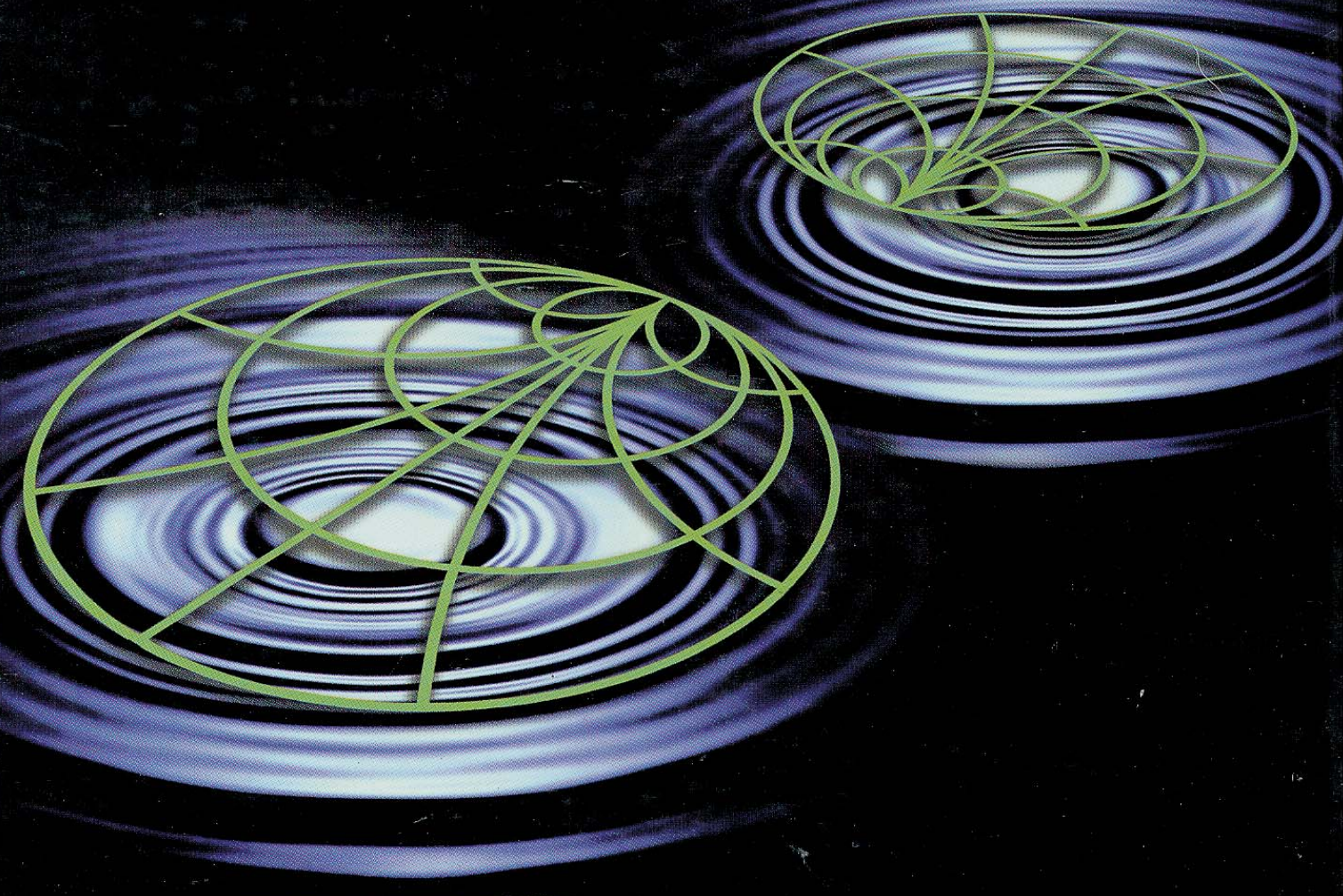


RF Circuit Design

Theory and Applications



Reinhold Ludwig ▶ Pavel Bretchko

RF Circuit Design

Theory and Applications

Reinhold Ludwig

Worcester Polytechnic Institute

Pavel Bretchko

Worcester Polytechnic Institute

Prentice Hall
Upper Saddle River, NJ 07458

Library of Congress Information Available

Publisher: **Tom Robbins**
Acquisitions editor: **Eric Frank**
Editor-in-chief: **Marcia Horton**
Marketing manager: **Danny Hoyt**
Production manager: **Rose Kernan**
Managing editor: **David George**
Executive managing editor: **Vince O'Brien**
Cover design: **Bruce Kenselaer**
Manufacturing coordinator: **Pat Brown**
Editorial assistant: **Jennie DiBlasi**

©2000 by Prentice-Hall, Inc.
Upper Saddle River, New Jersey 07458

All rights reserved. No part of this book may be reproduced, in any form
or by any means, without permission in writing from the publisher.

Printed in the United States of America

10 9 8 7 6 5 4 3 2 1

ISBN 0-13-095323-7

PRENTICE-HALL INTERNATIONAL (UK) LIMITED, *London*
PRENTICE-HALL OF AUSTRALIA PTY. LIMITED, *Sydney*
PRENTICE-HALL CANADA INC., *Toronto*
PRENTICE-HALL HISPANOAMERICANA, S.A., *Mexico*
PRENTICE-HALL OF INDIA PRIVATE LIMITED, *New Delhi*
PRENTICE-HALL OF JAPAN, INC., *Tokyo*
PRENTICE-HALL (SINGAPORE) PTE. LTD., *Singapore*
EDITORIA PRENTICE-HALL DO BRASIL, LTDA., *Rio de Janeiro*

DEDICATION

To our families and the memory of my father F. Ludwig

Preface

The field of high-frequency circuit design is receiving significant industrial attention due to a host of radio-frequency (RF) and microwave (MW) applications. Improved semiconductor devices have made possible a proliferation of high-speed digital and analog systems as observed in wireless communication, global positioning, RADAR, and related electrical and computer engineering disciplines. This interest has translated into a strong demand for engineers with comprehensive knowledge of high-frequency circuit design principles.

For the student, the professional engineer, and even the faculty member teaching this material there is, however, a general problem. The majority of existing textbooks appear to target two separate audiences: A) the advanced graduate-level population with a broad theoretical background, and B) the technologists with little interest in mathematical and physical rigor. As a result, RF circuit design has been presented in two very different formats. For the advanced students the entry into this field is often pursued through an electromagnetic field approach, while for the technologists the basic circuit aspect embedded in Kirchhoff's laws is the preferred treatment. Both approaches make it difficult to adequately address the theoretical and practical issues surrounding high-frequency design principles. The basic circuit approach lacks, or only superficially covers, the wave nature of currents and voltages whose reflection and transmission properties constitute indispensable ingredients of the RF circuit behavior. The electromagnetic field approach certainly covers the wave guide and transmission line aspect, but falls far short of reaching the important aspects of designing high-frequency amplifier, oscillator, and mixer circuits.

The objective of this textbook is to develop the RF circuit design aspects in such a way that the need for transmission line principles is made clear without adopting an electromagnetic field approach. Therefore, no EM background is necessary beyond a first year undergraduate physics course in fields and waves as provided by most colleges and universities. Students equipped with the knowledge of basic circuit theory and/or an exposure to microelectronics can use this book and cover the entire spectrum from the basic principles of transmission and microstrip lines to the various high-frequency circuit design procedures. Lengthy mathematical derivations are either relegated to the appendices or placed in examples, separated from the main text. This allows the omission of some of the dry theoretical details and thus focuses on the main concepts.

Accepting the challenge of providing a high degree of design experience, we have included many examples that discuss in considerable detail, in many cases extending over several pages, the philosophy and the intricacies of the various design approaches.

This has caused some problems as well, specifically with respect to the circuit simulations. Obviously, we cannot expect the reader to have ready access to modern computer simulation tools such as MMICAD or ADS to name but two of the popular choices. Professional high-frequency simulation packages are generally expensive and require familiarity to use them effectively. For this reason we have created a considerable number of MATLAB M-files that the interested student can download from our website listed in Appendix G. Since MATLAB is a widely used relatively inexpensive mathematical tool, many examples discussed in this book can be executed and the results graphically displayed in a matter of seconds. Specifically the various Smith-Chart computations of the impedance transformations should appeal to the reader. Nonetheless, all design examples, specifically the ones presented in Chapters 8 to 10, have been independently simulated and verified in MMICAD for the linear circuit models, and ADS for the non-linear oscillator and mixer models.

In terms of material coverage, this textbook purposely omitted the high-speed digital circuits as well as coding and modulation aspects. Although important, these topics would simply have required too many additional pages and would have moved the book too far away from its original intent of providing a fundamental, one- or two-semester, introduction to RF circuit design. At WPI this does not turn out to be a disadvantage, since most of the material can readily be acquired in available communication systems engineering courses.

The organization of this text is as follows: **Chapter 1** presents a general explanation of why basic circuit theory breaks down as the operating frequency is increased to a level where the wavelength becomes comparable with the discrete circuit components. In **Chapter 2** the transmission line theory is developed as a way to replace the low-frequency circuit models. Because of the voltage and current wave nature, **Chapter 3** introduces the Smith Chart as a generic tool to deal with the impedance behavior on the basis of the reflection coefficient. **Chapter 4** discusses two-port networks with their flow-chart representations and how they can be described on the basis of the so-called scattering parameters. These network models and their scattering parameter descriptions are utilized in **Chapter 5** to develop passive RF filter configurations. Before covering active devices, **Chapter 6** provides a review of some of the key semiconductor fundamentals, followed by their circuit models representation in **Chapter 7**. The impedance matching and biasing of bipolar and field effect transistors is taken up in **Chapter 8** in an effort to eliminate potentially dangerous reflections and to provide optimal power flow. **Chapter 9** focuses on a number of key high-frequency amplifier configurations and their design intricacies ranging from low noise to high power applications. Finally, **Chapter 10** introduces the reader to nonlinear systems and their designs in oscillator and mixer circuits.

This book is used in the Electrical and Computer Engineering Department at WPI as required text for the standard 7-week (5 lecture hours per week) course in RF circuit design (EE 3113, Introduction to RF Circuit Design). The course has primarily attracted an audience of 3rd and 4th year undergraduate students with a background in microelectronics. The course does not include a laboratory, although six videotapes of practical circuit performances conducted at *Philips Semiconductors* and in-class RF circuit measurements with a network analyzer are included. In addition, MMICAD and ADS simulations are incorporated as part of the regular lectures. Each chapter is fairly self-contained, with the goal of providing wide flexibility in organizing the course material. At WPI the content of approximately one three semester hour course is compressed into a 7-week period (consisting of a total of 25–28 lectures). The topics covered are shown in the table below.

EE 3113, Introduction to RF Circuit Design

| | |
|---|-------------------|
| Chapter 1, Introduction | Sections 1.1–1.6 |
| Chapter 2, Transmission Line Analysis | Sections 2.1–2.12 |
| Chapter 3, Smith Chart | Sections 3.1–3.5 |
| Chapter 4, Single- and Multi-Port Networks | Sections 4.1–4.5 |
| Chapter 7, Active RF Component Modeling | Sections 7.1–7.2 |
| Chapter 8, Matching and Biasing Networks | Sections 8.1–8.4 |
| Chapter 9, RF Transistor Amplifier Designs | Sections 9.1–9.4 |

The remaining material is targeted for a second (7-week) term covering more advanced topics such as microwave filters, equivalent circuit models, oscillators and mixers. An organizational plan is provided below.

Advanced Principles of RF Circuit Design

| | |
|--|--------------------|
| Chapter 5, A Brief Overview of RF Filter Design | Sections 5.1–5.5 |
| Chapter 6, Active RF Components | Sections 6.1–6.6 |
| Chapter 7, Active RF Component Modeling | Sections 7.3–7.5 |
| Chapter 9, RF Transistor Amplifier Designs | Sections 9.5–9.8 |
| Chapter 10, Oscillators and Mixers | Sections 10.1–10.4 |

However, the entire course organization will always remain subject to change depending on total classroom time, student background, and interface requirements with related courses.

Please refer to the companion website at <http://www.prenhall.com/ludwig> for more material including all of the art files in this text in pdf format.

ACKNOWLEDGEMENTS

The authors are grateful to a number of colleagues, students, and practicing engineers. Prof. John Orr, head of the ECE department, WPI, was instrumental in introducing this course and he provided the funding for the RF simulation packages. Our thanks go to Korne Vennema, Jarek Lucek, and Scott Blum of Philips Semiconductors for providing technical expertise, sponsoring senior student projects, and making available measurement equipment. Profs. John Sullivan, Jr., William Michalson, and Sergey Makarov assisted through extensive technical help. Linda Gu, Qiang Lai, Joe Plunkett, Dr. Funan Shi, Gene Bogdanov, Minhua Liu, and Josh Resnik are current and former graduate students who provided much needed ambience and support in the EM and RF lab at WPI. R. L. is particularly thankful to Prof. J. Thomas Vaughan of the University of Minnesota's MRI Center who introduced him to the importance of transmission line principles in the design of RF coils for high-field magnetic resonance imaging. P.B. would like to express his sincere thanks to Mikhail Shirokov of Lehigh University for helpful discussions on all aspects of RF/MW circuits and devices. The staff of Prentice-Hall, specifically Eric Frank, Tom Robbins, and Rose Kerman are thanked for their insight and support in making this book a reality.

Donation of the MIMICAD RF simulation design package by Optotek and a university license of ADS provided by Hewlett-Packard Corporation are gratefully acknowledged.

Contents

| | |
|---|-----------|
| Preface | v |
| Chapter 1. Introduction | 1 |
| 1.1 Importance of Radiofrequency Design | 2 |
| 1.2 Dimensions and Units | 6 |
| 1.3 Frequency Spectrum | 8 |
| 1.4 RF Behavior of Passive Components | 10 |
| 1.4.1 High-Frequency Resistors | 14 |
| 1.4.2 High-Frequency Capacitors | 17 |
| 1.4.3 High-Frequency Inductors | 21 |
| 1.5 Chip Components and Circuit Board Considerations | 24 |
| 1.5.1 Chip Resistors | 24 |
| 1.5.2 Chip Capacitors | 25 |
| 1.5.3 Surface-Mounted Inductors | 26 |
| 1.6 Summary | 28 |
| Chapter 2. Transmission Line Analysis | 37 |
| 2.1 Why Transmission Line Theory? | 37 |
| 2.2 Examples of Transmission Lines | 41 |
| 2.2.1 Two-Wire Lines | 41 |
| 2.2.2 Coaxial Line | 42 |
| 2.2.3 Microstrip Lines | 42 |
| 2.3 Equivalent Circuit Representation | 45 |
| 2.4 Theoretical Foundation | 47 |
| 2.4.1 Basic Laws | 47 |
| 2.5 Circuit Parameters for a Parallel Plate Transmission Line | 53 |
| 2.6 Summary of Different Line Configurations | 57 |
| 2.7 General Transmission Line Equation | 58 |
| 2.7.1 Kirchhoff Voltage and Current Law Representations | 58 |
| 2.7.2 Traveling Voltage and Current Waves | 62 |
| 2.7.3 General Impedance Definition | 63 |
| 2.7.4 Lossless Transmission Line Model | 64 |
| 2.8 Microstrip Transmission Lines | 64 |
| 2.9 Terminated Lossless Transmission Line | 69 |
| 2.9.1 Voltage Reflection Coefficient | 69 |
| 2.9.2 Propagation Constant and Phase Velocity | 71 |
| 2.9.3 Standing Waves | 72 |
| 2.10 Special Termination Conditions | 75 |
| 2.10.1 Input Impedance of Terminated Lossless Line | 75 |

| | | |
|--|---|------------|
| 2.10.2 | Short Circuit Transmission Line | 76 |
| 2.10.3 | Open-Circuit Transmission Line | 79 |
| 2.10.4 | Quarter-Wave Transmission Line | 81 |
| 2.11 | Sourced and Loaded Transmission Line | 84 |
| 2.11.1 | Phasor Representation of Source | 85 |
| 2.11.2 | Power Considerations for a Transmission Line | 87 |
| 2.11.3 | Input Impedance Matching | 90 |
| 2.11.4 | Return Loss and Insertion Loss | 91 |
| 2.12 | Summary | 93 |
| Chapter 3. The Smith Chart | | 101 |
| 3.1 | From Reflection Coefficient to Load Impedance | 102 |
| 3.1.1 | Reflection Coefficient in Phasor Form | 102 |
| 3.1.2 | Normalized Impedance Equation | 104 |
| 3.1.3 | Parametric Reflection Coefficient Equation | 106 |
| 3.1.4 | Graphical Representation | 108 |
| 3.2 | Impedance Transformation | 110 |
| 3.2.1 | Impedance Transformation for General Load | 110 |
| 3.2.2 | Standing Wave Ratio | 113 |
| 3.2.3 | Special Transformation Conditions | 115 |
| 3.2.4 | Computer Simulations | 119 |
| 3.3 | Admittance Transformation | 122 |
| 3.3.1 | Parametric Admittance Equation | 122 |
| 3.3.2 | Additional Graphical Displays | 125 |
| 3.4 | Parallel and Series Connections | 126 |
| 3.4.1 | Parallel Connection of R and L Elements | 127 |
| 3.4.2 | Parallel Connection of R and C Elements | 128 |
| 3.4.3 | Series Connection of R and L Elements | 128 |
| 3.4.4 | Series Connection of R and C Elements | 129 |
| 3.4.5 | Example of a T-Network | 130 |
| 3.5 | Summary | 133 |
| Chapter 4. Single- and Multiport Networks | | 143 |
| 4.1 | Basic Definitions | 144 |
| 4.2 | Interconnecting Networks | 153 |
| 4.2.1 | Series Connection of Networks | 153 |
| 4.2.2 | Parallel Connection of Networks | 154 |
| 4.2.3 | Cascading Networks | 155 |
| 4.2.4 | Summary of ABCD Network Representations | 156 |
| 4.3 | Network Properties and Applications | 161 |
| 4.3.1 | Interrelations between Parameter Sets | 161 |
| 4.3.2 | Analysis of Microwave Amplifier | 164 |
| 4.4 | Scattering Parameters | 168 |
| 4.4.1 | Definition of Scattering Parameters | 168 |

| | | |
|---|---|------------|
| 4.4.2 | Meaning of S-Parameters | 171 |
| 4.4.3 | Chain Scattering Matrix | 175 |
| 4.4.4 | Conversion between Z- and S-Parameters | 177 |
| 4.4.5 | Signal Flow Chart Modeling | 178 |
| 4.4.6 | Generalization of S-Parameters | 184 |
| 4.4.7 | Practical Measurements of S-Parameters | 188 |
| 4.5 | Summary | 194 |
| Chapter 5. An Overview of RF Filter Design | | 201 |
| 5.1 | Basic Resonator and Filter Configurations | 202 |
| 5.1.1 | Filter Types and Parameters | 202 |
| 5.1.2 | Low-Pass Filter | 206 |
| 5.1.3 | High-Pass Filter | 209 |
| 5.1.4 | Bandpass and Bandstop Filters | 210 |
| 5.1.5 | Insertion Loss | 217 |
| 5.2 | Special Filter Realizations | 220 |
| 5.2.1 | Butterworth-Type Filters | 221 |
| 5.2.2 | Chebyshev-Type Filters | 224 |
| 5.2.3 | Denormalization of Standard Low-Pass Design | 231 |
| 5.3 | Filter Implementation | 241 |
| 5.3.1 | Unit Elements | 243 |
| 5.3.2 | Kuroda's Identities | 243 |
| 5.3.3 | Examples of Microstrip Filter Design | 245 |
| 5.4 | Coupled Filter | 253 |
| 5.4.1 | Odd and Even Mode Excitation | 254 |
| 5.4.2 | Bandpass Filter Section | 257 |
| 5.4.3 | Cascading bandpass filter elements | 258 |
| 5.4.4 | Design Example | 260 |
| 5.5 | Summary | 263 |
| Chapter 6. Active RF Components | | 271 |
| 6.1 | Semiconductor Basics | 272 |
| 6.1.1 | Physical Properties of Semiconductors | 272 |
| 6.1.2 | PN-Junction | 279 |
| 6.1.3 | Schottky Contact | 289 |
| 6.2 | RF Diodes | 293 |
| 6.2.1 | Schottky Diode | 293 |
| 6.2.2 | PIN Diode | 296 |
| 6.2.3 | Varactor Diode | 302 |
| 6.2.4 | IMPATT Diode | 305 |
| 6.2.5 | Tunnel Diode | 307 |
| 6.2.6 | TRAPATT, BARRITT, and Gunn Diodes | 311 |
| 6.3 | Bipolar-Junction Transistor | 312 |
| 6.3.1 | Construction | 312 |

| | | |
|---|---|------------|
| 6.3.2 | Functionality | 314 |
| 6.3.3 | Frequency Response | 321 |
| 6.3.4 | Temperature Behavior | 323 |
| 6.3.5 | Limiting Values | 327 |
| 6.4 | RF Field Effect Transistors | 328 |
| 6.4.1 | Construction | 329 |
| 6.4.2 | Functionality | 331 |
| 6.4.3 | Frequency Response | 337 |
| 6.4.4 | Limiting Values | 337 |
| 6.5 | High Electron Mobility Transistors | 338 |
| 6.5.1 | Construction | 339 |
| 6.5.2 | Functionality | 339 |
| 6.5.3 | Frequency Response | 343 |
| 6.6 | Summary | 343 |
| Chapter 7. Active RF Component Modeling | | 351 |
| 7.1 | Diode Models | 352 |
| 7.1.1 | Nonlinear Diode Model | 352 |
| 7.1.2 | Linear Diode Model | 354 |
| 7.2 | Transistor Models | 357 |
| 7.2.1 | Large-Signal BJT Models | 357 |
| 7.2.2 | Small-Signal BJT Models | 366 |
| 7.2.3 | Large-Signal FET Models | 378 |
| 7.2.4 | Small-Signal FET Models | 382 |
| 7.3 | Measurement of Active Devices | 385 |
| 7.3.1 | DC Characterization of Bipolar Transistor | 385 |
| 7.3.2 | Measurements of AC Parameters of Bipolar Transistors | 387 |
| 7.3.3 | Measurements of Field Effect Transistor Parameters | 392 |
| 7.4 | Scattering Parameter Device Characterization | 393 |
| 7.5 | Summary | 397 |
| Chapter 8. Matching and Biasing Networks | | 405 |
| 8.1 | Impedance Matching Using Discrete Components | 406 |
| 8.1.1 | Two-Component Matching Networks | 406 |
| 8.1.2 | Forbidden Regions, Frequency Response, and Quality Factor | 415 |
| 8.1.3 | T and Pi Matching Networks | 426 |
| 8.2 | Microstrip Line Matching Networks | 431 |
| 8.2.1 | From Discrete Components to Microstrip Lines | 431 |
| 8.2.2 | Single-Stub Matching Networks | 435 |
| 8.2.3 | Double-Stub Matching Networks | 440 |
| 8.3 | Amplifier Classes of Operation and Biasing Networks | 444 |
| 8.3.1 | Classes of Operation and Efficiency of Amplifiers | 444 |
| 8.3.2 | Bipolar Transistor Biasing Networks | 449 |
| 8.3.3 | Field Effect Transistor Biasing Networks | 455 |

| | | |
|---|--|------------|
| 8.4 | Summary | 456 |
| Chapter 9. RF Transistor Amplifier Designs | | 463 |
| 9.1 | Characteristics of Amplifiers | 464 |
| 9.2 | Amplifier Power Relations | 465 |
| 9.2.1 | RF Source | 465 |
| 9.2.2 | Transducer Power Gain | 466 |
| 9.2.3 | Additional Power Relations | 468 |
| 9.3 | Stability Considerations | 470 |
| 9.3.1 | Stability Circles | 470 |
| 9.3.2 | Unconditional Stability | 473 |
| 9.3.3 | Stabilization Methods | 480 |
| 9.4 | Constant Gain | 483 |
| 9.4.1 | Unilateral Design | 483 |
| 9.4.2 | Unilateral Figure of Merit | 490 |
| 9.4.3 | Bilateral Design | 492 |
| 9.4.4 | Operating and Available Power Gain Circles | 495 |
| 9.5 | Noise Figure Circles | 502 |
| 9.6 | Constant VSWR Circles | 506 |
| 9.7 | Broadband, High-Power, and Multistage Amplifiers | 511 |
| 9.7.1 | Broadband Amplifiers | 511 |
| 9.7.2 | High-Power Amplifiers | 522 |
| 9.7.3 | Multistage Amplifiers | 526 |
| 9.8 | Summary | 529 |
| Chapter 10. Oscillators and Mixers | | 539 |
| 10.1 | Basic Oscillator Model | 540 |
| 10.1.1 | Negative Resistance Oscillator | 541 |
| 10.1.2 | Feedback Oscillator Design | 543 |
| 10.1.3 | Design Steps | 546 |
| 10.1.4 | Quartz Oscillators | 550 |
| 10.2 | High-Frequency Oscillator Configuration | 552 |
| 10.2.1 | Fixed-Frequency Oscillators | 556 |
| 10.2.2 | Dielectric Resonator Oscillators | 563 |
| 10.2.3 | YIG-Tuned Oscillator | 569 |
| 10.2.4 | Voltage-Controlled Oscillator | 570 |
| 10.2.5 | Gunn Element Oscillator | 573 |
| 10.3 | Basic Characteristics of Mixers | 574 |
| 10.3.1 | Basic Concepts | 575 |
| 10.3.2 | Frequency Domain Considerations | 578 |
| 10.3.3 | Single-Ended Mixer Design | 580 |
| 10.3.4 | Single-Balanced Mixer | 588 |
| 10.3.5 | Double-Balanced Mixer | 590 |
| 10.4 | Summary | 590 |

| | |
|--|------------|
| Appendix A. Useful Physical Quantities and Units | 597 |
| Appendix B. Skin Equation for a Cylindrical Conductor | 601 |
| Appendix C. Complex Numbers | 603 |
| C.1 Basic Definition | 603 |
| C.2 Magnitude Computations | 603 |
| C.3 Circle Equation | 604 |
| Appendix D. Matrix Conversions | 605 |
| Appendix E. Physical Parameters of Semiconductors | 608 |
| Appendix F. Long and Short Diode Models | 609 |
| F.1 Long Diode | 610 |
| F.2 Short Diode | 610 |
| Appendix G. Couplers | 612 |
| G.1 Wilkinson Divider | 612 |
| G.2 Branch Line Coupler | 616 |
| G.3 Lange Coupler | 619 |
| Appendix H. Noise Analysis | 620 |
| H.1 Basic Definitions | 620 |
| H.2 Noisy Two-Port Networks | 623 |
| H.3 Noise Figure for Two-Port Network | 625 |
| H.4 Noise Figure for Cascaded Multiport Network | 629 |
| Appendix I. Introduction to MATLAB | 631 |
| I.1 Background | 631 |
| I.2 Brief Example of Stability Evaluation | 633 |
| I.3 Simulation Software on Compact Disk | 635 |
| I.3.1 Overview | 635 |
| I.3.2 Software Installation | 635 |
| I.3.3 File Organization | 636 |
| Index | 637 |

Introduction

It is common knowledge that both analog and digital design engineers are continually developing and refining circuits for increasingly higher operational frequencies. Analog circuits for wireless communication in the gigahertz (GHz) range and the ever-increasing clock speeds of computer circuits in high-performance mainframes, workstations, and, of course, personal computers exemplify this trend. Global positioning systems require carrier frequencies in the range of 1227.60 and 1575.42 MHz. The low-noise amplifier in a personal communication system may operate at 1.9 GHz and fit on a circuit board smaller in size than a dime. Satellite broadcasting in the C band involves 4 GHz uplink and 6 GHz downlink systems. In general, due to the rapid expansion of wireless communication, more compact amplifier, filter, oscillator, and mixer circuits are being designed and placed in service at frequencies generally above 1 GHz. There is little doubt that this trend will continue unabated, resulting not only in engineering systems with unique capabilities, but also special design challenges not encountered in conventional low-frequency systems.

This chapter reviews the evolution from low- to high-frequency circuit operations. It motivates and provides the physical rationales that have prompted the need for new engineering approaches to design and optimize these circuits. The example of a cellular phone circuit, components of which will be analyzed in more detail in later chapters, serves as a vehicle to outline the goals and objectives of this textbook and its organization.

The chapter begins with a brief historical discussion explaining the transition from direct current (DC) to high-frequency modes of operation. As the frequency increases and the associated wavelengths of the electromagnetic waves becomes comparable to the dimensions of the discrete circuit components such as resistors, capacitors, and inductors, these components start to deviate in their electric responses from the ideal frequency behavior. It is the purpose of this chapter to provide the reader with an appre-

ciation and understanding of high-frequency passive component characteristics. In particular, due to the availability of sophisticated measurement equipment, the design engineer must know exactly why and how the high-frequency behavior of his or her circuit differs from the low-frequency realization. Without this knowledge it will be impossible to develop and understand the special requirements of high-performance systems.

1.1 Importance of Radiofrequency Design

The beginning of electrical circuit design is most likely traced back to the late eighteenth and early nineteenth centuries when the first reliable batteries became available. Named after their inventor A. Volta (1745–1827), the Voltaic cells permitted the supply of reliable DC energy to power the first crude circuits. However, it soon became apparent that low-frequency alternating current (AC) power sources can transport electricity more efficiently and with less electric losses when transmitted over some distance and that rerouting the electric energy could be facilitated through transformers that operate in accordance with Faraday's induction law. Due to pioneering work by such eminent engineers as Charles Steinmetz, Thomas Edison, Werner Siemens, and Nikolas Tesla, the power generation and distribution industry quickly gained entry into our everyday life. It was James Maxwell (1831–1879) who, in a paper first read in 1864 to the Royal Society in London, postulated the coupling of the electric and magnetic fields whose linkage through space gives rise to wave propagation. In 1887 Heinrich Hertz experimentally proved the radiation and reception of electromagnetic energy through air. This discovery heralded the rapidly expanding field of wireless communication, from radio and TV transmissions in the 1920s and 1930s to cellular phones and Global Positioning Systems (GPS) in the 1980s and 1990s. Unfortunately, the design and development of suitable high-frequency circuits for today's wireless communication applications is not so straightforward. As will be discussed in detail, conventional Kirchhoff-type voltage and current law analysis tools, as presented to first- and second-year undergraduate electrical engineering students, apply strictly only to DC and low-frequency lumped parameter systems consisting of networks of resistors, capacitors, and inductors. They fail when applied to circuits governed by electromagnetic wave propagation.

The main purpose of this textbook is to provide the reader with theoretical and practical aspects of analog circuit design when the frequency of operation extends into the **radio frequency (RF)** and **microwave (MW)** domains. Here conventional circuit analysis principles fail. The following questions arise:

- At what upper frequency does conventional circuit analysis become inappropriate?

- What characteristics make the high-frequency behavior of electric components so different from their low-frequency behavior?
- What “new” circuit theory has to be employed?
- How is this theory applied to the practical design of high-frequency analog circuits?

This book intends to provide comprehensive answers to these questions by developing not only the theoretical framework but also delivering the practical applications through a host of examples and design projects.

To identify more clearly the issues that we will address, let us examine the generic RF system shown in Figure 1-1.

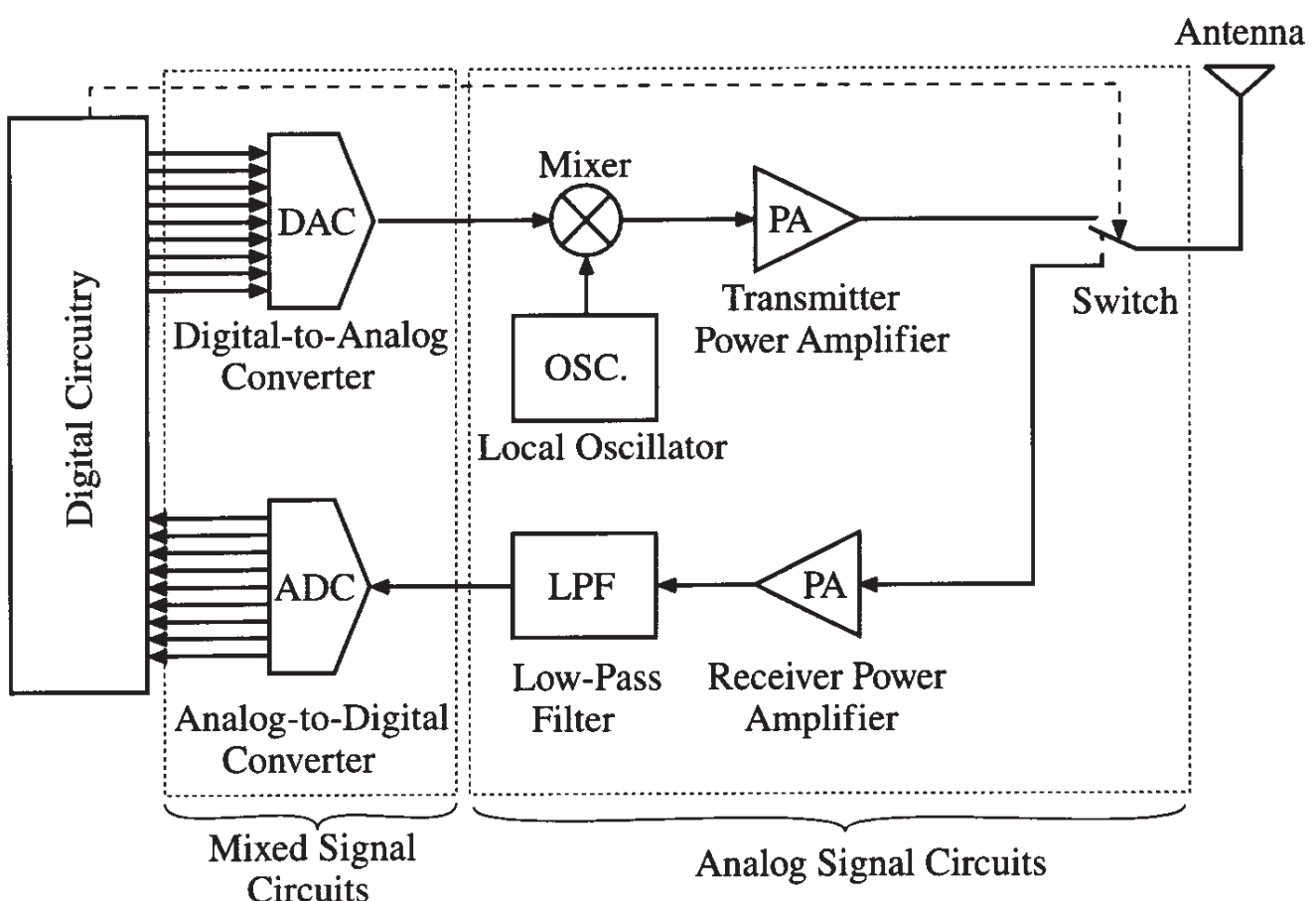


Figure 1-1 Block diagram of a generic RF system.

Typical applications of this configuration are **cellular phones** and **wireless local area networks (WLANs)**. The entire block diagram in Figure 1-1 can be called a **transceiver**, since it incorporates both transmitter and receiver circuits and uses a single antenna for communication. In this configuration the input signal (either a voice or a digital signal from a computer) is first digitally processed. If the input signal is a voice signal, as is the case in cellular phones, it is first converted into digital form; then compressed to reduce the time of transmission; and finally appropriately coded to suppress noise and communication errors.

After the input signal has been digitally preprocessed, it is converted back to analog form via a **digital-to-analog converter** (DAC). This low-frequency signal is mixed with a high-frequency carrier signal provided by a local oscillator. The combined signal is subsequently amplified through a **power amplifier** (PA) and then routed to the antenna, whose task is to radiate the encoded information as electromagnetic waves into free space.

In the block diagram of Figure 1-1 let us focus on the transmitter PA. This could be a 2 GHz PA for cellular phones that may be implemented as a dual-stage amplifier. Details of the circuit diagram for the first stage PA are shown in Figure 1-2(a).

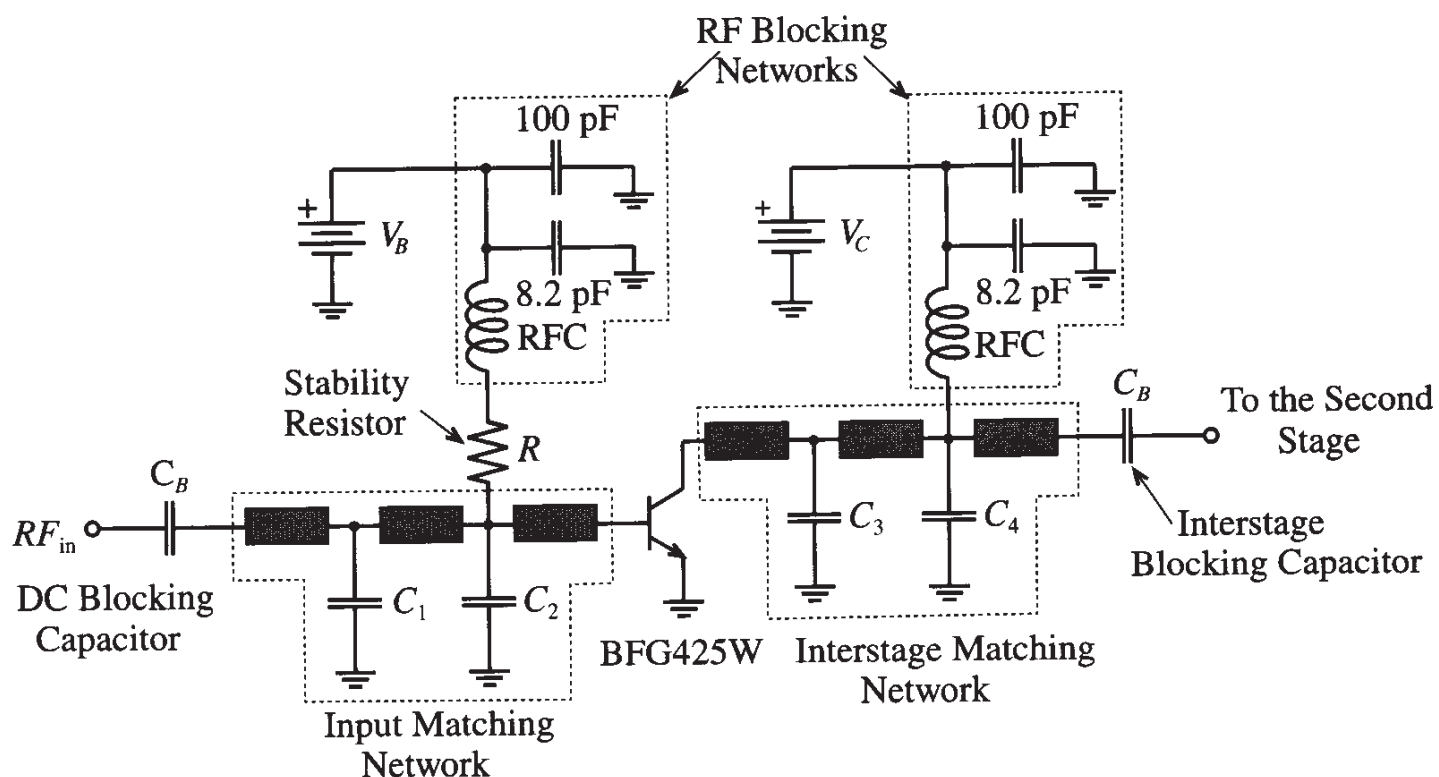


Figure 1-2(a) Simplified circuit diagram of the first stage of a 2 GHz power amplifier for a cellular phone.

We notice that the input signal is fed through a DC blocking capacitor into an **input matching network**, needed to match the input impedance of the transistor (type BFG425W of Philips Semiconductors), operated in common emitter configuration, to the output impedance of the mixer that precedes the PA. The matching is needed to ensure optimal power transfer as well as to eliminate performance degrading reflections. The **interstage matching network** must then match the output impedance of the transistor to the input impedance of the second stage of the PA. Key components in the matching networks are microstrip lines shown by the shaded rectangles in Figure 1-2(a). At high frequency these distributed elements exhibit unique electric properties that differ significantly from low-frequency lumped circuit elements. We also notice

additional networks to bias the input and output ports of the transistor. The separation of high-frequency signals from the DC bias conditions is achieved through two RF blocking networks that feature so-called **radio frequency coils** (RFCs).

The actual dual-stage circuit board implementation is given in Figure 1-2(b), which shows the microstrip lines as copper traces of specific lengths and widths. Attached to the microstrip lines are chip capacitors, resistors, and inductors.

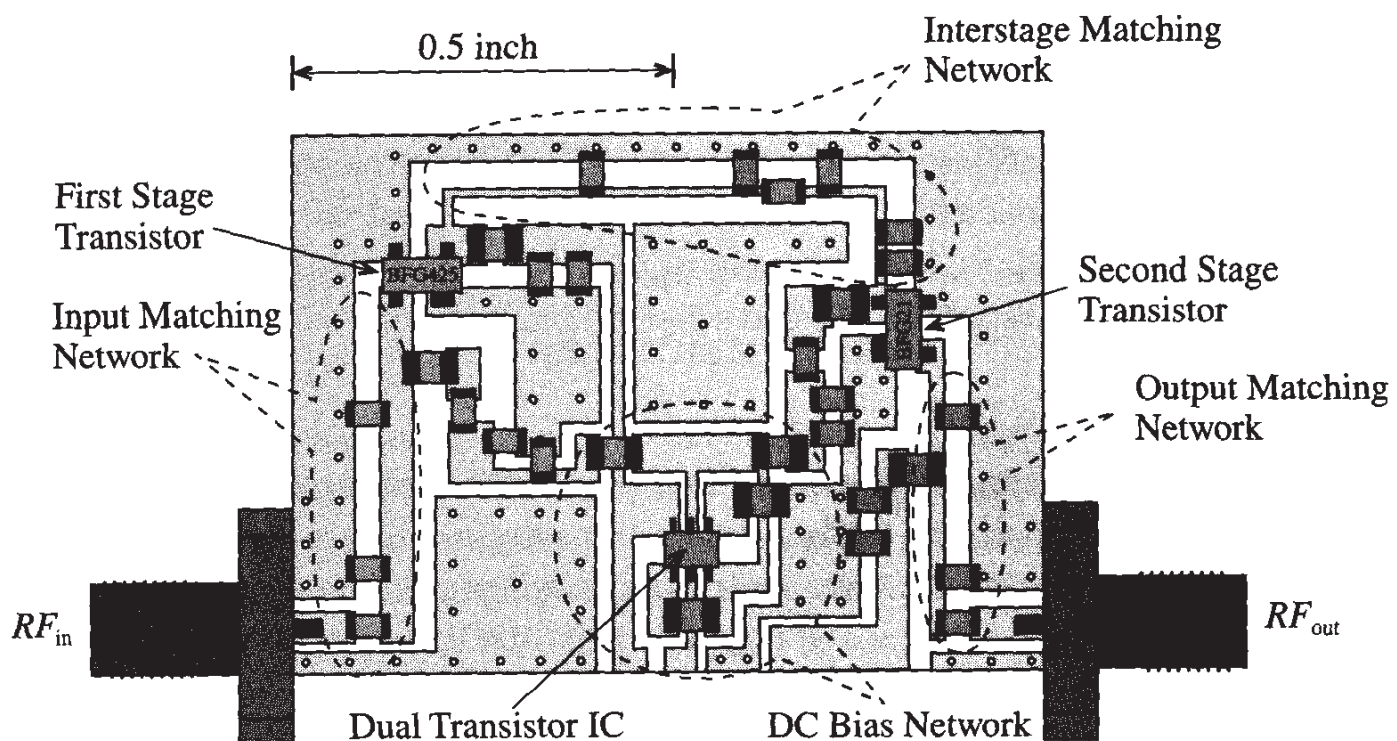


Figure 1-2(b) Printed circuit board layout of the power amplifier.

To understand, analyze, and ultimately build such a PA circuit requires knowledge of a number of crucial RF topics discussed in this textbook:

- Microstrip line impedance behavior is discussed in “Transmission Line Analysis” (Chapter 2) and its quantitative evaluation is considered in Chapter 3, “The Smith Chart.”
- The ability to reduce a complicated circuit into simpler constituents whose input-output is described through two-port network description. This is discussed in Chapter 4, “Single- and Multiport Networks.”
- Strategies of generically developing particular impedance versus frequency responses as encountered in filter design. Chapter 5, “A Brief Overview of RF Filter Design,” outlines the basic discrete and distributed filter theories, and Chapter 8, “Matching Networks,” delves into a detailed circuit implementation as related to Figure 1-2(b).

- High-frequency bipolar junction and field effect transistors as well as RF diodes are investigated in “Active RF Components” (Chapter 6) in terms of their physical basis followed by “Active Circuit Device Models” (Chapter 7), where large signal and small signal circuit models are analyzed.
- The overall amplification requirements, as related to gain, linearity, noise, and stability, are basis of “RF Transistor Amplifier Design” (Chapter 9).
- In addition to amplifiers, Chapter 10, “Oscillators and Mixers,” focuses on additional important RF circuit design concepts, as shown in Figure 1-1.

A successful RF design engineer knows about and applies all these concepts in the design, construction, and testing of a particular RF circuit project. As the preceding example implies, our concern in this textbook is mostly geared toward analog RF circuit theory and applications. We purposely neglect mixed and digital RF signals since their treatment would exceed the size and scope of this textbook.

1.2 Dimensions and Units

To understand the upper frequency limit, beyond which conventional circuit theory can no longer be applied to analyze an electric system, we should recall the representation of an electromagnetic wave. In free space, plane electromagnetic (EM) wave propagation in the positive z -direction is typically written in sinusoidal form:

$$E_x = E_{0x} \cos(\omega t - \beta z) \quad (1.1a)$$

$$H_y = H_{0y} \cos(\omega t - \beta z) \quad (1.1b)$$

where E_x and H_y are the x -directed electric and the y -directed magnetic field vector components, as shown qualitatively in Figure 1-3. Here E_{0x} and H_{0y} represent constant amplitude factors in units of V/m and A/m .

These waves possess an angular frequency ω , and a propagation constant β that defines the spatial extent in terms of the **wavelength** λ , such that $\beta = 2\pi/\lambda$. Classical field theory based on Maxwell's equations reveals that the ratio between electric and magnetic field components is defined in terms of the so-called **intrinsic impedance** Z_0

$$\frac{E_x}{H_y} = Z_0 = \sqrt{\mu/\epsilon} = \sqrt{(\mu_0\mu_r)/(\epsilon_0\epsilon_r)} = 377 \Omega \sqrt{\mu_r/\epsilon_r} \quad (1.2)$$

based on the material dependent permeability $\mu = \mu_0\mu_r$ and permittivity $\epsilon = \epsilon_0\epsilon_r$, with μ_0 and ϵ_0 being absolute permeability and permittivity of free space and μ_r and ϵ_r denoting relative values. We also point out that the field components are orthogonal to each other and both are orthogonal to the direction of propagation. This is known as **transverse electromagnetic mode (TEM)** and, since we deal exclusively with RF, it is

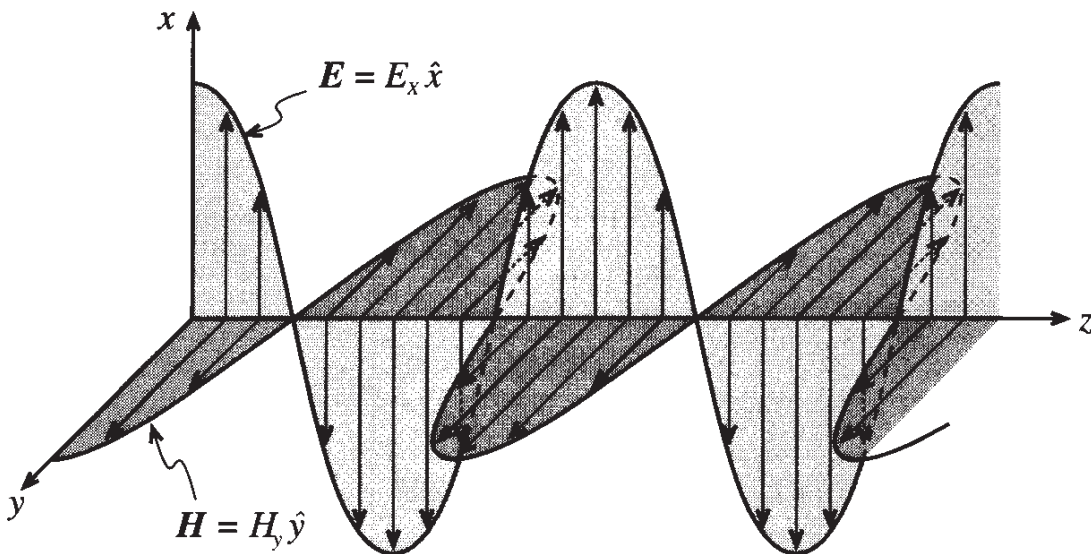


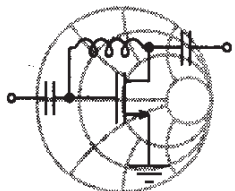
Figure 1-3 Electromagnetic wave propagation in free space. The electric and magnetic fields are recorded at a fixed instance in time as a function of space (\hat{x} , \hat{y} are unit vectors in x - and y -direction).

the only mode that is considered in this text. TEM wave propagation is in stark contrast to the various **transverse electric** (TE) and **transverse magnetic** (TM) wave modes, which are the underlying principles of MW and optical communication. In these cases the field vectors are no longer perpendicular to the direction of propagation.

The phase velocity v_p of the TEM wave can be found via

$$v_p = \frac{\omega}{\beta} = \frac{1}{\sqrt{\epsilon\mu}} \quad (1.3)$$

Relevant quantities, units and symbols used throughout the book are summarized in Tables A-1 and A-2 in Appendix A. Although we are dealing here with rather abstract concepts of electromagnetic wave quantities, we can immediately relate (1.1) to circuit parameters by observing that the electric field, as the unit of V/m already implies, can intuitively be understood as a normalized voltage wave. Similarly, the magnetic field, given in units of A/m, is a normalized current wave.



RF & MW →

Example 1-1: Intrinsic wave impedance, phase velocity, and wavelengths

Compute the intrinsic wave impedance, phase velocity, and wavelengths of an electromagnetic wave in free space for the frequencies $f = 30 \text{ MHz}$, 300 MHz , 30 GHz .

Solution: Relative permeability and permittivity of free space are equal to unity. Therefore, from (1.2) we determine that intrinsic impedance in this case is equal to

$$Z_0 = \sqrt{\frac{\mu}{\epsilon}} = \sqrt{\frac{\mu_0}{\epsilon_0}} = \sqrt{\frac{4\pi \times 10^{-7}}{8.85 \times 10^{-12}}} = 377 \Omega$$

The phase velocity according to (1.3) is equal to

$$v_p = \frac{1}{\sqrt{\epsilon\mu}} = \frac{1}{\sqrt{\epsilon_0\mu_0}} = 2.999 \times 10^8 \text{ m/s}$$

which happens to be the speed of light $v_p = c$. The wavelength is evaluated by the following expression:

$$\lambda = \frac{2\pi}{\beta} = \frac{2\pi v_p}{\omega} = \frac{v_p}{f} \quad (1.4)$$

where f is the operating frequency. Using equation (1.4), we find that the wavelength for an electromagnetic wave propagating in free space at a frequency of 30 MHz is equal to $\lambda = 10$ m; at 300 MHz it is already reduced to $\lambda = 1$ m; and at 30 GHz the wavelength is a minute $\lambda = 1$ cm.

This example conveys an appreciation of how the wavelength changes as a function of frequency. As the frequency increases, the wavelength reduces to dimensions comparable to the size of circuit boards or even individual discrete components. The implication of this fact will be analyzed in Chapter 2.

1.3 Frequency Spectrum

Because of the vast scope of applications, engineers have to deal with a broad range of frequencies of circuit operation. Over the years several attempts have been made to classify the frequency spectrum. The first designations for industrial and government organizations were introduced in the United States by the Department of Defense during and shortly after World War II. However, the most common frequency spectrum classification in use today was created by the Institute of Electrical and Electronic Engineers (IEEE) and is listed in Table 1-1.

Table 1-1 IEEE Frequency Spectrum

| Frequency Band | Frequency | Wavelength |
|------------------------------|--------------|----------------|
| ELF (Extreme Low Frequency) | 30–300 Hz | 10,000–1000 km |
| VF (Voice Frequency) | 300–3000 Hz | 1000–100 km |
| VLF (Very Low Frequency) | 3–30 kHz | 100–10 km |
| LF (Low Frequency) | 30–300 kHz | 10–1 km |
| MF (Medium Frequency) | 300–3000 kHz | 1–0.1 km |
| HF (High Frequency) | 3–30 MHz | 100–10 m |
| VHF (Very High Frequency) | 30–300 MHz | 10–1 m |
| UHF (Ultrahigh Frequency) | 300–3000 MHz | 100–10 cm |
| SHF (Superhigh Frequency) | 3–30 GHz | 10–1 cm |
| EHF (Extreme High Frequency) | 30–300 GHz | 1–0.1 cm |
| Decimillimeter | 300–3000 GHz | 1–0.1 mm |
| P Band | 0.23–1 GHz | 130–30 cm |
| L Band | 1–2 GHz | 30–15 cm |
| S Band | 2–4 GHz | 15–7.5 cm |
| C Band | 4–8 GHz | 7.5–3.75 cm |
| X Band | 8–12.5 GHz | 3.75–2.4 cm |
| Ku Band | 12.5–18 GHz | 2.4–1.67 cm |
| K Band | 18–26.5 GHz | 1.67–1.13 cm |
| Ka Band | 26.5–40 GHz | 1.13–0.75 cm |
| Millimeter wave | 40–300 GHz | 7.5–1 mm |
| Submillimeter wave | 300–3000 GHz | 1–0.1 mm |

Based on Table 1-1 and calculations carried out in Example 1-1 we note that the VHF/UHF band, as typically encountered in television sets, constitutes the point at which the wavelength first reaches dimensions equivalent to the physical extent of the electronic system. It is this region where we need to begin to take into account the wave nature of current and voltage signals in the respective electronic circuits. The situation becomes even more critical when for instance 30 GHz frequency in the EHF band is considered. Without being able to assign exact limits, the RF frequency range is customarily associated from VHF to the S band. The MW frequency range has been traditionally associated with radar systems operating in the C band and above.

1.4 RF Behavior of Passive Components

From conventional AC circuit analysis we know that a resistance R is frequency independent and that a capacitor C and an inductor L can simply be specified by their reactances X_C and X_L as follows:

$$X_C = \frac{1}{\omega C} \quad (1.5a)$$

$$X_L = \omega L \quad (1.5b)$$

The implications of (1.5), for example, are such that a capacitor of $C = 1 \text{ pF}$ and an inductor of $L = 1 \text{ nH}$ at low frequencies of 60 Hz represent, respectively, either an open or short circuit condition because

$$X_C(60 \text{ Hz}) = \frac{1}{2\pi \cdot 60 \cdot 10^{-12}} \cong 2.65 \times 10^9 \Omega \approx \infty \quad (1.6a)$$

$$X_L(60 \text{ Hz}) = 2\pi \cdot 60 \cdot 10^{-9} \cong 3.77 \times 10^{-7} \Omega \approx 0 \quad (1.6b)$$

It is important to point out that resistances, inductances, and capacitances are not only created by wires, coils, and plates as typically encountered in conventional low-frequency electronics. Even a single straight wire or a copper segment of a **printed circuit board** (PCB) layout possesses frequency dependent resistance and inductance. For instance, a cylindrical copper conductor of radius a , length l , and conductivity σ_{cond} has a DC resistance of

$$R_{DC} = \frac{l}{\pi a^2 \sigma_{\text{cond}}} \quad (1.7)$$

For a DC signal the entire conductor cross-sectional area is utilized for the current flow. At AC the situation is complicated by the fact that the alternating charge carrier flow establishes a magnetic field that induces an electric field (according to Faraday's law) whose associated current density opposes the initial current flow. The effect is strongest at the center $r = 0$, therefore significantly increasing the resistance in the center of the conductor. The result is a current flow that tends to reside at the outer perimeter with increasing frequency. As derived in Appendix B, the z -directed current density J_z can be represented by

$$J_z = \frac{pI}{2\pi a} \frac{J_0(pr)}{J_1(pa)} \quad (1.8)$$

where $p^2 = -j\omega\mu\sigma_{\text{cond}}$, and $J_0(pr)$, $J_1(pa)$ are Bessel functions of zeroth and first order, and I is the total current flow in the conductor. Further calculations reveal that the

normalized resistance and inductance under high-frequency conditions ($f \geq 500$ MHz) can be put in the form

$$R/R_{DC} \approx a/(2\delta) \quad (1.9)$$

and

$$(\omega L)/R_{DC} \approx a/(2\delta) \quad (1.10)$$

In these expressions δ is the so-called **skin depth**

$$\delta = (\pi f \mu \sigma_{cond})^{-1/2} \quad (1.11)$$

which describes the spatial drop-off in resistance and reactance as a function of frequency f , permeability μ , and conductivity σ_{cond} . For the equations (1.9) and (1.10) to be valid it is assumed that $\delta \ll a$. In most cases, the relative permeability of the conductor is equal to unity (i.e., $\mu_r = 1$). Because of the inverse square root frequency behavior, the skin depth is large for low frequencies and rapidly decreases for increasing frequencies. Figure 1-4 exemplifies the skin depth behavior as a function of frequency for material conductivities of copper, aluminum, and gold.

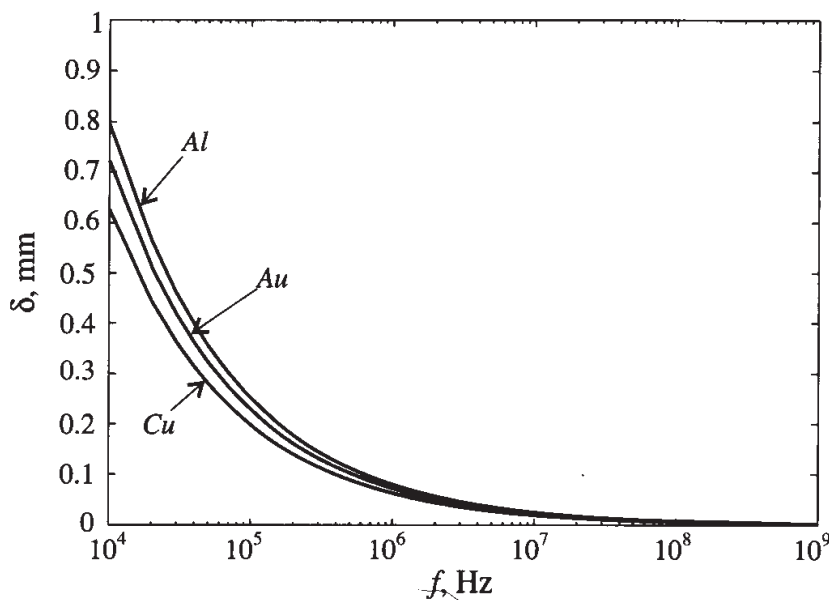


Figure 1-4 Skin depth behavior of copper $\sigma_{Cu} = 64.516 \times 10^6$ S/m, aluminum $\sigma_{Al} = 40.0 \times 10^6$ S/m, and gold $\sigma_{Au} = 48.544 \times 10^6$ S/m.

If we consider the conductivity of copper, we can plot the AC current density (1.8) normalized with respect to the DC current density $J_{z0} = I/(\pi a^2)$ as schematically shown for the axisymmetric wire depicted in Figure 1-5(a).

For a fixed wire radius of, let us say, $a = 1$ mm we can now plot J_z/J_{z0} as a function of radius r for various frequencies as given in Figure 1-5(b).

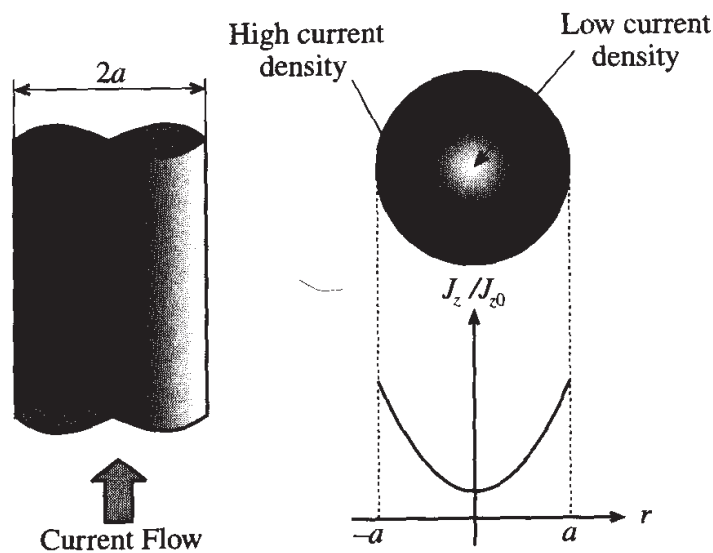


Figure 1-5(a) Schematic cross-sectional AC current density representation normalized to DC current density.

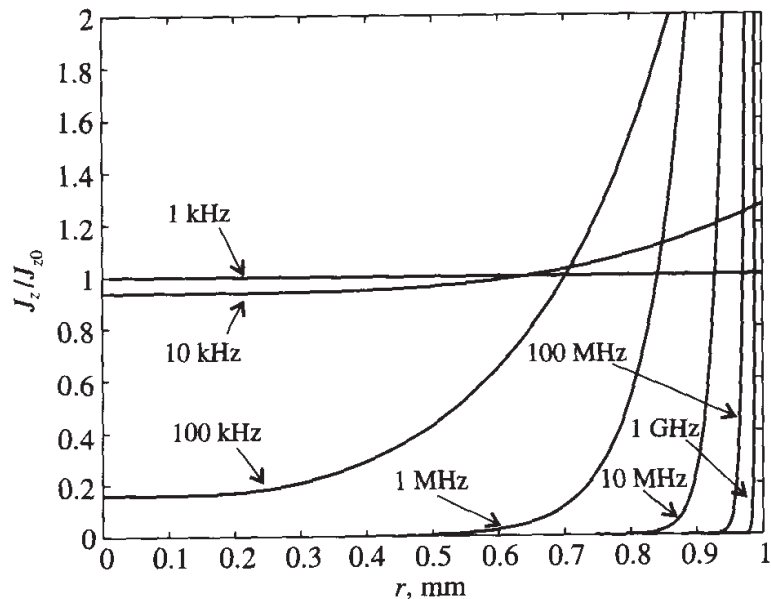


Figure 1-5(b) Frequency behavior of normalized AC current density for a copper wire of radius $a = 1 \text{ mm}$.

We notice the significant increase in current flow at the outer perimeter of the wire even for moderate frequencies of less than 1 MHz. At frequencies around 1 GHz, the current flow is almost completely confined to the surface of the wire with negligible radial penetration. An often used high-frequency approximation for the z -directed current density is

$$J_z \approx \frac{I_p}{j2\pi a \sqrt{r}} e^{-(1+j)\frac{a-r}{\delta}} \quad (1.12)$$

As seen in (1.12), the skin depth δ has a simple physical meaning. It denotes the reduction in the current density to the e^{-1} factor (approximately 37%) of its original DC value. If we rewrite (1.9) slightly, we find

$$R = R_{DC} \frac{a}{2\delta} = R_{DC} \frac{\pi a^2}{2\pi a \delta} \quad (1.13)$$

This equation shows that the resistance increases inverse proportionally with the cross-sectional skin area, see Figure 1-6.

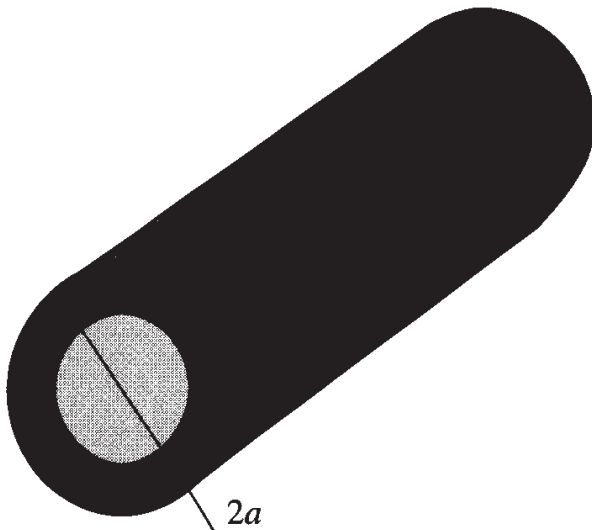
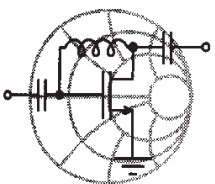


Figure 1-6 Increase in resistance over the cross sectional surface area. The current flow is confined to a small area defined by the skin depth δ .

To standardize the sizes of wires, the American Wire Gauge (AWG) system is commonly used in the United States. For instance, the diameter of the wire can be determined by its AWG value. A complete listing of all AWG values and their corresponding diameters is given in Table A-4 in Appendix A. The general rule is that in the AWG system, the diameter of the wire roughly doubles every six wire gauges starting with 1 mil for a AWG 50 wire (see Table A-4).



RF & MW →

Example 1-2: Conversion between wire diameter and AWG size

Determine the radius of the AWG 26 wire if the diameter of the AWG 50 wire is 1.0 mil (or 2.54×10^{-5} m).

Solution: The increase in diameter is computed as follows:

$$\text{AWG 50} \quad d = 1 \text{ mil}$$

$$\text{AWG 44} \quad d = 2 \text{ mils}$$

$$\text{AWG 38} \quad d = 4 \text{ mils}$$

$$\text{AWG 32} \quad d = 8 \text{ mils}$$

$$\text{AWG 26} \quad d = 16 \text{ mils}$$

Thus we determined that the diameter of a AWG 26 wire is equal to 16 mils. Therefore, the radius is

$$8 \text{ mil} = 8 \times (2.54 \times 10^{-5} \text{ m}) = 0.2032 \text{ mm}$$

Even in today's increasingly metric world, AWG has retained its importance, and knowledge of how to convert mil-based AWG size wires into millimeters often proves indispensable.

1.4.1 High-Frequency Resistors

Perhaps the most common circuit element in low-frequency electronics is a resistor whose purpose is to produce a voltage drop by converting some of the electric energy into heat. We can differentiate among several types of resistors:

- Carbon-composite resistors of high-density dielectric granules
- Wire-wound resistors of nickel or other winding material
- Metal-film resistors of temperature stable materials
- Thin-film chip resistors of aluminum or beryllium based materials

Of these types mainly the thin-film chip resistors find application nowadays in RF and MW circuits as **surface mounted devices** (SMDs). This is due to the fact that they can be produced in extremely small sizes, as Figure 1-7 shows.

As the previous section has shown, even a straight wire possesses an associated inductance. Consequently, the electric equivalent circuit representation of a high-frequency resistor of nominal value R is more complicated and has to be modified such that the finite lead dimensions as well as parasitic capacitances are taken into account. This situation is depicted in Figure 1-8.

The two inductances L model the leads, while the capacitances are needed to account for the actual wire arrangement, which always represents a certain charge sepa-

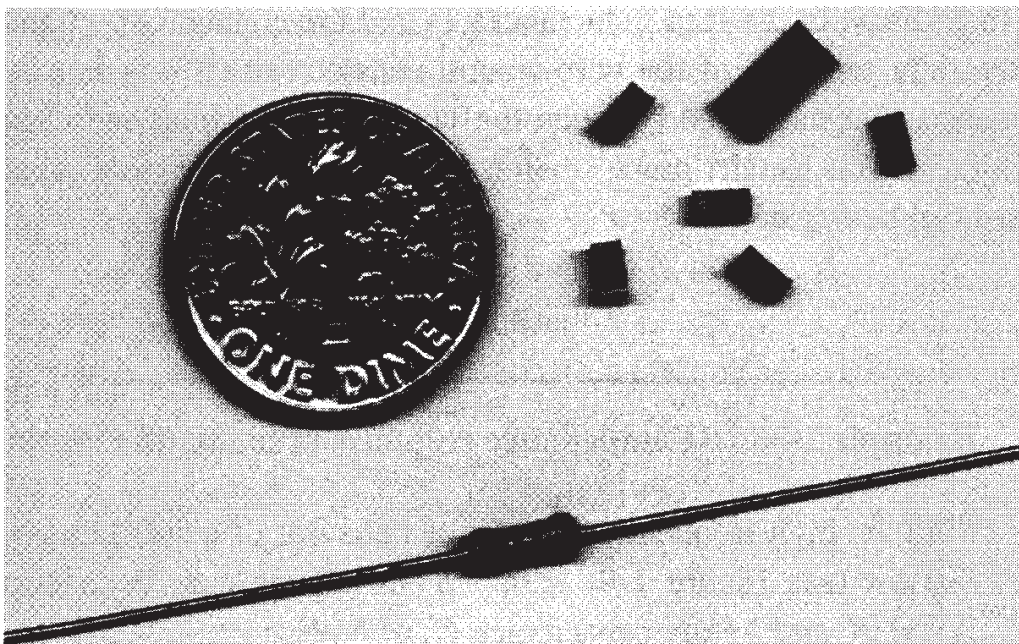


Figure 1-7 One- and quarter-watt thin-film chip resistors in comparison with a conventional quarter-watt resistor.

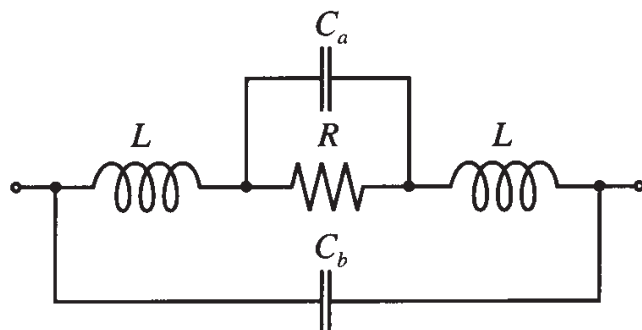


Figure 1-8 Electric equivalent circuit representation of the resistor.

ration effect modeled by capacitance C_a , and interlead capacitance C_b . The lead resistance is generally neglected when compared with the nominal resistance R . For a wire-wound resistor the model is more complex, as Figure 1-9 shows.

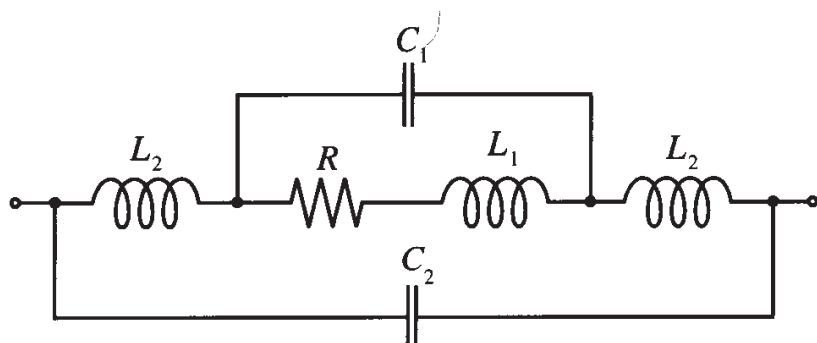
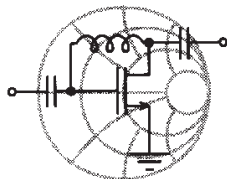


Figure 1-9 Electric equivalent circuit representation for a high-frequency wire-wound resistor.

Here, in addition to the lead inductances L_2 and the contact capacitance, we need to include the inductance L_1 of the wire-wound resistor, which acts as a coil, and the stray capacitance C_1 established between the windings. The interlead capacitance C_2 (or C_b in Figure 1-8) is usually much smaller than the internal or stray capacitance and in many cases can be neglected.



RF & MW →

Example 1-3: RF impedance response of metal film resistors

Find the high frequency impedance behavior of a 500Ω metal film resistor (see Figure 1-8) with 2.5 cm copper wire connections of AWG 26 and a stray capacitance C_a of 5 pF.

Solution: In Example 1-2 we have determined that the radius of an AWG 26 wire is $a = 2.032 \times 10^{-4} \text{ m}$. According to (1.10) the inductance of the straight wire at high frequency is approximately equal to $L = R_{DC}a/(2\omega\delta)$. Substituting (1.11) for the skin depth, we get the following expression of a lead inductance (we set the conductivity of copper to be $\sigma_{Cu} = 64.516 \times 10^6 \Omega^{-1} \cdot \text{m}^{-1}$):

$$L = R_{DC} \frac{a}{2\omega} \sqrt{\pi f \mu_0 \sigma_{Cu}} = \frac{2l}{\sigma \pi a^2 4\pi f} \sqrt{\pi f \mu_0 \sigma_{Cu}} = \frac{2l}{4\pi a} \sqrt{\frac{\mu_0}{\pi \sigma_{Cu} f}} = \frac{1.54}{\sqrt{f}} \mu\text{H}$$

where the length of the leads is doubled to account for two connections. The preceding formula for the computation of the lead inductance is applicable only for frequencies where the skin depth is smaller than the radius of the wire [i.e., $\delta = (\pi f \mu \sigma)^{-1/2} \ll a$] or in terms of frequency $f \gg 1/(\pi \mu \sigma_{Cu} a^2) = 95 \text{ kHz}$.

Knowing the inductance of the leads, we can now compute the impedance of the entire circuit as

$$Z = j\omega L + \frac{1}{j\omega C + 1/R}$$

The result of the computation is presented in Figure 1-10, where the absolute value of the impedance of the resistor is plotted versus frequency.

As seen, at low frequencies the impedance of the resistor is equal to R . However, as the frequency increases and exceeds

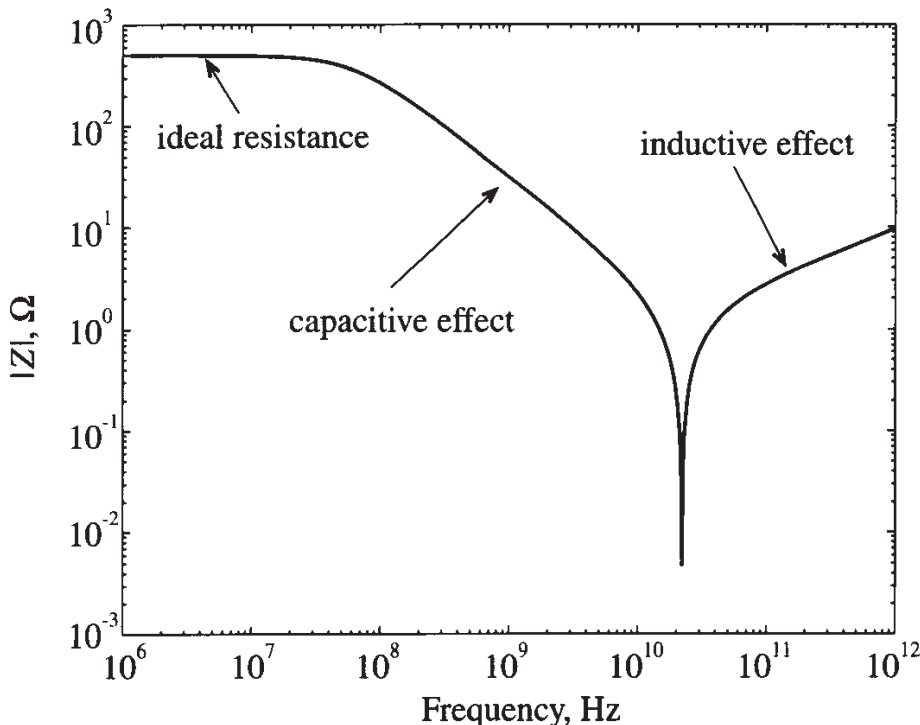


Figure 1-10 Absolute impedance value of a $500\text{-}\Omega$ thin-film resistor as a function of frequency.

10 MHz, the effect of the stray capacitance becomes dominant, which causes the impedance of the resistor to decrease. Beyond the resonance at approximately 20 GHz, the total impedance increases due to the lead inductance, which represents an open circuit or infinite impedance at very high frequencies.

This example underscores the care that is required when dealing with the ubiquitous, seemingly frequency-independent resistors. While not all resistors exhibit exactly the same response as shown in Figure 1-10, it is the single, often multiple, resonance point that occurs when the frequency reaches into the GHz range.

1.4.2 High-Frequency Capacitors

In most RF circuits chip capacitors find widespread application for the tuning of filters and matching networks as well as for biasing active components such as transistors. It is therefore important to understand their high-frequency behavior. Elementary circuit analysis defines capacitance for a parallel plate capacitor whose plate dimensions are large compared to its separation as follows:

$$C = \frac{\epsilon A}{d} = \epsilon_0 \epsilon_r \frac{A}{d} \quad (1.14)$$

where A is the plate surface area and d denotes the plate separation. Ideally there is no current flow between the plates. However, at high frequencies the dielectric materials become lossy (i.e., there is a conduction current flow). The impedance of a capacitor must thus be written as a parallel combination of conductance G_e and susceptance ωC :

$$Z = \frac{1}{G_e + j\omega C} \quad (1.15)$$

In this expression the current flow at DC is due to the conductance $G_e = \sigma_{\text{diel}} A/d$, with σ_{diel} being the conductivity of the dielectric. It is now customary to introduce the **series loss tangent** $\tan \Delta_s = \omega \epsilon / \sigma_{\text{diel}}$ and insert it into the expression for G_e to yield

$$G_e = \frac{\sigma_{\text{diel}} A}{d} = \frac{\omega \epsilon A}{d \tan \Delta_s} = \frac{\omega C}{\tan \Delta_s} \quad (1.16)$$

Some practical values for the loss tangent are summarized in Table A-3. The corresponding electric equivalent circuit with parasitic lead inductance L , series resistance R_s describing losses in the lead conductors, and dielectric loss resistance $R_e = 1/G_e$, is shown in Figure 1-11.

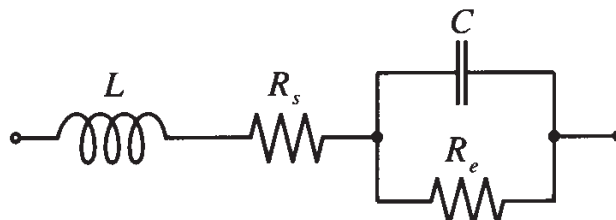
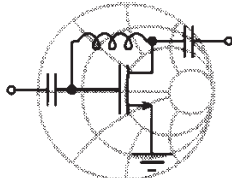


Figure 1-11 Electric equivalent circuit for a high-frequency capacitor.



RF & MW →

Example 1-4: RF impedance response of capacitor

Compute the high frequency impedance of a 47 pF capacitor whose dielectric medium consists of an aluminum oxide (Al_2O_3) possessing a series loss tangent of 10^{-4} (assumed to be frequency independent) and whose leads are 1.25 cm AWG 26 copper wires ($\sigma_{\text{Cu}} = 64.516 \times 10^6 \Omega^{-1} \cdot \text{m}^{-1}$).

Solution: Similar to Example 1-3, the inductance associated with the leads is given by

$$L = R_{DC} \frac{a}{2\omega} \sqrt{\pi f \mu_0 \sigma_{Cu}} = \frac{2l}{4\pi a} \sqrt{\frac{\mu_0}{\pi \sigma_{Cu} f}} = \frac{771}{\sqrt{f}} \text{nH}$$

The series resistance of the leads is computed from (1.13) to be

$$R_s = R_{DC} \frac{a}{2\delta} = \frac{2l}{2\pi a \sigma_{Cu}} \sqrt{\pi f \mu_0 \sigma_{Cu}} = \frac{l}{a} \sqrt{\frac{\mu_0 f}{\pi \sigma_{Cu}}} = 4.8 \sqrt{f} \text{ } \mu\Omega$$

Finally, in accordance with (1.16), the parallel leakage resistance is equal to

$$R_e = \frac{1}{G_e} = \frac{1}{2\pi f C \tan \Delta_s} = \frac{33.9 \times 10^6}{f} \text{ M}\Omega$$

The frequency response of the magnitude of the impedance based on equation (1.15) for the capacitor is shown in Figure 1-12.

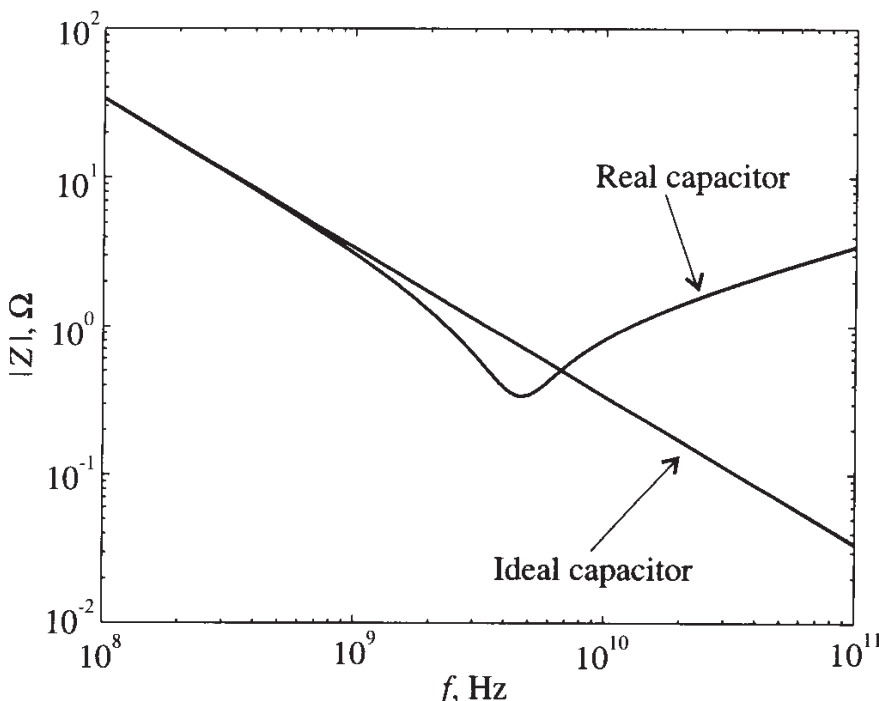


Figure 1-12 Absolute value of the capacitor impedance as a function of frequency.

In computing the parallel leakage resistance R_e we have assumed the loss tangent $\tan \Delta_s$ to be frequency independent. In reality, however, this factor may significantly depend upon the operating frequency. Unfortunately, data sheets often do not, or only very incompletely, report this behavior.

Since the loss tangent can also be defined as the ratio of an **equivalent series resistance** (ESR) to the capacitor's reactance, many data sheets list ESR instead of $\tan\Delta_s$. The ESR value is thus given as

$$ESR = \frac{\tan\Delta_s}{\omega C}$$

This indicates that $ESR \rightarrow 0$ as $\tan\Delta_s \rightarrow 0$.

As already known from the RF resistor impedance response in Example 1-3, the capacitor reveals a similar resonance behavior due to the presence of dielectric losses and finite lead wires.

The construction of a surface-mounted ceramic capacitor is shown in Figure 1-13. The capacitor is a rectangular block of a ceramic dielectric into which a number of interleaved metal electrodes are sandwiched. The purpose of this type of packaging is to provide a high capacitance per unit volume by maximizing the electrode surface area. Capacitance values range from 0.47 pF to 100 nF with operating voltage ranging from 16 V to 63 V. The loss tangent is usually listed by the manufacturer as $\tan\Delta_s \leq 10^{-3}$ at a 1 MHz test frequency. Again, this loss tangent can significantly increase as the frequency reaches into the GHz range.

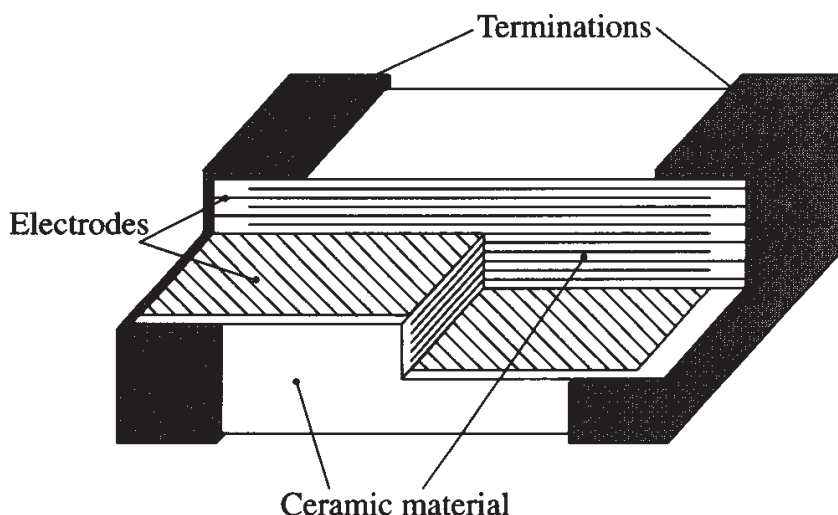


Figure 1-13 Actual construction of a surface-mounted ceramic multilayer capacitor.

Besides capacitance and loss tangent, manufacturers list a nominal voltage that cannot be exceeded at a particular operating temperature (for instance, $T \leq 85^{\circ}\text{C}$). Furthermore, the capacitance is temperature dependent, as further discussed in the problem section of this chapter.

1.4.3 High-Frequency Inductors

Although not employed as often as resistors and capacitors, inductors generally are used in transistor biasing networks, for instance as **RF coils** (RFCs) to short circuit the device to DC voltage conditions. Since a coil is generally formed by winding a straight wire on a cylindrical former, we know from our previous discussion that the windings represent an inductance in addition to the frequency-dependent wire resistance. Moreover, adjacently positioned wires constitute separated moving charges, thus giving rise to a parasitic capacitance effect as shown in Figure 1-14.

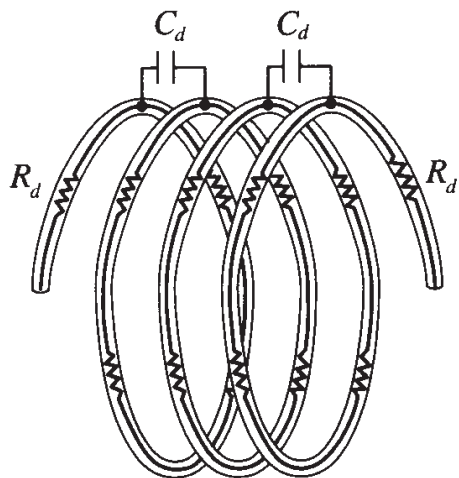


Figure 1-14 Distributed capacitance and series resistance in the inductor coil.

The equivalent circuit model of the inductor is shown in Figure 1-15. The parasitic shunt capacitance C_s and series resistance R_s represent composite effects of distributed capacitance C_d and resistance R_d , respectively.

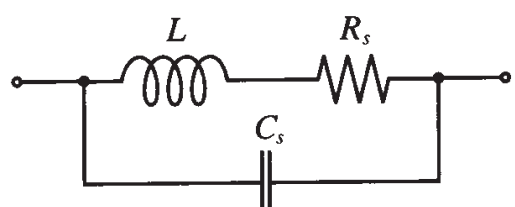
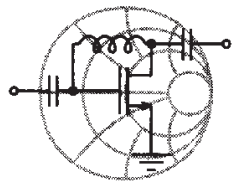


Figure 1-15 Equivalent circuit of the high-frequency inductor.



RF & MW →

Example 1-5: RF impedance response of an RFC

Estimate the frequency response of an RFC formed by $N = 3.5$ turns of AWG 36 copper wire on a 0.1 inch air core. Assume that the length of the coil is 0.05 inch.

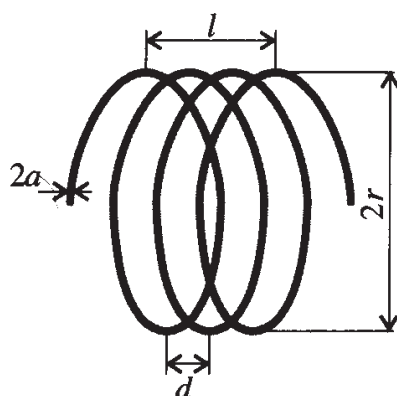


Figure 1-16 Inductor dimensions of an air-core coil.

Solution: The dimensions of the coil are shown in Figure 1-16. From Table A-4 in Appendix A, we find that the radius of the AWG 36 wire is $a = 2.5$ mils = $63.5 \mu\text{m}$. The radius of the coil core is $r = 50$ mils = 1.27 mm . The length of the coil is $l = 50$ mils = 1.27 mm . The distance between two adjacent turns is $d = l/N \approx 3.6 \times 10^{-4} \text{ m}$.

To estimate the inductance of the coil we will use a well-known formula for the inductance of an air core solenoid:

$$L = \frac{\pi r^2 \mu_0 N^2}{l} \quad (1.17)$$

Strictly speaking, this formula is valid only for the case when $r \ll l$ and the number of turns N is large. In our case, the length of the coil is comparable with its radius and the number of turns is relatively small. Therefore, (1.17) will not give an exact value for the inductance, but a rather good approximation. Substituting the given values into (1.17), we obtain $L = 61.4 \text{ nH}$.

To approximate the effect of the capacitance C_s , we will use the formula for an ideal parallel-plate capacitor (1.14). In our case

the separation d between the plates is assumed to be equal to the distance between the turns $d = l/N \approx 3.6 \times 10^{-4}$ m, and the area A can be estimated as $A = 2al_{\text{wire}}$, where $l_{\text{wire}} = 2\pi rN$ is the length of the wire. We conclude that

$$C_s = \frac{\epsilon_0 \cdot 2\pi rN \cdot 2a}{l/N} = 4\pi\epsilon_0 \frac{raN^2}{l} = 0.087 \text{ pF}$$

Since the radius of the wire is only $63.5 \mu\text{m}$, we can neglect the skin effect and compute the series resistance R_s as a DC resistance of the wire.

$$R_s = \frac{l_{\text{wire}}}{\sigma_{\text{Cu}} \pi a^2} = \frac{2\pi rN}{\sigma_{\text{Cu}} \pi a^2} = 0.034 \Omega$$

The frequency response of the RFC impedance just analyzed is shown in Figure 1-17.

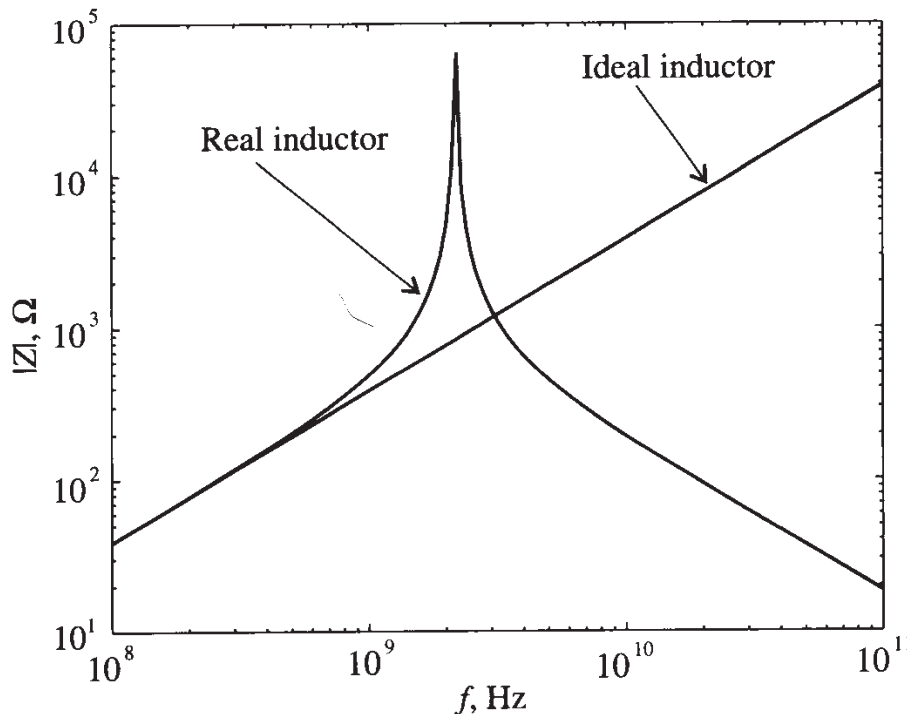


Figure 1-17 Frequency response of the impedance of an RFC.

RFCS find widespread use for biasing RF circuits. However, as Figure 1-17 shows, the frequency dependency can form complicated resonance conditions with additional elements in an RF system. Indeed, certain matching circuits rely on the RFCS as tuning elements.

As can be seen from Figure 1-17, the behavior of the RFC deviates from the expected behavior of an ideal inductance at high frequencies. First, the impedance of the RFC increases more rapidly as the frequency approaches resonance. Second, as the frequency continues to increase, the influence of the parasitic capacitance C_s becomes dominant and the impedance of the coil decreases.

If the RFC had zero series resistance, then the overall impedance behavior at resonance would reach infinity, but due to the nonzero value of R_s the maximum value of the impedance is of finite value. To characterize the impact of the coil resistance, the quality factor Q is commonly used:

$$Q = \frac{X}{R_s} \quad (1.18)$$

where X is the reactance and R_s is the series resistance of the coil. The quality factor characterizes the resistive loss in this passive circuit, and for tuning purposes it is desirable that this factor is as high as possible.

1.5 Chip Components and Circuit Board Considerations

The practical realization of passive components on printed RF circuit boards is primarily accomplished in chip form and placed on specially fabricated board materials. In the following section we examine the three most common passive chip elements in terms of their sizes and electric characteristics.

1.5.1 Chip Resistors

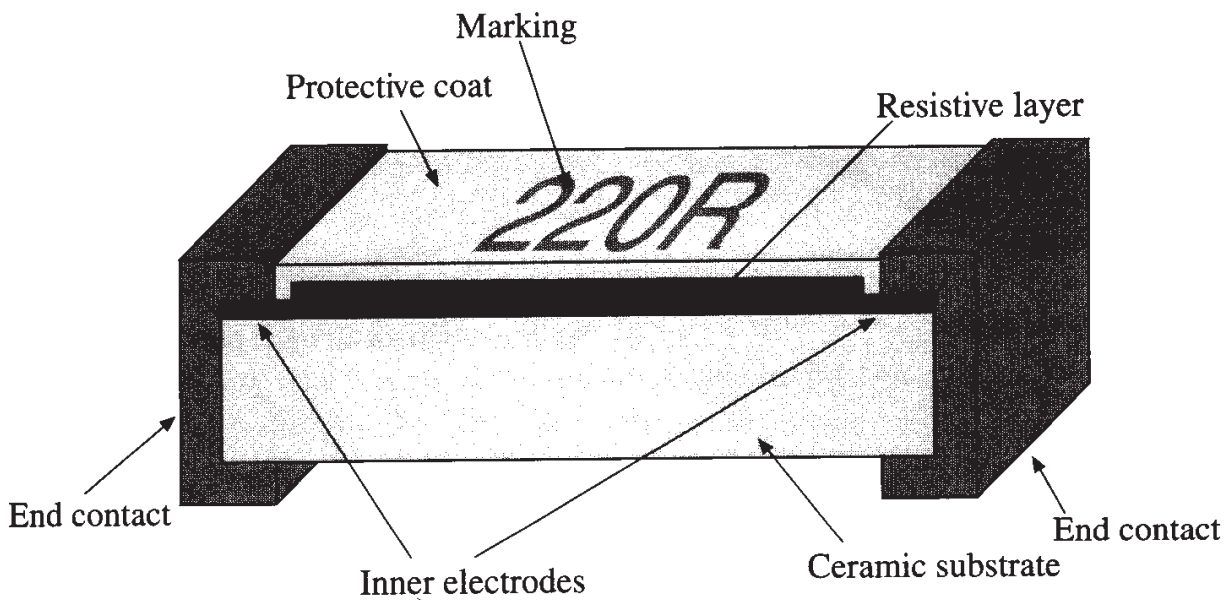
The size of chip resistors can be as small as 40 by 20 mils (where 1 mil = 0.001 inch = 0.0254 mm) for 0.5 W power ratings and up to 1 by 1 inch for 1000 W ratings in RF power amplifiers. The chip resistor sizes that are most commonly used in circuits operating up to several hundred watts are summarized in Table 1-2.

A general rule of thumb in determining the size of the chip components from the known size code is as follows: the first two digits in the code denote the length L in terms of tens of mils, and the last two digits denote the width W of the component. The thickness of the chip resistors is not standardized and depends on the particular component type.

The resistance value range from $1/10 \Omega$ up to several $M\Omega$. Higher values are difficult to manufacture and result in high tolerances. Typical resistor tolerance values range from $\pm 5\%$ to $\pm 0.01\%$. Another difficulty that arises with high-value resistors is that they are prone to produce parasitic fields, adversely affecting the linearity of the resistance versus frequency behavior. A conventional chip resistor realization is shown in Figure 1-18.

Table 1-2 Standard sizes of chip resistors

| Geometry | Size Code | Length L, mils | Width W, mils |
|----------|-----------|----------------|---------------|
| | 0402 | 40 | 20 |
| | 0603 | 60 | 30 |
| | 0805 | 80 | 50 |
| | 1206 | 120 | 60 |
| | 1218 | 120 | 180 |

**Figure 1-18** Cross-sectional view of a typical chip resistor.

A metal film (usually nichrome) layer is deposited on a ceramic body (usually aluminum oxide). This resistive layer is trimmed to the desired nominal value by reducing its length and inserting inner electrodes. Contacts are made on both ends of the resistor that allow the component to be soldered to the board. The resistive film is coated with a protective layer to prevent environmental interferences.

1.5.2 Chip Capacitors

The chip capacitors are implemented either as a conventional single-plate configuration, as shown in Figure 1-19, or a multiple-layer design (see Figure 1-13).

Frequently, single-plate capacitors are combined in clusters of two or four elements sharing a single dielectric material and a common electrode, as shown in Figure 1-20.

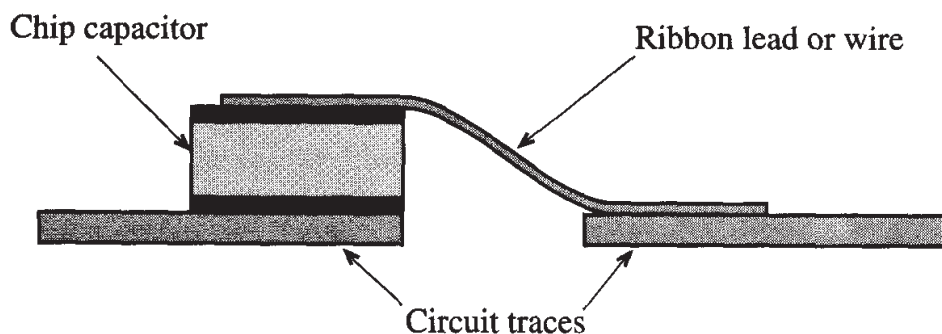


Figure 1-19 Cross section of a typical single-plate capacitor connected to the board.

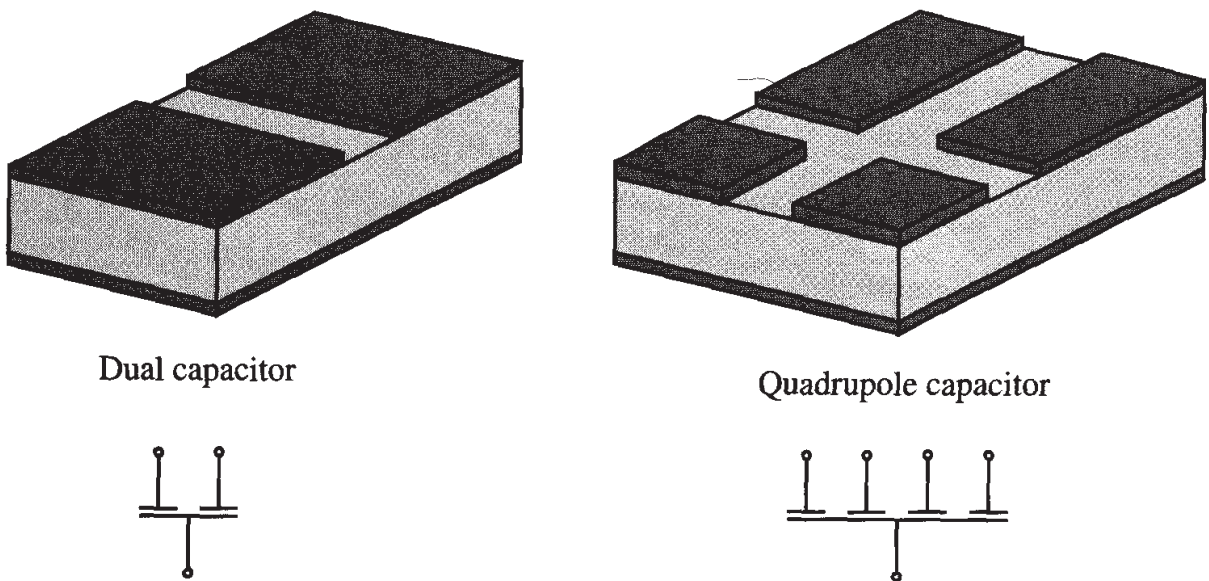


Figure 1-20 Clusters of single-plated capacitors sharing a common dielectric material.

The standard sizes of the capacitors range from a minimum of 15 mils square in a single layer configuration to 400 by 425 mils at higher values. Typical values for commercial capacitors range from 0.1 pF to several μF . The tolerances vary from $\pm 2\%$ to $\pm 50\%$. For small capacitances tolerances are usually expressed in terms of pF instead of percent; for example, we often encounter capacitors with the nominal values given as (0.5 ± 0.25) pF.

1.5.3 Surface-Mounted Inductors

The most common implementation of surface-mounted inductors is still the wire-wound coil. A typical example of such an inductor with air core is shown in Figure 1-21. Modern manufacturing technology allows us to make these inductors extremely small. Their dimensions are comparable to those of chip resistors and capacitors. Typical sizes



Figure 1-21 Typical size of an RF wire-wound air-core inductor in comparison with a cellular phone antenna (courtesy of Coilcraft, Inc.).

of the surface-mounted wire-wound inductors range from 60 by 30 mils to 180 by 120 mils. The inductance values cover the range from 1 nH to 1000 μ H.

When thickness constraints of the circuit play a major role, flat inductors are often employed that can be integrated with microstrip transmission lines. A generic configuration of a flat coil is shown in Figure 1-22. Although such thin-wire coils have relatively low inductances on the order of 1 to 500 nH, it is the frequency in the GHz range that helps push the reactance beyond 1 $k\Omega$. The physical construction can be as small as 2 mm by 2 mm.

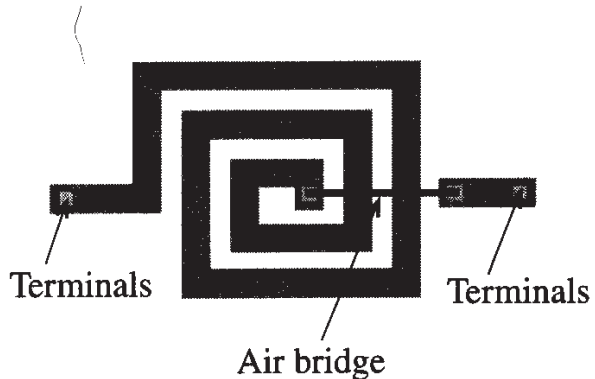


Figure 1-22 Flat coil configuration. An air bridge is made by using either a wire or a conductive ribbon.

Flat coils are used in both integrated and **hybrid circuits**. Hybrid circuits are very similar to an ordinary circuit, but discrete semiconductor elements are placed on the dielectric substrate in die form (without case) and are connected to the conductors on

the board using bond wires. After the entire circuit is assembled, it is then placed into a single case to protect it from environmental interferences. Resistors and capacitors for hybrid circuits can directly be implemented on the board by metal-film deposition. This approach permits significant reduction in the size of the circuit.

1.6 Summary

In this chapter the evolution from low- to high-frequency systems is discussed and placed in a historical context. A key concept when dealing with high-frequency applications is the fact that the electromagnetic wave nature begins to dominate over Kirchhoff's current and voltage laws. Issues such as propagation constant and phase velocity,

$$\beta = 2\pi/\lambda \text{ and } v_p = \frac{\omega}{\beta} = \frac{1}{\sqrt{\epsilon\mu}}$$

gain importance.

A consequence of the electromagnetic wave nature is the skin effect, which forces the current to flow close to the surface of the conducting structures. The depth of penetration from the surface can be determined via the skin depth equation:

$$\delta = \frac{1}{\sqrt{\pi f \mu \sigma}}$$

With the skin depth we can approximately characterize the frequency dependent resistance and reactance of components at RF frequency. As an example, the simple cylindrical lead wires exhibit resistances and reactances that become a function of frequency

$$R \approx R_{DC} \frac{a}{2\delta} \text{ and } X = \omega L \approx R_{DC} \frac{a}{2\delta}$$

These wires, in conjunction with the respective R , C , and L elements, form electric equivalent circuits whose performance markedly deviate from the ideal element behavior. We find that the constant resistance at low frequency is no longer constant, but displays a second-order system response with a resonant dip. The dielectric material in a capacitor becomes lossy at high frequencies (i.e., allows the flow of a small conduction current). The degree of loss is quantified by the loss tangent, which is tabulated for a range of engineering materials. Therefore, a capacitor exhibits an impedance behavior that follows an inverse frequency response only at low frequencies. Finally, inductors represent an impedance response that follows a linear increase at low frequencies before deviating from the ideal behavior by reaching a resonance peak and then turning capacitive.

A passive RF component vendor will always attempt to keep the physical dimensions of resistors, capacitors, and inductors as small as possible. This is desired since the wavelength of high-frequency voltage and current waves becomes ever smaller,

eventually reaching the characteristic sizes of the circuit components. As discussed in subsequent chapters, when the wavelength is comparable in size with the discrete electronic components, basic circuit analysis no longer applies.

Further Reading

- I. Bohl and P. Bhartia, *Microwave Solid State Design*, John Wiley, New York, 1988.
- C. Bowick, *RF Circuit Design*, Newmes, Newton, MA, 1982.
- D. K Chen, *Fundamentals of Engineering Electromagnetics*, Addison-Wesley, Reading, MA, 1993.
- R. A. Chipman, *Transmission Lines*, Schaum Outline Series, McGraw-Hill, New York, 1968.
- L. N. Dworsky, *Modern Transmission Line Theory and Applications*, Robert E. Krieger, Malabar, FL, 1988.
- M. F. Iskander, *Electromagnetic Fields and Waves*, Prentice Hall, Upper Saddle River, NJ, 1992.
- T. S. Laverghetta, *Practical Mircowaves*, Prentice Hall, Upper Saddle River, NJ, 1996.
- H. P. Neff, *Basic Electromagnetic Fields*, 2nd ed. Harper & Row, New York, 1987.
- K. F. Sander, *Microwave Components and Systems*, Addison-Wesley, 1987.
- K. F. Sander and G. A. L. Read, *Transmission and Propagation of Electromagnetic Waves*, 2nd ed. Cambridge University Press, Cambridge, UK, 1986.
- W. Sinnema, *Electronic Transmission Line Technology*, 2nd ed., Prentice Hall, Upper Saddle River, NJ, 1988.
- F. T. Ulaby, *Fundamentals of Applied Electromagnetics*, Prentice Hall, Upper Saddle River, NJ, 1997.

Problems

- 1.1 Compute the phase velocity and wavelength in an FR4 printed circuit board whose relative dielectric constant is 4.6 and where the operational frequency is 1.92 GHz.

- 1.2 The current flowing in a microstrip line (assumed to be infinite and lossless) is specified to be $i(t) = 0.6 \cos(9 \times 10^9 t - 500z)$ A. Find the (a) phase velocity, (b) frequency, (c) wavelength, and (d) phasor expression of the current.

- 1.3 A coaxial cable that is assumed lossless has a wavelength of the electric and magnetic fields of $\lambda = 20$ cm at 960 MHz. Find the relative dielectric constant of the insulation.

- 1.4 The electric wave field of a positive z -traveling wave in a medium with relative dielectric constant of $\epsilon_r = 4$ and with frequency of 5 GHz is given by

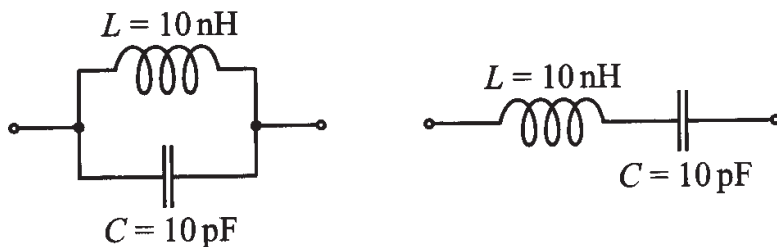
$$E_x = E_{0x} \cos(\omega t - kz) \text{ V/m}$$

(a) Find the magnetic field if $E_{0x} = 10^6$ V/m.

(b) Determine phase velocity and wavelength.

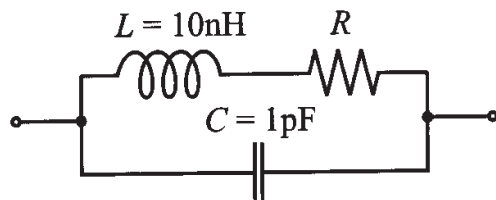
(c) Compute the spatial advance of the traveling wave between time intervals $t_1 = 3\mu\text{s}$ and $t_2 = 7\mu\text{s}$.

- 1.5 Find the frequency response of the impedance magnitude of the following series and parallel LC circuits:

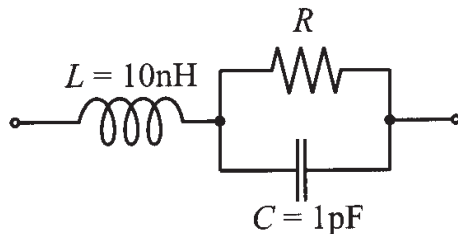


Compare your results to the situation when the ideal inductance is replaced by the same inductance and a 5Ω resistance connected in series. Assume that these circuits operate in the VHF/UHF frequency band of 30–3000 MHz.

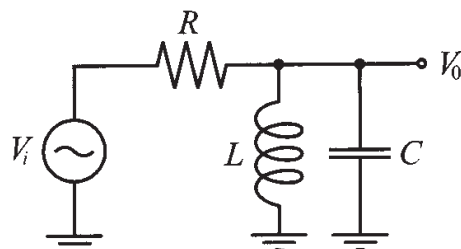
- 1.6 For the circuit shown, derive the resonance frequency and plot the resonance frequency behavior as a function of the resistance R .



- 1.7 Repeat Problem 1.6 for the following circuit.



- 1.8 For the following circuit we chose $R \ll (\sqrt{L/C})/2$.



Find $|V_0/V_i|$ as a function of frequency and identify the dominant circuit portions for the low-, mid-, and high-frequency domains.

- 1.9 One of the objectives of Chapter 1 is to sensitize the reader to high-frequency phenomena that are usually neglected in a low-frequency circuit analysis. One such phenomenon is the skin effect. To show its importance in RF calculations, (a) compute the frequency behavior of an inductor formed by 10 turns of AWG 26 copper wire on a 5 mm air core. The length of the coil is 5 mm. (b) repeat the computations by first neglecting the skin effect and then including it.
- 1.10 The leads of a resistor in an RF circuit are treated as straight aluminum wires ($\sigma_{Al} = 4.0 \times 10^7 \text{ S/m}$) of AWG size 14 and of total length of 5 cm. (a) Compute the DC resistance. (b) Find the AC resistance and inductance at 100 MHz, 1 GHz, and 10 GHz operating frequencies.
- 1.11 Compute the skin depths for copper ($\sigma_{Cu} = 64.516 \times 10^6 \text{ S/m}$), aluminum ($\sigma_{Al} = 40 \times 10^6 \text{ S/m}$), and gold ($\sigma_{Au} = 48.544 \times 10^6 \text{ S/m}$) at 1 GHz and 10 GHz, and find the resistance of a 10 cm wire with diameter of 1 mm.
- 1.12 A typical PCB substrate consists of Al_2O_3 with a relative dielectric constant of 10 and a loss tangent of 0.0004 at 10 GHz. Find the conductivity of the substrate.

- 1.13 For the series *RLC* circuit with $R = 1 \Omega$, $L = 1 \text{ nH}$, and $C = 1 \text{ pF}$, compute the resonance frequency and quality factor at $\pm 10\%$ of the resonance frequency. Does the presence of the resistor affect the resonance frequency?
- 1.14 A 4.7 pF capacitor with relative dielectric constant of 4.6 and series loss tangent of 0.003 is used in a circuit operated at 10 GHz. For a combined copper lead length of 6 cm and diameter of 0.5 mm, determine (a) the lead resistance and lead reactance, and (b) the conductance and the total impedance. The conductivity of copper is given as $\sigma_{\text{Cu}} = 64.516 \times 10^6 \Omega^{-1} \cdot \text{m}^{-1}$.
- 1.15 A manufacturer data sheet records the series loss tangent of a capacitor to be 10^{-4} at 5 GHz. For a total plate dimension of 10^{-2} cm^2 and plate separation of 0.01 mm and a relative dielectric constant of 10, find the conductance.
- 1.16 A two-element impedance of the generic form

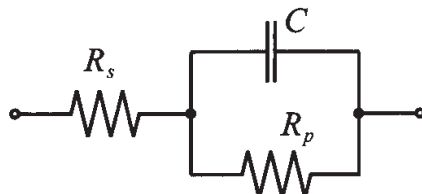
$$Z = R + jX$$

has to be converted into an equivalent admittance form $Y = 1/Z$ such that

$$Y = G + jB$$

Find the conductance G and susceptance B in terms of resistance R and reactance X .

- 1.17 A more elaborate model of a capacitor is sometimes represented by the following circuit:

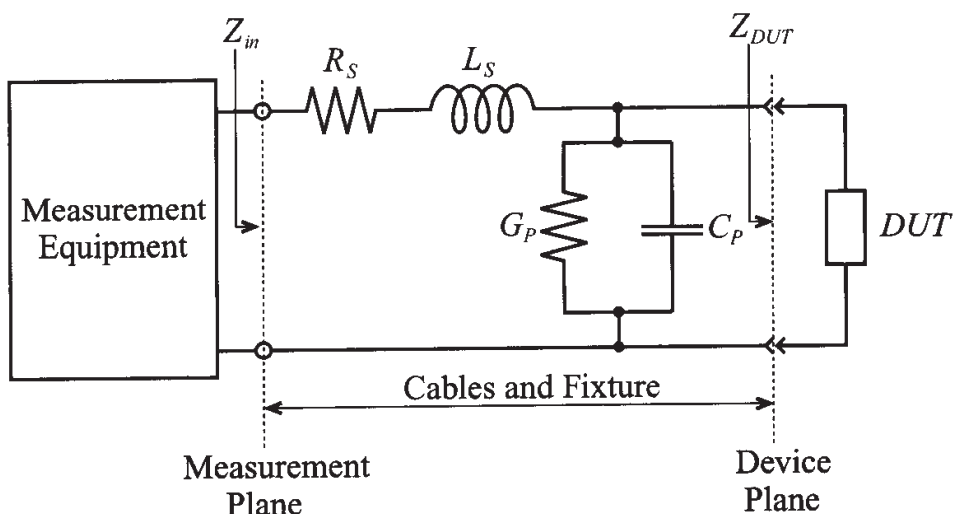


Here the loss tangent is specified as consisting of two parts involving the admittance $Y_p = 1/R_p + j\omega C$ with a parallel-circuit loss tangent $\tan\Delta_p = |\text{Re}\{Y_p\}/\text{Im}\{Y_p\}|$ and series impedance $Z_S = R_S + 1/(j\omega C)$ with a series-circuit loss tangent $\tan\Delta_S = |\text{Re}\{Z_S\}/\text{Im}\{Z_S\}|$ (it is noted that R_S is different from Example 1-4). Show that for low-loss capacitances we approximately obtain $\tan\Delta \approx \tan\Delta_S + \tan\Delta_p$, where $\tan\Delta = |\text{Re}\{Z\}/\text{Im}\{Z\}|$ and Z is the total impedance.

- 1.18 When recording the capacitance with a measurement equipment, the user has often the choice to select a suitable circuit representation. For the series representation, the instrument attempts to predict R_S and C_S , while for the

parallel representation the prediction involves R_P and C_P . Which mode should be chosen if large capacitors of more than $100 \mu\text{F}$ are to be measured? Is this mode also suitable for small values of less than $10 \mu\text{F}$? Explain your answers.

- 1.19 The ability to store electric charge, expressed through the capacitance, depends on the operating temperature. This behavior can be quantified through the relation $C = C_0[1 + \alpha(T - 20^\circ\text{C})]$, where C_0 is the nominal capacitance and α is a temperature coefficient that can be positive or negative. If the capacitance C at $T = 20^\circ\text{C}$ is recorded to be 4.6 pF , which increases to 4.8 pF at $T = 40^\circ\text{C}$, what is the temperature coefficient α ? Determine the capacitance at 0°C and 80°C .
- 1.20 When measuring impedance at low frequency we connect the measurement equipment to a device using a pair of wires and assume that the reading reflects the impedance of the device under test (DUT). As we have seen in this chapter, at high frequencies we have to take into account the influence of the parasitic elements. The typical circuit representation of the measurement arrangement is as follows.

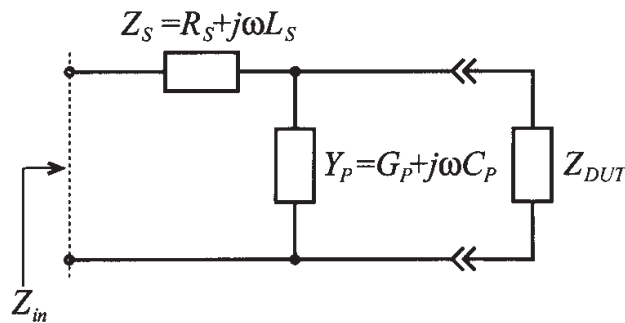


Here the fixture and cables are replaced by an equivalent circuit of the lead impedance ($R_S + j\omega L_S$) and stray admittance ($G_P + j\omega C_P$). Ideally, we would like to perform the measurement at the device plane. However, due to the influence of the fixture, the measurement plane is shifted away from the DUT.

To measure accurately the impedance of the DUT, the test fixture with connecting cables has to be taken into account. The methodology adopted by most manufacturers is to compensate for these undesired, fixture-related influences through an open- and short-circuit calibration. The first step is to

replace the DUT by a short circuit and record the resulting impedance. Due to the influence of the fixture, the measured impedance will not be equal to zero. Next, the short circuit is replaced by an open circuit and the impedance is recorded again. These two measurements allow us to quantify the parasitic influence of the fixture.

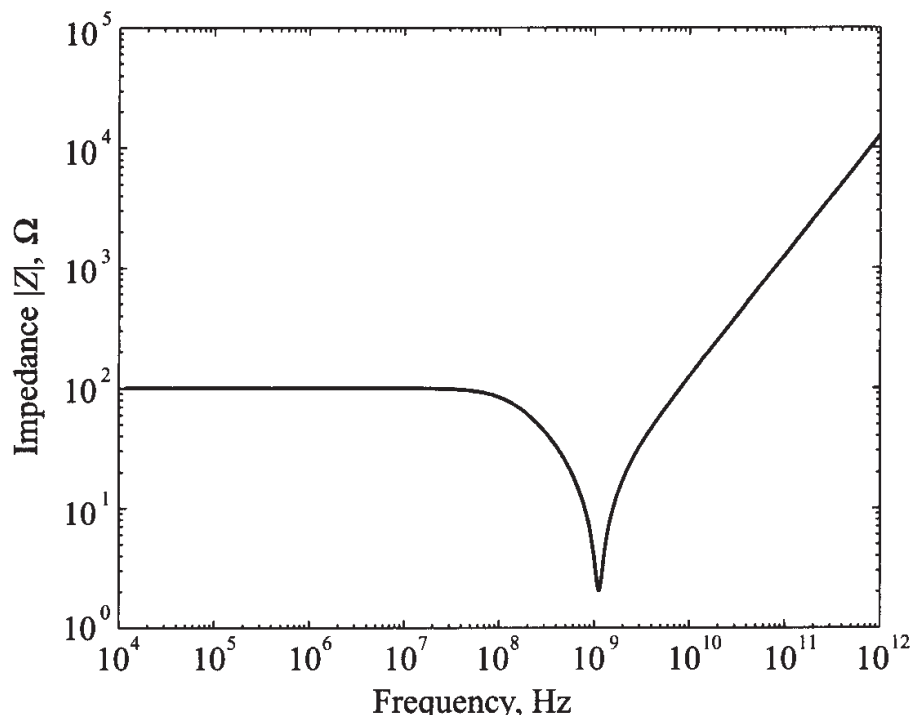
After calibration, we can connect the DUT and measure the input impedance. The equivalent circuit in this case is as follows.



Knowing the values of the parasitic elements (Z_S and Y_P), we can now compute the true impedance of the DUT.

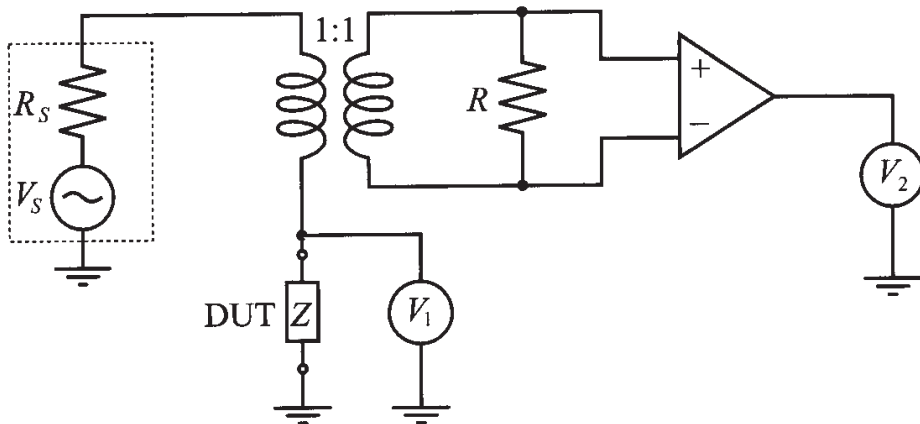
Explain the procedure with all necessary equations, and specify under what conditions such a calibration is possible. Next, develop the formula that allows us to find the desired DUT impedance in the absence of the fixture.

- 1.21** The results of a frequency sweep impedance measurement of an unknown passive device are shown in the following figure.



Based on the shape of the impedance response, develop a circuit that can be used as an equivalent circuit to replicate this device under test. What device can it be: resistor, inductor, or capacitor?

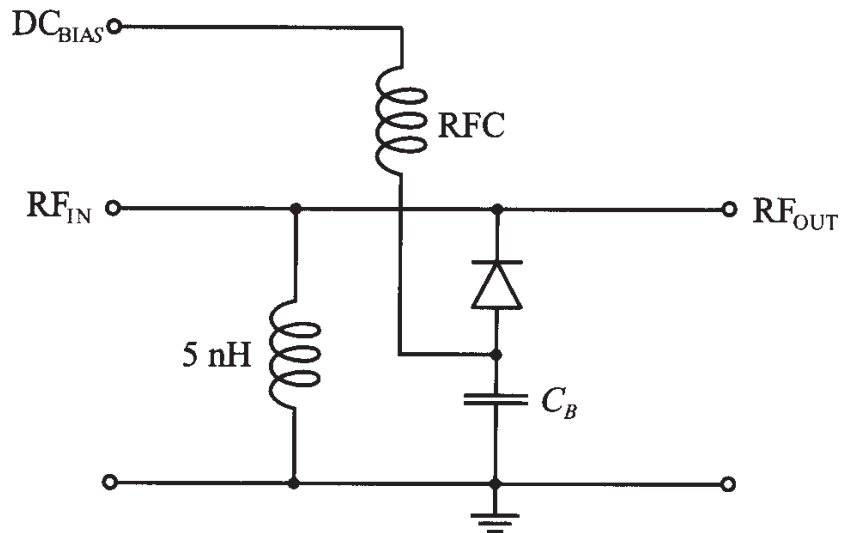
- 1.22 To measure the impedance of a passive component at RF frequencies is quite a challenge. Conventional techniques such as bridge circuits and resonance techniques fail beyond a few MHz. A technique pursued by several instrument manufactures is the current voltage recording based on the following simplified schematic.



Here the voltages are measured with vector voltmeters that allow the recording of magnitude and phase. Explain how the impedance of the component under test is determined and discuss the purpose of the transformer and operational amplifier.

- 1.23 An RFC is constructed by winding four turns of AWG 38 copper wire on a 2 mm ceramic core diameter ($\mu_r = 1$) of 0.1 mm length. Based on Example 1-5, estimate the inductance, stray capacitance, resistance, and resonance frequency.
- 1.24 Using data and the equivalent circuit diagram developed in the previous problem, find values of the equivalent circuit parameters for the magnitude of the impedance if the device is 100Ω under DC conditions and 1257Ω at 100 GHz. Assume the resonance frequency point to be at 1.125 GHz.
- 1.25 A quadrupole capacitor as shown in Figure 1-18 consists of four equal-size electrodes of 25 mils square separated 5 mils from a common ground plane through a dielectric medium of a relative dielectric constant of 11. Find the individual and total capacitance that can be achieved.

1.26 Consider the following diode circuit.



As will be shown in Chapter 6, a reverse biased diode can be represented as a series combination of a resistor R_S and junction capacitor C , where the capacitance is bias dependent. Its value is approximately given by the expression

$$C = C_0 \left(1 - \frac{V_{\text{bias}}}{V_{\text{diff}}}\right)^{-1/2}$$

Assuming that RFC and blocking capacitor C_B have infinite values, find the biasing voltage such that the circuit exhibits a resonance at the frequency of 1 GHz. The diode is characterized as follows: $C_0 = 10 \text{ pF}$, $R_S = 3 \Omega$, and barrier voltage $V_{\text{diff}} = 0.75 \text{ V}$.

Transmission Line Analysis

As we already know, higher frequencies imply decreasing wavelengths. The consequence for an RF circuit is that voltages and currents no longer remain spatially uniform when compared to the geometric size of the discrete circuit elements: They have to be treated as propagating waves. Since Kirchhoff's voltage and current laws do not account for these spatial variations, we must significantly modify the conventional lumped circuit analysis.

The purpose of this chapter is to outline the physical reason for transitioning from lumped to distributed circuit representation and, in the process, develop one of the most useful equations: the spatially dependent impedance representation of a generic RF transmission line configuration. The application of this equation to the analysis and design of high-frequency circuits is going to assume central importance in subsequent chapters. Developing the background of transmission line theory in this chapter, we have purposely attempted to minimize (albeit not eliminate) the reliance on electromagnetics. The motivated reader who would like to delve deeper into the concepts of electromagnetic wave theory is referred to a host of excellent books listed at the end of this chapter.

2.1 Why Transmission Line Theory?

Let us once again return to the wave field representation (1.1a): $E_x = E_{0x} \cos(\omega t - \beta z)$. Here we have an x -directed electric field propagating in the positive z -direction. For propagation in free space the orthogonality between electric field and direction of propagation is always assured. If, on the other hand, we assume that the wave is confined to a conducting medium that is aligned with the z -axis, we will find that the electric field has a longitudinal component E_z that, when integrated in z -direction, gives us a voltage drop (i.e., $V = -\int E_z dl_z$, where dl_z is the line element in the

z -direction). Let us now consider more closely the argument of the cosine term in (1.1a). It couples space and time in such a manner that the sinusoidal space behavior is characterized by the wavelength λ along the z -axis. Moreover, the sinusoidal temporal behavior can be quantified by the time period $T = 1/f$ along the *time*-axis. In mathematical terms this leads to the method of characteristics, where the differential change in space over time denotes the speed of evolution, in our case the constant phase velocity in the form v_p :

$$v_p = \frac{\omega}{\beta} = \lambda f = \frac{1}{\sqrt{\epsilon\mu}} = \frac{c}{\sqrt{\epsilon_r\mu_r}} \quad (2.1)$$

For a frequency of, let us say, $f = 1$ MHz and medium parameters of $\epsilon_r = 10$ and $\mu_r = 1$ ($v_p = 9.49 \times 10^7$ m/s), a wavelength of $\lambda = 94.86$ m is obtained. This situation is spatially and temporally depicted in Figure 2-1 for the voltage wave $V = -\int \cos(\omega t - \beta z) dz = \sin(\omega t - \beta z)/\beta$.

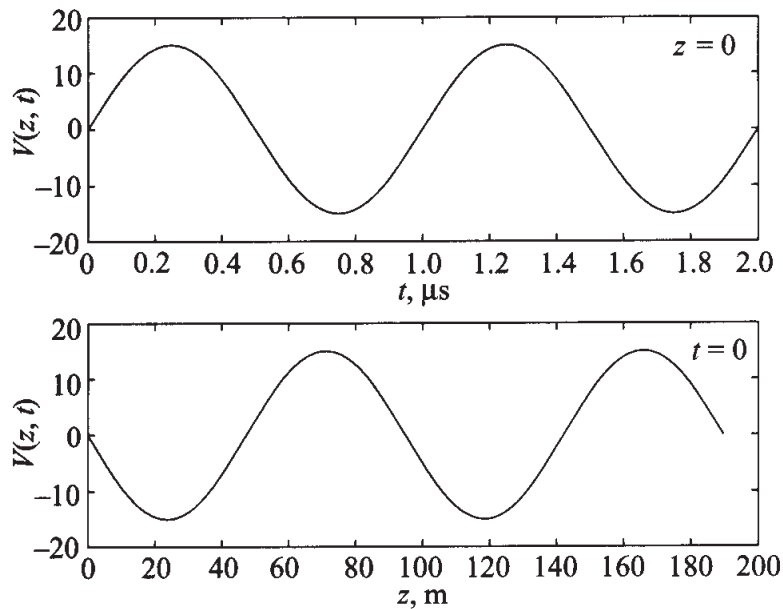


Figure 2-1 Voltage distribution as a function of time ($z = 0$) and as a function of space ($t = 0$).

We next direct our attention to a simple electric circuit consisting of load resistor R_L and sinusoidal voltage source V_G with internal resistance R_G connected to the load by means of 1.5 cm long copper wires. We further assume that those wires are aligned along the z -axis and their resistance is negligible. If the generator is set to a frequency of 1 MHz, then, as computed before, the wavelength will be 94.86 m. A 1.5 cm long wire connecting source with load will experience spatial voltage variations on such a minute scale that they are insignificant.

When the frequency is increased to 10 GHz, the situation becomes dramatically different. In this case the wavelength reduces to $\lambda = v_p/10^{10} \text{ m} = 0.949 \text{ cm}$ and thus is approximately two-thirds the length of the wire. Consequently, if voltage measurements are now conducted along the 1.5 cm wire, location becomes very important in determining the phase reference of the signal. This fact would readily be observed if an oscilloscope were to measure the voltage at the beginning (location A), at the end (location B), or somewhere along the wire, where distance A-B is 1.5 cm measured along the z-axis in Figure 2-2.

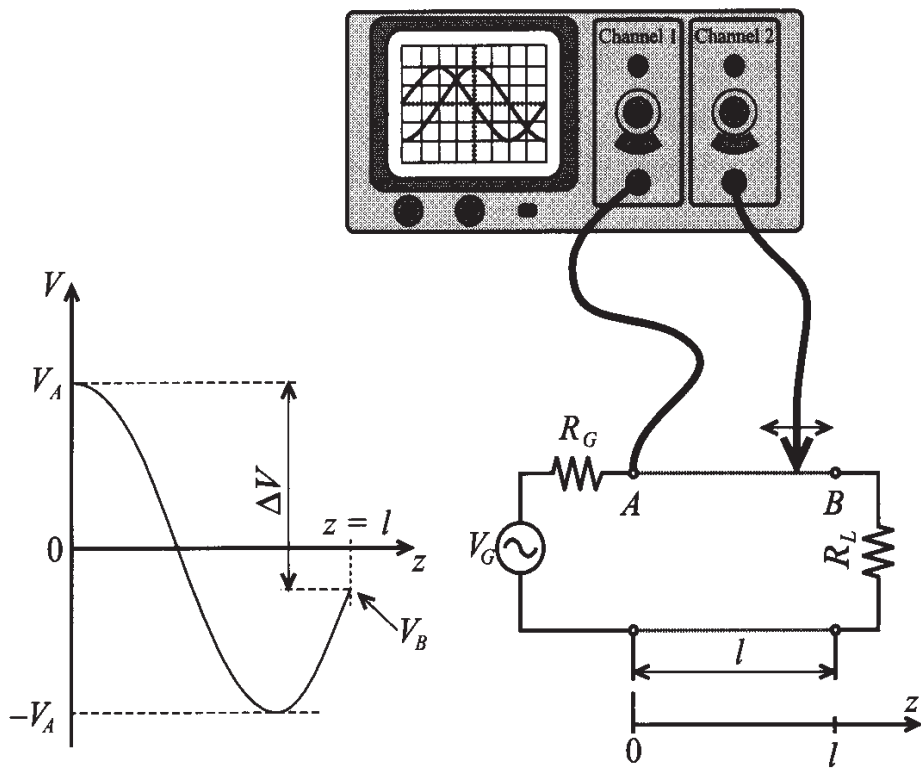


Figure 2-2 Amplitude measurements of 10 GHz voltage signal at the beginning (location A) and somewhere in between a wire connecting load to source.

We are now faced with a dilemma. A simple circuit, seen in Figure 2-2, with a voltage source V_G and source resistance R_G connected to a load resistor R_L through a two-wire line of length l , whose resistance is assumed negligible, can only be analyzed with Kirchhoff's voltage law

$$\sum_{i=1}^N V_i = 0 \quad (2.2)$$

when the line connecting source with load does not possess a spatial voltage variation, as is the case in low-frequency circuits. In (2.2) V_i ($i = 1, \dots, N$) represents the voltage drops over N discrete components. When the frequency attains such high values that the

spatial behavior of the voltage, and also the current, has to be taken into account, Kirchhoff's circuit laws cannot be directly applied. The situation can be remedied, however, if the line is subdivided into elements of small, (mathematically speaking) infinitesimal length, over which voltage and current can be assumed to remain constant, as depicted in Figure 2-3.

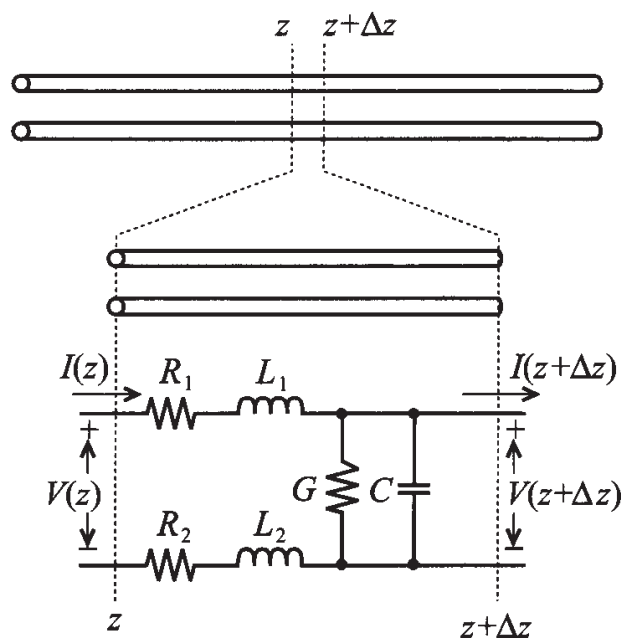


Figure 2-3 Partitioning an electric line into small elements Δz over which Kirchhoff's laws of constant voltage and current can be applied.

For each section of length Δz , we can devise an equivalent electric circuit representation. With reference to our discussions in Chapter 1 it is immediately concluded that there will be some series resistance and inductance associated with each wire. In addition, due to the relative proximity of the two wires, a capacitive effect will also be observed. Since in reality no perfect insulator does exist, a small current flow through the dielectric occurs. A more accurate analysis of all these effects will be given in Section 2.2. At this point we need to stress that equivalent elements, briefly described here, represent only a small segment of the line. To build the complete model of the entire line we would have to replicate Δz a large number of times. Therefore, the transmission line in general cannot be represented in terms of *lumped* parameters, but must be viewed as *distributed* parameters R , L , C , and G , where all circuit parameters are given in terms of unit length.

The question of when a wire, or a discrete component, has to be treated as a transmission line cannot precisely be answered with a single number. The transition from lumped circuit analysis obeying Kirchhoff's laws to distributed circuit theory involving

voltage and current waves depends on the wavelength in comparison with the average component size. The transition takes place gradually as the wavelength becomes increasingly comparable with the circuit elements. As a rule of thumb, *when the average size l_A of the discrete circuit component is more than a tenth of the wavelength, transmission line theory should be applied ($l_A \geq \lambda/10$)*. For the example of the 1.5 cm wire we would determine the following frequency estimation:

$$f = \frac{v_p}{10l} = \frac{9.49 \times 10^7 \text{ m/s}}{0.15 \text{ m}} = 633 \text{ MHz}$$

Can the RF design engineer deal with the simple circuit in Figure 2-2 as a lumped element representation at 700 MHz? Perhaps. Can Kirchhoff's circuit theory be applied to the circuit at 1 GHz? Not without having to take into account a significant loss in precision. Additional reasons why the use of transmission line theory is needed will become apparent in later chapters.

2.2 Examples of Transmission Lines

2.2.1 Two-Wire Lines

The two-wire transmission line discussed in Section 2.1 is one example of a system capable of transporting high-frequency electric energy from one location to another. Unfortunately, it is perhaps the most unsuitable way of transmitting high-frequency voltage and current waves. As shown schematically in Figure 2-4, the two conductors separated over a fixed distance suffer from the drawback that the electric and magnetic field lines emanating from the conductors extend to infinity and thus influence electronic equipment in the vicinity of the line.

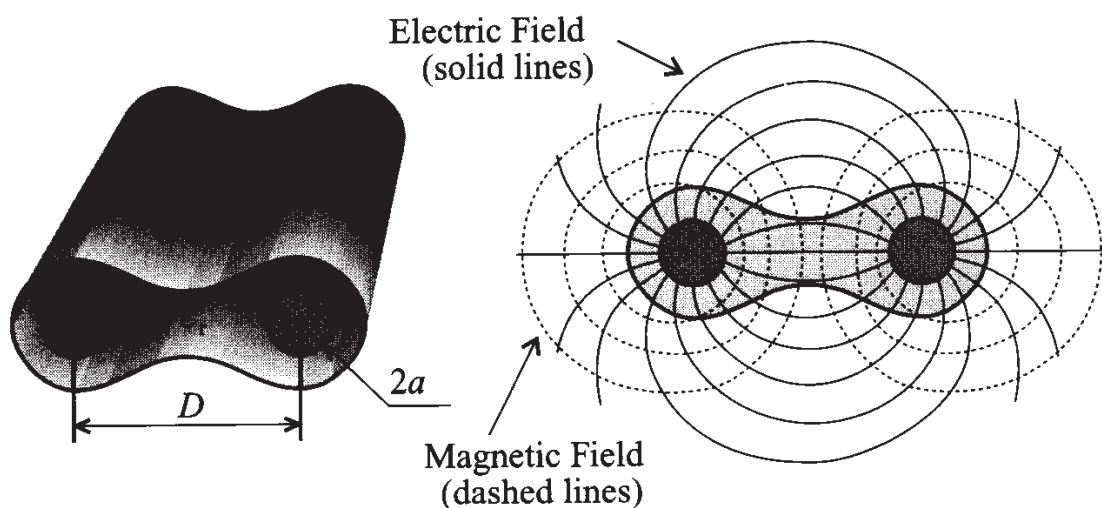


Figure 2-4 Geometry and field distribution in two-wire parallel conductor transmission line.

Further, due to the fact that the wire pair acts as a large antenna, radiation loss tends to be very high. Therefore, the two-wire line finds only limited applications in the RF domain (for instance, when connecting private TV sets to receiving antennas). However, it is commonly used in 50–60 Hz power lines and local telephone connections. Even though the frequency is low, the distance can easily extend over several kilometers, thus making the wire size comparable to the wavelength (as an example, $\lambda = c/f = 3 \times 10^8 / 60 = 5000$ km). Here again, distributed circuit behavior may have to be taken into account.

2.2.2 Coaxial Line

A more common example of a transmission line is the coaxial cable. It is used for almost all cases of externally connected RF systems or measurement equipment at frequencies of up to 10 GHz. As shown in Figure 2-5, a typical coaxial line consists of an inner cylindrical conductor of radius a , an outer conductor of radius b , and a dielectric medium layered in between. Usually the outer conductor is grounded, thus minimizing radiation loss and field interference. Several of the most commonly used dielectric materials include polystyrene ($\epsilon_r = 2.5$, $\tan\Delta_s = 0.0003$ at 10 GHz), polyethylene ($\epsilon_r = 2.3$, $\tan\Delta_s = 0.0004$ at 10 GHz), or teflon ($\epsilon_r = 2.1$, $\tan\Delta_s = 0.0004$ at 10 GHz).

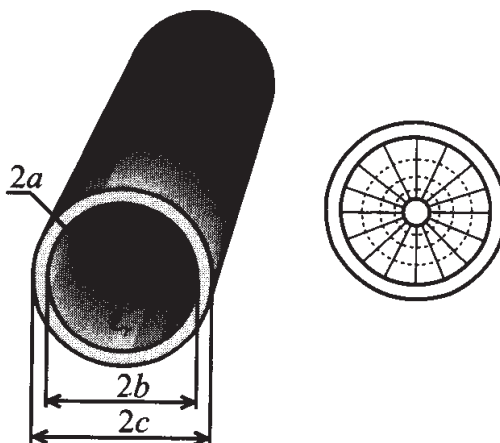
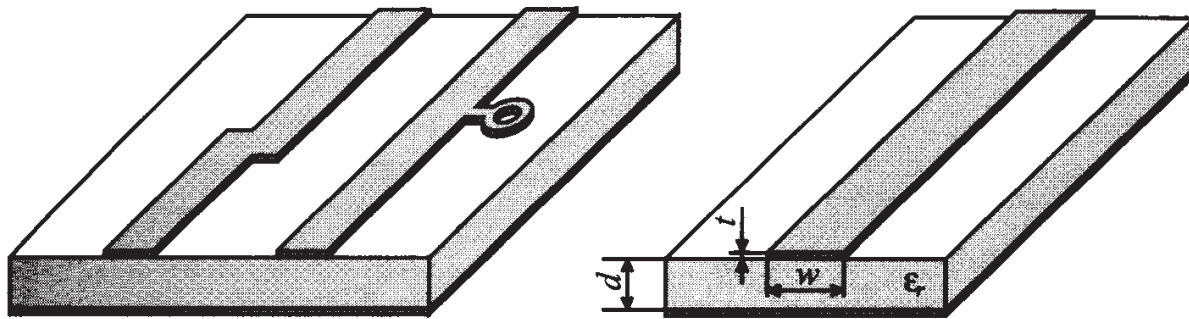


Figure 2-5 Coaxial cable transmission line.

2.2.3 Microstrip Lines

It is a common practice to use planar printed circuit boards (PCBs) as the basic medium to implement most electronic systems. When dealing with actual RF circuits, we need to consider the high-frequency behavior of the conducting strips etched on the PCBs, as depicted qualitatively in Figure 2-6.

The ground plane below the current carrying conductor traces helps prevent excessive field leakage and thus reduces radiation loss. The use of PCBs simplifies the access



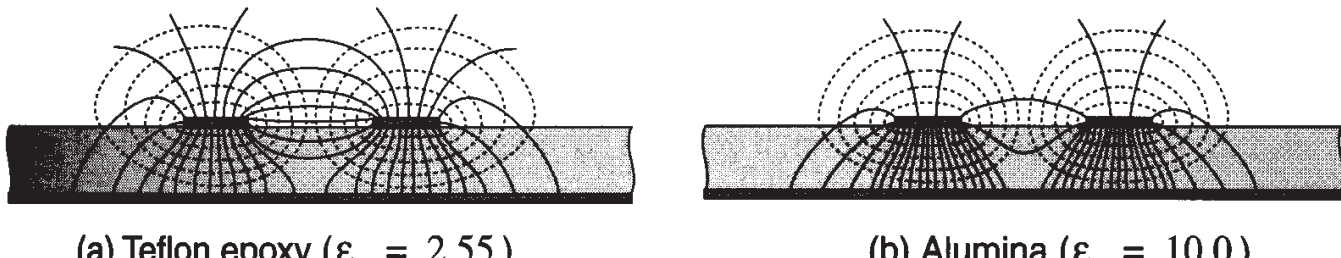
(a) Printed circuit board section

(b) Microstrip line

Figure 2-6 Microstrip transmission line representation.

to the active and passive devices on the board and reduces the cost of the manufacturing process. In addition, PCBs allow the tuning of circuits by simply changing the position of the components and manually adjusting variable tuning capacitors and inductors.

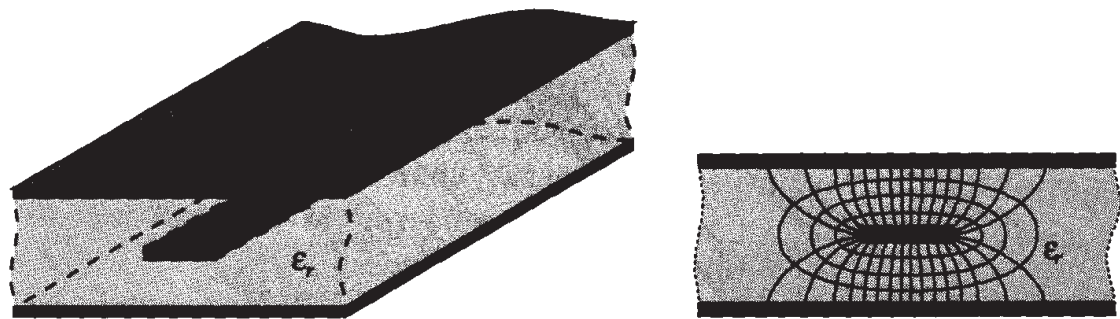
One of the disadvantages of single layered PCBs is that they have rather high radiation loss and are prone to “crosstalk” (interference) between neighboring conductor traces. As noted in Figure 2-7, the severity of field leakage depends on the relative dielectric constants, as shown qualitatively in the electric field line displays for teflon epoxy ($\epsilon_r = 2.55$) and alumina ($\epsilon_r = 10.0$) dielectrics.

(a) Teflon epoxy ($\epsilon_r = 2.55$)(b) Alumina ($\epsilon_r = 10.0$)**Figure 2-7** Electric field leakage as a function of dielectric constants.

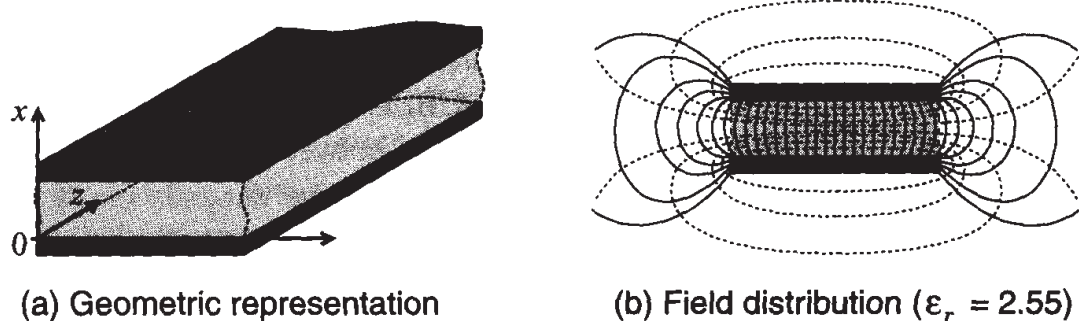
Direct comparison of the field lines in Figure 2-7 suggests that to achieve high board density of the component layout, we should use substrates with high dielectric constants since they minimize field leakage and cross coupling.

Another way to reduce radiation losses and interference is to use multilayer techniques to achieve balanced circuit board designs where the microstrip line is “sandwiched” between two ground planes, resulting in the triple-layer configuration seen in Figure 2-8.

A microstrip configuration that is primarily used for low impedance, high-power applications is the parallel-plate line. Here the current and voltage flow is confined to two plates separated by a dielectric medium. This configuration and the corresponding field distribution are shown in Figure 2-9 for the dielectric medium of teflon epoxy ($\epsilon_r = 2.55$).

(a) Sandwich structure ($\epsilon_r = 2.55$)

(b) Cross-sectional field distribution

Figure 2-8 Triple-layer transmission line configuration.

(a) Geometric representation

(b) Field distribution ($\epsilon_r = 2.55$)**Figure 2-9** Parallel-plate transmission line.

There are many more transmission line configurations used for a number of special-purpose applications. However, a detailed coverage of the pros and cons of all possible combinations would go beyond the objectives of this book.

The preceding transmission line examples all have the commonality that the electric and magnetic field components between the current-carrying conductors are transversely orientated (or polarized); that is, they form a transverse electromagnetic (TEM) field pattern similar to the one shown in Figure 1-3. As mentioned in Chapter 1, the TEM behavior has to be seen in contrast to guided modes, where the electromagnetic wave propagation is accomplished through wave reflections and refractions between conducting plates or indexed dielectric media in optical fibers. The analysis is broken down into so-called transverse magnetic (TM) and transverse electric (TE) modes. Such modes of operation are of major interest in the microwave range for satellite communication, radar, and remote sensing applications. Due to their extremely high frequency of operation, well above the RF range, waveguides and optical fiber cables require special electromagnetic treatment and are not considered further. Instead, we refer the reader to a number of references listed at the end of this chapter.

2.3 Equivalent Circuit Representation

As mentioned previously, voltages and currents are no longer spatially constant on the geometric scale of interest to RF circuit design engineers. As a consequence, Kirchhoff's voltage and circuit laws cannot be applied over the macroscopic line dimension. However, this problem can be circumvented when the transmission line is broken down into smaller (in the limit infinitesimally small) segments. Those segments are still large enough to contain all relevant electric characteristics such as loss, as well as inductive and capacitive line effects. The main advantage of this reduction to a microscopic representation is the fact that a distributed parameter description can now be introduced whose analysis follows Kirchhoff's laws on a microscopic scale. Besides providing an intuitive picture, the approach also lends itself to a two-port network analysis, as discussed in Chapter 4.

To develop an electric model, let us consider once again a two-wire transmission line. As Figure 2-10 indicates, the transmission line is aligned along the z -axis and segmented into elements of length Δz .

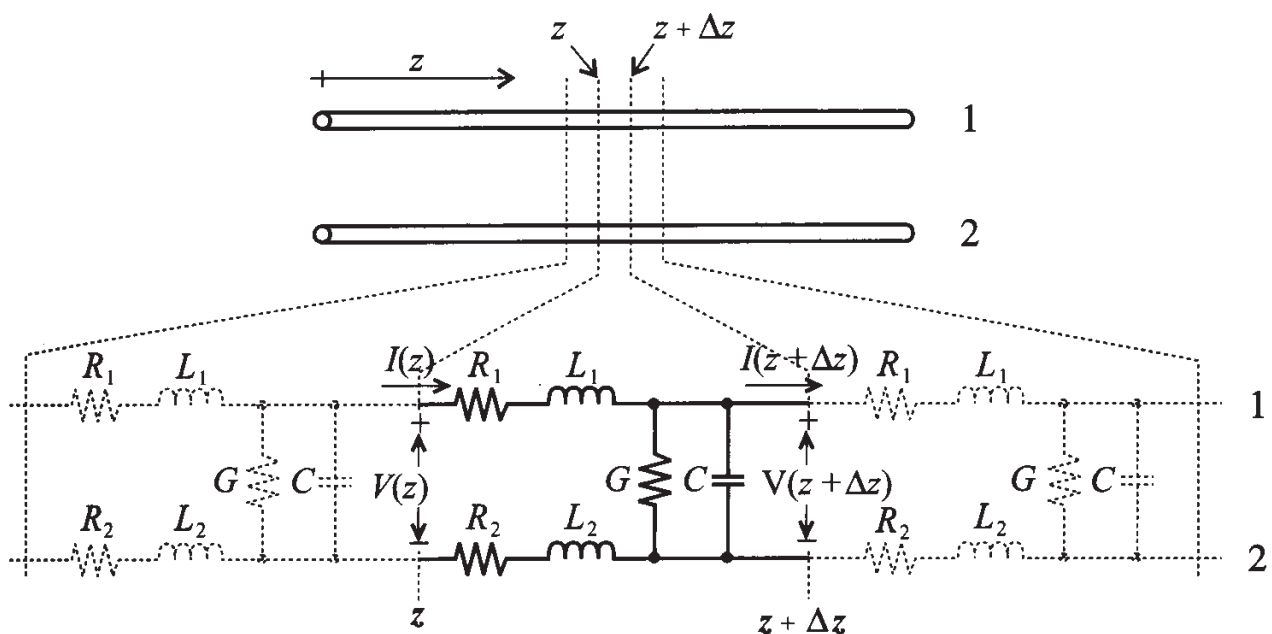


Figure 2-10 Segmentation of two-wire transmission line into Δz -long sections suitable for lumped parameter analysis.

If we focus our attention on a single section residing between z and $z + \Delta z$, we notice that each conductor (1 and 2) is described as a series connection of resistor and inductor (R_1, L_1 , and R_2, L_2). In addition, the charge separation created by conductors 1 and 2 gives rise to a capacitive effect denoted by C . Recognizing that all dielectrics suffer losses (see our discussion in Section 1.4.2), we need to include a

conductance G . Again attention is drawn to the fact that all circuit parameters R , L , C , and G are given in values per unit length.

Similar to the two-wire transmission line, the coaxial cable in Figure 2-11 can also be recognized as a two-conductor configuration with the same lumped parameter representation.

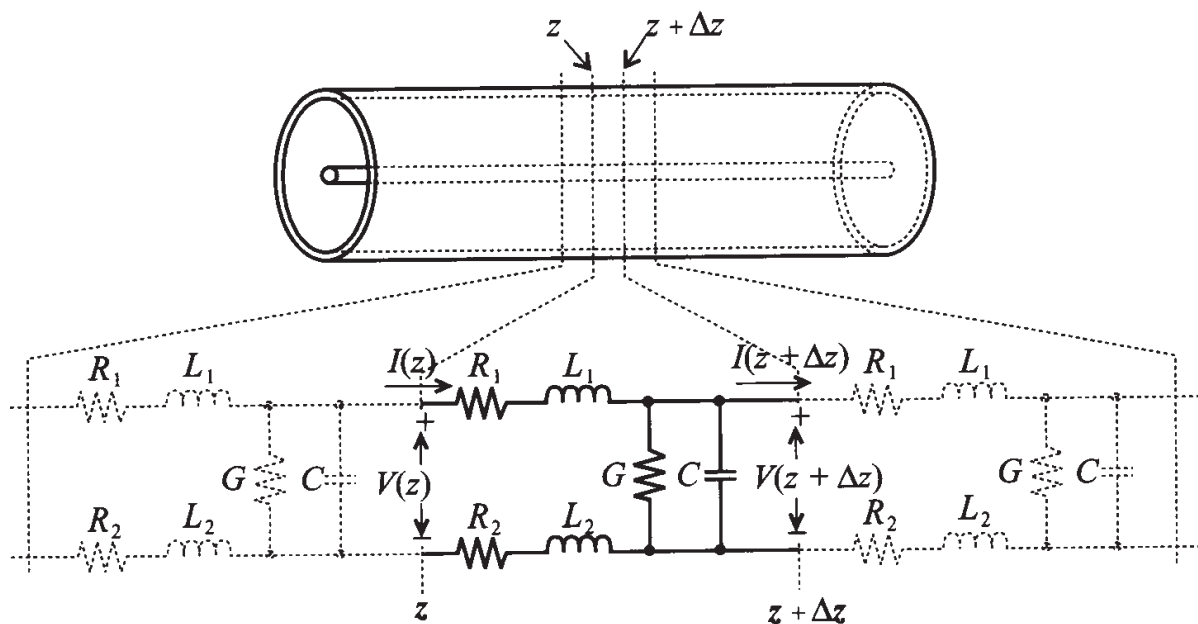


Figure 2-11 Segmentation of a coaxial cable into Δz length elements suitable for lumped parameter analysis.

A generic form of an electric equivalent circuit is developed as shown in Figure 2-12, where the resistances and inductances of the two conductors are usually combined into single elements. This representation is not suitable for all transmission line applications. For instance, when dealing with transient wave propagation and signal integrity issues of inductive and capacitive crosstalks, it generally makes more sense to retain the parameter representation shown in Figure 2-11. However, for our treatment of transmission lines we will exclusively use the model shown in Figure 2-12.

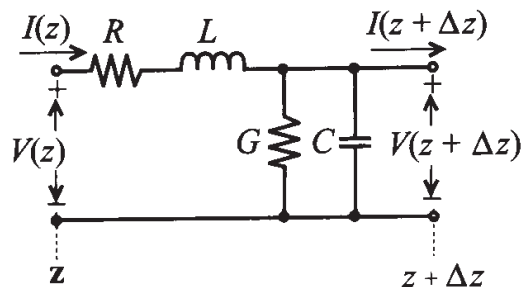


Figure 2-12 Generic electric equivalent circuit representation.

It should be recalled from the discussion in Chapter 1 that the aforementioned R , L , C , and G elements are frequency-dependent parameters that change significantly depending on the operational frequency and the employed transmission line type. Further, L not only incorporates the inductance of the wire (self-inductance; see Section 1.4.3) but also takes into account the mutual inductance between the wires. In general, the self-inductance is so small compared with the mutual inductance that it can be safely neglected. To summarize the advantages of the electric circuit representation, we observe that it

- provides a clear intuitive physical picture
- lends itself to a standardized two-port network representation
- permits the analysis with Kirchhoff's voltage and current laws
- provides building blocks that allow the expansion from microscopic to macroscopic forms

There are also two significant disadvantages worth noting:

- It is basically a one-dimensional analysis that does not take into account field fringing in the plane orthogonal to the direction of propagation and therefore cannot predict interference with other components of the circuit.
- Material-related nonlinearities due to hysteresis effects are neglected.

Despite these disadvantages, the equivalent circuit representation is a powerful mathematical model for describing the characteristic transmission line behavior. With this model in place, we can now embark on developing generalized transmission line equations.

2.4 Theoretical Foundation

2.4.1 Basic Laws

The next question that we should ask ourselves is how to determine the distributed circuit parameters if we know the physical dimensions and electric properties of the transmission line. The answer is provided through the use of two central laws of electromagnetics: Faraday's law and Ampère's law.

Rooted in experimental observations, Faraday's and Ampère's laws establish two fundamental relations linking electric and magnetic field quantities. As such, both laws provide cornerstones of Maxwell's theory by stating so-called source-field relations. In other words, the time-varying electric field as a source gives rise to a rotational magnetic field. Alternatively, the time-varying magnetic field as a source results in a time-varying electric field that is proportional to the rate of change of the magnetic field. The

mutual linkage between electric and magnetic fields is ultimately responsible for wave propagation and traveling voltage and current waves in RF circuits.

By stating Faraday's and Ampère's laws in integral and differential forms, we possess the necessary tools to calculate, at least in principle, the line parameters R , L , C , and G for the electric circuit elements. They are needed to characterize various transmission line systems. By going through the subsequent calculations, we will observe how abstract theoretical laws can be used as a starting point to derive practical circuit parameters for a particular type of transmission line.

Ampère's Law

This fundamental law states that moving charges, which are characterized by the current density \mathbf{J} , give rise to a rotational magnetic field \mathbf{H} surrounding the charge flow as expressed by the integral relation

$$\oint \mathbf{H} \cdot d\mathbf{l} = \iint \mathbf{J} \cdot d\mathbf{S} \quad (2.3)$$

where the line integral is taken along the path characterized by the differential element $d\mathbf{l}$ that defines the edge of the surface element \mathbf{S} in such a manner that the surface \mathbf{S} always stays on the left side. In equation (2.3) the total current density can be written as $\mathbf{J} = \mathbf{J}_0 + \sigma\mathbf{E} + \partial(\epsilon\mathbf{E})/\partial t$. It is comprised of (a) the impressed source current density \mathbf{J}_0 , (b) the conduction current density $\sigma\mathbf{E}$, which is induced by an electric field \mathbf{E} in the conductor and is responsible for conduction losses; and (c) the displacement current density $\partial(\epsilon\mathbf{E})/\partial t$, which is responsible for radiation losses. Here and in the following equations we use again bold letters to denote vector quantities such that

$$\mathbf{E}(\mathbf{r}, t) = E_x(x, y, z, t)\hat{x} + E_y(x, y, z, t)\hat{y} + E_z(x, y, z, t)\hat{z}$$

where E_x , E_y , E_z are the vector components and \hat{x} , \hat{y} , \hat{z} are unit vectors in x , y , z directions in a Cartesian coordinate system. Figure 2-13 illustrates the meaning of equation (2.3).

Perhaps less intuitive than the integral relation, nonetheless perfectly identical to (2.3), is Ampère's law in differential or point form:

$$(\nabla \times \mathbf{H}) \cdot \mathbf{n} = \lim_{\Delta S \rightarrow 0} \frac{1}{\Delta S} \oint \mathbf{H} \cdot d\mathbf{l} = \lim_{\Delta S \rightarrow 0} \frac{1}{\Delta S} \iint_{\Delta S} \mathbf{J} \cdot d\mathbf{S} = \mathbf{J} \cdot \mathbf{n} \quad (2.4)$$

where $\nabla \times$ is the *curl* operator and \mathbf{n} is a unit vector perpendicular to the surface element $\Delta\mathbf{S}$. When using vector components in a rectangular coordinate system, this differential operator can be represented in the matrix form

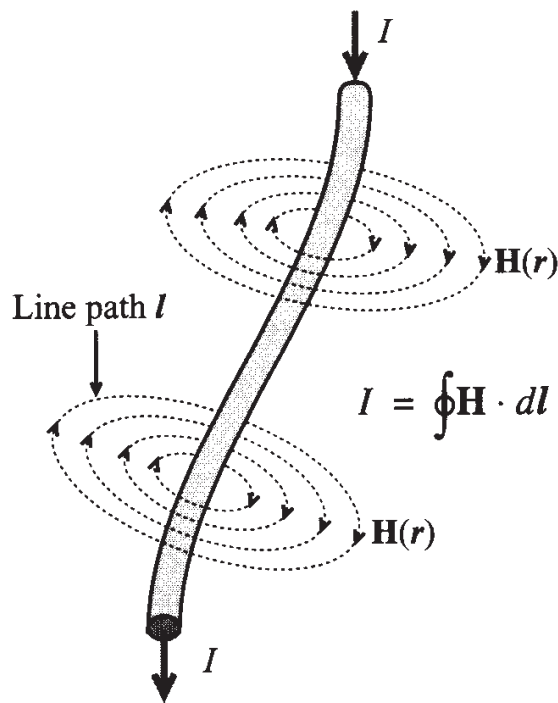


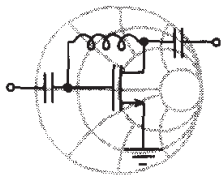
Figure 2-13 Ampère's law linking the current flow to the magnetic field.

$$\nabla \times = \begin{bmatrix} 0 & -\frac{\partial}{\partial z} & \frac{\partial}{\partial y} \\ \frac{\partial}{\partial z} & 0 & -\frac{\partial}{\partial x} \\ -\frac{\partial}{\partial y} & \frac{\partial}{\partial x} & 0 \end{bmatrix} \quad (2.5)$$

Therefore, by applying the *curl* to the vector field \mathbf{H} , we obtain

$$\nabla \times \mathbf{H} = \begin{bmatrix} 0 & -\frac{\partial}{\partial z} & \frac{\partial}{\partial y} \\ \frac{\partial}{\partial z} & 0 & -\frac{\partial}{\partial x} \\ -\frac{\partial}{\partial y} & \frac{\partial}{\partial x} & 0 \end{bmatrix} \begin{Bmatrix} H_x \\ H_y \\ H_z \end{Bmatrix} = \begin{Bmatrix} J_x \\ J_y \\ J_z \end{Bmatrix} \quad (2.6)$$

where H_x, H_y, H_z and J_x, J_y, J_z are x, y , and z components of the magnetic field vector \mathbf{H} , and the current density \mathbf{J} .



RF & MW →

Example 2-1: Magnetic field generated by a constant current flow in a conductor

Plot the graph of the radial magnetic field $H(r)$ inside and outside an infinitely long wire of radius $a = 5$ mm aligned along the z -axis and carrying a DC current of 5 A. The surrounding medium is assumed to be air.

Solution: This is a typical example for Ampère's law in integral form as given by (2.3). Inside the conductor the current density \mathbf{J} is uniform and is equal to $\mathbf{J} = I/(\pi a^2)\hat{z}$. Therefore, the application of (2.3) yields the following result:

$$H2\pi r = \frac{I}{\pi a^2}\pi r^2 \quad \Rightarrow \quad H = \frac{Ir}{2\pi a^2}$$

where $0 \leq r \leq a$. Outside of the conductor the current density is equal to zero and the surface integral in (2.3) gives the total current I flowing through the conductor. Thus, the magnetic field H outside the wire is obtained as

$$H2\pi r = I \quad \Rightarrow \quad H = \frac{I}{2\pi r}$$

where $r \geq a$. The total magnetic field inside and outside of the infinitely long wire is thus

$$H(r) = \begin{cases} \frac{Ir}{2\pi a^2}, & r \leq a \\ \frac{I}{2\pi r}, & r \geq a \end{cases} = \begin{cases} 31.83r \text{ kA/m}, & r \leq 5 \text{ mm} \\ 0.796/r \text{ A/m}, & r \geq 5 \text{ mm} \end{cases}$$

The graph of this radial magnetic field distribution is plotted in Figure 2-14.

We make the important observation that inside the wire the magnetic field linearly increases from the center to the outer con-

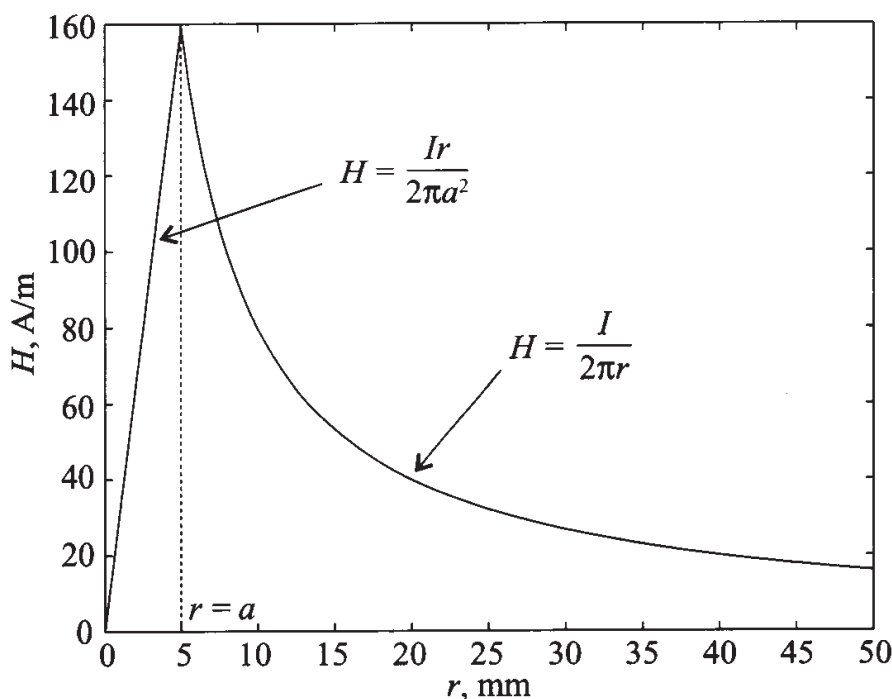


Figure 2-14 Magnetic field distribution inside and outside of an infinitely long wire of radius $a = 5$ mm carrying a current of 5 A.

ductor periphery since more current contributes to the magnetic field.

Faraday's law

This law implies that the time rate of change of the magnetic flux density $\mathbf{B} = \mu \mathbf{H}$ ($\mu = \mu_0 \mu_r$) as a source gives rise to a rotating electric field

$$\oint \mathbf{E} \cdot d\mathbf{l} = -\frac{d}{dt} \iint \mathbf{B} \cdot d\mathbf{S} \quad (2.7)$$

The line integral is again taken along the edge of the surface S as previously described for Ampère's law. The integration of the electric field along a wire loop as shown in Figure 2-15 yields an induced voltage $V = -\oint \mathbf{E} \cdot d\mathbf{l} = \frac{d}{dt} \iint \mathbf{B} \cdot d\mathbf{S}$.

Similar to Ampère's law, we can convert (2.7) into a differential, or point form:

$$\nabla \times \mathbf{E} = -\frac{\partial \mathbf{B}}{\partial t} \quad (2.8)$$

Equation (2.8) makes it clear that we need a time-dependent magnetic flux density to obtain an electric field, which in turn creates a magnetic field according to Ampère's law.

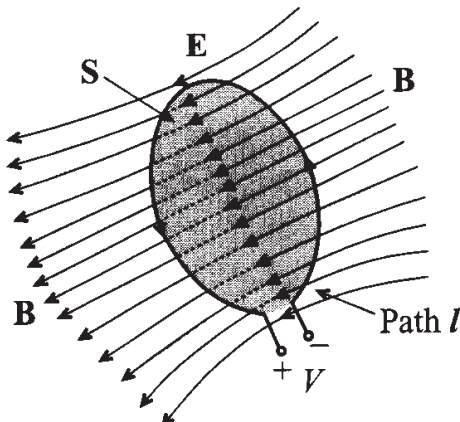
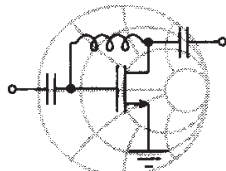


Figure 2-15 The time rate of change of the magnetic flux density induces a voltage.



RF & MW →

Example 2-2: Induced voltage in a stationary wire loop

Find the induced voltage of a thin wire loop of radius $a = 5 \text{ mm}$ in air subjected to a time-varying magnetic field $H = H_0 \cos(\omega t)$, where $H_0 = 5 \text{ A/m}$, and the operating frequency is $f = 100 \text{ MHz}$.

Solution: The voltage induced in the loop is equal to the line integral of the electrical field \mathbf{E} along the loop. Employing Faraday's law (2.7) results in the following:

$$V = -\oint \mathbf{E} \cdot d\mathbf{l} = \frac{d}{dt} \iint \mathbf{B} \cdot d\mathbf{S}$$

Since the surrounding medium is air, the relative permeability μ_r equals unity and the magnetic flux density is $\mathbf{B} = \mu_0 \mathbf{H} = \mu_0 H_0 \cos(\omega t) \hat{z}$. Substituting \mathbf{B} into the preceding integral leads to an expression for the induced voltage V in the loop:

$$V = \frac{d}{dt} \iint \mathbf{B} \cdot d\mathbf{S} = \frac{d}{dt} \mu_0 H_0 \cos(\omega t) \pi a^2 = -\pi a^2 \omega \mu_0 H_0 \sin(\omega t)$$

This can be further simplified to $V = -0.31 \sin(6.28 \times 10^8 t) \text{ V}$.

The result of this example is also known as the transformer form of Faraday's law whereby a time-varying field produced by a primary coil induces a voltage response in a secondary loop.

2.5 Circuit Parameters for a Parallel Plate Transmission Line

Our goal is to compute the line parameters R , L , C , and G for a section of a transmission line seen in Figure 2-16. To avoid any confusion we explicitly use σ_{cond} and $\sigma_{\text{dielectric}}$ to denote, respectively, conductivity in the conductor and conductivity in the dielectric medium.

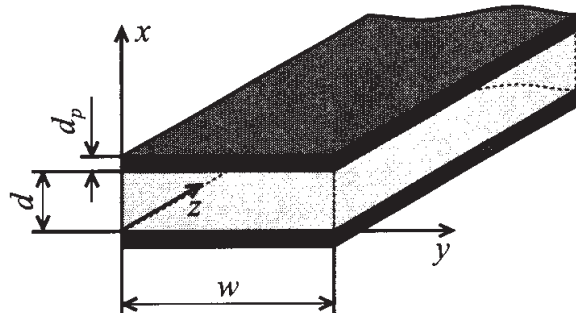


Figure 2-16 Parallel-plate transmission line geometry. The plate width w is large compared with the separation d .

For the analysis we must assume that the plate width w is large compared with the plate separation d for a one-dimensional analysis to apply. Further, we assume that the skin depth δ is small compared to the thickness d_p of the plates to simplify the derivation of the parameters. Under these conditions we are able to cast the electric and magnetic fields in the conducting plates in the form

$$\mathbf{E} = \hat{z} E_z(x, z) e^{j\omega t} \quad (2.9a)$$

$$\mathbf{H} = \hat{y} H_y(x, z) e^{j\omega t} \quad (2.9b)$$

The term $e^{j\omega t}$ represents the time dependence of the sinusoidal electric and magnetic fields, and phasors $E_z(x, z)$ and $H_y(x, z)$ encode spatial variations. We do not have any field dependency upon y , because the plates are assumed very wide, and thus the electromagnetic fields do not change appreciably along the y -axis. Application of the differential forms of Faraday's and Ampère's laws

$$\nabla \times \mathbf{E} = -\mu \frac{\partial \mathbf{H}}{\partial t} \quad (2.10)$$

$$\nabla \times \mathbf{H} = \sigma_{\text{cond}} \mathbf{E} \quad (2.11)$$

results in two differential equations:

$$\begin{bmatrix} 0 & \frac{\partial}{\partial z} & \frac{\partial}{\partial y} \\ \frac{\partial}{\partial z} & 0 & -\frac{\partial}{\partial x} \\ -\frac{\partial}{\partial y} & \frac{\partial}{\partial x} & 0 \end{bmatrix} \begin{Bmatrix} 0 \\ 0 \\ E_z \end{Bmatrix} = -\frac{\partial E_z}{\partial x} = -\mu \frac{d}{dt} \begin{Bmatrix} 0 \\ H_y \\ 0 \end{Bmatrix} = -\mu \frac{dH_y}{dt} = -j\omega \mu H_y \quad (2.12)$$

and

$$\begin{bmatrix} 0 & \frac{\partial}{\partial z} & \frac{\partial}{\partial y} \\ \frac{\partial}{\partial z} & 0 & -\frac{\partial}{\partial x} \\ -\frac{\partial}{\partial y} & \frac{\partial}{\partial x} & 0 \end{bmatrix} \begin{Bmatrix} 0 \\ H_y \\ 0 \end{Bmatrix} = -\frac{\partial H_y}{\partial x} = \sigma_{\text{cond}} \begin{Bmatrix} 0 \\ 0 \\ E_z \end{Bmatrix} = \sigma_{\text{cond}} E_z \quad (2.13)$$

By differentiating (2.13) with respect to x and substituting (2.12), we find

$$\frac{d^2 H_y}{dx^2} = j\omega \sigma_{\text{cond}} \mu H_y = p^2 H_y \quad (2.14)$$

where $p^2 = j\omega \sigma_{\text{cond}} \mu$. The general solution for this second-order ordinary differential equation (2.14) is $H_y(x) = Ae^{-px} + Be^{px}$. The coefficients A and B are integration constants. We can now perform the following manipulations:

$$p = \sqrt{j\omega \sigma_{\text{cond}} \mu} = \sqrt{j\omega \sigma_{\text{cond}} \mu} = (1+j)\sqrt{(\omega \sigma_{\text{cond}} \mu)/2} = (1+j)/\delta \quad (2.15)$$

where $\delta = \sqrt{2/(\omega \sigma_{\text{cond}} \mu)}$ is recognized as the skin depth. Since p has a positive real component, constant A should be equal to zero to satisfy the condition that the magnetic field in the lower plate must decay in amplitude for negative x . A similar argument can be made for the upper plate by setting $B = 0$. Thus, for the magnetic field in the lower conducting plate we have a simple exponential solution

$$H_y = H_0 e^{px} = H_0 e^{(1+j)x/\delta} \quad (2.16)$$

where $B = H_0$ is a yet to be determined constant factor. Since the current density can be written as

$$J_z = \sigma E_z = \frac{\partial H_y}{\partial x} = \frac{(1+j)H_0}{\delta} e^{(1+j)x/\delta} \quad (2.17)$$

we are now able to relate the current density J_z to the total current flow I in the lower plate

$$I = \iint_S J_z dx dy = w \int_{-d_p}^0 J_z dx = w H_0 e^{(1+j)x/\delta} \Big|_{-d_p}^0 = w H_0 (1 - e^{-(1+j)d_p/\delta}) \quad (2.18)$$

where S is the cross sectional area of the lower plate and d_p is the thickness of that plate. Since we assume that $d_p \gg \delta$, the exponential term in (2.18) drops out and $I = w H_0$. From this we conclude that $H_0 = I/w$. The electric field at the surface of the conductor ($x = 0$) can be specified as

$$E_z(0) = \frac{J_z(0)}{\sigma_{\text{cond}}} = \frac{(1+j)H_0}{\sigma_{\text{cond}}\delta} = \frac{1+j}{\sigma_{\text{cond}}\delta} \frac{I}{w} \quad (2.19)$$

Equation (2.19) allows us to compute the surface impedance per unit length, Z_s , by eliminating the current I as follows:

$$Z_s = E_z/I = \frac{1}{w\sigma_{\text{cond}}\delta} + \frac{j}{w\sigma_{\text{cond}}\delta} = R_s + j\omega L_s \quad (2.20)$$

The surface resistance and surface inductance per unit length are then identified as

$$R_s = \frac{1}{w\sigma_{\text{cond}}\delta} \quad (2.21)$$

$$L_s = \frac{1}{w\sigma_{\text{cond}}\omega\delta} \quad (2.22)$$

Both are dependent on the skin depth δ . It is important to point out that (2.21) and (2.22) apply for a single conductor. Since we have two conductors in our system (upper and lower plates) the total series resistance and inductance per unit length will be twice the value of R_s and L_s , respectively.

To obtain the inductive and capacitive behavior of the mutual line coupling, we must employ the definitions of capacitance and inductance:

$$C = \frac{Q}{V} = \frac{\oint \mathbf{D} \cdot d\mathbf{S}}{V} = \frac{\epsilon \iint E_x dS}{\int E_x dl_x} = \frac{\epsilon E_x w}{E_x d} = \frac{\epsilon w}{d} \quad (2.23)$$

and

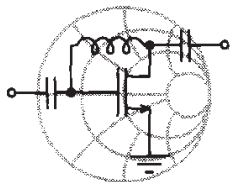
$$L = \frac{\iint \mathbf{B} \cdot d\mathbf{S}}{I} = \frac{\iint \mu H_y dS}{I} = \frac{\mu H_y d}{I} = \frac{\mu H_y d}{H_y w} = \frac{\mu d}{w} \quad (2.24)$$

where we have used the result of (2.18) to compute the current $I = wH_y$. Both in (2.23) and (2.24) the capacitance and inductance are given per unit length.

Finally, we can express the conductance G in a similar way as derived in (2.23):

$$G = \frac{\iint \mathbf{J} \cdot d\mathbf{S}}{V} = \frac{\sigma_{\text{diel}} \iint E_x dS}{\int E_x dl} = \frac{\sigma_{\text{diel}} E_x w}{E_x d} = \frac{\sigma_{\text{diel}} w}{d} \quad (2.25)$$

Thus we have succeeded in deriving all relevant parameters for the parallel-plate transmission line. From a practical point of view, at RF frequencies the magnitude of L_s is typically much smaller than L and therefore is neglected.



RF & MW →

Example 2-3: Line parameters of a parallel-plate transmission line

For a parallel copper-plate transmission line operated at 1 GHz, the following parameters are given: $w = 6 \text{ mm}$, $d = 1 \text{ mm}$, $\epsilon_r = 2.25$, and $\sigma_{\text{diel}} = 0.125 \text{ mS/m}$. Find the line parameters R , L , G , and C per unit length.

Solution: The skin depth for copper with conductivity $\sigma_{\text{cond}} = 64.516 \times 10^6 \Omega^{-1} \text{m}^{-1}$ at operating frequency of 1 GHz is $\delta = 1/\sqrt{\pi\sigma_{\text{cond}}\mu_0 f} = 1.98 \mu\text{m}$, which is assumed to be much smaller than the thickness of the conductor. Therefore, the resistance of each plate is determined by (2.21). Since we have two plates, the total resistance is $R = 2R_s = 2/(w\sigma_{\text{cond}}\delta) = 2.6 \Omega/\text{m}$. The series inductance due to the skin effect is $L_s = 2/(w\sigma_{\text{cond}}\omega\delta) = 0.42 \text{ nH/m}$, where the factor 2 takes into account both plates. The mutual inductance between plates is determined by (2.24) and for our problem is equal to $L = 209.4 \text{ nH/m}$. As seen, the series inductance is much smaller than the mutual inductance and therefore can safely be neglected. According to

(2.23), the capacitance of the line is given by $C = (\epsilon_0 \epsilon_r w)/d = 119.5 \text{ pF/m}$. Finally, the conductance G is determined from (2.25) and equals $G = 0.75 \text{ mS/m}$.

The RF surface resistance due to the skin depth phenomenon does, in general, contribute much more significantly to the line losses than does the DC resistance.

2.6 Summary of Different Line Configurations

The previous computations were carried out for the relatively simple case of a parallel-plate transmission line. Similar analyses apply when dealing with more complicated line geometries, such as coaxial cables and twisted wire pairs. Table 2-1 summarizes the three common transmission line types.

Table 2-1 Transmission line parameters for three line types

| Parameter | Two-Wire Line | Coaxial Line | Parallel-Plate Line | Unit |
|-----------|---|---|---|-------------------|
| R | $\frac{1}{\pi a \sigma_{\text{cond}} \delta}$ | $\frac{1}{2\pi \sigma_{\text{cond}} \delta} \left(\frac{1}{a} + \frac{1}{b} \right)$ | $\frac{2}{w \sigma_{\text{cond}} \delta}$ | Ω/m |
| L | $\frac{\mu}{\pi} \text{acosh}\left(\frac{D}{2a}\right)$ | $\frac{\mu}{2\pi} \ln\left(\frac{b}{a}\right)$ | $\mu \frac{d}{w}$ | H/m |
| G | $\frac{\pi \sigma_{\text{diel}}}{\text{acosh}(D/(2a))}$ | $\frac{2\pi \sigma_{\text{diel}}}{\ln(b/a)}$ | $\sigma_{\text{diel}} \frac{w}{d}$ | S/m |
| C | $\frac{\pi \epsilon}{\text{acosh}(D/(2a))}$ | $\frac{2\pi \epsilon}{\ln(b/a)}$ | $\epsilon \frac{w}{d}$ | F/m |

The geometric dimensions for the two-wire (D, a), coaxial (a, b), and parallel-plate (w, d) lines are depicted in Figures 2-4, 2-5, and 2-16. The term acosh in Table 2-1 denotes the inverse hyperbolic cosine function. For more complex transmission line configurations, significant mathematical effort must be exerted, and resorting to numerical analysis procedures is often the only available solution. This is seen when dealing with microstrip transmission lines (Section 2.8).

2.7 General Transmission Line Equation

2.7.1 Kirchhoff Voltage and Current Law Representations

Having developed the background of Faraday's and Ampère's laws in Section 2.4.1, we are well positioned to exploit both equations from a circuit point of view. This is identical with applying Kirchhoff's voltage and current laws (KVL and KCL, respectively) to the loop and node a shown in Figure 2-17.

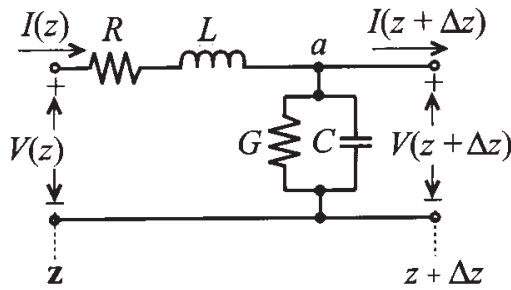


Figure 2-17 Segment of a transmission line with voltage loop and current node.

Adopting phasor notation, we can use Kirchhoff's voltage law to conclude

$$(R + j\omega L)I(z)\Delta z + V(z + \Delta z) = V(z) \quad (2.26)$$

which is re-expressed as a differential equation by combining the voltage drop on either side of the differential transmission line segment into a differential quotient:

$$\lim_{\Delta z \rightarrow 0} \left(-\frac{V(z + \Delta z) - V(z)}{\Delta z} \right) = -\frac{dV(z)}{dz} = (R + j\omega L)I(z) \quad (2.27)$$

or

$$-\frac{dV(z)}{dz} = (R + j\omega L)I(z) \quad (2.28)$$

where R and L are the combined resistance and inductance of the two lines. Applying Kirchhoff's current law to the designated node a in Figure 2-17 yields

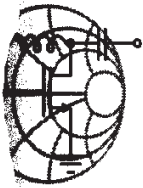
$$I(z) - V(z + \Delta z)(G + j\omega C)\Delta z = I(z + \Delta z) \quad (2.29)$$

which can be converted into a differential equation similar to (2.27). The result is

$$\lim_{\Delta z \rightarrow 0} \frac{I(z + \Delta z) - I(z)}{\Delta z} = \frac{dI(z)}{dz} = -(G + j\omega C)V(z) \quad (2.30)$$

Equations (2.28) and (2.30) are coupled first-order differential equations. They can also be derived from a more fundamental point of view, revealing the definitions of R , G , C ,

and L as discussed in Example 2-4 for the previously analyzed parallel-plate transmission line example.



RF & MW →

Example 2-4: Derivation of the parallel-plate transmission line equations

Establish the transmission line equations for the parallel-plate conductors.

Solution: The purpose of this example is to show how the transmission line equations (2.28) and (2.30) can be derived from the fundamental physical concepts of Faraday's and Ampère's laws.

Let us first consider Faraday's law (2.7). The surface element over which the line and surface integrations are performed is shown as a shadowed area in Figure 2-18.

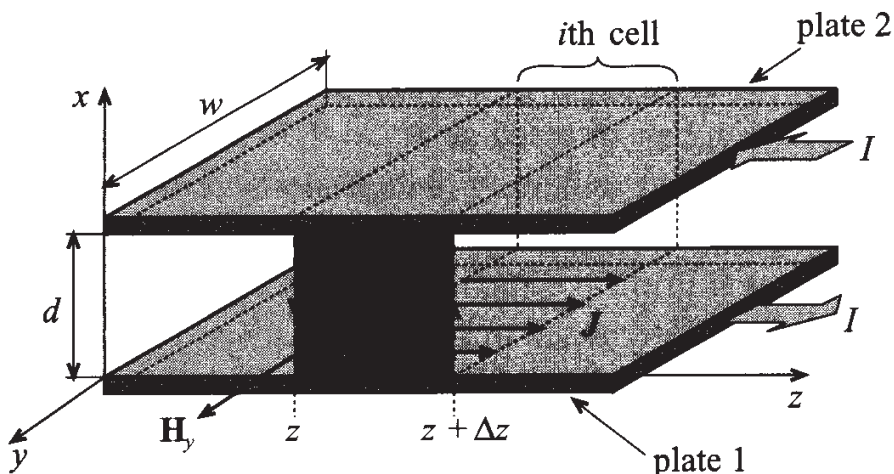


Figure 2-18 Integration surface element for Faraday's law application.

The line integral in (2.7) is taken along the edge of the shaded region with the integration direction denoted by arrows in Figure 2-18. Evaluation of this line integration yields the following contributions:

$$\oint_i \mathbf{E} \cdot d\mathbf{l} = \mathbf{E}^1 \cdot \hat{\mathbf{z}} \Delta z + \mathbf{E}(z + \Delta z) \cdot \hat{\mathbf{x}} d - \mathbf{E}^2 \cdot (-\hat{\mathbf{z}}) \Delta z + \mathbf{E}(z) \cdot (-\hat{\mathbf{x}}) d$$

where $E_z^1 = \mathbf{E}^1 \cdot \hat{\mathbf{z}}$ and $E_z^2 = \mathbf{E}^2 \cdot \hat{\mathbf{z}}$ are the electric fields in the lower (denoted by index 1) and upper (index 2) plates, respectively; and $E_x(z) = \mathbf{E}(z) \cdot \hat{\mathbf{x}}$ and $E_x(z + \Delta z) = \mathbf{E}(z + \Delta z) \cdot \hat{\mathbf{x}}$ are the electric fields in the dielectric medium between locations z and $z + \Delta z$. It is important to note that the direction of the electric field in the upper conductor is opposite to that of the electric field in the lower conductor, whereas the direction of the field in the dielectric is the same regardless of position. The minus sign in front of the unit vectors indicates that the integration is performed counterclockwise. Combining terms, we obtain

$$\oint_i \mathbf{E} \cdot d\mathbf{l} = E_z^1 \Delta z + E_z^2 \Delta z + E_x(z + \Delta z) d - E_x(z) d$$

Since the magnetic field in the dielectric is assumed uniform, the integration over the surface in (2.7) gives

$$\iint \mu \mathbf{H} \cdot d\mathbf{S} = \mu H_y \Delta z d$$

Substitution of these two integrals into (2.7) results in

$$E_z^1 \Delta z + E_z^2 \Delta z + E_x(z + \Delta z) d - E_x(z) d = -\frac{d}{dt} \mu H_y \Delta z d$$

Similar to discussions in Section 2.5, the magnetic field in the dielectric can be expressed as $H_y = I/w$. The electric field in the conductor at high frequency is dependent on the skin effect and is $E_z^1 = E_z^2 = I/(w\sigma_{\text{cond}}\delta) + jI/(w\sigma_{\text{cond}}\delta) = E_z$. At low frequency, the skin effect does not affect the electric field behavior. The field is solely determined by the DC resistivity of the plates and current I : $E_z = I/(w\sigma_{\text{cond}}d_p)$. Since we are primarily concerned with the high-frequency performance, we must assume that the skin depth δ is much smaller than the thickness of the plates. Thus, d_p has to be replaced with δ . Combining expressions for H_y and E_z , and taking into account the relation for the potential between the plates, $V = E_x d$, we obtain

$$2\left(\frac{I}{w\sigma_{\text{cond}}\delta} + \frac{jI}{w\sigma_{\text{cond}}\delta}\right)\Delta z + V(z + \Delta z) - V(z) = -\mu \frac{d\Delta z}{w} \frac{dI}{dt} = -j\omega \mu \frac{d\Delta z}{w} I$$

or

$$2R_s I + j\omega I(L + 2L_s) = -\frac{V(z + \Delta z) - V(z)}{\Delta z} = -\frac{\partial V}{\partial z}$$

where $R_s = 1/(w\sigma_{cond}\delta)$ is the surface resistance of the plates, $L_s = 1/(w\sigma_{cond}\omega\delta)$ is the high-frequency self-inductance of the plates, and $L = \mu d/w$ is the mutual inductance between both plate conductors.

For the application of Ampère's law (2.3) we use the surface element shown in Figure 2-19.

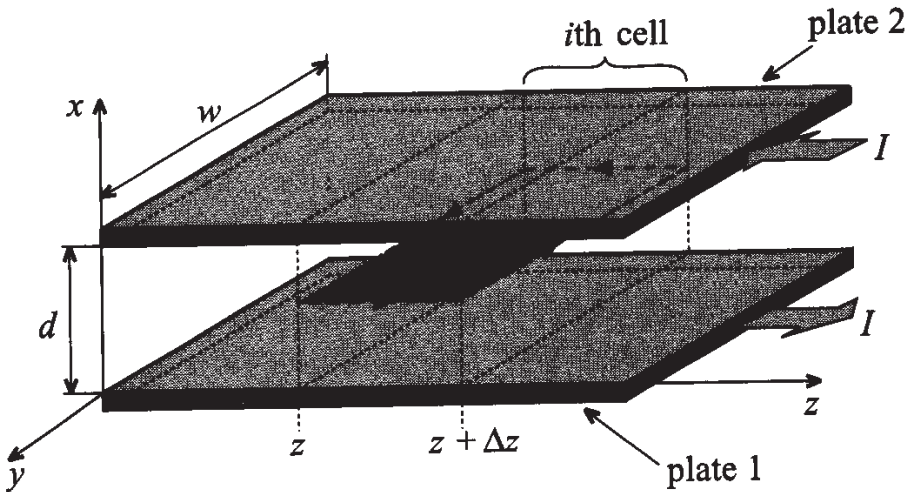


Figure 2-19 Surface element used to apply Ampère's law.

The surface integral of the current density \mathbf{J} in the dielectric medium results in the following expression

$$\iint \mathbf{J} \cdot d\mathbf{S} = J_x \Delta z w = \sigma_{dielectric} E_x w \Delta z + \epsilon \frac{\partial E_x}{\partial t} w \Delta z$$

where the $\sigma_{dielectric} E_x w \Delta z$ term represents the conduction current in the dielectric, and $\epsilon (\partial E_x / \partial t) w \Delta z$ is the contribution of the displacement current. The line integration of the magnetic field yields

$$\oint \mathbf{H} \cdot d\mathbf{l} = -H_y(z + \Delta z)w + H_y(z)w = -I(z + \Delta z) + I(z)$$

Taking into account the relation between the electric field and the potential drop V between z and $z + \Delta z$, that is, $E_x = V/d$, we combine both integrals:

$$\frac{\sigma_{dielectric} w}{d} V + \frac{\epsilon w}{d} \frac{dV}{dt} = -\frac{I(z + \Delta z) - I(z)}{\Delta z}$$

or, after introducing the differential quotient,

$$-\frac{\partial I}{\partial z} = \frac{\sigma_{dielectric} w}{d} V + \frac{\epsilon w}{d} \frac{dV}{dt} = \frac{\sigma_{dielectric} w}{d} V + \frac{\epsilon w}{d} j\omega V = (G + j\omega C)V$$

Thus, we succeeded in deriving the equations for the parallel-plate transmission line. To obtain the voltage and current distribution of such a line, the following system of coupled first-order differential equations must be solved:

$$\left\{ \begin{array}{l} -\frac{\partial V}{\partial z} = [2R_s + j\omega(L + 2L_s)]I \\ -\frac{\partial I}{\partial z} = (G + j\omega C)V \end{array} \right.$$

Usually, the self-inductance due to the skin effect L_s is much smaller than the mutual inductance L and is often neglected.

This example underscores the effort and assumptions required to develop closed-form expressions for the parallel-plate transmission line. However, if w is comparable in size to d , the preceding treatment breaks down and one has to resort to numerical simulations.

2.7.2 Traveling Voltage and Current Waves

The solution of equations (2.28) and (2.30) is greatly facilitated if these first-order differential equations are decoupled. This can be accomplished by spatially differentiating both sides of (2.28) and substituting (2.30) for the space derivative of the current. The result is a standard second-order differential equation

$$\frac{d^2V(z)}{dz^2} - k^2V(z) = 0 \quad (2.31)$$

describing the voltage behavior in phasor form. Here the factor k is known as a complex propagation constant

$$k = k_r + jk_i = \sqrt{(R + j\omega L)(G + j\omega C)} \quad (2.32)$$

that depends on the type of transmission line. For simple line configurations, Table 2-1 provides explicit parameters. Reversing the order of decoupling by differentiating (2.30) and substituting (2.28) results in an identical differential equation describing the current:

$$\frac{d^2 I(z)}{dz^2} - k^2 I(z) = 0 \quad (2.33)$$

Solutions to these decoupled equations are two exponential functions for the voltage

$$V(z) = V^+ e^{-kz} + V^- e^{+kz} \quad (2.34)$$

and for the current

$$I(z) = I^+ e^{-kz} + I^- e^{+kz} \quad (2.35)$$

It is important to observe that (2.34) and (2.35) are general solutions for transmission lines aligned along the z -axis. The convention is such that the first term represents wavefronts propagating in the $+z$ -direction, whereas the second term denotes wave propagation in the $-z$ -direction. This makes physical sense since the negative sign in conjunction with $k, \geq 0$ ensures diminishing amplitudes for the positive ($+z$) traveling wave. Conversely, negative traveling waves are attenuated due to the diminishing exponential term.

2.7.3 General Impedance Definition

Equation (2.35) is related to (2.34). This can be seen if (2.34) is substituted into (2.35). Differentiating and rearranging provides us with a current expression in the following form:

$$I(z) = \frac{k}{(R + j\omega L)} (V^+ e^{-kz} - V^- e^{+kz}) \quad (2.36)$$

Since voltage and current are generally related via an impedance, we can introduce the so-called characteristic line impedance Z_0 by defining

$$Z_0 = \frac{(R + j\omega L)}{k} = \sqrt{\frac{(R + j\omega L)}{(G + j\omega C)}} \quad (2.37)$$

Substituting the current expression (2.35) into the left-hand side of (2.36), we also find

$$Z_0 = \frac{V^+}{I^+} = -\frac{V^-}{I^-} \quad (2.38)$$

The characteristic impedance allows us to express the current (2.36) in the concise form

$$I(z) = \frac{1}{Z_0} (V^+ e^{-kz} - V^- e^{+kz}) \quad (2.39)$$

The importance of Z_0 will become apparent in the following sections. Here it is noteworthy to point out that Z_0 is not an impedance in the conventional circuit sense. Its definition is based on the *positive and negative traveling voltage and current waves*. As such this definition has nothing in common with the *total voltage and current expressions* used to define a conventional circuit impedance.

2.7.4 Lossless Transmission Line Model

The characteristic line impedance defined in (2.37) is, in general, a complex quantity and therefore takes into account losses that are always present when dealing with realistic lines. However, for short line segments, as mostly encountered in RF and MW circuits, it does not create an appreciable error to deal with lossless line conditions. This implies $R = G = 0$ and the characteristic impedance (2.37) simplifies to

$$Z_0 = \sqrt{L/C} \quad (2.40)$$

Since Z_0 is independent of frequency, current and voltage waves are only scaled by a constant factor. It is instructive to substitute values for a particular transmission line type. If we use the parallel-plate transmission line with L and C given in Table 2-1, we find the explicit form

$$Z_0 = \sqrt{\frac{\mu d}{\epsilon w}} \quad (2.41)$$

where the square root term is known as the wave impedance, which yields ($\mu = \mu_0$, $\epsilon = \epsilon_0$), a value of approximately 377Ω in free space. This value is typical when dealing with radiation systems whereby an antenna emits electromagnetic energy into free space. However, unlike electromagnetic field radiation into open space, the transmission line introduces geometric constraints as expressed through w and d for the parallel-plate line configuration.

2.8 Microstrip Transmission Lines

As we have seen in Figures 2-6 and 2-7, a simple treatment of the strip line as a parallel-plate capacitor that formed the basis of computing C in Table 2-1 does not apply in the general case. If the substrate thickness h increases or if the conductor width w decreases, fringing fields become more prominent and cannot be ignored in the mathematical model. Over the years a number of researchers have developed approximate expressions for the calculation of the characteristic line impedance, taking into account conductor width and thickness. As often encountered in engineering, we have to strike a balance between complexity and the accuracy of our computations. The most precise

expressions describing microstrip lines are derived by using **conformal mapping**, but these expressions are also the most complex, requiring substantial computational efforts. For the purposes of obtaining fast and generally reliable estimations of the line parameters, simpler empirical formulas are more beneficial.

As a first approximation, we assume that the thickness t of the conductor forming the line is negligible compared to the substrate height h ($t/h < 0.005$). In this case, we can use empirical formulas that depend only on the line dimensions (w and h) and the dielectric constant ϵ_r . They require two separate regions of applicability depending on whether the ratio w/h is larger or less than unity. For narrow strip lines, $w/h < 1$, we obtain the line impedance

$$Z_0 = \frac{Z_f}{2\pi\sqrt{\epsilon_{\text{eff}}}} \ln\left(8\frac{h}{w} + \frac{w}{4h}\right) \quad (2.42)$$

where $Z_f = \sqrt{\mu_0/\epsilon_0} = 376.8 \Omega$ is the wave impedance in free space, and ϵ_{eff} is the **effective dielectric constant** given by

$$\epsilon_{\text{eff}} = \frac{\epsilon_r + 1}{2} + \frac{\epsilon_r - 1}{2} \left[\left(1 + 12\frac{h}{w}\right)^{-1/2} + 0.04 \left(1 - \frac{w}{h}\right)^2 \right] \quad (2.43)$$

For a wide line, $w/h > 1$, we need to resort to a different characteristic line impedance expression:

$$Z_0 = \frac{Z_f}{\sqrt{\epsilon_{\text{eff}}} \left(1.393 + \frac{w}{h} + \frac{2}{3} \ln\left(\frac{w}{h} + 1.444\right) \right)} \quad (2.44)$$

with

$$\epsilon_{\text{eff}} = \frac{\epsilon_r + 1}{2} + \frac{\epsilon_r - 1}{2} \left(1 + 12\frac{h}{w} \right)^{-1/2} \quad (2.45)$$

It is important to note that the characteristic impedances given by (2.42) and (2.44) are only approximations and do not produce continuous functions over the entire range of w/h . In particular, we notice that at $w/h = 1$ the characteristic impedance computed according to (2.42) and (2.44) displays a small discontinuity. Since the error introduced by this discontinuity is less than 0.5%, we still can use the preceding expressions for the computation of both the characteristic line impedance and the effective dielectric constant, as shown in Figures 2-20 and 2-21. In these figures the quantities Z_0 and ϵ_{eff} are plotted as functions of w/h ratios and ϵ_r values. The parameter range of w/h and ϵ_r

is chosen such that it spans the domain of typically encountered practically relevant circuit values.

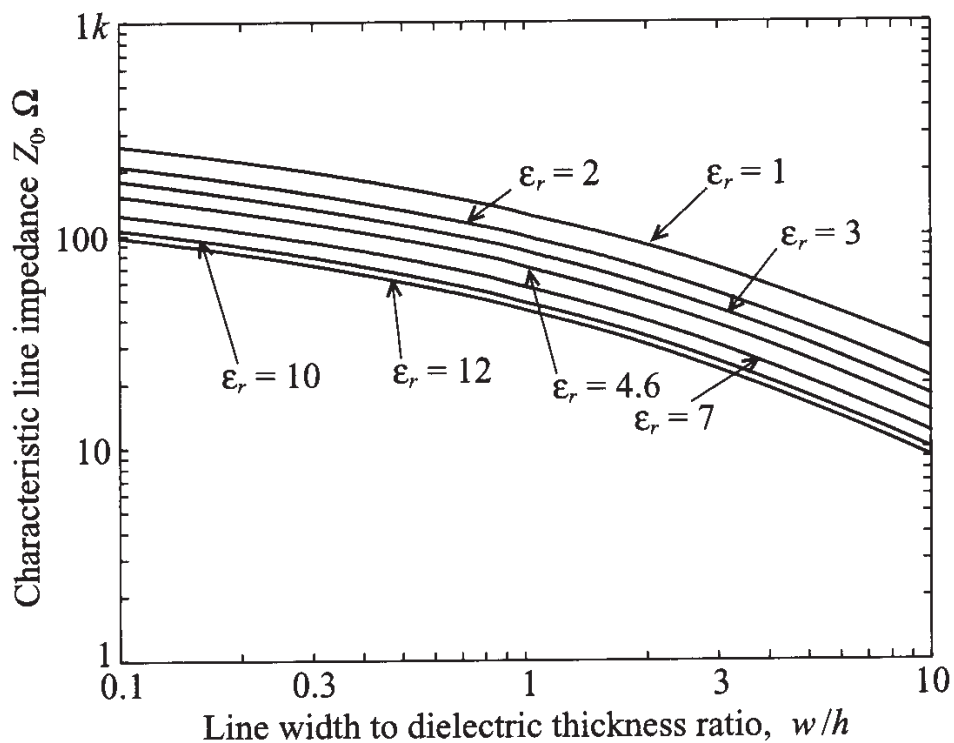


Figure 2-20 Characteristic line impedance as a function of w/h .

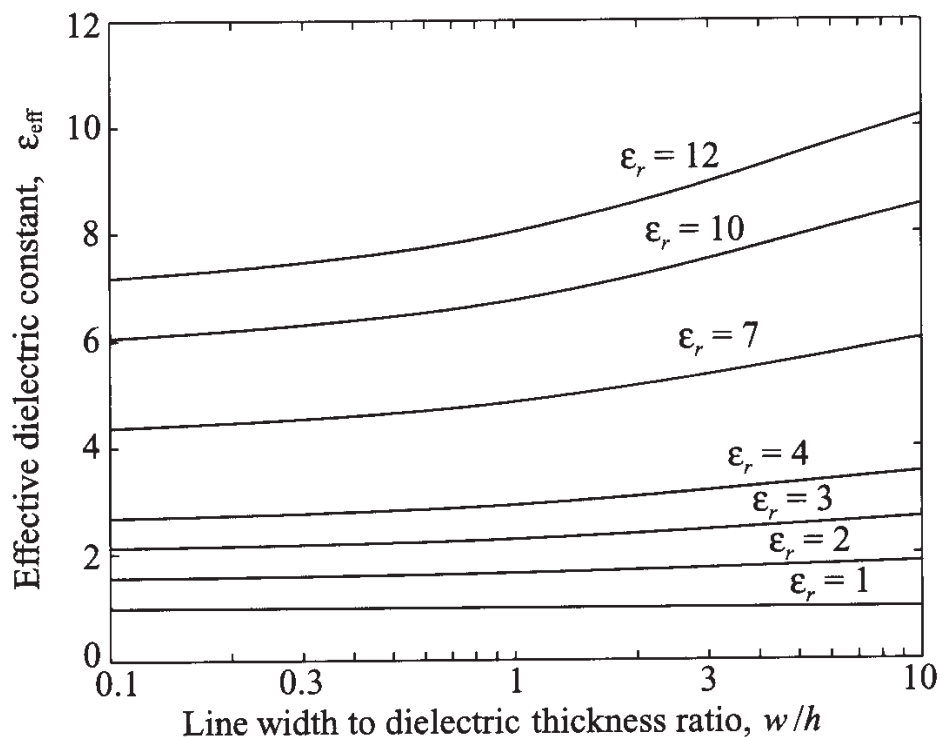


Figure 2-21 Effective dielectric constant as a function of w/h for different dielectric constants.

In the preceding formulas the effective dielectric constant is viewed as the dielectric constant of a homogeneous material that fills the entire space around the line, replacing dielectric substrate and surrounding air. With the knowledge of the effective dielectric constant we can compute the phase velocity of the strip line as $v_p = c/\sqrt{\epsilon_{\text{eff}}}$. This leads to an expression for the wavelength of

$$\lambda = \frac{v_p}{f} = \frac{c}{f\sqrt{\epsilon_{\text{eff}}}} = \frac{\lambda_0}{\sqrt{\epsilon_{\text{eff}}}},$$

where, as before, c is the speed of light and f is the operating frequency.

For design purposes we would like to have a relation that allows us to compute w/h ratios based on a given characteristic impedance Z_0 and dielectric constant ϵ_r of the substrate. Assuming an infinitely thin line conductor, we can write (see Sobol's article in Further Reading at the end of the chapter) for $w/h \leq 2$:

$$\frac{w}{h} = \frac{8e^A}{e^{2A} - 2} \quad (2.46a)$$

where the factor A is given by

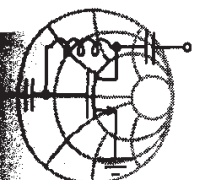
$$A = 2\pi \frac{Z_0}{Z_f} \sqrt{\frac{\epsilon_r + 1}{2}} + \frac{\epsilon_r - 1}{\epsilon_r + 1} \left(0.23 + \frac{0.11}{\epsilon_r} \right)$$

For $w/h \geq 2$ we obtain:

$$\frac{W}{h} = \frac{2}{\pi} \left\{ B - 1 - \ln(2B - 1) + \frac{\epsilon_r - 1}{2\epsilon_r} \left[\ln(B - 1) + 0.39 - \frac{0.61}{\epsilon_r} \right] \right\} \quad (2.46b)$$

where the factor B is given by

$$B = \frac{Z_f \pi}{2Z_0 \sqrt{\epsilon_r}}$$



RF & MW →

Example 2-5: Design of a microstrip line

A particular RF circuit requires that a line impedance of 50Ω is to be maintained. The selected PCB board material is FR-4 with a relative dielectric constant of 4.6 and a thickness of 40 mil. What are the width of the trace, phase velocity, and wavelength at 2 GHz?

Solution: At first we can use Figure 2-20 to determine an approximate ratio of w/h . Choosing a curve corresponding to $\epsilon_r = 4.6$, we find that for $Z_0 = 50 \Omega$, w/h is approximately 1.9. Therefore, in (2.46) we have to chose the case where $w/h \leq 2$. This leads to

$$A = 2\pi \frac{Z_0}{Z_f} \sqrt{\frac{\epsilon_r + 1}{2}} + \frac{\epsilon_r - 1}{\epsilon_r + 1} \left(0.23 + \frac{0.11}{\epsilon_r} \right) = 1.5583$$

Substituting this result into (2.46a), we find

$$\frac{w}{h} = \frac{8e^A}{e^{2A} - 2} = 1.8477$$

Then, by using (2.45), we obtain the effective dielectric constant to be

$$\epsilon_{\text{eff}} = \frac{\epsilon_r + 1}{2} + \frac{\epsilon_r - 1}{2} \left(1 + 12 \frac{h}{w} \right)^{-1/2} = 3.4575$$

We can compute the characteristic impedance of the line (2.44) to verify our result:

$$Z_0 = \frac{Z_f}{\sqrt{\epsilon_{\text{eff}}} \left(1.393 + \frac{w}{h} + \frac{2}{3} \ln \left(\frac{w}{h} + 1.444 \right) \right)} = 50.2243 \Omega$$

which is very close to the target impedance of 50Ω and therefore indicates that our result is correct.

Using the obtained ratio for w/h , we find the trace width to be $w = 73.9$ mil. Finally, the effective dielectric constant just computed allows us to evaluate the phase velocity of the microstrip line

$$v_p = c / \sqrt{\epsilon_{\text{eff}}} = 1.61 \times 10^8 \text{ m/s}$$

and the effective wave length at 2 GHz

$$\lambda = v_p / f = 80.67 \text{ mm}$$

Strictly speaking, this example focuses on a single trace of infinite length only. In reality, proximity to neighboring traces and bends is an issue of practical importance that is most easily accounted for in RF/MW computer aided design (CAD) programs.

For many applications the assumption of zero thickness of the strip line may not be valid and corrections to the preceding equations are needed. The effect of nonzero copper strip thickness is approximated as an increase in **effective width** w_{eff} of the conductor since more fringing fields will occur. In other words, a finite thickness is modeled by simply replacing the width of the strip in (2.42)–(2.45) with an effective width computed as

$$w_{\text{eff}} = w + \frac{t}{\pi} \left(1 + \ln \frac{2x}{t} \right) \quad (2.47)$$

where t is the thickness of the conductor, and either $x = h$ if $w > h/(2\pi) > 2t$, or $x = 2\pi w$ if $h/(2\pi) > w > 2t$.

The influence of nonzero thickness on the characteristic line impedance for a standard FR-4 substrate with $h = 25\text{ mil}$ is illustrated in Figure 2-22.

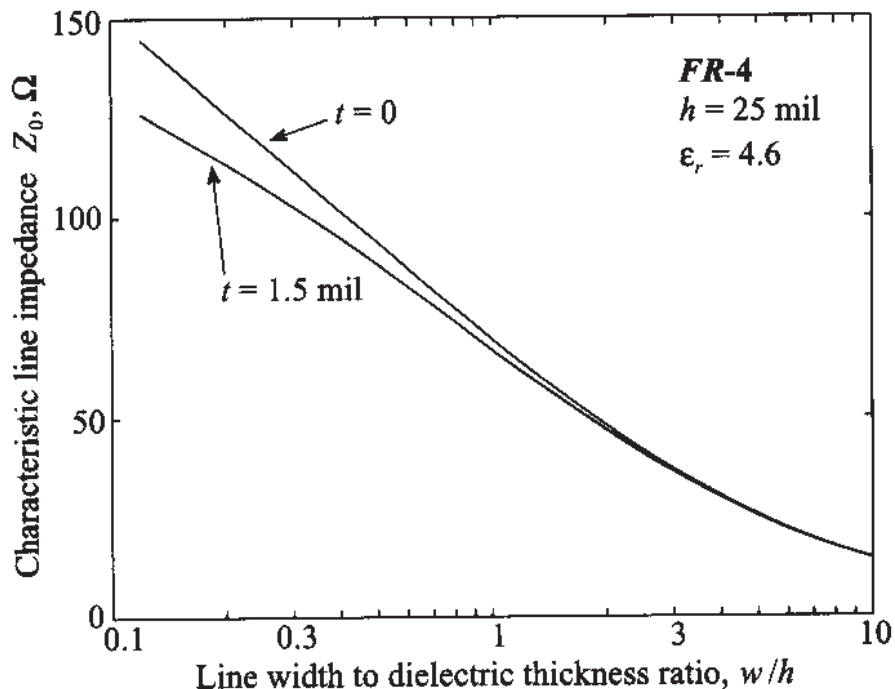


Figure 2-22 Effect of conductor thickness on the characteristic impedance of a microstrip line placed on a 25 mil thick FR-4 printed circuit board.

As seen in the figure, the effect is most noticeable for narrow strips, while it becomes almost negligible for cases when the width is greater than the thickness of the dielectric.

2.9 Terminated Lossless Transmission Line

2.9.1 Voltage Reflection Coefficient

High-frequency electric circuits can be viewed as a collection of finite transmission line sections connected to various discrete active and passive devices. Therefore,

let us take at first a closer look at the simple configuration of a load impedance connected to a finite transmission line segment of length l depicted in Figure 2-23. Such a system forces us to investigate how an incident voltage wave propagating along the positive z -axis interacts with a load impedance representing a generic line termination.

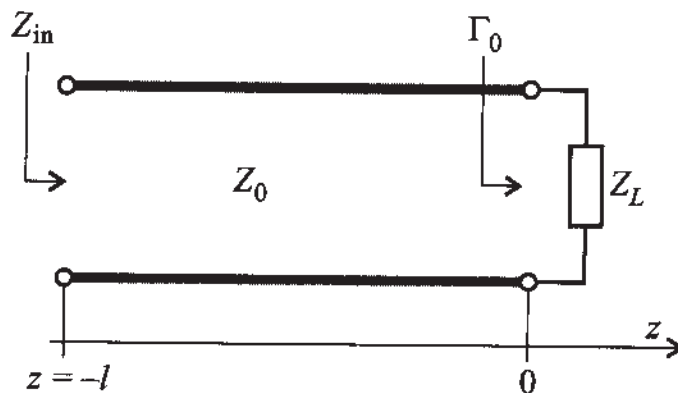


Figure 2-23 Terminated transmission line at location $z = 0$.

Without a loss of generality, the load is assumed to be located at $z = 0$ and the voltage wave is coupled into the line at $z = -l$. As we know, the voltage anywhere along the line is generically given by (2.34). The second term in (2.34) has the meaning of a reflection from the terminating load impedance for values $z < 0$. We introduce the **voltage reflection coefficient** Γ_0 as the ratio of reflected to incident voltage wave

$$\Gamma_0 = \frac{V^-}{V^+} \quad (2.48)$$

at the load location $z = 0$. As a consequence of this definition, the voltage and current waves can be re-expressed in terms of the reflection coefficient as

$$V(z) = V^+(e^{-kz} + \Gamma_0 e^{+kz}) \quad (2.49)$$

and

$$I(z) = \frac{V^+}{Z_0}(e^{-kz} - \Gamma_0 e^{+kz}) \quad (2.50)$$

If (2.49) is divided by (2.50), we find the impedance as a function of space $Z(z)$ anywhere along the z -axis $-l \leq z \leq 0$. For instance at $z = -l$ the total input impedance Z_{in} is recorded, and for location $z = 0$ the impedance becomes the load impedance

$$Z(0) = Z_L = Z_0 \frac{1 + \Gamma_0}{1 - \Gamma_0} \quad (2.51)$$

Equation (2.51) can be solved for the reflection coefficient Γ_0 with the result

$$\Gamma_0 = \frac{Z_L - Z_0}{Z_L + Z_0} \quad (2.52)$$

This is a more useful representation than (2.48) since it involves known circuit quantities independent of particular voltage wave amplitude ratios.

We conclude that for an open line ($Z_L \rightarrow \infty$) the reflection coefficient becomes 1, which means the reflected wave returns with the same polarity as the incident voltage. In contrast, for a short circuit ($Z_L = 0$) the reflected voltage returns with inverted amplitude, resulting in $\Gamma_0 = -1$. For the case where the load impedance matches the line impedance, $Z_0 = Z_L$, no reflection occurs and $\Gamma_0 = 0$. If there is no reflection we have the case where the incident voltage wave is completely absorbed by the load. This can be regarded as if a second transmission line with the same characteristic impedance, but infinite length, is attached at $z = 0$.

2.9.2 Propagation Constant and Phase Velocity

The definition of the complex propagation constant (2.32) assumes a very simple form for the lossless line ($R = G = 0$). For this case we obtain

$$k = k_r + jk_i = j\omega\sqrt{LC} \quad (2.53)$$

This is identified in generally accepted engineering notation as

$$\alpha \equiv k_r = 0 \quad (2.54)$$

and

$$\beta \equiv k_i = \omega\sqrt{LC} \quad (2.55)$$

where α represents the attenuation coefficient and β is the wave number or propagation constant for lossless lines. The propagation constant is now purely imaginary, resulting in

$$V(z) = V^+(e^{-j\beta z} + \Gamma_0 e^{+j\beta z}) \quad (2.56)$$

and

$$I(z) = \frac{V^+}{Z_0}(e^{-j\beta z} - \Gamma_0 e^{+j\beta z}) \quad (2.57)$$

Here, the characteristic impedance is again given by (2.40). Furthermore, from (2.1) it is known that the wavelength λ can be related to the frequency f via the phase velocity v_p :

$$\lambda = v_p/f \quad (2.58)$$

and the phase velocity v_p is given in terms of the line parameters L, C as

$$v_p = \frac{1}{\sqrt{LC}} \quad (2.59)$$

Because of (2.55), we can relate the wave number to the phase velocity:

$$\beta = \frac{\omega}{v_p} \quad (2.60)$$

Substituting the appropriate line parameters from Table 2-1, it is noticed that for all three transmission line types the phase velocity is independent of frequency. The implication of this fact is as follows: If we assume a pulsed voltage signal propagating down a line, we can decompose the pulse into its frequency components, and each frequency component propagates with the same fixed phase velocity. Thus, the original pulse will appear at a different location without having changed in shape. This phenomenon is known as **dispersion-free** transmission. Unfortunately, in reality we always have to take into account a certain degree of frequency dependence or dispersion of the phase velocity that causes signal distortion.

2.9.3 Standing Waves

It is instructive to insert the reflection coefficient for a short-circuit line ($\Gamma_0 = -1$) into the voltage expression (2.56) and change to a new coordinate d representation such that $z = 0$ in the old system coincides with the origin of the new coordinate system but extends in opposite, $-z$ direction, as shown in Figure 2-24.

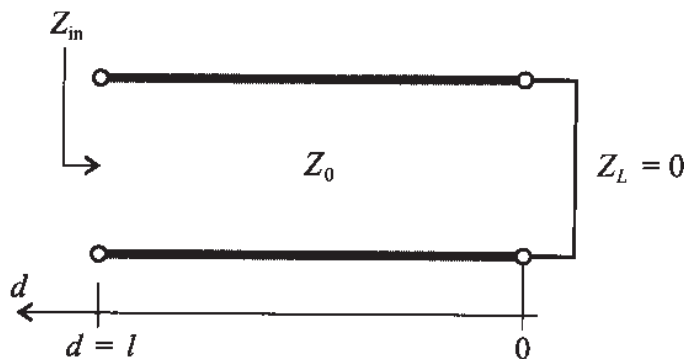


Figure 2-24 Short-circuit transmission line and new coordinate system d .

Equation (2.56) now reads

$$V(d) = V^+ (e^{+j\beta d} - e^{-j\beta d}) \quad (2.61)$$

We notice that the bracket can be replaced by $2j \sin(\beta d)$, and upon converting the phasor expression back into the time domain, we obtain

$$\begin{aligned} v(d, t) &= \operatorname{Re}\{V e^{j\omega t}\} = \operatorname{Re}\{2jV^+ \sin(\beta d)e^{j\omega t}\} \\ &= 2V^+ \sin(\beta d) \cos(\omega t + \pi/2) \end{aligned} \quad (2.62)$$

The sin-term ensures that the voltage maintains the short circuit condition for $d = 0$ at all time instances t , see Figure 2-25. Because time and space are now decoupled, no wave propagation, as discussed in Chapter 1, occurs. This phenomenon can physically be explained by the fact that the incident wave is 180° out of phase with the reflected wave, giving rise to fixed zero crossings of the wave at spatial locations $0, \lambda/2, \lambda, 3\lambda/2$, and so on.

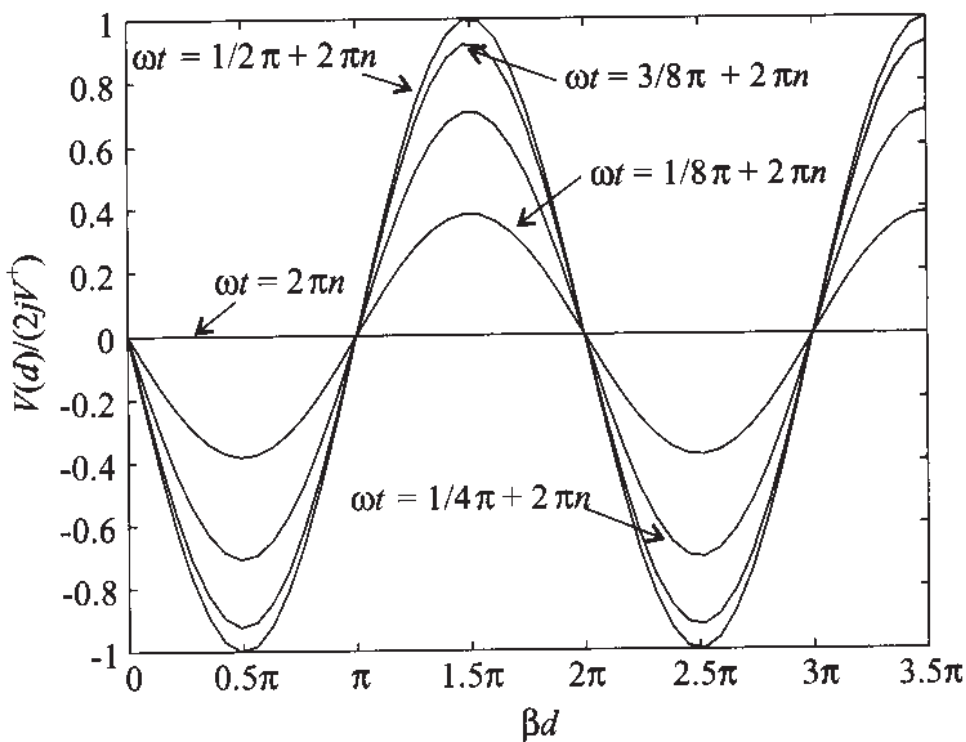


Figure 2-25 Standing wave pattern for various instances of time.

Introducing the new coordinate d into (2.56), this equation becomes

$$V(d) = V^+ e^{+j\beta d} (1 + \Gamma_0 e^{-j2\beta d}) = A(d)[1 + \Gamma(d)] \quad (2.63)$$

where we set $A(d) = V^+ e^{+j\beta d}$ and define a reflection coefficient

$$\Gamma(d) = \Gamma_0 e^{-j2\beta d} \quad (2.64)$$

valid anywhere along the length of the line d . The far-reaching implications of equation (2.64) as part of the Smith Chart will be subject of Chapter 3. Similarly, the current in the new spatial reference frame can be defined as

$$I(d) = \frac{V^+}{Z_0} e^{+j\beta d} (1 - \Gamma_0 e^{-j2\beta d}) = \frac{A(d)}{Z_0} [1 - \Gamma(d)] \quad (2.65)$$

Under matched condition ($\Gamma_0 = 0$) the reflection coefficient $\Gamma(d)$ is zero, thus maintaining only a right-propagating wave. To quantify the degree of mismatch, it is customary to introduce the **standing wave ratio (SWR)** as the ratio of the maximum voltage (or current) over the minimum voltage (or current) as follows:

$$\text{SWR} = \frac{|V_{\max}|}{|V_{\min}|} = \frac{|I_{\max}|}{|I_{\min}|} \quad (2.66)$$

We note that the extreme values of (2.64) can only be +1 and -1. Knowing that the exponential function has a magnitude of 1, we find for (2.66) the form

$$\text{SWR} = \frac{1 + |\Gamma_0|}{1 - |\Gamma_0|} \quad (2.67)$$

which has a range of $1 \leq \text{SWR} < \infty$, as seen in Figure 2-26.

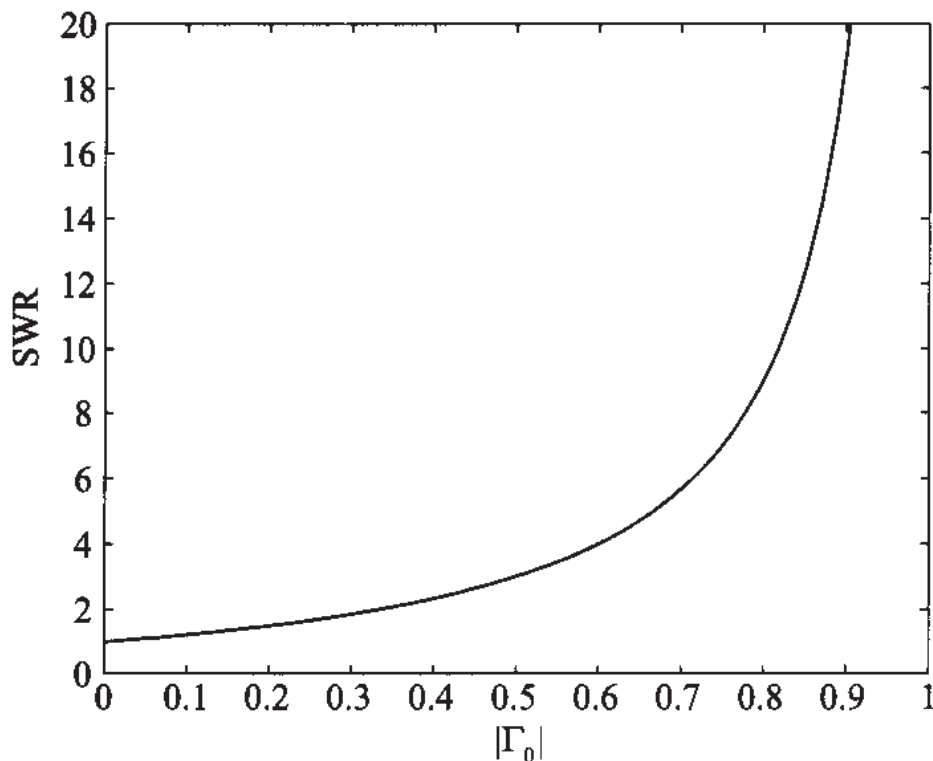


Figure 2-26 SWR as a function of load reflection coefficient $|\Gamma_0|$.

In many cases engineers use the term **voltage standing wave ratio** (VSWR) instead of SWR by defining it as the ratio of the maximum absolute voltage value to its minimum. It is concluded from the definition (2.66) and from Figure 2-26 that the ideal case of matched termination yields an SWR of 1, whereas the worst case of either open or short-circuit termination results in $\text{SWR} \rightarrow \infty$. Strictly speaking, SWR can only be applied to lossless lines, since it is impossible to define a SWR for lossy transmission systems. This is because the magnitude of the voltage or current waves diminishes as a function of distance due to attenuation and thus invalidates (2.67), which, as a single descriptor, is independent of where along the transmission line the measurement is taken. Because most RF systems possess very low losses, (2.67) can be safely applied. Upon inspection of the exponent in (2.64) we see that the distance between the maximum and minimum of the reflection coefficient is $2\beta d = \pi$ or $d = \lambda/4$ and the distance between two maxima is $d = \lambda/2$.

2.10 Special Termination Conditions

2.10.1 Input Impedance of Terminated Lossless Line

At a distance d away from the load the input impedance is given by the expression

$$Z_{\text{in}}(d) = \frac{V(d)}{I(d)} = Z_0 \frac{V^+ e^{j\beta d} (1 + \Gamma_0 e^{-2j\beta d})}{V^+ e^{j\beta d} (1 - \Gamma_0 e^{-2j\beta d})} \quad (2.68)$$

where (2.63) and (2.65) are used for the voltage and current expressions. Equation (2.68) can be converted into the form

$$Z_{\text{in}}(d) = Z_0 \frac{1 + \Gamma(d)}{1 - \Gamma(d)} \quad (2.69)$$

and, upon using (2.52) to replace Γ_0 , we obtain

$$\begin{aligned} Z_{\text{in}}(d) &= \frac{e^{j\beta d} + \left(\frac{Z_L - Z_0}{Z_L + Z_0}\right) e^{-j\beta d}}{e^{j\beta d} - \left(\frac{Z_L - Z_0}{Z_L + Z_0}\right) e^{-j\beta d}} Z_0 \\ &= \frac{Z_L(e^{j\beta d} + e^{-j\beta d}) + Z_0(e^{j\beta d} - e^{-j\beta d})}{Z_L(e^{j\beta d} - e^{-j\beta d}) + Z_0(e^{j\beta d} + e^{-j\beta d})} Z_0 \\ &= \frac{Z_L \cos(\beta d) + jZ_0 \sin(\beta d)}{Z_0 \cos(\beta d) + jZ_L \sin(\beta d)} Z_0 \end{aligned} \quad (2.70)$$

Division by the cosine term gives us the final form of the input impedance for the terminated transmission line:

$$Z_{in}(d) = Z_0 \frac{Z_L + jZ_0 \tan(\beta d)}{Z_0 + jZ_L \tan(\beta d)} \quad (2.71)$$

This important result allows us to predict how the load impedance Z_L is transformed along a transmission line of characteristic impedance Z_0 and length d . It takes into account the frequency of operation through the wave number β . Depending on the application, β can be expressed either in terms of frequency and phase velocity, $\beta = (2\pi f)/v_p$, or wavelength, $\beta = 2\pi/\lambda$.

2.10.2 Short Circuit Transmission Line

If $Z_L = 0$ (which means the load is represented by a short circuit) expression (2.71) simplifies to

$$Z_{in}(d) = jZ_0 \tan(\beta d) \quad (2.72)$$

Equation (2.72) can also directly be derived by the division of voltage through current wave for the short circuit condition ($\Gamma_0 = -1$):

$$V(d) = V^+ [e^{+j\beta d} - e^{-j\beta d}] = 2jV^+ \sin(\beta d) \quad (2.73)$$

and

$$I(d) = \frac{V^+}{Z_0} [e^{+j\beta d} + e^{-j\beta d}] = \frac{2V^+}{Z_0} \cos(\beta d) \quad (2.74)$$

so that $Z_{in}(d) = V/I = jZ_0 \tan(\beta d)$. A plot of voltage, current, and impedance as a function of line length is shown in Figure 2-27.

It is interesting to note the periodic transitions of the impedance as the distance from the load increases. If $d = 0$, the impedance is equal to the load impedance, which is zero. For increasing d the impedance of the line is purely imaginary and increases in magnitude. The positive sign of the impedance at this location shows that the line exhibits inductive behavior. When d reaches a quarter-wave length, the impedance is equal to infinity, which represents an open-circuit condition. Further increase in distance leads to negative imaginary impedance, which is equivalent to a capacitive behavior. At distance $d = \lambda/2$ the impedance becomes zero and the entire periodic process is repeated for $d > \lambda/2$.

From a practical point of view, it is difficult to conduct electric measurements at various locations along the line, or alternatively by considering a multitude of lines of different lengths. Much easier (for instance, through the use of a network analyzer) is

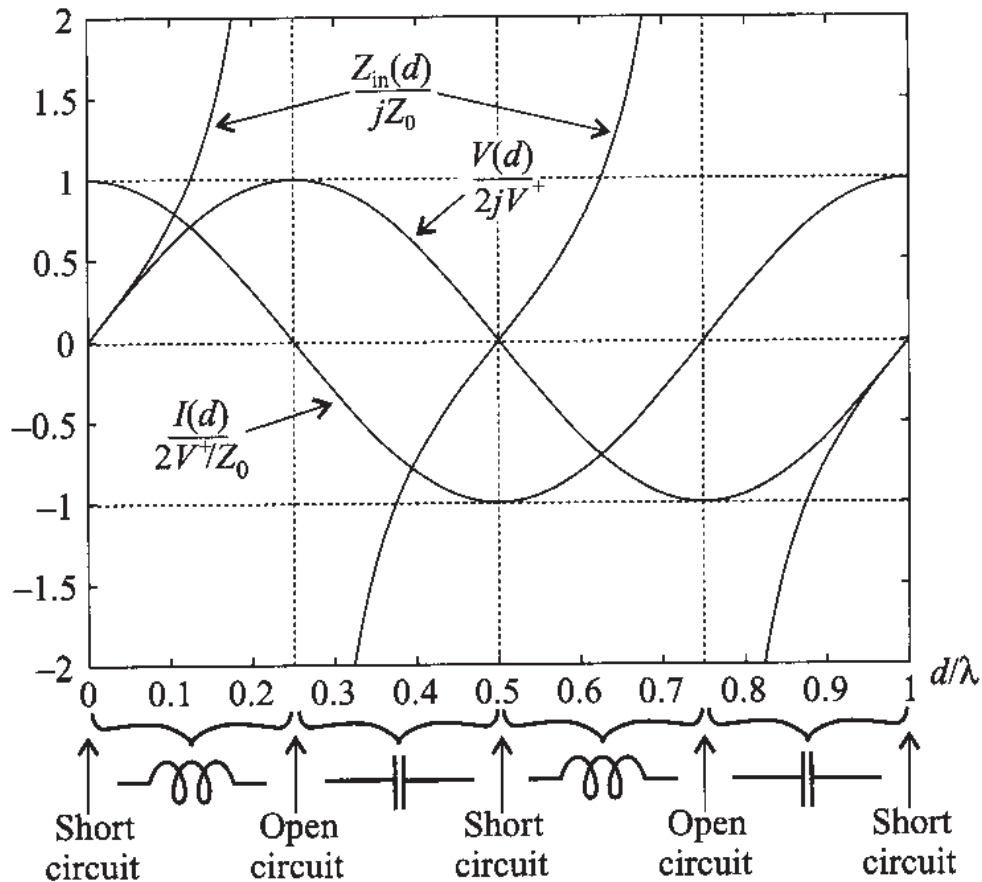


Figure 2-27 Voltage, current, and impedance as a function of line length for a short circuit termination.

the recording of the impedance as a function of frequency. In this case d is fixed, and the frequency is swept over a specified range, as discussed in the following example.

RF & MW

Example 2-6: Input impedance of a short-circuit transmission line as a function of frequency

For a short-circuit transmission line of $l = 10$ cm compute the magnitude of the input impedance when the frequency is swept from $f = 1$ GHz to 4 GHz. Assume the line parameters are the same as the ones given in Example 2.3 (i.e., $L = 209.4$ nH/m and $C = 119.5$ pF/m).

Solution: Based on the line parameters L and C , the characteristic impedance is found to be $Z_0 = \sqrt{L/C} = 41.86 \Omega$. Further, the phase velocity is given by $v_p = 1/\sqrt{LC}$ and is equal to

1.99×10^8 m/s. The input impedance of the transmission line $Z_{in}(d = l)$ as a function of frequency can then be expressed in the form

$$Z_{in}(d = l) = jZ_0 \tan(\beta l) = jZ_0 \tan\left(\frac{2\pi f}{v_p} l\right) \quad (2.75)$$

The magnitude of the impedance is shown in Figure 2-28 for the frequency range of 1 GHz to 4 GHz. Again we notice the periodic short- or open-circuit behavior of this line segment. In other words, depending on the frequency, the line exhibits an open-circuit behavior (for instance at 1.5 GHz) or a short-circuit behavior (for instance at 2 GHz).

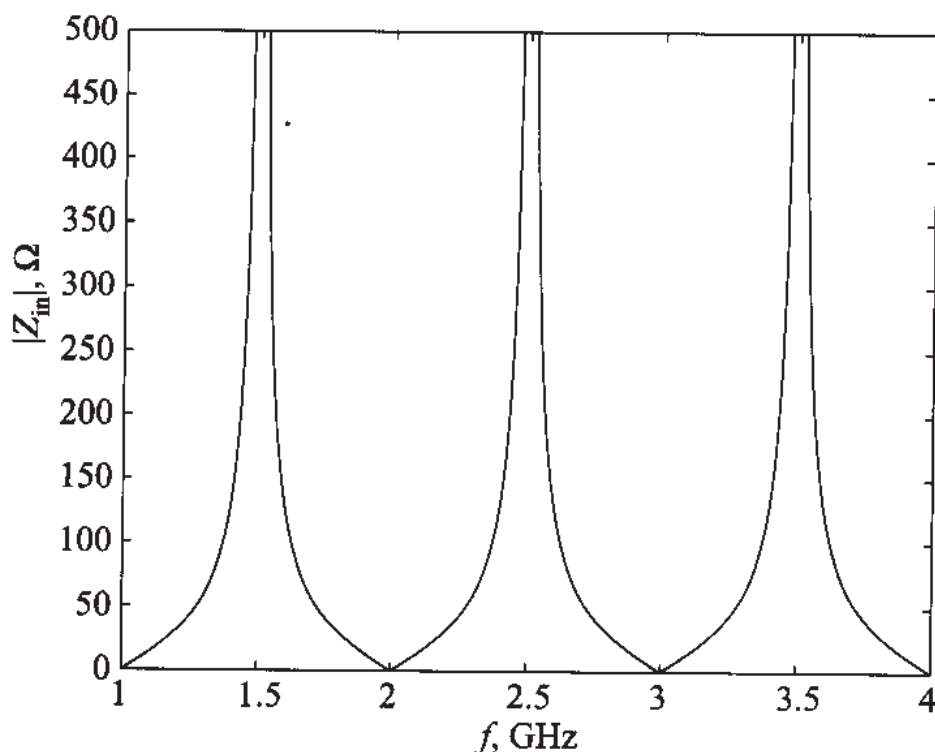


Figure 2-28 Magnitude of the input impedance for a 10 cm long, short-circuit transmission line as a function of frequency.

Practical measurements with a network analyzer permit the recording of graphs as the one seen in Figure 2-28. Had we fixed the frequency and varied the line length, we would have gotten an identical response.

2.10.3 Open-Circuit Transmission Line

If $Z_L \rightarrow \infty$ the input impedance (2.71) simplifies to the expression

$$Z_{\text{in}}(d) = -jZ_0 \frac{1}{\tan(\beta d)} \quad (2.76)$$

which can be directly derived when we divide the voltage (2.63) by the current wave (2.65) for the open circuit condition ($\Gamma_0 = +1$):

$$V(d) = V^+ [e^{+j\beta d} + e^{-j\beta d}] = 2V^+ \cos(\beta d) \quad (2.77)$$

and

$$I(d) = \frac{V^+}{Z_0} [e^{+j\beta d} - e^{-j\beta d}] = \frac{2jV^+}{Z_0} \sin(\beta d) \quad (2.78)$$

so that $Z_{\text{in}}(d) = V/I = -jZ_0 \cot(\beta d)$. Plotting voltage, current, and impedance as a function of line length is shown in Figure 2-29.

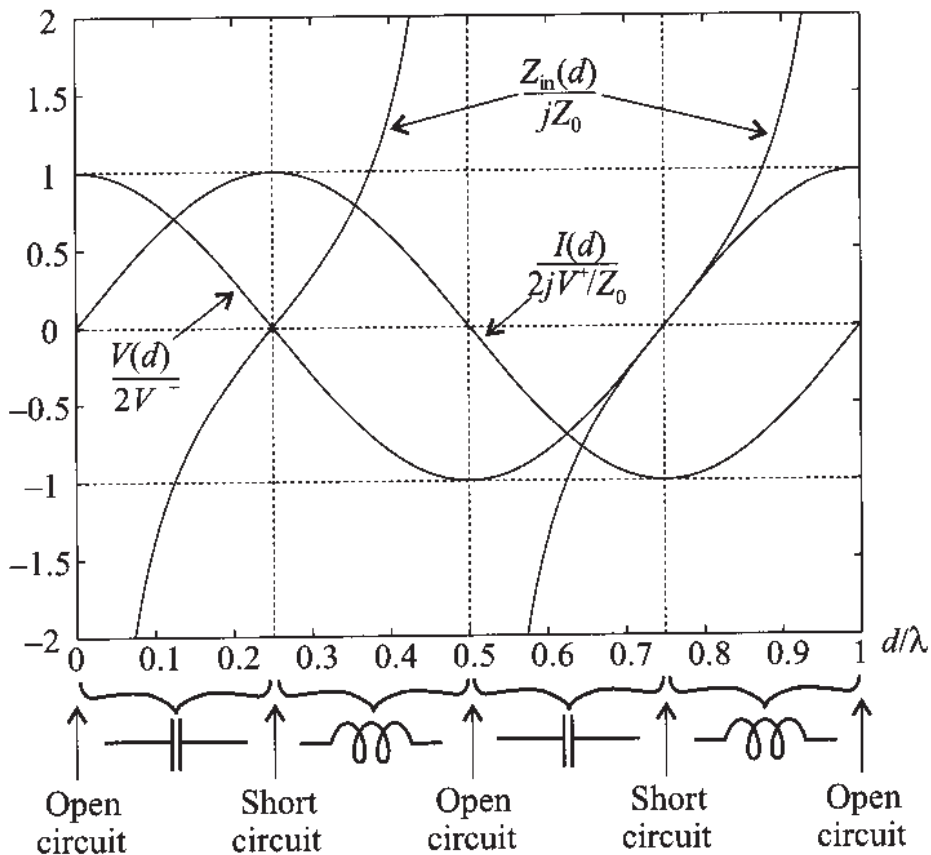
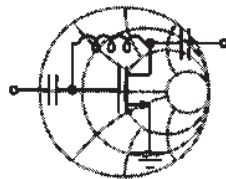


Figure 2-29 Voltage, current, and impedance as a function of line length for an open-circuit termination.

It is again of interest to keep the length d fixed, and sweep the frequency over a specified range, as the next example illustrates.



RF & MW →

Example 2-7: Input impedance of an open-circuit transmission line as a function of frequency

For an open-circuit transmission line of $l = 10 \text{ cm}$, repeat the calculations of Example 2-6.

Solution: All calculations remain the same, except that the input impedance is changed to

$$Z_{\text{in}}(d = l) = -jZ_0 \cot(\beta l) = -jZ_0 \cot\left(\frac{2\pi f}{v_p} l\right) \quad (2.79)$$

The magnitude of the impedance is displayed in Figure 2-30 for the frequency range of 1 GHz to 4 GHz. The points where the cotangent approaches infinity correspond to values where the argument reaches 90° , 180° , 270° , and so on. In reality, small losses due to the presence of R and G tend to limit the amplitude to finite peaks. The physical reason for these peaks is due to a phase shift between

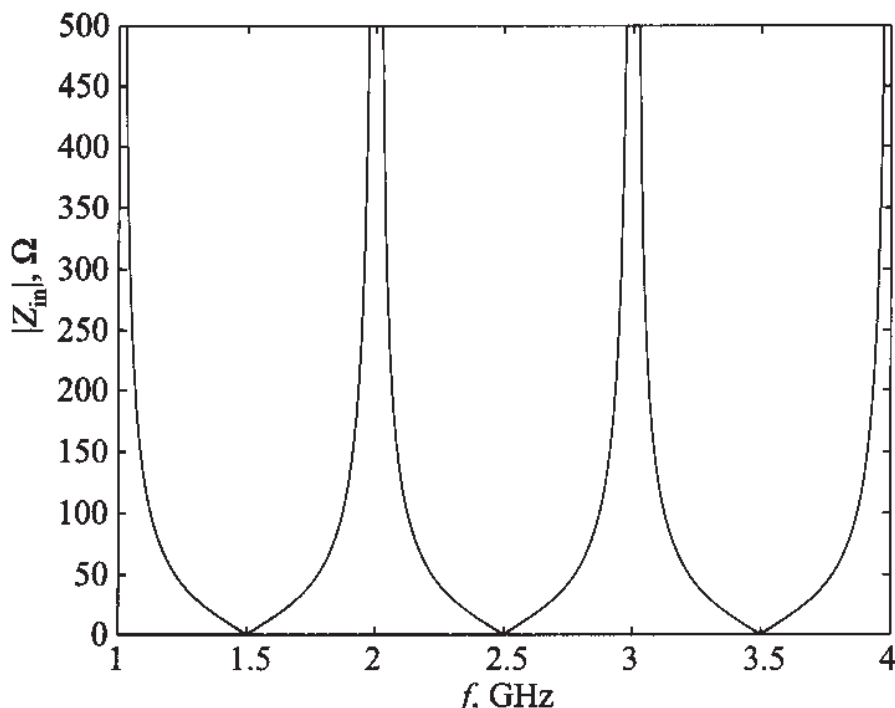


Figure 2-30 Magnitude of impedance for a 10 cm long, open-circuit transmission line as a function of frequency.

voltage and current wave. Specifically, when the current wave approaches zero and the voltage is finite, the line impedance assumes a maximum. This is equivalent to the mechanical effect where, for instance, a sound wave at particular discrete frequencies (so-called eigen frequencies) forms standing waves between the walls of a confining structure.

Figures 2-28 and 2-30 teach us that impedance matching to a particular impedance value is only possible at a fixed frequency. Any deviations can result in significantly different impedances.

2.10.4 Quarter-Wave Transmission Line

As evident from (2.70), if the line is matched, $Z_L = Z_0$, we see that $Z_{in}(d) = Z_0$ regardless of the line length. We can also ask ourselves the question: Is it possible to make the input impedance of the line equal to the load impedance ($Z_{in}(d) = Z_L$)? The answer is found by setting $d = \lambda/2$ (or more generally $d = \lambda/2 + m(\lambda/2)$, $m = 1, 2, \dots$), i.e.,

$$Z_{in}(d = \lambda/2) = Z_0 \frac{Z_L + jZ_0 \tan\left(\frac{2\pi}{\lambda} \cdot \frac{\lambda}{2}\right)}{Z_0 + jZ_L \tan\left(\frac{2\pi}{\lambda} \cdot \frac{\lambda}{2}\right)} = Z_L \quad (2.80)$$

In other words, if the line is exactly a half wavelength long, the input impedance is equal to the load impedance, independent of the characteristic line impedance Z_0 .

As a next step, let us reduce the length to $d = \lambda/4$ (or $d = \lambda/4 + m(\lambda/2)$, $m = 1, 2, \dots$). This yields

$$Z_{in}(d = \lambda/4) = Z_0 \frac{Z_L + jZ_0 \tan\left(\frac{2\pi}{\lambda} \cdot \frac{\lambda}{4}\right)}{Z_0 + jZ_L \tan\left(\frac{2\pi}{\lambda} \cdot \frac{\lambda}{4}\right)} = \frac{Z_0^2}{Z_L} \quad (2.81)$$

The implication of (2.81) leads to the **lambda-quarter transformer**, which allows the matching of a real load impedance to a desired real input impedance by choosing a transmission line segment whose characteristic impedance can be computed as the geometric mean of load and input impedances:

$$Z_0 = \sqrt{Z_L Z_{in}} \quad (2.82)$$

This is shown in Figure 2-31, where Z_{in} and Z_L are known impedances and Z_0 is determined based on (2.82).

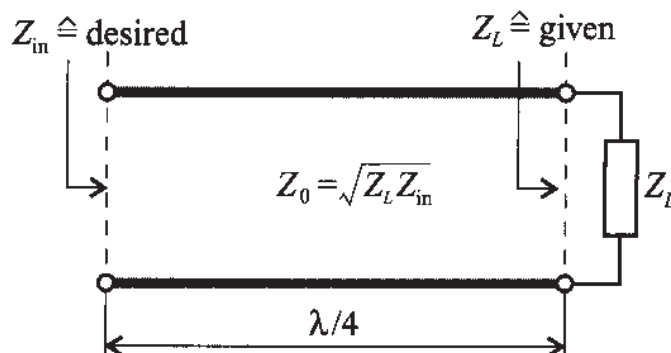
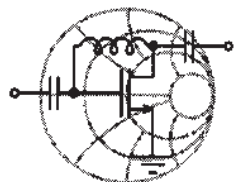


Figure 2-31 Input impedance matched to a load impedance through a $\lambda/4$ line segment Z_0 .

The idea of impedance matching has important practical design implications and is investigated extensively in Chapter 8. In terms of a simple example we place the preceding formula in context with the reflection coefficient.



RF & MW →

Example 2-8: Impedance matching via a $\lambda/4$ transformer

A transistor has an input impedance of $Z_L = 25 \Omega$ which is to be matched to a 50Ω microstrip line at an operating frequency of 500 MHz (see Figure 2-32). Find the length, width, and characteristic impedance of the quarter-wave parallel-plate line transformer for which matching is achieved. The thickness of the dielectric is $d = 1 \text{ mm}$ and the relative dielectric constant of the material is $\epsilon_r = 4$. Assume that the surface resistance R and shunt conductance G (see Table 2-1) can be neglected.

Solution: We can directly apply (2.81) by using the given impedances from the problem statement. For the line impedance we find

$$Z_{line}(l = \lambda/4) = \sqrt{Z_0 Z_L} = 35.355 \Omega$$

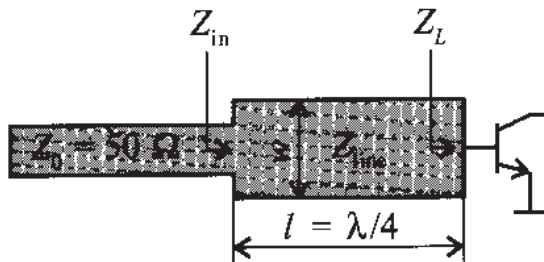


Figure 2-32 Input impedance of quarter-length transformer.

On the other hand, the characteristic impedance of the parallel-plate line is

$$Z_{line} = \sqrt{L/C} = (d_p/w)\sqrt{\mu/\epsilon}$$

Thus, the width of the line is

$$w = \frac{d_p}{Z_{line}} \sqrt{\frac{\mu_0}{\epsilon_0 \epsilon_r}} = 5.329 \text{ mm}$$

From Table 2-1 we find the values for capacitance and inductance of the line:

$$L = \mu d_p / w = 235.8 \text{ nH/m}$$

$$C = \epsilon w / d_p = 188.6 \text{ pF/m}$$

The line length l follows from the condition

$$l = \frac{\lambda}{4} = \frac{1}{4f\sqrt{LC}} = 74.967 \text{ mm}$$

The input impedance of the combined transmission line and the load is shown in Figure 2-32.

$$Z_{in} = Z_{line} \frac{Z_L + jZ_{line} \tan(\beta d)}{Z_{line} + jZ_L \tan(\beta d)} = Z_{line} \frac{1 + \Gamma(d)}{1 - \Gamma(d)}$$

where $d = l = \lambda/4$ and the reflection coefficient is given by

$$\Gamma(d) = \Gamma_0 e^{-2j\beta d} = \frac{Z_L - Z_{line}}{Z_L + Z_{line}} \exp\left(-j2\frac{2\pi f}{v_p} d\right)$$

The reflection coefficient is next inserted into the expression for Z_{in} . Plotting the impedance magnitude is shown in Figure 2-33.

We note that Z_{in} is matched to the line impedance of 50Ω not only at 500 MHz, but also at 1.5 GHz. Since the quarter-wave trans-

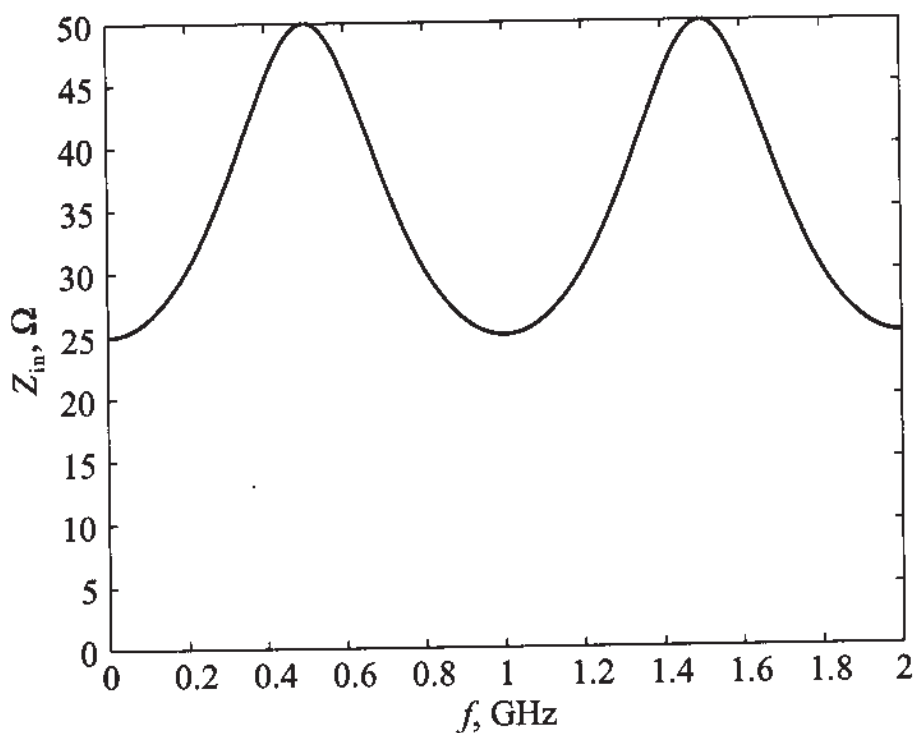


Figure 2-33 Magnitude of Z_{in} for frequency range of 0 to 2 GHz and fixed length d .

former is designed to achieve matching only at 500 MHz for a particular line length l , we cannot expect matching to occur for frequencies away from the 500 MHz point. In fact, for circuits required to operate over a wide frequency band, this approach may not be a suitable strategy.

The $\lambda/4$ transformer plays an important role in many applications as an easy-to-build, narrowband matching circuit.

2.11 Sourced and Loaded Transmission Line

Thus far our discussion has only relied on the transmission line and its termination through a load impedance. In completing our investigation, we need to attach a source to the line. This results in the added complication of not only having to deal with an impedance mismatch between transmission line and load, but having to take into considerations possible line-to-source mismatches as well.

2.11.1 Phasor Representation of Source

The generic transmission line circuit is shown in Figure 2-34 and involves a voltage source consisting of a generator voltage V_G and source impedance Z_G .

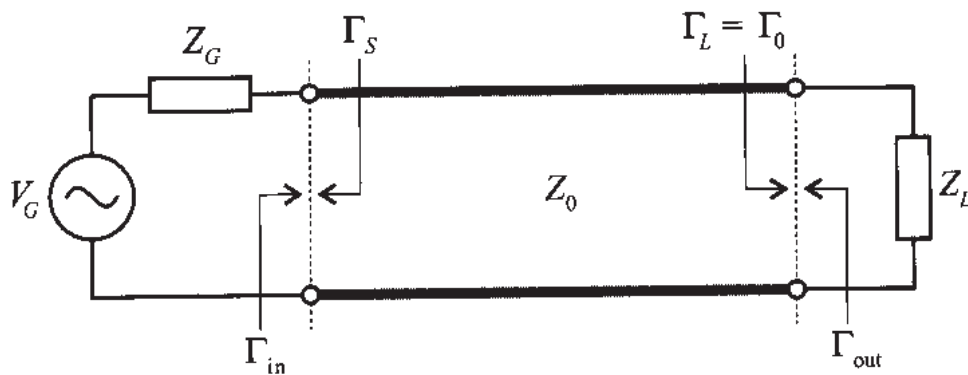


Figure 2-34 Generic transmission line circuit involving source and load terminations.

The input voltage recorded at the beginning of the transmission line can be written in general form

$$V_{in} = V_{in}^+ + V_{in}^- = V_{in}^+(1 + \Gamma_{in}) = V_G \left(\frac{Z_{in}}{Z_{in} + Z_G} \right) \quad (2.83)$$

where the last expression follows from the voltage divider rule. The input reflection coefficient Γ_{in} is obtained by looking from the source into the transmission line of length $d = l$:

$$\Gamma_{in} = \Gamma(d = l) = \frac{Z_{in} - Z_0}{Z_{in} + Z_0} = \Gamma_0 e^{-2j\beta l} \quad (2.84)$$

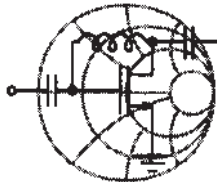
In (2.84), Γ_0 is the load reflection coefficient as defined in (2.52). In addition, it is often useful to introduce transmission coefficients, which take the form

$$T_{in} = 1 + \Gamma_{in} = \frac{2Z_{in}}{Z_{in} + Z_0} \quad (2.85)$$

at the beginning of the line, and

$$T_0 = 1 + \Gamma_0 = \frac{2Z_L}{Z_L + Z_0} \quad (2.86)$$

at the load end. The formal derivation of the transmission coefficient for a terminated transmission line is presented in the following example.



RF & MW →

Example 2-9: Determination of transmission coefficient

Consider a transmission line aligned along the z -axis whose characteristic line impedance is Z_0 and has a load Z_L at $d = 0$. Derive the transmission coefficient T_0 .

Solution: To the left of the load impedance ($d > 0$) we can write for the voltage wave

$$V(d) = V^+(e^{+j\beta d} + \Gamma_0 e^{-j\beta d})$$

and for the transmitted voltage at the load impedance ($d = 0$) we set generically

$$V(d = 0) = V^+ T_0$$

Since the voltage has to maintain continuity at $d = 0$, we obtain

$$1 + \Gamma_0 = T_0$$

from which we can find the transmission coefficient

$$T_0 = 1 + \frac{Z_L - Z_0}{Z_L + Z_0} = \frac{2Z_L}{Z_L + Z_0}$$

The argument of matching incident voltage with transmitted voltage wave can be applied to any discontinuity between two lines involving different characteristic impedances.

Reflection and transmission coefficients are easier to measure at high frequency than impedances. They are therefore more commonly used to characterize an interface between two dissimilar transmission line segments.

In addition to the preceding reflection and transmission coefficients, the connected source introduces an additional difficulty. Since the voltage reflected from the load is traveling toward the source, we need to consider a mismatch between the transmission

line and the source impedance. Accordingly, when looking from the line into the source we can define the source reflection coefficient:

$$\Gamma_s = \frac{Z_G - Z_0}{Z_G + Z_0} \quad (2.87)$$

The output reflection coefficient shown in Figure 2-34 is then computed similar to (2.84), but moving in opposite direction: $\Gamma_{\text{out}} = \Gamma_s e^{-j2\beta l}$.

2.11.2 Power Considerations for a Transmission Line

From the definition of time-averaged power

$$P_{\text{av}} = \frac{1}{2} \operatorname{Re}\{VI^*\} \quad (2.88)$$

we can compute the total power at the beginning of the transmission line. To accomplish this task, the complex input voltage $V_{\text{in}} = V_{\text{in}}^+(1 + \Gamma_{\text{in}})$ and current $I_{\text{in}} = (V_{\text{in}}^+ / Z_0)(1 - \Gamma_{\text{in}})$ have to be inserted in (2.88). The result is

$$P_{\text{in}} = P_{\text{in}}^+ + P_{\text{in}}^- = \frac{1}{2} \frac{|V_{\text{in}}^+|^2}{Z_0} (1 - |\Gamma_{\text{in}}|^2) \quad (2.89)$$

We notice here again that, just like voltage and current, power is also treated as being comprised of a positive and negative traveling wave.

Since V_{in}^+ in (2.89) is not directly accessible, it is more useful to re-express (2.89) in terms of the generator voltage V_G as follows:

$$V_{\text{in}}^+ = \frac{V_{\text{in}}}{1 + \Gamma_{\text{in}}} = \frac{V_G}{1 + \Gamma_{\text{in}}} \left(\frac{Z_{\text{in}}}{Z_{\text{in}} + Z_G} \right) \quad (2.90)$$

where (2.83) is used. As already known from (2.69), the input impedance is rewritten

$$Z_{\text{in}} = Z_0 \frac{1 + \Gamma_{\text{in}}}{1 - \Gamma_{\text{in}}} \quad (2.91)$$

The generator impedance follows from (2.87) as

$$Z_G = Z_0 \frac{1 + \Gamma_s}{1 - \Gamma_s} \quad (2.92)$$

Inserting (2.91) and (2.92) into (2.90) yields, after some algebra,

$$V_{\text{in}}^+ = \frac{V_G}{2} \frac{(1 - \Gamma_S)}{(1 - \Gamma_S \Gamma_{\text{in}})} \quad (2.93)$$

Using (2.93) in (2.89), the final expression for the input power is therefore

$$P_{\text{in}} = \frac{1}{8} \frac{|V_G|^2}{Z_0} \frac{|1 - \Gamma_S|^2}{|1 - \Gamma_S \Gamma_{\text{in}}|^2} (1 - |\Gamma_{\text{in}}|^2) \quad (2.94)$$

Upon using (2.84), we obtain the following expression for the input power for a lossless line:

$$P_{\text{in}} = \frac{1}{8} \frac{|V_G|^2}{Z_0} \frac{|1 - \Gamma_S|^2}{|1 - \Gamma_S \Gamma_0 e^{-2j\beta l}|^2} (1 - |\Gamma_0 e^{-2j\beta l}|^2) \quad (2.95)$$

Since the line is lossless, the power delivered to the load will be equal to the input power. If source and load impedances both are matched to the transmission line impedance (implying $\Gamma_S = 0$ and $\Gamma_0 = 0$), then (2.95) simplifies to

$$P_{\text{in}} = \frac{1}{8} \frac{|V_G|^2}{Z_0} = \frac{1}{8} \frac{|V_G|}{Z_G} \quad (2.96)$$

which represents the power produced by the source under perfectly matched conditions and which constitutes the *maximum available power provided by the source*. When the load Z_L is matched to the transmission line, but the source impedance Z_G is mismatched, then part of the power will be reflected and only portion of the maximum available power will be transmitted into the line at location $d = l$:

$$P_{\text{in}} = \frac{1}{8} \frac{|V_G|^2}{Z_0} |1 - \Gamma_S|^2 \quad (2.97)$$

For the case where both source and load impedances are mismatched, reflections will occur on both sides of the transmission line and the power that will be delivered to the load is defined by (2.95). Besides *watts* (W), the unit that is widely used to quantify power in RF circuit design is dBm, which is defined as follows:

$$P[\text{dBm}] = 10 \log \frac{P[\text{W}]}{1 \text{ mW}} \quad (2.98)$$

In other words, power is measured relative to 1 milliwatt.



Example 2-10: Power considerations of transmission line

For the circuit shown in Figure 2-34, assume a lossless line with $Z_0 = 75 \Omega$, $Z_G = 50 \Omega$, and $Z_L = 40 \Omega$. Compute the input power and power delivered to the load. Give your answer both in W and dBm. Assume the length of the line to be $\lambda/2$ with a source voltage of $V_G = 5 \text{ V}$.

Solution: Since the line is lossless, the power delivered to the load is exactly the same as the input power. To find the input power, we use expression (2.95). Because the length of the line is $\lambda/2$, all exponential terms in (2.95) are equal to unity; that is, $e^{-2j\beta l} = e^{-2j(2\pi/\lambda)(\lambda/2)} = 1$ and (2.95) can be rewritten as

$$P_{\text{in}} = \frac{1}{8} \frac{|V_G|^2}{Z_0} \frac{|1 - \Gamma_S|^2}{|1 - \Gamma_S \Gamma_0|^2} (1 - |\Gamma_0|^2)$$

where the reflection coefficient at the source end is $\Gamma_S = (Z_G - Z_0)/(Z_G + Z_0) = -0.2$ and the reflection coefficient at the load is $\Gamma_0 = (Z_L - Z_0)/(Z_L + Z_0) = -0.304$. Substitution of the obtained values into the preceding equation yields

$$P_L = P_{\text{in}} = 61.7 \text{ mW}$$

or

$$P_L = P_{\text{in}} = 17.9 \text{ dBm}.$$

Most RF data sheets and application notes specify the output power in dBm. It is therefore important to gain a “feel” of the relative magnitudes of mW and dBm.

The previous analysis is easy to extend to a lossy transmission line. Here we find that the input power is no longer equal to the load power due to signal attenuation.

However, with reference to Figure 2-34 the power absorbed by the load can be expressed similarly to (2.89) as

$$P_L = \frac{|V_L^+|^2}{2Z_0} (1 - |\Gamma_L|^2) \quad (2.99)$$

where the voltage $|V_L^+|$ for a lossy transmission is $|V_L^+| = |V_{in}^+| e^{-\alpha l}$, with α again being the attenuation coefficient. Inserting (2.93) into (2.99) gives as the final expression

$$P_L = \frac{1}{8} \frac{|V_G|^2}{Z_0} \frac{|1 - \Gamma_S|^2}{|1 - \Gamma_S \Gamma_{in}|^2} e^{-2\alpha l} (1 - |\Gamma_L|^2) \quad (2.100)$$

where all parameters are defined in terms of the source voltage and the reflection coefficients.

2.11.3 Input Impedance Matching

Employing an electric equivalent circuit representation for the transmission line configuration shown in Figure 2-34 allows us to examine optimal conditions for the matching of the generator to the line.

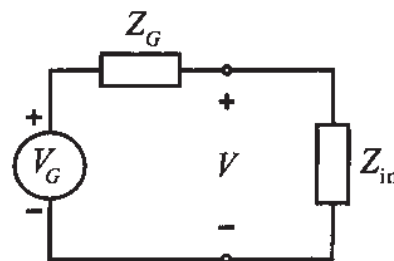


Figure 2-35 Equivalent lumped input network for a transmission line configuration.

In a lumped parameter expression, and consistent with Figure 2-35, we can express (2.95) as

$$P_{in} = \frac{1}{2} \operatorname{Re} \left\{ V_{in} \left(\frac{V_{in}^*}{Z_{in}^*} \right) \right\} = \frac{1}{2} \frac{|V_G|^2}{\operatorname{Re}\{Z_{in}^*\}} \left| \frac{Z_{in}}{Z_G + Z_{in}} \right|^2 \quad (2.101)$$

If we assume the generator impedance to be of fixed complex value $Z_G = R_G + jX_G$, we can find the conditions that have to be imposed on Z_{in} to obtain maximum power transfer into the transmission line. Treating P_{in} as a function of two independent variables R_{in} and X_{in} , we find the maximum power value by taking the first derivatives of P_{in} with respect to R_{in} and X_{in} and setting the values to zero:

$$\frac{\partial P_{\text{in}}}{\partial R_{\text{in}}} = \frac{\partial P_{\text{in}}}{\partial X_{\text{in}}} = 0 \quad (2.102)$$

The two conditions that result are

$$R_G^2 - R_{\text{in}}^2 + (X_G^2 + 2X_G X_{\text{in}} + X_{\text{in}}^2) = 0 \quad (2.103a)$$

$$X_{\text{in}}(X_G + X_{\text{in}}) = 0 \quad (2.103b)$$

Solving (2.103b) gives $X_{\text{in}} = -X_G$ and, upon substituting this result into (2.103a), yields $R_{\text{in}} = R_G$. This derivation shows that optimal power transfer requires conjugate complex matching of the transmission line to the generator impedance:

$$Z_{\text{in}} = Z_G^* \quad (2.104)$$

Though this is done for the case of generator to input impedance matching, an identical analysis can be carried out to match the output impedance to the load impedance. Again we will find that the impedances require conjugate complex matching for maximum power transfer:

$$Z_{\text{out}} = Z_L^*$$

Here, Z_{out} represents the impedance looking into the transmission line from the load side.

2.11.4 Return Loss and Insertion Loss

Practical circuit realizations always suffer a certain degree of mismatch between available source power and power delivered to the transmission line; that is, Γ_{in} in (2.89) is not zero. This mismatch is customarily defined as **return loss** (RL), which is the ratio of reflected power, $P_r = P_{\text{in}}^-$, to incident power, $P_i = P_{\text{in}}^+$, or

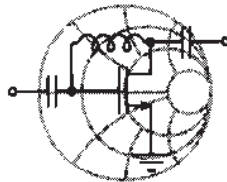
$$\text{RL} = -10\log\left(\frac{P_r}{P_i}\right) = -10\log|\Gamma_{\text{in}}|^2 = -20\log|\Gamma_{\text{in}}| \quad (2.105a)$$

$$\text{RL} = -\ln|\Gamma_{\text{in}}| \quad (2.105b)$$

Equation (2.105a) specifies the *return loss* in decibel (dB) based on the logarithm to the base 10, whereas (2.105b) specifies RL in Nepers (Np) based on the natural logarithm. A conversion between Np and dB is accomplished by noting that

$$\text{RL} = -20\log|\Gamma_{\text{in}}| = -20(\ln|\Gamma_{\text{in}}|)/(\ln 10) = -(20\log e)\ln|\Gamma_{\text{in}}| \quad (2.106)$$

Therefore, $1 N_p = 20 \log e = 8.686 \text{ dB}$. As seen from (2.106), if the line is matched $\Gamma_{in} \rightarrow 0$, then $RL \rightarrow \infty$.



RF & MW →

Example 2-11: Return loss of transmission line section

For the circuit in Figure 2-35 a return loss of 20 dB is measured. Assuming real impedance values only, what is the source resistance R_G if the transmission line has a characteristic line impedance of $R_{in} = 50 \Omega$? Is the answer unique?

Solution: The reflection coefficient is found from (2.105a) as

$$|\Gamma_{in}| = 10^{-RL/20} = 10^{-20/20} = 0.1$$

The source resistance is now computed by using (2.91):

$$R_G = R_{in} \frac{1 + \Gamma_{in}}{1 - \Gamma_{in}} = 50 \left(\frac{1 + 0.1}{1 - 0.1} \right) \Omega = 61.1 \Omega$$

In the preceding calculations, we assumed that the reflection coefficient Γ_{in} is positive and therefore is equal to its absolute value. However, it can also be negative, and in that case the source resistance would be

$$R_G = R_{in} \frac{1 + \Gamma_{in}}{1 - \Gamma_{in}} = 50 \left(\frac{1 - 0.1}{1 + 0.1} \right) \Omega = 40.9 \Omega$$

The return loss, which can be recorded with a network analyzer, provides immediate access to the reflection coefficient and thus the degree of impedance mismatch between the transmission line and generator.

In addition to the return loss, which involves the reflected power, it is useful to introduce the **insertion loss** (IL) defined as a ratio of transmitted power P_t to incident power P_i . In practice insertion loss is measured in dB according to the following formula:

$$IL = -10 \log \frac{P_t}{P_i} = -10 \log \frac{P_i - P_r}{P_i} = -10 \log (1 - |\Gamma_{in}|^2) \quad (2.107)$$

The meaning of (2.107) in circuit design is straightforward. As the name implies, if an unmatched circuit is connected to an RF source, reflections occur that result in a loss of power delivered to the circuit. For instance, if the circuit represents an open- or short-circuit condition, the insertion loss reaches a maximum ($IL \rightarrow \infty$). Alternatively, if the circuit is matched to the source, all power is transferred to the circuit, and the insertion loss becomes a minimum ($IL = 0$).

2.12 Summary

In this chapter a detailed description is given of the fundamental concepts of distributed circuit theory. The topic is motivated by the fact that when the wavelengths of the voltage and current waves shrink to roughly 10 times the size of the circuit components, a transition must be made from lumped element analysis, based on Kirchhoff's current and voltage laws, to distributed theory according to wave principles. This transition from low- to high-frequency circuit analysis may not be as clear-cut as the definition of less than or equal to 10λ implies; in fact, a considerable "gray area" does exist. Nevertheless, starting at a particular frequency a transition is needed to obtain meaningful design results.

The underlying concepts of distributed theory can best be understood by developing an equivalent circuit representation (Section 2.3) of a microscopic section of the transmission line. The required circuit parameters per unit length R , L , G , C are obtained directly from Table 2-1 for three common transmission line types (Section 2.3) without going into much theoretical detail. However, for the readers who are interested in how the parameters can be found, Section 2.4 introduces the necessary tools of Faraday's and Ampère's laws, followed by Section 2.5, which derives all four circuit parameters for the parallel-plate transmission line.

In either case, the knowledge of the circuit parameters ultimately leads to the characteristic line impedance of a generic transmission line system:

$$Z_0 = \sqrt{\frac{(R + j\omega L)}{(G + j\omega C)}}$$

In this representation the input impedance of a terminated transmission line is developed. The result is perhaps one of the single most important RF equations:

$$Z_{in}(d) = Z_0 \frac{Z_L + jZ_0 \tan(\beta d)}{Z_0 + jZ_L \tan(\beta d)}$$

The application of this equation for the special cases of open, short, and matched load impedances are investigated in terms of their spatial and frequency domain behaviors. Furthermore, the lambda-quarter or quarter-wave transformer is introduced as a way of matching a load impedance to a desired input impedance.

As an alternative to the input impedance equation, it is often very useful to represent the line impedance in terms of the reflection coefficients at load and source end:

$$\Gamma_0 = \frac{Z_L - Z_0}{Z_L + Z_0}, \quad \Gamma_s = \frac{Z_G - Z_0}{Z_G + Z_0}$$

It is found that the reflection coefficient is spatially dependent, as shown by

$$\Gamma(d) = \Gamma_0 e^{-j2\beta d}$$

The reflection coefficient concept allows concise expressions for power flow considerations. Similar to the input impedance we found the input power

$$P_{in} = \frac{1}{8} \frac{|V_G|^2}{Z_0} \frac{|1 - \Gamma_s|^2}{|1 - \Gamma_s \Gamma_0 e^{-2j\beta l}|^2} (1 - |\Gamma_0 e^{-2j\beta l}|^2)$$

This equation permits the investigation of various matching or mismatching conditions at the load/source side. Chapter 2 concludes with a brief discussion of insertion loss and return loss.

Further Reading

- R. Collin, *Foundations of Microwave Engineering*, McGraw-Hill, New York, 1966.
- G. Gonzales, *Microwave Transistor Amplifiers, Analysis and Design*, 2nd edition, Prentice Hall, Upper Saddle River, New Jersey, 1997.
- H. A. Haus and J. R. Melcher, *Electromagnetic Fields and Energy*, Prentice Hall, Englewood Cliffs, NJ, 1989.
- M. F. Iskander, *Electromagnetic Fields and Waves*, Prentice Hall, Upper Saddle River, New Jersey, 1992.
- C. T. A. Johnk, *Engineering Electromagnetic Fields and Waves*, 2nd ed., John Wiley & Sons, New York, 1989.
- J. A. Kong, *Electromagnetic Wave Theory*, 2nd ed., John Wiley & Sons, New York, 1996.

S. Y. Liao, *Engineering Applications of Electromagnetic Theory*, West Publishing Company, St. Paul, MN, 1988.

D. M. Pozar, *Microwave Engineering*, 2nd ed., John Wiley & Sons, New York, 1998.

P. A. Rizzi, *Microwave Engineering, Passive Circuits*, Prentice Hall, Englewood Cliffs, New Jersey, 1988.

H. Sobol, "Applications of Integrated Circuit Technology to Microwave Frequencies," *Proceedings of the IEEE*, August 1971.

D. H. Staelin, A. W. Morgenthaler, and J. A. Kong, *Electromagnetic Waves*, Prentice Hall, Upper Saddle River, New Jersey, 1994.

Problems

- 2.1 To estimate the effective relative permittivity ϵ_r of a dielectric material used in a transmission line, you decide to measure the voltage distribution along the line using a similar setup as depicted in Figure 2-2. Your measurements at 1 GHz excitation frequency have shown that the wavelength of the signal in the cable is equal to 10 m. Using this information, compute the effective relative permittivity of the material. Discuss how this experimental setup could be used to measure the attenuation factor α .
- 2.2 As discussed in this chapter, a single signal trace on a printed circuit board (PCB) can be treated as a transmission line and can be modeled using an equivalent circuit, shown in Figure 2-12. Nevertheless, when the size of the PCB gets smaller, the distance between the traces decreases and they can no longer be treated as separate transmission lines. Therefore, the interaction between them has to be accounted for. Using the configuration shown in Figure 2-7, suggest a new equivalent circuit that takes into account interaction between two signal traces.
- 2.3 In Example 2-1 we showed how to compute the magnetic field distribution produced by the wire carrying current I . Repeat your computations for a system consisting of two parallel wires each of radius 5 mm and carrying a current of 5 A in the same direction. Plot the field distribution of the magnetic field $H(r)$ as a function of distance r starting at the center-line position between the two wires.
- 2.4 Consider a system consisting of a circular loop of radius $r = 1$ cm of thin wire (assume the radius of the wire to be equal to zero) and carrying a con-

stant current $I = 5 \text{ A}$. Compute the magnetic field along the center line of the loop as a function of distance h from the center of the loop.

- 2.5 Find k_r and k_i in terms of L , C , G , R , and ω in equation (2.32).
- 2.6 In the text we have derived the transmission line parameters (R , L , G , and C) for a parallel-plate line. Derive these parameters for a two-wire configuration, see Figure 2-4. Assume that $D \gg a$.
- 2.7 Repeat Problem 2.6 for a coaxial cable, see Figure 2-5.
- 2.8 An RG6A/U cable has a characteristic impedance of 75Ω . The capacitance of a 0.5 m long cable is measured and the value is found to be 33.6 pF . What is the cable inductance per unit length, if the cable is lossless?
- 2.9 Assuming that dielectric and conductor losses in a transmission line are small (i.e. $G \ll \omega C$ and $R \ll \omega L$), show that propagation constant k can be written as

$$k = \alpha + j\beta = \frac{1}{2} \left(\frac{R}{Z_0} + GZ_0 \right) + j\omega \sqrt{LC}$$

where $Z_0 = \sqrt{L/C}$ is the characteristic impedance of the line in the absence of loss.

- 2.10 Using the results from the previous problem and the transmission line parameters given in Table 2-1,

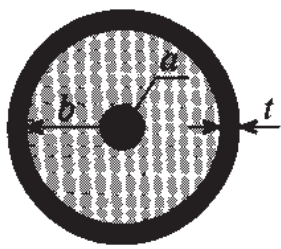
(a) show that the attenuation constant in a coaxial cable with small losses is

$$\alpha = \frac{1}{2} \frac{1}{\sigma_{\text{cond}} \delta} \sqrt{\frac{\epsilon}{\mu}} \frac{1}{\ln(b/a)} \left(\frac{1}{a} + \frac{1}{b} \right) + \frac{\sigma_{\text{diel}}}{2} \sqrt{\frac{\mu}{\epsilon}}$$

where σ_{diel} and σ_{cond} are the conductivities of the dielectric material and the conductors, respectively.

- (b) show that the attenuation in this case is minimized for conductor radii such that $x \ln x = 1 + x$, where $x = b/a$.
- (c) show that for a coaxial cable with dielectric constant $\epsilon_r = 1$ the condition of minimum losses results in the characteristic impedance of $Z_0 = 76.7 \Omega$.

- 2.11 Compute the transmission-line parameters for a coaxial cable, which characteristics are listed as follows:



Inner Conductor: Copper
 $a = 0.5\text{mm}$, $\sigma_{\text{Cu}} = 64.516 \times 10^6 \text{ S/m}$
Dielectric: Polyethylene
 $b = 1.5\text{mm}$, $\sigma_{\text{Poly}} = 10^{-14} \text{ S/m}$
Outer Conductor: Copper
 $t = 0.5\text{mm}$, $\sigma_{\text{Cu}} = 64.516 \times 10^6 \text{ S/m}$

- 2.12 An RG58A/U cable has a characteristic line impedance of 50Ω . The measurements performed on a section of this cable produce the following results

- capacitance of 1 meter of cable: 101 pF
- phase velocity: 66% of speed of light
- attenuation at 1 GHz: 0.705 dB/m
- outer diameter of the insulation layer: 2.95 mm
- center conductor is made out of AWG 20 copper wire, $\sigma_{\text{Cu}} = 64.516 \times 10^6 \text{ S/m}$
- dielectric layer is made out of polyethylene, $\sigma_{\text{Poly}} = 10^{-14} \text{ S/m}$

From this list of information, find the following quantities:

- inductance L per unit length of the cable assuming that cable is lossless
- relative permeability ϵ_r of the dielectric material
- resistance R per unit length of the cable at operating frequency of 1 GHz (*Hint:* use the formula for the attenuation constant derived in Problem 2.10)
- conductance G of the dielectric per unit length

- 2.13 Using the coaxial cable from the previous problem, compute its characteristic impedance. Plot the frequency behavior of the real and imaginary components of the characteristic impedance. Is the result what you expected to see? Explain any discrepancies.

- 2.14 A distortionless transmission line results if $R = G = 0$, which results in $k = j\omega\sqrt{LC} = \alpha + j\beta$, or $\alpha = 0$ and $\beta = \omega/v_p$ with the phase velocity independent of frequency [i.e., $v_p = 1/\sqrt{LC}$]. A signal propagating along this transmission line will not suffer any pulse distortion or attenuation. If we allow $R \neq G \neq 0$, find the condition for which $\alpha = \sqrt{RG}$ and $\beta = \omega\sqrt{LC}$. In other words, the line is attenuative but remains distortionless.

- 2.15 It is desired to construct a 50Ω microstrip line. The relative dielectric constant is 2.23 and the board height is $h = 0.787 \text{ mm}$. Find the width, wavelength, and effective dielectric constant when the thickness of the copper trace is negligible. Assume an operating frequency of 1 GHz.

- 2.16 Starting with basic definition for the standing wave ratio (SWR)

$$\text{SWR} = \frac{|V_{\max}|}{|V_{\min}|} = \frac{|I_{\max}|}{|I_{\min}|}$$

show that it can be re-expressed as

$$\text{SWR} = \frac{1 + |\Gamma_0|}{1 - |\Gamma_0|}$$

- 2.17 The characteristic impedance of a coax cable is 50Ω and assumed lossless. If the load is a short circuit, find the input impedance if the cable is 2 wavelength, 0.75 wavelength, and 0.5 wavelength in length.

- 2.18 An experiment similar to the one shown in Figure 2-2 is performed with the following results: The distance between successive voltage minima is 2.1 cm; the distance of the first voltage minimum from the load impedance is 0.9 cm; the SWR of the load is 2.5. If $Z_0 = 50 \Omega$, find the load impedance.

- 2.19 In this chapter we have derived the equation for the input impedance of the loaded lossless line, (2.65). Using the same approach, show that for a loaded lossy transmission line (i.e., $R \neq 0, G \neq 0$) the input impedance is

$$Z_{\text{in}}(d) = Z_0 \frac{Z_L + Z_0 \tanh(\gamma d)}{Z_0 + Z_L \tanh(\gamma d)}$$

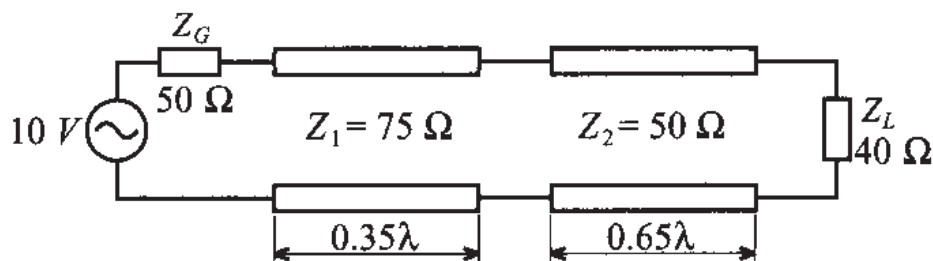
where γ is the complex propagation constant and tanh denotes the hyperbolic tangent

$$\tanh(x) = \frac{e^x - e^{-x}}{e^x + e^{-x}}$$

- 2.20 Using the result from the previous problem, compute the input impedance of a 10 cm long lossy coaxial cable connected to a $Z_L = (45 + j5) \Omega$ load impedance. The system is operated at 1 GHz frequency, and the coaxial cable has the following parameters: $R = 123(\mu\Omega/\text{m})$, $L = 123(\text{nH/m})$, $G = 123(\mu\text{S}/\text{m})$, and $C = 123(\text{pF/m})$.

- 2.21 Show that the input impedance of a lossless transmission line repeats itself every half wavelength [i.e., $Z_{\text{in}}(l_d) = Z_{\text{in}}\{l_d + m(\lambda/2)\}$], where l_d is an arbitrary length and m is an integer 0, 1, 2, ...

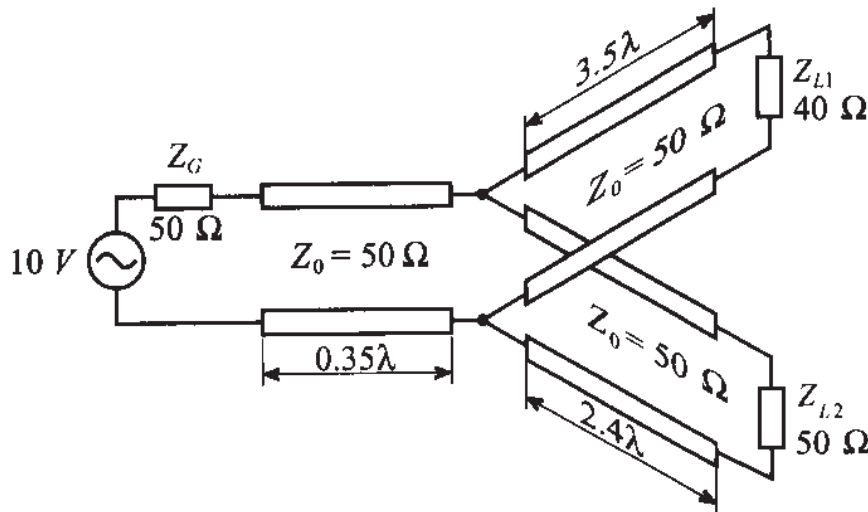
- 2.22 A radio transmitter is capable of producing 3 W output power. The transmitter is connected to an antenna having a characteristic impedance of 75Ω . The connection is made using a lossless coaxial cable with 50Ω characteristic impedance. Calculate the power delivered to the antenna if the source impedance is 45Ω and the cable length is 11λ .
- 2.23 For an RF circuit project an open-circuit impedance has to be created with a 75Ω microstrip line placed on a circuit board with relative dielectric constant of 10 and operated at 1.96 GHz. The line is terminated with a short circuit on one side. To what length does the line have to be cut to measure an infinite impedance on the other side?
- 2.24 A short-circuited microstrip line of $Z_0 = 85 \Omega$ and $(3/4)\lambda$ in length is used as a lumped circuit element. What is the input impedance if the line is assumed lossless?
- 2.25 For the following system, compute the input power, power delivered to the load, and insertion loss. Assume that all transmission lines are lossless.



- 2.26 Repeat Problem 2.25 for a 50Ω load impedance.
- 2.27 The complex load impedance $Z_L = (75 - j50)\Omega$ is attached to a lossless transmission line of 100Ω characteristic impedance. The frequency is selected such that the wavelength is 30 cm for a 50 cm long line. Find (a) the input impedance, (b) the impedance looking toward the load 10 cm away from the load, and (c) the voltage reflection coefficient at the load and 10 cm away from the load.
- 2.28 A 100Ω microstrip line is connected to a 75Ω line. Determine Γ , SWR, percentage power reflected, return loss, percentage power transmitted, and insertion loss.
- 2.29 A 50Ω transmission line is matched to a source and feeds a load of $Z_L = 75 \Omega$. If the line is 3.4λ long and has an attenuation constant

$\alpha = 0.5 \text{ dB}/\lambda$, find the power that is (a) delivered by the source, (b) lost in the line, and (c) delivered to the load. The amplitude of the signal produced by the source is 10 V.

- 2.30 A measurement technique is proposed to determine the characteristic line impedance of a coaxial cable via the determination of open, Z_{in}^{oc} , and short circuit, Z_{in}^{sc} input impedances with a network analyzer. It is assumed that the line impedance is real. How does one have to process these impedances to obtain Z_0 ?
- 2.31 A signal generator is used to feed two loads, as shown in the following figure.



Find the both the power produced by the source and the power delivered to each load.

- 2.32 A lossless 50Ω microstrip line is terminated into a load with an admittance of 0.05 mS . (a) what additional impedance has to placed in parallel with the load to assure an input impedance of 50Ω ? (b) If the input voltage is 10 V, find the voltage, current, and power absorbed by the combined load.
- 2.33 Show that return loss and insertion loss can be expressed in terms of the voltage standing wave ratio SWR as

$$RL = 20 \log \frac{SWR + 1}{SWR - 1} \text{ and } IL = 20 \log \frac{SWR + 1}{2\sqrt{SWR}}.$$

The Smith Chart

A transmission line changes its impedance depending on material properties and geometric dimensions. Typical practical realizations include microstrip line, coaxial cable, and parallel-plate line. In addition, both the length and operating frequency of the transmission line significantly influence the input impedance. In the previous chapter we derived the fundamental equation describing the input impedance of a terminated transmission line. We found that this equation incorporates the characteristic line impedance, load impedance, and, through the argument of the tangent function, line length and operating frequency. As we saw in Section 2.9, the input impedance can equivalently be evaluated by using the spatially dependent reflection coefficient. To facilitate the evaluation of the reflection coefficient, P. H. Smith developed a graphical procedure based on conformal mapping principles. This approach permits an easy and intuitive display of the reflection coefficient as well as the line impedance in one single graph. Although this graphical procedure, nowadays known as the Smith Chart, was developed in the 1930s prior to the computer age, it has retained its popularity and today can be found in every data book describing passive and active RF/MW components and systems. Almost all computer-aided design programs utilize the Smith Chart for the analysis of circuit impedances, design of matching networks, and computations of noise figures, gain, and stability circles. Even instruments such as the ubiquitous network analyzer have the option to represent certain measurements in a Smith Chart format.

This chapter reviews the steps necessary to convert the input impedance in its standard complex plane into a suitable complex reflection coefficient representation via a specific conformal transformation originally proposed by Smith. The graphical dis-

play of the reflection coefficient in this new complex plane can then be utilized directly to find the input impedance of the transmission line. Moreover, the Smith Chart facilitates evaluation of more complicated circuit configurations, which will be employed in subsequent chapters to build filters and matching networks for active devices.

The following sections present a step-by-step derivation of the Smith Chart followed by several examples of how to use this graphical design tool in computing the impedance of passive circuits.

3.1 From Reflection Coefficient to Load Impedance

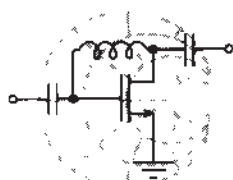
In Section 2.9 the reflection coefficient is defined as the ratio of reflected voltage wave to incident voltage wave at a certain fixed spatial location along the transmission line. Of particular interest is the reflection coefficient at the load location $d = 0$. From a physical point of view this coefficient Γ_0 describes the mismatch in impedance between the characteristic line impedance Z_0 and the load impedance Z_L as expressed by (2.52). In moving away from the load in the positive d -direction toward the beginning of the transmission line, we have to multiply Γ_0 by the exponential factor $\exp(-j2\beta d)$, as seen in (2.64), to obtain $\Gamma(d)$. It is this transformation from Γ_0 to $\Gamma(d)$ that constitutes one of the key ingredients in the **Smith Chart** as a graphical design tool.

3.1.1 Reflection Coefficient in Phasor Form

The representation of the reflection coefficient Γ_0 can be cast in the following complex notation.

$$\Gamma_0 = \frac{Z_L - Z_0}{Z_L + Z_0} = \Gamma_{0r} + j\Gamma_{0i} = |\Gamma_0|e^{j\theta_L} \quad (3.1)$$

where $\theta_L = \tan^{-1}(\Gamma_{0i}/\Gamma_{0r})$. We recall that pure short- and open-circuit conditions in (3.1) correspond to Γ_0 values of -1 and $+1$, located on the real axis in the complex Γ -plane.



Example 3-1: Reflection coefficient representations

A transmission line with a characteristic line impedance of $Z_0 = 50 \Omega$ is terminated into the following load impedances:

- (a) $Z_L = 0$ (short circuit)

RF & MW →

- (b) $Z_L \rightarrow \infty$ (open circuit)
- (c) $Z_L = 50 \Omega$
- (d) $Z_L = (16.67 - j16.67) \Omega$
- (e) $Z_L = (50 + j150) \Omega$

Find the individual reflection coefficients Γ_0 and display them in the complex Γ -plane.

Solution: Based on (3.1) we compute the following numbers for the reflection coefficients:

- (a) $\Gamma_0 = -1$ (short circuit)
- (b) $\Gamma_0 = 1$ (open circuit)
- (c) $\Gamma_0 = 0$ (matched circuit)
- (d) $\Gamma_0 = 0.54 \angle 221^\circ$
- (e) $\Gamma_0 = 0.83 \angle 34^\circ$

The values are displayed in polar form in Figure 3-1.

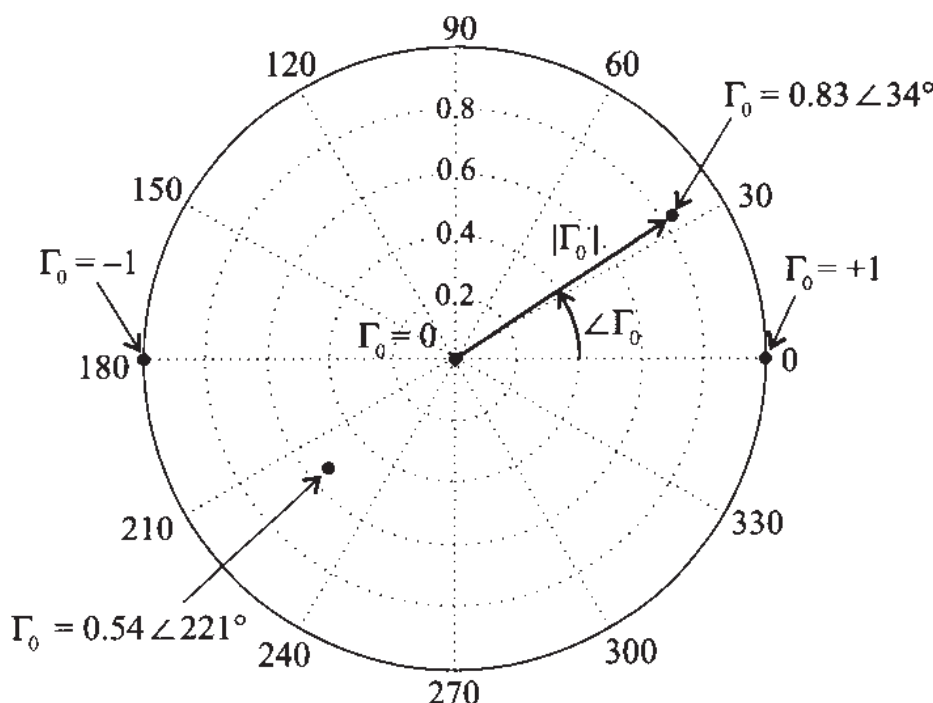


Figure 3-1 Complex Γ -plane and various locations of Γ_0 .

The reflection coefficient is represented in phasor form as done when dealing with the conventional voltages and currents in basic circuit theory.

3.1.2 Normalized Impedance Equation

Let us return to our general input impedance expression (2.69), into which we substitute the reflection coefficient

$$\Gamma(d) = |\Gamma_0| e^{j\theta_L} e^{-j2\beta d} = \Gamma_r + j\Gamma_i \quad (3.2)$$

This results in

$$Z_{in}(d) = Z_0 \frac{1 + \Gamma_r + j\Gamma_i}{1 - \Gamma_r - j\Gamma_i} \quad (3.3)$$

In order to generalize the subsequent derivations, we normalize (3.3) with respect to the characteristic line impedance as follows

$$Z_{in}(d)/Z_0 = z_{in} = r + jx = \frac{1 + \Gamma(d)}{1 - \Gamma(d)} = \frac{1 + \Gamma_r + j\Gamma_i}{1 - \Gamma_r - j\Gamma_i} \quad (3.4)$$

The preceding equation represents a mapping from one complex plane, the z_{in} -plane, to a second complex plane, the Γ -plane. Multiplying numerator and denominator of (3.4) by the complex conjugate of the denominator allows us to isolate real and imaginary parts of z_{in} in terms of the reflection coefficient. This means

$$z_{in} = r + jx = \frac{1 - \Gamma_r^2 - \Gamma_i^2 + 2j\Gamma_i}{(1 - \Gamma_r)^2 + \Gamma_i^2} \quad (3.5)$$

can be separated into

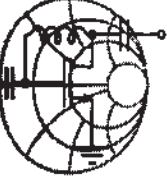
$$r = \frac{1 - \Gamma_r^2 - \Gamma_i^2}{(1 - \Gamma_r)^2 + \Gamma_i^2} \quad (3.6)$$

and

$$x = \frac{2\Gamma_i}{(1 - \Gamma_r)^2 + \Gamma_i^2} \quad (3.7)$$

Equations (3.6) and (3.7) are explicit transformation rules of finding z_{in} if the reflection coefficient is specified in terms of Γ_r and Γ_i . Therefore, the mapping from the complex Γ -plane into the z_{in} -plane is straightforward, as the following example underscores.

RF & MW →



Example 3-2: Input impedance of a terminated transmission line

A load impedance $Z_L = (30 + j60) \Omega$ is connected to a 50Ω transmission line of 2 cm length and operated at 2 GHz. Use the reflection coefficient concept and find the input impedance Z_{in} under the assumption that the phase velocity is 50% of the speed of light.

Solution: We first determine the load reflection coefficient

$$\Gamma_0 = \frac{Z_L - Z_0}{Z_L + Z_0} = \frac{30 + j60 - 50}{30 + j60 + 50} = 0.2 + j0.6 = \sqrt{2/5}e^{j71.56^\circ} \quad (3.8)$$

Next we compute $\Gamma(d = 2\text{cm})$ based on the fact that

$$\beta = \frac{2\pi}{\lambda} = \frac{2\pi f}{v_p} = \frac{2\pi f}{0.5c} = 83.77 \text{ m}^{-1}$$

This results in $2\beta d = 191.99^\circ$ and yields for the reflection coefficient

$$\Gamma = \Gamma_0 e^{-j2\beta d} = \Gamma_r + j\Gamma_i = -0.32 - j0.55 = \sqrt{2/5}e^{-j120.43^\circ}$$

Having thus determined the reflection coefficient, we can now directly find the corresponding input impedance:

$$Z_{in} = Z_0 \frac{1 + \Gamma}{1 - \Gamma} = R + jX = 14.7 - j26.7 \Omega$$

We note that the reflection coefficient phasor form at the load, Γ_0 , is multiplied with a rotator that incorporates twice the electric line length βd . This mathematical statement thus conveys the idea that voltage/current waves have to travel to the load and return back to the source to define the input impedance.

Example 3.2 could have been solved just as efficiently by using the impedance equation (2.65) developed in Section 2.9.

3.1.3 Parametric Reflection Coefficient Equation

The goal of our investigation is to pursue a different approach toward computing the input impedance. This new approach involves the inversion of (3.6) and (3.7). In other words, we ask ourselves how a point in the z_{in} -domain, expressed through its normalized real, r , and imaginary, x , components, is mapped into the complex Γ -plane, where it then can be expressed in terms of the real, Γ_r , and imaginary, Γ_i , components of the reflection coefficient. Since Γ appears in the numerator and denominator, we have to suspect that straight lines in the impedance plane z_{in} may not be mapped into straight lines in the Γ -plane. All we can say at this point is that the matching of the load impedance to the transmission line impedance $Z_{in} = Z_0$, or $z_{in} = 1$, results in a zero reflection coefficient (i.e., $\Gamma_r = \Gamma_i = 0$) located in the center of the Γ -plane.

The inversion of (3.6) is accomplished by going through the following basic algebraic operations:

$$r[(1 - \Gamma_r)^2 + \Gamma_i^2] = 1 - \Gamma_r^2 - \Gamma_i^2 \quad (3.9a)$$

$$\Gamma_r^2(r + 1) - 2r\Gamma_r + \Gamma_i^2(r + 1) = 1 - r \quad (3.9b)$$

$$\Gamma_r^2 - \frac{2r}{r+1}\Gamma_r + \Gamma_i^2 = \frac{1-r}{r+1} \quad (3.9c)$$

At this point the trick consists in recognizing that Γ_r can be written as a complete binomial expression (see also Appendix C)

$$\left(\Gamma_r - \frac{r}{r+1}\right)^2 - \frac{r^2}{(r+1)^2} + \Gamma_i^2 = \frac{1-r}{r+1} \quad (3.9d)$$

This finally can be cast in the form

$$\left(\Gamma_r - \frac{r}{r+1}\right)^2 + \Gamma_i^2 = \left(\frac{1}{r+1}\right)^2 \quad (3.10)$$

In an identical way as done previously, we proceed to invert (3.7). The result for the normalized reactance is

$$(\Gamma_r - 1)^2 + \left(\Gamma_i - \frac{1}{x}\right)^2 = \left(\frac{1}{x}\right)^2 \quad (3.11)$$

Both (3.10) and (3.11) are parametric equations of circles in the complex Γ -plane that can be written in the generic form $(\Gamma_r - a)^2 + (\Gamma_i - b)^2 = c^2$. Here a, b denote shifts along the real and imaginary Γ axes, and c is the radius of the circle.

Figure 3-2 depicts the parametric circle equations of (3.10) for various resistances. For example, if the normalized resistance r is zero, the circle is centered at the origin and possesses a radius of 1, since (3.10) reduces to $\Gamma_r^2 + \Gamma_i^2 = 1$. For $r = 1$ we find $(\Gamma_r - 1/2)^2 + \Gamma_i^2 = (1/2)^2$, which represents a circle of radius $1/2$ shifted in the positive Γ_r direction by $1/2$ units. We conclude that as r increases, the radii of the circles are continually reduced and shifted further to the right toward the point 1 on the real axis. In the limit for $r \rightarrow \infty$ we see that the shift converges to the point $r/(r+1) \rightarrow 1$ and the circle radius approaches $1/(r+1)^2 \rightarrow 0$.

It is important to realize that this mapping transforms fixed values of r only and does not involve x . Thus, for a fixed r an infinite range of reactance values x , as indicated by the straight lines in the z -plane, maps onto the same resistance circle. The mapping involving r alone is therefore not a unique point-to-point correspondence.

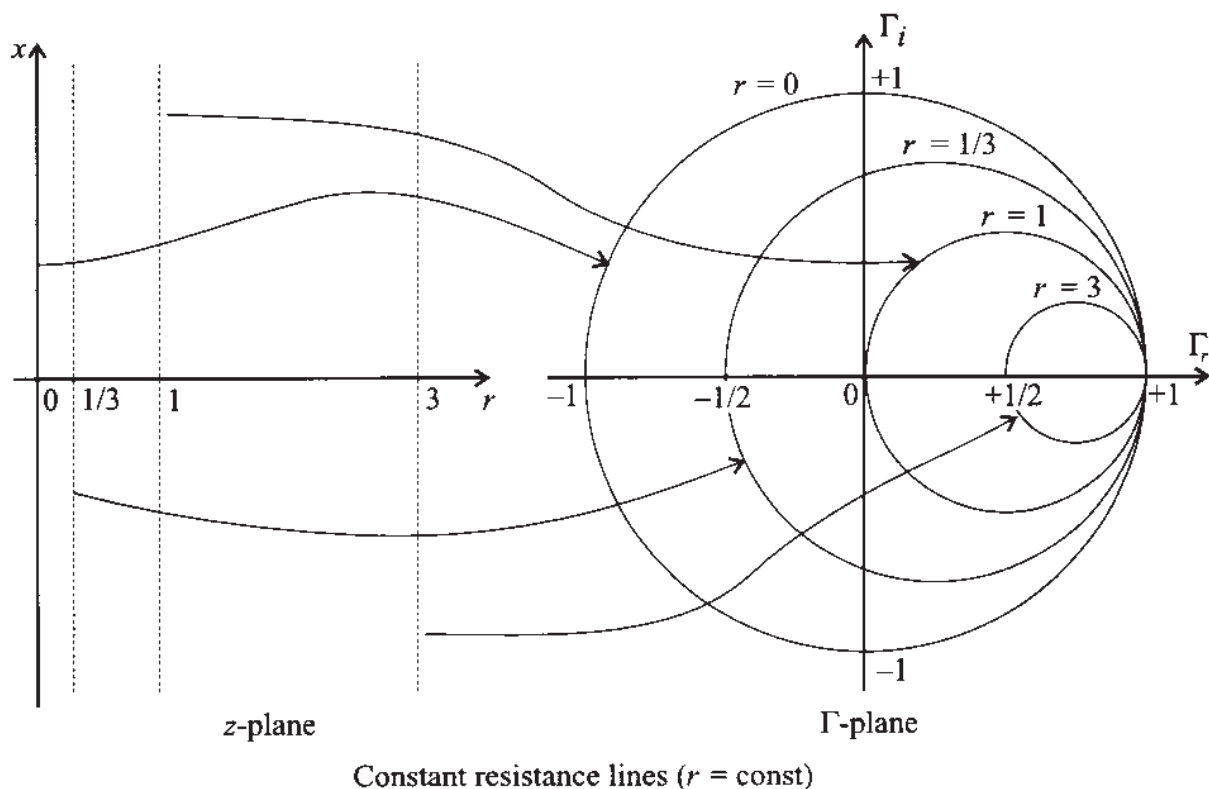


Figure 3-2 Parametric representation of the normalized resistance r in the complex Γ -plane.

A different graphical display results for the circle equation (3.11), which involves the normalized reactance. Here the centers of the circles reside all along a line perpendicular to the $\Gamma_r = 1$ point. For instance, for $x = \infty$ we note that $(\Gamma_r - 1)^2 + \Gamma_i^2 = 0$, which is a circle of zero radius, or a point located at $\Gamma_r = 1$ and $\Gamma_i = 0$. For $x = 1$ we see that the circle equation becomes $(\Gamma_r - 1)^2 + (\Gamma_i - 1)^2 = 1$. As $x \rightarrow 0$ the radii and shifts along the positive imaginary axis approach infinity. Interestingly, the shifts

can also be along the negative imaginary axis. Here for $x = -1$ we notice that the circle equation becomes $(\Gamma_r - 1)^2 + (\Gamma_i + 1)^2 = 1$ with the center located at $\Gamma_r = 1$ and $\Gamma_i = -1$. We observe that negative x -values refer to capacitive impedances residing in the lower half of the Γ -plane. Figure 3-3 shows the parametric form of the normalized imaginary impedance. For better readability the circles are displayed inside the unit circle only. In contrast to Figure 3-2 we notice that fixed x -values are mapped into circles in the Γ -plane for arbitrary resistance values $0 \leq r < \infty$, as indicated by the straight lines in the impedance plane.

The transformations (3.10) and (3.11) taken individually do not constitute unique mappings from the normalized impedance into the reflection coefficient plane. In other words, impedance points mapped into the Γ -plane by either (3.10) or (3.11) cannot uniquely be inverted back into the original impedance points. However, since the transformations complement each other, a unique mapping can be constructed by combining both transformations, as discussed in the next section.

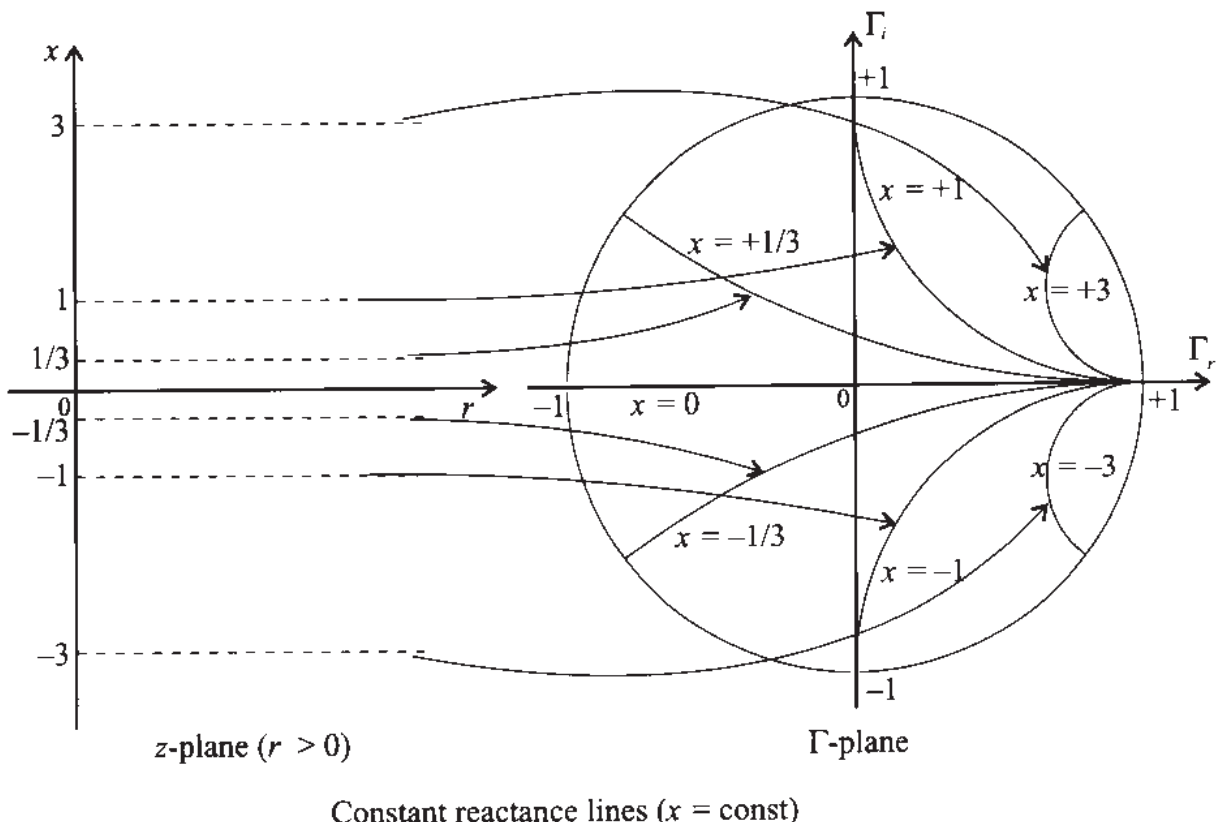


Figure 3-3 Parametric representation of the normalized reactance x in the complex Γ -plane.

3.1.4 Graphical Representation

Combining the parametric representations for normalized resistance and reactance circles (i.e., Figures 3-2 and 3-3) for $|\Gamma| \leq 1$ results in the Smith Chart as illustrated in

Figure 3-4. An important observation of the Smith Chart is that there is a *one-to-one mapping* between the normalized impedance plane and the reflection coefficient plane. We notice also that the normalized resistance circles r have a range $0 \leq r < \infty$ and the normalized reactance circles x can represent either negative (i.e., capacitive) or positive (i.e., inductive) values in the range $-\infty < x < +\infty$.

It should be pointed out that the reflection coefficient does not have to satisfy $|\Gamma| \leq 1$. Negative resistances, encountered for instance as part of the oscillation condition for resonators, lead to the case $|\Gamma| > 1$ and consequently map to points residing outside the unit circle. Graphical displays where the reflection coefficient is greater than 1 are known as **compressed Smith Charts**. These charts, however, play a rather limited role in RF/MW engineering designs and are therefore not further pursued in this text. The interested reader may consult specialized literature (see the Hewlett-Packard application note listed at the end of this chapter).

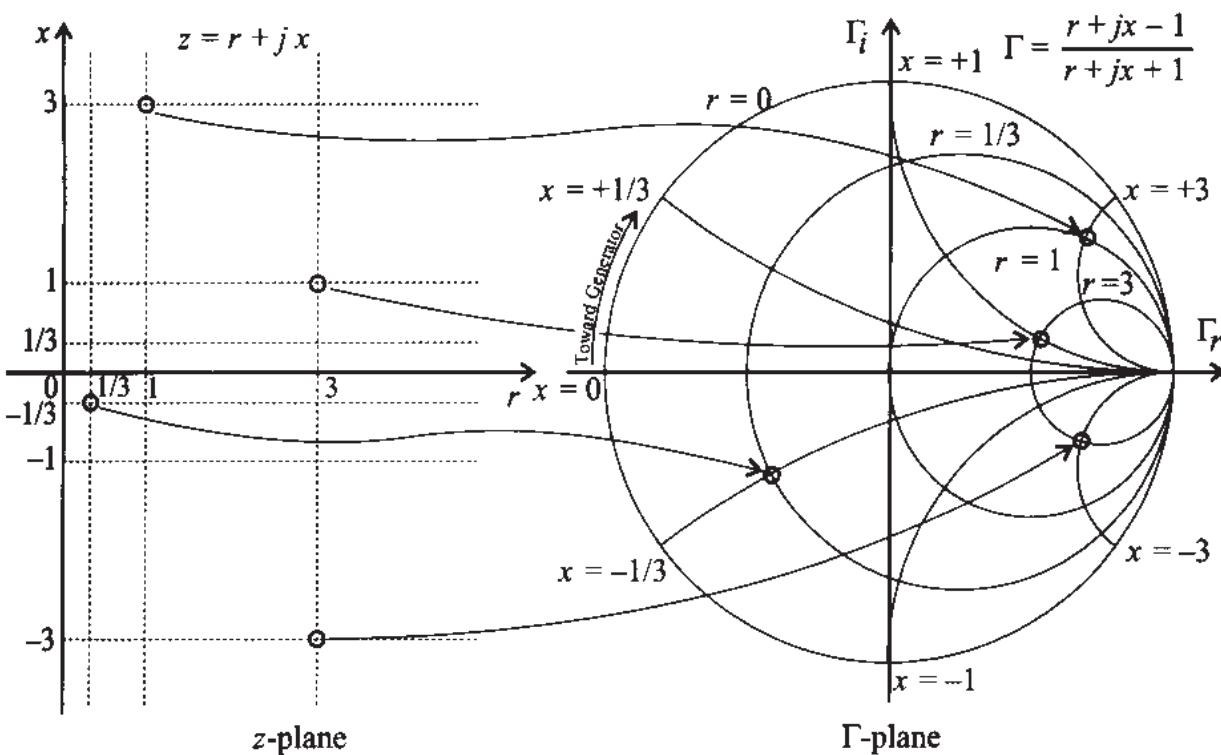


Figure 3-4 Smith Chart representation by combining r and x circles for $|\Gamma| \leq 1$.

In Figure 3-4 we must note that the angle of rotation $2\beta d$ introduced by the length of the transmission line is measured from the phasor location of $\Gamma_0 = |\Gamma_0| e^{j\theta_L}$ in clockwise (mathematically negative) direction due to the negative exponent ($-2j\beta d$) in the reflection coefficient expression (3.2). For the computation of the input impedance of a terminated transmission line, the motion is thus always *away from the load impedance or toward the generator*. This rotation is indicated by an arrow on the periphery of the chart. We further observe that a complete revolution around the unit circle requires

$$2\beta d = 2\frac{2\pi}{\lambda}d = 2\pi$$

where $d = \lambda/2$ or 180° . The quantity βd is sometimes referred to as the **electrical length** of the line.

3.2 Impedance Transformation

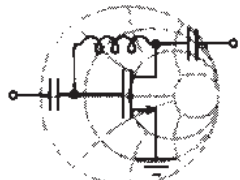
3.2.1 Impedance Transformation for General Load

The determination of the impedance response of a high-frequency circuit is often a critical issue for the RF design engineer. Without detailed knowledge of the impedance behavior, RF/MW system performance cannot adequately be predicted. In this section we will elaborate on how the impedance can be determined easily and efficiently with the aid of the previously introduced Smith Chart.

A typical Smith Chart computation involving a load impedance Z_L connected to a transmission line of characteristic line impedance Z_0 and length d proceeds according to the following six steps:

1. Normalize the load impedance Z_L with respect to the line impedance Z_0 to determine z_L .
2. Locate z_L in the Smith Chart.
3. Identify the corresponding load reflection coefficient Γ_0 in the Smith Chart both in terms of its magnitude and phase.
4. Rotate Γ_0 by twice its electrical length βd to obtain $\Gamma_{in}(d)$.
5. Record the normalized input impedance z_{in} at this spatial location d .
6. Convert z_{in} into the actual impedance Z_{in} .

Example 3-3 goes through these steps, which are the standard procedure to arrive at the graphical impedance solution.



RF & MW →

Example 3-3: Transmission line input impedance determination with the Smith Chart

Solve Example 3-2 by following the six-step Smith Chart computations given in the preceding list.

Solution: We commence with the load impedance $Z_L = (30 + j60) \Omega$ and proceed according to the previously outlined steps:

1. The normalized load impedance is

$$z_L = (30 + j60)/50 = 0.6 + j1.2$$

2. This point can be identified in the Smith Chart as the intersection of the circle of constant resistance $r = 0.6$ with the circle of constant reactance $x = 1.2$, as seen in Figure 3-5.

3. The straight line connecting the origin to point z_L determines the load reflection coefficient Γ_0 . The associated angle is recorded with respect to the positive real axis.

4. Keeping in mind that the outside circle on the Smith Chart corresponds to the unity reflection coefficient ($|\Gamma_0| = 1$), we can find its magnitude as the length of the vector connecting the origin to z_L . Rotating this vector by twice the electrical length of the line (i.e., $2 \times \beta d = 2 \times 96^\circ = 192^\circ$) yields the input reflection coefficient Γ_{in} .

5. This point uniquely identifies the associated normalized input impedance $z_{in} = 0.3 - j0.53$.

6. The preceding normalized impedance can be converted back into actual input impedance values by multiplying it by $Z_0 = 50 \Omega$, resulting in the final solution: $Z_{in} = (15 - j26.5)\Omega$.

We recall that the exact value of the input impedance obtained in Example 3-2 is $(14.7 - j26.7) \Omega$. The small discrepancy is understandable because of the approximate processing of the graphical data in the Smith Chart. The entire sequence of steps leading to the determination of the input impedance of the line connected to the load is shown in Figure 3-5.

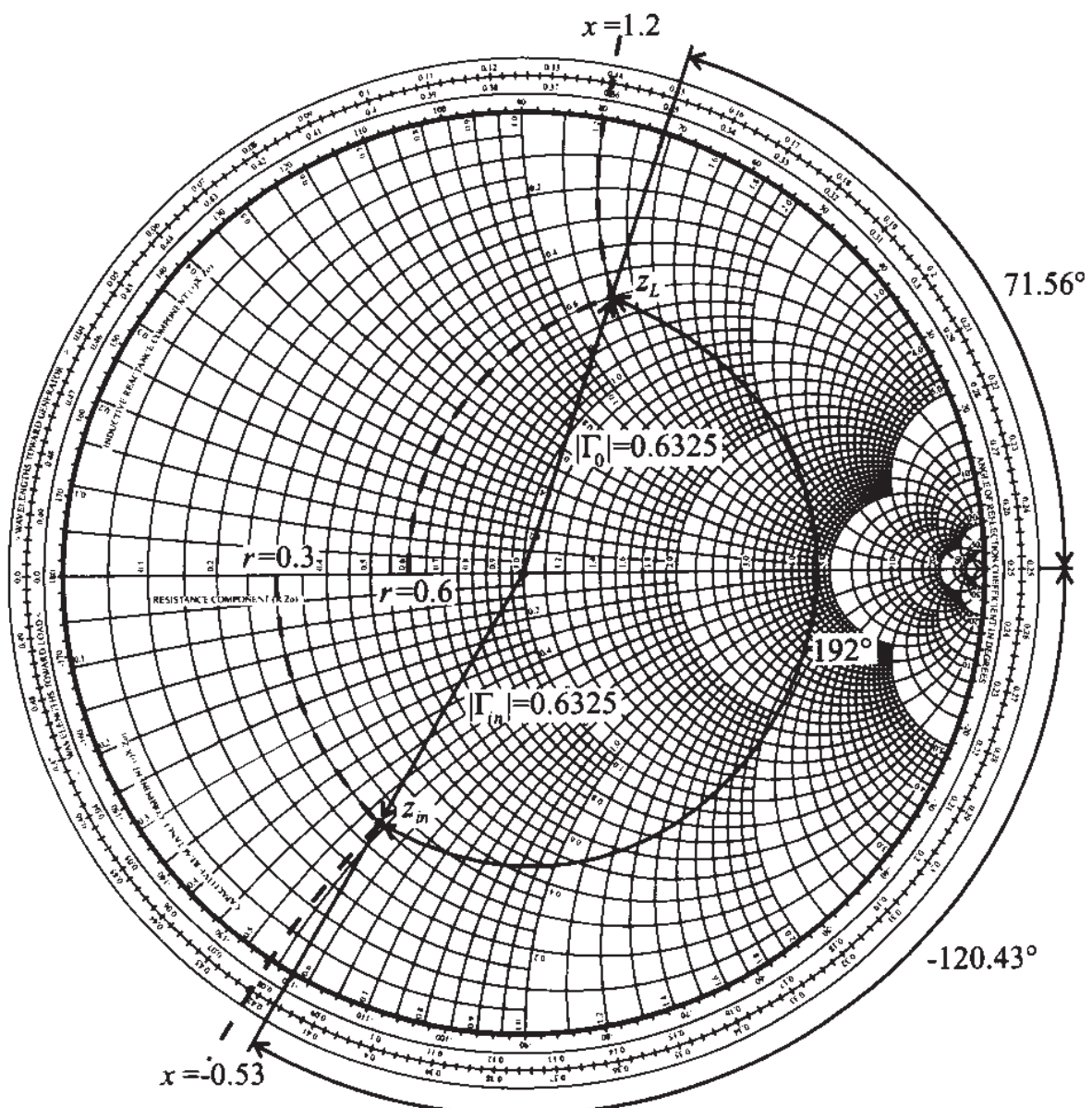


Figure 3-5 Usage of the Smith Chart to determine the input impedance for Example 3-3.

These steps appear at first cumbersome and prone to error if carried out by hand. However, using mathematical spreadsheets and relying on modern computer-based instrumentation, the calculations are routinely done in seconds and with a high degree of accuracy.

3.2.2 Standing Wave Ratio

From the basic definition of the SWR in Section 2.8.3 it follows that for an arbitrary distance d along the transmission line, the standing wave ratio is written

$$\text{SWR}(d) = \frac{1 + |\Gamma(d)|}{1 - |\Gamma(d)|} \quad (3.12)$$

where $\Gamma(d) = \Gamma_0 \exp(-j2\beta d)$. Equation (3.12) can be inverted to give

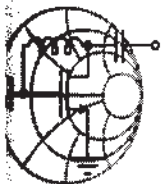
$$|\Gamma(d)| = \frac{\text{SWR} - 1}{\text{SWR} + 1} \quad (3.13)$$

This form of the reflection coefficient permits the representation of the SWR as circles in the Smith Chart with the matched condition $\Gamma(d) = 0$ (or $\text{SWR} = 1$) being the origin.

It is interesting to note that equation (3.12) is very similar in appearance to the expression for determining the impedance from a given reflection coefficient:

$$Z(d) = Z_0 \frac{1 + \Gamma(d)}{1 - \Gamma(d)} \quad (3.14)$$

This similarity, together with the fact that for $|\Gamma(d)| \leq 1$ the SWR is greater or equal to unity, suggests that the actual numerical value for the SWR can be found from the Smith Chart by finding the intersection of the circle of radius $|\Gamma(d)|$ with the right-hand side of the real axis.



RF & MW →

Example 3-4: Reflection coefficient, voltage standing wave ratio, and return loss

Four different load impedances:

- (a) $Z_L = 50 \Omega$,
 - (b) $Z_L = 48.5 \Omega$,
 - (c) $Z_L = (75 + j25) \Omega$, and
 - (d) $Z_L = (10 - j5) \Omega$,
- are sequentially connected to a 50Ω transmission line. Find the reflection coefficients and the SWR circles, and determine the return loss in dB.

Solution: The normalized load impedances and corresponding reflection coefficients, return loss, and SWR values are computed as follows:

- (a) $z_L = 1$, $\Gamma = (z_L - 1)/(z_L + 1) = 0$, $RL_{dB} = \infty$, $SWR = 1$
- (b) $z_L = 0.97$, $\Gamma = (z_L - 1)/(z_L + 1) = -0.015$, $RL_{dB} = 36.3$, $SWR = 1.03$
- (c) $z_L = 1.5 + j0.5$, $\Gamma = (z_L - 1)/(z_L + 1) = 0.23 + j0.15$, $RL_{dB} = 11.1$, $SWR = 1.77$
- (d) $z_L = 0.2 - j0.1$, $\Gamma = (z_L - 1)/(z_L + 1) = -0.66 - j0.14$, $RL_{dB} = 3.5$, $SWR = 5.05$

To determine the approximate values of the SWR requires us to exploit the similarity with the input impedance, as discussed previously. To this end, we first plot the normalized impedance values in the Smith Chart (see Figure 3-6). Then we draw circles with centers at the origin and radii whose lengths reach the respective impedance points defined in the previous step. From these circles we see that the load reflection coefficient for zero load reactance ($x_L = 0$) is

$$\Gamma_0 = \frac{z_L - 1}{z_L + 1} = \frac{r_L - 1}{r_L + 1} = \Gamma_r$$

The SWR can be defined in term of the real load reflection coefficient along the real Γ -axis:

$$SWR = \frac{1 + |\Gamma_0|}{1 - |\Gamma_0|} = \frac{1 + \Gamma_r}{1 - \Gamma_r}$$

This requires $|\Gamma_0| = \Gamma_r \geq 0$. In other words, for $\Gamma_r \geq 0$ we have to enforce $r_L \geq 1$, meaning that only the intersects of the right-hand-side circles with the real axis define the SWR.

As a graphical design tool, the Smith Chart allows immediate observation of the degree of mismatch between line and load impedances by plotting the radius of the SWR circle.

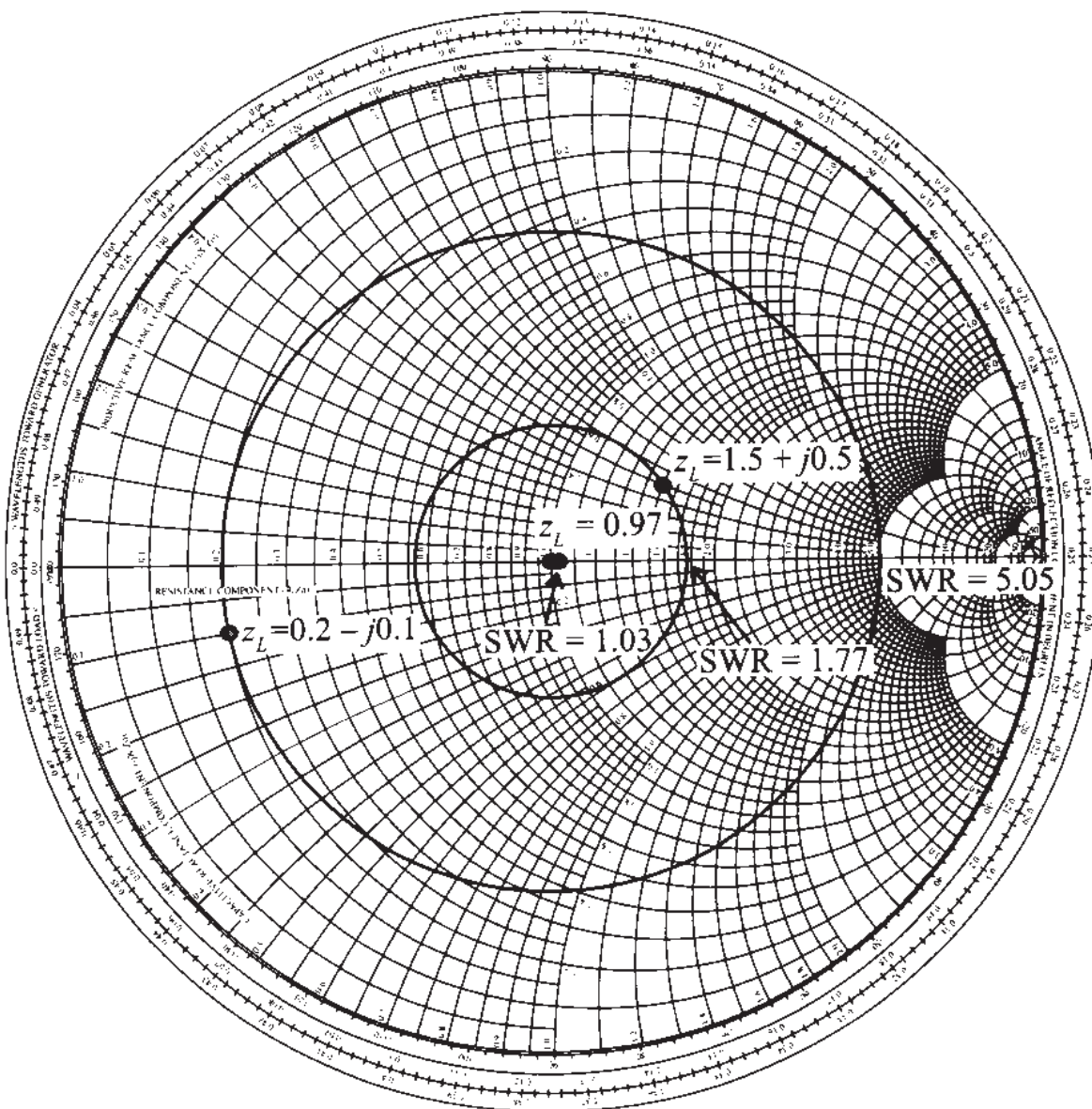


Figure 3-6 SWR circles for various reflection coefficients.

3.2.3 Special Transformation Conditions

The amount of rotation by which the point of the normalized transmission line impedance circles around the Smith Chart is controlled by the length of the line, or alternatively the operating frequency. Consequently, both inductive (upper plane) and capacitive (lower plane) impedances can be generated based on the line length and the termination conditions at a given frequency. These lumped circuit parameter representations, realized through distributed circuit analysis techniques, are of significant practical importance.

The cases of open- and short-circuit line termination are of particular interest in generating inductive and capacitive behavior and are examined in more detail next.

Open Circuit Transformations

To obtain a pure inductive or capacitive impedance behavior, we need to operate along the $r = 0$ circle. The starting point is the right-hand location ($\Gamma_0 = 1$) with rotation toward the generator in a clockwise sense.

A capacitive impedance $-jX_C$ is obtained through the condition

$$\frac{1}{j\omega C} \frac{1}{Z_0} \equiv z_{in} = -j \cot(\beta d_1) \quad (3.15)$$

as direct comparison with (2.70) shows. The line length d_1 is found to be

$$d_1 = \frac{1}{\beta} \left[\cot^{-1} \left(\frac{1}{\omega C Z_0} \right) + n\pi \right] \quad (3.16)$$

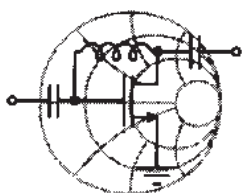
where $n\pi$ ($n = 1, 2, \dots$) is required due to the periodicity of the cotangent function. Alternatively, an inductive impedance jX_L can be realized via the condition

$$j\omega L \frac{1}{Z_0} \equiv z_{in} = -j \cot(\beta d_2) \quad (3.17)$$

The line length d_2 is now found to be

$$d_2 = \frac{1}{\beta} \left[\pi - \cot^{-1} \left(\frac{\omega L}{Z_0} \right) + n\pi \right] \quad (3.18)$$

Both conditions are schematically depicted in Figure 3-7. How to choose a particular open-circuit line length to exhibit capacitive or inductive behavior is discussed in the following example.



RF & MW →

Example 3-5: Representation of passive circuit elements through transmission line section

For an open-ended 50Ω transmission line operated at 3 GHz and with a phase velocity of 77% of the speed of light, find the line lengths to create a 2 pF capacitor and a 5.3 nH inductor. Perform your computations both by relying on (3.16) and (3.18) and by using the Smith Chart.

Solution: For a given value of phase velocity, the propagation constant is

$$\beta = 2\pi f / v_p = 2\pi f / (0.77c) = 81.6 \text{ m}^{-1}$$

Substituting this value into (3.16) and (3.18), we conclude that for the representation of a 2 pF capacitor we need an open-circuit line or stub with line length $d_1 = 13.27 + n38.5$ mm. For the realization of a 5.3 nH inductor, a $d_2 = 32.81 + n38.5$ mm stub is required.

The alternative method for computing the lengths of the required stubs is through the use of the Smith Chart (see Figure 3-7). At a 3-GHz frequency, the reactance of a 2 pF capacitor is $X_C = 1/(\omega C) = 26.5\Omega$. The corresponding normalized imped-

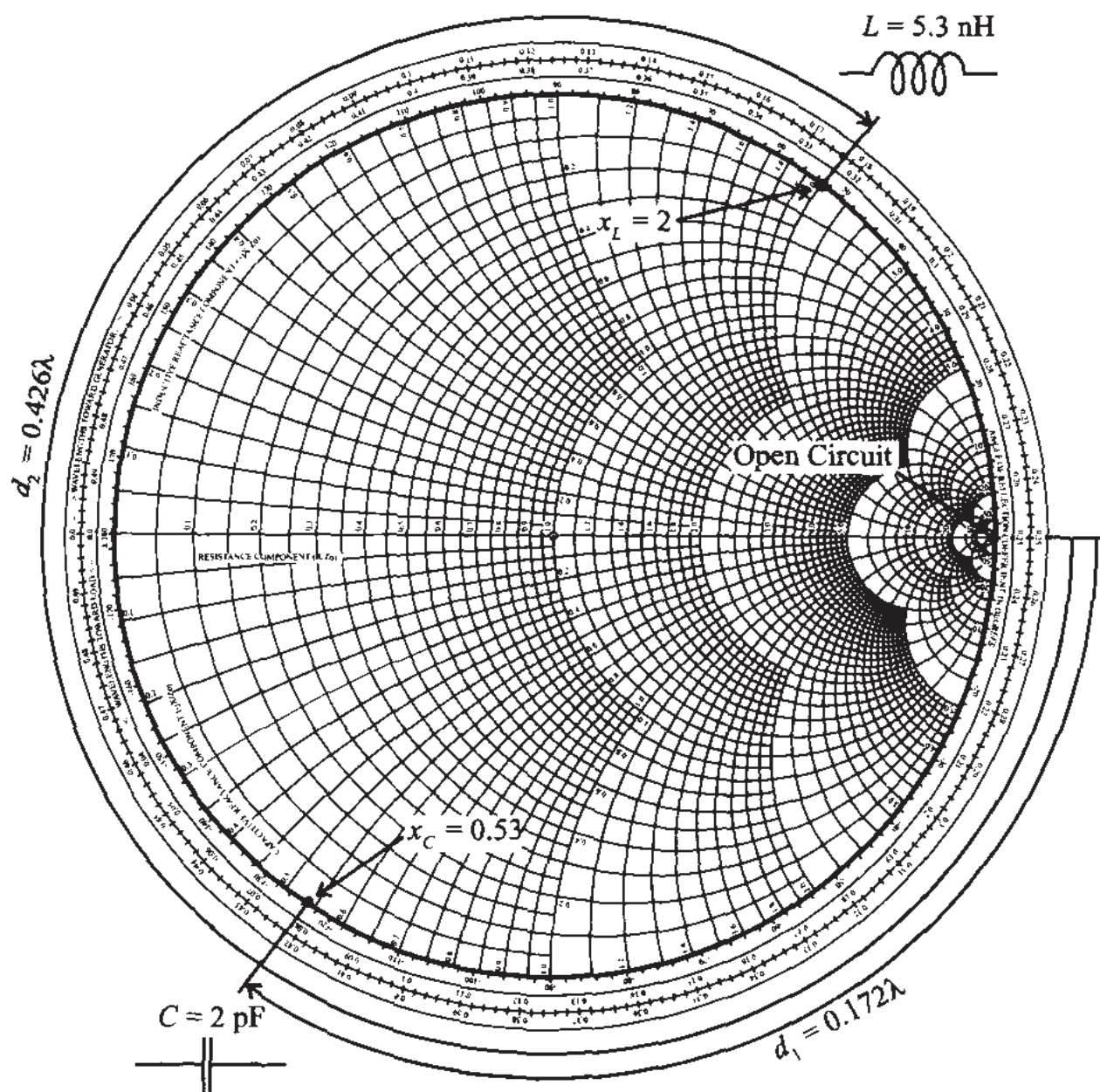


Figure 3-7 Creating capacitive and inductive impedances via an open-circuit transmission line.

ance in this case is $z_C = -jX_C = -j0.53$. From the Smith Chart we can deduce that the required transmission line length has to be approximately 0.172 of one wavelength. We note that for the given phase velocity, the wavelength is $\lambda = v_p/f = 77$ mm. This results in a line length of $d_1 = 13.24$ mm which is very close to the previously computed value of 13.27 mm. Similarly, for the inductance we obtain $z_L = j2$. The line length in this case is 0.426 of one wavelength, which is equal to 32.8 mm.

Circuits are often designed with lumped elements before converting them into transmission line segments, similar to the procedure described in this example.

Short-Circuit Transformations

Here the transformation rules follow similar procedures as outlined previously, except that the starting point in the Smith Chart is now the $\Gamma_0 = -1$ point on the real axis, as indicated in Figure 3-8.

A capacitive impedance $-jX_C$ follows from the condition

$$\frac{1}{j\omega C} \frac{1}{Z_0} \equiv z_{in} = j \tan(\beta d_1) \quad (3.19)$$

where use is made of (2.66). The line length d_1 is found to be

$$d_1 = \frac{1}{\beta} \left[\pi - \tan^{-1} \left(\frac{1}{\omega C Z_0} \right) + n\pi \right] \quad (3.20)$$

Alternatively, an inductive impedance jX_L can be realized via the condition

$$j\omega L \frac{1}{Z_0} \equiv z_{in} = j \tan(\beta d_2) \quad (3.21)$$

The line length d_2 is now found to be

$$d_2 = \frac{1}{\beta} \left[\tan^{-1} \left(\frac{\omega L}{Z_0} \right) + n\pi \right] \quad (3.22)$$

At high frequencies, it is very difficult to maintain perfect open-circuit conditions because of changing temperatures, humidity, and other parameters of the medium surrounding the open transmission line. For this reason short-circuit conditions are more preferable in practical applications. However, even a short-circuit termination becomes

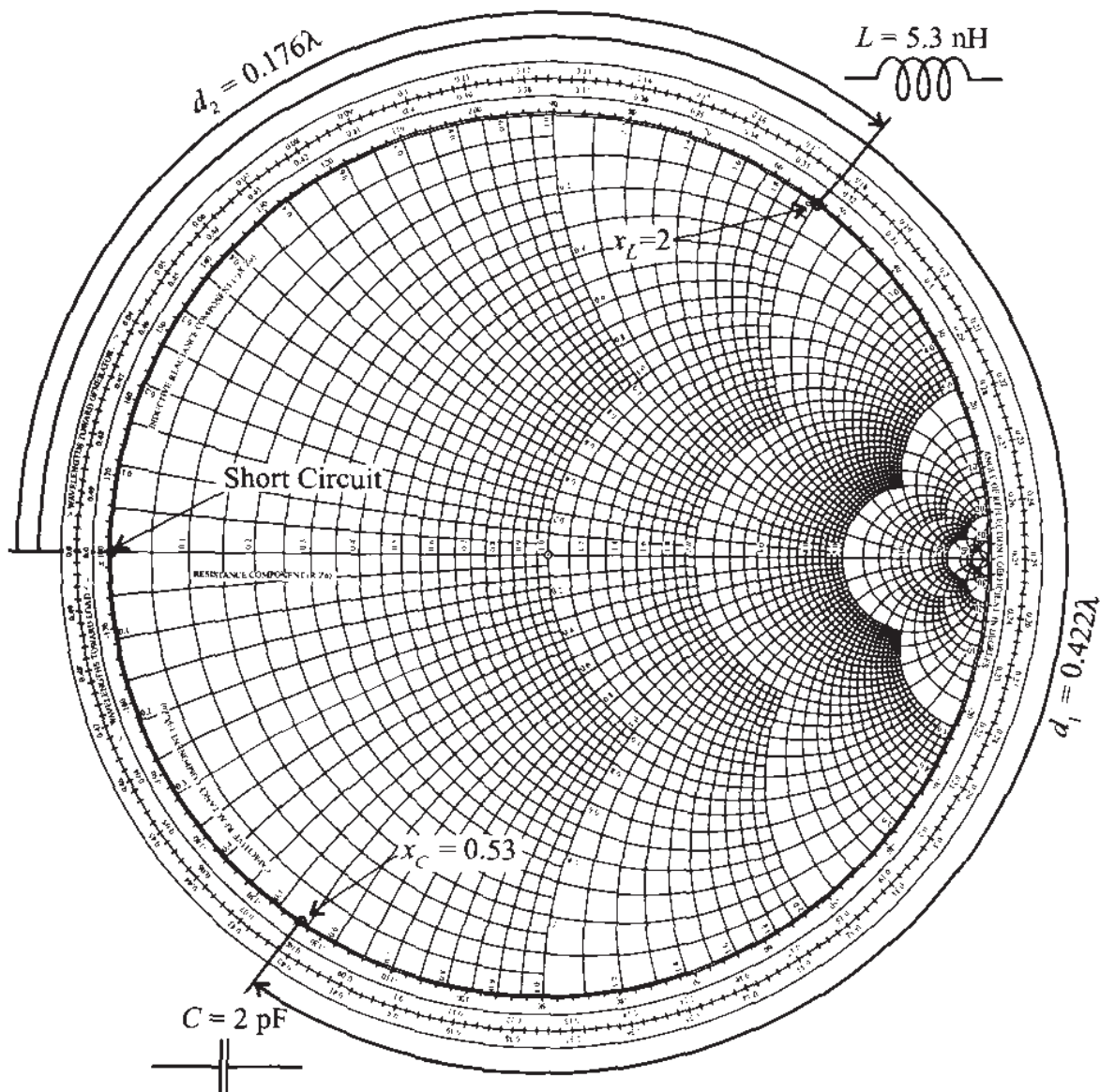


Figure 3-8 Creating capacitive and inductive impedances via a short-circuit transmission line.

problematic at very high frequencies or when through-hole connections in printed circuit boards are involved, since they result in additional parasitic inductances. Moreover, a design engineer may not have a choice if the circuit layout area is to be minimized by requiring the selection of the shortest line segments. For instance, the realization of a capacitor always yields the shortest length for an open-circuit line.

3.2.4 Computer Simulations

There are many **computer aided design** (CAD) programs available to facilitate the RF/MW circuit design and simulation processes. These programs can perform a multitude of tasks, varying from simple impedance calculations to complex circuit optimizations and circuit board layouts. One commercial software package that is used throughout

this textbook is called **Monolithic and Microwave Integrated Circuit Analysis and Design (MMICAD)** (Optotek Ltd., Kanata, Ontario, Canada), which is a linear simulator program with optimization tools. Another well-known program with advanced features is EESof's **Libra** package (Hewlett-Packard Corporation, Westlake Village, CA, USA), which is capable of performing linear as well as nonlinear analyses and optimizations.

It is not the purpose of this textbook to review and discuss the various CAD programs presently in industrial and academic use. However, to reproduce the subsequent simulation results, Appendix I provides a brief introduction to the basic features of MATLAB, which was chosen as a tool to carry out most simulations presented in this book.

The main reason for using MATLAB is its wide-spread use as a mathematical spreadsheet which permits easy programming and direct graphical display. This eliminates the need to rely on complex and expensive programs accessible to only a few readers. The benefit of a MATLAB routine will immediately become apparent when the Smith Chart computations have to be performed repetitively for a range of operating frequencies or line lengths as the following discussion underscores.

In this section we revisit Example 3-2, which computed the input reflection coefficient and input impedance of a generic transmission line connected to a load. We now extend this example beyond a single operating frequency and a fixed line length. Our goal is to examine the effect of a frequency sweep in the range from 0.1 GHz to 3 GHz and a change in line length varying from 0.1 cm to 3 cm. The example MATLAB routine, which performs the analysis of the transmission line length changing from 0.1 cm to 3 cm at a fixed operating frequency 2 GHz, is as follows:

```

smith_chart;          % plot smith chart
Set_z0(50);          % set characteristic impedance to 50 Ohm
s_Load(30+j*60);    % set load impedance to 30+j60 Ohm
vp=0.5*3e8;          % compute phase velocity
f=2e9;               % set frequency to 2 GHz
d=0.0:0.001:0.03;   % set the line length to a range from 0 to
                     % 3 cm in 1 mm increments
betta=2*pi*f/vp;    % compute propagation constant
Gamma=(ZL-Z0)/(ZL+Z0); % compute load reflection coefficient
rd=abs(Gamma);       % magnitude of the reflection coefficient
alpha=angle(Gamma)-2*betta*d; % phase of the reflection
                               % coefficient
plot(rd*cos(alpha),rd*sin(alpha)); % plot the graph

```

In the first line of the MATLAB code (see file fig3_9.m on the accompanying CD) we generate the Smith Chart with the necessary resistance and reactance circles. The next lines define the characteristic line impedance $Z_0 = 50 \Omega$, load impedance

$Z_L = (30 + j60) \Omega$, operation frequency $f = 2 \times 10^9$ Hz, and phase velocity $v_p = 0.5 \times 3 \times 10^8$ m/s. The command line $d=0.0:0.001:0.03$ creates an array d representing the transmission line length, which is varied from 0 mm to 3 cm in 1-mm increments. After all parameters have been identified, the magnitude and phase of the input reflection coefficients have to be computed. This is accomplished by determining the propagation constant $\beta = 2\pi f/v_p$, load reflection coefficient $\Gamma_0 = (Z_L - Z_0)/(Z_L + Z_0)$ and its magnitude $|\Gamma_0|$, and the total angle of rotation $\alpha = \angle(\Gamma_0) - 2\beta d$. Finally, the display of the impedance as part of the Smith Chart is done through the plot command, which requires both real and imaginary phasor arguments $|\Gamma_0|\cos(\alpha)$ and $|\Gamma_0|\sin(\alpha)$. The final result is shown in Figure 3-9.

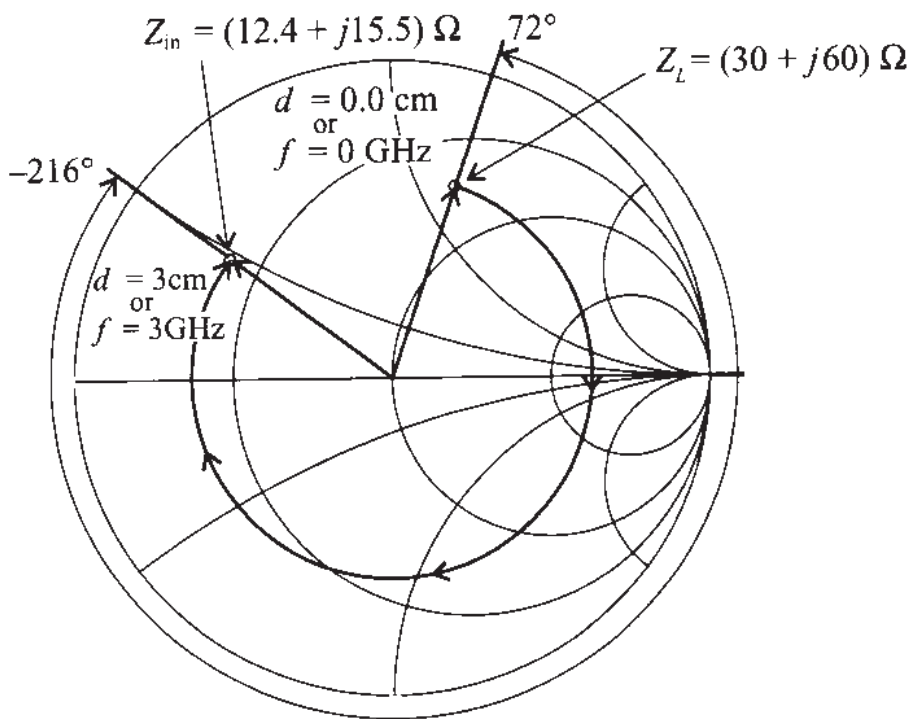


Figure 3-9 Input impedance of a loaded line of 2 cm length for a sweep in operating frequency from 0.0 to 3 GHz. If the operating frequency is fixed at 2 GHz and the line length is varied from 0.0 to 3 cm, the same impedance curve is obtained.

For the case where the length of the line is fixed to be 2 cm and the frequency is swept from values ranging from 0.0 to 3 GHz, the only necessary modification to the above input file is to set $d=0.02$, followed by specifying the frequency range in increments of 100 MHz (i.e., $f=0.0:1e7:3e9$). We should note that in both cases the electrical length (βd) of the line changes from 0° to 144° . Therefore, the impedance graphs produced for both cases are identical.

At the end of the rotation, either by fixing the frequency and varying the length or vice versa, the input impedance is found to be $Z_{in} = (12.4 + j15.5) \Omega$. It is reassuring that for a fixed frequency $f = 2$ GHz and a line length range $d = 0 \dots 2$ cm, weulti-

mately arrive at the same input impedance of $Z_{in} = (14.7 - j26.7) \Omega$ as obtained in Example 3-2.

3.3 Admittance Transformation

3.3.1 Parametric Admittance Equation

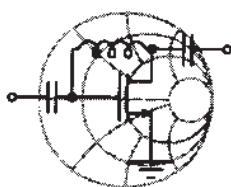
From the representation of the normalized input impedance (3.4), it is possible to obtain a normalized admittance equation by simple inversion:

$$y_{in} = \frac{Y_{in}}{Y_0} = \frac{1}{z_{in}} = \frac{1 - \Gamma(d)}{1 + \Gamma(d)} \quad (3.23)$$

where $Y_0 = 1/Z_0$. To represent (3.23) graphically in the Smith Chart, we have several options. A very intuitive way of displaying admittances in the conventional Smith Chart or **Z-Smith Chart** is to recognize that (3.23) can be found from the standard representation (3.4) via

$$\frac{1 - \Gamma(d)}{1 + \Gamma(d)} = \frac{1 + e^{-j\pi}\Gamma(d)}{1 - e^{-j\pi}\Gamma(d)} \quad (3.24)$$

In other words, we take the normalized input impedance representation and multiply the reflection coefficient by $-1 = e^{-j\pi}$, which is equivalent to a 180° rotation in the complex Γ -plane.



RF & MW →

Example 3-6: Use of the Smith Chart for converting impedance to admittance

Convert the normalized input impedance $z_{in} = 1 + j1 = \sqrt{2}e^{j(\pi/4)}$ into normalized admittance and display it in the Smith Chart.

Solution: The admittance can be found by direct inversion, that is

$$y_{in} = \frac{1}{\sqrt{2}}e^{-j(\pi/4)} = \frac{1}{2} - j\frac{1}{2}$$

In the Smith Chart we simply rotate the reflection coefficient corresponding to z_{in} by 180° to obtain the impedance. Its *numerical* value is equal to y_{in} as shown in Figure 3-10. To denormalize y_{in}

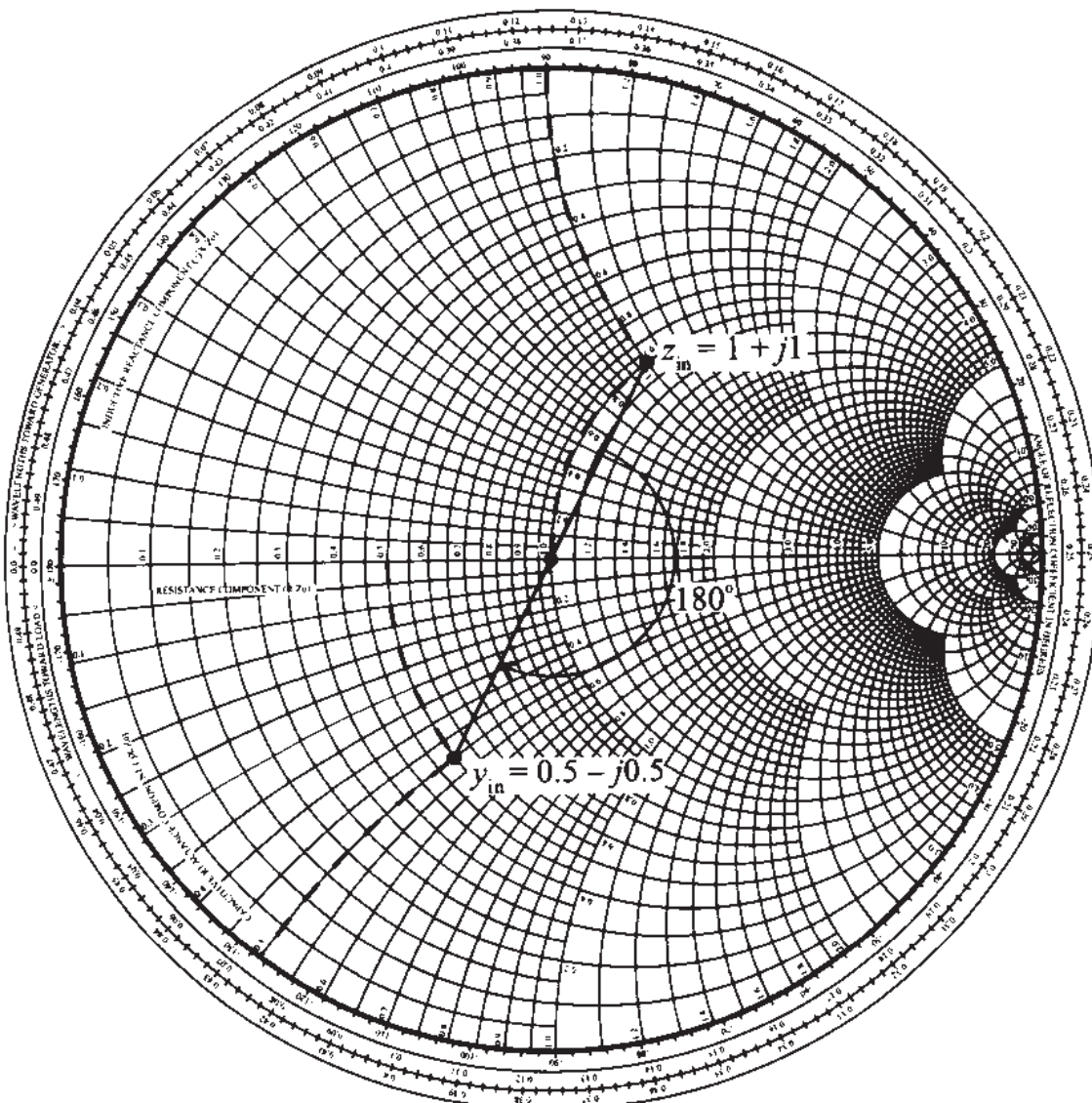


Figure 3-10 Conversion from impedance to admittance by 180° rotation.

we multiply by the inverse of the impedance normalization factor. Thus,

$$Y_{in} = \frac{1}{Z_0} y_{in} = Y_0 y_{in}.$$

Rotations by 180 degrees to convert from the impedance to the admittance representation require only a reflection about the origin in the Γ -plane.

In addition to the preceding operation, there is a widely used additional possibility. Instead of rotating the reflection coefficient by 180° in the Z-Smith Chart, we can

rotate the Smith Chart itself. The chart obtained by this transformation is called the **admittance Smith Chart** or the **Y -Smith Chart**. The correspondences are such that normalized resistances become normalized conductances and normalized reactances become normalized susceptances. That is,

$$r = \frac{R}{Z_0} \Rightarrow g = \frac{G}{Y_0} = Z_0 G$$

and

$$x = \frac{X}{Z_0} \Rightarrow b = \frac{B}{Y_0} = Z_0 B$$

This reinterpretation is depicted in Figure 3-11 for a particular normalized impedance point $z = 0.6 + j1.2$.

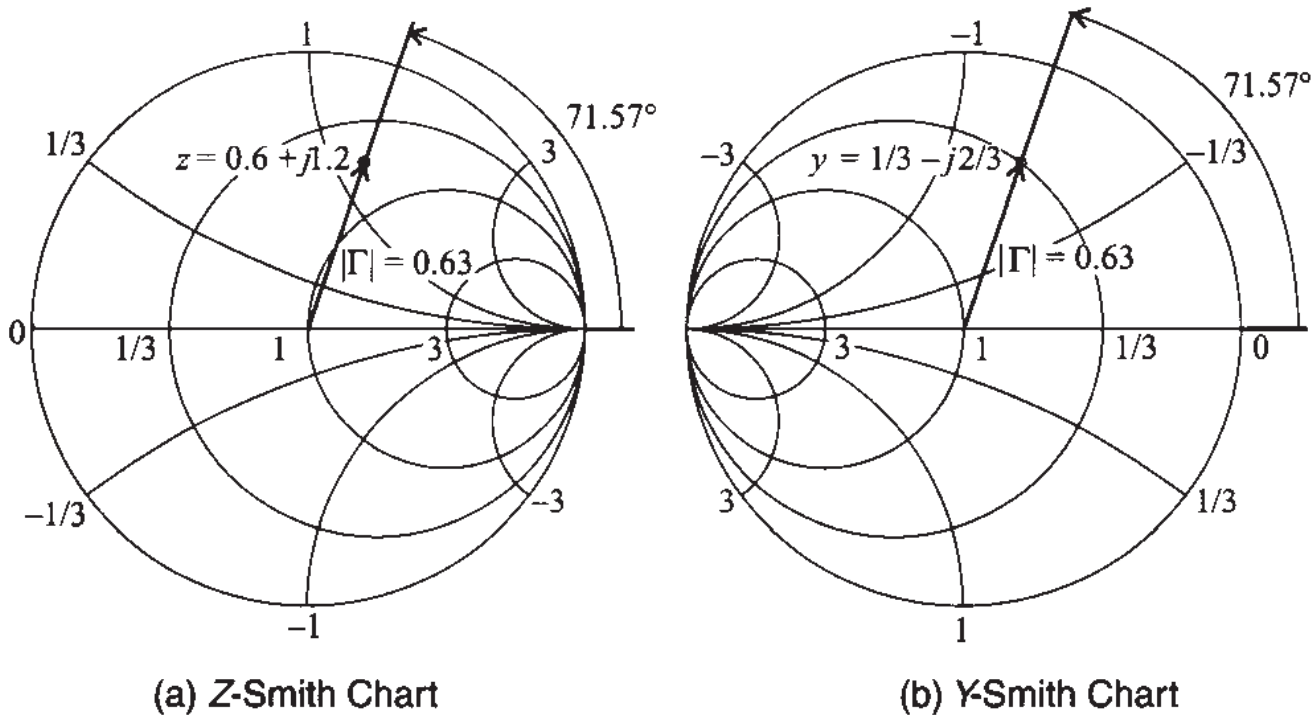


Figure 3-11 Reinterpretation of the Z-Smith Chart as a Y-Smith Chart.

As seen in Figure 3-11, the transformation preserves (a) the direction in which the angle of the reflection coefficient is measured and (b) the direction of rotation (either toward or away from the generator). Attention has to be paid to the proper identification of the extreme points: A short-circuit condition $z_L = 0$ in the Z-Smith Chart is $y_L = \infty$ in the Y-Smith Chart, and conversely an open-circuit $z_L = \infty$ in the Z-Smith Chart is $y_L = 0$ in the Y-Smith Chart. Furthermore, negative values of susceptance are plotted now in the upper half of the chart, corresponding to inductive behavior, and positive values in the bottom half, corresponding to capacitive behavior. The real component of the admittance increases from right to left.

To complete our discussion of the *Y-Smith Chart*, we should mention an additional, often employed definition of the admittance chart. Here the admittance is represented in exactly the same manner as the impedance chart without a 180° rotation. In this case the reflection coefficient phase angle is measured from the opposite end of the chart (see the book by Gonzalez listed in Further Reading at the end of this chapter).

3.3.2 Additional Graphical Displays

In many practical design applications it is necessary to switch frequently from impedance to admittance representations and vice versa. To deal with those situations a combined, or so-called **ZY-Smith Chart**, can be obtained by overlaying the *Z*- and *Y*-Smith Charts, as shown in Figure 3-12.

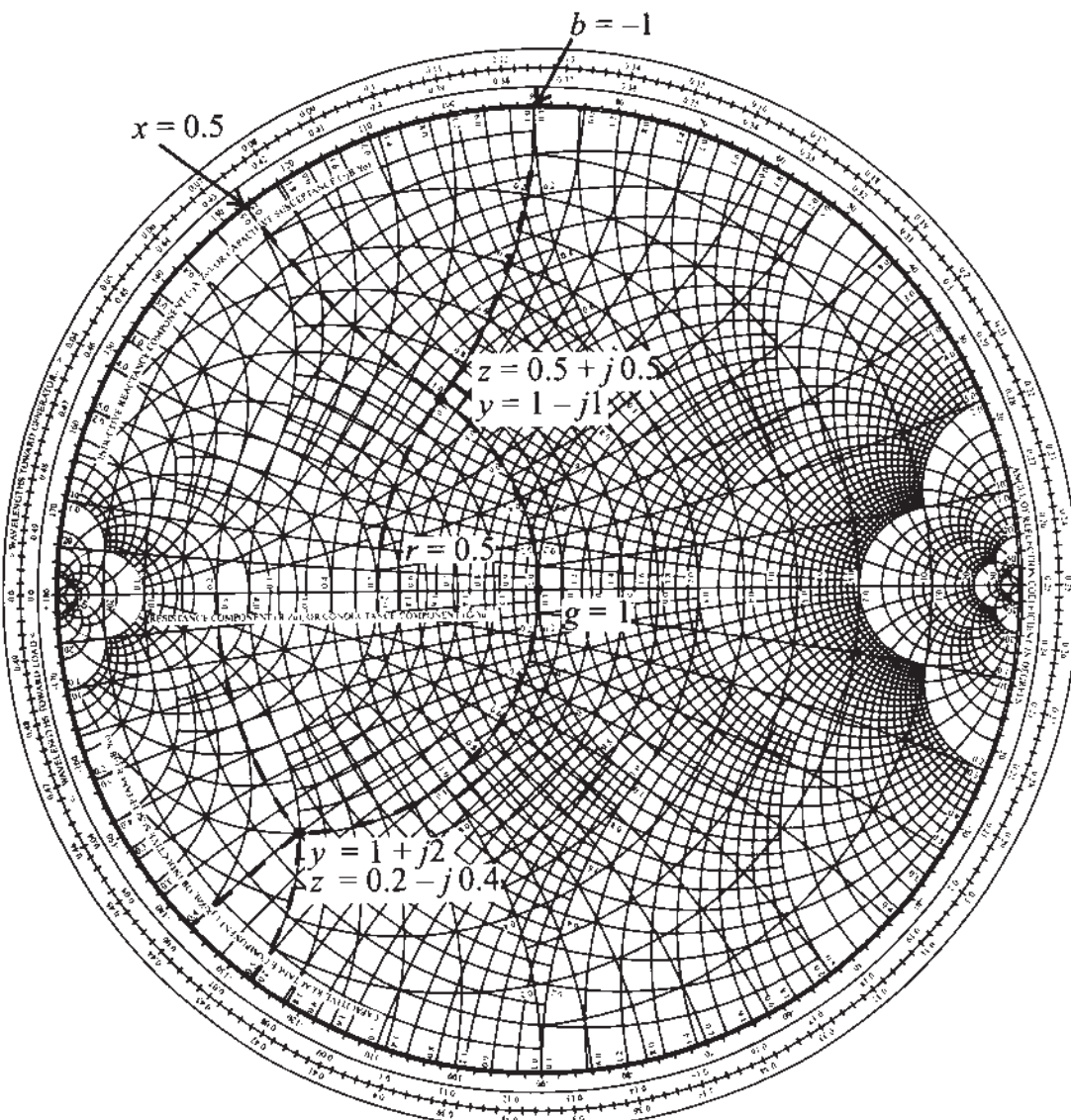
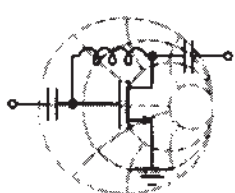


Figure 3-12 The *ZY-Smith Chart* superimposes the *Z*- and *Y*-Smith Charts in one graphical display.

This combined ZY-Smith Chart allows direct conversion between impedances and admittances. In other words, a point in this combined chart has two interpretations depending on whether the Z-Chart or Y-Chart display is chosen.



RF & MW →

Example 3-7: Use of the combined ZY-Smith Chart

Identify (a) the normalized impedance value $z = 0.5 + j0.5$ and (b) the normalized admittance value $y = 1 + j2$ in the combined ZY-Smith Chart and find the corresponding values of normalized admittance and impedance.

Solution: Let us first consider the normalized impedance value $z = 0.5 + j0.5$. In the combined ZY-Smith Chart we locate the impedance by using circles of constant resistance $r = 0.5$ and constant reactance $x = 0.5$, as shown in Figure 3-12. The intersection of these two circles determines the specified impedance value $z = 0.5 + j0.5$. To find the corresponding admittance value we simply move along the circles of constant conductance g and susceptance b . The intersection gives us $g = 1$ and $jb = -j1$ (i.e., the admittance for part (a) of this example is $y = 1 - j1$). The solution for the normalized admittance $y = 1 + j2$ is obtained in identical fashion and is also illustrated in Figure 3-12.

The ZY-Smith Chart requires a fair amount of practice due to its “busy” appearance and the fact that inductors and capacitors are counted either in positive or negative units depending on whether an impedance or admittance representation is needed.

3.4 Parallel and Series Connections

In the following sections several basic circuit element configurations are analyzed and their impedance responses are displayed in the Smith Chart as a function of frequency. The aim is to develop insight into how the impedance/admittance behaves over a range of frequencies for different combinations of lumped circuit parameters. A prac-

tical understanding of these circuit responses is needed later in the design of matching networks (see Chapter 8) and in the development of equivalent circuit models.

3.4.1 Parallel Connection of R and L Elements

Recognizing that $g = Z_0/R$ and $b_L = +Z_0/(\omega L)$, we can locate the normalized admittance value in the upper Y-Smith Chart plane for a particular, fixed normalized conductance g at a certain angular frequency ω_L :

$$y_{in}(\omega_L) = g - j \frac{Z_0}{\omega_L L} \quad (3.25)$$

As the angular frequency is increased to the upper limit ω_U , we trace out a curve along the constant conductance circle g . Figure 3-13 schematically shows the frequency-dependent admittance behavior for various constant conductance values $g = 0.3, 0.5, 0.7$, and 1 and for frequencies ranging from 500 MHz to 4 GHz. For a fixed inductance value of $L = 10$ nH and a characteristic line impedance $Z_0 = 50 \Omega$, the susceptance always starts at -1.59 (500 MHz) and ends at -0.20 (4 GHz).

In Figure 3-13 and the following three additional cases, the transmission line characteristic impedance is represented as a lumped impedance of $Z_0 = 50 \Omega$. This is permissible since our interest is focused on the impedance and admittance behavior of different load configurations. For these cases the characteristic line impedance serves only as a normalization factor.

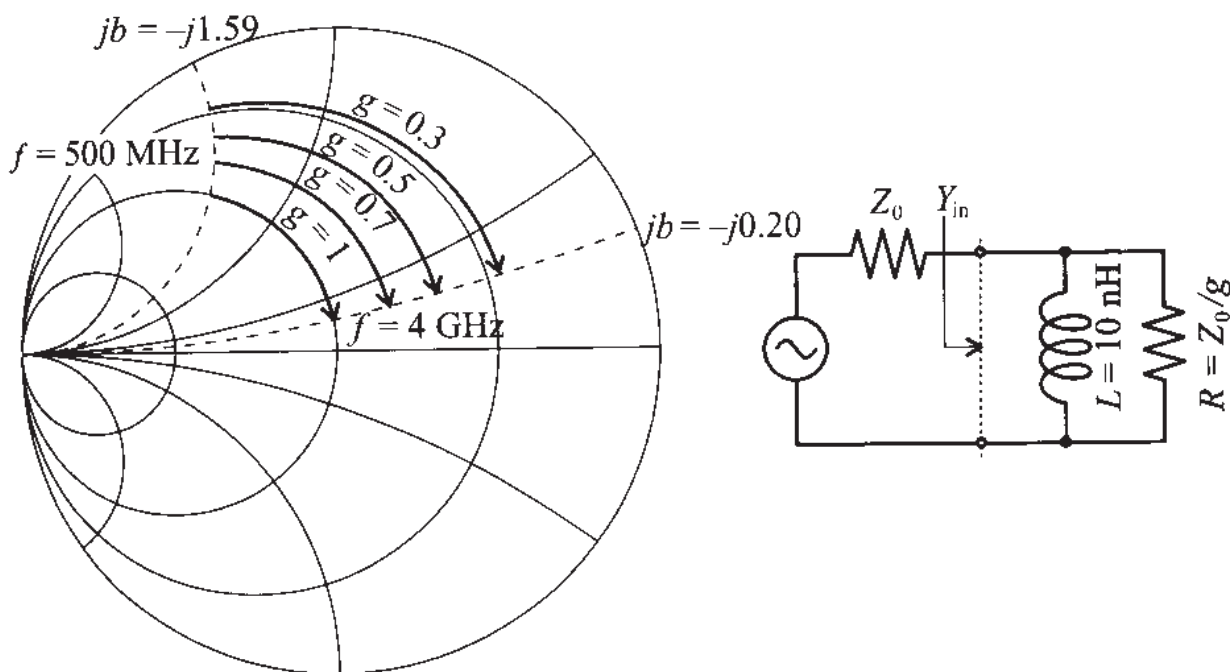


Figure 3-13 Admittance response of parallel RL circuit for $\omega_L \leq \omega \leq \omega_U$ at constant conductances $g = 0.3, 0.5, 0.7$, and 1 .

3.4.2 Parallel Connection of R and C Elements

Here we operate in the lower Y -Chart plane because susceptance $b_C = Z_0\omega C$ remains positive. To locate the normalized admittance value for a particular, fixed normalized conductance g and angular frequency ω_L we have

$$y_{in}(\omega_L) = g + jZ_0\omega_L C \quad (3.26)$$

Figure 3-14 depicts the frequency-dependent admittance behavior as a function of various constant conductance values $g = 0.3, 0.5, 0.7$, and 1 . The normalized susceptance for $C = 1 \text{ pF}$ and characteristic line impedance $Z_0 = 50 \Omega$ always starts at 0.16 (500 MHz) and ends at 1.26 (4 GHz).

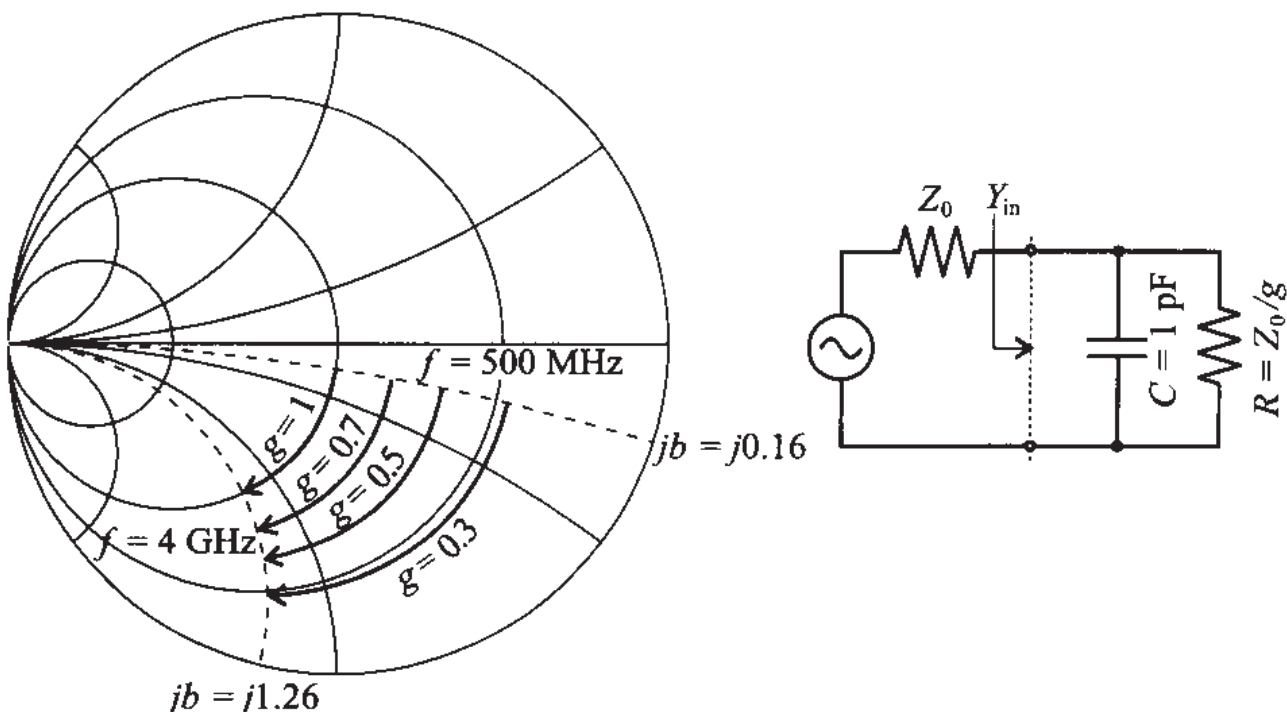


Figure 3-14 Admittance response of parallel RC circuit for $\omega_L \leq \omega \leq \omega_U$ at constant conductances $g = 0.3, 0.5, 0.7$, and 1 .

3.4.3 Series Connection of R and L Elements

When dealing with series connections, we can conveniently choose the Z -Smith Chart for the impedance display. Identifying the normalized reactive component as $x_L = \omega L / Z_0$, it is straightforward to locate the normalized impedance value for a particular, fixed normalized resistance r at a given angular frequency ω_L :

$$z_{in}(\omega_L) = r + j\omega_L L / Z_0 \quad (3.27)$$

In Figure 3-15 the frequency-dependent impedance behavior is shown as a function of various constant resistance values $r = 0.3, 0.5, 0.7$, and 1 . For the same inductance of 10 nH and characteristic line impedance of 50Ω as used in Figure 3-13, we now pick

reactance circles associated with 0.63 (500 MHz) and with 5.03 (4 GHz). Because the reactance is positive and since we use the Z-Smith Chart, all impedances have to reside in the upper half plane.

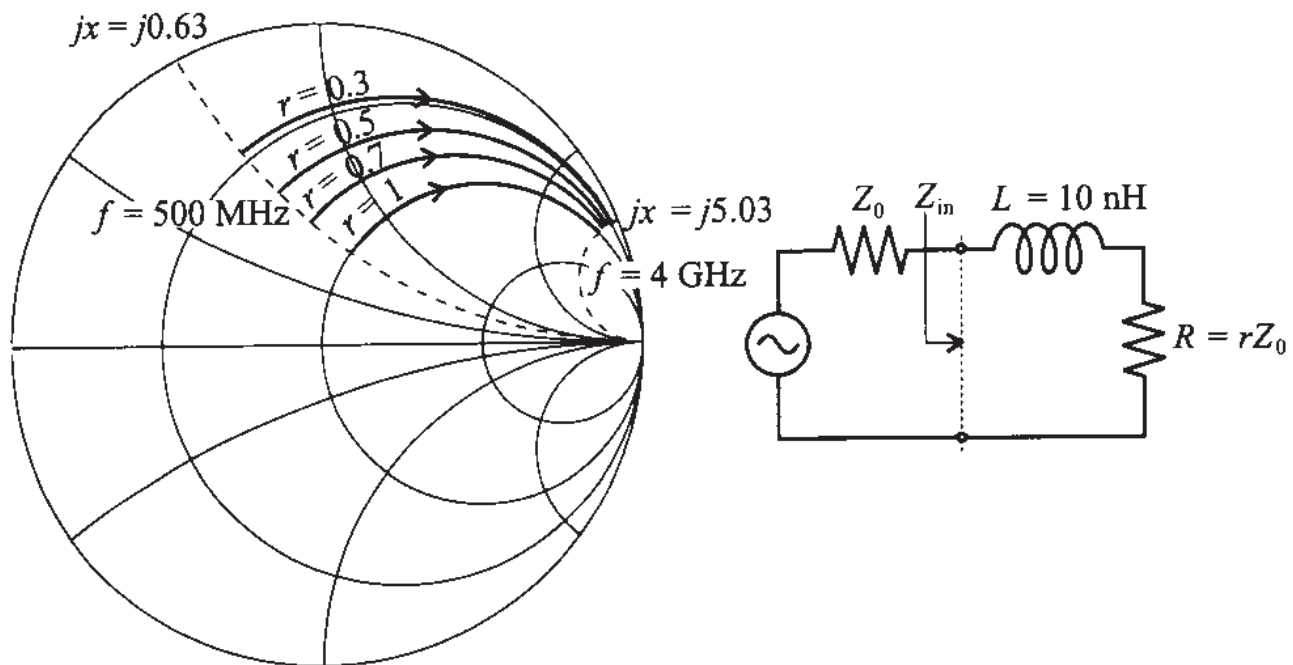


Figure 3-15 Impedance response of series RL circuit for $\omega_L \leq \omega \leq \omega_U$ and constant resistances $r = 0.3, 0.5, 0.7$, and 1 .

3.4.4 Series Connection of R and C Elements

We again choose the Z-Smith Chart for the impedance display. The normalized reactive component is $x_C = +1/(\omega C Z_0)$, indicating that all curves will reside in the lower half of the Smith Chart. The normalized impedance value for a particular, fixed normalized resistance r at an angular frequency ω_L reads

$$z_{in}(\omega_L) = r - j \frac{1}{\omega_L C Z_0} \quad (3.28)$$

Figure 3-16 displays the frequency-dependent impedance behavior as a function of various constant resistance values $r = 0.3, 0.5, 0.7$, and 1 . The capacitance of 1 pF in series with the variable resistance connected to a characteristic line impedance of 50Ω now yields circles associated with the reactances of -6.03 (500 MHz) and -0.8 (4 GHz), which intersect with the four resistance circles, uniquely determining upper and lower impedance values.

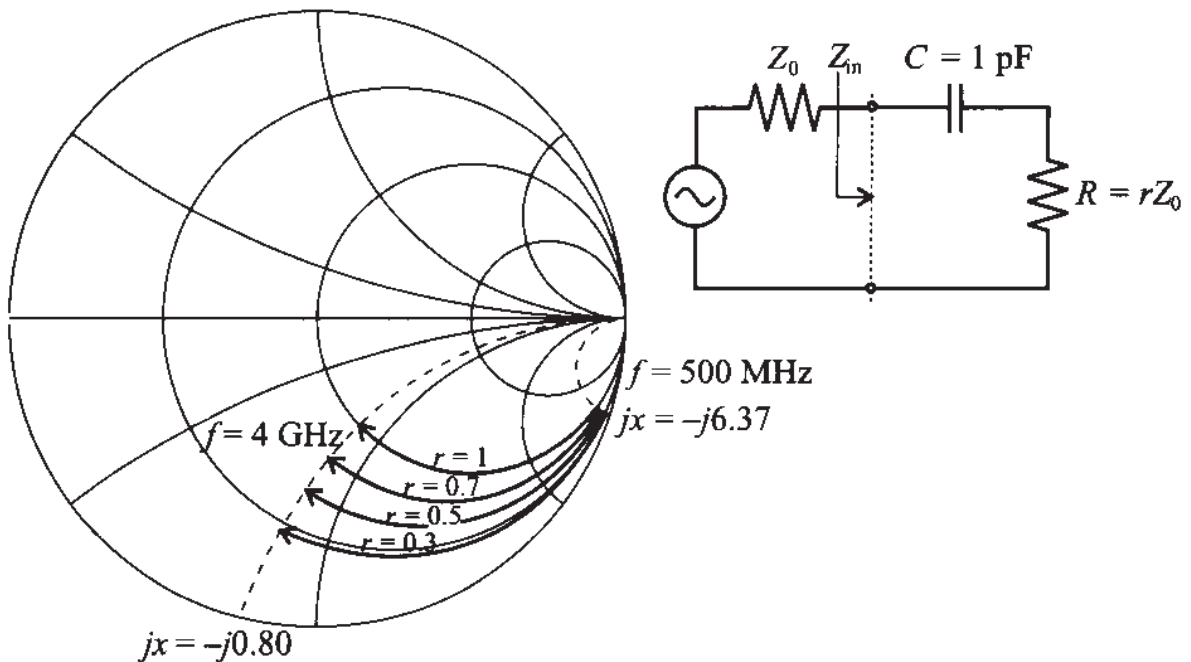


Figure 3-16 Impedance response of series RC circuit for $\omega_L \leq \omega \leq \omega_U$ at constant resistances $r = 0.3, 0.5, 0.7$, and 1 .

3.4.5 Example of a T-Network

In the previous examples only pure series or shunt configurations have been analyzed. In reality, however, one often encounters combinations of both. To show how easily the ZY Chart allows transitions between series and shunt connections, let us investigate by way of an example the behavior of a **T-type network** connected to the input of a bipolar transistor. The input port of the transistor is modeled as a parallel RC network as depicted in Figure 3-17. As we will see in Chapter 6, R_L approximates the base-emitter resistance and C_L is the base-emitter junction capacitance. The numerical parameter values are listed in Figure 3-17.

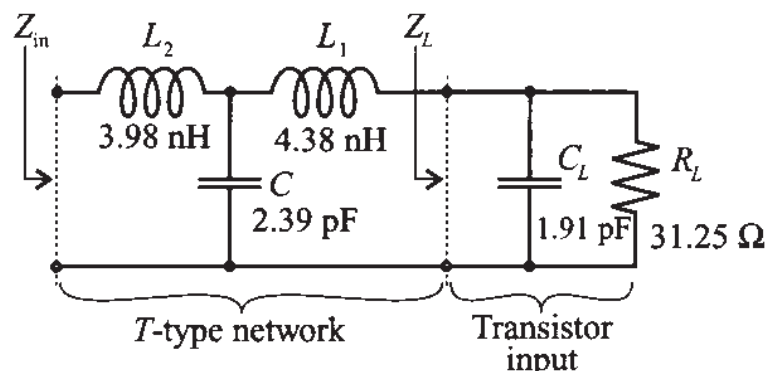


Figure 3-17 T network connected to the base-emitter input impedance of a bipolar transistor.

To use the Smith Chart for the computation of the input impedance of this more complicated network, we first analyze this circuit at 2 GHz and then show the entire response of the circuit for a frequency range from 500 MHz to 4 GHz by employing the commercial MMICAD software simulation package.

To obtain the load impedance, or the input impedance of the transistor, we use the Y-Smith Chart to identify the conductance point corresponding to the load resistor $R_L = 31.25 \Omega$. Assuming a 50Ω characteristic line impedance, we determine the normalized admittance for this case to be $g_A = 1.6$, which corresponds to point A in Figure 3-18.

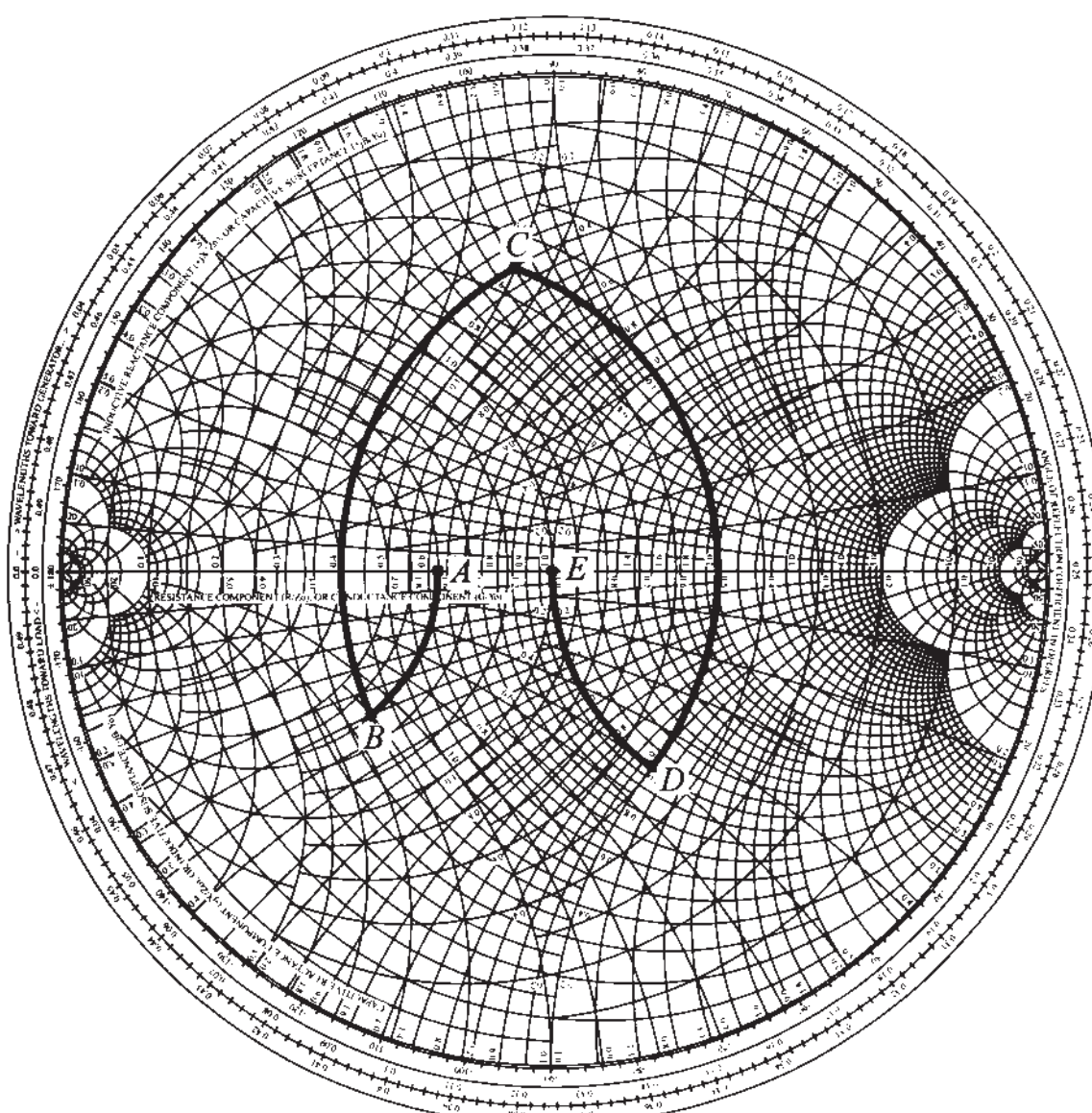


Figure 3-18 Computation of the normalized input impedance of the T network shown in Figure 3-17 for a center frequency $f = 2$ GHz.

The next step is to connect the capacitance $C_L = 1.91 \text{ pF}$ in shunt with the resistor R_L . At the angular frequency of $\omega_L = 2\pi 2 \times 10^9 \text{ s}^{-1}$, the susceptance of this capacitor becomes $B_{C_L} = \omega_L C_L = 24 \text{ mS}$, which corresponds to a rotation of the original point A into the new location B . The amount of rotation is determined by the normalized susceptance of the capacitor $b_{C_L} = B_{C_L} Z_0 = 1.2$ and is carried out along the circle of constant conductance in the Y-Smith Chart (see Figure 3-18).

Re-evaluating point B in the Z-Smith Chart, we obtain the normalized impedance of the parallel combination of resistor R_L and capacitor C_L to be $z_B = 0.4 - j0.3$. The series connection of the inductance L_1 results in the new location C . This point is obtained through a rotation from $x_B = -0.3$ by an amount $x_{L_1} = \omega_L L_1 / Z_0 = 1.1$ to $x_C = 0.8$ along the circle of constant resistance $r = 0.4$ in the Z-Smith Chart as discussed in Section 3.4.3.

Converting point C into a Y-Smith Chart value results in $y_C = 0.5 - j1.0$. The shunt connected capacitance requires the addition of a normalized susceptance $b_C = \omega C Z_0 = 1.5$, which results in the admittance value of $y_D = 0.5 + j0.5$ or point D in the Y-Smith Chart. Finally, converting point D into the impedance value $z_D = 1 - j1$ in the Z-Smith Chart allows us to add the normalized reactance $x_{L_2} = \omega_L L_2 / Z_0 = 1$ along the constant $r = 1$ circle. Therefore, we reach $z_{in} = 1$ or point E in Figure 3-18. This value happens to match the 50Ω characteristic transmission line impedance at the given frequency 2 GHz. In other words, $Z_{in} = Z_0 = 50 \Omega$.

When the frequency changes we need to go through the same steps but will arrive at a different input impedance point z_{in} . It would be extremely tedious to go through the preceding computations for a range of frequencies. This is most efficiently done by the computer.

Relying on the previously mentioned CAD program MMICAD we are able to produce a graphical display of the input impedance in the Z-Smith Chart over the entire frequency range in preselected increments of 10 MHz, as shown in Figure 3-19. This figure can also be generated as part of the MATLAB software (see file fig3_18.m on the accompanying CD).

We notice that the impedance trace ranging from 0.5 to 4 GHz is in agreement with our previous calculations at 2 GHz. Also, as the frequency approaches 4 GHz, the capacitor of $C = 2.39 \text{ pF}$ behaves increasingly like a short circuit in series with a single inductor L_2 . For this reason, the normalized resistance r approaches zero and the reactance grows to large positive values.

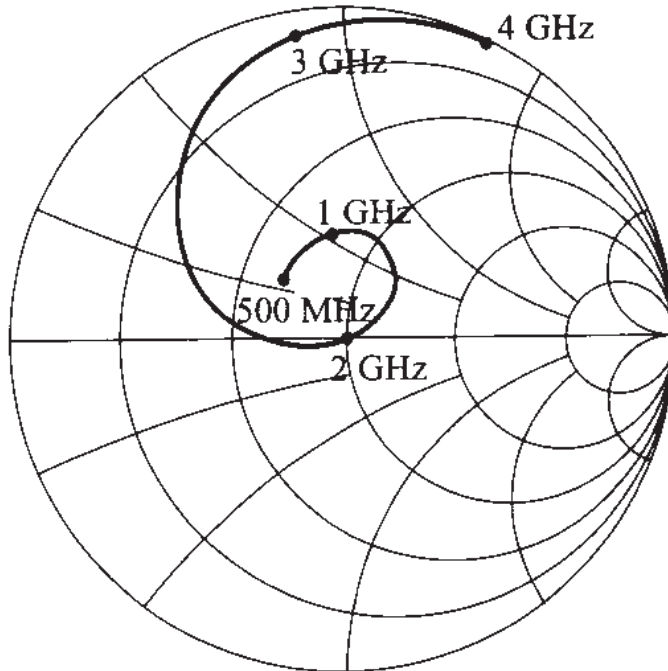


Figure 3-19 CAD simulation of the normalized input impedance Z_{in} for the network depicted in Figure 3-17 over the entire frequency range $500 \text{ MHz} \leq f \leq 4 \text{ GHz}$.

3.5 Summary

This chapter has derived the *Smith Chart* as the most widely used RF graphical design tool to display the impedance behavior of a transmission line as a function of either line length or frequency. Our approach originated from the representation of the normalized input impedance of a terminated transmission line in the form

$$z_{in} = r + jx = \frac{1 + \Gamma(d)}{1 - \Gamma(d)} = \frac{1 + \Gamma_r + j\Gamma_i}{1 - \Gamma_r - j\Gamma_i}$$

which can be inverted in terms of the reflection coefficient to yield two circle equations (3.10) and (3.11), which take on the following expressions for the normalized resistance r :

$$\left(\Gamma_r - \frac{r}{r+1} \right)^2 + \Gamma_i^2 = \left(\frac{1}{r+1} \right)^2$$

and for the normalized reactance x

$$(\Gamma_r - 1)^2 + \left(\Gamma_i - \frac{1}{x} \right)^2 = \left(\frac{1}{x} \right)^2$$

Superimposing the circles described by both equations over the complex polar form of the normalized impedance z -plane on the unit circle yields the Smith Chart. The key feature to remember is that one full rotation is equal to *half a wavelength* because of the

exponent $2\beta d$ in the reflection coefficient expression (3.2). In addition to observing the impedance behavior, we can also quantify in the Smith Chart the degree of mismatch expressed by the *standing wave ratio* (SWR) equation (3.12), or

$$\text{SWR}(d) = \frac{1 + |\Gamma(d)|}{1 - |\Gamma(d)|}$$

which can be directly obtained from the chart.

To facilitate computer-based evaluation of the Smith Chart, a wide range of commercial programs can be utilized. Due to its ease of implementation on a PC and its user-friendly interface, throughout this book we have used the package *MMICAD* developed by Optotek. However, for the relatively uncomplicated circuits analyzed in this Chapter, one can also create a custom-tailored Smith Chart and perform simple computations by relying on mathematical spreadsheets such as *Mathematica*, *MATLAB*, or *MathCad*. To demonstrate the procedure, a number of *MATLAB* modules have been developed, and the use of these so-called *m.files* as part of a basic Smith Chart computation is demonstrated in Section 3.2.4.

A transition to the admittance, or *Y-Smith Chart*, can be made via (3.23):

$$y_{in} = \frac{Y_{in}}{Y_0} = \frac{1}{z_{in}} = \frac{1 - \Gamma(d)}{1 + \Gamma(d)}$$

and it is found that the only difference to (3.4) is a sign reversal in front of the reflection coefficient. Consequently, rotating the reflection coefficient in the *Z-Smith Chart* by 180° results in the *Y-Smith Chart*. In practice, this rotation can be avoided by turning the chart itself. Superimposing the rotated chart over the original *Z-Smith Chart* provides a combined *ZY-Smith Chart* display. The benefit of such a display is the easy transition from parallel to series connection in circuit designs. This ease is demonstrated by a *T-network* configuration connected to the input port of a bipolar transistor consisting of a parallel *RC* network. To investigate the impedance behavior as a function of frequency sweep, however, is most easily accomplished through the use of CAD programs.

Further Reading

- G. Gonzalez, *Microwave Transistor Amplifiers: Analysis and Design*, 2nd ed., Prentice Hall, Upper Saddle River, NJ, 1997.
- K. C. Gupta, R. Garg, and I. J. Bohl, *Microstrip Lines and Slotlines*, Artech House, Dedham, MA, 1979.
- J. Helszajn, *Passive and Active Microwave Circuits*, John Wiley, New York, 1978.

Hewlett-Packard Application Note 154, "S-Parameter Design," 1972.

H. Howe, *Stripline Circuit Design*, Artech House, Dedham, MA, 1974.

S. Y. Liao, *Microwave Devices and Circuits*, Prentice Hall, Englewood Cliffs, NJ, 1980.

MMICAD for Windows, Reference Manual, Optotek, Ltd., 1997.

D. M. Pozar, *Microwave Engineering, 2nd edition*, John Wiley, New York, 1998.

P. A. Rizzi, *Microwave Engineering, Passive Circuits*, Prentice Hall, Englewood Cliffs, NJ, 1988.

P. H. Smith, "Transmission-Line Calculator," *Electronics*, Vol. 12, pp. 29–31, 1939.

P. H. Smith, "An Improved Transmission-Line Calculator," *Electronics*, Vol. 17, p. 130, 1944.

Problems

- 3.1 Consider a load $Z_L = (80 + j40) \Omega$ connected to a lossy transmission line with characteristic line impedance of

$$Z_0 = \sqrt{\frac{0.1 + j200}{0.05 - j0.003}}$$

Determine the reflection coefficient and the standing wave ratio (SWR) at the load.

- 3.2 A coaxial cable of characteristic line impedance $Z_0 = 75 \Omega$ is terminated by a load impedance of $Z_L = (40 + j35) \Omega$. Find the input impedance of the line for each of the following pairs of frequency f and cable length d assuming that the propagation velocity is 77% of the speed of light:

- (a) $f = 1 \text{ GHz}$ and $d = 50 \text{ cm}$
- (b) $f = 5 \text{ GHz}$ and $d = 25 \text{ cm}$
- (c) $f = 9 \text{ GHz}$ and $d = 5 \text{ cm}$

- 3.3 The attenuation coefficient of a transmission line can be determined by shortening the load side and recording the VSWR at the beginning of the line. We recall that the reflection coefficient for a lossy line takes on the form $\Gamma(d) = \Gamma_0 \exp(-kl) = \Gamma_0 \exp(-\alpha l) \exp(-j\beta l)$. If the line is 100 m in length and the VSWR is 3, find the attenuation coefficient α in Np/m, and dB/m.

- 3.4 A load impedance of $Z_L = (150 - j50) \Omega$ is connected to a 5 cm long transmission line with characteristic line impedance of $Z_0 = 75 \Omega$. For a wavelength of 6 cm, compute
- the input impedance
 - the operating frequency, if the phase velocity is 77% the speed of light
 - the SWR
- 3.5 Identify the following normalized impedances and admittances in the Smith Chart:
- $z = 0.1 + j0.7$
 - $y = 0.3 + j0.5$
 - $z = 0.2 + j0.1$
 - $y = 0.1 + j0.2$
- Also find the corresponding reflection coefficients and SWRs.
- 3.6 An unknown load impedance is connected to a 0.3λ long, 50Ω lossless transmission line. The SWR and phase of the reflection coefficient measured at the input of the line are 2.0 and -20° , respectively. Using the Smith Chart, determine the input and load impedances.
- 3.7 In Section 3.1.3 the circle equation (3.10) for the normalized resistance r is derived from (3.6). Start with (3.7); that is,

$$x = \frac{2\Gamma_i}{(1 - \Gamma_r)^2 + \Gamma_i^2}$$

and show that the circle equation

$$(\Gamma_r - 1)^2 + \left(\Gamma_i - \frac{1}{x}\right)^2 = \left(\frac{1}{x}\right)^2$$

can be derived.

- 3.8 Starting with the equation for normalized admittance

$$y = g + jb = \frac{1 - \Gamma}{1 + \Gamma}$$

prove that the circle equations for the Y-Smith Chart are given by the following two formulas:

- (a) For the constant conductance circle as

$$\left(\Gamma_r + \frac{g}{1 + g}\right)^2 + \Gamma_i^2 = \left(\frac{1}{1 + g}\right)^2$$

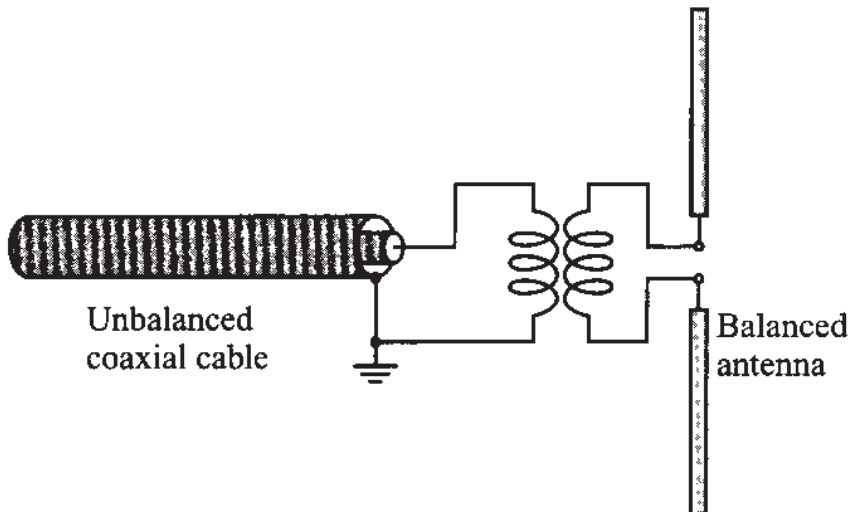
- (b) For the constant susceptance circle as

$$(\Gamma_r + 1)^2 + (\Gamma_i + 1/b) = (1/b)^2$$

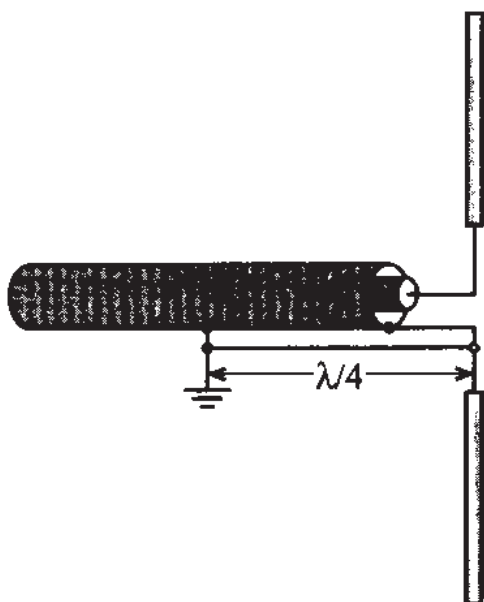
- 3.9 A lossless transmission line ($Z_0 = 50 \Omega$) is 10 cm long ($f = 800 \text{ MHz}$, $v_p = 0.77c$). If the input impedance is $Z_{\text{in}} = j60 \Omega$
- Find Z_L (using the Smith Chart)
 - What length of a short-circuit transmission line would be needed to replace Z_L ?
- 3.10 A transmission line of characteristic impedance $Z_0 = 50 \Omega$ and length $d = 0.15\lambda$ is terminated into a load impedance of $Z_L = (25 - j30) \Omega$. Find Γ_0 , $Z_{\text{in}}(d)$, and the SWR by using the Z-Smith Chart.
- 3.11 A short-circuited 50Ω transmission line section is operated at 1 GHz and possesses a phase velocity of 75% of the speed of light. Use both the analytical and the Smith Chart approach to determine the shortest lengths required to obtain (a) a 5.6 pF capacitor, and (b) a 4.7 nH inductor.
- 3.12 Determine the shortest length of a 75Ω open-circuit transmission line that equivalently represents a capacitor of 4.7 pF at 3 GHz. Assume the phase velocity is 66% of the speed of light.
- 3.13 A circuit is operated at 1.9 GHz and a lossless section of a 50Ω transmission line is short circuited to construct a reactance of 25Ω . (a) If the phase velocity is $3/4$ of the speed of light, what is the shortest possible length of the line to realize this impedance? (b) If an equivalent capacitive load of 25Ω is desired, determine the shortest possible length based on the same phase velocity.
- 3.14 A microstrip line with 50Ω characteristic line impedance is terminated into a load impedance consisting of a 200Ω resistor in shunt with a 5 pF capacitor. The line is 10 cm in length and the phase velocity is 50% the speed of light. (a) Find the input impedance in the Smith Chart at 500 MHz, 1 GHz, and 2 GHz, and (b) use the MATLAB routine (see Section 3.2.4) and plot the frequency response from 100 MHz to 3 GHz in the Smith Chart.
- 3.15 For an FM broadcasting station operated at 100 MHz, the amplifier output impedance of 250Ω has to be matched to a 75Ω dipole antenna.
- Determine the length and characteristic impedance of a quarter-wave transformer with $v_p = 0.7c$.
 - Find the spacing D for a two-wire lossless transmission line with AWG

26 wire size and a polystyrene dielectric ($\epsilon_r = 2.55$).

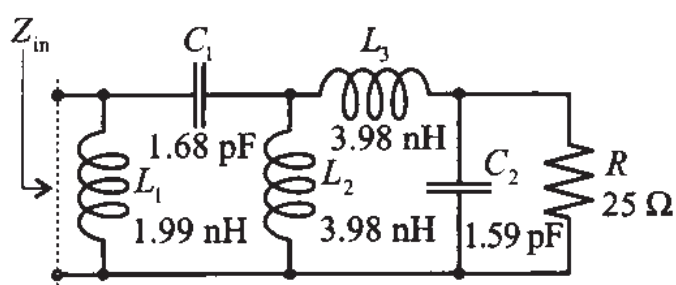
- 3.16 Consider the case of matching a 73Ω load to a 50Ω line by means of a $\lambda/4$ transformer. Assume the matching is achieved for a center frequency of $f_C = 2 \text{ GHz}$. Plot the SWR for the frequency range $1/3 \leq f/f_C \leq 3$.
- 3.17 A line of characteristic impedance of 75Ω is terminated by a load consisting of a series connection of $R = 30 \Omega$, $L = 10 \text{ nH}$, and $C = 2.5 \text{ pF}$. Find the values of the SWR and minimum line lengths at which a match of the input impedance to the characteristic line is achieved. Consider the following range of frequencies: (a) 100 MHz, (b) 500 MHz, and (c) 2 GHz.
- 3.18 A 50Ω lossless coaxial cable ($\epsilon_r = 2.8$) is connected to a 75Ω antenna operated at 2 GHz. If the cable length is 25 cm, find the input impedance by using the analytical equation (2.71) and the Z-Smith Chart.
- 3.19 A **balanced to unbalanced** (balun) transformation is often needed to connect a dipole antenna (balanced) to a coaxial cable (unbalanced). The following figure depicts the basic concept.



As an alternative of using a transformer, one often uses the following antenna connection.

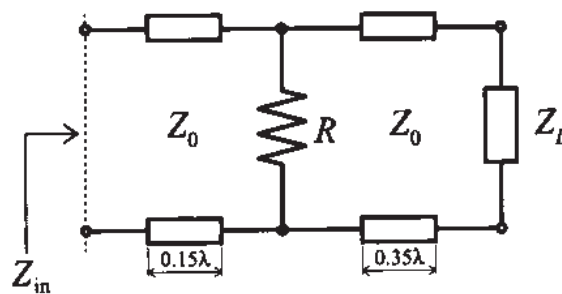


- (a) Explain why one leg of the dipole antenna is connected a distance $\lambda/4$ away from the end of the coax cable.
- (b) For an FM broadcast band antenna in the frequency range from 88 to 108 MHz, find the average length where the connection has to be made.
- 3.20 Using the ZY-Smith Chart, find the input impedance of the following network at 2 GHz.

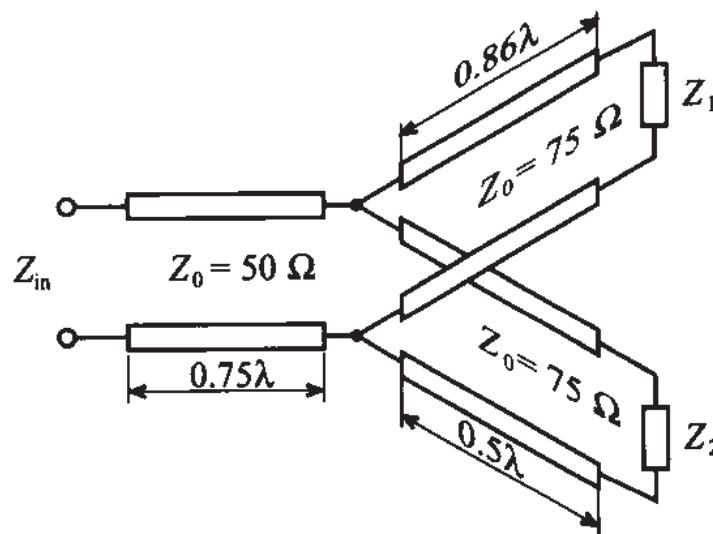


What is the input impedance of this network at 1 GHz?

- 3.21 A $Z_0 = 50\Omega$ transmission line is 0.5λ in length and terminated into a load of $Z_L = (50 - j30)\Omega$. At 0.35λ away from the load, a resistor of $R = 25\Omega$ is connected in shunt configuration (see figure below). Find the input impedance with the help of the ZY Smith Chart.



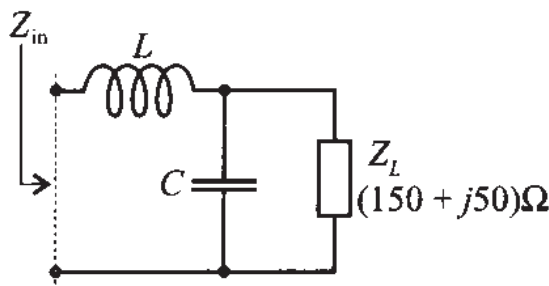
- 3.22 A 50Ω transmission line of $3/4$ wavelength in length is connected to two transmission line sections each of 75Ω in impedance and length of 0.86 and 0.5 wavelength, respectively, as illustrated in the following figure.



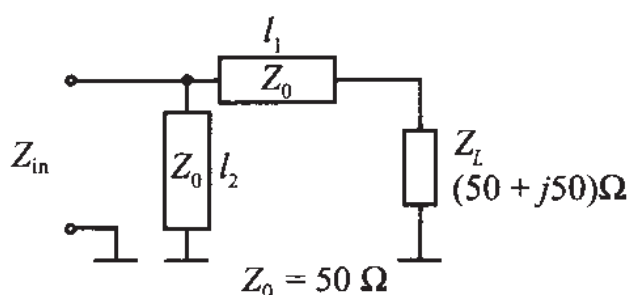
The termination for line 1 is $Z_1 = (30 + j40)\Omega$ and $Z_2 = (75 - j80)\Omega$ for line 2. Employ the Smith Chart and find the input impedance.

- 3.23 Repeat the previous problem if all characteristic line impedances are $Z_0 = 50\Omega$ and all transmission line sections are $\lambda/4$ in length.
- 3.24 A dipole antenna of impedance $Z_L = (75 + j20)\Omega$ is connected to a 50Ω lossless transmission whose length is $\lambda/3$. The voltage source $V_G = 25V$ is attached to the transmission line via an unknown resistance R_G . It is determined that an average power of $3W$ is delivered to the load under load-side matching ($Z_L^{\text{match}} = 50\Omega$). Find the generator resistance R_G , and determine the power delivered to the antenna if the generator impedance is matched to the line via a quarter-wave transformer.

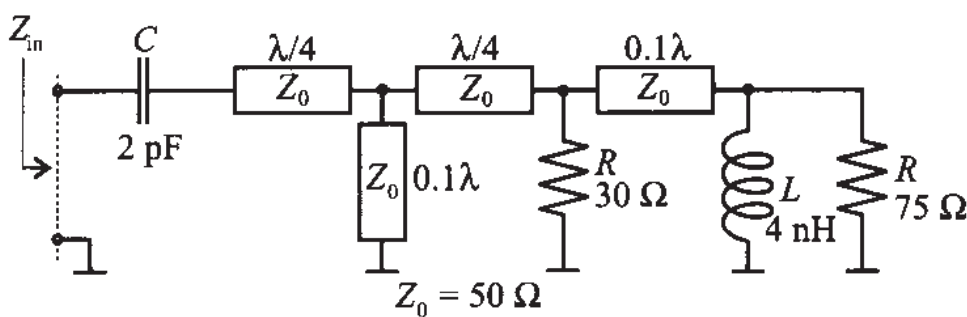
- 3.25 Determine the values of the inductance L and the capacitance C such that they result in a 50Ω input impedance at 3 GHz operating frequency for the following network.



- 3.26 An open-circuit transmission line (50Ω) is operated at 500 MHz ($v_p = 0.7c$). Use the ZY Smith Chart and find the impedance Z_{in} if the line is 65 cm in length. Find the shortest distance for which the admittance is $Y_{in} = -j0.05S$.
- 3.27 Find the minimum line length l_1 and the minimum length of the short-circuited stub l_2 in terms of wavelength λ , such that the input impedance of the circuit is equal to 50Ω .

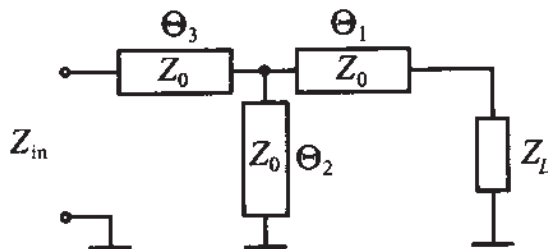


- 3.28 Find the input impedance in terms of magnitude and phase of the following network at an operating frequency of 950 MHz.



- 3.29 Repeat your computation and solve Problem 3.28 for a 1.5 GHz operating frequency. Comment on the differences in your results.

3.30 A specific transmission line configuration is as follows:



The characteristic line impedance for all three elements is $Z_0 = 50 \Omega$. The load impedance has a value of $Z_L = (20 + j40) \Omega$, and the electrical lengths of the corresponding line segments are $\Theta_1 = 164.3^\circ$, $\Theta_2 = 57.7^\circ$, and $\Theta_3 = 25.5^\circ$.

- Find the input impedance.
- Find the input impedance if transmission line segment Θ_2 is open circuit.

(This problem and Problem 3.27 become very important in Chapter 8, when we discuss the problem of matching a particular load impedance to a desired input impedance.)

Single- and Multiport Networks

Ever since single- and multiple port networks were first introduced into the electrical engineering profession through Guillemin and Feldkeller, they have quickly become indispensable tools in restructuring and simplifying complicated circuits as well as in providing fundamental insight into the performance of active and passive electronic devices. Moreover, the importance of network modeling has extended far beyond electrical engineering and has influenced such diverse fields as vibrational analysis in structural and mechanical engineering as well as biomedicine. For example, today's piezoelectric medical transducer elements and their electrical-mechanical conversion mechanisms are most easily modeled as a three-port network.

The ability to reduce most passive and active circuit devices, irrespective of their complicated and often nonlinear behavior, to simple input-output relations has many advantages. Chief among them is the experimental determination of input and output port parameters without the need to know the internal structure of the system. The "black box" methodology has tremendous appeal to engineers whose concern is mostly focused on the overall circuit performance rather than the analysis of individual components. This approach is especially important in RF and MW circuits, where complete field theoretical solutions to Maxwell's equations are either too difficult to derive or the solutions provide more information than is normally needed to develop functional, practical designs involving systems such as filters, resonators, and amplifiers.

In the following sections our objective is to establish the basic network input-output parameter relations such as impedance, admittance, hybrid, and *ABCD*-parameters. We then develop conversions between these sets. Rules of connecting networks are presented to show how more complicated circuits can be constructed by series and parallel cascading of individual network blocks. Finally, the scattering parameters are presented

as an important practical way of characterizing RF/MW circuits and devices through the use of power wave relations.

4.1 Basic Definitions

Before embarking on a discussion of electrical networks we have to identify some general definitions pertaining to directions and polarity of voltages and currents. For our purposes we use the convention shown in Figure 4-1. Regardless of whether we deal with a single-port or an N -port network, the port-indexed current is assumed to flow into the respective port and the associated voltage is recorded as indicated.

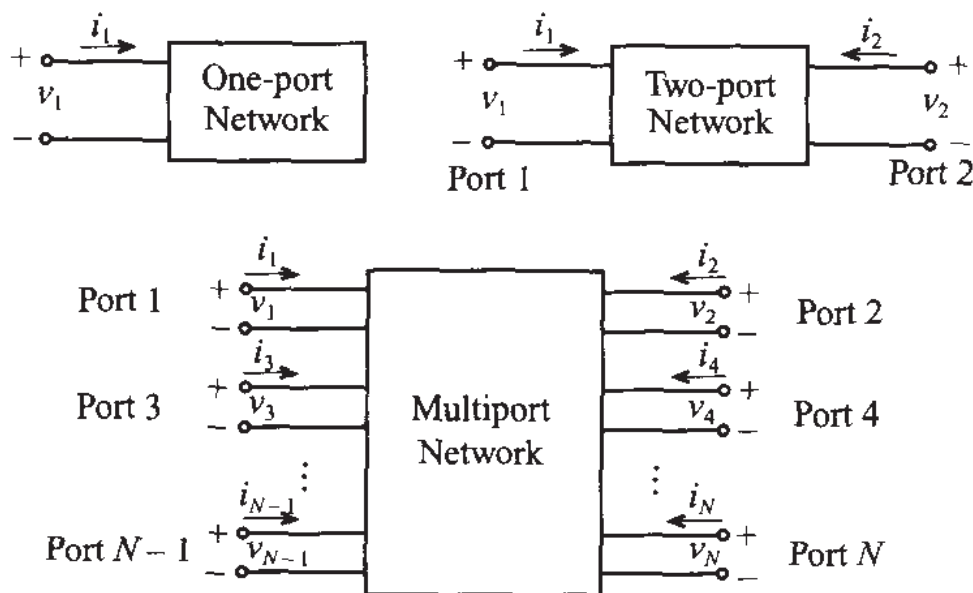


Figure 4-1 Basic voltage and current definitions for single- and multiport network.

In establishing the various parameter conventions we begin with the voltage-current relations through double-indexed impedance coefficients Z_{nm} , where indices n and m range between 1 and N . The voltage at each port $n = 1 \dots N$ is given by

$$v_1 = Z_{11}i_1 + Z_{12}i_2 + \dots + Z_{1N}i_N \quad (4.1a)$$

for port 1,

$$v_2 = Z_{21}i_1 + Z_{22}i_2 + \dots + Z_{2N}i_N \quad (4.1b)$$

for port 2, and

$$v_N = Z_{N1}i_1 + Z_{N2}i_2 + \dots + Z_{NN}i_N \quad (4.1c)$$

for port N . We see that each port n is affected by its own impedance Z_{nn} as well as by a linear superposition of all other ports. In a more concise notation, (4.1) can be converted into an **impedance** or **Z-matrix** form:

$$\begin{Bmatrix} v_1 \\ v_2 \\ \vdots \\ v_N \end{Bmatrix} = \begin{bmatrix} Z_{11} & Z_{12} & \cdots & Z_{1N} \\ Z_{21} & Z_{22} & \cdots & Z_{2N} \\ \vdots & \vdots & \ddots & \vdots \\ Z_{N1} & Z_{N2} & \cdots & Z_{NN} \end{bmatrix} \begin{Bmatrix} i_1 \\ i_2 \\ \vdots \\ i_N \end{Bmatrix} \quad (4.2)$$

or, in matrix notation,

$$\{\mathbf{V}\} = [\mathbf{Z}]\{\mathbf{I}\} \quad (4.3)$$

where $\{\mathbf{V}\}$ and $\{\mathbf{I}\}$ are vectors of voltages v_1, v_2, \dots, v_N and currents i_1, i_2, \dots, i_N , respectively, and $[\mathbf{Z}]$ is the impedance matrix.

Each impedance element in (4.2) can be determined via the following protocol:

$$Z_{nm} = \left. \frac{v_n}{i_m} \right|_{i_k=0 \text{ (for } k \neq m\text{)}} \quad (4.4)$$

which means that the voltage v_n is recorded at port n while port m is driven by current i_m and the rest of the ports are maintained under open terminal conditions (i.e. $i_k = 0$ where $k \neq m$).

Instead of voltages as the dependent variable, we can specify currents such that

$$\begin{Bmatrix} i_1 \\ i_2 \\ \vdots \\ i_N \end{Bmatrix} = \begin{bmatrix} Y_{11} & Y_{12} & \cdots & Y_{1N} \\ Y_{21} & Y_{22} & \cdots & Y_{2N} \\ \vdots & \vdots & \ddots & \vdots \\ Y_{N1} & Y_{N2} & \cdots & Y_{NN} \end{bmatrix} \begin{Bmatrix} v_1 \\ v_2 \\ \vdots \\ v_N \end{Bmatrix} \quad (4.5)$$

or

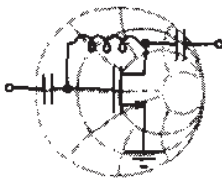
$$\{\mathbf{I}\} = [\mathbf{Y}]\{\mathbf{V}\} \quad (4.6)$$

where, similar to (4.4), we define the individual elements of the **admittance** or **Y-matrix** as

$$Y_{nm} = \left. \frac{i_n}{v_m} \right|_{v_k=0 \text{ (for } k \neq m\text{)}} \quad (4.7)$$

Comparing (4.2) and (4.5), it is apparent that impedance and admittance matrices are the inverse of each other:

$$[\mathbf{Z}] = [\mathbf{Y}]^{-1} \quad (4.8)$$



RF & MW

Example 4-1: Matrix representation of Pi-network

For the pi-network (the name of the network comes from the resemblance with the greek letter Π) shown in Figure 4-2 with generic impedances Z_A , Z_B , and Z_C find the impedance and admittance matrices.

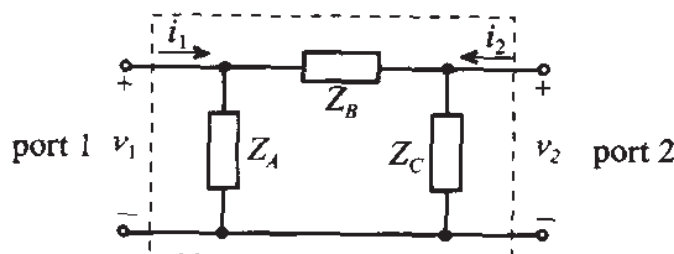


Figure 4-2 Pi-network as a two-port network.

Solution: The impedance elements are found by using (4.4) and the appropriate open- and short-circuit termination conditions.

To find Z_{11} we must compute the ratio of the voltage drop v_1 across port 1 to the current i_1 flowing into this port when the current into port 2 equals zero. The requirement $i_2 = 0$ is equivalent to an open-circuit condition. Thus, the impedance Z_{11} is equal to the parallel combination of impedances Z_A and $Z_B + Z_C$.

$$Z_{11} = \left. \frac{v_1}{i_1} \right|_{i_2=0} = Z_A \parallel (Z_B + Z_C) = \frac{Z_A(Z_B + Z_C)}{Z_A + Z_B + Z_C}$$

The value for Z_{12} can be found as the ratio of voltage drop v_1 measured across port 1 to the current i_2 . In this case we must ensure that the current i_1 remains zero (i.e., we must treat port 1 as open). Voltage v_1 is equal to the voltage drop across impedance Z_A and can be obtained using the voltage divider rule:

$$v_1 = \frac{Z_A}{Z_B + Z_C} v_{AB}$$

where v_{AB} is a voltage drop across impedances Z_A and Z_B connected in series and computed as $v_{AB} = i_2[Z_C \parallel (Z_A + Z_B)]$. Thus,

$$Z_{12} = \left. \frac{v_1}{i_2} \right|_{i_1=0} = \frac{Z_A}{Z_A + Z_B} [Z_C \parallel (Z_A + Z_B)] = \frac{Z_A Z_C}{Z_A + Z_B + Z_C}$$

Similarly, we can obtain the remaining two coefficients of the impedance matrix:

$$Z_{21} = \left. \frac{v_2}{i_1} \right|_{i_2=0} = \frac{Z_C}{Z_B + Z_C} [Z_A \parallel (Z_B + Z_C)] = \frac{Z_A Z_C}{Z_A + Z_B + Z_C}$$

$$Z_{22} = \left. \frac{v_2}{i_2} \right|_{i_1=0} = Z_C \parallel (Z_A + Z_B) = \frac{Z_C(Z_A + Z_B)}{Z_A + Z_B + Z_C}$$

Thus, the impedance matrix for the generic pi-network is written in the form

$$[Z] = \frac{1}{Z_A + Z_B + Z_C} \begin{bmatrix} Z_A(Z_B + Z_C) & Z_A Z_C \\ Z_A Z_C & Z_C(Z_A + Z_B) \end{bmatrix}$$

The coefficients for the admittance matrix can be derived using (4.7). To find the value for Y_{11} we must find the ratio of current flow into port 1 to the voltage drop across this port when the second port is shortened (i.e., $v_2 = 0$).

$$Y_{11} = \left. \frac{i_1}{v_1} \right|_{v_2=0} = \frac{1}{Z_A} + \frac{1}{Z_B}$$

The value for coefficient Y_{12} of the admittance matrix can be obtained by shortening port 1 (i.e., forcing $v_1 = 0$) and measuring the ratio of the current i_1 to the voltage drop across port 2. We note that, when a positive voltage is applied to port 2, the current i_1 will flow away from port 1, resulting in a negative current:

$$Y_{12} = \left. \frac{i_1}{v_2} \right|_{v_1=0} = -\frac{1}{Z_B}$$

The rest of the admittance matrix can be derived in the same way, leading to the following final form

$$[\mathbf{Y}] = \begin{bmatrix} \frac{1}{Z_A} + \frac{1}{Z_B} & -\frac{1}{Z_B} \\ -\frac{1}{Z_B} & \frac{1}{Z_B} + \frac{1}{Z_C} \end{bmatrix} = \begin{bmatrix} Y_A + Y_B & -Y_B \\ -Y_B & Y_B + Y_C \end{bmatrix}$$

where $Y_A = Z_A^{-1}$, $Y_B = Z_B^{-1}$, and $Y_C = Z_C^{-1}$.

Direct evaluation shows that the obtained impedance and admittance matrices are indeed inversely related, which supports the validity of (4.8).

The practical determination of the matrix coefficients can be accomplished easily by enforcing open- and short-circuit conditions. However, as the frequency reaches RF limits, parasitic terminal effects can no longer be ignored and a different measurement approach becomes necessary.

Example 4-1 indicates that both impedance and admittance matrices are symmetric. This is generally true for linear, passive networks. *Passive* in this context implies not containing any current or voltage sources. We can state the symmetry as

$$Z_{nm} = Z_{mn} \quad (4.9)$$

which also applies for admittances because of (4.8). In fact, it can be proved that any reciprocal (that is, nonactive, linear) and lossless N -port network is symmetric.

Besides impedance and admittance network descriptions, there are two more useful parameter sets depending on how the voltage and currents are arranged. Restricting our discussion to two-port networks and with reference to Figure 4-1, we define the **chain or ABCD-matrix** as

$$\begin{Bmatrix} v_1 \\ i_1 \end{Bmatrix} = \begin{bmatrix} A & B \\ C & D \end{bmatrix} \begin{Bmatrix} v_2 \\ -i_2 \end{Bmatrix} \quad (4.10)$$

and the **hybrid or h-matrix** as

$$\begin{Bmatrix} v_1 \\ i_2 \end{Bmatrix} = \begin{bmatrix} h_{11} & h_{12} \\ h_{21} & h_{22} \end{bmatrix} \begin{Bmatrix} i_1 \\ v_2 \end{Bmatrix} \quad (4.11)$$

The determination of the individual matrix coefficients is identical to the method introduced for the impedance and admittance matrices. For instance, to find h_{12} in (4.11), we set i_1 to zero and compute the ratio of v_1 over v_2 ; that is,

$$h_{12} = \left. \frac{v_1}{v_2} \right|_{i_1 = 0}$$

It is interesting to note that in the hybrid representation parameters h_{21} and h_{12} define the forward current and reverse voltage gain, respectively. The remaining two parameters determine the input impedance (h_{11}) and output admittance (h_{22}) of the network. These properties of the hybrid representation explain why it is most often used for low-frequency transistor models. The following example shows the derivation of the hybrid matrix representation for a **bipolar-junction transistor (BJT)** for low-frequency operation.

RF & MW → Example 4-2: Low-frequency hybrid network description of a BJT

Describe the common-emitter BJT transistor in terms of its hybrid network parameters for the low-frequency, small-signal transistor model shown in Figure 4-3.

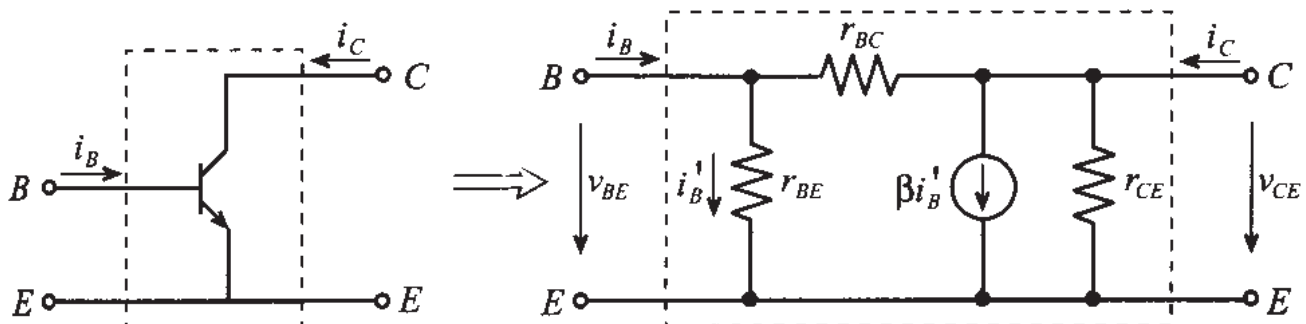


Figure 4-3 Common-emitter low-frequency, small-signal transistor model.

Solution: In the transistor model shown in Figure 4-3 r_{BE} , r_{BC} , and r_{CE} represent base-emitter, base-collector, and collector-emitter internal resistances of the transistor. The current through the current-controlled current source is dependent on the current i'_B flowing through the base-emitter resistance.

To evaluate the h_{11} parameter of the hybrid matrix according to (4.10) we must short-circuit the collector and emitter terminals, thus setting $v_2 = v_{CE} = 0$, and compute the ratio of the base-emitter voltage to the base current. Using the notation established in Figure 4-3, we notice that h_{11} is equal to the parallel combination of r_{BE} and r_{BC} :

$$h_{11} = \left. \frac{v_{BE}}{i_B} \right|_{v_{CE}=0} = \frac{r_{BC}r_{BE}}{r_{BE} + r_{BC}} \quad (\text{input impedance})$$

Following a similar procedure, the relations for the remaining three parameters of the hybrid representation can be established as follows:

$$h_{12} = \left. \frac{v_{BE}}{v_{CE}} \right|_{i_B=0} = \frac{r_{BE}}{r_{BE} + r_{BC}} \quad (\text{voltage feedback ratio})$$

$$h_{21} = \left. \frac{i_C}{i_B} \right|_{v_{CE}=0} = \frac{\beta r_{BC} - r_{BE}}{r_{BE} + r_{BC}} \quad (\text{small-signal current gain})$$

$$h_{22} = \left. \frac{i_C}{v_{CE}} \right|_{i_B=0} = \frac{1}{r_{CE}} + \frac{1+\beta}{r_{BE} + r_{BC}} \quad (\text{output admittance})$$

In the majority of all practical transistor designs, the current amplification coefficient β is usually much greater than unity and the collector-base resistance is much larger than the base-emitter resistance. Keeping these relations in mind, we can simplify the expressions derived for the h -matrix representation of the transistor:

$$h_{11} = \left. \frac{v_{BE}}{i_B} \right|_{v_{CE}=0} = r_{BE} \quad (\text{input impedance})$$

$$h_{12} = \left. \frac{v_{BE}}{v_{CE}} \right|_{i_B=0} = 0 \quad (\text{voltage feedback ratio})$$

$$h_{21} = \left. \frac{i_C}{i_B} \right|_{v_{CE}=0} = \beta \quad (\text{small-signal current gain})$$

$$h_{22} = \left. \frac{i_C}{v_{CE}} \right|_{i_B=0} = \frac{1}{r_{CE}} + \frac{\beta}{r_{BC}} \text{ (output admittance)}$$

The hybrid network description is a very popular way to characterize the BJT, and its h-parameter coefficients are widely reported in many data sheets.

Due to the presence of the current source in Example 4-2, the h-matrix is no longer symmetric ($h_{12} \neq h_{21}$) and the transistor model is nonreciprocal. In low-frequency electronic circuit design the coefficients of the hybrid matrix representation are often listed as h_{ie} for h_{11} , h_{re} for h_{12} , h_{fe} for h_{21} , and h_{oe} for h_{22} .

Up to this point we considered the problem of deriving the matrix representation based on a known topology and element values of the circuit. However, in practical design tasks it is often required to solve an **inverse** problem and obtain the equivalent circuit for an unknown or incompletely defined device based on a few measurements. This becomes extremely important when the characterization of the device is performed under a particular set of operating conditions, but it becomes necessary to evaluate its performance under completely different circuit conditions. In this case the use of the equivalent circuit representation enables an engineer to predict with reasonable accuracy the response of the device or circuit under changing operating conditions. In the following example we will derive the values of the internal resistances of the BJT from known h-matrix parameters.

RF & MW →

Example 4-3: Determination of internal resistances and current gain of a BJT based on h-parameter measurements

Use the equivalent circuit representation of the BJT shown in Figure 4-3 and employ the following measured hybrid parameters: $h_{ie} = 5 \text{ k}\Omega$, $h_{re} = 2 \times 10^{-4}$, $h_{fe} = 250$, $h_{oe} = 20 \mu\text{S}$ (these parameters correspond to the 2n3904 transistor manufactured by

Motorola). Find the internal resistances r_{BE} , r_{BC} , and r_{CE} , and the current gain β .

Solution: As derived in Example 4-2, the values of the h-matrix for the equivalent circuit shown in Figure 4-3 are given by the following four equations:

$$h_{ie} = \frac{r_{BC}r_{BE}}{r_{BE} + r_{BC}} \quad (\text{input impedance}) \quad (4.12)$$

$$h_{re} = \frac{r_{BE}}{r_{BE} + r_{BC}} \quad (\text{voltage feedback ratio}) \quad (4.13)$$

$$h_{fe} = \frac{\beta r_{BC} - r_{BE}}{r_{BE} + r_{BC}} \quad (\text{small-signal current gain}) \quad (4.14)$$

$$h_{oe} = \frac{1}{r_{CE}} + \frac{1 + \beta}{r_{BE} + r_{BC}} \quad (\text{output admittance}) \quad (4.15)$$

If we divide (4.12) by (4.13), we determine that the base-collector resistance is equal to the ratio of h_{ie} over h_{re} . Accordingly, for values given in the problem formulation, we obtain: $r_{BC} = h_{ie}/h_{re} = 71 \text{ M}\Omega$. Substituting this value into either equation (4.12) or (4.13), we find $r_{BE} = h_{ie}/(1 - h_{re}) = 5 \text{ k}\Omega$. Knowing r_{BC} and r_{BE} , (4.14) allows us to find the current gain coefficient $\beta = (h_{re} - h_{fe})/(h_{re} - 1) = 300.02$. Finally, the collector-emitter resistance can be evaluated from (4.15) as

$$r_{CE} = \frac{h_{ie}}{h_{oe}h_{ie} - h_{re}h_{fe} + 2h_{re}^2 - h_{re}} = 63.35 \text{ k}\Omega$$

We note from the obtained values that r_{BE} is indeed much smaller than r_{BC} .

This example provides a first idea of how the measured h-parameters can be used as a basis to characterize the BJT circuit model. The concept of “inverting” the measurements to determine circuit model parameters will be further analyzed in Chapter 7.

4.2 Interconnecting Networks

4.2.1 Series Connection of Networks

A series connection consisting of two two-port networks is shown in Figure 4-4. The individual networks are shown in impedance matrix representation.

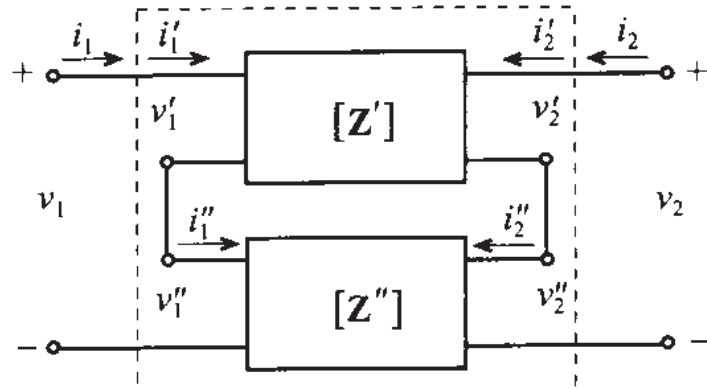


Figure 4-4 Series connection of two two-port networks.

In this case the individual voltages are additive while the currents remain the same. This results in

$$\begin{Bmatrix} v_1 \\ v_2 \end{Bmatrix} = \begin{Bmatrix} v_1' + v_1'' \\ v_2' + v_2'' \end{Bmatrix} = [\mathbf{Z}] \begin{Bmatrix} i_1 \\ i_2 \end{Bmatrix} \quad (4.16)$$

where the new composite network $[\mathbf{Z}]$ takes the form

$$[\mathbf{Z}] = [\mathbf{Z}'] + [\mathbf{Z}''] = \begin{bmatrix} Z_{11}' + Z_{11}'' & Z_{12}' + Z_{12}'' \\ Z_{21}' + Z_{21}'' & Z_{22}' + Z_{22}'' \end{bmatrix} \quad (4.17)$$

Caution has to be exercised in not indiscriminately connecting individual networks, as short circuits may be created. This situation is exemplified in Figure 4-5 (a). The problem can be avoided by including a transformer, as seen in Figure 4-5 (b). The transformer in this case decouples input and output ports of the second network. However, this approach will only work for AC signals since the transformer acts as a high-pass filter and rejects all DC contributions.

When two networks are connected with the output interchanged, as shown in Figure 4-6, the most suitable representation is the hybrid form.

In the network connection that is shown in Figure 4-6, the voltages on the input ports and currents on the output ports are additive (i.e., $v_1 = v_1' + v_1''$ and $i_2 = i_2' + i_2''$), while the voltages on the output ports and currents on input ports are

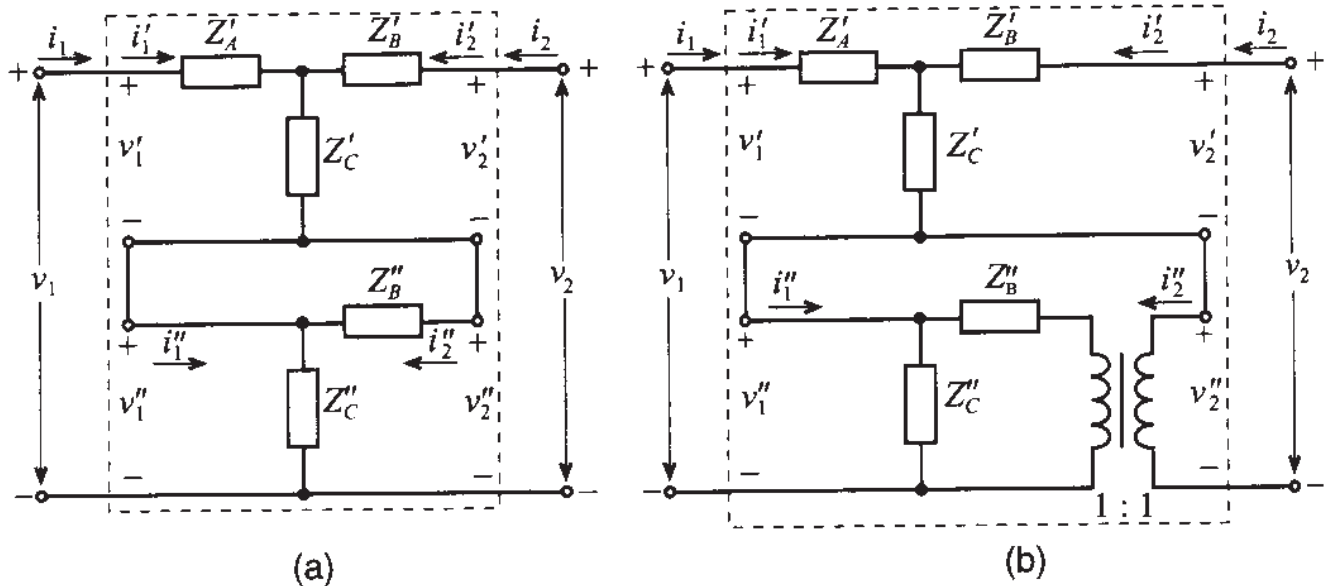


Figure 4-5 (a) Short circuit in series connection. (b) Transformer to avoid short circuit.

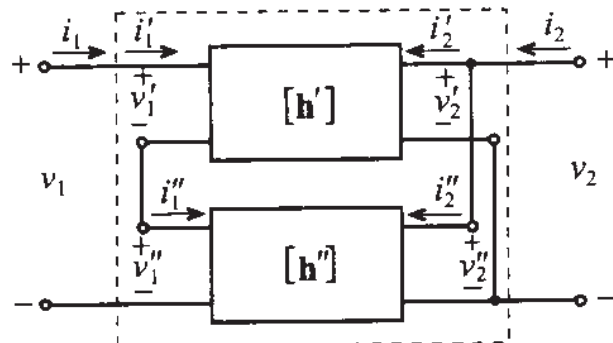


Figure 4-6 Connection of two-port networks suitable for hybrid representation.

the same (i.e., $v_2 = v'_2 = v''_2$ and $i_1 = i'_1 = i''_1$). From this observation we can conclude that the resulting h -matrix for the overall system is equal to the sum of the h -matrices of the individual networks:

$$\begin{Bmatrix} v_1 \\ i_2 \end{Bmatrix} = \begin{Bmatrix} v'_1 + v''_1 \\ i'_2 + i''_2 \end{Bmatrix} = \begin{bmatrix} h_{11}' + h_{11}'' & h_{12}' + h_{12}'' \\ h_{21}' + h_{21}'' & h_{22}' + h_{22}'' \end{bmatrix} \begin{Bmatrix} i_1 \\ v_2 \end{Bmatrix} \quad (4.18)$$

An example of this type of connection is the Darlington transistor pair Q_1 and Q_2 shown in Figure 4-7.

4.2.2 Parallel Connection of Networks

A parallel connection of two dual-port networks is shown in Figure 4-8 for the admittance matrices \mathbf{Y}' and \mathbf{Y}'' , where, unlike (4.16), the currents are now additive

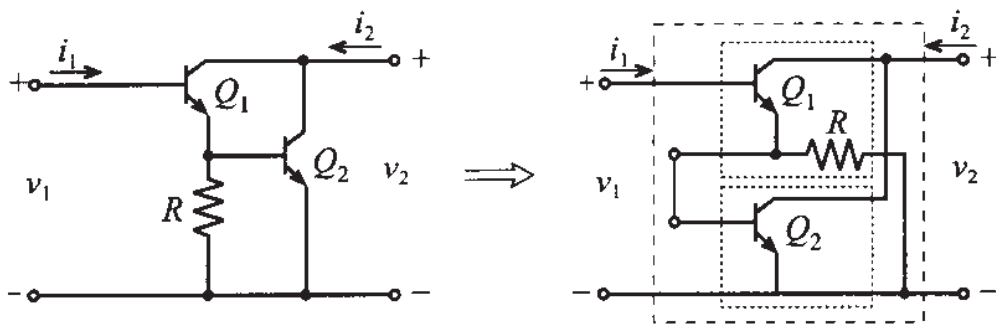


Figure 4-7 Series connection of two hybrid networks.

$$\begin{Bmatrix} i_1 \\ i_2 \end{Bmatrix} = \begin{Bmatrix} i_1' + i_1'' \\ i_2' + i_2'' \end{Bmatrix} = [\mathbf{Y}] \begin{Bmatrix} v_1 \\ v_2 \end{Bmatrix} \quad (4.19)$$

and the new admittance matrix is defined as the sum of the individual admittances

$$[\mathbf{Y}] = [\mathbf{Y}'] + [\mathbf{Y}''] = \begin{bmatrix} Y_{11}' + Y_{11}'' & Y_{12}' + Y_{12}'' \\ Y_{21}' + Y_{21}'' & Y_{22}' + Y_{22}'' \end{bmatrix} \quad (4.20)$$

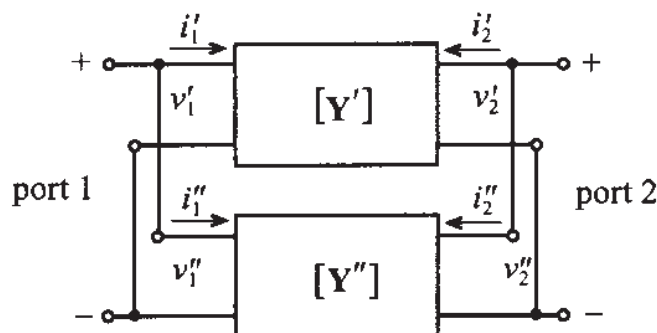


Figure 4-8 Parallel connection of two two-port networks.

4.2.3 Cascading Networks

The $ABCD$ -parameter description is most suitable when cascading networks, as depicted in Figure 4-9 for the example of a two-transistor configuration. In this case the current on the output of the first network is equal in value, but opposite in sign, to the input current of the second network (i.e., $i_2' = -i_1''$). The voltage drop v_2' across the output port of the first network is equal to the voltage drop v_1'' across the input port of the second network. Thus, we can write the following relations:

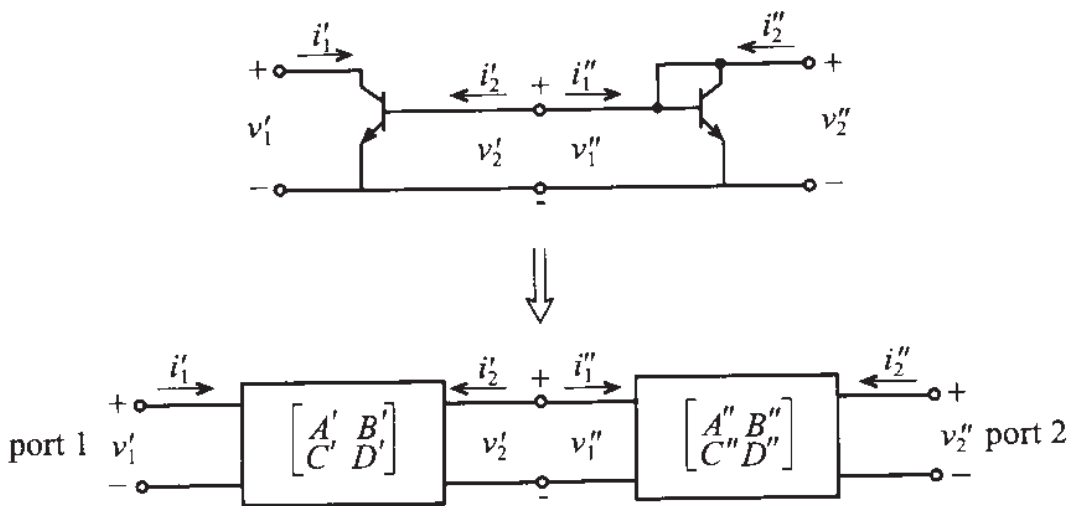


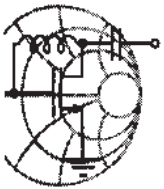
Figure 4-9 Cascading two networks.

$$\begin{aligned}
 \left\{ \begin{array}{c} v_1 \\ i_1 \end{array} \right\} &= \left\{ \begin{array}{c} v_1' \\ i_1' \end{array} \right\} = \begin{bmatrix} A' & B' \\ C' & D' \end{bmatrix} \left\{ \begin{array}{c} v_2' \\ -i_2' \end{array} \right\} = \begin{bmatrix} A' & B' \\ C' & D' \end{bmatrix} \left\{ \begin{array}{c} v_1'' \\ i_1'' \end{array} \right\} \\
 &= \begin{bmatrix} A' & B' \\ C' & D' \end{bmatrix} \begin{bmatrix} A'' & B'' \\ C'' & D'' \end{bmatrix} \left\{ \begin{array}{c} v_2'' \\ -i_2'' \end{array} \right\}
 \end{aligned} \tag{4.21}$$

The overall system **ABCD**-matrix is equal to the product of the **ABCD**-matrices of the individual networks.

4.2.4 Summary of **ABCD** Network Representations

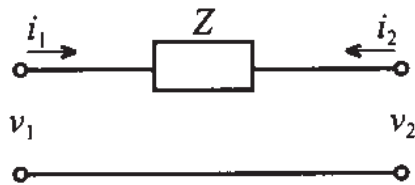
As we will see in subsequent chapters, microwave circuits can usually be represented as the result of cascading simpler networks. It is therefore important to develop **ABCD**-matrix representations for simple two-port networks that can be used as building blocks of more complex configurations. In this section several examples are considered for which we will derive **ABCD**-parameters such as transmission line, series impedance, and passive *T*-network. Other very useful circuits, such as parallel impedance, passive pi-network, and transformer, are left as exercises at the end of this chapter (see Problems 4.10–4.12). The results of all the computations are summarized in Table 4-1 at the end of this section.



RF & MW

Example 4-4: ABCD network representation of an impedance element

Compute the *ABCD*-matrix representation for the following network:



Solution: Guided by the definition (4.10), to determine parameter *A* we have to compute the ratio of the voltage drop across port 1 to the voltage drop across port 2 when the current into this port is equal to zero (i.e., port 2 is disconnected). In this case, it is apparent that for the circuit under consideration, the voltages on both ports are equal to their ratio, which is equal to unity

$$A = \frac{v_1}{v_2} \Big|_{i_2=0} = 1$$

To obtain the value for *B*, we need to find the ratio of the voltage drop across port 1 to the current flowing from port 2 when the terminals of port 2 are shortened. From the circuit topology, this ratio is equal to the impedance *Z*:

$$B = \frac{v_1}{-i_2} \Big|_{v_2=0} = Z$$

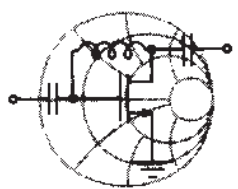
The remaining two parameters are found according to (4.10) of the *ABCD*-representation and can be shown to be

$$C = \frac{i_1}{v_2} \Big|_{i_2=0} = 0 \text{ and } D = \frac{i_1}{-i_2} \Big|_{v_2=0} = 1$$

The ABCD-matrix coefficients are determined in a similar manner as the previously discussed Z-, Y-, and h-matrix coefficients.

The accurate prediction of the coefficients again depends on the ability to enforce open- and short-circuit terminal conditions.

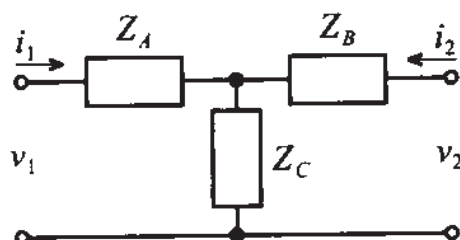
In the following example the *ABCD*-parameters of the passive *T*-network are determined. In the derivation of the parameters we will rely on the knowledge of *ABCD* parameters for series and parallel connections of the impedance.



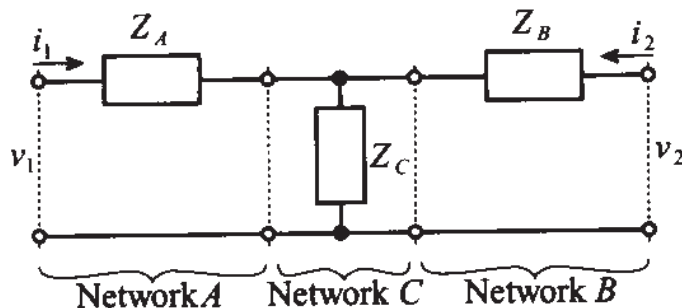
RF & MW

Example 4-5: ABCD matrix computation of a T-network

Compute the *ABCD*-matrix representation for the following *T*-network:



Solution: This problem can be solved using two different approaches. The first approach involves directly applying the definition of the *ABCD*-matrix coefficients and compute them as done in the previous example. Another approach is to utilize the knowledge of the *ABCD*-parameters for parallel and series connections of a single impedance. If we choose this method, we first have to break the initial circuit into subcircuits as follows:

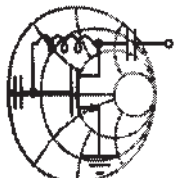


As discussed previously, the **ABCD**-matrix representation of the entire circuit is equal to the product of the **ABCD**-matrices of the individual subcircuits. Using the results from Example 4-4 and Problem 4.8, we can write

$$[\mathbf{ABCD}] = \begin{bmatrix} 1 & Z_A \\ 0 & 1 \end{bmatrix} \begin{bmatrix} 1 & 0 \\ Z_C^{-1} & 1 \end{bmatrix} \begin{bmatrix} 1 & Z_B \\ 0 & 1 \end{bmatrix} = \begin{bmatrix} 1 + \frac{Z_A}{Z_C} & Z_A + Z_B + \frac{Z_A Z_B}{Z_C} \\ \frac{1}{Z_C} & 1 + \frac{Z_B}{Z_C} \end{bmatrix}$$

*Here we see the advantage of using the **ABCD**-matrix representation in that a more complex network can be constructed by multiplication of simpler building blocks.*

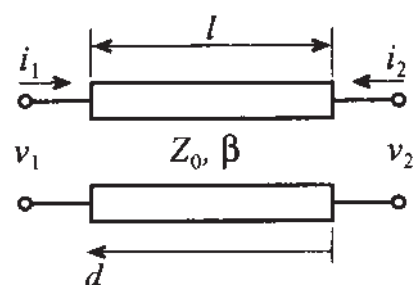
As a last example, let us consider the computation of the **ABCD** parameters for a transmission line.



RF & MW →

Example 4-6: ABCD-matrix coefficient computation of a transmission line section

Compute the **ABCD**-matrix representation of the following transmission line with characteristic impedance Z_0 , propagation constant β , and length l .



Solution: Similar to Example 4-4, we have to apply open- and short-circuit conditions at port 2. For a transmission line these con-

ditions are equivalent to the analysis of open- and short-circuit stub lines. Such lines are simply the open/short-circuit transmission line representations discussed in Sections 2.9.3 and 2.9.2. In these sections we found that for the open-circuit stub the voltage and current are given by the following expressions [see (2.71) and (2.72)]:

$$V(d) = 2V^+ \cos(\beta d) \text{ and } I(d) = \frac{2jV^+}{Z_0} \sin(\beta d)$$

where distance d is measured from the open port (i.e., in our case from port 2).

For a short-circuit stub of length l voltages and currents are determined by (2.67) and (2.68):

$$V(d) = 2jV^+ \sin(\beta d) \text{ and } I(d) = \frac{2V^+}{Z_0} \cos(\beta d)$$

where distance d is again measured from port 2 to port 1. In addition to these relations, it is important to recall that the current is defined as flowing *toward the load*. Therefore, the current is equal to i_1 at port 1 and equal to $-i_2$ at port 2.

Having determined the relations for voltages and currents, it is now possible to establish equations for the *ABCD*-parameters of the transmission line. Parameter *A* is defined as the ratio of the voltages at ports 1 and 2 when port 2 is open (i.e., we have to use the formulas for the open-circuit stub):

$$A = \left. \frac{v_1}{v_2} \right|_{i_2=0} = \frac{2V^+ \cos(\beta l)}{2V^+} = \cos(\beta l)$$

where we employ the fact that $d = 0$ at port 2 and $d = l$ at port 1.

Parameter *B* is defined as the ratio of the voltage drop across port 1 to the current flowing from port 2 (i.e., toward the load) when port 2 is shorted. For this case we have to use the formulas for voltage and current defined for a short-circuit stub. This yields

$$B = \left. \frac{v_1}{-i_2} \right|_{v_2=0} = \frac{2jV^+ \sin(\beta l)}{2V^+/Z_0} = jZ_0 \sin(\beta l)$$

The remaining two coefficients are obtained in a similar manner:

$$C = \left. \frac{i_1}{v_2} \right|_{i_2=0} = \frac{\frac{2jV^+}{Z_0} \sin(\beta l)}{2V^+} = jY_0 \sin(\beta l)$$

$$D = \left. \frac{i_1}{-i_2} \right|_{v_2=0} = \frac{\frac{2V^+}{Z_0} \cos(\beta l)}{\frac{2V^+}{Z_0}} = \cos(\beta l)$$

Thus, a transmission line with characteristic impedance Z_0 , propagation constant β , and length l has the following matrix representation:

$$\begin{bmatrix} A & B \\ C & D \end{bmatrix} = \begin{bmatrix} \cos(\beta l) & jZ_0 \sin(\beta l) \\ jY_0 \sin(\beta l) & \cos(\beta l) \end{bmatrix}$$

The ABCD transmission line representation has the expected periodic parameter behavior similar to the line input impedance formula derived in Chapter 2.

In Table 4-1 six of the most common circuit configurations are summarized in terms of their $ABCD$ two-port network representations. From these six basic models, more complicated circuits are readily constructed by suitably combining these elementary networks.

4.3 Network Properties and Applications

4.3.1 Interrelations between Parameter Sets

Depending on the particular circuit configuration, we may be forced to convert between different parameter sets to arrive at a particular input/output description. For instance, the low-frequency transistor parameters are often recorded in **h**-matrix form. However, when cascading the transistor with additional networks, a more useful **ABCD**-matrix form may be appropriate. Thus, converting the **h**-matrix into an **ABCD**-matrix form and vice versa can greatly simplify the analysis.

Table 4-1 ABCD-Parameters of Some Useful Two-Port Circuits.

| Circuit | ABCD-Parameters | |
|---------|--|--|
| | $A = 1$ $C = 0$ | $B = Z$ $D = 1$ |
| | $A = 1$ $C = Y$ | $B = 0$ $D = 1$ |
| | $A = 1 + \frac{Z_A}{Z_C}$ $C = \frac{1}{Z_C}$ | $B = Z_A + Z_B + \frac{Z_A Z_B}{Z_C}$ $D = 1 + \frac{Z_B}{Z_C}$ |
| | $A = 1 + \frac{Y_B}{Y_C}$ $C = Y_A + Y_B + \frac{Y_A Y_B}{Y_C}$ | $B = \frac{1}{Y_C}$ $D = 1 + \frac{Y_A}{Y_C}$ |
| | $A = \cos \beta l$ $C = \frac{j \sin \beta l}{Z_0}$ | $B = j Z_0 \sin \beta l$ $D = \cos \beta l$ |
| | $A = N$ $C = 0$ | $B = 0$ $D = \frac{1}{N}$ |

To show how the conversion between the individual parameter sets can be accomplished, let us find an ABCD-matrix representation of a given h-matrix. From the definition (4.11) we can express parameter A as follows

$$A = \left. \frac{v_1}{v_2} \right|_{i_2=0} = \frac{h_{11}i_1 + h_{12}v_2}{v_2} \quad (4.22)$$

In this expression we are able to re-express the current i_1 in (4.11) in terms of the voltage v_2 because $i_2 = 0$. The result is

$$A = \left. \frac{v_1}{v_2} \right|_{i_2=0} = \frac{h_{11}\left(-\frac{h_{22}}{h_{21}}v_2\right) + h_{12}v_2}{v_2} = \frac{1}{h_{21}}(h_{22}h_{11} - h_{12}h_{21}) = -\frac{\Delta h}{h_{21}} \quad (4.23)$$

where $\Delta h = h_{11}h_{22} - h_{12}h_{21}$ denotes the determinant of the **h**-matrix. Similarly, for the remaining coefficients we compute

$$B = \left. -\frac{v_1}{i_2} \right|_{v_2=0} = -\frac{h_{11}i_1}{i_2} = -\frac{h_{11}\left(\frac{i_2}{h_{21}}\right)}{i_2} = -\frac{h_{11}}{h_{21}} \quad (4.24)$$

$$C = \left. \frac{i_1}{v_2} \right|_{i_2=0} = \frac{\frac{-h_{22}}{h_{21}}v_2}{v_2} = -\frac{h_{22}}{h_{21}} \quad (4.25)$$

$$D = \left. -\frac{i_1}{i_2} \right|_{v_2=0} = -\frac{\frac{i_2}{h_{21}}}{i_2} = -\frac{1}{h_{21}} \quad (4.26)$$

This concludes the conversion from **h**-parameters to **ABCD** form. A similar procedure could have been performed from **ABCD**-parameters to **h**-matrix form.

As an additional case, let us investigate the conversion from **ABCD**-parameters to the **Z**-representation. Starting with (4.2) and using (4.11), we can develop the following relations:

$$Z_{11} = \left. \frac{v_1}{i_1} \right|_{i_2=0} = \frac{Av_2}{Cv_2} = \frac{A}{C} \quad (4.27)$$

$$Z_{12} = \left. \frac{v_1}{i_2} \right|_{i_1=0} = \frac{Av_2 - Bi_2}{\frac{C}{D}v_2} = \frac{Av_2 - \frac{BC}{D}v_2}{\frac{C}{D}v_2} = \frac{AD - BC}{C} = \frac{\Delta ABCD}{C} \quad (4.28)$$

$$Z_{21} = \left. \frac{v_2}{i_1} \right|_{i_2=0} = \frac{v_1/A}{Cv_2} = \frac{Av_2/A}{Cv_2} = \frac{1}{C} \quad (4.29)$$

$$Z_{22} = \left. \frac{v_2}{i_2} \right|_{i_1=0} = \frac{v_2}{Cv_2/D} = \frac{D}{C} \quad (4.30)$$

where $\Delta ABCD = AD - BC$ is the determinant of the ABCD-matrix.

By relying on the respective defining voltage and current relations, it is relatively straightforward to work out all parameter conversions. For convenience, Table 4-2 summarizes the formulas for the previously defined four network parameter sets (see also Appendix H for a complete list of all conversion formulas).

Table 4-2 Conversion between Different Network Representations

| | [Z] | [Y] | [h] | [ABCD] |
|--------|---|---|---|--|
| [Z] | $Z_{11} Z_{12}$ | $\frac{Z_{22}}{\Delta Z} - \frac{Z_{12}}{\Delta Z}$ | $\frac{\Delta Z}{Z_{22}} \frac{Z_{12}}{Z_{22}}$ | $\frac{Z_{11}}{Z_{21}} \frac{\Delta Z}{Z_{21}}$ |
| | $Z_{21} Z_{22}$ | $-\frac{Z_{21}}{\Delta Z} \frac{Z_{11}}{\Delta Z}$ | $-\frac{Z_{21}}{Z_{22}} \frac{1}{Z_{22}}$ | $\frac{1}{Z_{21}} \frac{Z_{22}}{Z_{21}}$ |
| [Y] | $\frac{Y_{22}}{\Delta Y} - \frac{Y_{12}}{\Delta Y}$ | $Y_{11} Y_{12}$ | $\frac{1}{Y_{11}} - \frac{Y_{12}}{Y_{11}}$ | $-\frac{Y_{22}}{Y_{21}} - \frac{1}{Y_{21}}$ |
| | $-\frac{Y_{21}}{\Delta Y} \frac{Y_{11}}{\Delta Y}$ | $Y_{21} Y_{22}$ | $\frac{Y_{21}}{Y_{11}} \frac{\Delta Y}{Y_{11}}$ | $-\frac{\Delta Y}{Y_{21}} - \frac{Y_{11}}{Y_{21}}$ |
| [h] | $\frac{\Delta h}{h_{22}} \frac{h_{12}}{h_{22}}$ | $\frac{1}{h_{11}} - \frac{h_{12}}{h_{11}}$ | $h_{11} h_{12}$ | $-\frac{\Delta h}{h_{21}} - \frac{h_{11}}{h_{21}}$ |
| | $-\frac{h_{21}}{h_{22}} \frac{1}{h_{22}}$ | $\frac{h_{21}}{h_{11}} \frac{\Delta h}{h_{11}}$ | $h_{21} h_{22}$ | $-\frac{h_{22}}{h_{21}} - \frac{1}{h_{21}}$ |
| [ABCD] | $\frac{A}{C} \frac{\Delta ABCD}{C}$ | $\frac{D}{B} - \frac{\Delta ABCD}{B}$ | $\frac{B}{D} \frac{\Delta ABCD}{D}$ | $A \ B$ |
| | $\frac{1}{C} \frac{D}{C}$ | $-\frac{1}{B} \frac{A}{B}$ | $\frac{1}{D} \frac{C}{D}$ | $C \ D$ |

4.3.2 Analysis of Microwave Amplifier

In this section we consider, by way of an example, the usage of the conversion between different network representations to analyze a relatively complicated circuit. Basis of the analysis is the circuit diagram of a particular microwave amplifier shown in Figure 4-10.

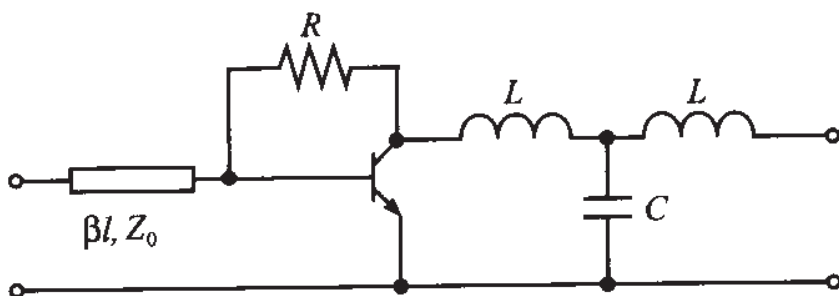


Figure 4-10 Microwave amplifier circuit diagram.

The first step is to break down the circuit into smaller, simpler subnetworks. This can be accomplished in several ways, one of which is shown in Figure 4-11.

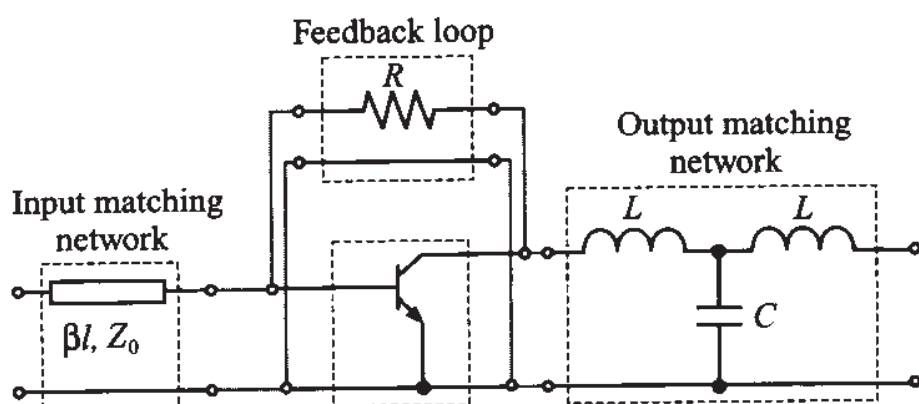


Figure 4-11 Subnetwork representation of the microwave amplifier.

As shown in this figure, the amplifier is divided into a set of four subcircuits. The input matching network consists of a transmission line (for convenience only the upper trace is shown) and is cascaded with a parallel combination of the transistor and a feedback loop. This circuit is then cascaded with an output matching network.

For the transistor we will use a high-frequency hybrid pi-network model (see also Chapter 7), which is shown in Figure 4-12.

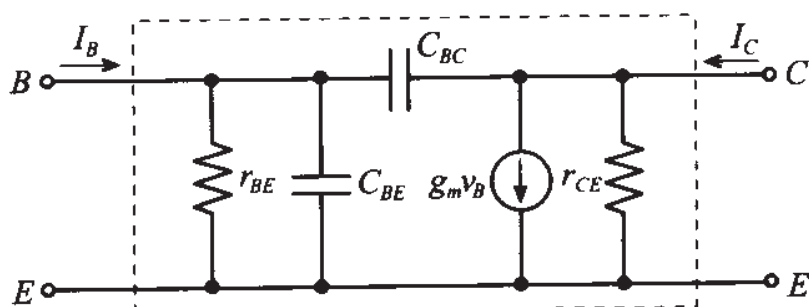


Figure 4-12 High-frequency hybrid transistor model.

The derivation of the h -parameters is left as a problem (Problem 4.13 at the end of this chapter). Here we only list the resulting \mathbf{h} -matrix for the transistor:

$$h_{11} = h_{ie} = \frac{r_{BE}}{1 + j\omega(C_{BE} + C_{BC})r_{BE}} \quad (4.31a)$$

$$h_{12} = h_{re} = \frac{j\omega C_{BC}r_{BE}}{1 + j\omega(C_{BE} + C_{BC})r_{BE}} \quad (4.31b)$$

$$h_{21} = h_{fe} = \frac{r_{BE}(g_m - j\omega C_{BC})}{1 + j\omega(C_{BE} + C_{BC})r_{BE}} \quad (4.31c)$$

$$h_{22} = h_{oe} = \frac{1}{r_{CE}} + \frac{j\omega C_{BC}(1 + g_m r_{BE} + j\omega C_{BE}r_{BE})}{1 + j\omega(C_{BE} + C_{BC})r_{BE}} \quad (4.31d)$$

To compute the matrix for the parallel combination of the transistor and the feedback loop resistor we have to convert the \mathbf{h} -matrix into a \mathbf{Y} -matrix called $[\mathbf{Y}]_{tr}$ in order to apply the summation rule (4.20). To accomplish this, we can use formulas from Table 4-2 and add the result to the \mathbf{Y} -matrix of the feedback resistor. The admittance matrix for the feedback resistor can be derived either directly using the definition of the \mathbf{Y} -matrix or by converting the $ABCD$ -parameters derived in Example 4-4 into the \mathbf{Y} -form. The result of these computations is

$$\begin{bmatrix} Y_{11} & Y_{12} \\ Y_{21} & Y_{22} \end{bmatrix}_R = \begin{bmatrix} R^{-1} & -R^{-1} \\ -R^{-1} & R^{-1} \end{bmatrix} \quad (4.32)$$

After the summation we obtain the admittance matrix for the parallel combination of the transistor and the feedback resistor $[\mathbf{Y}]_{tr+R}$.

The same result could have been obtained if we had noticed that the feedback resistor is connected in parallel with the capacitor C_{BC} of the transistor. Thus, to obtain the admittance matrix of the parallel combination of the feedback resistor and the transistor, we simply need to replace C_{BC} in the \mathbf{h} -matrix of the transistor with $C_{BC} + 1/(j\omega R)$ and then convert the resulting matrix into \mathbf{Y} -representation.

The final step in the analysis is to multiply the $ABCD$ -matrices for the input matching network (index: IMN), the transistor with feedback resistor (index: $tr + R$), and the output matching network (index: OMN)

$$\begin{bmatrix} A & B \\ C & D \end{bmatrix}_{amp} = \begin{bmatrix} A & B \\ C & D \end{bmatrix}_{IMN} \begin{bmatrix} A & B \\ C & D \end{bmatrix}_{tr+R} \begin{bmatrix} A & B \\ C & D \end{bmatrix}_{OMN} \quad (4.33)$$

where the **ABCD**-matrices for the matching networks are found using the results from Table 4-1:

$$\begin{bmatrix} A & B \\ C & D \end{bmatrix}_{IMN} = \begin{bmatrix} \cos \beta l & jZ_0 \sin \beta l \\ \frac{j \sin \beta l}{Z_0} & \cos \beta l \end{bmatrix} \quad (4.34)$$

$$\begin{bmatrix} A & B \\ C & D \end{bmatrix}_{OMN} = \begin{bmatrix} 1 - \omega^2 LC & 2j\omega L - j\omega^3 L^2 C \\ j\omega C & 1 - \omega^2 LC \end{bmatrix} \quad (4.35)$$

Due to rather lengthy expressions we are not presenting the final result for the **ABCD**-parameters of the entire amplifier. Instead we urge the interested readers to perform these computations by relying on a mathematical spreadsheet program of their choice (MathCad, MATLAB, Mathematica, etc.). One of the results of these computations is shown in Figure 4-13, where the small-signal current gain for the amplifier with short-circuited output (inverse of the *D*-coefficient) is plotted versus frequency for different values of the feedback resistor.

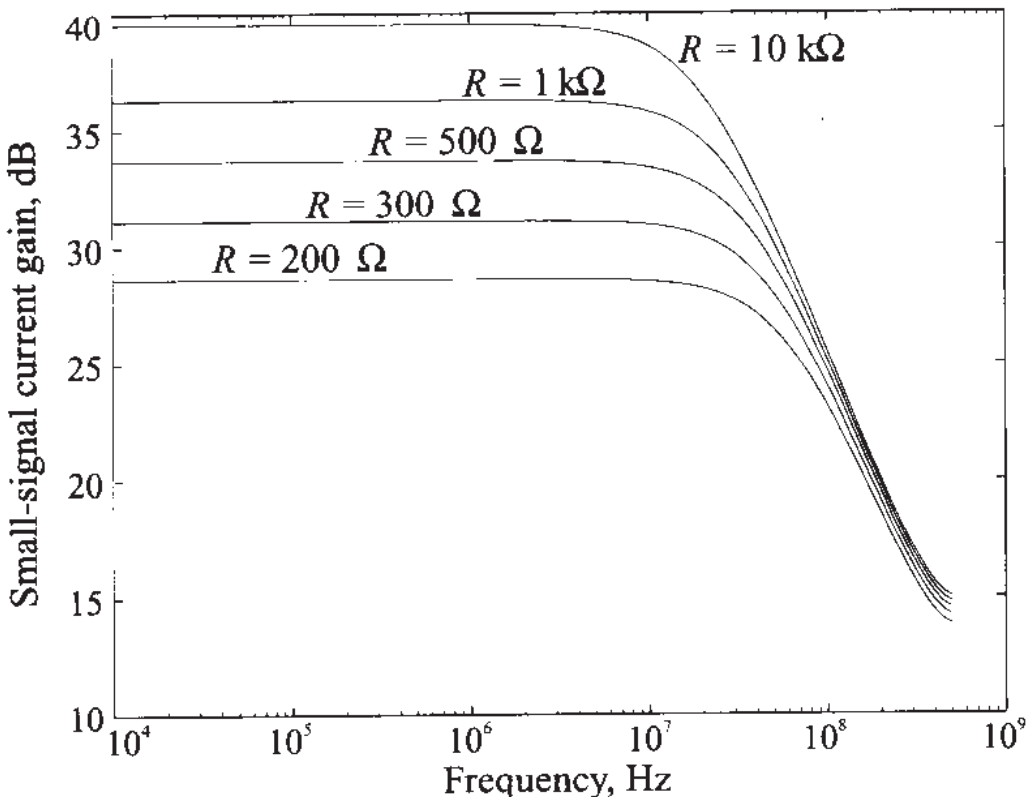


Figure 4-13 Small-signal current gain of the amplifier versus frequency for different values of the feedback resistor.

The computations are based on the circuit in Figure 4-11 with $L = 1 \text{ nH}$, $C = 10 \text{ pF}$, transmission line length of $l = 5 \text{ cm}$, and phase velocity equal to 65% of the speed of light. The transistor is described by the following set of values: $r_{BE} = 520 \Omega$, $r_{CE} = 80k \Omega$, $C_{BE} = 10 \text{ pF}$, $C_{BC} = 1 \text{ pF}$, and $g_m = 0.192 \text{ s}$.

4.4 Scattering Parameters

In almost all databooks and technical literature regarding RF systems, the **scattering** or **S-parameter** representation plays a central role. This importance is derived from the fact that practical system characterizations can no longer be accomplished through simple open- or short-circuit measurements, as it is customarily done in low-frequency applications and as discussed at the beginning of this chapter. We should recall what happens when we attempt to create a short circuit with a wire: The wire itself possesses an inductance that can be of substantial magnitude at high frequency. Also, the open circuit leads to capacitive loading at the terminal. In either case, the open/short-circuit conditions needed to determine Z -, Y -, h -, and $ABCD$ -parameters can no longer be guaranteed. Moreover, when dealing with wavepropagation phenomena, it is not desirable to introduce a reflection coefficient whose magnitude is unity. For instance, the terminal discontinuity will cause undesirable voltage and/or current wave reflections, leading to oscillations that can result in the destruction of the device. With the **S**-parameters, the RF engineer has a tool to characterize the two-port network description of practically all RF devices without requiring unachievable terminal conditions or causing harm to the **device under test (DUT)**.

4.4.1 Definition of Scattering Parameters

Simply put, **S**-parameters are power wave descriptors that permit us to define the input-output relations of a network in terms of incident and reflected power waves. With reference to Figure 4-14 we define an incident *normalized* power wave a_n and a reflected *normalized* power wave b_n as follows:

$$a_n = \frac{1}{2\sqrt{Z_0}}(V_n + Z_0 I_n) \quad (4.36a)$$

$$b_n = \frac{1}{2\sqrt{Z_0}}(V_n - Z_0 I_n) \quad (4.36b)$$

where the index n refers either to port number 1 or 2. The impedance Z_0 is the characteristic impedance of the connecting lines on the input and output side of the network. Under more general conditions the line impedance on the input side can differ from the

line impedance on the output side. However, for our initial discussion, we will keep things simple and assume that both impedances are the same.

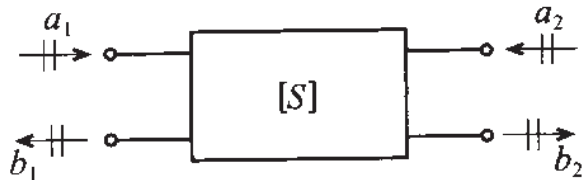


Figure 4-14 Convention used to define S -parameters for a two-port network.

Inverting (4.36) leads to the following voltage and current expressions:

$$V_n = \sqrt{Z_0}(a_n + b_n) \quad (4.37a)$$

$$I_n = \frac{1}{\sqrt{Z_0}}(a_n - b_n) \quad (4.37b)$$

The physical meaning of (4.36) becomes clear when we recall the equations for power:

$$P_n = \frac{1}{2}\text{Re}\{V_n I_n^*\} = \frac{1}{2}(|a_n|^2 - |b_n|^2) \quad (4.38)$$

Isolating forward and backward traveling wave components in (4.37), we immediately see

$$a_n = \frac{V_n^+}{\sqrt{Z_0}} = \sqrt{Z_0} I_n^+ \quad (4.39a)$$

$$b_n = \frac{V_n^-}{\sqrt{Z_0}} = -\sqrt{Z_0} I_n^- \quad (4.39b)$$

which is consistent with the definitions (4.37) since

$$V_n = V_n^+ + V_n^- = Z_0 I_n^+ - Z_0 I_n^- \quad (4.40)$$

Based on the directional convention shown in Figure 4-14 we are now in a position to define the S -parameters:

$$\begin{Bmatrix} b_1 \\ b_2 \end{Bmatrix} = \begin{bmatrix} S_{11} & S_{12} \\ S_{21} & S_{22} \end{bmatrix} \begin{Bmatrix} a_1 \\ a_2 \end{Bmatrix} \quad (4.41)$$

where the terms are

$$S_{11} = \left. \frac{b_1}{a_1} \right|_{a_2=0} = \frac{\text{reflected power wave at port 1}}{\text{incident power wave at port 1}} \quad (4.42a)$$

$$S_{21} = \left. \frac{b_2}{a_1} \right|_{a_2=0} = \frac{\text{transmitted power wave at port 2}}{\text{incident power wave at port 1}} \quad (4.42b)$$

$$S_{22} = \left. \frac{b_2}{a_2} \right|_{a_1=0} = \frac{\text{reflected power wave at port 2}}{\text{incident power wave at port 2}} \quad (4.42c)$$

$$S_{12} = \left. \frac{b_1}{a_2} \right|_{a_1=0} = \frac{\text{transmitted power wave at port 1}}{\text{incident power wave at port 2}} \quad (4.42d)$$

We observe that the conditions $a_2 = 0$ and $a_1 = 0$ imply that no power waves are returned to the network at either port 2 or port 1. However, these condition can only be ensured when the connecting transmission lines are terminated into their characteristic impedances.

Since the S -parameters are closely related to power relations, we can express the normalized input and output waves in terms of time averaged power. With reference to Section 2.10.2 we note that the average power at port 1 is given by

$$P_1 = \frac{1}{2} \frac{|V_1^+|^2}{Z_0} (1 - |\Gamma_{\text{in}}|^2) = \frac{1}{2} \frac{|V_1^+|^2}{Z_0} (1 - |S_{11}|^2) \quad (4.43)$$

where the reflection coefficient at the input side is expressed in terms of S_{11} under matched output according to the following argument:

$$\Gamma_{\text{in}} = \frac{V_1^-}{V_1^+} = \left. \frac{b_1}{a_1} \right|_{a_2=0} = S_{11}. \quad (4.44)$$

This also allows us to redefine the VSWR at port 1 in terms of S_{11} as

$$\text{VSWR} = \frac{1 + |S_{11}|}{1 - |S_{11}|} \quad (4.45)$$

Furthermore, based on (4.39a) we can identify the incident power in (4.43) and express it in terms of a_1 :

$$\frac{1}{2} \frac{|V_1^+|^2}{Z_0} = P_{\text{inc}} = \frac{|a_1|^2}{2} \quad (4.46)$$

which is the maximal available power from the generator. Using (4.46) and (4.44) in (4.43) finally gives us the total power at port 1 (under matched output condition) expressed as a combination of incident and reflected powers:

$$P_1 = P_{\text{inc}} + P_{\text{ref}} = \frac{1}{2}(|a_1|^2 - |b_1|^2) = \frac{|a_1|^2}{2}(1 - |\Gamma_{\text{in}}|^2) \quad (4.47)$$

If the reflection coefficient, or S_{11} , is zero, all available power from the source is delivered to port 1 of the network. An identical analysis at port 2 yields

$$P_2 = \frac{1}{2}(|a_2|^2 - |b_2|^2) = \frac{|a_2|^2}{2}(1 - |\Gamma_{\text{out}}|^2) \quad (4.48)$$

4.4.2 Meaning of S-Parameters

As already mentioned in the previous section, the S -parameters can only be determined under conditions of perfect matching on the input or output side. For instance, in order to record S_{11} and S_{21} we have to ensure that on the output side the line impedance Z_0 is matched for $a_2 = 0$ to be enforced, as shown in Figure 4-15.

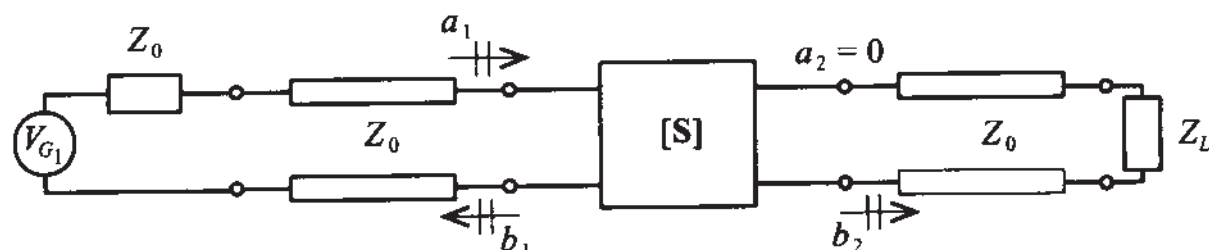


Figure 4-15 Measurement of S_{11} and S_{21} by matching the line impedance Z_0 at port 2 through a corresponding load impedance $Z_L = Z_0$.

This configuration allows us to compute S_{11} by finding the input reflection coefficient:

$$S_{11} = \Gamma_{\text{in}} = \frac{Z_{\text{in}} - Z_0}{Z_{\text{in}} + Z_0} \quad (4.49)$$

In addition, taking the logarithm of the magnitude of S_{11} gives us the return loss in dB

$$\text{RL} = -20 \log |S_{11}| \quad (4.50)$$

Moreover, with port 2 properly terminated, we find

$$S_{21} = \left. \frac{b_2}{a_1} \right|_{a_2=0} = \left. \frac{V_2^-/\sqrt{Z_0}}{(V_1 + Z_0 I_1)/(2\sqrt{Z_0})} \right|_{I_2^+ = V_2^+ = 0} \quad (4.51)$$

Since $a_2 = 0$, we can set to zero the positive traveling voltage and current waves at port 2. Replacing V_1 by the generator voltage V_{G1} minus the voltage drop over the source impedance Z_0 , $V_{G1} - Z_0 I_1$ gives

$$S_{21} = \frac{2V_2^-}{V_{G1}} = \frac{2V_2}{V_{G1}} \quad (4.52)$$

Here we observe that the voltage recorded at port 2 is directly related to the generator voltage and thus specifies the **forward voltage gain** of the network. To find the **forward power gain**, we square (4.52) to obtain

$$G_0 = |S_{21}|^2 = \left| \frac{V_2}{V_{G1}/2} \right|^2 \quad (4.53)$$

If we reverse the measurement procedure and attach a generator voltage V_{G2} to port 2 and properly terminate port 1, as shown in Figure 4-16, we can determine the remaining two S -parameters, S_{22} and S_{12} .

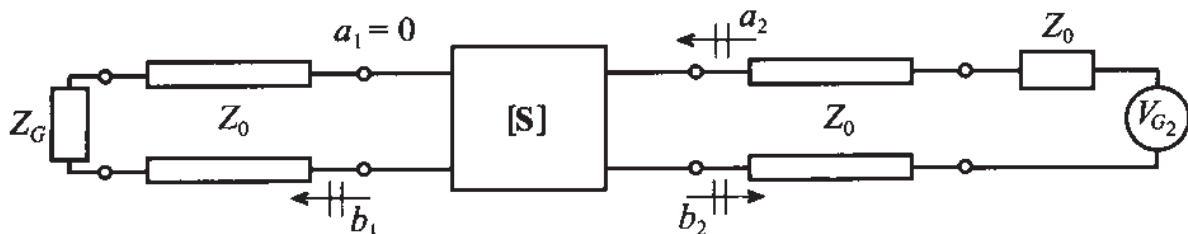


Figure 4-16 Measurement of S_{22} and S_{12} by matching the line impedance Z_0 at port 1 through a corresponding input impedance $Z_G = Z_0$.

To compute S_{22} we need to find the output reflection coefficient Γ_{out} in a similar way as already discussed for S_{11} :

$$S_{22} = \Gamma_{\text{out}} = \frac{Z_{\text{out}} - Z_0}{Z_{\text{out}} + Z_0} \quad (4.54)$$

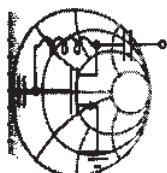
and for S_{12}

$$S_{12} = \left. \frac{b_1}{a_2} \right|_{a_1 = 0} = \left. \frac{V_1^- / \sqrt{Z_0}}{(V_2 + Z_0 I_2) / (2\sqrt{Z_0})} \right|_{I_1^+ = V_1^+ = 0} \quad (4.55)$$

The term S_{12} can further be manipulated through the substitution of V_2 by $V_{G2} - Z_0 I_2$, leading to the form

$$S_{12} = \frac{2V_1^-}{V_{G2}} = \frac{2V_1}{V_{G2}} \quad (4.56)$$

known as the **reverse voltage gain** and whose square $|S_{12}|^2$ is identified as **reverse power gain**. While determining S_{11} and S_{22} can be directly computed as part of the impedance definitions, S_{12} and S_{21} require the replacement of the defining voltages by the appropriate network parameters. In the following example, the S -parameters are computed for a simple, three element network.



RF & MW →

Example 4-7: Determination of a T-network elements

Find the S -parameters and the resistive elements for the 3 dB attenuator network shown in Figure 4-17(a) assuming that the network is placed into a transmission line section with a characteristic line impedance of $Z_0 = 50 \Omega$.

Solution: An attenuator should be matched to the line impedance and must therefore meet the requirement $S_{11} = S_{22} = 0$. As a result, based on Figure 4-17(b) and consistent with (4.49), we set

$$Z_{in} = R_1 + \frac{R_3(R_2 + 50 \Omega)}{(R_3 + R_2 + 50 \Omega)} = 50 \Omega$$

Because of symmetry, it is immediately clear that $R_1 = R_2$. We now investigate the voltage $V_2 = V_2^-$ at port 2 in terms of $V_1 = V_1^+$. According to the circuit configuration shown in Figure 4-17(c), the following expression is obtained

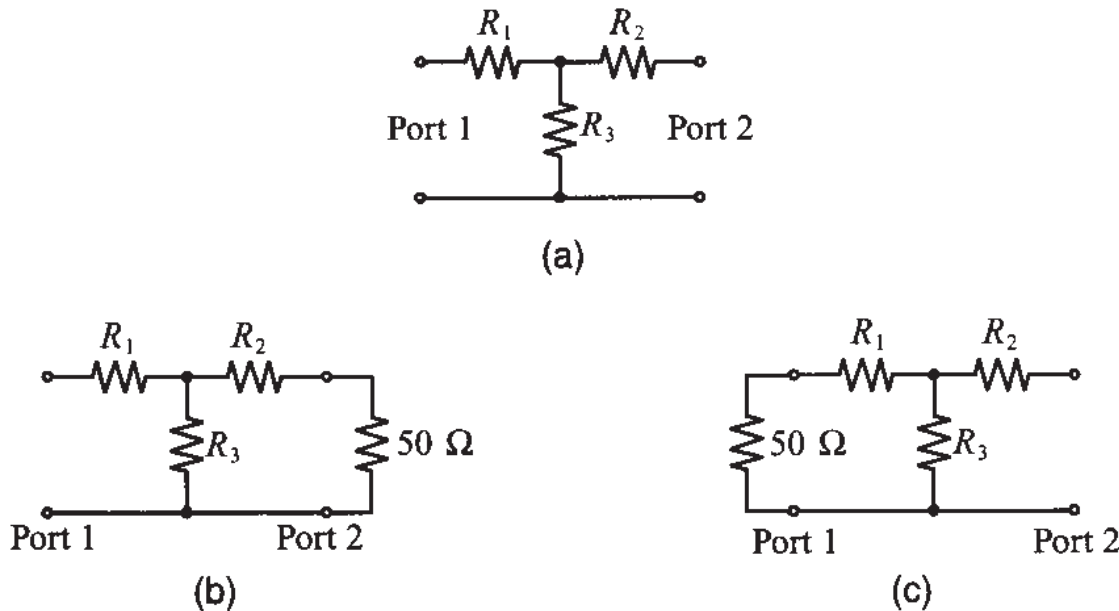


Figure 4-17 S-parameter computation for a T-network. (a) circuit diagram; (b) circuit for S_{11} and S_{21} measurements; (c) circuit for S_{12} and S_{22} measurements.

$$V_2 = \left(\frac{\frac{R_3(R_1 + 50\ \Omega)}{R_3 + R_1 + 50\ \Omega}}{\frac{R_3(R_1 + 50\ \Omega)}{R_3 + R_1 + 50\ \Omega} + R_1} \right) \left(\frac{50\ \Omega}{50\ \Omega + R_1} \right) V_1$$

For a 3 dB attenuation, we require

$$S_{21} = \frac{2V_2}{V_{G1}} = \frac{V_2}{V_1} = \frac{1}{\sqrt{2}} = 0.707 = S_{12}$$

Setting the ratio of V_2/V_1 to 0.707 in the preceding equation allows us, in combination with the input impedance expression, to determine R_1 and R_3 . After simplification it is seen that

$$R_1 = R_2 = \frac{\sqrt{2}-1}{\sqrt{2}+1} Z_0 = 8.58\ \Omega \text{ and } R_3 = 2\sqrt{2} \cdot Z_0 = 141.4\ \Omega$$

The choice of the resistor network ensures that at the input and output ports an impedance of $50\ \Omega$ is maintained. This implies that this network can be inserted into a $50\ \Omega$ transmission line section without causing undesired reflections, resulting in an insertion loss.

The definitions for the S -parameters require appropriate termination. For instance, if S_{11} is desired, the transmission line connected to port 2 has to be terminated into its characteristic line impedance. This does not necessarily mean that the output impedance Z_{out} of the network has to be matched to the line impedance Z_0 . Rather, the line impedance must be matched to ensure that no wave is reflected from the load, as implied by $a_2 = 0$. If this is not the case, we will see in Section 4.4.5 how S_{11} is modified.

4.4.3 Chain Scattering Matrix

To extend the concept of the S -parameter representation to cascaded networks, it is more efficient to rewrite the power wave expressions arranged in terms of input and output ports. This results in the **chain scattering matrix** notation. That is,

$$\begin{Bmatrix} a_1 \\ b_1 \end{Bmatrix} = \begin{bmatrix} T_{11} & T_{12} \\ T_{21} & T_{22} \end{bmatrix} \begin{Bmatrix} b_2 \\ a_2 \end{Bmatrix} \quad (4.57)$$

It is immediately seen that the cascading of two dual-port networks becomes a simple multiplication. This is apparent in Figure 4-18, where network A (given by matrix $[T]_A$) is connected to network B (given by matrix $[T]_B$).

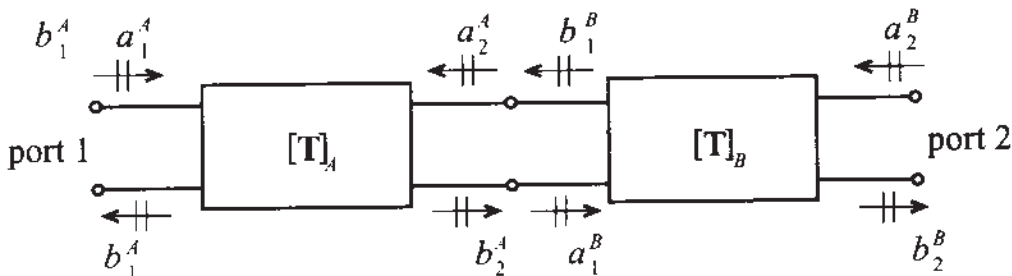


Figure 4-18 Cascading of two networks A and B .

If network A is described by the relation

$$\begin{Bmatrix} a_1^A \\ b_1^A \end{Bmatrix} = \begin{bmatrix} T_{11}^A & T_{12}^A \\ T_{21}^A & T_{22}^A \end{bmatrix} \begin{Bmatrix} b_2^A \\ a_2^A \end{Bmatrix} \quad (4.58a)$$

and network B by

$$\begin{Bmatrix} a_1^B \\ b_1^B \end{Bmatrix} = \begin{bmatrix} T_{11}^B & T_{12}^B \\ T_{21}^B & T_{22}^B \end{bmatrix} \begin{Bmatrix} b_2^B \\ a_2^B \end{Bmatrix} \quad (4.58b)$$

we notice, based on the parameter convention shown in Figure 4-18, that

$$\begin{Bmatrix} b_2^A \\ a_2^A \end{Bmatrix} = \begin{Bmatrix} a_1^B \\ b_1^B \end{Bmatrix} \quad (4.59)$$

Thus, for the combined system, we conclude

$$\begin{Bmatrix} a_1^A \\ b_1^A \end{Bmatrix} = \begin{bmatrix} T_{11}^A & T_{12}^A \\ T_{21}^A & T_{22}^A \end{bmatrix} \begin{bmatrix} T_{11}^B & T_{12}^B \\ T_{21}^B & T_{22}^B \end{bmatrix} \begin{Bmatrix} b_2^B \\ a_2^B \end{Bmatrix} \quad (4.60)$$

which is the desired matrix multiplication. Therefore, the chain scattering matrix plays a similar role as the ABCD-matrix discussed earlier.

The conversion from the S-matrix to the chain matrix notation follows identical steps as outlined in Section 4.3.1. In particular, to compute T_{11} for instance, we see that

$$T_{11} = \frac{a_1}{b_2} \Big|_{a_2=0} = \frac{a_1}{S_{21}a_1} = \frac{1}{S_{21}} \quad (4.61)$$

Similarly,

$$T_{12} = -\frac{S_{22}}{S_{21}} \quad (4.62)$$

$$T_{21} = \frac{S_{11}}{S_{21}} \quad (4.63)$$

$$T_{22} = \frac{-(S_{11}S_{22} - S_{12}S_{21})}{S_{21}} = \frac{-\Delta S}{S_{21}} \quad (4.64)$$

Conversely, when the chain scattering parameters are given and we need to convert to S-parameters, we find the following relations:

$$S_{11} = \frac{b_1}{a_1} \Big|_{a_2=0} = \frac{T_{21}b_2}{T_{11}b_2} = \frac{T_{21}}{T_{11}} \quad (4.65)$$

$$S_{12} = \frac{T_{11}T_{22} - T_{21}T_{12}}{T_{11}} = \frac{\Delta T}{T_{11}} \quad (4.66)$$

$$S_{21} = \frac{1}{T_{11}} \quad (4.67)$$

$$S_{22} = -\frac{T_{12}}{T_{11}} \quad (4.68)$$

Alternatively, a matrix manipulation as discussed in the next section could have been carried out with the same result.

4.4.4 Conversion between Z- and S-Parameters

We have already seen how certain S -parameters can be defined in terms of input and output impedances of a network [i.e., equations (4.49) and (4.54)]. In this section, we go through a formal conversion between the Z - and S -parameter sets. Once this interrelation is established, we are able to formulate conversion links between all six network parameter sets ($S, Z, Y, ABCD, h, T$).

To find the conversion between the previously defined S -parameters and the Z -parameters, let us begin with the defining S -parameter relation in matrix notation [i.e., (4.41)]

$$\{\mathbf{b}\} = [\mathbf{S}]\{\mathbf{a}\} \quad (4.69)$$

Multiplying by $\sqrt{Z_0}$ gives

$$\sqrt{Z_0}\{\mathbf{b}\} = \{\mathbf{V}^-\} = \sqrt{Z_0}[\mathbf{S}]\{\mathbf{a}\} = [\mathbf{S}]\{\mathbf{V}^+\} \quad (4.70)$$

Adding $\{\mathbf{V}^+\} = \sqrt{Z_0}\{\mathbf{a}\}$ to both sides results in

$$\{\mathbf{V}\} = [\mathbf{S}]\{\mathbf{V}^+\} + \{\mathbf{V}^+\} = ([\mathbf{S}] + [\mathbf{E}])\{\mathbf{V}^+\} \quad (4.71)$$

where $[\mathbf{E}]$ is the identity matrix. To compare this form with the impedance expression $\{\mathbf{V}\} = [\mathbf{Z}]\{\mathbf{I}\}$, we have to express $\{\mathbf{V}^+\}$ in terms of $\{\mathbf{I}\}$. This is accomplished by first subtracting $[\mathbf{S}]\{\mathbf{V}^+\}$ from both sides of $\{\mathbf{V}^+\} = \sqrt{Z_0}\{\mathbf{a}\}$; that is,

$$\{\mathbf{V}^+\} - [\mathbf{S}]\{\mathbf{V}^+\} = \sqrt{Z_0}(\{\mathbf{a}\} - \{\mathbf{b}\}) = Z_0\{\mathbf{I}\} \quad (4.72)$$

Now, by isolating $\{\mathbf{V}^+\}$, it is seen that

$$\{\mathbf{V}^+\} = Z_0([\mathbf{E}] - [\mathbf{S}])^{-1}\{\mathbf{I}\} \quad (4.73)$$

Substituting (4.73) into (4.71) yields the desired result of

$$\{\mathbf{V}\} = ([\mathbf{S}] + [\mathbf{E}])\{\mathbf{V}^+\} = Z_0([\mathbf{S}] + [\mathbf{E}])([\mathbf{E}] - [\mathbf{S}])^{-1}\{\mathbf{I}\} \quad (4.74)$$

or

$$[\mathbf{Z}] = Z_0([\mathbf{S}] + [\mathbf{E}])([\mathbf{E}] - [\mathbf{S}])^{-1} \quad (4.75)$$

Explicit evaluation yields

$$\begin{bmatrix} Z_{11} & Z_{12} \\ Z_{21} & Z_{22} \end{bmatrix} = Z_0 \begin{bmatrix} 1 + S_{11} & S_{12} \\ S_{21} & 1 + S_{22} \end{bmatrix} \begin{bmatrix} 1 - S_{11} & -S_{12} \\ -S_{21} & 1 - S_{22} \end{bmatrix}^{-1}$$

$$= \frac{Z_0 \begin{bmatrix} 1 + S_{11} & S_{12} \\ S_{21} & 1 + S_{22} \end{bmatrix}}{(1 - S_{11})(1 - S_{22}) - S_{21}S_{12}} \begin{bmatrix} 1 - S_{22} & S_{12} \\ S_{21} & 1 - S_{11} \end{bmatrix} \quad (4.76)$$

Identifying individual terms is now easily carried out. A complete summary of all network coefficient sets is given in Appendix C.

4.4.5 Signal Flow Chart Modeling

The analysis of RF networks and their overall interconnection is greatly facilitated through signal flow charts as commonly used in system and control theory. As originally introduced to seismology and remote sensing, wave propagation can be associated with directed paths and associated nodes connecting these paths. Even complicated networks are easily reduced to input-output relations in which the reflection and transmission coefficients play integral parts. In this section we will briefly summarize key principles needed for a signal flow network analysis.

The main concepts required to construct flow charts are as follows:

1. **Nodes** that are deployed to identify network parameters such as a_1, b_1, a_2, b_2 when dealing with S -parameters
2. **Branches** that are needed when connecting the network parameters
3. Addition and subtraction of branch values in accordance with the directions of the branches

We will now discuss these three items in detail. To this end let us consider a section of a transmission line that is terminated in a load impedance Z_L , as seen in Figure 4-19.

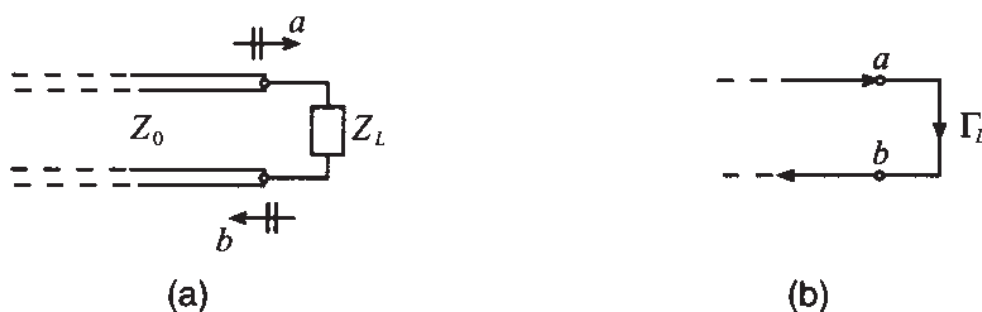


Figure 4-19 Terminated transmission line segment with incident and reflected S -parameter description. (a) Conventional form, and (b) Signal flow form.

Even though we could use voltage values as node identifier, it is the *S*-parameter representation that finds widespread use. In Figure 4-19(b) the nodes *a* and *b* are connected through the load reflection coefficient Γ_L . This makes sense since the reflection coefficient is the ratio b/a , so that it simply states that node *b* is found as a result of multiplying node *a* by Γ_L . This is depicted in generic form in Figure 4-20.

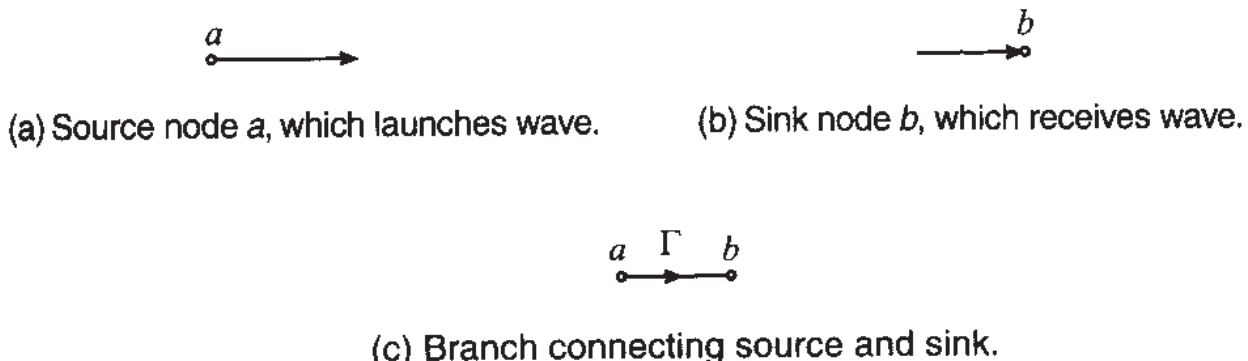


Figure 4-20 Generic source node (a), receiver node (b), and the associated (c) branch connection.

In terms of notation, we can encode the situation shown in Figure 4-20 as

$$b = \Gamma a \quad (4.77)$$

A more complicated situation arises when we need to make the transmission line circuit shown in Figure 4-19 more realistic by including a source term, as seen in Figure 4-21.

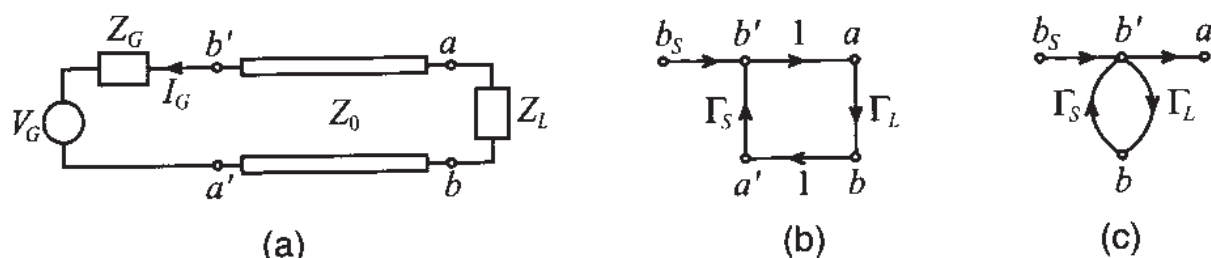


Figure 4-21 Terminated transmission line with source. (a) conventional form, (b) signal flow form, and (c) simplified signal flow form.

Unlike Figure 4-19, the nodes *a* and *b* are preceded by two additional nodes that we shall denote *a'* and *b'*. The ratio b'/a' defines the source reflection coefficient Γ_S as already discussed in Section 2.11. Here we also see that *b'* is given by multiplying *a'* with the source reflection coefficient. By relying on the concept of summation, we define *b'* as the sum of b_S and $a'\Gamma_S$. Thus, the source b_S is

$$b_S = b' - a'\Gamma_S \quad (4.78)$$

An explicit expression for b_S is obtained by noting that

$$V_S = V_G + I_G Z_G \quad (4.79)$$

based on an outflowing current convention (see Figure 4-21). This can be converted into the form

$$V_S^+ + V_S^- = V_G + Z_G \left(\frac{V_S^+}{Z_0} - \frac{V_S^-}{Z_0} \right) \quad (4.80)$$

Rearranging terms and division by $\sqrt{Z_0}$ gives

$$\frac{\sqrt{Z_0}}{Z_G + Z_0} V_G = \frac{V_S^-}{\sqrt{Z_0}} - \Gamma_S \frac{V_S^+}{\sqrt{Z_0}} \quad (4.81)$$

When comparing (4.81) with (4.78), we immediately see that

$$b_S = \frac{\sqrt{Z_0}}{Z_G + Z_0} V_G \quad (4.82)$$

An important conclusion can be drawn when expressing a' in (4.78) by $\Gamma_L b'$ so that we obtain

$$b' = b_S + \Gamma_L \Gamma_S b' = \frac{b_S}{1 - \Gamma_L \Gamma_S} \quad (4.83)$$

This is known as a self- or feedback loop (see Figure 4-22), which allows us to represent the nodes b_S and b' by a single branch whose value is given by (4.83).

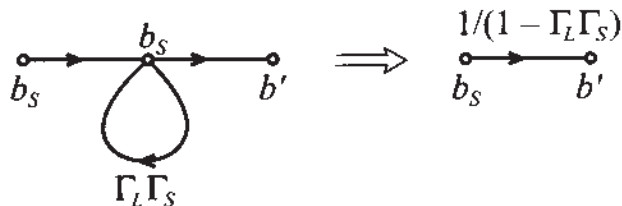


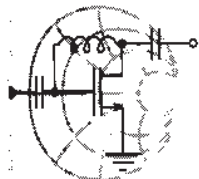
Figure 4-22 A self-loop that collapses to a single branch.

All signal flow chart principles can therefore be reduced to six building blocks, as summarized in Table 4-3.

By way of an example, let us analyze a more complicated RF circuit consisting of a sourced and terminated dual-port network.

Table 4-3 Signal flow chart building blocks

| Description | Graphical Representation |
|-----------------------|--------------------------|
| Nodal Assignment | |
| Branch | |
| Series Connection | |
| Parallel Connection | |
| Splitting of Branches | |
| Self-loop | |



RF & MW →

Example 4-8: Flow chart analysis of a dual-port network

For the network shown in Figure 4-23 find the ratios of b_1/a_1 and a_1/b_S . Assume unity for the multiplication factor of the transmission line segments.

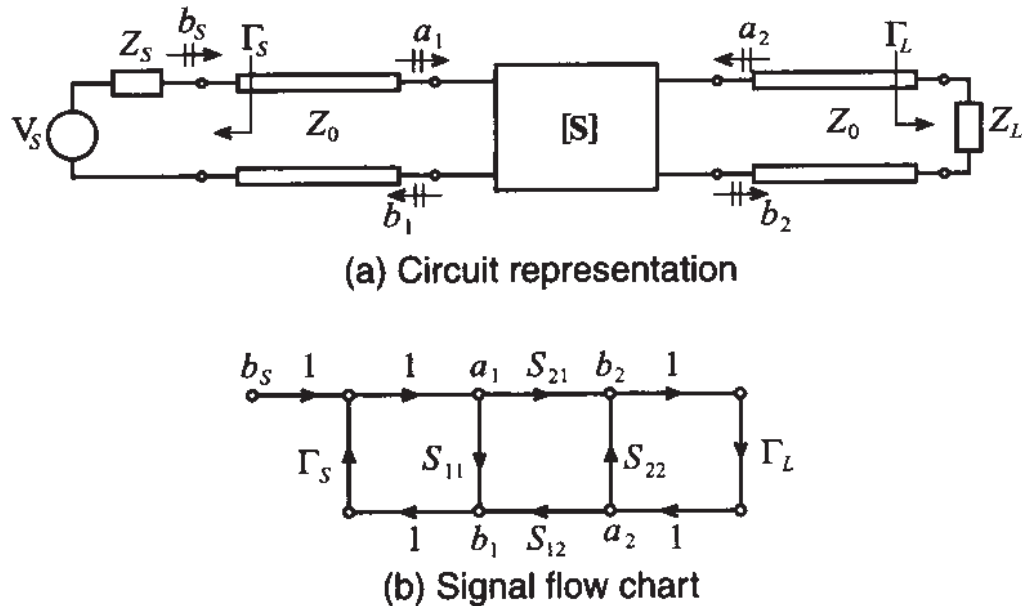


Figure 4-23 Sourced and terminated two-port network.

Solution: The process of setting up the individual ratios is explained best by going through a step-by-step simplification for the ratio a_1/b_s employing the rules summarized in Table 4-3. Figure 4-24 depicts the five steps.

Step 1: Splitting of the rightmost loop between b_2 and a_2 , leading to the self-loop $S_{22}\Gamma_L$

Step 2: Decomposition of the self-loop between branches a_1 and b_2 , resulting in the multiplication factor $S_{21}/(1 - S_{22}\Gamma_L)$, which can be combined with Γ_L and S_{12}

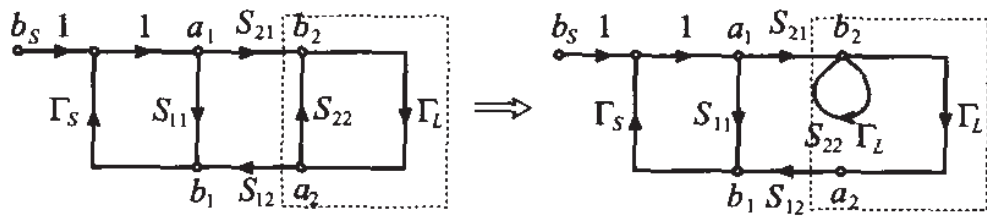
Step 3: Series and parallel connections between a_1 and b_1 , leading to the input reflection coefficient

$$\Gamma_{in} = \frac{b_1}{a_1} = S_{11} + \frac{S_{12}S_{21}}{1 - S_{22}\Gamma_L}\Gamma_L$$

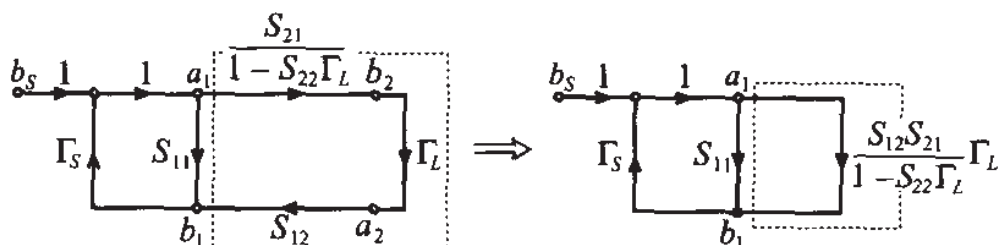
Step 4: Splitting the loop into a self-loop, resulting in the multiplication factor

$$\left(S_{11} + \frac{S_{12}S_{21}}{1 - S_{22}\Gamma_L}\Gamma_L \right)\Gamma_s$$

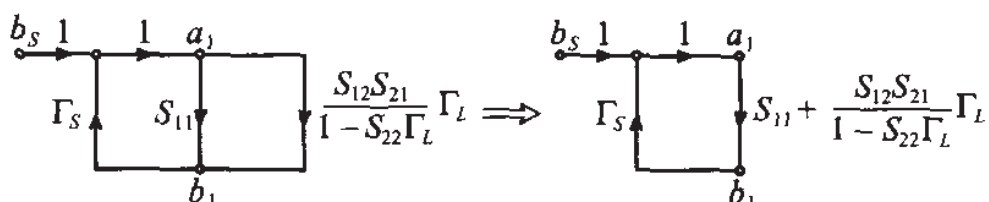
Step 5: Decomposition of the self-loop at a_1 , leading to the expression



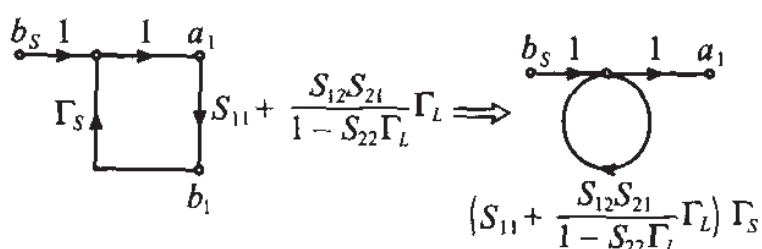
Step 1



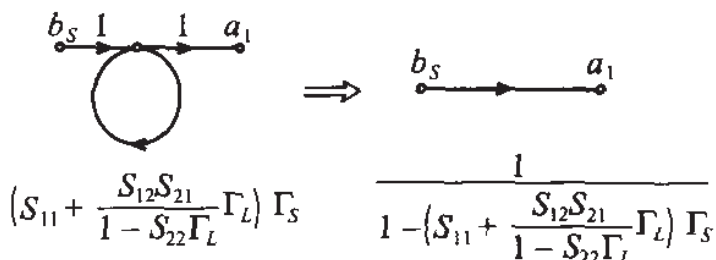
Step 2



Step 3



Step 4



Step 5

Figure 4-24 Step-by-step simplification to determine the ratio a_1/b_S .

$$a_1 = \frac{1}{1 - \left(S_{11} + \frac{S_{12}S_{21}}{1 - S_{22}\Gamma_L} \Gamma_L \right) \Gamma_S} b_S$$

Rearranging and simplification leads to the final form:

$$\frac{a_1}{b_S} = \frac{1 - S_{22}\Gamma_L}{1 - (S_{11}\Gamma_S + S_{22}\Gamma_L + S_{12}S_{21}\Gamma_S) + S_{11}S_{22}\Gamma_S\Gamma_L}$$

The preceding derivation follows a pattern similar to finding the transfer function of a control system or a signal processor. Even complicated circuits can be reduced efficiently and quickly to establish the nodal dependencies.

The preceding example points out what will happen if the matching condition for recording the S -parameters is not satisfied. As we know, if we compute S_{11} we need to ensure that $a_2 = 0$. However, if $a_2 \neq 0$, as is the case in the preceding example, we see that S_{11} is modified by the additional factor $S_{12}S_{21}\Gamma_L/(1 - S_{22}\Gamma_L)$.

4.4.6 Generalization of S-Parameters

In our discussion thus far it was assumed that the characteristic line impedance at both ports has the same value Z_0 . However, this does not have to be the case. Indeed, if we assume that port 1 is connected to line impedance Z_{01} and port 2 to impedance Z_{02} , we have to represent the voltage and current waves at the respective port ($n = 1, 2$) as

$$V_n = V_n^+ + V_n^- = \sqrt{Z_{0n}}(a_n + b_n) \quad (4.84)$$

and

$$I_n = \frac{V_n^+}{Z_{0n}} - \frac{V_n^-}{Z_{0n}} = \frac{a_n}{\sqrt{Z_{0n}}} - \frac{b_n}{\sqrt{Z_{0n}}} \quad (4.85)$$

where we immediately observe

$$a_n = \frac{V_n^+}{\sqrt{Z_{0n}}}, \quad b_n = \frac{V_n^-}{\sqrt{Z_{0n}}} \quad (4.86)$$

These equations allow the definition of the S -parameters as follows:

$$S_{ij} = \left. \frac{b_i}{a_j} \right|_{a_n = 0 (n \neq j)} = \left. \frac{V_i^- / \sqrt{Z_{0i}}}{V_j^+ / \sqrt{Z_{0j}}} \right|_{V_n^+ = 0 (n \neq j)} \quad (4.87)$$

When compared to the previous S -parameter definitions, we notice that scaling by the appropriate line impedances has to be taken into account. It should also be apparent that although the focus of our derivations was a two-port network, the preceding formulas can be extended to an N -port network where $n = 1, \dots, N$.

A second consideration is related to the fact that practical measurements involve the determination of the network S -parameters through transmission lines of finite length. In this case we need to investigate a system where the measurement planes are shifted away from the actual network, as depicted in Figure 4-25.

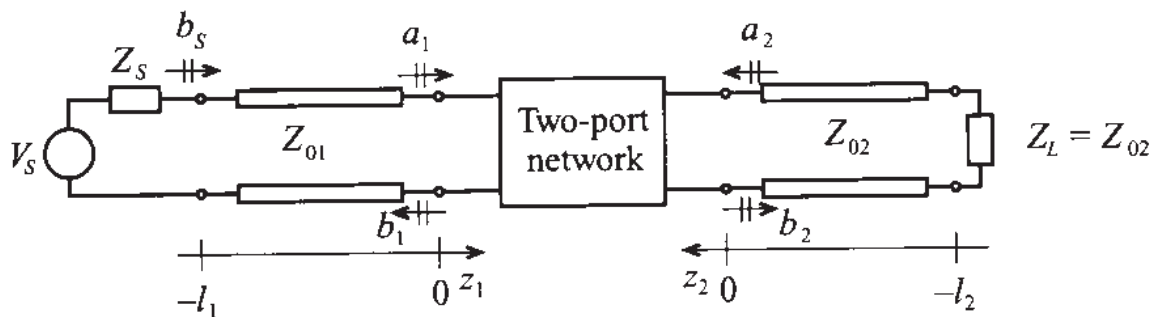


Figure 4-25 Two-port network with finite-length transmission line segments.

An incident voltage wave launched from the power supply will have to travel a distance l_1 in order to reach port 1. Consistent with the notation introduced in Section 2.9, we note that at port 1 the incident voltage is given as

$$V_{\text{in}}^+(z_1 = 0) = V_1^+ \quad (4.88)$$

and, at the generator side, as

$$V_{\text{in}}^+(z_1 = -l_1) = V_1^+ e^{-j\beta_1(-l_1)} \quad (4.89)$$

The reflected voltage wave at port 1 can be cast in the form

$$V_{\text{in}}^-(z_1 = 0) = V_1^- \quad (4.90)$$

and

$$V_{\text{in}}^-(z_1 = -l_1) = V_1^- e^{j\beta_1(-l_1)} \quad (4.91)$$

where, as usual, β_1 stands for the lossless propagation constant of line 1. In an identical fashion, the voltage behavior at port 2 can be formulated by simply replacing V_{in} in terms of V_{out} and V_1 in terms of V_2 as well as β_1 in terms of β_2 . The preceding equations can be combined in matrix form

$$\begin{Bmatrix} V_{in}^+(-l_1) \\ V_{out}^+(-l_2) \end{Bmatrix} = \begin{bmatrix} e^{j\beta_1 l_1} & 0 \\ 0 & e^{j\beta_2 l_2} \end{bmatrix} \begin{Bmatrix} V_1^+ \\ V_2^+ \end{Bmatrix} \quad (4.92)$$

which links the impinging waves at the network ports to the corresponding voltages shifted by the electric lengths of the attached transmission line segments. For the reflected voltage waves we get the matrix form

$$\begin{Bmatrix} V_{in}^-(-l_1) \\ V_{out}^-(-l_2) \end{Bmatrix} = \begin{bmatrix} e^{-j\beta_1 l_1} & 0 \\ 0 & e^{-j\beta_2 l_2} \end{bmatrix} \begin{Bmatrix} V_1^- \\ V_2^- \end{Bmatrix} \quad (4.93)$$

As the discussion in Section 4.4.1 taught us, the S -parameters are linked to the coefficients a_n and b_n , which in turn can be expressed through voltages (if we assume $Z_{01} = Z_{02}$).

$$\begin{Bmatrix} V_1^- \\ V_2^- \end{Bmatrix} = \begin{bmatrix} S_{11} & S_{12} \\ S_{21} & S_{22} \end{bmatrix} \begin{Bmatrix} V_1^+ \\ V_2^+ \end{Bmatrix} \quad (4.94)$$

It is apparent that if transmission line segments are added, we have to replace the above voltages by the previously derived expressions, leading to the form

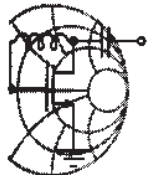
$$\begin{Bmatrix} V_{in}^-(-l_1) \\ V_{out}^-(-l_2) \end{Bmatrix} = \begin{bmatrix} e^{-j\beta_1 l_1} & 0 \\ 0 & e^{-j\beta_2 l_2} \end{bmatrix} \begin{bmatrix} S_{11} & S_{12} \\ S_{21} & S_{22} \end{bmatrix} \begin{bmatrix} e^{-j\beta_1 l_1} & 0 \\ 0 & e^{-j\beta_2 l_2} \end{bmatrix} \begin{Bmatrix} V_{in}^+(-l_1) \\ V_{out}^+(-l_2) \end{Bmatrix} \quad (4.95)$$

This final reveals that the S -parameters for the shifted network are comprised of three matrices. In terms of the coefficients, we see that

$$[S]^{SHIFT} = \begin{bmatrix} S_{11}e^{-j2\beta_1 l_1} & S_{12}e^{-j(\beta_1 l_1 + \beta_2 l_2)} \\ S_{21}e^{-j(\beta_1 l_1 + \beta_2 l_2)} & S_{22}e^{-j2\beta_2 l_2} \end{bmatrix} \quad (4.96)$$

The physical meaning of this form is easy to understand. The first matrix coefficient reveals that we have to take into account $2\beta_1 l_1$ or twice the travel time for the incident voltage to reach port 1 and, upon reflection, return. Similarly, for port 2 we see that the

phase shift is $2\beta_2 l_2$. Moreover, the cross terms, which are closely related to the forward and reverse gains, require the additive phase shifts associated with transmission line 1 ($\beta_1 l_1$) and transmission line 2 ($\beta_2 l_2$), since the overall input/output configuration now consists of both line segments.



RF & MW

Example 4-9: Input impedance computation of a transmission line based on the use of the signal flow chart

A lossless transmission line system with characteristic line impedance Z_0 and length l is terminated into a load impedance Z_L and attached to a source voltage V_G and source impedance Z_G , as shown in Figure 4-26. (a) Draw the signal flow chart and (b) derive the input impedance formula at port 1 from the signal flow chart representation.

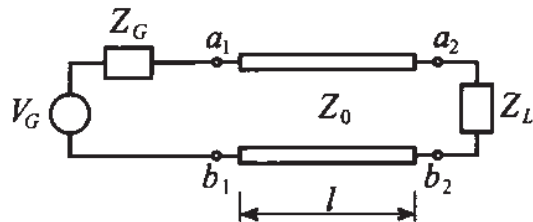


Figure 4-26 Transmission line attached to a voltage source and terminated by a load impedance.

Solution: (a) Consistent with our previously established signal flow chart notation, we can readily convert Figure 4-26 into the form seen in Figure 4-27.

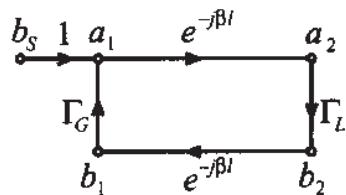


Figure 4-27 Signal flow chart diagram for transmission line system in Figure 4-26.

(b) The input reflection coefficient at port 1 is given by

$$b_1 = \Gamma_L e^{-j2\beta l} a_1$$

which is exactly in the form given in Section 3.1, with $\Gamma_L = \Gamma_0$ and $l = d$. Thus

$$\Gamma_{in}(l) = \Gamma_L e^{-j2\beta l} = \frac{Z_{in} - Z_0}{Z_{in} + Z_0}$$

Solving for Z_{in} yields the final result

$$Z_{in} = Z_0 \frac{1 + \Gamma_L e^{-j2\beta l}}{1 - \Gamma_L e^{-j2\beta l}}$$

This example shows how the input impedance of a transmission line can be found quickly and elegantly by using signal flow chart concepts.

4.4.7 Practical Measurements of S-Parameters

Measurement of the S-parameters of a two-port network requires reflection and transmission evaluations of traveling waves at both ports. One of the most popular methods is to use a vector network analyzer. The vector network analyzer is an instrument that can measure voltages in terms of magnitude and phase. Usually network analyzers have one output port, which provides the RF signal either from an internal source or an external signal generator, and three measurement channels, which are denoted as R , A , and B (see Figure 4-28).

The RF source is typically set to sweep over a specified frequency range. The measurement channel R is employed for measuring the incident wave. Channel R also serves as a reference port. Channels A and B usually measure the reflected and transmitted waves. In general, the measurement channels A and B can be configured to record any two parameters with a single measurement setup. An example of the test arrangement that allows us to measure S_{11} and S_{21} is shown in Figure 4-28.

In this case the value of S_{11} can be obtained by evaluating the ratio A/R , and S_{21} through computing B/R . To measure S_{12} and S_{22} we have to reverse the DUT. In Figure 4-28 the dual-directional coupler allows the separation of the incident and reflected waves at the input port of the DUT. The bias tees are employed to provide necessary biasing conditions, such as a quiescent point for the DUT. Since the most com-

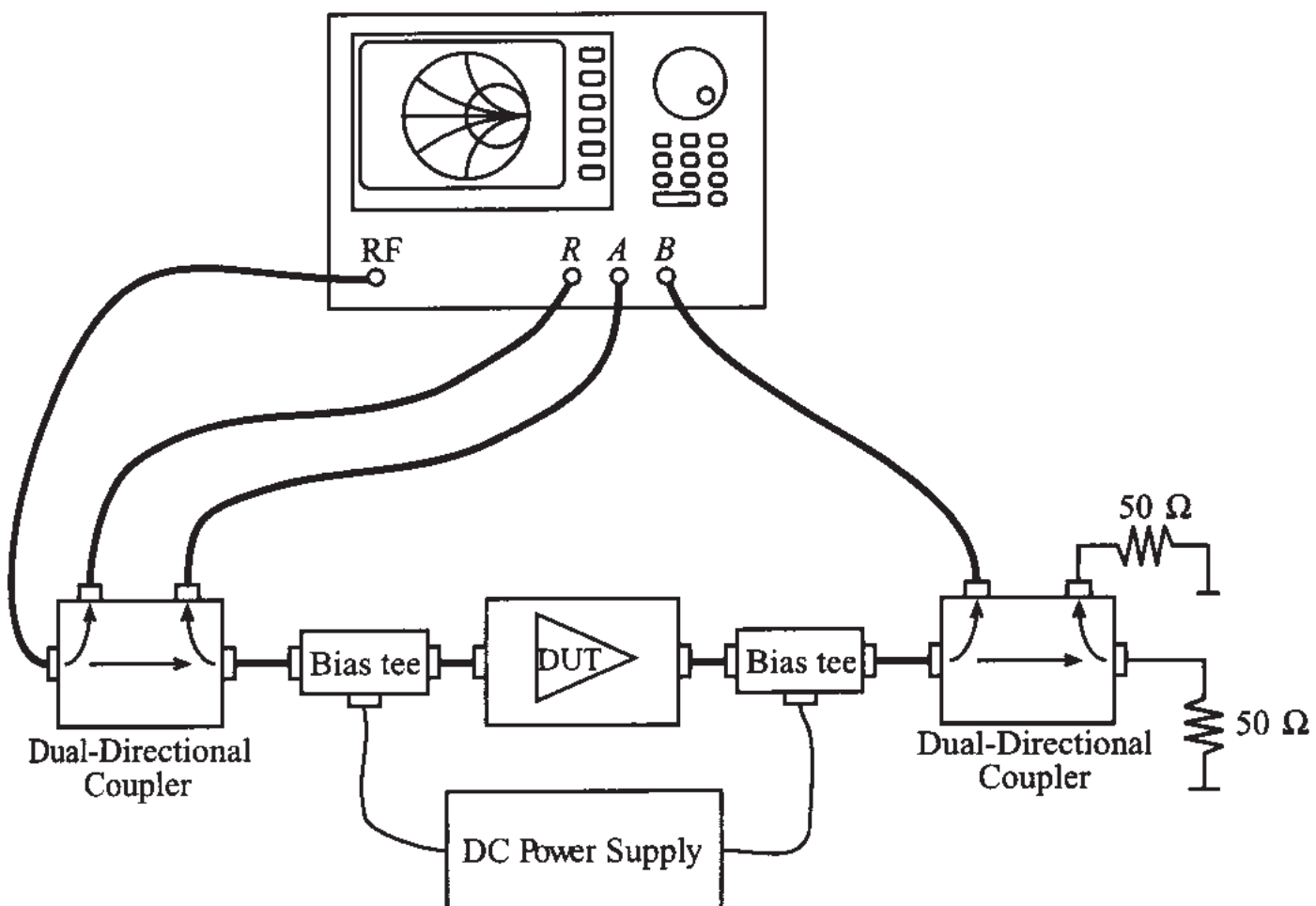


Figure 4-28 Measurement system for S_{11} and S_{21} parameters using a network analyzer.

mon use of network analyzers is the characterization of two-port devices, bias tees, directional couplers, and necessary electronic switches as well as the RF sweep signal generator are all integral parts of most modern analyzers.

As we can see, a practical test arrangement is more complicated when compared with the simple ideal system described in Sections 4.4.4 and 4.4.6, where we assume that the DUT is connected to perfectly matched transmission lines of equal (Section 4.4.4) or unequal (Section 4.4.6) characteristic impedance. In a realistic measurement system we cannot guarantee either matching conditions or ideality of the components. In fact, we have to consider all effects of the external components connected to the input and output ports of the DUT. Furthermore, the primary reference plane for measurements of complex voltages, which are then converted into S -parameters, is usually somewhere inside of the networks analyzer. As a result, it is necessary to take into account not only attenuation and phase shifts due to the external components, but also portions of the internal structure of the network analyzer itself.

In general, the measurement test arrangement can be reduced to the cascade of three networks depicted in Figure 4-29.

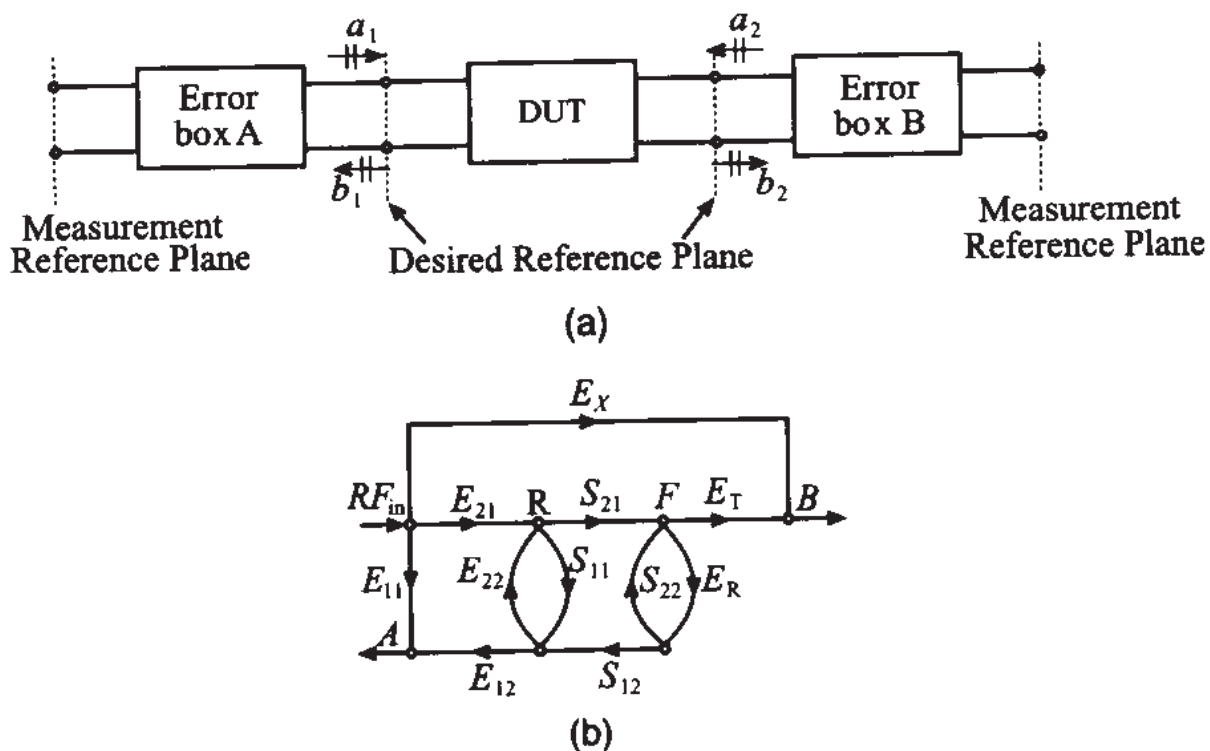


Figure 4-29 (a) Block diagram of the setup for measurement of S -parameters of a two-port network; (b) signal flow chart of the measurement test setup.

In Figure 4-29 the signals R , A , B correspond to the reference port and channels A and B of the network analyzer. RF_{in} is the output line from the signal source. The branch denoted E_X represents possible leakage between the output of the signal source and the channel B .

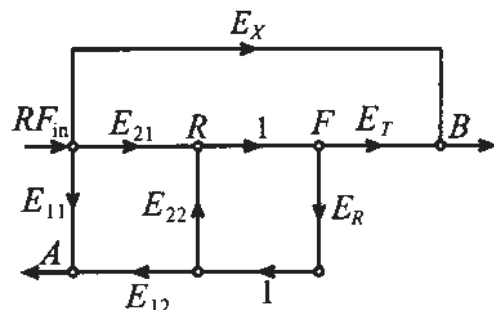
The network analyzer treats everything between the measurement reference planes as a single device. Therefore, our task is reduced to finding a way to calibrate the network analyzer in such a way that it becomes possible to eliminate the effect of all undesired influences or parasitics. The main goal of a **calibration procedure** is to characterize the error boxes prior to measuring the DUT. This information can then be used by an internal computer to evaluate the error-free S -parameters of the actual DUT.

Assuming that the error box A network is reciprocal, we can state $E_{12} = E_{21}$. Therefore, we have to find six parameters (E_{11} , E_{12} , E_{22} , E_X , E_R , and E_T) to characterize the error boxes.

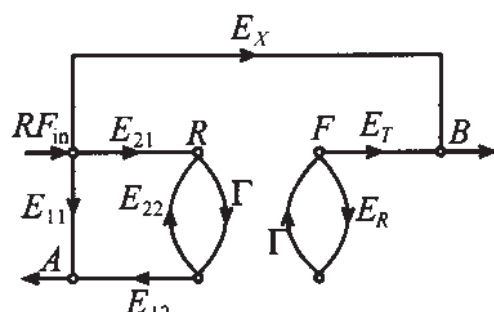
The simplest calibration method involves three or more known loads (open, short, and matched). The problem with this approach is that such standards are usually imperfect and are likely to introduce additional errors into the measurement procedures. These errors become especially significant at higher frequencies. To avoid the dependency on the accuracy of calibration standards, several methods have been developed (see Eul and Schiek and Engen and Hoer, listed in the Further Reading section at the

end of this chapter). In this section we will only consider the so-called **Through-Reflect-Line** (TRL) technique (see Engen and Hoer).

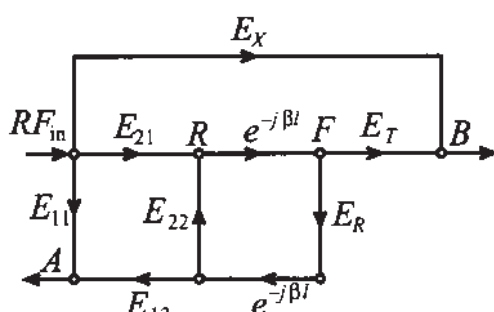
The TRL calibration scheme does not rely on known standard loads. Instead, it is based on the use of three types of connections, which are shown in Figure 4-30.



(a) Through



(b) Reflect



(c) Line

Figure 4-30 Signal flow graphs of TRL method: (a) Through, (b) Reflect, (c) Line configurations.

The *Through* connection is made by directly connecting ports 1 and 2 of the DUT. Next, the *Reflect* connection uses a load with high reflectivity. The reflection coefficient does not have to be known because it will be determined during the calibration process. The only requirement is that the load possesses the same reflection coefficient for both input and output ports. The *Line* connection is made by connecting ports 1 and 2 via a transmission line matched to the impedance of the error boxes. Usually, this impedance

is close to 50Ω . Before we continue with the actual analysis of each particular connection type, let us first consider the system as a general two-port network.

From Figure 4-29(b) it is seen that the signal at node B is a linear combination of the input RF signal and the signal at node F :

$$B = E_X + E_T F \quad (4.97)$$

Applying the self-loop rule, we can write that signal at node F as

$$F = \frac{S_{21}}{1 - E_R S_{22}} R \quad (4.98)$$

To compute the signal at port R , the same method as discussed in Example 4-8 can be used. In this example we first replaced the loop with the signal F through a self-loop and then performed the same transformation for the signal R . The result of these computations is

$$R = \frac{E_{21}}{1 - E_{22} \left(S_{11} + \frac{S_{12} S_{21} E_R}{1 - E_R S_{22}} \right)} \quad (4.99)$$

Substituting (4.99) into (4.98) followed by the substitution of (4.98) into (4.97), we obtain an expression for signal B :

$$B = E_X + E_T \frac{S_{21}}{1 - E_R S_{22}} \frac{E_{21}}{1 - E_{22} \left(S_{11} + \frac{S_{12} S_{21} E_R}{1 - E_R S_{22}} \right)} \quad (4.100)$$

Finally, the value for the signal at node A is obtained by using the summation rule:

$$A = E_{11} + \frac{E_{12} E_{21}}{1 - E_{22} \left(S_{11} + \frac{S_{12} S_{21} E_R}{1 - E_R S_{22}} \right)} \left(S_{11} + S_{12} E_R \frac{S_{21}}{1 - E_R S_{22}} \right) \quad (4.101)$$

If the measurement system does not introduce any errors, then $E_{12} = E_{21} = E_T = 1$ and $E_{11} = E_{22} = E_R = E_X = 0$. Substituting these values into (4.99), (4.100), and (4.101), we find that $R = 1$, $A = S_{11}$, and $B = S_{12}$, which shows the validity of the formulas.

Now we are ready to investigate the TRL connections in more detail. To avoid confusion, let us denote the measured signals R , A , and B for *Through* by subscript T , for *Reflect* by R , and for *Line* by L .

For the *Through* connection we know that $S_{11} = S_{22} = 0$ and $S_{12} = S_{21} = 1$. Setting $E_{12} = E_{21}$ it follows that

$$R_T = \frac{E_{12}}{1 - E_{22}E_R} \quad (4.102a)$$

$$A_T = E_{11} + \frac{E_{12}^2}{1 - E_{22}E_R}E_R \quad (4.102b)$$

$$B_T = E_X + E_T \frac{E_{12}}{1 - E_{22}E_R} \quad (4.102c)$$

For the *Reflect* connection we have $S_{11} = S_{22} = \Gamma$ and $S_{12} = S_{21} = 0$. This results in the equations

$$R_R = \frac{E_{12}}{1 - E_{22}\Gamma} \quad (4.103a)$$

$$A_R = E_{11} + \frac{E_{12}^2\Gamma}{1 - E_{22}\Gamma} \quad (4.103b)$$

$$B_R = E_X \quad (4.103c)$$

Finally, for the *Line* connection we see that $S_{11} = S_{22} = 0$ and $S_{12} = S_{21} = e^{-\gamma l}$, where l is the transmission line length and γ is a complex propagation constant ($\gamma = \alpha + j\beta$) that takes into account attenuation effects. The result is

$$R_L = \frac{E_{12}}{1 - E_{22}E_R e^{-2\gamma l}} \quad (4.104a)$$

$$A_L = E_{11} + \frac{E_{12}^2 E_R e^{-2\gamma l}}{1 - E_{22}E_R e^{-2\gamma l}} \quad (4.104b)$$

$$B_L = E_X + E_T e^{-\gamma l} \frac{E_{12}}{1 - E_{22}E_R e^{-2\gamma l}} \quad (4.104c)$$

Equations (4.102a)–(4.104b) allow us to solve for the unknown coefficients of the error boxes E_{11} , E_{12} , E_{22} , E_X , E_R , E_T , the reflection coefficient Γ , and the transmission line parameter $e^{-\gamma l}$. Knowing the error coefficients we are then in a position to process the measured data in order to obtain an error-free S -parameter set of the DUT.

4.5 Summary

Networks play an integral part in analyzing basic low-frequency circuits as well as RF/MW circuits. For instance, the admittance or Y -matrix for an N -port network can be written in generic form as

$$\begin{Bmatrix} i_1 \\ i_2 \\ \vdots \\ i_N \end{Bmatrix} = \begin{bmatrix} Y_{11} & Y_{12} & \cdots & Y_{1N} \\ Y_{21} & Y_{22} & \cdots & Y_{2N} \\ \vdots & \vdots & \ddots & \vdots \\ Y_{N1} & Y_{N2} & \cdots & Y_{NN} \end{bmatrix} \begin{Bmatrix} v_1 \\ v_2 \\ \vdots \\ v_N \end{Bmatrix}$$

where currents and voltages become the defining external port conditions. The evaluation of the matrix coefficients is accomplished through appropriate terminal conditions:

$$Y_{nm} = \left. \frac{i_n}{v_m} \right|_{v_k = 0 \text{ (for } k \neq m)}$$

The concepts of \mathbf{Z} -, \mathbf{Y} -, \mathbf{h} -, and \mathbf{ABCD} -matrix representations of networks can be directly extended to high-frequency circuits. Unfortunately, we encounter practical difficulties in applying the required open- and short-circuit network conditions needed when defining the respective parameter sets. It is for this reason that the scattering parameters as normalized forward and backward propagating power waves are introduced:

$$a_n = \frac{V_n^+}{\sqrt{Z_0}} = \sqrt{Z_0} I_n^+$$

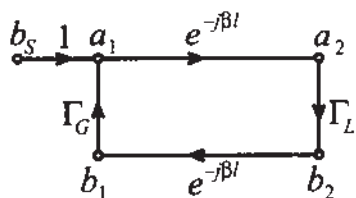
$$b_n = \frac{V_n^-}{\sqrt{Z_0}} = -\sqrt{Z_0} I_n^-$$

For a two-port network this results in the matrix form

$$\begin{Bmatrix} b_1 \\ b_2 \end{Bmatrix} = \begin{bmatrix} S_{11} & S_{12} \\ S_{21} & S_{22} \end{bmatrix} \begin{Bmatrix} a_1 \\ a_2 \end{Bmatrix}$$

Unlike open- or short-circuit network conditions, impedance line matching at the respective port is now required to establish the S -matrix set. The S -parameters can be directly related to the reflection coefficients at the input and output of the two-port network (S_{11}, S_{22}). Furthermore, forward and reverse power gains are readily identified ($|S_{21}|^2, |S_{12}|^2$).

The S -parameters are also very useful descriptors when dealing with signal flow diagrams. A signal flow diagram is a circuit representation involving nodes and paths for the sourced and terminated transmission line as follows:



With signal flow diagrams even complicated systems can be examined in terms of specific input output relations in a similar manner as done in control system theory.

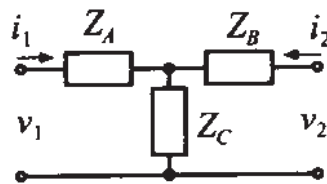
Chapter 4 finishes with a brief discussion of the practical recording of the S -parameters for a two-port network (DUT) through the use of a vector network analyzer. To compensate for various error sources associated with the measurement arrangement, the so-called TRL method is presented. Here the *Through*, *Reflect*, and *Line* calibrations are shown to account for the various errors and therefore permit the recording of the actual S -parameters needed to characterize the DUT.

Further Reading

- C. Bowick, *RF Circuit Design*, Howard Sams & Co., Indianapolis, IN, 1982.
- R. S. Elliot, *An Introduction to Guided Waves and Microwave Circuits*, Prentice Hall, Upper Saddle River, NJ, 1997.
- G. F. Engen and C. A. Hoer, "Thru-Reflect-Line: An Improved Technique for Calibrating the Dual Six-Port Automatic Network Analyzer," *IEEE Trans. Microwave Theory and Techniques*, Vol. MTT-27, pp. 987–998, 1979.
- H.J. Eul and B. Schiek, "Thru-Match-Reflect: One Result of a Rigorous Theory for De-embedding and Network Analyzer Calibration," Proceedings of the 18th European Microwave Conference, Stockholm, Sweden, 1988.
- G. Gonzales, *Microwave Transistor Amplifiers*, 2nd ed. Prentice Hall, Upper Saddle River, NJ, 1997.
- S-Parameter Design*, Hewlett-Packard Application Note 154, 1972.
- D. V. Morgan and M. J. Howes, eds., *Microwave Solid State Devices and Applications*, P. Peregrinus Ltd., New York, 1980.
- P. A. Rizzi, *Microwave Engineering-Passive Circuits*, Prentice Hall, Upper Saddle River, NJ, 1988.
- D. Roddy, *Microwave Technology*, Prentice Hall, Upper Saddle River, NJ.

Problems

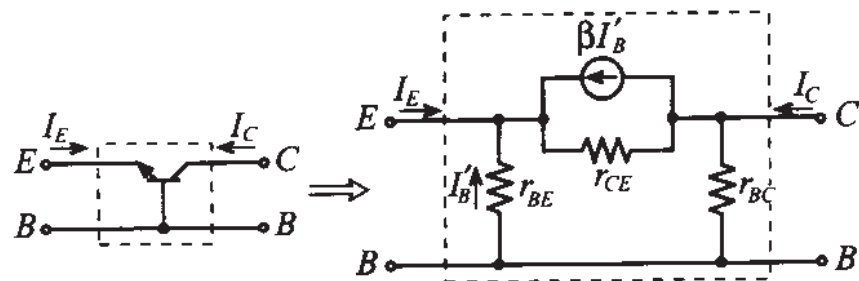
- 4.1 From the defining equations (4.3) and (4.6) for the impedance and admittance matrices, show that $[Z] = [Y]^{-1}$.
- 4.2 For the following generic T-network, find the impedance and admittance matrices.



- 4.3 Show that for a bipolar-junction transistor in a common-base configuration under small-signal low-frequency conditions (whose equivalent circuit is shown below) a hybrid parameter matrix can be established as follows:

$$[h] = \begin{bmatrix} \frac{r_{ce}r_{be}}{r_{be} + (1 + \beta)r_{ce}} & \frac{r_{be}}{r_{be} + (1 + \beta)r_{ce}} \\ -\frac{r_{be} + \beta r_{ce}}{r_{be} + (1 + \beta)r_{ce}} & \frac{1}{r_{bc}} + \frac{1}{r_{be} + (1 + \beta)r_{ce}} \end{bmatrix}$$

where the individual transistor parameters are denoted in the figure.

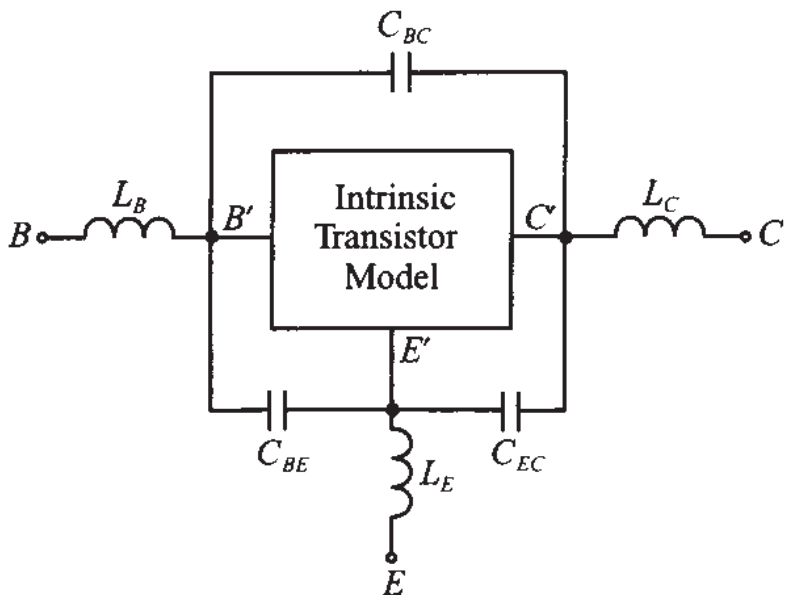


- 4.4 Using the results from Problem 4.3, compute the equivalent circuit parameters for a BJT in common-base configuration if the h-matrix is given as

$$[h] = \begin{bmatrix} 16.6 & 0.262 \times 10^{-3} \\ -0.99668 & 66.5 \times 10^{-9} \end{bmatrix}$$

- 4.5 Employ the conversion table for the different parameter representations of the two-port network and find the h-matrix representation for a Darlington pair shown in Figure 4-7 under the assumption that the transistors are specified by the same h-matrices derived in Example 4-2.

- 4.6 Using the definition of the $ABCD$ network representation, find the Y -parameter description.
- 4.7 From the results of Problem 4.3 and Example 4.2, establish the conversion equations between the \mathbf{h} -matrix parameters for the common-base and common-emitter transistor configurations.
- 4.8 Unlike the series connection discussed in Example 4-4, derive the $ABCD$ -parameters for a two-port network where the impedance Z is connected in parallel.
- 4.9 Find the $ABCD$ -parameters for a generic three-element pi-network, as depicted in Figure 4-2.
- 4.10 Compute the $ABCD$ -parameters for an RF transformer with turn ratio $N = N_1/N_2$, where N_1 is the number of turns a the primary winding and N_2 is the number of turns of the secondary winding.
- 4.11 Prove that the \mathbf{h} -matrix parameters for a high-frequency hybrid transistor model shown in Figure 4-12 are given by (4.31).
- 4.12 In this chapter we have mentioned several \mathbf{h} -matrix representations of the bipolar-junction transistor for different frequency conditions. In all cases we have neglected the influence of the parasitic components associated with the casing of the transistor. The modification to the equivalent circuit of the transistor that takes into account these parasitics is shown below:



Assuming that the intrinsic transistor model is given by a generic \mathbf{h} -matrix, derive the modified model that accounts for the casing.

- 4.13 Compute the return loss for a 25Ω resistor connected to a 75Ω lossless transmission line.
- 4.14 Find the forward gain of the circuit discussed in Example 4-8.
- 4.15 Given that the input of an amplifier has a VSWR of 2 and the output is given by $\text{VSWR} = 3$, find the magnitudes of the input and output reflection coefficients. What does your result mean in terms of S_{11} and S_{22} ?
- 4.16 Using the same approach as described in Section 4.4.4, show that the S -parameters of the network can be computed from the known Y -parameters using

$$[\mathbf{S}] = ([\mathbf{Y}] + Y_0[\mathbf{E}])^{-1}(Y_0[\mathbf{E}] - [\mathbf{Y}])$$

and the corresponding inverse relation

$$[\mathbf{Y}] = Y_0([\mathbf{E}] - [\mathbf{S}])([\mathbf{S}] + [\mathbf{E}])^{-1}$$

where $Y_0 = 1/Z_0$ is the characteristic line admittance.

- 4.17 The ideal transformer of Problem 4.10 can also be represented in S -parameter form. Show that the S -matrix is given by

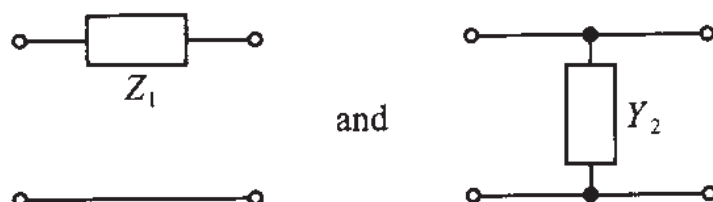
$$[\mathbf{S}] = \left(\frac{1}{1+N^2} \right) \begin{bmatrix} (N^2 - 1) & (2N) \\ (2N) & (1 - N^2) \end{bmatrix}$$

where $N = N_1/N_2$.

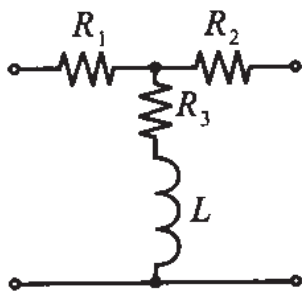
- 4.18 For the following two circuits, prove that the S -parameters are given as

$$[\mathbf{S}] = \begin{bmatrix} \Gamma_1 & 1 - \Gamma_1 \\ 1 - \Gamma_1 & \Gamma_1 \end{bmatrix} \text{ and } [\mathbf{S}] = \begin{bmatrix} \Gamma_2 & 1 + \Gamma_2 \\ 1 + \Gamma_2 & \Gamma_2 \end{bmatrix}$$

respectively, where $\Gamma_1 = (1 + 2Z_0/Z_1)^{-1}$ and $\Gamma_2 = -(1 + 2Y_0/Y_1)^{-1}$.



- 4.19 For the following *T*-network inserted into a transmission line with characteristic impedance of $Z_0 = 50 \Omega$, the three resistances are $R_1 = R_2 = 8.56 \Omega$, and $R_3 = 141.8 \Omega$. Find the *S*-parameters of this configuration and plot the insertion loss as a function of inductance L for the frequency of $f = 2 \text{ GHz}$ and L changing from 0 to 100 nH.



- 4.20 In practice, the resistors in the *T*-network of the previous problem are not frequency independent. At RF frequencies parasitic effects have to be taken into account. Compute the *S*-parameters at 2 GHz when all resistors have a 0.5 nH parasitic series inductance. Assume L is fixed at 10 nH.
- 4.21 A BJT is operated in a 50Ω circuit at 1.5 GHz. For the bias conditions of 4 mA collector current and collector-emitter voltage of 10 V, the manufacturer provides the *S*-parameters in magnitude and angle as follows:

$$S_{11} = 0.6 \angle -127^\circ; S_{21} = 3.88 \angle 87^\circ; S_{12} = 0.039 \angle 28^\circ; S_{22} = 0.76 \angle -35^\circ.$$

Find (a) the *Z*-parameter and (b) the *h*-parameter representation.

An Overview of RF Filter Design

After the discussion in Chapter 4, we are ready to extend and apply our knowledge of one- and two-port networks to develop RF filters. It is of particular interest in any analog circuit design to manipulate high-frequency signals in such a way as to enhance or attenuate certain frequency ranges or bands. This chapter examines the filtering of analog signals. As we know from elementary circuit courses, there are generally four types of filters: *low-pass*, *high-pass*, *bandpass*, and *bandstop*. The low-pass filter allows low-frequency signals to be transmitted from the input to the output port with little attenuation. However, as the frequency exceeds a certain *cut-off* point, the attenuation increases significantly with the result of delivering an amplitude-reduced signal to the output port. The opposite behavior is true for a high-pass filter, where the low-frequency signal components are highly attenuated or reduced in amplitude, while beyond a cut-off frequency point the signal passes the filter with little attenuation. Bandpass and bandstop filters restrict the passband between specific lower and upper frequency points where the attenuation is either low (bandpass) or high (bandstop) compared to the remaining frequency band.

In this chapter we first review several fundamental concepts and definitions pertaining to filters and resonators. Specifically, the key concept of loaded and unloaded quality factors will be examined in some detail. Then, we introduce the basic, multisection low-pass filter configuration for which tabulated coefficients have been developed both for the so-called maximally flat binomial, or Butterworth filter, and the equi-ripple or Chebyshev filter. The intent of Chapter 5 is not to introduce the reader to the entire filter theory, particularly how to derive these coefficients, but rather how to utilize the information to design specific filter types. We will see that the normalized low-pass filter serves as the basic building block from which all four filter types can be derived.

Once we know the procedures of converting a standard low-pass filter design in Butterworth or Chebyshev configuration into a particular filter type that meets our requirements, we then need to investigate ways of implementing the filter through distributed elements. This step is critical, since at frequencies above 500 MHz lumped elements such as inductors and capacitors are unsuitable. Relying on Richards transformation, which converts lumped into distributed elements, and Kuroda's identities, we are given powerful tools to develop a wide range of practically realizable filter configurations.

5.1 Basic Resonator and Filter Configurations

5.1.1 Filter Types and Parameters

It is convenient to begin our discussion by introducing the ideal behavior of the four basic filter types: low-pass, high-pass, bandpass, and bandstop. Figure 5-1 summarizes their attenuation α versus normalized angular frequency behavior.

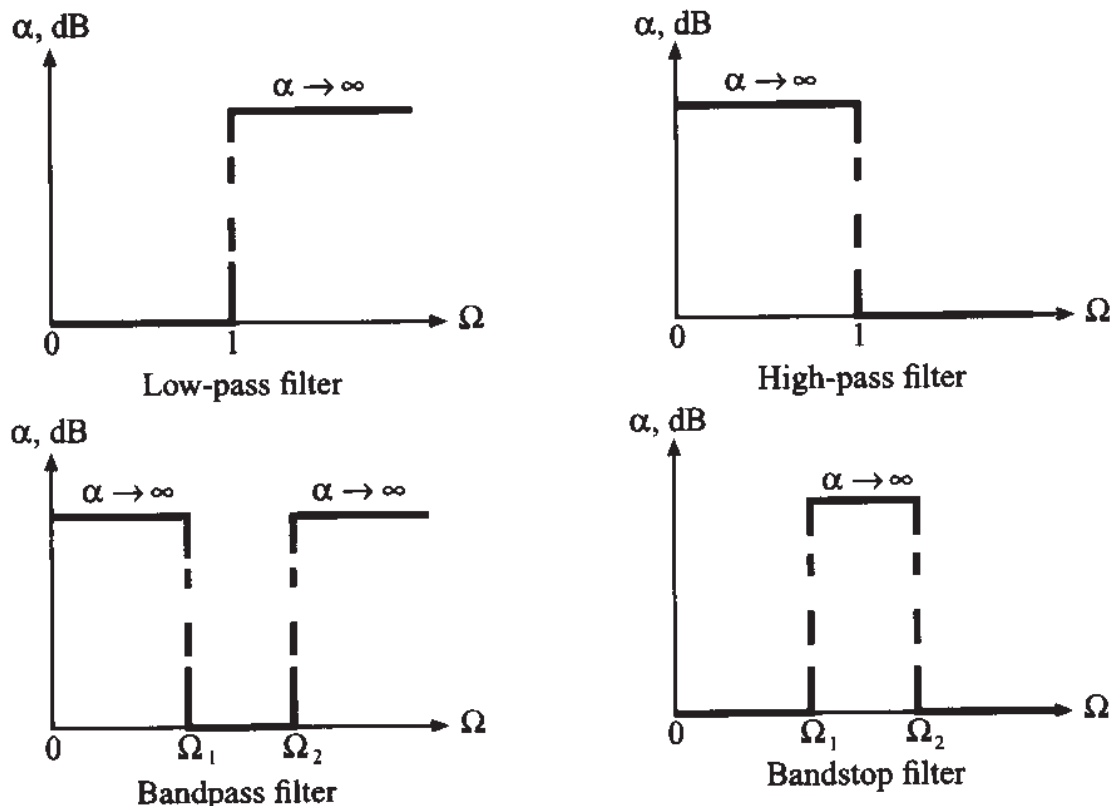


Figure 5-1 Four basic filter types.

We have chosen the parameter $\Omega = \omega/\omega_c$ as a normalized frequency with respect to the angular frequency ω_c , which denotes **cut-off frequency** for low-pass and high-pass filters and **center frequency** for bandpass and bandstop filters. As we will

see, this normalization will greatly simplify our task of developing standard filter approaches. Actual attenuation profiles are shown in Figure 5-2 for the so-called **binomial** (Butterworth), **Chebyshev**, and **elliptic** (Cauer) low-pass filters.

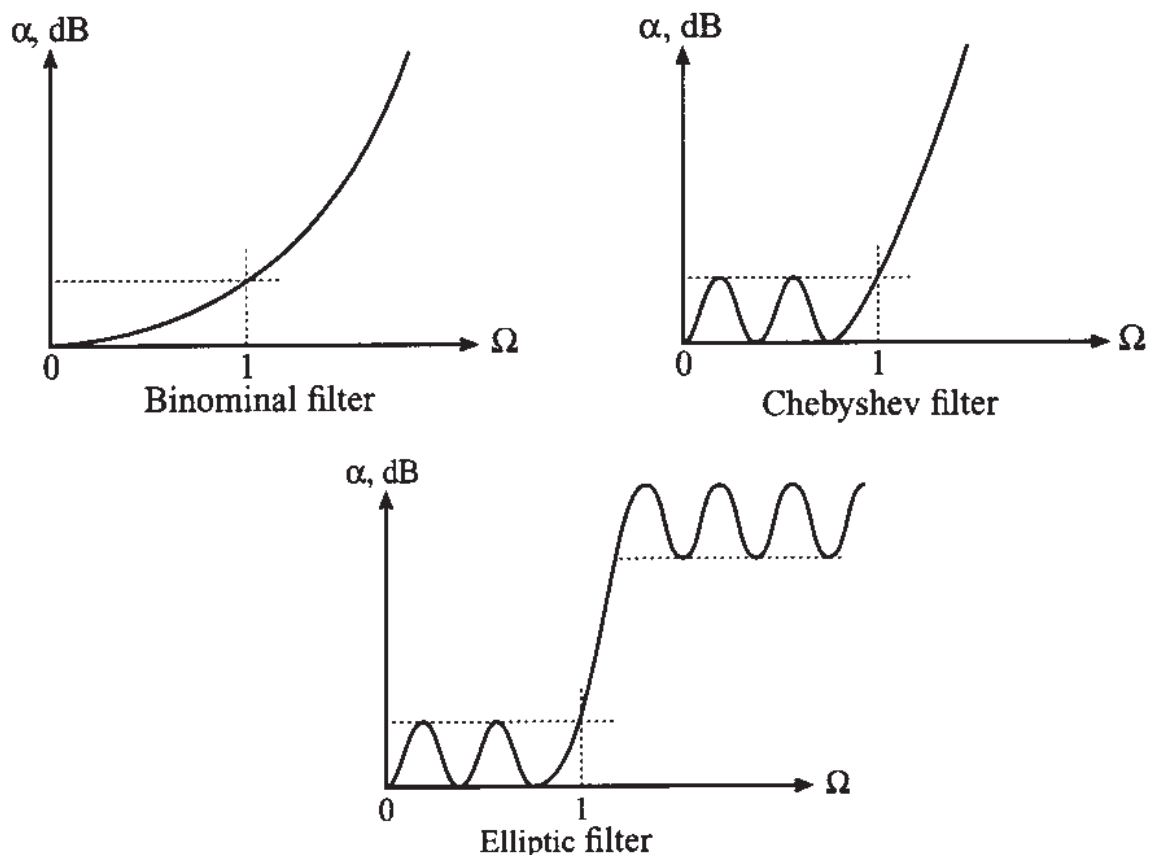


Figure 5-2 Actual attenuation profile for three types of low-pass filters.

The binomial filter exhibits a monotonic attenuation profile that is generally easy to implement. Unfortunately, to achieve a steep attenuation transition from pass- to stop band, a large number of components is needed. A better, steeper slope can be implemented if one permits a certain degree of variations, or ripples, in the passband attenuation profile. If these ripples maintain equal amplitude, either in the stopband or passband, we speak of a **Chebyshev filter** since the design relies on the so-called Chebyshev polynomials. For both the binomial and the Chebyshev filter we observe that the attenuation approaches infinity as $\Omega \rightarrow \infty$. This is in contrast to the elliptic filters, which allow the steepest transitions from passband to stopband at the expense of ripples in both bands. Because of their mathematical complexity in designing elliptic filters, we will not investigate them any further (for more information see Rizzi, listed in Further Reading at the end of this chapter).

In analyzing the various trade-offs when dealing with filters, the following parameters play key roles:

- **Insertion loss.** Ideally, a perfect filter inserted into the RF circuit path would introduce no power loss in the passband. In other words, it would have zero insertion loss. In reality, however, we have to expect a certain amount of power loss associated with the filter. The insertion loss quantifies how much below the 0 dB line the power amplitude response drops. In mathematical terms it states

$$IL = 10\log \frac{P_{in}}{P_L} = -10\log(1 - |\Gamma_{in}|^2) \quad (5.1)$$

where P_L is the power delivered to the load, P_{in} is the input power from the source, and $|\Gamma_{in}|$ is the reflection coefficient looking into the filter.

- **Ripple.** The flatness of the signal in the passband can be quantified by specifying the ripple or difference between maximum and minimum amplitude response in either dB or Nepers. As already mentioned, and as will be discussed further, the Chebyshev filter design allows us to precisely control the magnitude of the ripple.
- **Bandwidth.** For a bandpass filter, bandwidth defines the difference between upper and lower frequencies typically recorded at the 3 dB attenuation points above the passband:

$$BW^{3\text{dB}} = f_u^{3\text{dB}} - f_L^{3\text{dB}} \quad (5.2)$$

- **Shape factor.** This factor describes the sharpness of the filter response by taking the ratio between the 60 dB and the 3 dB bandwidths:

$$SF = \frac{BW^{60\text{dB}}}{BW^{3\text{dB}}} = \frac{f_u^{60\text{dB}} - f_L^{60\text{dB}}}{f_u^{3\text{dB}} - f_L^{3\text{dB}}} \quad (5.3)$$

- **Rejection.** For an ideal filter we would obtain infinite attenuation level for the undesirable signal frequencies. However, in reality we expect an upper bound due to the deployment of a finite number of filter components. Practical designs often specify 60 dB as the rejection rate since it can readily be combined with the shape factor (5.3).

The preceding filter parameters are best illustrated by way of a generic bandpass attenuation profile, as summarized in Figure 5-3. The magnitude of the filter's attenuation behavior is plotted with respect to the normalized frequency Ω . As a result, the center frequency f_c is normalized to $\Omega = 1$. The 3 dB lower and upper cut-off frequencies are symmetric with respect to this center frequency. Beyond these 3 dB points, we observe the attenuation response rapidly increasing and reaching the 60 dB rejection points at which the stopband begins.

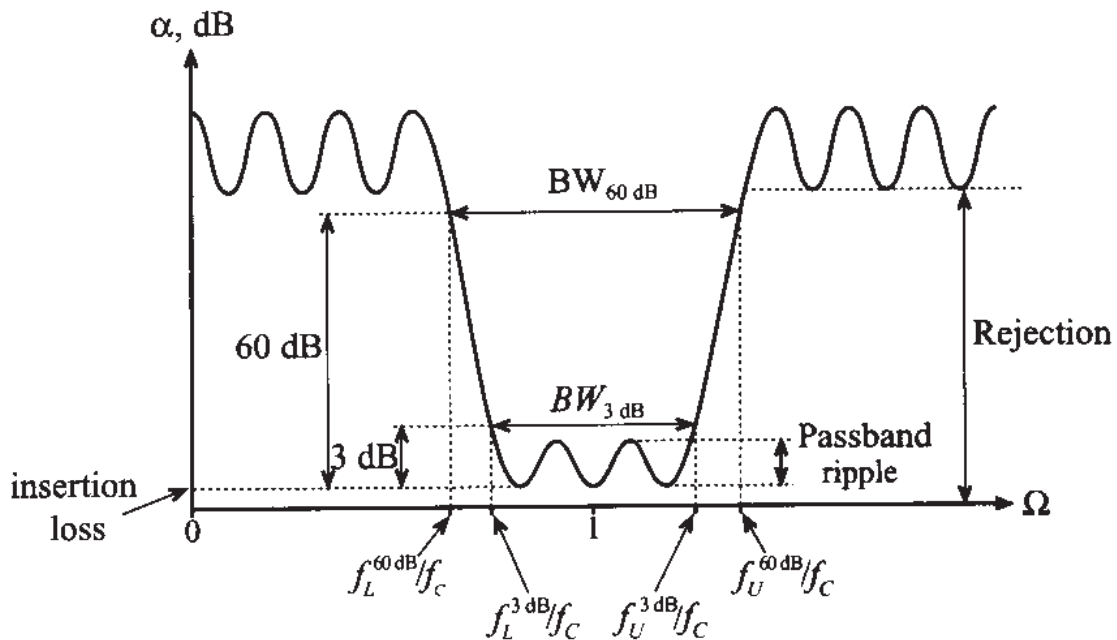


Figure 5-3 Generic attenuation profile for a bandpass filter.

There is one additional parameter describing the selectivity of the filter. This parameter is known as the **quality factor Q** , which generally defines the ratio of the average stored energy to the energy loss per cycle at the resonant frequency:

$$Q = \omega \frac{\text{average stored energy}}{\text{energy loss per cycle}} \Big|_{\omega = \omega_c} = \omega \frac{\text{average stored energy}}{\text{power loss}} \Big|_{\omega = \omega_c} = \omega \frac{W_{\text{stored}}}{P_{\text{loss}}} \Big|_{\omega = \omega_c} \quad (5.4)$$

where the power loss P_{loss} is equal to the energy loss per unit time. In applying this definition, care must be taken to distinguish between an unloaded and loaded filter. What is meant here is best seen by viewing the filter as a two-port network connected to a source at the input side and a load at the output, as shown in Figure 5-4.



Figure 5-4 Filter as a two-port network connected to an RF source and load.

It is customary to consider the power loss as consisting of the power loss associated with the external load and the filter itself. The resulting quality factor is named **loaded Q** , or Q_{LD} . Interestingly, if we take the inverse of the loaded Q , we see that

$$\frac{1}{Q_{LD}} = \frac{1}{\omega} \left(\frac{\text{power loss in filter}}{\text{average stored energy}} \right) \Big|_{\omega = \omega_r} + \frac{1}{\omega} \left(\frac{\text{power loss in load}}{\text{average stored energy}} \right) \Big|_{\omega = \omega_r} \quad (5.5)$$

since the total power loss is comprised of the power losses due to the presence of the filter and the load. This can be written in the concise form

$$\frac{1}{Q_{LD}} = \frac{1}{Q_F} + \frac{1}{Q_E} \quad (5.6)$$

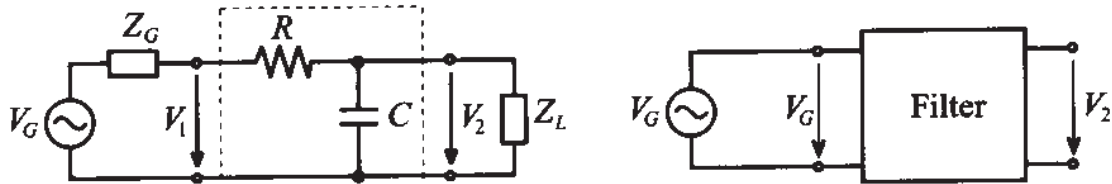
where Q_F and Q_E are the filter Q and the external Q . The precise meaning of (5.6) will be analyzed in Section 5.1.4. As we will also see in this section, (5.6) can be cast in the form

$$Q_{LD} = \frac{f_c}{f_U^{3dB} - f_L^{3dB}} \equiv \frac{f_c}{BW^{3dB}} \quad (5.7)$$

where f_c is the center or resonance frequency of the filter. In the following sections a summary is given of the salient features of the three most common filters. Emphasis is placed on the network description as previously developed in Chapter 4.

5.1.2 Low-Pass Filter

As one of the simplest examples we start our investigation by analyzing a first-order low-pass filter connected to a load resistance, as depicted in Figure 5-5.



(a) Low-pass filter with load resistance. (b) Network with input/output voltages

Figure 5-5 Low-pass filter connected between source and load resistance.

The focal point in any filter design is to find the output V_2 due to the input voltage V_1 , or even better, the generator voltage V_G . For our simple circuit this can best be accomplished by cascading four $ABCD$ -networks (labeled 1 through 4) as suggested in Figure 5-6.

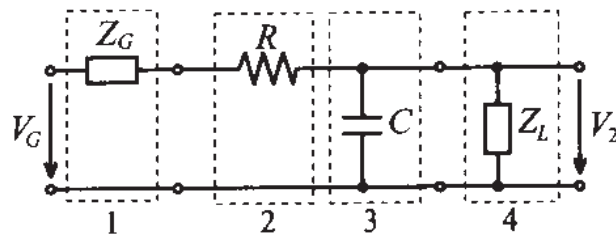


Figure 5-6 Cascading four *ABCD*-networks.

The overall *ABCD*-network is therefore

$$\begin{bmatrix} A & B \\ C & D \end{bmatrix} = \begin{bmatrix} 1 & R_G \\ 0 & 1 \end{bmatrix} \begin{bmatrix} 1 & R \\ 0 & 1 \end{bmatrix} \begin{bmatrix} 1 & 0 \\ j\omega C & 1 \end{bmatrix} \begin{bmatrix} 1 & 0 \\ 1/R_L & 1 \end{bmatrix} = \begin{bmatrix} 1 + (R + R_G) \left(j\omega C + \frac{1}{R_L} \right) R_G + R_L \\ j\omega C + \frac{1}{R_L} \end{bmatrix} \quad (5.8)$$

where we use the fact that both source and load impedances are resistive, i.e., $Z_G = R_G$ and $Z_L = R_L$. Since A is already the ratio V_G/V_2 , we only have to invert this single coefficient:

$$\frac{V_2}{V_G} = \frac{1}{A} = \frac{1}{1 + (R + R_G) \left(j\omega C + \frac{1}{R_L} \right)} \quad (5.9)$$

Equation (5.9) can be examined for the limiting cases where the frequency is either zero or approaches infinity. For $\omega \rightarrow 0$ we obtain

$$\frac{V_2}{V_G} = \frac{1}{1 + (R + R_G)/R_L} = \frac{R_L}{R_G + R + R_L} \quad (5.10a)$$

and for $\omega \rightarrow \infty$

$$\frac{V_2}{V_G} = 0 \quad (5.10b)$$

In the first case we notice that the voltage divider rule applies for the DC condition, while for the second case the filter exhibits the expected low-pass behavior of zero output voltage at high frequencies. Further, if the load resistance goes to infinity ($R_L \rightarrow \infty$), the filter becomes unloaded and in the limit a pure first-order system results:

$$\frac{V_2}{V_G} = H(\omega) = \frac{1}{1 + j\omega(R_G + R)C} \quad (5.11)$$

where $H(\omega)$ is known from system theory as **transfer function**. Besides specifying the transfer function, it is more common to compute the attenuation factor in Neper (Np) such that

$$\alpha(\omega) = -\ln|H(\omega)| = -\frac{1}{2}\ln|H(\omega)|^2 \quad (5.12a)$$

or in dB as

$$\alpha(\omega) = -20\log|H(\omega)| = -10\log|H(\omega)|^2 \quad (5.12b)$$

The corresponding phase is

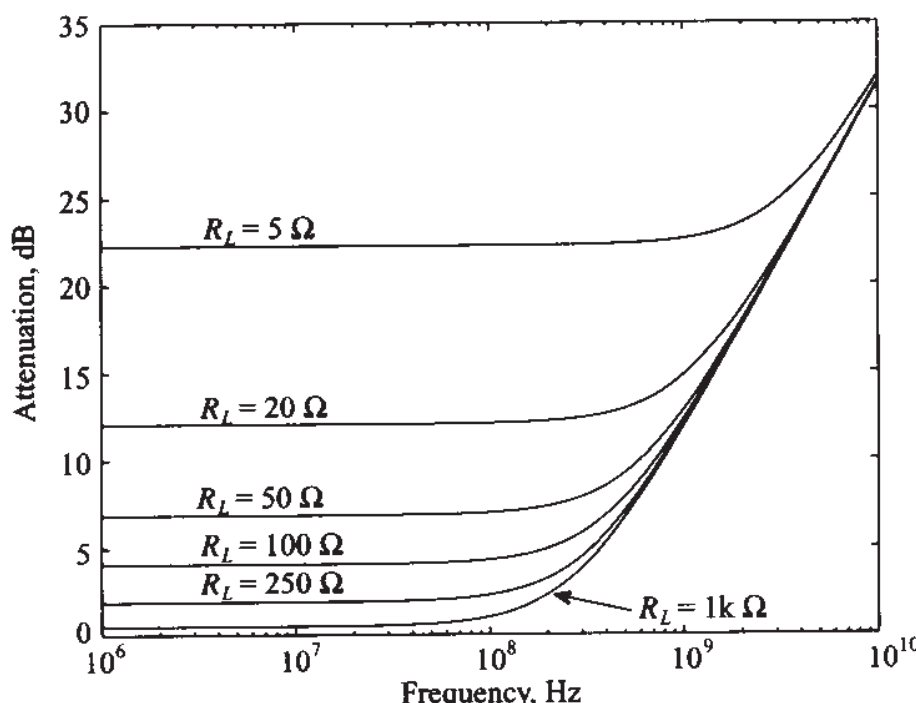
$$\phi(\omega) = \tan^{-1}\left(\frac{\text{Im}\{H(\omega)\}}{\text{Re}\{H(\omega)\}}\right) \quad (5.12c)$$

Directly related to phase is the so-called **group delay** t_g , which is defined as the frequency derivative of the phase.

$$t_g = \frac{d\phi(\omega)}{d\omega} \quad (5.12d)$$

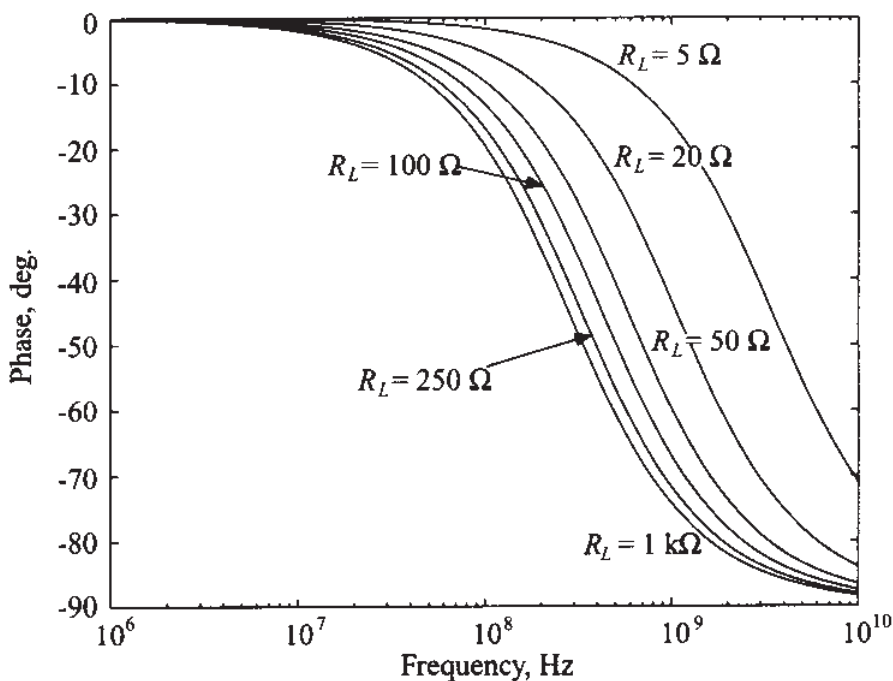
It is often desirable to design a filter with nearly linear phase (i.e., $\phi \propto \omega A$, with A being an arbitrary constant factor). The group delay is then simply a constant $t_g \propto A$.

A typical filter response for $C = 10 \text{ pF}$, $R = 10 \Omega$, $R_G = 50 \Omega$ and various load resistances is shown in Figure 5-7.



(a) Attenuation profile of the low-pass filter for various load resistances

Figure 5-7 First-order low-pass filter response as a function of various load resistances.



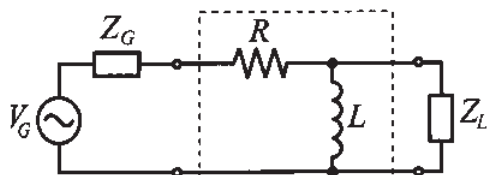
(b) Phase response of the low-pass filter for various load resistances

Figure 5-7 First-order low-pass filter response as a function of various load resistances. (Continued)

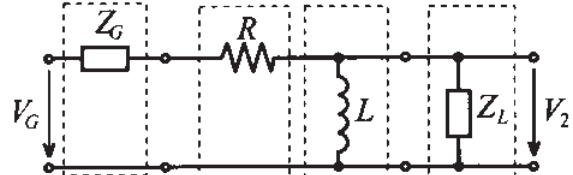
5.1.3 High-Pass Filter

Replacing the capacitor with an inductor in Figure 5-5 permits the construction of a first-order high-pass filter, as depicted in Figure 5-8. The analysis follows the same steps as outlined in (5.9), except that the capacitive reactance is replaced by an inductive reactance. The result is

$$\begin{bmatrix} A & B \\ C & D \end{bmatrix} = \begin{bmatrix} 1 & R_G \\ 0 & 1 \end{bmatrix} \begin{bmatrix} 1 & R \\ 0 & 1 \end{bmatrix} \begin{bmatrix} 1 & 0 \\ \frac{1}{j\omega L} & 1 \end{bmatrix} \begin{bmatrix} 1 & 0 \\ \frac{1}{R_L} & 1 \end{bmatrix} = \begin{bmatrix} 1 + (R + R_G)\left(\frac{1}{j\omega L} + \frac{1}{R_L}\right) & R_G + R_L \\ j\omega C + \frac{1}{R_L} & 1 \end{bmatrix} \quad (5.13)$$



(a) High-pass filter with load resistance



(b) Network and input/output voltages

Figure 5-8 First-order high-pass filter.

This gives us directly the result

$$\frac{V_2}{V_G} = \frac{1}{A} = \frac{1}{1 + (R + R_G)\left(\frac{1}{j\omega L} + \frac{1}{R_L}\right)} \quad (5.14)$$

As $\omega \rightarrow 0$, it is seen that

$$\frac{V_2}{V_G} = 0 \quad (5.15a)$$

and for $\omega \rightarrow \infty$ we conclude

$$\frac{V_2}{V_G} = \frac{1}{1 + (R + R_G)/R_L} = \frac{R_L}{R_G + R + R_L} \quad (5.15b)$$

which reveals that the inductive influence can be neglected. The filter response for $L = 100 \text{ nH}$, $R = 10 \Omega$, $R_G = 50 \Omega$, and various load resistances is shown in Figure 5-9.

5.1.4 Bandpass and Bandstop Filters

A bandpass filter can be constructed through an RLC series circuit or through a parallel connection of an RLC shunt circuit. The generic series circuit diagram, including generator and load impedances, is displayed in Figure 5-10.

The network representation in $ABCD$ notation takes on the form

$$\begin{bmatrix} A & B \\ C & D \end{bmatrix} = \begin{bmatrix} 1 & Z_G \\ 0 & 1 \end{bmatrix} \begin{bmatrix} 1 & Z \\ 0 & 1 \end{bmatrix} \begin{bmatrix} 1 & 0 \\ 1/Z_L & 1 \end{bmatrix} = \begin{bmatrix} 1 + \frac{Z + Z_G}{Z_L} & Z_G + Z \\ \frac{1}{Z_L} & 1 \end{bmatrix} \quad (5.16)$$

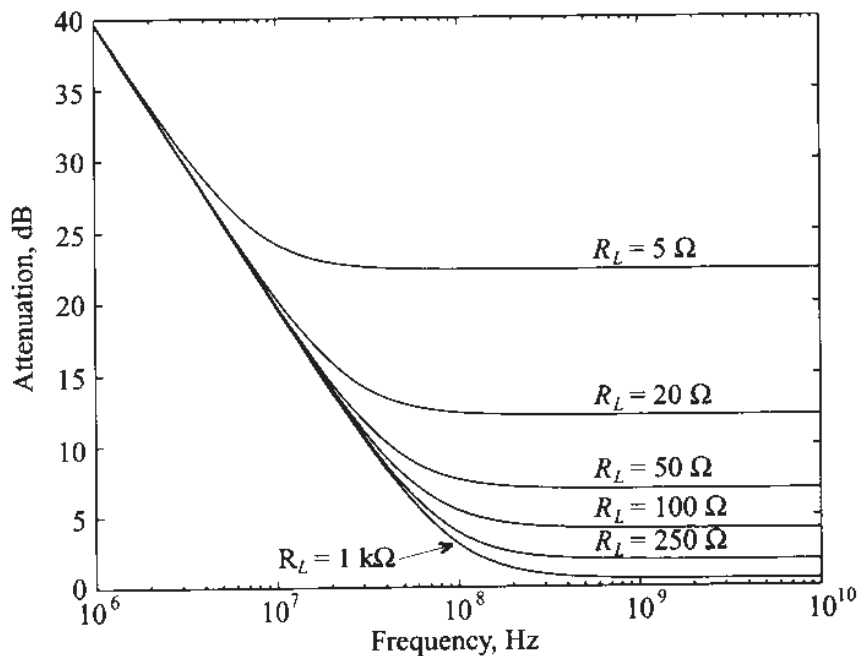
where impedance Z is specified from conventional circuit analysis as

$$Z = R + j\left(\omega L - \frac{1}{\omega C}\right) \quad (5.17)$$

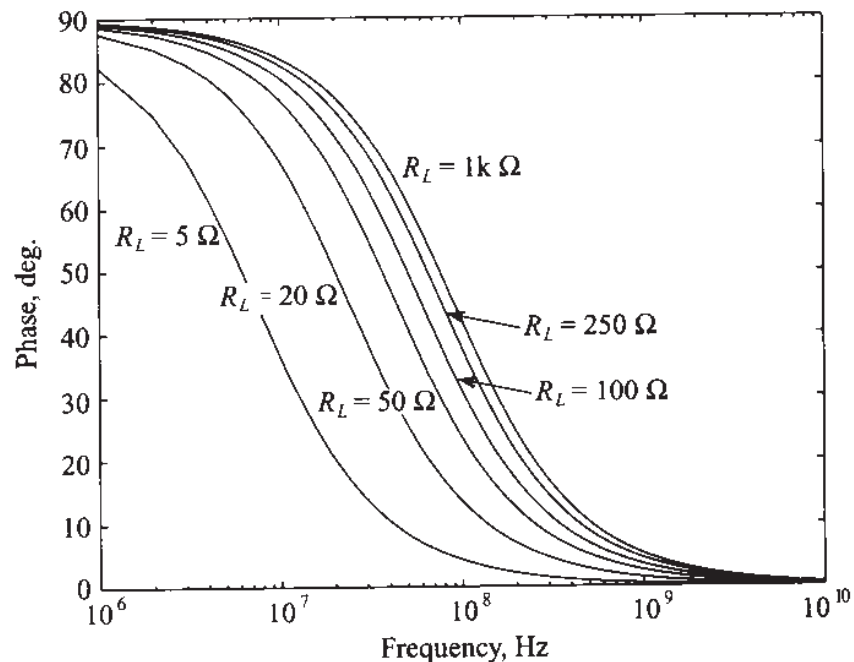
The transfer function $H(\omega) = 1/A$ is found to be

$$\frac{V_2}{V_G} = H(\omega) = \frac{Z_L}{(Z_L + Z_G) + R + j[\omega L - 1/(\omega C)]} \quad (5.18)$$

Explicit plots of the transfer function and the attenuation profile are discussed in the following example.



(a) Attenuation profile of the filter for various load resistances



(b) Phase response of the filter for various load resistances

Figure 5-9 Low-pass filter response as a function of various load resistances.

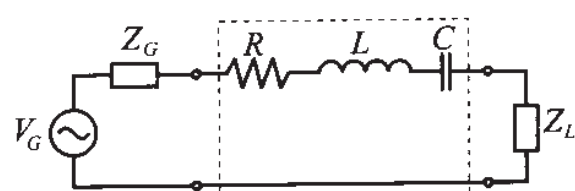
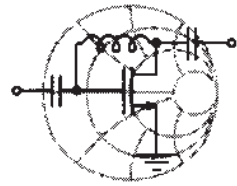


Figure 5-10 Bandpass filter implemented in series configuration.



RF & MW →

Example 5-1: Bandpass filter response

For a bandpass filter with $Z_L = Z_G = 50 \Omega$ the following components are selected: $R = 20 \Omega$, $L = 5 \text{ nH}$, and $C = 2 \text{ pF}$. Find the resonance frequency, and plot the frequency response of the phase of the transfer function and the associated attenuation profile in dB.

Solution: To solve this problem we use the definition of the transfer function for the bandpass filter presented in (5.18). The attenuation profile of the filter expressed in dB is computed as $\alpha = 20\log[H(\omega)^{-1}] = -20\log[H(\omega)]$. Both the attenuation and phase profiles of the filter are shown in Figure 5-11. From the graph we can estimate the resonance frequency f_0 of the filter to be approximately 1.5 GHz. The exact numerical value is $f_0 = 1/(2\pi\sqrt{LC}) = 1.59 \text{ GHz}$.

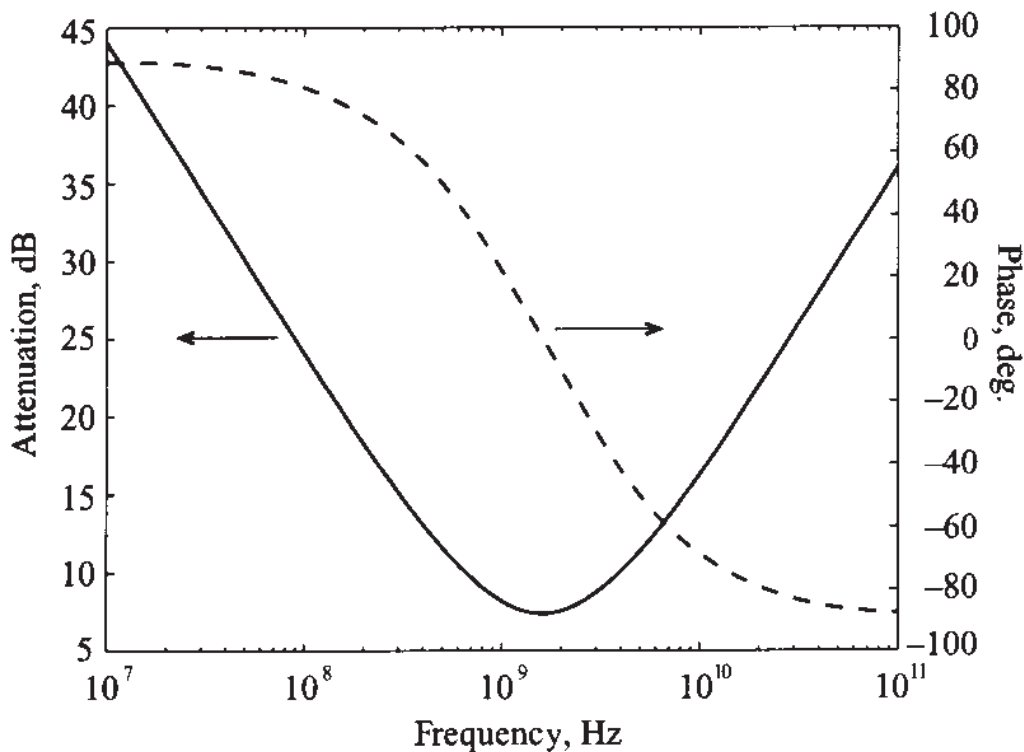


Figure 5-11 Bandpass filter response.

As expected, our bandpass filter assumes a minimum attenuation at the resonance point, but the transitions from stopband to passband are very gradual.

If the series circuit is replaced by a shunt circuit, as shown in Figure 5-12, we only have to replace Z by $1/Y$ in (5.17), which leads to

$$\frac{V_2}{V_G} = \frac{Z_L}{Z_L + Z_G + 1/Y} \quad (5.19)$$

where the admittance is

$$Y = G + j\left(\omega C - \frac{1}{\omega L}\right) \quad (5.20)$$

and upon insertion into (5.19) yields

$$\frac{V_2}{V_G} = H(\omega) = \frac{Z_L \left[G + j\left(\omega C - \frac{1}{\omega L}\right) \right]}{(Z_L + Z_G) \left[G + j\left(\omega C - \frac{1}{\omega L}\right) \right] + 1} \quad (5.21)$$

A typical transfer function response of magnitude and phase for the values listed in Example 5-1 is seen in Figure 5-12.

Working with energy storage systems or *LC*-based networks, we can use the quality factor as introduced in Section 5.1.1 to specify the bandwidth of the 3 dB passband or stopband of a filter:

$$BW = \frac{f_0}{Q} \quad (5.22)$$

where f_0 is the resonance frequency. This quality factor is the inverse of the **dissipation factor** d , which depends on whether we deal with a series (*RLC*) or a parallel connected (*GLC*) circuit. Table 5-1 summarizes all relevant definitions for the series and parallel resonance circuits.

The quality factor provides important insight into the losses generated by a particular resonator circuit configuration. The circuits shown in Table 5-1 depict unloaded filters (i.e., filters in the absence of any external load connections).

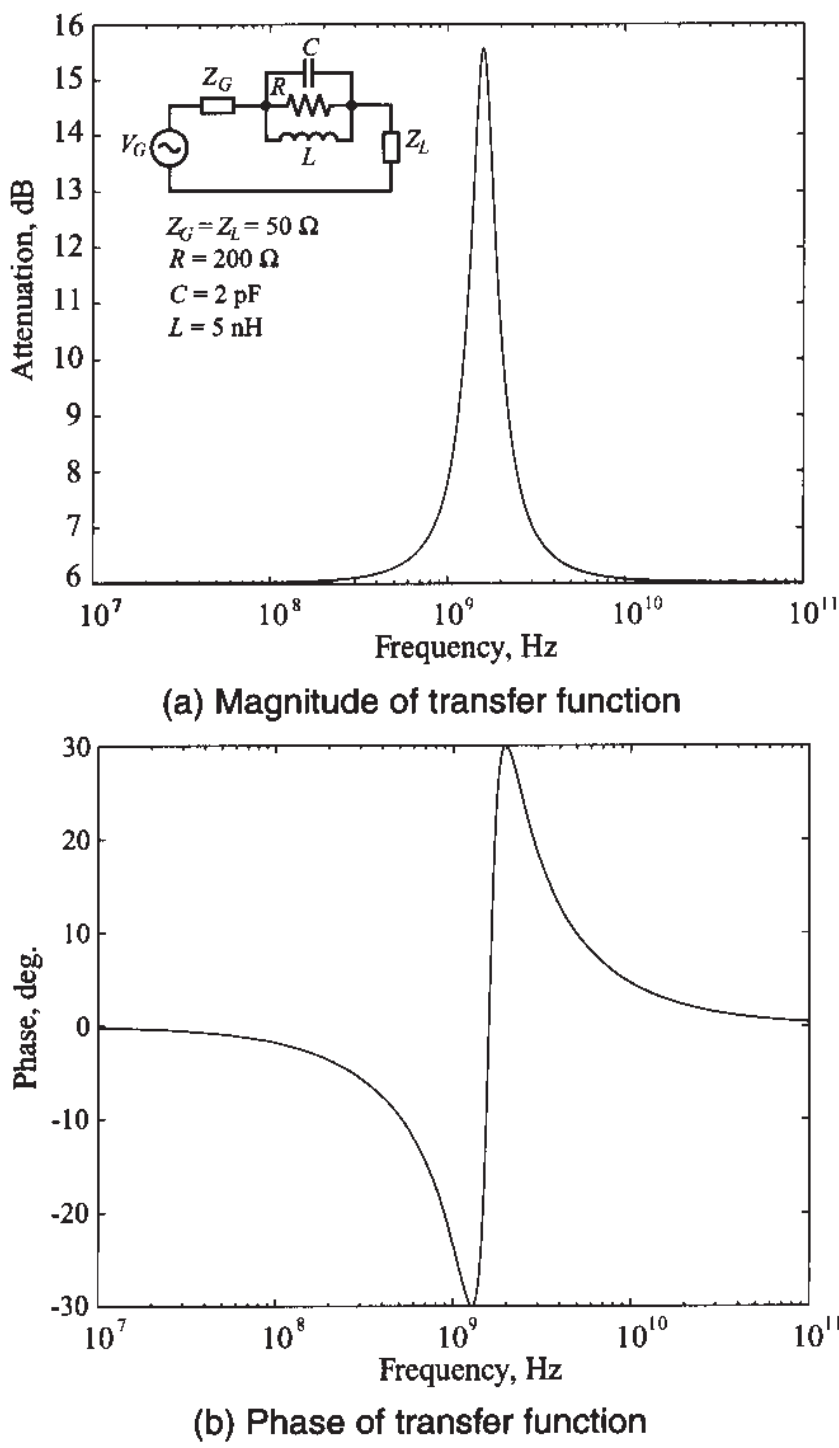
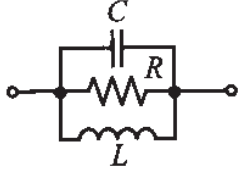
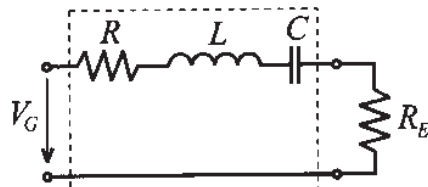


Figure 5-12 Bandstop filter response.

When dealing with the loaded situation we are confronted with the additional complication of generator and load impedances attached to the resonator. With reference to Figure 5-10, let us take a more detailed look at how the three different quality factors arise. To this end, our aim is to analyze the series resonance, or bandpass filter, connected to the generator resistance R_G and load R_L . Without loss of generality, we can combine both resistances into the configuration shown in Figure 5-13.

Table 5-1 Series and parallel resonators

| Parameter |  |  |
|--------------------------------|---|---|
| Impedance or Admittance | $Z = R + j\omega L + \frac{1}{j\omega C}$ | $Y = G + j\omega C + \frac{1}{j\omega L}$ |
| Resonance Frequency | $\omega_0 = \frac{1}{\sqrt{LC}}$ | $\omega_0 = \frac{1}{\sqrt{LC}}$ |
| Dissipation Factor | $d = \frac{R}{\omega_0 L} = R\omega_0 C$ | $d = \frac{G}{\omega_0 C} = G\omega_0 L$ |
| Quality Factor | $Q = \frac{\omega_0 L}{R} = \frac{1}{R\omega_0 C}$ | $Q = \frac{\omega_0 C}{G} = \frac{1}{G\omega_0 L}$ |
| Bandwidth | $BW = \frac{f_0}{Q} = \frac{1}{2\pi L} R$ | $BW = \frac{f_0}{Q} = \frac{1}{2\pi C} G$ |

**Figure 5-13** Circuit used for the definitions of loaded and unloaded quality factors.

where $R_E = R_G + R_L$ and V_G is understood as a Thévenin-equivalent source. The losses can now be partitioned as originating from an external resistance R_E , an internal resistance R , or both. Therefore, we need to differentiate three cases:

External quality factor ($R_E \neq 0, R = 0$)

$$Q_E = \frac{\omega_0 L}{R_E} = \frac{1}{R_E \omega_0 C}$$

Internal or filter quality factor ($R_E = 0, R \neq 0$)

$$Q_F = \frac{\omega_0 L}{R} = \frac{1}{R \omega_0 C}$$

Loaded quality factor ($R_E \neq 0, R \neq 0$)

$$Q_{LD} = \frac{\omega_0 L}{R + R_E} = \frac{1}{(R + R_E)\omega_0 C}$$

Identical expressions are derived for a shunt resonator circuit if we replace R and R_E by G and G_E . It is customary to introduce the normalized frequency deviation from the resonance point

$$\epsilon = \frac{\omega}{\omega_0} - \frac{\omega_0}{\omega} \quad (5.23)$$

and expand it as follows:

$$\epsilon = \frac{f_0 + f - f_0}{f_0} - \frac{f_0}{f_0 + f - f_0} = \left(1 + \frac{\Delta f}{f_0}\right) - \left(1 + \frac{\Delta f}{f_0}\right)^{-1} \approx 2 \frac{\Delta f}{f_0} \quad (5.24)$$

with $\Delta f = f_0 - f$. Equation (5.24) leads to the expression of the differential change in quality factor

$$\Delta Q_{LD} = Q_{LD} \epsilon \approx 2 \frac{\Delta f}{f_0} Q_{LD} \quad (5.25)$$

If (5.25) is solved for Q_{LD} , and using $X = \omega L$, we obtain

$$Q_{LD} = \frac{\Delta Q_{LD}}{\epsilon} = \frac{f_0}{2(R_E + R)} \frac{dX}{df} \Big|_{f=f_0} \quad (5.26a)$$

for the series circuit configuration.

Alternatively, for a parallel circuit with $B = 1/(\omega L)$ we have

$$Q_{LD} = \frac{\Delta Q_{LD}}{\epsilon} = \frac{f_0}{2(G_E + G)} \frac{dB}{df} \Big|_{f=f_0} \quad (5.26b)$$

The equations (5.26a) and (5.26b) show that generically the loaded quality factor for complex impedances (or admittances) can be computed as

$$Q_{LD} = \frac{\Delta Q_{LD}}{\epsilon} = \frac{f_0}{2\operatorname{Re}\{Z\}} \frac{d\operatorname{Im}\{Z\}}{df} \Big|_{f=f_0}$$

or

$$Q_{LD} = \frac{\Delta Q_{LD}}{\epsilon} = \frac{f_0}{2\operatorname{Re}\{Y\}} \frac{d\operatorname{Im}\{Y\}}{df} \Big|_{f=f_0}$$

where $\text{Re}\{Z\}$, $\text{Im}\{Z\}$, $\text{Re}\{Y\}$, and $\text{Im}\{Y\}$ are real and imaginary parts of the total impedance or admittance of the resonance circuit.

5.1.5 Insertion Loss

The previously developed quality factor expressions are very useful in RF circuit design, since the Q of a filter can more easily be measured (for instance, with a network analyzer) than the actual impedance or admittance. It is therefore helpful to re-express the impedance or admittance values of bandpass or bandstop filters in terms of the various Q -factors. For example, the impedance of the series resonance circuit can be rewritten as:

$$Z = R + j\left(\omega L - \frac{1}{\omega C}\right) = (R_E + R)\left[\frac{R}{R_E + R} + j\left(\frac{\omega L}{R_E + R} - \frac{1}{\omega C(R_E + R)}\right)\right] \quad (5.27)$$

which leads to

$$Z = (R_E + R)\left[\frac{Q_{LD}}{Q_F} + jQ_{LD}\epsilon\right] \quad (5.28)$$

Following the same steps as described for a series resonator, a very similar expression can be derived for the admittance Y of a parallel resonator:

$$Y = (G_E + G)\left[\frac{Q_{LD}}{Q_F} + jQ_{LD}\epsilon\right] \quad (5.29)$$

We now turn our attention to the following situation: a transmission line system with characteristic line impedance Z_0 is matched at the load and generator sides ($Z_L = Z_G = Z_0$) as seen in Figure 5-14(a).

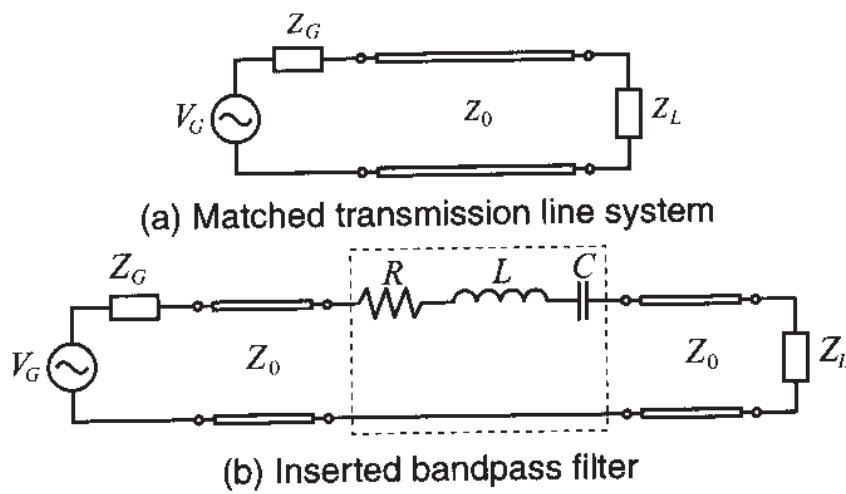


Figure 5-14 Insertion loss considerations.

In Figure 5-14(a) the power delivered to the load P_L is the total available power from the source P_{in} :

$$P_L = P_{\text{in}} = |V_G|^2 / (8Z_0) \quad (5.30)$$

If the filter is inserted as shown in Figure 5-14(b), the power delivered to the load becomes

$$P_L = \frac{1}{2} \left| \frac{V_G}{2Z_0 + Z} \right|^2 Z_0 = \frac{|V_G|^2 / (8Z_0)}{\frac{1}{4Z_0^2} \left| 2Z_0 + (2Z_0 + R) \left[\frac{Q_{LD}}{Q_F} + j\varepsilon Q_{LD} \right] \right|^2} \quad (5.31)$$

which, after some algebra and the use of (5.6), yields

$$P_L = P_{\text{in}} \frac{1}{(1 + \varepsilon^2 Q_{LD}^2) Q_E^2 / Q_{LD}^2} \quad (5.32)$$

The insertion loss in dB due to the presence of the filter is then computed as

$$IL = 10 \log \left(\frac{1 + \varepsilon^2 Q_{LD}^2}{Q_{LD}^2 / Q_E^2} \right) = 10 \log (1 + \varepsilon^2 Q_{LD}^2) - 10 \log (1 - Q_{LD} / Q_F)^2 \quad (5.33)$$

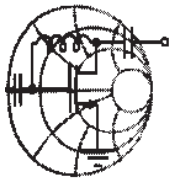
At resonance, $\varepsilon = 0$, the first term drops out and the second term quantifies the associated resonator losses. However, if the filter is off resonance, then the first term quantifies the sensitivity. If we consider the frequency at which the power delivered to the load is half, or 3 dB, of the power at resonance frequency, we can immediately write that $1 + \varepsilon^2 Q_{LD}^2 = 2$, or, taking into account relation (5.24), we obtain

$$BW_{3\text{dB}} = 2\Delta f = \varepsilon f_0 = f_0 / Q_{LD}$$

Recalling Section 2.11, we notice that (5.33) can be related to the input reflection coefficient:

$$1 - |\Gamma_{\text{in}}|^2 = 1 - \left| \frac{Z_{\text{in}} - Z_G}{Z_{\text{in}} + Z_G} \right|^2 = \frac{Q_{LD}^2 / Q_E^2}{1 + \varepsilon^2 Q_{LD}^2} = \frac{1}{LF} \quad (5.34)$$

where LF is known as the **loss factor**. This loss factor plays a central role when developing the desired filter attenuation profiles.



RF & MW →

Example 5-2: Calculation of various quality factors for a filter

For the filter configuration shown in Figure 5-14(b), the following parameters are given: $Z_0 = 50 \Omega$, $Z_G = Z_L = Z_0$, $R = 10 \Omega$, $L = 50 \text{ nH}$, $C = 0.47 \text{ pF}$, and the generator voltage is $V_G = 5 \text{ V}$. Find the loaded, unloaded (filter), and external quality factors; power generated by the source; power absorbed by the load at resonance; and plot the insertion loss in the range of $\pm 20\%$ of the resonance frequency.

Solution: The first step in the solution of this problem is to find the resonance frequency of the filter:

$$f_0 = \frac{1}{2\pi\sqrt{LC}} = 1.038 \text{ GHz}$$

Knowing this value we are now capable of computing the various quality factors of the filter:

$$\text{External quality factor: } Q_E = \frac{\omega_0 L}{2Z_0} = 3.26$$

$$\text{Internal or filter quality factor: } Q_F = \frac{\omega_0 L}{R} = 32.62$$

$$\text{Loaded quality factor: } Q_{LD} = \frac{\omega_0 L}{R + 2Z_0} = 2.97$$

To determine the input power, or maximum available power from the source, we use (5.30):

$$P_{in} = |V_G|^2 / (8Z_0) = 62.5 \text{ mW}$$

Due to nonzero internal resistance of the filter ($R = 10 \Omega$), the signal will suffer some attenuation even at the resonance frequency and the power delivered to the load will be less than the available power:

$$P_L = P_{in} \frac{1}{(1 + \epsilon^2 Q_{LD}^2) Q_E^2 / Q_{LD}^2} \Big|_{f=f_0} = P_{in} \frac{1}{Q_E^2 / Q_{LD}^2} = 51.7 \text{ mW}$$

Finally, substituting the loaded and external quality factors into (5.33), we proceed to find the insertion loss of the filter in the range

of $\pm 20\%$ of the resonance frequency by plotting the frequency response of IL , as shown in Figure 5-15. As we see from the graph, the 3 dB bandwidth of this filter is approximately equal to 350 MHz, which agrees with the result obtained using our formula derived earlier in this section (i.e., $BW_{3dB} = f_0/Q_{LD} = 350.07\text{MHz}$).

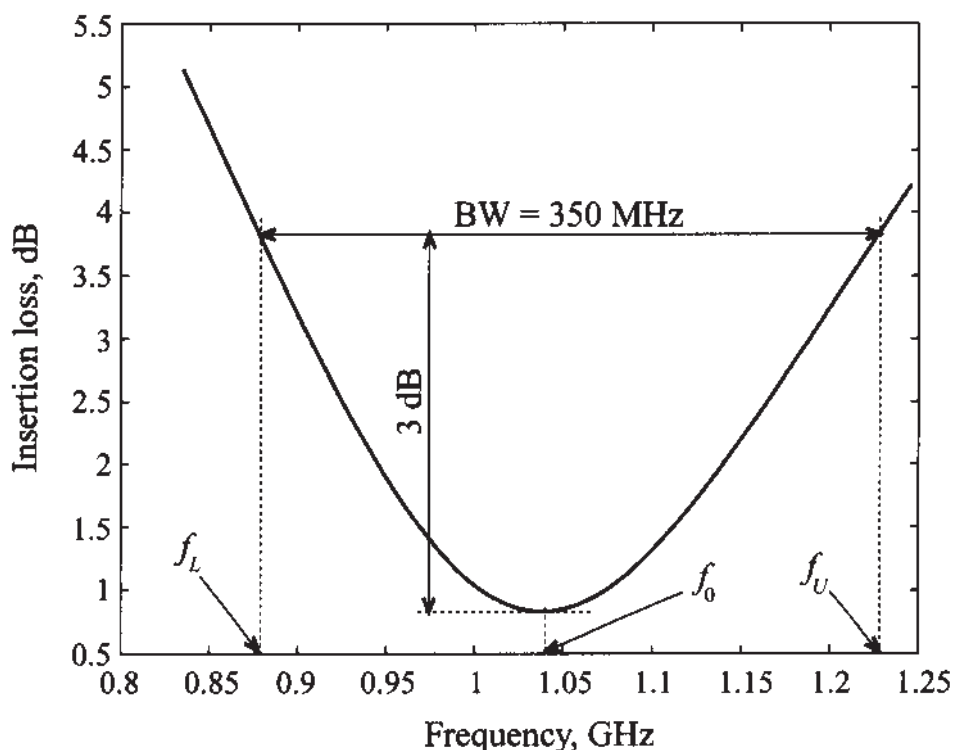


Figure 5-15 Insertion loss versus frequency.

Although not as distinctively observed in practice, the example shows that the loaded quality is lower than both the external and internal filter quality factors.

5.2 Special Filter Realizations

The analytical synthesis of special filter characteristics such as low-pass, high-pass, and bandpass/bandstop filters is generally very complicated. In our brief introductory treatment we are going to concentrate on two filter types: the maximally flat **Butterworth** and the equi-ripple **Chebyshev** filter realizations. Both filter types are analyzed first in a normalized low-pass configuration, before the low-pass behavior is frequency scaled to implement the remaining filter types through a frequency transformation.

5.2.1 Butterworth-Type Filters

This filter type is also known as maximally flat filter since no ripple is permitted in its attenuation profile. For the low-pass filter, the insertion loss is determined through the loss factor,

$$IL = -10\log(1 - |\Gamma_{in}|^2) = 10\log\{LF\} = 10\log\{1 + a^2\Omega^{2N}\} \quad (5.35)$$

where Ω is again the normalized frequency as introduced in Section 5.1.1 and where N denotes the order of the filter. It is customary to select the constant $a = 1$ so that at $\Omega = \omega/\omega_c = 1$ the insertion loss becomes $IL = 10\log\{2\}$, which is the 3 dB point at the cut-off frequency. In Figure 5-16 the insertion loss for several values N is plotted.

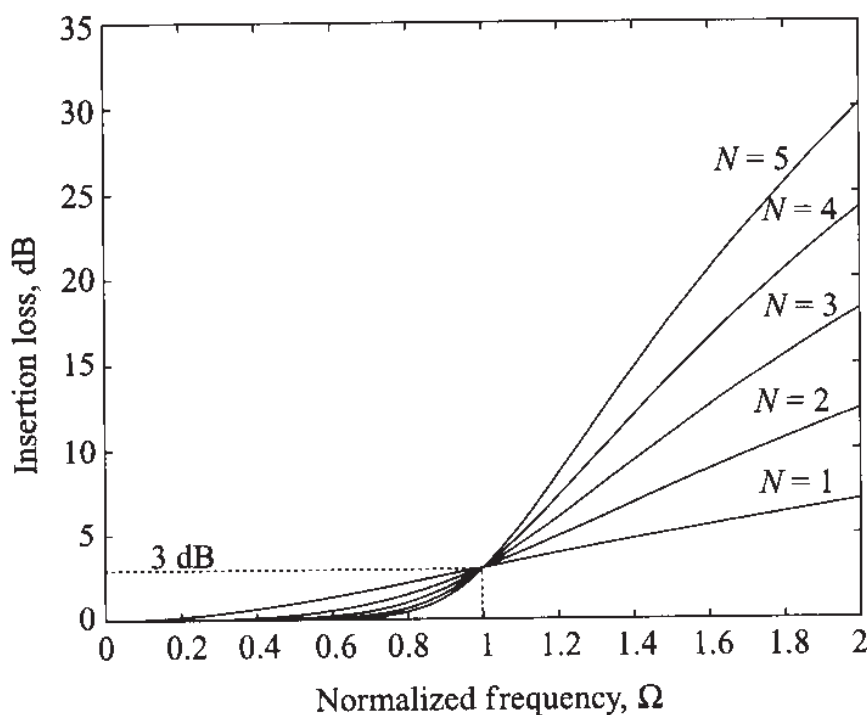


Figure 5-16 Butterworth low-pass filter design.

Two possible realizations of the generic normalized low-pass filter are shown in Figure 5-17, where we set $R_G = 1$.

The element values in the circuits in Figure 5-17 are numbered from g_0 at the generator side to g_{N+1} at the load location. The elements in the circuit alternate between series inductance and shunt capacitance. The corresponding elements g are defined as follows:

$$g_0 = \begin{cases} \text{internal generator resistance for circuit in Figure 5-17(a)} \\ \text{internal generator conductance for circuit in Figure 5-17(b)} \end{cases}$$

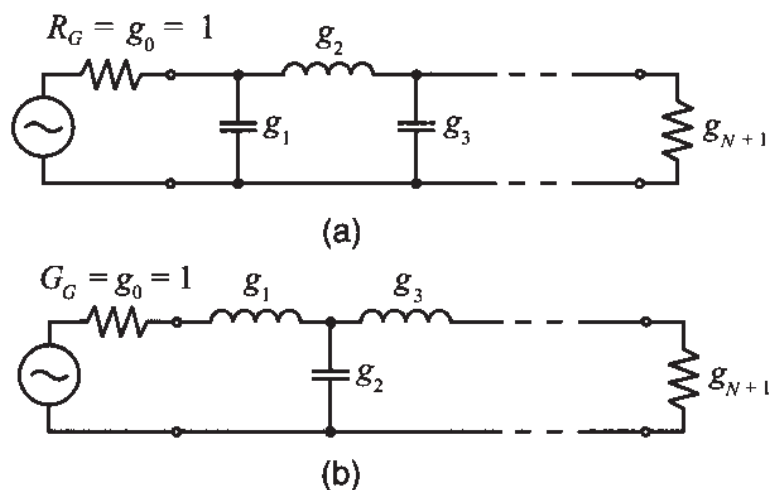


Figure 5-17 Two equivalent realizations of the generic multisection low-pass filter with normalized elements.

$$g_m = \left\{ \begin{array}{l} \text{inducance for series inductor} \\ \text{capacitance for shunt capacitor} \end{array} \right\} \quad (m = 1, \dots, N)$$

$$g_{N+1} = \left\{ \begin{array}{l} \text{load resistance if the last element is a shunt capacitor} \\ \text{load conductance if the last element is a series inductor} \end{array} \right.$$

The values for the g 's are tabulated and can be found in the literature (see Pozar and Rizzi, listed in Further Reading). For N up to 10, Table 5-2 summarizes the respective g -values for the maximally flat low-pass filter based on $g_0 = 1$ and cut-off frequency $\omega_c = 1$.

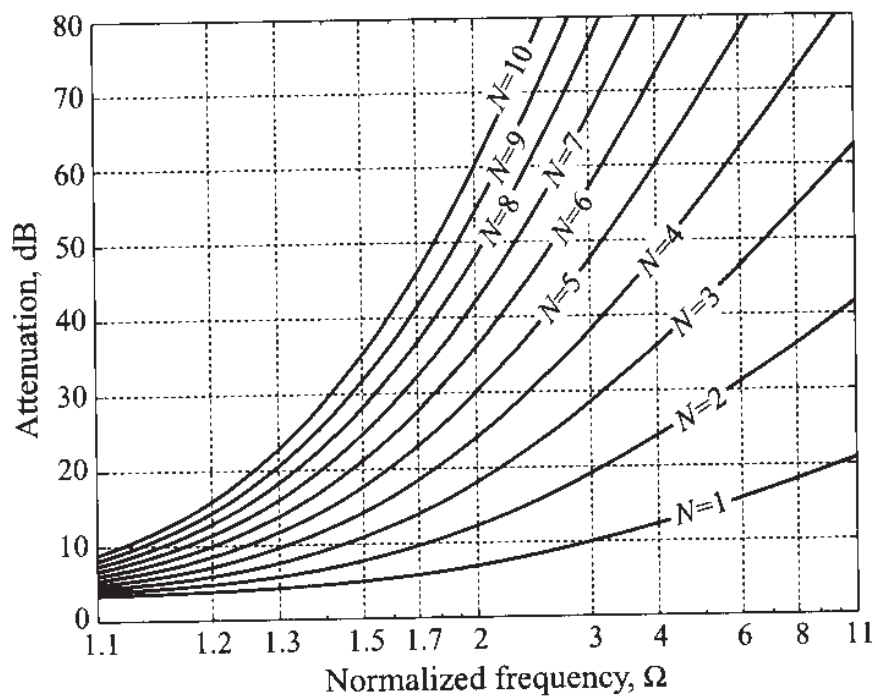
The corresponding attenuation versus frequency behavior for various filter orders N is seen in Figure 5-18. We note that $\Omega = 1$ is the 3 dB cut-off frequency point. The attenuation curves in Figure 5-18 are very useful in determining the required order of the filter. For instance, if a maximally flat low-pass filter is to be designed with attenuation of at least 60 dB at $\Omega = 2$, we see that an order of $N = 10$ is required.

Figure 5-18 exhibits a steep increase in attenuation after cut-off. We notice that for $\Omega \gg 1$ or $\omega \gg \omega_c$ the loss factor increases as Ω^{2N} , which is a rate of 20N dB per decade. However, nothing is said about the phase response of such a filter. In many wireless communication applications, a **linear phase** behavior may be a more critical issue than a rapid attenuation or amplitude transition. Unfortunately, linear phase and rapid amplitude change are opposing requirements. If linear phase is desired, we demand a functional behavior similar to (5.35)

$$\phi(\Omega) = A_1 \Omega (1 + A_2 \Omega^{2N}) \quad (5.36)$$

Table 5-2 Coefficients for maximally flat low-pass filter ($N = 1$ to 10)

| N | g_1 | g_2 | g_3 | g_4 | g_5 | g_6 | g_7 | g_8 | g_9 | g_{10} | g_{11} |
|-----|--------|--------|--------|--------|--------|--------|--------|--------|--------|----------|----------|
| 1 | 2.0000 | 1.0000 | | | | | | | | | |
| 2 | 1.4142 | 1.4142 | 1.0000 | | | | | | | | |
| 3 | 1.0000 | 2.0000 | 1.0000 | 1.0000 | | | | | | | |
| 4 | 0.7654 | 1.8478 | 1.8478 | 0.7654 | 1.0000 | | | | | | |
| 5 | 0.6180 | 1.6180 | 2.0000 | 1.6180 | 0.6180 | 1.0000 | | | | | |
| 6 | 0.5176 | 1.4142 | 1.9318 | 1.9318 | 1.4142 | 0.5176 | 1.0000 | | | | |
| 7 | 0.4450 | 1.2470 | 1.8019 | 2.0000 | 1.8019 | 1.2470 | 0.4450 | 1.0000 | | | |
| 8 | 0.3902 | 1.1111 | 1.6629 | 1.9615 | 1.9615 | 1.6629 | 1.1111 | 0.3902 | 1.0000 | | |
| 9 | 0.3473 | 1.0000 | 1.5321 | 1.8794 | 2.0000 | 1.8794 | 1.5321 | 1.0000 | 0.3473 | 1.0000 | |
| 10 | 0.3129 | 0.9080 | 1.4142 | 1.7820 | 1.9754 | 1.9754 | 1.7820 | 1.4142 | 0.9080 | 0.3129 | 1.0000 |

**Figure 5-18** Attenuation behavior of maximally flat low-pass filter versus normalized frequency.

with A_1 and A_2 being arbitrary constants. The associated group delay t_g is

$$t_g = \frac{d\phi(\Omega)}{d\Omega} = A_1[1 + A_2(2N + 1)\Omega^{2N}] \quad (5.37)$$

In Table 5-3, the first 10 coefficients for a linear phase response with group delay $t_g = 1$ are listed.

Since steep filter transition and linear phase are generally competing requirements, it has to be expected that the shape factor is reduced. The question of how a linear phase design based on Table 5-3 compares with a standard design of Table 5-2 is discussed in Example 5-3 for the case $N = 3$.

Table 5-3 Coefficients for linear phase low-pass filter ($N = 1$ to 10).

| N | g_1 | g_2 | g_3 | g_4 | g_5 | g_6 | g_7 | g_8 | g_9 | g_{10} | g_{11} |
|-----|--------|--------|--------|--------|--------|--------|--------|--------|--------|----------|----------|
| 1 | 2.0000 | 1.0000 | | | | | | | | | |
| 2 | 1.5774 | 0.4226 | 1.0000 | | | | | | | | |
| 3 | 1.2550 | 0.5528 | 0.1922 | 1.0000 | | | | | | | |
| 4 | 1.0598 | 0.5116 | 0.3181 | 0.1104 | 1.0000 | | | | | | |
| 5 | 0.9303 | 0.4577 | 0.3312 | 0.2090 | 0.0718 | 1.0000 | | | | | |
| 6 | 0.8377 | 0.4116 | 0.3158 | 0.2364 | 0.1480 | 0.0505 | 1.0000 | | | | |
| 7 | 0.7677 | 0.3744 | 0.2944 | 0.2378 | 0.1778 | 0.1104 | 0.0375 | 1.0000 | | | |
| 8 | 0.7125 | 0.3446 | 0.2735 | 0.2297 | 0.1867 | 0.1387 | 0.0855 | 0.0289 | 1.0000 | | |
| 9 | 0.6678 | 0.3203 | 0.2547 | 0.2184 | 0.1859 | 0.1506 | 0.1111 | 0.0682 | 0.0230 | 1.0000 | |
| 10 | 0.6305 | 0.3002 | 0.2384 | 0.2066 | 0.1808 | 0.1539 | 0.1240 | 0.0911 | 0.0557 | 0.0187 | 1.0000 |

5.2.2 Chebyshev-Type Filters

The design of an equi-ripple filter type is based on an insertion loss whose functional behavior is described by the **Chebyshev polynomials** $T_N(\Omega)$ in the following form:

$$IL = 10\log\{LF\} = 10\log\{1 + a^2 T_N^2(\Omega)\} \quad (5.38)$$

where

$$T_N(\Omega) = \cos\{N[\cos^{-1}(\Omega)]\}, \text{ for } |\Omega| \leq 1$$

$$T_N(\Omega) = \cosh\{N[\cosh^{-1}(\Omega)]\}, \text{ for } |\Omega| \geq 1$$

To appreciate the behavior of the Chebyshev polynomials in the normalized frequency range $-1 < \Omega < 1$, we list the first five terms:

$$T_0 = 1, T_1 = \Omega, T_2 = -1 + 2\Omega^2, T_3 = -3\Omega + 4\Omega^3, T_4 = 1 - 8\Omega^2 + 8\Omega^4$$

The functional behavior of the first two terms is a constant and a linear function, and the subsequent three terms are quadratic, cubic, and fourth-order functions, as seen in Figure 5-19.

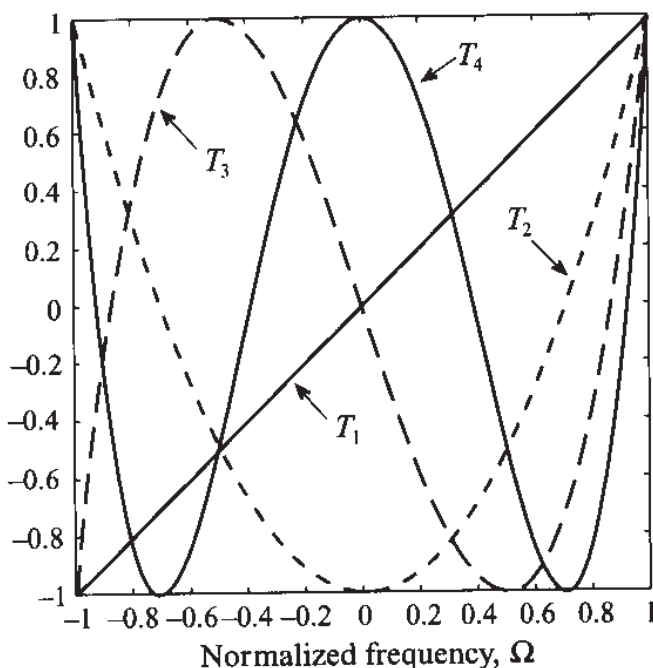


Figure 5-19 Chebyshev polynomials $T_1(\Omega)$ through $T_4(\Omega)$ in the normalized frequency range $-1 \leq \Omega \leq 1$.

It can be observed that all polynomials oscillate within a ± 1 interval, a fact that is exploited in the equi-ripple design. The magnitude of the transfer function $|H(j\Omega)|$ is obtained from the Chebyshev polynomial as follows:

$$|H(\Omega)| = \sqrt{H(\Omega)H(\Omega)^*} = \frac{1}{\sqrt{1 + a^2 T_N^2(\Omega)}} \quad (5.39)$$

where $T_N(\Omega)$ is the Chebyshev polynomial of order N and a is a constant factor that allows us to control the height of the passband ripples. For instance, if we choose $a = 1$, then at $\Omega = 1$ we have

$$|H(0)| = \frac{1}{\sqrt{2}} = 0.707$$

which is the 3 dB level that applies uniformly throughout the passband (equiripple). We do not go any further into the general theory of Chebyshev filter design, but rather refer the reader to a classical textbook that covers this topic comprehensively (see Matthaei et al.).

In Figure 5-20 the loss factor and insertion loss are plotted for a Chebyshev filter with coefficient $a = 1$, which again results in a 3 dB attenuation response at resonance frequency ($\Omega = 1$).

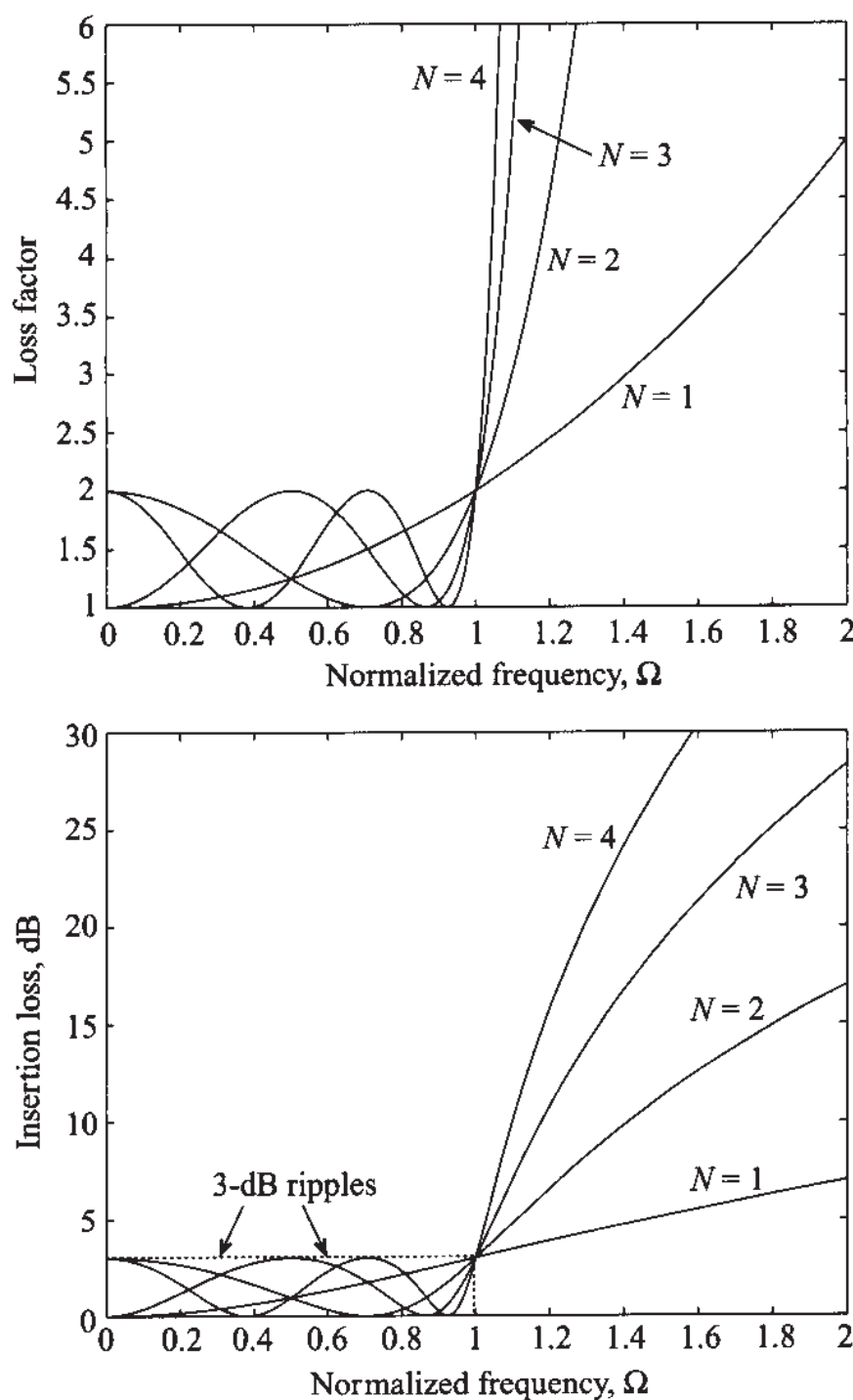


Figure 5-20 Frequency dependence of the loss factor and insertion loss of the Chebyshev low-pass filter.

As mentioned, the magnitude of the ripple can be controlled by suitably choosing factor a . Since Chebyshev polynomials oscillate in the range from -1 to $+1$ for $-1 \leq \Omega \leq 1$, the squared value of these polynomials will change from 0 to $+1$ in the same frequency range. Therefore, in the frequency range of $-1 \leq \Omega \leq 1$ the minimum attenuation that is introduced by the filter is 0 dB and the maximum attenuation, or equivalently the magnitude of the ripples, is $IL = 10\log(1 + a^2)$. Thus, if the desired magnitude of the ripples is denoted as RPL_{dB} , then a should be chosen as

$$a = \sqrt{10^{RPL_{dB}/10} - 1}$$

For instance, to obtain a ripple level of 0.5 dB we have to select $a = (10^{0.5/10} - 1)^{1/2} = 0.3493$. The associated attenuation profiles for the first 10 orders are shown in Figure 5-21 for a 3 dB ripple, and in Figure 5-22 for a 0.5 dB ripple.

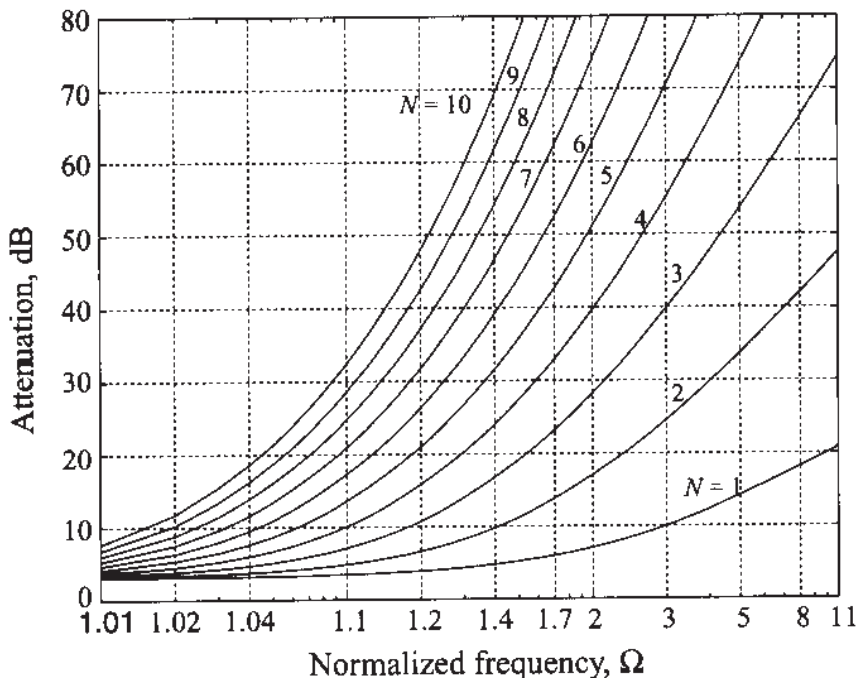


Figure 5-21 Attenuation response for 3 dB Chebyshev design.

Upon comparing Figure 5-21 with 5-22, it is apparent that the disadvantage of a higher ripple in the passband has as an advantage a steeper transition to the stopband. For instance, a fifth-order, 3 dB ripple Chebyshev filter design at $\Omega = 1.2$ has an attenuation of 20 dB, whereas the same order 0.5 dB ripple filter reaches only 12 dB at the same frequency point. The trend remains the same for higher frequencies and different orders. As a case in point, at $\Omega = 5$ the fourth-order, 0.5 dB filter has an attenuation of 65 dB compared with the 3 dB design, which has an attenuation of approximately 73 dB.

With reference to the prototype filter circuit, Figure 5-17, the corresponding coefficients are listed in Table 5-4.

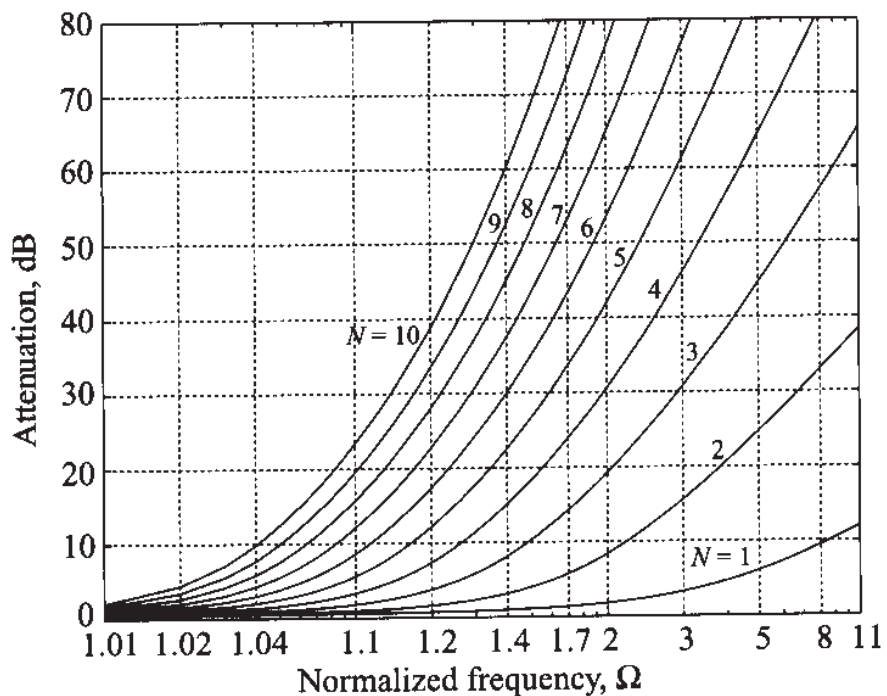


Figure 5-22 Attenuation response for 0.5 dB Chebyshev design.

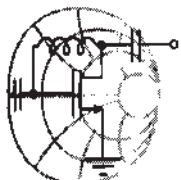
Table 5-4 (a) Chebyshev filter coefficients; 3 dB filter design ($N = 1$ to 10)

| N | g_1 | g_2 | g_3 | g_4 | g_5 | g_6 | g_7 | g_8 | g_9 | g_{10} | g_{11} |
|-----|--------|--------|--------|--------|--------|--------|--------|--------|--------|----------|----------|
| 1 | 1.9953 | 1.0000 | | | | | | | | | |
| 2 | 3.1013 | 0.5339 | 5.8095 | | | | | | | | |
| 3 | 3.3487 | 0.7117 | 3.3487 | 1.0000 | | | | | | | |
| 4 | 3.4389 | 0.7483 | 4.3471 | 0.5920 | 5.8095 | | | | | | |
| 5 | 3.4817 | 0.7618 | 4.5381 | 0.7618 | 3.4817 | 1.0000 | | | | | |
| 6 | 3.5045 | 0.7685 | 4.6061 | 0.7929 | 4.4641 | 0.6033 | 5.8095 | | | | |
| 7 | 3.5182 | 0.7723 | 4.6386 | 0.8039 | 4.6386 | 0.7723 | 3.5182 | 1.0000 | | | |
| 8 | 3.5277 | 0.7745 | 4.6575 | 0.8089 | 4.6990 | 0.8018 | 4.4990 | 0.6073 | 5.8095 | | |
| 9 | 3.5340 | 0.7760 | 4.6692 | 0.8118 | 4.7272 | 0.8118 | 4.6692 | 0.7760 | 3.5340 | 1.0000 | |
| 10 | 3.5384 | 0.7771 | 4.6768 | 0.8136 | 4.7425 | 0.8164 | 4.7260 | 0.8051 | 4.5142 | 0.6091 | 5.8095 |

Table 5-4 (b) Chebyshev filter coefficients; 0.5 dB filter design ($N = 1$ to 10)

| N | g_1 | g_2 | g_3 | g_4 | g_5 | g_6 | g_7 | g_8 | g_9 | g_{10} | g_{11} |
|----|--------|--------|--------|--------|--------|--------|--------|--------|--------|----------|----------|
| 1 | 0.6986 | 1.0000 | | | | | | | | | |
| 2 | 1.4029 | 0.7071 | 1.9841 | | | | | | | | |
| 3 | 1.5963 | 1.0967 | 1.5963 | 1.0000 | | | | | | | |
| 4 | 1.6703 | 1.1926 | 2.3661 | 0.8419 | 1.9841 | | | | | | |
| 5 | 1.7058 | 1.2296 | 2.5408 | 1.2296 | 1.7058 | 1.0000 | | | | | |
| 6 | 1.7254 | 1.2479 | 2.6064 | 1.3137 | 2.4758 | 0.8696 | 1.9841 | | | | |
| 7 | 1.7372 | 1.2583 | 2.6381 | 1.3444 | 2.6381 | 1.2583 | 1.7372 | 1.0000 | | | |
| 8 | 1.7451 | 1.2647 | 2.6564 | 1.3590 | 2.6964 | 1.3389 | 2.5093 | 0.8796 | 1.9841 | | |
| 9 | 1.7504 | 1.2690 | 2.6678 | 1.3673 | 2.7939 | 1.3673 | 2.6678 | 1.2690 | 1.7504 | 1.0000 | |
| 10 | 1.7543 | 1.2721 | 2.6754 | 1.3725 | 2.7392 | 1.3806 | 2.7231 | 1.3485 | 2.5239 | 0.8842 | 1.9841 |

Unlike the previously discussed Butterworth filter, the Chebyshev filter approach provides us with a steeper passband/stopband transition. For higher normalized frequencies $\Omega \gg 1$, the Chebyshev polynomials $T_N(\Omega)$ can be approximated as $(1/2)(2\Omega)^N$. This means that the filter has an improvement in attenuation of roughly $(2^{2N})/4$ over the Butterworth design.

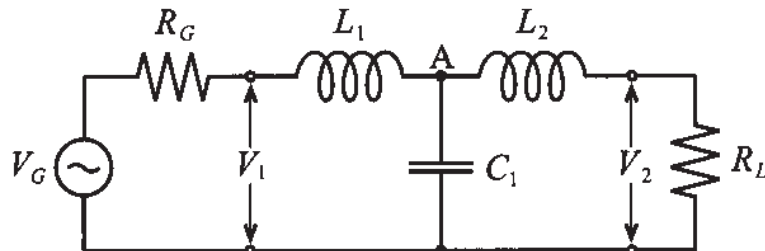


RF & MW →

Example 5-3: Comparison between Butterworth, linear phase Butterworth, and Chebyshev filters

Compare the attenuation versus frequency behavior of the third-order low-pass filter for (a) standard 3 dB Butterworth, (b) linear phase Butterworth, and (c) 3 dB Chebyshev design.

Solution: If we choose the first element of the filter to be an inductor connected in series with the source, then the circuit topology of the third order filter is given by



where the inductances and the capacitor are obtained from Tables 5-2, 5-3, and 5-4. Specifically,

- Standard Butterworth: $L_1 = L_2 = 1 \text{ H}$, $C_1 = 2 \text{ F}$
- Linear phase Butterworth: $L_1 = 1.255 \text{ H}$, $C_1 = 0.5528 \text{ F}$, $L_2 = 0.1922 \text{ H}$
- 3 dB Chebyshev filter: $L_1 = L_2 = 3.3487 \text{ H}$, $C_1 = 0.7117 \text{ F}$
- generator and load: $R_G = R_L = 1 \Omega$

As we can see from the preceding circuit diagram, under DC condition the inductances become short circuits and the capacitor acts like an open circuit. The voltage across the load is equal to one-half of the voltage at the source due to the voltage divider formed by the load and source impedances (i.e. $V_2 = 0.5V_G$). When the frequency is not equal to zero the voltage across the load can be obtained by applying the voltage divider rule twice; first, to obtain the voltage at node A:

$$V_A = \frac{Z_C \parallel (Z_{L_2} + R_L)}{Z_C \parallel (Z_{L_2} + R_L) + Z_{L_1} + R_G} V_G$$

and, second, to obtain the voltage across the load with reference to V_A :

$$V_2 = \frac{R_L}{R_L + Z_{L_2}} V_A$$

where $Z_C = R_G + j\omega L_1$. If we find the ratio of the circuit gain at AC to the gain under DC conditions, it is possible to compute the attenuation that is introduced by the filter:

$$\alpha = 2 \frac{R_L}{R_L + Z_{L_2}} \frac{Z_C \parallel (Z_{L_2} + R_L)}{Z_C \parallel (Z_{L_2} + R_L) + Z_{L_1} + R_G}$$

The graph of the attenuation coefficient expressed in dB for the three filter realizations is shown in Figure 5-23. As expected, the Chebyshev filter has the steepest slope of the attenuation profile, while the linear phase filter exhibits the lowest roll-off with fre-

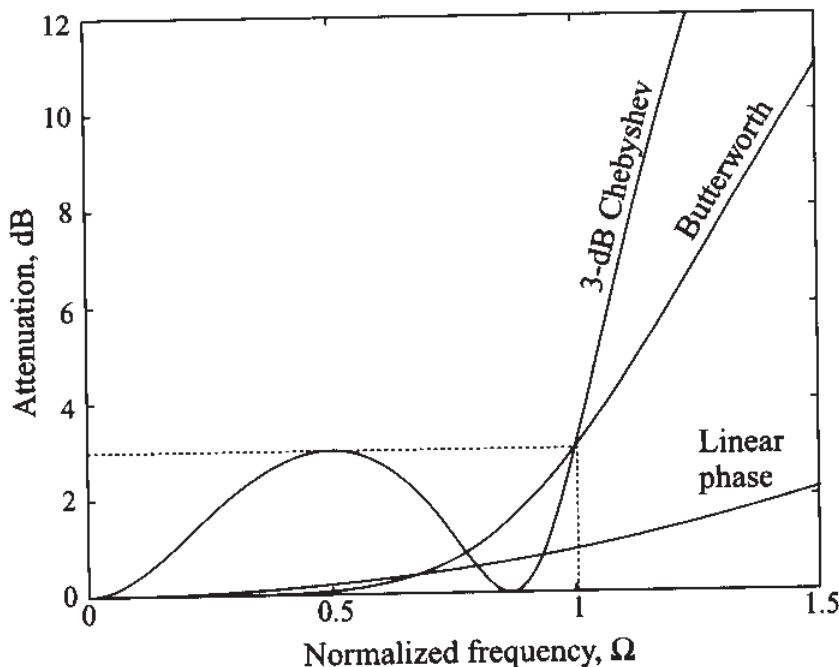


Figure 5-23 Comparison of the frequency response of the Butterworth, linear phase, and 3-dB Chebyshev third-order filters.

quency. Therefore, if a sharp transition from passband to stopband is required, and ripples can be tolerated, the most appropriate choice would be a Chebyshev filter implementation. We also note that the attenuation of the Chebyshev filter at cut-off frequency is equal to the ripple size in the passband.

Even though the linear phase Butterworth filter suffers from a shallow transition, it is the linear phase that makes it particularly attractive for modulation and mixer circuits.

5.2.3 Denormalization of Standard Low-Pass Design

To arrive at realizable filters, we have to denormalize the aforementioned coefficients to meet realistic frequency and impedance requirements. In addition, the standard low-pass filter prototype should be convertible into high-pass or bandpass/bandstop filter types depending on the application. Those objectives can be achieved by considering two distinct steps:

- **Frequency transformation** to convert from normalized frequency Ω to actual frequency ω . This step implies the scaling of the standard inductances and capacitances.
- **Impedance transformation** to convert standard generator and load resistances g_0 and $g_{(N+1)}$ to actual resistances R_L and R_G .

We begin by examining the frequency transformation and its implications in terms of the various filter types. To eliminate confusing notation, we drop the index denoting individual components (i.e., $L_n(n = 1, \dots, N) \rightarrow L$ and $C_n(n = 1, \dots, N) \rightarrow C$). This makes sense since the transformation rules to be developed will be applicable to all components equally.

Frequency Transformation

A standard fourth-order low-pass Chebyshev filter with 3 dB ripples in the passband response is shown in Figure 5-24, where we have included negative frequencies to display more clearly the symmetry of the attenuation profile in the frequency domain. Furthermore, by appropriately scaling and shifting, we notice that all four filter types, Figures 5-25, 5-26, 5-28, and 5-29, can be generated. This is now examined in detail.

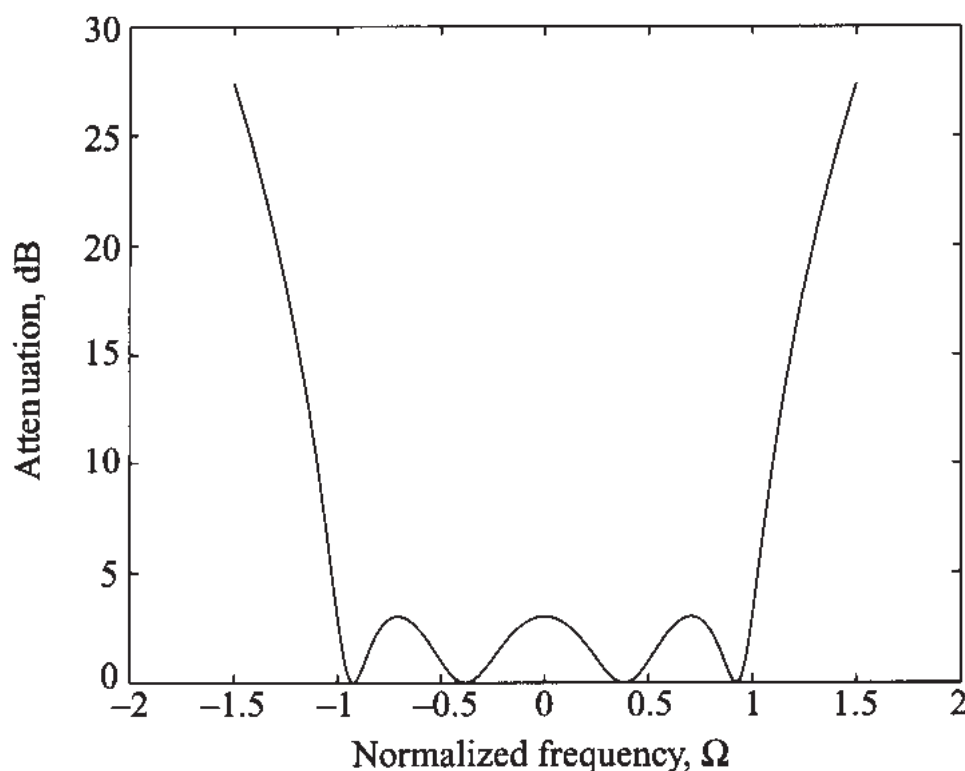


Figure 5-24 Fourth-order low-pass Chebyshev filter with 3 dB ripples in the passband.

For the *low-pass filter* we see that a simple multiplication by the angular cut-off frequency ω_c accomplishes the desired scaling (see Figure 5-25):

$$\omega = \Omega\omega_c \quad (5.40)$$

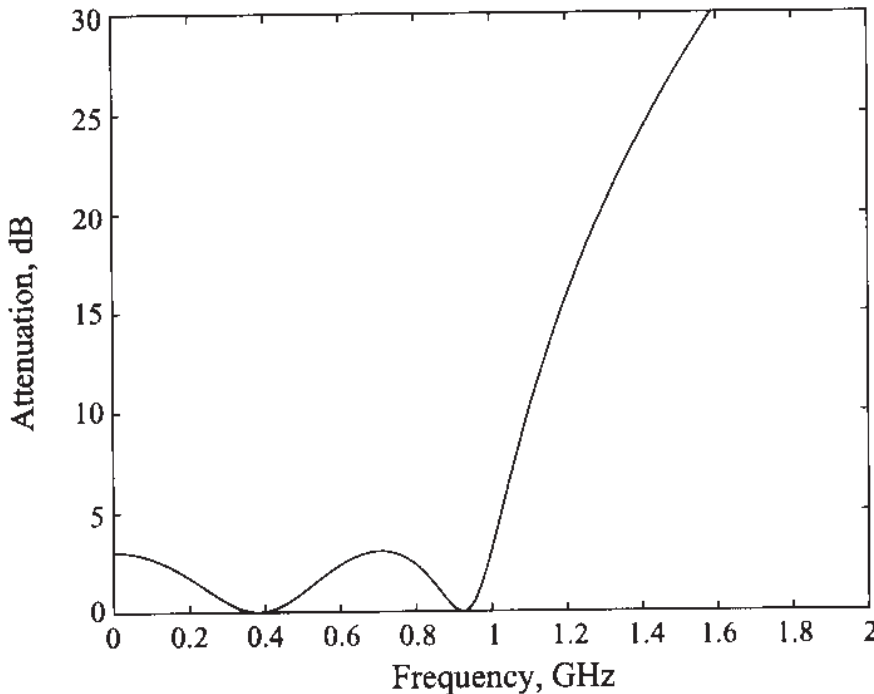


Figure 5-25 Conversion of standard low-pass filter prototype into low-pass realization. Cut-off frequency is $f_c = 1$ GHz.

For the scaling we picked an arbitrary cut-off frequency of 1 GHz. In the corresponding insertion loss and loss factor expressions, Ω is simply replaced by $\Omega\omega_c$. For the inductive and capacitive elements, we have to compare normalized with actual reactances:

$$jX_L = j\Omega L = j(\omega/\omega_c)L = j\omega\tilde{L} \quad (5.41a)$$

$$jX_c = \frac{1}{j\Omega C} = \frac{1}{j(\omega/\omega_c)C} = \frac{1}{j\omega\tilde{C}} \quad (5.41b)$$

This reveals that the actual inductance and capacitance \tilde{L} and \tilde{C} are computed from the normalized L and C as

$$\tilde{L} = L/\omega_c \quad (5.42a)$$

$$\tilde{C} = C/\omega_c \quad (5.42b)$$

For the *high-pass filter* the parabolically shaped frequency response has to be mapped into a hyperbolic frequency domain behavior. This can be accomplished through the transformation

$$\omega = \frac{-\omega_c}{\Omega} \quad (5.43)$$

The correctness of this transformation is immediately apparent when the normalized cut-off frequency $\Omega = \pm 1$ is substituted in (5.43). This assigns the actual cut-off frequency $\omega = \mp\omega_c$ to the high-pass filter, consistent with Figure 5-26.

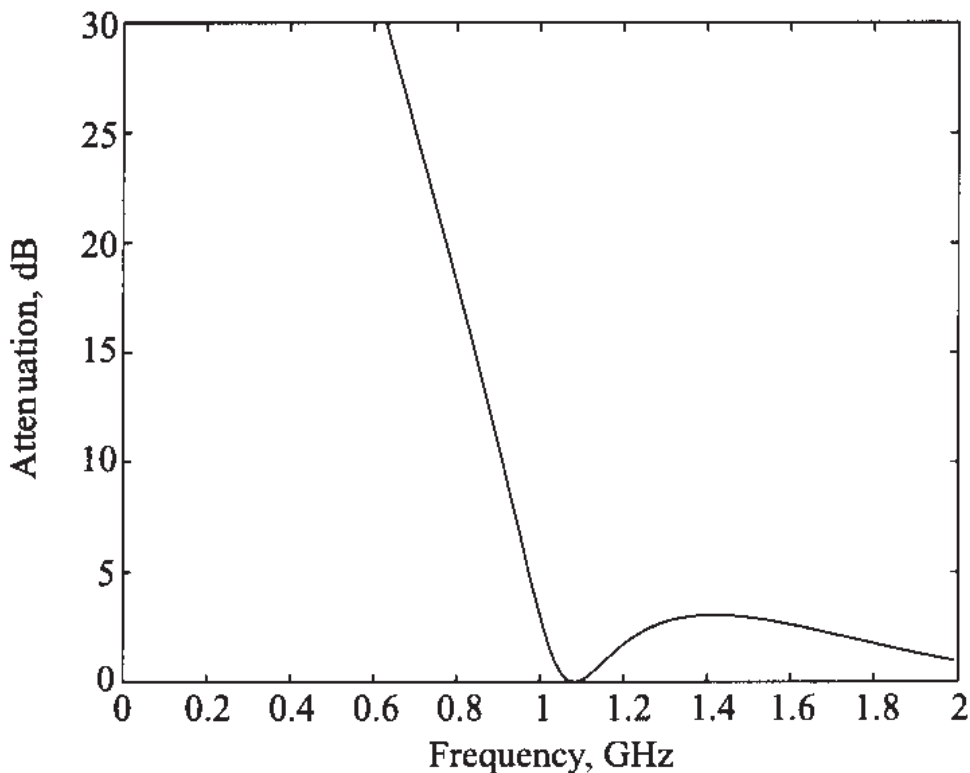


Figure 5-26 Conversion of standard low-pass filter prototype into high-pass realization. Cut-off frequency is $f_c = 1$ GHz.

Care has to be exercised in de-normalizing the circuit parameters. We note

$$jX_L = j\Omega L = -j\frac{\omega_c}{\omega}L = \frac{1}{j\omega\tilde{C}} \quad (5.44a)$$

$$jX_c = \frac{1}{j\Omega C} = -\frac{\omega}{j\omega_c C} = j\omega\tilde{L} \quad (5.44b)$$

Thus, it follows that

$$\tilde{C} = \frac{1}{\omega_c L} \quad (5.45a)$$

$$\tilde{L} = \frac{1}{\omega_c C} \quad (5.45b)$$

This makes intuitive sense since it is known from fundamental circuit theory that a first-order high-pass filter can be obtained from a low-pass filter by replacing the inductors with capacitors or vice versa. Equations (5.45) are the logical extension to higher-order filters.

The *bandpass filter* requires a more sophisticated transformation. In addition to scaling, we also have to shift the standard low-pass filter response. The mapping from the normalized frequency Ω to the actual frequency ω is best explained by considering Figure 5-27.

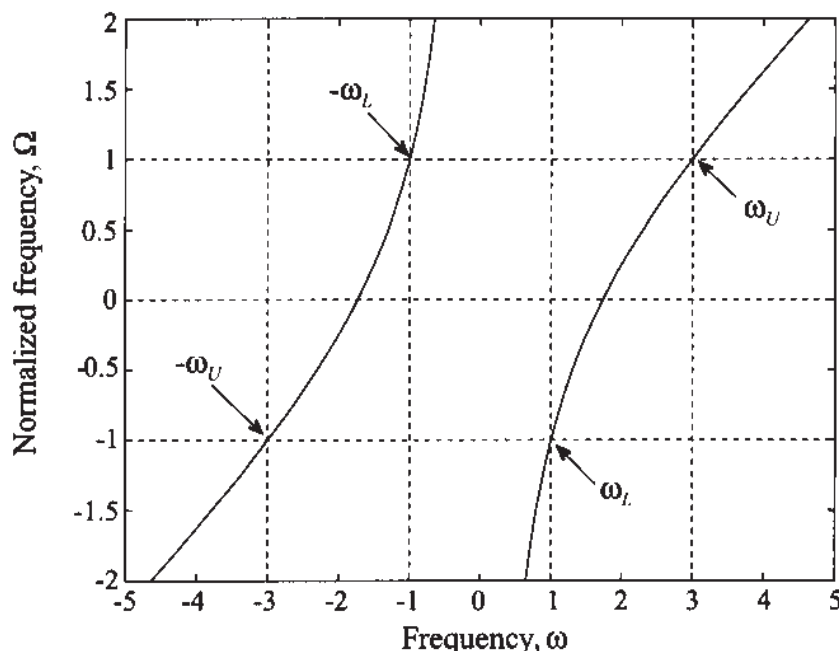


Figure 5-27 Mapping from standard frequency Ω into actual frequency ω . Lower cut-off frequency is $\omega_L = 1$ and upper cut-off frequency is $\omega_U = 3$.

The functional relation that achieves scaling and shifting is

$$\Omega = \frac{1}{\omega_U/\omega_c - \omega_L/\omega_c} \left(\frac{\omega}{\omega_c} - \frac{1}{\omega/\omega_c} \right) = \frac{\omega_c}{\omega_U - \omega_L} \left(\frac{\omega}{\omega_c} - \frac{\omega_c}{\omega} \right) \quad (5.46)$$

where the upper and lower frequencies ω_U , ω_L define the bandwidth expressed in rad/s ($BW = \omega_U - \omega_L$) of the passband located at $\omega_c = \omega_0$. In other words, the cut-off frequency ω_c now defines the center frequency ω_0 as mentioned earlier. Using ω_0 and (5.23), it is possible to rewrite (5.46) as

$$\Omega = \frac{\omega_0}{\omega_U - \omega_L} \epsilon \quad (5.47)$$

The upper and lower frequencies are the inverse of each other:

$$\frac{\omega_U}{\omega_0} = \frac{\omega_0}{\omega_L} \quad (5.48)$$

a fact that can be employed to specify the center frequency as the geometric mean of the upper and lower frequencies, $\omega_0 = \sqrt{\omega_U \omega_L}$. The mapping of this transformation is verified if we first consider $\Omega = 1$. Equation (5.46) is unity for $\omega = \omega_U$ and $\omega = \omega_L$. For $\Omega = 0$ we obtain $\omega = \pm\omega_0$. The frequency transformations are therefore as follows:

$$0 \leq \Omega \leq 1 \rightarrow \omega_0 \leq \omega \leq \omega_U$$

$$-1 \leq \Omega \leq 0 \rightarrow \omega_L \leq \omega \leq -\omega_0$$

The result of this transformation applied to the low-pass filter prototype is shown in Figure 5-28.

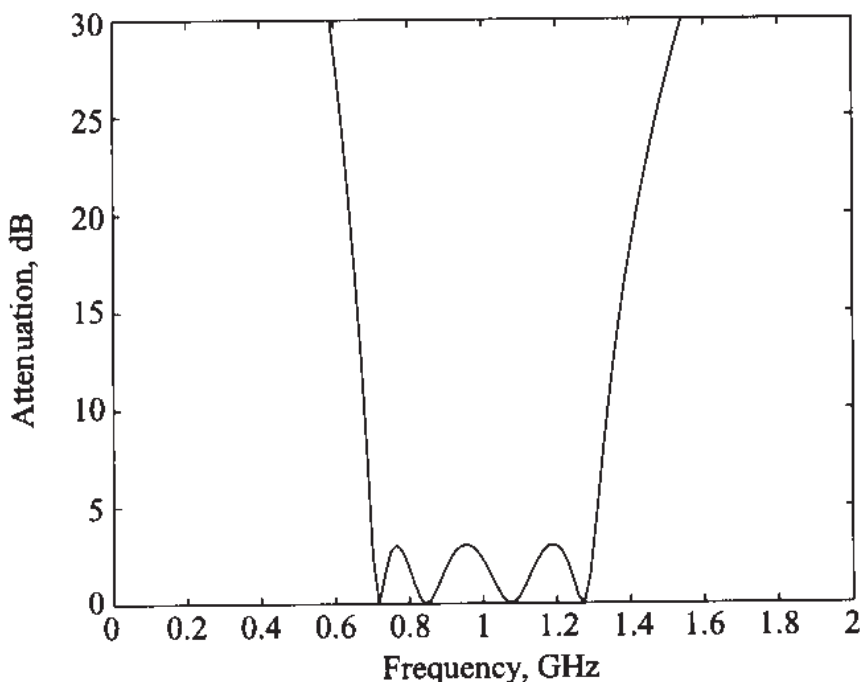


Figure 5-28 Conversion of standard low-pass filter prototype into bandpass realization with lower cut-off frequency $f_L = 0.7$ GHz, upper cut-off frequency $f_U = 1.3$ GHz, and center frequency of $f_0 = 1$ GHz.

The circuit parameters are next transformed according to the assignment

$$jX_L = j\Omega L = j\left(\frac{\omega_0}{\omega_U - \omega_L}\epsilon\right)L = j\omega\tilde{L} + \frac{1}{j\omega\tilde{C}} \quad (5.49)$$

which yields for the series inductor L in (5.49) the denormalized series inductor \tilde{L}

$$\tilde{L} = \frac{L}{\omega_U - \omega_L} \quad (5.50a)$$

and the denormalized series capacitance \tilde{C}

$$\tilde{C} = \frac{\omega_U - \omega_L}{\omega_0^2 L} \quad (5.50b)$$

The shunt capacitor is transformed based on the equation

$$jB_C = j\Omega C = j\left(\frac{\omega_0}{\omega_U - \omega_L}\epsilon\right)C = j\omega\tilde{C} + \frac{1}{j\omega\tilde{L}} \quad (5.51)$$

to the following two shunt elements:

$$\tilde{L} = \frac{\omega_U - \omega_L}{\omega_0^2 C} \quad (5.52a)$$

$$\tilde{C} = \frac{C}{\omega_U - \omega_L} \quad (5.52b)$$

Referring to Figure 5-17, we see that a normalized inductor is transformed into a series inductor and capacitor with values given by (5.50). On the other hand, the normalized capacitor is transformed into shunt inductor and capacitor, whose values are stated by (5.52).

The *bandstop filter* transformation rules are not explicitly derived, since they can be developed through an inverse transform of (5-47) or by using the previously derived high-pass filter and applying (5.49). In either case, we find for the series inductor the series combination

$$\tilde{L} = (\omega_U - \omega_L)L/\omega_0^2 \quad (5.53a)$$

$$\tilde{C} = 1/[(\omega_U - \omega_L)L] \quad (5.53b)$$

and for the shunt capacitor the shunt combination

$$\tilde{L} = 1/[(\omega_U - \omega_L)C] \quad (5.54a)$$

$$\tilde{C} = (\omega_U - \omega_L)C/\omega_0^2 \quad (5.54b)$$

The resulting frequency response for the band-stop filter is shown in Figure 5-29.

Table 5-5 summarizes the conversion from the standard low-pass filter to the four filter realizations.

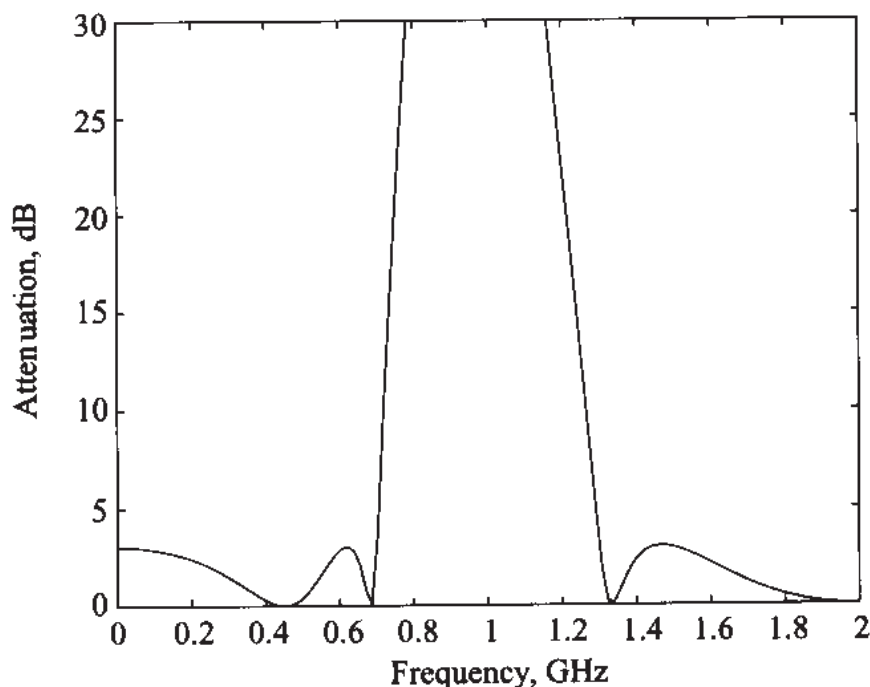


Figure 5-29 Conversion of standard low-pass filter prototype into band-stop realization with center frequency of $f_0 = 1$ GHz. Lower cut-off frequency is $f_L = 0.7$ GHz and upper cut-off frequency is $f_U = 1.3$ GHz.

Table 5-5 Transformation between normalized low-pass filter and actual bandpass and bandstop filter ($BW = \omega_U - \omega_L$)

| Low-pass prototype | Low-pass | High-pass | Bandpass | Bandstop |
|--------------------|----------------------|------------------------|---|---|
| $L = g_k$ | $\frac{L}{\omega_c}$ | $\frac{1}{\omega_c L}$ | $\frac{L}{BW}$ $\frac{BW}{\omega_0^2 L}$ | $\frac{1}{(BW)L}$ $\frac{(BW)L}{\omega_0^2}$ |
| $C = g_k$ | $\frac{C}{\omega_c}$ | $\frac{1}{\omega_c C}$ | $\frac{C}{BW}$ $\frac{BW}{\omega_0^2 C}$ | $\frac{1}{(BW)C}$ $\frac{(BW)C}{\omega_0^2}$ |

Impedance transformation

In the original filter prototype shown in Figure 5-17 we have unit source and load resistances except for the even-numbered Chebyshev filter coefficients listed in Table 5-4. If, however, either the generator resistance g_0 or the load resistance R_L is required to be unequal to unity, we need to scale the entire impedance expression. This is accomplished by scaling all filter coefficients by the actual resistance R_G . That is,

$$\tilde{R}_G = 1R_G \quad (5.55a)$$

$$\tilde{L} = LR_G \quad (5.55b)$$

$$\tilde{C} = \frac{C}{R_G} \quad (5.55c)$$

$$\tilde{R}_L = R_L R_G \quad (5.55d)$$

where the tilde expressions are again the resulting actual parameters and L , C , and R_L are the values of the original prototype.

In Example 5-4 we demonstrate the design of a Chebyshev bandpass filter based on the low-pass prototype.

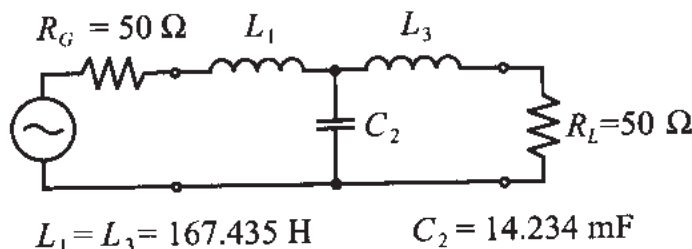


Example 5-4: Chebyshev bandpass filter design

An $N = 3$ Chebyshev bandpass filter is to be designed with a 3 dB passband ripple for a communication link. The center frequency is at 2.4 GHz and the filter has to meet a bandwidth requirement of 20%. The filter has to be inserted into a 50Ω characteristic line impedance. Find the inductive and capacitive elements and plot the attenuation response in the frequency range 1 to 4 GHz.

Solution: From Table 5-4(a) we find that the coefficients for a standard low-pass $N = 3$ Chebyshev filter with 3 dB ripples in the pass-band are $g_0 = g_4 = 1$, $g_1 = g_3 = 3.3487$, and $g_2 = 0.7117$. In this filter prototype we assumed that both generator and load impedances are equal to unity. In our problem, however, we have to match the filter to 50Ω line impedances. Thus we must

apply scaling as described by (5.55). The resulting circuit is shown in the following figure:



This is still a low-pass filter with cut-off frequency of $\omega_c = 1$ or $f_c = 1/(2\pi) = 0.159 \text{ Hz}$. We can next apply the frequency transformation to change the low-pass filter into a bandpass filter:

$$\omega_U = 1.1(2\pi 2.4 \times 10^9) = 16.59 \times 10^9$$

$$\omega_L = 0.9(2\pi 2.4 \times 10^9) = 13.57 \times 10^9$$

and

$$\omega_0 = \sqrt{\omega_L \omega_U} = 15 \times 10^9$$

The actual inductive and capacitive values are defined in (5.50) and (5.52):

$$\tilde{L}_1 = \tilde{L}_3 = \frac{L_1}{\omega_U - \omega_L} = 55.5 \text{ nH}$$

$$\tilde{C}_1 = \tilde{C}_3 = \frac{\omega_U - \omega_L}{\omega_0^2 L_1} = 80 \text{ fF}$$

$$\tilde{L}_2 = \frac{\omega_U - \omega_L}{\omega_0^2 C_2} = 0.94 \text{ nH}$$

$$\tilde{C}_2 = \frac{C_2}{\omega_U - \omega_L} = 4.7 \text{ pF}$$

The final circuit is shown in Figure 5-30 together with the resulting graph for the attenuation response.

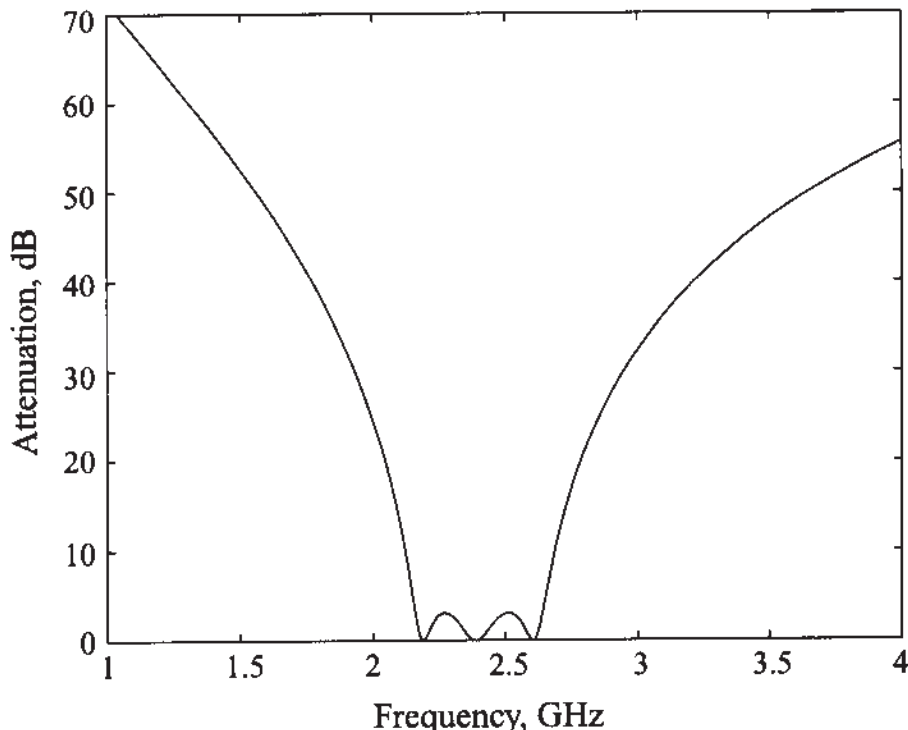
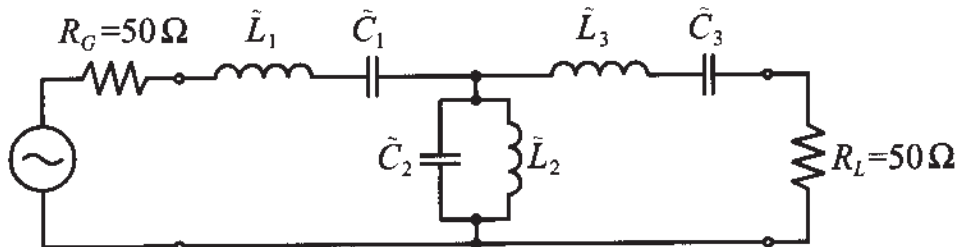


Figure 5-30 Attenuation response of a third-order 3-dB ripple bandpass Chebyshev filter centered at 2.4 GHz. The lower cut-off frequency is $f_L = 2.16$ GHz and the upper cut-off frequency is $f_U = 2.64$ GHz.

The filter design becomes almost a cook-book approach if we start from the standard low-pass filter and subsequently apply the appropriate frequency transformation and component scaling.

5.3 Filter Implementation

Filter designs beyond 500 MHz are difficult to realize with discrete components because the wavelength becomes comparable with the physical filter element dimensions, resulting in various losses severely degrading the circuit performance. Thus, to arrive at practical filters, the lumped component filters discussed in Section 5.2 must be

converted into distributed element realizations. In this section, some of the necessary tools are introduced—namely, Richards transformation, the concept of the unit element, and Kuroda's identities.

To accomplish the conversion between lumped and distributed circuit designs, Richards proposed a special transformation that allows open- and short-circuit transmission line segments to emulate the inductive and capacitive behavior of the discrete components. We recall that the input impedance Z_{in} of a short-circuit transmission line ($Z_L = 0$) of characteristic line impedance Z_0 is purely reactive:

$$Z_{in} = jZ_0 \tan(\beta l) = jZ_0 \tan\theta \quad (5.56)$$

Here, the electric length θ can be rewritten in such a way as to make the frequency behavior explicit. If we pick the line length to be $\lambda_0/8$ at a particular reference frequency $f_0 = v_p/\lambda_0$, the electric length becomes

$$\theta = \beta \frac{\lambda_0}{8} = \frac{2\pi f}{v_p} \frac{v_p}{8f_0} = \frac{\pi f}{4f_0} = \frac{\pi}{4}\Omega \quad (5.57)$$

By substituting (5.57) into (5.56), a direct link between the frequency-dependent inductive behavior of the transmission line and the lumped element representation can be established:

$$jX_L = j\omega L \equiv jZ_0 \tan\left(\frac{\pi}{4}\Omega\right) = jZ_0 \tan\left(\frac{\pi}{4}\Omega\right) = SZ_0 \quad (5.58)$$

where $S = j\tan(\pi\Omega/4)$ is the actual Richards transform. The capacitive lumped element effect can be replicated through the open-circuit transmission line section

$$jB_C = j\omega C \equiv jY_0 \tan\left(\frac{\pi}{4}\Omega\right) = SY_0 \quad (5.59)$$

Thus, Richards transformation allows us to replace lumped inductors with short-circuit stubs of characteristic impedance $Z_0 = L$ and capacitors with open-circuit stubs of characteristic impedance $Z_0 = 1/C$.

It is interesting to note that the choice of $\lambda_0/8$ as line length is somewhat arbitrary. Indeed, several authors use $\lambda_0/4$ as the basic length. However, $\lambda_0/8$ is more convenient since it results in smaller physical circuits and the cut-off frequency point in the standard low-pass filter response is preserved (i.e., $S = j1$ for $f = f_0 = f_c$). In

In Section 5.5.3 we will encounter a bandstop filter that requires a $\lambda_0/4$ line length to meet the expected attenuation profile.

Richards transformation maps the lumped element frequency response in the range of $0 \leq f < \infty$ into the range $0 \leq f \leq 4f_0$ due to the periodic behavior of the tangent function and the fact that all lines are $\lambda_0/8$ in length, a property that is known as **commensurate line length**. To obtain the inductive responses, we need to restrict the domain to $0 \leq f \leq 2f_0$. Because of this periodic property, the frequency response of such a filter cannot be regarded as broadband.

5.3.1 Unit Elements

When converting lumped elements into transmission line sections, there is a need to separate the transmission line elements spatially to achieve practically realizable configurations. This is accomplished by inserting so-called **unit elements** (UEs). The unit element has an electric length of $\theta = \frac{\pi}{4}(f/f_0)$ and a characteristic impedance Z_{UE} . The two-port network expression in chain parameter representation is immediately apparent from our discussion in Chapter 4. We recall that the transmission line representation is

$$[UE] = \begin{bmatrix} A_{UE} & B_{UE} \\ C_{UE} & D_{UE} \end{bmatrix} = \begin{bmatrix} \cos\theta & jZ_{UE}\sin\theta \\ j\sin\theta & \cos\theta \end{bmatrix} = \frac{1}{\sqrt{1-S^2}} \begin{bmatrix} 1 & Z_{UE}S \\ S & 1 \end{bmatrix} \quad (5.60)$$

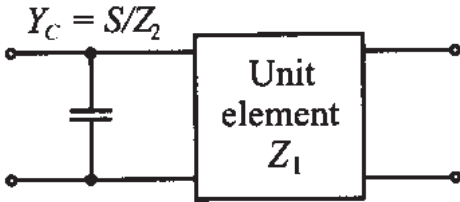
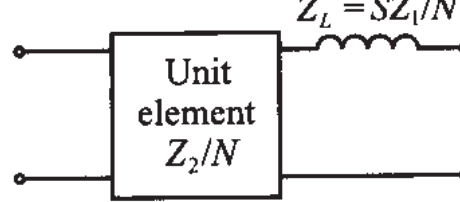
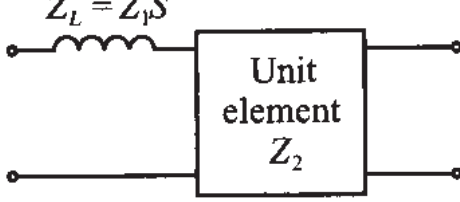
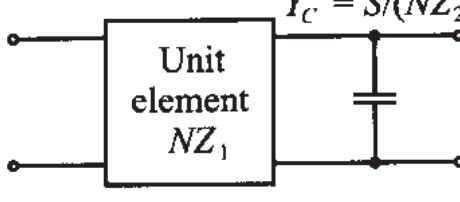
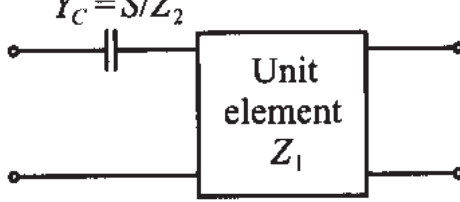
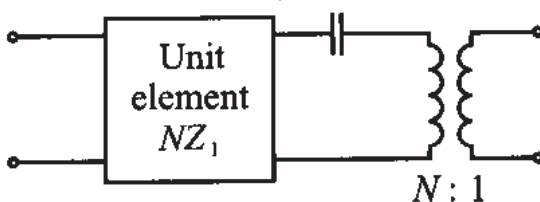
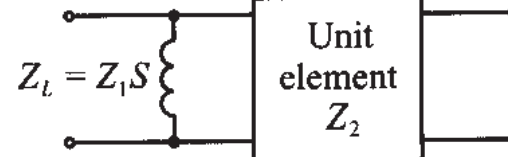
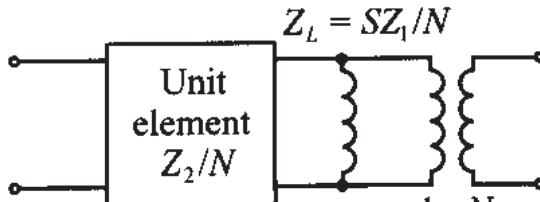
where the definition of S is given by (5.58). The use of the unit elements is discussed best by way of a few examples, as presented in Section 5.3.4.

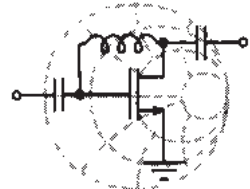
5.3.2 Kuroda's Identities

In addition to the unit element, it is important to be able to convert a practically difficult-to-implement design to a more suitable filter realization. For instance, a series inductance implemented by a short-circuit transmission line segment is more complicated to realize than a shunt stub line. To facilitate the conversion between the various transmission line realizations, Kuroda has developed four identities which are summarized in Table 5-6.

We should note that in Table 5-6 all inductances and capacitances are represented by their equivalent Richards transformations. As an example we will prove one of the identities and defer proof of the remaining identities to the problems at the end of this chapter.

Table 5-6 Kuroda's Identities

| Initial Circuit | Kuroda's Identity |
|--|---|
| $Y_C = S/Z_2$  | $Z_L = SZ_1/N$  |
| $Z_L = Z_p S$  | $Y_C = S/(NZ_2)$  |
| $Y_C = S/Z_2$  | $Y_C = S/(NZ_2)$  |
| $Z_L = Z_1 S$  | $Z_L = SZ_1/N$  |
| $N = 1 + Z_2/Z_1$ | |



RF & MW →

Example 5-5: Prove the fourth of Kuroda's identities from Table 5-6

Solution: It is convenient to employ chain parameter representation of the shunt connected inductor (see Table 4-1 for the corresponding ABCD-matrix) and the unit element as given in (5.60) to write the left-hand side as follows:

$$\begin{bmatrix} A & B \\ C & D \end{bmatrix}_L = \begin{bmatrix} 1 & 0 \\ \frac{1}{SZ_1} & 1 \end{bmatrix} \frac{1}{\sqrt{1-S^2}} \begin{bmatrix} 1 & Z_2S \\ \frac{S}{Z_2} & 1 \end{bmatrix} = \frac{1}{\sqrt{1-S^2}} \begin{bmatrix} 1 & Z_2S \\ \frac{1}{SZ_1} + \frac{S}{Z_2} & 1 + \frac{Z_2}{Z_1} \end{bmatrix}$$

Similarly, we can write the ABCD-matrix for Kuroda's fourth identity, or the right-hand side:

$$\begin{bmatrix} A & B \\ C & D \end{bmatrix}_R = \frac{1}{\sqrt{1-S^2}} \begin{bmatrix} 1 & \frac{Z_2S}{N} \\ \frac{SN}{Z_2} & 1 \end{bmatrix}_{UE} \begin{bmatrix} 1 & 0 \\ \frac{N}{SZ_1} & 1 \end{bmatrix}_{ind} \begin{bmatrix} 1/N & 0 \\ 0 & N \end{bmatrix}_{trans}$$

where subscripts *UE*, *ind*, and *trans* indicate chain parameter matrices for unit element, inductor, and transformer, respectively. After carrying out the multiplication between the matrices, we obtain the following ABCD-matrix describing Kuroda's identity:

$$\begin{bmatrix} A & B \\ C & D \end{bmatrix}_R = \frac{1}{\sqrt{1-S^2}} \begin{bmatrix} \frac{1}{N} \left(1 + \frac{Z_2}{Z_1} \right) & Z_2S \\ \frac{S}{Z_2} + \frac{1}{SZ_1} & N \end{bmatrix}$$

which is identical with the left-hand side, if we set $N = 1 + Z_2/Z_1$. The remaining three Kuroda identities can be proved in a similar fashion.

We see again the importance of the ABCD network representation, which allows us to directly multiply the individual element networks.

5.3.3 Examples of Microstrip Filter Design

In the following two examples we will concentrate on the design of a low-pass bandstop filter. The bandstop design will be conducted based on the aforementioned Richards transformation followed by employing Kudora's identities. Specifically, the bandstop design requires some attention in converting from lumped to distributed elements.

The practical filter realization proceeds in four steps:

1. Select the normalized filter parameters to meet the design criteria.
2. Replace the inductances and capacitances by equivalent $\lambda_0/8$ transmission lines.
3. Convert series stub lines to shunt stubs through Kudora's identities.
4. De-normalize and select equivalent microstrip lines (length, width, and dielectric constant).

Specifically, step 4 requires knowledge of the appropriate geometric dimensions of the respective microstrip lines, a subject that is discussed in detail in Chapter 2. According to these four steps, let us now discuss the two examples.

The first design task involves a low-pass filter which is formulated as follows:

Project I

Design a low-pass filter whose input and output are matched to a 50Ω impedance and that meets the following specifications: cut-off frequency of 3 GHz; equi-ripple of 0.5 dB; and rejection of at least 40 dB at approximately twice the cut-off frequency. Assume a dielectric material that results in a phase velocity of 60% of the speed of light.

In solving this problem, we proceed according to the previously outlined four steps.

Step 1 From Figure 5-22, it is seen that the filter has to be of order $N = 5$, with coefficients

$$g_1 = 1.7058 = g_5, g_2 = 1.2296 = g_4, g_3 = 2.5408, g_6 = 1.0$$

The normalized low-pass filter is given in Figure 5-31.

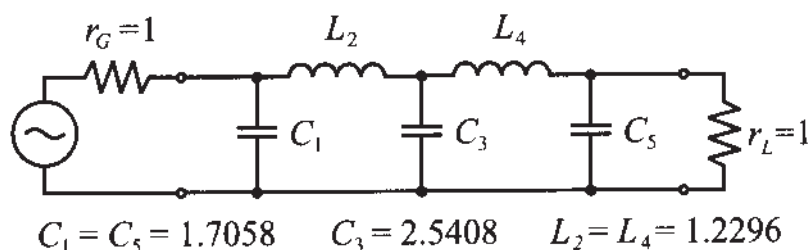


Figure 5-31 Normalized low-pass filter of order $N = 5$.

Step 2 The inductances and capacitances in Figure 5-31 are replaced by open and short circuit series and shunt stubs as shown in Figure 5-32. This is a direct consequence of applying Richards transformation (5.58) and (5.59). The characteristic line impedances and admittances are

$$Y_1 = Y_5 = g_1, Y_3 = g_3, Z_2 = Z_4 = g_4$$

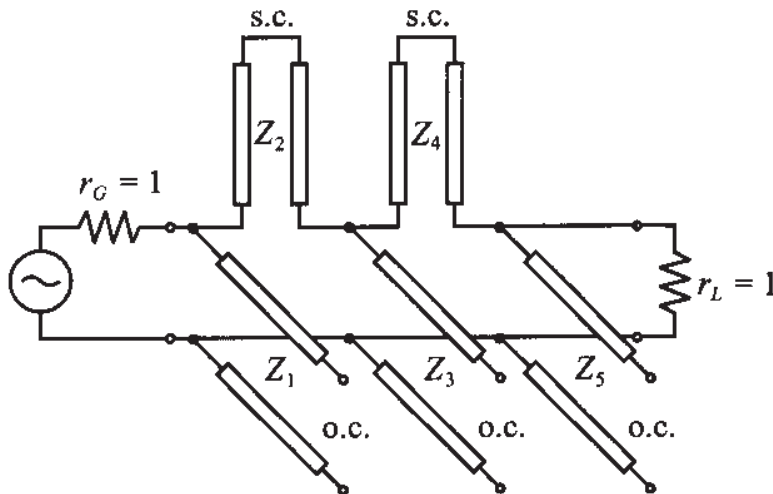


Figure 5-32 Replacing inductors and capacitors by series and shunt stubs (o.c. = open circuit line, s.c. = short circuit line).

Step 3 To match source and load sides, and to make the filter realizable, unit elements are introduced with the intent to apply the first and second of Kudora's identities (see Table 5-6) to convert all series stubs into shunt stubs. Since we have a fifth-order filter we must deploy a total of four unit elements to convert all series connected short-circuited stubs into shunt connected open-circuit stubs. To clarify this process we divide this step into several substeps.

First, we introduce two unit elements on the input and output ends of the filter, as shown in Figure 5-33.

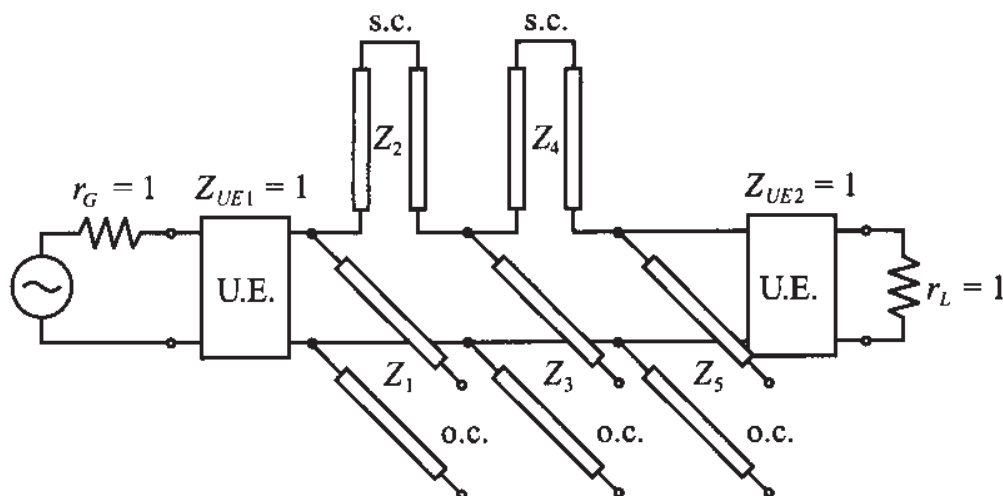


Figure 5-33 Deployment of the first set of unit elements (U.E. = unit element).

The introduction of unit elements does not affect the filter performance since they are matched to source and load impedances. The result of applying Kuroda's identities to the first and last shunt stubs is shown in Figure 5-34.

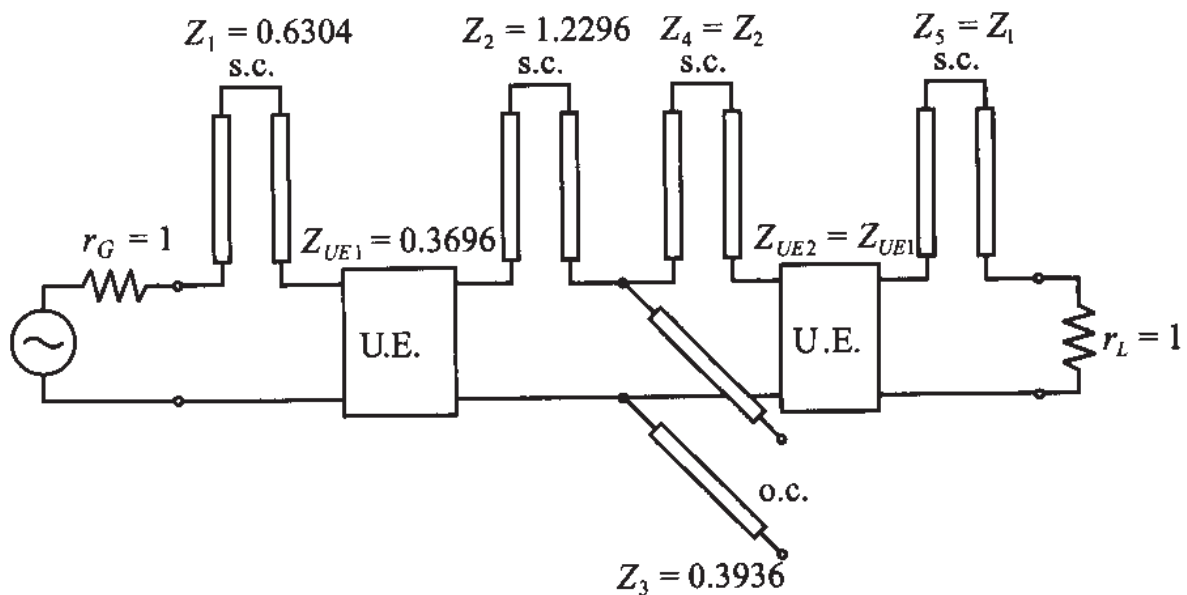


Figure 5-34 Converting shunt stubs to series stubs.

This version of the circuit is still nonrealizable because we have four series stubs. To convert them to shunt connections, we have to deploy two more unit elements, as shown in Figure 5-35.

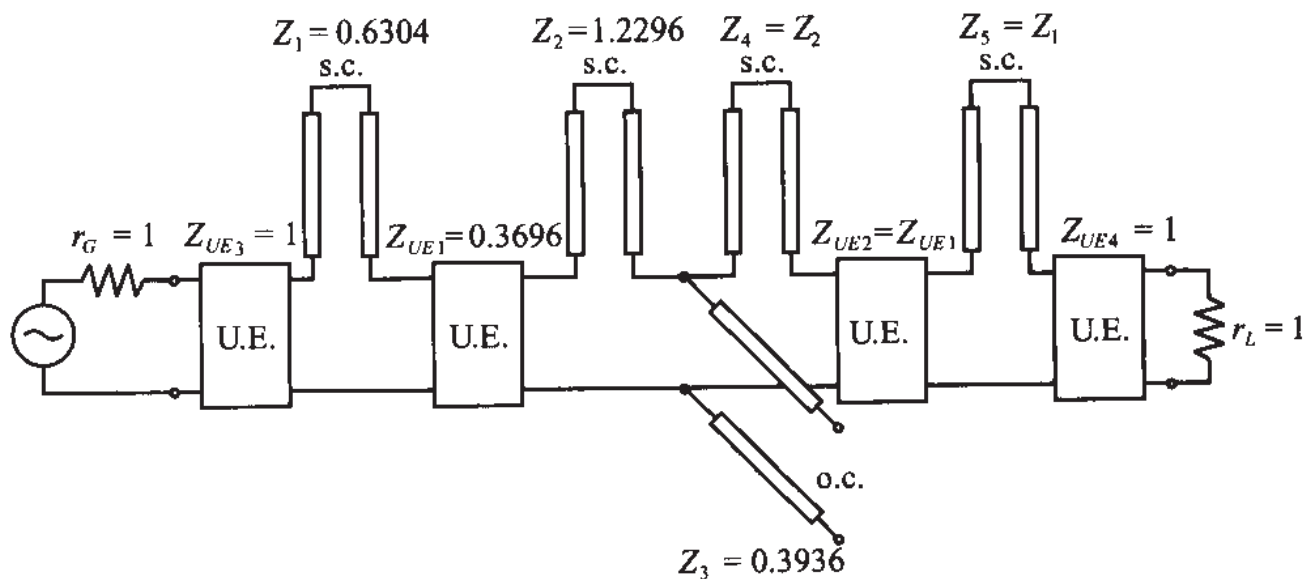


Figure 5-35 Deployment of the second set of unit elements to the fifth-order filter.

Again, the introduction of unit elements does not affect the performance of the filter since they are matched to the source and load impedances. Applying Kuroda's identities to the circuit shown in Figure 5-35, we finally arrive at the realizable filter design, depicted in Figure 5-36.

Step 4 De-normalization involves scaling the unit elements to the 50Ω input and output impedances and computing the length of the lines based on (5.57). Using

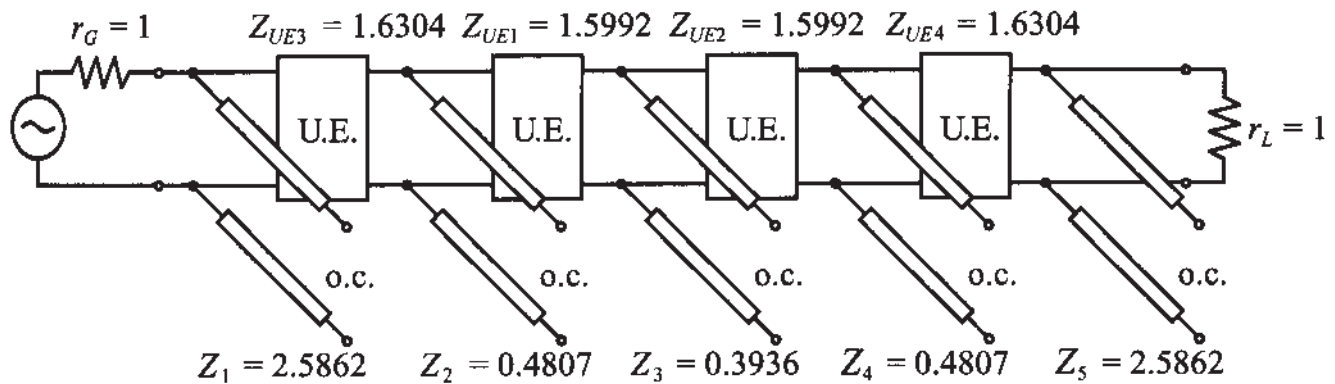


Figure 5-36 Realizable filter circuit obtained by converting series and shunt stubs using Kuroda's identities.

$v_p = 0.6c = 1.8 \times 10^8$ m/s, the length is found to be $l = (\lambda_0/8) = v_p/(8f_0) = 7.5$ mm. The final design implemented in microstrip lines is shown in Figure 5-37(a). Figure 5-37(b) plots the attenuation profile in the frequency range 0 to 3.5 GHz. We notice that the passband ripple does not exceed 0.5 dB up to the cut-off frequency of 3 GHz.

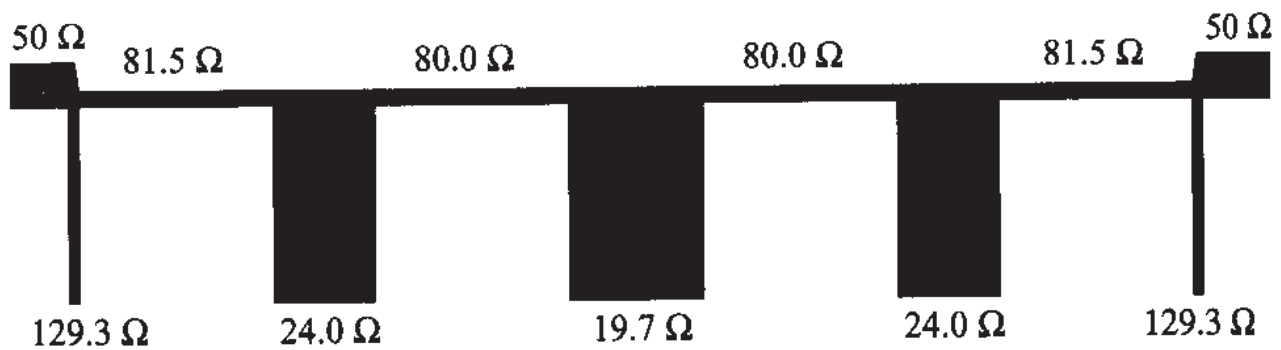
The second design project involves a more complicated bandstop filter, which requires the transformation of the standard low-pass prototype with a unity cut-off frequency into a design with specified center frequency and lower and upper 3 dB frequency points.

Project II

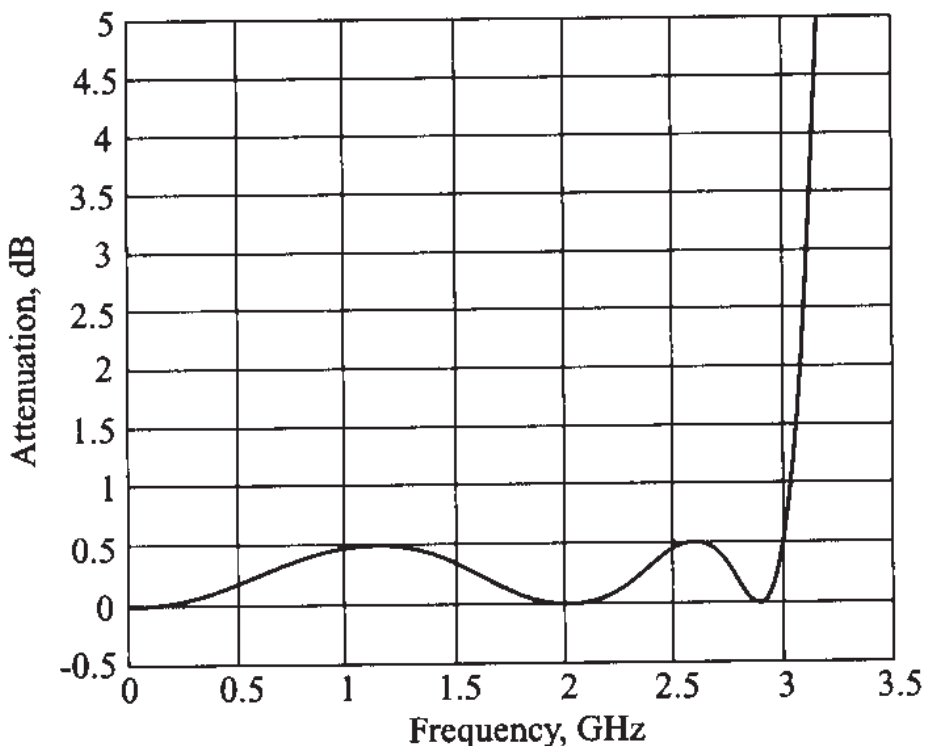
Design a maximally flat third-order **bandstop filter** whose input and output are matched to a 50Ω impedance that meets the following design specifications: center frequency of 4 GHz and bandwidth of 50%. Again, we assume a dielectric material that results in a phase velocity of 60% of the speed of light.

This design requires a careful analysis when converting from lumped to distributed elements. Specifically, when dealing with bandstop designs, we require either maximal or minimal impedance at the center frequency f_0 depending on whether series or shunt connections are involved. With our previous definition of Richards transformation based on $\lambda_0/8$ line segments, we encounter the difficulty that at $f = f_0$, (5.58) yields a tangent value of 1, and not a maximum. However, if a line length of $\lambda_0/4$ is used, then the tangent will go to infinity as required for a bandstop design. Another aspect that we have to take into account is the fact that we want the $\Omega = 1$ cut-off frequency of the low-pass prototype filter to be transformed into lower and upper cut-off frequencies of the bandstop filter. This is done by introducing a so-called **bandwidth factor** bf .

$$bf = \cot\left(\frac{\pi}{2} \frac{\omega_L}{\omega_0}\right) = \cot\left[\frac{\pi}{2} \left(1 - \frac{sbw}{2}\right)\right] \quad (5.61)$$



(a) Microstrip line low-pass filter implementation



(b) Attenuation versus frequency response

Figure 5-37 Final microstrip line low-pass filter.

where $sbw = (\omega_U - \omega_L)/\omega_0$ is the **stopband width** and $\omega_0 = (\omega_U + \omega_L)/2$ is the center frequency. Multiplying the Richards transformation for $\lambda_0/4$ line lengths by bf at the lower or upper frequency points reveals that the magnitude of the product is equal to unity. For instance, for the lower frequency point ω_L , it follows that

$$(bf)S|_{\omega = \omega_L} = \cot\left(\frac{\pi\omega_L}{2\omega_0}\right)\tan\left(\frac{\pi\omega_L}{2\omega_0}\right) \equiv 1$$

This corresponds to a $\Omega = 1$ cut-off frequency in the normalized low-pass filter response. Similarly, for the upper cut-off frequency ω_U we have

$$(bf)S|_{\omega = \omega_U} = \cot\left(\frac{\pi\omega_L}{2\omega_0}\right)\tan\left(\frac{\pi\omega_U}{2\omega_0}\right) = \cot\left(\frac{\pi\omega_L}{2\omega_0}\right)\tan\left[\frac{\pi}{2}\left(\frac{2\omega_0 - \omega_L}{\omega_0}\right)\right] \equiv -1$$

which corresponds to a $\Omega = -1$ cut-off frequency in the normalized low-pass filter. With these preliminary remarks, we are now ready to proceed according to the four steps.

Step 1 From Table 5-2, the coefficients for a maximally flat normalized low-pass filter prototype of third order are

$$g_1 = 1.0 = g_3, g_2 = 2.0, g_4 = 1.0$$

Thus, the normalized low-pass filter has the form shown in Figure 5-38.

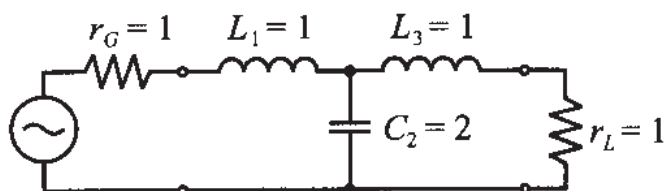


Figure 5-38 Normalized third-order low-pass filter.

Step 2 The inductances and capacitances in Figure 5-38 are replaced by open and short circuit series and shunt stubs, as depicted in Figure 5-39. The line impedances and the admittance are multiplied by the bandwidth factor (5.61).

$$Z_1 = Z_3 = bf \cdot g_1, \quad Y_2 = bf \cdot g_2$$

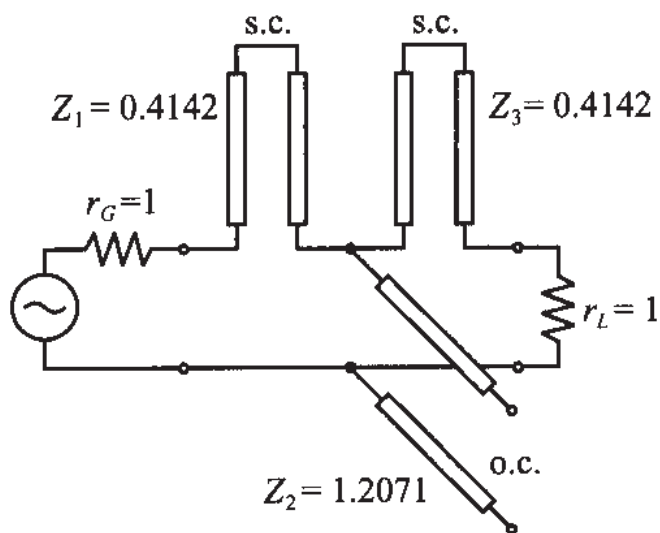


Figure 5-39 Replacing inductors and capacitors by series and shunt stubs.

Step 3 Unit elements of $\lambda_0/4$ line length are inserted and Kudora's identity is used to convert all series stubs into shunt stubs as seen in Figure 5-40.

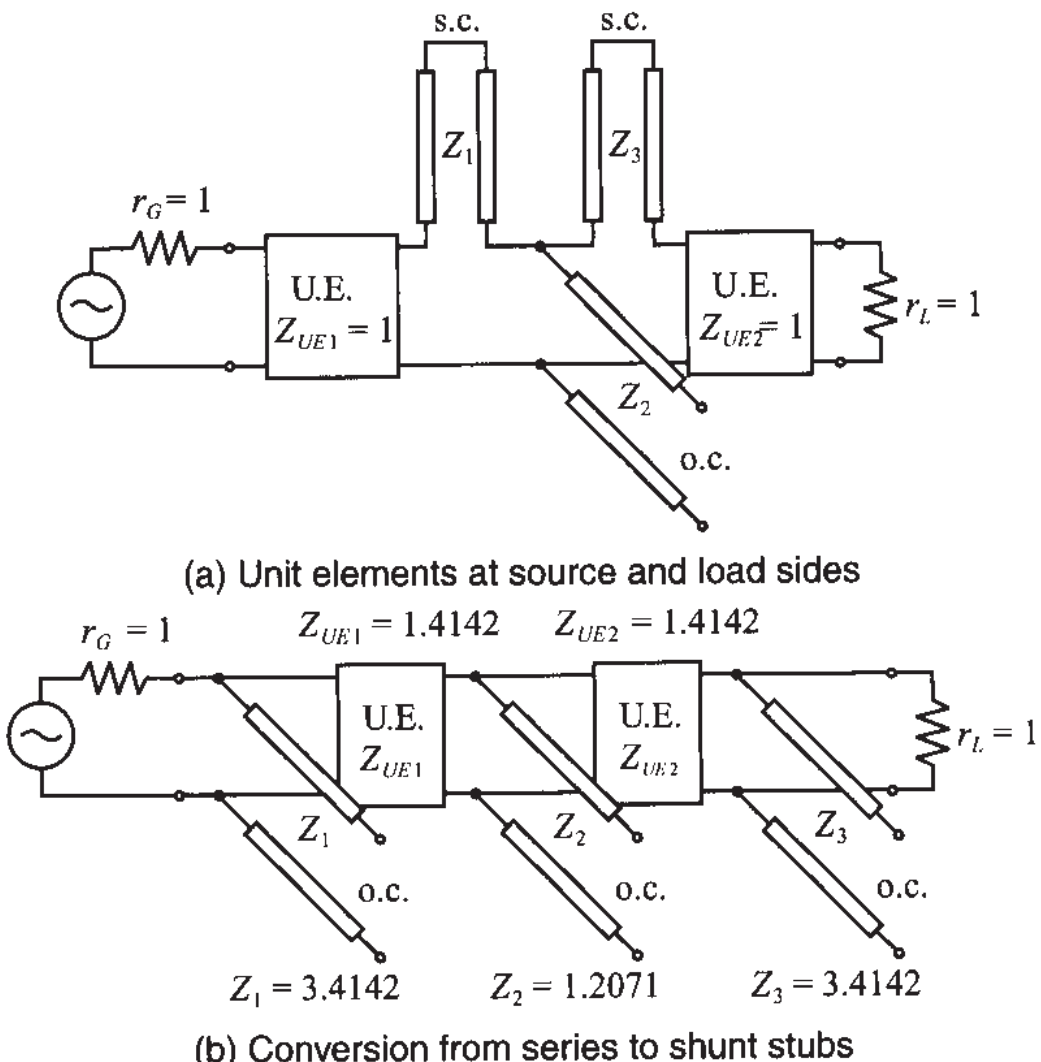


Figure 5-40 Introducing unit elements and converting series stubs to shunt stubs.

Step 4 De-normalization the unit elements and explicit computation of the individual line lengths can now be conducted. Using the phase velocity $v_p = 0.6c = 1.8 \times 10^8 \text{ m/s}$, the length is computed to be $l = (\lambda_0/4) = v_p/(4f_0) = 15 \text{ mm}$. Thus, the resulting design in microstrip line implementation is as shown in Figure 5-41.

Finally, for this bandstop filter we can also utilize a commercial simulation package such as MMICAD to simulate the filter response of the microstrip line configuration shown in Figure 5-41. The attenuation profile is given in Figure 5-42, and shows that the filter specifications are met.

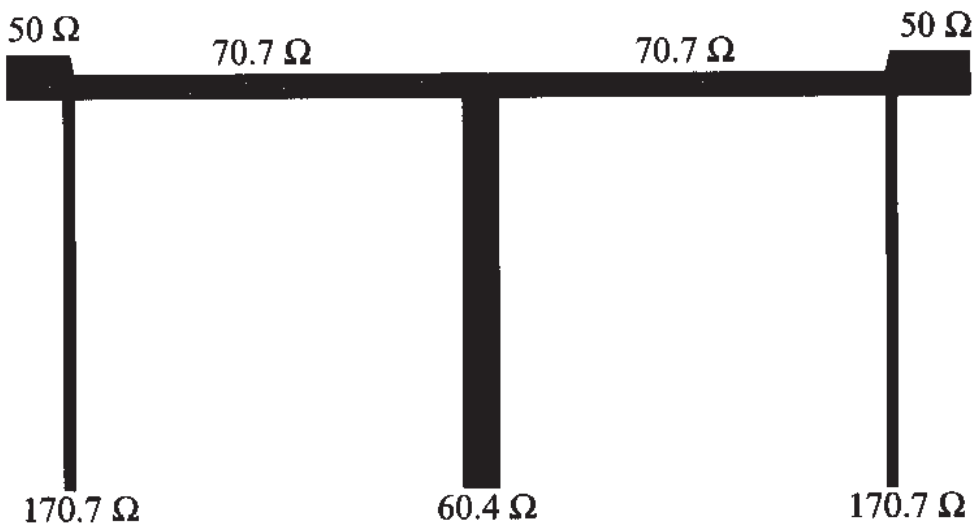


Figure 5-41 Characteristic impedances of final microstrip line implementation of bandstop filter design.

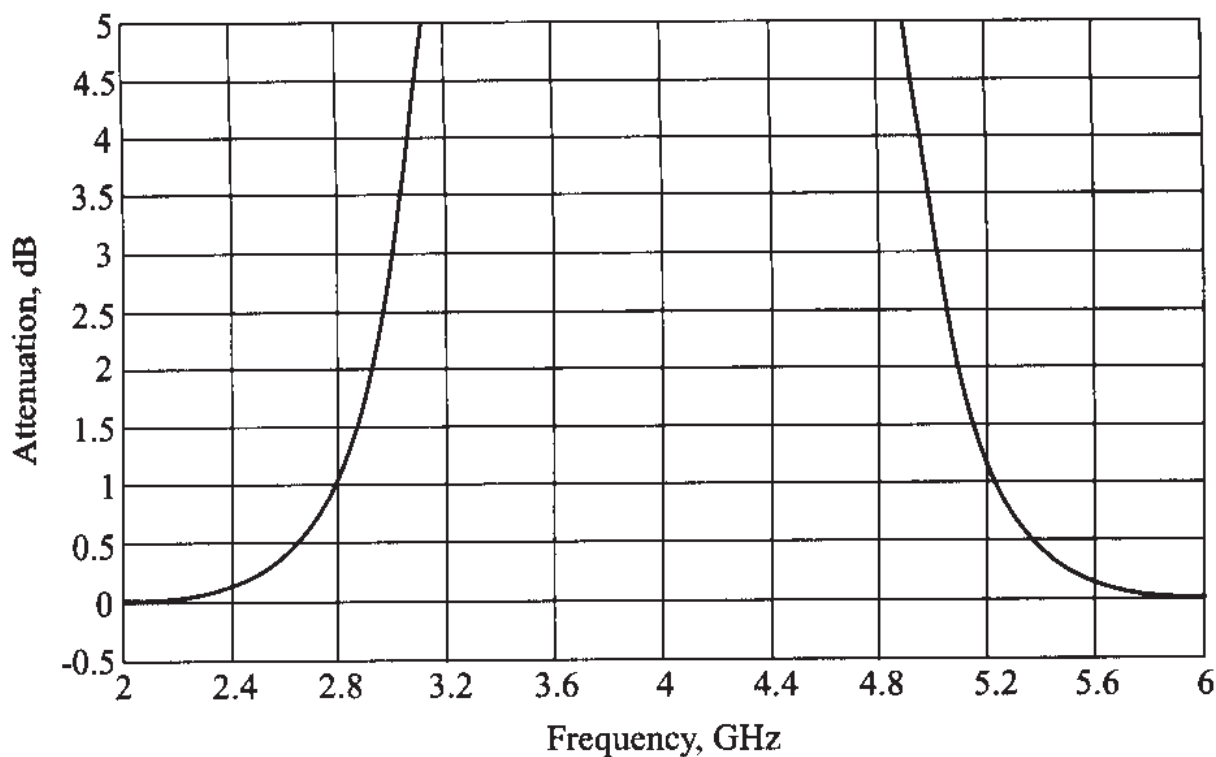


Figure 5-42 Attenuation versus frequency response for third-order bandstop filter.

5.4 Coupled Filter

The literature is extensive when dealing with coupled filter designs and analyses. For our cursory treatment we will introduce only the most salient points and refer the reader to the references listed at the end of this chapter.

Our discussion briefly covers the odd and even wave coupling of transmission lines through a common ground plane, which results in odd and even characteristic line

impedances. This sets the stage to an understanding of the coupling between two strip lines and their input/output impedances as part of a two-port chain matrix representation. Cascading these elements gives rise to bandpass filter structures that are most easily designed with the aid of RF circuit simulation packages.

5.4.1 Odd and Even Mode Excitation

A simple modeling approach of coupled microstrip line interaction is established when considering the geometry depicted in Figure 5-43. The configuration consists of two lines separated over a distance S and attached to a dielectric medium of thickness d and dielectric constant ϵ_r . The strip lines are W wide, and the thickness is negligible when compared with d . The capacitive and inductive coupling phenomena between the lines and ground is schematically given in Figure 5-44. Here equal indices denote self-capacitances and inductances, whereas index 12 stands for coupling between line 1 and line 2 (which is equal to coupling between line 2 and line 1).

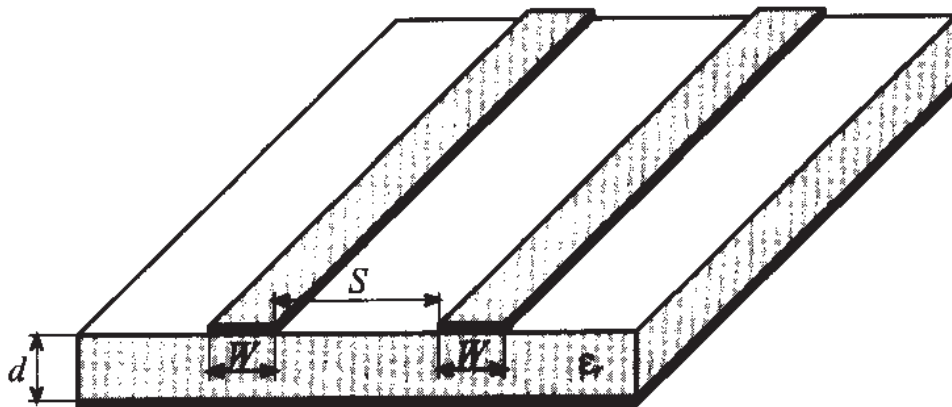


Figure 5-43 Coupled microstrip lines.

We can now define an even mode voltage V_e and current I_e and an odd mode voltage V_{od} and current I_{od} in terms of the total voltages and currents at terminals 1 and 2 such that

$$V_e = \frac{1}{2}(V_1 + V_2), \quad I_e = \frac{1}{2}(I_1 + I_2) \quad (5.62a)$$

and

$$V_{od} = \frac{1}{2}(V_1 - V_2), \quad I_{od} = \frac{1}{2}(I_1 - I_2) \quad (5.62b)$$

This is consistent with the voltage and current convention shown in Figure 5-44. For even mode of operation (V_e, I_e), voltages are additive and currents flow in the same direction. However, for odd mode of operation (V_{od}, I_{od}) the terminal voltages are subtractive and currents flow in opposite directions.

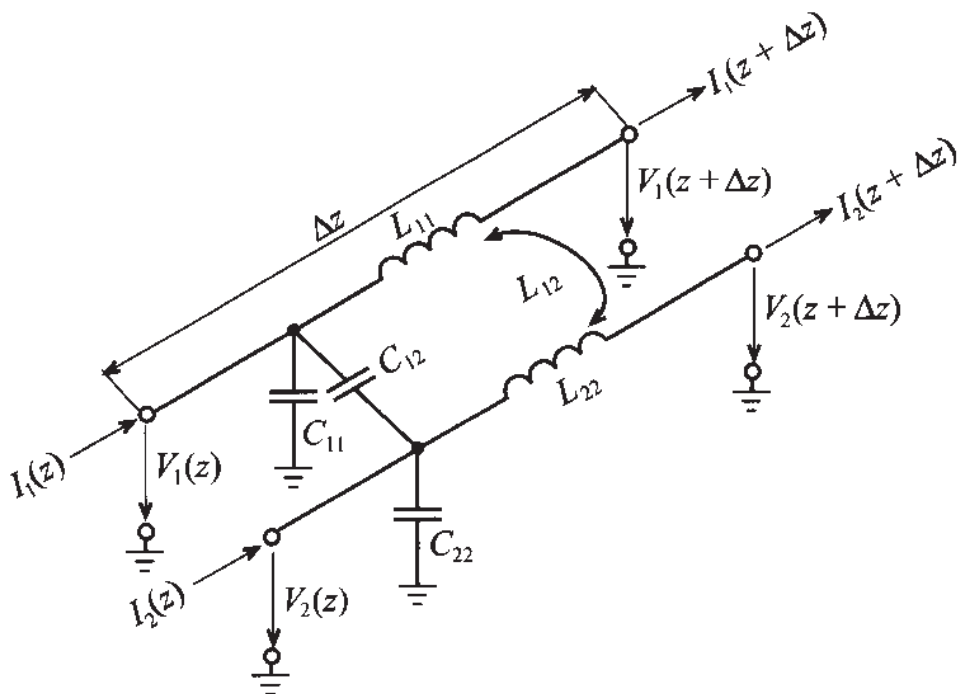


Figure 5-44 Equivalent circuit diagram and appropriate voltage and current definitions for a system of two lossless coupled transmission lines.

The benefit of introducing odd and even modes of operation is seen when establishing the fundamental equations. It can be shown that for two lines we get a set of first-order, coupled ordinary differential equations similar in form to the transmission line equations in Chapter 2:

$$-\frac{dV_e}{dz} = j\omega(L_{11} + L_{12})I_e \quad (5.63a)$$

$$-\frac{dI_e}{dz} = j\omega(C_{11} + C_{12})V_e \quad (5.63b)$$

and

$$-\frac{dV_{od}}{dz} = j\omega(L_{11} - L_{12})I_{od} \quad (5.64a)$$

$$-\frac{dI_{od}}{dz} = j\omega(C_{11} - C_{12})V_{od} \quad (5.64b)$$

What is important to notice is the fact that even and odd modes allow us to decouple the governing equations. The characteristic line impedances Z_{0e} and Z_{0o} for the even and odd modes can be defined in terms of even and odd mode capacitances C_e , C_{od} , and the respective phase velocities as follows:

$$Z_{oe} = \frac{1}{v_{pe} C_e}, \quad Z_{0o} = \frac{1}{v_{po} C_{od}} \quad (5.65)$$

If both conductors are equal in size and location, we can conclude for the even mode

$$C_e = C_{11} = C_{22} \quad (5.66a)$$

and for the odd mode

$$C_{od} = C_{11} + 2C_{12} = C_{22} + 2C_{12} \quad (5.66b)$$

The capacitances are, in general, difficult to find since fringing fields and different media have to be taken into account. For instance, even the strip line conductor over a dielectric substrate cannot be computed based on the simple capacitance per unit length formula $C_{11} = \epsilon_0 \epsilon_r (w/d)$ because the width-to-thickness ratio is not sufficiently large for this formula to apply. Moreover, the cross-coupling capacitance C_{12} requires a very intricate treatment. For this reason, it is common practice to resort to a numerically computed impedance grid, such as the one shown in Figure 5-45.

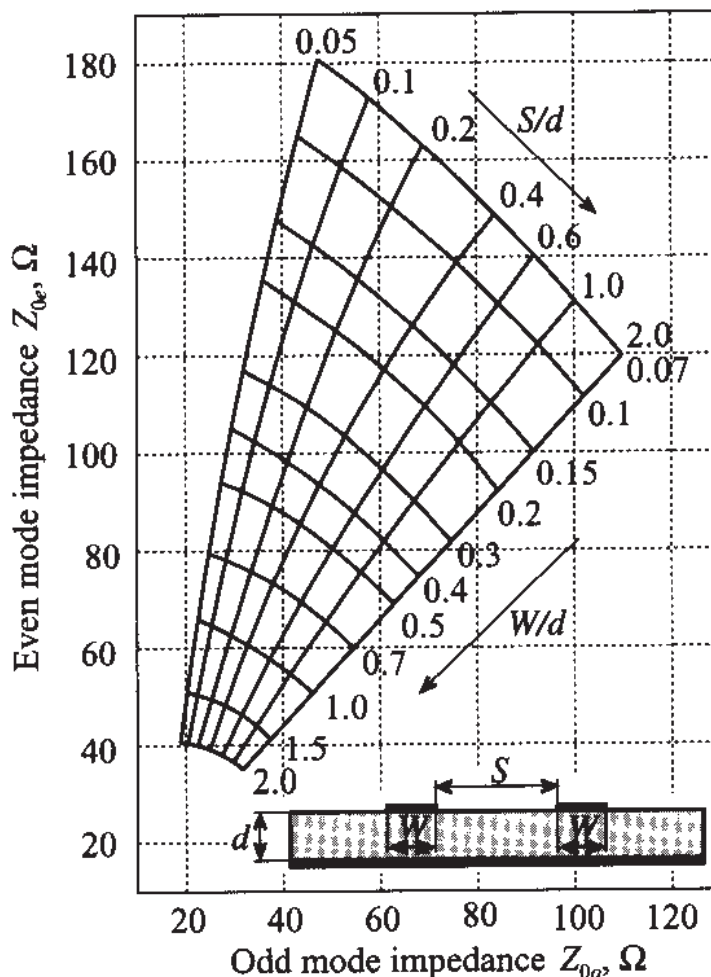


Figure 5-45 Even and odd characteristic impedance for microstrip lines.

5.4.2 Bandpass Filter Section

We turn our attention to two microstrip lines as the main building block of a bandpass filter shown in Figure 5-46. Both the geometric arrangement with input and output ports and open-circuit conditions and the corresponding transmission line representation are depicted.

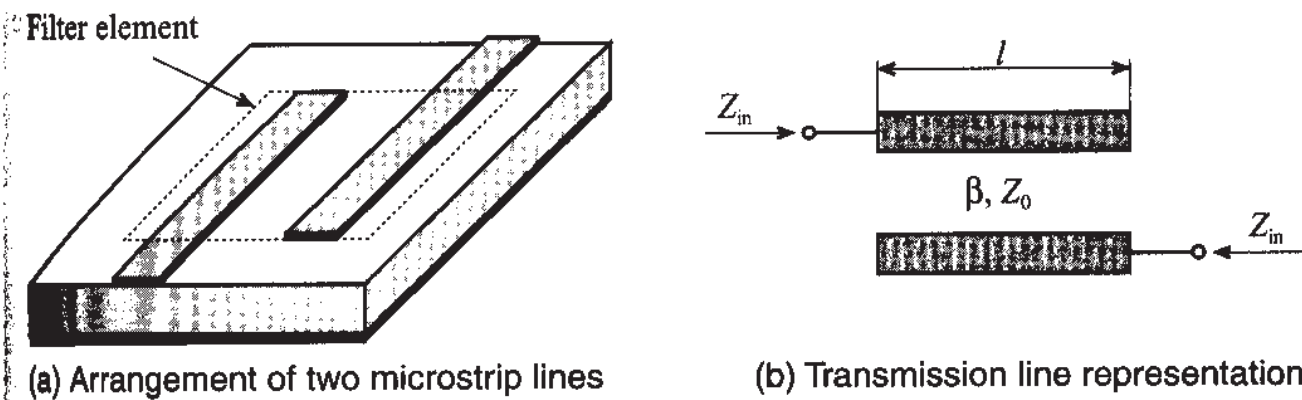


Figure 5-46 Bandpass filter element.

Without delving into details of the rather complicated treatment (see Gupta in *Further Reading*), this configuration has the impedance matrix coefficients for open transmission line segments in the form

$$Z_{11} = -j \frac{1}{2} (Z_{0e} + Z_{0o}) \cot(\beta l) = Z_{22} \quad (5.67a)$$

$$Z_{12} = -j \frac{1}{2} (Z_{0e} - Z_{0o}) \frac{1}{\sin(\beta l)} = Z_{21} \quad (5.67b)$$

When cascading these building blocks into multiblock filter configurations, our desire is to match both ports of this segment to the adjacent elements. This is also known as finding the **image impedance**. For the input impedance at port 1 we can write

$$Z_{in} = \frac{V_1}{I_1} = \frac{AZ_L + B}{CZ_L + D} \quad (5.68a)$$

and the output impedance at port 2

$$Z_L = \frac{-V_2}{I_2} = \frac{DZ_{in} + B}{CZ_{in} + A} \quad (5.68b)$$

Since we require $Z_{in} = Z_L$, we find from (5.68) that $A = D$ and

$$Z_{in} = \sqrt{\frac{B}{C}} \quad (5.69)$$

If (5.67) is converted into a chain matrix form the coefficients A, B, C, D can be determined. Inserting B and C into (5.69), one finds for the input, or image impedance

$$Z_{\text{in}} = \frac{1}{2 \sin(\beta l)} \sqrt{(Z_{0e} - Z_{0o})^2 - (Z_{0e} + Z_{0o})^2 \cos^2(\beta l)} \quad (5.70)$$

The bandpass filter behavior of (5.70) becomes apparent when plotting the real part of the input impedance response as a function of the electric length in the range $0 \leq \beta l \leq 2\pi$, as depicted in Figure 5-47.

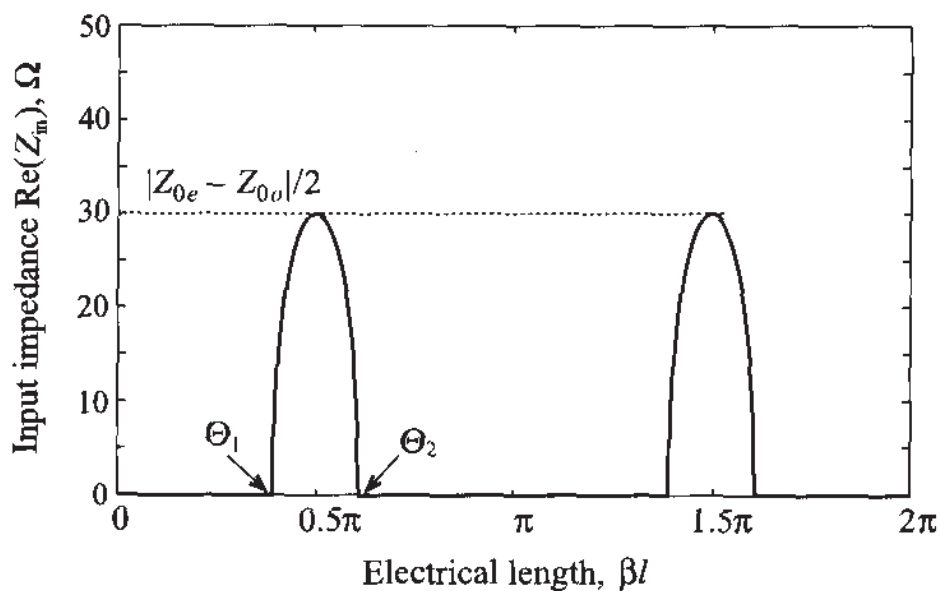


Figure 5-47 Input impedance behavior of equation (5.70). Z_{0e} and Z_{0o} are arbitrarily set to 120Ω and 60Ω , respectively.

According to Figure 5-47, the characteristic bandpass filter performance is obtained when the length is selected to be $\lambda/4$ or $\beta l = \pi/2$. For this case the upper and lower cut-off frequencies are found as

$$(\beta l)_{1,2} = \Theta_{1,2} = \pm \cos^{-1} \left[\frac{Z_{0e} - Z_{0o}}{Z_{0e} + Z_{0o}} \right] \quad (5.71)$$

Also noticeable is the periodic impedance response in Figure 5-47, which indicates that the upper operating frequency has to be band limited to avoid multiple bandpass filter responses at higher frequencies.

5.4.3 Cascading bandpass filter elements

A single bandpass element as discussed in the previous section does not result in a good filter performance with steep passband to stopband transitions. However, it is the

bility to cascade these building blocks that ultimately results in high-performance filters. Figure 5-48 depicts a generic multielement design.

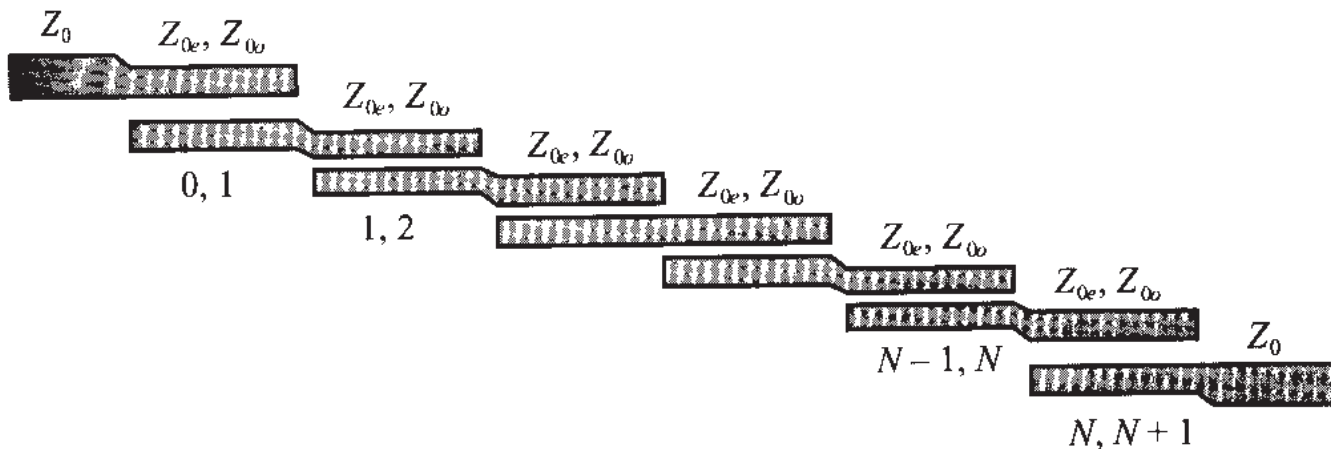


Figure 5-48 Multielement configuration of a fifth-order coupled-line bandpass filter ($N = 5$).

To design such a structure that meets a particular bandpass filter specification, a number of computations have to be performed. The following sequence of steps is needed to translate a set of design requirements into a practical filter realization (see Matthaei et al. in Further Reading).

- *Selection of standard low-pass filter coefficients.* Depending on whether a Butterworth or Chebyshev design with desired rejection and ripple is needed, the designer can directly select the appropriate standard low-pass filter coefficients $g_0, g_1, \dots, g_N, g_{N+1}$ listed in Tables 5-2 to 5-6.
- *Identification of normalized bandwidth, upper, and lower frequencies.* From the desired filter specifications for lower and upper frequencies ω_L , ω_U and the center frequency $\omega_0 = (\omega_U + \omega_L)/2$, we define the normalized bandwidth of the filter as

$$BW = \frac{\omega_U - \omega_L}{\omega_0} \quad (5.72)$$

This factor allow us to compute the following parameters:

$$J_{0,1} = \frac{1}{Z_0} \sqrt{\frac{\pi BW}{2g_0g_1}} \quad (5.73a)$$

$$J_{i,i+1} = \frac{1}{Z_0} \frac{\pi BW}{2\sqrt{g_i g_{i+1}}} \quad (5.73b)$$

$$J_{N,N+1} = \frac{1}{Z_0} \sqrt{\frac{\pi BW}{2g_N g_{N+1}}} \quad (5.73c)$$

which in turn permit us to determine the odd and even characteristic line impedances:

$$Z_{0o}|_{i,i+1} = Z_0 [1 - Z_0 J_{i,i+1} + (Z_0 J_{i,i+1})^2] \quad (5.74a)$$

and

$$Z_{0e}|_{i,i+1} = Z_0 [1 + Z_0 J_{i,i+1} + (Z_0 J_{i,i+1})^2] \quad (5.74b)$$

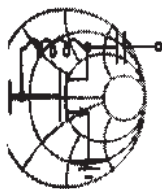
where the indices $i, i+1$ refer to the overlapping elements seen in Figure 5-48. Here Z_0 is the characteristic line impedance at the beginning and the end of the filter structure.

- *Selection of actual strip line dimensions.* Based on Figure 5-45, the individual odd and even line impedances can be converted into strip line dimensions. For instance, if the dielectric material and the thickness of the PCB board are given, we can determine separation S , and width W of the copper strips. Normally, the width will conform with the width of the other microstrip lines. Therefore, the separation is the most common parameter that can be varied to achieve the impedances required by (5.74). The length of each coupled line segment has to be equal to $\lambda/4$ at the center frequency, as described in Section 5.4.2.

The preceding steps result in a first and often crude design, which can be made more precise by introducing length and width corrections to account for fringing field effects. In addition, the use of simulation packages often allows further adjustments and fine-tuning to ensure a design that actually performs according to the specifications.

5.4.4 Design Example

In the following example we go through the steps outlined in the previous section by designing a particular bandpass filter.



Example 5-6: Bandpass filter design with coupled line transmission line segments

A coupled-line bandpass filter with 3 dB ripples in the passband is to be designed for a center frequency of 5 GHz and lower and upper cut-off frequencies of 4.8 and 5.2 GHz, respectively. The attenuation should be at least 30 dB at 5.3 GHz. Select the number of elements and find odd and even mode characteristic impedances of the coupled transmission lines.

Solution: According to Section 5.4.3, the first step in the design of this filter is to choose an appropriate low-pass filter prototype. The order of the filter can be selected from the requirement of 30 dB attenuation at 5.3 GHz. Using frequency conversion for the bandpass filter (5.46), we find that for 5.3 GHz the normalized frequency of the low-pass filter prototype is

$$\Omega = \frac{\omega_c}{\omega_U - \omega_L} \left(\frac{\omega}{\omega_c} - \frac{\omega_c}{\omega} \right) = 1.4764$$

From Figure 5-21 we determine that the order of the filter should be at least $N = 5$ to achieve 30 dB attenuation at $\Omega = 1.4764$. The coefficients for an $N = 5$ Chebyshev filter with 3 dB ripples are

$$g_1 = g_5 = 3.4817, g_2 = g_4 = 0.7618, g_3 = 4.5381, g_6 = 1.$$

The next step in the design is to find the even and odd excitation mode characteristic impedances of the coupled transmission lines as described by (5.74). The results of these computations are listed in the following table.

| i | $Z_{0J_{i,i+1}}$ | $Z_{0o}(\Omega)$ | $Z_{0e}(\Omega)$ |
|-----|------------------|------------------|------------------|
| 0 | 0.1900 | 42.3056 | 61.3037 |
| 1 | 0.0772 | 46.4397 | 54.1557 |
| 2 | 0.0676 | 46.8491 | 53.6077 |
| 3 | 0.0676 | 46.8491 | 53.6077 |
| 4 | 0.0772 | 46.4397 | 54.1557 |
| 5 | 0.1900 | 42.3056 | 61.3037 |

To confirm the validity of our theoretical design, we can use MMICAD to analyze the performance of the bandpass filter just designed. The result of the simulation is shown in Figure 5-49.

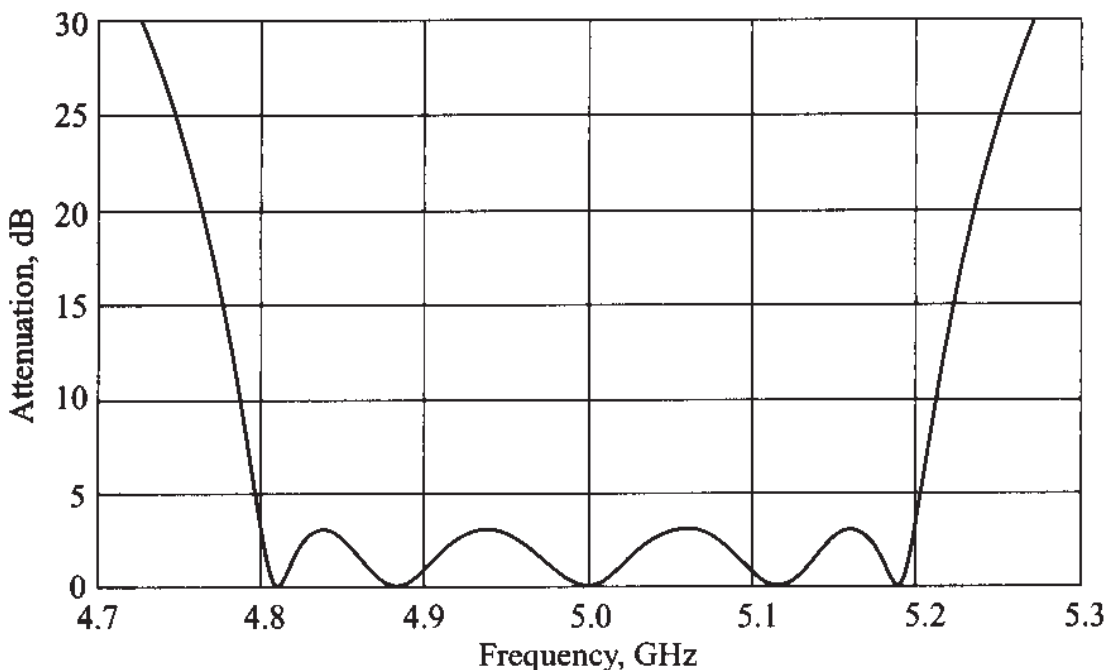


Figure 5-49 MMICAD simulations of the fifth-order coupled-line Chebyshev bandpass filter with 3 dB ripple in the passband. The lower cut-off frequency is 4.8 GHz and the upper cut-off frequency is 5.2 GHz.

The filter response in Figure 5-49 confirms that the specifications are met for f_L and f_U and that the attenuation at 5.3 GHz even exceeds the 30 dB requirement.

Often the theoretical filter design leads to coefficients whose validity must be double-checked against an RF circuit simulator to test the actual performance.

Another reason for resorting to a simulation package is the need to verify the design methodology independently and to test the filter performance over a range of parameter variations in terms of geometry and dielectric properties. Most of these parametric studies can be accomplished with little effort on a computer. After the initial theoretical design idea, the computer simulations typically precede the actual board construction and testing.

5.5 Summary

Our emphasis in this chapter has been an exposure to filter design concepts that are ubiquitous in many RF/MW circuit designs. Rather than going into detailed derivations, the intent of this chapter is to present a generic discussion of some of the key issues facing a design engineer in the construction of practical filter types.

Beginning with a general classification of high-pass, low-pass, bandpass, and bandstop filters, we introduce a common terminology that is needed to understand the common descriptors when developing filter specifications. Terms that are often used such as cut-off, lower, upper, and center frequencies, shape factor, bandwidth, insertion loss, and rejection, are defined and placed in context with simple first-order high- and low-pass filters as well as series and parallel resonant circuits. Since the resonator circuits permit the realization of bandpass and bandstop designs, the sharpness of the impedance or admittance behavior is quantified through the so-called quality factor:

$$Q = \omega \frac{\text{averaged stored energy}}{\text{energy loss per cycle}} \Big|_{\omega = \omega_c}$$

a measure that can be further broken down into the filter Q_F and external Q_E quality factors. Specifically, the notation of insertion loss

$$IL = 10 \log \frac{P_{in}}{P_L} = -10 \log(1 - |\Gamma_{in}|^2)$$

which defines the amount of power lost by inserting the filter between the source and load ports, is of central importance in the design of high-frequency filters. Depending on the attenuation profile necessary to realize the various filter types, the loss factor

$$LF = \frac{1}{1 - |\Gamma_{in}|^2}$$

is employed to realize a particular response.

To enable a more comprehensive approach, the low-pass filter design based on a normalized frequency scale is chosen as the standard type. Through frequency scaling and shifting, all filter types can then be readily realized. The benefit of this approach is that only a few sets of standard low-pass filter coefficients have to be derived depending on whether a Butterworth filter with a maximally flat profile or Chebyshev filter with an equiripple attenuation profile is desired.

The practical implementation is achieved through Richards transformation:

$$S = j \tan\left(\frac{\pi}{4}\Omega\right)$$

This transformation is central in establishing a link between lumped capacitive and inductive elements and distributed transmission line theory. The various series and shunt transmission line segments can be spatially separated through unit elements before Kudora's identities permit the conversion of some of the transmission sections into easy-to-implement segmental elements. In particular, series inductive configurations are often easier to implement than stub elements. With the aid of Kudora's identities this can be accomplished elegantly.

The fact that the proximity of strip lines causes electromagnetic coupling is exploited to design bandpass and bandstop filters. Without delving into the theoretical explanations too deeply, two line segments are used as the basic building block of a two-port network representation. Through odd and even mode impedance analysis we can find the image impedance

$$Z_{in} = \frac{1}{2\sin(\beta l)} \sqrt{(Z_{0e} - Z_{0o})^2 - (Z_{0e} + Z_{0o})^2 \cos^2(\beta l)}$$

as the characteristic bandpass response. This single element can be cascaded into multiple section filters to fulfill various design requirements. By using an RF/MW simulation package, the same example is revisited and the coupled filter response is computed as a function of various element numbers and geometric dimensions of the microstrip lines.

Although the topic of filter design could only cursorily be covered, Chapter 5 should convey the basic engineering steps needed to arrive at a functional high-frequency filter realization. We attempted to make the process of picking the appropriate filter coefficients, scaling the results to actual frequencies, and implementing the process in microstrip lines as much of a cookbook approach as possible. However, Chapter 5 should also make clear the usefulness of commercial simulation packages in carrying out a detailed numerical analysis. Indeed, for most modern filter design examples, an RF/MW simulation package is an indispensable tool to predict the filter performance. Moreover, from the circuit schematic it is relatively straightforward to use special layout programs to generate the actual PCB layout file that becomes the basis for the physical board construction.

Further Reading

S. Butterworth, "On the Theory of Filter Amplifiers," *Wireless Eng.*, Vol. 7, pp. 536-541, 1930.

K. C. Gupta, R. Garg, and I. J. Bahl, *Microstrip Lines and Slot Lines*, Artech House, Dedham, MA, 1979.

G. L. Matthaei, et al., *Microwave Filters, Impedance-Matching Networks, and Coupling Structures*, McGraw-Hill, New York, 1964.

C. G. Montgomery, R. H Dicke, and E. M. Purcell, *Principles of Microwave Circuits*, MIT Radiation Laboratory Series, Vol. 8, McGraw-Hill, New York, 1948.

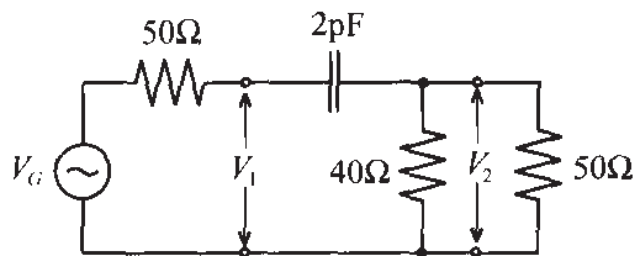
D. M. Pozar, *Microwave Engineering*, 2nd ed., John Wiley, New York, 1998.

P. A. Rizzi, *Microwave Engineering: Passive Circuits*, Prentice Hall, Englewood Cliffs, NJ, 1988.

L. Weinberg, *Network Analysis and Synthesis*, McGraw-Hill, New York, 1962.

Problems

- 5.1 For the simple integrator circuit shown,

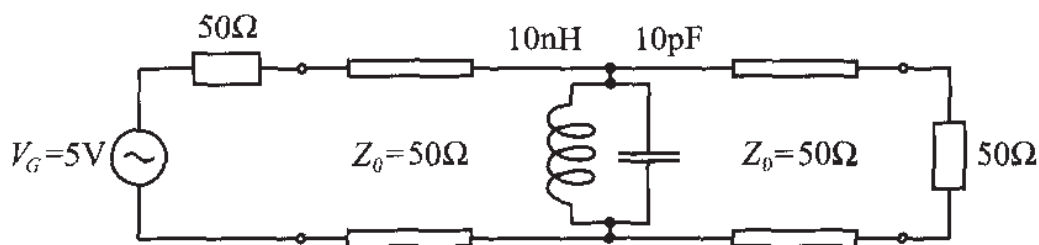


determine the following quantities:

- Transfer function $H(\omega) = V_2/V_G$
- Attenuation versus frequency behavior $\alpha(\omega)$
- Phase versus frequency behavior $\phi(\omega)$
- Group delay t_g

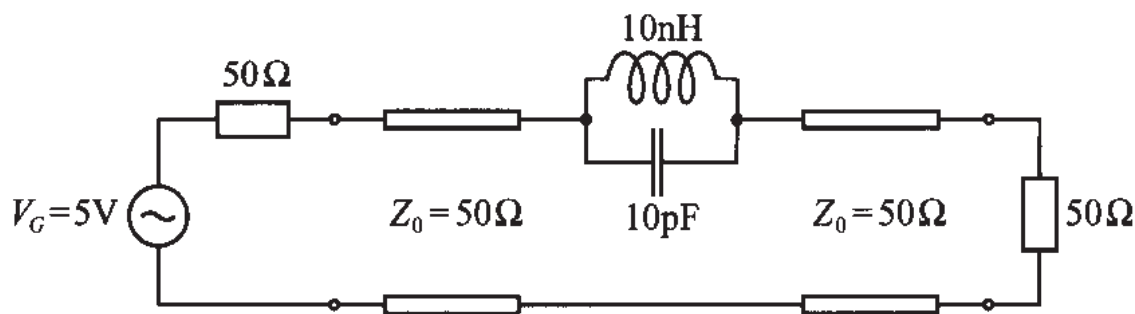
Plot these factors for the frequency range from DC to 1 GHz.

- 5.2 Derive expressions for internal, external, and loaded quality factors for the standard series and parallel resonance circuits discussed in Section 5.1.4.
- 5.3 In Section 5.1.5 the admittance of the parallel resonance circuit is expressed in terms of a quality factor expression. Prove the resulting equation (5.29).
- 5.4 For the filter circuit shown,



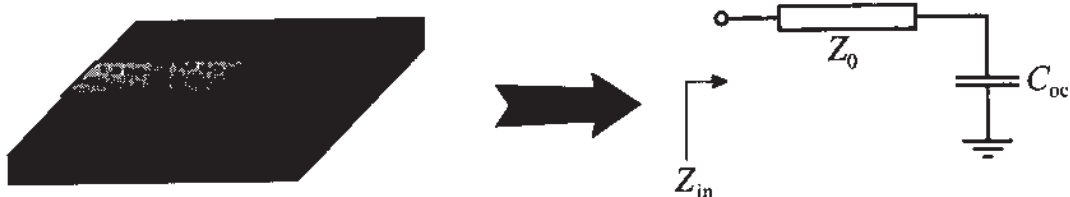
Find the loaded, unloaded, and external quality factors. In addition determine the power generated by the source as well as the power absorbed by the load at resonance. Furthermore, plot the insertion loss as a function of frequency in the range of $\pm 50\%$ of the resonance frequency.

5.5 Repeat Problem 5.4 for the following filter circuit:



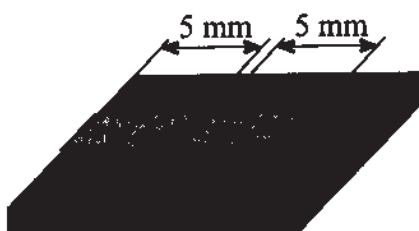
- 5.6** You are required to build a low-pass Butterworth filter that provides an attenuation value of at least 50 dB at $f = 1.5f_{3\text{dB}}$. Which filter order is required? How many components (inductors and capacitors) do you need to realize this filter?
- 5.7** Design a prototype low-pass Butterworth filter that will provide at least 20 dB attenuation at the frequency of $f = 2f_{3\text{dB}}$.
- 5.8** Plot the insertion loss of a low-pass Chebyshev filter that has 6 dB ripple in the passband and at least 50 dB attenuation at $f = 2f_{\text{cut-off}}$.
- 5.9** Using the low-pass prototype developed in Problem 5.7, design a high-pass filter with cut-off frequency of 1 GHz. Plot the attenuation profile.
- 5.10** To suppress noise in a digital communication system a bandpass RF filter is required with a passband from 1.9 GHz to 2 GHz. The minimum attenuation of the filter at 2.1 GHz and 1.8 GHz should be 30 dB. Assuming that a 0.5 dB ripple in the passband can be tolerated, design a filter that will use a minimum number of components.
- 5.11** In the design of an amplifier for cellular phone applications it is discovered that the circuit exhibits excessive noise at 3 GHz. Develop a bandstop filter with a center frequency of $f_c = 3\text{GHz}$ and bandwidth of 10% at f_c with 30 dB minimum attenuation in the stopband.

- 5.12 In previous chapters we examined the input impedance behavior of an open-circuit stub assuming that open-circuit conditions at the end are ideal. In practical realizations, due to fringing fields, leakage occurs. This can be modeled as an additional parasitic capacitance, as shown below:

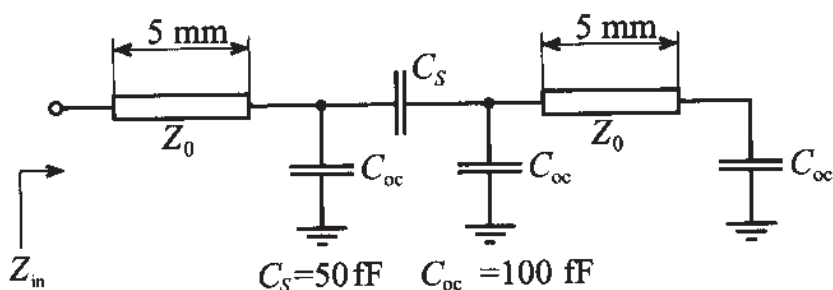


Using your favorite mathematical program, find the input impedance of the 50Ω open-circuit stub of length $l = 1 \text{ cm}$ for frequencies ranging from 10 MHz to 100 GHz. In your computations assume that an equivalent load capacitance is $C_{oc} = 0.1 \text{ pF}$ and the phase velocity of the line is $v_p = 1.5 \times 10^8 \text{ m/s}$. Compare your results to the input impedance behavior of the ideal open-circuit and short-circuit stubs.

- 5.13 Assuming all physical parameters of the open-circuit stub to be the same as in Problem 5.12, find the effective fringing capacitance C_{oc} if the lowest frequency (at which the input impedance of the stub is equal zero) is 3.3 GHz.
- 5.14 After reconsidering the design in Problem 5.12, it is decided to use an open-circuit stub of half of the length (i.e., $l = 5 \text{ mm}$). Since the board is already manufactured with a 1 cm stub, you cut a slit in the middle so that the length of the resulting stub is 5 mm, as shown below.



Due to proximity effects, the equivalent circuit in this case is as follows:

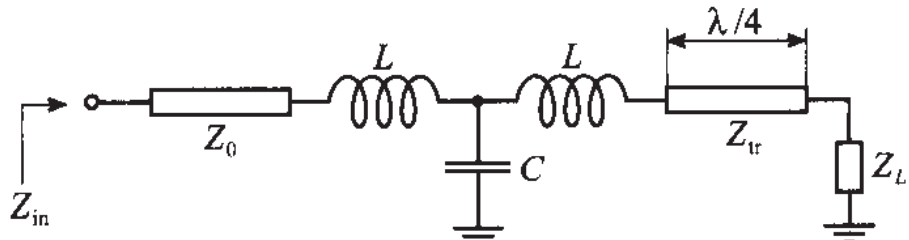


Using a mathematical spreadsheet, compute the input impedance of this configuration for frequencies ranging from 10 MHz to 20 GHz, assuming that the characteristic line impedance is 50Ω and the phase velocity is $v_p = 1.5 \times 10^8 \text{ m/s}$. Compare the results with the input impedance behavior of the 5 mm open-circuit stub taking into account a fringing capacitance $C_{oc} = 100 \text{ fF}$.

- 5.15 In Chapter 2 we introduced a quarter-wave strip line transformer that is able to transform any real load impedance into any other real value. In our analysis we always assumed that there are no parasitic elements involved. In reality, the connection of two transmission lines with different impedances leads to discontinuity in the line width as follows:



Due to this discontinuity, additional parasitic elements have to be taken into account. The equivalent circuit for the above configuration is:



For a load impedance of $Z_L = 25 \Omega$ and a $Z_0 = 100 \Omega$ line impedance find a characteristic impedance Z_{tr} of the quarter-wave transformer and compute the input impedance Z_{in} of the entire system for a frequency range from 10 MHz to 20 GHz, assuming that the transmission line is quarter-wave long and parasitic elements have the following values: $L = 10 \text{ pH}$, $C = 100 \text{ fF}$.

- 5.16 Prove the first three Kuroda's identities given in Table 5-6 by computing the appropriate ABCD matrices.
- 5.17 Develop a low-pass filter with cut-off frequency of 200 MHz and attenuation of 50 dB at 250 MHz. The flatness of the filter response is not a design consideration. Choose the filter implementation that requires the least number of components.

- 5.18 Design a three-section bandpass filter with 3 dB ripples in the passband. The center frequency is 900 MHz and the bandwidth is 30 MHz. Use a mathematical spreadsheet and plot the insertion loss of the filter.
- 5.19 In Project I of Section 5.3.3 we designed a microstrip realization of the Chebyshev-type low-pass filter with 3 GHz cut-off frequency. Repeat this design using an FR-4 substrate with dielectric constant of $\epsilon_r = 4.6$ and thickness of $h = 25$ mil. In addition, obtain the physical width and length of each microstrip line.
- 5.20 Design a five-section bandstop filter having a maximally flat response. The bandwidth of the filter should be 15% with a center frequency of 2.4 GHz. The filter has to be matched to a 75Ω impedance at both sides.
- 5.21 Design a fifth-order low-pass filter with linear phase response. The cut-off frequency of the filter is 5 GHz. Provide two designs: the first one using lumped elements and the second design using microstrip lines. In both cases assume that a FR-4 substrate is used ($\epsilon_r = 4.6$, $h = 20$ mil).
- 5.22 As a part of a satellite communication link, a bandpass filter for image rejection in the downconversion stage has to be designed. The bandwidth of a signal is 300 MHz and the center frequency is 10 GHz. It is essential to provide maximally flat response in the passband and obtain at least 40 dB attenuation at 10.4 GHz.
- 5.23 Prove equations (5.68a) and (5.68b) and show how (5.70) results.

Active RF Components

Our focus in the first five chapters has been primarily geared toward passive RF devices and their electric circuit behavior. In this chapter we extend and broaden our scope to include an investigation of various active circuit elements. Of specific interest for the design of amplifiers, mixers, and oscillators are solid-state devices such as diodes and transistors. What complicates a unified treatment is the wealth of special purpose components developed and marketed by a range of companies for a wide host of industrial applications. We cannot adequately address the multitude of technological advances currently shaping the RF/MW commercial markets. This is not the intent of this text; rather we emphasize a number of key concepts driving the technological RF/MW evolution. These concepts are utilized later for the design of amplifiers, mixers, oscillators, and other circuits developed in subsequent chapters. Our approach intends to enable the reader to formulate and develop his or her own network descriptions as part of an integrated strategy to construct suitable models of analog RF circuits.

Before developing appropriate network models for active devices, a short discussion of solid-state physics involving *pn* and metal-semiconductor junctions is presented. The aim is to provide a solid-state perspective of the electric circuit representations derived from the physical device level. This is needed because

- at high-frequency modes of operation, additional capacitive and inductive effects enter the solid-state devices and affect their performance
- the high-frequency behavior of many active devices markedly departs from that of low-frequency components and therefore requires special treatment
- to utilize simulation tools such as SPICE, or more dedicated RF CAD programs, a working knowledge of the physical parameters must be obtained that directly or indirectly influence the circuit behavior

Chapter 6 provides a concise summary of the most important semiconductor fundamentals that are encountered at high frequencies.

By analyzing the *pn*-junction and the Schottky contact, we gain a more complete picture of electronic circuit functions that form the foundation of rectifier, amplifier, tuning, and switching systems. In particular, the metal-semiconductor interface is shown to be especially useful for high-frequency operations. It is the RF domain that has seen many specialized diode developments. Chief among them are the Schottky, *PIN*, and tunnel diode, to name but a few.

Next, our attention is turned toward the bipolar and field effect transistors, which are more complex implementations of the previously investigated *pn*-junction and Schottky contact. We learn about the construction, functionality, temperature, and noise performance of the bipolar and the metal-semiconductor field effect transistors.

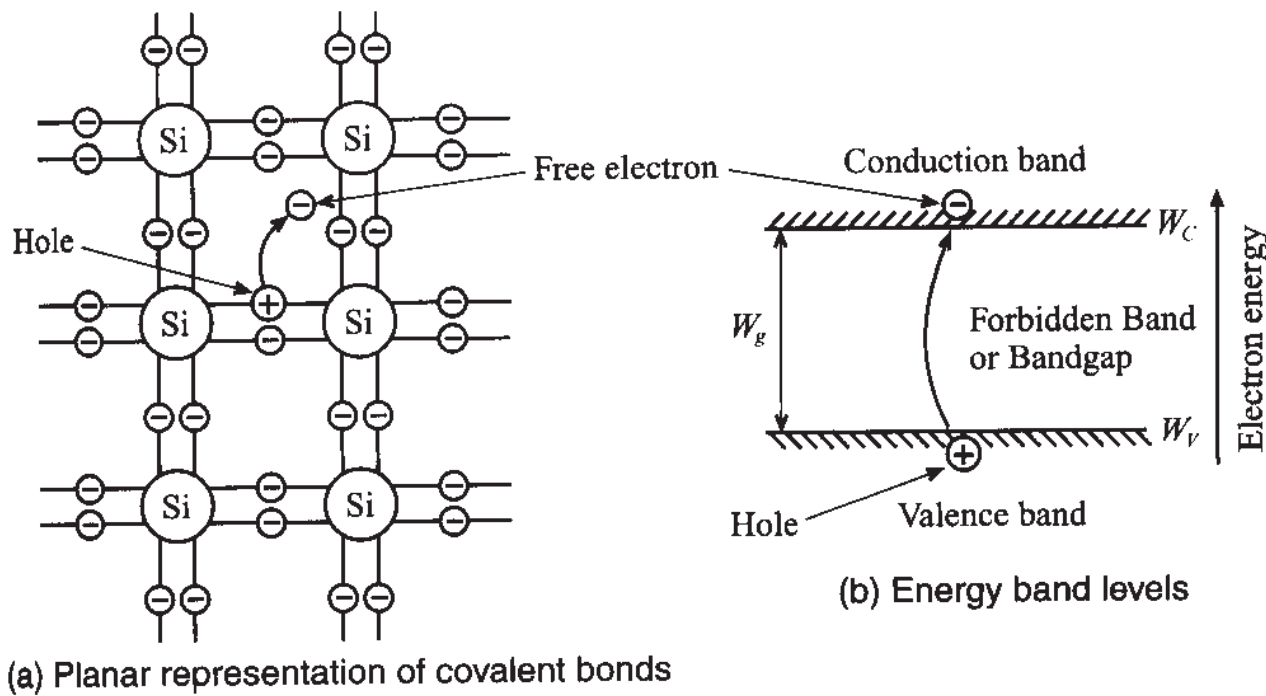
6.1 Semiconductor Basics

6.1.1 Physical Properties of Semiconductors

The operation of semiconductor devices is naturally dependent on the physical behavior of the semiconductors themselves. This section presents a brief introduction to the basic building blocks of semiconductor device modeling, particularly the operation of the *pn*-junction. In our discussion we will concentrate on the three most commonly used semiconductors: germanium (Ge), silicon (Si), and gallium arsenide (GaAs). Figure 6-1(a) schematically shows the bonding structure of pure silicon: Each silicon atom shares its four valence electrons with the four neighboring atoms, forming four covalent bonds.

In the absence of thermal energy (i.e., when the temperature is equal to zero degree Kelvin [$T^{\circ}\text{K} = 0$ or $T^{\circ}\text{C} = -273.15$, where $T^{\circ}\text{K} = 273.15 + T^{\circ}\text{C}$]) all electrons are bonded to the corresponding atoms and the semiconductor is not conductive. However, when the temperature increases, some of the electrons obtain sufficient energy to break up the covalent bond and cross the energy gap $W_g = W_C - W_V$, as shown in Figure 6-1(b) (at room temperature $T = 300^{\circ}\text{K}$ the **bandgap energy** is equal to 1.12 eV for Si, 0.62 eV for Ge, and 1.42 eV for GaAs). These free electrons form negative charge carriers that allow electric current conduction. The concentration of the conduction electrons in the semiconductor is denoted as n . When an electron breaks the covalent bond it leaves behind a positively charged vacancy, which can be occupied by another free electron. These types of vacancies are called **holes** and their concentration is denoted by p .

Electrons and holes undergo random motion through the semiconductor lattice as a result of the presence of thermal energy ($T > 0^{\circ}\text{K}$). If an electron happens to meet a



(a) Planar representation of covalent bonds

Figure 6-1 Lattice structure and energy levels of silicon.

(a) schematic planar crystal arrangement with thermal breakup of one valent bond resulting in a hole and a moving electron for $T > 0^{\circ}\text{K}$.

(b) equivalent energy band level representation whereby a hole is created in the valence band W_V and an electron is produced in the conduction band W_C . The energy gap between both bands is indicated by W_g .

hole, they recombine and both charge carriers disappear. In thermal equilibrium we have equal number of recombinations and generations of holes and electrons. The concentrations obey the Fermi statistics according to

$$n = N_C \exp\left[-\frac{W_C - W_F}{kT}\right] \quad (6.1a)$$

$$p = N_V \exp\left[-\frac{W_F - W_V}{kT}\right] \quad (6.1b)$$

where

$$N_{C,V} = 2(2m_{n,p}^* \pi kT/h^2)^{3/2} \quad (6.2)$$

are the **effective carrier concentration** in the conduction (N_C) and valence (N_V) bands, respectively. The terms W_C and W_V denote the energy levels associated with the conduction and valence bands and W_F is the **Fermi energy level**, which indicates the energy level that has a 50% probability of being occupied by an electron. For **intrinsic** (i.e., pure) semiconductors at room temperature the Fermi level is very close

to the middle of the bandgap. In (6.2), m_n^* and m_p^* refer to the effective mass of electrons and holes in the semiconductor that are different from the free electron rest mass due to interaction with the crystal lattice; k is Boltzmann's constant; \hbar is Planck's constant; and T is the absolute temperature measured in Kelvin.

In an intrinsic semiconductor the number of free electrons produced by thermal excitation is equal to the number of holes (i.e. $n = p = n_i$). Therefore, electron and hole concentrations are described by the concentration law

$$np = n_i^2 \quad (6.3)$$

where n_i is the intrinsic concentration. Equation (6.3) is true not only for intrinsic but also for doped semiconductors, which are discussed later in this section.

Substitution of (6.1) into (6.3) results in the expression for the intrinsic carrier concentration:

$$n_i = \sqrt{N_C N_V} \exp\left[-\frac{W_C - W_V}{2kT}\right] = \sqrt{N_C N_V} \exp\left[-\frac{W_g}{2kT}\right] \quad (6.4)$$

The effective electron and hole masses as well as the concentrations N_C , N_V , and n_i for $T = 300^\circ\text{K}$ are summarized in Table 6-1 and are also listed in Table E-1 in Appendix E.

Table 6-1 Effective concentrations and effective mass values at $T = 300^\circ\text{K}$

| Semiconductor | m_n^*/m_0 | m_p^*/m_0 | $N_C(\text{cm}^{-3})$ | $N_V(\text{cm}^{-3})$ | $n_i(\text{cm}^{-3})$ |
|-------------------------|-------------|-------------|-----------------------|-----------------------|-----------------------|
| Silicon (Si) | 1.08 | 0.56 | 2.8×10^{19} | 1.04×10^{19} | 1.45×10^{10} |
| Germanium (Ge) | 0.55 | 0.37 | 1.04×10^{19} | 6.0×10^{18} | 2.4×10^{13} |
| Gallium Arsenide (GaAs) | 0.067 | 0.48 | 4.7×10^{17} | 7.0×10^{18} | 1.79×10^6 |

Classical electromagnetic theory specifies the electrical conductivity in a material to be $\sigma = J/E$, where J is the current density and E is the applied electric field. The conductivity in the classical model (Drude model) can be found through the carrier concentration N , the associated elementary charge q , the drift velocity v_d , and the applied electric field E :

$$\sigma = qNv_d/E \quad (6.5)$$

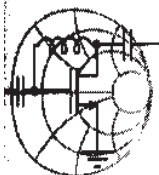
In semiconductors, we have both electrons and holes contributing to the conductivity of the material. At low electric fields the drift velocity v_d of the carriers is proportional to

the applied field strength through a proportionality constant known as **mobility** μ . Thus, for semiconductors we can rewrite (6.5) as

$$\sigma = qn\mu_n + qp\mu_p \quad (6.6)$$

where μ_n , μ_p are the mobilities of electrons and holes, respectively. For intrinsic semiconductors we can simplify (6.6) further by recalling that $n = p = n_i$, that is,

$$\sigma = qn_i(\mu_n + \mu_p) = q\sqrt{N_C N_V} \exp\left[-\frac{W_g}{2kT}\right](\mu_n + \mu_p) \quad (6.7)$$



RF & MW

Example 6-1: Computation of the temperature dependence of the intrinsic semiconductor conductivity

It is desired to find the conductivities for the intrinsic materials of Si, Ge, and GaAs as a function of temperature. To make the computations not too difficult, we assume that the bandgap energy and the mobilities for holes and electrons are temperature independent over the range of interest $-50^\circ\text{C} \leq T \leq 200^\circ\text{C}$.

Solution: As a first step it is convenient to combine into one parameter $\sigma_0(T)$ all factors without the exponential term in (6.7); that is,

$$\sigma_0(T) = q\sqrt{N_C N_V}(\mu_n + \mu_p)$$

where electron and hole mobilities are found from Table E-1:

$$\mu_n = 1350(\text{Si}), 3900(\text{Ge}), 8500(\text{GaAs})$$

$$\mu_p = 480(\text{Si}), 1900(\text{Ge}), 400(\text{GaAs})$$

All values are given in units of $\text{cm}^2/(\text{V} \cdot \text{s})$. N_C , N_V are computed according to (6.2) as

$$N_{C,V}(T) = N_{C,V}(300^\circ\text{K}) \left(\frac{T}{300}\right)^{3/2}$$

This leads to the form

$$\sigma = \sigma_0(T) \exp\left(-\frac{W_g}{2kT}\right) = q(\mu_n + \mu_p)\sqrt{N_C N_V} \left(\frac{T}{300}\right)^{3/2} \exp\left(-\frac{W_g}{2kT}\right)$$

where the bandgap energy $W_g = W_C - W_V$ is, respectively, 1.12 eV (Si), 0.62 eV (Ge), and 1.42 eV (GaAs). The three conductivities are plotted in Figure 6-2.

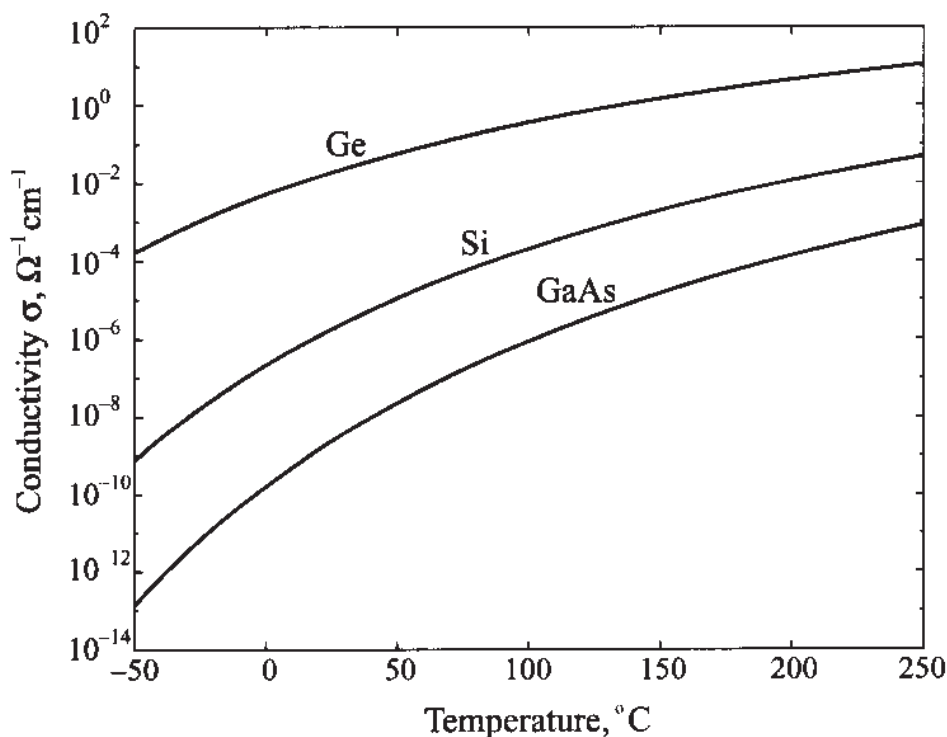


Figure 6-2 Conductivity of Si, Ge, GaAs in the range from -50°C to 250°C .

The electric properties of semiconductors are strongly influenced by the ambient temperature. In this example we have neglected the temperature dependence of the bandgap energy, which is discussed in Chapter 7. Knowledge of the temperature behavior of active devices is an important design consideration where internal heating, due to power dissipation, can easily result in temperature values exceeding $100\text{--}150^{\circ}\text{C}$.

A major change in the electrical properties of a semiconductor can be initiated by introducing impurity atoms. This process is called **doping**. To achieve **n-type** doping (which supplies additional electrons to the conduction band) we introduce atoms with a larger number of valence electrons than the atoms in the intrinsic semiconductor lattice that they substitute. For instance, the implantation of phosphorous (P) atoms into Si introduces loosely bound electrons into the neutral crystal lattice, as shown in Figure 6-3(b).

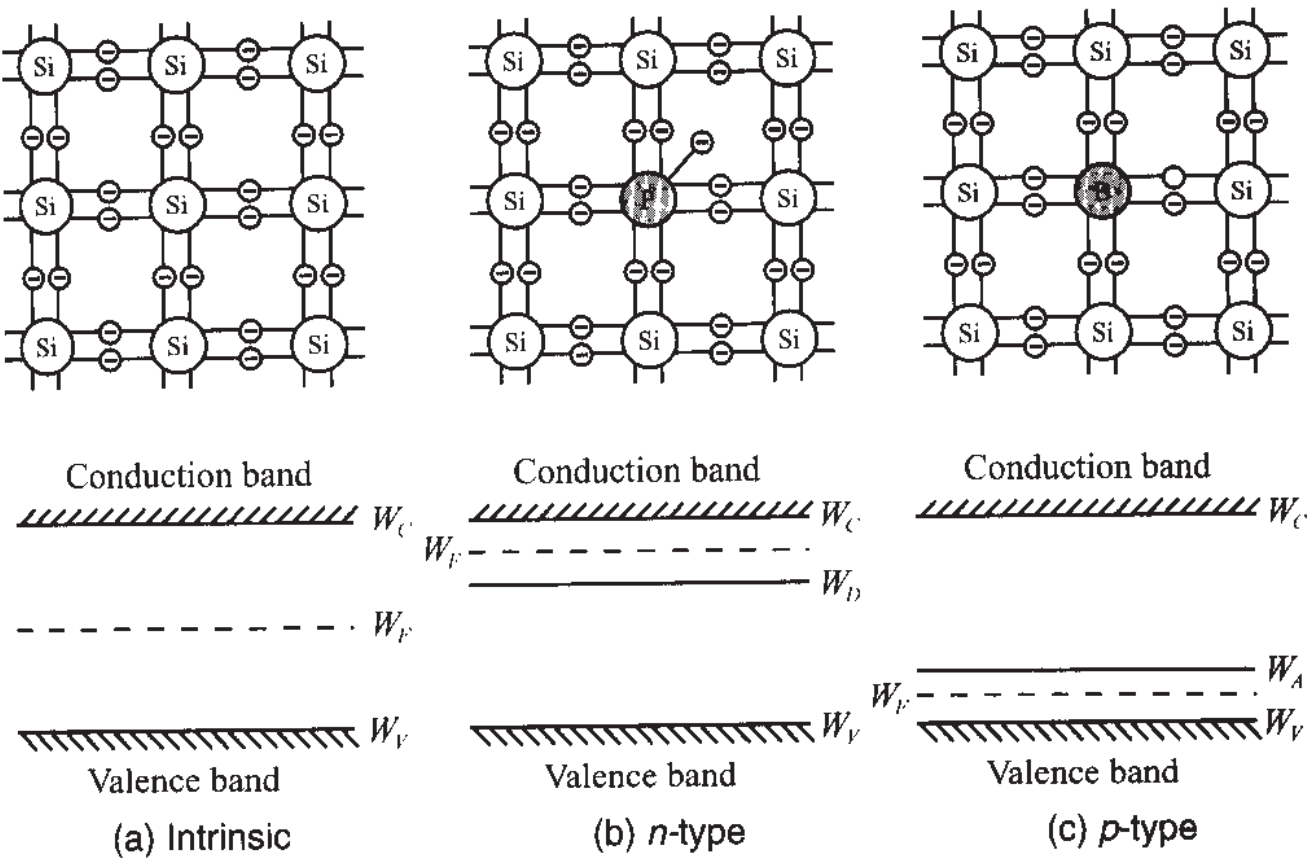


Figure 6-3 Lattice structure and energy band model for (a) intrinsic, (b) n -type, and (c) p -type semiconductors at no thermal energy. W_D and W_A are donor and acceptor energy levels.

It is intuitively apparent that the energy level of this “extra” electron is closer to the conduction band than the energy of the remaining four valence electrons. When the temperature is increased above absolute zero, the loosely bound electron separates from the atom, forming a free negative charge and leaving behind the fixed positive ion of phosphorous. Thus, while still maintaining charge neutrality, the atom has donated an electron to the conduction band without creating a hole in the valence band. This results in an increase in the Fermi level since more electrons are located in the conduction band. Contrary to the intrinsic semiconductor (n_i, p_i) we now have an **n -type** semiconductor in which the electron concentration is related to the hole concentration as

$$n_n = N_D + p_n \quad (6.8)$$

where N_D is the donor concentration and p_n represents the minority hole concentration. To find n_n and p_n we have to solve (6.8) in conjunction with (6.3). The result is

$$n_n = \frac{N_D + \sqrt{N_D^2 + 4n_i^2}}{2} \quad (6.9a)$$

$$p_n = \frac{-N_D + \sqrt{N_D^2 + 4n_i^2}}{2} \quad (6.9b)$$

If the donor concentration N_D is much greater than the intrinsic electron concentration n_i , then

$$n_n \approx N_D \quad (6.10a)$$

$$p_n \approx \frac{-N_D + N_D(1 + 2n_i^2/N_D^2)}{2} = \frac{n_i^2}{N_D} \quad (6.10b)$$

Let us now consider adding impurity atoms with fewer valence electrons than the atoms forming the intrinsic semiconductor lattice. These types of elements are called **acceptors**, and an example of such an element for the Si lattice is boron (B). As seen in Figure 6-3(c), one of the covalent bonds appears to be empty. This empty bond introduces additional energy states in the bandgap that are closely situated to the valence band. Again, when the temperature is increased from absolute zero, some electrons gain extra energy to occupy empty bonds but do not possess sufficient energy to cross the bandgap. Thus, impurity atoms will accept additional electrons, forming negative net charges. At the sites where the electrons are removed, holes will be created. These holes are free to migrate and will contribute to the conduction current of the semiconductor. By doping the semiconductor with acceptor atoms we have created a **p-type** semiconductor with

$$p_p = N_A + n_p \quad (6.11)$$

where N_A , n_p are the acceptor and minority electron concentrations. Solving (6.11) together with (6.3), we find hole p_p and electron n_p concentrations in the p-type semiconductor:

$$p_p = \frac{N_A + \sqrt{N_A^2 + 4n_i^2}}{2} \quad (6.12a)$$

$$n_p = \frac{-N_A + \sqrt{N_A^2 + 4n_i^2}}{2} \quad (6.12b)$$

Similar to (6.9), for high doping levels, when $N_A \gg n_i$, we observe

$$p_p \approx N_A \quad (6.13a)$$

$$n_p \approx \frac{-N_A + N_A(1 + 2n_i^2/N_A^2)}{2} = \frac{n_i^2}{N_A} \quad (6.13b)$$

Minority and majority concentrations play key roles in establishing the current flow characteristics in the semiconductor materials.

6.1.2 PN-Junction

The physical contact of a *p*-type with an *n*-type semiconductor leads to one of the most important concepts when dealing with active semiconductor devices: the ***pn*-junction**. Because of the difference in the carrier concentrations between the two types of semiconductors a current flow will be initiated across the interface. This current is commonly known as a **diffusion current** and is composed of electrons and holes. To simplify our discussion we consider a one-dimensional model of the *pn*-junction as seen in Figure 6-4.

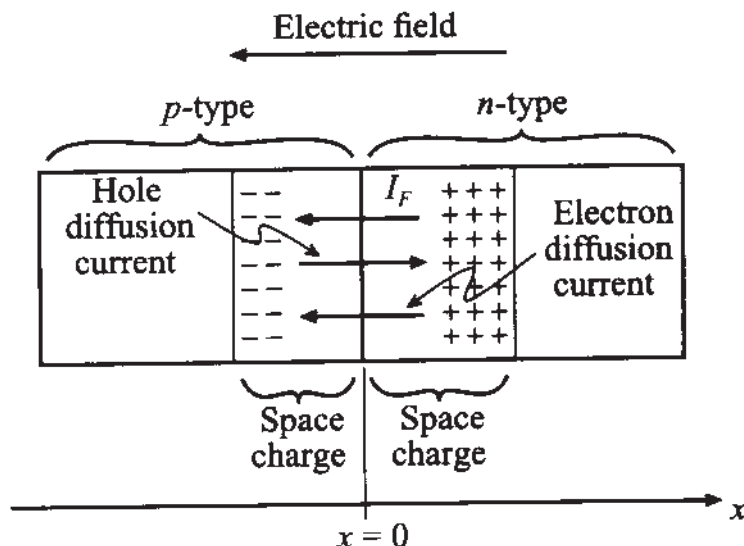


Figure 6-4 Current flow in the *pn*-junction

The diffusion current is composed of $I_{n_{\text{diff}}}$ and $I_{p_{\text{diff}}}$ components:

$$I_{\text{diff}} = I_{n_{\text{diff}}} + I_{p_{\text{diff}}} = qA \left(D_n \frac{dn}{dx} + D_p \frac{dp}{dx} \right) \quad (6.14)$$

where A is the semiconductor cross-sectional area orthogonal to the x -axis, and D_n , D_p are the diffusion constants for electrons and holes in the form (Einstein relation)

$$D_{n, p} = \mu_{n, p} \frac{kT}{q} = \mu_{n, p} V_T \quad (6.15)$$

The thermal potential $V_T = kT/q$ is approximately 26 mV at room temperature of 300°K.

Since the *p*-type semiconductor was initially neutral, the diffusion current of holes is going to leave behind a negative space charge. Similarly, the electron current flow

from the *n*-semiconductor will leave behind positive space charges. As the diffusion current flow takes place, an electric field *E* is created between the net positive charge in the *n*-semiconductor and the net negative charge in the *p*-semiconductor. This field in turn induces a current $I_F = \sigma A E$ which opposes the diffusion current such that $I_F + I_{\text{diff}} = 0$. Substituting (6.6) for the conductivity, we find

$$I_F = qA(n\mu_n + p\mu_p)E = I_{n_F} + I_{p_F} \quad (6.16)$$

Since the total current is equal to zero, the electron portion of the current is also equal to zero; that is,

$$I_{n_{\text{diff}}} + I_{n_F} = qD_n A \frac{dn}{dx} + qn\mu_n AE = q\mu_n A \left(V_T \frac{dn}{dx} - n \frac{dV}{dx} \right) = 0 \quad (6.17)$$

where the electric field *E* has been replaced by the derivative of the potential $E = -dV/dx$. Integrating (6.17), we obtain the **diffusion barrier voltage** or, as it is often called, the **built-in potential**:

$$\int_0^{V_{\text{diff}}} dV = V_{\text{diff}} = V_T \int_{n_p}^{n_n} n^{-1} dn = V_T \ln \left(\frac{n_n}{n_p} \right) \quad (6.18)$$

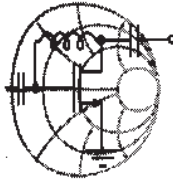
where again n_n is the electron concentration in the *n*-type and n_p is the electron concentration in the *p*-type semiconductor. The same diffusion barrier voltage could have been found had we considered the hole current flow from the *p* to the *n*-semiconductor and the corresponding balancing field-induced current flow I_{p_F} . The resulting equation describing the barrier voltage is

$$V_{\text{diff}} = V_T \ln \left(\frac{p_p}{p_n} \right) \quad (6.19)$$

If the concentration of acceptors in the *p*-semiconductor is $N_A \gg n_i$ and the concentration of donors in the *n*-semiconductor is $N_D \gg n_i$, then $n_n = N_D$, $n_p = n_i^2/N_A$, see (6.13b), and by using (6.18) we obtain

$$V_{\text{diff}} = V_T \ln \left(\frac{N_A N_D}{n_i^2} \right) \quad (6.20)$$

Exactly the same result is obtained from (6.19) if we substitute $p_p = N_A$ and $p_n = n_i^2/N_D$.



RF & MW →

Example 6-2: Determining the diffusion barrier or built-in voltage of a *pn*-junction

For a particular Si *pn*-junction the doping concentrations are given to be $N_A = 10^{18} \text{ cm}^{-3}$ and $N_D = 5 \times 10^{15} \text{ cm}^{-3}$ with an intrinsic concentration of $n_i = 1.5 \times 10^{10} \text{ cm}^{-3}$. Find the barrier voltages for $T = 300^\circ\text{K}$.

Solution: The barrier voltage is directly determined from (6.20):

$$V_{\text{diff}} = V_T \ln\left(\frac{N_A N_D}{n_i^2}\right) = \frac{kT}{q} \ln\left(\frac{N_A N_D}{n_i^2}\right) = 0.796 \text{ (V)}$$

We note that the built-in potential is strongly dependent on the doping concentrations and temperature.

For different semiconductor materials such as GaAs, Si, Ge, the built-in voltage will be different even if the doping densities are the same. This is due to significantly different intrinsic carrier concentrations.

If we want to determine the potential distribution along the x -axis, we can employ Poisson's equation, which for a one-dimensional analysis is written as

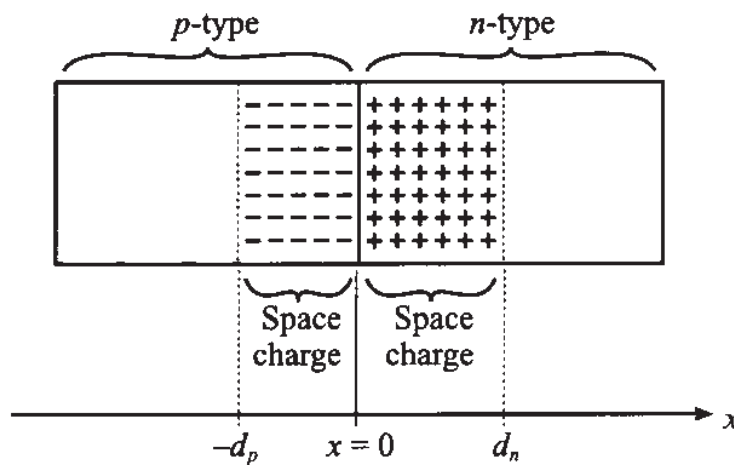
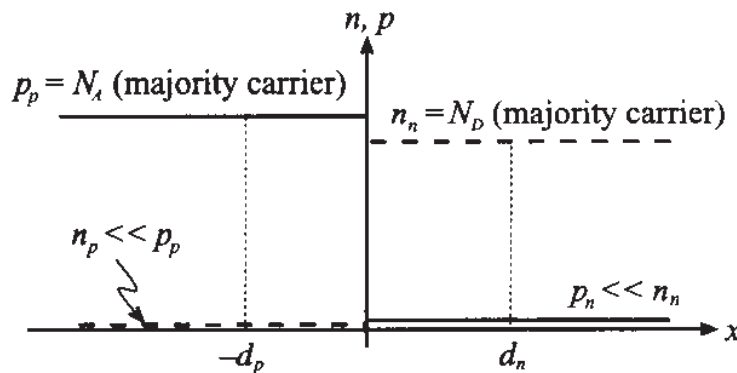
$$\frac{d^2 V(x)}{dx^2} = -\frac{\rho(x)}{\epsilon_r \epsilon_0} = -\frac{dE}{dx} \quad (6.21)$$

where $\rho(x)$ is the charge density and ϵ_r is the relative dielectric constant of the semiconductor. Assuming uniform doping and the **abrupt junction approximation**, as shown in Figure 6-5(b), the charge density in each material is

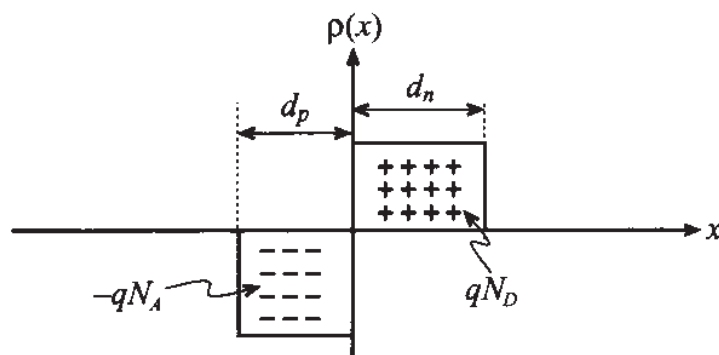
$$\rho(x) = -qN_A, \quad \text{for } -d_p \leq x \leq 0 \quad (6.22a)$$

$$\rho(x) = qN_D, \quad \text{for } 0 \leq x \leq d_n \quad (6.22b)$$

where d_p and d_n are the extents of the space charges in the *p*- and *n*-type semiconductors.

(a) *pn*-junction with space charge extent

(b) Acceptor and donor concentrations



(c) Polarity of charge density distribution

Figure 6-5 The *pn*-junction with abrupt charge carrier transition in the absence of an externally applied voltage.

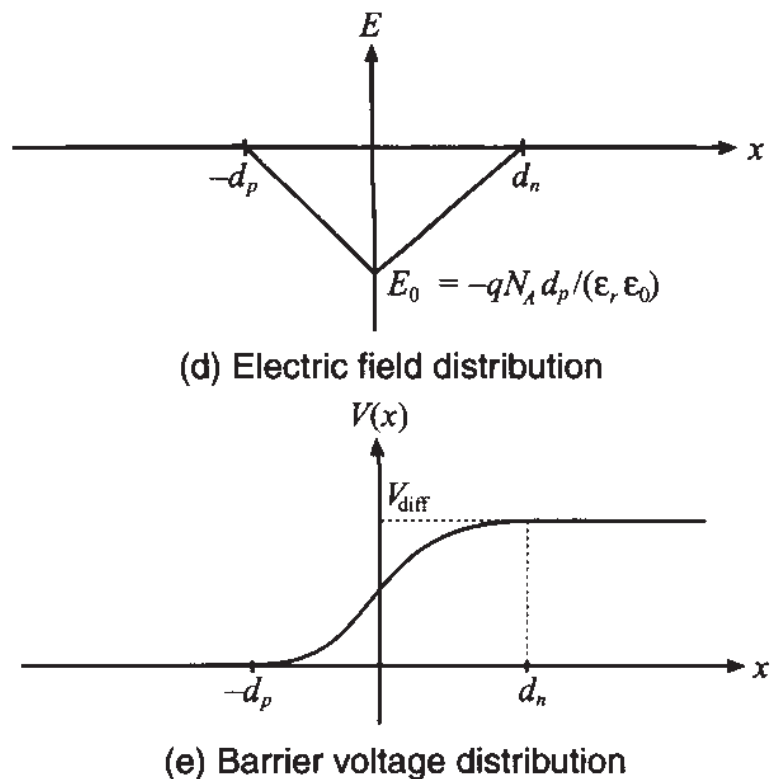


Figure 6-5 The *pn*-junction with abrupt charge carrier transition in the absence of an externally applied voltage. (Continued)

The electric field in the semiconductor is found by integrating (6.21) in the spatial limits $-d_p \leq x \leq d_n$ such that

$$E(x) = \int_{-d_p}^x \frac{\rho(x)}{\epsilon_r \epsilon_0} dx = \begin{cases} -\frac{qN_A}{\epsilon_r \epsilon_0}(x + d_p), & \text{for } -d_p \leq x \leq 0 \\ -\frac{qN_D}{\epsilon_r \epsilon_0}(d_n - x), & \text{for } 0 \leq x \leq d_n \end{cases} \quad (6.23)$$

The resulting electric field profile is depicted in Figure 6-5(d). In deriving (6.23) we used the fact that the charge balance law demands that the total space charge in the semiconductor equals zero, which for highly doped semiconductors is equivalent to the condition

$$N_A \cdot d_p = N_D \cdot d_n \quad (6.24)$$

To obtain the voltage distribution profile we now carry out the integration of (6.23) as follows:

$$V(x) = - \int_{-d_p}^x E(x) dx = \begin{cases} \frac{qN_A}{2\epsilon_r\epsilon_0}(x + d_p)^2, & \text{for } -d_p \leq x \leq 0 \\ \frac{q}{2\epsilon_r\epsilon_0}(N_A d_p^2 + N_D d_n^2) - \frac{qN_D}{2\epsilon_r\epsilon_0}(d_n - x)^2, & \text{for } 0 \leq x \leq d_n \end{cases} \quad (6.25)$$

Since the total voltage drop must be equal to the diffusion voltage V_{diff} , it is found that

$$V(d_n) = V_{\text{diff}} = \frac{qN_A d_p^2}{2\epsilon_r\epsilon_0} + \frac{qN_D d_n^2}{2\epsilon_r\epsilon_0} \quad (6.26)$$

Substituting $d_p = d_n N_D / N_A$ and solving (6.26) for d_n , we obtain the extent of the positive space charge domain into the n -semiconductor:

$$d_n = \left\{ \frac{2\epsilon V_{\text{diff}} N_A}{q} \left(\frac{1}{N_A + N_D} \right) \right\}^{1/2} \quad (6.27)$$

where $\epsilon = \epsilon_0 \epsilon_r$. An identical derivation involving $d_n = d_p N_A / N_D$ gives us the space charge extent into the p -semiconductor:

$$d_p = \left\{ \frac{2\epsilon V_{\text{diff}} N_D}{q} \left(\frac{1}{N_A + N_D} \right) \right\}^{1/2} \quad (6.28)$$

The entire length is then the addition of (6.27) and (6.28):

$$d_s = \left\{ \frac{2\epsilon V_{\text{diff}}}{q} \left(\frac{1}{N_A} + \frac{1}{N_D} \right) \right\}^{1/2} \quad (6.29)$$

We next turn our attention to the computation of the **junction capacitance**. This is an important parameter for RF devices, since low capacitances imply rapid switching speeds and suitability for high-frequency operations. The junction capacitance can be found via the well-known one-dimensional capacitor formula

$$C = \frac{\epsilon A}{d_s}$$

Substituting (6.29) for the distance d_s , we express the capacitance as

$$C = A \left\{ \frac{q\epsilon}{2V_{\text{diff}}} \frac{N_A N_D}{N_A + N_D} \right\}^{1/2} \quad (6.30)$$

If an external voltage V_A is applied across the junction, two situations arise that explain the rectifier action of the diode, as shown in Figure 6-6.

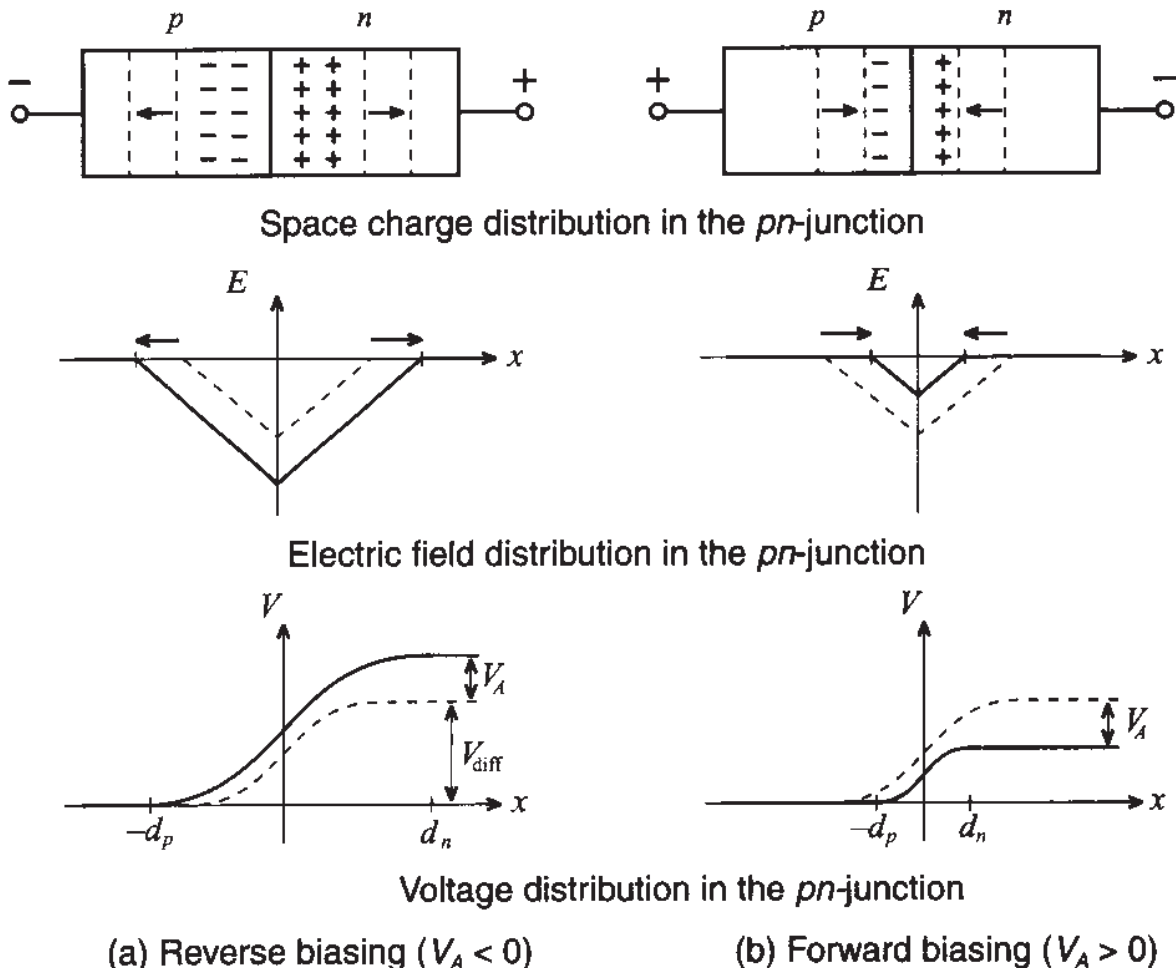


Figure 6-6 External voltage applied to the *pn*-junction in reverse and forward directions.

The reverse polarity [Figure 6-6(a)] increases the space charge domain and prevents the flow of current except for a small leakage current involving the minority carrier concentration (holes in the *n*-semiconductor, and electrons in the *p*-semiconductor). In contrast, the forward polarity reduces the space charge domain by injecting excessive electrons into the *n*- and holes into the *p*-type semiconductor. To describe these situations, the previously given equations (6.27) and (6.28) have to be modified by replacing the barrier voltage V_{diff} with $V_{\text{diff}} - V_A$; that is,

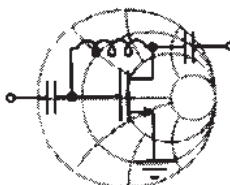
$$d_p = \left\{ \frac{2\epsilon(V_{\text{diff}} - V_A)N_D}{q} \frac{1}{N_A(N_A + N_D)} \right\}^{\frac{1}{2}} \quad (6.31)$$

$$d_n = \left\{ \frac{2\epsilon(V_{\text{diff}} - V_A)N_A}{q} \frac{1}{N_D(N_A + N_D)} \right\}^{\frac{1}{2}} \quad (6.32)$$

which leads to a total length of the space charge or depletion domain

$$d_S = \left\{ \frac{2\epsilon(V_{\text{diff}} - V_A)}{q} \left(\frac{1}{N_A} + \frac{1}{N_D} \right) \right\}^{\frac{1}{2}} \quad (6.33)$$

Depending on the polarity of V_A , we notice from (6.31)–(6.33) that either the space charge domain is enlarged or diminished.



RF & MW

Example 6-3: Computation of the junction capacitance and the space charge region length of a pn -junction

For an abrupt pn -junction Si semiconductor at room temperature ($\epsilon_r = 11.9$, $n_i = 1.5 \times 10^{10} \text{ cm}^{-3}$) with donor and acceptor concentrations equal to $N_D = 5 \times 10^{15} \text{ cm}^{-3}$ and $N_A = 10^{15} \text{ cm}^{-3}$, we desire to find the space charge regions d_p and d_n and the junction capacitance at zero biasing voltage. Show that the depletion-layer capacitance of a pn -junction can be cast into the form

$$C_J = C_{J0} \left(1 - \frac{V_A}{V_{\text{diff}}} \right)^{-1/2}$$

and determine C_{J0} . Sketch the depletion capacitance as a function of applied voltage. Assume that the cross-sectional area of the pn -junction is $A = 10^{-4} \text{ cm}^2$.

Solution: We return to the capacitance expression (6.30) where we introduce the applied voltage V_A . Thus,

$$C_J = A \left[\frac{q\epsilon}{2V_{\text{diff}}(1 - V_A/V_{\text{diff}})N_A + N_D} \right]^{1/2}$$

which is immediately recognized as the preceding formula, if we set

$$C_{J0} = A \left[\frac{q\epsilon}{2V_{\text{diff}}} \frac{N_A N_D}{N_A + N_D} \right]^{1/2}$$

Substituting $V_{\text{diff}} = V_T \ln(N_A N_D / n_i^2) = 0.6159$ V, it is found that $C_{J0} = 10.68$ pF.

For the space charge extents we use (6.28) and (6.29):

$$d_n = \left\{ \frac{2\epsilon V_{\text{diff}} N_A}{q} \left(\frac{1}{N_A + N_D} \right) \right\}^{1/2} = 0.1643 \mu\text{m}$$

$$d_p = \left\{ \frac{2\epsilon V_{\text{diff}} N_D}{q} \left(\frac{1}{N_A + N_D} \right) \right\}^{1/2} = 0.8214 \mu\text{m}$$

The dependence of the junction capacitance on the applied voltage is depicted in Figure 6-7.

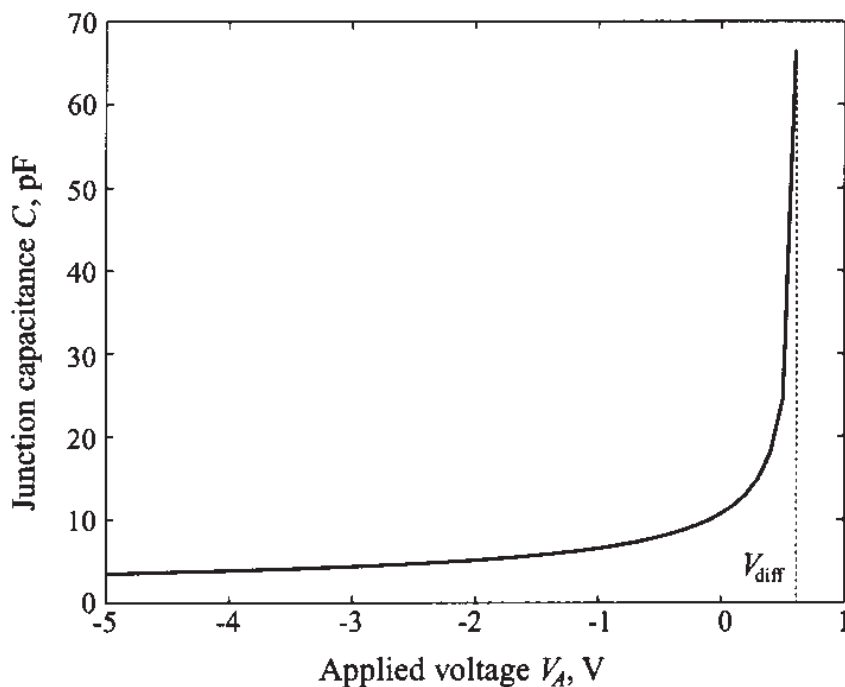


Figure 6-7 The *pn*-junction capacitance as a function of applied voltage.

In Figure 6-7 the junction capacitance for applied voltages near the built-in potential will approach infinity. However, in reality the value begins to saturate, as further discussed in Chapter 7.

For the current flow through the diode we list the Shockley diode equation, which is derived in Appendix F:

$$I = I_0(e^{V_A/V_T} - 1) \quad (6.34)$$

where I_0 is the **reverse saturation or leakage current**. The current-voltage characteristic, often called the ***I-V curve***, is generically depicted in Figure 6-8.

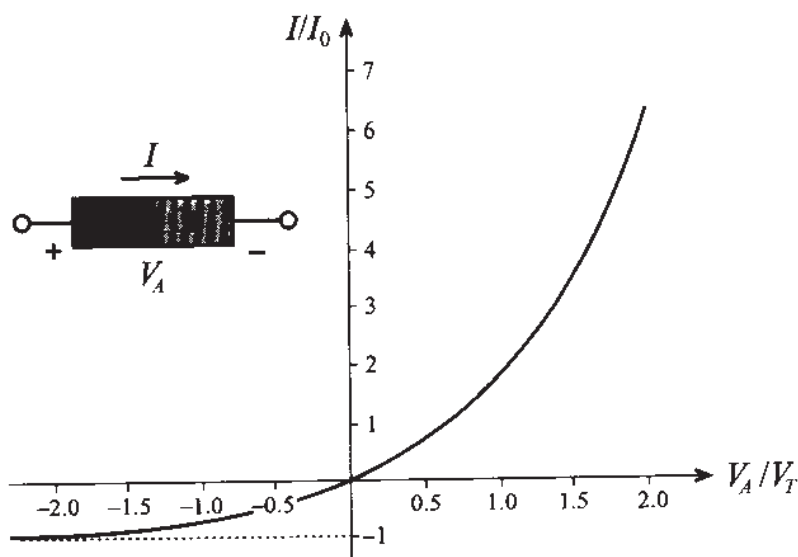


Figure 6-8 Current-voltage behavior of *pn*-junction based on Shockley equation.

This curve reveals that for negative voltages a small, voltage independent, current $-I_0$ will flow, whereas for positive voltages an exponentially increasing current is observed. The function shown in Figure 6-8 is an idealization since it does not take into account breakdown phenomena. Nonetheless (6.34) reveals clearly the rectifier property of the *pn*-junction when an alternating voltage is applied.

The existence of the depletion layer or junction capacitance requires a reverse-biased *pn*-junction diode. This implies, with reference to Example 6-3, the condition that $V_A < V_{\text{diff}}$. However, under forward bias condition we encounter an additional **diffusion capacitance** due to the presence of diffusion charges Q_d (minority carriers) stored in the semiconductor layers which become dominant if $V_A > V_{\text{diff}}$. This charge can be quantified by realizing that the charge Q_d can be computed as diode current I multiplied by the transition time of carriers through the diode τ_T or

$$Q_d = I\tau_T = \tau_T I_0(e^{V_A/V_T} - 1) \quad (6.35)$$

It is apparent that the diffusion capacitance assumes a nonlinear relation with the applied voltage and the junction temperature. The diffusion capacitance is computed as

$$C_d = \frac{dQ_d}{dV_A} = \frac{I_0 \tau_T}{V_T} e^{V_A/V_T} \quad (6.36)$$

and is seen to be strongly dependent on the operating voltage.

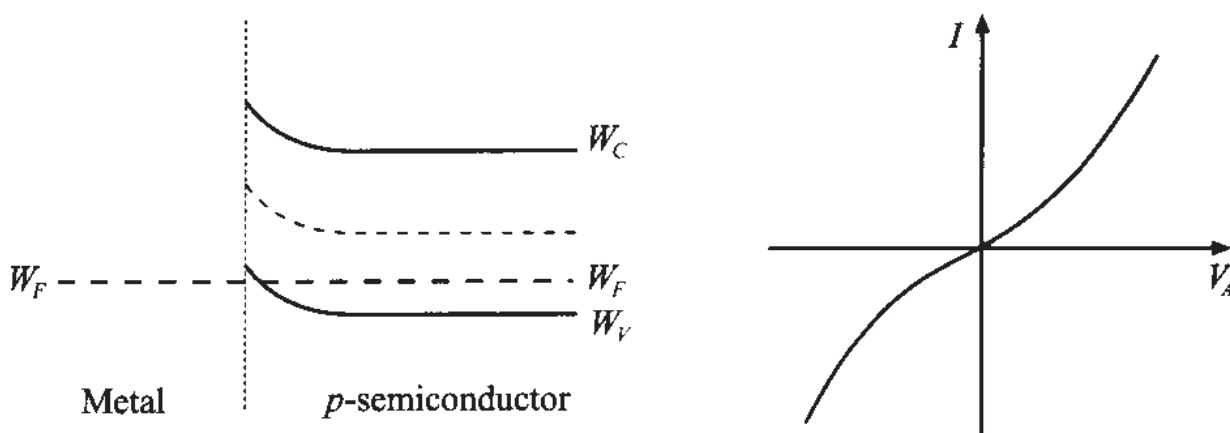
In general, the total capacitance C of a pn -diode can roughly be divided into three regions:

1. $V_A < 0$: only the depletion capacitance is significant: $C = C_J$
2. $0 < V_A < V_{\text{diff}}$: depletion and diffusion capacitances combine: $C = C_J + C_d$
3. $V_A > V_{\text{diff}}$: only the diffusion capacitance is significant: $C = C_d$

The influence of the diffusion capacitance is appreciated if we consider a diode that is operated at $V_A = 1$ V and that has an assumed transition time of $\tau_T = 100$ ps = 10^{-10} s and a reverse saturation current of $I_0 = 1$ fA = 10^{-15} A measured at room temperature of 300°K (i.e., $V_T = 26$ mV). Substituting these values into (6.36), we find $C = C_d = 194$ nF which is rather large and for typical resistances of $R = 0.1 \dots 1 \Omega$ results in large RC time constants that restrict the high-frequency use of conventional pn -junction diodes.

6.1.3 Schottky Contact

W. Schottky analyzed the physical phenomena involved when a metallic electrode is contacting a semiconductor. For instance, if a p -semiconductor is in contact with a copper or aluminum electrode, there is a tendency for the electrons to diffuse into the metal, leaving behind an increased concentration of holes in the semiconductor. The consequences of this effect are modified valence and conduction band energy levels near the interface. This can be displayed by a local change in the energy band structure depicted in Figure 6-9(a).



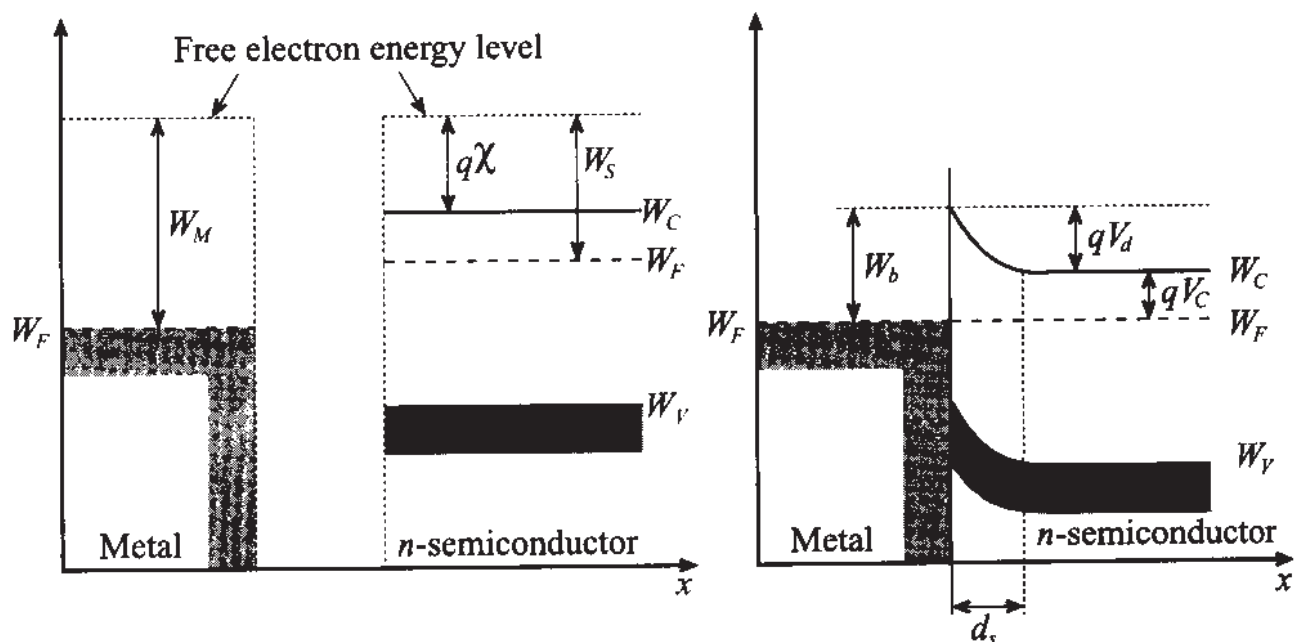
(a) Energy band model

(b) Voltage-current characteristic

Figure 6-9 Metal electrode in contact with p -semiconductor.

Because of the higher concentration of holes, the valence band bends toward the Fermi level. The conduction band, as the result of a lower electron concentration, bends away from the Fermi level. For such a configuration we always obtain a low resistance contact [(see Figure 6-9(b)], irrespective of the polarity of the applied voltage.

The situation becomes more complicated, but technologically much more interesting, when a metallic electrode is brought in contact with an *n*-semiconductor. Here the more familiar behavior of a *pn*-junction emerges: A small positive volume charge density is created in the semiconductor due to electron migration from the semiconductor to the metal. This mechanism is due to the fact that the Fermi level is higher in the semiconductor (lower work function) than in the metal (higher work function) when the two materials are apart. However, as both materials are contacted, the Fermi level again has to be the same and band distortions are created. Electrons diffuse from the *n*-semiconductor and leave behind positive space charges. The depletion zone grows until the electrostatic repulsion of the space charges prevents further electron diffusion. To clarify the issues associated with a metal *n*-semiconductor contact, Figure 6-10 shows the two materials before and after bonding.



(a) Metal and semiconductor do not interact

(b) Metal-semiconductor contact

Figure 6-10 Energy-band diagram of Schottky contact, (a) before and (b) after contact.

The energy $W_b = qV_b$ is related to the metal work function $W_M = qV_M$ (V_M is recorded from the Fermi level to the reference level where the electron becomes a detached free particle; values of V_M for some commonly used metals are summarized in Table 6-2) and the electron affinity $q\chi$, where χ is 4.05V for Si, 4.0V for Ge, and

4.07V for GaAs and is measured from the conduction band to the same reference level where the electron becomes a free carrier, according to

$$W_b = q(V_M - \chi) \quad (6.37)$$

Table 6-2 Work function potentials of some metals

| Material | Work function potential, V_M |
|-----------------|--------------------------------|
| Silver (Ag) | 4.26 V |
| Aluminum (Al) | 4.28 V |
| Gold (Au) | 5.1 V |
| Chromium (Cr) | 4.5 V |
| Molybdenum (Mo) | 4.6 V |
| Nickel (Ni) | 5.15 V |
| Palladium (Pd) | 5.12 V |
| Platinum (Pt) | 5.65 V |
| Titanium (Ti) | 4.33 V |

An expression for a built-in Schottky barrier voltage V_d is established just as in the *pn*-junction, which involves (6.37) and the additional voltage V_C between conduction and Fermi levels:

$$V_d = (V_M - \chi) - V_C \quad (6.38)$$

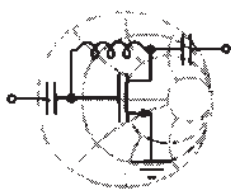
where V_C is dependent on the doping N_D and the concentration of states in the conduction band N_C according to $N_C = N_D \exp(V_C/V_T)$. Solving for the voltage gives $V_C = V_T \ln(N_C/N_D)$. Although real metal-semiconductor interfaces usually involve an additional very narrow isolation layer, we will neglect the influence of this layer and only deal with the length of the space charge in the semiconductor:

$$d_S = \left\{ \frac{2\epsilon}{q} \frac{(V_d - V_A)}{N_D} \right\}^{\frac{1}{2}} \quad (6.39)$$

Therefore, it is found that the junction capacitance of the Schottky contact

$$C_J = A \frac{\epsilon}{d_s} = A \left\{ \frac{q\epsilon}{2(V_d - V_A) N_D} \right\}^{\frac{1}{2}} \quad (6.40)$$

is almost identical to (6.30). A simple computation now can predict a typical value for V_d as illustrated in the following example.



RF & MW

Example 6-4: Computation of the barrier voltage, depletion capacitance, and space charge region width for a Schottky diode

A Schottky diode is created as an interface between a gold contact material and an n -type silicon semiconductor. The semiconductor is doped to $N_D = 10^{16} \text{ cm}^{-3}$ and the work function V_M for gold is 5.1 V. Also, as mentioned above, the affinity for Si is $\chi = 4.05 \text{ V}$. Find the Schottky barrier V_d , space charge width d_s , and capacitance C_J if the dielectric constant of silicon is $\epsilon_r = 11.9$. Assume the cross-sectional diode area to be $A = 10^{-4} \text{ cm}^2$ and the temperature equal to 300°K .

Solution: Since the concentration of states in the conduction band of silicon is $N_C = 2.8 \times 10^{19} \text{ cm}^{-3}$, we can compute the conduction band potential as

$$V_C = V_T \ln\left(\frac{N_C}{N_D}\right) = \frac{1.38 \times 10^{-23} 300}{1.6 \times 10^{-19}} \ln\left(\frac{2.8 \times 10^{19}}{10^{16}}\right) \text{ V} = 0.21 \text{ V}$$

Substituting the obtained value for V_C into (6.38), we find the built-in barrier voltage

$$V_d = (V_M - \chi) - V_C = (5.1 \text{ V} - 4.05 \text{ V}) - 0.21 \text{ V} = 0.84 \text{ V}$$

The space charge width is obtained from (6.39)

$$d_s = \sqrt{\frac{2\epsilon_0 \epsilon_r V_d}{q N_D}} = \sqrt{\frac{2(8.85 \times 10^{-12})(11.9)(0.84)}{1.6 \times 10^{-19} 10^{16}}} \text{ m} = 332 \mu\text{m}$$

Finally, the junction capacitance according to the formula for the parallel-plate capacitor, see (6.40), gives us

$$C_J = A \frac{\epsilon_0 \epsilon_r}{d_s} = 10^{-8} \frac{8.85 \times 10^{-12} \cdot 11.9}{332 \times 10^{-6}} \text{ F} = 3.2 \text{ fF}$$

This example shows that the metal-semiconductor junction diode for similar size and doping has a depletion capacitance significantly smaller than that of a pn-junction, which permits higher operational frequencies of the device.

6.2 RF Diodes

In this section we will review some practical realizations of the diodes that are most commonly used in RF and MW circuits. As presented in the previous section, a classical *pn*-junction diode is not very suitable for high-frequency applications because of the high junction capacitance. In contrast, diodes formed by a metal-semiconductor contact possess smaller junction capacitances and consequently reach higher frequency limits. Today, Schottky diodes find widespread applications in RF detectors, mixers, attenuators, oscillators, and amplifiers.

After discussing the Schottky diode in Section 6.2.1, we will continue investigating a number of special RF diodes. In Section 6.2.2 the PIN diode is analyzed and placed in context with its primary use as a variable resistor and high-frequency switch.

Besides relying on the rectifier property of diodes, we can also exploit the dependence of the junction capacitance on the applied voltage to construct voltage-controlled tuning circuits, where diodes are used as variable capacitors. An example of such a specialized diode is the varactor diode, covered in Section 6.2.3.

At the end of this section we will discuss a few more exotic diode configurations, such as IMPATT, Tunnel, TRAPATT, BARRITT, and Gunn diodes, which are less frequently used but which are still of interest due to their unique electric properties.

6.2.1 Schottky Diode

Compared with the conventional *pn*-junction, the Schottky barrier diode has a different reverse-saturation current mechanism, which is determined by the thermionic emission of the majority carriers across the potential barrier. This current is orders of magnitude larger than the diffusion-driven minority carriers constituting the reverse-saturation current of the ideal *pn*-junction diode. For instance, the Schottky diode has a

typical reverse-saturation current density on the order of 10^{-6} A/cm^2 compared with 10^{-11} A/cm^2 of a conventional Si-based *pn*-junction diode. The schematic diagram of a cross-sectional view of the Schottky diode with the corresponding circuit elements is given in Figure 6-11.

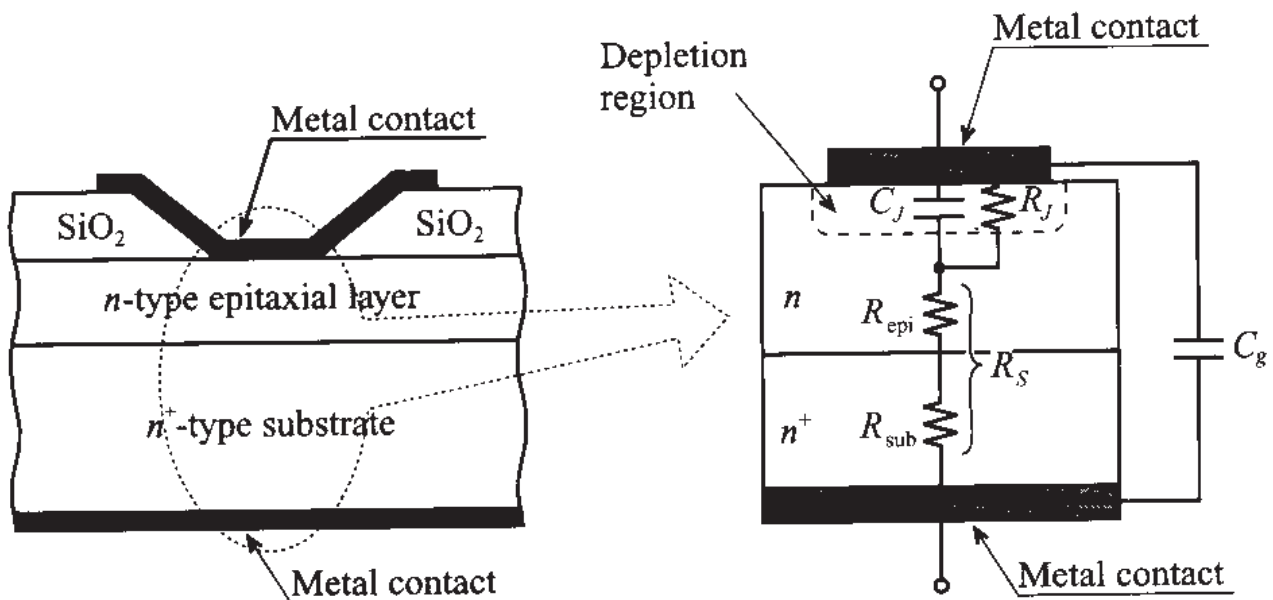


Figure 6-11 Cross-sectional view of Si Schottky diode.

The metal electrode (tungsten, aluminum, gold, etc.) is in contact with a weakly doped *n*-semiconductor layer epitaxially grown on a highly doped *n*⁺ substrate. The dielectric is assumed to be ideal; that is, the conductance is zero. The current-voltage characteristic is described by the following equation:

$$I = I_S(e^{(V_A - IR_S)} - 1) \quad (6.41)$$

where the reverse-saturation current is given by

$$I_S = A \left(R^* T^2 \exp \left[\frac{-q V_b}{kT} \right] \right) \quad (6.42)$$

and R^* is the so-called **Richardson constant** for thermionic emission of the majority carrier across the potential barrier. A typical value of R^* for Si is $100 \text{ A/cm}^2 \text{ K}^2$.

The corresponding **small-signal** equivalent circuit model is illustrated in Figure 6-12. In this circuit we note that the junction resistance R_j is dependent on the bias current, just as is the diode series resistance, which is comprised of epitaxial and substrate resistances $R_S = R_{\text{epi}} + R_{\text{sub}}$. The bond wire inductance is fixed and its value is approximately on the order of $L_g = 0.1 \text{ nH}$. As discussed above, the junction capacitance C_j is given by (6.40). Because of the resistance R_S , the actual junction voltage is

equal to the applied voltage minus the voltage drop over the diode series resistance, resulting in the modified exponential expression (6.41).

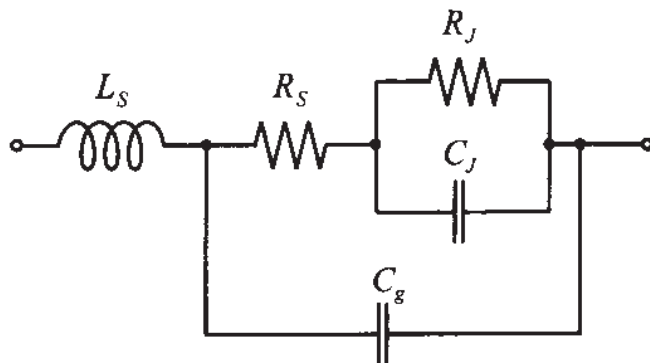


Figure 6-12 Circuit model of typical Schottky diode.

Typical component values for Schottky diodes are $R_S \approx 2 \dots 5 \Omega$, $C_g = 0.1 \dots 0.2 \text{ pF}$, and $R_J = 200 \dots 2 \text{ k}\Omega$. Often, the additional IR_S term in (6.41) is neglected for small bias currents below 0.1 mA. However, for certain applications, the series resistance may form a feedback loop, which means the resistance is multiplied by a gain factor of potentially large magnitude. For this situation, the IR_S term has to be taken into account.

In circuit realizations of high-frequency Schottky diodes, the planar configuration in Figure 6-11 gives rise to relatively large parasitic capacitances for very small metal contacts of typically $10 \mu\text{m}$ diameter and less. The stray capacitances can be somewhat minimized through the addition of an isolation ring, as depicted in Figure 6-13.

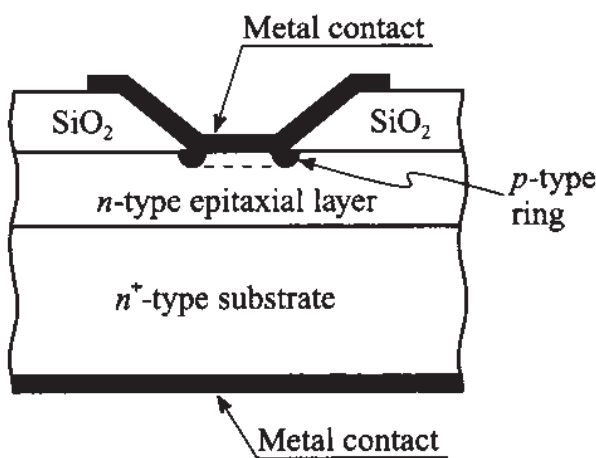


Figure 6-13 Schottky diode with additional isolation ring suitable for very-high-frequency applications.

The small signal junction capacitance and junction resistance can be found by expanding the electric current expression (6.41) around the quiescent or operating

point V_Q . That means the total diode voltage is written as a DC bias V_Q and a small AC signal carrier frequency component v_d :

$$V = V_Q + v_d \quad (6.43)$$

The substitution of (6.43) in (6.41) for a negligible IR_S term yields

$$I = I_S(e^{V/V_T} - 1) = I_S(e^{V_Q/V_T} e^{v_d/V_T} - 1) \quad (6.44)$$

Expanding this equation in a Taylor series about the Q -point and retaining the first two terms gives

$$I(V) \approx I_Q + \frac{dI}{dV} \Big|_{V_Q} v_d = I_Q + \frac{I_S v_d}{V_T} e^{V_Q/V_T} = I_Q + (I_Q + I_S) \frac{v_d}{V_T} = I_Q + \frac{v_d}{R_J} \quad (6.45)$$

Here the junction resistance $R_J(V_Q)$ is identified as

$$R_J(V_Q) = \frac{V_T}{I_Q + I_S} \quad (6.46)$$

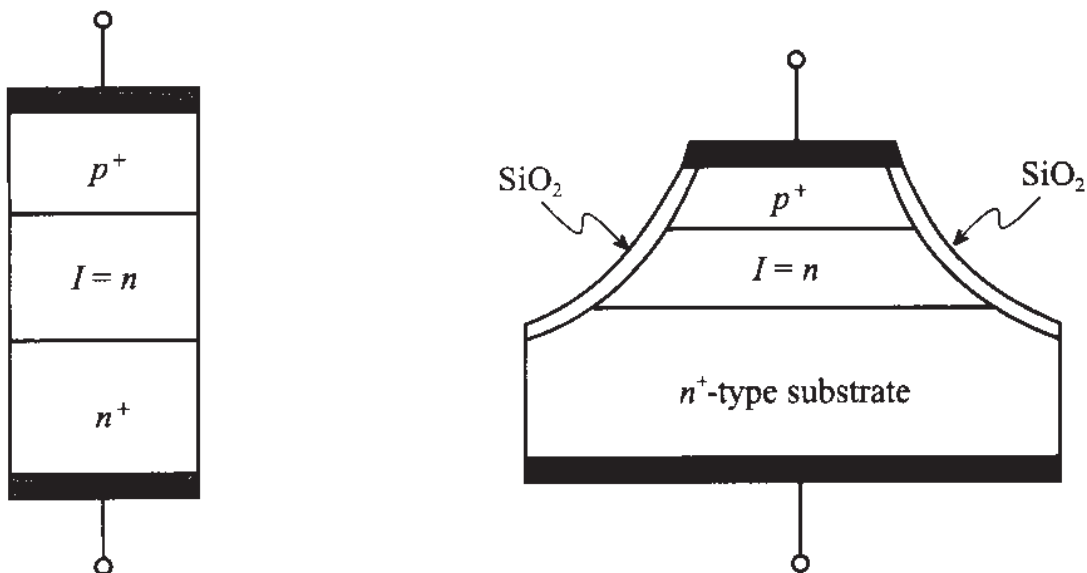
and the junction capacitance is given by (6.40), with V_Q replacing V_A .

6.2.2 PIN Diode

PIN diodes find applications as high-frequency switches and variable resistors (attenuators) in the range from $10\text{ k}\Omega$ to less than $1\text{ }\Omega$ for RF signals up to 50 GHz. They contain an additional layer of an intrinsic (*I-layer*) or lightly doped semiconductor sandwiched between highly doped p^+ and n^+ layers. Depending upon application and frequency range, the thickness of the middle layer ranges from 1 to 100 μm . In forward direction, the diode behaves as if it possesses a variable resistance controlled by the applied current. However, in reverse direction the lightly doped inner layer creates space charges whose extent reaches the highly doped outer layers. This effect takes place even for small reverse voltages and remains essentially constant up to high voltages, with the consequence that the diode behaves similar to a dual plate capacitor. For instance, a Si-based PIN diode with an internal *I-layer* of $20\text{ }\mu\text{m}$ and a surface area of 200 by $200\text{ }\mu\text{m}$ has a diffusion capacitance on the order of 0.2 pF .

A generic PIN diode and its practical implementation in **mesa processing technology** is presented in Figure 6-14. The advantage of the mesa configuration over the conventional planar construction is a significant reduction in fringing capacitance.

The mathematical representation of the *I-V* characteristic depends on the level and direction of current flow. To keep things simple, we will rely to a large extent on discussions already outlined for the *pn*-junction.



(a) Simplified structure of a PIN diode (b) Fabrication in mesa processing technology
Figure 6-14 PIN diode construction.

In the forward direction and for a weakly doped n -type intrinsic layer the current through the diode is

$$I = A \left(\frac{qn_i^2 W}{N_D \tau_p} \right) \left(e^{V_A/(2V_T)} - 1 \right) \quad (6.47)$$

where W is the width of the intrinsic layer; τ_p is the **excess minority carrier lifetime**, which can be on the order of up to $\tau_p = 1 \mu\text{s}$; and N_D is the doping concentration in the middle layer of the lightly doped n -semiconductor. The factor 2 in the exponent takes into account the presence of two junctions. For a pure intrinsic layer $N_D = n_i$, (6.47) leads to the form

$$I = A \left(\frac{qn_i W}{\tau_p} \right) \left(e^{V_A/(2V_T)} - 1 \right) \quad (6.48)$$

The total charge can be calculated from the relation $Q = I\tau_p$. This allows us to find the diffusion capacitance:

$$C_d = \frac{dQ}{dV_A} = \tau_p \left(\frac{dI}{dV_A} \right) = \frac{I\tau_p}{2V_T} \quad (6.49a)$$

In the reverse direction, the capacitance is dominated by the bias-dependent space charge length of the I -layer. For small voltages C_J is approximately

$$C_J = \epsilon_I \left(\frac{A}{W} \right) \quad (6.49b)$$

where ϵ_I is the dielectric constant of the intrinsic layer.

The dynamic resistance of a PIN diode can be found through a Taylor series expansion around the Q -point as already discussed for the Schottky diode. The result is

$$R_J(V_Q) = \left. \frac{dV}{dI} \right|_{I=I_Q} = \frac{2V_T}{I_Q + I_{P0}} \quad (6.50)$$

where, with reference to (6.47), we have set $I_{P0} = A(qn_i^2 W)/(N_D \tau_p)$.

Based on the PIN diode's resistive behavior under forward bias ("switch on") and capacitive behavior under reverse bias ("switch off" or **isolation**) we can proceed to construct simple small signal models. For the PIN diode in series connection, the electric circuit model is seen in Figure 6-15 terminated with source and load resistances. The junction resistance and diffusion capacitance, as derived in (6.49) and (6.50), may in practice model the PIN diode behavior only very approximately. More quantitative information is obtained through measurements or sophisticated computational modeling efforts.

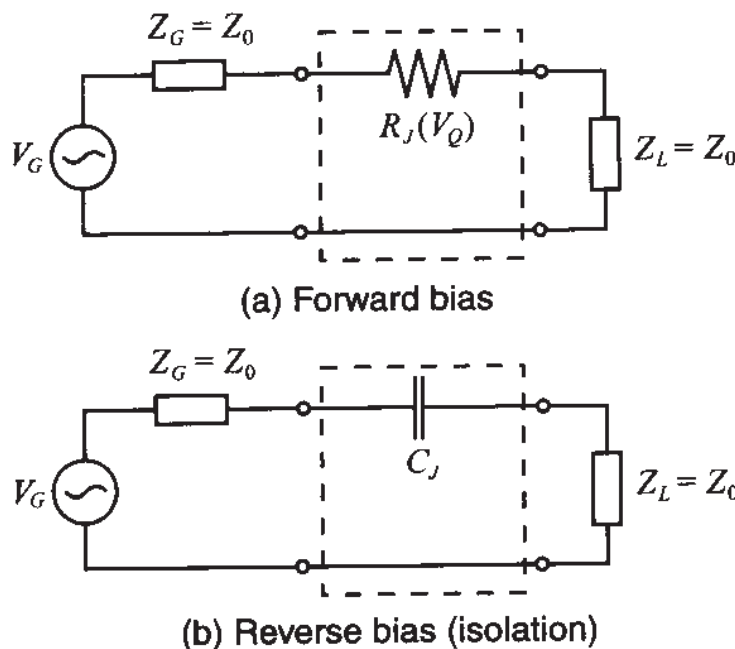


Figure 6-15 PIN diode in series connection.

The bias point setting required to operate the PIN diode has to be provided through a DC circuit that must be separated from the RF signal path. The DC isolation is achieved by a **radio frequency coil (RFC)**, representing a short circuit at DC and an open circuit at high frequency. Conversely, **blocking capacitors (C_B)** represent an

open circuit at DC and a short circuit at RF. Figure 6-16 shows a typical attenuator circuit where the PIN diode is used either in series or shunt connection.

Although in the following discussion we will use a DC bias, a low-frequency AC bias can also be employed. In this case the current through the diode consists of two components such that $I = (dQ/dt) + Q/\tau_p$. The implication of this is deferred to the problem section.

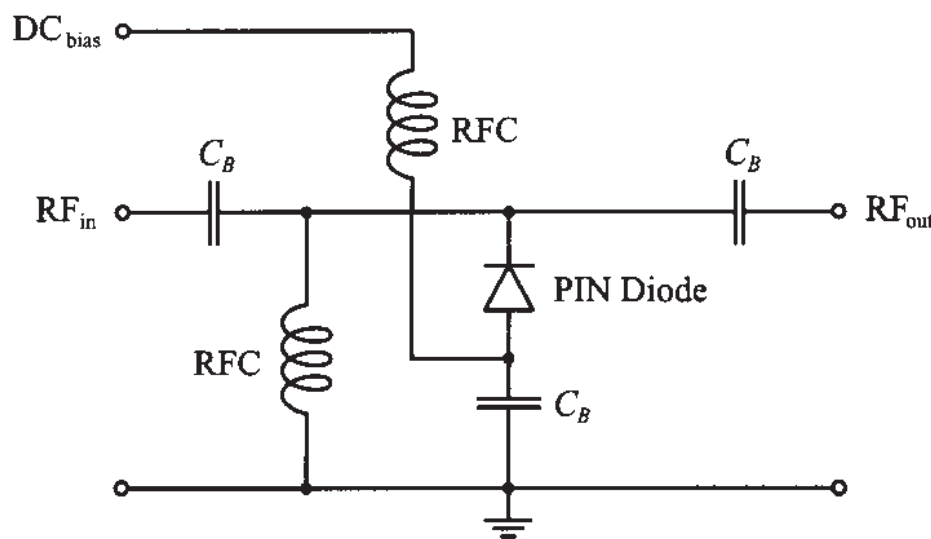
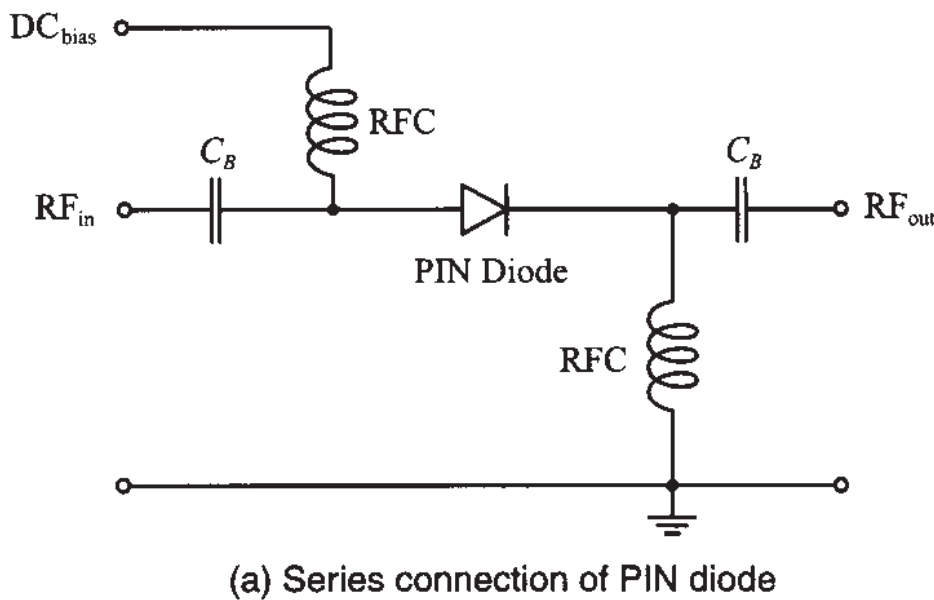


Figure 6-16 Attenuator circuit with biased PIN diode in series and shunt configurations.

For positive DC bias voltage, the series connected PIN diode represents a low resistance to the RF signal. The shunt connected PIN diode, however, creates a short-circuit condition, permitting only a negligibly small RF signal to appear at the output port.

The shunt connection acts like a high attenuation device with high insertion loss. The situation is reversed for negative bias condition where the series connected PIN diode behaves like a capacitor with high impedance or high insertion loss, whereas the shunt connected diode with a high shunt impedance does not affect the RF signal appreciably.

An often used notation is the **transducer loss** TL conveniently expressed in terms of the S parameter $|S_{21}|$ so that with (4.52)

$$TL = -20\log|S_{21}| = -20\log\left|\frac{2V_2}{V_G}\right| \quad (6.51)$$

The following example computes the transducer loss for a PIN diode in series configuration.



RF & MW

Example 6-5: Computation of transducer loss of a PIN diode in series configuration for forward and reverse bias conditions

Find the transducer loss of a forward and reverse biased PIN diode in series connection ($Z_G = Z_L = Z_0 = 50 \Omega$). Assume the junction resistance R_J under forward bias ranges between 1 and 20Ω . Furthermore, assume that the reverse bias operating conditions result in the junction capacitance being $C_J = 0.1, 0.3, 0.6, 1.3$, and 2.5 pF , and the frequency range of interest extends from 10 MHz to 50 GHz.

Solution: Based on (6.51) and Figure 6-15, the transducer loss is found with the aid of the voltage divider rule to be

$$TL_{\text{forward}} = -20\log\left(\frac{100}{100 + R_J}\right) = 20\log\left(1 + \frac{R_J}{100}\right)$$

and

$$TL_{\text{reverse}} = -20\log\left|\frac{100}{100 - j1/(\omega C_P)}\right| = 10\log\left[1 + \left(\frac{1}{100\omega C_P}\right)^2\right]$$

Figure 6-17 plots the transducer loss in dB under forward bias condition for the given range of junction resistances. In contrast, Figure 6-18 graphs the reverse bias condition where the PIN diode essentially has a purely capacitive response.

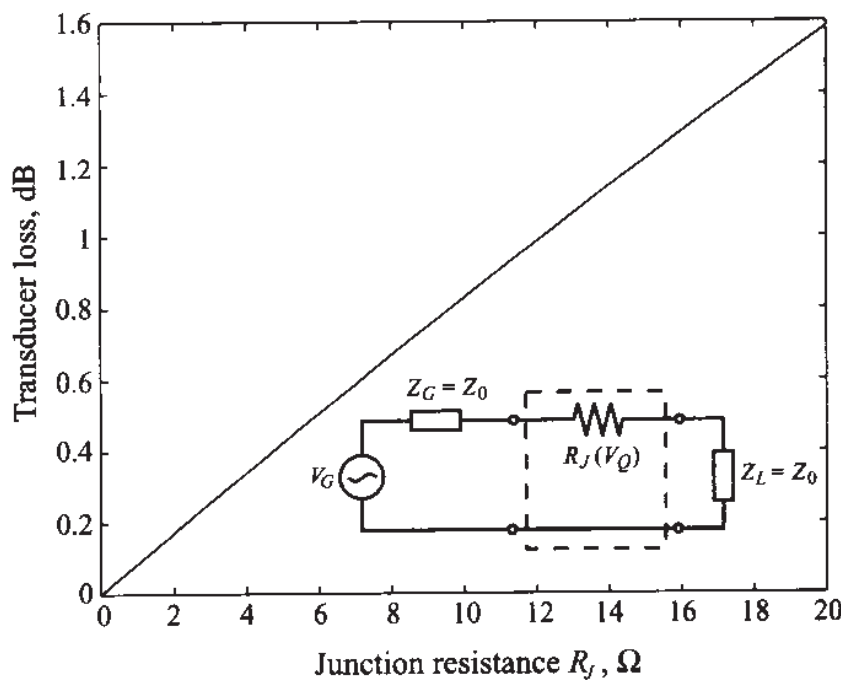


Figure 6-17 Transducer loss of series connected PIN diode under forward bias condition. The diode behaves as a resistor.

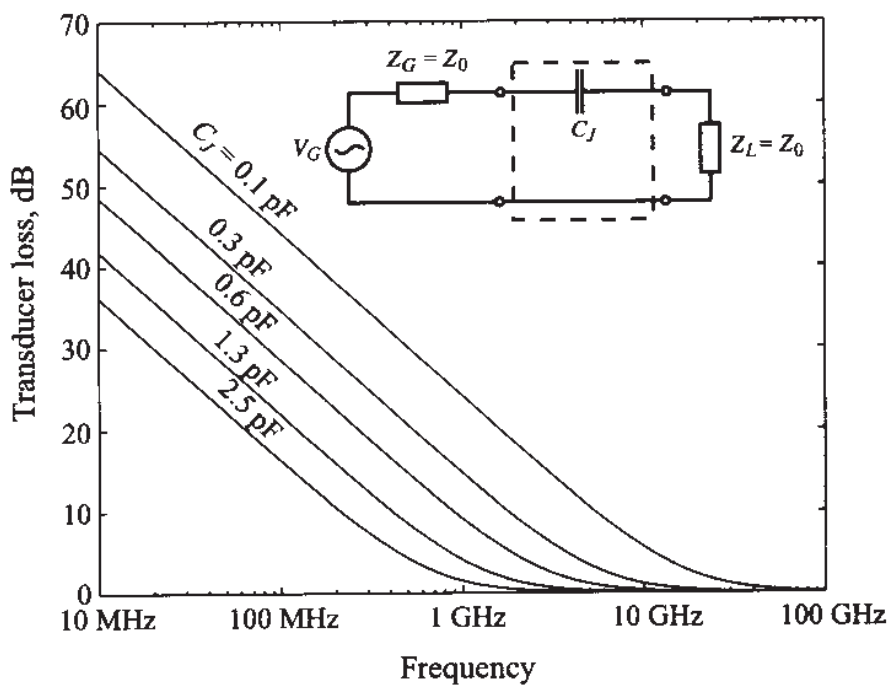
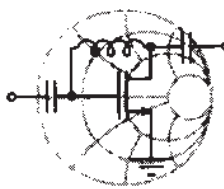


Figure 6-18 Transducer loss of series connected PIN diode under reverse bias condition. The diode behaves as a capacitor.

6.2.3 Varactor Diode

The PIN diode with its capacitive behavior under reverse bias already suggests that a variable capacitance versus voltage characteristic can be created by a specific middle layer doping profile. A varactor diode exactly accomplishes this task by a suitable choice of the intrinsic layer thickness W in addition to selecting a particular doping distribution $N_D(x)$.



RF & MW

Example 6-6: Determination of the required doping profile for a particular capacitance-voltage behavior

Find the appropriate doping concentration profile $N_D(x)$ that ensures that the varactor diode capacitance changes depending on the applied reverse biasing voltage as $C(V_A) = C_0'/(V_A - V_{\text{diff}})$, where $C_0' = 5 \times 10^{-12} \text{ FV}$ and the cross-sectional diode area is $A = 10^{-4} \text{ cm}^2$.

Solution: The extent of the space charge length can be predicted based on (6.39) to be

$$x = \left\{ \frac{2\epsilon_I(V_{\text{diff}} - V_A)}{q} \left(\frac{1}{N_D} \right) \right\}^{1/2}$$

which determines the junction capacitance $C = \epsilon_I A/x$. In the derivation of the preceding formula we assumed that the doping concentration in the I -layer is much lower than the doping in the adjacent layers. If the space charge domain is increased by a small increment ∂x , the charge is modified to

$$\partial Q = q N_D(x) A \partial x$$

This differential increase in length can be expressed by a corresponding decrease in capacitance. By differentiating the capacitor formula, we obtain

$$\partial x = -\epsilon_I A \partial C / C^2$$

Upon substitution of ∂x into the expression for ∂Q and noting that $\partial Q = C \partial V_A$, we have

$$\partial Q \equiv C \partial V_A = -q N_D(x) A^2 \epsilon_I \partial C / C^2$$

This gives us the desired expression for the doping profile:

$$N_D(x) = -\frac{C^3}{q \epsilon_I A^2} \left(\frac{\partial V_A}{\partial C} \right)$$

For the desired capacitance, we find

$$N_D(x) = \frac{C_0'}{qAx} = \frac{2 \times 10^{11}}{x} \text{ cm}^{-2}$$

Naturally we cannot enforce the doping profile to reach infinity as x approaches the beginning of the I-layer. Nonetheless, by approximating a hyperbolic function, it is possible to ensure the desired capacitance-voltage behavior.

Figure 6-19 presents the simplified electric circuit model of the varactor diode consisting of a substrate resistance and voltage-dependent capacitance of the form $(V_{\text{diff}} - V_A)^{-1/2}$. This is the case when the doping profile is constant. Therefore we have for the capacitance in generic representation:

$$C_V = C_{V0} \left(1 - \frac{V_Q}{V_{\text{diff}}} \right)^{-1/2} \quad (6.52)$$

where V_Q is the reverse bias.

One of the main applications of this diode is the frequency tuning of microwave circuits. This is due to the fact that the cut-off frequency f_V of the first-order varactor model

$$f_V = \frac{1}{2\pi R_S C_V(V_Q)} \quad (6.53)$$

can be controlled through the reverse bias V_Q .

In addition, the varactor diode can be used to generate short pulses as schematically explained in Figure 6-20. An applied voltage V_A across a series connection of resistor and diode creates a current flow I_V . This current is in phase with the voltage over the positive cycle. During the negative voltage cycle the stored carriers in the middle layer contribute to the continued current flow until all carriers are removed. At this point the current

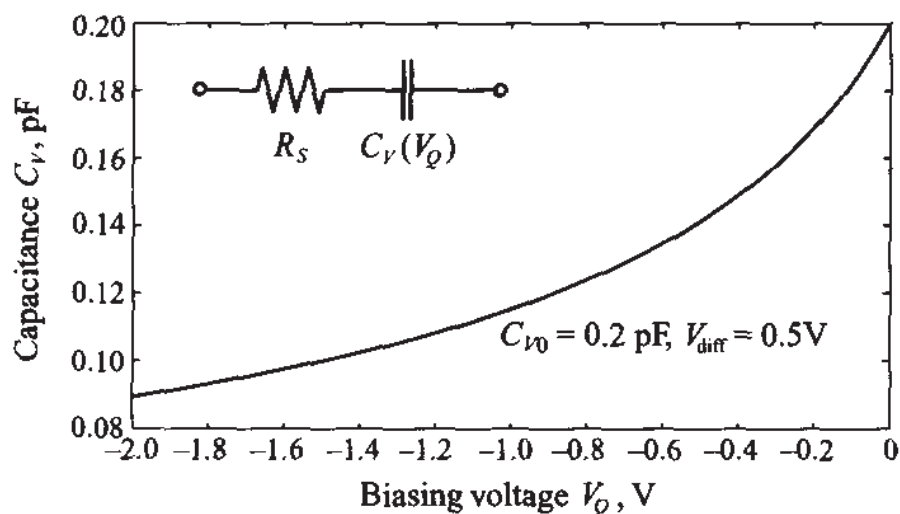


Figure 6-19 Simplified electric circuit model and capacitance behavior of varactor diode.

drops abruptly to zero. A transformer can now couple out a voltage pulse according to Faraday's law $V_{\text{out}} = L(dI_V/dt)$. The pulse width can be approximated based on the length of the middle layer W and the saturation drift velocity $v_{d\max}$ of the injected carrier concentration.

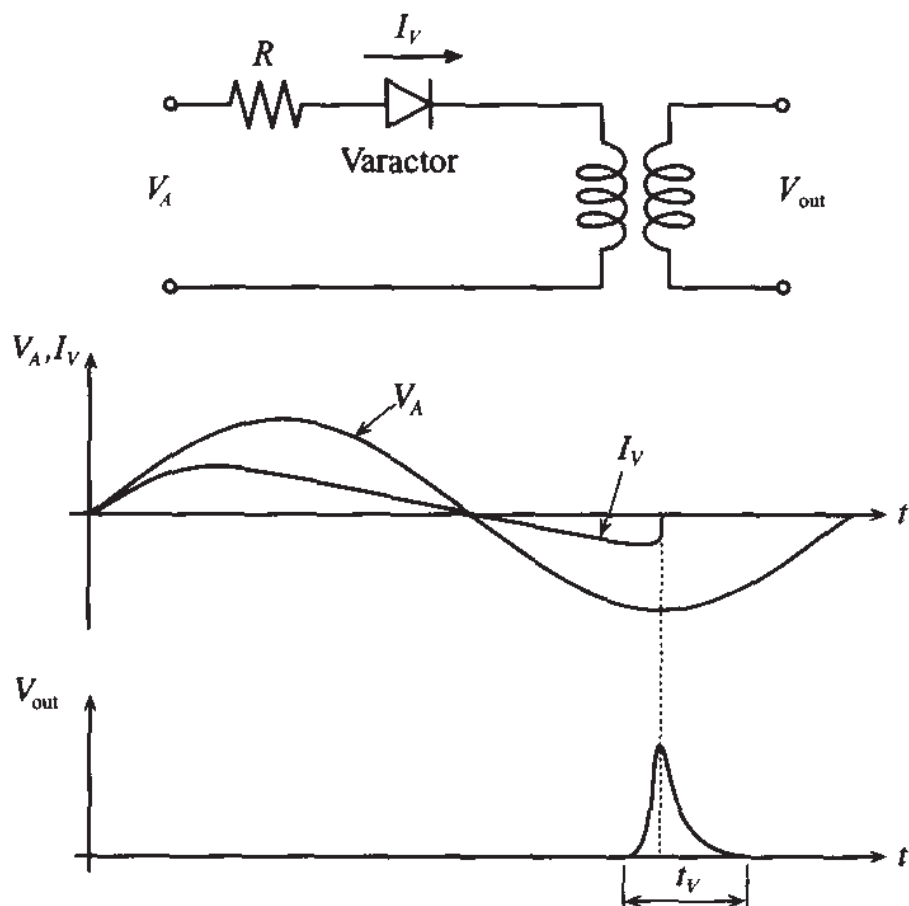


Figure 6-20 Pulse generation with a varactor diode.

If we assume $W = 10 \mu\text{m}$ and $v_{d\max} \approx 10^6 \text{ cm/s}$ we obtain a transit time that is equivalent to a pulse width of

$$t_v = \frac{W}{v_{d\max}} = \frac{10 \mu\text{m}}{10^4 \text{ m/s}} = 1 \text{ ns} \quad (6.54)$$

6.2.4 IMPATT Diode

IMPATT stands for **I**MPact **A**valanche and **T**ransit **T**ime diode and exploits the **a**valanche **e**ffect as originally proposed by Read. The principle of this diode construction, which is very similar to the PIN diode, is depicted in Figure 6-21. The key difference is the high electric field strength that is generated at the interface between the n^+ and p layer resulting in an avalanche of carriers through **i**mpact **ionization.**

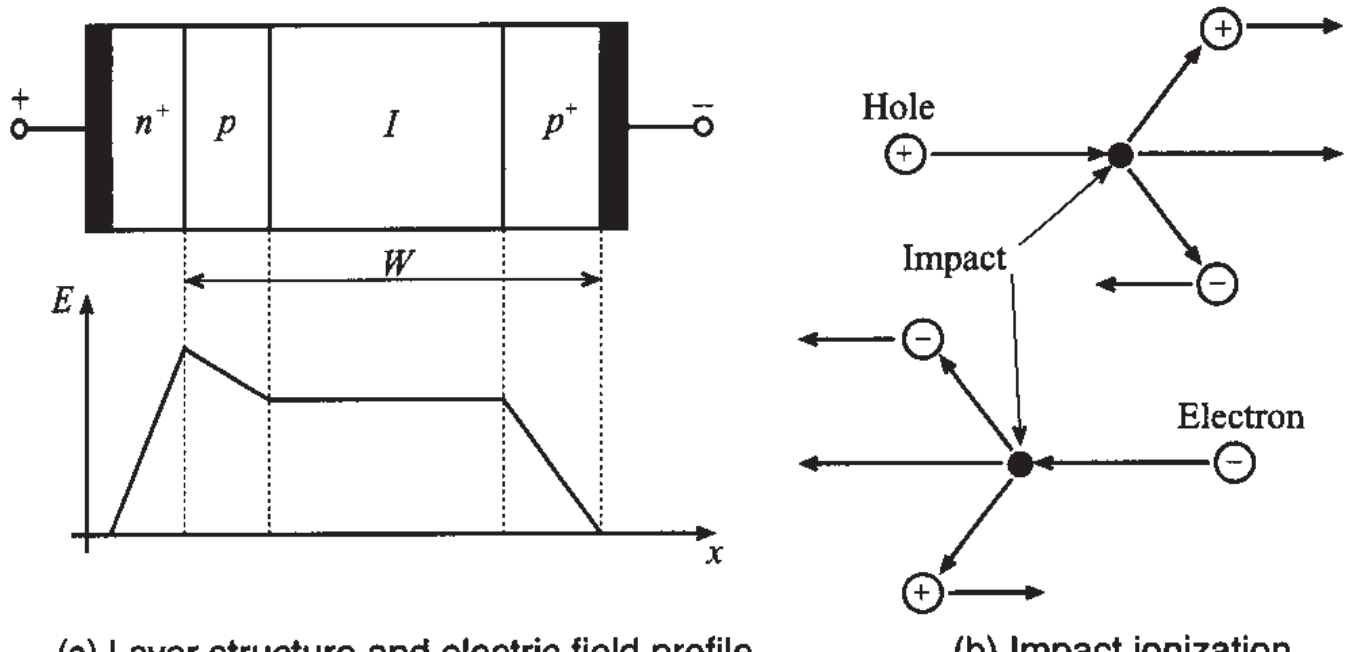


Figure 6-21 IMPATT diode behavior.

The additional ionization current I_{ion} that is generated when the applied RF voltage V_A produces an electric field that exceeds the critical threshold level is seen in Figure 6-22. The current slowly decreases during the negative voltage cycle as the excess carriers are removed. The phase shift between this ionization current and the applied voltage can be tailored so as to reach 90° . The total diode current suffers an additional delay since the excess carriers have to travel through the intrinsic layer to the p^+ layer. The time constant is dependent on the length and drift velocity as given in (6.47). Choosing the intrinsic layer length appropriately in conjunction with a suitable doping concentration can create an additional time delay of 90° .

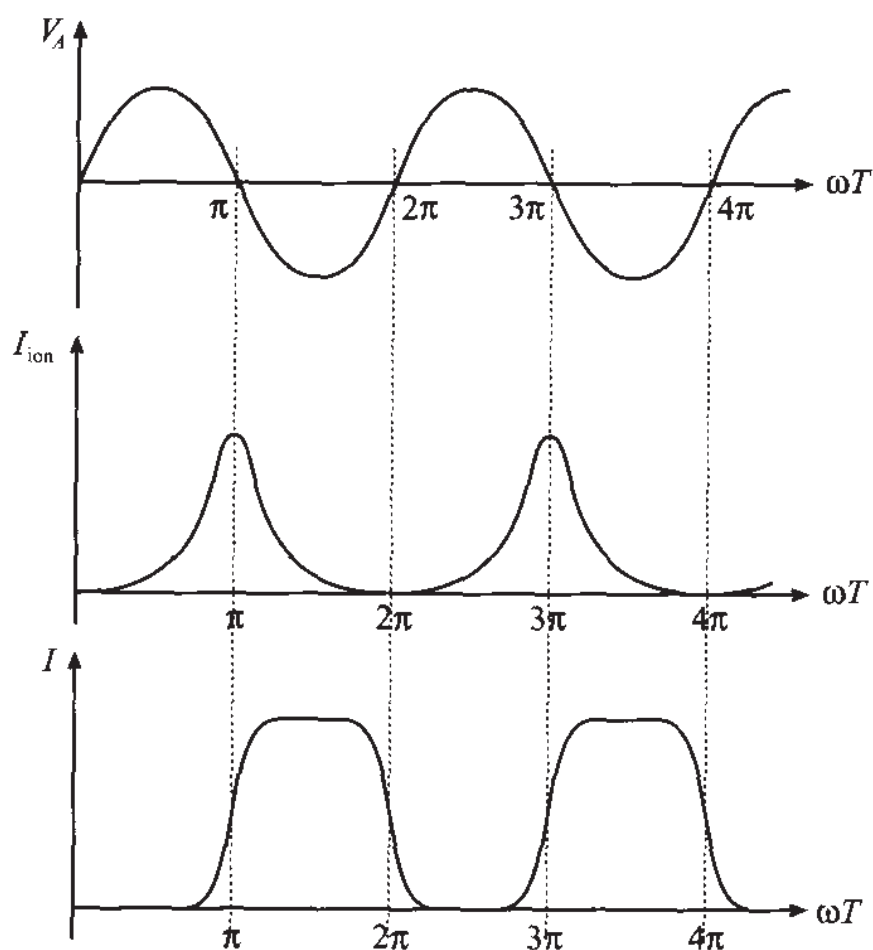


Figure 6-22 Applied voltage, ionization current, and total current of an IMPATT diode.

The electric circuit diagram of an IMPATT device shown in Figure 6-23 is more intricate than the PIN diode and the reactance reveals an inductive behavior below the diode's resonance frequency f_0 before turning capacitive above the resonance frequency. The total resistance is positive for $f < f_0$ and becomes negative for $f > f_0$.

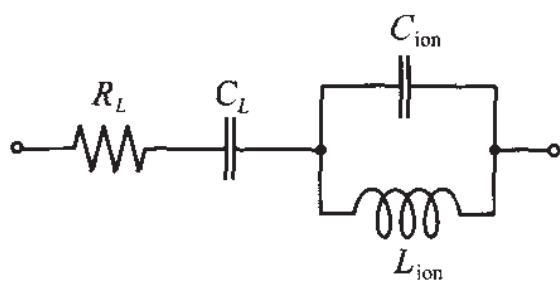


Figure 6-23 Electric circuit representation for the IMPATT diode.

The resonance frequency is determined based on the operating current I_Q , dielectric constant, saturation drift velocity $v_{d\max}$, and the differential change in the ioniza-

tion coefficient α with respect to the differential change in electric field strength $\alpha' = \partial\alpha/\partial E$. The resonance frequency is predicted as

$$f_0 = \frac{1}{2\pi} \sqrt{2I_Q \frac{v_{d\max}}{\epsilon} \alpha'} \quad (6.55)$$

The additional circuit parameters are specified as follows

$$R = R_L + \frac{v_{d\max}}{2\pi^2 f_0^2 C_L W [1 - (f/f_0)^2]} \quad (6.56a)$$

$$C_L = \frac{\epsilon A}{W} \quad (6.56b)$$

$$C_{\text{ion}} = \frac{\epsilon A}{d} \quad (6.56c)$$

$$L_{\text{ion}} = \frac{1}{(2\pi f_0)^2 C_{\text{ion}}} \quad (6.56d)$$

where R_L is the combined resistance of the semiconductor layers, d is the length of the avalanche region of the p -layer, and W is the total length, as shown in Figure 6-19. The negative resistance of this diode above the resonance frequency can be understood in terms of returning electric energy to the RF or MW resonance circuit; which means the diode operates as an active device. Thus, the circuit attenuation can be substantially reduced to the point where additional power is transferred to the load impedance. Unfortunately, the 180-degree phase shift comes with a price: The **efficiency** of converting DC to RF power at operating frequencies of 5 to 10 GHz is very low, with typical values in the range of 10 to 15%.

6.2.5 Tunnel Diode

Tunnel diodes are pn -junction diodes that are made of n and p layers with extremely high doping (concentrations approach 10^{19} – 10^{20} cm $^{-3}$) that create very narrow space charge zones. This can be seen immediately from equations (6.27) and (6.28). The result is that the electrons and holes exceed the effective state concentrations in the conduction and valence bands. The Fermi level is shifted into the conduction band W_{Cn} of the n^+ layer and into the valence band W_{Vp} of the p^+ semiconductor. We notice from Figure 6-24 that the permissible electron states in either semiconductor layer are only separated through a very narrow potential barrier.

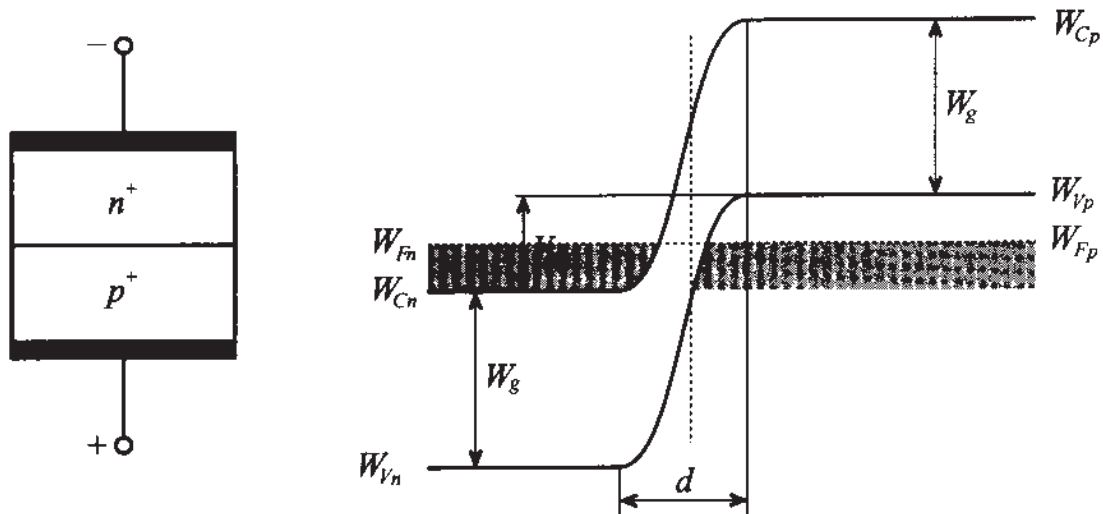
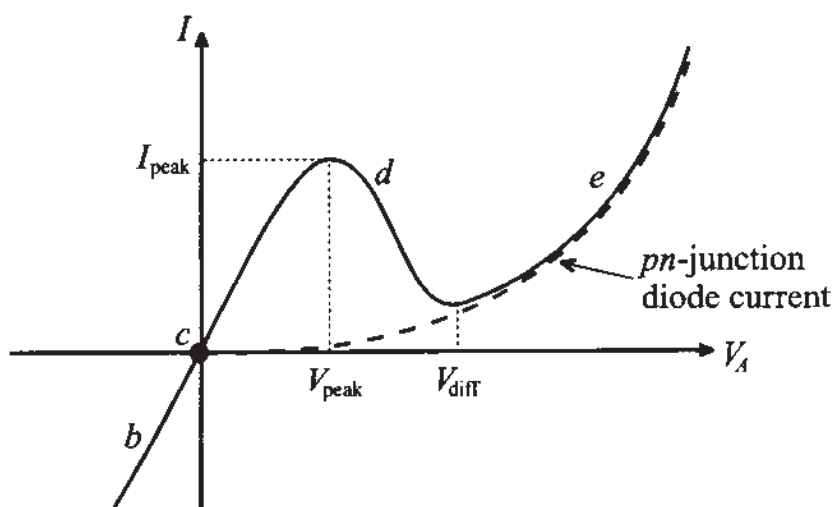


Figure 6-24 Tunnel diode and its band energy representation.

Based on quantum mechanical considerations, there is a finite probability that electrons can be exchanged across the narrow gap rather than having to overcome the potential barrier through an externally supplied voltage. This phenomenon is known as **tunneling**. In thermal equilibrium the electron tunneling from the *n* to *p* layer is balanced by the opposite tunneling from the *p* to *n* layer. No net current flow results.

The peculiar current-voltage response of the tunnel diode is best explained with reference to the corresponding energy band deformation for four distinct situations, as shown in Figure 6-25(b)–(e).



- (a) *I*-*V* curve of tunnel diode. At high positive biasing voltages the corresponding current of the tunnel diode approaches the current of the conventional *pn*-junction diode.

Figure 6-25 Current-voltage behavior of the tunnel diode and comparison with energy band structure.

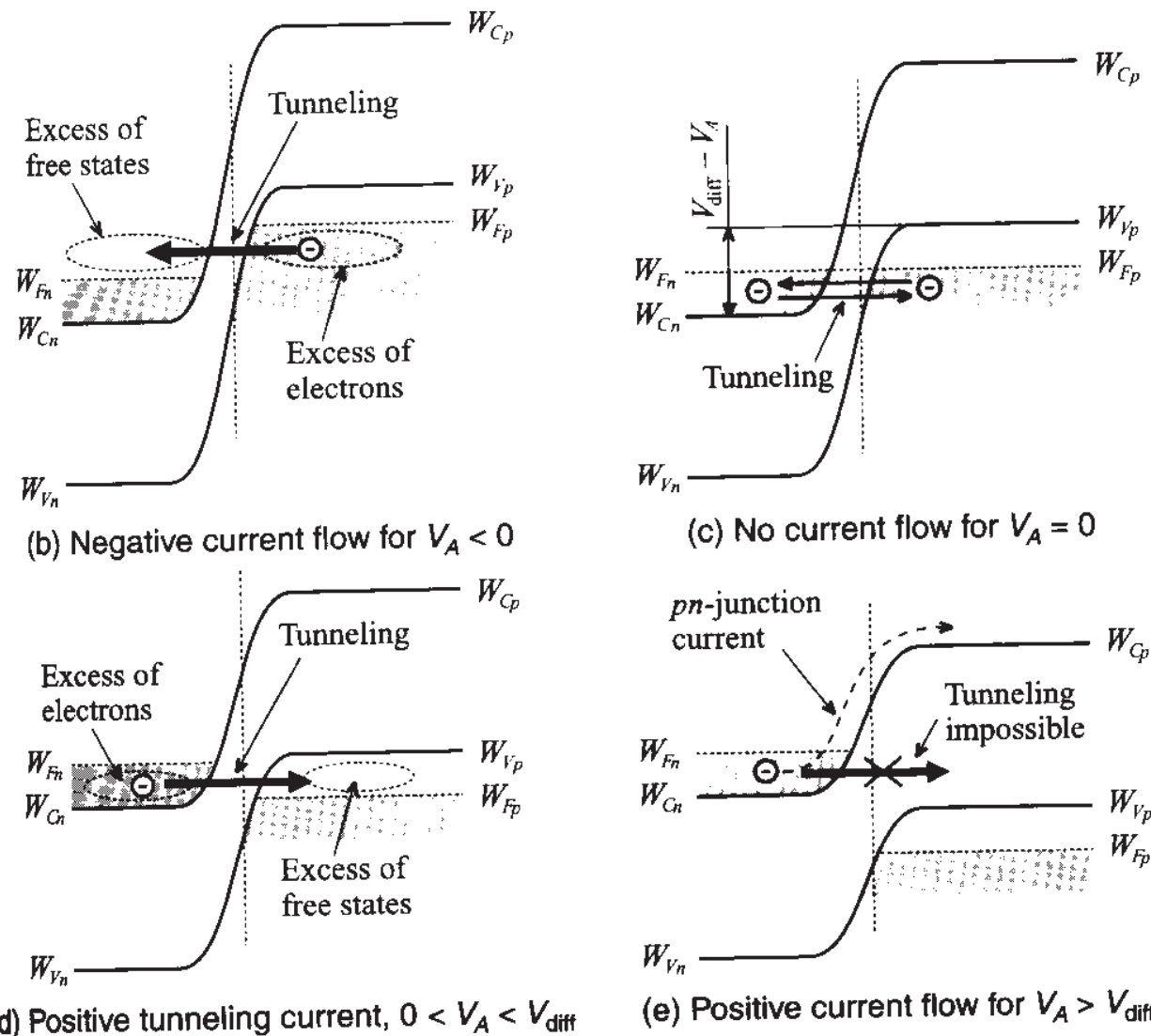


Figure 6-25 Current-voltage behavior of the tunnel diode and comparison with energy band structure. (Continued)

Unlike the equilibrium condition shown in Figure 6-24 and Figure 6-25(c), for a negative applied voltage V_A a higher concentration of electron states is created in the p -layer, which results in a higher probability to tunnel into the n -layer than vice versa. The consequence is that even for small negative voltages, a steep increase in current can be observed [Figure 6-25(b)]. For a small positive voltage the reservoir of free electrons is shifted to the n -semiconductor and an increase in free electron states is created in the p -semiconductor. The consequence is a positive current flow [Figure 6-25(d)] in response to the tunneling of electrons from the n to the p layer. However, if the applied voltage reaches a critical value $V_A \approx V_{\text{diff}}$ no overlapping band structures occur [i.e., the condition $W_{Cn} < W_{Vp}$ responsible for the tunneling effect no longer exists, see Figure 6-25(e)]. The current flow through the tunnel diode approaches a minimum. Above

this critical voltage point V_{diff} the diode behaves again like a conventional *pn*-junction diode and current increases exponentially.

The electric circuit of the tunnel diode, Figure 6-26, is very similar to the IMPATT diode shown in Figure 6-23. Here R_S and L_S are resistance of the semiconductor layer and associated lead inductance. The junction capacitance C_T is in shunt with a negative conductance $-g = dI/dV$, which is utilized in the negative slope of the *I-V* curve shown in Figure 6-25(a).

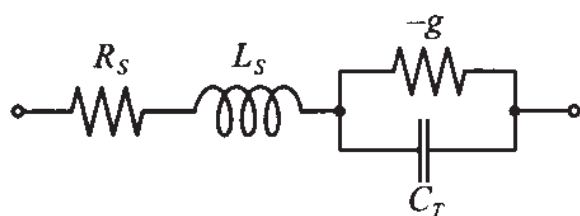


Figure 6-26 Electric circuit representation of a tunnel diode.

A simplified amplifier circuit involving a tunnel diode is depicted in Figure 6-27. If we consider the power amplification factor G_T as the ratio of the power delivered to the load R_L to the maximally available power from the source $P_S = |V_G|^2/(8R_G)$, we obtain at resonance

$$|G_T| = \frac{4}{R_L} \frac{1}{R_G(1/R_L + 1/R_G - g)^2} \quad (6.57)$$

where the influence of R_S is neglected. If g is chosen appropriately (i.e., $g = 1/R_L + 1/R_G$), the denominator approaches zero and we have the behavior of an oscillator.

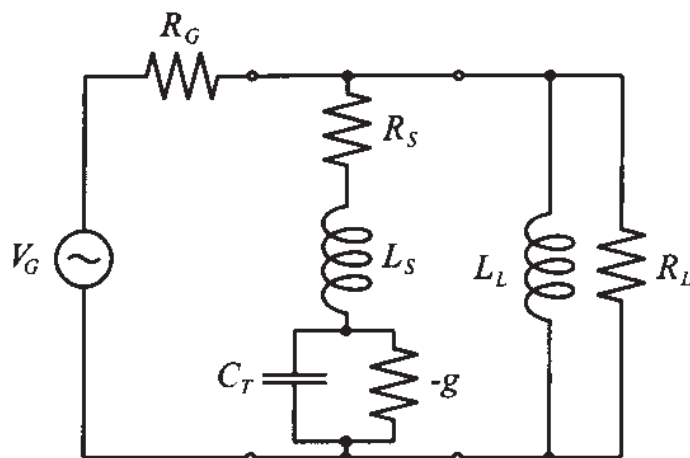


Figure 6-27 Tunnel diode circuit for amplification/oscillation behavior.

6.2.6 TRAPATT, BARRITT, and Gunn Diodes

For completeness we briefly mention these additional three diode types without going into any detail of their circuit representation and quantitative electric parameter derivations.

The TRApped Plasma Avalanche Triggered Transit (TRAPATT) diode can be considered an enhancement of the IMPATT diode in that a higher efficiency (up to 75%) is realized through the use of bandgap traps. Such traps are energy levels that are situated inside the bandgap and allow the capture of electrons. External circuits ensure that during the positive cycle a high barrier voltage is generated, resulting in carrier multiplication of the electron-hole plasma. The consequence is a breakdown in the rectifier properties of the diode during the negative cycle. The operating frequency is slightly lower than the IMPATT diode. This is due to the fact that the buildup of the electron-hole plasma is slower than the transit time through the middle layer in an IMPATT diode.

For the BARRier Injection Transit Time (BARRIT) we are essentially dealing with a transit time diode whose $p^+ n p^+$ doping profile acts like a transistor without base contact. The space charge domain extends from the cathode through the middle layer into the anode. The small-signal circuit model consists of a resistor and shunt capacitor whose values are dependent on the DC current bias. Unlike the IMPATT diode, this RC circuit can create a negative phase of up to -90 degrees at a relatively low efficiency of 5% and less. The BARRIT diode finds applications in RADAR mixer and detector circuits.

The **Gunn** diode is named after its inventor J. B. Gunn, who found in 1963 that in certain semiconductors (GaAs, InP) a sufficiently high electric field can cause electrons to scatter into regions where the bandgap separation increases. As a result of this increase in bandgap energy, the electrons suffer a loss in mobility μ_n . This phenomenon is so dramatic that, for instance in GaAs, the drift velocity ($v_d = nq\mu_n$) can drop from 2×10^7 cm/s to less than 10^7 cm/s for electric field strengths growing from 5 kV/cm to 7 kV/cm. The negative differential mobility

$$\mu_n = \frac{dv_d}{dE} < 0$$

is again used for oscillator circuits as we will see in later chapters. To exploit the Gunn effect for RF and MW applications, a special doping profile is needed to ensure that once the voltage exceeds the required threshold a stable single-carrier space domain is created.

6.3 Bipolar-Junction Transistor

The transistor was invented in 1948 by Bardeen and Brattain at the former AT&T Bell Laboratories and has over the past 50 years received a long lists of improvements and refinements. Initially developed as a point-contact, single device, the transistor has proliferated into a wide host of sophisticated types ranging from the still popular **bipolar junction transistors** (BJTs) over the modern **GaAs field effect transistors** (GaAs FETs) to the most recent **high electron mobility transistors** (HEMTs). Although transistors are often arranged in the millions in integrated circuits (ICs) as part of microprocessor, memory, and peripheral chips, in RF and MW applications the single transistor has retained its importance. Many RF circuits still rely on discrete transistors in low-noise, linear, and high-power configurations. It is for this reason that we need to investigate both the DC and RF behavior of the transistors in some detail.

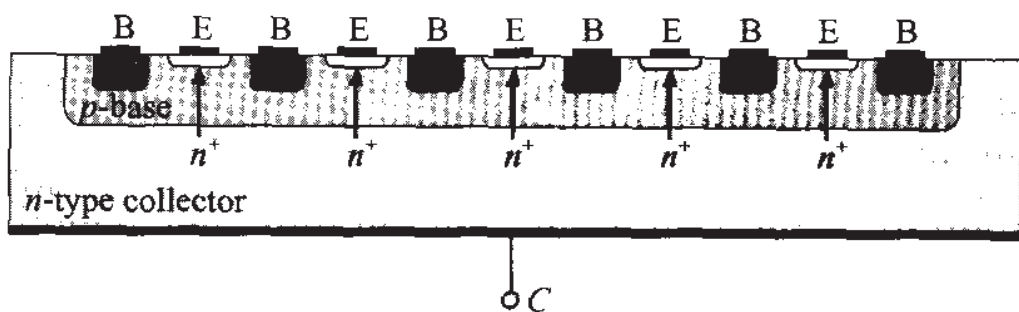
The constituents of a bipolar transistor are three alternatively doped semiconductors, in *npn* or *pnp* configuration. As the word *bipolar* implies, the internal current flow is due to both minority and majority carriers. In the following we recapitulate some of the salient characteristics.

6.3.1 Construction

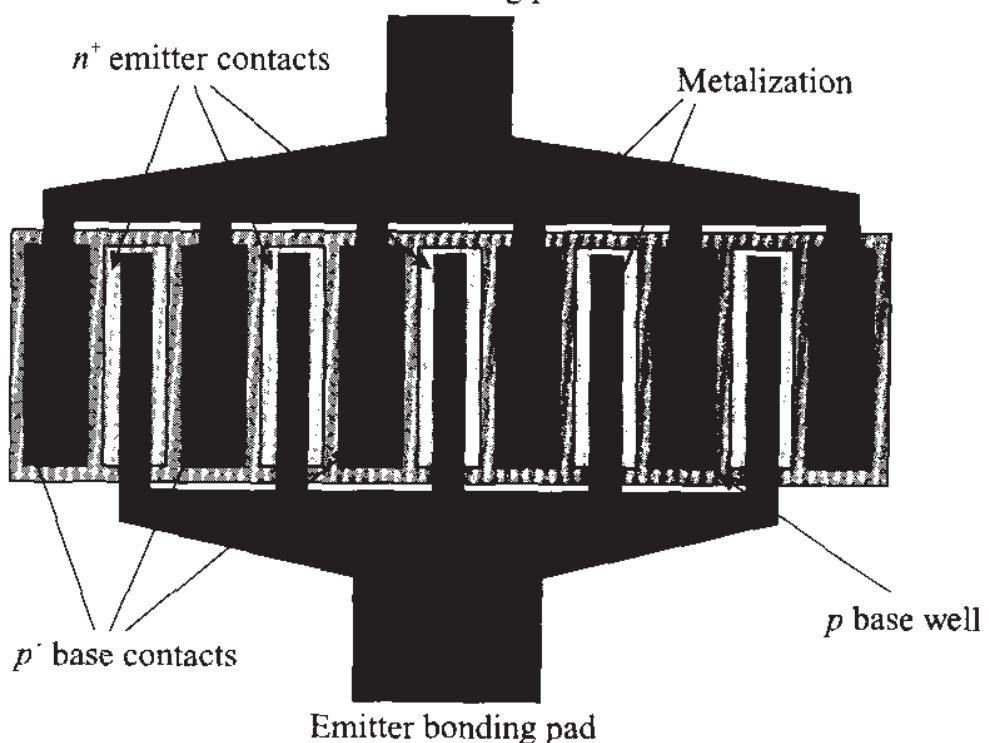
The BJT is one of the most widely used active RF elements due to its low-cost construction, relatively high operating frequency, low-noise performance, and high-power handling capacity. The high-power capacity is achieved through a special interdigital emitter-base construction as part of a planar structure. Figure 6-28 shows both the cross-sectional planar construction and the top view of an interdigital emitter-base connection.

Because of the interleaved construction shown in Figure 6-28(b) the base-emitter resistance is kept at a minimum while not compromising the gain performance. As we will see, a low base resistance directly improves the signal-to-noise ratio by reducing the current density through the base-emitter junction (shot noise) and by reducing the random thermal motion in the base (thermal noise), see Chapter 7 for more details.

For frequency applications exceeding 1 GHz it is important to reduce the emitter width to typically less than 1 μm size while increasing the doping to levels of $10^{20} \dots 10^{21} \text{ cm}^{-3}$ to both reduce base resistance and increase current gain. Unfortunately, it becomes extremely difficult to ensure the tight tolerances, and self-aligning processes are required. Furthermore, the acceptor and donor doping concentrations reach quickly the solubility limits of the Si or GaAs semiconductor materials, providing a physical limitation of the achievable current gain. For these reasons, **heterojunction bipolar transistors** (HBTs) are becoming increasingly popular. HBTs achieve high



(a) Cross-sectional view of a multifinger bipolar junction transistor
Base bonding pad



(b) Top view of a multifinger bipolar junction transistor

Figure 6-28 Interdigitated structure of high-frequency BJT.

current gains without having to dope the emitter excessively. Due to additional semiconductor layers (for instance, GaAlAs-GaAs sandwich structures) an enhanced electron injection into the base is achieved while the reverse hole injection into the emitter is suppressed. The result is an extremely high **emitter efficiency** as defined by the ratio of electron current into the base to the sum of the same electron current and reverse emitter hole current. Figure 6-29 shows a cross-sectional view of such a structure.

Besides GaAs, heterojunctions have been accomplished with InP emitter and InGaAs base interfaces; even additional heterojunction interfaces between the GaInAs base and InP collector (double heterojunctions) have been fabricated. The material InP has the advantage of high breakdown voltage, larger bandgap, and higher thermal conductivity compared to GaAs. Operational frequencies exceeding 100 GHz, and a carrier

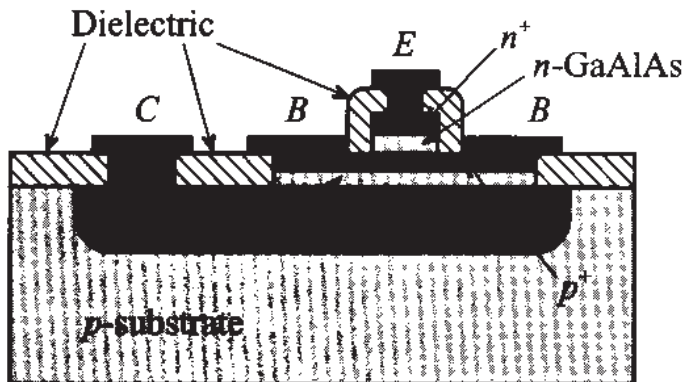


Figure 6-29 Cross-sectional view of a GaAs heterojunction bipolar transistor involving a GaAlAs-GaAs interface.

transition time between base and collector of less than 0.5 ps have been achieved. Unfortunately, InP is a difficult material to handle and the manufacturing process has not yet matured to a level that allows it to compete with the Si and GaAs technologies.

6.3.2 Functionality

In general, there are two types of BJTs: *npn* and *pnp* transistors. The difference between these two types lies in the doping of the semiconductor used to produce base, emitter, and collector. For an *npn*-transistor, collector and emitter are made of *n*-type semiconductor, while the base is of *p*-type. For a *pnp*-transistor, the semiconductor types are reversed (*n*-type for base, and *p*-type for emitter and collector). Usually, the emitter has the highest and the base has the lowest concentration of doping atoms. The BJT is a *current-controlled device* that is best explained by referring to Figure 6-30, which shows the structure, electrical symbol, and diode model with associated voltage and current convention for the *npn*-structure. We omit the discussion of the *pnp*-transistor since it requires only a reversal of voltage polarity and diode directions.

The first letter in the voltage designation always denotes the positive and the second letter gives the negative voltage reference points. Under normal mode of operation (i.e., the **forward active mode**), the emitter-base diode is operated in forward direction (with $V_{BE} \approx 0.7$ V) and the base-collector diode in reverse. Thus the emitter injects electrons into the base, and conversely from the base a hole current reaches the emitter. If we maintain the collector-emitter voltage to be larger than the so-called **saturation voltage** (typically around 0.1 V), and since the base is a very thin (on the order of $d_B \leq 1$ μm) and lightly doped *p*-type layer, only a small amount of electrons recombine with the holes supplied through the base current. The vast majority of electrons reach the base-collector junction and are collected by the applied reverse voltage V_{BC} .

For the **reverse active mode**, the collector-emitter voltage is negative (typically $V_{CE} < -0.1$ V) and the base-collector diode is forward biased, while the base-emitter

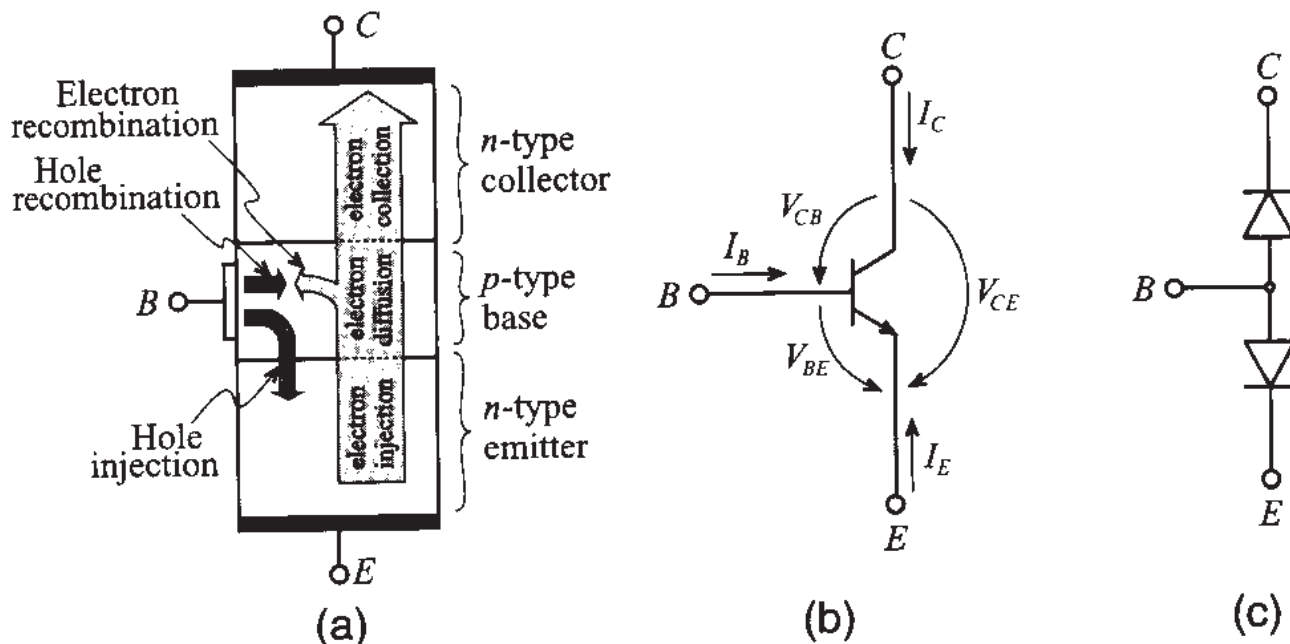


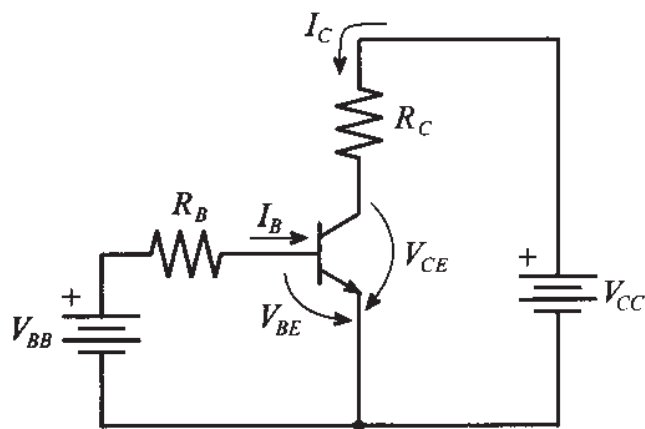
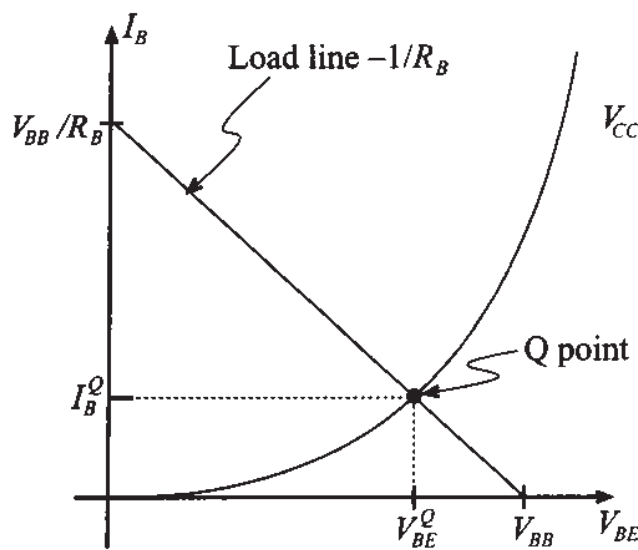
Figure 6-30 *npn* transistor: (a) structure with electrical charge flow under forward active mode of operation, (b) transistor symbol with voltage and current directions, and (c) diode model.

diode is now operated in reverse direction. Unlike the forward active mode, it is now the electron flow from the collector that bridges the base and reaches the emitter.

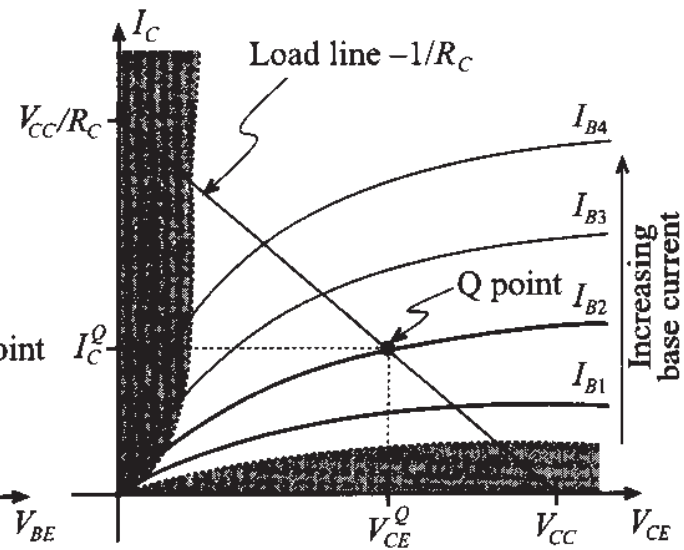
Finally, the **saturation mode** involves the forward biasing of both the base-emitter and base-collector junctions. This mode typically plays an important role when dealing with switching circuits.

For a common emitter configuration, Figure 6-31(a) depicts a generic biasing arrangement, where the base current is fixed through an appropriate choice of biasing resistor R_B and voltage source V_{BB} , resulting in a suitable Q -point. The base current versus base-emitter voltage, Figure 6-31(b), follows a typical diode I - V behavior, which constitutes the input characteristic of the transistor. The base current and base-emitter voltage at the intersection point between the load line and the transistor input characteristic are identified as I_B^Q and V_{BE}^Q . The collector current versus collector-emitter voltage behavior as part of the transistor output characteristic follows a more complicated pattern since the collector current must be treated as a parametric curve dependent on the base current ($I_B 1 < I_B 2 \dots$) as seen in Figure 6-31(c).

The quantitative BJT behavior is analyzed by investigating the three modes of operation in terms of setting appropriate operating points and formulating the various current flows. For simplicity, we will neglect the spatial extent of the individual space charge domains and assume typical representative voltage and current conditions. To keep track of the different minority/majority and doping conditions in the three semiconductor layers, Table 6-3 summarizes the parameters and corresponding notation.

(a) Biasing circuit for *n*p*n* BJT in common-emitter configuration

(b) Input characteristic of transistor



(c) Output characteristic of transistor

Figure 6-31 Biasing and input, output characteristics of an *n*p*n* BJT.**Table 6-3** BJT parameter nomenclature

| Parameter description | Emitter (<i>n</i> -type) | Base (<i>p</i> -type) | Collector (<i>n</i> -type) |
|---|-----------------------------|-----------------------------|-----------------------------|
| Doping level | N_D^E | N_A^B | N_D^C |
| Minority carrier concentration in thermal equilibrium | $p_{n_0}^E = n_i^2 / N_D^E$ | $n_{p_0}^B = n_i^2 / N_A^B$ | $p_{n_0}^C = n_i^2 / N_D^C$ |
| Majority carrier concentration in thermal equilibrium | $n_{n_0}^E$ | $p_{p_0}^B$ | $n_{n_0}^C$ |
| Spatial extent | d_E | d_B | d_C |

For the following BJT analysis, it is implicitly understood that the concentrations obey the inequality $p_{n0}^E \ll n_p^B \ll p_n^C$.

Forward Active Mode ($V_{CE} > V_{CE\text{sat}} = 0.1 \text{ V}$, $I_B > 0$)

To find the minority charge concentrations, we consider the configuration shown in Figure 6-32. Here the concentration is plotted as a function of distance across the three semiconductor layers. For predicting the spatial minority carrier concentrations in the respective layer, we rely on the so-called **short diode** (see Appendix F) analysis, which approximates the exponentials as linear charge concentration gradients.

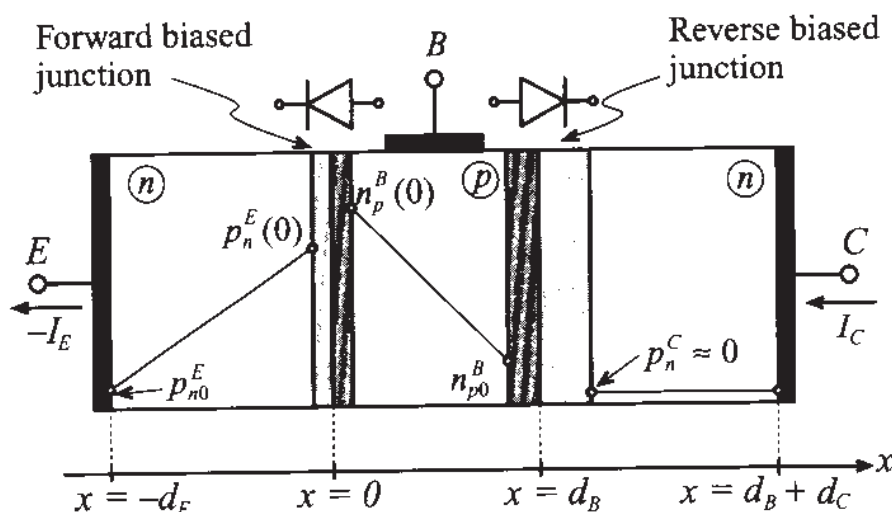


Figure 6-32 Minority carrier concentrations in forward active BJT.

The minority charge concentrations in each layer are given as follows:

- Emitter: $p_n^E(-d_E) = p_{n0}^E$ and $p_n^E(0) = p_{n0}^E e^{-V_{BE}/V_T}$
- Base: $n_p^B(0) = n_{p0}^B e^{-V_{BE}/V_T}$ and $n_p^B(d_B) = n_{p0}^B e^{-V_{BC}/V_T} \approx 0$
- Collector: $p_n^C(d_B) = p_{n0}^C e^{-V_{BC}/V_T} \approx 0$

The last two concentrations are zero because the base-collector voltage is negative (for instance, for typical transistor values of $V_{CE} = 2.5 \text{ V}$ and $V_{BE} = 0.7 \text{ V}$ we find $V_{BC} = -1.8 \text{ V}$, which yields $\exp[V_{BC}/V_T] = \exp[-1.8/0.026] \rightarrow 0$). Based on the aforementioned carrier concentrations we can now predict the diffusion current density of holes $J_{p\text{diff}}^E$ in the emitter:

$$J_{p\text{diff}}^E = -qD_p^E \frac{dp_n^E(x)}{dx} = -\frac{qD_p^E}{d_E} [p_n^E(0) - p_n^E(-d_E)] = -\frac{qD_p^E p_{n0}^E}{d_E} (e^{V_{BE}/V_T} - 1) \quad (6.58)$$

For the diffusion current density of electrons in the base layer $J_{n\text{diff}}^B$ we similarly obtain

$$J_{n\text{diff}}^B = qD_n^B \left[\frac{dn_p^B(x)}{dx} \right] = \frac{qD_n^B}{d_B} [n_p^B(d_B) - n_p^B(0)] = -\frac{qD_n^B n_{p0}^B}{d_B} e^{V_{BE}/V_T} \quad (6.59)$$

From the preceding two equations, the collector and base currents can be established as

$$I_{FC} = -J_{n\text{diff}}^B A = \frac{qD_n^B n_{p0}^B}{d_B} A e^{V_{BE}/V_T} = I_S e^{V_{BE}/V_T} \quad (6.60)$$

and

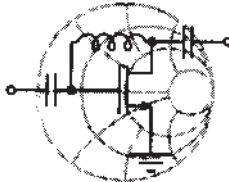
$$I_{FB} = -J_{p\text{diff}}^E A = \frac{qD_p^E p_{n0}^E}{d_E} A (e^{V_{BE}/V_T} - 1) \quad (6.61)$$

where index F denotes forward current, A is the junction cross-sectional area, and $I_S = (qD_n^B n_{p0}^B A)/d_B$ is the **saturation current**. The emitter current is directly found by adding (6.60) and (6.61). The forward current gain β_F under constant collector emitter voltage is defined as

$$\beta_F = \left. \frac{I_{FC}}{I_{FB}} \right|_{V_{CE}} = \frac{D_n^B n_{p0}^B d_E}{D_p^E p_{n0}^E d_B} \quad (6.62)$$

To arrive at (6.62) it is assumed that the exponential function in (6.61) is much larger than 1, allowing us to neglect the factor -1 . Moreover, the ratio between collector and emitter currents, or α_F , is expressed as

$$\alpha_F = \frac{I_{FC}}{(-I_{FE})} = \frac{\beta_F}{1 + \beta_F} \quad (6.63)$$



RF & MW

Example 6-7: Computation of the maximum forward current gain in a bipolar-junction transistor

Find the maximum forward current gain for a silicon-based BJT with the following parameters: donor concentration in the emitter, $N_D^E = 10^{19} \text{ cm}^{-3}$; acceptor concentration in the base, $N_A^B = 10^{17} \text{ cm}^{-3}$; space charge extent in the emitter, $d_E = 0.8 \mu\text{m}$; and space charge extent in the base, $d_B = 1.2 \mu\text{m}$.

Solution: To apply (6.62), we need to determine the diffusion constants in base and emitter as described by the Einstein relation (6.15). Substituting this relation into (6.62), we obtain the forward current gain:

$$\beta_F = \frac{\mu_n n_p^B d_E}{\mu_p p_{n0}^E d_B}$$

Furthermore, using the expressions for the minority carrier concentrations in base and emitter from Table 6-3, we arrive at the final expression for β_F :

$$\beta_F = \frac{\mu_n N_D^E d_E}{\mu_p N_A^B d_B} = 187.5$$

As discussed in Section 6.3.3 and in the following chapter, the current gain is only approximately constant. In general, it depends on the transistor operating conditions and temperature behavior.

Reverse Active Mode ($V_{CE} < -0.1$ V, $I_B > 0$)

The minority carrier concentrations are shown in Figure 6-33 with the associated space charge domains (i.e., the base-emitter diode is reversed biased whereas the base-collector diode is forward biased).

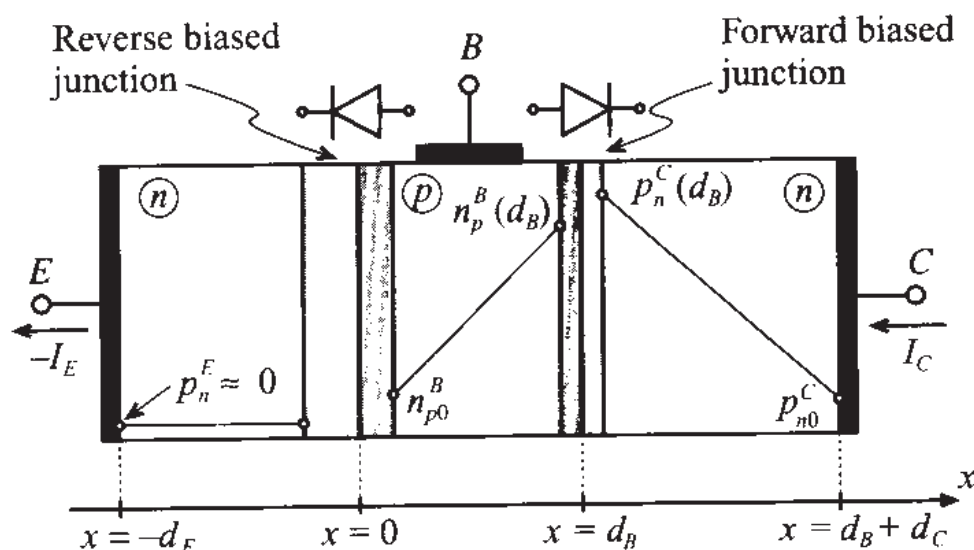


Figure 6-33 Reverse active mode of BJT.

The minority charge concentrations in each layer are as follows:

- Emitter: $p_n^E(-d_E) \approx 0$ and $p_n^E(0) = p_{n0}^E e^{V_{BE}/V_T} \approx 0$
- Base: $n_p^B(0) = n_{p0}^B e^{V_{BE}/V_T} \approx 0$ and $n_p^B(d_B) = n_{p0}^B e^{V_{BC}/V_T}$
- Collector: $p_n^C(d_B) = p_{n0}^C e^{V_{BC}/V_T}$ and $p_n^C(d_B + d_C) \approx p_{n0}^C$

From the diffusion current density, we can find the reverse emitter current

$$I_{RE} = -J_{ndiff}^B A = -qD_n^B \left(\frac{dn_p^B}{dx} \right)_A = \frac{qD_n^B n_{p0}^B}{d_B} A e^{V_{BC}/V_T} = I_S e^{V_{BC}/V_T} \quad (6.64)$$

and the reverse base current

$$I_{RB} = -J_{pdiff}^C A = -qD_p^C \left(\frac{dp_n^C}{dx} \right)_A = \frac{qD_p^C p_{n0}^C}{d_C} A \left(e^{V_{BC}/V_T} - 1 \right) \quad (6.65)$$

In a similar manner as done for the forward current gain, we define the **reverse current gain** β_R

$$\beta_R = \left. \frac{I_{RE}}{I_{RB}} \right|_{V_{BC}} = \frac{D_n^B n_{p0}^B d_C}{D_p^C p_{n0}^C d_B} \quad (6.66)$$

and the collector emitter ratio α_R

$$\alpha_R = \left. \frac{I_{RC}}{(-I_{RE})} \right|_{V_{BC}} = \frac{\beta_R}{1 + \beta_R} \quad (6.67)$$

Saturation Mode ($V_{BE}, V_{BC} > V_T, I_B > 0$)

This mode of operation implies the forward bias of both diodes, so that the diffusion current density in the base is the combination of forward and reverse carrier flows; that is, with (6.60) and (6.64):

$$J_{ndiff}^B = J_{RE} - J_{FC} = -\frac{I_S}{A} e^{V_{BE}/V_T} + \frac{I_S}{A} e^{V_{BC}/V_T} \quad (6.68)$$

From (6.68) it is possible to find the emitter current by taking into account the forward base current. This forward base current (6.61) injects holes into the emitter and thus has to be taken with a negative sign to comply with our positive emitter current direction convention. Making the exponential expressions in (6.68) compatible with (6.61), we add and subtract unity and finally obtain

$$I_E = -I_S \left(e^{V_{BE}/V_T} - 1 \right) - \frac{I_S}{\beta_F} \left(e^{V_{BC}/V_T} - 1 \right) + I_S \left(e^{V_{BC}/V_T} - 1 \right) \quad (6.69)$$

Because the BJT can be treated as a symmetric device, the collector current is expressible in a similar manner as the contribution of three currents: the forward collector and reverse emitter currents, given by the negative of (6.68), and an additional hole diffusion contribution as the result of the reverse base current I_{RB} . The resulting equation is

$$I_C = I_S \left(e^{V_{BE}/V_T} - 1 \right) - \frac{I_S}{\beta_R} \left(e^{V_{BC}/V_T} - 1 \right) - I_S \left(e^{V_{BC}/V_T} - 1 \right) \quad (6.70)$$

Finally, the base current $I_B = -I_C - I_E$ is found from the preceding two equations:

$$I_B = I_S \left\{ \frac{1}{\beta_R} \left(e^{V_{BC}/V_T} - 1 \right) + \frac{1}{\beta_F} \left(e^{V_{BE}/V_T} - 1 \right) \right\} \quad (6.71)$$

Here again, it is important to recall that the internal emitter current flow is denoted opposite in sign to the customary external circuit convention.

6.3.3 Frequency Response

The **transition frequency** f_T (also known as the **cut-off frequency**) of a microwave BJT is an important figure of merit since it determines the operating frequency at which the common-emitter, short-circuit current gain h_{fe} decreases to unity. The transition frequency f_T is related to the transit time τ that is required for carriers to travel through the emitter-collector structure:

$$f_T = \frac{1}{\tau} \quad (6.72)$$

This transition time is generally composed of three delays:

$$\tau = \tau_E + \tau_B + \tau_C \quad (6.73)$$

where τ_E , τ_B , and τ_C are delays in emitter, base, and collector, respectively. The base-emitter depletion region charging time is given by

$$\tau_E = r_E C = \frac{V_T}{I_E} (C_E + C_C) \equiv \frac{V_T}{I_C} (C_E + C_C) \quad (6.74a)$$

where C_E , C_C are emitter and collector capacitances, and r_E is the emitter resistance obtained by differentiation of the emitter current with respect to base-emitter voltage. The second delay in (6.73) is the base layer charging time, and its contribution is given as

$$\tau_B = \frac{d_B^2}{\eta D_n} \quad (6.74b)$$

where the factor η is doping profile dependent and ranges from $\eta = 2$ for uniformly doped base layers up to $\eta = 60$ for highly nonuniform layers. Finally, the transition time τ_C through the base-collector junction space charge zone w_C can be computed as

$$\tau_C = \frac{w_C}{v_s} \quad (6.74c)$$

with v_s representing the saturation drift velocity. In the preceding formulas we have neglected the collector charging time $\tau_{CC} = r_C C_C$, which is typically very small when compared with τ_E .

As seen in (6.74a), the emitter charging time is inversely proportional to the collector current, resulting in higher transition frequencies for increasing collector currents. However, as the current reaches sufficiently high values, the concentration of charges injected into the base becomes comparable with the doping level of the base, which causes an increase of the effective base width and, in turn, reduces the transition frequency. Usually, BJT data sheets provide information about the dependence of the transition frequency on the collector current. For instance, Figure 6-34 shows the transition frequency as a function of collector current for the wideband *npn*-transistor BFG403W measured at $V_{CE} = 2$ V, $f = 2$ GHz, and at an ambient temperature of 25°C.

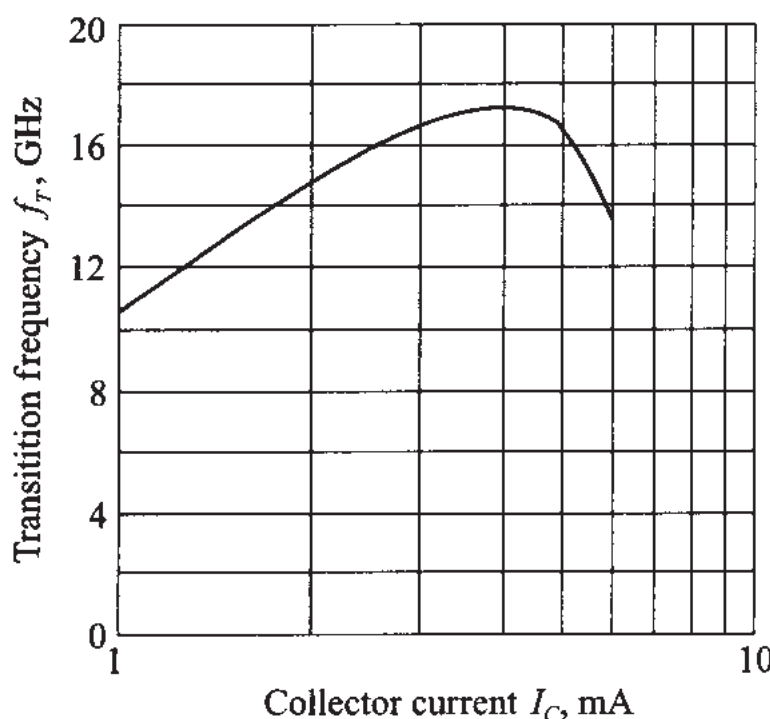


Figure 6-34 Transition frequency as a function of collector current for the 17 GHz *npn* wideband transistor BFG403W (courtesy of Philips Semiconductors).

Another aspect of the BJT operated at RF and MW frequencies is that at high frequencies the skin effect physically restricts current flow to the outer perimeter of the emitter (see also Section 1.4). To keep the charging time as low as possible, the emitter is constructed in a grid pattern of extremely narrow (less than 1 μm) strips. Unfortunately, the trade-off is a high current density over the small surface area, limiting the power handling capabilities. Additional ways to increase the cut-off frequency are to reduce the base transition time constant τ_B by high doping levels and concomitantly fabricate very short base layers of less than 100 nm. In addition, a small base thickness has as an advantage a reduction in power loss.

6.3.4 Temperature Behavior

We have seen in this chapter that almost all parameters describing both the static and dynamic behavior of semiconductor devices are influenced by the junction temperature T_j . As an example of such a dependence, in Figure 6-35 the forward current gain β_F for a given V_{CE} is plotted as a function of collector current I_C for various junction temperatures T_j . As we can see from this graph, the current gain raises from 40 at $I_C = 3.5 \text{ mA}$ and $T_j = -50^\circ\text{C}$ to more than 80 at $T_j = 50^\circ\text{C}$.

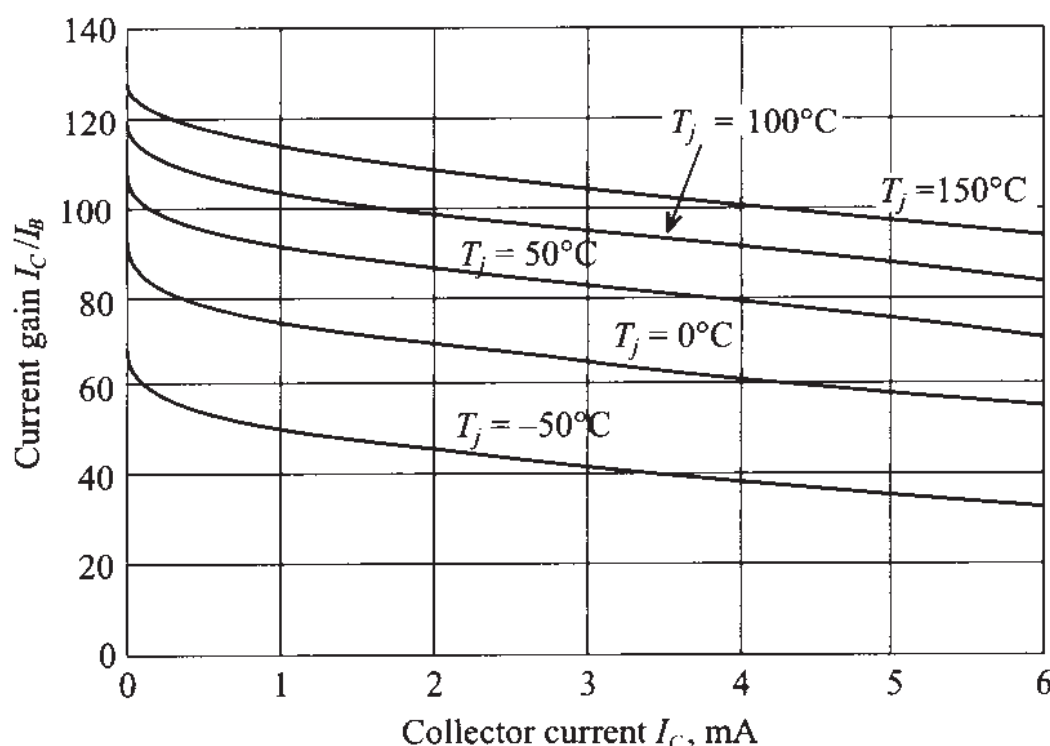


Figure 6-35 Current gain $\beta_F = \alpha_F / (1 - \alpha_F)$ as a function of collector current for various junction temperatures at a fixed V_{CE} .

Another example that shows the strong temperature influence is the dependence of the input characteristic of a transistor described by the base current as a function of base-emitter voltage, as depicted in Figure 6-36.

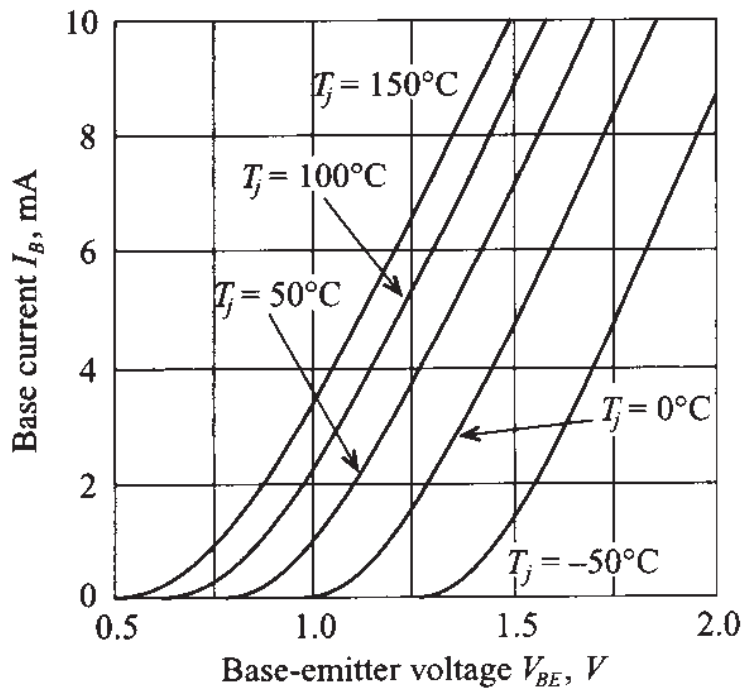


Figure 6-36 Typical base current as a function of base-emitter voltage for various junction temperatures at a fixed V_{CE} .

Again, if we compare the behavior of the transistor at $T_j = -50^\circ\text{C}$ and $T_j = 50^\circ\text{C}$, we notice that at $T_j = -50^\circ\text{C}$ and a base-emitter voltage of 1.25 V the transistor is in cut-off state, whereas at $T_j = 50^\circ\text{C}$ the BJT already conducts 4 mA base current. These two examples underscore the importance of temperature considerations in the design of RF circuits. For instance, the design of a cellular phone for worldwide use must ensure that our circuit performs according to specifications under all temperature conditions encountered by the operator. Standard specifications usually cover the temperature range from -50°C to 80°C .

The junction temperature also plays an important role when dealing with the maximum power dissipation. In general, the manufacturer provides a **power derating curve** that specifies the temperature T_S up to which the transistor can be operated at the maximum available power P_{tot} . For junction temperatures T_j exceeding this value, the power has to be reduced to values dictated by the thermal resistance between the junction and the soldering point (or case) R_{thjs} according to

$$P = P_{\text{tot}} \frac{T_{j\max} - T_j}{T_{j\max} - T_S} = \frac{T_{j\max} - T_j}{R_{\text{thjs}}} \quad (6.75)$$

where $T_{j\max}$ is the maximum junction temperature. Typical BJT values vary between 150 and 200°C.

For the RF transistor BFG403W the maximum total power P_{tot} of 16 mW can be maintained up to $T_s = 140^\circ\text{C}$. For higher temperatures $T_s \leq T_j \leq T_{j\max}$, the power must be derated until the maximum junction temperature $T_{j\max}$ of 150°C is reached. The corresponding slope is 820°K/W. This value implies that if the power dissipation of the device decreases by 10 mW, the junction temperature can be increased by 8.2°C up to the maximum junction temperature. Obviously, transistor cases with such a high slope (or high thermal resistance) are not acceptable for high-power applications and manufacturers have to develop effective ways to dissipate the thermal energy generated by the transistor. Usually, this is done by employing heat sinks and using materials with high thermal conductivity. Instead of the thermal resistance at the soldering point R_{thjs} , the manufacturer may supply additional information involving heat resistances between junction-to-case (R_{thjc}), case-to-sink (R_{thcs}), and sink-to-air (R_{thha}) interfaces.

To simplify the thermal analysis it is convenient to resort to a thermal equivalent circuit with the following correspondences:

- Thermal power dissipation = electric current
- Temperature = electric voltage

A typical thermal circuit in equilibrium is shown in Figure 6-37, where the total electric power supplied to the device is balanced through a thermal circuit involving thermal resistances. In particular, we recognize the thermal resistance of junction to soldering point which is assumed to be equal to R_{thjc} . Therefore

$$R_{\text{thjc}} = R_{\text{thjs}} = \frac{T_j - T_s}{P_w} = \frac{1}{\gamma_{\text{th}} A_{\text{BJT}}} \quad (6.76)$$

where junction and soldering point temperatures T_j and T_s and thermal power P_w determine the thermal resistance in Kelvin per Watt (°K/W), and whose value can also be expressed in terms of the thermal conductivity γ_{th} and the surface area A_{BJT} of the BJT. The solder point temperature is affected by the transition between casing and heat sink. This constitutes a thermal resistance R_{thcs} with values up to 5 °K/W. Finally, the heat sink represents a thermal resistance of

$$R_{\text{thha}} = \frac{1}{\delta_{\text{hs}} A_{\text{hs}}} \quad (6.77)$$

where δ_{hs} is a convection coefficient that can vary widely between $10 \text{ W}/(\text{K}\cdot\text{m}^2)$ for still air, $100 \text{ W}/(\text{K}\cdot\text{m}^2)$ for forced air, up to $1000 \text{ W}/(\text{K}\cdot\text{m}^2)$ for water cooling, and A_{hs} is the total area of the heat sink.

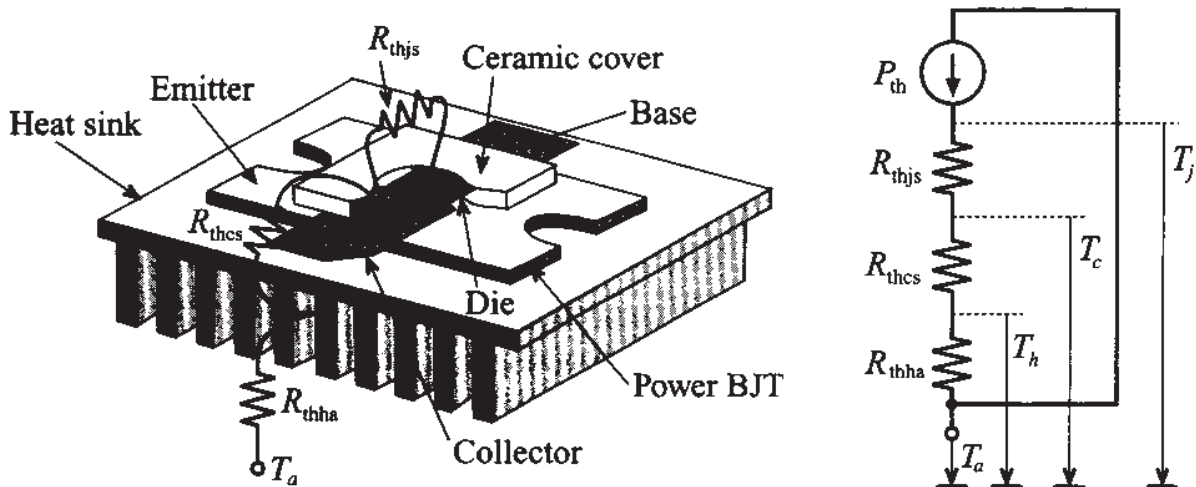
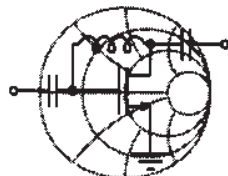


Figure 6-37 Thermal equivalent circuit of BJT.

The following example provides an often encountered design problem.



RF & MW →

Example 6-8: Thermal analysis involving a BJT mounted on a heat sink

An RF power BJT generates a total power P_W of 15 W at case temperature of 25°C. The maximum junction temperature is 150°C and the maximum ambient operating temperature is specified by the user to be $T_a = 60^\circ\text{C}$. What is the maximum dissipated power if the thermal resistances between case-to-sink and sink-to-air is 2°K/W and 10°K/W, respectively.

Solution: With reference to Figure 6-37, we are dealing with three thermal resistances: R_{thjs} , R_{thcs} , and R_{thha} . The junction-to-soldering resistance can be found based on equation (6.76):

$$R_{\text{thjs}} = \frac{T_j - T_s}{P_W} = \frac{150^\circ\text{C} - 25^\circ\text{C}}{15 \text{ W}} = 8.33^\circ\text{K}/\text{W}$$

Adding up all resistances gives us a total thermal resistance of

$$R_{\text{thtot}} = R_{\text{thjs}} + R_{\text{thca}} + R_{\text{thhs}} = 20.333^\circ\text{K}/\text{W}$$

The dissipated power P_{th} follows from the temperature drop (junction temperature T_j minus ambient temperature T_a) divided by the total thermal resistance:

$$P_{\text{th}} = \frac{T_j - T_a}{R_{\text{thtot}}} = \frac{150^\circ\text{C} - 60^\circ\text{C}}{20.33^\circ\text{ K/W}} = 4.43 \text{ W}$$

To operate the BJT in thermal equilibrium, we have to reduce the total electric power $P_{\text{tot}} = P_w$ to the point where it is in balance with the computed thermal power $P_{\text{tot}} = P_{\text{th}}$. Thus a reduction from 15 W to 4.43 W is required.

While the design engineer cannot influence the junction-to-soldering point heat resistance, it is the choice of casing and heat sink that typically allows major improvements in thermal performance.

6.3.5 Limiting Values

The total power dissipation capabilities at a particular temperature restrict the range of safe operation of the BJT. In our discussion we will exclusively focus on the active mode in the common-emitter configuration and will neglect the switch-mode behavior whereby the BJT is operated either in saturation or cut-off mode. For a given maximum BJT power rating, we can either vary the collector-emitter voltage V_{CE} and plot the allowable collector current $I_C = P_{\text{tot}}/V_{CE}$ (here we assume that base current is negligibly small compared to the collector current due to high β) or vary I_C and plot the allowable collector-emitter voltage $V_{CE} = P_{\text{tot}}/I_C$. The result is the **maximum power hyperbola**. This does not mean that I_C and V_{CE} can be increased without bound. In fact, we need to ensure that $I_C \leq I_{C\max}$ and $V_{CE} \leq V_{CE\max}$, as depicted in Figure 6-38. The **safe operating area** (SOAR) is defined as a set of biasing points where the transistor can be operated without risk of unrecoverable damage to the device. The SOAR domain, shown as a shaded region in Figure 6-38, is more restrictive than a subset bounded by the maximum power hyperbola, since we have to take into account two more breakdown mechanisms:

1. **Breakdown of first kind.** Here the collector current density exhibits a nonuniform distribution that results in a local temperature increase, which in turn lowers the resistance of a portion of the collector domain, creating a channel. The consequence is a further increase in current density through this channel until the positive feedback begins to destroy the crystal structure (**avalanche breakdown**), ultimately destroying the transistor itself.

2. Breakdown of second kind. This breakdown mechanism can take place independently of the first mechanism and affects primarily power BJTs. Internal overheating may cause an abrupt increase in the collector current for constant V_{CE} . This breakdown mechanism usually occurs at the base-collector junction when the temperature increases to such high values that the intrinsic concentration is equal to the collector doping concentration. At this point the resistance of the junction is abruptly reduced, resulting in a dramatic current increase and melting of the junction.

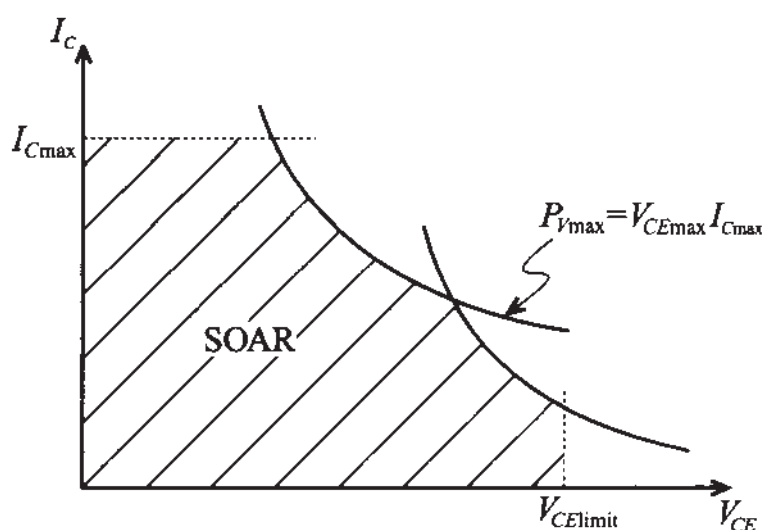


Figure 6-38 Operating domain of BJT in active mode with breakdown mechanisms.

It is interesting to point out that the BJT can exceed the SOAR, indeed even the maximum power hyperbola, for a short time since the temperature response has a much larger time constant (on the order of microseconds) in comparison with the electric time constants.

Additional parameters of importance to a design engineer are the maximum voltage conditions for open emitter, base and collector conditions; that is, V_{CBO} (collector-base voltage, open emitter), V_{CEO} (collector-emitter, open base), and V_{EBO} (emitter-base voltage, open collector). For instance, values for the BFG403W are as follows: $V_{CBO}|_{\max} = 10 \text{ V}$, $V_{CEO}|_{\max} = 4.5 \text{ V}$, and $V_{EBO}|_{\max} = 1.0 \text{ V}$.

6.4 RF Field Effect Transistors

Unlike BJTs, field effect transistors (FETs) are monopolar devices, meaning that only one carrier type, either holes or electrons, contributes to the current flow through the channel. If hole contributions are involved we speak of *p*-channel, otherwise of *n*-channel FETs. Moreover, the FET is a voltage-controlled device. A variable

electric field controls the current flow from **source** to **drain** by changing the applied voltage on the **gate** electrode.

6.4.1 Construction

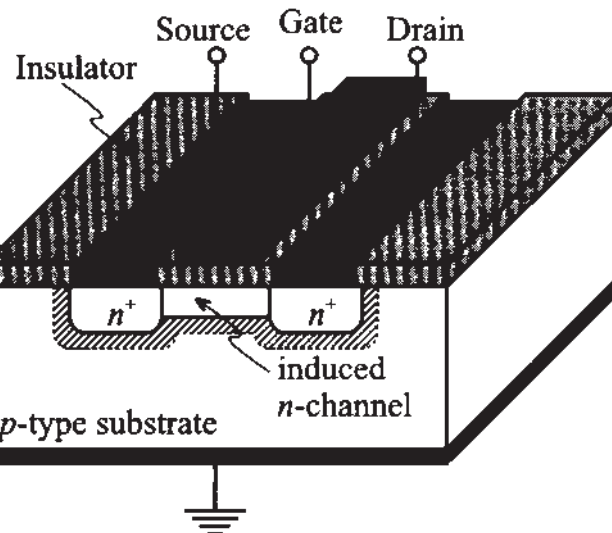
Traditionally FETs are classified according to how the gate is connected to the conducting channel. Specifically, the following four types are used:

1. **Metal Insulator Semiconductor FET (MISFET)**. Here the gate is separated from the channel through an insulation layer. One of the most widely used types, the **Metal Oxide Semiconductor FET (MOSFET)**, belongs to this class.
2. **Junction FET (JFET)**. This type relies on a reverse biased *pn*-junction that isolates the gate from the channel.
3. **MEtal Semiconductor FET (MESFET)**. If the reverse biased *pn*-junction is replaced by a Schottky contact, the channel can be controlled just as in the JFET case.
4. **Hetero FET**. As the name implies (and unlike the previous three cases, whose constructions rely on a single semiconductor material such as Si, GaAs, SiGe, or InP) the hetero structures utilize abrupt transitions between layers of different semiconductor materials. Examples are GaAlAs to GaAs or GaInAs to GaAlAs interfaces. The **High Electron Mobility Transistor (HEMT)** belongs to this class.

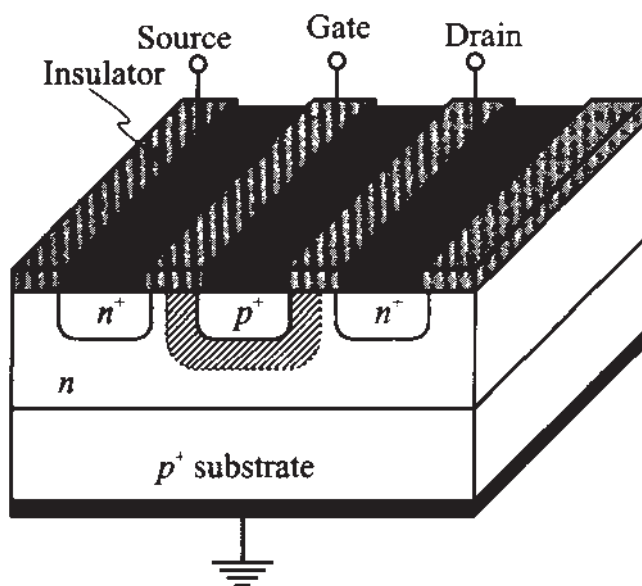
Figure 6-39 provides an overview of the first three types. In all cases the current flow is directed from the **source** to **drain**, with the **gate** controlling the current flow.

Due to the presence of a large capacitance formed by the gate electrode and the insulator or reverse biased *pn*-junction, MISFETs and JFETs have a relatively low cut-off frequency and are usually operated in low and medium frequency ranges of typically up to 1 GHz. GaAs MESFETs find applications up to 60–70 GHz, and HEMT can operate beyond 100 GHz. Since our interest is geared toward RF applications, the emphasis will be on the last two types.

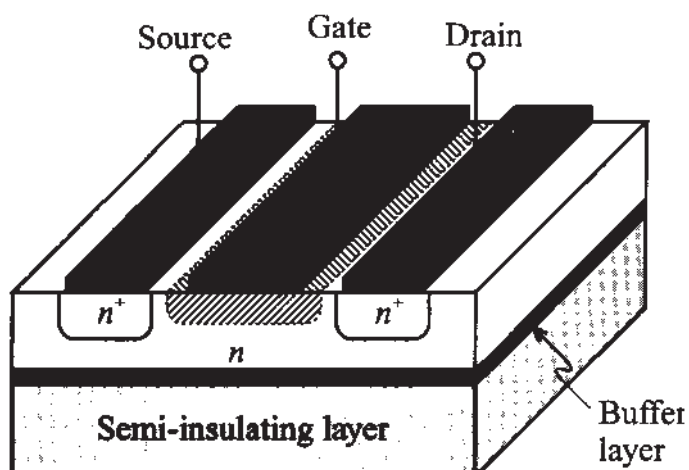
In addition to the above physical classification, it is customary to electrically classify FETs according to **enhancement** and **depletion** types. This means that the channel either experiences an increase in carriers (for instance the *n*-type channel is injected with electrons) or a depletion in carriers (for instance the *n*-type channel is depleted of electrons). In Figure 6-39 (a) the FET is nonconducting, or **normally-off**, until a sufficiently positive gate voltage sets up a conduction channel. Normally-off FETs can only be operated in **enhancement mode**. Alternatively, **normally-on** FETs can be of both enhancement and depletion types.



(a) Metal insulator semiconductor FET (MISFET)



(b) Junction field effect transistor (JFET)



(c) Metal semiconductor FET (MESFET)

Figure 6-39 Construction of (a) MISFET, (b) JFET, and (c) MESFET. The shaded areas depict the space charge domains.

6.4.2 Functionality

Because of its importance in RF and MW amplifier, mixer, and oscillator circuits, we focus our analysis on the MESFET, whose physical behavior is in many ways similar to the JFET. The analysis is based on the geometry shown in Figure 6-40 where the transistor is operated in depletion mode.

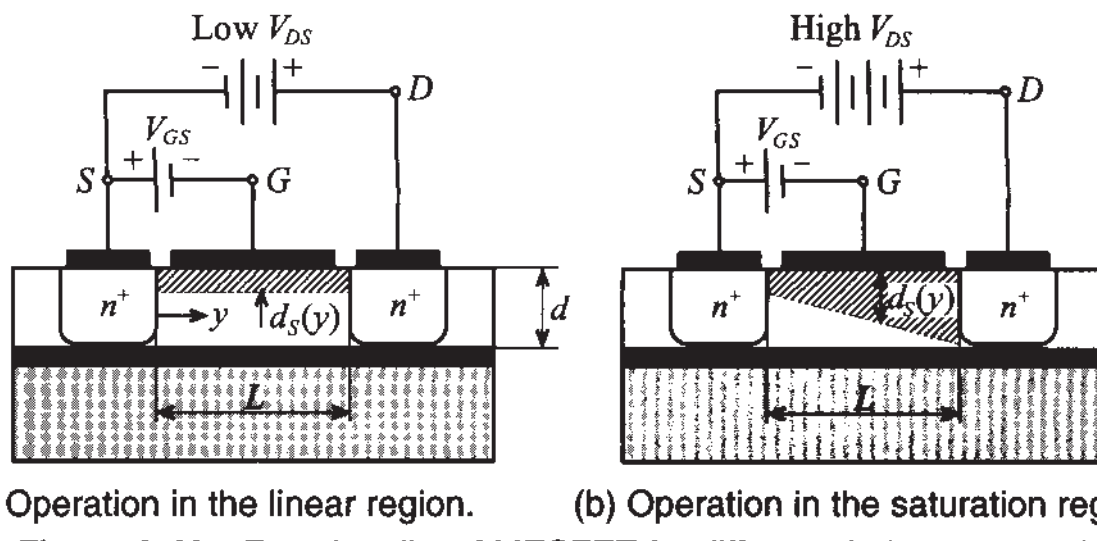


Figure 6-40 Functionality of MESFET for different drain-source voltages.

The Schottky contact builds up a channel space charge domain that affects the current flow from source to drain. The space charge extent d_S can be controlled via the gate voltage in accordance to our discussion in Section 6.1.3, where (6.39) is adjusted such that V_A is replaced by the gate source voltage V_{GS} :

$$d_S = \sqrt{\frac{2\epsilon}{q} \left(\frac{V_d - V_{GS}}{N_D} \right)} \quad (6.78)$$

For instance, the barrier voltage V_d is approximately 0.9 V for a GaAs-Au interface. The resistance R between source and drain is predicted by

$$R = \frac{L}{\sigma(d - d_S)W} \quad (6.79)$$

with the conductivity given by $\sigma = q\mu_n N_D$ and W being the gate width. Substituting (6.78) into (6.79) yields the drain-current equation:

$$I_D = \frac{V_{DS}}{R} = G_0 \left[1 - \sqrt{\frac{2\epsilon}{qd^2} \left(\frac{V_d - V_{GS}}{N_D} \right)} \right] V_{DS} \quad (6.80)$$

where we have defined the conductance $G_0 = \sigma W d / L$. This equation shows that the drain current depends linearly on the drain source voltage, a fact that is only true for small V_{DS} .

As the drain-source voltage increases, the space charge domain near the drain contact increases as well, resulting in a nonuniform distribution of the depletion region along the channel; see Figure 6-40(b). If we assume that the voltage along the channel changes from 0 at the source location to V_{DS} at the drain end, then we can compute the drain current for the nonuniform space charge region. This approach is also known as the **gradual-channel approximation**. The approximation rests primarily on the assumption that the cross-sectional area at a particular location y along the channel is given by $A(y) = \{d - d_s(y)\}W$ and the electric field E is only y -directed. The channel current is thus

$$I_D = -\sigma EA(y) = \sigma \frac{dV(y)}{dy} \{d - d_s(y)\} W \quad (6.81)$$

where the difference between V_d and V_{GS} in the expression for $d_s(y)$ has to be augmented by the additional drop in voltage $V(y)$ along the channel; that is, (6.78) becomes

$$d_s(y) = \left[\frac{2\epsilon}{qN_D} (V_d - V_{GS} + V(y)) \right]^{1/2} \quad (6.82)$$

Substituting (6.82) into (6.81) and carrying out the integration on both sides of the equation yields

$$\int_0^L I_D dy = I_D L = \sigma W \int_0^{V_{DS}} \left(d - \sqrt{\frac{2\epsilon}{qN_D}} \sqrt{V + V_d - V_{GS}} \right) dV \quad (6.83)$$

The result is the **output characteristic** of the MESFET in terms of the drain current as a function of V_{DS} for a given fixed V_{GS} , or

$$I_D = G_0 \left(V_{DS} - \frac{2}{3} \sqrt{\frac{2\epsilon}{qN_D d^2}} [\{V_{DS} + V_d - V_{GS}\}^{3/2} - \{V_d - V_{GS}\}^{3/2}] \right) \quad (6.84)$$

This equation reduces for small V_{DS} to (6.80).

An interesting phenomenon occurs when the space charge extends over the entire channel depth d . The drain-source voltage for this situation is called **drain saturation voltage** $V_{D\text{sat}}$ and is given by

$$d_s(L) = d = \sqrt{\frac{2\epsilon}{qN_D} (V_d - V_{GS} + V_{D\text{sat}})} \quad (6.85)$$

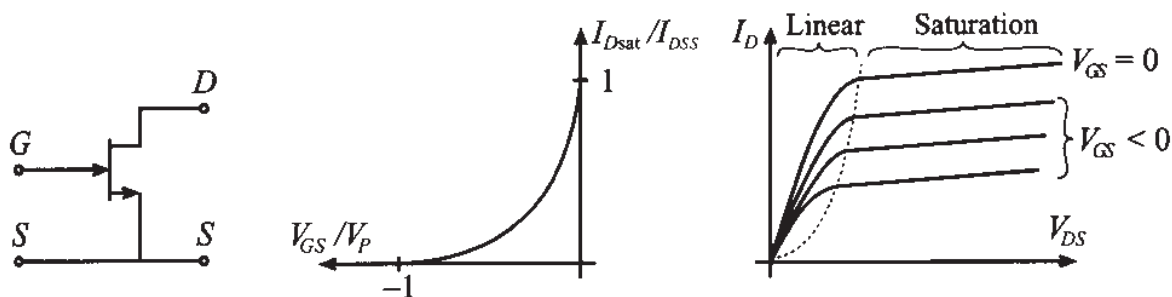
or, explicitly,

$$V_{D\text{sat}} = \frac{qN_D d^2}{2\epsilon} - (V_d - V_{GS}) = V_p - V_d + V_{GS} = V_{GS} - V_{T0} \quad (6.86)$$

where we introduced the so-called **pinch-off voltage** $V_p = qN_D d^2/(2\epsilon)$ and **threshold voltage** $V_{T0} = V_d - V_p$. The associated drain saturation current is found by inserting (6.86) into (6.84) with the result

$$I_{D\text{sat}} = G_0 \left[\frac{V_p}{3} - (V_d - V_{GS}) + \frac{2}{3\sqrt{V_p}} (V_d - V_{GS})^{3/2} \right] \quad (6.87)$$

The maximum saturation current in (6.87) is obtained when $V_{GS} = 0$, which we define as $I_{D\text{sat}}(V_{GS} = 0) = I_{DSS}$. In Figure 6-41 the typical input/output transfer as well as the output characteristic behavior is shown.



(a) Circuit symbol

(b) Transfer characteristic

(c) Output characteristic

Figure 6-41 Transfer and output characteristics of an *n*-channel MESFET.

The saturation drain current (6.87) is often approximated by the simple relation

$$I_{D\text{sat}} = I_{DSS} \left(1 - \frac{V_{GS}}{V_{T0}} \right)^2 \quad (6.88)$$

How well (6.88) approximates (6.87) is discussed in the following example.



RF & MW →

Example 6-9: Drain saturation current in a MESFET

A GaAs MESFET has the following parameters: $N_D = 10^{16} \text{ cm}^{-3}$, $d = 0.75 \mu\text{m}$, $W = 10 \mu\text{m}$, $L = 2 \mu\text{m}$, $\epsilon_r = 12.0$, $V_d = 0.8 \text{ V}$, and $\mu_n = 8500 \text{ cm}^2/(\text{Vs})$. Determine (a) the pinch-

off voltage, (b) the threshold voltage, (c) the maximum saturation current I_{DSS} ; and plot the drain saturation current based on (6.87) and (6.88) for V_{GS} ranging from -4 to 0 V.

Solution: The pinch-off voltage for the FET is independent of the gate-source voltage and is computed as

$$V_p = \frac{qN_D d^2}{2\epsilon} = 4.24 \text{ V}$$

Knowing V_p and the barrier voltage $V_d = 0.8$ V, we find the threshold voltage to be $V_{T0} = V_d - V_p = -3.44$ V. The maximum saturation drain current is again independent of the applied drain-source voltage and, based on (6.87), is equal to

$$I_{DSS} = G_0 \left[\frac{V_p}{3} - V_d + \frac{2}{3\sqrt{V_p}} V_d^{3/2} \right] = 6.89 \text{ A}$$

where $G_0 = \sigma q N_D W d / L = q^2 \mu_n N_D^2 W d / L = 8.16 \text{ S}$.

Figure 6-42 shows results for the saturation drain current computed by using the exact formula (6.87) and by using the quadratic law approximation given by (6.88).

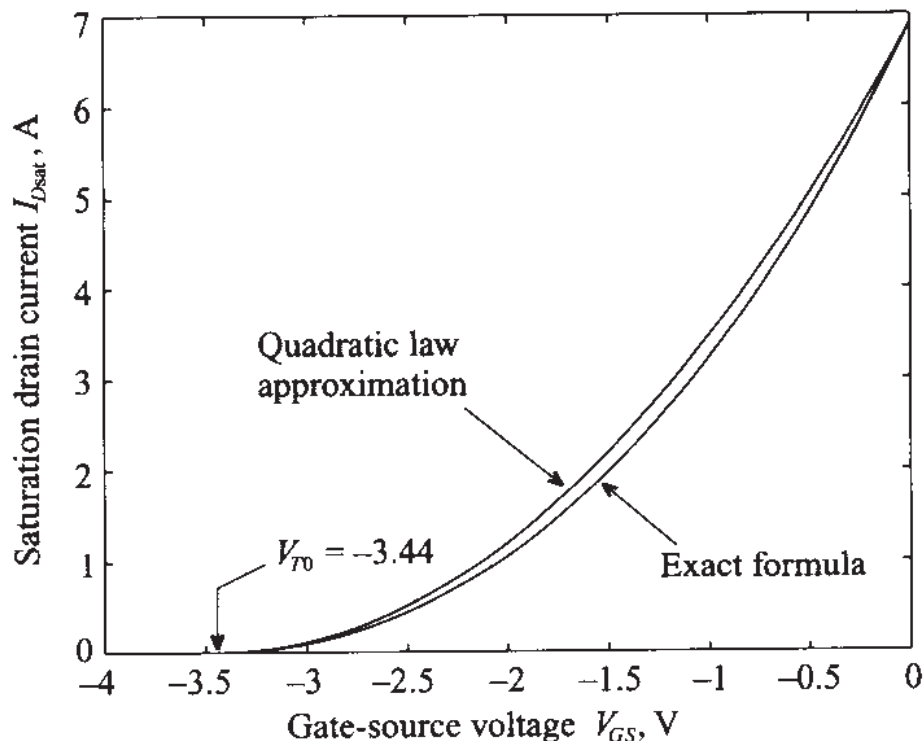


Figure 6-42 Drain current versus V_{GS} computed using the exact and the approximate equations (6.87) and (6.88).

Because of the excellent agreement, the quadratic law approximation (6.88) is more widely used in the literature and data sheets than the exact equation.

If V_{DS} reaches the saturation voltage $V_{D\text{sat}}$ for a given V_{GS} , the space charges pinch off the channel. This implies that the drain current saturates. Interestingly, *pinch-off does not imply a zero I_D* since there is no charge barrier impeding the flow of carriers. It is the electric field as a result of the applied voltage V_{DS} that “pulls” the electrons across the depletion space charge domain. Any additional increase $V_{DS} > V_{D\text{sat}}$ will result in a shortening of the channel length from the original length L to the new length $L' = L - \Delta L$. The result is that (6.87) must be modified to

$$I'_D = I_D \left(\frac{L}{L - \Delta L} \right) = I_D \left(\frac{L}{L'} \right) \quad (6.89)$$

The change in channel length as a function of V_{DS} is heuristically taken into account through the so-called **channel length modulation parameter** $\lambda = \Delta L / (L' V_{DS})$. This is particularly useful when expressing the drain current in the saturation region:

$$I'_{D\text{sat}} = I_{D\text{sat}} (1 + \lambda V_{DS}) \quad (6.90)$$

where measurements show a slight increase in drain current as V_{DS} is increased.



RF & MW

Example 6-10: I - V characteristic of a MESFET

For discrete gate-source voltages $V_{GS} = -1, -1.5, -2$, and -2.5 V, plot the drain current I_D of a MESFET as a function of drain-source voltage V_{DS} in the range from 0 to 5 V. Assume that the device parameters are the same as in the previous example and that the channel length modulation parameter λ is set to be 0.03 V $^{-1}$. Compare your results with the case where $\lambda = 0$.

Solution: In the analysis of the MESFET behavior we have to be careful about choosing the appropriate formulas. At very low drain-source voltages, the drain current can be described by a simple linear relation (6.80). As the voltage increases, this approximation

becomes invalid and a more complicated expression for I_D has to be employed; see (6.84). Further increase in V_{DS} ultimately leads to channel pinch-off, where $V_{DS} \geq V_{D\text{sat}} = V_{GS} - V_{T0}$. In this case the drain current is equal to the saturation current given by (6.87). Additional increases in V_{DS} beyond the saturation voltage result only in minor increases of the drain current due to a shortening of the channel. At this point, I_D is linearly dependent on V_{DS} . Substituting (6.87) into (6.90) for $V_{DS} \geq V_{D\text{sat}}$, we obtain

$$I_D = G_0 \left\{ \frac{V_P}{3} - (V_d - V_{GS}) + \frac{2}{3} \frac{\sqrt{(V_d - V_{GS})^3}}{\sqrt{V_p}} \right\} (1 + \lambda V_{DS})$$

To provide a smooth transition from normal to saturation region for nonzero λ we multiply (6.84) by $(1 + \lambda V_{DS})$. Thus, the final expression for the drain current for $V_{DS} \leq V_{D\text{sat}}$ is

$$I_D = G_0 \left\{ V_{DS} - \frac{2}{3} \frac{\sqrt{(V_{DS} + V_d - V_{GS})^3} - \sqrt{(V_d - V_{GS})^3}}{\sqrt{V_p}} \right\} (1 + \lambda V_{DS})$$

The results of applying these formulas to predict I_D for zero (dashed line) as well as nonzero λ (solid line) are shown in Figure 6-43.

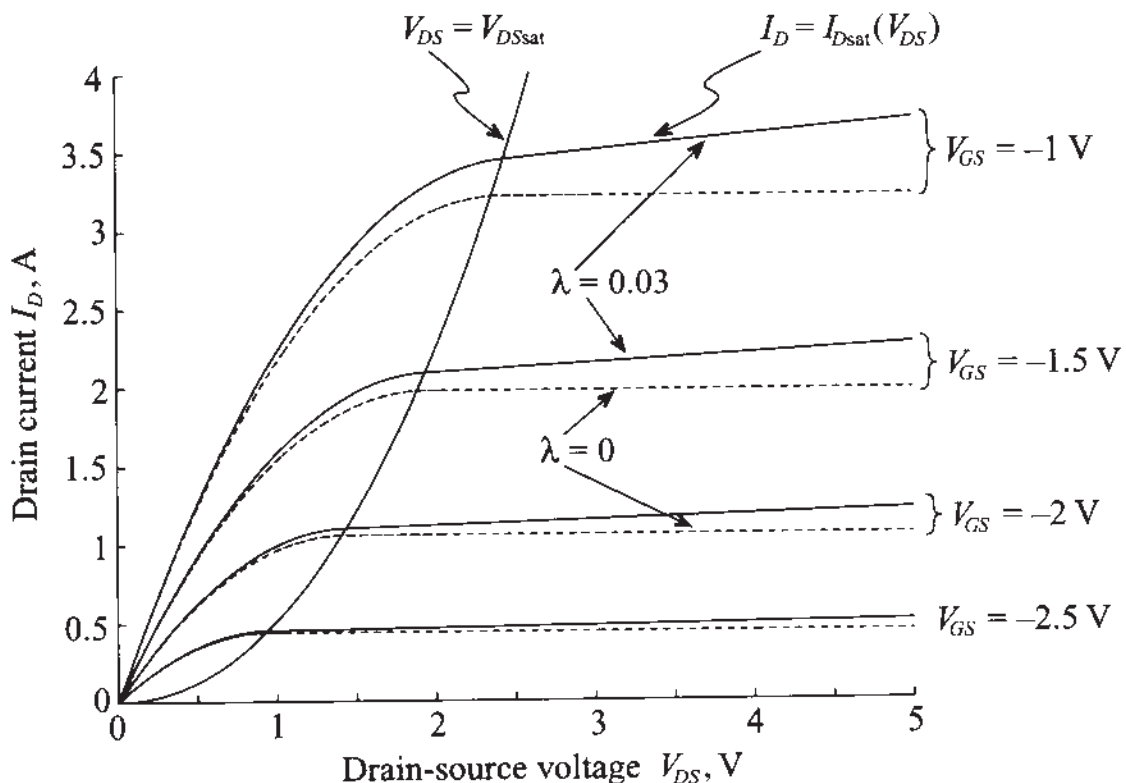


Figure 6-43 Drain current as a function of applied drain-source voltage for different gate-source biasing conditions.

The channel length modulation is similar to the Early effect encountered in a BJT, where the collector current in saturation mode increases slightly for increasing collector emitter voltage as discussed in Chapter 7.

6.4.3 Frequency Response

The high-frequency MESFET performance is determined by the transit time of charge carriers traveling between source and drain and the *RC* time constant of the device. Here we will focus our attention on the transit time only and defer the time constant computation, which requires knowledge of the channel capacitance, to Chapter 7. Since electrons in silicon and GaAs have much higher mobility than holes, *n*-channel MESFETs are used in RF and MW applications almost exclusively. Furthermore, since the electron mobility of GaAs is roughly five times higher than that of Si, GaAs MESFETs are usually preferred over Si devices.

The transit time τ of the electrons traveling through the channel of gate length L is computed as

$$\tau = \frac{L}{v_{\text{sat}}} \quad (6.91)$$

where we have assumed a fixed saturation velocity v_{sat} . As an example, the transition frequency $f_T = 1/(2\pi\tau)$ for a gate length of 1.0 μm and a saturation velocity of approximately 10^7 cm/s is 15 GHz.

6.4.4 Limiting Values

The MESFET must be operated in a domain limited by maximum drain current $I_{D\text{max}}$, maximum gate-source voltage $V_{GS\text{max}}$, and maximum drain-source voltage $V_{DS\text{max}}$. The maximum power P_{max} is dictated by the product of V_{DS} and I_D , or

$$P_{\text{max}} = V_{DS}I_D \quad (6.92)$$

which in turn is related to the channel temperature T_C and ambient temperature T_a and the thermal resistance between channel and soldering point R_{thjs} , according to

$$T_C = T_a + R_{\text{thjs}}P \quad (6.93)$$

Figure 6-44 clarifies this point. Also shown in this figure are three possible operating points. Bias point 3 indicates low amplification and possible clipping of the output current. However, the power consumption is at a minimum. Bias point 2 reveals accept-

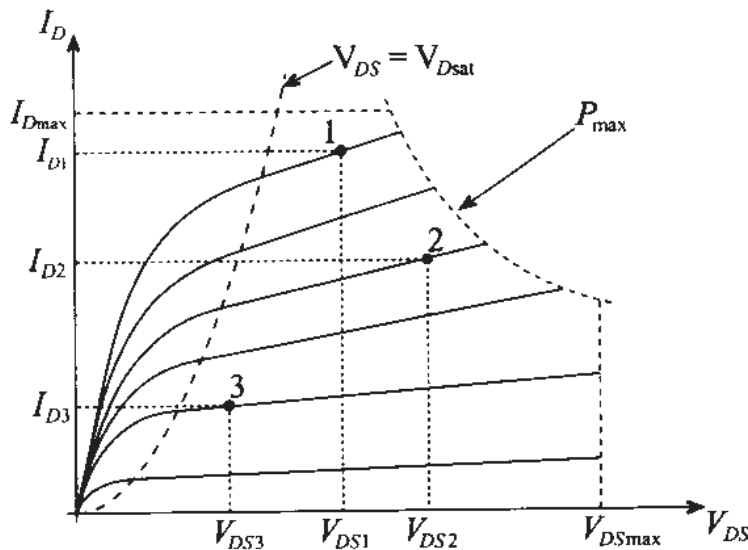


Figure 6-44 Typical maximum output characteristics and three operating points of MESFET.

able amplification at substantially increased power consumption. Finally, bias point 1 shows high amplification at high power consumption and low output current swing. Choosing appropriate bias points for specific applications will be investigated in-depth in subsequent chapters.

6.5 High Electron Mobility Transistors

The **high electron mobility transistor** (HEMT), also known as **modulation-doped field effect transistor** (MODFET), exploits the differences in band gap energy between dissimilar semiconductor materials such as GaAlAs and GaAs in an effort to *substantially surpass the upper frequency limit of the MESFET while maintaining low noise performance and high power rating*. At present, transit frequencies of 100 GHz and above have been achieved. The high frequency behavior is due to a separation of the carrier electrons from their donor sites at the interface between the doped GaAlAs and undoped GaAs layer (**quantum well**), where they are confined to a very narrow (about 10 nm thick) layer in which motion is possible only parallel to the interface. Here we speak of a **two-dimensional electron gas** (2DEG) or plasma of very high mobility, up to $9000 \text{ cm}^2/(\text{V}\cdot\text{s})$. This is a major improvement over GaAs MESFETs with $\mu_n \approx 4500 \text{ cm}^2/(\text{V}\cdot\text{s})$. Because of the thin layer, the carrier density is often specified in terms of a surface density, typically on the order of 10^{12} – 10^{13} cm^{-2} .

To further reduce carrier scattering by impurities it is customary to insert a spacer layer ranging between 20 and 100 nm of undoped GaAlAs. The layer is grown through a molecular beam epitaxial process and has to be sufficiently thin so as to allow the gate voltage V_{GS} to control the electron plasma through electrostatic force mechanism. Besides single layer heterostructures (GaAlAs on GaAs), multilayer heterostructures

involving several 2DEG channels have also been proposed. As can be expected, manufacturing an HEMT is significantly more expensive when compared with the relatively inexpensive GaAs MESFET due to the precisely controlled thin-layer structures, steep doping gradients, and the use of more difficult to fabricate semiconductor materials.

6.5.1 Construction

The basic heterostructure is shown in Figure 6-45, where a GaAlAs *n*-doped semiconductor is followed by an undoped GaAlAs spacer layer of the same material, an undoped GaAs layer, and a high resistive semi-insulating (s.i.) GaAl substrate.

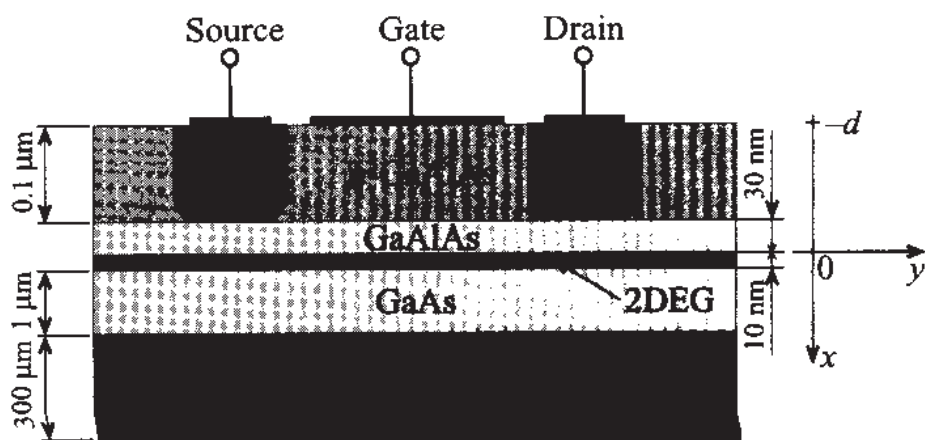


Figure 6-45 Generic heterostructure of a depletion-mode HEMT.

The 2DEG is formed in the undoped GaAs layer for zero gate bias condition because the Fermi level is above the conduction band so that electrons accumulate in this narrow potential well. As discussed later, the electron concentration can be depleted by applying an increasingly negative gate voltage.

HEMTs are primarily constructed of heterostructures with matching lattice constants to avoid mechanical tensions between layers. Specific examples are the GaAlAs-GaAs and InGaAs-InP interfaces. Research is also ongoing with mis-matched lattices whereby, for instance, a larger InGaAs lattice is compressed onto a smaller GaAs lattice. Such device configurations are known as **pseudomorphic HEMTs**, or pHEMTs.

6.5.2 Functionality

The key issue that determines the drain current flow in a HEMT is the narrow interface between the GaAlAs and the GaAs layers. For simplicity, we neglect the spacer layer and concentrate our attention at the energy band model shown in Figure 6-46.

A mathematical model similar to (6.21) can be developed by writing down the one-dimensional Poisson equation in the form

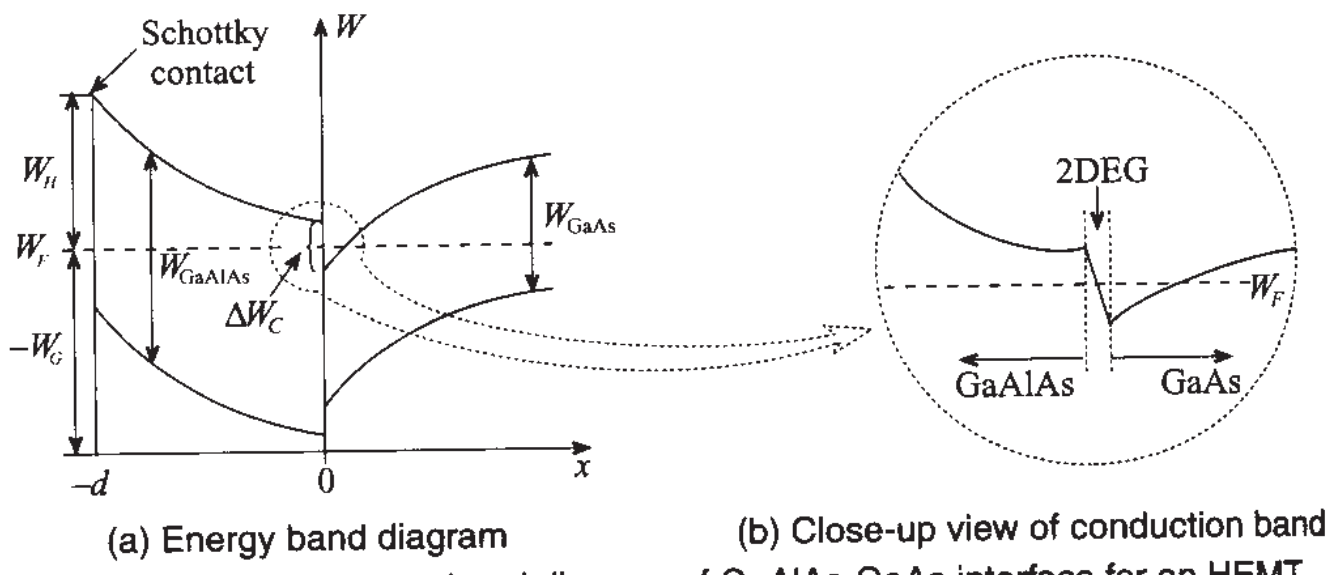


Figure 6-46 Energy band diagram of GaAlAs-GaAs interface for an HEMT.

Figure 6-46 Energy band diagram of GaAlAs-GaAs interface for an HEMT.

$$\frac{d^2V}{dx^2} = -\frac{qN_D}{\epsilon_H} \quad (6.94)$$

where N_D and ϵ_H are the donor concentration and dielectric constant in the GaAlAs heterostructure. The boundary conditions for the potential are imposed such that $V(x = 0) = 0$ and at the metal-semiconductor side $V(x = -d) = -V_b + V_G + \Delta W_C/q$. Here V_b is the barrier voltage, see (6.38); ΔW_C is the energy difference in the conduction levels between the n -doped GaAlAs and GaAs; and V_G is comprised of the gate-source voltage as well as the channel voltage drop $V_G = -V_{GS} + V(y)$. To find the potential, (6.94) is integrated twice. At the metal-semiconductor we set

$$V(-d) = \frac{qN_D}{2\epsilon_H}x^2 - E_y(0)d \quad (6.95)$$

which yields

$$E(0) = \frac{1}{d}(V_{GS} - V(y) - V_{T0}) \quad (6.96)$$

where we defined the HEMT threshold voltage V_{T0} as $V_{T0} = V_b - \Delta W_C/q - V_p$. Here we have used the previously defined pinch-off voltage $V_p = qN_D d^2/(2\epsilon_H)$. From the known electric field at the interface, we find the electron drain current

$$I_D = \sigma E_y A = -q\mu_n N_D E W d = q\mu_n N_D \left(\frac{dV}{dy}\right) W d \quad (6.97)$$

As mentioned previously, the current flow is restricted to a very thin layer so that it is appropriate to carry out the integration over a surface charge density Q_s at $x = 0$. The

result is $\sigma = -\mu_n Q/(WLd) = -\mu_n Q_S/d$. For the surface charge density we find with Gauss's law $Q_S = \epsilon_H E(0)$. Inserted in (6.97), we obtain

$$\int_0^L I_D dy = \mu_n W \int_0^{V_{DS}} Q_S dV \quad (6.98a)$$

Upon using (6.96), it is seen that the drain current can be found

$$I_D L = \mu_n W \int_0^{V_{DS}} \frac{\epsilon_H}{d} (V_{GS} - V - V_{T0}) dV \quad (6.98b)$$

or

$$I_D = \mu_n \frac{W \epsilon_H}{L d} \left\{ V_{DS} (V_{GS} - V_{T0}) - \frac{V_{DS}^2}{2} \right\} \quad (6.98c)$$

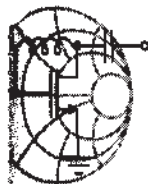
Pinch-off occurs when the drain-source voltage is equal to or less than the difference of gate-source and threshold voltages (i.e., $V_{DS} \leq V_{GS} - V_{T0}$). If the equality of this condition is substituted in (6.98c), it is seen

$$I_D = \mu_n \frac{W \epsilon_H}{2 L d} (V_{GS} - V_{T0})^2 \quad (6.99)$$

The threshold voltage allows us to determine if the HEMT is operated as an enhancement or depletion type. For the depletion type we require $V_{T0} < 0$, or $V_b - (\Delta W_C/q) - V_P < 0$. Substituting the pinch-off voltage $V_P = q N_D d^2 / (2 \epsilon)$ and solving for d , this implies

$$d > \left\{ \frac{2 \epsilon_H}{q N_D} \left(V_b - \frac{\Delta W_C}{q} \right) \right\}^{1/2} \quad (6.100)$$

and if d is less than the preceding expression (i.e., $V_{T0} > 0$), we deal with an enhancement HEMT.



RF & MW →

Example 6-11: Computation of HEMT-related electric characteristics

Determine typical numerical values for a HEMT device such as pinch-off voltage, threshold voltage, and drain current for $V_{GS} = -1, -0.75, -0.5, -0.25$, and 0 V as a function of drain-

source voltage V_{DS} . Assume the following parameters: $N_D = 10^{18} \text{ cm}^{-3}$, $V_b = 0.81 \text{ V}$, $\epsilon_H = 12.5\epsilon_0$, $d = 50 \text{ nm}$, $\Delta W_C = 3.5 \times 10^{-20} \text{ W}\cdot\text{s}$, $W = 10 \mu\text{m}$, $L = 0.5 \mu\text{m}$, and $\mu_n = 8500 \text{ cm}^2/(\text{V}\cdot\text{s})$.

Solution: The pinch-off voltage of a HEMT is evaluated as

$$V_P = qN_D d^2 / (2\epsilon_H) = 1.81 \text{ V}$$

Knowing V_P we can find the threshold voltage as

$$V_{T0} = V_b - \Delta W_C / q - V_P = -1.22 \text{ V}$$

Using these values the drain current is computed by relying either on equation (6.98c) for $V_{DS} \leq V_{GS} - V_{T0}$ or equation (6.99) for $V_{DS} \geq V_{GS} - V_{T0}$. The results of these computations are plotted in Figure 6-47. We notice in this graph that unlike the GaAs MESFET in Figure 6-43, a channel length modulation is not taken into account. In practical simulations such a heuristic adjustment can be added.

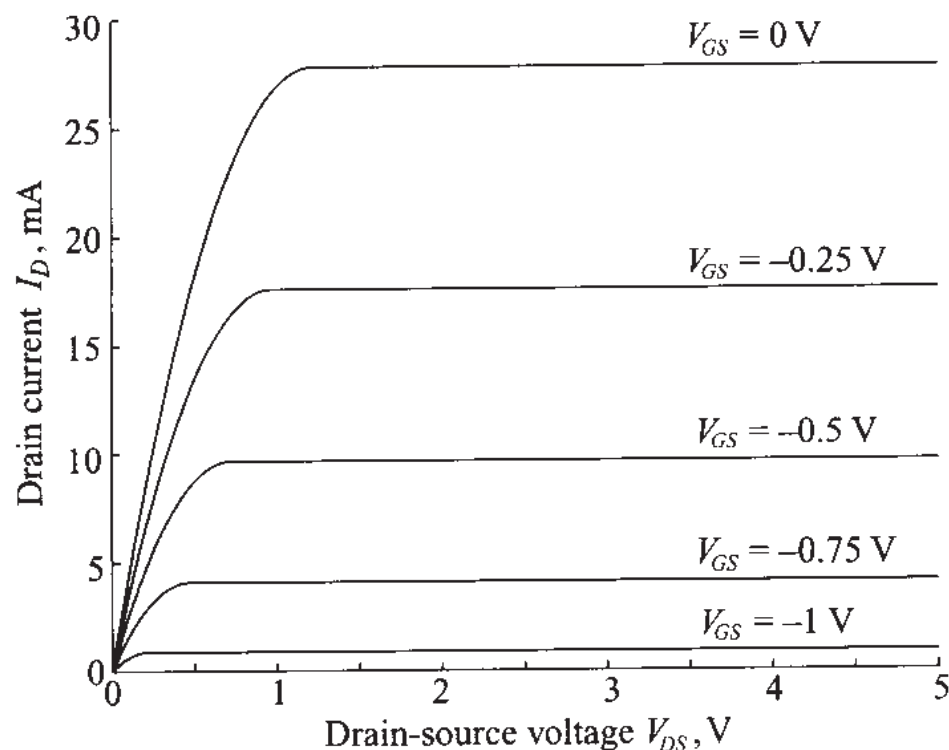


Figure 6-47 Drain current in a GaAs HEMT.

Both GaAs MESFET and HEMT exhibit similar output characteristics and are thus represented by the same electric circuit model.

6.5.3 Frequency Response

The high-frequency performance of the HEMT is determined by the transit time similar to the MESFET. However, the transit time τ is expressed best through the electron mobility μ_n and the electric field E of the drain-source voltage according to

$$\tau = \frac{L}{v_{\text{sat}}} = \frac{L}{\mu_n E_y} = \frac{L^2}{\mu_n V_{DS}} \quad (6.101)$$

We therefore obtain a transit frequency $f_T = 1/(2\pi\tau)$ of approximately 190 GHz for the gate length of 1.0 μm and a mobility of $\mu_n = 8000 \text{ cm}^2/(\text{V}\cdot\text{s})$ at a typical drain voltage V_{DS} of 1.5 V.

6.6 Summary

To understand the functionality and limitations of the most widely employed active RF solid-state devices, we commenced this chapter with a review of the key elements of semiconductor physics. The concepts of conduction, valence, and Fermi levels as part of the energy band model are used as the starting point to examine the various solid-state mechanisms.

We next turned our attention to the *pn*-junction, where we derived the barrier voltage

$$V_{\text{diff}} = V_T \ln\left(\frac{N_A N_D}{n_i^2}\right)$$

and the depletion and diffusion capacitances C_d and C_s in the forms

$$C_d = \frac{C_0}{\sqrt{1 - V_A/V_{\text{diff}}}} \quad \text{and} \quad C_s = \frac{\tau I_0}{V_T} e^{V_A/V_T}$$

Both capacitances are of primary importance when dealing with the frequency response of a *pn*-diode whose current is given by the Shockley equation

$$I = I_s \left(e^{V_A/V_T} - 1 \right)$$

This equation underscores the nonlinear current-voltage diode characteristics.

Unlike the *pn*-junction, the Schottky contact involves an *n*-type semiconductor and a metal interface. The Schottky barrier potential V_d is now modified and requires the work function of metal, qV_M , semiconductor, $q\chi$, and the conduction band potential V_C , expressed via

$$V_d = (V_M - \chi) - V_C$$

Unlike the 0.7 V of a *pn*-junction, we obtain a typical value of 0.84 V for a Si-Au interface. Technologically, this contact is exploited in the Schottky diode, which has become ubiquitous in many RF applications such as modulators and mixers. The *I-V* characteristic remains the same as for the *pn*-junction diode, except that the reverse saturation current I_S is theoretically more intricate.

Additional special-purpose RF diodes are the PIN, varactor, and tunnel diodes. The PIN diode incorporates an additional intrinsic layer sandwiched between the *p* and *n* layers. This allows the switching between a low-resistance forward bias to a capacitive reverse, or isolation, bias. PIN diodes find applications in switchers and attenuators. The *I-V* characteristic of a PIN diode is very similar to a *pn*-junction diode but differs by the factor 2 in the exponent:

$$I = A \left(\frac{qn_i W}{\tau_p} \right) \left(e^{V_A/(2V_T)} - 1 \right)$$

The varactor diode incorporates the *I*-layer based on a special doping profile to achieve a particular capacitance-voltage behavior. Such a response is beneficial for frequency tuning and the generation of short pulses. The tunnel diode exhibits a negative slope during a particular portion of its *I-V* curve, thus making it suitable for oscillator circuits. Additional diodes of interest in the RF field are the IMPATT, TRAPATT, BARRITT, and Gunn diodes.

The BJT in many ways can be regarded as an extension of our previous diode discussion since the *npn*-structure constitutes the series connection of two diodes. The three transistor modes forward active, reverse active, and saturation are reflected in the emitter, collector, and base current expressions (6.69)–(6.71):

$$\begin{aligned} I_E &= -I_S(e^{V_{BE}/V_T} - 1) - \frac{I_S}{\beta_F}(e^{V_{BC}/V_T} - 1) + I_S(e^{V_{BC}/V_T} - 1) \\ I_C &= I_S(e^{V_{BE}/V_T} - 1) - \frac{I_S}{\beta_R}(e^{V_{BC}/V_T} - 1) - I_S(e^{V_{BC}/V_T} - 1) \\ I_B &= I_S \left\{ \frac{1}{\beta_R}(e^{V_{BC}/V_T} - 1) + \frac{1}{\beta_F}(e^{V_{BE}/V_T} - 1) \right\} \end{aligned}$$

The frequency response of a BJT is determined by the transit or transition frequency $f_T = 1/(2\pi\tau)$ at which the short-circuit current gain is equal to unity. The time constant is comprised of three delays $\tau = \tau_E + \tau_B + \tau_C$ associated with emitter, base, and collector domains.

Unlike the bipolar BJT, the FET is a monopolar device that displays superior high-frequency and low-noise performances. In particular, *n*-channel GaAs MESFETs are commonly found in many RF amplifiers, mixers, and oscillators. The key equation that determines the output characteristic of a MESFET is the drain current (6.84):

$$I_D = G_0 \left(V_{DS} - \frac{2}{3} \sqrt{\frac{2\epsilon}{qN_D d^2}} [\{ V_{DS} + V_d - V_{GS} \}^{3/2} - \{ V_d - V_{GS} \}^{3/2}] \right)$$

Additional modifications to the drain current are required when the channel is pinched off and the FET is operated in the saturation domain with channel length modulation.

Finally, the HEMT device is almost identical in construction with the MESFET, but exploits the differences in bandgap energies between heterogeneous semiconductors. Here the current flow is restricted to a very narrow, quantum well layer where the charge mobility can attain twice the value of a MESFET. Because of carrier separation from the donor sites, extremely high operational frequencies have been reported (exceeding 100 GHz). The drain-current representation is almost identical with the one discussed for the MESFET.

Further Reading

- R. S. Cobbold, *Theory and Applications of Field-Effect Transistors*, John Wiley, New York, 1970.
- A. M. Cowley and S. M. Sze, "Surface States and Barrier Height of Semiconductor Systems," *J. Appl. Physics*, Vol. 36, pp. 3212–3220, 1965.
- M. B. Das, "Millimeter-Wave Performance of Ultra-Submicrometer Gate Field-Effect Transistors. A Comparison of MODFET, MESFET, and HBT-Structures," *IEEE Trans. on Electron Devices*, Vol. 34, pp. 1429–1440, 1987.
- A. S. Grove, *Physics and Technology of Semiconductor Devices*, John Wiley, New York, 1967.
- G. Massobrio and P. Antognetti, *Semiconductor Device Modeling with SPICE*, McGraw-Hill, New York, 1993.
- J. L. Moll, *Physics of Semiconductors*, McGraw-Hill, New York, 1964.
- D. V. Morgan and N. Parkman, *Physics and Technology of Heterojunction Devices*, P. Peregrinus Ltd., London, UK, 1991.
- M. H. Norwood and E. Schatz, "Voltage Variable Capacitor Tuning—A Review," *Proceed. IEEE*, Vol. 56, pp. 788–798, 1968.

R.S. Pengelly, *Microwave Field-effect Transistors—Theory, Design and Applications*, Research Studies Press, London, UK, 1982.

C. T. Sah, "Characteristics of the Metal-Oxide Semiconductor Field-Effect Transistor," *IEEE Trans. on Electron Devices*, Vol. 11, pp. 324–345, 1964.

W. Shockley, *Electrons and Holes in Semiconductors*, Van Nostrand Reinhold, New York, 1950.

M. Shur, *GaAs Devices and Circuits*, Plenum Press, New York, 1987.

S. M. Sze, *Physics of Semiconductor Devices*, John Wiley, New York, 1981.

C. Weisbuch. *Physics and Fabrication of Microstructures and Microdevices*, Springer-Verlag, New York, 1986.

Problems

- 6.1 To appreciate the large number of atoms in semiconductors, let us consider the following simple calculation: A silicon semiconductor is a body-centered cubic semiconductor with a lattice constant of $a = 5.43 \times 10^{-8}$ cm. The atom arrangement is such that a corner atom contributes one-eighth plus one center atom. Find the density of atoms per cubic centimeter.
- 6.2 The conduction and valence band carrier concentration is determined by integration of the density of states based on the Fermi statistics.

$$N = \int g(E) dE$$

For effective electron mass m_n^* , quantum mechanical considerations lead to the density function

$$g(E) = 4\pi(2m_n^*)^{3/2} \sqrt{E}/h^3$$

- (a) Determine the generic electron concentration of states N for energy values up to 1.5 eV.
 (b) For an effective electron mass of $1.08 m_n$ or $1.08 \times 9.11 \times 10^{-31}$ kg, explicitly find the number of states.

- 6.3 Let us consider a *p*-type Si semiconductor whose doping concentration at room temperature contains $N_A = 5 \times 10^{16}$ boron atoms per cubic centimeter ($n_i = 1.5 \times 10^{10}$ cm⁻³). Find the minority and majority carrier concentrations as well as the conductivity of the semiconductor.

- 6.4 The Fermi-Dirac probability for indistinguishable particles is the underlying statistical theory describing the quantum mechanical distribution of particles per unit volume and per unit energy $N(E)$ normalized with respect to the number of quantum states per unit voltage and per unit energy $g(E)$ according to

$$f(E) = \frac{N(E)}{g(E)} = \frac{1}{1 + \exp([E - E_F]/[kT])}$$

- (a) Plot both the probability of states being occupied, $f(E)$, as well as the probability of states being empty, $1 - f(E)$, at room temperature and for $E_F = 5$ eV.
 - (b) Determine the temperature at which we have a 5% probability of encountering an empty state.
- 6.5 The intrinsic carrier concentration is typically recorded at room temperature. For GaAs we find at $T = 300^\circ\text{K}$ the effective densities of state $N_C = 4.7 \times 10^{17} \text{ cm}^{-3}$, $N_V = 7.0 \times 10^{18} \text{ cm}^{-3}$. Assuming that the band-gap energy of 1.42 eV remains constant,
- (a) Find the intrinsic carrier concentration at room temperature.
 - (b) Compute n_i at $T = 400^\circ\text{K}$.
 - (c) Compute n_i at $T = 450^\circ\text{K}$.
- 6.6 It is interesting to observe that a significant diffusion current density can be created even for moderate carrier concentration gradients. We can assume for a *p*-type Si semiconductor a linear hole concentration changing from $5 \times 10^{17} \text{ cm}^{-3}$ to 10^{18} cm^{-3} over a distance of 100 μm . Find the current density if the diffusion coefficient is given at $T = 300^\circ\text{K}$ to be $D_p = 12.4 \text{ cm}^2/\text{s}$.
- 6.7 In Section 6.1.2 we derived the expressions for the electric field and potential distributions in the *pn*-diode with abrupt junction. Repeat these computations for a case of gradual junction where the charge density changes linearly according to the following relation:

$$\rho(x) = \begin{cases} qN_A(x/d_p), & -d_p \leq x \leq 0 \\ qN_D(x/d_n), & 0 \leq x \leq d_n \end{cases}$$

- 6.8 The built-in potential barrier of a *pn*-junction remains relatively constant even though the doping concentration may change over several orders of magnitude. We recall that the typical barrier potential in solid state circuits is

assumed to be 0.5–0.9 V. In this problem we intend to show how one arrives at this voltage. Let us assume a *p*-type semiconductor with $N_A = 10^{18} \text{ cm}^{-3}$ joined with an *n*-type semiconductor of concentration $N_D = 5 \times 10^{15} \text{ cm}^{-3}$.

- (a) Find the barrier voltage at room temperature ($n_i = 1.45 \times 10^{10} \text{ cm}^{-3}$).
- (b) Recompute the barrier voltage if N_A is reduced to $N_A = 5 \times 10^{16} \text{ cm}^{-3}$.

- 6.9 An abrupt *pn*-junction made of Si has the acceptor and donor concentrations of $N_A = 10^{18} \text{ cm}^{-3}$ and $N_D = 5 \times 10^{15} \text{ cm}^{-3}$, respectively. Assuming that the device operates at room temperature, determine
- (a) the barrier voltage
 - (b) the space charge width in the *p*- and *n*-type semiconductors
 - (c) the peak electric field across the junction
 - (d) the junction capacitance for a cross sectional area of 10^{-4} cm^2 and a relative dielectric constant of $\epsilon_r = 11.7$
- 6.10 For two *pn*-diodes with abrupt junction, one of which is made of Si and another is made of GaAs, with $N_A = 10^{17} \text{ cm}^{-3}$ and $N_D = 2 \times 10^{14} \text{ cm}^{-3}$ in both cases:
- (a) Find the barrier voltage.
 - (b) Find the maximum electric field and the space charge region width.
 - (c) Plot the space charge, potential, and electric field distribution along the diode axis.
- 6.11 A silicon *pn* junction has a conductivity of 10 S/cm and 4 S/cm for *p* and *n* layers, respectively. Using the necessary properties of silicon, calculate the built-in voltage of the junction at room temperature.
- 6.12 A Schottky contact between a metal and a semiconductor can be made of various materials. For both Si and GaAs we would like to investigate the barrier voltage if the metal is either aluminum or gold. Use Table 6-2 and Table E-1 to find the four barrier voltages and associated depletion layer thicknesses at room temperature.
- 6.13 Consider a Schottky diode formed by the contact between *n*-type GaAs and silver. The diode is operated at forward biasing current of 1 mA. The Richardson constant $R^* = 4 \text{ A}/(\text{cm}^2 \text{K}^2)$, the parasitic series resistance is 15 Ω, and the device cross section $A = 10^{-2} \text{ mm}^2$. Compute the barrier voltage V_d and plot the magnitude and phase of the impedance of diode ver-

sus frequency ranging from 1 MHz to 100 GHz for two doping densities $N_D: 10^{15}$ and 10^{17} cm^{-3} . Assume that the device is operated at the temperature of 300°K.

- 6.14 It is often of enormous practical interest to investigate the nonlinear current behavior of a Schottky diode for a given applied voltage. We recall

$$I = I_S \left(e^{(V_A - IR_S)} - 1 \right)$$

with the reverse saturation current given to be $I_S = 2 \times 10^{-11} \text{ A}$. For a substrate resistance $R_S = 1.8 \Omega$ write a computer program to predict the current if the applied voltage is allowed to vary within $0 \leq V_A \leq 10 \text{ V}$.

- 6.15 A PIN diode is a semiconductor device with an intrinsic layer sandwiched between two highly doped *n*- and *p*-type materials. In the intrinsic layer, the charged minority and majority carriers possess a finite life time τ_p before recombination takes place. On the basis of the recombination lifetime a simple PIN model can be constructed involving the diode current I and the stored charge Q :

$$I = \frac{Q}{\tau_p} + \frac{dQ}{dt}$$

- (a) Establish the frequency domain response $Q(\omega)$ of this first-order system.
- (b) Plot the normalized charge response $20\log[Q(\omega)/(I\tau_p)]$ versus angular frequency for τ_p of 10 ps, 1 ns, and 1 μs .

Note: For frequencies well below the cut-off frequency $f_p = 1/\tau_p$ the PIN diode behaves like a normal *pn*-junction diode. However, at frequencies above f_p , the PIN diode becomes a pure linear resistor whose value is controlled by the biasing signal.

- 6.16 The fabrication of two different types of varactor diodes calls for the following two capacitance-voltage behaviors:

- (a) $C = 5 \text{ pF} \sqrt{V_A/(V_A - V_{\text{diff}})}$
- (b) $C = 5 \text{ pF} (V_A/(V_A - V_{\text{diff}}))^{1/3}$

Determine the necessary donor doping profile $N_D(x)$ for the intrinsic layer. Assume the cross-sectional area of the varactor diode to be 10^{-4} cm^2 .

- 6.17 Consider a Si bipolar junction transistor whose emitter, base, and collector are uniformly doped with the following concentrations: $N_D^E = 10^{21} \text{ cm}^{-3}$, $N_A^B = 2 \times 10^{17} \text{ cm}^{-3}$, $N_D^C = 10^{19} \text{ cm}^{-3}$. Assume that the base-emitter volt-

age is 0.75 V and the collector-emitter potential is set to 2 V. The cross-sectional area of both junctions is 10^{-4} cm^2 and the emitter, base, and collector thicknesses are $d_E = 0.8 \mu\text{m}$, $d_B = 1.2 \mu\text{m}$, and $d_C = 2 \mu\text{m}$, respectively. Assuming that the device is operated at room temperature:

- (a) Find the space charge region extents for both junctions.
- (b) Draw the energy band diagram.
- (c) Compute the base, emitter, and collector currents.
- (d) Calculate the forward and reverse current gains β_F and β_R .

- 6.18 For a GaAs BJT the maximum junction temperature is 420°C (which far exceeds the maximum junction temperature of Si with 200°C). The supplied power is 90 W. The thermal resistance between the BJT and the heat sink is estimated to be $1.5^\circ\text{C}/\text{W}$
- (a) Determine the maximum thermal resistance of the heat sink if the ambient operating temperature does not exceed 50°C .
 - (b) For a heat convection coefficient of $100 \text{ W}/^\circ\text{C} \cdot \text{m}^2$ find the required surface area.
- 6.19 A BJT is encapsulated in a plastic housing and mounted on a heat sink ($R_{\text{thha}} = 3.75^\circ\text{C}/\text{W}$). Under these conditions the total power dissipation is supposed to be 20 W at an ambient temperature of 20°C . What rating has the engineer to choose for the BJT casing if the maximum junction temperature should not exceed 175°C ?
- 6.20 Prove that the drain current (6.84) for a MESFET under gradual-channel approximation reduces to (6.80) for small V_{DS} .
- 6.21 Derive the saturation drain current equation (6.88).
- 6.22 The junction field-effect transistor with *n*-type channel has the following parameters: $W/L = 10$, $\mu_n = 1000 \text{ m}^2/(\text{V}\cdot\text{s})$, $d = 2 \mu\text{m}$, $\epsilon_r = 11.7$, and $V_{T0} = -3 \text{ V}$. Compute the saturation drain current at $V_{GS} = -1 \text{ V}$.
- 6.23 Compute the output current I_D versus V_{DS} characteristics of the transistor from Problem 6.22 for drain-source voltage ranging from 0 to 5 V. First assume that channel length modulation effect is negligible (i.e., $\lambda = 0$), and then repeat your computation for a case when $\lambda = 0.01$.

Active RF Component Modeling

Almost all circuit designs of any complexity have to be modeled as part of computer-aided design (CAD) programs prior to their practical realizations to assess quantitatively whether or not these circuits meet design specifications. For the purpose of electric circuit simulation, a large number of software analysis packages offer a host of equivalent circuit models attempting to replicate the electric performance of the various discrete elements. Special electric circuit models have been developed to address such important design requirements as low- or high-frequency operation, linear or nonlinear system behavior, and normal or reverse mode of operation to name but a few.

It is the purpose of this chapter to examine several active devices in terms of suitable equivalent circuit representations for diodes as well as mono- and bipolar transistors. The physical foundation of these devices is reviewed in Chapter 6. By developing a close link with the previous chapter, we will be able to observe how a basic understanding of solid-state device physics naturally leads to large signal (nonlinear) circuit models. Subsequent discussions will focus on modifications that can be made to linearize these models and to refine them for high-frequency operations.

Considering the various BJT models, we restrict our discussion to only the most popular types such as the Ebers-Moll and Gummel-Poon models. Both types, and a number of linear derivatives, find widespread applications in such simulation tools as SPICE, ADS, MMICAD, and others. Often the situation arises where the device manufacturer may not be able to specify all the required electric parameters, since they can easily exceed 40 independent parameters, and a so-called SPICE model representation is unattainable. Under those circumstances, the *S*-parameters are recorded for various bias conditions and operating frequencies to characterize the high-frequency behavior.

In most cases, these *S*-parameters may provide the design engineer with sufficient information to complete the simulation task.

7.1 Diode Models

7.1.1 Nonlinear Diode Model

The typical large-scale circuit model treats both the *pn* and Schottky diode in the same fashion, as shown in Figure 7-1.

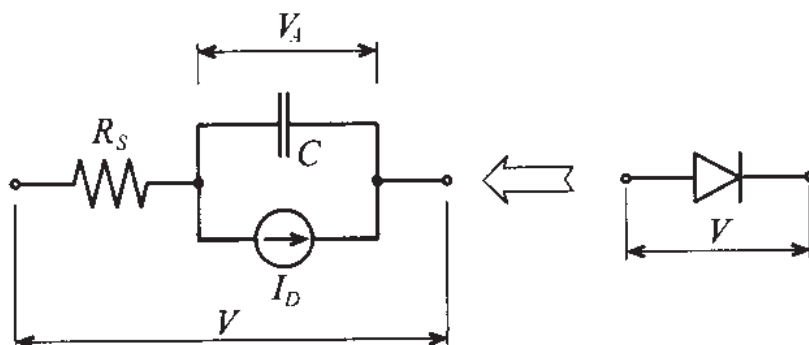


Figure 7-1 Large-scale diode model.

This model takes into account the nonlinear *I-V* characteristics of the Shockley diode equation (6.34) in slightly modified form

$$I_D = I_S (e^{V_A/(nV_T)} - 1) \quad (7.1)$$

where the **emission coefficient** *n* is chosen as an additional parameter aimed at bringing the model in closer agreement with actual measurements. This coefficient for most applications is close to 1.0. Furthermore, in Section 6.1.2 the diffusion and junction (or depletion layer) capacitances C_d and C_J are discussed. Both effects are combined in a single capacitance *C*, but in a more general form. Specifically, for the junction capacitance, we have to consider the space charge Q_J , which is differentiated with respect to the applied voltage, leading to

$$C_J = \frac{dQ_J}{dV_A} = \frac{C_{J0}}{\left[1 - V_A/V_{\text{diff}}\right]^m} \quad (7.2)$$

where *m* is known as the **junction grading coefficient**. It assumes a value of 0.5 for the abrupt junction that is subject of our analysis in Section 6.1.2. For the more realistic case of a gradual transition *m* lies in the range $0.2 \leq m \leq 0.5$. As mentioned in Chapter 6, the formula given in (7.2) is applicable only for certain positive applied voltages. If the applied voltage V_A approaches the built-in potential V_{diff} , the junction

capacitance computed using (7.2) approaches infinity which is obviously physically impossible. In practice, the junction capacitance becomes almost linearly dependent on the applied voltage once it exceeds a threshold potential V_m , which is usually equal to half of the built-in potential, $V_m \approx 0.5V_{\text{diff}}$. Therefore, the approximate formula capable of describing the junction capacitance over the entire range of applied voltages is given by

$$C_J = \begin{cases} \frac{C_{J0}}{(1 - V_A/V_{\text{diff}})^m}, & V_A \leq V_m \\ \frac{C_{J0}}{(1 - V_m/V_{\text{diff}})^m} \left(1 + m \frac{V_A - V_m}{V_{\text{diff}} - V_m}\right), & V_A \geq V_m \end{cases} \quad (7.3)$$

We also observe that C_d is dependent on V_A . For the diffusion capacitance, we can use

$$C_d = \frac{dQ_d}{dV_A} = \frac{I_S \tau_T}{nV_T} e^{V_A/(nV_T)} \quad (7.4)$$

with the transition time τ_T .

In a realistic diode the injection and extraction of charges is accomplished by the electric field that constitutes a voltage drop in the charge neutral domains. This voltage drop is modeled as a series resistance R_s . Thus the total voltage in Figure 7-1 is composed of two contributions:

$$V = R_s I_D + nV_T \ln(1 + I_D/I_S) \quad (7.5)$$

Temperature dependencies can also be introduced into this model. Besides the obvious thermal voltage $V_T = kT/q$ it is primarily the reverse saturation current I_S that is found to be strongly influenced by temperature according to

$$I_S(T) = I_S(T_0) \left(\frac{T}{T_0}\right)^{p_t/n} \exp\left[-\frac{W_g(T)}{V_T} \left(1 - \frac{T}{T_0}\right)\right] \quad (7.6)$$

where T_0 is a reference temperature at which the saturation current is recorded. The literature primarily uses $T_0 = 300^\circ\text{K}$ (or 27°C). The **reverse saturation current temperature coefficient** p_t is either 3 or 2 depending on whether a *pn* or Schottky diode is modeled. The model parameter can thus account for the difference in temperature behavior between the two diode types. Also, the **bandgap energy** $W_g(T)$ is considered. As the temperature increases, this bandgap decreases, making it easier for charge carriers to transition from the valence into the conduction band. The semi-empirical

formula assumes a specific bandgap energy $W_g(0)$ recorded at $T = 0^\circ\text{K}$ and then adjusts this value as follows

$$W_g(T) = W_g(0) - \left(\frac{\alpha_T T^2}{\beta_T + T} \right) \quad (7.7)$$

For instance, the experimentally determined parameters for Si are $W_g(0) = 1.16\text{ eV}$, $\alpha_T = 7.02 \times 10^{-4}\text{ eV}/^\circ\text{K}$, and $\beta_T = 1108^\circ\text{K}$. Additional temperature dependencies affecting the capacitances are usually small and are neglected.

Perhaps the most popular circuit simulation program in industry and academia is SPICE, which is capable of taking into account the nonlinear diode model depicted in Figure 7-1. This simulation program incorporates a range of physical model parameters; some of them are so specialized that they are beyond the scope of our textbook. The most important ones are summarized in Table 7-1. Also listed are the differences between the standard *pn* and Schottky diode.

Table 7-1 Diode model parameters and their corresponding SPICE parameters

| Symbol | SPICE | Description | Typical values |
|-------------------|-------|--|---|
| I_S | IS | saturation current | 1 fA–10 μA |
| n | N | emission coefficient | 1 |
| τ_T | TT | transit time | 5 ps–500 μs |
| R_S | RS | ohmic resistance | 0.1–20 Ω |
| V_{diff} | VJ | barrier voltage | 0.6–0.8 V (<i>pn</i>) 0.5–0.6 V (Schottky) |
| C_{J0} | CJ0 | zero-bias junction capacitance | 5–50 pF (<i>pn</i>) 0.2–5 pF (Schottky) |
| m | M | grading coefficient | 0.2–0.5 |
| W_g | EG | bandgap energy | 1.11 eV (Si) 0.69 eV (Si-Schottky) |
| p_t | XTI | saturation current temperature coefficient | 3 (<i>pn</i>) 2 (Schottky) |

7.1.2 Linear Diode Model

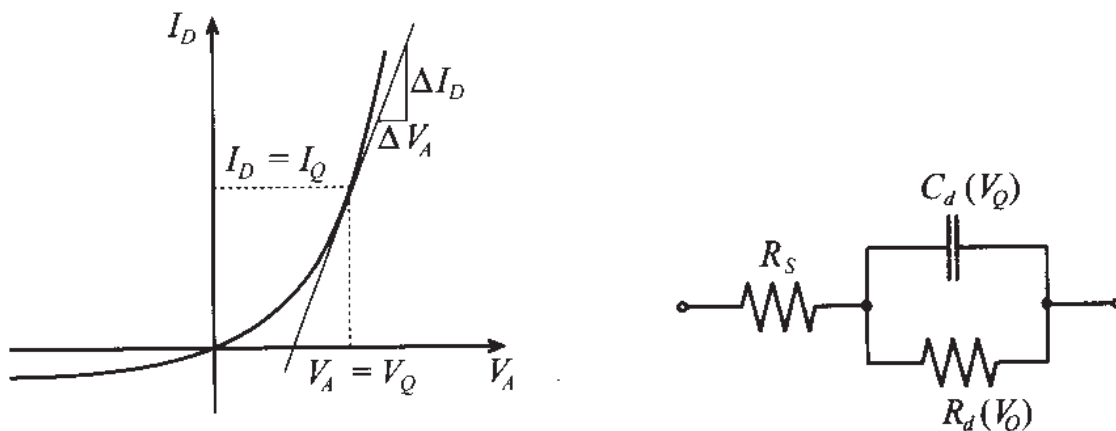
The nonlinear model is based on the device physics developed in Chapter 6. As such, this model can be used for static and dynamic analyses under practically any circuit conditions. However, if the diode is operated at a particular DC voltage bias point and the signal variations about this point are small, we can develop a linear or small-

signal model. The concept of linearization implies the approximation of the exponential I - V characteristic through a tangent at the bias or Q -point V_Q . The tangent at this Q -point is the differential conductance G_d , which we can find as

$$G_d = \frac{1}{R_d} = \left. \frac{dI_D}{dV_A} \right|_{V_Q} = \frac{I_Q + I_S}{nV_T} \equiv \frac{I_Q}{nV_T} \quad (7.8)$$

The tangent approximation is shown in Figure 7-2 along with the simplified, linear circuit model. It is important to emphasize that the differential capacitance is now the diffusion capacitance at bias point V_Q , or

$$C_d = \frac{I_S \tau_T}{nV_T} e^{V_Q/(nV_T)} \quad (7.9)$$

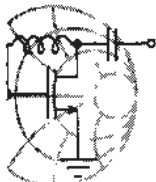


(a) tangent approximation at Q -point

(b) linear circuit model.

Figure 7-2 Small-signal diode model.

An apparent benefit of such a linearized circuit model is the ability to decouple the RF diode operation from the DC bias condition, as the following design example underscores.



RF & MW →

Example 7-1: Derivation of the small-signal *pn* diode model

A conventional Si-based *pn*-diode is operated at 300°K and has the following electric parameters at this temperature: $\tau_T = 500$ ps, $I_S = 5 \times 10^{-15}$ A, $R_S = 1.5 \Omega$, $n = 1.16$. The DC operating conditions are chosen such that $I_Q = 50$ mA. To characterize the per-

formance of a particular RF system in which this diode is used, we need to obtain

- (a) the impedance behavior of the diode in the frequency range $10 \text{ MHz} \leq f \leq 1 \text{ GHz}$ at 300°K , and
- (b) the impedance response of the diode in the same frequency range, but for temperatures of 250°K , 350°K , and 400°K .

Solution: At a temperature of 300°K , we first determine from $I_Q = 50 \text{ mA}$ the corresponding V_Q , which is found from (7.1)

$$V_Q = nV_T \ln(1 + I_Q/I_S) = 0.898 \text{ V}$$

Next we can compute the differential resistance and capacitance as

$$R_d = \frac{nV_T}{I_Q} = 0.6 \Omega \text{ and } C_d = \frac{I_S \tau_T}{nV_T} e^{V_Q/(nV_T)} = 832.9 \text{ pF}$$

Knowing these parameters, we can find the impedance of the diode as a resistor R_S connected in series with the parallel combination of R_d and C_d :

$$Z = R_S + \frac{R_d}{1 + j\omega C_d R_d}$$

The resulting frequency behavior is shown in Figure 7-3.

As temperature changes and the biasing current I_Q is maintained constant, the biasing voltage V_Q should change due to the temperature dependence of the thermal potential $V_T = kT/q$, bandgap energy W_g given by (7.7), and saturation current I_S described in (7.6). Results of these computations are presented in Table 7-2, and the corresponding frequency behavior of the diode impedance is shown in Figure 7-3.

Table 7-2 Diode model parameters for different temperatures

| $T, ^\circ\text{K}$ | 250 | 300 | 350 | 400 |
|---------------------|-----------------------|-----------------------|-----------------------|-----------------------|
| $W_g(T), \text{eV}$ | 1.128 | 1.115 | 1.101 | 1.086 |
| $I_s(T), \text{A}$ | 5.1×10^{-19} | 5.0×10^{-15} | 3.3×10^{-12} | 3.8×10^{-10} |
| V_Q, V | 0.979 | 0.898 | 0.821 | 0.748 |
| R_d, Ω | 0.5 | 0.6 | 0.7 | 0.8 |
| C_d, pF | 999.5 | 832.9 | 713.9 | 624.7 |

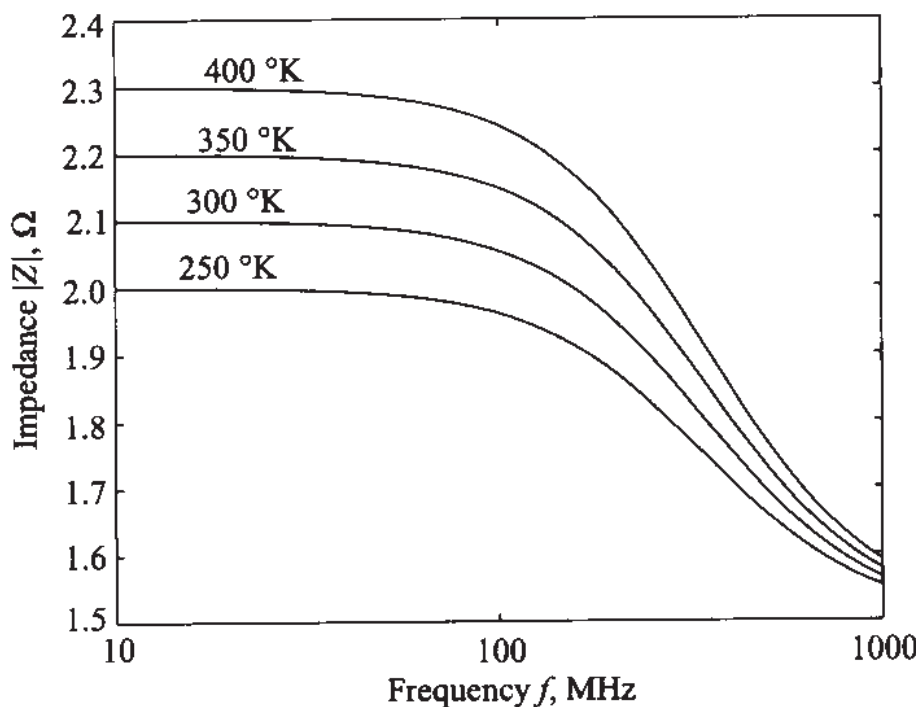


Figure 7-3 Frequency behavior of the diode impedance for different junction temperatures.

We observe how the physical parameters developed for the pn-junction in Chapter 6 directly translate into the small-signal circuit model. The DC bias conditions influence the AC behavior because they affect the differential capacitance and resistance.

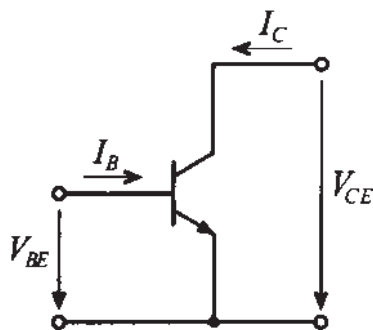
7.2 Transistor Models

Over the years a number of large- and small-signal bipolar and monopolar transistor models have been developed. Perhaps the best-known one is the Ebers-Moll BJT model, which was initially introduced to characterize static and low-frequency transistor modes. The need to expand into RF/MW frequencies and high power applications required taking into account many important second-order effects, such as low-current and high-injection phenomena. This has resulted in the Gummel-Poon model as a more refined BJT circuit representation.

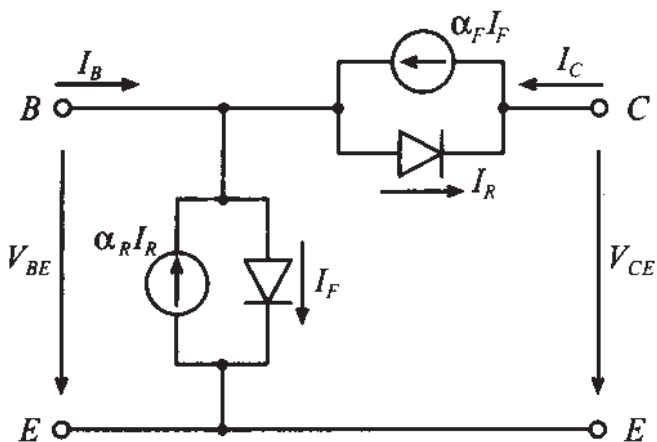
7.2.1 Large-Signal BJT Models

We begin our discussion with the static **Ebers-Moll model**, which is one of the most popular large-signal models. Although this model was first introduced in December of 1954, it still is indispensable to understand the basic model requirements and its extensions to more sophisticated large-signal models as well as the derivation of most

small signal models. Figure 7-4 shows the generic *npn* transistor with the associated Ebers-Moll circuit model in the so-called **injection version**.



(a) Voltage and current convention for *npn* transistor



(b) Ebers-Moll circuit model

Figure 7-4 Large-signal Ebers-Moll circuit model.

In Figure 7-4 we encounter two diodes connected in forward and reverse polarity, as already seen in Chapter 6. In addition, two current-controlled current sources permit the mutual coupling of the two diodes as part of the base contact. The forward and reverse current gains (in common-base configuration) α_F and α_R possess typical values of $\alpha_F = 0.95 \dots 0.99$ and $\alpha_R = 0.02 \dots 0.05$. As a direct extension of the previously discussed single-diode model, the dual-diode Ebers-Moll equations take on the form

$$I_E = \alpha_R I_R - I_F \quad (7.10)$$

$$I_C = \alpha_F I_F - I_R \quad (7.11)$$

with the diode currents

$$I_R = I_{CS} (e^{V_{BE}/V_T} - 1) \quad (7.12)$$

$$I_F = I_{ES} (e^{V_{BC}/V_T} - 1) \quad (7.13)$$

where the **reverse collector and emitter saturation currents** I_{CS} and I_{ES} (whose numerical values range from 10^{-9} A to 10^{-18} A) can be related to the transistor saturation current I_S as follows:

$$\alpha_F I_{ES} = \alpha_R I_{CS} = I_S \quad (7.14)$$

Despite their simplicity, the Ebers-Moll equations are capable of describing all major physical phenomena developed in Chapter 6. For the important cases of forward and reverse active modes, the circuit model can be simplified. The following two situations arise:

- Forward Active Mode ($V_{CE} > V_{CE_{sat}} = 0.1$ V, $V_{BE} \approx 0.7$ V). With the base-emitter diode I_F conducting, and the base-collector diode in reverse direction (i.e., $V_{BC} < 0$ V), we conclude that $I_R \approx 0$, and also $\alpha_R I_R \approx 0$. The base-collector diode and the base-emitter current source can thus be neglected.
- Reverse Active Mode ($V_{CE} < -0.1$ V, $V_{BC} \approx 0.7$ V). Here the base-collector diode I_R is conducting, and the base-emitter diode is biased in reverse direction (i.e., $V_{BE} < 0$ V), which results in $I_F \approx 0$ and $\alpha_F I_F \approx 0$.

Figure 7-5 summarizes these two modes of operation when the emitter is chosen as common reference point.

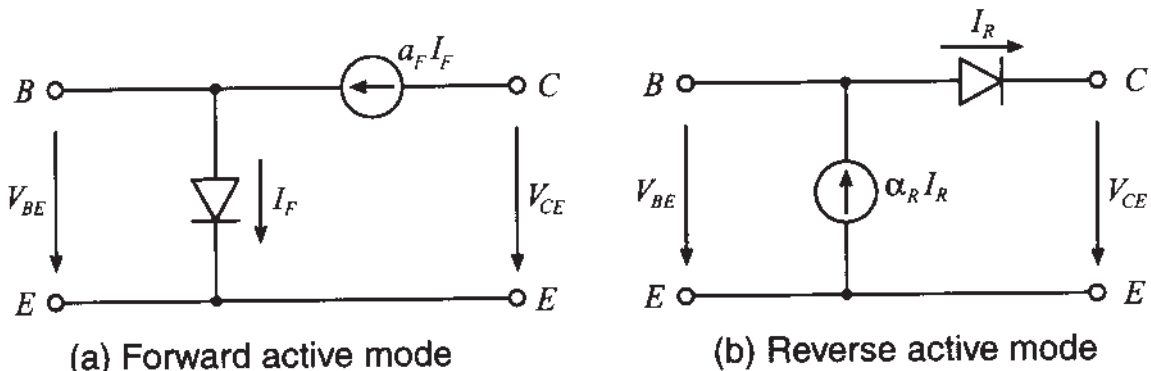
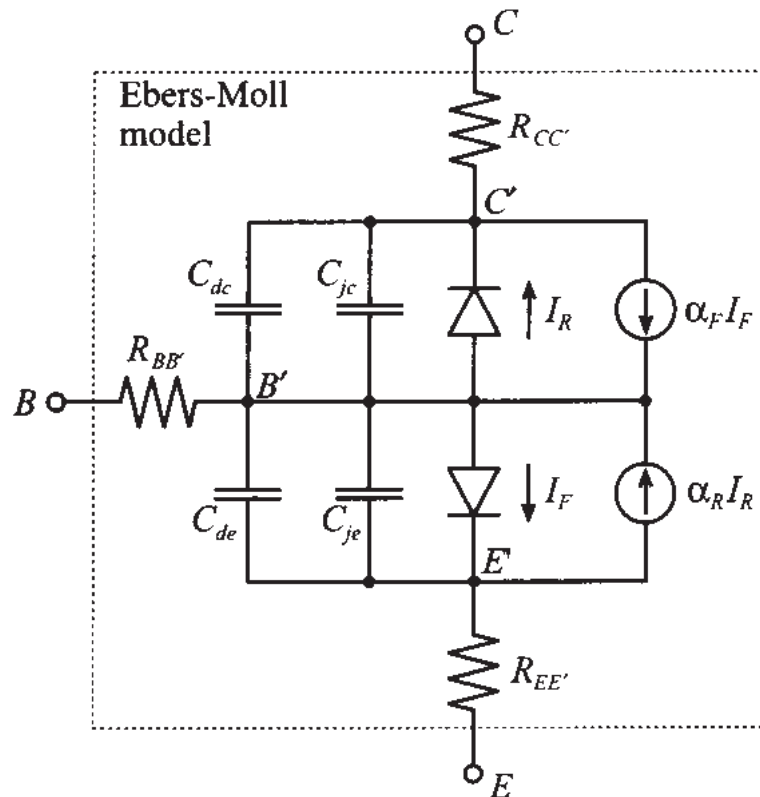
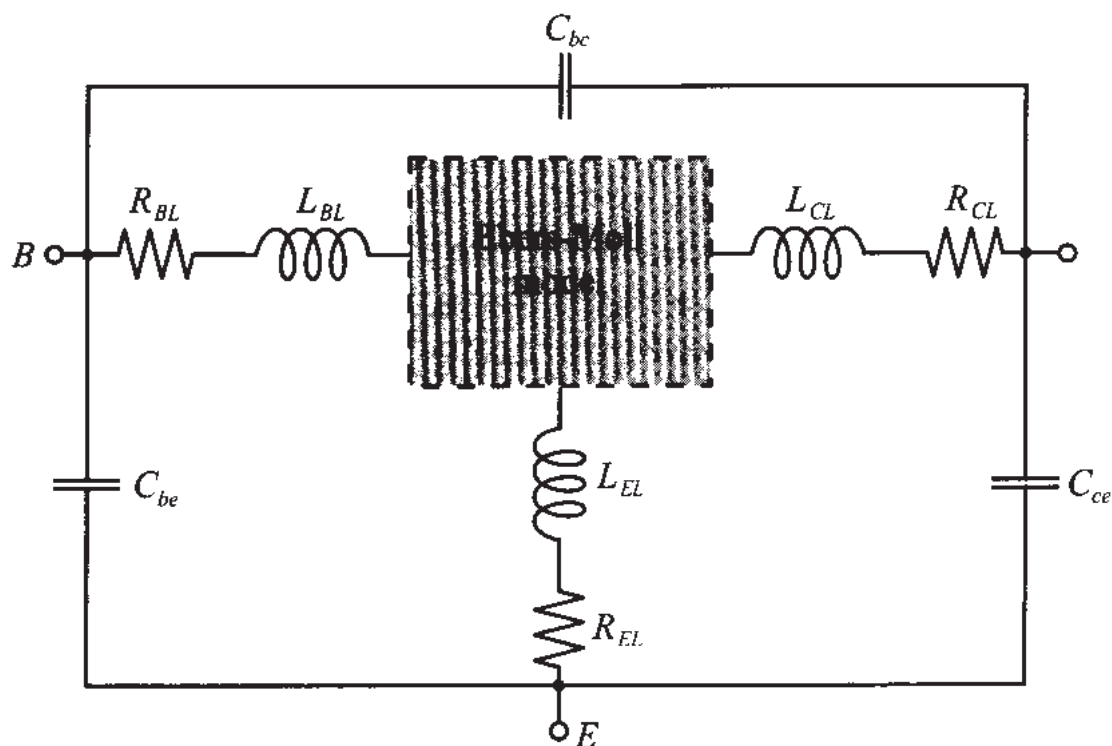


Figure 7-5 Simplified Ebers-Moll equations for forward and reverse active modes.

This model can be modified to account for dynamic operations by including the familiar base-emitter and base-collector diffusion (C_{de} , C_{dc}) and junction (C_{je} , C_{jc}) diode capacitances. Unlike the simple charge analysis presented for the single-diode model, a more elaborate treatment is required for the BJT. For instance, the charge accounting for the emitter diffusion capacitance is comprised of minority charges stored in (a) the neutral emitter zone, (b) the emitter-base, (c) the collector-base space charge regions, and (d) the neutral base zone. An identical analysis applies to the collector diffusion capacitance. Figure 7-6 depicts the dynamic Ebers-Moll chip-model. Further refine-



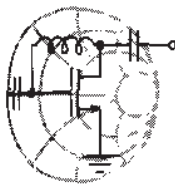
(a) Dynamic Ebers-Moll chip model



(b) RF model with parasitic terminal effects

Figure 7-6 Dynamic Ebers-Moll model and parasitic element refinements.

ments for RF operations are often made by including the resistive and inductive properties of the lead wires as well as parasitic capacitances between the terminal points, see Figure 7-6(b).



RF & MW →

Example 7-2: Transport versus injection form of the Ebers-Moll large-signal model

Instead of the injection model, it is the transport model that typically finds use in SPICE simulations. Let us go through the qualitative steps to arrive at this important representation.

Solution: We begin our discussion with the static BJT model, since the diffusion and junction capacitances can be added later in the derivation. First, we can show that the injection model Figure 7-4 is equivalent to the transport model in Figure 7-7.

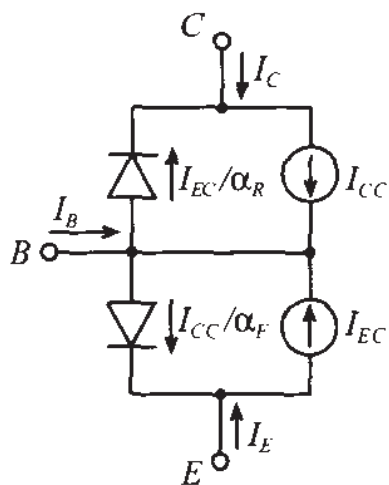


Figure 7-7 Transport representation of static Ebers-Moll injection model.

The equivalence of both models can be established if we re-express collector and emitter currents as follows:

$$I_C = I_{CC} - I_{EC}/\alpha_R$$

$$I_E = -I_{CC}/\alpha_F + I_{EC}$$

with the current controlled sources now given as

$$I_{CC} = I_S(e^{V_{BE}/V_T} - 1)$$

$$I_{EC} = I_S(e^{V_{BC}/V_T} - 1)$$

A slightly different form can be obtain if both current sources are combined to a single source $I_{\text{com}} = I_{CC} - I_{EC}$ and the diode currents are re-expressed as

$$\frac{I_{EC}}{\alpha_R} \rightarrow \frac{1 - \alpha_R}{\alpha_R} I_{EC} = \frac{I_{EC}}{\beta_R}$$

$$\frac{I_{CC}}{\alpha_F} \rightarrow \frac{1 - \alpha_F}{\alpha_F} I_{CC} = \frac{I_{CC}}{\beta_F}$$

This model configuration is shown in Figure 7-8 with base, collector, and emitter resistances. Also shown in Figure 7-8 are the combined diffusion and junction capacitances C_{be} and C_{bc} associated with the base-emitter and base-collector diodes.

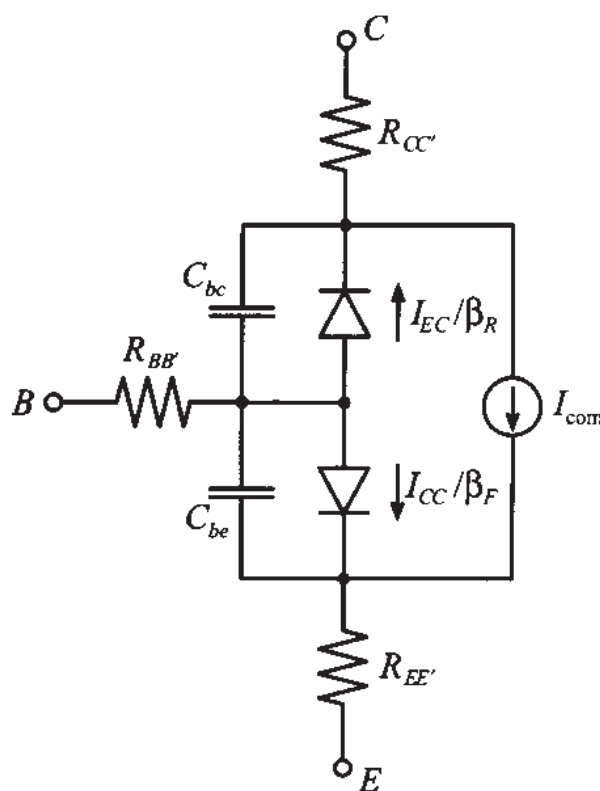


Figure 7-8 Dynamic Ebers-Moll transport model with single current source.

The Figure 7-8 configuration is important since it leads directly to the large-signal BJT model under forward active mode

condition. This mode allows us to neglect the base-collector diode current, but not its capacitative effect. Renaming the electric parameters, we arrive at the circuit depicted in Figure 7-9, where we replaced the forward-biased diode with an equivalent current source.

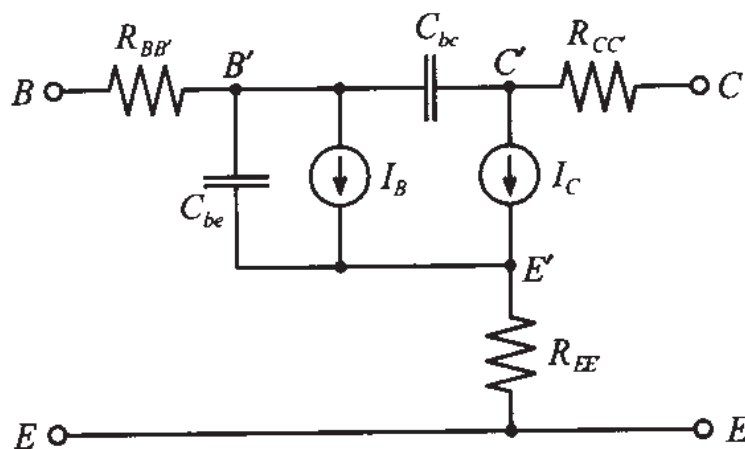


Figure 7-9 Large-signal BJT model in forward active mode.

This final form can be found in the SPICE library as a nonlinear representation of the standard BJT.

We notice how the dynamic transport model of the Ebers-Moll equations naturally lead to the SPICE large-signal model. An inherent difficulty for all circuit models is the unique determination of the model parameters through appropriate measurement strategies.

The Ebers-Moll model was one of the first BJT circuit representations and has retained its popularity and wide acceptance. However, shortly after its introduction, it became apparent that a number of physical phenomena could not be taken into account by this original model. Specifically, research has shown that (1) β_F and β_R are current dependent, and (2) the saturation current I_S is affected by the base-collector voltage (**Early effect**). Both effects significantly influence the overall BJT performance. For this reason a number of refinements have been introduced to the original Ebers-Moll model, culminating in the Gummel-Poon model shown in Figure 7-10.

In this model we immediately notice the addition of two extra diodes to deal with the collector-dependent forward and reverse current gains $\beta_F(I_C)$ and $\beta_R(I_C)$. Figure 7-11 depicts a typical curve for β_F .

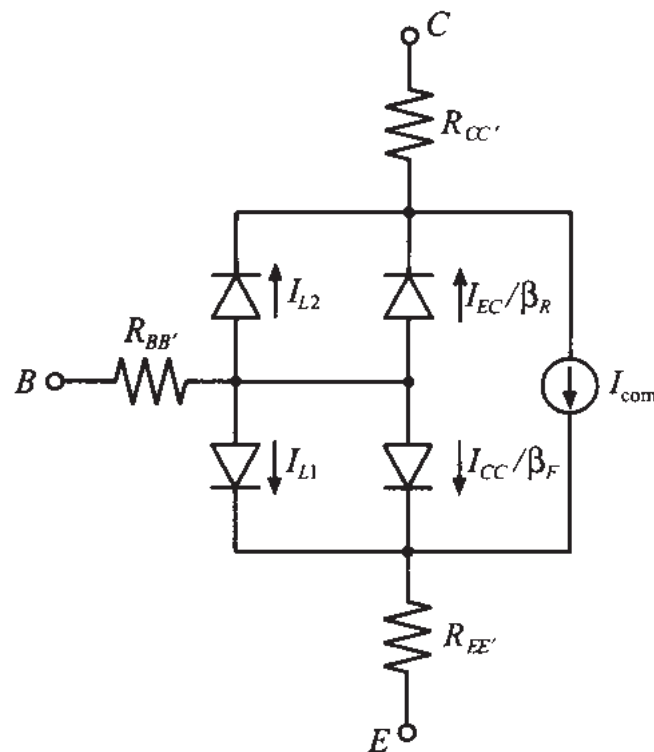


Figure 7-10 Static Gummel-Poon model.

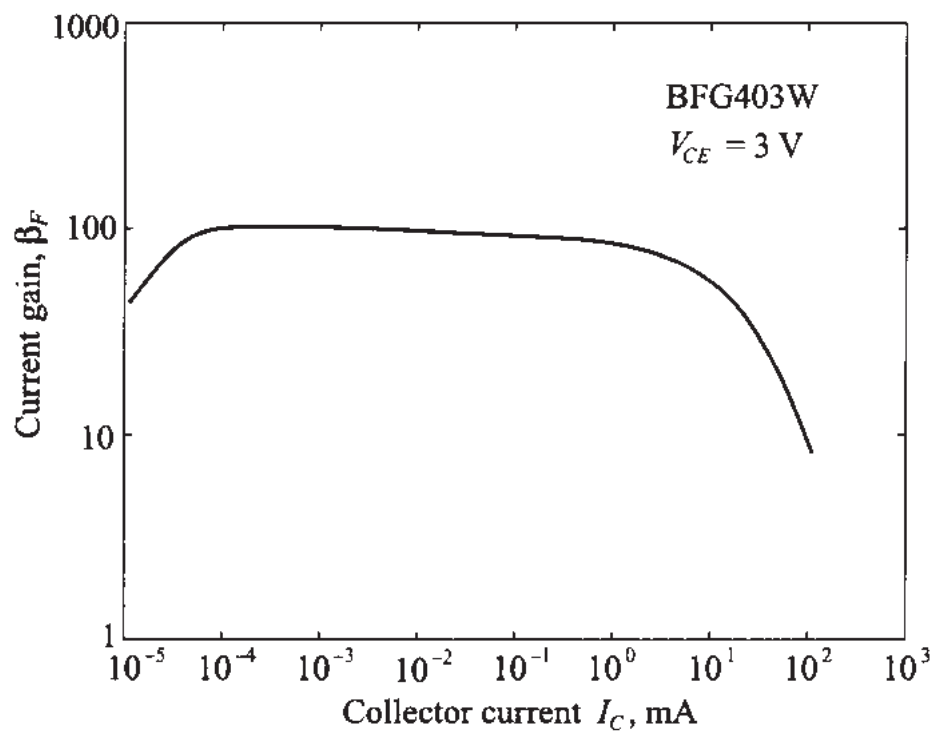


Figure 7-11 Typical dependency of β_F on the collector current I_C for a fixed collector-emitter voltage V_{CE} .

The two **leakage diodes** L_1, L_2 provide four new design parameters: coefficients I_{S1}, n_{EL} in $I_{L1} = I_{S1}(\exp[V_{BE}/(n_{EL}V_T)] - 1)$ for low-current normal mode operation, and I_{S2}, n_{CL} in $I_{L2} = I_{S2}(\exp[V_{BC}/(n_{CL}V_T)] - 1)$ for low-current inverse mode operation. Additionally, the Gummel-Poon model can handle the Early effect,

whereby with increasing collector-emitter voltage the space charge domain begins to extend far into the base region. The result is an increase in collector current for a fixed base current. If one draws tangents to each collector current curve (see Figure 7-12), they all converge approximately at a single voltage point $-V_{AN}$ known as the **forward Early voltage**. An identical analysis can be conducted if the BJT is operated in the reverse active mode, resulting in a voltage point V_{BN} known as the **inverse Early voltage**.

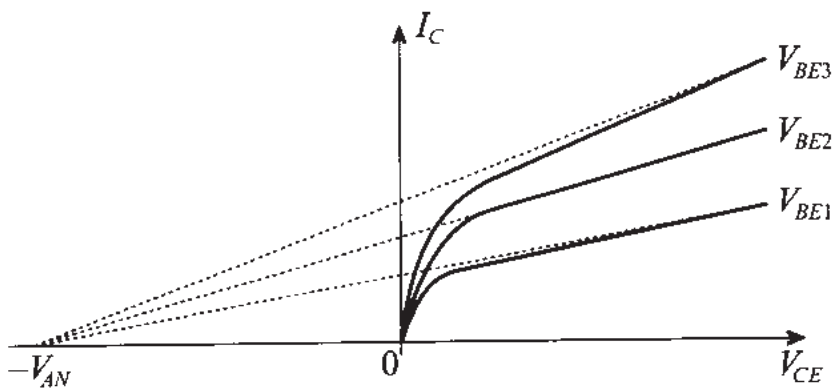


Figure 7-12 Collector current dependence on V_{CE} and its approximation through the Early voltage V_{AN} .

Both voltages are incorporated as additional factors in the model. Moreover, Gummel-Poon also permits the specification of a current-dependent base resistance and a distributed base-collector junction capacitance C_{jbc} . We will not go into any details of the various underlying physical reasonings leading to the requirement of these additional model parameters. The interested reader is referred to the sources listed at the end of this chapter. Converting the static Gummel-Poon model (Figure 7-10) into dynamic form by including the diode capacitances and C_{jbc} leads to the equivalent circuit shown in Figure 7-13.

This circuit is similar to the large-signal Ebers-Moll form (Figure 7-9) but with the differences that the base resistance $R_{BB'}$ is current dependent, the collector current takes into account the Early effect, and a distributed base-collector junction capacitance C_{jbc} enters the model.

In SPICE both BJT models can be invoked, with Ebers-Moll requiring the specification of 26 circuit parameters and up to 41 parameters for Gummel-Poon. Generally, the BJT manufacturers supply these parameters in their data sheets. Unfortunately, one increasingly encounters the situation where instead of the generally applicable SPICE model parameters, only the measured S-parameters are given. Since these measurements are recorded for particular operating frequencies and under certain bias conditions, it is then left to the circuit design engineer to interpolate the data for a particular transistor operation not found in the data sheet.

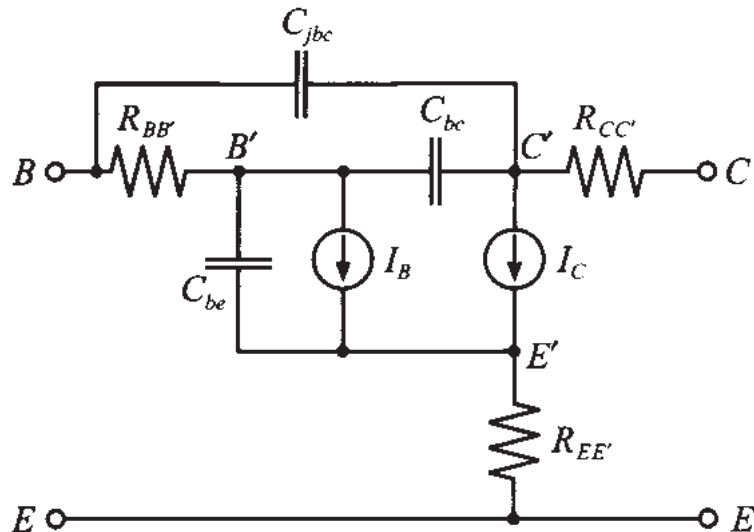


Figure 7-13 Large-signal Gummel-Poon model in normal active mode.

7.2.2 Small-Signal BJT Models

From the large-signal Ebers-Moll equations it is now easy to derive a small-signal model in the normal active mode. To this end, the large signal model (Figure 7-9) is converted into the linear hybrid- π model shown in Figure 7-14.

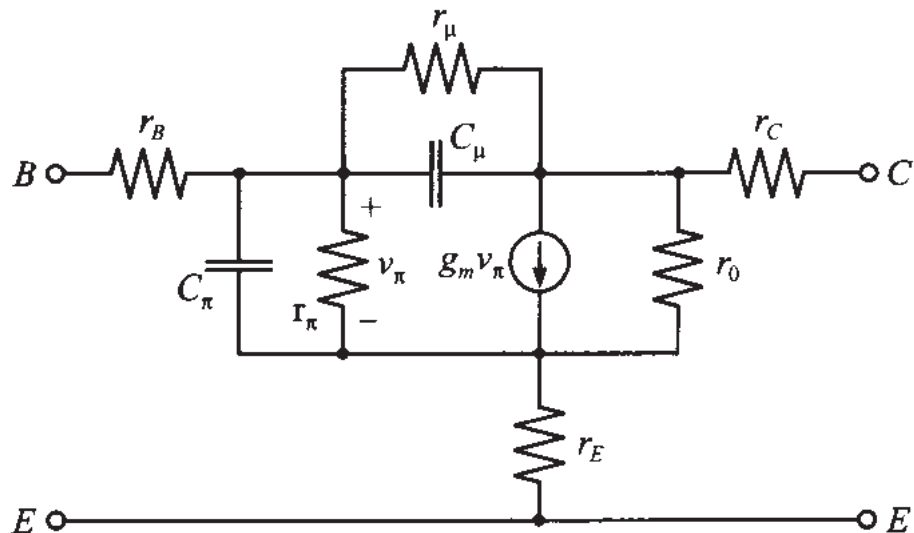


Figure 7-14 Small-signal hybrid- π Ebers-Moll BJT model.

We see that the base-emitter diode is replaced by a small-signal diode model and the collector current source is substituted by a voltage-controlled current source. To make the model more realistic, a resistor r_μ is connected in shunt to the feedback capacitor C_μ . For this model we can directly establish the small-circuit parameters by expanding the input voltage V_{BE} and output current I_C about the biasing or Q -point in terms of small AC voltage v_{be} and current i_c as follows:

$$V_{BE} = V_{BE}^Q + v_{be} \quad (7.15a)$$

$$I_C = I_C^Q + i_c = I_S \exp[(V_{BE}^Q + v_{be})/V_T] = I_C^Q \left[1 + \left(\frac{v_{be}}{V_T} \right) + \frac{1}{2} \left(\frac{v_{be}}{V_T} \right)^2 + \dots \right] \quad (7.15b)$$

Truncating the series expansion of the exponential expression after the linear term, we find for the small-signal collector current

$$i_c = \left(\frac{I_C^Q}{V_T} \right) v_{be} = g_m v_{be} \quad (7.16)$$

where we identify the **transconductance**

$$g_m = \left. \frac{dI_C}{dV_{BE}} \right|_Q = \left. \frac{d}{dV_{BE}} I_S e^{(V_{BE}/V_T)} \right|_Q \approx \frac{I_C^Q}{V_T} \quad (7.17)$$

and the **small-signal current gain** at the operating point

$$\beta_F|_Q = \left. \frac{dI_C}{dI_B} \right|_Q = \beta_0 \quad (7.18)$$

The **input resistance** is determined through the chain rule:

$$r_\pi = \left. \frac{dV_{BE}}{dI_B} \right|_Q = \left. \frac{dI_C}{dI_B} \right|_Q \left. \frac{dV_{BE}}{dI_C} \right|_Q = \frac{\beta_0}{g_m} \quad (7.19)$$

For the **output conductance** we have

$$\frac{1}{r_0} = \left. \frac{dI_C}{dV_{CE}} \right|_Q = \left. \frac{d}{dV_{CE}} \left(I_S e^{V_{BE}/V_T} \left[1 + \frac{V_{CE}}{V_{AN}} \right] \right) \right|_Q \equiv \frac{I_C^Q}{V_{AN}} \quad (7.20)$$

which includes the Early effect, also known as the **base-width modulation** because of the increased depletion layer extent into the base.

It is directly seen that this model in its simplest form at the terminals $B'-C'-E'$ reduces for the static case and, under negligence of the collector-emitter resistance, to our familiar low-frequency transistor model. Here the output current can simply be expressed in term of the input voltage v_{be} as

$$i_c = \frac{v_{be}}{r_\pi} + g_m v_{be} = (1 + g_m r_\pi) \frac{v_{be}}{r_\pi} = (1 + \beta_0) \frac{v_{be}}{r_\pi} \quad (7.21)$$

Often additional small-signal BJT circuit models can be developed on the basis of the h -parameter network representation. For instance, if we recall the definitions of the h -parameters and apply them to a BJT in common-emitter configuration, we obtain

$$v_{be} = h_{11} i_b + h_{12} v_{ce} \quad (7.22)$$

$$i_c = h_{21} i_b + h_{22} v_{ce} \quad (7.23)$$

which is encoded in generic form in Figure 7-15.

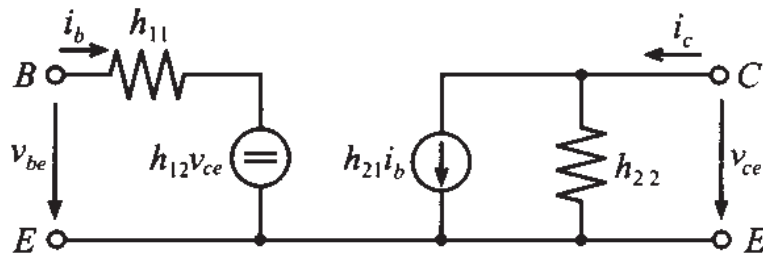


Figure 7-15 Generic h -parameter BJT representation with two sources.

In this notation the indices denote $11 \Rightarrow$ input, $21 \Rightarrow$ reverse, $21 \Rightarrow$ forward, and $22 \Rightarrow$ output. The individual parameter can be computed via the following relations:

$$h_{11} = \left. \frac{v_{be}}{i_b} \right|_{v_{ce} = 0} \quad \text{input impedance} \quad (7.24a)$$

$$h_{21} = \left. \frac{i_c}{i_b} \right|_{v_{ce} = 0} \quad \text{forward current gain } \beta_F \quad (7.24b)$$

$$h_{12} = \left. \frac{v_{be}}{v_{ce}} \right|_{i_b = 0} \quad \text{reverse voltage gain} \quad (7.24c)$$

$$h_{22} = \left. \frac{i_c}{v_{ce}} \right|_{i_b = 0} \quad \text{output admittance} \quad (7.24d)$$

It is observed that h_{12} represents the influence of the output voltage “fed back” to the input as part of a voltage-controlled voltage source. Conversely, h_{21} models the influence of the input “fed forward” to the output, or gain, as part of a current-controlled current source. The output to input feedback is modeled by the reverse biased collector-base junction capacitance C_{cb} , which is generally on the order of 0.1 to 0.5 pF and a resistor r_{cb} , with values ranging in the low $M\Omega$. Therefore, for low and intermediary frequencies up to approximately 50 MHz, this feedback can safely be neglected. However, in the GHz range, it may profoundly affect the BJT operation.

If the feedback resistor r_{bc} is neglected, a high-frequency circuit model results, as displayed in Figure 7-16. Also shown in this figure is a converted circuit such that the feedback capacitance C_{cb} appears as the Miller capacitance on the input and output sides. The Miller effect allows us to decouple the input from the output port by redistributing the feedback capacitance, as the following example shows.

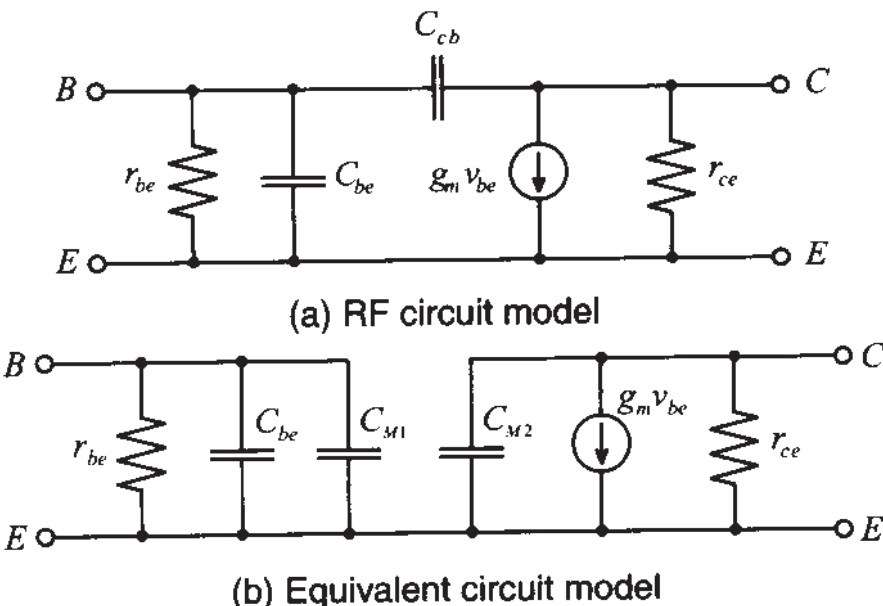
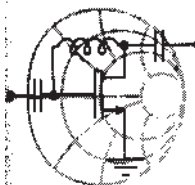


Figure 7-16 RF small-signal circuit model and converted circuit model using the Miller effect.



RF & MW →

Example 7-3: The Miller effect

Show that the feedback capacitance C_{cb} can be expressed as $C_{M1} = C_{cb}(1 - v_{ce}/v_{be})$ on the input port and as $C_{M2} = C_{cb}(1 - v_{be}/v_{ce})$ on the output port. Assume that the input and output voltages are approximately constant, and keep in mind that v_{ce} is negative under common emitter configuration.

Solution: We need to convince ourselves that the two generic circuits shown in Figure 7-17 are equivalent.

The current I_p is found by taking the voltage difference between output and input divided by the feedback impedance

$$I_p = (V_1 - V_2)/Z_{12}$$

and for the equivalent input and output impedances Z_{11} , Z_{22}

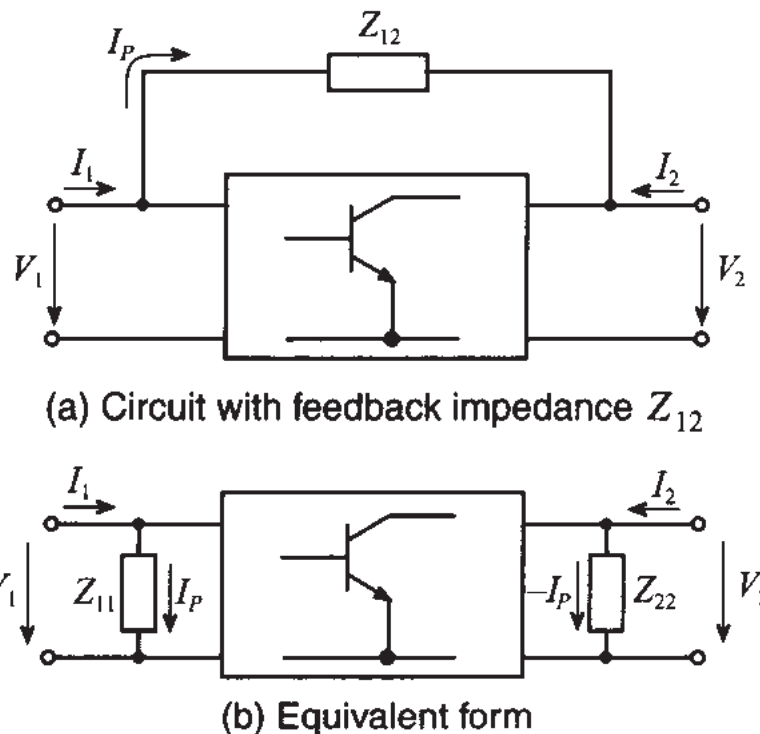


Figure 7-17 Miller transformation of feedback impedance.

$$Z_{11} = \frac{V_1}{I_p} = \frac{Z_{12} V_1}{(V_1 - V_2)} = Z_{12} (1 - V_2/V_1)^{-1}$$

and

$$Z_{22} = \frac{V_2}{(-I_p)} = \frac{Z_{12} V_2}{(V_2 - V_1)} = Z_{12} (1 - V_1/V_2)^{-1}$$

With the assignments \$Z_{12} = 1/(j\omega C_{cb})\$, \$Z_{11} = 1/(j\omega C_{M1})\$, \$Z_{22} = 1/(j\omega C_{M2})\$ and \$V_1 = v_{be}\$, \$V_2 = v_{ce}\$, we find the equivalent capacitances

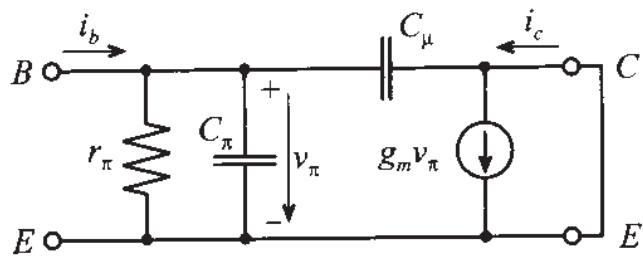
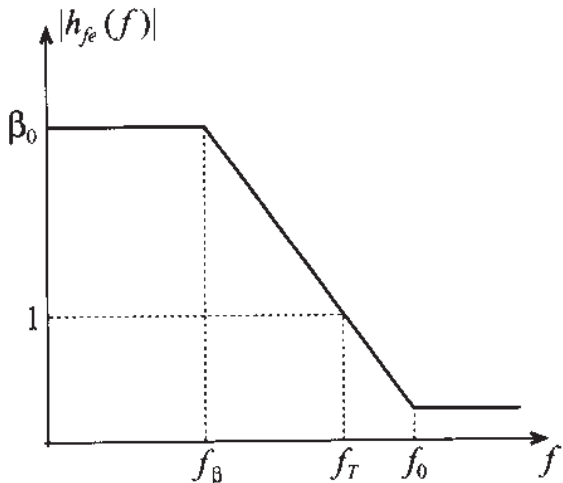
$$C_{M1} = C_{be} (1 - v_{ce}/v_{be}) \quad (7.25)$$

and

$$C_{M2} = C_{be} (1 - v_{be}/v_{ce}) \quad (7.26)$$

Decoupling of the input from the output port is accomplished by computing an equivalent capacitance that depends on a constant voltage amplification factor \$v_{ce}/v_{be}\$.

Another important factor that is directly related to the BJT frequency behavior is the short-circuit current gain \$h_{fe}(\omega)\$, which implies the connection of the collector with the emitter as depicted in Figure 7-18.

(a) Short-circuit hybrid- π model

(b) Amplification versus frequency behavior

Figure 7-18 Short-circuit current gain of BJT model.

Since the output is short circuited and thus $v_{ce} = 0$, the Miller effect does not enter the analysis. We find $h_{fe}(\omega)$ by computing the ratio of collector to base currents

$$h_{fe}(\omega) = \frac{i_c}{i_b} = \frac{g_m Z_{in} (1 - j\omega C_\mu / g_m)}{1 + j\omega C_\mu Z_{in}} \quad (7.27)$$

where $Z_{in} = r_\pi / (1 + j\omega r_\pi C_\pi)$. Substituting Z_{in} into (7.27) and using (7.19) results in

$$h_{fe}(\omega) = \frac{\beta_0 (1 - j\omega C_\mu / g_m)}{1 + j\omega r_\pi (C_\pi + C_\mu)} = \frac{\beta_0 [1 - j(f/f_0)]}{1 + j(f/f_\beta)} \quad (7.28)$$

with the maximum frequency f_0 and the beta cut-off frequency f_β

$$f_0 = \frac{g_m}{2\pi C_\mu} \text{ and } f_\beta = \frac{1}{2\pi r_\pi (C_\pi + C_\mu)} \quad (7.29)$$

The transition frequency f_T denotes the point where the magnitude of the current gain is unity (or 0 dB) under short-circuit output condition. Setting the absolute value of (7.28) equal unity, we find

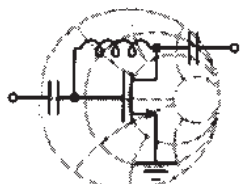
$$f_T = \frac{1}{2\pi} \sqrt{\frac{\beta_0^2 - 1}{r_\pi^2(C_\pi^2 + 2C_\pi C_\mu)}} \quad (7.30)$$

Since usually $\beta_0 \gg 1$ and $C_\pi \gg C_\mu$ we can rewrite (7.30) as

$$f_T \approx \frac{\beta_0}{2\pi r_\pi C_\pi} = \frac{g_m}{2\pi C_\pi} \quad (7.31)$$

As already seen in Chapter 6, this frequency is related to the emitter-collector time delay, which is composed of the delays associated with base, emitter, and collector. Another name for f_T is the **gain-bandwidth product**, which is specified in data sheets for a particular collector-emitter voltage and collector current bias condition. Additional figures of merit can be established when one considers $|S_{21}|^2$, where the power gain of the transistor is recorded under zero source and load reflection coefficients. This condition will be investigated in greater detail in Chapter 9.

Finally, let us discuss a design project involving the BJT. In this project, we will go through the steps of deciding upon bias conditions, determining the input and output impedances as a function of frequency, and converting the impedance values to the relevant *S*-parameters. The transistor parameters used for this example are summarized in Table 7-3. The MATLAB routine ex7_4.m provides computational details.



RF & MW

Example 7-4: Setting bias conditions, determining input/output impedances, and computing the *S*-parameters for a BJT

Our task is to design an amplifier for a portable communication system. The system is supposed to operate from a 3.6 V battery source. Taking into considerations the maximum available current and battery lifetime, we demand that the current for the amplifier should not exceed approximately 10 mA. Assuming $V_{CE} = 2$ V and $I_C = 10$ mA as bias conditions for this transistor, and the BJT parameters given in Table 7-3, we need to determine the hybrid- π model. In addition, the resulting input/output impedances and the corresponding *S*-parameters for the frequency range of 1 MHz $< f <$ 100 GHz have to be found.

Table 7-3 Parameters of the BJT transistor

| Symbol | Description | Typical value |
|------------------------|--|---------------|
| β_F | forward current gain | 145 |
| I_S | saturation current | 5.5 fA |
| V_{AN} | forward Early voltage | 30 V |
| τ_F | forward transition time | 4 ps |
| C_{JC0} | base-collector junction capacitance at zero applied junction voltage | 16 fF |
| C_{JE0} | base-emitter junction capacitance at zero applied junction voltage | 37 fF |
| m_C | collector capacitance grading coefficient | 0.2 |
| m_E | emitter capacitance grading coefficient | 0.35 |
| $V_{\text{diff}_{BE}}$ | base-emitter diffusion potential | 0.9 V |
| $V_{\text{diff}_{BC}}$ | base-collector diffusion potential | 0.6 V |
| r_B | base body resistance | 125 Ω |
| r_C | collector body resistance | 15 Ω |
| r_E | emitter body resistance | 1.5 Ω |
| L_B | base lead inductance | 1.1 nH |
| L_C | collector lead inductance | 1.1 nH |
| L_E | emitter lead inductance | 0.5 nH |

Solution: We begin this design by developing a standard voltage divider biasing network, as shown in Figure 7-19.

With the power supply voltage of $V_{CC} = 3.6$ V, desired collector-emitter voltage of $V_{CE} = 2$ V, and collector current of $I_C = 10$ mA, we can find a value for the collector resistor R_C as follows:

$$R_C = \frac{V_{CC} - V_{CE}}{I_C} = 160 \Omega$$

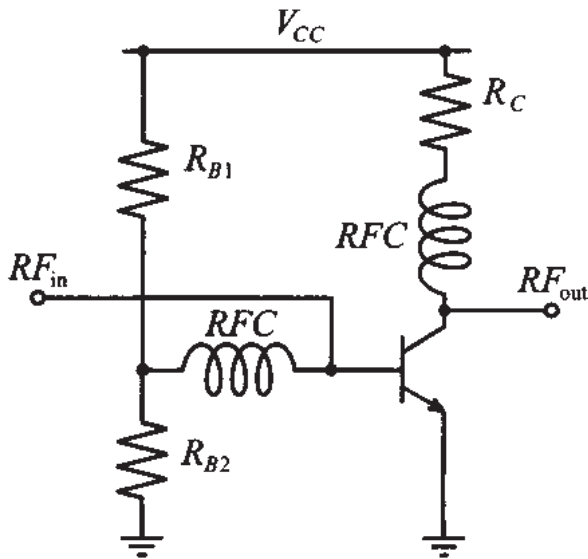


Figure 7-19 Biasing a BJT in common-emitter configuration.

Based on the current gain of $\beta = 145$ and collector current of $I_C = 10 \text{ mA}$, we find the base current to be $I_B = I_C/\beta = 69 \mu\text{A}$. The current through the resistor R_{B1} is equal to the sum of the current flowing through resistor R_{B2} and I_B . In practice, the values of R_{B1} and R_{B2} are selected such that they make the magnitude of I_B equal to 10% of the current through resistor R_{B2} . Keeping this in mind and realizing that the base-emitter voltage drop V_{BE} is approximately equal to the base-emitter built-in potential $V_{\text{diff}_{BE}}$, we find

$$R_{B2} = \frac{V_{\text{diff}_{BE}}}{10I_B} = 1300 \Omega$$

and

$$R_{B1} = \frac{V_{CC} - V_{\text{diff}_{BE}}}{11I_B} = 3560 \Omega$$

Now we are ready to compute the hybrid- π model parameters. From equations (7.17)–(7.20) we obtain $g_m = I_C/V_T = 386 \text{ mS}$, $r_\pi = \beta_0/g_m = 375 \Omega$, and $r_0 = V_{AN}/I_C = 3 \text{ k}\Omega$. To find C_μ and C_π we have to resort to the *pn*-junction analysis. Since the base-collector voltage is negative, the base-collector capacitance is only determined by the junction capacitance. From (7.3) we find

$$C_\mu = \frac{C_{JC0}}{(1 - V_{BC}/V_{\text{diff}_{BC}})^{m_C}} = 13 \text{ fF}$$

Because the base-emitter voltage is positive, C_π is a combination of both the junction and diffusion capacitances. From (7.3), and by assuming $V_{m_E} = 0.5 V_{\text{diff}_{BE}}$, we have

$$C_{\pi_{\text{junct}}} = \frac{C_{JE0}}{0.5^{m_E}} \left(1 + m_E \frac{V_{BE} - 0.5 V_{\text{diff}_{BE}}}{0.5} \right) = 55 \text{ fF}$$

and

$$C_{\pi_{\text{diff}}} = \frac{I_S \tau_T}{V_T} e^{V_{BE}/V_T} = 1.085 \text{ pF}$$

Thus, the total base-emitter capacitance is

$$C_\pi = C_{\pi_{\text{junct}}} + C_{\pi_{\text{diff}}} = 1.14 \text{ pF}$$

After establishing all parameters of the hybrid- π model, we can compute the corresponding h -parameter matrix as described in (7.24). The result takes into account only the transistor die hybrid- π parameters without incorporating base, collector, and emitter resistances and parasitic inductances.

To consider the influence of the lead resistance and inductance, we can employ a network analysis as described in Chapter 4. Specifically, we can partition the equivalent transistor circuit into four two-port networks, as shown in Figure 7-20.

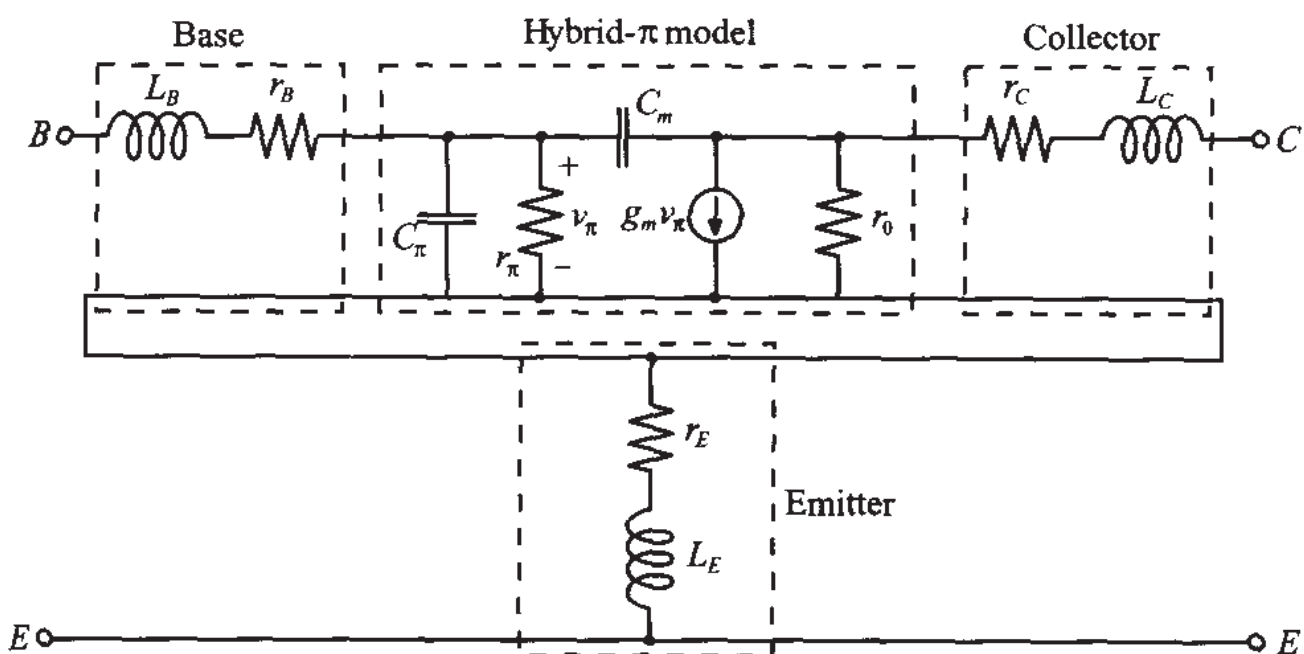


Figure 7-20 Complete transistor model divided into four two-port networks.

Relying on this network partitioning we proceed as follows: To obtain the Z -parameters of the entire transistor we first convert the h -parameters of the hybrid- π model into $ABCD$ representation. Next, this converted hybrid- π model is multiplied by the $ABCD$ -matrix representations for base and collector leads.

The matrix equation is as follows:

$$\begin{bmatrix} A & B \\ C & D \end{bmatrix}_{\text{tr}} = \begin{bmatrix} 1 & r_B + j\omega L_B \\ 0 & 1 \end{bmatrix}_{\text{base}} \begin{bmatrix} A & B \\ C & D \end{bmatrix}_{h\text{-model}} \begin{bmatrix} 1 & r_C + j\omega L_C \\ 0 & 1 \end{bmatrix}_{\text{collector}}$$

Finally, we convert the $ABCD$ representation of the transistor with the attached base and collector leads into Z -parameter form and add the resulting matrix to the Z -matrix of the emitter lead.

$$\begin{bmatrix} Z_{11} & Z_{12} \\ Z_{21} & Z_{22} \end{bmatrix}_{\text{trans}} = \begin{bmatrix} Z_{11} & Z_{12} \\ Z_{21} & Z_{22} \end{bmatrix}_{\text{tr}} + \begin{bmatrix} r_E + j\omega L_E & r_E + j\omega L_E \\ r_E + j\omega L_E & r_E + j\omega L_E \end{bmatrix}_{\text{emitter}}$$

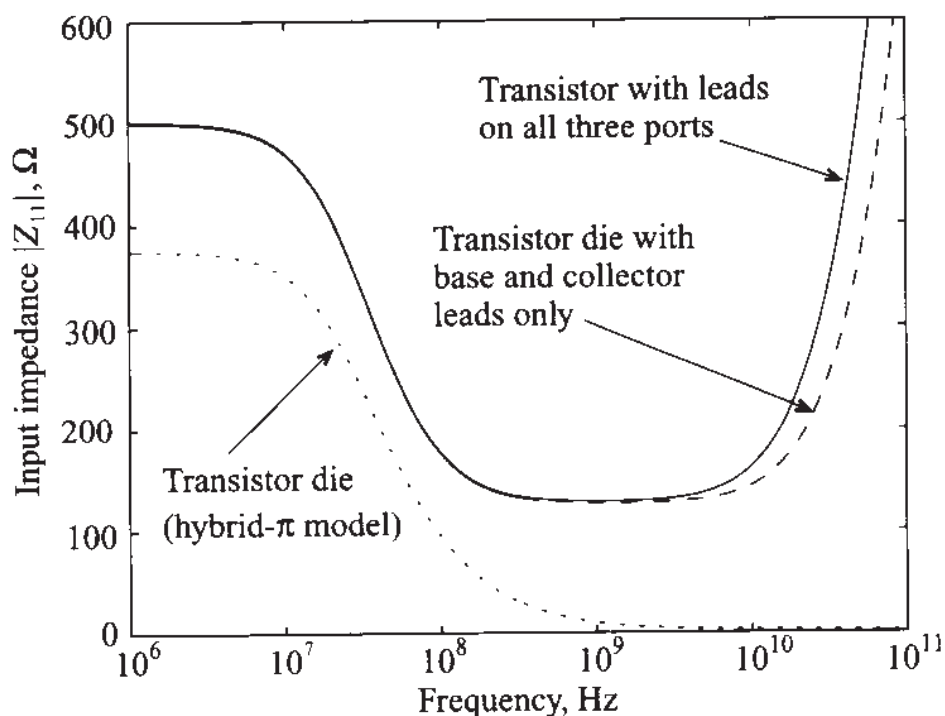
The frequency responses of coefficients Z_{11} and Z_{22} are shown in Figure 7-21.

As we see from Figure 7-21(a), the addition of the lead impedance to the basic hybrid- π model at low frequencies results in a significant increase in the input impedance due to the large base resistance. At high frequencies the effect of base and emitter inductances become noticeable in terms of a sharp rise in the impedance.

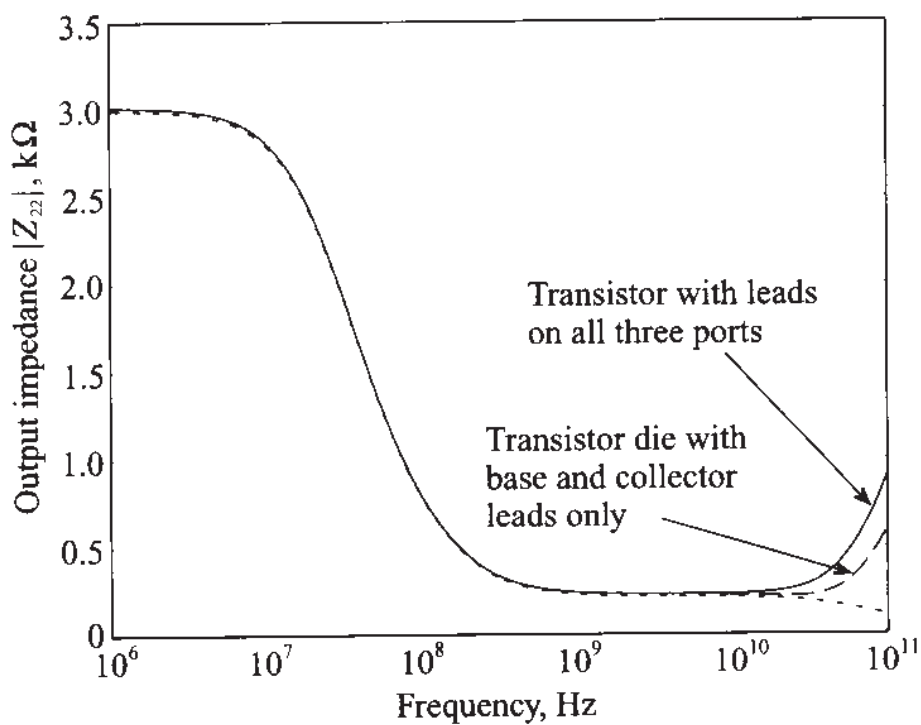
For the output impedance the situation is quite different. Since the base resistance does not have any effect on Z_{22} , the output impedance remains virtually unaffected by the addition of the leads and is dominated by the resistance r_0 up to very high frequencies. At that point the inductive effect of the leads become dominant.

From the known Z -parameter representation of the transistor we can easily compute the S -parameters using the conversion described in Chapter 4. The resulting input reflection coefficient, S_{11} , and gain, S_{21} , of the transistor are shown in Figure 7-22 as part of the Smith Chart and a polar plot, respectively.

As we notice in Figure 7-22(b), even though the emitter resistance and inductance seem to be negligible compared to the values of the other components in the model, their addition results in a significant drop in gain over the entire frequency range. This shows once again the influence of parasitic elements in RF circuits.

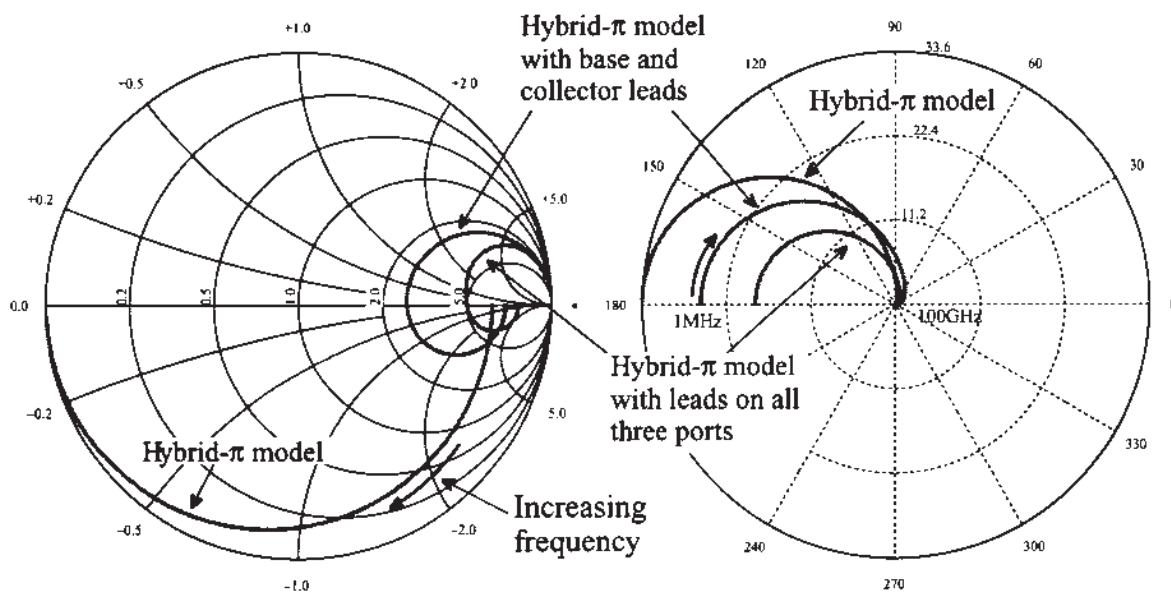


(a) Input impedance of the transistor



(b) Output impedance of the transistor

Figure 7-21 Input and output impedances as a function of frequency.

(a) Input reflection coefficient, S_{11} (b) Gain of the transistor, S_{21} **Figure 7-22** S_{11} and S_{21} responses of a BJT for various model configurations.

We have demonstrated an approach of computing the small-signal parameters of the transistor from known operating conditions of the underlying SPICE model. Even though a simple topology is investigated, this method can be directly applied to more complicated internal structures by breaking them down into a set of interconnected two-port networks.

7.2.3 Large-Signal FET Models

FETs offer a number of advantages but also suffer some disadvantages over BJTs. In choosing the appropriate active device for a particular circuit, one should take into consideration the following FET-related benefits:

- FETs exhibit a better temperature behavior.
- The noise performance of a FET is, in general, superior.
- The input impedance of FETs is normally very high, making them ideal for preamplification stages.
- The drain current of a FET shows a quadratic (and thus a more linear) functional behavior compared with the exponential collector current curve of a BJT.
- The upper frequency limit exceeds, often by a substantial margin, that of a BJT.
- The power consumption of a FET is smaller.

In terms of the disadvantages one often hears:

- FETs generally possess smaller gains.

- Because of the high input impedance, matching networks are more difficult to construct.
- The power handling capabilities tend to be inferior compared with BJTs.

The preceding list is debatable, since new device concepts and fabrication improvements continuously affect various transistor performance aspects.

For our FET modeling purposes we will focus on the **noninsulated gate FET**. To this group we count the MESFET, often identified as GaAs FET (pronounced “gasfet”), and the HEMT. Both types are discussed in Chapter 6. In Figure 7-23 the basic *n*-channel, depletion mode MESFET model (with negative threshold voltage) is shown along with the transfer and output characteristics.

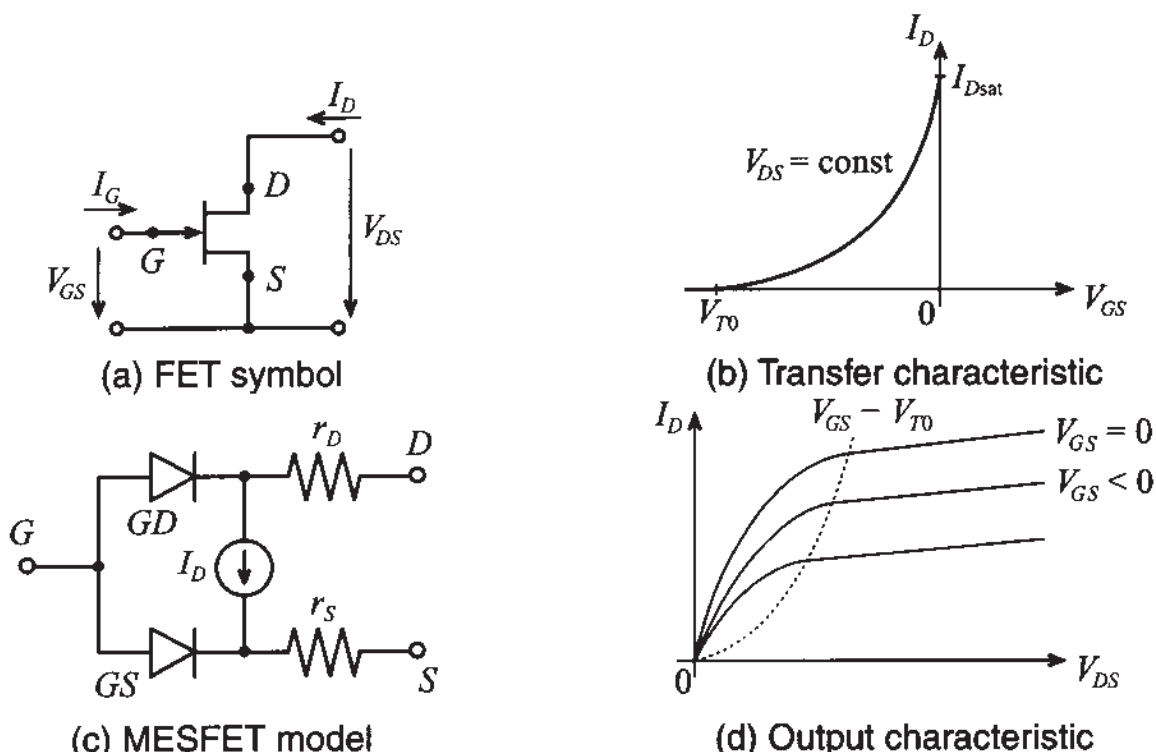


Figure 7-23 Static *n*-channel MESFET model.

The key equations for the drain current in forward, or normal, mode of operation follow from the analysis developed in Section 6.4. There we obtained the drain current for both the linear and saturation regions. These current expressions constitute the starting point of deriving the model for the FET.

Saturation region ($V_{DS} \geq V_{GS} - V_{T0} > 0$)

The saturation drain current given by (6.94) is repeated here for convenience

$$I_{D\text{sat}} = G_0 \left[\frac{V_p}{3} - (V_d - V_{GS}) + \frac{2}{3\sqrt{V_p}} (V_d - V_{GS})^{3/2} \right] \quad (7.32)$$

If we substitute in (7.32) the combination of threshold voltage V_{T0} and pinch-off voltage V_P (in other words, $V_d = V_{T0} + V_P$) an alternate form is obtained:

$$I_{D\text{sat}} = G_0 \frac{V_P}{3} \left\{ 1 - 3 \left(1 - \frac{V_{GS} - V_{T0}}{V_P} \right) + 2 \left[1 - \frac{V_{GS} - V_{T0}}{V_P} \right]^{3/2} \right\} \quad (7.33)$$

Making a binomial expansion of the square bracketed expression up to the second term allows us to write (7.33) as

$$I_{D\text{sat}} = G_0 \frac{V_P}{3} \left(\frac{3}{4} \right) (V_{GS} - V_{T0})^2 \quad (7.34)$$

The constant factors in front of the square term in (7.34) are combined to the **conduction parameter** β_n

$$\beta_n = \frac{1}{4} \left(\frac{G_0}{V_P} \right) = \frac{\mu_n \epsilon Z}{2Ld} \quad (7.35)$$

where the definitions for the conductance $G_0 = \sigma Z d / L = \mu_n N_D q Z d / L$ and the pinch-off voltage $V_P = (q N_D d^2) / (2\epsilon)$ from Section 6.4 have been used. If the channel modulation effect is included, we arrive at

$$I_D = \beta_n (V_{GS} - V_{T0})^2 (1 + \lambda V_{DS}) \quad (7.36)$$

Here the parameter $\lambda \approx 0.01 \dots 0.1 \text{ V}^{-1}$ models the slight increase in drain current for increasing drain-source voltage in the saturation region, see Figure 7-23(d).

Linear region ($0 < V_{DS} < V_{GS} - V_{T0}$)

Identical steps, as outlined for the saturation region, can be invoked to manipulate the drain current expression (6.91) to yield

$$I_D = \beta_n [2(V_{GS} - V_{T0})V_{DS} - V_{DS}^2] (1 + \lambda V_{DS}) \quad (7.37)$$

where again the channel modulation is considered to achieve a smooth transition from the linear into the saturation region. For instance, if $V_{DS} = V_{GS} - V_{T0}$ (that is, the transition from linear to saturation region) both drain currents are identical.

The FET can also be operated in reverse or inverted mode if $V_{DS} < 0$. For completeness, the two drain current relations are given without further comments.

Reverse saturation region ($-V_{DS} \geq V_{GD} - V_{T0} > 0$)

$$I_D = -\beta_n (V_{GD} - V_{T0})^2 (1 - \lambda V_{DS}) \quad (7.38)$$

Reverse linear region ($0 < -V_{DS} < V_{GD} - V_{T0}$)

$$I_D = \beta_n [2(V_{GD} - V_{T0})V_{DS} - V_{DS}^2](1 + \lambda V_{DS}) \quad (7.39)$$

Under reverse operation, the gate-drain diode (GD) is negatively biased.

Making the transition from the static to the dynamic FET model requires only the addition of gate-drain and gate-source capacitances, as illustrated in Figure 7-24. Also shown in this model are source and drain resistors associated with source-gate and drain-gate channel resistances. A gate resistor is typically not included because the gate current, although substantially higher than for a MOSFET, is still negligible.

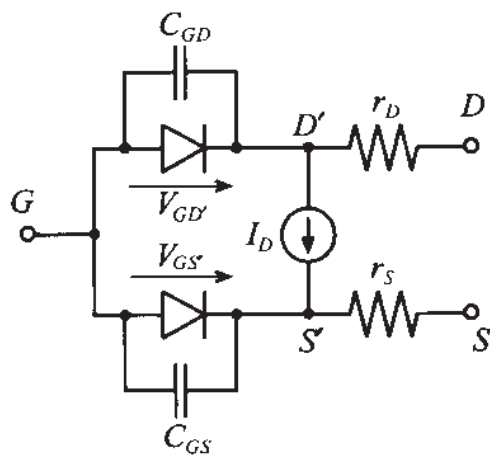


Figure 7-24 Dynamic FET model.

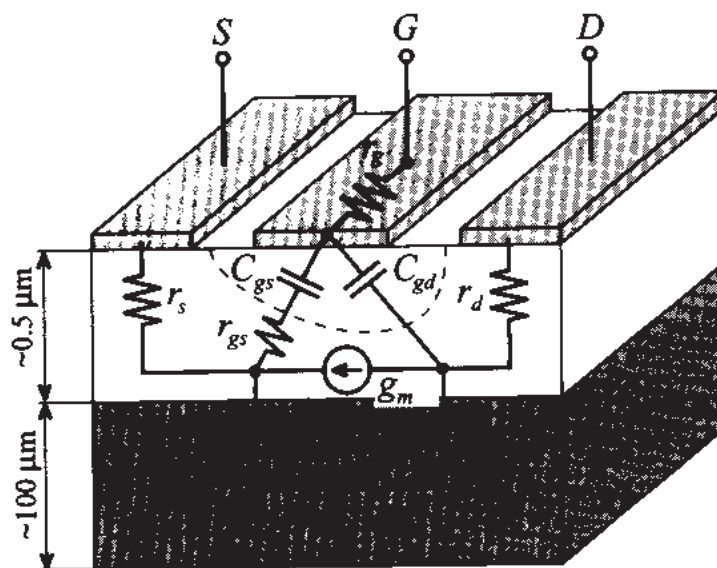
A summary of the most relevant SPICE modeling parameters for a MESFET is presented in Table 7-4.

Table 7-4 SPICE modeling parameters for a MESFET

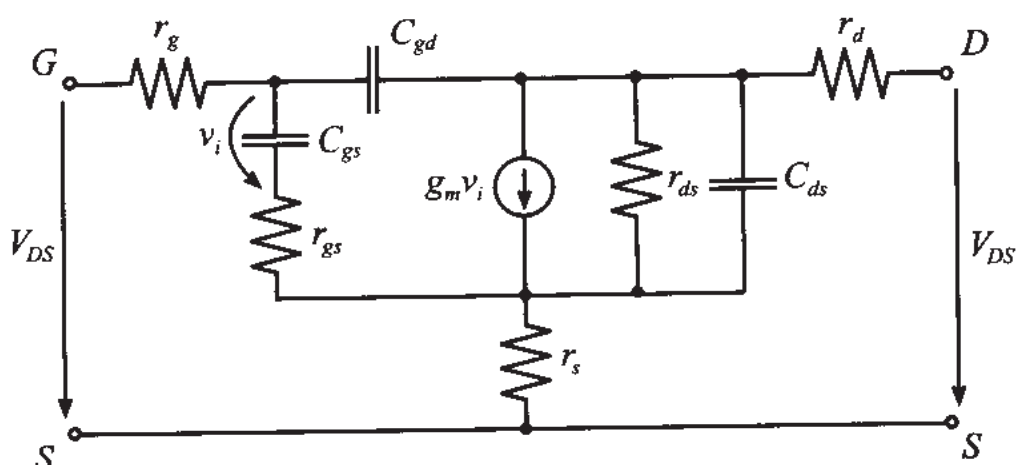
| Symbol | SPICE | Description |
|-----------|--------|---------------------------------------|
| V_{T0} | VTO | Threshold voltage |
| λ | LAMBDA | Channel-length modulation coefficient |
| β | BETA | Conduction parameter |
| C_{GD} | CGD | Zero-bias gate-to-drain capacitance |
| C_{GS} | CGS | Zero-bias gate-to-source capacitance |
| r_D | RD | Drain resistance |
| r_S | RS | Source resistance |

7.2.4 Small-Signal FET Models

A small-signal FET circuit can directly be derived from the large-signal FET model (Figure 7-24). In this model we simply replace the gate-drain and the gate-source diodes by their small-signal representations derived in Section 7.1. In addition, the voltage-controlled current source is modeled via a transconductance g_m and a shunt conductance $g_0 = 1/r_{ds}$. The model can be tied in with a physical device correspondence, as Figure 7-25 shows.



(a) Idealized MESFET device structure



(b) Circuit model

Figure 7-25 Small-signal MESFET model.

This model can be described by a two-port Y-parameter network in the form

$$i_g = y_{11}v_{gs} + y_{12}v_{ds} \quad (7.40a)$$

$$i_d = y_{21}v_{gs} + y_{22}v_{ds} \quad (7.40b)$$

Under realistic conditions, the input conductance of y_{11} and the feedback conductance of y_{12} are very small and can thus be neglected. This is consistent with the fact that the gate current is too small to be of practical consequence. However, for high-frequency operations the capacicances are typically included, resulting in the circuit model shown in Figure 7-26.

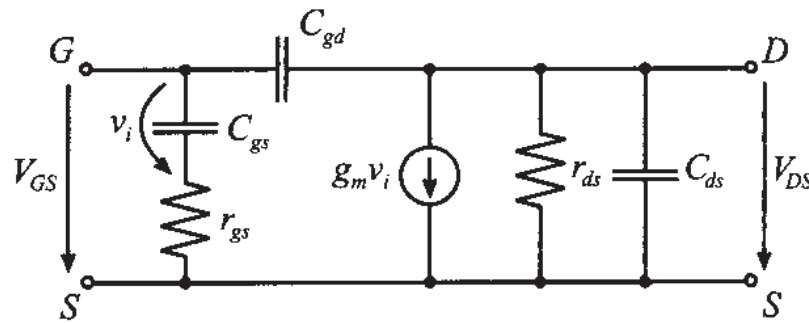


Figure 7-26 High-frequency FET model.

For DC and low-frequency operation, the model in Figure 7-26 simplifies to the condition where the input is completely decoupled from the output. Transconductance g_m and output conductance g_0 can be readily computed for the forward saturation region from the drain current equation (7.36):

$$y_{21} = g_m = \left. \frac{dI_D}{dV_{GS}} \right|_Q = 2\beta_n(V_{GS}^Q - V_{T0})(1 + \lambda V_{DS}^Q) \quad (7.41)$$

$$y_{22} = \frac{1}{r_{ds}} = \left. \frac{dI_D}{dV_{DS}} \right|_Q = \beta_n \lambda (V_{GS}^Q - V_{T0})^2 \quad (7.42)$$

with the operating point, or Q -point, denoted by V_{DS}^Q and V_{GS}^Q .

The gate-source and gate-drain capacitances play a crucial role in determining the frequency performance. For the transition frequency f_T we again have to consider the short-circuit current gain for the situation where the magnitude of the input current I_G is equal to the magnitude of the output current I_D , or specifically

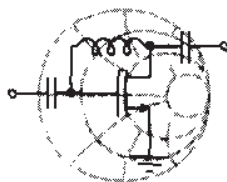
$$|I_G| = \omega_T(C_{gs} + C_{gd})|V_{GS}| = |I_D| = g_m|V_{GS}| \quad (7.43)$$

which gives us

$$f_T = \frac{g_m}{2\pi(C_{gs} + C_{gd})} \quad (7.44)$$

For low-frequency FET applications, it is primarily the charging time defined by these capacitances that severely limits the FET frequency response. This is in contrast to the

channel transition time, as defined in Section 6.4.3, which for high-frequency applications limits the FET's operation as the following example shows.



RF & MW

Example 7-5: Approximate determination of cut-off frequency of a GaAs MESFET

A GaAs MESFET with a gold gate is fabricated to be $1.0 \mu\text{m}$ in length and $200 \mu\text{m}$ in width, and $d = 0.5 \mu\text{m}$ in depth. The following electric characteristics are known: $\epsilon_r = 13.1$, $N_D = 10^{16} \text{ cm}^{-3}$, and $\mu_n = 8,500 \text{ cm}^2/\text{V}\cdot\text{s}$. Under suitably chosen approximations, we would like to find the cut-off frequency at room temperature.

Solution: To apply (7.44), it is necessary to find an approximate expression for the transconductance and capacitances. The transconductance can be found by knowing that the drain saturation current (7.33) is maximum for $V_{GS} = 0$, which gives

$$g_m = \left. \frac{dI_{D\text{sat}}}{dV_{GS}} \right|_{V_{GS}=0} = G_0(1 - \sqrt{V_d/V_P})$$

where the built-in voltage V_d for the Schottky contact is found from (6.39) to be

$$V_d = (V_M - \chi) - V_C$$

with $V_C = V_T \ln(N_C/N_D) = 0.1 \text{ V}$, $V_M = 5.1 \text{ V}$, and $\chi = 4.07 \text{ V}$. Substituting these values yields $V_d = 0.93 \text{ V}$. The pinch-off voltage and the conductance are, respectively,

$$V_P = \frac{qN_D d^2}{2\epsilon_0 \epsilon_r} = 1.74 \text{ V} \quad \text{and} \quad G_0 = \frac{q\mu_n N_D W d}{L} = 34 \text{ mS}$$

Thus, $g_m \approx 9.1 \text{ mS}$. For the capacitance we can approximately compute the surface area of the channel times the dielectric constant divided by the channel thickness:

$$C_{gs} + C_{gd} = \epsilon_0 \epsilon_r \left(\frac{WL}{d} \right) = 0.046 \text{ pF}$$

From these values we can finally estimate f_T to be

$$f_T = \frac{g_m}{2\pi(C_{gs} + C_{gd})} = 31.5 \text{ GHz}$$

In contrast to an approximate channel transit time of 15 GHz discussed in Section 6.4.3, we now have the situation that the RC time constant is smaller. In other words, the channel transition time becomes the limiting factor in the high-speed performance of this MESFET.

An often used approximate formula for (7.44) can be derived if we set $g_m \approx G_0$. The explicit result is

$$f_T \approx \frac{q\mu_n N_D d^2}{2\pi\epsilon L^2} \quad (7.45)$$

This expression applied to the above example would have yielded 29.3 GHz, a value very close to the computed frequency of 31.5 GHz.

7.3 Measurement of Active Devices

7.3.1 DC Characterization of Bipolar Transistor

We commence our analysis with the Ebers-Moll equations (7.10) and (7.11), re-expressed as collector and base currents:

$$I_C = I_S(e^{V_{BE}/V_T} - e^{V_{BC}/V_T}) - \frac{I_S}{\beta_R}(e^{V_{BC}/V_T} - 1) \quad (7.46a)$$

$$I_B = \frac{I_S}{\beta_F}(e^{V_{BE}/V_T} - 1) + \frac{I_S}{\beta_R}(e^{V_{BC}/V_T} - 1) \quad (7.46b)$$

The unknown coefficients to be determined through measurements are I_S , β_R , and β_F . In addition, forward and reverse Early voltages V_{AN} and V_{BN} become important when the BJT is operated for large V_{CE} . To separate forward and reverse current gain measurements, we resort to two measurement protocols, shown in Figure 7-27.

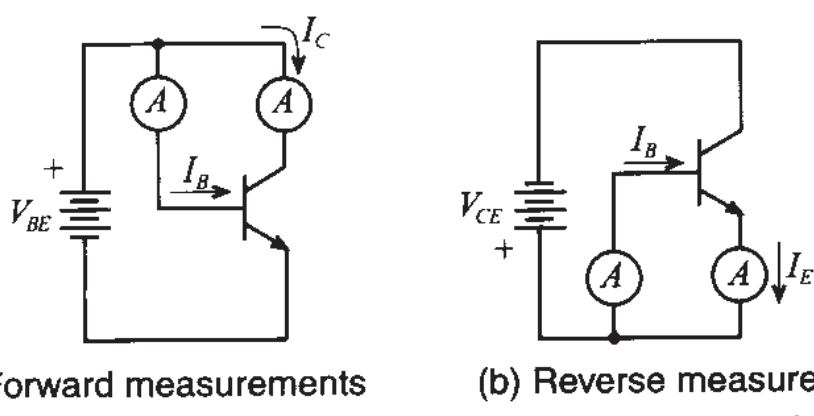


Figure 7-27 Forward and reverse measurements to determine Ebers-Moll BJT model parameters.

Under the forward measurement condition, the base-collector is short circuited ($V_{BC} = 0$), simplifying (7.46) to

$$I_C = I_S(e^{V_{BE}/V_T} - 1) \quad (7.47a)$$

$$I_B = \frac{I_S}{\beta_F}(e^{V_{BE}/V_T} - 1) \quad (7.47b)$$

Monitoring the base and collector currents as a function of V_{BE} results in the graph shown in Figure 7-28.

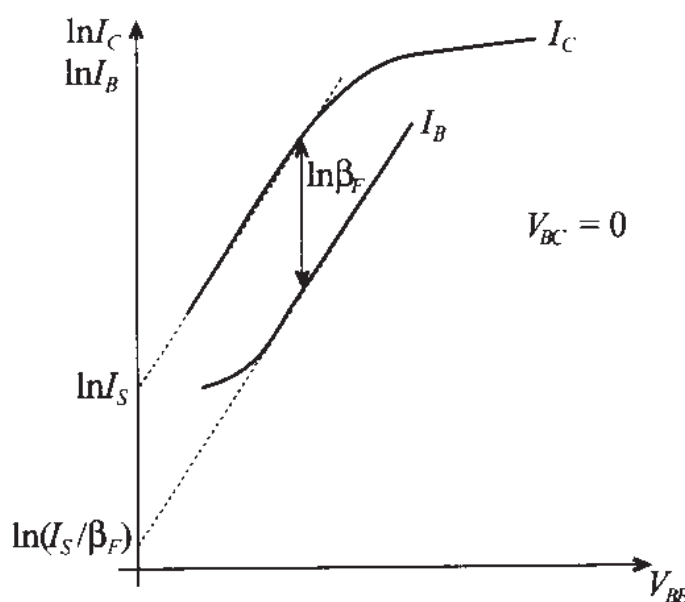


Figure 7-28 I_C and I_B versus V_{BE} .

Both currents are logarithmically plotted and shown for sufficiently large V_{BE} values, where the exponential terms dominates over the factor 1. A linear slope of $1/V_T$ for both currents is obtained, since

$$\ln I_C = \ln I_S + \frac{V_{BE}}{V_T} \quad (7.48a)$$

$$\ln I_B = \ln I_S - \ln \beta_F + \frac{V_{BE}}{V_T} \quad (7.48b)$$

From these two curves we can first extrapolate the collector current to get $\ln I_S$ and thus I_S . Extrapolating the base current next yields a value for $\ln I_S - \ln \beta_F$, from which we can determine β_F . From Figure 7-28 it is apparent that the current gain is constant only over a very narrow collector-emitter voltage domain. For low and high current injections significant deviations occur. The Early effect is expressed as a linear gradient of the collector current:

$$I_C = I_S(e^{V_{CE}/V_T} - 1) \left(1 + \frac{V_{CE}}{V_{AN}}\right) \approx I_S e^{V_{CE}/V_T} \left(1 + \frac{V_{CE}}{V_{AN}}\right) \quad (7.49)$$

This allows us to find V_{AN} by projecting the tangent, applied to the collector current in the saturation region, to the intercept point with the V_{CE} -axis in the second quadrant. The intercept point is the same for various base currents, as shown in Figure 7-12. The determination of the reverse mode parameters β_R , V_{BN} is carried out by interchanging the collector with the emitter terminal [see Figure 7-27(b)], and then following the identical procedure as done in the forward direction.

7.3.2 Measurements of AC Parameters of Bipolar Transistors

The determination of the AC parameters is more of a challenge depending on the model involved and the details required. To extract analytically the large-signal Ebers-Moll or Gummel-Poon circuit elements is an actively pursued research endeavor. For our purposes we concentrate on the small-signal, low-frequency circuit model shown in Figure 7-29.

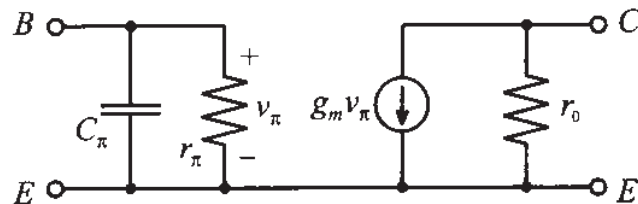


Figure 7-29 Small-signal, low-frequency h -parameter representation.

This model is related to the hybrid- π model presented in Figure 7-14, but without the output feedback ($h_{12} = 0$) and ohmic contributions $r_B \approx r_E \approx r_C \approx 0$. For a Q -point in the active forward region, and consistent with (7.15)–(7.20), we can derive the following parameters:

Transconductance

$$g_m = \left. \frac{dI_C}{dV_{BE}} \right|_{V_{CE} = 0} = \frac{I_C^Q}{V_T} \quad (7.50a)$$

Input capacitance

$$C_\pi = \tau_{be} \frac{I_S}{V_T} e^{V_{BE}^Q/V_T} = \tau_{be} \frac{I_C^Q}{V_T} \quad (7.50b)$$

Input resistance

$$r_\pi = \left. \frac{dV_{BE}}{dI_B} \right|_{V_{CE}^Q} = \left. \frac{v_{be}}{i_b} \right|_{v_{ce} = 0} = \frac{\beta_0}{g_m} \quad (7.50c)$$

Output conductance

$$\frac{1}{r_0} = \left. \frac{dI_C}{dV_{CE}} \right|_{V_{BE}^Q} = \frac{I_C^Q}{V_{AN}} \quad (7.50d)$$

where it is understood that the collector current in the presence of the Early effect is given by $I_C = g_m I_B (1 + V_{CE}/V_{AN})$. Furthermore, since we decided to operate in the forward active mode, C_π denotes the diffusion capacitance, with the forward transit time τ_{be} of the base-emitter diode.

The parameter extraction for this simplified hybrid- π model begins with the process of setting the desired Q -point, resulting in known I_C^Q , I_B^Q , and V_{AN} . Thus, a measurement protocol would sequence through the following steps:

- Transconductance $g_m = I_C^Q/V_T$ for a given junction temperature
- DC current gain $\beta_0 = I_C^Q/I_B^Q$
- Input resistance $r_\pi = \beta_0/g_m$
- Output resistance $r_0 = V_{AN}/I_C^Q$
- Input impedance $Z_{in} = (1/r_\pi + j\omega C_\pi)^{-1}$ recorded at a particular angular frequency and then solved for the capacitance C_π

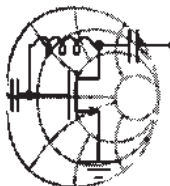
Instead of recording the input impedance and indirectly determining C_π , we can more elegantly find the transition frequency and thus C_π . This is accomplished by noting that the AC current gain at the transition frequency f_T is unity:

$$\frac{|i_c|}{|i_b|} = \left| \frac{\beta_0}{1 + j\omega_T r_\pi C_\pi} \right| \equiv 1 \quad (7.51)$$

Knowing that $\beta_0 \gg 1$ leads to $f_T \approx \beta_0 / (2\pi C_\pi r_\pi)$, from which it follows that

$$C_\pi \approx \frac{\beta_0}{2\pi f_T r_\pi} \quad (7.52)$$

This approach can be implemented quite easily with a network analyzer. Sweeping the frequency until the base current is equal to the collector current would allow us to enforce (7.51). The resulting transition frequency can then be substituted into (7.52) to find C_π .



RF & MW

Example 7-6: Small-signal hybrid- π parameter extraction without Miller effect

An *npn*-transistor is operated under DC bias of $I_C^Q = 6 \text{ mA}$, $I_B^Q = 40 \mu\text{A}$, and the Early voltage is recorded to be $V_{AN} = 30 \text{ V}$. Through a network analyzer measurement the transition frequency is determined to be $f_T = 37 \text{ GHz}$ at room temperature. It is required to determine the hybrid- π parameters: β_0 , r_π , C_π , r_0 , and g_m .

Solution: Neglecting feedback from the output to the input, we can use the preceding equations directly and find

$$g_m = \frac{I_C^Q}{V_T} = \frac{6 \times 10^{-3} \text{ A}}{0.026 \text{ V}} = 232 \text{ mS}$$

The forward DC current gain β_0 of the transistor can be found simply as a ratio of the collector current to the base current:

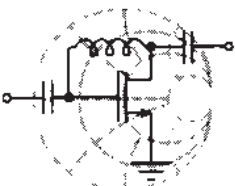
$$\beta_0 = I_C^Q / I_B^Q = 150$$

From the known β_0 and transconductance g_m we find the input resistance as $r_\pi = \beta_0 / g_m = 647 \Omega$. The output resistance is a ratio of the forward Early voltage to the collector current $r_0 = V_{AN} / I_C^Q = 5 \text{ k}\Omega$. Finally, the capacitance is found from (7.52):

$$C_\pi = \frac{\beta_0}{2\pi f_T r_\pi} = 1.00 \text{ pF}$$

The small-signal parameter determination is almost a cook-book design process. However, the constant forward current gain may not always reflect a realistic transistor behavior.

While Example 7-6 is applicable for low- and medium-range frequencies, the situation becomes more complicated for values approaching 1 GHz and beyond. Here we cannot neglect the Miller effect, and our attempt must be directed toward finding a strategy to obtain C_μ . As discussed in Chapter 4, electric measurements at high frequencies cannot rely on impedance, admittance, or h -parameter determinations because of the difficulties associated with enforcing short- and open-circuit conditions. At these frequencies we must resort to S -parameter measurements. How the S -parameters can be utilized to find the feedback capacitor C_μ is explained in the following example.



RF & MW

Example 7-7: Small signal hybrid- π parameter extraction with Miller effect included

We re-examine the previous example, but this time use the network analyzer to record the following S -parameters based on the characteristic impedance of 50Ω at 500 MHz:

$$[S] = \begin{bmatrix} 0.74e^{-j20.7^\circ} & 0.006e^{j82.5^\circ} \\ 9.78e^{j157.2^\circ} & 0.97e^{-j7.8^\circ} \end{bmatrix}$$

Our goal is to find the feedback capacitance C_μ . In addition, we would like to observe how the input and output impedances are affected if C_μ is excluded.

Solution: Since the DC measurements do not change, we will not repeat them. For given S -parameters we can easily compute the

input impedance of the transistor using matrix transformations described in Chapter 4:

$$Z_{\text{in}} = Z_0 \frac{(1 + S_{11})(1 - S_{22}) + S_{12}S_{21}}{(1 - S_{11})(1 - S_{22}) - S_{12}S_{21}} = R_{\text{in}} + jX_{\text{in}} = (77.5 - j24.4) \Omega$$

Setting the input impedance equal to the circuit model yields

$$R_{\text{in}} + jX_{\text{in}} = \frac{1}{1/r_\pi + j\omega(C_\pi + C_{M1})}$$

where C_{M1} is the Miller-transformed capacitance. Rearranging this equation leads to the form

$$C_{M1} = \frac{1}{\omega} \sqrt{\frac{1}{r_\pi R_{\text{in}}} - \frac{1}{r_\pi^2}} \approx \frac{1}{\sqrt{r_\pi R_{\text{in}}} \omega} - C_\pi$$

where the real part of the input impedance is used and $\omega = 2\pi f$ is the angular frequency at which the S -parameters are recorded. Explicitly, we find $C_{M1} = 1.42 \text{ pF} - 1.00 \text{ pF} = 0.42 \text{ pF}$. To compute the actual feedback capacitance C_μ , we can use (7.25), where the ratio of collector-emitter to base-emitter voltage is equal to the h_{12} parameter. This yields finally $C_\mu = C_{M1}/(1 + |h_{12}|) = 7.22 \text{ fF}$.

To compute the frequency behavior of the input and output impedances we can first calculate the h -parameters of the transistor as given by (7.24) and then convert them into Z -parameter representation. Both input and output impedances are plotted with and without the feedback ($C_\mu = 0$) in Figure 7-30.

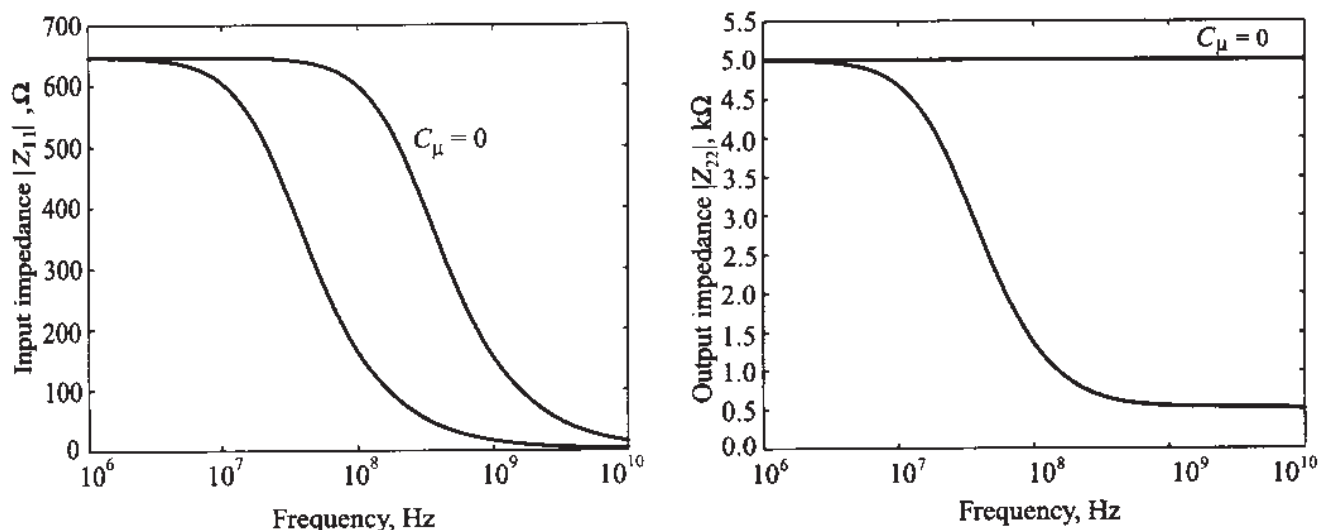


Figure 7-30 Input and output impedances with and without feedback.

This example underscores the importance to include the feed-back effect once the frequency begins to exceeds 100 MHz.

Although the preceding examples are simple extraction cases, they convey an appreciation of how difficult a realistic situation can become if the entire SPICE parameter set is attempted to be extracted. For the nonlinear large signal circuit models, this is a research task with no clear solution methodology. Many manufacturers have therefore resorted to *S*-parameter characterization alone. This approach greatly simplifies the BJT characterization by utilizing an appropriate test fixture or jig and relying on a network analyzer to measure the *S*-parameters at certain bias conditions and operation frequencies.

7.3.3 Measurements of Field Effect Transistor Parameters

Because the GaAs MESFET has gained such prominence in many RF circuits, it is important to take a closer look at its parameter extraction. Since the circuit model is the same for the HEMT, we can treat both cases in parallel. The fundamental equation for the *drain current in the linear region* is derived in Chapter 6 and is repeated here for convenience:

$$I_D = \mu_n \frac{\epsilon}{d} \frac{W}{L} \left\{ (V_{GS} - V_{T0}) V_{DS} - \frac{1}{2} V_{DS}^2 \right\} \approx \beta (V_{GS} - V_{T0}) V_{DS} \quad (7.53)$$

The only difference between MESFET and HEMT lies in the definition of the threshold voltage V_{T0} . Specifically, with the Schottky barrier voltage V_d , pinch-off voltage V_p , and energy difference ΔW_c between the conduction bands of the heterostructure in a HEMT, we obtain the following two expressions:

$$V_{T0} = V_d - V_p \text{ (MESFET)} \quad (7.54a)$$

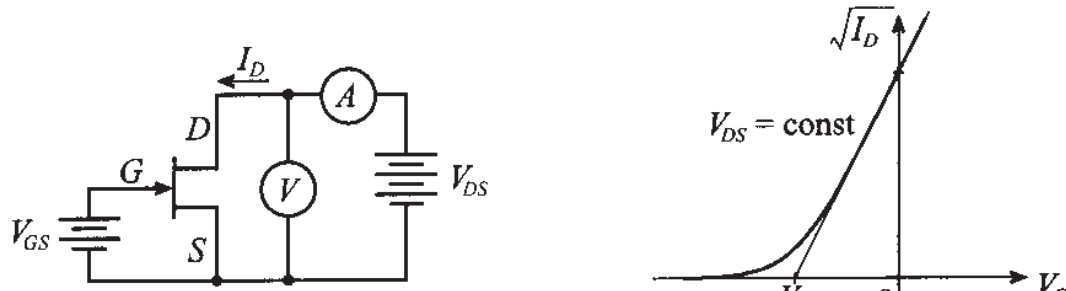
$$V_{T0} = V_d - \Delta W_c / q - V_p \text{ (HEMT)} \quad (7.54b)$$

For the saturation region, when $V_{DS} = V_{GS} - V_{T0}$, (7.53) becomes the quadratic equation

$$I_D = I_{D\text{sat}} = \beta (V_{GS} - V_{T0})^2 \quad (7.55)$$

Using (7.55) we can easily extract values for conduction parameter β and threshold voltage V_{T0} by plotting the square root of the drain current versus the applied gate-

source voltage V_{GS} . A measurement arrangement of a MESFET for obtaining V_{T0} and β is shown in Figure 7-31.



(a) Measurement arrangement

(b) I_D versus V_{GS} transfer characteristic

Figure 7-31 Generic measurement arrangement and transfer characteristics in saturation region.

The threshold voltage is determined indirectly by setting two different gate-source voltages V_{GS1} and V_{GS2} while maintaining a constant drain-source voltage $V_{DS} = \text{const} \geq V_{GS} - V_{T0}$ so that the transistor is operated in the saturation region. The result of these two measurements gives

$$\sqrt{I_{D1}} = \sqrt{\beta}(V_{GS1} - V_{T0}) \quad (7.56a)$$

$$\sqrt{I_{D2}} = \sqrt{\beta}(V_{GS2} - V_{T0}) \quad (7.56b)$$

Here we assume that the channel length modulation effect is negligible; therefore, the measured current is close to the saturation drain current as given by (7.55). Taking the ratio of (7.56 a) to (7.56 b) and solving for V_{T0} , we obtain

$$V_{T0} = \frac{V_{GS1} - (\sqrt{I_{D1}}/\sqrt{I_{D2}})V_{GS2}}{1 - \sqrt{I_{D1}}/\sqrt{I_{D2}}} \quad (7.57)$$

Next we substitute (7.57) into (7.56a) and solve this equation for β . The extraction process can further be simplified if we choose $I_{D2} = 4I_{D1}$ so that (7.57) becomes $V_{T0} = 2V_{GS1} - V_{GS2}$. Upon substituting this expression in (7.56a), we see that $\beta = I_{D1}/(V_{GS2} - V_{GS1})^2$.

7.4 Scattering Parameter Device Characterization

The S -parameter measurement approach greatly simplifies the device-under-test (DUT) characterization by utilizing an appropriate test fixture or jig and relying on a vector voltmeter or network analyzer to record the frequency and bias dependent four S -parameters.

Although nowadays a vector voltmeter is seldom used for recording the S-parameters, it nonetheless allows us to gain valuable insight into the basic measurement procedure that is also at the heart of a network analyzer. We will therefore investigate this approach first. It is generically depicted in Figure 7-32 and requires an RF signal generator, two dual-directional couplers, transistor biasing networks, the actual transistor fixture, and calibration kit to create short-circuit and through-line conditions.

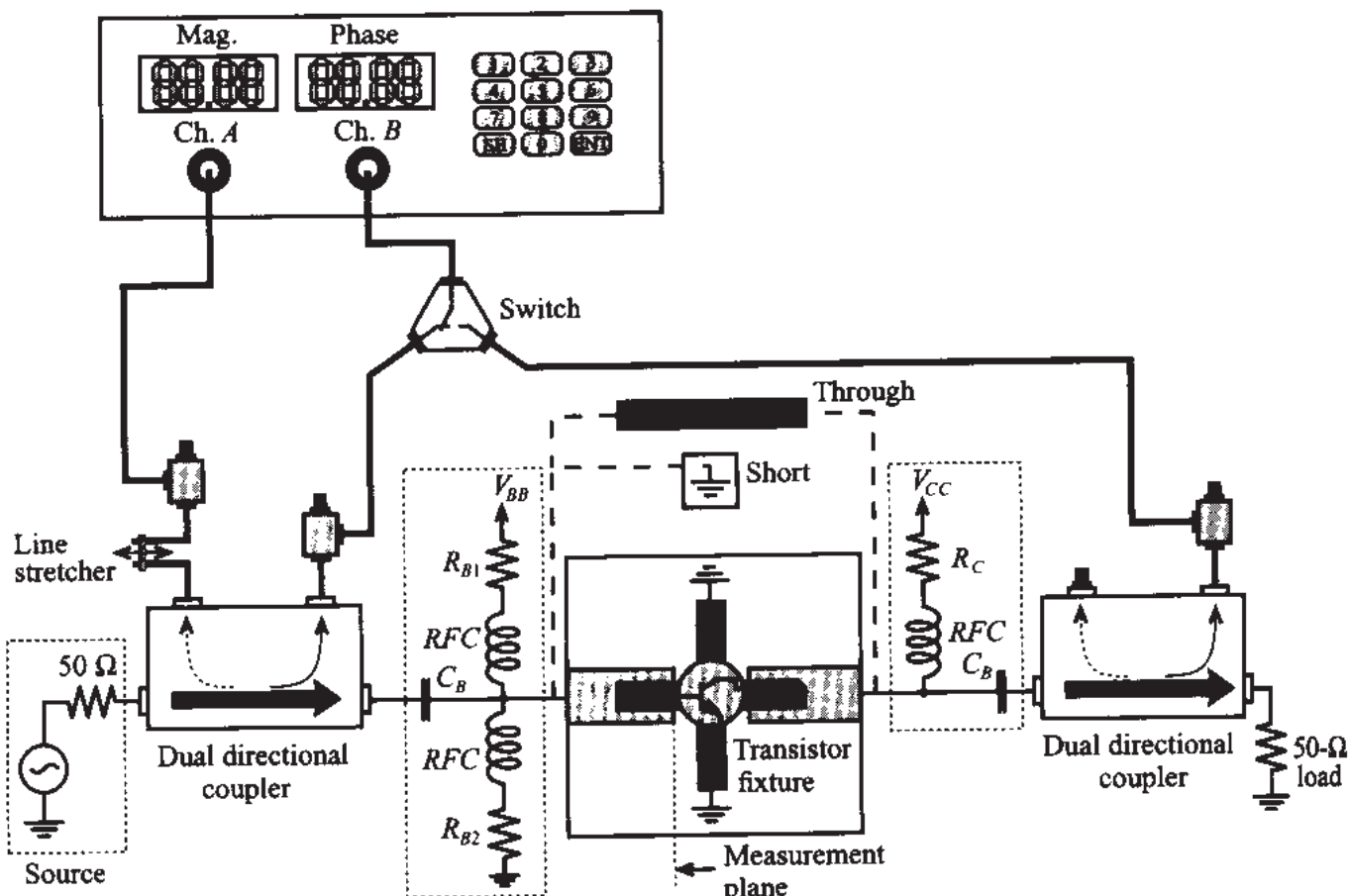


Figure 7-32 Recording of S-parameters with a vector voltmeter.

The function of a **dual-directional coupler** in Figure 7-32 is to isolate the incident from the reflected power wave. How this is accomplished can be explained with reference to Figure 7-33, where a cross-sectional view of a coaxial coupler is shown. For incident power coming from the left through the main arm, two slots, spaced $\lambda/4$ apart, couple the energy into an auxiliary path labeled 4. The incident wave does not produce any coupling into direction 3, since there is a 180° phase delay between signals coming from slot B and slot A, essentially canceling the entire wave. However, a reflected wave from the DUT will enter the coupler at port 2 coming from the right and subsequently couple out the wave energy through the auxiliary path labeled 3, canceling any wave leaving port 4. Therefore, port 3 provides an output for the reflected power, whereas port 4 records the incident power. The two figures of merit for a direc-

tional coupler are the **coupling factor** cf and its **directivity factor** df . The factor cf is defined as

$$cf = 10\log\left(\frac{P_i}{P_n}\right) \quad (7.58a)$$

and denotes the logarithmic ratio of the power in the main port, either 1 or 2 ($i = 1, 2$), over the power in the auxiliary port, either 3 or 4 ($n = 3, 4$). The directivity df

$$df = 10\log\left(\frac{P_3}{P_4}\right) \quad (7.58b)$$

specifies the ratio of the powers in the auxiliary arm for the condition of equal forward and reverse power levels applied to the main ports 1 and 2. For high signal discrimination we expect to see a large directivity value.

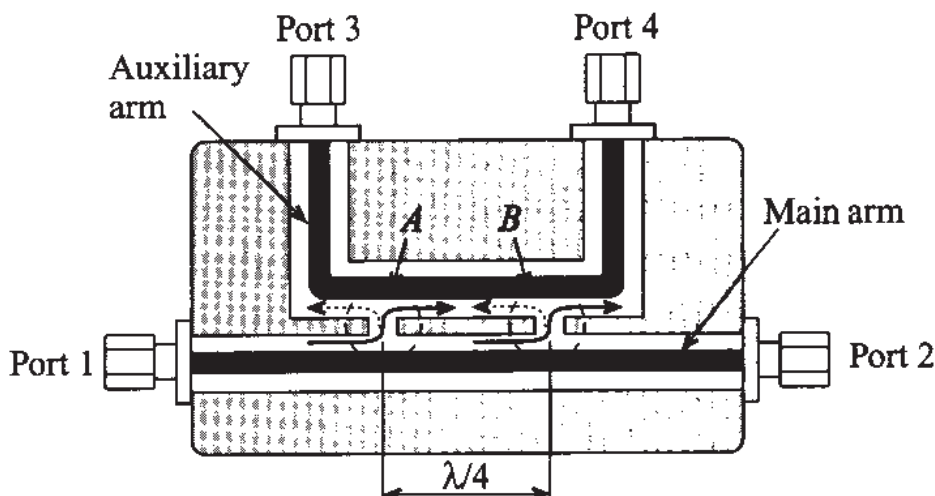


Figure 7-33 Cross-sectional view of directional coupler and signal path adjustment.

The actual signal propagation paths are observed in Figure 7-32. Here the vector voltmeter records with channels A and B the incident and reflected powers from the input port of the active device. Taking the ratio of the voltage magnitudes yields $|S_{11}|$. For recording the phase angle it is important to obtain an appropriate phase reference. For this reason, the DUT is removed and a short circuit is inserted for phase reference. To ensure equal path length (i.e., from the signal source to channel A , and from the short to channel B), a line stretcher is used to perform the necessary adjustment to achieve a zero phase difference.

The same test setup can also be utilized to find the forward gain S_{21} . Switching channel B to the directional coupler situated on the output side of the DUT yields the ratio between the output and input voltages or $|S_{21}|$. The phase adjustment now calls

for replacing the DUT with a through section element and again equalizing the signal paths with the line stretcher.

The remaining two S-parameters, S_{22} and S_{12} , are measured by reversing the DUT jig and exchanging the biasing networks. As Figure 7-32 implies, the S-parameter measurements depend on the setting of an appropriate bias or Q -point and the signal source frequency. As a result, a wide range of parametric curves could be generated.

Instead of employing a vector voltmeter, a more common approach involves the use of the network analyzer. This instrument is capable of processing magnitude and phase of a single or dual-port RF network. A simplified block diagram highlighting the functionality is shown in Figure 7-34.

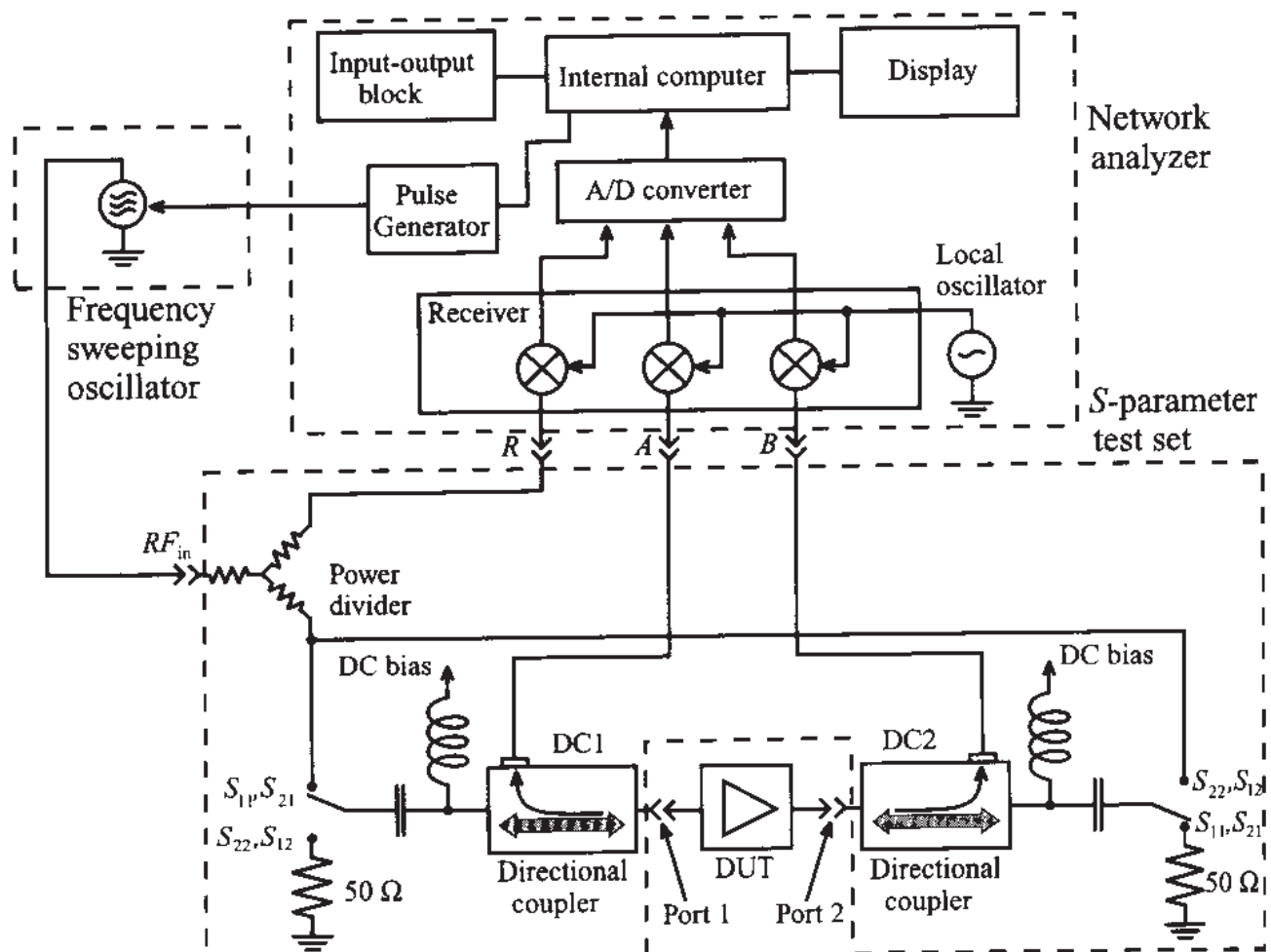


Figure 7-34 Block diagram of a network analyzer with S-parameter test set.

The advantage of a network analyzer lies in the fact that all the separate functional units associated with the vector voltmeter based measurement procedures are incorporated into one single instrument for an entirely automated testing of the RF or MW device. The operation is such that a sweeping RF generator applies the RF signal to the directional couplers. In forward direction, the reference channel R records the incident power wave and channel A provides the S_{11} parameter via directional coupler 1 (DC1).

At the same time, parameter S_{21} is recorded via directional coupler 2 (DC2). Switching to reverse direction, the reference channel R records the incident power launched into port 2 of the device under test, while channel B records S_{22} and channel A then yields S_{12} . This arrangement allows electronic switching between calibration and testing conditions, permitting the recording of the entire S -parameter set without changing the test jig. An interfrequency mixing and amplification stage feeds the signal into an analog-to-digital conversion unit and subsequently into a microcomputer and display system. The computer provides the user with the computed S -parameters (in magnitude and phase) as well as such postprocessed parameters as group delay, return and insertion losses, voltage standing wave ratio, input and output impedances, and many additional features.

The computer system allows for the software compensation of many imperfections introduced by the test arrangement. As a case in point, we recall the recording of the S -parameters in Section 4.4.7 via the through-reflect-line (TRL) technique. This is only one of a number of calibration schemes proposed to compensate for the various error sources introduced by the measurement process.

7.5 Summary

Electric circuit models for active devices form the backbone of most CAD software packages. These circuits range from simple linear models to very sophisticated large-signal models. Specifically, a large-scale BJT SPICE model that takes into account temperature influences can involve over 40 adjustable parameters whose determination is a daunting task.

In this chapter we reviewed the basic large-scale diode model that is used for modeling both the conventional pn -junction diode and the Schottky diode. Junction and diffusion capacitances and the temperature-dependent saturation current are the key ingredients constituting this model. By identifying a bias or Q -point and considering only small-signal responses, we arrive at the linear diode model with the differential conductance and diffusion capacitance

$$G_d = \frac{1}{R_d} = \left. \frac{dI_D}{dV_A} \right|_{V_Q} = \frac{I_Q}{nV_T} \text{ and } C_d = \frac{I_Q \tau_T}{nV_T} e^{V_Q/(nV_T)}$$

The diode model is utilized as the basic building block to develop the static large-scale BJT model as originally proposed by Ebers and Moll. Issues such as forward active and reverse active modes are explained by simplifying the basic Ebers-Moll equations. Starting from the injection model, we converted the Ebers-Moll BJT equations to the transport representation and subsequently to the large-scale BJT model in forward active mode. Additional refinements and modifications of the Ebers-Moll model have

resulted in the more sophisticated Gummel-Poon model, whose large-signal normal active mode circuit is shown in Figure 7-13. For the small-signal representation the hybrid- π is a popular linearization of the large-scale Ebers-Moll representation. The hybrid- π parameters are computed for a given collector current operating point:

$$g_m = I_C^Q/V_T, r_\pi = \beta_0/g_m, \beta_F|_Q = \beta_0, \text{ and } 1/r_0 = I_C^Q/V_{AN}$$

For high-frequency operations the capacitive coupling between input and output ports significantly influence the transistor operation. By taking into account the so-called Miller effect, the collector-base capacitance is transformed into input and output capacitances, thus permitting us again to separate the two ports. Since lead inductances and resistances also influence the high-frequency performance, we go through a detailed design project to investigate, among other topics, how the input and output impedances are affected as the frequency increases.

Attention is next directed toward the FET circuit models, specifically the high-frequency relevant types of MESFET and HEMT. Saturation, linear, reverse saturation, and reverse linear regions are defined in close relation with Chapter 6. Specifically, the drain currents in the saturation region

$$I_D = \beta_n(V_{GS} - V_{T0})^2(1 + \lambda V_{DS})$$

and in the linear region

$$I_D = \beta_n[2(V_{GS} - V_{T0})V_{DS} - V_{DS}^2](1 + \lambda V_{DS})$$

form the basis of the static and dynamic circuit models. Of particular interest are the small-signal low- and high-frequency FET models. The cut-off frequency allows us to quantify the frequency limitations of the device. For low to medium frequencies it is the charging time of the capacitors that determines the frequency performance, whereas for very high speed operations it is the channel transit time that becomes the limiting factor.

Finally, we discuss some of the electric parameters of the active devices. For the DC characterization of the BJT we can primarily rely on the collector and base currents as a function of base-emitter voltage. From these curves, the saturation current, current gain, and Early voltage are obtained. Measurement of the AC parameters is more of a challenge, and only the linear hybrid- π model allows a cook-book approach as outlined by equations (7.50). The FET model characterization follows a similar path as outlined for the DC BJT model and involves the recording of the drain-current versus gate-source voltage.

In many cases, both for BJT and FET, the *S*-parameter representation is the most common way to characterize an active device for a given bias and operating frequency. For this purpose either a vector voltmeter or network analyzer is used to record the

input/output power waves of the device under test. Measurements with the vector voltmeter require directional couplers, signal sources, switches, and a forward and reverse measurement protocol. This is all automated by connecting an S -parameter test set to the three channels of a network analyzer. The recording of S_{11} , S_{22} , S_{21} , and S_{12} for particular bias conditions and operating frequencies generally provides sufficient information for the circuit designer to characterize the device.

Further Reading

P. Antognetti and G. Massobrio, *Semiconductor Device Modeling with SPICE*, McGraw-Hill, New York, 1988.

J. J. Ebers and J. L. Moll, "Large-Scale Behaviour of Junction Transistors," *Proc. of IRE*, Vol. 42, pp. 1761–1778, December 1954.

H. K. Gummel and H. C. Poon, "An Integral Charge Control Model of Bipolar Transistors," *Bell System Tech. Journal*, Vol. 49, pp. 827–851, 1970.

T.-H. Hsu and C. P. Snapp, "Low-Noise Microwave Bipolar Transistor with Sub-Half-Micrometer Emitter Width," *IEEE Trans. on Electron Devices*, Vol. ED-25, No. 6, June 1978.

E. S. Yang, *Microelectronic Devices*, McGraw-Hill, NY, 1988.

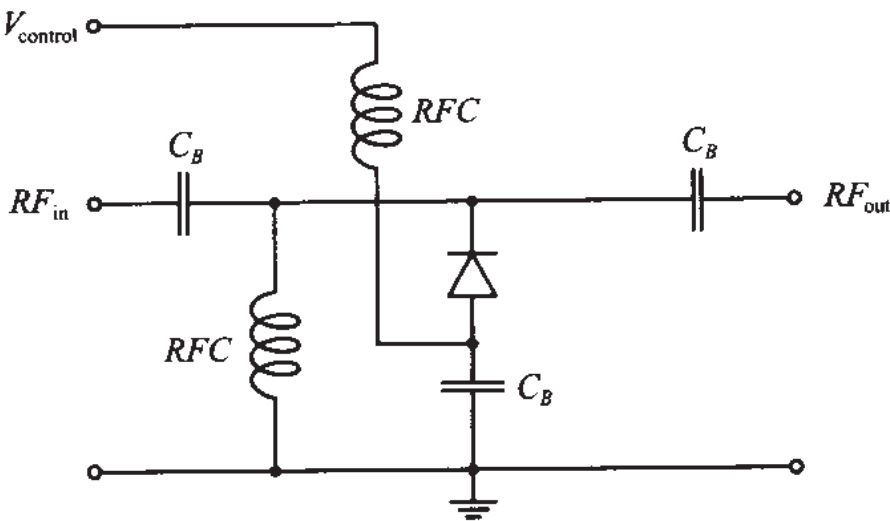
Problems

- 7.1 A silicon pn -junction diode has the following parameters at $T = 300^\circ\text{K}$, $I_S = 5 \times 10^{-15} \text{ A}$, $n = 1.2$, $\tau_T = 100 \text{ ps}$, and $R_S = 10 \Omega$. Assuming that the diode is operated under such biasing conditions that the applied junction voltage is maintained at 0.7 V, find the differential resistance and the diode capacitance for temperatures ranging from 200 to 450°K .
- 7.2 The reverse saturation current of a pn -diode is $I_S = 0.01 \text{ pA}$ at $T_j = 25^\circ\text{C}$ and has an emission coefficient of 1.6. For a junction temperature of 120°C find the reverse saturation current and the diode current I_D at an applied diode voltage of $V_A = 0.8 \text{ V}$.
- 7.3 The task for a process engineer is to obtain the model parameters for a Schottky diode. From measurements it is determined that the saturation current is equal to $I_S = 2 \text{ pA}$. To obtain the remaining parameters (n and τ_T) the engineer decides to use the differential capacitance of the diode. It is assumed that the electric measurements at room temperature indicate a dif-

fusion capacitance of $C_d = 0.329 \text{ pF}$ at an applied junction voltage of $V_A = 0.5 \text{ V}$, and $C_d = 0.371 \text{ nF}$ at $V_A = 0.7 \text{ V}$. Find the emission coefficient n and the transit time τ_T .

- 7.4 A GaAs Schottky diode with gold contact is operated at 80 mA. The following parameters are given at 300°K: $\tau_T = 40 \text{ ps}$, $R_S = 3 \Omega$, $n = 1.2$, $I_S = 10^{-14} \text{ A}$. (a) Plot the magnitude of the small signal impedance behavior in the frequency range from 1 MHz to 5 GHz. (b) Repeat the calculations for a temperature of 400°K.

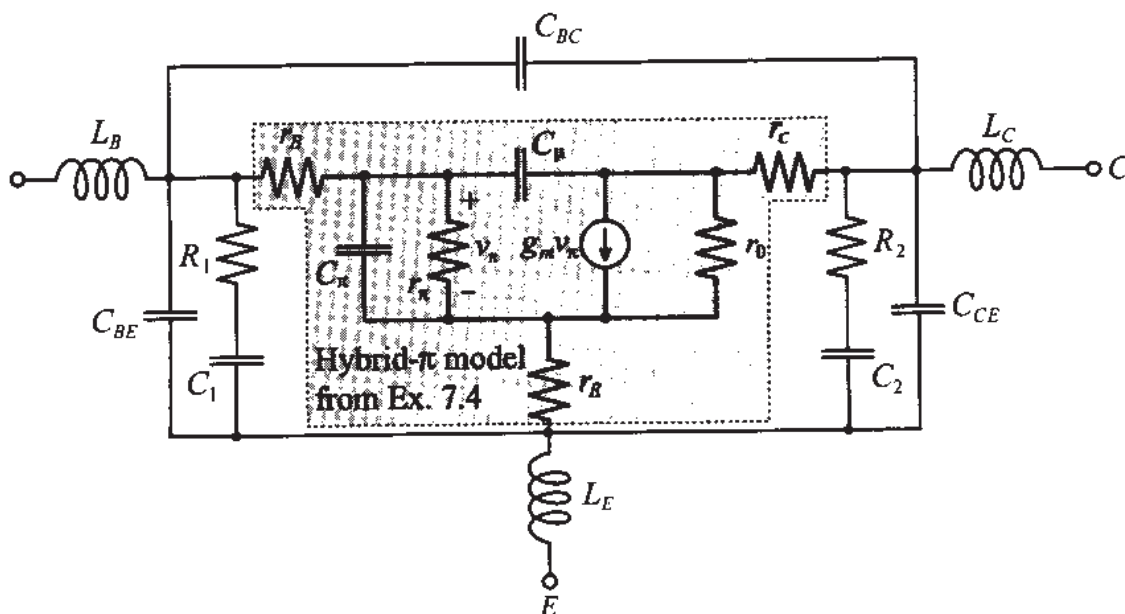
- 7.5 For the PIN diode configuration shown below, compute the S -parameters of the circuit when the control voltage equals either +1 V or -1 V and the frequency ranges from 1 MHz to 10 GHz. The diode model parameters are $I_S = 5 \times 10^{-15} \text{ A}$, $n = 1.2$, $\tau_T = 100 \text{ ps}$, $m = 0.5$, $C_{J0} = 10 \text{ pF}$, $V_{\text{diff}} = 0.7 \text{ V}$, and $R_S = 10 \Omega$. The ambient operating temperature is $T = 300^\circ\text{K}$, and we set infinite values for the blocking capacitors and RFCs.



- 7.6 Determine the change in the forward-bias voltage of an ideal Si pn -junction diode with change in temperature from -20°C to 80°C . Assume that current is kept constant and the initial bias voltage was 0.7 V at $T = 300^\circ\text{K}$.
- 7.7 Find the maximum operation frequency of the ideal pn -junction diode whose parameters are given in Example 7-1. The maximum frequency can be estimated based on the RC constant of the diode.
- 7.8 Consider three ideal pn -junction diodes whose parameters are identical except for the bandgap energy. Find the ratio of the forward-biased currents for these diodes if the applied voltage is the same in each case and the diodes are made of Ge, Si, and GaAs, respectively.

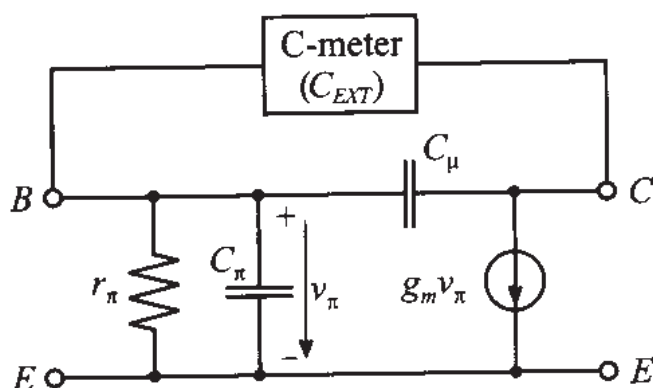
- 7.9 The terminal base current is constrained to be zero in an *npn*-BJT (open-circuit condition). Assuming that the device is operated at room temperature and has $\alpha_F = 0.99$ and $\alpha_R = 0.05$, use the large-signal Ebers-Moll model to find the base-emitter voltage as a function of the applied collector-emitter voltage V_{CE} .
- 7.10 Express the transconductance g_m of a bipolar junction transistor in terms of its collector current. Compare this expression with the expression for a differential resistance of a *pn*-diode.
- 7.11 Show that for a small-signal transistor model as depicted in Figure 7-16, the input Miller capacitance can be written as $C_{M1} = (1 + g_m r_{ce}) C_\mu$. In addition, obtain an upper frequency limit for which this formula is still applicable.
- 7.12 For a hybrid- π BJT model plot the short-circuit current gain h_{fe} in the frequency range from 10 MHz to 10 GHz. Assume the following parameters are given at a collector bias point of 20 mA and $T = 300^\circ\text{K}$: $\beta_0 = 140$, $C_\mu = 0.1 \text{ pF}$, and $C_\pi = 5 \text{ pF}$.
- 7.13 In Example 7-4 we discussed the relatively complicated case of a microwave transistor analysis where we have taken into account effects associated with parasitic elements such as lead inductances and resistances. In most practical applications, the situation is even more complicated due to the presence of internal matching and stability networks incorporated into the transistor housing by the manufacturer.

For the internal circuit shown, compute the *S*-parameters in the frequency range of 100 MHz to 20 GHz.



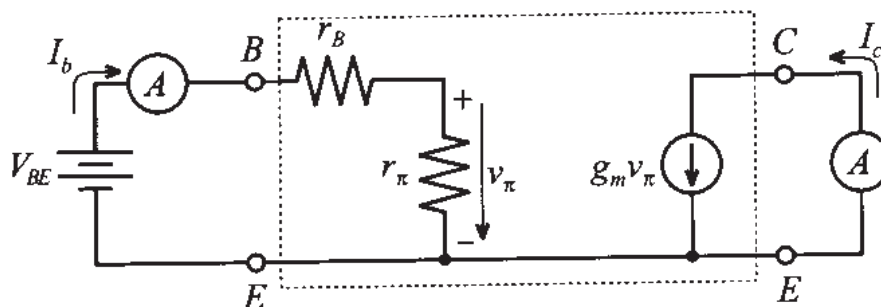
The following component values are given: $R_1 = 25 \Omega$, $R_2 = 20 \Omega$, $C_1 = C_2 = 0.2 \text{ pF}$, $C_{BE} = C_{CE} = 0.1 \text{ pF}$, and $C_{BC} = 10 \text{ fF}$. Assume that the biasing conditions and the values for all inductances and components in the hybrid- π model are the same as in Example 7-4.

- 7.14 An easy way to determine the capacitance C_μ in the hybrid- π BJT model is to make a capacitance measurement between base and collector, as follows.



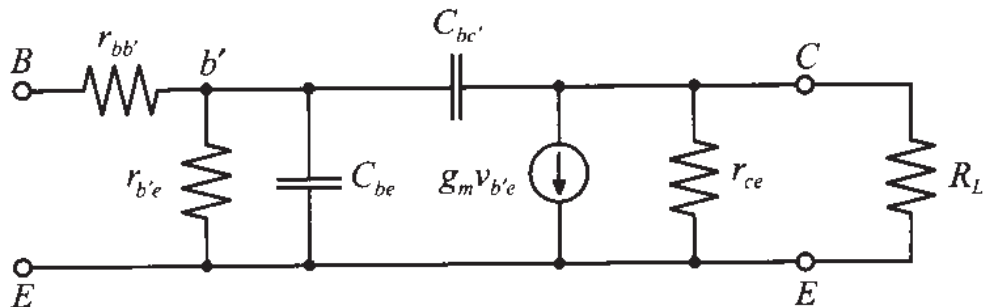
If the frequency is sufficiently low such that $1/(\omega C_\mu) \gg r_B$, we can directly relate the externally recorded capacitance to the feedback capacitance C_μ . Show that this is true by proving that the voltage v_π is zero and that r_π , C_π , and g_m do not influence the measurement. If a precision instrument measures an external capacitance $C_{ext} = 0.6 \text{ pF}$ at 1 MHz, can r_B , which typically ranges between 25 and 200 Ω , be neglected?

- 7.15 For the hybrid- π model it is required to find the parameters r_π , r_B , and g_m from low-frequency measurements (which allow us to neglect C_μ and C_π). The following measurement arrangement is given:

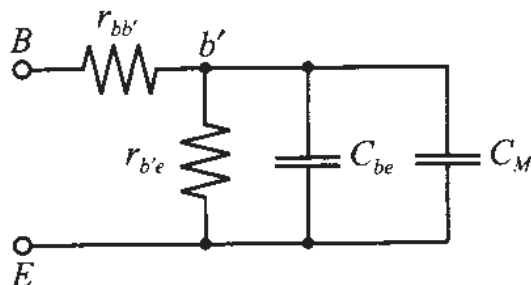


At the operating point and at room temperature (25°C) we record a DC base current of $I_B = 100 \mu\text{A}$ at a base emitter voltage of $V_{BE} = 11.8 \text{ V}$, and a short-circuit collector current of $I_C = 25 \text{ mA}$.

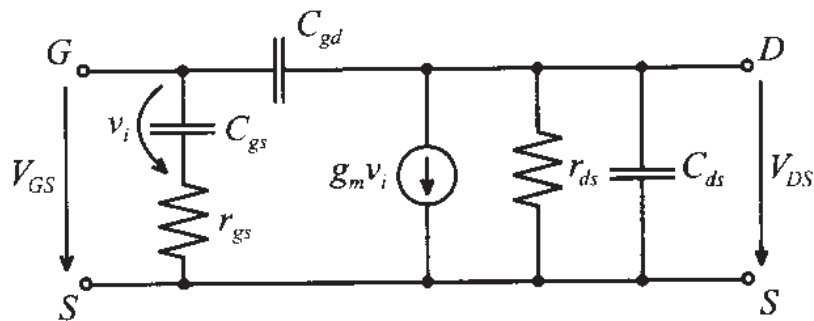
- 7.16 A small-signal BJT model has the following parameters: $g_m = 40 \text{ mS}$, $f_T = 600 \text{ MHz}$, $h_{21} = 100$, $r_{ce} = 2.5 \text{ k}\Omega$, $r_{bb'} = 125 \Omega$, and $C_{b'c} = 2 \text{ pF}$. A load $R_L = 50 \Omega$ is attached as shown.



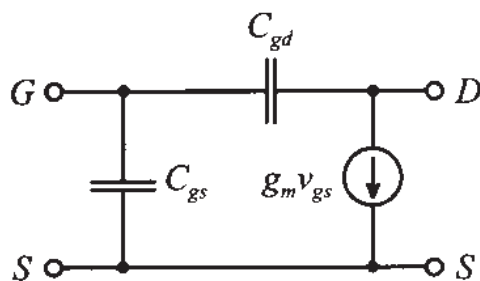
Under the assumption that $V_L \approx -g_m V_{b'e} R_L$, find the Miller capacitance C_M such that the circuit can be approximated as



- 7.17 Neglecting all parasitic elements, including base, emitter, and collector resistances in the transistor described in Example 7-4, find the maximum frequency f_0 , the beta cut-off frequency f_β , and the transition frequency f_T .
- 7.18 Obtain the h -parameter representation for a BJT in common-base configuration, neglecting base, emitter, and collector resistances (r_B , r_E , and r_C).
- 7.19 Derive the h -parameter representation for the following high-frequency FET model:

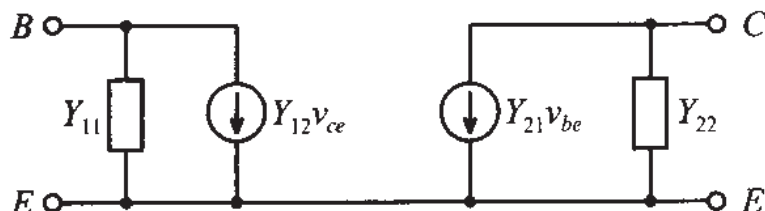


- 7.20 Using the equivalent circuit shown in Problem 7.19, obtain the h -parameter representation for a FET in common-gate configuration.
- 7.21 For the FET circuit model in Problem 7.19, find the equivalent input and output impedances by replacing C_{gd} with its equivalent Miller capacitances. Under what condition is this approximation valid?
- 7.22 For the simplified FET model shown, determine the capacitances C_{gs} and C_{gd} as well as g_m .

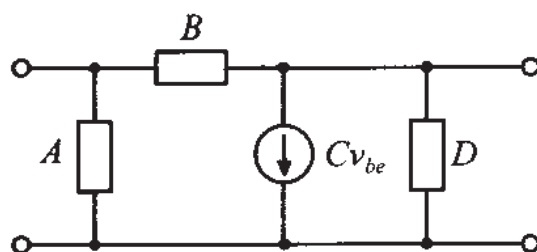


Show that for low frequency operation it is sufficient to record the drain-current and gate-source voltage under short-circuit output condition. Further, design a measurement protocol to predict C_{gs} and C_{gd} .

- 7.23 FET models are often given in terms of Y -parameters, as the following generic figure shows:



Convert this model into a π -network and determine its coefficients A , B , C , and D .



- 7.24 For the model parameters in Problem 7.16, plot the cut-off frequency f_T as a function of load resistance in the range $10 \Omega \leq R_L \leq 200 \Omega$.

Matching and Biasing Networks

As pointed out in Chapter 2, to achieve maximum power transfer, we need to match the impedance of the load to that of the source. Usually this is accomplished by incorporating additional passive networks connected in-between source and load. These networks are generically referred to as matching networks. However, their functionality is not simply limited to matching source and load impedances for optimal power flow. In fact, for many practical circuits matching networks are not only designed to meet the requirement of minimum power loss but are also based on additional constraints, such as minimizing the noise influence, maximizing power handling capabilities, and linearizing the frequency response. In a more general context, the purpose of a matching network can be defined as a transformation to convert a given impedance value to another, more suitable value.

In this chapter we restrict our coverage to the techniques of performing impedance transformation using passive matching networks. The emphasis is to ensure minimum reflections between source and load. All remaining considerations, such as noise figure and linearity, are left for discussions in Chapter 9.

We commence with a study of networks based on discrete components. These networks are easy to analyze and can be used up to frequencies in the low GHz range. Next, we continue with the analysis and design of matching networks using distributed elements, such as strip lines and stub sections. These networks are more suitable for operational frequencies exceeding 1 GHz, or for cases where vertical circuit dimensions are of importance, as required in RF integrated circuit designs.

To simplify our treatment and to gain clarity in the design methodology, the Smith Chart will be utilized extensively throughout as a primary design tool.

8.1 Impedance Matching Using Discrete Components

8.1.1 Two-Component Matching Networks

In a generic sense our engineering efforts primarily strive for two main goals: first, to meet system specifications, and second, to find the most inexpensive and reliable way to accomplish this first task. The cheapest and most reliable matching networks are usually those that contain the least number of components.

The topic of this section is to analyze and design the simplest possible type of matching networks: so-called **two-component networks**, also known as **L-sections** due to their element arrangement. These networks use two reactive components to transform the load impedance (Z_L) to the desired input impedance (Z_{in}). In conjunction with the load and source impedances, the components are alternatively connected in series and shunt configuration, as shown in Figure 8-1, which depicts eight possible arrangements of capacitors and inductors.

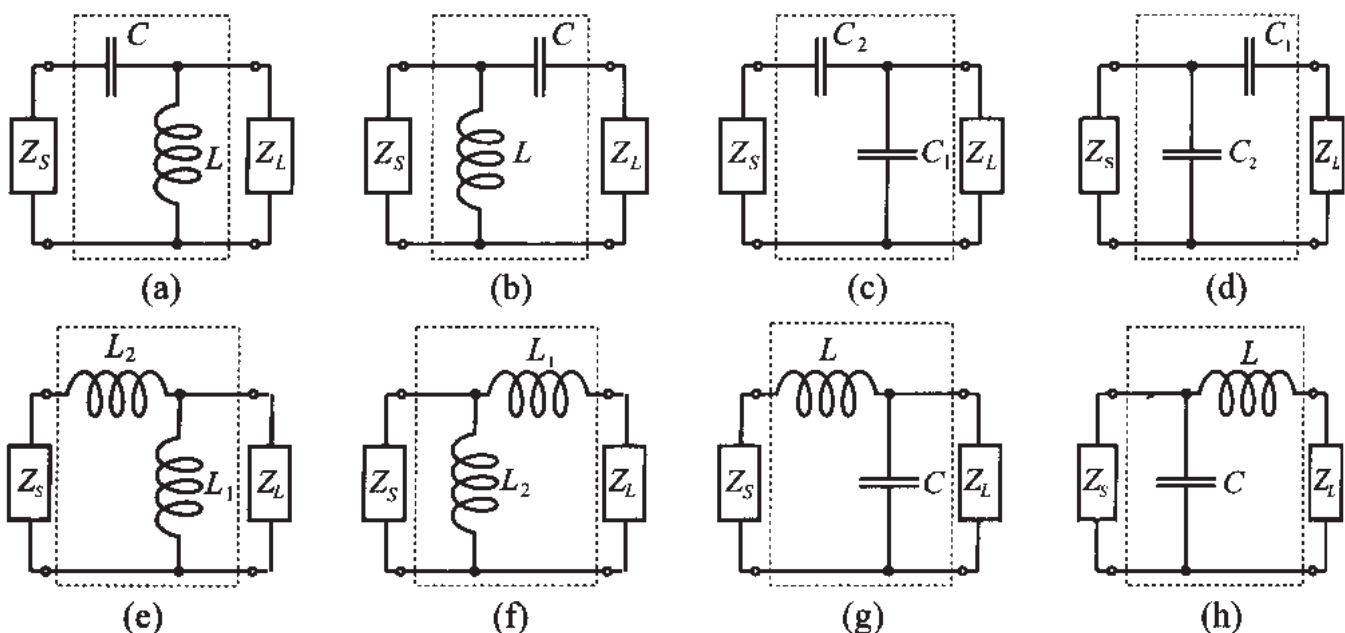
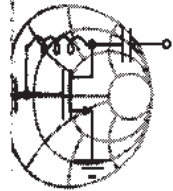


Figure 8-1 Eight possible configurations of the discrete two-component matching networks.

In designing a matching network we have two broad approaches at our disposal:

1. To derive the values of the elements analytically
2. To rely on the Smith Chart as a graphical design tool

The first approach yields very precise results and is suitable for computer synthesis. Alternatively, the second approach is more intuitive, easier to verify, and faster for an initial design, since it does not require complicated computations. The example below details the use of the analytical approach to design a particular L-section matching network.



Example 8-1: Analytical approach to the design of an L-section matching network

The output impedance of a transmitter operating at a frequency of 2 GHz is $Z_T = (150 + j75)\Omega$. Design an L-section matching network, as shown in Figure 8-2, such that maximum power is delivered to the antenna whose input impedance is $Z_A = (75 + j15)\Omega$.

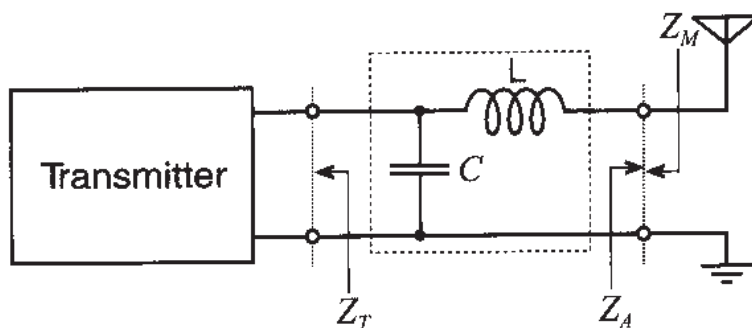


Figure 8-2 Transmitter to antenna matching circuit design.

Solution: The condition of maximum power transfer from the source to the load requires the source impedance to be equal to the complex conjugate of the load impedance. In our case this implies that the output impedance Z_M of the matching network has to be equal to the complex conjugate of Z_A [i.e., $Z_M = Z_A^* = (75 - j15)\Omega$].

The impedance Z_M can be computed as a series connection of an inductor L and a parallel combination of C and Z_T :

$$Z_M = \frac{1}{Z_T^{-1} + jB_C} + jX_L = Z_A^* \quad (8.1)$$

where $B_C = \omega C$ is the susceptance of the capacitor and $X_L = \omega L$ is the reactance of the inductor. Expressing transmitter and antenna impedances in terms of their real and imaginary parts (i.e., $Z_T = R_T + jX_T$ and $Z_A = R_A + jX_A$), we can rewrite (8.1) as

$$\frac{R_T + jX_T}{1 + jB_C(R_T + jX_T)} + jX_L = R_A - jX_A \quad (8.2)$$

Separating real and imaginary parts in (8.2), a system of two equations is found:

$$R_T = R_A(1 - B_C X_T) + (X_A + X_L)B_C R_T \quad (8.3a)$$

$$X_T = R_T R_A B_C - (1 - B_C X_T)(X_A + X_L) \quad (8.3b)$$

Solving (8.3a) for X_L and substituting into (8.3b) results in a quadratic equation for B_C whose solution is

$$B_C = \frac{X_T \pm \sqrt{\frac{R_T}{R_A}(R_T^2 + X_T^2) - R_T^2}}{R_T^2 + X_T^2} \quad (8.4)$$

Since $R_T > R_A$, the argument of the square root is positive and greater than X_T^2 . Therefore, to ensure a positive B_C we must choose the “plus” sign in (8.4). Substituting (8.4) into (8.3a) yields X_L as

$$X_L = \frac{1}{B_C} - \frac{R_A(1 - B_C X_T)}{B_C R_T} - X_A \quad (8.5)$$

Inserting numerical values into (8.4) and (8.5), we find

$$B_C = 9.2 \text{ mS} \Rightarrow C = B_C / \omega = 0.73 \text{ pF}$$

$$X_L = 76.9 \Omega \Rightarrow L = X_L / \omega = 6.1 \text{ nH}$$

This example shows the analytical approach of designing an L-section matching network by solving a quadratic equation for C and then a linear equation for L. The process is tedious but can be easily implemented on a mathematical spreadsheet.

As we may anticipate from Example 8-1, the analytical approach of designing matching networks can become very complicated and computationally intensive even for simple L-sections. Instead of the preceding method, we can use the Smith Chart for rapid and relatively precise designs of the matching circuits. The appeal of this approach is that its complexity remains almost the same independent of the number of components in the network. Moreover, by observing the impedance transformation on the Smith Chart we obtain a “feel” of how the individual circuit elements contribute to achieving a particular matching condition. Any errors in component selection and value assignment are observed immediately and the design engineer can directly intervene. With the help of a personal computer, this process is carried out in real time. That is, the parameter choice (L or C) and its value assignment can be instantaneously displayed as part of the Smith Chart on the computer screen.

The effect of connecting a single reactive component (either capacitor or inductor) to a complex load is described in considerable detail in Section 3.4. Here we just point out the following:

- The addition of a reactance connected in series with a complex impedance results in motion along a constant-resistance circle in the combined Smith Chart
- A shunt connection produces motion along a constant-conductance circle.

This is indicated in Figure 8-3 for the combined ZY Smith Chart. Concerning the direction of the rotation, the general rule of thumb is that whenever an inductor is involved, we rotate in the direction that moves the impedance into the upper half of the Smith Chart. In contrast, a capacitance results in the movement toward the lower half.

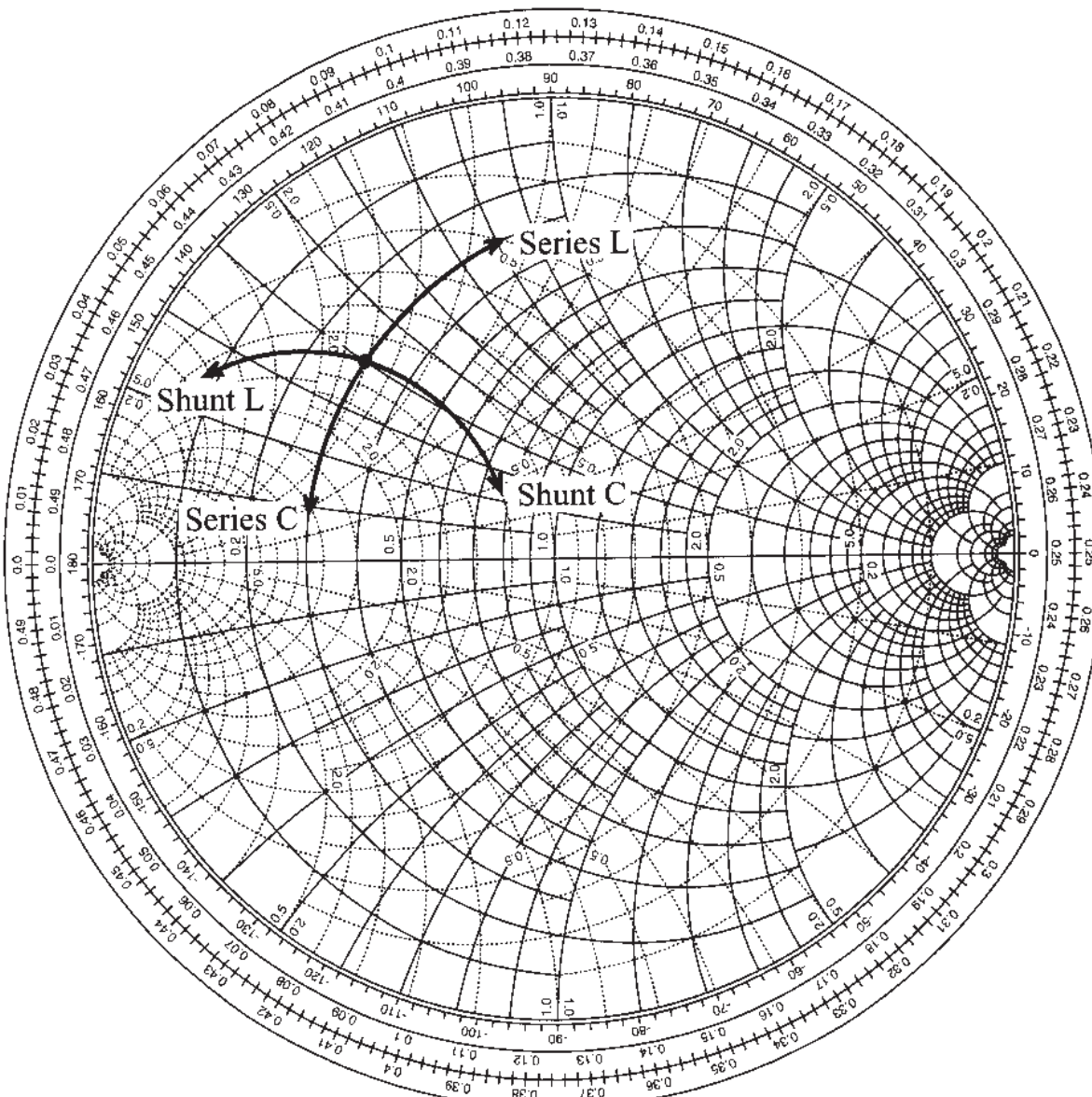
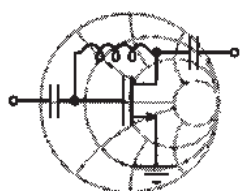


Figure 8-3 Impedance effect of series and shunt connections of L and C to a complex load in the Smith Chart.

Having established the effect of connecting a single component to the load, we can now develop suitable two-component matching networks that perform the transformation from any load impedance to any specified input impedance. In general, designing an L-type matching network, or for that matter any passive network, in the ZY Smith Chart consists of moving along either constant resistance or constant conductance circles.

In the following example we illustrate this graphical design technique as an alternative to the analytical approach discussed in Example 8-1. Most modern CAD programs allow us to conduct this graphical approach interactively on the computer screen. In fact, simulation packages such as MMICAD directly permit the placement of components with the corresponding impedance behavior displayed on the Smith Chart.



RF & MW →

Example 8-2: Graphical approach to the design of the L-section matching network

Design the L-type reactive matching network discussed in Example 8-1 by using the Smith Chart as a graphical design tool.

Solution: The first step is to compute normalized transmitter and antenna impedances. Since no characteristic impedance Z_0 is given, we arbitrarily select $Z_0 = 75 \Omega$. Therefore, the normalized transmitter and antenna impedances are $z_T = Z_T/Z_0 = 2 + j1$ and $z_A = Z_A/Z_0 = 1 + j0.2$, respectively. Since the first component connected to the transmitter is a shunt capacitor, the total impedance of this parallel combination is positioned somewhere on the circle of constant conductance that passes through the point z_T in the combined Smith Chart (see Figure 8-4).

Next, an inductor is added in series with the parallel combination of transmitter z_T and capacitor; the resulting impedance will move along the circle of constant resistance. For maximum power gain we require an output impedance of the matching network connected to the transmitter to be equal to the complex conjugate of the antenna impedance. This circle has to pass through $z_M = z_A^* = 1 - j0.2$, as shown in Figure 8-4.

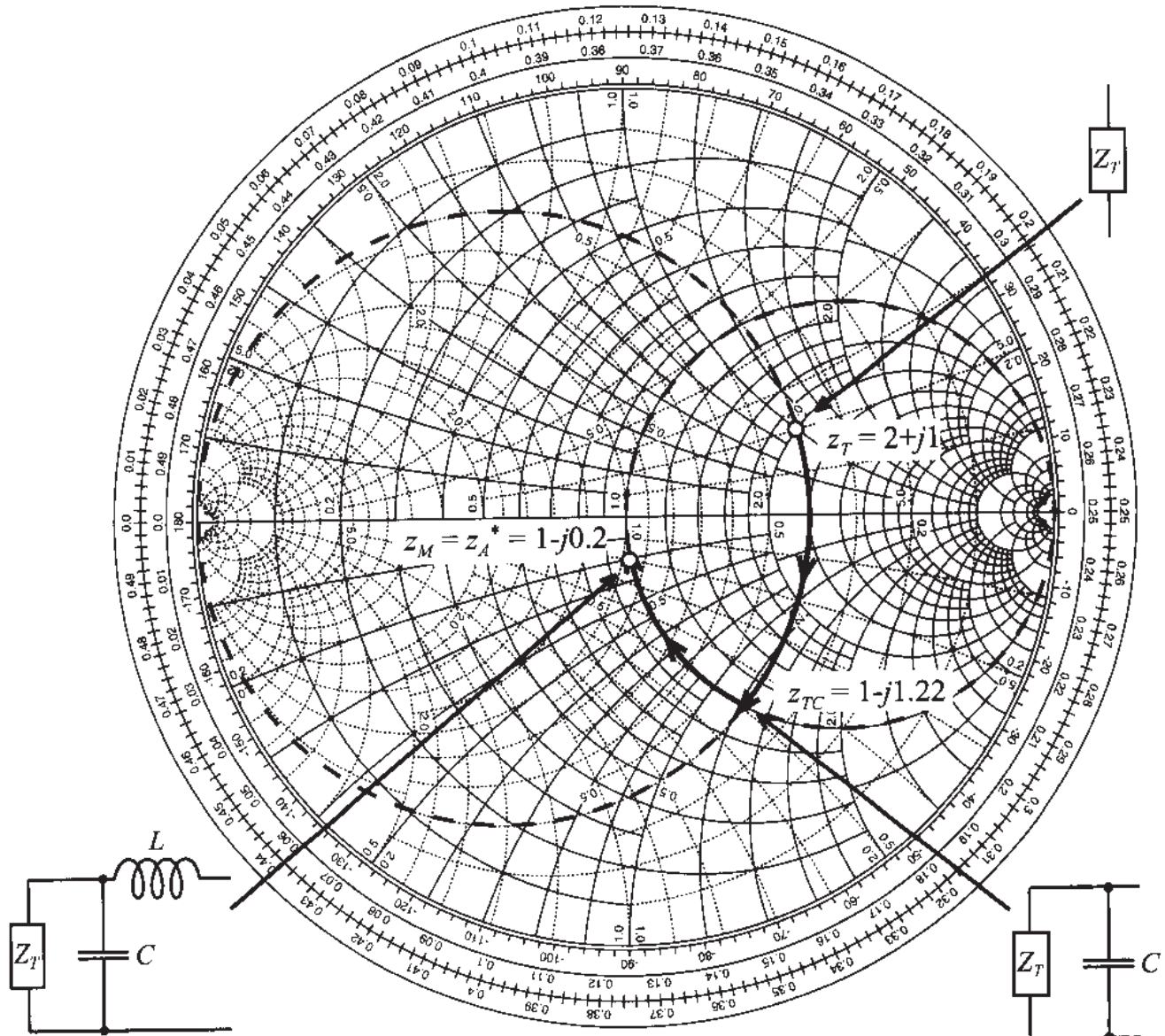


Figure 8-4 Design of the two-element matching network as part of the ZY Smith Chart.

The intersection of two circles in the Smith Chart determines the normalized impedance formed by the shunt connection of transmitter and capacitor. Reading from the Smith Chart, we find that this impedance is approximately $z_{TC} = 1 - j1.22$ with the corresponding admittance of $y_{TC} = 0.4 + j0.49$. Therefore, the normalized susceptance of the shunt capacitor is $j b_C = y_{TC} - y_T = j0.69$ and the normalized reactance of the inductor is $j x_L = z_A - z_{TC} = j1.02$. Finally, the actual values for the inductor and capacitor are

$$L = (x_L Z_0) / \omega = 6.09 \text{ nH}$$

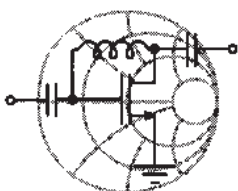
$$C = b_C / (\omega Z_0) = 0.73 \text{ pF}$$

This example presents a simple and yet precise graphical approach to design L-section matching networks. The method can be readily extended to more complicated systems.

The design procedure described in Example 8-2 can be applied to any L-section matching network shown in Figure 8-1. The generic solution procedure for optimal power transfer includes the following six steps:

1. Find the normalized source and load impedances.
2. In the Smith Chart plot circles of constant resistance and conductance that pass through the point denoting the source impedance.
3. Plot circles of constant resistance and conductance that pass through the point of the *complex conjugate* of the load impedance.
4. Identify the intersection points between the circles in steps 2 and 3. The number of intersection points determines the number of possible L-section matching networks.
5. Find the values of the normalized reactances and susceptances of the inductors and capacitors by tracing a path along the circles from the source impedance to the intersection point and then to the complex conjugate of the load impedance.
6. Determine the actual values of inductors and capacitors for a given frequency.

In the preceding steps it is not necessary to move from the source to the complex conjugate load impedance. As a matter of fact, we can transform the load to the complex conjugate source impedance. The following example illustrates the first approach, whereas Section 8.1.2 discusses the second method.



RF & MW

Example 8-3: Design of general two-component matching networks

Using the Smith Chart, design all possible configurations of discrete two-element matching networks that match the source impedance $Z_S = (50 + j25)\Omega$ to the load $Z_L = (25 - j50)\Omega$. Assume a characteristic impedance of $Z_0 = 50 \Omega$ and an operating frequency of $f = 2 \text{ GHz}$.

Solution: We follow the six steps listed previously.

1. The normalized load and source impedances are:

$$z_L = Z_L/Z_0 = 1 + j0.5 \text{ or } y_L = 0.8 - j0.4$$

$$z_S = Z_S/Z_0 = 0.5 - j1 \text{ or } y_S = 3 + j0.8$$

2. We plot circles of constant resistance and constant conductance that pass through the points of the normalized source impedance (dashed line circles in Figure 8-5), and

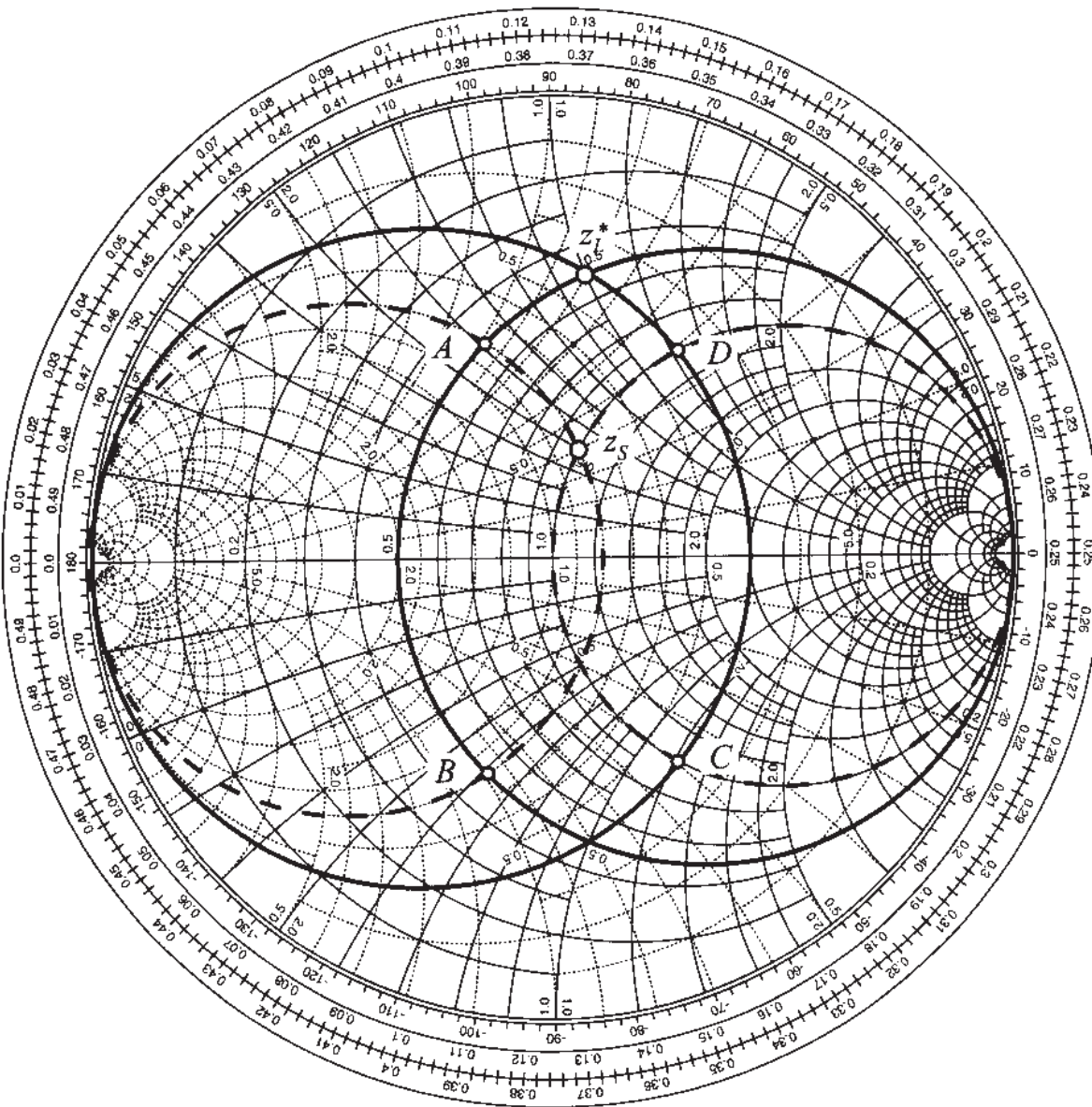


Figure 8-5 Design of a matching network using the Smith Chart

3. Complex conjugate of the load impedance (solid line circles in Figure 8-5).

4. These circles intersect in four points denoted as A , B , C , and D , with the normalized impedances and admittances being as follows:

$$z_A = 0.5 + j0.6, \quad y_A = 0.8 - j1$$

$$z_B = 0.5 - j0.6, \quad y_B = 0.8 + j1$$

$$z_C = 1 - j1.2, \quad y_C = 3 + j0.5$$

$$z_D = 1 + j1.2, \quad y_D = 3 - j0.5$$

5. Since there are four intersection points, we expect four possible configurations of L-section matching networks. Indeed, if we move along the $z_S \rightarrow z_A \rightarrow z_L^*$ path we see that from point z_S to z_A the impedance is transformed along the circle of constant conductance indicating shunt connection. Moreover, we move toward the upper half of the Smith Chart (see Figure 8-3), which indicates that the first component connected to the source should be a shunt inductor. From points z_A to z_L^* the impedance is transformed along the circle of constant resistance, with movement toward the upper half of the chart indicating series connection of the inductance. Therefore, the $z_S \rightarrow z_A \rightarrow z_L^*$ path results in a “shunt L, series L” matching network, as shown in Figure 8-1(f). If the $z_S \rightarrow z_B \rightarrow z_L^*$ path is chosen, we obtain a “shunt C, series L” network [Figure 8-1(h)]. For $z_S \rightarrow z_C \rightarrow z_L^*$ the matching network is “series C, shunt L” [Figure 8-1(a)]. Finally, for the $z_S \rightarrow z_D \rightarrow z_L^*$ path, a matching network is constructed by a “series L, shunt L” combination, which is shown in Figure 8-1(e).
6. We finally have to find the actual component values for the matching networks identified in the previous step. If we direct our attention again to the $z_S \rightarrow z_A \rightarrow z_L^*$ path, we see that from the source impedance to the point z_A the normalized admittance of the circuit is changed by

$$jb_{L_2} = y_A - y_S = (0.8 - j1) - (0.8 - j0.4) = -j0.6$$

From here the value of the shunt inductor is:

$$L_2 = -\frac{Z_0}{b_{L_2}\omega} = 6.63nH$$

Transformation from point z_A to z_L^* is done by adding an inductor connected in series to the impedance z_A . Therefore,

$$jx_{L_1} = z_L^* - z_A = (0.5 + j1) - (0.5 + j0.6) = j0.4$$

and the value of this inductor is

$$L_1 = \frac{x_{L_1} Z_0}{\omega} = 1.59 \text{ nH}$$

The values of the components for the remaining three matching networks are found in the same way. The results are shown in Figure 8-6.

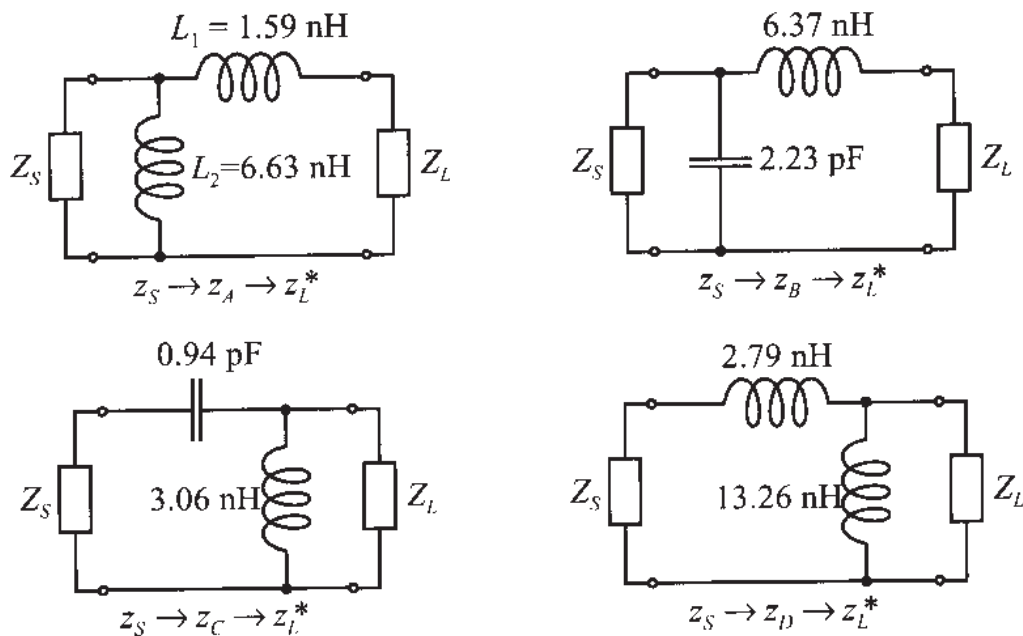


Figure 8-6 Matching networks for four different paths in the Smith Chart.

The Smith Chart allows us immediate observation whether or not a particular impedance transformation is capable of achieving the desired matching. Moreover, the total number of possible network connections can readily be seen.

8.1.2 Forbidden Regions, Frequency Response, and Quality Factor

Before continuing with the frequency analysis of L-type matching networks, let us first note that not every network topology depicted in Figure 8-1 can perform the required matching between arbitrary load and source impedances. For example, if the source is $Z_S = Z_0 = 50 \Omega$ and if we use a matching network shown in Figure 8-1(h), then the addition of the capacitor in parallel with the source produces motion in clockwise direction away from the circle of constant resistance that passes through the origin. This implies that all load impedances that fall into the shaded region in Figure 8-7(a) cannot be matched to the 50Ω source by this particular network.

Similar “forbidden regions” can be developed for all L-type matching network topologies depicted in Figure 8-1. Examples of such regions for several other networks

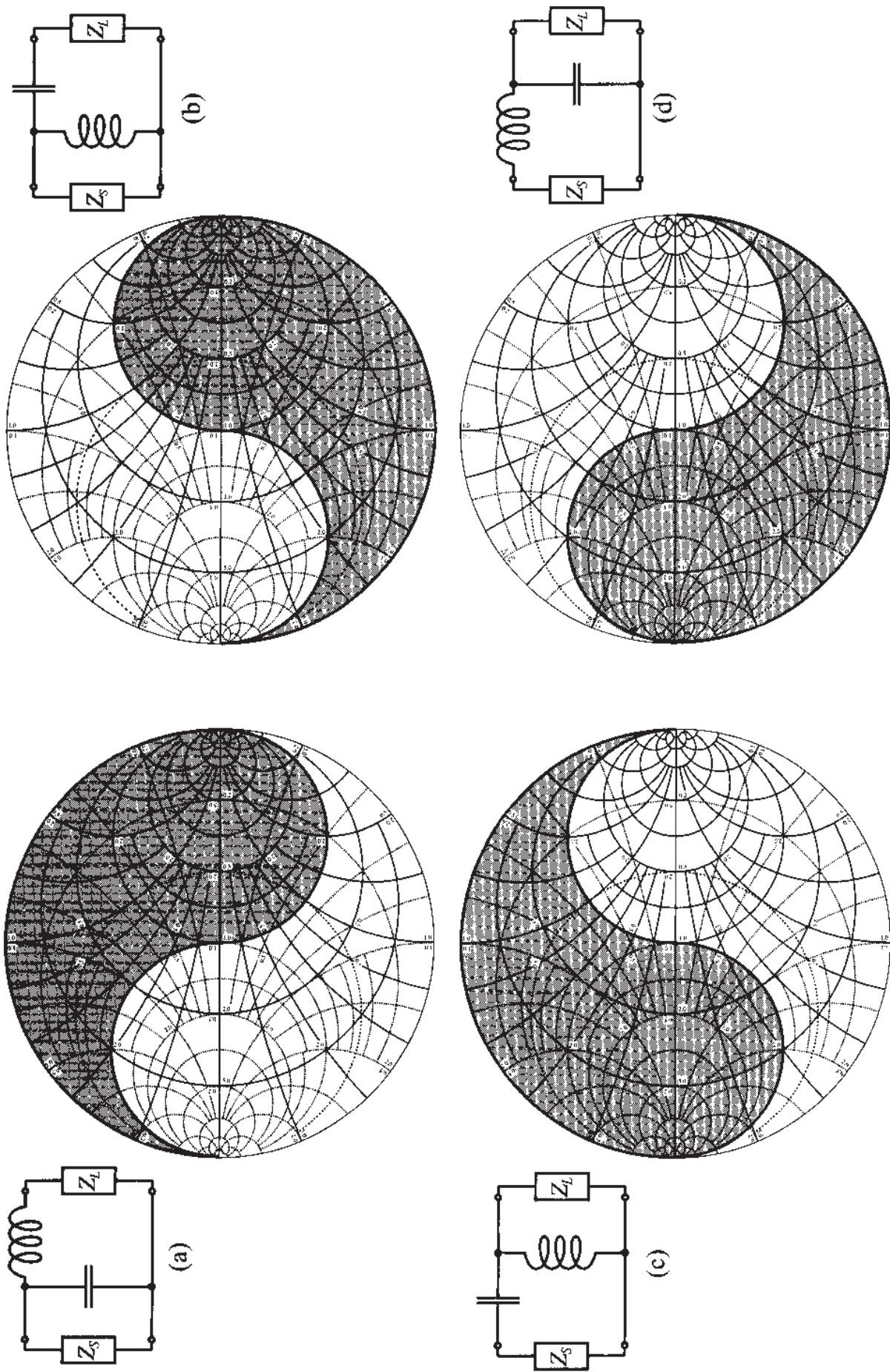


Figure 8-7 Forbidden regions for L-type matching networks with $Z_S = Z_0 = 50 \Omega$.

based on a 50Ω source impedance are shown in Figure 8-7. Here the shaded areas denote values of the load impedance that cannot be matched to the 50Ω source. It is important to keep in mind that the forbidden regions in Figure 8-7 are applicable only when dealing with a $Z_S = Z_0 = 50 \Omega$ source impedance. The regions take on totally different shapes for other source impedance values.

As explained in Example 8-3 and displayed in Figure 8-7, for any given load and input impedances there are at least two possible configurations of L-type networks that accomplish the required match. The question now is, what is the difference between these realizations and which network should ultimately be chosen?

Besides the obvious reasons for selecting one network over another (for instance, availability of components with required values), there are key technical considerations, including DC biasing, stability, and frequency response. In the remainder of this section we concentrate primarily on the frequency response and quality factor of the L-type matching networks, whereas DC biasing issues are covered later in Section 8.3. Stability is deferred to Chapter 9.

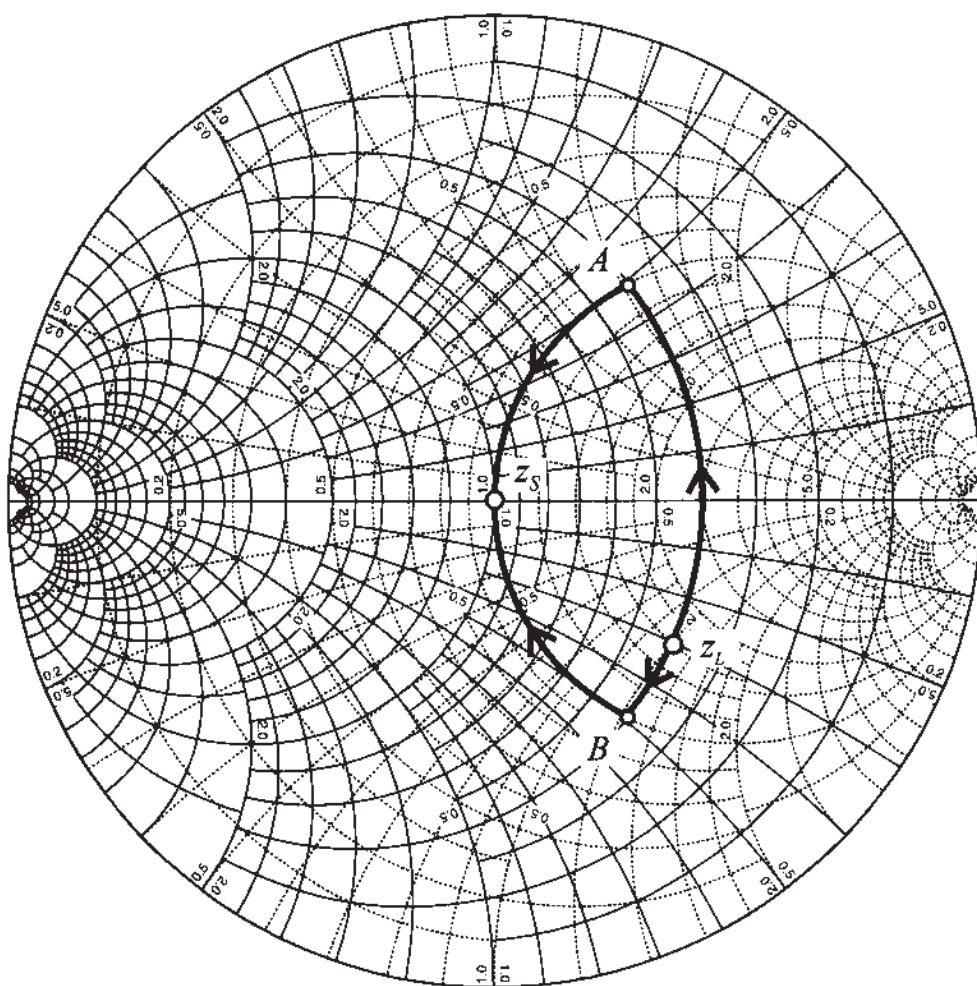
Since any L-type matching network consists of series and shunt combinations of capacitors and/or inductors, the frequency response of these networks can be classified as either low-pass, high-pass, or bandpass filters. To demonstrate such behavior, let us consider a matching network that transforms a complex load, consisting of resistance $R_L = 80 \Omega$ connected in series with capacitor $C_L = 2.65 \text{ pF}$, into a 50Ω input impedance. Let us further assume that the operational frequency for this circuit is $f_0 = 1 \text{ GHz}$.

At 1 GHz the normalized load impedance is $z_L = 1.6 - j1.2$, and according to Figure 8-7 we can use either one of the matching networks shown in Figure 8-7(c) or Figure 8-7(d), following a similar design procedure as described in Example 8-2. However, because the source impedance z_S is real ($z_S = 50 \Omega$) it is easier to transform from the load to the source impedance since $z_S^* = z_S = 50 \Omega$. This is shown in Figure 8-8(a). The corresponding matching networks are shown in Figures 8-8(b) and 8-8(c).

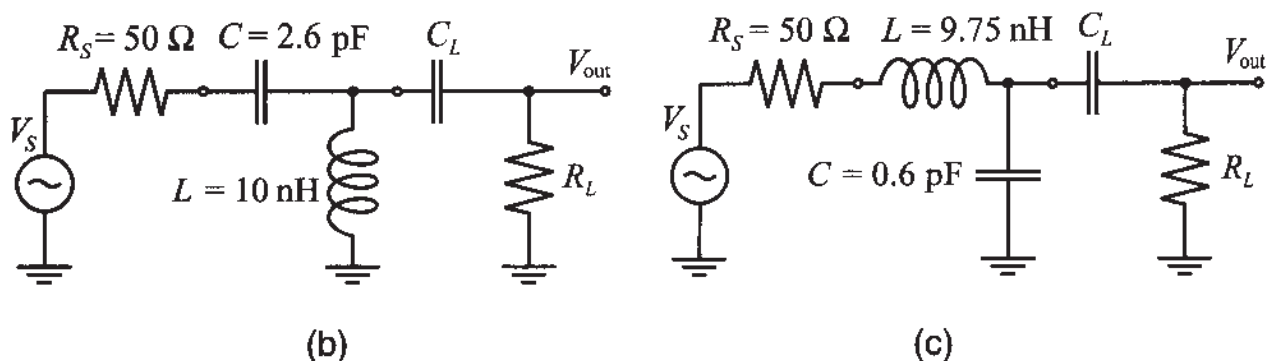
The frequency responses of these two networks in terms of the input reflection coefficient $\Gamma_{\text{in}} = (Z_{\text{in}} - Z_S)/(Z_{\text{in}} + Z_S)$ and the transfer function $H = V_{\text{out}}/V_S$ (where the output voltage V_{out} is measured across the load resistance $R_L = 80 \Omega$) are shown in Figures 8-9(a) and (b), respectively.

It is apparent from Figure 8-9 that both networks exhibit perfect matching only at a particular frequency $f_0 = 1 \text{ GHz}$ and begin to deviate quickly when moving away from f_0 .

The previously developed matching networks can also be viewed as resonance circuits with f_0 being the resonance frequency. As discussed in Section 5.1.1, these



(a) Impedance transformations displayed in Smith Chart

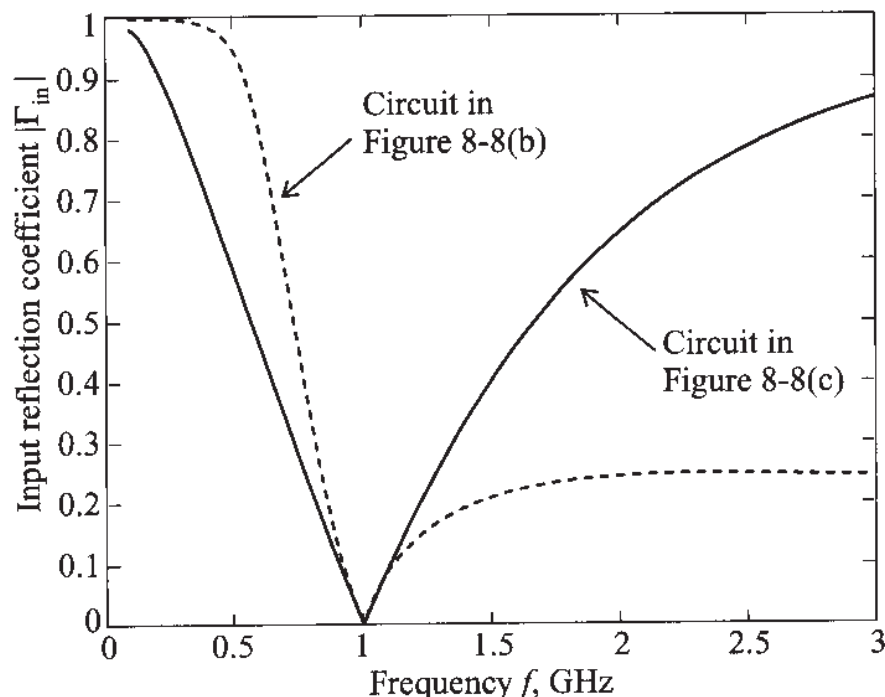


Resulting matching networks

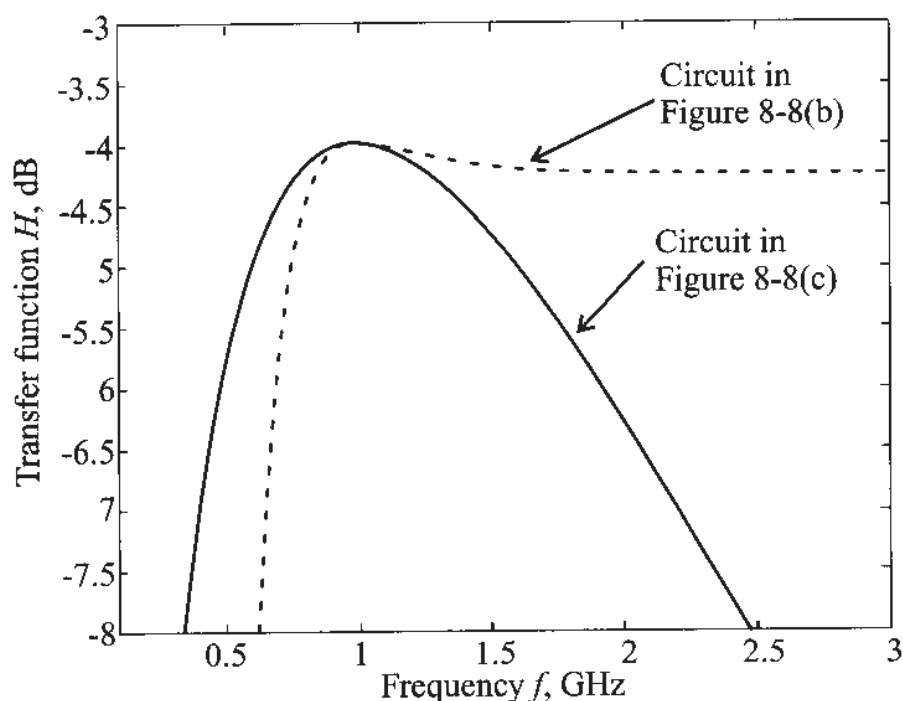
Figure 8-8 Two design realizations of an L-type matching network.

networks may be described by a loaded quality factor, Q_L , which is equal to the ratio of the resonance frequency f_0 over the 3 dB bandwidth BW

$$Q_L = \frac{f_0}{BW} \quad (8.6)$$



(a) Frequency response of input reflection coefficient



(b) Transfer function of the matching networks

Figure 8-9 Frequency response of the two matching network realizations.

where both f_0 and BW are expressed in Hz. The question now is how to find the bandwidth of the matching network. To answer this, we will exploit the similarity between the bell-shaped response of the matching network's transfer function near f_0 [see Figure 8-9(b)] and the frequency response of a bandpass filter.

For frequencies close to f_0 , the matching network in Figure 8-8(c) can be redrawn as a bandpass filter with a loaded quality factor calculated based on (8.6). The equivalent bandpass filter is shown in Figure 8-10(a). The equivalent capacitance C_T in this circuit is obtained by replacing the series combination of R_L and C_L in Figure 8-8(c) with an equivalent parallel connection of R_{LP} and C_{LP} and then adding the capacitances C and C_{LP} : $C_T = C + C_{LP}$. The equivalent shunt inductance L_{LN} is obtained by first replacing the series connection of the voltage source V_S , resistance R_S , and inductance L with the Norton equivalent current source $I_N = V_S/(R_S + j\omega_0 L)$ connected to the parallel combination of conductance G_{SN} and inductance L_N , where the admittance is given as follows: $G_{SN} + (j\omega_0 L_N)^{-1} = (R_S + j\omega_0 L)^{-1}$. Next, the current source I_N and conductance G_{SN} are converted back into a Thévenin equivalent voltage source

$$V_T = I_N/G_{SN} = V_S \frac{R_S - j\omega_0 L}{R_S} = V_S(1 - j1.2255) \quad (8.7)$$

and series resistance

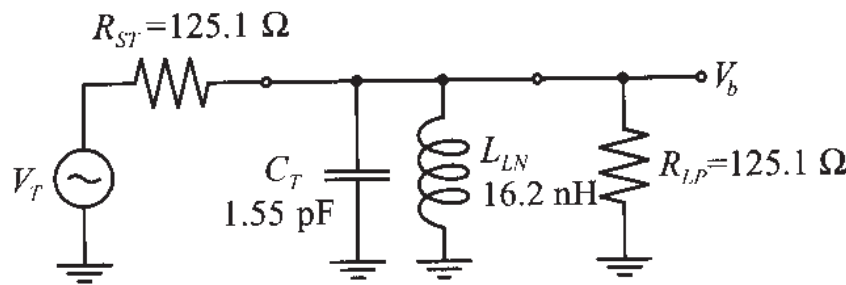
$$R_{ST} = G_{SN}^{-1} = \frac{R_S^2 + (\omega_0 L)^2}{R_S} \quad (8.8)$$

The resonance circuit in Figure 8-10 is loaded by the combined resistance $R_T = R_L \parallel R_{ST} = 62.54 \Omega$. Thus, the loaded quality factor Q_L of the equivalent bandpass filter is given by

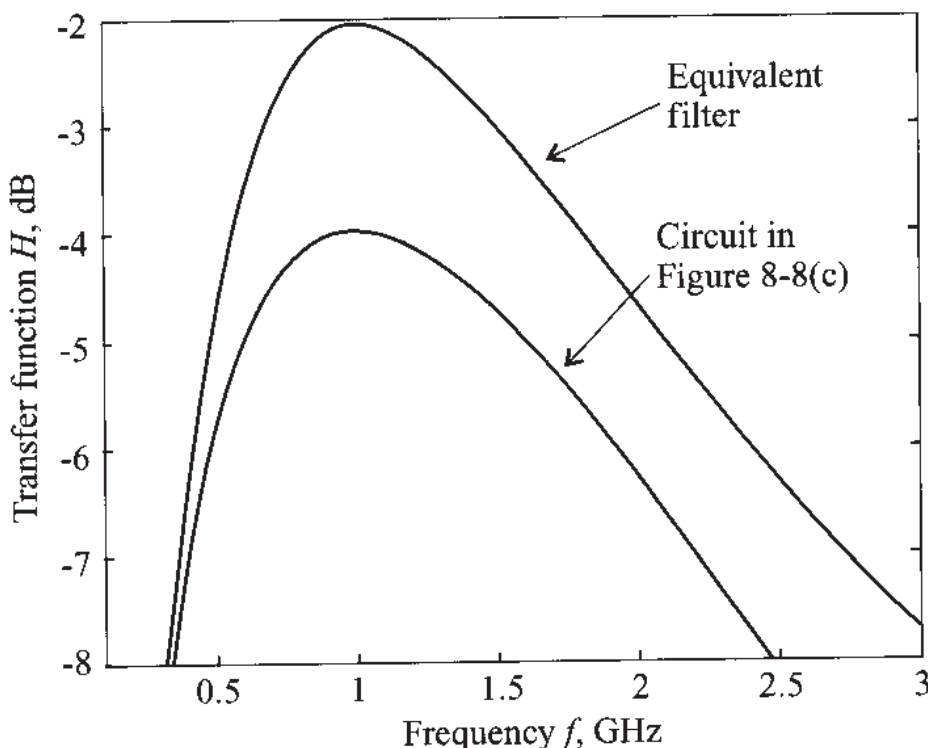
$$Q_L = \frac{f_0}{BW} = \omega_0 R_T C = \frac{R_T}{|X_C|} = 0.61 \quad (8.9)$$

It is immediately noticed that the maximum gain for the equivalent bandpass filter is higher than the gain of the original matching network. This is explained by the fact that for the matching network we measure the output voltage on the load R_L , while for the equivalent filter we measure the output voltage at the equivalent load resistance R_{LP} , which is connected in parallel with the capacitance C_T . Therefore, the conversion from V_b to V_{out} at the resonance frequency can be found through the voltage divider rule:

$$|V_{out}| = |V_b| \frac{R_L}{R_L + \frac{1}{j\omega_0 C_L}} = 0.7908 |V_b|$$



(a) Equivalent bandpass filter



(b) Frequency response of the matching network compared to the equivalent filter response

Figure 8-10 Comparison of the frequency response of the L-type matching network and an equivalent bandpass filter.

which gives us

$$20 \log \frac{|V_{\text{out}}|}{|V_S|} = -2.0382 + 20 \log \frac{|V_b|}{|V_S|} = -3.9794 \text{ dB}$$

a result that agrees very well with Figure 8-9(b).

From the known Q_L we can directly find the bandwidth of the filter: $BW = f_0/Q_L = 1.63 \text{ GHz}$. The frequency response in Figure 8-9(b) shows that the 3 dB point for $f < f_0$ occurs at $f_{\min} = 0.40 \text{ GHz}$ and for $f > f_0$ the 3 dB point corresponds to $f_{\max} = 2.19 \text{ GHz}$. Thus, the bandwidth of the matching network is

$BW = f_{\max} - f_{\min} = 1.79$ GHz, which again agrees reasonably well with the result obtained for the equivalent bandpass filter.

The equivalent bandpass filter analysis allows us to explain the bell-shaped response of the matching network in the neighborhood of f_0 and provides us with a good estimation of the bandwidth of the circuit. The only drawback to this approach is its complexity. It would be desirable to develop a simpler method of estimating the quality factor of the matching network without having first to develop an equivalent bandpass filter or even computing the frequency response of the network. This is accomplished through the use of a so-called **nodal quality factor** Q_n .

Let us go back to Figure 8-8(a), where we illustrate the impedance transformation as we move from one node of the circuit to another. We note that at each node of the matching network the impedance can be expressed in terms of an equivalent series impedance $Z_S = R_S + jX_S$ or admittance $Y_P = G_P + jB_P$. Hence, at each node we can find Q_n as the ratio of the absolute value of the reactance X_S to the corresponding resistance R_S

$$Q_n = \frac{|X_S|}{R_S} \quad (8.10)$$

or as the ratio of the absolute value of susceptance B_P to the conductance G_P

$$Q_n = \frac{|B_P|}{G_P} \quad (8.11)$$

Using (8.10) and (8.11) and the impedance transformations in Figure 8-8(a), we can deduce that for the matching network shown in Figure 8-8(c) the maximum nodal quality factor is obtained at point *B* where the normalized impedance is $1 - j1.23$, resulting in

$$Q_n = |1.23|/1 = 1.23 \quad (8.12)$$

To relate the nodal quality factor Q_n to Q_L , we compare the result of (8.12) with (8.9) and find

$$Q_L = \frac{Q_n}{2} \quad (8.13)$$

This result is true for any L-type matching network. For more complicated configurations the loaded quality factor of the matching network is usually estimated as simply the maximum nodal quality factor. Even though this approach does not yield a quantitative estimate of the circuit bandwidth, it nonetheless allows us to compare networks qualitatively and to select a network with higher or lower bandwidth.

To simplify the matching network design process even further we can draw constant- Q_n contours in the Smith Chart. Figure 8-11 shows such contours for Q_n valued 0.3, 1, 3, and 10.

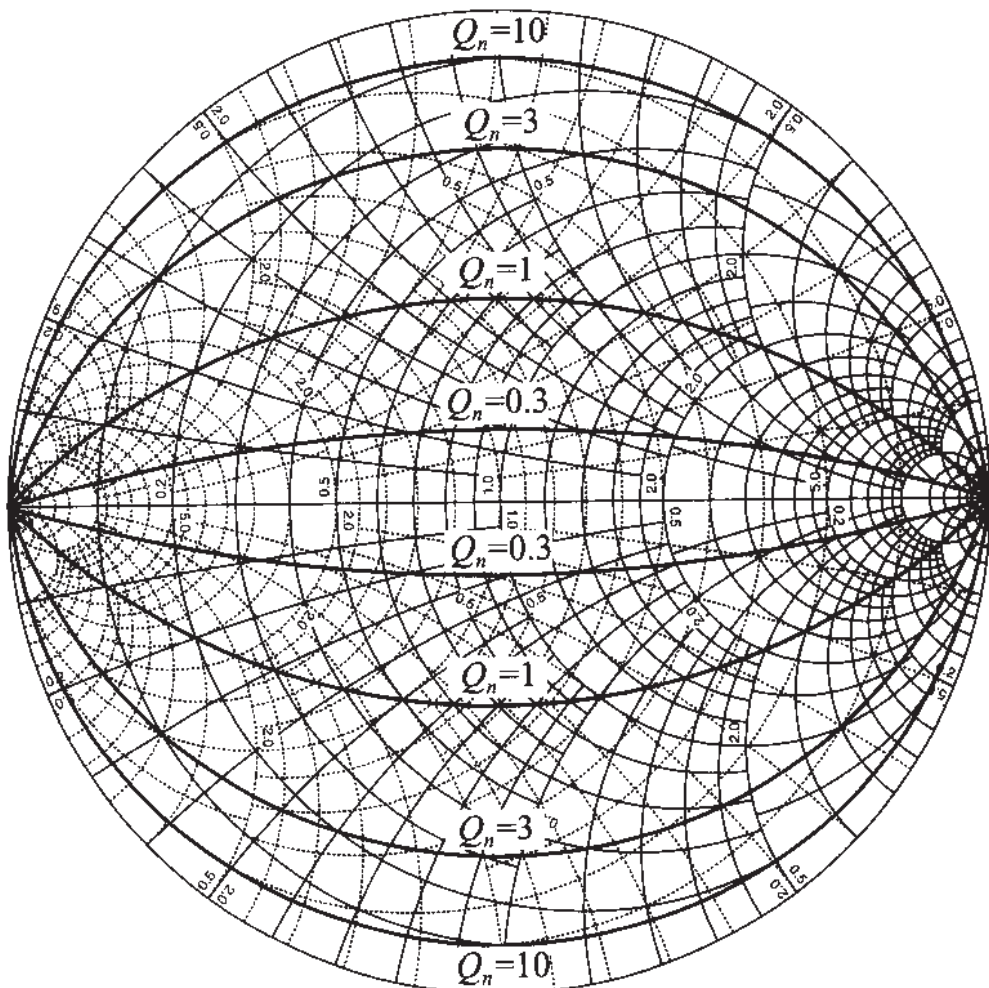


Figure 8-11 Constant Q_n contours displayed in the Smith Chart.

To obtain the equations for these contours we refer back to the general derivation of the Smith Chart in Chapter 3. There it is shown in (3.6) and (3.7) that the normalized impedance can be written as

$$z = r + jx = \frac{1 - \Gamma_r^2 - \Gamma_i^2}{(1 - \Gamma_r)^2 + \Gamma_i^2} + j \frac{2\Gamma_i}{(1 - \Gamma_r)^2 + \Gamma_i^2} \quad (8.14)$$

Thus, the nodal quality factor can be written as

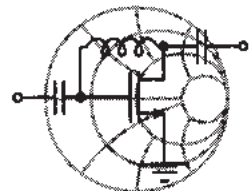
$$Q_n = \frac{|x|}{r} = \frac{2|\Gamma_i|}{1 - \Gamma_r^2 - \Gamma_i^2} \quad (8.15)$$

Rearranging terms in (8.15), it follows that a circle equation is found in the form

$$\Gamma_i^2 + \left(\Gamma_r \pm \frac{1}{Q_n} \right)^2 = 1 + \frac{1}{Q_n^2} \quad (8.16)$$

where the “plus” sign is taken for positive reactance x and the “minus” sign for negative x .

With these constant Q_n circles in the Smith Chart it is possible to find the loaded quality factor of an L-type matching network by simply reading the corresponding Q , and dividing it by 2. This procedure is discussed in Example 8-4.



RF & MW →

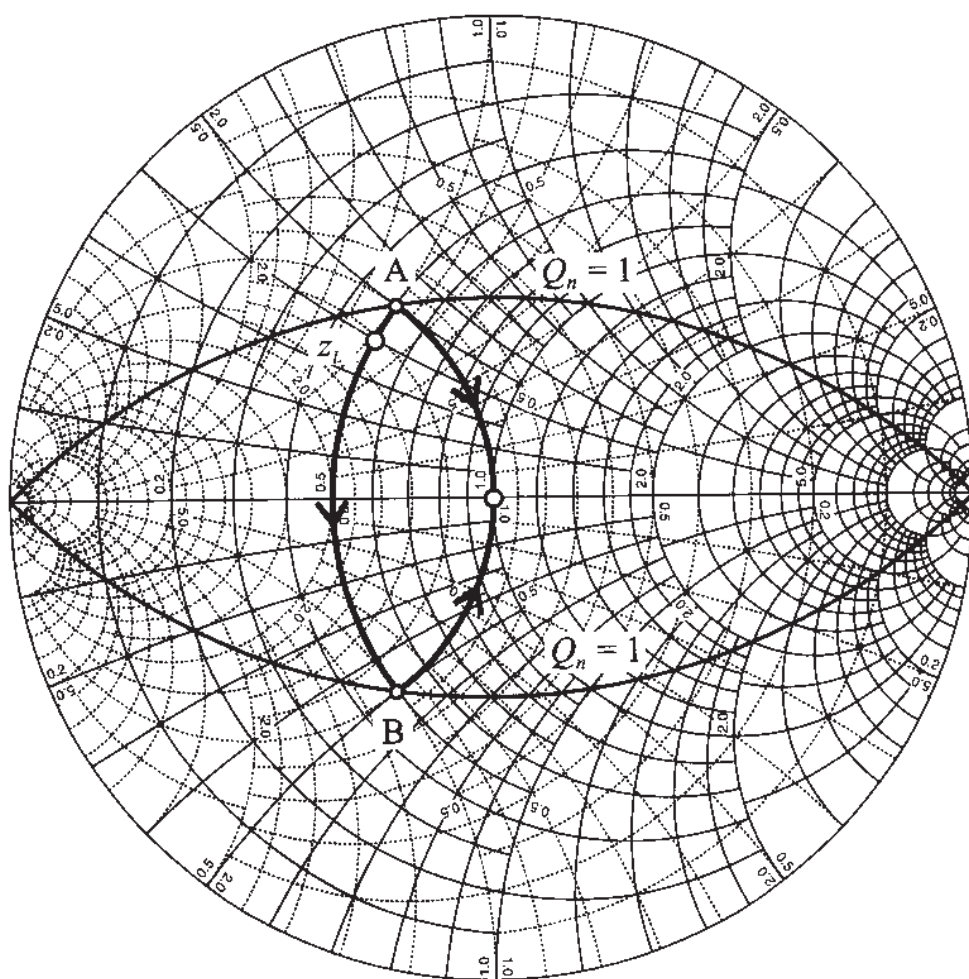
Example 8-4: Design of narrow-band matching network

Using the forbidden regions in Figure 8-7, design two L-type networks that match a $Z_L = (25 + j20)\Omega$ load impedance to a 50Ω source at 1 GHz. Determine the loaded quality factors of these networks from the Smith Chart and compare them to the bandwidth obtained from their frequency response. Assume that the load consists of a resistance and inductance connected in series.

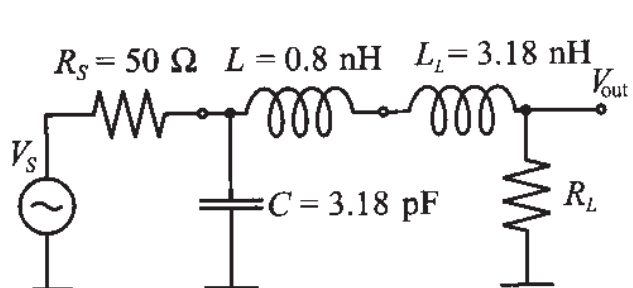
Solution: As we see from Figure 8-7, the normalized load impedance $z_L = 0.5 + j0.4$ lies inside of the constant conductance circle $g = 1$. There are two L-type matching networks that satisfy our requirements. The first consists of a series inductor and shunt capacitor, as shown in Figure 8-7(a), and the second is a series capacitor with shunt inductor, as shown in Figure 8-7(b). Following the same procedure as described in Example 8-2, we obtain the two matching networks shown in Figure 8-12.

According to Figure 8-12(a), the nodal quality factor for both networks is equal to $Q_n = 1$. Thus, we can expect that the bandwidth should be equal to $BW = f_0/Q_L = 2f_0/Q_n = 2$ GHz. This is checked by plotting the corresponding frequency responses for the designed matching networks, as depicted in Figure 8-13.

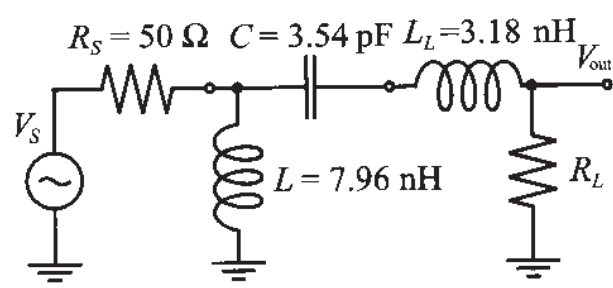
We observe that the bandwidth for the network corresponding to Figure 8-12(c) is approximately $BW_c = 2.4$ GHz. Interestingly, the matching network corresponding to Figure 8-12(b) does not possess a lower cut-off frequency. However, if we assume that the frequency



(a) Impedance transformation in the Smith Chart



(b)



(c)

Resulting matching networks

Figure 8-12 Two L-type matching networks for a 50Ω source and a $Z_L = (25 + j20)\Omega$ load impedance operated at a frequency of 1 GHz.

response is symmetric around the resonance frequency $f_0 = 1 \text{ GHz}$, then the bandwidth will be $BW_b = 2(f_{\max} - f_0) = 1.9 \text{ GHz}$, with the upper cut-off frequency being $f_{\max} = 1.95 \text{ GHz}$.

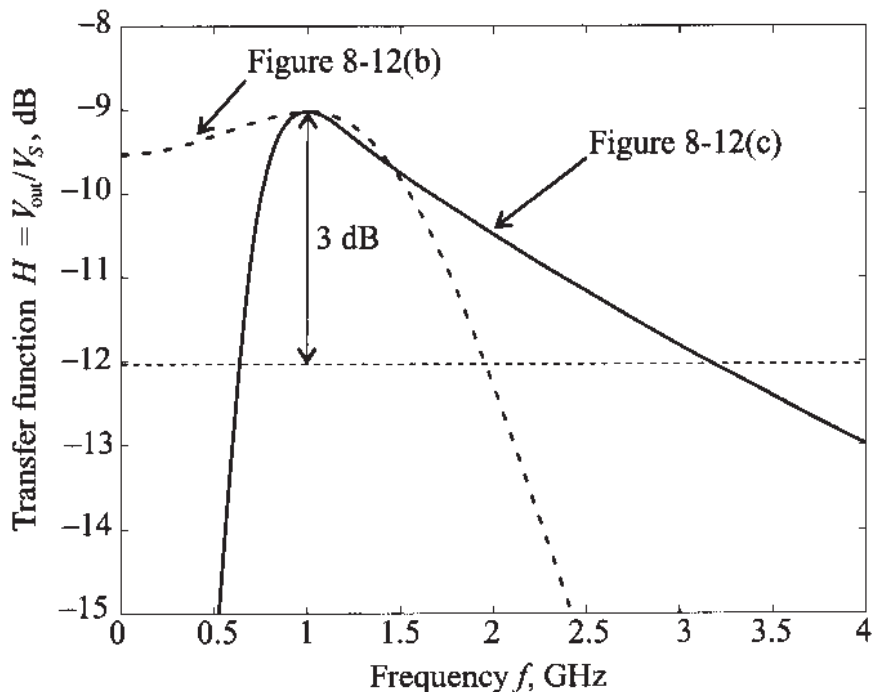


Figure 8-13 Frequency responses for the two matching networks.

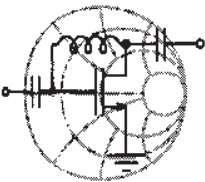
Despite their design for the same resonance frequency, certain matching network configurations exhibit better high or low frequency rejection, as Figure 8-13 exemplifies.

In many practical applications the quality factor of the matching network is of importance. For example, if we design a broadband amplifier we would like to utilize networks with low Q in order to increase the bandwidth. However, for oscillator design it is desirable to achieve high- Q networks to eliminate unwanted harmonics in the output signal. Unfortunately, as we have seen in the previous example, L-type matching networks provide no control over the value of Q_n and we must either accept or reject the resulting quality factor. To gain the freedom of choosing the values of Q and thus affect the bandwidth behavior of the circuit, we can introduce a third element in the matching network. The addition of this third element results in either a T- or Pi-network, both of which are discussed next.

8.1.3 T and PI Matching Networks

As already pointed out, the loaded quality factor of the matching network can be estimated from the maximum nodal Q_n . The addition of the third element into the matching network produces an additional node in the circuit and allows us to control the value of Q_L by choosing an appropriate impedance at that node.

The following two examples illustrate the design of T- and Pi-type matching networks with specified Q_n factor.



RF & MW →

Example 8-5: Design of a T matching network

Design a T-type matching network that transforms a load impedance $Z_L = (60 - j30)\Omega$ into a $Z_{in} = (10 + j20)\Omega$ input impedance and that has a maximum nodal quality factor of 3. Compute the values for the matching network components, assuming that matching is required at $f = 1$ GHz.

Solution: There are several possible solutions that satisfy the design specifications. In this example, we investigate only one design since the rest can easily be obtained by using the same approach.

The general topology of the T-type matching network is shown in Figure 8-14.

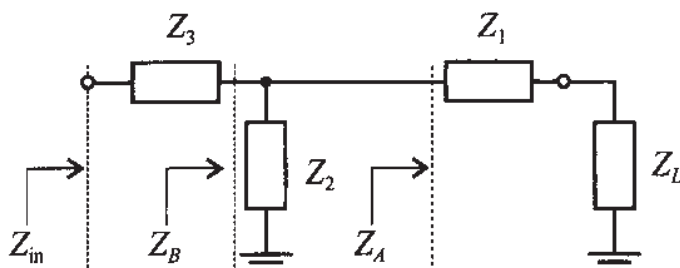


Figure 8-14 General topology of a T-type matching network.

The first element in this network is connected in series with the load impedance. Because Z_1 is purely reactive, the combined impedance Z_A will reside somewhere on the constant resistance circle described by $r = r_L$. Similarly, Z_3 is connected in series with the input so that the combined impedance Z_B (consisting of Z_L , Z_1 , and Z_2) is positioned somewhere on the constant resistance circle with $r = r_{in}$. Because the network should have a nodal quality factor $Q_n = 3$, we can choose the impedance values in such a way that Z_B is located on the intersection of the constant resistance circle $r = r_{in}$ and the $Q_n = 3$ circle (see point *B* in Figure 8-15).

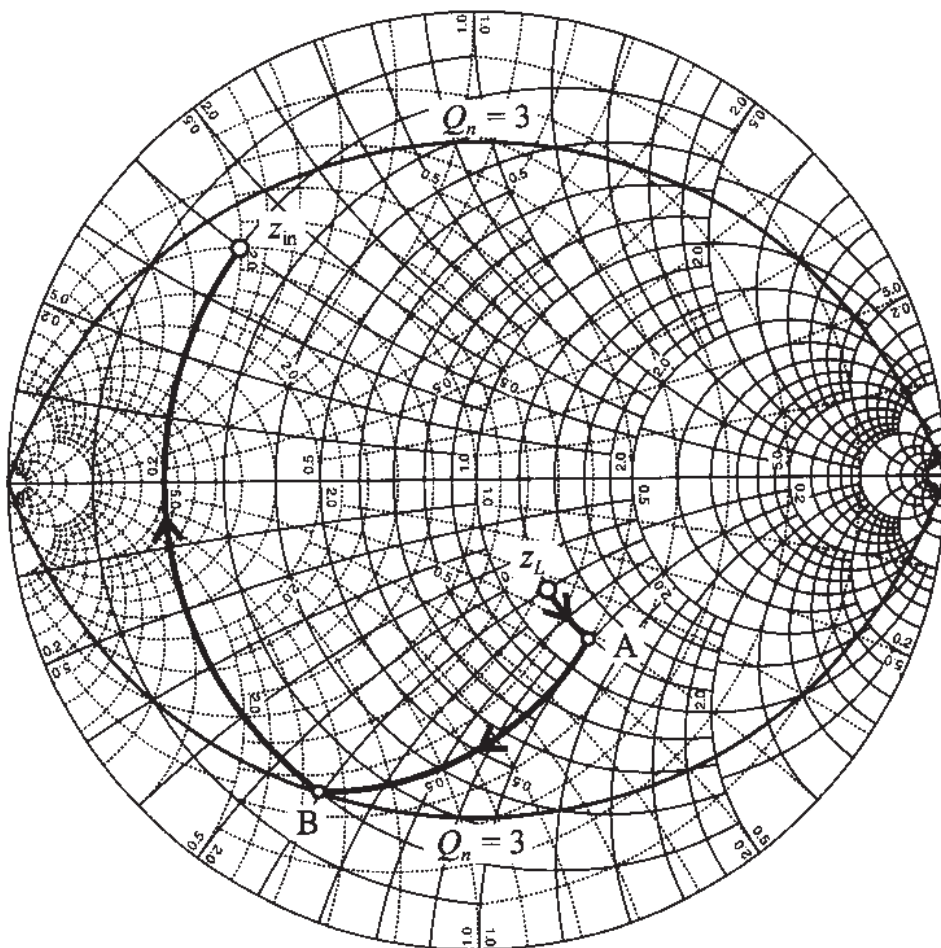


Figure 8-15 Design of a T-type matching network for a specified $Q_n = 3$.

We next find the intersection point A of the constant conductance circle that passes through the point B obtained from the previous step. The circle of constant resistance $r = r_L$ now allows us to determine the required value of the remaining component of the network to reach the point z_{in} .

The complete T-type matching network with the actual component values is illustrated in Figure 8-16. The computed elements are based on the required matching frequency of $f = 1$ GHz.

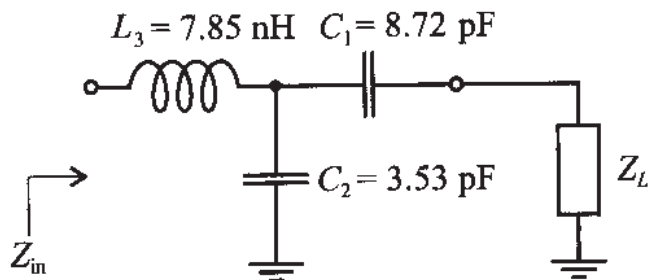
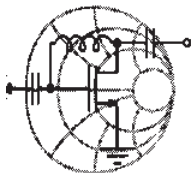


Figure 8-16 T-type matching network circuit schematics.

The extra degree of freedom to adjust the quality factor (bandwidth) of a matching network comes at the expense of an additional circuit element.

In the following example the design of a Pi-type matching network is developed with the intent to achieve a minimum nodal quality factor. A low quality factor design directly translates into a wider bandwidth of the network, as required, for instance, in broadband FET and BJT amplifiers.



RF & MW →

Example 8-6: Design of a Pi-type matching network

For a broadband amplifier it is required to develop a Pi-type matching network that transforms a load impedance of $Z_L = (10 - j10)\Omega$ into an input impedance of $Z_{in} = (20 + j40)\Omega$. The design should involve the lowest possible nodal quality factor. Find the component values, assuming that matching should be achieved at a frequency of $f = 2.4$ GHz.

Solution: Since the load and input impedances are fixed, we cannot produce a matching network that has a quality factor lower than the highest Q_n computed at the locations Z_L and Z_{in} . Therefore, the minimum value for Q_n is determined at the input impedance location as $Q_n = |X_{in}|/R_{in} = 40/20 = 2$. The Smith Chart design of the Pi-type matching network based on $Q_n = 2$ is depicted in Figure 8-17.

In the design we employ a method very similar to the one used in Example 8-5. First, we plot a constant conductance circle $g = g_{in}$ and find its intersection with the $Q_n = 2$ contour in the Smith Chart. This intersection is denoted as point B . Next, we find the intersection point of the constant conductance circle $g = g_L$ with the constant resistance circle that passes through the point B . The resulting point is denoted as A in Figure 8-17.

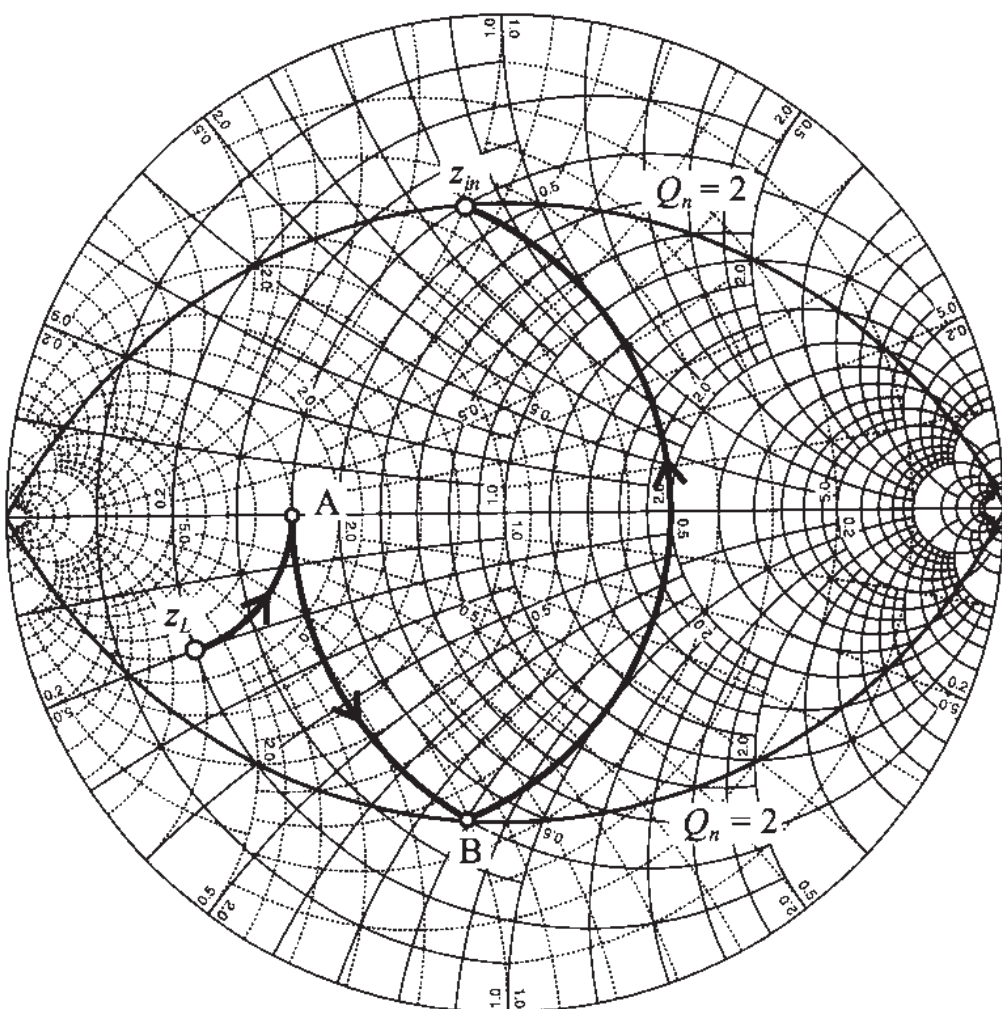


Figure 8-17 Design of a Pi-type matching network using a minimal Q_n .

The network components can be determined based on converting the Smith Chart points into actual capacitances and inductances as detailed in Example 8-2. The resulting circuit configuration is shown in Figure 8-18.

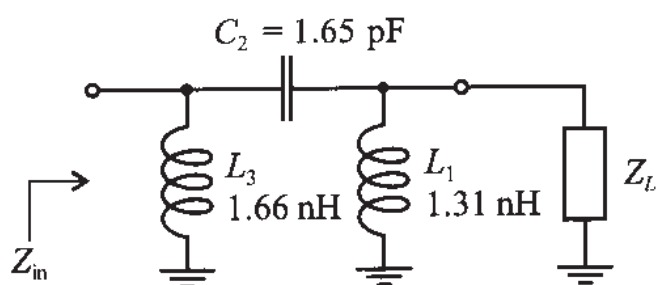


Figure 8-18 Pi-type matching network configuration.

It is interesting to note that unlike the situation discussed in Example 8-5, the relative positions of Z_L and Z_{in} in this example are such that only one possible Pi-type network configuration with

$Q_n = 2$ exists. All other realizations of the Pi-type network will result in an increased nodal quality factor. Furthermore, if we had a lower load resistance, we would not be able to implement this Pi-type network for the given Q_n .

As this example shows, the bandwidth cannot be increased arbitrarily by reducing the nodal quality factor. The limits are set by the desired input and output impedances.

8.2 Microstrip Line Matching Networks

In the previous sections we have discussed the design of matching networks involving discrete components. However, with increasing frequency and correspondingly reduced wavelength, the influence of parasitics in the discrete elements becomes more noticeable. The design now requires us to take these parasitics into account, thus significantly complicating the component value computations. This, along with the fact that discrete components are only available for certain values, limits their use in high-frequency circuit applications. As an alternative to lumped elements, distributed components are widely used when the wavelength becomes sufficiently small compared with the characteristic circuit component length, a fact already discussed in Chapter 2.

8.2.1 From Discrete Components to Microstrip Lines

In the mid-GHz range, design engineers often employ a mixed approach by combining lumped and distributed elements. These types of matching networks usually contain a number of transmission lines connected in series and capacitors spaced in a parallel configuration, as illustrated in Figure 8-19. The reader is also referred to Figure 1-2(a) for a practical example.

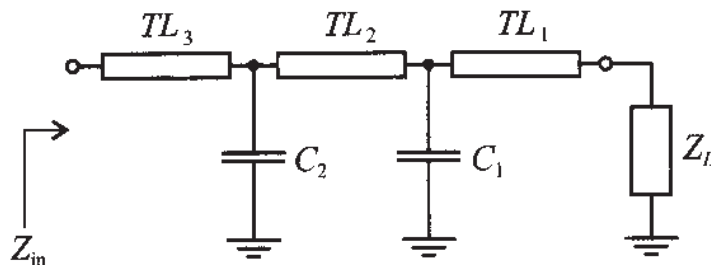
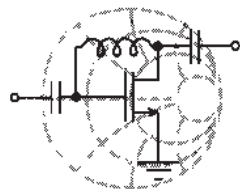


Figure 8-19 Mixed design of matching network involving transmission line sections (TL) and discrete capacitive elements.

Inductors are usually avoided in such designs because they tend to have higher resistive losses than capacitors. In general, only one shunt capacitor with two transmission lines connected in series on both sides is sufficient to transform any given load impedance to any input impedance. Similar to the L-type matching networks, such configurations may involve the additional requirement of a fixed Q_n , necessitating additional components to control the quality factor of the circuit.

The arrangement of components shown in Figure 8-19 is very attractive in practice, since it permits tuning the circuit after it has been manufactured. Changing the values of the capacitors as well as placing them at different locations along the transmission lines offers a wide range of flexibility. The tuning capability makes these types of matching networks very popular for prototyping. Usually, all transmission lines have the same width (i.e., the same characteristic impedance) to simplify the actual tuning.

Example 8-7 discusses the Smith Chart approach to the design of a matching network containing two 50Ω transmission lines connected in series and a single shunt capacitor placed in-between them.



RF & MW →

Example 8-7: Design of a matching network with lumped and distributed components

Design a matching network that transforms the load $Z_L = (30 + j10)\Omega$ to an input impedance $Z_{in} = (60 + j80)\Omega$. The matching network should contain only two series transmission lines and a shunt capacitance. Both transmission lines have a 50Ω characteristic line impedance, and the frequency at which matching is desired is $f = 1.5$ GHz.

Solution: The first step involves identifying the normalized load impedance $z_L = 0.6 + j0.2$ as a point in the Smith Chart. We can then draw a SWR circle that indicates the combined impedance of the load connected to the 50Ω transmission line. The position on the SWR circle is determined by the length of the transmission line, as investigated in Chapter 3.

The second step requires plotting a SWR circle that passes through the normalized input impedance point $z_{in} = 1.2 + j1.6$ shown in Figure 8-20.

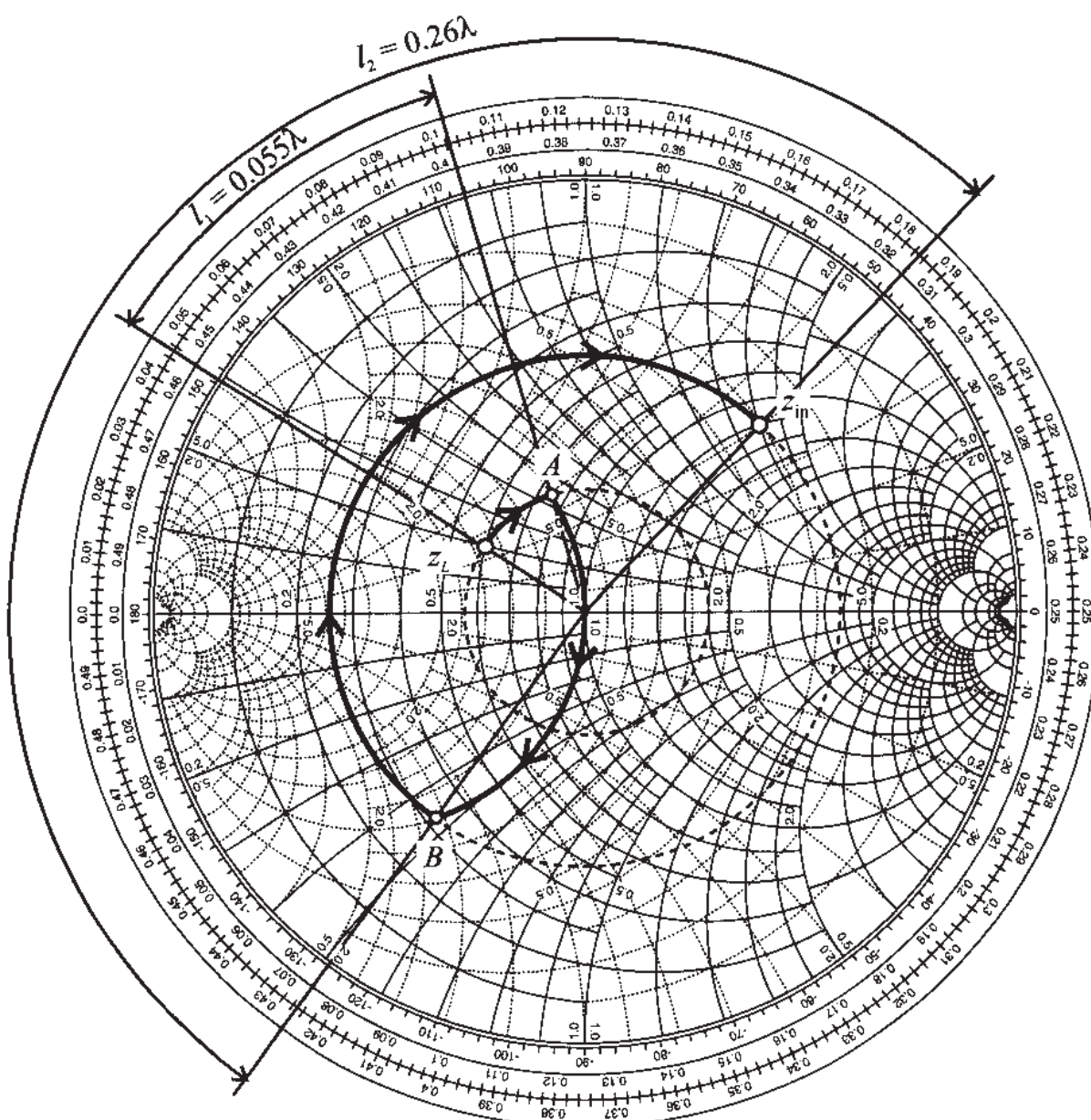


Figure 8-20 Design of the distributed matching network for Example 8-7.

The choice of the point from which we transition from the load SWR circle to the input SWR circle can be made arbitrarily. In Figure 8-20 the point A is chosen, which approximately corresponds to a normalized admittance value of $y_A = 1 - j0.6$. The addition of the parallel capacitor results in the movement along the circle of constant conductance $g = 1$ and transforms the impedance from point A to point B on the input SWR circle of the Smith Chart. From point B an impedance transformation is required along the constant SWR circle by adding a series connected transmission line.

As a final step, the electrical length of the transmission lines must be determined. This can be done by reading the two lengths l_1 ,

l_2 from the so-called WTG (wavelength toward generator) scale displayed on the outer perimeter of the Smith Chart (see Figure 8-20). The resulting circuit schematics for the matching network is shown in Figure 8-21

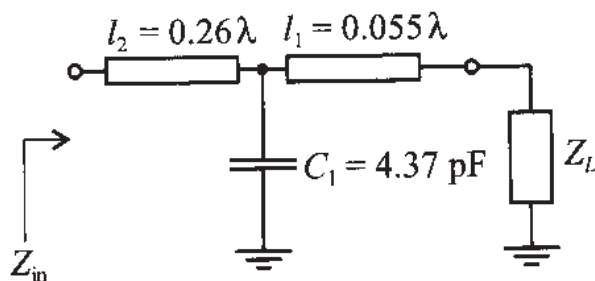


Figure 8-21 Matching network combining series transmission lines and shunt capacitance.

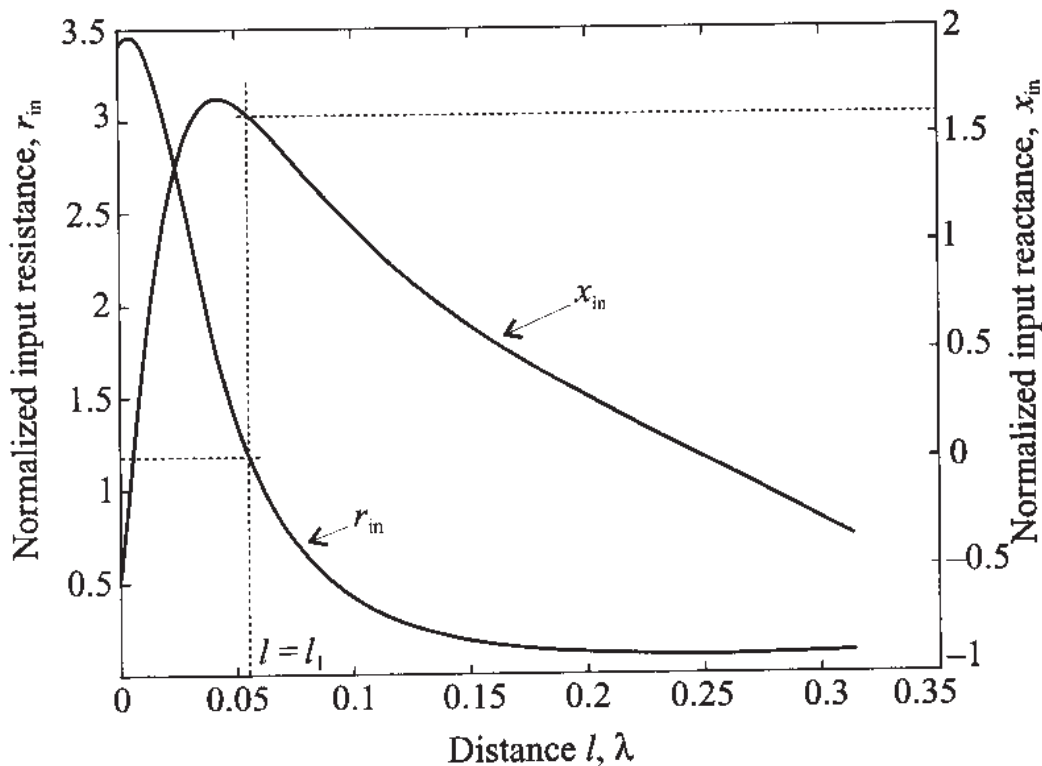


Figure 8-22 Input impedance as a function of the position of the shunt capacitor in Example 8-7.

It is interesting to investigate the tuning capability range for this circuit configuration. Figure 8-22 shows the dependency of the real r_{in} and imaginary x_{in} parts of the input impedance as a function of the distance l between the load and the capacitor location. In other words, the total length $l_1 + l_2$ is kept fixed and the placement of the capacitor is varied from the load end to the beginning of the

network (i.e., $0 \leq l \leq l_1 + l_2$). The dashed lines indicate the original design. It is noticed that x_{in} undergoes the expected inductive (positive values) to capacitive (negative values) transition.

In this example we have designed a combined matching network that involves both distributed (transmission lines) and a lumped (capacitor) element. These types of networks have rather large tuning capabilities, but are very sensitive to the placement of the capacitor along the transmission line. Even small deviations from the target location result in drastic changes in the input impedance.

8.2.2 Single-Stub Matching Networks

The next logical step in the transition from lumped to distributed element networks is the complete elimination of all lumped components. This is accomplished by employing open- and/or short-circuit stub lines.

In this section we consider matching networks that consist of a series transmission line connected to a parallel open-circuit or short-circuit stub. Let us investigate two topologies: The first one involves a series transmission line connected to the parallel combination of load and stub, as shown in Figure 8-23(a), and the second involves a parallel stub connected to the series combination of the load and transmission line, as depicted in Figure 8-23(b).

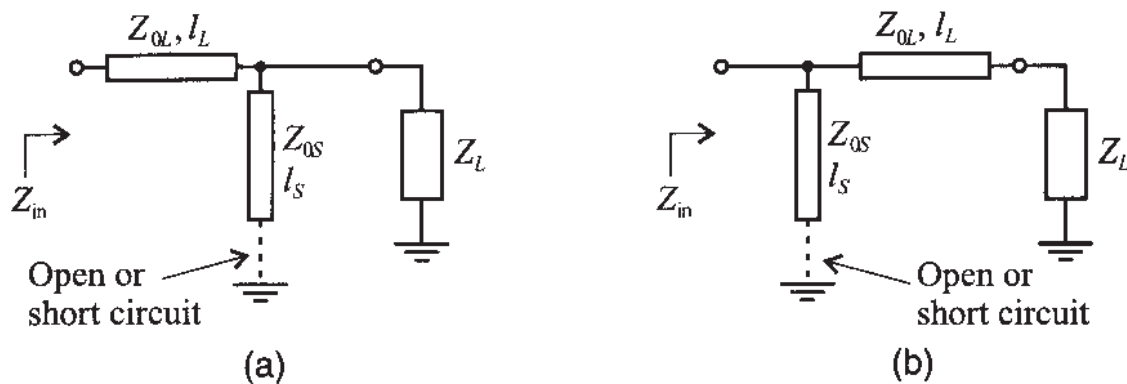
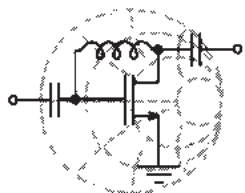


Figure 8-23 Two topologies of single-stub matching networks.

The matching networks in Figure 8-23 possess four adjustable parameters: length l_S and characteristic impedance Z_{0S} of the stub, and length l_L and characteristic impedance Z_{0L} of the transmission line.

Example 8-8 demonstrates the design procedure for the matching network topology shown in Figure 8-23(a) with the characteristic impedances of both stub Z_{0S} and transmission line Z_{0L} fixed to the same arbitrary value Z_0 and their electrical length variable to meet the particular input impedance requirement.



RF & MW

Example 8-8: Single-stub matching network design with fixed characteristic impedances

For a load impedance of $Z_L = (60 - j45)\Omega$, design two single-stub matching networks that transform the load to a $Z_{in} = (75 + j90)\Omega$ input impedance. Assume that both stub and transmission line in Figure 8-23(a) have a characteristic impedance of $Z_0 = 75 \Omega$.

Solution: The basic concept is to select the length l_S of the stub such that it produces a susceptance B_S sufficient to move the load admittance $y_L = 0.8 + j0.6$ to the SWR circle that passes through the normalized input impedance point $z_{in} = 1 + j1.2$, as illustrated in Figure 8-24.

We notice that the input SWR circle associated with $z_{in} = 1 + j1.2$ intersects the constant conductance circle $g = 0.8$ in two points (at $y_A = 0.8 + j1.05$ and at $y_B = 0.8 - j1.05$) suggesting two possible solutions. The corresponding susceptance values for the stub are $jb_{SA} = y_A - y_L = j0.45$ and $jb_{SB} = y_B - y_L = -j1.65$, respectively. In the first case, the length of an open-circuit stub can be found in the Smith Chart by measuring the length l_{SA} , starting from the $y = 0$ point (open circuit) and moving along the outer perimeter of the Smith Chart $g = 0$ toward the generator (clockwise) to the point where $y = j0.45$. The length for this case is $l_{SA} = 0.067\lambda$. The open-circuit stub can be replaced by a short-circuit stub if its length is increased by a quarter wavelength. Such a substitution may become necessary if a coaxial cable is used because of excessive radiation losses due to the large cross-sectional area. In printed circuit design, open-circuit stubs are sometimes preferred because they eliminate the deployment of a via,

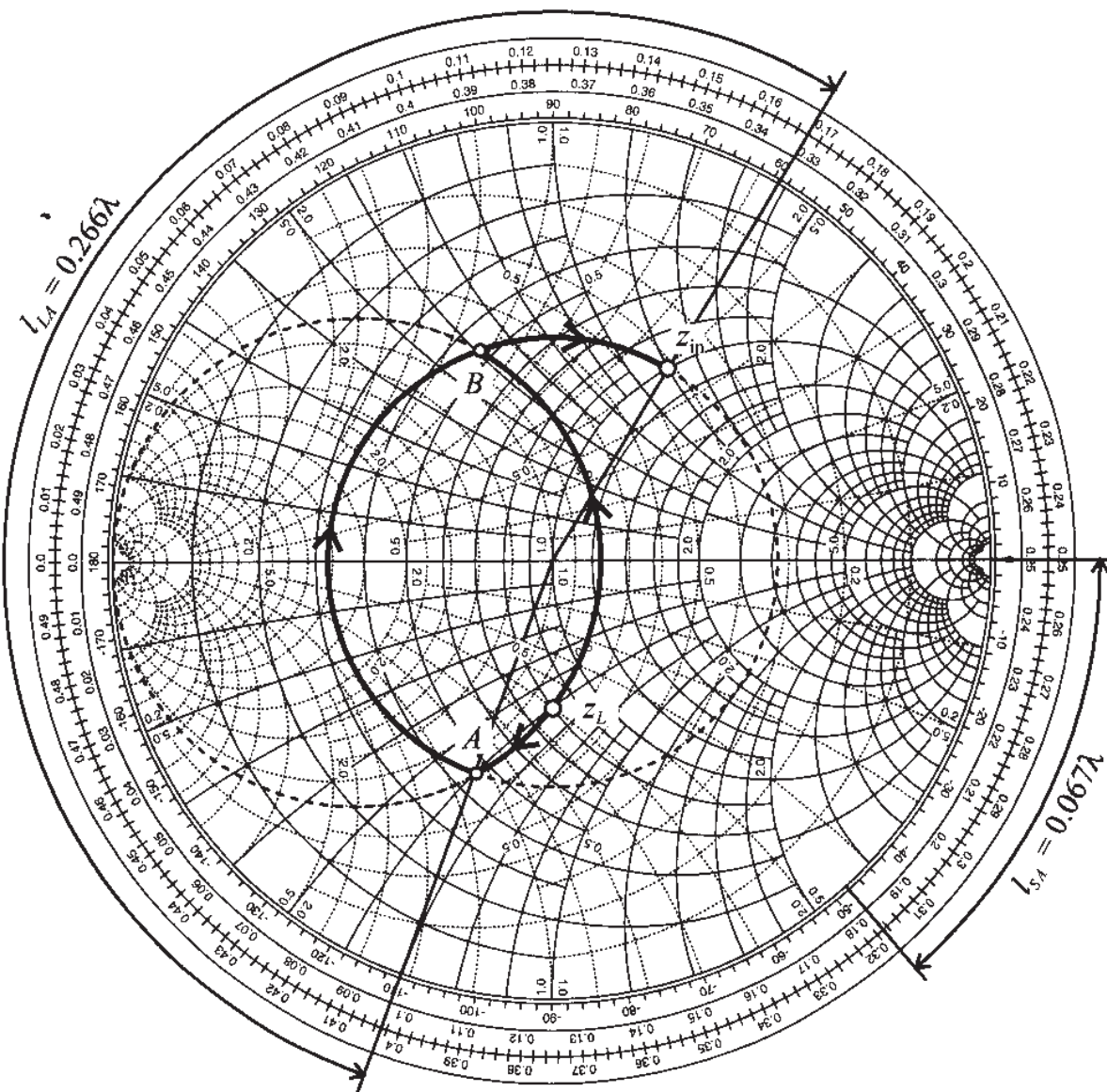


Figure 8-24 Smith Chart design for the single-stub matching network based on Example 8-8.

which is otherwise necessary to obtain the ground connection for a short-circuit stub.

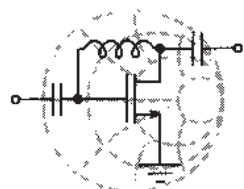
Similar to the first solution, b_{SB} yields the length $l_{SB} = 0.337\lambda$ for the open-circuit stub, and $l_{SB} = 0.087\lambda$ for the short-circuit stub. For this case we also notice that creating a short-circuit stub requires a shorter length than an open-circuit stub. This is due to the fact that the open-circuit stub models a negative susceptance.

The length of the series transmission line segment is found in the same way as described in Example 8-7 and is equal to

$l_{LA} = 0.266\lambda$ for the first solution and $l_{LB} = 0.07\lambda$ for the second solution.

A circuit designer often has to minimize the size of the circuit board and therefore must be concerned about employing the shortest possible transmission line segments. Depending on the impedance requirements, this can either be an open- or short-circuit stub section.

In the next example we illustrate the generic design procedure for the matching network topology shown in Figure 8-23(b). Unlike the previous example, we now fix the lengths of both the stub and the transmission line segment but vary their characteristic impedances. In a microstrip line circuit design this is typically accomplished by changing the width of the lines.



RF & MW →

Example 8-9: Design of a single-stub matching network using transmission lines with different characteristic impedances

Using the matching network topology shown in Figure 8-23(b), choose the characteristic impedances of the stub and transmission line such that the load impedance $Z_L = (120 - j20)\Omega$ is transformed into the input impedance $Z_{in} = (40 + j30)\Omega$. Assume that the length of the transmission line is $l_L = 0.25\lambda$ and the stub has the length of $l_S = 0.375\lambda$. Furthermore, determine whether a short-circuit or an open-circuit stub is necessary for this circuit.

Solution: The combined impedance Z_1 of the series connection of the load impedance with the transmission line can be computed using the formula for the quarter-wave transformer:

$$Z_1 = Z_{0L}^2 / Z_L \quad (8.17)$$

The addition of the open-circuit stub results in an input admittance of

$$Y_{\text{in}} = Y_1 + jB_S \quad (8.18)$$

where $Y_1 = Z_1^{-1}$ is the admittance of the previously computed series combination of load impedance and transmission line and $jB_S = \pm jZ_{0S}^{-1}$ is the susceptance of the stub. The “plus” or “minus” signs correspond to either a short-circuit or an open-circuit stub.

Combining (8.17) and (8.18), we find

$$G_{\text{in}} = R_L/Z_{0L}^2 \quad (8.19a)$$

$$B_{\text{in}} = X_L/Z_{0L}^2 \pm Z_{0S}^{-1} \quad (8.19b)$$

where we have used the input admittance and load impedance representation in terms of their real and imaginary components: $Y_{\text{in}} = G_{\text{in}} + jB_{\text{in}}$, $Z_L = R_L + jX_L$.

Using (8.19a), we find the characteristic impedance of the transmission line to be

$$Z_{0L} = \sqrt{\frac{R_L}{G_{\text{in}}}} = \sqrt{\frac{120}{0.016}} = 86.6 \Omega$$

Substituting the obtained value into (8.19b), we find that the “minus” sign should be used; that is, we need to implement an open-circuit stub with a characteristic impedance of

$$Z_{0S} = \frac{1}{X_L/Z_{0L}^2 - B_{\text{in}}} = 107.1 \Omega$$

This design approach is very easy to implement as long as the characteristic impedance stays within reasonable limits ranging approximately from 20 to 200 Ω.

In practical realizations single-sided unbalanced stubs are often replaced by the balanced design, as shown in Figure 8-25.

Naturally, the combined susceptance of the parallel connection of stubs *ST1* and *ST2* has to be equal to the susceptance of the unbalanced stub. Therefore, the susceptance of each side of the balanced stub must be equal to half of the susceptance of the

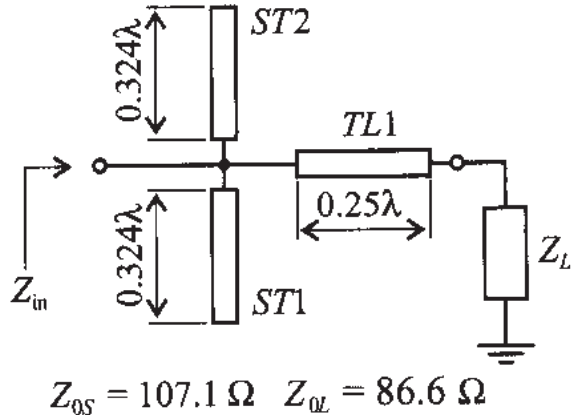


Figure 8-25 Balanced stub design for Example 8-9.

unbalanced stub. We note that the length l_{SB} of each side does not scale linearly. In other words, the length of the balanced stub is not half of the length of the unbalanced stub l_S . Rather, it has to be computed as

$$l_{SB} = \frac{\lambda}{2\pi} \tan^{-1} \left(2 \tan \frac{2\pi l_S}{\lambda} \right) \quad (8.20)$$

for open-circuit stub, or

$$l_{SB} = \frac{\lambda}{2\pi} \tan^{-1} \left(\frac{1}{2} \tan \frac{2\pi l_S}{\lambda} \right) \quad (8.21)$$

for short-circuit stub. This result can also be found graphically by using the Smith Chart.

8.2.3 Double-Stub Matching Networks

The single-stub matching networks in the previous section are quite versatile and allow matching between any input and load impedances, so long as they have a nonzero real part. One of the main drawbacks of such matching networks is that they require a variable-length transmission line between stub and input port, or between stub and load impedance. Usually this does not pose a problem for fixed networks, but it may create difficulties for variable tuners. In this section we examine matching networks that overcome this drawback by incorporating a second stub. The general topology of such a network that matches an arbitrary load impedance to an input impedance $Z_{in} = Z_0$ is shown in Figure 8-26.

In double-stub matching networks two short- or open-circuit stubs are connected in parallel with a fixed-length transmission line placed in between. The length l_2 of this line is usually chosen to be one-eighth, three-eighth, or five-eighth of a wavelength. The

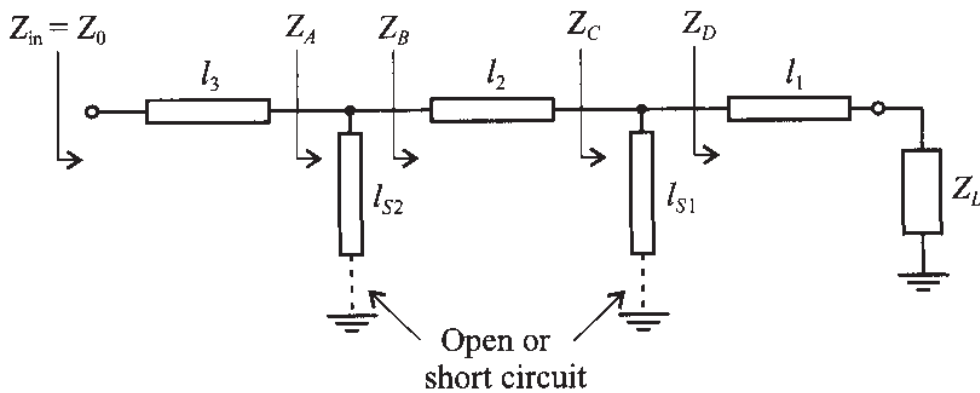


Figure 8-26 Double-stub matching network arrangement.

three-eighth and five-eighth wavelength spacings are typically employed in high-frequency applications to simplify the tuner construction.

Let us assume for our subsequent discussion that the length of the line segment between the two stubs is $l_2 = (3/8)\lambda$. To facilitate the analysis we start from the input side of the tuner and work backward to the load end.

For a perfect match it is required that $Z_{in} = Z_0$ and therefore $y_A = 1$. Since it is assumed that the lines are lossless, the normalized admittance $y_B = y_A - jb_{S2}$ is located somewhere on the constant conductance circle $g = 1$ in the Smith Chart. Here b_{S2} is the susceptance of the stub and l_{S2} is the associated length. For an $l_2 = (3/8)\lambda$ line the $g = 1$ circle is rotated by $2\beta l_2 = 3\pi/2$ radians or 270° toward the load (i.e., in counter-clockwise direction, as depicted in Figure 8-27). The admittance y_C (being the series connection of Z_L with line l_1 in parallel to stub l_{S1}) needs to reside on this rotated $g = 1$ circle (called the y_C circle) in order to ensure matching.

By varying the length of the l_{S1} stub we can transform point y_D in such a way that the resulting y_C is indeed located on the rotated $g = 1$ circle. This procedure can be done for any load impedance except for the case when point y_D (i.e., the series connection of Z_L and line l_1) is located inside the $g = 2$ circle. This represents the forbidden region that has to be avoided. To overcome this problem in practical applications, commercial double-stub tuners usually have input and output transmission lines whose lengths are related according to $l_1 = l_3 \pm \lambda/4$. In this case, if a particular load impedance cannot be matched, one simply connects the load to the opposite end of the tuner, which moves y_D out of the forbidden region.

The following example demonstrates the computation of the stub lengths to achieve matching for a specific load impedance.

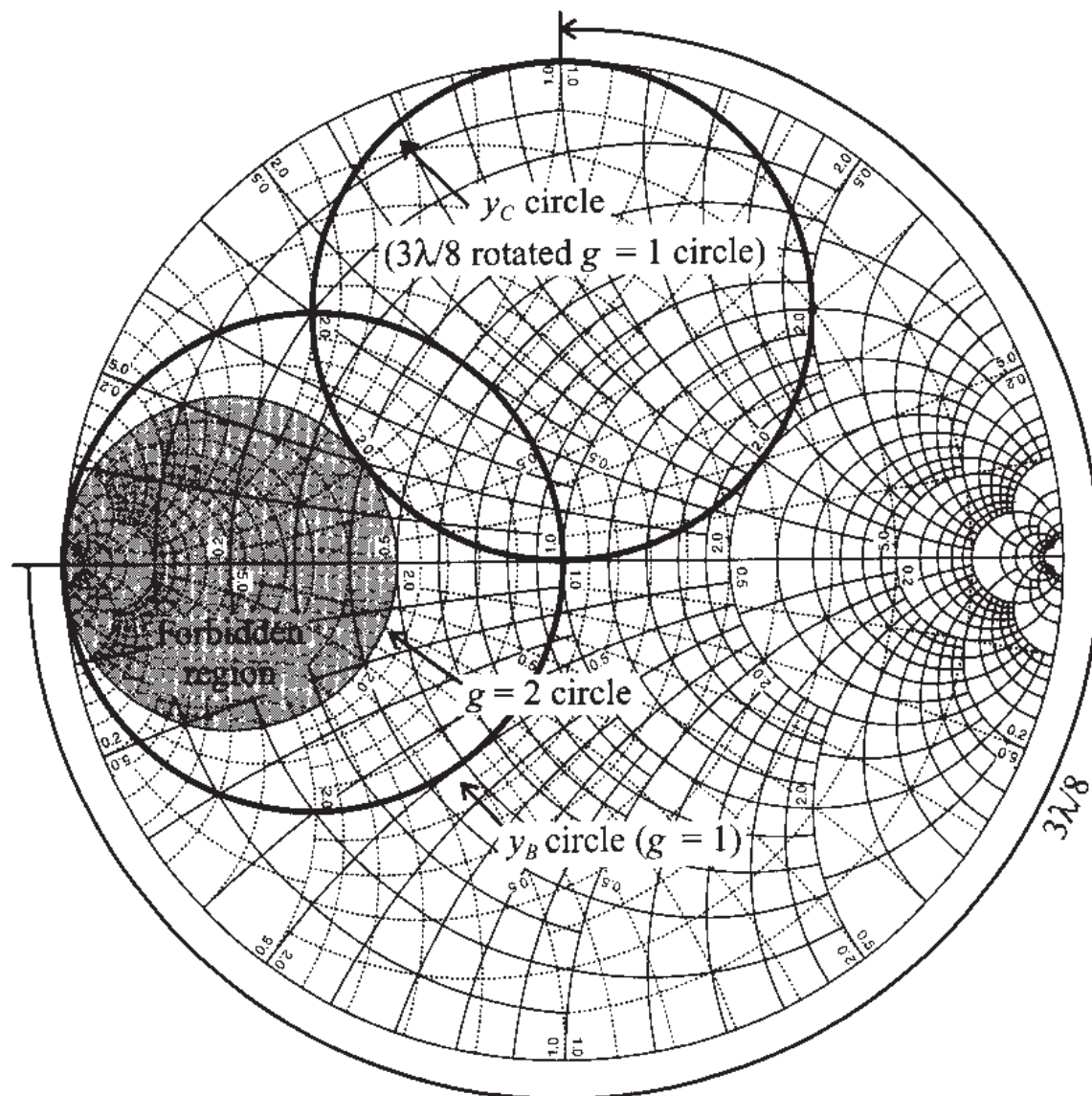
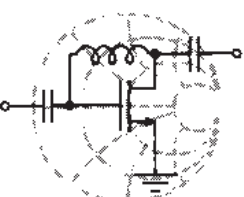


Figure 8-27 Smith Chart analysis of a double-stub matching network shown in Figure 8-26.



RF & MW →

Example 8-10: Design of a double-stub matching network

It is assumed that in the double-stub matching network shown in Figure 8-26 the lengths of the transmission lines are $l_3 = l_2 = 3\lambda/8$ and $l_1 = \lambda/8$. Find the lengths of the short-circuit stubs that match the load impedance $Z_L = (50 + j50)\Omega$ to a 50Ω input impedance. The characteristic line impedance for all components is $Z_0 = 50 \Omega$.

Solution: First the normalized admittance y_D has to be determined and checked that it does not fall inside the forbidden region. Using the Smith Chart (see Figure 8-28), we find $y_D = 0.4 + j0.2$. Since $g_D < 2$, we are assured that the admittance y_D does not fall into the forbidden region. Next we plot the rotated $g = 1$ circle as explained previously. This allows us to fix the intersection of the rotated $g = 1$ circle with the constant conductance circle that passes through the point y_D . The intersection point gives us the value of y_C . In fact, there are two intersection points that yield two possible solutions. If we choose $y_C = 0.4 - j1.8$, then the susceptance of the first stub should be $jb_{S1} = y_C - y_D = -j2$, which permits us to determine the length of the first short-circuit stub: $l_{S1} = 0.074\lambda$.

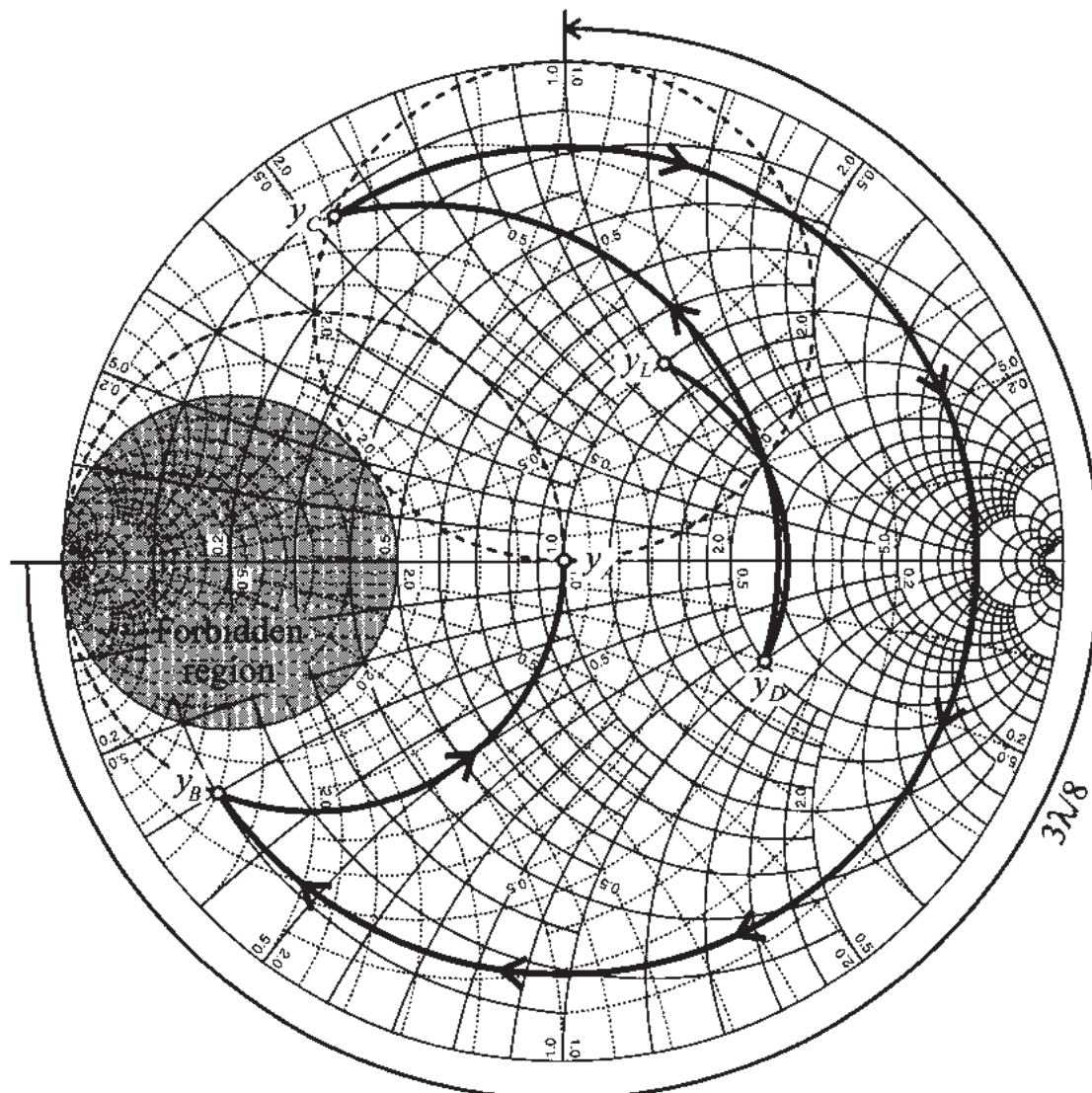


Figure 8-28 Double-stub tuning network design for Example 8-10.

Rotating y_C by $l_2 = 3\lambda/8$ we find $y_B = 1 + j3$, which means that we have to make the susceptance of the second stub equal to $jb_{S2} = -j3$ so that $y_{in} = y_A = 1$. Using the Smith Chart, we find that the length of the second stub is $l_{S2} = 0.051\lambda$.

In some practical realizations the stubs are replaced by varactor diodes. This allows an electronic tuning of the diode capacitances and thus the shunt admittances.

8.3 Amplifier Classes of Operation and Biasing Networks

An indispensable building block in any RF circuit is the active or passive biasing network. The purpose of biasing is to provide the appropriate quiescent point for the active devices under specified operating conditions and maintain a constant setting irrespective of transistor parameter variations and temperature fluctuations.

In the following section we introduce a general analysis of the different classes of amplifier operation. This will enable us to develop an understanding of how BJT and FET need to be appropriately biased.

8.3.1 Classes of Operation and Efficiency of Amplifiers

Depending on the application for which the amplifier is designed, specific bias conditions are required. There are several classes of amplifier operation that describe the biasing of an active device in an RF circuit.

In Figure 8-29 the transfer function characteristic of an ideal transistor is displayed. It is assumed that the transistor does not reach saturation or breakdown regions and in the linear operating region the output current is proportional to the input voltage. The voltage V^* corresponds either to the threshold voltage in case of FETs or the base-emitter built-in potential in case of BJTs.

The distinction between different classes of operation is made based upon the so-called **conduction angle**, which indicates the portion of the signal cycle when the current is flowing through the load. As depicted in Figure 8-29(a), in **Class A** operation the current is present during the entire output signal cycle. This corresponds to a $\Theta_A = 360^\circ$ conduction angle. If the transfer characteristic of the transistor in the linear region is close to that of a linear function, then the output signal is an amplified replica of the input signal without suffering any distortion. In practical circuits, however,

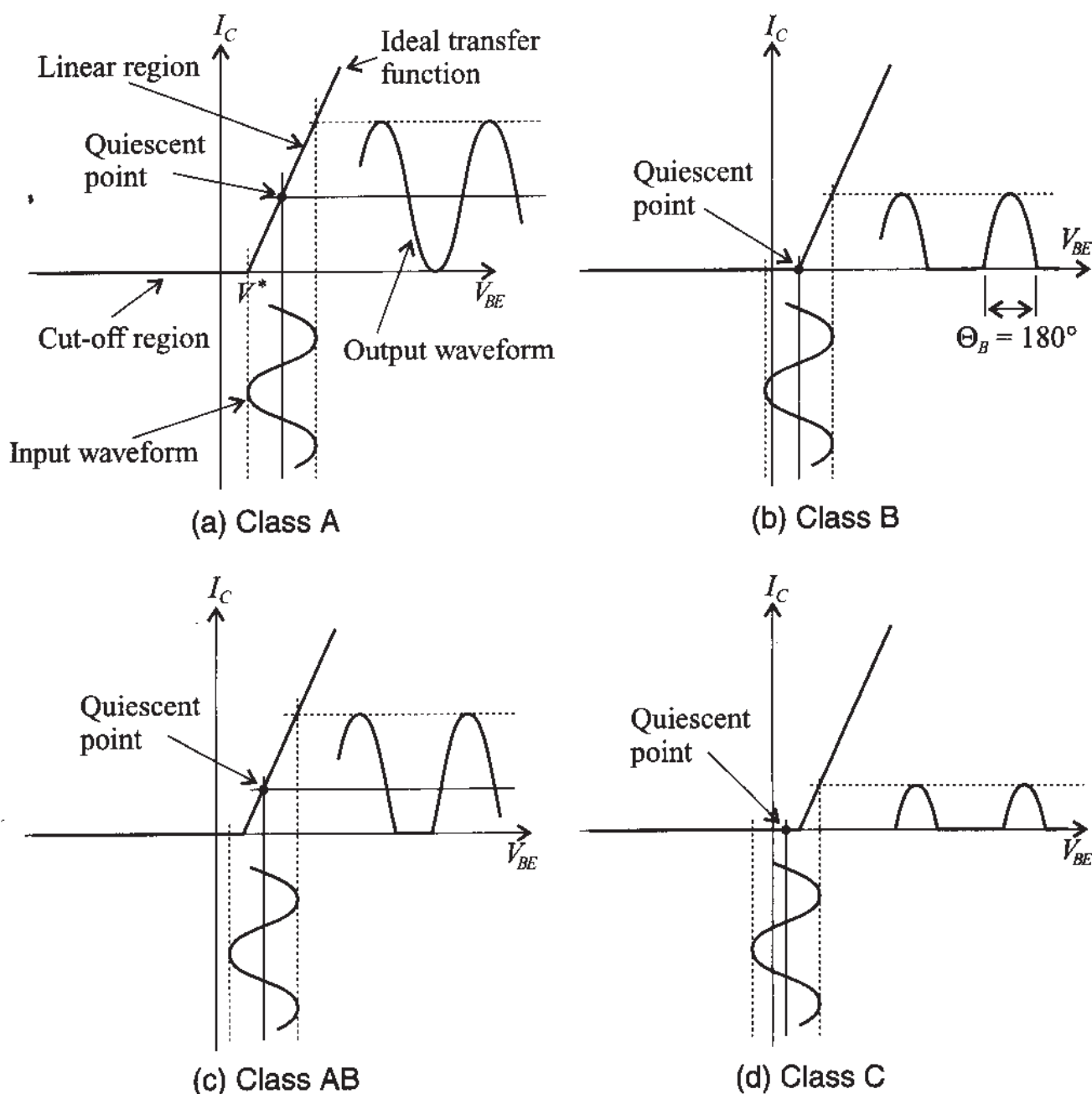


Figure 8-29 Various classes of amplifier operation.

there is always a certain degree of nonlinearity present which results in a distorted output signal of the amplifier.

In **Class B** [Figure 8-29(b)] the current is present during only half of the cycle, corresponding to a $\Theta_B = 180^\circ$ conduction angle. During the second half of the cycle, the transistor is in the cut-off region and no current flows through the device. **Class AB** [Figure 8-29(c)] combines the properties of the classes A and B and has a conduction angle Θ_{AB} ranging from 180° to 360° . This type of amplifier is typically employed when a high-power “linear” amplification of the RF signal is required.

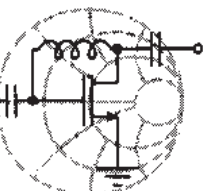
In a **Class C** amplifier [Figure 8-29(d)] we have a nonzero current for less than half of the cycle (i.e., the conduction angle is $0 < \Theta_C < 180^\circ$). This results in maximum distortion of the output signal.

A logical question that arises is why are not all amplifiers operated in Class A since this mode delivers the least signal distortion? The answer is directly linked to the amplifier efficiency. Efficiency, η , is defined as the ratio of the average RF power P_{RF} delivered to the load over the average power P_S supplied by the source, and is usually measured in percent:

$$\eta = \frac{P_{RF}}{P_S} 100\% \quad (8.22)$$

The theoretical maximum efficiency of the Class A amplifier is only 50%, but the efficiency of Class C can reach values close to 100%. Fifty percent efficiency of Class A amplifiers means that half of the power supplied by the source is dissipated as heat. This situation may not be acceptable in portable communication systems where most devices are battery operated. In practical applications, designers usually choose the class of operation that gives maximum efficiency but still preserves the informational content of the RF signal.

In the following example we derive the maximum theoretical efficiency η of the amplifier as a function of conduction angle.



RF & MW

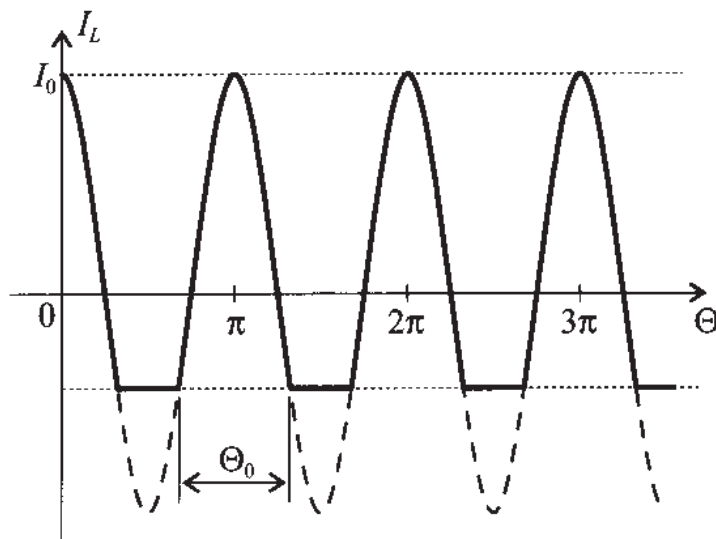
Example 8-11: Amplifier efficiency computation

Derive the general expression for the amplifier efficiency η as a function of conduction angle Θ_0 . List the values of η for both Class A and Class B amplifiers.

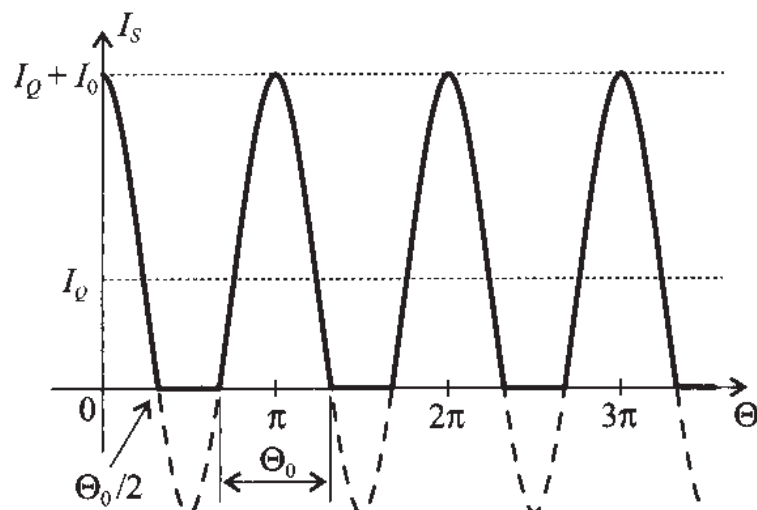
Solution: The electrical current through the load for a conduction angle of Θ_0 has a waveform shown in Figure 8-30(a), where the cosine current amplitude is given by I_0 .

Similarly, the power supply current I_S has a maximum value of I_0 plus the quiescent current I_Q :

$$I_S = I_Q + I_0 \cos \Theta \quad (8.23)$$



(a) Load current waveform at the output of the transistor



(b) Corresponding power supply current waveform

Figure 8-30 Load and power supply current waveforms as a function of conduction angle.

The value of the quiescent current necessary to ensure the specified conduction angle Θ_0 can be found from (8.23) by setting I_S to zero at $\Theta = \Theta_0/2$:

$$I_Q = -I_0 \cos(\Theta_0/2) \quad (8.24)$$

The average power supply current is then computed as an integral over the conduction angle ranging between the limits of $\Theta = -\Theta_0/2$ and $\Theta = \Theta_0/2$; that is,

$$\langle I_S \rangle = \frac{1}{2\pi} \int_{-\Theta_0/2}^{\Theta_0/2} I_S d\Theta = -\frac{I_0}{2\pi} \left[\Theta_0 \cos\left(\frac{\Theta_0}{2}\right) - 2 \sin\left(\frac{\Theta_0}{2}\right) \right] \quad (8.25)$$

Thus, the average power from the power supply is

$$P_S = V_{CC} \langle I_S \rangle = -\frac{I_0 V_{CC}}{2\pi} \left[\Theta_0 \cos\left(\frac{\Theta_0}{2}\right) - 2 \sin\left(\frac{\Theta_0}{2}\right) \right] \quad (8.26)$$

where V_{CC} is the supply voltage.

Since the voltage on the load changes together with the current, the average RF power is computed as an integral of the product of load current and load voltage:

$$P_{RF} = \frac{1}{2\pi} \int_{-\Theta_0/2}^{\Theta_0/2} I_0 V_{CC} \cos^2 \Theta d\Theta = \frac{I_0 V_{CC}}{4\pi} (\Theta_0 - \sin \Theta_0) \quad (8.27)$$

Dividing (8.27) by (8.26), we find an amplifier efficiency

$$\eta = \frac{\Theta_0 - \sin \Theta_0}{2[\Theta_0 \cos(\Theta_0/2) - 2 \sin(\Theta_0/2)]} \quad (8.28)$$

where the conduction angle Θ_0 is measured in radians.

The graph of η as a function of the conduction angle Θ_0 is shown in Figure 8-31.

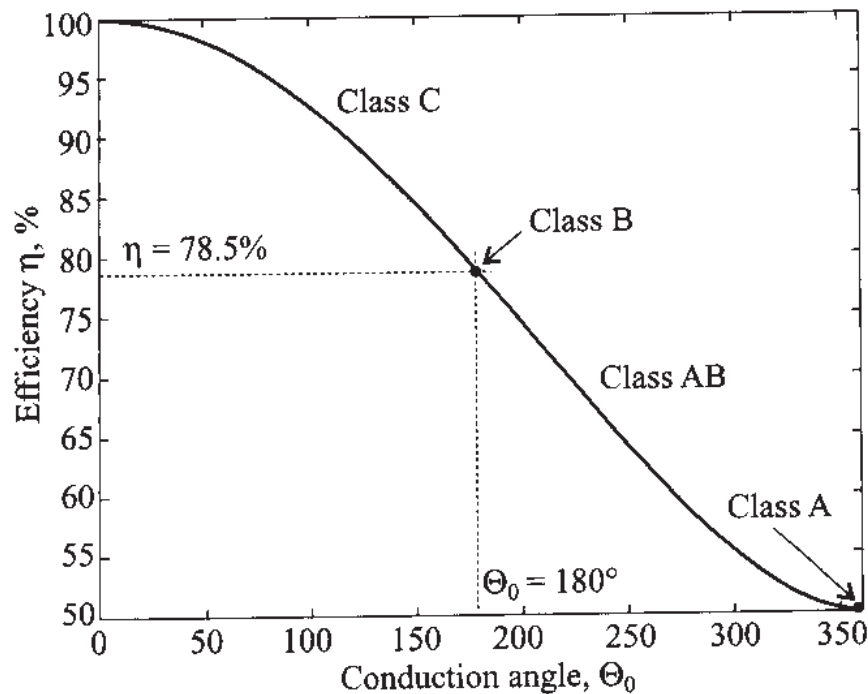


Figure 8-31 Maximum theoretical efficiency of an ideal amplifier as a function of conduction angle.

Substituting $\Theta_0 = 2\pi$ into (8.28), we find that the efficiency of a Class A amplifier is indeed 50%. To determine the efficiency of a Class B amplifier, we simply use the conduction angle $\Theta_0 = \pi$ in (8.28), which yields

$$\eta_B = -\frac{\pi - \sin \pi}{2[\pi \cos(\pi/2) - 2 \sin(\pi/2)]} = \frac{\pi}{4} = 0.785$$

That is, Class B yields an efficiency of 78.5%.

Efficiency is an important design consideration when dealing with low power consumption, as required, for instance, in personal communication systems, where battery lifetime must be maximized.

8.3.2 Bipolar Transistor Biasing Networks

There are generally two types of biasing networks: passive and active. **Passive (or self-biased)** networks are the simplest type of biasing circuits and usually incorporate a resistive network, which provides the appropriate voltages and currents for the RF transistor. The main disadvantages of such networks are that they are very sensitive to changes in transistor parameters and that they provide poor temperature stability. To compensate for these drawbacks **active biasing** networks are often employed.

In this section we consider several network configurations for biasing RF BJTs. Two possible topologies are shown in Figure 8-32.

The combination of the blocking capacitor C_B and the RFC connected to the base and collector terminals of the transistor in Figure 8-32 serve the purpose to isolate the

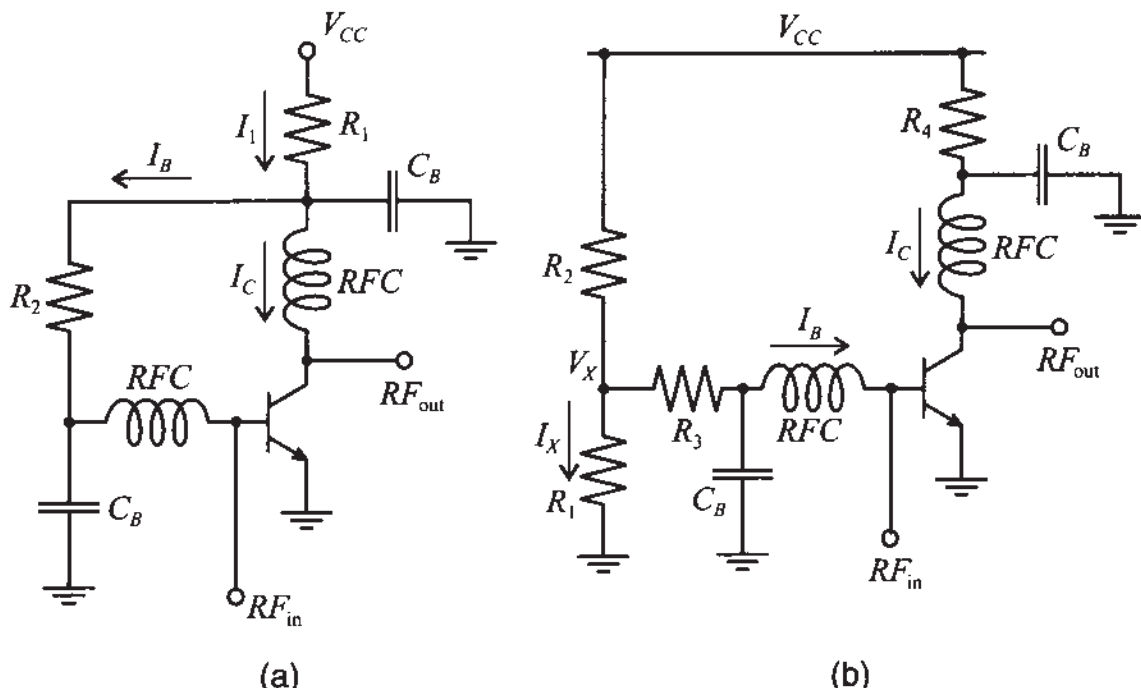
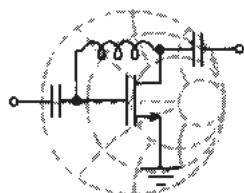


Figure 8-32 Passive biasing networks for an RF BJT in common-emitter configuration.

RF signal from the DC power source. At high frequencies, the RFCs are usually replaced by quarter wave transmission lines that convert the short-circuit condition on the C_B side to an open-circuit condition on the transistor side.

The following example discusses how to compute the resistors for the two biasing networks shown in Figure 8-32.



RF & MW →

Example 8-12: Design of passive biasing networks for a BJT in common-emitter configuration

Design biasing networks according to Figures 8-32(a) and (b) for the BJT settings of $I_C = 10 \text{ mA}$, $V_{CE} = 3 \text{ V}$, and $V_{CC} = 5 \text{ V}$. Assume that the transistor has a $\beta = 100$ and $V_{BE} = 0.8 \text{ V}$.

Solution: As seen in Figure 8-32(a), the current I_1 through resistor R_1 is equal to the sum of the collector and base currents. Since $I_B = I_C/\beta$, we obtain

$$I_1 = I_C + I_B = I_C(1 + \beta^{-1}) = 10.1 \text{ mA}$$

The value of R_1 can be found as

$$R_1 = \frac{V_{CC} - V_{CE}}{I_1} = 198 \Omega$$

Similarly, the base resistor R_2 is computed as

$$R_2 = \frac{V_{CE} - V_{BE}}{I_B} = \frac{V_{CE} - V_{BE}}{I_C/\beta} = 22 \text{ k}\Omega$$

For the circuit in Figure 8-32(b) the situation is slightly more complicated. Here we have the freedom of choosing the value of the voltage potential V_X and the current I_X through the voltage divider resistor R_2 . Arbitrarily setting V_X to 1.5 V, we determine the base resistor R_3 to be

$$R_3 = \frac{V_X - V_{BE}}{I_B} = \frac{V_X - V_{BE}}{I_C/\beta} = 7 \text{ k}\Omega$$

The value of I_X is usually chosen to be 10 times larger than I_B . Therefore, $I_X = 10I_B = 1 \text{ mA}$ and the values of the resistances for the voltage divider are computed as

$$R_1 = \frac{V_X}{I_X} = 1.5 \text{ k}\Omega \text{ and } R_2 = \frac{V_{CC} - V_X}{I_X + I_B} = 3.18 \text{ k}\Omega$$

Finally, the collector resistor is found as

$$R_4 = (V_{CC} - V_{CE})/I_C = 200 \text{ }\Omega$$

The freedom of selecting particular voltages and currents is in practice restricted by the need to choose electric settings that result in standardized resistance values.

An example of an active biasing network for a BJT in common-emitter configuration is shown in Figure 8-33. Here we employ a low-frequency transistor Q_1 to provide the necessary base current for the RF transistor Q_2 . The resistor R_{E1} connected to the emitter of the transistor Q_1 improves stability of the quiescent point. If transistors Q_1 and Q_2 have the same thermal properties, then this biasing network also results in good temperature stability.

Example 8-13 illustrates the determination of the component values for the active biasing network depicted in Figure 8-33.

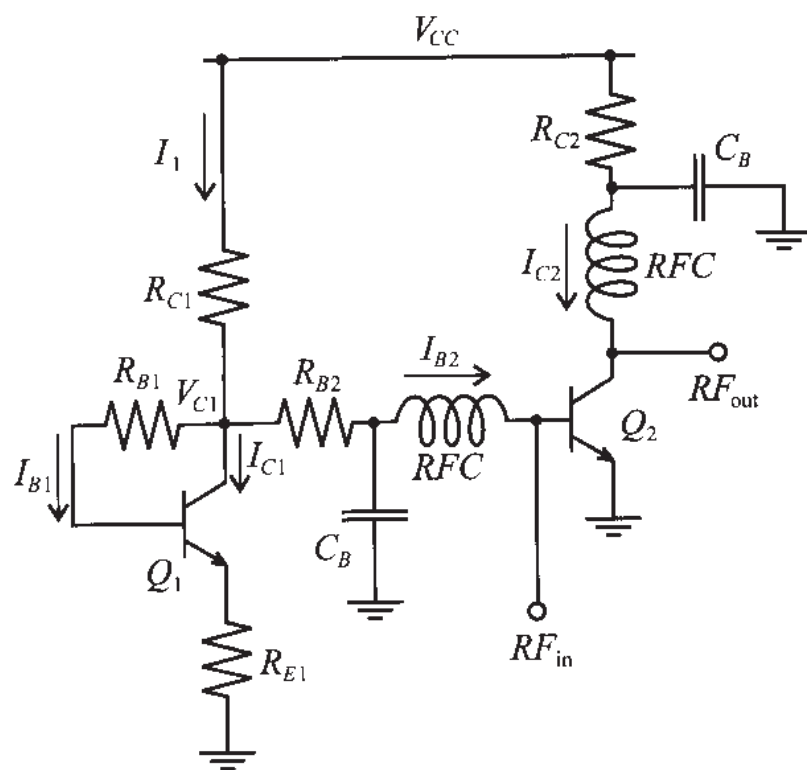
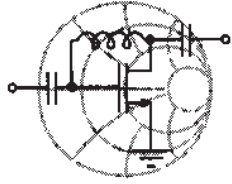


Figure 8-33 Active biasing network for a common-emitter RF BJT.



RF & MW →

Example 8-13: Design of an active biasing network for a BJT transistor in common-emitter configuration

Design a biasing network as shown in Figure 8-33 for $I_{C2} = 10 \text{ mA}$, $V_{CE2} = 3 \text{ V}$, and $V_{CC} = 5 \text{ V}$. Assume that both transistors have $\beta = 100$ and $V_{BE} = 0.8 \text{ V}$.

Solution: Similar to the previous example we have several degrees of freedom in this biasing network. First, we can pick the value for a voltage potential V_{C1} at the collector of transistor Q_1 . Second, we are free in our choice of the collector current through Q_1 . Since I_{B2} should not be affected by current fluctuations in I_{C1} , we choose I_{C1} such that $I_{C1} = 10I_{B2}$ (i.e., $I_{C1} = 1 \text{ mA}$). Then the current I_1 through resistor R_{C1} is composed of collector current I_{C1} and two base currents I_{B1} and I_{B2} ; that is,

$$I_1 = I_{C1} + I_{B1} + I_{B2} = I_{C1}(1 + \beta_1^{-1}) + I_{C2}/\beta_2 = 1.11 \text{ mA}$$

Assuming $V_{C1} = 3 \text{ V}$, we find

$$R_{B2} = \frac{V_{C1} - V_{BE2}}{I_{B2}} = 22 \text{ k}\Omega \text{ and } R_{C1} = \frac{V_{CC} - V_{C1}}{I_1} = 1.8 \text{ k}\Omega$$

Another degree of freedom is the choice of voltage V_{E1} at the emitter terminal of the transistor Q_1 . Setting V_{E1} to 1 V, we find

$$R_{B1} = \frac{V_{C1} - V_{BE1} - V_{E1}}{I_{B1}} = 120 \text{ k}\Omega$$

and

$$R_{E1} = \frac{V_{E1}}{I_{C1} - I_{B1}} = 1.11 \text{ k}\Omega$$

Finally, the collector resistor R_{C2} is determined to be

$$R_{C2} = (V_{CC} - V_{CE2})/I_{C2} = 200 \text{ }\Omega$$

Although active biasing offers a number of performance advantages over passive networks, certain disadvantages also arise:

specifically, additional circuit board space, possible layout complications, and added power requirements.

Another active biasing network for a BJT in common-emitter configuration is shown in Figure 8-34. Here diodes D_1 and D_2 provide a fixed reference for the voltage drop across the base-emitter junctions of both transistors. Resistor R_1 is used to adjust the biasing current to the base of transistor Q_1 and R_2 limits the range of this adjustment. Ideally, for temperature compensation, transistor Q_1 and one of the diodes should remain at ambient temperature, whereas the second diode should be placed on the same heat-sink as RF transistor Q_2 .

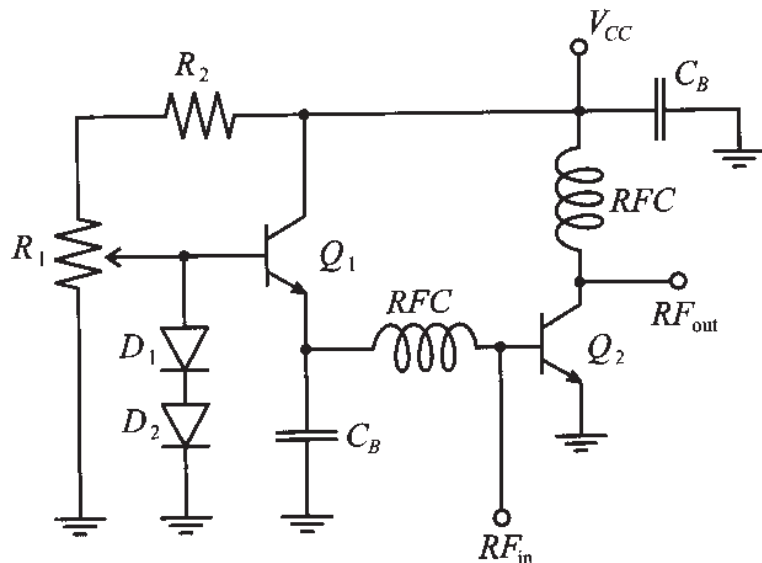


Figure 8-34 Active biasing network containing low-frequency transistor and two diodes.

As a final remark, it is important to point out that in all biasing networks the operational conditions (common-base, common-emitter, or common-collector) of the transistor at RF frequencies are entirely independent of the DC configuration. For instance, we can take an active biasing network, shown in Figure 8-33, and modify it for common-base RF operation, as seen in Figure 8-35.

At DC all blocking capacitors represent an open circuit and all RFCs behave like short circuits. Therefore, this biasing network can be redrawn as shown in Figure 8-36(a), indicating the common-emitter configuration. However, at RF frequency all blocking capacitors become short circuits and all RFCs behave like open circuits. This transforms the biasing network into a common-base mode, as depicted in Figure 8-36(b).

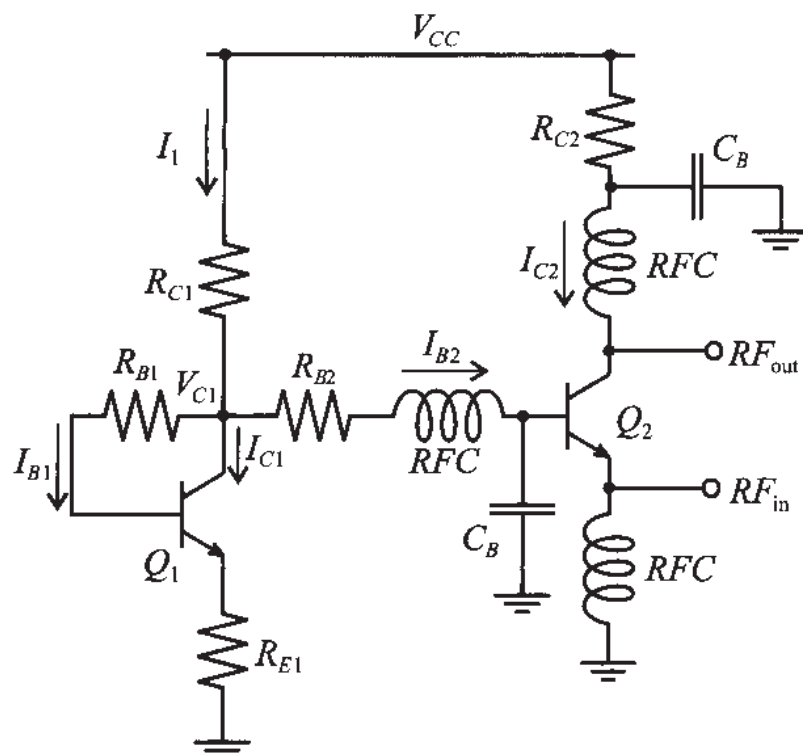


Figure 8-35 Modification of the active biasing network shown in Figure 8-33 for a common-base RF operation.

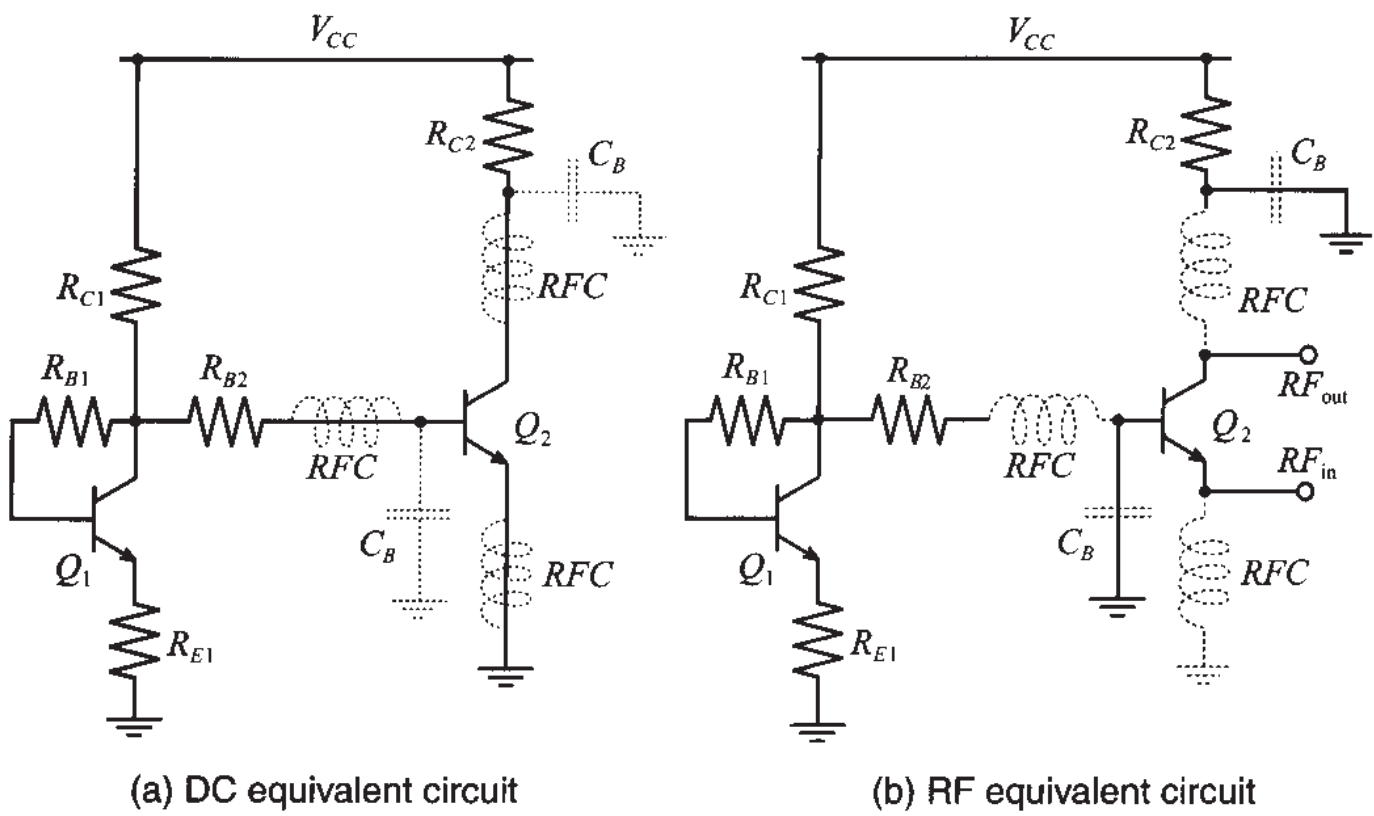


Figure 8-36 DC and RF equivalent circuits for the active biasing network in Figure 8-35.

8.3.3 Field Effect Transistor Biasing Networks

The biasing networks for field effect transistors are in many ways very similar to the BJT networks covered in the previous section. One key distinction is that MESFET usually require a negative gate voltage as part of the bias conditions.

The most basic passive bipolar biasing network for FETs is shown in Figure 8-37.

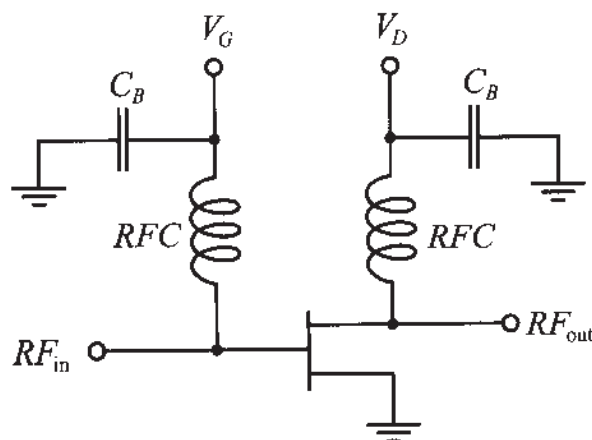


Figure 8-37 Bipolar passive biasing network for FETs.

The main disadvantage of such a network is the need of a bipolar power supply for $V_G < 0$ and $V_D > 0$. If such a bipolar power supply is unavailable one can resort to a strategy where instead of the gate, the source terminal of the transistor is biased. The gate in this case is grounded. Two examples of such networks are shown in Figure 8-38.

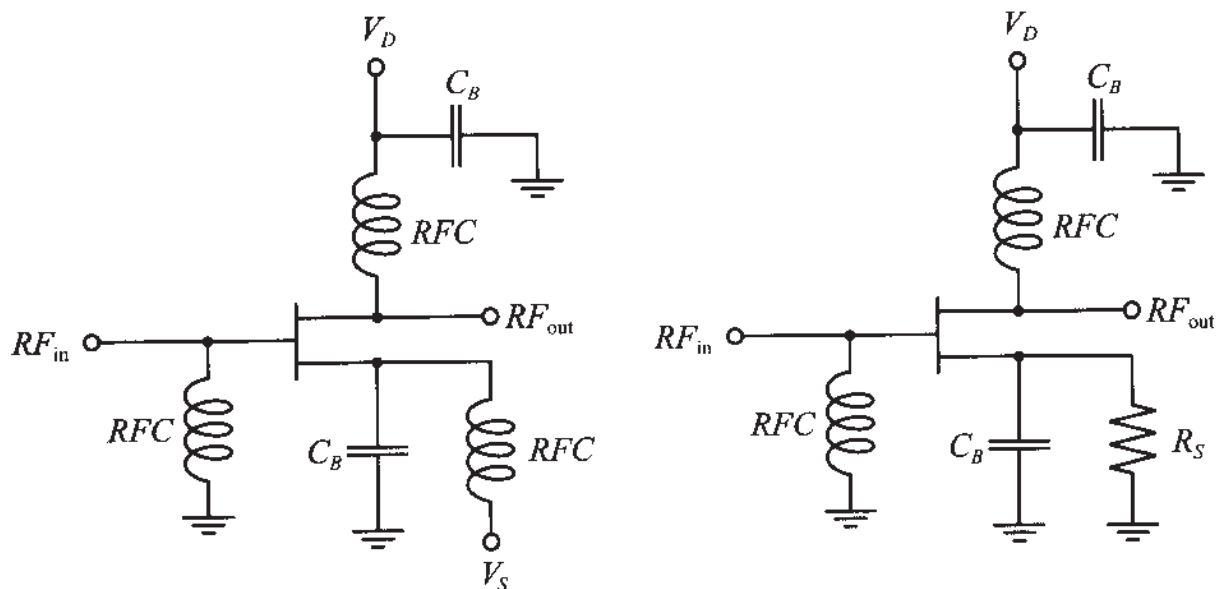


Figure 8-38 Unipolar passive biasing networks for FETs.

The temperature compensation of the FET biasing networks is typically accomplished through the use of thermistors.

8.4 Summary

The material covered in this chapter is geared toward providing an understanding of two key issues encountered in any RF/MW system: interfacing various components of different impedance values, and suitably biasing the active devices depending on their class of operation.

To ensure optimal power transfer between systems of different impedances, we investigate at first two-element L-type matching configurations. In the context of two-port network analysis, the conjugate complex matching requirement at the input and output ports results in optimal power transfer at a particular target frequency. The technique is simple and can be compared with the design of a bandpass or bandstop filter. Care must be exercised in selecting a suitable L-type network to avoid the forbidden regions for which a given load impedance cannot be matched to the desired input impedance. From the knowledge of the network transfer function, the loaded quality factor

$$Q_L = \frac{f_0}{BW}$$

and the simpler to compute nodal quality factor

$$Q_n = \frac{|X_S|}{R_S} = \frac{|B_P|}{G_P}$$

can be utilized as a measure to assess the frequency behavior of the matching networks. Unfortunately, L-type networks do not allow any flexibility in conditioning the frequency response and are therefore mostly used for narrow band RF designs. To affect the frequency behavior, a third element must be added, resulting in T- and Pi-type networks. With these configurations a certain nodal quality factor, and indirectly a desired bandwidth, can be implemented.

While the lumped element design is appropriate at low frequencies, distributed transmission line elements must be employed when the frequency extends into the GHz range. The hybrid configurations of using series connected transmission line elements and shunt connected capacitors are very attractive for prototyping since the location and value of the capacitors can easily be varied. If the capacitors are replaced by open- and short-circuit transmission lines, one arrives at the single- and double-stub matching networks.

Depending on the application (for instance, linear small signal or nonlinear large signal amplification), various classes of transistor amplifiers are identified. The classification is done by computing the RF to supply power ratio, known as efficiency:

$$\eta = \frac{P_{RF}}{P_S} 100\%$$

which can be expressed in terms of the conduction angle Θ_0 quantifying the amount of load current flow through the relation

$$\eta = \frac{\Theta_0 - \sin \Theta_0}{2[\Theta_0 \cos(\Theta_0/2) - 2 \sin(\Theta_0/2)]}$$

For instance, Class A offers the highest linearity at the expense of the lowest efficiency of 50%, whereas Class B compromises linearity but improves efficiency to 78.5%.

Once the class of operation is identified, a biasing network is chosen to set the appropriate quiescent point of the transistor. Passive biasing networks are normally easy to implement. However, they are not as flexible as biasing networks involving active devices. The biasing not only sets the DC operating conditions but must also ensure isolation of the RF signal through the use of RFCs and blocking capacitors.

Further Reading

W. A. Davis, *Microwave Semiconductor Circuit Design*, Van Nostrand Reinhold Company, New York, 1984.

N. Dye and H. Granberg, *Radio Frequency Transistors: Principles and Practical Applications*, Butterworth-Heinemann, 1993.

G. Gonzalez, *Microwave Transistor Amplifiers: Analysis and Design*, Prentice Hall, Upper Saddle River, NJ, 1997.

P. Horowitz and W. Hill, *The Art of Electronics*, Cambridge University Press, Cambridge, UK, 1993.

D. Pozar, *Microwave Engineering*, John Wiley & Sons, New York, 1998.

P. Rizzi, *Microwave Engineering: Passive Circuits*, Prentice Hall, Englewood Cliffs, NJ, 1988.

Problems

- 8.1 Obtain the “forbidden” regions for the two-element matching networks shown in Figures 8-1(c)–(f). Assume that the load is matched to the normalized input impedance (i.e., $z_{in} = 1$).

- 8.2 Use the analytical approach and design a two-component matching network that matches the $Z_L = (100 + j20)\Omega$ load impedance to a given $Z_S = (10 + j25)\Omega$ source, at the frequency of $f_0 = 960$ MHz.
- 8.3 Develop a two-component matching network for a $Z_L = (30 - j40)\Omega$ load and a $50\ \Omega$ source. How many network topologies exist that can be used? Find the values of the components if a perfect match is desired at $f_0 = 450$ MHz.
- 8.4 Repeat Problem 8.3 for a $Z_L = (40 + j10)\Omega$ load and a matching frequency of $f_0 = 1.2$ GHz.
- 8.5 Measurements indicate that the source impedance in Problem 8.3 is not purely resistive but has a parasitic inductance of $L_S = 2\text{ nH}$. Recompute the values for the matching network components that take into account the presence of L_S .
- 8.6 A load $Z_L = (20 + j10)\Omega$ consisting of a series $R-L$ combination is to be matched to a $50\ \Omega$ microstrip line at $f_0 = 800$ MHz. Design two two-element matching networks and specify the values of their components. Plot a frequency response for both networks and find the corresponding bandwidths.
- 8.7 In Example 8-5 a T-network is discussed that matches a load impedance of $Z_L = (60 - j30)\Omega$ to an input impedance of $Z_{in} = (10 + j20)\Omega$ at 1 GHz, under the constraint that Q_n does not exceed the factor of 3. Step-by-step go through this design and identify each point in the Smith Chart in terms of its impedance or admittance values. Verify the final results shown in Figure 8-16.
- 8.8 Go through Example 8-6 and find each point in the Smith Chart shown in Figure 8-17 and verify the final network components depicted in Figure 8-18.
- 8.9 Repeat the Pi-type matching network design in Example 8-6 for a nodal quality factor of $Q_n = 2.5$. Plot $Z_{in}(f)$ for this Q_n value and compare it against the $Q_n = 2$ design in Example 8-6. As frequency range, choose $1\text{ GHz} < f < 4\text{ GHz}$.

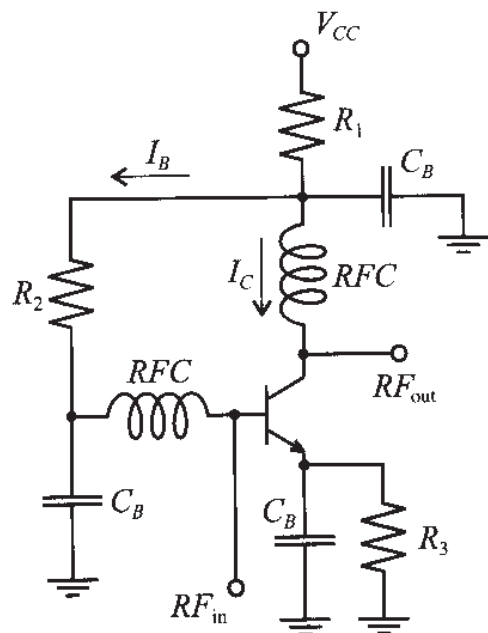
- 8.10 Design two T-type matching networks that transform a $Z_L = 100 \Omega$ load to an $Z_{in} = (20 - j40)\Omega$ input impedance at a nodal quality factor of $Q_n = 4$. The matching should be achieved at $f_0 = 600$ MHz.
- 8.11 Design two Pi-type matching networks for the same conditions as in Problem 8.10.
- 8.12 To achieve matching conditions for a specified Q_n , the circuit designer has to use more than two or three elements in the matching network. Using a graphical approach, design a multisection matching network that transforms $Z_L = 10 \Omega$ into $Z_S = 250 \Omega$ at $f_0 = 500$ MHz while maintaining a nodal quality factor of $Q_n = 1$. The multisection matching network should consist of a series of two-element sections each of which is a “series inductor, shunt capacitor” combination [see Figure 8-1(h)].
- 8.13 For an increased frequency of $f_0 = 1$ GHz it was decided that the network designed in Problem 8.12 should be replaced by a combined matching network shown in Figure 8-19. Determine the total number of capacitors and transmission line sections necessary to achieve matching and find the values of all components in the network.
- 8.14 Using the design from Example 8-7, find the length and width of each transmission line if an FR-4 substrate with dielectric constant of $\epsilon_r = 4.6$ and height of $h = 25$ mil is used. Find the maximum deviation of the input impedance of the matching network if the capacitor that is used in the circuit has a $\pm 10\%$ tolerance and the automatic component placement equipment has a ± 2 mil precision (i.e., the capacitor can be placed within ± 2 mil of the intended position).
- 8.15 In Example 8-7 it is argued that open-circuit stubs can be replaced by short-circuit ones if the length is increased by a quarter wavelength. Matching is achieved only for a single frequency, and over a broader frequency range the network response can significantly differ from the target impedance values. Design a single-stub matching network that transforms a $Z_L = (80 + j20)\Omega$ load impedance into a $Z_{in} = (30 - j10)\Omega$ input impedance. Compare the frequency response over the $\pm 0.8f_0$ frequency range for two different realizations of the matching network: open-circuit stub, and using an equivalent short-circuit stub. Assume that the matching frequency is $f_0 = 1$ GHz and the load is a series combination of resistance and inductance.

- 8.16 Using the matching network shown in Figure 8-23(b), find the stub length l_S , the characteristic line impedance Z_{0L} , and the transmission line length l_L such that the $Z_L = (80 - j40)\Omega$ load impedance is matched to 50Ω source. Assume that the characteristic impedance of the stub is $Z_{0S} = 50\Omega$.
- 8.17 For a double-stub tuner shown in Figure 8-26 with parameters $l_1 = \lambda/8$, $l_2 = 5\lambda/8$, and $l_3 = 3\lambda/8$, determine to which end of the tuner a $Z_L = (20 - j20)\Omega$ load has to be connected and find the length of the short-circuited stubs such that the load is matched to a 50Ω line. Assume that all stubs and transmission lines in the tuner have a 50Ω characteristic impedance.
- 8.18 Discuss a circuit configuration that replaces in the previous problem the stub tuners with varactor diodes in series with inductors. Choose the appropriate inductances if the varactor diodes can change their capacitances in the range from 1 pF to 6 pF. For a frequency of 1.5 GHz discuss the tuning capabilities in terms of possible load impedance variations.
- 8.19 An ideal amplifier has a transfer function given by the equation

$$V_{\text{out}} = \begin{cases} 30(V_{\text{in}} - V^*), & V_{\text{in}} \geq V^* \\ 0, & V_{\text{in}} < V^* \end{cases}$$

where $V^* = 60$ mV. Find the quiescent point (V_Q and I_Q) and the corresponding maximum efficiency such that the amplifier is operated in the AB class and has conductance angle of $\Theta_0 = 270^\circ$. Assume that the input signal is a sinusoidal voltage wave of 100 mV amplitude.

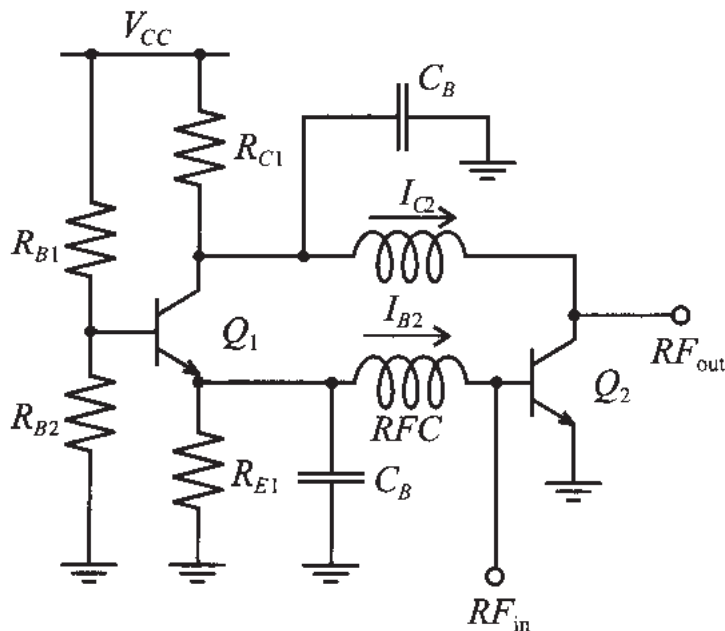
- 8.20 Find the component values for a low-GHz range biasing network for a BJT with bypassed emitter resistor R_3 , as shown below:



Assume that the power supply voltage is $V_{CC} = 12$ V and the transistor has the following parameters: $I_C = 20$ mA, $V_{CE} = 5$ V, $\beta = 125$, and $V_{BE} = 0.75$ V.

- 8.21 For stability purposes a feedback resistor $R_F = 1\text{ k}\Omega$ has been added between base and collector of the transistor in the biasing network shown in Figure 8-32(b). Compute the values of all resistors in the biasing network if the following biasing conditions must be satisfied: supply voltage of $V_{CC} = 5$ V, collector current of $I_C = 10$ mA, and collector-emitter voltage of $V_{CE} = 3$ V. Assume that the transistor has a $\beta = 100$ and a $V_{BE} = 0.8$ V.

- 8.22 Design a biasing network (shown in the following figure) for $I_{C2} = 10 \text{ mA}$, $V_{CE2} = 3 \text{ V}$, and $V_{CC} = 5 \text{ V}$. Assume that $\beta_1 = 150$, $\beta_2 = 80$, and both transistors have $V_{BE} = 0.7 \text{ V}$.



- 8.23 Redraw the active biasing network shown in Figure 8-34 for a common-base and a common-collector operating mode, respectively.
- 8.24 For the passive FET biasing network shown in Figure 8-38, find the value of the source resistance R_S if $V_{GS} = -4 \text{ V}$, $V_{DS} = 10 \text{ V}$, and the drain current is given to be $I_D = 50 \text{ mA}$.

RF Transistor Amplifier Designs

Amplifier designs at RF differ significantly from the conventional low-frequency circuit approaches and consequently require special considerations. In particular, the fact that *voltage and current waves* impinge upon the active device necessitates appropriate matching to reduce the VSWR and avoid undesirable oscillations. For this reason a stability analysis is usually the first step in the design process and, in conjunction with gain and noise figure circles, is a basic ingredient needed to develop amplifier circuits that meet the often competing requirements of gain, gain flatness, output power, bandwidth, and bias conditions.

This chapter expands upon the material covered in Chapters 2 and 3, where power relations of terminated transmission lines are investigated. However, unlike the passive circuit presentations, Chapter 9 deals with active devices where gain and feedback considerations assume central importance. Issues such as power gain, unilateral and bilateral circuit designs and their graphical display in the Smith Chart constitute the starting point of an extensive analysis into quantifying high-frequency transistor amplifier performance. The reader will note the flexibility of the Smith Chart, which allows constant gain, VSWR, and stability circle displays to be superimposed over the reflection coefficient and impedance representation discussed in Chapter 3. Moreover, even a noise analysis can be conducted by converting the noise figure of an amplifier into circles that are displayed in the Smith Chart.

After covering the basic design tools, Chapter 9 also investigates various types of power amplifiers and their characteristics such as gain flatness, bandwidth, and intermodular distortion as well as the differences between single- and multistage amplifiers.

9.1 Characteristics of Amplifiers

Perhaps the most important and complex task in analog circuit theory is the amplification of an input signal through either a single or multistage transistor circuit. A generic single-stage amplifier configuration embedded between input and output matching networks is shown in Figure 9-1.

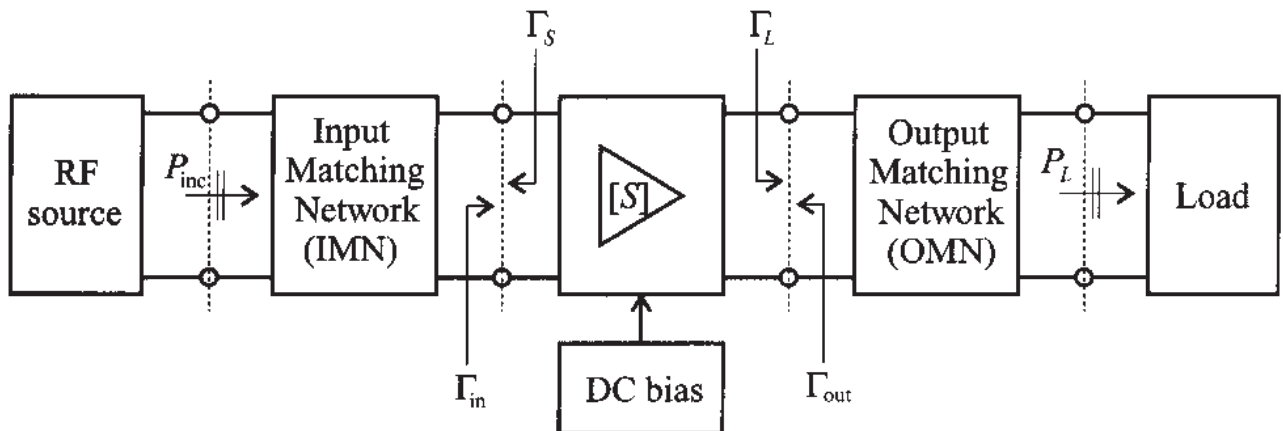


Figure 9-1 Generic amplifier system.

Input and output matching networks, discussed in Chapter 8, are needed to reduce undesired reflections and thus improve the power flow capabilities. In Figure 9-1 the amplifier is characterized through its S -matrix at a particular DC bias point. In terms of performance specifications, the following list constitutes a set of key amplifier parameters:

- Gain and gain flatness (in dB)
- Operating frequency and bandwidth (in Hz)
- Output power (in dBm)
- Power supply requirements (in V and A)
- Input and output reflection coefficients (VSWR)
- Noise figure (in dB)

In addition, one often must consider such parameters as intermodular distortion (IMD) products, harmonics, feedback, and heating effects, all of which can seriously affect the amplifier performance.

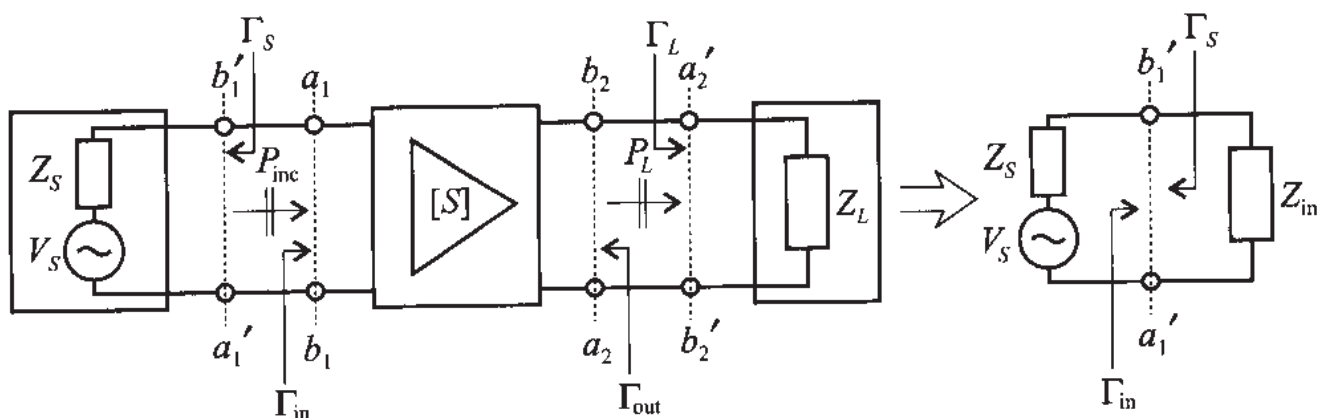
To approach the amplifier design process systematically, we need first to establish a number of definitions regarding various power relations. This is followed by several important analysis tools required to define stability, gain, noise, and VSWR performance. The common denominator of all four topics is that they can be expressed as circle equations and displayed in the Smith Chart.

9.2 Amplifier Power Relations

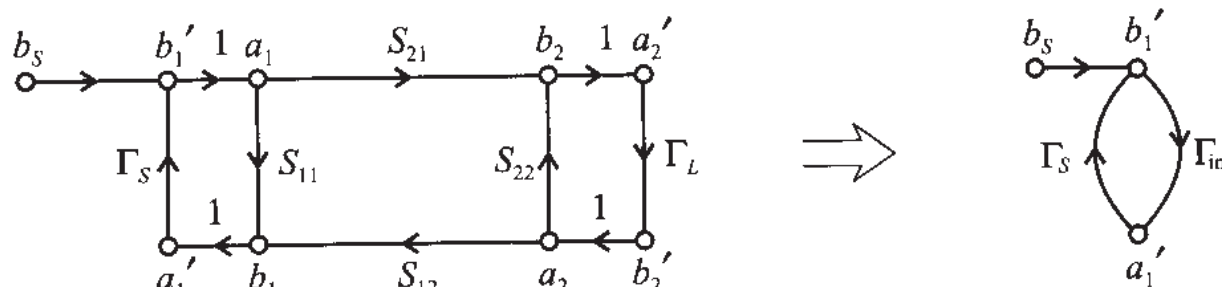
9.2.1 RF Source

There are various power gain definitions that are critical to the understanding of how an RF amplifier functions. For this reason, let us examine Figure 9-1 in terms of its power flow relations under the assumption that the two matching networks are included in the source and load impedances. This simplifies our system to the configuration shown in Figure 9-2(a). The starting point of our power analysis is the RF source connected to the amplifier network. For the convention depicted in Figure 9-2 we recall our signal flow discussion in Section 4.4.5 [see (4.82) and (4.83)] and write for the source voltage

$$b_S = \frac{\sqrt{Z_0}}{Z_S + Z_0} V_S = b_1' - a_1' \Gamma_S = b_1'(1 - \Gamma_{in} \Gamma_S) \quad (9.1)$$



(a) Simplified schematics of a single-stage amplifier



(b) Signal flow graph

Figure 9-2 Source and load connected to a single-stage amplifier network.

The incident power wave associated with b_1' is given as

$$P_{\text{inc}} = \frac{|b_1'|^2}{2} = \frac{1}{2} \frac{|b_s|^2}{|1 - \Gamma_{in}\Gamma_s|^2} \quad (9.2)$$

which is the power launched toward the amplifier. The actual input power P_{in} observed at the input terminal of the amplifier is composed of the incident and reflected power waves. With the aid of the input reflection coefficient Γ_{in} we can therefore write:

$$P_{\text{in}} = P_{\text{inc}}(1 - |\Gamma_{in}|^2) = \frac{1}{2} \frac{|b_s|^2}{|1 - \Gamma_{in}\Gamma_s|^2} (1 - |\Gamma_{in}|^2) \quad (9.3)$$

The **maximum power transfer** from the source to the amplifier is achieved if the input impedance is complex conjugate matched ($Z_{in} = Z_S^*$) or, in terms of the reflection coefficients, if $\Gamma_{in} = \Gamma_S^*$. Under maximum power transfer condition, we define the **available power** P_A as

$$P_A = P_{\text{in}} \Big|_{\Gamma_{in} = \Gamma_S^*} = \frac{1}{2} \frac{|b_s|^2}{|1 - \Gamma_{in}\Gamma_s|^2} \Bigg|_{\Gamma_{in} = \Gamma_S^*} (1 - |\Gamma_{in}|^2) = \frac{1}{2} \frac{|b_s|^2}{1 - |\Gamma_S|^2} \quad (9.4)$$

This expression makes clear the dependence on Γ_S . If $\Gamma_{in} = 0$ and $\Gamma_S \neq 0$ it is seen from (9.2) and (9.4) that $P_{\text{inc}} = |b_s|^2/2$.

9.2.2 Transducer Power Gain

We can next investigate the **transducer power gain** G_T , which quantifies the gain of the amplifier placed between source and load.

$$G_T = \frac{\text{power delivered to the load}}{\text{available power from the source}} = \frac{P_L}{P_A}$$

or with $P_L = \frac{1}{2}|b_2|^2 \cdot (1 - |\Gamma_L|^2)$ we obtain

$$G_T = \frac{P_L}{P_A} = \frac{|b_2|^2}{|b_s|^2} (1 - |\Gamma_L|^2)(1 - |\Gamma_S|^2) \quad (9.5)$$

In this expression, the ratio b_2/b_S has to be determined. With the help of our signal flow discussion in Section 4.4.5 and based on Figure 9-2, we establish

$$b_2 = \frac{S_{21}a_1}{1 - S_{22}\Gamma_L} \quad (9.6a)$$

$$b_S = \left[1 - \left(S_{11} + \frac{S_{21}S_{12}\Gamma_L}{1-S_{22}\Gamma_L} \right) \Gamma_S \right] a_1 \quad (9.6b)$$

The required ratio is therefore given by

$$\frac{b_2}{b_S} = \frac{S_{21}}{(1-S_{11}\Gamma_S)(1-S_{22}\Gamma_L) - S_{21}S_{12}\Gamma_L\Gamma_S} \quad (9.7)$$

Inserting (9.7) into (9.5) results in

$$G_T = \frac{(1-|\Gamma_L|^2)|S_{21}|^2(1-|\Gamma_S|^2)}{|(1-S_{11}\Gamma_S)(1-S_{22}\Gamma_L) - S_{21}S_{12}\Gamma_L\Gamma_S|^2} \quad (9.8)$$

which can be rearranged by defining the input and output reflection coefficients (see Problem 9.2)

$$\Gamma_{in} = S_{11} + \frac{S_{21}S_{12}\Gamma_L}{1-S_{22}\Gamma_L} \quad (9.9a)$$

$$\Gamma_{out} = S_{22} + \frac{S_{12}S_{21}\Gamma_S}{1-S_{11}\Gamma_S} \quad (9.9b)$$

With these two definitions, two more transducer power gain expressions can be derived. First, by incorporating (9.9a) into (9.8), it is seen that

$$G_T = \frac{(1-|\Gamma_L|^2)|S_{21}|^2(1-|\Gamma_S|^2)}{|1-\Gamma_S\Gamma_{in}|^2|1-S_{22}\Gamma_L|^2} \quad (9.10)$$

Second, using (9.9b) in (9.8) results in the expression

$$G_T = \frac{(1-|\Gamma_L|^2)|S_{21}|^2(1-|\Gamma_S|^2)}{|1-\Gamma_L\Gamma_{out}|^2|1-S_{11}\Gamma_S|^2} \quad (9.11)$$

An often employed approximation for the transducer power gain is the so-called **unilateral power gain**, G_{TU} , which neglects the feedback effect of the amplifier ($S_{12} = 0$). This simplifies the form (9.11) to

$$G_{TU} = \frac{(1-|\Gamma_L|^2)|S_{21}|^2(1-|\Gamma_S|^2)}{|1-\Gamma_L S_{22}|^2|1-S_{11}\Gamma_S|^2} \quad (9.12)$$

As discussed in Section 9.4.1, equation (9.12) is often used as a basis to develop approximate designs for an amplifier and its input and output matching networks.

9.2.3 Additional Power Relations

The transducer power gain is a fundamental expression from which additional important power relations can be derived. For instance, the **available power gain** for load side matching ($\Gamma_L = \Gamma_{\text{out}}^*$) is defined as

$$G_A = G_T \Big|_{\Gamma_L = \Gamma_{\text{out}}^*} = \frac{\text{power available from the amplifier}}{\text{power available from the source}}$$

or, with the aid of (9.11),

$$G_A = \frac{|S_{21}|^2 (1 - |\Gamma_S|^2)}{(1 - |\Gamma_{\text{out}}|^2) |1 - S_{11} \Gamma_S|^2} \quad (9.13)$$

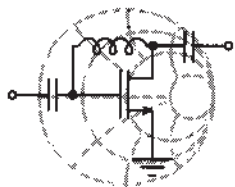
Further, the **power gain (operating power gain)** is defined as the ratio of the power delivered to the load to the power supplied to the amplifier.

$$G = \frac{\text{power delivered to the load}}{\text{power supplied to the amplifier}} = \frac{P_L}{P_{\text{in}}} = \frac{P_L}{P_A} \cdot \frac{P_A}{P_{\text{in}}} = G_T \frac{P_A}{P_{\text{in}}}$$

Combining (9.3), (9.4), and (9.10), we find

$$G = \frac{(1 - |\Gamma_L|^2) |S_{21}|^2}{(1 - |\Gamma_{\text{in}}|^2) |1 - S_{22} \Gamma_L|^2} \quad (9.14)$$

It is interesting to note that (9.14) can be obtained from (9.10) by setting $\Gamma_S = \Gamma_{\text{in}}^*$ since in this case $P_{\text{in}} = P_A$. The following example goes through the computation of some of these expressions for an amplifier with given S-parameters.



RF & MW →

Example 9-1: Power relations for an RF amplifier

An RF amplifier has the following S-parameters: $S_{11} = 0.3 \angle -70^\circ$, $S_{21} = 3.5 \angle 85^\circ$, $S_{12} = 0.2 \angle -10^\circ$, and $S_{22} = 0.4 \angle -45^\circ$. Furthermore, the input side of the amplifier is connected to a voltage source with $V_S = 5V \angle 0^\circ$ and source impedance $Z_S = 40 \Omega$. The output is utilized to drive an antenna which has an impedance of $Z_L = 73 \Omega$. Assuming that the S-parameters of the amplifier are

measured with reference to a $Z_0 = 50 \Omega$ characteristic impedance, find the following quantities:

- (a) transducer gain G_T , unilateral transducer gain G_{TU} , available gain G_A , operating power gain G , and
- (b) power delivered to the load P_L , available power P_A , and incident power to the amplifier P_{inc} .

Solution: First we find the source and load reflection coefficients assuming a $Z_0 = 50 \Omega$ characteristic impedance:

$$\Gamma_S = \frac{Z_S - Z_0}{Z_S + Z_0} = -0.111 \text{ and } \Gamma_L = \frac{Z_L - Z_0}{Z_L + Z_0} = 0.187$$

Next, the input and output impedances, as given in (9.9a) and (9.9b), are determined:

$$\Gamma_{\text{in}} = S_{11} + \frac{S_{21}S_{12}\Gamma_L}{1 - S_{22}\Gamma_L} = 0.146 - j0.151$$

$$\Gamma_{\text{out}} = S_{22} + \frac{S_{12}S_{21}\Gamma_S}{1 - S_{11}\Gamma_S} = 0.265 - j0.358$$

Substituting the obtained values along with the S -parameters into (9.11), (9.12), (9.13), and (9.14), the transducer gain G_T , unilateral transducer gain G_{TU} , available gain G_A , and operating power gain G are computed as follows:

$$G_T = \frac{(1 - |\Gamma_L|^2)|S_{21}|^2(1 - |\Gamma_S|^2)}{|1 - \Gamma_L\Gamma_{\text{out}}|^2|1 - S_{11}\Gamma_S|^2} = 12.56 \text{ or } 10.99 \text{ dB}$$

$$G_{TU} = \frac{(1 - |\Gamma_L|^2)|S_{21}|^2(1 - |\Gamma_S|^2)}{|1 - \Gamma_L S_{22}|^2|1 - S_{11}\Gamma_S|^2} = 12.67 \text{ or } 11.03 \text{ dB}$$

$$G_A = \frac{|S_{21}|^2(1 - |\Gamma_S|^2)}{|1 - |\Gamma_{\text{out}}|^2||1 - S_{11}\Gamma_S|^2} = 14.74 \text{ or } 11.68 \text{ dB}$$

$$G = \frac{(1 - |\Gamma_L|^2)|S_{21}|^2}{|1 - |\Gamma_{\text{in}}|^2||1 - S_{22}\Gamma_L|^2} = 13.74 \text{ or } 11.38 \text{ dB}$$

Using (9.2) in conjunction with (9.1) allows us to find the incident power flow into the amplifier:

$$P_{\text{inc}} = \frac{1}{2} \frac{|b_S|^2}{|1 - \Gamma_{\text{in}} \Gamma_S|^2} = \frac{1}{2} \frac{Z_0}{(Z_S + Z_0)^2} \frac{|V_S|^2}{|1 - \Gamma_{\text{in}} \Gamma_S|^2} = 74.7 \text{ mW}$$

Often P_{inc} is expressed in dBm as

$$P_{\text{inc}}(\text{dBm}) = 10 \log [P_{\text{inc}}/(1 \text{ mW})] = 18.73 \text{ dBm}$$

Similarly, from (9.2) we find the available power to be $P_A = 78.1 \text{ mW}$ or $P_A = 18.93 \text{ dBm}$. Finally, the power delivered to the load is the available power multiplied by the transducer gain. This results in $P_L = P_A G_T = 981.4 \text{ mW}$, or, expressed in dBm,

$$P_L(\text{dBm}) = P_A(\text{dBm}) + G_T(\text{dB}) = 29.92 \text{ dBm}$$

It is interesting to point out that the unilateral power gain often matches the actual transducer power gain very closely. As discussed further, the use of the unilateral amplifier gain significantly simplifies the amplifier design task.

9.3 Stability Considerations

9.3.1 Stability Circles

One of the first requirements that an amplifier circuit must meet is a stable performance in the frequency range of interest. This is a particular concern when dealing with RF circuits, which tend to oscillate depending on operating frequency and termination. The phenomenon of oscillations can be understood in the context of a voltage wave along a transmission line. If $|\Gamma_0| > 1$, then the return voltage increases in magnitude (positive feedback) causing instability. Conversely, $|\Gamma_0| < 1$ causes a diminished return voltage wave (negative feedback).

Let us regard the amplifier as a two-port network characterized through its S -parameters and external terminations described by Γ_L and Γ_S . Stability then implies that the magnitudes of the reflection coefficients are less than unity. Namely,

$$|\Gamma_L| < 1, |\Gamma_S| < 1 \quad (9.15a)$$

$$|\Gamma_{\text{in}}| = \left| \frac{S_{11} - \Gamma_L \Delta}{1 - S_{22} \Gamma_L} \right| < 1 \quad (9.15\text{b})$$

$$|\Gamma_{\text{out}}| = \left| \frac{S_{22} - \Gamma_S \Delta}{1 - S_{11} \Gamma_S} \right| < 1 \quad (9.15\text{c})$$

where $\Delta = S_{11}S_{22} - S_{12}S_{21}$ has been used to re-express (9.9a) and (9.9b). Since the S -parameters are fixed for a particular frequency, the only factors that have a parametric effect on the stability are Γ_L and Γ_S .

In terms of the amplifier's *output port*, we need to establish the condition for which (9.15b) is satisfied. To this end the complex quantities

$$S_{11} = S_{11}^R + jS_{11}^I, S_{22} = S_{22}^R + jS_{22}^I, \Delta = \Delta^R + j\Delta^I, \Gamma_L = \Gamma_L^R + j\Gamma_L^I \quad (9.16)$$

are substituted into (9.15b), resulting after some algebra in the **output stability circle** equation

$$(\Gamma_L^R - C_{\text{out}}^R)^2 + (\Gamma_L^I - C_{\text{out}}^I)^2 = r_{\text{out}}^2 \quad (9.17)$$

where the circle radius is given by

$$r_{\text{out}} = \frac{|S_{12}S_{21}|}{|S_{22}|^2 - |\Delta|^2} \quad (9.18)$$

and the center of this circle is located at

$$C_{\text{out}} = C_{\text{out}}^R + jC_{\text{out}}^I = \frac{(S_{22} - S_{11}^* \Delta)^*}{|S_{22}|^2 - |\Delta|^2} \quad (9.19)$$

as depicted in Figure 9-3(a). In terms of the *input port*, substituting (9.16) into (9.15c) yields the **input stability circle** equation

$$(\Gamma_S^R - C_{\text{in}}^R)^2 + (\Gamma_S^I - C_{\text{in}}^I)^2 = r_{\text{in}}^2 \quad (9.20)$$

where

$$r_{\text{in}} = \frac{|S_{12}S_{21}|}{|S_{11}|^2 - |\Delta|^2} \quad (9.21)$$

and

$$C_{\text{in}} = C_{\text{in}}^R + jC_{\text{in}}^I = \frac{(S_{11} - S_{22}^* \Delta)^*}{|S_{11}|^2 - |\Delta|^2} \quad (9.22)$$

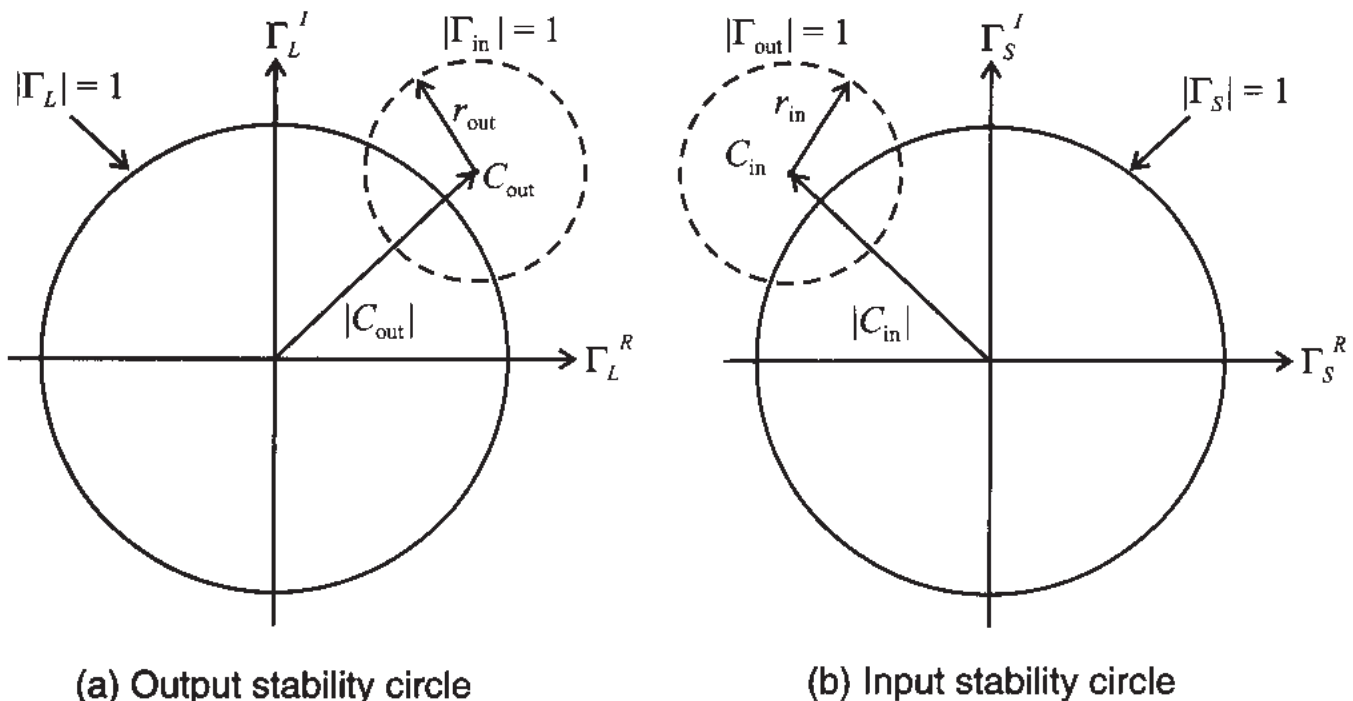


Figure 9-3 Stability circle $|\Gamma_{\text{in}}| = 1$ in the complex Γ_L plane and stability circle $|\Gamma_{\text{out}}| = 1$ in the complex Γ_S plane.

When plotted in the Γ_S -plane we obtain a response as schematically shown in Figure 9-3(b).

To interpret the meaning of Figure 9-3 correctly, a critical issue arises that is investigated for the output circle [Figure 9-3(a)], although the same argument holds for the input circle. If $\Gamma_L = 0$, then $|\Gamma_{\text{in}}| = |S_{11}|$ and two cases have to be differentiated depending on $|S_{11}| < 1$ or $|S_{11}| > 1$. For $|S_{11}| < 1$, the origin (the point $\Gamma_L = 0$) is part of the stable region, see Figure 9-4(a). However, for $|S_{11}| > 1$ the matching condition $\Gamma_L = 0$ results in $|\Gamma_{\text{in}}| = |S_{11}| > 1$, i.e. the origin is part of the unstable region. In this case the only stable region is the shaded domain between the output stability circle $|\Gamma_{\text{in}}| = 1$ and the $|\Gamma_L| = 1$ circle, see Figure 9-4(b).

For completeness, Figure 9-5 shows the two stability domains for the input stability circle. The rule-of-thumb is the inspection if $|S_{22}| < 1$, which leads to the conclusion that the center ($\Gamma_S = 0$) must be stable; otherwise the center becomes unstable for $|S_{22}| > 1$.

Care has to be exercised in correctly interpreting the stability circles if the circle radius is larger than $|C_{\text{in}}|$ or $|C_{\text{out}}|$. Figure 9-6 depicts the input stability circles for $|S_{22}| < 1$ and the two possible stability domains depending on $r_{\text{in}} < |C_{\text{in}}|$ or $r_{\text{in}} > |C_{\text{in}}|$.

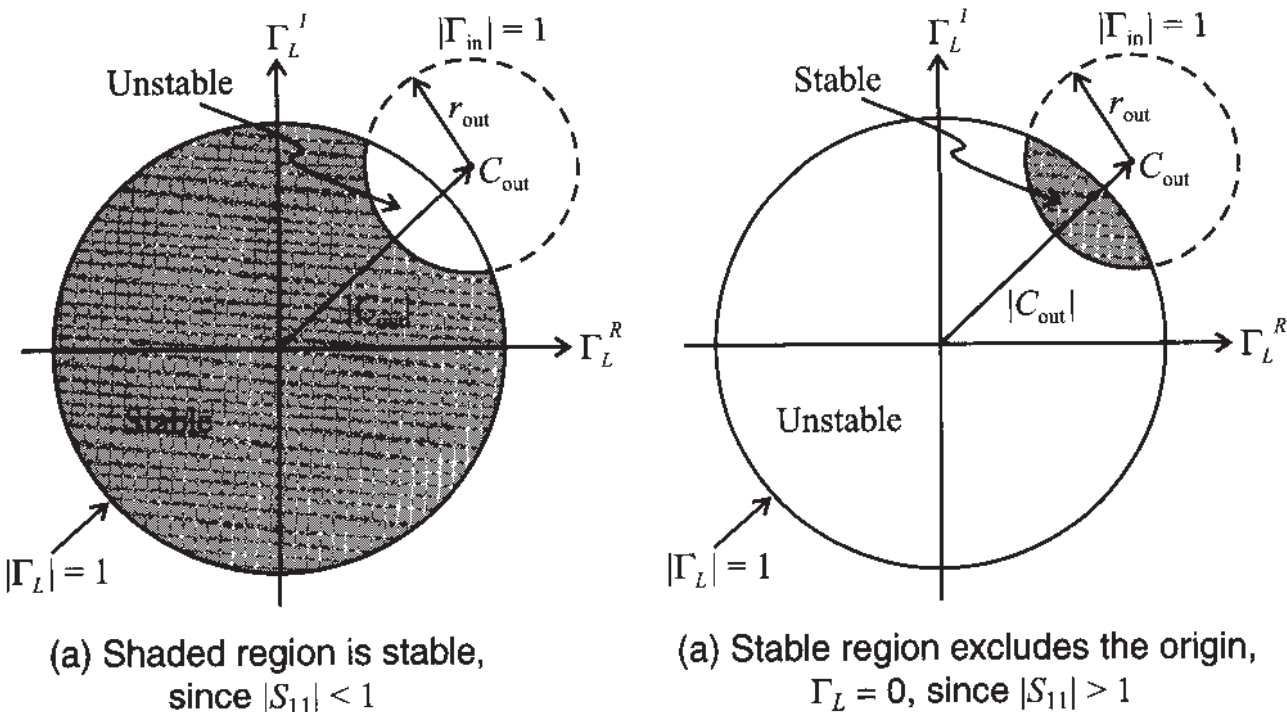


Figure 9-4 Output stability circles denoting stable and unstable regions.

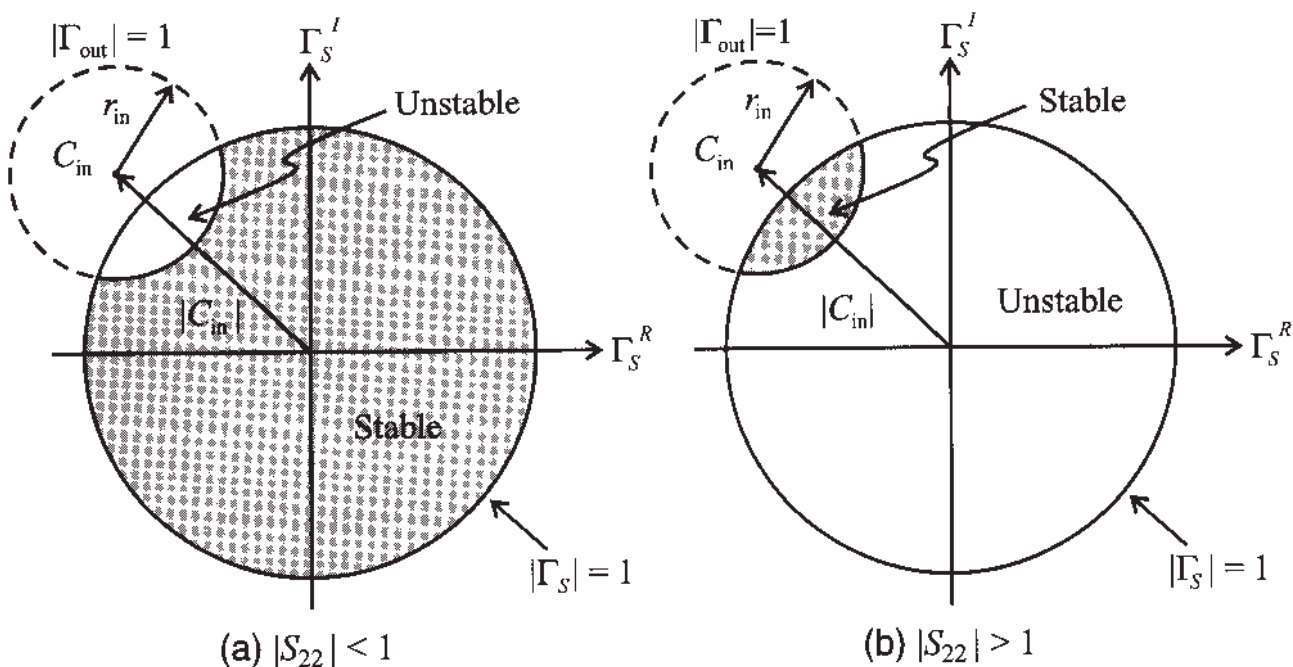


Figure 9-5 Input stability circles denoting stable and unstable regions.

9.3.2 Unconditional Stability

As the name implies, unconditional stability refers to the situation where the amplifier remains stable throughout the entire domain of the Smith Chart at the selected frequency and bias conditions. This applies to both the input and output ports. For $|S_{11}| < 1$ and $|S_{22}| < 1$ it is stated as

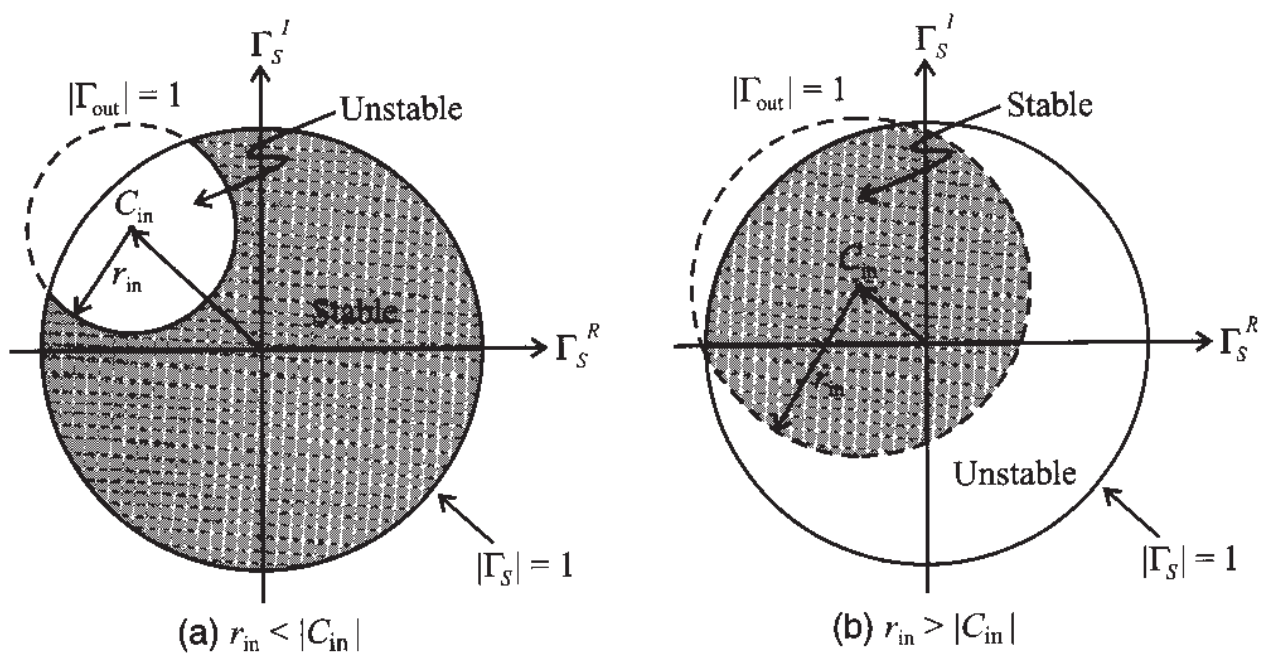


Figure 9-6 Different input stability regions for $|S_{22}| < 1$ depending on ratio between r_s and $|C_{in}|$.

$$||C_{in}| - r_{in}| > 1 \quad (9.23a)$$

$$||C_{out}| - r_{out}| > 1 \quad (9.23b)$$

In other words, the stability circles have to reside completely outside the $|\Gamma_S| = 1$ and $|\Gamma_L| = 1$ circles. In the following discussion we concentrate on the $|\Gamma_S| = 1$ circle shown in Figure 9-7(a). It is shown in Example 9-2 that condition (9.23a) can be reexpressed in terms of the stability or Rollett factor k :

$$k = \frac{1 - |S_{11}|^2 - |S_{22}|^2 + |\Delta|^2}{2|S_{12}||S_{21}|} > 1 \quad (9.24)$$

Alternatively, unconditional stability can also be viewed in terms of the Γ_S behavior in the complex $\Gamma_{out} = \Gamma_{out}^R + j\Gamma_{out}^I$ plane. Here, the $|\Gamma_S| \leq 1$ domain must reside completely within the $|\Gamma_{out}| = 1$ circle, as depicted in Figure 9-7(b). Plotting $|\Gamma_S| = 1$ in the Γ_{out} plane produces a circle whose center is located at

$$C_S = S_{22} + \frac{S_{12}S_{21}S_{11}^*}{1 - |S_{11}|^2} \quad (9.25)$$

and which possesses a radius of

$$r_S = \frac{|S_{12}S_{21}|}{1 - |S_{11}|^2} \quad (9.26)$$

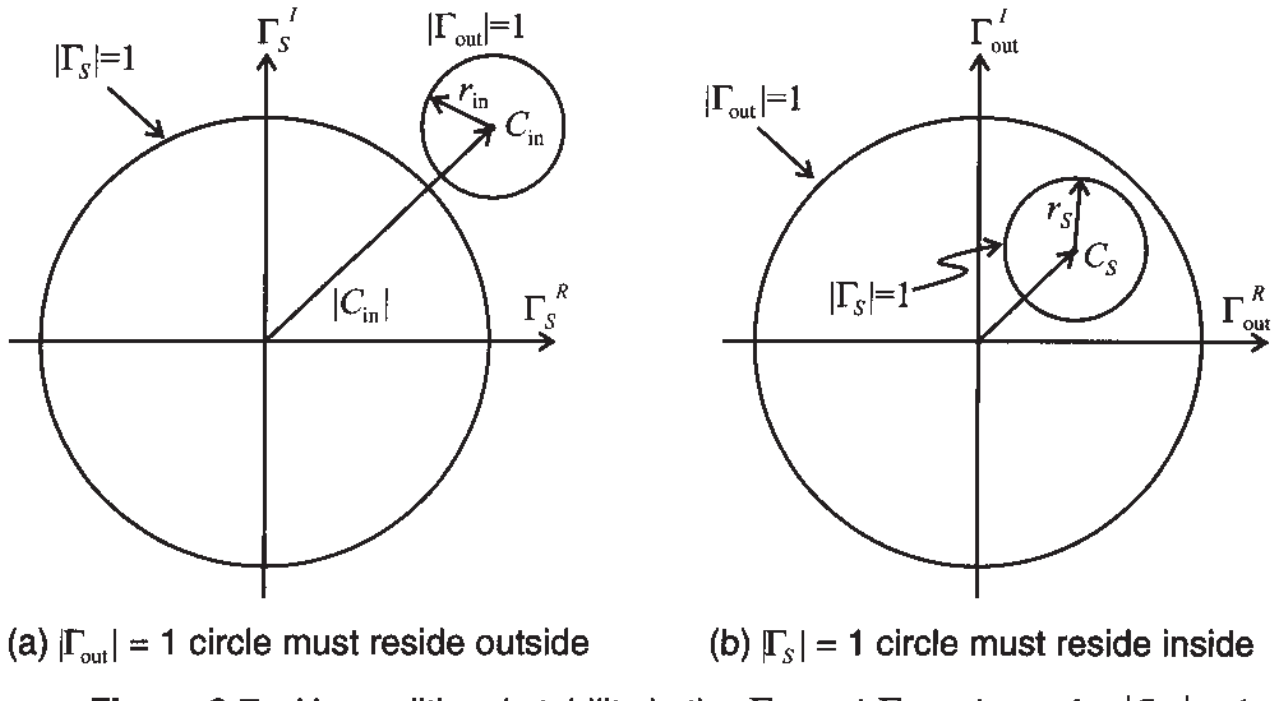


Figure 9-7 Unconditional stability in the Γ_s and Γ_{out} planes for $|S_{11}| < 1$.

where the condition $|C_s| + r_s < 1$ must hold. We note that (9.25) can be rewritten as $C_s = (S_{22} - \Delta S_{11}^*)/(1 - |S_{11}|^2)$. Employing $|C_s| + r_s < 1$ and (9.26) it is seen that

$$|S_{22} - \Delta S_{11}^*| + |S_{12}S_{21}| < 1 - |S_{11}|^2 \quad (9.27a)$$

and since $|S_{12}S_{21}| \leq |S_{22} - \Delta S_{11}^*| + |S_{12}S_{21}|$ we conclude

$$|S_{12}S_{21}| < 1 - |S_{11}|^2 \quad (9.27b)$$

A similar analysis can be established for Γ_L in the complex Γ_{in} plane. From the corresponding circle center C_L and radius r_L , we set $|C_L| = 0$ and $r_S < 1$. Thus,

$$|S_{12}S_{21}| < 1 - |S_{22}|^2 \quad (9.28)$$

However, as long as $|\Delta| < 1$, (9.24) remains the sufficient requirement to ensure unconditional stability. This follows from the fact that when (9.27b) and (9.28) are added, it is seen that

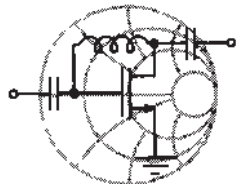
$$2|S_{12}S_{21}| < 2 - |S_{11}|^2 - |S_{22}|^2$$

Introducing the inequality $|\Delta| = |S_{11}S_{22} - S_{12}S_{21}| \leq |S_{11}S_{22}| + |S_{12}S_{21}|$ results in

$$|\Delta| < 1 - \frac{1}{2}(|S_{11}|^2 + |S_{22}|^2 - 2|S_{11}||S_{22}|) = 1 - \frac{1}{2}(|S_{11}| - |S_{22}|)^2$$

Since $(1/2)(|S_{11}| - |S_{22}|)^2 < 1$, it is seen that (9.27b) and (9.28) are equivalent to

$$|\Delta| < 1 \quad (9.29)$$



RF & MW →

Example 9-2: Stability factor derivation

Derive the stability factor k (Rollett factor) from (9.23a).

Solution: Substituting (9.21) and (9.22) into (9.23a) gives

$$\left| \frac{|S_{11} - S_{22}^* \Delta| - |S_{12} S_{21}|}{|S_{11}|^2 - |\Delta|^2} \right| > 1 \quad (9.30a)$$

Squaring and rearranging (9.30a) results in

$$2|S_{11} - S_{22}^* \Delta| |S_{12} S_{21}| < |S_{11} - S_{22}^* \Delta|^2 + |S_{12} S_{21}|^2 - (|S_{11}|^2 - |\Delta|^2)^2 \quad (9.30b)$$

The term $|S_{11} - S_{22}^* \Delta|^2$ in (9.30b) can be re-expressed as

$$|S_{11} - S_{22}^* \Delta|^2 = |S_{12} S_{21}|^2 + (1 - |S_{22}|^2)(|S_{11}|^2 - |\Delta|^2) \quad (9.30c)$$

Squaring (9.30b) again and rearranging terms finally gives

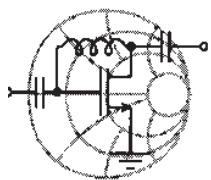
$$(|S_{11}|^2 - |\Delta|^2)^2 \left\{ [(1 - |S_{22}|^2) - (|S_{11}|^2 - |\Delta|^2)]^2 - 4|S_{12} S_{21}|^2 \right\} > 0 \quad (9.30d)$$

The terms inside the curly brackets are recognized as the desired stability factor:

$$k = \frac{1 - |S_{11}|^2 - |S_{22}|^2 + |\Delta|^2}{2|S_{12}||S_{21}|} > 1 \quad (9.30e)$$

A stability analysis starting from (9.23b) would have resulted in exactly the same inequality. Thus, the stability factor k applies for both input and output ports.

It is always prudent to determine that both the $|\Delta| < 1$ and $k > 1$ conditions are fulfilled to ensure an unconditionally stable design. The next example investigates a transistor in common-emitter configuration in terms of its input and output stability behavior.



RF & MW

Example 9-3: Stability circles for a BJT at different operating frequencies

Determine the stability regions of the bipolar junction transistor BFG505W (Philips Semiconductors) biased at $V_{CE} = 6$ V and $I_C = 4$ mA. The corresponding S -parameters as a function of frequency are given in Table 9-1.

Table 9-1 BFG505W S -parameters as a function of frequency

| Frequency | S_{11} | S_{12} | S_{21} | S_{22} |
|-----------|------------------------|----------------------|-----------------------|-----------------------|
| 500 MHz | $0.70\angle-57^\circ$ | $0.04\angle47^\circ$ | $10.5\angle136^\circ$ | $0.79\angle-33^\circ$ |
| 750 MHz | $0.56\angle-78^\circ$ | $0.05\angle33^\circ$ | $8.6\angle122^\circ$ | $0.66\angle-42^\circ$ |
| 1000 MHz | $0.46\angle-97^\circ$ | $0.06\angle22^\circ$ | $7.1\angle112^\circ$ | $0.57\angle-48^\circ$ |
| 1250 MHz | $0.38\angle-115^\circ$ | $0.06\angle14^\circ$ | $6.0\angle104^\circ$ | $0.50\angle-52^\circ$ |

Solution: Based on the definitions for k , $|\Delta|$, C_{in} , r_{in} , C_{out} , and r_{out} , we compute the values via a MATLAB routine (see m-file ex9_3.m). A summary of the results is given in Table 9-2 for the four frequencies listed in Table 9-1.

Table 9-2 Stability parameters for BFG505W for frequencies listed in Table 9-1

| k | $ \Delta $ | C_{in} | r_{in} | C_{out} | r_{out} |
|------|------------|-------------------------|----------|----------------------|-----------|
| 0.41 | 0.69 | $39.04\angle108^\circ$ | 38.62 | $3.56\angle70^\circ$ | 3.03 |
| 0.60 | 0.56 | $62.21\angle119^\circ$ | 61.60 | $4.12\angle70^\circ$ | 3.44 |
| 0.81 | 0.45 | $206.23\angle131^\circ$ | 205.42 | $4.39\angle69^\circ$ | 3.54 |
| 1.02 | 0.37 | $42.42\angle143^\circ$ | 41.40 | $4.24\angle68^\circ$ | 3.22 |

The example input and output stability circles for the frequencies of $f = 750$ MHz and $f = 1.25$ GHz are shown in Figure 9-8. We notice that $|S_{11}| < 1$ and $|S_{22}| < 1$ in all cases. This implies that the $\Gamma_L = 0$ and $\Gamma_S = 0$ points are stable, indicating that the interior domain of the Smith Chart up to the stability circles denotes the stable region.

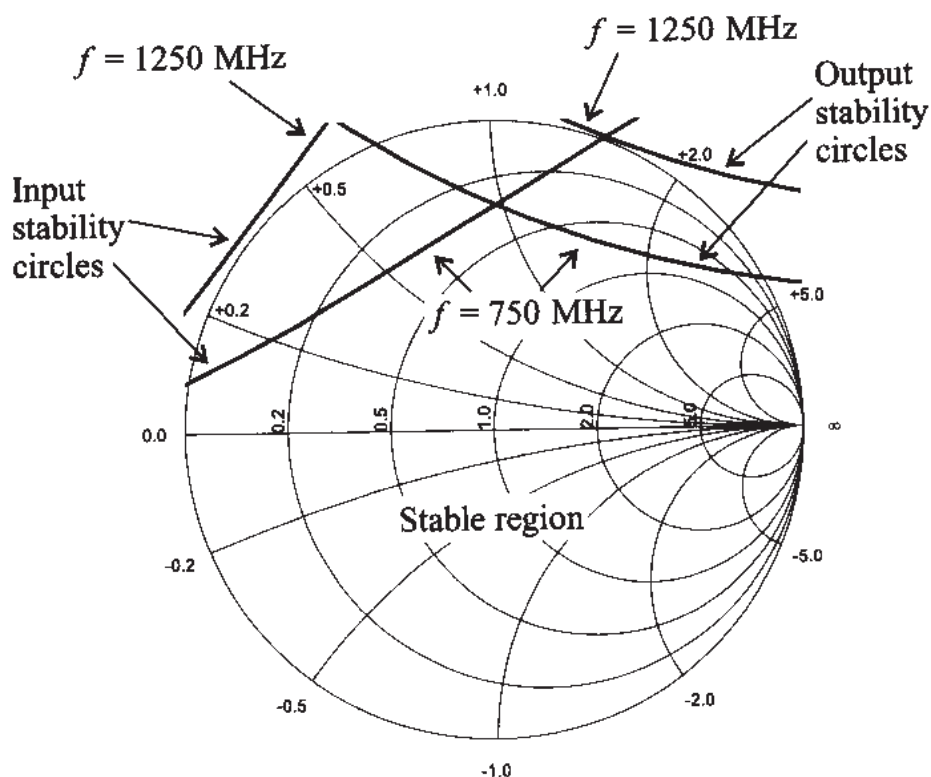
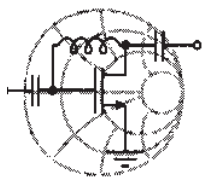


Figure 9-8 Input and output stability circles for BFG505W computed at $f = 750$ MHz and $f = 1.25$ GHz.

Also, as can be seen from Figure 9-8 and Table 9-2, the transistor is unconditionally stable at $f = 1.25$ GHz and both input and output stability circles are located completely outside of the $|\Gamma| = 1$ circle. At all other frequencies transistor is potentially unstable.

The stability circles are not only affected by frequency, but also by the bias conditions. We recall that the S-parameters are given for particular bias conditions. The entire stability analysis must be repeated if biasing, or even temperature, changes.

Even though k can vary widely, most unstable practical designs fall into the range $0 \leq k \leq 1$. Oscillators, discussed in Chapter 10, target the entire Smith Chart as the unstable domain, resulting in negative values of k . It is also interesting to observe that in the absence of any output to input feedback ($S_{12} = 0$) the transistor is inherently stable, since the stability factor yields $k \rightarrow \infty$. In practice, one often examines k alone without paying attention to the $|\Delta| < 1$ condition. This can cause potential problems, as the following example highlights.



RF & MW

Example 9-4: Stable versus unstable region of a transistor

Investigate the stability regions of a transistor whose S -parameters are recorded as follows: $S_{11} = 0.7 \angle -70^\circ$, $S_{12} = 0.2 \angle -10^\circ$, $S_{21} = 5.5 \angle 85^\circ$, and $S_{22} = 0.7 \angle -45^\circ$

Solution: We again compute the values k , $|\Delta|$, C_{in} , r_{in} , C_{out} , and r_{out} . The results are $k = 1.15$, $|\Delta| = 1.58$, $C_{\text{in}} = 0.21 \angle 52^\circ$, $r_{\text{in}} = 0.54$, $C_{\text{out}} = 0.21 \angle 27^\circ$, and $r_{\text{out}} = 0.54$ (see Figure 9-9). It is seen that even though $k > 1$, the transistor is still potentially unstable because $|\Delta| > 1$. This results in input and output stability

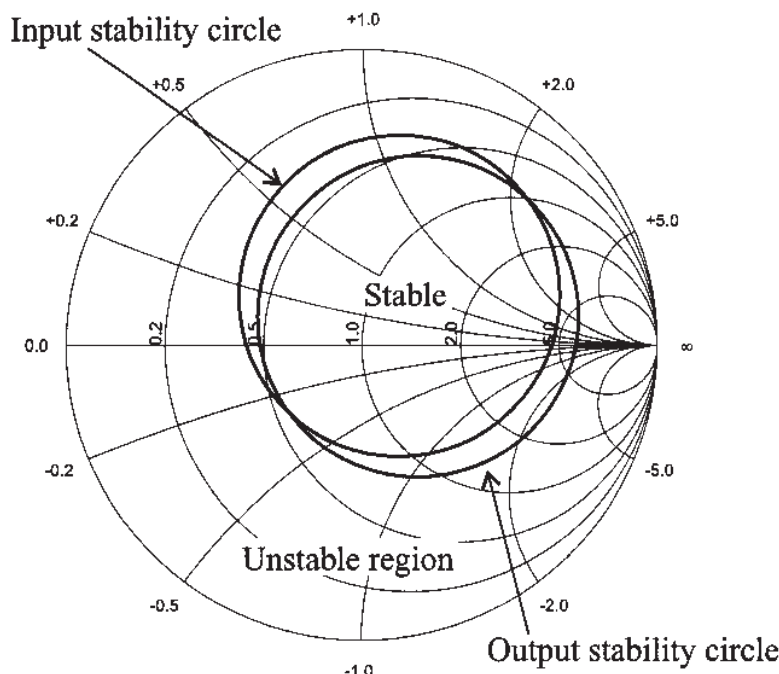


Figure 9-9 Stability circles for $k > 1$ and $|\Delta| > 1$.

circles being located inside of the Smith Chart. Since both $|S_{11}|$ and $|S_{22}|$ are less than unity, the center of the Smith Chart is a stable point. Therefore, since $|C_{in}| < r_{in}$ and $|C_{out}| < r_{out}$, the area inside of the stability circles represents the stable region, as shown in Figure 9-9.

Usually manufacturers avoid producing transistors with both $k > 1$ and $|\Delta| > 1$ by incorporating matching networks housed inside the transistor casing.

9.3.3 Stabilization Methods

If the operation of a FET or BJT is found to be unstable in the desired frequency range, an attempt can be made to stabilize the transistor. We recall that $|\Gamma_{in}| > 1$ and $|\Gamma_{out}| > 1$ can be written in terms of the input and output impedances:

$$|\Gamma_{in}| = \left| \frac{Z_{in} - Z_0}{Z_{in} + Z_0} \right| > 1 \text{ and } |\Gamma_{out}| = \left| \frac{Z_{out} - Z_0}{Z_{out} + Z_0} \right| > 1$$

which imply $\operatorname{Re}\{Z_{in}\} < 0$ and $\operatorname{Re}\{Z_{out}\} < 0$. One way to stabilize the active device is to add a series resistance or a shunt conductance to the port. Figure 9-10 shows the configuration for the input port. This loading in conjunction with $\operatorname{Re}\{Z_S\}$ must compensate the negative contribution of $\operatorname{Re}\{Z_{in}\}$. Thus, we require

$$\operatorname{Re}\{Z_{in} + R_{in}' + Z_S\} > 0 \text{ or } \operatorname{Re}\{Y_{in} + G_{in}' + Y_S\} > 0 \quad (9.31a)$$

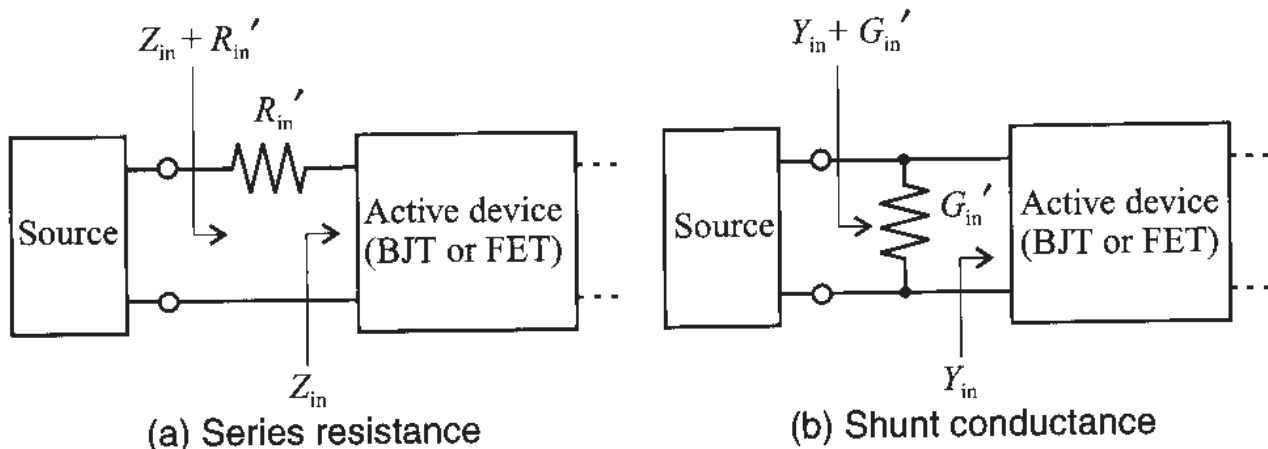


Figure 9-10 Stabilization of input port through series resistance or shunt conductance.

Following an identical argument, Figure 9-11 shows the stabilization of the output port. The corresponding condition is

$$\operatorname{Re}\{Z_{\text{out}} + R_{\text{out}}' + Z_L\} > 0 \text{ or } \operatorname{Re}\{Y_{\text{out}} + G_{\text{out}}' + Y_L\} > 0 \quad (9.31b)$$

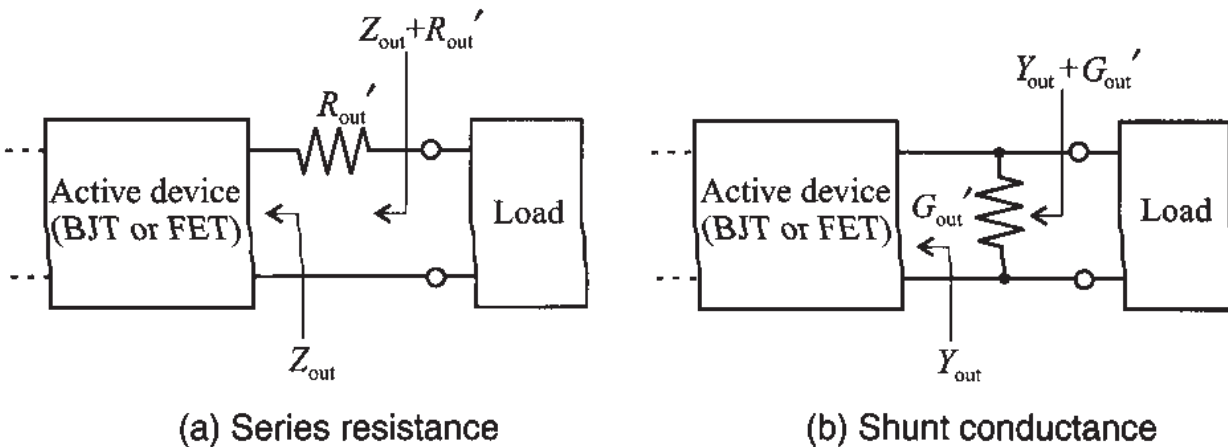
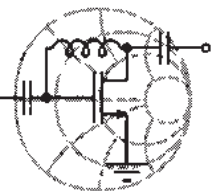


Figure 9-11 Stabilization of output port through series resistance or shunt conductance.

The next example explains the stabilization procedure for transistor.



RF & MW →

Example 9-5: Stabilization of a BJT

Using the transistor BFG505W from Example 9-3 operated at $f = 750$ MHz (and with the S -parameters given as follows: $S_{11} = 0.56\angle-78^\circ$, $S_{21} = 0.05\angle33^\circ$, $S_{12} = 8.64\angle122^\circ$, and $S_{22} = 0.66\angle-42^\circ$), attempt to stabilize the transistor by finding a series resistor or shunt conductance for the input and output ports.

Solution: With given S -parameters we can identify the input and output stability circles by computing their radii and center positions: $C_{\text{in}} = 62.21\angle119^\circ$, $r_{\text{in}} = 61.60$, and $C_{\text{out}} = 4.12\angle70^\circ$, $r_{\text{out}} = 3.44$. The corresponding stability circles are shown in Figure 9-12. A constant resistance circle $r' = 0.33$ in the Z -chart indicates the minimal series resistance that has to be connected to the input of the transistor to make this port stable. If a passive network is connected in series to the resistor with the value of $R_{\text{in}}' = r'Z_0 = 16.5 \Omega$, then the combined impedance will be located inside of the $r' = 0.33$ circle and therefore in the stable

region. Similarly, by tracing a constant conductance circle $g' = 2.8$ we find the shunt admittance $G_{in}' = g'/Z_0 = 56 \text{ mS}$ that stabilizes the input of the transistor. This time any passive network connected to G_{in}' will have the combined admittance residing inside of the $g' = 2.8$ circle in the Y-chart, which is inside the stable region for the input port of the transistor.

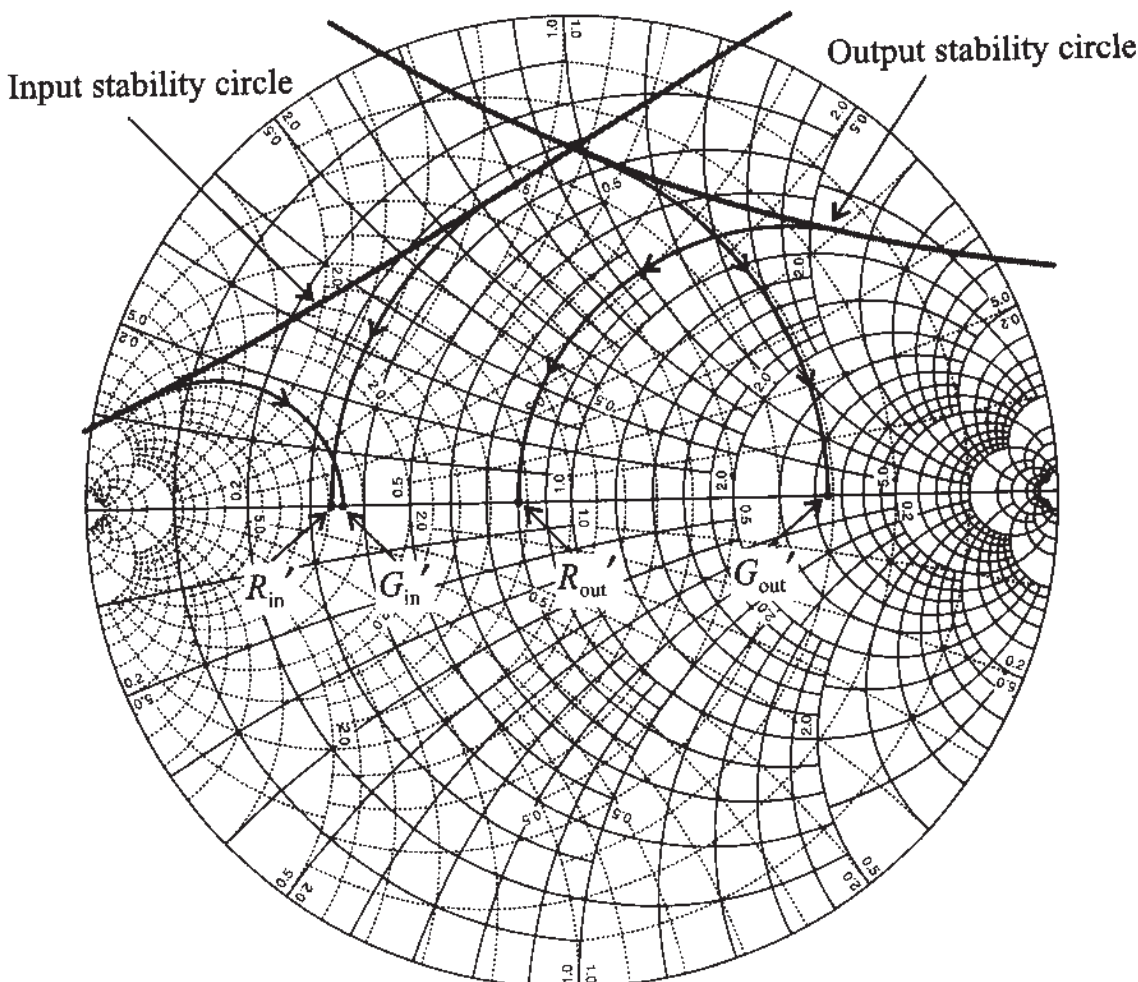


Figure 9-12 Input and output stability circles and circles for finding stabilizing series resistance and shunt conductances.

Following an identical procedure we can find a series resistance of $R_{out}' = 40 \Omega$ and a shunt conductance $G_{out}' = 6.2 \text{ mS}$, which stabilize the output port of the transistor.

Due to the coupling between input and output ports of the transistor it is usually sufficient to stabilize one port. The choice of which port is generally up to the circuit designer. However, one

attempts to avoid resistive elements at the input port since they cause additional noise to be amplified.

Stabilization through the addition of resistors comes at a prize: the impedance matching can suffer, there may be a loss in power flow, and the noise figure typically worsens due to the additional thermal noise sources that the resistors present.

9.4 Constant Gain

9.4.1 Unilateral Design

Besides ensuring stability, the need to obtain a desired gain performance is another important consideration in the amplifier design task. If, as sometimes done in practice, the influence of the transistor's feedback is neglected ($S_{12} \approx 0$), we can employ the unilateral power gain G_{TU} described by (9.12). This equation is rewritten such that the individual contributions of the matching networks become identifiable. With reference to Figure 9-13, we write

$$G_{TU} = \frac{1 - |\Gamma_S|^2}{|1 - S_{11}\Gamma_S|^2} \times |S_{21}|^2 \times \frac{1 - |\Gamma_L|^2}{|1 - \Gamma_L S_{22}|^2} = G_S \times G_0 \times G_L \quad (9.32)$$

where the individual blocks are

$$G_S = \frac{1 - |\Gamma_S'|^2}{|1 - S_{11}\Gamma_S'|^2}, \quad G_0 = |S_{21}|^2, \quad G_L = \frac{1 - |\Gamma_L'|^2}{|1 - \Gamma_L S_{22}|^2} \quad (9.33)$$

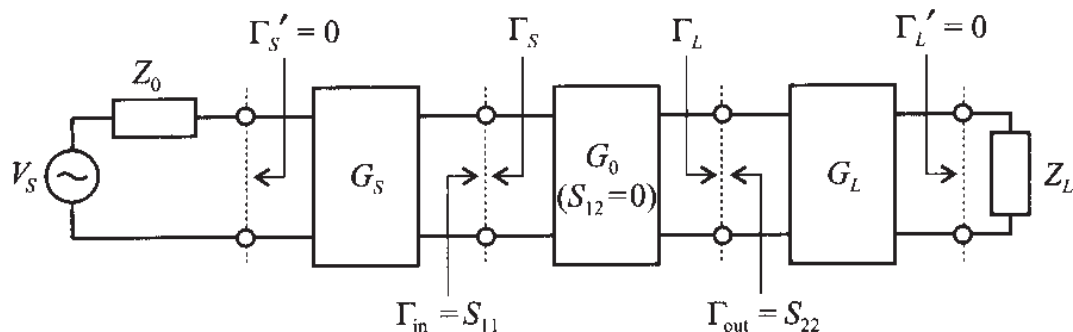


Figure 9-13 Unilateral power gain system arrangement.

Because most gain calculations are done in dB, (9.32) is frequently expressed as

$$G_{TU}(\text{dB}) = G_S(\text{dB}) + G_0(\text{dB}) + G_L(\text{dB}) \quad (9.34)$$

where G_S and G_L are gains associated with input and output matching networks and G_0 is the insertion gain of the transistor. As seen from (9.33), the network gains can be greater than unity which at first glance might appear stronger since they do not contain any active devices. The reason for this seemingly contradictory behavior is that without any matching a significant power loss can occur at the input and output sides of the amplifier. The use of G_S and G_L attempts to reduce these inherent losses, which is considered a gain.

If $|S_{11}|$ and $|S_{22}|$ are less than unity, the maximal unilateral power gain $G_{TU\max}^*$ results when both input and output are matched (i.e., $\Gamma_S = S_{11}^*$ and $\Gamma_L = S_{22}^*$). For this case it is seen that

$$G_{S\max} = \frac{1}{1 - |S_{11}|^2} \quad (9.35)$$

$$G_{L\max} = \frac{1}{1 - |S_{22}|^2} \quad (9.36)$$

The contributions from G_S and G_L can be normalized with respect to their maximum values such that

$$g_S = \frac{G_S}{G_{S\max}} = \frac{1 - |\Gamma_S|^2}{|1 - S_{11}\Gamma_S|^2} (1 - |S_{11}|^2) \quad (9.37a)$$

$$g_L = \frac{G_L}{G_{L\max}} = \frac{1 - |\Gamma_L|^2}{|1 - S_{22}\Gamma_L|^2} (1 - |S_{22}|^2) \quad (9.37b)$$

where the normalized gain is given in both cases as $0 \leq g_i \leq 1$, with $i = S, L$.

Even though we have explicit gain equations for the input and output matching networks, they are not directly usable in terms of providing parametric curves of constant gain. The key question that must be answered is formulated as follows: For a given S_{11} (or S_{22}) and a desired normalized gain g_S (or g_L), what is the range of values for Γ_S (or Γ_L) that achieves a particular gain? The solution requires the inversion of (9.37)

$$g_i = \frac{1 - |\Gamma_i|^2}{|1 - S_{ii}\Gamma_i|^2} (1 - |S_{ii}|^2) \quad (9.38)$$

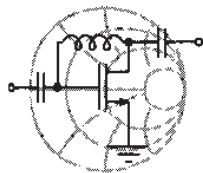
for the reflection coefficient Γ_i . Here $ii = 11, 22$ depending on $i = S, L$. The result is a set of circles with center locations at

$$d_{g_i} = \frac{g_i S_{ii}^*}{1 - |S_{ii}|^2(1 - g_i)} \quad (9.39)$$

and radii of size

$$r_{g_i} = \frac{\sqrt{1 - g_i}(1 - |S_{ii}|^2)}{1 - |S_{ii}|^2(1 - g_i)} \quad (9.40)$$

Example 9-6 details the necessary steps to derive the unilateral constant gain circle equations (9.39) and (9.40).



RF & MW

Example 9-6: Derivation of the constant gain circles

Find the expressions for d_{g_i} and r_{g_i} as given in (9.39) and (9.40).

Solution: The derivation begins with (9.38), which is rewritten as

$$g_i(1 + |S_{ii}\Gamma_i|^2 - S_{ii}^*\Gamma_i^* - S_{ii}\Gamma_i) = 1 - |S_{ii}|^2 - |\Gamma_i|^2 + |S_{ii}|^2|\Gamma_i|^2 \quad (9.41a)$$

The reflection coefficient Γ_i can be factored out such that

$$\begin{aligned} |\Gamma_i|^2 - \frac{g_i S_{ii}}{1 - |S_{ii}|^2(1 - g_i)}\Gamma_i - \frac{g_i S_{ii}^*}{1 - |S_{ii}|^2(1 - g_i)}\Gamma_i^* + \\ + \frac{g_i^2 |S_{ii}|^2}{(1 - |S_{ii}|^2(1 - g_i))^2} = \frac{(1 - g_i)(1 - |S_{ii}|^2)^2}{(1 - |S_{ii}|^2(1 - g_i))^2} \end{aligned} \quad (9.41b)$$

This equation is the complex form of a circle expression

$$(\Gamma_i - d_{g_i})(\Gamma_i^* - d_{g_i}^*) = r_{g_i}^2 \quad (9.41c)$$

with

$$d_{g_i} = \frac{g_i S_{ii}^*}{1 - |S_{ii}|^2(1 - g_i)} \text{ and } r_{g_i} = \frac{\sqrt{1 - g_i}(1 - |S_{ii}|^2)}{1 - |S_{ii}|^2(1 - g_i)}$$

Multiplying out (9.41c) results in the more familiar from

$$(\Gamma_i^R - d_{g_i}^R)^2 + (\Gamma_i^I - d_{g_i}^I)^2 = r_{g_i}^2 \quad (9.41d)$$

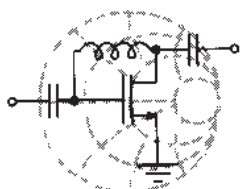
where superscripts R and I denote real and imaginary parts of Γ_i and d_{g_i} .

Because of the unilateral assumption we are able to derive separate gain circle equations for input and output ports.

The following observations can be made from the constant gain circle equations (9.39) and (9.40):

- The maximum gain $G_{i\max} = 1/(1 - |S_{ii}|^2)$ is obtained for $\Gamma_i = S_{ii}^*$, which coincides with the gain circle whose center is at $d_{g_i} = S_{ii}^*$ and of radius $r_{g_i} = 0$.
- The constant gain circles all have their centers on a line connecting the origin to S_{ii}^* . The smaller the gain values, the closer the center d_{g_i} moves to the origin and the larger the radius r_{g_i} .
- For the special case $\Gamma_i = 0$, the normalized gain becomes $g_i = 1 - |S_{ii}|^2$ and both d_{g_i} and r_{g_i} have the same value $d_{g_i} = r_{g_i} = |S_{ii}|/(1 + |S_{ii}|^2)$. This implies that the $G_i = 1$ (or 0 dB) circle always passes through the origin of the Γ_i -plane.

Example 9-7 demonstrates the source gain circles for an amplifier design under unilateral approximation.



RF & MW

Example 9-7: Computation of the source gain circles for a unilateral design

A FET is operated at $f = 4$ GHz and is biased such that $S_{11} = 0.7 \angle 125^\circ$. It is assumed that the transistor is unconditionally stable so that the unilateral approximation can be applied. Find the maximum source gain $G_{S\max}$ and plot the constant source gain circles for several values of G_S .

Solution: First we find the maximum source gain $G_{S\max}$ using (9.35). The result is

$$G_{S_{\max}} = \frac{1}{1 - |S_{11}|^2} = \frac{1}{1 - 0.7^2} = 1.96 \text{ or } G_{S_{\max}} = 2.92 \text{ dB}$$

We can now plot the constant gain circles by using (9.39) and (9.40) for the computation of circle centers d_{g_S} and radii r_{g_S} . A summary of several arbitrary source gains G_S is presented in Table 9-3.

Table 9-3 Parameters for constant source gain circles in Example 9-7.

| G_S | g_S | d_{g_S} | r_{g_S} |
|--------|-------|--------------------------|-----------|
| 2.6 dB | 0.93 | $0.67 \angle -125^\circ$ | 0.14 |
| 2 dB | 0.81 | $0.62 \angle -125^\circ$ | 0.25 |
| 1 dB | 0.64 | $0.54 \angle -125^\circ$ | 0.37 |
| 0 dB | 0.51 | $0.47 \angle -125^\circ$ | 0.47 |
| -1 dB | 0.41 | $0.40 \angle -125^\circ$ | 0.56 |

As seen from Table 9-3, the radius r_{g_S} of the $G_S = 0$ dB circle is equal to the magnitude of its center position d_{g_S} and the circle indeed passes through the center of the Smith Chart. We also observe that the centers for all G_S circles are located on the $\Theta = \angle S_{11}^* = -125^\circ$ line, and as G_S approaches $G_{S_{\max}}$, the radius of the corresponding circle reduces to zero and its center position becomes $S_{11}^* = 0.7 \angle -125^\circ$.

Figure 9-14 illustrates the source gain circles based on the computed numerical values given in Table 9-3. The figure points out clearly that, despite the input matching network being passive, the gain can be greater than 0 dB, indicating amplification. The physical meaning for such a behavior lies in the fact that the matching network reduces the input reflection coefficient of the overall system, thus effectively creating an “additional” gain.

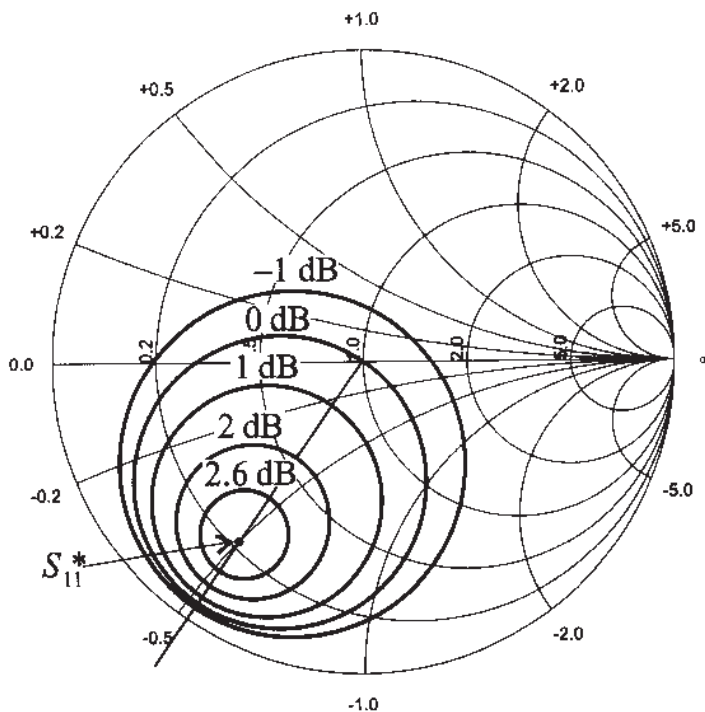
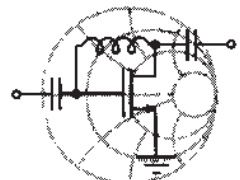


Figure 9-14 Constant source gain circles in the Smith Chart.

The underlying assumption of this example is that the gain associated with the matched input port is not affected by the output since the unilateral approximation neglects the reverse gain.

We next discuss a typical application that requires the use of the constant gain circle approach. Specifically, let us develop a unilateral amplifier for a predetermined fixed gain value.



RF & MW →

Example 9-8: Design of a 18 dB single-stage MESFET amplifier operated at 5.7 GHz

A MESFET operated at 5.7 GHz has the following S -parameters:
 $S_{11} = 0.5 \angle -60^\circ$, $S_{12} = 0.02 \angle 0^\circ$, $S_{21} = 6.5 \angle 115^\circ$, and
 $S_{22} = 0.6 \angle -35^\circ$.

- (a) Determine if the circuit is unconditionally stable.

- (b) Find the maximum power gain under optimal choice of the reflection coefficients, assuming the unilateral design ($S_{12} = 0$).
- (c) Adjust the load reflection coefficient such that the desired gain is realized using the concept of constant gain circles.

Solution: (a) The stability of the device is tested via (9.24) and (9.29), with the results

$$k = \frac{1 - |S_{11}|^2 - |S_{22}|^2 + |\Delta|^2}{2|S_{12}||S_{21}|} = 2.17$$

and

$$|\Delta| = |S_{11}S_{22} - S_{12}S_{21}| = 0.42$$

Because $k > 1$ and $|\Delta| < 1$, the transistor is unconditionally stable.

(b) We next compute the maximum gain for the optimal choice of the reflection coefficients (i.e., $\Gamma_L = S_{22}^*$ and $\Gamma_S = S_{11}^*$)

$$G_{S\max} = \frac{1}{1 - |S_{11}|^2} = 1.33 \text{ or } 1.25 \text{ dB}$$

$$G_{L\max} = \frac{1}{1 - |S_{22}|^2} = 1.56 \text{ or } 1.94 \text{ dB}$$

$$G_0 = |S_{21}|^2 = 42.25 \text{ or } 16.26 \text{ dB}$$

Therefore, the maximum unilateral transducer gain is given by

$$G_{TU\max} = G_{S\max} G_0 G_{L\max} = 88.02 \text{ or } 19.45 \text{ dB}$$

(c) Since the source matching network ($\Gamma_S = S_{11}^*$) and the transistor combined already provide a gain of 17.51 dB, we have to choose Γ_L in such a way that $G_L = 0.49$ dB. This means that Γ_L has to reside on the $r_{g_L} = 0.38$, $d_{g_L} = 0.48 \angle 35^\circ$ circle, as shown in Figure 9-15. If we choose $\Gamma_L = 0.03 + j0.17$, the output matching network reduces to a single element (i.e., a series inductor with a value of $L = 0.49$ nH) provided the load is equal to the characteristic impedance ($Z_L = Z_0$).

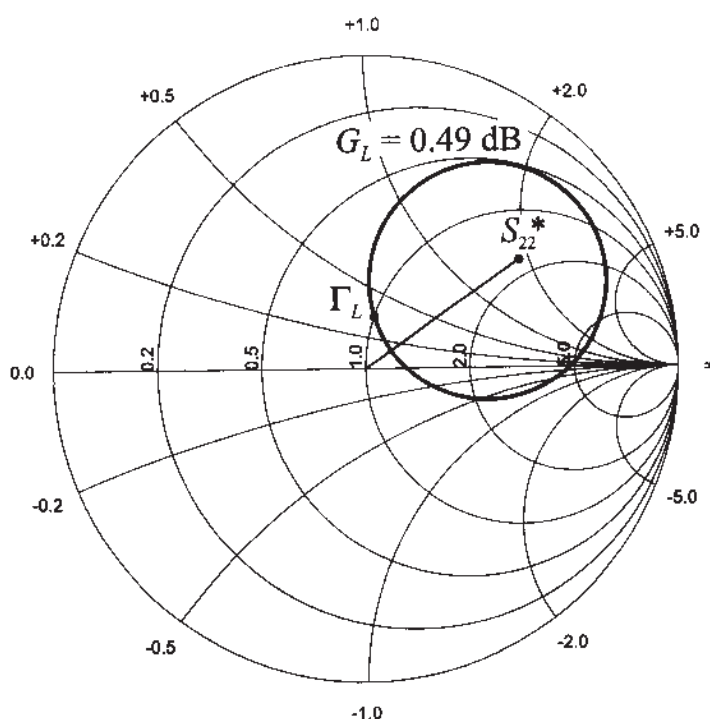


Figure 9-15 Constant load gain circle in the Smith Chart.

If the amplifier is operated over a range of frequencies, the gain has to be determined for a corresponding number of discrete frequency points due to the changing S-parameters.

For the case where $|S_{ii}| > 1$ ($ii = 11$ for the input port and $ii = 22$ for the output port) it is possible for a passive network to produce an infinite value of G_i ($i = S$ or L , respectively). This situation occurs when $\Gamma_i = S_{ii}^{-1}$, meaning that the real component of the impedance associated with Γ_i is equal in magnitude to the negative resistance related to S_{ii} . Thus, the two resistances cancel each other and oscillations will result: the amplifier is unstable. To avoid this problem, we plot the constant gain circles for $|S_{ii}| > 1$ and the corresponding stability circle and choose Γ_i in such a way that it is located on the desired gain circle but also resides inside the stable region.

9.4.2 Unilateral Figure of Merit

The unilateral design approach discussed in Example 9-8 involves the approximation that the feedback effect, or the reverse gain, of the amplifier is negligible ($S_{12} = 0$). To estimate the error due to this assumption, the ratio between the transducer gain G_T , which takes into account S_{12} , and the unilateral transducer gain G_{TU} can be formed. Using definitions (9.8) and (9.12), we find

$$\frac{G_T}{G_{TU}} = \frac{1}{\left| 1 - \frac{S_{12}S_{21}\Gamma_L\Gamma_S}{(1-S_{11}\Gamma_S)(1-S_{22}\Gamma_L)} \right|^2} \quad (9.42)$$

where $G_T \leq G_{TU}$.

The maximum value of G_{TU} , and therefore the maximum error, is obtained for the input and output matching conditions ($\Gamma_S = S_{11}^*$ and $\Gamma_L = S_{22}^*$). Therefore, (9.42) becomes

$$\frac{G_T}{G_{TU\max}} = \frac{1}{\left| 1 - \frac{S_{12}S_{21}S_{22}^*S_{11}^*}{(1-\lvert S_{11} \rvert^2)(1-\lvert S_{22} \rvert^2)} \right|^2} \quad (9.43)$$

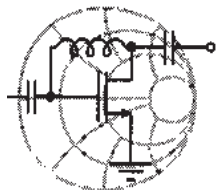
This can be used to set bounds on the error fluctuation

$$(1+U)^{-2} \leq \frac{G_T}{G_{TU}} \leq (1-U)^{-2} \quad (9.44)$$

where U is known as the frequency-dependent **unilateral figure of merit**:

$$U = \frac{\lvert S_{12} \rvert \lvert S_{21} \rvert \lvert S_{22} \rvert \lvert S_{11} \rvert}{(1-\lvert S_{11} \rvert^2)(1-\lvert S_{22} \rvert^2)} \quad (9.45)$$

To justify a unilateral amplifier design approach, this figure of merit should be as small as possible. In the limit, as G_T approaches G_{TU} for the ideal case of $S_{12} = 0$, we see that the error does indeed vanish (i.e., $U = 0$).



RF & MW →

Example 9-9: Unilateral design applicability test

For the amplifier discussed in Example 9-8 estimate the error that is introduced by making the unilateral design approximation.

Solution: Substituting the S -parameter values into (9.45), the unilateral figure of merit is found to be

$$U = \frac{\lvert S_{12} \rvert \lvert S_{21} \rvert \lvert S_{22} \rvert \lvert S_{11} \rvert}{(1-\lvert S_{11} \rvert^2)(1-\lvert S_{22} \rvert^2)} = 0.0812$$

The maximum error can then be estimated from (9.44):

$$0.86 \leq \frac{G_T}{G_{TU}} \leq 1.18$$

This implies that the theoretical value for the transducer gain can deviate from its unilateral approximation by as much as 18%. Practically, however, the actual difference often is much smaller. This becomes apparent if we substitute the values obtained in Example 9-8 into the transducer power gain definition (9.8). It is found that $G_T = 62.86$ or 17.98 dB, which compares favorably with $G_{TU} = 63.10$ or 18 dB. In other words, we introduced an error of less than 1%.

The unilateral figure of merit computation constitutes a very conservative, worst case error estimation.

9.4.3 Bilateral Design

For many practical situations the unilateral approach may not be appropriate because the error committed by setting $S_{12} = 0$ could result in an intolerably imprecise design. The **bilateral design** takes into account this feedback. Instead of the unilateral matching $\Gamma_S^* = S_{11}$ and $\Gamma_L^* = S_{22}$, it deals with the complete equations [see (9.15b) and (9.15c)] for the input and output reflection coefficients

$$\Gamma_S^* = S_{11} + \frac{S_{12}S_{21}\Gamma_L}{1 - S_{22}\Gamma_L} = \frac{S_{11} - \Gamma_L\Delta}{1 - S_{22}\Gamma_L} \quad (9.46a)$$

$$\Gamma_L^* = S_{22} + \frac{S_{12}S_{21}\Gamma_S}{1 - S_{11}\Gamma_S} = \frac{S_{22} - \Gamma_S\Delta}{1 - S_{11}\Gamma_L} \quad (9.46b)$$

which require a **simultaneous conjugate match**. The meaning of *simultaneous* implies that matched source and load reflection coefficients Γ_{MS} and Γ_{ML} have to be found that satisfy both coupled equations. If the device is potentially unstable, then a simultaneous complex conjugate does not exist. The solution approach to obtain these optimal coefficients is outlined in Example 9-10. The final results, for the **matched source reflection coefficient** Γ_{MS} is

$$\Gamma_{MS} = \frac{B_1}{2C_1} - \frac{1}{2}\sqrt{\left(\frac{B_1}{C_1}\right)^2 - 4\frac{C_1^*}{C_1}} \quad (9.47)$$

where

$$C_1 = S_{11} - S_{22}^* \Delta \text{ and } B_1 = 1 - |S_{22}|^2 - |\Delta|^2 + |S_{11}|^2 \quad (9.48)$$

Similarly, the matched load reflection coefficient Γ_{ML} is

$$\Gamma_{ML} = \frac{B_2}{2C_2} - \frac{1}{2}\sqrt{\left(\frac{B_2}{C_2}\right)^2 - 4\frac{C_2^*}{C_2}} \quad (9.49)$$

where

$$C_2 = S_{22} - S_{11}^* \Delta \text{ and } B_2 = 1 - |S_{11}|^2 - |\Delta|^2 + |S_{22}|^2 \quad (9.50)$$

The solutions (9.47) and (9.49) are derived under the assumption of unconditional stability.

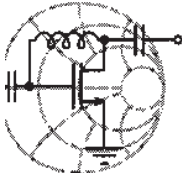
With Γ_{ML} and Γ_{MS} given by (9.47) and (9.49), the optimal matching can be rewritten as

$$\Gamma_{MS}^* = S_{11} + \frac{S_{12}S_{21}\Gamma_{ML}}{1 - S_{22}\Gamma_{ML}} \quad (9.51a)$$

and

$$\Gamma_{ML}^* = S_{22} + \frac{S_{12}S_{21}\Gamma_{MS}}{1 - S_{11}\Gamma_{MS}} \quad (9.51b)$$

It is noted that the unilateral approach, which decouples input and output ports, is a subset of the bilateral design approach.



RF & MW →

Example 9-10: Derivation of simultaneous conjugate matched reflection coefficients

Derive the reflection coefficient expression (9.47).

Solution: Starting from (9.46a) and (9.46b), we see that

$$(1 - S_{22}\Gamma_L)(\Gamma_S^* - S_{11}) = \Gamma_L S_{12}S_{21} \quad (9.52a)$$

$$(1 - S_{11}\Gamma_S)(\Gamma_L^* - S_{22}) = \Gamma_S S_{12} S_{21} \quad (9.52b)$$

Solving (9.52a) for Γ_L yields

$$\Gamma_L = \frac{S_{11} - \Gamma_S^*}{\Delta - S_{22}\Gamma_S^*} \quad (9.52c)$$

Substituting (9.52c) into (9.52b) results, after some algebra, in

$$\Gamma_S^2(S_{11} - S_{22}^*\Delta) - \Gamma_S(1 + |S_{11}|^2 - |S_{22}|^2 - |\Delta|^2) = -S_{11}^* + S_{22}\Delta^* \quad (9.52d)$$

Identifying $C_1 = (S_{11} - S_{22}^*\Delta)$, $B_1 = (1 + |S_{11}|^2 - |S_{22}|^2 - |\Delta|^2)$ leads to the standard quadratic equation

$$\Gamma_S^2 - \frac{B_1}{C_1}\Gamma_S = -C_1^* \quad (9.52e)$$

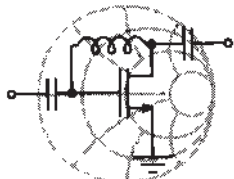
whose solution is

$$\Gamma_{MS} = \frac{B_1}{2C_1} - \frac{1}{2}\sqrt{\left(\frac{B_1}{C_1}\right)^2 - 4\frac{C_1^*}{C_1}} \quad (9.52f)$$

The negative sign in front of the square root is picked to ensure stability ($k > 1$).

An identical analysis approach for the load side leads to a quadratic equation for Γ_L whose solution yields Γ_{ML} .

Example 9-11 demonstrates the use of simultaneously complex conjugate reflection coefficients for the design of an amplifier with maximum gain.



RF & MW →

Example 9-11: Amplifier design for maximum gain

A BJT with $I_C = 10$ mA and $V_{CE} = 6$ V is operated at a frequency of $f = 2.4$ GHz. The corresponding S -parameters are: $S_{11} = 0.3\angle 30^\circ$, $S_{12} = 0.2\angle -60^\circ$, $S_{21} = 2.5\angle -80^\circ$, and $S_{22} = 0.2\angle -15^\circ$. Determine whether the transistor is uncondition-

ally stable and find the values for source and load reflection coefficients that provide maximum gain.

Solution: The stability of the transistor is determined by computing k and $|\Delta|$ based on (9.24) and (9.29) with the explicit result of $k = 1.18$, $|\Delta| = 0.56$. Since $k > 1$ and $|\Delta| < 1$, the transistor is unconditionally stable.

As we see from the S-parameters of the transistor, S_{12} has a relatively large magnitude and the use of the unilateral design method for the amplifier does not appear appropriate, suggesting the bilateral approach instead.

Using (9.48) and (9.50), we find the coefficients $C_1 = 0.19 + j0.06$, $B_1 = 0.74$, and $C_2 = 0.03 + j0.07$, $B_2 = 0.64$, which allow us to compute the simultaneously complex conjugate source and load reflection coefficients $\Gamma_{MS} = 0.30\angle-18^\circ$ and $\Gamma_{ML} = 0.12\angle69^\circ$, respectively. It should be noted that these values differ significantly from S_{11}^* and S_{22}^* , which are the basis for the unilateral design.

Applying (9.8), with Γ_L and Γ_S replaced by Γ_{ML} and Γ_{MS} , we find the transducer gain to be $G_T = 8.42$ dB. This also happens to be the maximum transducer gain $G_{T_{max}}$.

The discrepancy between unilateral and bilateral gain is best seen in the large differences in phase between S_{11}^ and Γ_{MS} as well as S_{22}^* and Γ_{ML} .*

9.4.4 Operating and Available Power Gain Circles

For the situation where the reverse gain of S_{12} cannot be neglected, the input impedance is dependent on the load reflection coefficient. Conversely, the output impedance becomes a function of the source reflection coefficient. Because of this mutual coupling, the unilateral approach described in Section 9.4.1 is not appropriate to design an amplifier for a predetermined gain.

In the bilateral case, which takes into account the mutual coupling between input and output ports, there are two alternative design methods to develop amplifiers with a specified gain.

The first method is based on the use of the operating power gain G given by (9.14). Here we attempt to find the load reflection coefficient Γ_L , assuming that the source is complex conjugate matched to the input reflection coefficient [i.e., $\Gamma_S = \Gamma_{in}^*$, where Γ_{in} is computed based on (9.9a)]. This method yields an input voltage standing wave ratio of $VSWR_{in} = 1$.

The second method uses the available power gain G_A definition of (9.13). In this case we assume perfect match on the output side of the amplifier ($\Gamma_L = \Gamma_{out}^*$), and the load is chosen in such a way as to satisfy the gain requirement. This method is preferable if the output standing wave ratio should be unity (i.e., $VSWR_{out} = 1$).

Operating Power Gain

To develop the design procedure based on using the operating power gain (and thus ensuring $VSWR_{in} = 1$), we rewrite (9.14) in the form

$$G = \frac{(1 - |\Gamma_L|^2)|S_{21}|^2}{(1 - |\Gamma_{in}|^2)|1 - S_{22}\Gamma_L|^2} = \frac{(1 - |\Gamma_L|^2)|S_{21}|^2}{\left(1 - \left|S_{11} + \frac{S_{21}S_{12}\Gamma_L|^2}{1 - S_{22}\Gamma_L}\right|^2\right)|1 - S_{22}\Gamma_L|^2} = g_o |S_{21}|^2 \quad (9.53)$$

where we use (9.9a) for Γ_{in} . The factor g_o defines a proportionality factor given by

$$g_o = \frac{1 - |\Gamma_L|^2}{\left(1 - \left|S_{11} + \frac{S_{21}S_{12}\Gamma_L|^2}{1 - S_{22}\Gamma_L}\right|^2\right)|1 - S_{22}\Gamma_L|^2} = \frac{1 - |\Gamma_L|^2}{|1 - S_{22}\Gamma_L|^2 - |S_{11} - \Delta\Gamma_L|^2} \quad (9.54)$$

As shown in Example 9-12, (9.54) can be rewritten in terms of a circle equation for the load reflection coefficient Γ_L ; that is,

$$|\Gamma_L - d_{g_o}| = r_{g_o} \quad (9.55)$$

where the center position d_{g_o} is

$$d_{g_o} = \frac{g_o(S_{22} - \Delta S_{11}^*)}{1 + g_o(|S_{22}|^2 - |\Delta|^2)} \quad (9.56)$$

and the radius r_{g_o} is defined as

$$r_{g_o} = \frac{\sqrt{1 - 2kg_0|S_{12}S_{21}| + g_0^2|S_{12}S_{21}|^2}}{|1 + g_0(|S_{22}|^2 - |\Delta|^2)|} \quad (9.57)$$

with k denoting the Roulette stability factor as defined in (9.24).

RF & MW

Example 9-12: Operating power gain circle derivation

Starting from (9.54), derive the circle equation (9.55) in the complex Γ_L -plane.

Solution: First we rewrite (9.54) in the form

$$g_o = \frac{1 - |\Gamma_L|^2}{1 - |S_{11}|^2 + |\Gamma_L|^2(|S_{22}|^2 - |\Delta|^2) - 2\operatorname{Re}\{\Gamma_L(S_{22} - \Delta S_{11}^*)\}} \quad (9.58)$$

After multiplying both sides of (9.58) by the denominator and rearranging terms, we see that

$$\begin{aligned} |\Gamma_L|^2[1 + g_o(|S_{22}|^2 - |\Delta|^2)] - 2g_o\operatorname{Re}\{\Gamma_L(S_{22} - \Delta S_{11}^*)\} &= \\ &= 1 - g_o(1 - |S_{11}|^2) \end{aligned} \quad (9.59)$$

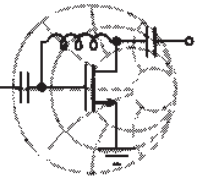
Dividing (9.59) by $[1 + g_o(|S_{22}|^2 - |\Delta|^2)]$, we find

$$|\Gamma_L|^2 - \frac{2g_o\operatorname{Re}\{\Gamma_L(S_{22} - \Delta S_{11}^*)\}}{1 + g_o(|S_{22}|^2 - |\Delta|^2)} = \frac{1 - g_o(1 - |S_{11}|^2)}{1 + g_o(|S_{22}|^2 - |\Delta|^2)}$$

This equation can already be recognized as a circle equation of the form $|\Gamma_L - d_{g_o}|^2 = r_{g_o}^2$, where the circle center d_{g_o} is given by (9.56) and the radius r_{g_o} is computed from

$$\begin{aligned} r_{g_o}^2 &= \frac{1 - g_o(1 - |S_{11}|^2)}{1 + g_o(|S_{22}|^2 - |\Delta|^2)} + \left| \frac{g_o(S_{22} - \Delta S_{11}^*)^*}{1 + g_o(|S_{22}|^2 - |\Delta|^2)} \right|^2 \\ &= \frac{[1 - g_o(1 - |S_{11}|^2)][1 + g_o(|S_{22}|^2 - |\Delta|^2)] + [g_o|S_{22} - \Delta S_{11}^*|]^2}{[1 + g_o(|S_{22}|^2 - |\Delta|^2)]^2} \\ &= \frac{1 - g_o(1 - |S_{11}|^2 - |S_{22}|^2 + |\Delta|^2) - g_o^2 M}{[1 + g_o(|S_{22}|^2 - |\Delta|^2)]^2} \\ &= \frac{1 - 2g_o|S_{12}S_{21}|k - g_o^2 M}{[1 + g_o(|S_{22}|^2 - |\Delta|^2)]^2} \end{aligned}$$

where k is the stability factor defined in (9.24) and M is a constant given by

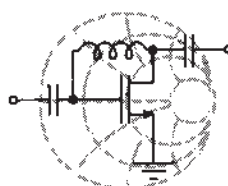


$$M = (1 - |S_{11}|^2)(|S_{22}|^2 - |\Delta|^2) - |S_{22} - \Delta S_{11}^*|^2 = -|S_{12}S_{21}|^2$$

Thus, for the square of the circle radius we obtain

$$r_{g_o}^2 = \frac{1 - 2g_o|S_{12}S_{21}|k + g_o^2|S_{12}S_{21}|^2}{[1 + g_o(|S_{22}|^2 - |\Delta|^2)]^2}$$

which agrees with (9.57).



RF & MW

Example 9-13: Amplifier design using the constant operating gain circles

Use the same BJT as described in Example 9-11, but instead of $G_{T_{\max}} = 8.42$ dB, design an amplifier with 8 dB power gain. In addition, ensure a perfect match on the input port of the amplifier.

Solution: As shown in Example 9-11, the transistor is unconditionally stable. Because a perfect match on the input port must be maintained, we employ the operating power gain circles in our design.

First we compute the value of factor g_o ; that is,

$$g_o = \frac{G}{|S_{21}|^2} = 1.0095$$

where $G = 6.31$ is the required 8 dB operating gain. Substituting g_o into (9.56) and (9.57), we find center and radius of the constant operating gain circle in the Γ_L -plane. The corresponding values are $d_{g_o} = 0.11 \angle 69^\circ$ and $r_{g_o} = 0.35$. The constant gain circle is shown in Figure 9-16.

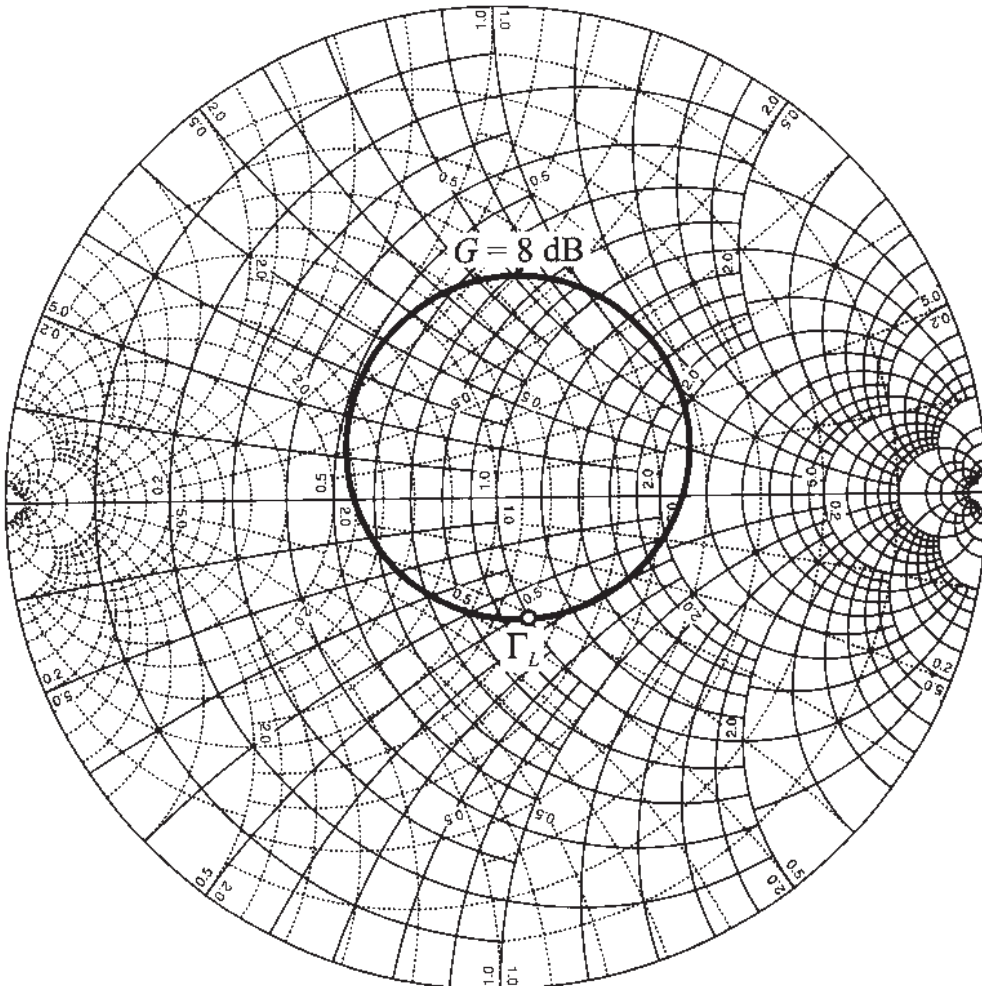


Figure 9-16 Constant operating power circle in the Γ_L -plane.

There is a great variety of possible choices for the load reflection coefficient that ensures a $G = 8 \text{ dB}$ operating gain. To simplify the output matching network, we pick Γ_L at the intersection of the constant gain circle with the constant resistance circle $r = 1$ (see Figure 9-16). The value obtained at that point is $\Gamma_L = 0.26\angle-75^\circ$. With Γ_L known, we can next find the source reflection coefficient that must be the conjugate to the input reflection coefficient as given in (9.9a):

$$\Gamma_S = \left(\frac{S_{11} - \Delta\Gamma_L}{1 - S_{22}\Gamma_L} \right)^* = 0.28\angle-55^\circ$$

Based on the previously computed values, we check the correctness of our approach. Substituting Γ_{in} and Γ_L into (9.10), we find that the transducer power gain is indeed 8 dB.

The complexity of the input matching network is directly affected by the appropriate choice of Γ_L because of the requirement $\Gamma_S = \Gamma_{in}^*$ where Γ_{in} is a function of Γ_L .

In Example 9-13 we pick the value of Γ_L arbitrarily (residing on the desired gain circle) and compute a corresponding input impedance such that $\Gamma_S = \Gamma_{in}^*$, assuming that there are no restrictions imposed on the value of Γ_S . Unfortunately, in many practical applications, Γ_S has to satisfy certain constraints (for example, to stay within a desired noise performance). Such additional conditions may therefore restrict our freedom in using Γ_S and, as a consequence, limit the possible choices for Γ_L . One way to satisfy both requirements (Γ_L residing within an appropriate gain circle, and Γ_S satisfy a particular noise requirement) is via trial-and-error, whereby we arbitrarily pick Γ_L and see whether the corresponding Γ_S meets design specifications. This method is simple but very tedious and time-consuming.

A more scientific approach relies upon mapping the constant gain circle (9.55) in the Γ_L -plane into a circle in the Γ_S -plane, i.e.,

$$|\Gamma_S - d_{g_S}| = r_{g_S} \quad (9.60)$$

where the equations for the circle radius r_{g_S} and its center d_{g_S} are obtained from the requirement that $\Gamma_S = \Gamma_{in}^*$. This can be written as

$$\Gamma_S^* = \frac{S_{11} - \Delta \Gamma_L}{1 - S_{22} \Gamma_L} \quad (9.61)$$

or

$$\Gamma_L = \frac{S_{11} - \Gamma_S^*}{\Delta - S_{22} \Gamma_S^*} \quad (9.62)$$

Substituting (9.62) into (9.55) gives us

$$\left| \frac{S_{11} - \Gamma_S^*}{\Delta - S_{22} \Gamma_S^*} - d_{g_o} \right|^2 = r_{g_o}^2 \quad (9.63)$$

which can be rewritten in the form of (9.60), where the circle radius is

$$r_{g_S} = \frac{r_{g_o} |S_{12} S_{21}|}{\left| 1 - S_{22} d_{g_o} \right|^2 - r_{g_o}^2 |S_{22}|^2} \quad (9.64)$$

and the center is given by

$$d_{g_s} = \frac{(1 - S_{22}d_{g_o})(S_{11} - \Delta d_{g_o})^* - r_{g_o}^2 \Delta^* S_{22}}{|1 - S_{22}d_{g_o}|^2 - r_{g_o}^2 |S_{22}|^2} \quad (9.65)$$

The derivation of (9.64) and (9.65) is left as a problem at the end of this chapter. The example of constant gain circle mapping is discussed further in Section 9.5, Example 9-14.

Available Power Gain

In those cases where perfect matching on the output side of the amplifier is required ($VSWR_{out} = 1$), the available power gain approach should be used instead of the previously presented operating gain method. For this situation, a constant available gain circle equation can be derived in the same fashion as (9.55) is obtained. The result of such a derivation is a circle equation which relates the source reflection coefficient to the desired gain:

$$|\Gamma_S - d_{g_a}| = r_{g_a} \quad (9.66)$$

where the center position d_{g_a} is

$$d_{g_a} = \frac{g_a(S_{11} - \Delta S_{22})^*}{1 + g_a(|S_{11}|^2 - |\Delta|^2)} \quad (9.67)$$

and the radius r_{g_a} is defined as

$$r_{g_a} = \frac{\sqrt{1 - 2kg_a|S_{12}S_{21}| + g_a^2|S_{12}S_{21}|^2}}{|1 + g_a(|S_{11}|^2 - |\Delta|^2)|} \quad (9.68)$$

The proportionality factor g_a is computed as

$$g_a = \frac{G_A}{|S_{21}|^2} \quad (9.69)$$

where G_A is the desired power level.

Similar to the constant operating power circles, a constant available power circle can be mapped into the Γ_L -plane using

$$|\Gamma_L - d_{g_l}| = r_{g_l} \quad (9.70)$$

with the circle radius given by

$$r_{g_l} = \frac{r_{g_a}|S_{12}S_{21}|}{||1 - S_{11}d_{g_a}|^2 - r_{g_a}^2|S_{11}|^2|} \quad (9.71)$$

and the center location defined by

$$d_{g_l} = \frac{(1 - S_{11}d_{g_a})(S_{22} - \Delta d_{g_a})^* - r_{g_a}^2 \Delta^* S_{11}}{|1 - S_{11}d_{g_a}|^2 - r_{g_a}^2|S_{11}|^2} \quad (9.72)$$

We see that r_{g_l} and d_{g_l} for $VSWR_{out} = 1$ have their correspondence to r_{g_s} and d_{g_s} for $VSWR_{in} = 1$ with S_{11} in (9.71) and (9.72) replaced by S_{22} .

9.5 Noise Figure Circles

In many RF amplifiers, the need for signal amplification at low noise level becomes an essential system requirement. Unfortunately, designing a low-noise amplifier competes with such factors as stability and gain. For instance, a minimum noise performance at maximum gain cannot be obtained. It is therefore important to develop a method that allows us to display the influence of noise as part of the Smith Chart to conduct comparisons and observe trade-offs between gain and stability.

From a practical perspective, the key ingredient of a noise analysis is the **noise figure** of a two-port amplifier in the admittance form

$$F = F_{min} + \frac{R_n}{G_S} |Y_S - Y_{opt}|^2 \quad (9.73)$$

or in the equivalent impedance representation

$$F = F_{min} + \frac{G_n}{R_S} |Z_S - Z_{opt}|^2 \quad (9.74)$$

where $Z_S = 1/Y_S$ is the source impedance.

Both expressions are derived in Appendix H. When using transistors, typically four noise parameters are known either through datasheets from the FET or BJT manufacturers or through direct measurements. They are:

- The **minimum (also called optimum) noise figure** F_{min} whose behavior depends on biasing condition and operating frequency. If the device were noise free, we would obtain $F_{min} = 1$.
- The **equivalent noise resistance** $R_n = 1/G_n$ of the device.

- The optimum source admittance $Y_{\text{opt}} = G_{\text{opt}} + jB_{\text{opt}} = 1/Z_{\text{opt}}$. Instead of the impedance or admittance, the optimum reflection coefficient Γ_{opt} is often listed. The relationship between Y_{opt} and Γ_{opt} is given by

$$Y_{\text{opt}} = Y_0 \frac{1 - \Gamma_{\text{opt}}}{1 + \Gamma_{\text{opt}}} \quad (9.75)$$

Since the S -parameter representation is a more suitable choice for high-frequency designs, we convert (9.73) into a form that replaces the admittances by reflection coefficients. Besides (9.75) we use

$$Y_S = Y_0 \frac{1 - \Gamma_S}{1 + \Gamma_S} \quad (9.76)$$

in (9.73). Recognizing that G_S can be written as $G_S = Y_0(1 - |\Gamma_S|^2)/|1 + \Gamma_S|^2$, the final result becomes

$$F = F_{\text{min}} + \frac{4R_n}{Z_0} \frac{|\Gamma_S - \Gamma_{\text{opt}}|^2}{(1 - |\Gamma_S|^2)|1 + \Gamma_{\text{opt}}|^2} \quad (9.77)$$

In (9.77) the quantities F_{min} , R_n , and Γ_{opt} are known. In general, the design engineer has the freedom to adjust Γ_S to affect the noise figure. For $\Gamma_S = \Gamma_{\text{opt}}$ we see that the lowest possible noise figure is achieved, $F = F_{\text{min}}$. To answer the question of how a particular noise figure, let us say F_k , relates to Γ_S , (9.77) is put into the form

$$|\Gamma_S - \Gamma_{\text{opt}}|^2 = (1 - |\Gamma_S|^2)|1 + \Gamma_{\text{opt}}|^2 \left(\frac{F_k - F_{\text{min}}}{4R_n/Z_0} \right) \quad (9.78)$$

which on the right-hand side already suggests the form of a circle equation. Introducing a constant Q_k such that

$$Q_k = |1 + \Gamma_{\text{opt}}|^2 \left(\frac{F_k - F_{\text{min}}}{4R_n/Z_0} \right) \quad (9.79)$$

and rearranging terms gives

$$(1 + Q_k)|\Gamma_S|^2 - 2\text{Re}\{\Gamma_S \Gamma_{\text{opt}}^*\} + |\Gamma_{\text{opt}}|^2 = Q_k \quad (9.80)$$

Division by $(1 + Q_k)$ and forming a complete square yields, after some algebra,

$$\left| \Gamma_S - \frac{\Gamma_{\text{opt}}}{1 + Q_k} \right|^2 = Q_k \left[\frac{1}{1 + Q_k} - \frac{|\Gamma_{\text{opt}}|^2}{(1 + Q_k)^2} \right] = \frac{Q_k^2 + Q_k(1 - |\Gamma_{\text{opt}}|^2)}{(1 + Q_k)^2} \quad (9.81)$$

This is the required circle equation in standard form that can be displayed as part of the Smith Chart:

$$|\Gamma_S - d_{F_k}|^2 = (\Gamma_S^R - d_{F_k}^R)^2 + (\Gamma_S^I - d_{F_k}^I)^2 = r_{F_k}^2 \quad (9.82)$$

with the circle center location d_{F_k} denoted by the complex number

$$d_{F_k} = d_{F_k}^R + j d_{F_k}^I = \frac{\Gamma_{\text{opt}}}{1 + Q_k} \quad (9.83)$$

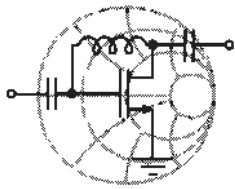
and the associated radius

$$r_{F_k} = \frac{\sqrt{(1 - |\Gamma_{\text{opt}}|^2)Q_k + Q_k^2}}{1 + Q_k} \quad (9.84)$$

There are two noteworthy conclusions that can be drawn from (9.83) and (9.84):

- The minimum noise figure is obtained for $F_k = F_{\min}$, which coincides with the location $d_{F_k} = \Gamma_{\text{opt}}$ and radius $r_{F_k} = 0$.
- All constant noise circles have their centers located along a line drawn from the origin to point Γ_{opt} . The larger the noise figure, the closer the center d_{F_k} moves to the origin and the larger the radius r_{F_k} .

The following example points out the trade-offs between gain and noise figure for a small-signal amplifier.



RF & MW →

Example 9-14: Design of a small-signal amplifier for minimum noise figure and specified gain

Using the same transistor as in Example 9-13, design a low-noise power amplifier with 8 dB gain and a noise figure that is less than 1.6 dB. Assume that the transistor has the following noise parameters: $F_{\min} = 1.5$ dB, $R_n = 4 \Omega$, and $\Gamma_{\text{opt}} = 0.5 \angle 45^\circ$.

Solution: The noise figure is independent of the load reflection coefficient. However, it is a function of the source impedance. It is therefore convenient to map the constant gain circle obtained in Example 9-13 into the Γ_S -plane. Applying equations (9.64) and

(9.65) and values from Example 9-13, we find the center and radius of the mapped constant gain circle: $d_{g_S} = 0.29 \angle -18^\circ$ and $r_{g_S} = 0.18$. A Γ_S residing anywhere on this circle will satisfy our gain requirement. However, for the noise figure specifications to be met we have to ensure that Γ_S resides inside the $F_k = 2$ dB constant noise circle.

The noise circle center and its radius are computed using (9.83) and (9.84), respectively. They are listed below together with the coefficient Q_k , see (9.79):

$$Q_k = 0.2, d_{F_k} = 0.42 \angle 45^\circ, r_{F_k} = 0.36$$

The obtained $G = 8$ dB and $F_k = 1.6$ dB circles are shown in Figure 9-17.

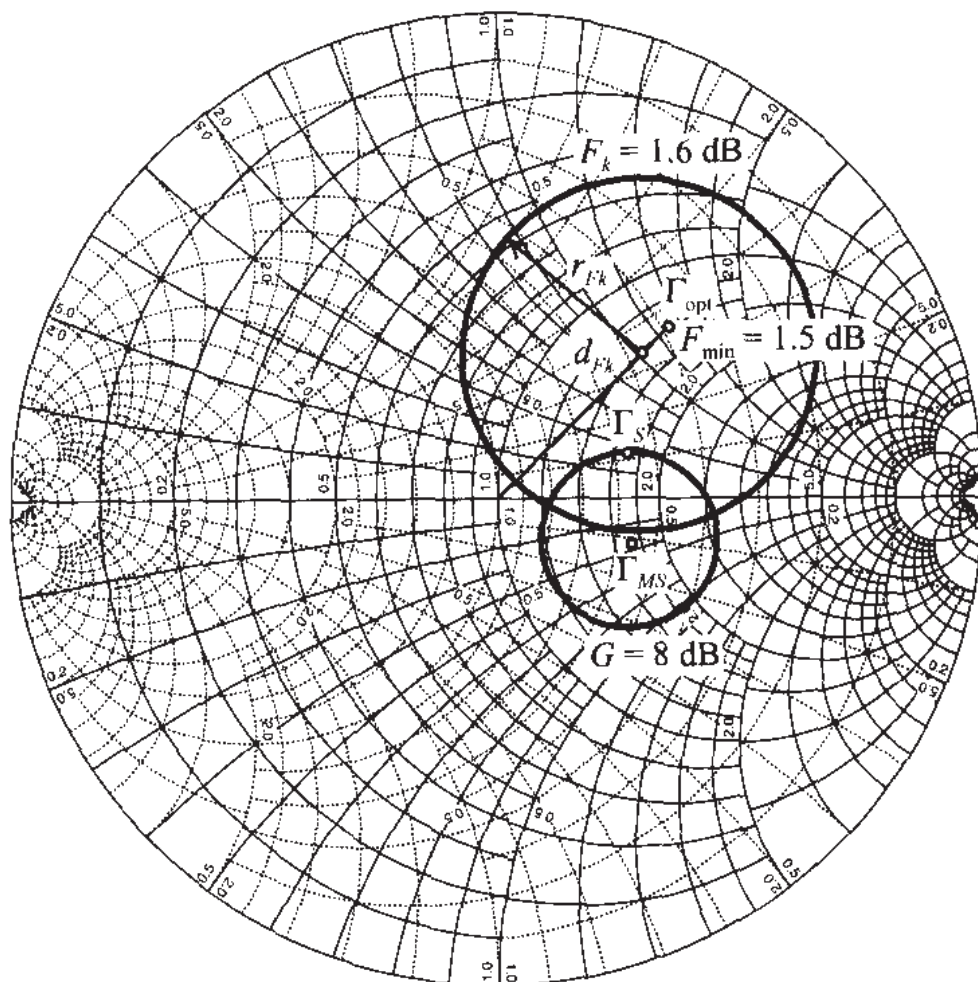


Figure 9-17 Constant noise figure circle and constant operating gain circle mapped into the Γ_S -plane.

Notice that the maximum power gain is obtained at the point where $\Gamma_{MS} = 0.30 \angle -18^\circ$ (see Example 9-11 for the detailed computations). However, the minimum noise figure is obtained at

$\Gamma_S = \Gamma_{\text{opt}} = 0.5\angle 45^\circ$, which shows for this example that it is impossible to achieve maximum gain and minimum noise figure simultaneously. Clearly, some compromises have to be made.

To minimize the noise figure for a given gain, we should pick the source reflection coefficient as close as possible to the location of Γ_{opt} while still residing on the constant gain circle. Arbitrarily choosing $\Gamma_S = 0.29\angle 19^\circ$, the corresponding load reflection coefficient is found to be $\Gamma_L = 0.45\angle 50^\circ$ by applying (9.62). The obtained amplifier noise figure is then computed using (9.77):

$$F = F_{\min} + \frac{4R_n}{Z_0} \frac{|\Gamma_S - \Gamma_{\text{opt}}|^2}{(1 - |\Gamma_S|^2)|1 + \Gamma_{\text{opt}}|^2} = 1.54 \text{ dB}$$

The requirements of maximum gain and minimum noise figure will always be design trade-offs and cannot be met simultaneously.

9.6 Constant VSWR Circles

In many cases the amplifier has to stay below a specified VSWR as measured at the input or output port of the amplifier. Typical values range between $1.5 \leq \text{VSWR} \leq 2.5$. As we know from our discussion in Chapter 8, the purpose of matching networks is primarily motivated by the desire to reduce the VSWR at the transistor. The complication arises from the fact that the input VSWR (or VSWR_{IMN}) is determined at the input matching network (IMN), which in turn is affected by the active device, and, through feedback, by the output matching network (OMN). Conversely, the output VSWR (or VSWR_{OMN}) is determined by the OMN and, again through feedback, by the IMN. This calls for a bilateral design approach, as discussed in Section 9.4.3.

To set the stage, let us consider the arrangement depicted in Figure 9-18. The two VSWRs that are part of an RF amplifier specification are

$$\text{VSWR}_{\text{IMN}} = \frac{1 + |\Gamma_{\text{IMN}}|}{1 - |\Gamma_{\text{IMN}}|} \text{ and } \text{VSWR}_{\text{OMN}} = \frac{1 + |\Gamma_{\text{OMN}}|}{1 - |\Gamma_{\text{OMN}}|} \quad (9.85)$$

The reflection coefficients Γ_{IMN} , Γ_{OMN} require further clarification. If we concentrate on Γ_{IMN} , it is apparent from Section 9.2.1 that the input power P_{in} (under the assumption $\Gamma_S' = 0$) can be expressed as a function of the available power P_A :

$$P_{\text{in}} = P_A(1 - |\Gamma_{\text{IMN}}|^2) \quad (9.86)$$

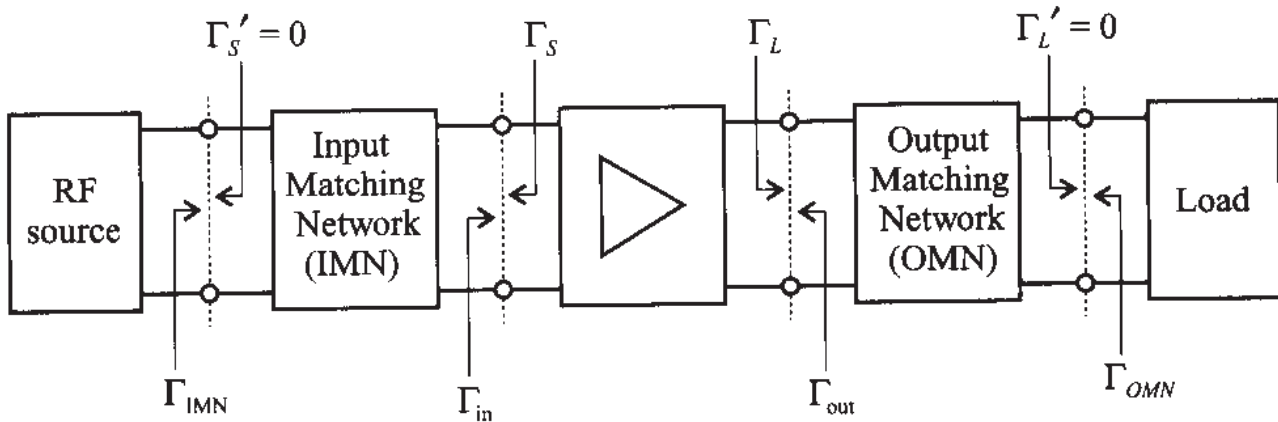


Figure 9-18 System configuration for input and output VSWR.

Postulating that the matching network is lossless, the same power is also present at the input terminal of the active device

$$P_{in} = P_A \frac{(1 - |\Gamma_S|^2)(1 - |\Gamma_{in}|^2)}{|1 - \Gamma_S \Gamma_{in}|} \quad (9.87)$$

in the absence of any matching. Setting both equations equal and solving for $|\Gamma_{IMN}|$ yields

$$|\Gamma_{IMN}| = \sqrt{1 - \frac{(1 - |\Gamma_S|^2)(1 - |\Gamma_{in}|^2)}{|1 - \Gamma_S \Gamma_{in}|}} = \left| \frac{\Gamma_{in} - \Gamma_S^*}{1 - \Gamma_S \Gamma_{in}} \right| = \left| \frac{\Gamma_{in}^* - \Gamma_S}{1 - \Gamma_S \Gamma_{in}} \right| \quad (9.88)$$

Equation (9.88) can be converted into a circle equation for Γ_S that is centered at location $d_{V_{IMN}}$ with radius $r_{V_{IMN}}$ such that

$$(\Gamma_S^R - d_{V_{IMN}}^R)^2 + (\Gamma_S^I - d_{V_{IMN}}^I)^2 = r_{V_{IMN}}^2 \quad (9.89)$$

where

$$d_{V_{IMN}} = d_{V_{IMN}}^R + j d_{V_{IMN}}^I = \frac{(1 - |\Gamma_{IMN}|^2)\Gamma_{in}^*}{1 - |\Gamma_{IMN}\Gamma_S|^2} \quad (9.90)$$

and

$$r_{V_{IMN}} = \frac{(1 - |\Gamma_{in}|^2)|\Gamma_{IMN}|}{1 - |\Gamma_{IMN}\Gamma_S|^2} \quad (9.91)$$

Here the subscript V_{IMN} in $d_{V_{IMN}}$ and $r_{V_{IMN}}$ is used to denote the VSWR at the IMN location.

In an identical procedure, the circle equation for the output VSWR is found. The voltage source is attached to the output side and impedance Z_L is treated as source impedance, whereas Z_S is the load impedance. Therefore, in a perfectly analogous way the output reflection coefficient becomes

$$|\Gamma_{OMN}| = \sqrt{1 - \frac{(1 - |\Gamma_L|^2)(1 - |\Gamma_{out}|^2)}{|1 - \Gamma_L \Gamma_{out}|}} = \left| \frac{\Gamma_{out} - \Gamma_L^*}{1 - \Gamma_L \Gamma_{out}} \right| = \left| \frac{\Gamma_{out}^* - \Gamma_L}{1 - \Gamma_L \Gamma_{out}} \right| \quad (9.92)$$

We convert (9.92) into a circle equation for Γ_L that is centered at location $d_{V_{OMN}}$ with radius $r_{V_{OMN}}$ such that

$$(\Gamma_L^R - d_{V_{OMN}}^R)^2 + (\Gamma_L^I - d_{V_{OMN}}^I)^2 = r_{V_{OMN}}^2 \quad (9.93)$$

where

$$d_{V_{OMN}} = d_{V_{OMN}}^R + j d_{V_{OMN}}^I = \frac{(1 - |\Gamma_{OMN}|^2)\Gamma_{out}^*}{1 - |\Gamma_{OMN}\Gamma_L|^2} \quad (9.94)$$

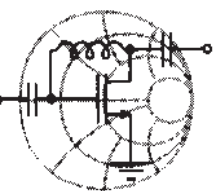
and

$$r_{V_{OMN}} = \frac{(1 - |\Gamma_{out}|^2)|\Gamma_{OMN}|}{1 - |\Gamma_{OMN}\Gamma_L|^2} \quad (9.95)$$

The previous derivations allow us to draw the following conclusions regarding the constant VSWR circles:

- For minimum VSWR (on the input side: $VSWR_{IMN} = 1$, $|\Gamma_{IMN}| = 0$; on the output side: $VSWR_{OMN} = 1$, $|\Gamma_{OMN}| = 0$) the circles are located at $d_{V_{IMN}}|_{|\Gamma_{IMN}|=0} = \Gamma_{in}^*$ (for the input) and $d_{V_{OMN}}|_{|\Gamma_{OMN}|=0} = \Gamma_{out}^*$ (for the output) with both radii equal to zero.
- All VSWR circles reside on the line extending from the origin to Γ_{in}^* (input) or Γ_{out}^* (output).

It is important to be aware of the fact that under *bilateral matching* the input and output reflection coefficients are functions of source and load reflection coefficients (Γ_S , Γ_L). Therefore, the input and output VSWR circles cannot be plotted simultaneously, but rather have to be considered one at a time in the iterative process of adjusting Γ_S and Γ_L .



RF & MW →

Example 9-15: Constant VSWR design for given gain and noise figure

Using the results of Example 9-14, plot the $VSWR_{IMN} = 1.5$ circle in the Γ_S -plane as part of the Smith Chart. Plot the graph of $VSWR_{OMN}$ as a function of the Γ_S position for a $VSWR_{IMN} = 1.5$. Find Γ_S that gives a minimum reflection on the output port of the amplifier and compute its corresponding gain.

Solution: In Example 9-14 we have found $\Gamma_S = 0.29 \angle 19^\circ$ and $\Gamma_L = 0.45 \angle 50^\circ$ as source and load reflection coefficients that meet specifications in terms of power gain and noise figure. Since we use the design based on constant operating gain circles, we obtain a perfect match at the input port of the amplifier. However, the output port is mismatched and the $VSWR_{OMN}$ can be computed from $|\Gamma_{OMN}|$, which is found from (9.92) in conjunction with (9.9b):

$$|\Gamma_{OMN}| = \left| \frac{\Gamma_{out}^* - \Gamma_L}{1 - \Gamma_L \Gamma_{out}} \right| = 0.26$$

The result is

$$VSWR_{OMN} = \frac{1 + |\Gamma_{OMN}|}{1 - |\Gamma_{OMN}|} = 1.69$$

To improve the $VSWR_{OMN}$, we can relax the requirements on $VSWR_{IMN}$ and introduce some mismatch at the input. If we set $VSWR_{IMN} = 1.5$, the corresponding input VSWR circle can be plotted in the Smith Chart, as shown in Figure 9-19.

The center of the $VSWR_{IMN} = 1.5$ circle and its radius are found from (9.90) and (9.91), respectively. The numerical values yield $d_{V_{IMN}} = 0.28 \angle 19^\circ$ and $r_{V_{IMN}} = 0.18$.

Every point on the $VSWR_{IMN} = 1.5$ circle can be expressed in the polar form

$$\Gamma_S = d_{V_{IMN}} + r_{V_{IMN}} \exp(j\alpha)$$

where the angle α changes from 0 to 360° . As α changes, we obtain a changing Γ_S , which in turn results in a corresponding Γ_{out}

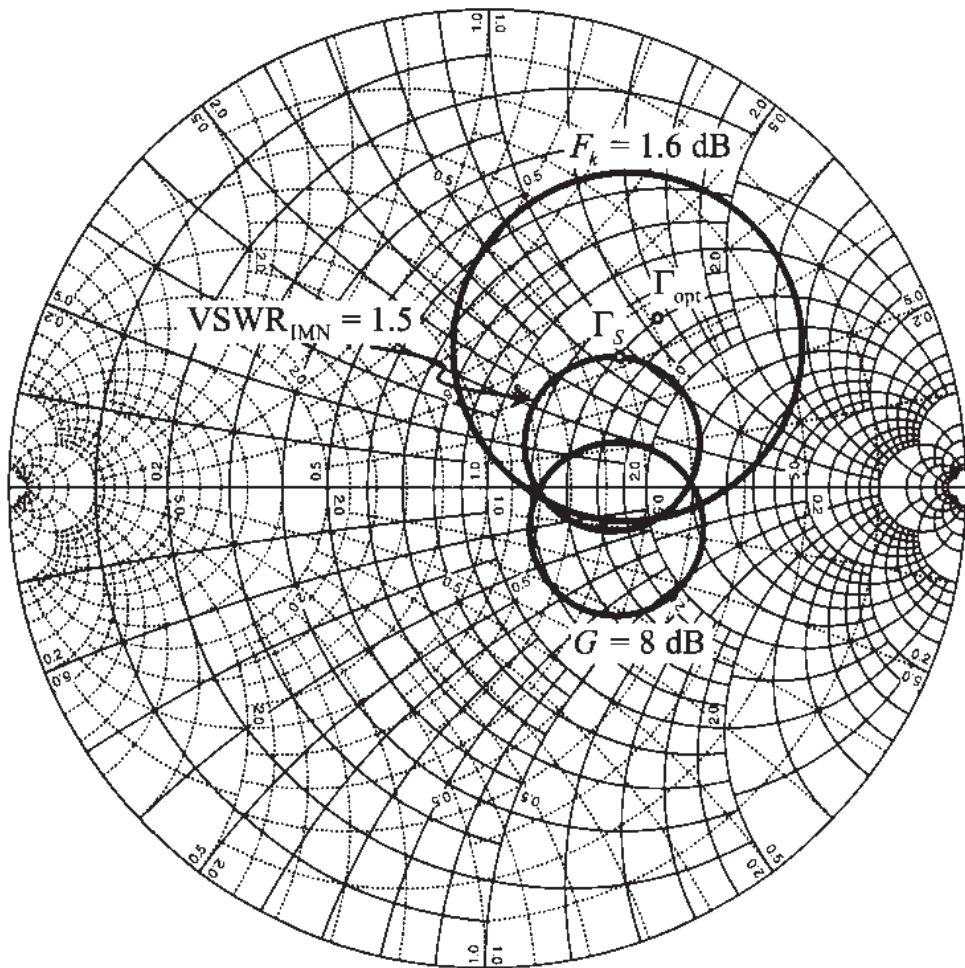


Figure 9-19 Constant operating power gain, noise figure, and input VSWR circle in Γ_S -plane.

and a computed $VSWR_{OMN}$. The graph of such a dependence is shown in Figure 9-20.

As can be observed in Figure 9-20, the $VSWR_{OMN}$ reaches its minimum value of 1.37 at approximately $\alpha = 85^\circ$. The corresponding source and output reflection coefficients, transducer gain, and noise figure are as follows:

$$\Gamma_S = 0.39\angle 45^\circ, \Gamma_{out} = 0.32\angle -52^\circ$$

$$G_T = 7.82 \text{ dB}, F = 1.51 \text{ dB}$$

An improvement in $VSWR_{OMN}$ has been achieved at the expense of a reduced gain. If the gain reduction becomes unacceptable, then both source and load reflection coefficients have to be adjusted simultaneously.

Many specifications explicitly prescribe a maximum tolerable VSWR that the amplifier design must meet. This becomes particu-

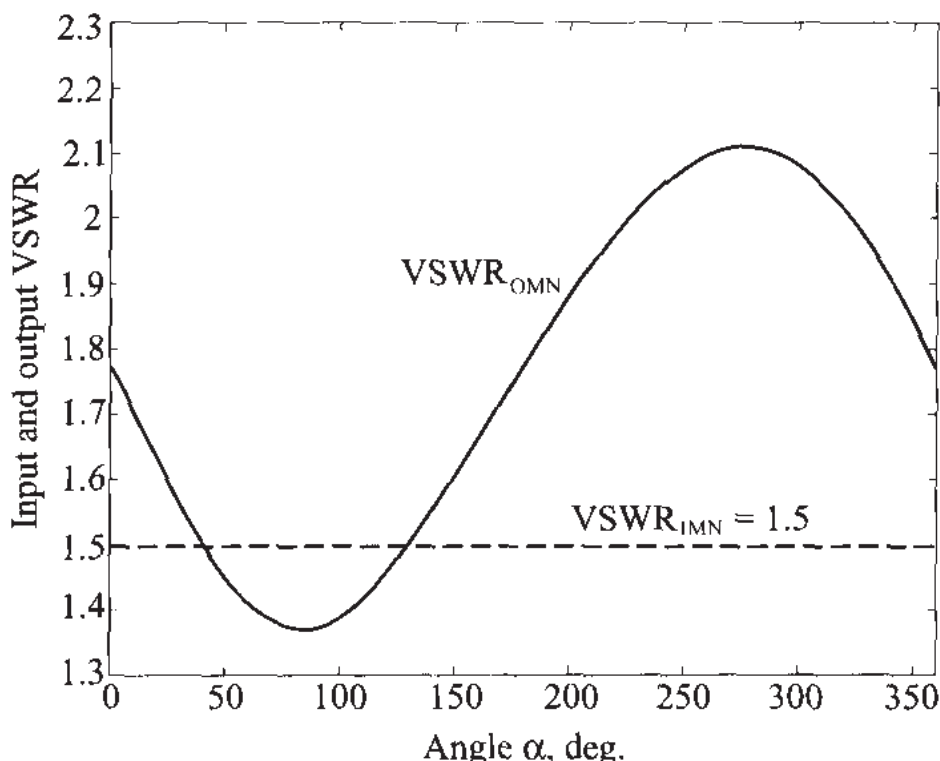


Figure 9-20 Input and output VSWR as a function of angle α .

larly important when dealing with system integration issues where several units are cascaded.

9.7 Broadband, High-Power, and Multistage Amplifiers

9.7.1 Broadband Amplifiers

Many modulation and coding circuits require amplifier with a wide or broad frequency band of operation. From the RF point of view, one of the major problems in broadband amplifier design is the limitation imposed by the gain-bandwidth product of the active device. As pointed out in Chapter 7, any active device has a gain roll-off at higher frequencies due to the base-collector capacitance in the BJTs or the gate-source and gate-drain capacitances in the FETs. Eventually, as the frequency reaches the transition frequency f_T , the transistor stops functioning as an amplifier and turns attenuative.

Unfortunately $|S_{21}|$ seldom remains constant over the wide frequency band of operation, necessitating compensation measures. Besides forward gain $|S_{21}|$ degradation, other complications that arise in the design of broadband amplifiers include

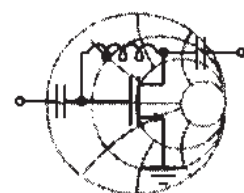
- Increase in the reverse gain $|S_{12}|$, which degrades the overall gain even further and increases the possibility for a device to fall into oscillation
- Frequency variation of S_{11} and S_{22}
- Noise figure degradation at high frequencies

To account for these effects, two different amplifier design approaches are used: frequency compensated matching networks and negative feedback. In the subsequent sections we investigate both design techniques.

Frequency Compensated Matching Networks

Frequency compensated matching networks introduce a mismatch on either the input or output port of the device to compensate for the frequency variation introduced by the S-parameters. The difficulty with these types of matching networks is that they are rather difficult to design and the procedures involved are more an art than a well-defined engineering approach that guarantees success. Frequency compensated matching networks have to be custom tailored for each particular case.

The following example demonstrates some of the key steps required to design a frequency compensated matching network.



RF & MW →

Example 9-16: Design of a broadband amplifier using a frequency compensated matching network

Design a broadband amplifier with 7.5 dB nominal gain and ± 0.2 dB gain flatness in the frequency range from 2 GHz to 4 GHz. For the design use Hewlett-Packard's AT41410 BJT, which is biased with $I_C = 10$ mA collector current and $V_{CE} = 8$ V collector-emitter voltage. The corresponding S-parameters measured at frequencies of 2, 3, and 4 GHz under unilateral assumption are summarized in Table 9-4.

Solution: According to the data provided in Table 9-4 the insertion gain of the transistor is $|S_{21}|^2 = 11.41$ dB at $f = 2$ GHz, 8.16 dB at 3 GHz, and 5.85 dB at 4 GHz. To realize an amplifier with a nominal gain of 8.7 dB, source and load matching networks must be designed that decrease the gain by 2.71 dB at 2 GHz and increase the gain by 0.54 dB at 3 GHz and 2.85 dB at 4 GHz.

Table 9-4 S-parameters of AT41410 BJT ($I_C = 10 \text{ mA}$, $V_{CE} = 8 \text{ V}$)

| f, GHz | $ S_{21} $ | S_{11} | S_{22} |
|-----------------|------------|-------------------------|-------------------------|
| 2 | 3.72 | $0.61 \angle 165^\circ$ | $0.45 \angle -48^\circ$ |
| 3 | 2.56 | $0.62 \angle 149^\circ$ | $0.44 \angle -58^\circ$ |
| 4 | 1.96 | $0.62 \angle 130^\circ$ | $0.48 \angle -78^\circ$ |

The maximum gain provided by the source and load are found from (9.35) and (9.36) and are as follows:

$$f = 2 \text{ GHz}: G_{S_{\max}} = 2.02 \text{ dB}, G_{L_{\max}} = 0.98 \text{ dB}$$

$$f = 3 \text{ GHz}: G_{S_{\max}} = 2.11 \text{ dB}, G_{L_{\max}} = 0.93 \text{ dB}$$

$$f = 4 \text{ GHz}: G_{S_{\max}} = 2.11 \text{ dB}, G_{L_{\max}} = 1.14 \text{ dB}$$

Although for the general case source and load matching networks would have to be designed, in this example an additional gain G_S that can be produced by the source matching is already sufficient to meet the amplifier specifications. Therefore, we concentrate on the development of the source matching network and leave the output port of the transistor without any matching network.

Since the output of the transistor is directly connected to the load, we have $G_L = 0 \text{ dB}$. The input matching network should produce an additional gain of $(-3.9 \pm 0.2) \text{ dB}$ at $f = 2 \text{ GHz}$, $(-0.7 \pm 0.2) \text{ dB}$ at 3 GHz , and $(1.7 \pm 0.2) \text{ dB}$ at 4 GHz . The corresponding constant gain circles are shown in Figure 9-21.

The required input matching network must be capable of transforming points on the constant gain circles in Figure 9-21 to the center of the Smith Chart. There are a number of networks that can accomplish this task. One solution involves a combination of two capacitors, one in shunt with the transistor and one in series with the input port of the amplifier, as shown in Figure 9-22. From a known Γ_S we can compute the transducer gain by setting $\Gamma_L = 0$ in (9.10). We can next find the input and output VSWR. Since $\Gamma_L = 0$, the values for VSWR_{OMN} is equal to VSWR_{out} and is found as

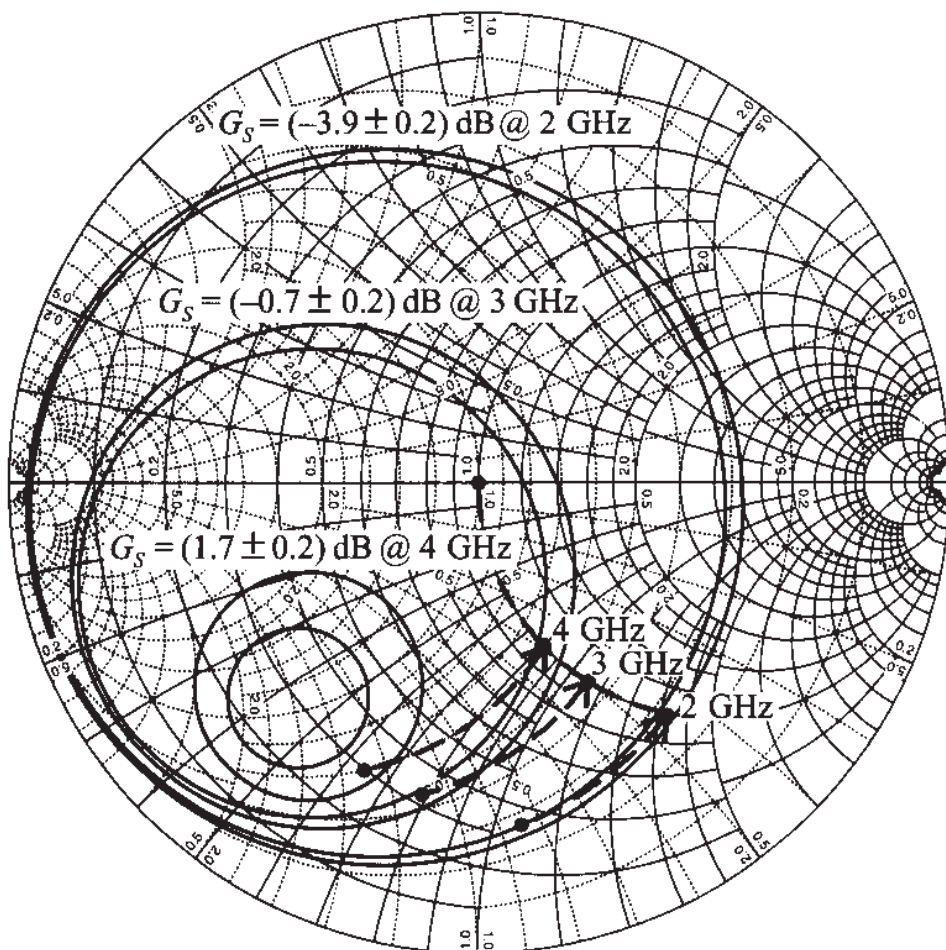


Figure 9-21 Smith Chart design of a broadband amplifier in Example 9-16.

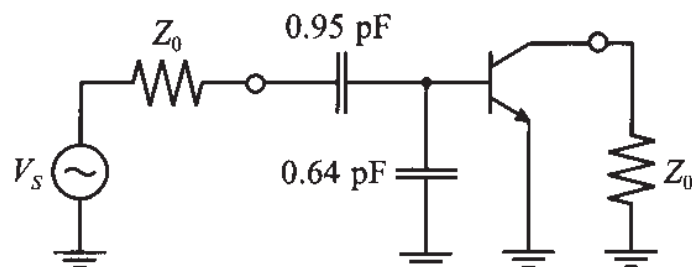


Figure 9-22 Broadband amplifier with 8.7 dB gain and ± 0.2 dB gain flatness over a frequency range from 2 to 4 GHz.

$$\text{VSWR}_{\text{out}} = \frac{1 + |S_{22}|}{1 - |S_{22}|}$$

For the computation of the VSWR at the input port we use

$$\text{VSWR}_{\text{IMN}} = \frac{1 + |\Gamma_{\text{IMN}}|}{1 - |\Gamma_{\text{IMN}}|}$$

where $|\Gamma_{\text{IMN}}|$ is computed based on (9.88):

$$|\Gamma_{IMN}| = \left| \frac{\Gamma_{in}^* - \Gamma_S}{1 - \Gamma_S \Gamma_{in}} \right| = \left| \frac{S_{11}^* - \Gamma_S}{1 - \Gamma_S S_{11}} \right|$$

The obtained values are summarized in Table 9-5.

Table 9-5 Parameters of a broadband amplifier

| f , GHz | Γ_S | G_T , dB | $VSWR_{IMN}$ | $VSWR_{OMN}$ |
|-----------|------------------------|------------|--------------|--------------|
| 2 | $0.74\angle-83^\circ$ | 7.65 | 13.1 | 2.6 |
| 3 | $0.68\angle-101^\circ$ | 7.57 | 5.3 | 2.6 |
| 4 | $0.66\angle-112^\circ$ | 7.43 | 2.0 | 2.8 |

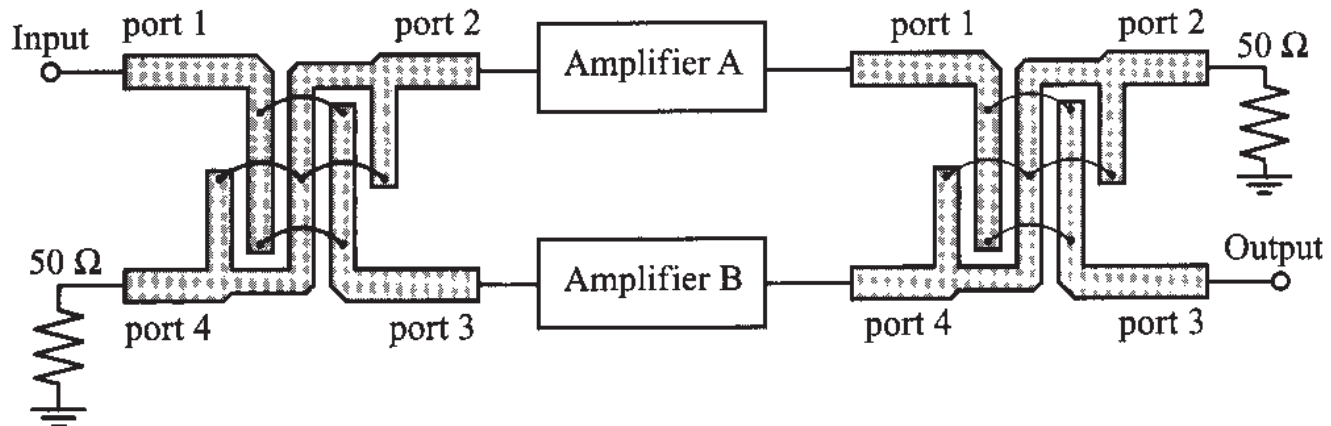
As seen from the values provided in Table 9-5, gain linearity is achieved at the expense of significantly higher VSWR.

As demonstrated in Example 9-16, the addition of a frequency compensated matching network to obtain an improved gain flatness may result in significant impedance mismatch, degrading the amplifier performance. To circumvent this problem, a balanced amplifier can be employed.

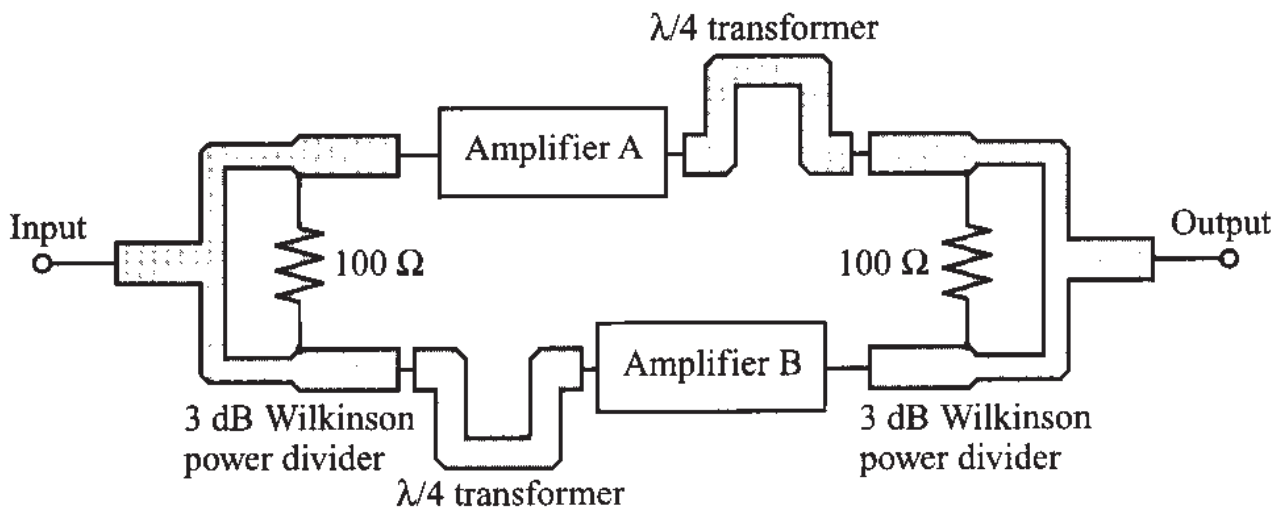
Balanced Amplifier Design

The typical balanced amplifier block-diagram using a 3 dB Lange or hybrid coupler and a 3 dB Wilkinson power divider and combiner are shown in Figures 9-23(a) and (b), respectively. The input signal power is split into two, amplified, and combined at the output. A complete discussion of the theory behind the operation of couplers and power dividers is given in Appendix G.

Let us first discuss the operation of the balanced amplifier in Figure 9-23(a). Here the input power launched into port 1 of the input coupler is equally divided in magnitude, but with a 90° phase shift between ports 2 and 3. No power is present at port 4. The output coupler combines the output signals of amplifiers A and B by introducing an additional 90° phase shift, thus bringing them in phase again. We denote the S-parameters of amplifier A as S_{11}^A , S_{12}^A , S_{21}^A , S_{22}^A , and the corresponding S-parameters of amplifier B with superscript B. The equations that relate the S-parameters of the entire amplifier to the S-parameters of individual branches are as follows



(a) Balanced amplifier using 3 dB coupler



(b) Balanced amplifier using 3 dB Wilkinson power divider and combiner

Figure 9-23 Block diagram of a balanced broadband amplifier.

$$\begin{aligned}
 |S_{11}| &= \frac{1}{2} |S_{11}^A - S_{11}^B| \\
 |S_{21}| &= \frac{1}{2} |S_{21}^A + S_{21}^B| \\
 |S_{12}| &= \frac{1}{2} |S_{12}^A + S_{12}^B| \\
 |S_{22}| &= \frac{1}{2} |S_{22}^A - S_{22}^B|
 \end{aligned} \tag{9.96}$$

where coefficients 1/2 take into account the 3 dB attenuation, and the minus sign is due to the 90° phase shift at port 3 that is traversed twice, adding up to 180° .

If the amplifiers in the two branches are identical, then $|S_{11}| = |S_{22}| = 0$ and the forward and reverse gain of the balanced amplifier are equal to the corresponding gains of each branch.

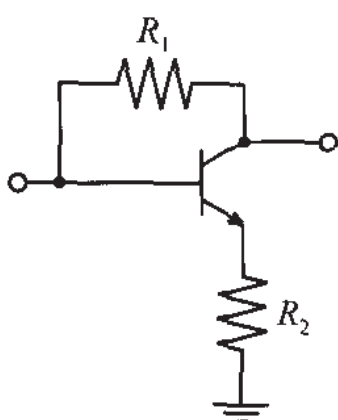
The operation of the balanced amplifier with Wilkinson power dividers [see Figure 9-23(b)] is identical. The only difference compared to the power divider is that the signals are in phase, and we need to add additional $\lambda/4$ transformers to produce a 90° phase shift between branches.

The main advantages of balanced amplifiers are that they possess very good impedance match at the input and output ports (provided that the amplifiers in both branches have similar characteristics), and one of the two amplifiers can continue operating even if the other branch should fail completely. The chief disadvantages of balanced amplifiers include increased circuit size and a reduction in frequency response introduced by the bandwidth of the couplers.

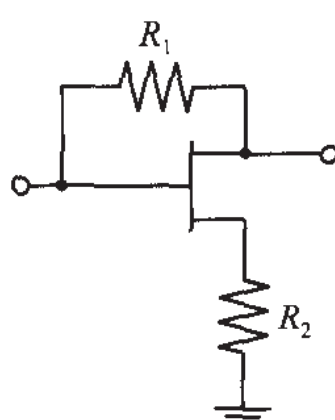
Negative Feedback Circuits

The alternative to frequency compensating networks is the use of negative feedback. This allows a flat gain response and reduces the input and output VSWR over a wide frequency range. An additional advantage of the negative feedback is that it makes the circuit less sensitive to transistor-to-transistor parameter variations. The disadvantage of such circuits is that they tend to limit the maximum power gain of the transistor and increase its noise figure.

The term *negative feedback* implies that part of the signal from the output of the transistor is coupled back to the input with opposite phase so that it subtracts from the input signal, thereby reducing it. If the signals are added in phase, the resulting response will grow and a positive feedback is obtained. The most general resistive feedback circuits for BJT and FET are shown in Figure 9-24, where resistor R_1 constitutes a shunt feedback and resistor R_2 a series feedback.



(a) Feedback in BJTs



(b) Feedback in FETs

Figure 9-24 Negative resistive feedback circuits.

As discussed in Chapter 7, both circuits in Figure 9-24 at low-frequencies can be replaced by the equivalent π -models, as shown in Figure 9-25, where the input resistance r_π is equal to infinity for FETs.

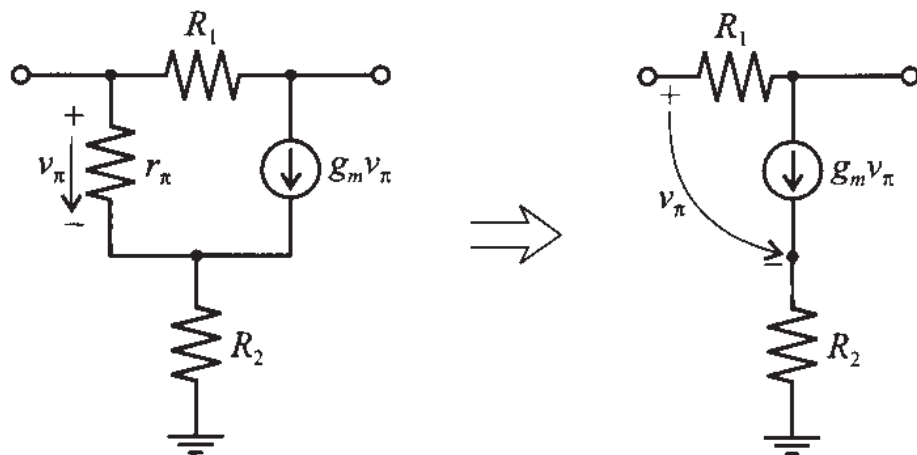


Figure 9-25 Low-frequency model of negative feedback circuit.

If we assume for the BJT that

$$r_\pi(1 + g_m R_2) \gg R_1 \quad (9.97)$$

then r_π in Figure 9-25 can be replaced by an open circuit and the h -parameter representation can be written as

$$[h] = \begin{bmatrix} R_1 & 1 \\ \frac{g_m R_1}{1 + g_m R_2} - 1 & \frac{g_m}{1 + g_m R_2} \end{bmatrix} \quad (9.98)$$

Using the matrix conversion formula from Appendix D, we find the corresponding S -parameter representation

$$[S] = \frac{1}{\Delta} \begin{bmatrix} \frac{R_1}{Z_0} - \frac{g_m Z_0}{1 + g_m R_2} & 2 \\ 2 \left(1 - \frac{g_m R_1}{1 + g_m R_2} \right) & \frac{R_1}{Z_0} - \frac{g_m Z_0}{1 + g_m R_2} \end{bmatrix} \quad (9.99)$$

where

$$\Delta = 2 + \frac{R_1}{Z_0} + \frac{g_m Z_0}{1 + g_m R_2} \quad (9.100)$$

Assuming ideal matching conditions $S_{11} = S_{22} = 0$ (i.e., the input and output VSWRs equal unity) yields the following equation relating the value of the shunt feedback resistor to the series feedback resistor R_1 :

$$R_2 = \frac{Z_0^2}{R_1} - \frac{1}{g_m} \quad (9.101)$$

where the characteristic impedance Z_0 and transconductance g_m are used.

Substituting (9.101) into (9.100) and (9.99) gives

$$[S] = \begin{bmatrix} 0 & \frac{Z_0}{R_1 + Z_0} \\ 1 - \frac{R_1}{Z_0} & 0 \end{bmatrix} \quad (9.102)$$

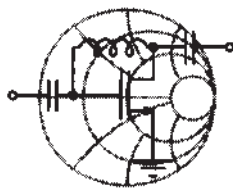
As seen from (9.99) and (9.102), both gain flattening and perfect match can be achieved by choosing appropriate values for the feedback resistors R_1 and R_2 . The only limitation arises from the requirement that R_2 in (9.101) must be nonnegative; that is, there exists a minimum value $g_{m_{\min}}$ that limits the range of g_m to

$$g_m \geq g_{m_{\min}} = \frac{R_1}{Z_0^2} = \frac{1 - S_{21}}{Z_0} \quad (9.103)$$

Any transistor with g_m satisfying condition (9.103) can be used in the negative feedback configuration shown in Figure 9-24.

The analysis of the feedback circuit is applicable only for ideal devices operated in the low-frequency range where all reactances are neglected. In practical applications the presence of the parasitic resistances in the transistor must be taken into account, resulting in modified values of the feedback resistors. In addition, at RF and MW frequencies the influence of internal capacitances and inductances cannot be neglected, and additional reactive components in the feedback loops enter the analysis. The most common practice is to add an inductance in series with the feedback resistor R_1 . This is done to reduce the feedback from higher frequencies and thus compensate for S_{21} -related roll-off.

The following example demonstrates the use of negative feedback for a broadband amplifier design where the feedback resistors are first computed theoretically and then adjusted using a CAD software package.



RF & MW →

Example 9-17: Design of a negative feedback loop broadband amplifier

The BJT BFG403W is biased with $V_{CE} = 3$ V and $I_C = 3.3$ mA ($\beta = 125$). The corresponding S -parameters in common-emitter configuration are listed in Table 9-6, where a $500\ \Omega$ resistor has been added to ensure stability.

Design a broad-band amplifier with $G_T = 10$ dB and a bandwidth ranging from 10 MHz to 2 GHz by using a negative feedback loop.

Table 9-6 S-parameters for the transistor in Example 9-17

| f , MHz | $ S_{11} $ | $\angle S_{11}$ | $ S_{21} $ | $\angle S_{21}$ | $ S_{12} $ | $\angle S_{12}$ | $ S_{22} $ | $\angle S_{22}$ |
|-----------|------------|-----------------|------------|-----------------|--------------------|-----------------|------------|-----------------|
| 10 | 0.877 | -0.3 | 7.035 | 179.6 | 1×10^{-4} | 66.8 | 0.805 | -0.1 |
| 100 | 0.876 | -2.4 | 7.027 | 176.1 | 7×10^{-4} | 85.9 | 0.805 | -1.4 |
| 250 | 0.870 | -5.9 | 6.983 | 170.2 | 0.002 | 84.3 | 0.803 | -3.4 |
| 500 | 0.850 | -11.5 | 6.834 | 160.6 | 0.003 | 80.5 | 0.797 | -6.6 |
| 750 | 0.820 | -16.9 | 6.607 | 151.4 | 0.004 | 76.0 | 0.789 | -9.8 |
| 1000 | 0.783 | -21.7 | 6.327 | 142.8 | 0.005 | 68.2 | 0.777 | -12.7 |
| 1500 | 0.700 | -29.6 | 5.711 | 127.2 | 0.007 | 74.1 | 0.755 | -18.1 |
| 2000 | 0.619 | -35.7 | 5.119 | 113.8 | 0.007 | 74.1 | 0.735 | -23.0 |

Solution: As seen from Table 9-6, the minimum gain of 14.2dB is attained at $f = 2\text{GHz}$, which is well above the required transducer power gain of $G_T = 10\text{dB}$.

Before continuing our approximate analysis, we have to ensure that condition (9.103) is satisfied. The value of r_π is found to be $r_\pi = \beta/g_m = 984\ \Omega$, where the transconductance g_m is computed as $g_m = I_C/V_T = 0.127\text{ S}$. Thus, the negative feedback

analysis is applicable since condition (9.103) is satisfied even for $R_2 = 0$.

The next step involves an estimation of the resistances R_1 and R_2 . Because the desired gain is $G = 10$ dB, the low-frequency S_{21} coefficient should be equal to -3.16 . Here the minus sign is due to the 180° phase shift of the common-emitter configuration. Substituting this value into (9.103) yields

$$R_1 = Z_0(1 - S_{21}) = 208 \Omega$$

Applying (9.101), we compute the value for the series feedback resistor R_2 :

$$R_2 = \frac{Z_0^2}{R_1} - \frac{1}{g_m} = 4.1 \Omega$$

The resulting insertion gain of the feedback network is listed in the second column of Table 9-7. It is observed that the negative feedback makes the gain response of the amplifier more uniform at the lower frequencies, unfortunately at too low a level. The discrepancy between the expected gain of 10 dB and the obtained value of $|S_{21}|^2 = 7.5$ dB is largely due to the fact that we neglected all parasitic resistances in the transistor. Such parasitics include the base resistance that is connected in series with r_π and thus reduces the effective transconductance g_m . Furthermore, the emitter resistance, which is in series with R_2 , has to be subtracted from the obtained value of R_2 .

Optimization of the circuit for frequencies up to 500 MHz using CAD tools results in the following modified values of the feedback resistances: $R_1 = 276 \Omega$ and $R_2 = 1.43 \Omega$. The corresponding insertion gain is listed in the third column of Table 9-7.

As observed from Table 9-7, these new values for the feedback resistances bring the transistor gain closer to the 10 dB specification at lower frequency, but it degrades quickly as the frequency increases. This indicates that a $R_1 = 276 \Omega$ feedback resistor is too small at those frequencies and has to be increased. This can be done by connecting an additional $L_1 = 4.5$ nH inductor in series with the resistor R_1 (the value of L_1 is predicted by a separate CAD optimization procedure).

Table 9-7 Insertion gain of the feedback amplifier

| f , MHz | $ S_{21} ^2$, dB | | |
|-----------|--|--|--|
| | $R_1 = 208 \Omega$, $R_2 = 4.1 \Omega$ | $R_1 = 276 \Omega$, $R_2 = 1.4 \Omega$ | $R_1 = 276 \Omega$, $R_2 = 1.4 \Omega$, $L_1 = 4.5 \text{ nH}$ |
| 10 | 7.50 | 10.01 | 10.01 |
| 100 | 7.50 | 10.01 | 10.01 |
| 250 | 7.50 | 10.00 | 10.01 |
| 500 | 7.50 | 9.97 | 10.00 |
| 750 | 7.50 | 9.93 | 10.00 |
| 1000 | 7.50 | 9.88 | 10.00 |
| 1500 | 7.51 | 9.75 | 9.99 |
| 2000 | 7.54 | 9.59 | 9.99 |

The resulting gain is listed in the last column in Table 9-7. As seen from the values presented, the addition of an inductor flattens the frequency response and improves the gain flatness to better than 0.1% over the entire bandwidth.

As the frequency increases, the negative feedback design approach becomes increasingly prone to parasitic influences. Above approximately 5 GHz, this lumped element method begins to break down.

9.7.2 High-Power Amplifiers

Thus far we have discussed the design of amplifiers based on linear, small-signal S-parameters. When dealing with high-power amplifiers, however, a small-signal approximation is usually not valid because the amplifier operates in a nonlinear region and large-signal S-parameters or impedances have to be obtained to conduct the appropriate design. Small-signal S-parameters can still be used when designing a Class A

amplifier. Here the signal amplification is largely restricted to the linear region of the transistor. However, the small-signal *S*-parameters become progressively unsuitable for Class AB, B, or C amplifiers, which operate in the saturation region.

One of the important characteristics of a high-power amplifier is the so-called **gain compression**. As the input signal to the amplifier approaches the saturation region, the gain begins to fall off, or compress. The typical relationship between input and output power can be plotted on a log-log scale, as shown in Figure 9-26.

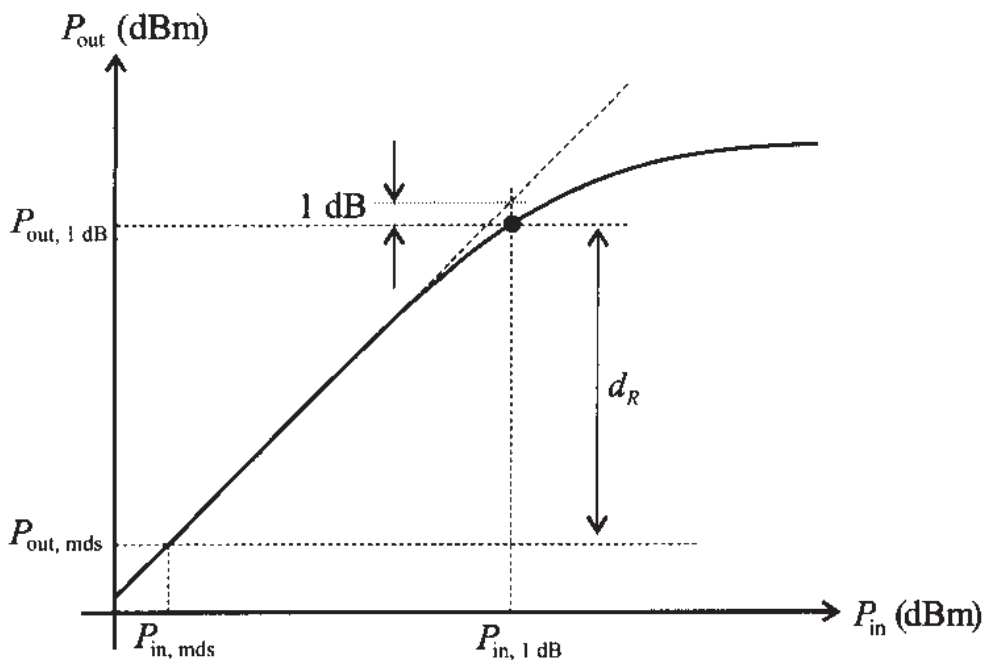


Figure 9-26 Output power of the amplifier as a function of input power.

At low drive levels, the output is proportional to the input power. However, as the power increases beyond a certain point, the gain of the transistor decreases, and eventually the output power reaches saturation. The point where the gain of the amplifier deviates from the linear, or small-signal gain by 1 dB is called the **1 dB compression point** and is used to characterize the power handling capabilities of the amplifier. The gain corresponding to the 1 dB compression point is referred to as $G_{1\text{dB}}$ and is computed as $G_{1\text{dB}} = G_0 - 1 \text{ dB}$, where G_0 is the small-signal gain. If the output power $P_{\text{out}, 1\text{dB}}$ at the 1 dB compression point is expressed in dBm, it can be related to the corresponding input power $P_{\text{in}, 1\text{dB}}$ as

$$\begin{aligned} P_{\text{out}, 1\text{dB}}(\text{dBm}) &= G_{1\text{dB}}(\text{dB}) + P_{\text{in}, 1\text{dB}}(\text{dBm}) \\ &= G_0(\text{dB}) - 1 \text{ dB} + P_{\text{in}, 1\text{dB}}(\text{dBm}) \end{aligned} \quad (9.104)$$

Another important characteristic of an amplifier is its **dynamic range** labeled d_R . The dynamic range signifies the region where the amplifier has a linear power gain

expressed as the difference between $P_{\text{out}, 1\text{dB}}$ and the output power of the **minimum detectable signal** $P_{\text{out}, \text{mds}}$. The quantity $P_{\text{out}, \text{mds}}$ is defined as a level X dB above the output noise power $P_{n, \text{out}}$. In most of the specifications, X is chosen to be 3 dB. The output noise power of an amplifier is given as

$$P_{n, \text{out}} = kTBG_0F \quad (9.105)$$

which, if expressed in dBm, can be cast in the form

$$P_{n, \text{out}}(\text{dBm}) = 10\log(kT) + 10\log B + G_0(\text{dB}) + F(\text{dB}) \quad (9.106)$$

where $10\log(kT) = -173.8$ dBm at $T = 300^\circ\text{K}$ and B is the bandwidth.

As with any nonlinear circuit, high-power amplifiers create **harmonic distortions** (multiples of the fundamental frequency). They appear as a power loss in the fundamental frequency. In general, Class A operation produces the lowest distortion figures. For higher-power applications where Class A operation is not feasible, due to low efficiency, Class AB push-pull amplifiers are employed to achieve nearly comparable distortion levels. Harmonic distortion is specified as the harmonic content of the overall output expressed in *dB* below the output power at the fundamental frequency.

An undesirable property of power amplifiers is the occurrence of so-called **intermodulation distortion (IMD)**. Although present in any amplifier (like harmonic distortion) it is most prominent in the high-power region of an active device where the nonlinear behavior has to be taken into account. Unlike harmonic distortions, IMD is the result of applying two unmodulated harmonic signals of slightly different frequencies to the input of an amplifier and observing the output, as shown in Figure 9-27.

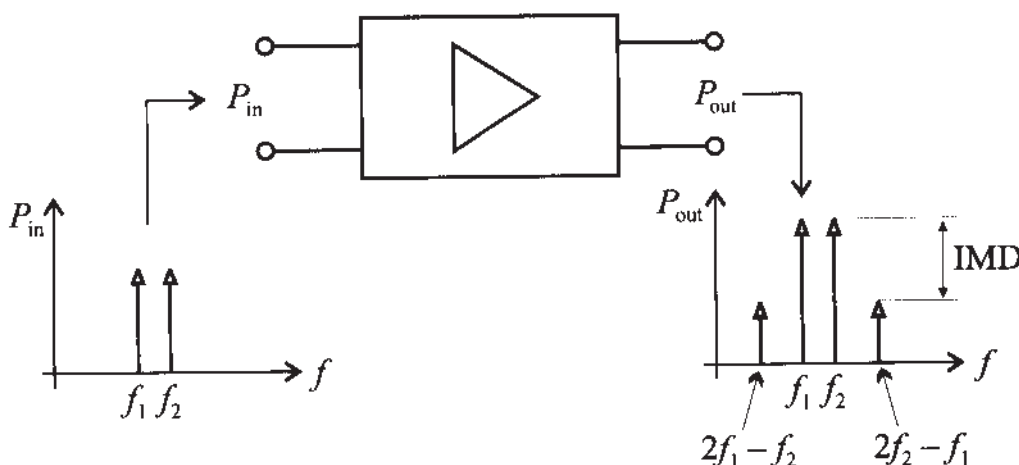


Figure 9-27 Observing the intermodular distortion of an amplifier.

Due to third-order nonlinearities of the amplifier, the input signals $P_{\text{in}}(f_1)$ and $P_{\text{in}}(f_2)$ create, besides the expected output signals $P_{\text{out}}(f_1)$ and $P_{\text{out}}(f_2)$, additional

frequencies $P_{\text{out}}(2f_1 - f_2)$ and $P_{\text{out}}(2f_2 - f_1)$. The additional frequency components can serve a desirable purpose when dealing with mixer circuits (see Chapter 10). However, for an amplifier one would like to see these contributions to be as small as possible. The difference between the desired and the undesired power level (in dBm) at the output port is typically defined as IMD in dB; that is,

$$\text{IMD(dB)} = P_{\text{out}}(f_2)(\text{dBm}) - P_{\text{out}}(2f_2 - f_1)(\text{dBm}) \quad (9.107)$$

In Figure 9-28 the output powers $P_{\text{out}}(f_2)$ and $P_{\text{out}}(2f_2 - f_1)$ are plotted versus the input power $P_{\text{in}}(f_2)$ on a log-log scale. In the region of linear amplification, the output power $P_{\text{out}}(f_2)$ increases proportionally to the input power $P_{\text{in}}(f_2)$, let us say $P_{\text{out}}(f_2) = \alpha P_{\text{in}}(f_2)$. However, the third order product $P_{\text{out}}(2f_2 - f_1)$ increases proportional to the third power [i.e., $P_{\text{out}}(2f_2 - f_1) = \alpha^3 P_{\text{in}}(f_2)$]. Thus, the IMD is reduced in proportion to the inverse square of the input power. Projecting the linear region of $P_{\text{out}}(f_2)$ and $P_{\text{out}}(2f_2 - f_1)$ results in a fictitious point called the **intercept point (IP)**. In practice, if higher than third order products can be neglected, the IP becomes a fixed point, independent of the particular power gain of the amplifier. This allows us to use the IP as a single number to quantify the IMD behavior.

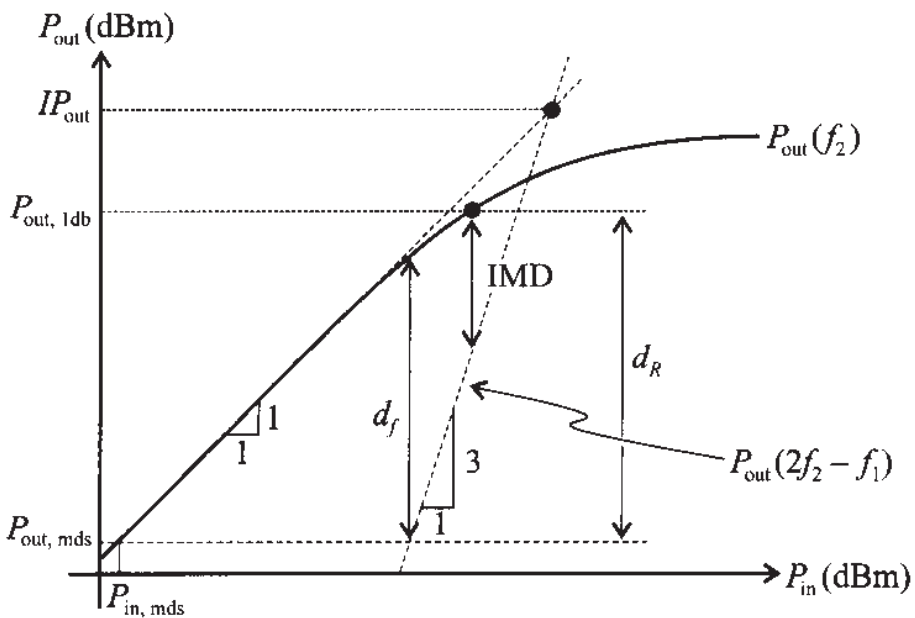


Figure 9-28 Recording of IMD based on input-output power relation.

Also shown in Figure 9-28 is a quantity called **spurious free dynamic range**, d_f , which is defined as

$$d_f(\text{dB}) = \frac{2}{3}[\text{IP}(\text{dBm}) - G_0(\text{dB}) - P_{\text{in, mds}}(\text{dBm})] \quad (9.108)$$

Typical values for a MESFET are $P_{\text{in, mds}} = -100 \text{ dBm}$, $IP = 40 \text{ dBm}$, and $d_f = 85 \text{ dB}$.

9.7.3 Multistage Amplifiers

A multistage amplifier circuit should be considered if the power gain requirement of the amplifier is so high that a single stage may not be able to achieve it. A typical example of a dual-stage BJT amplifier is shown in Figure 9-29.

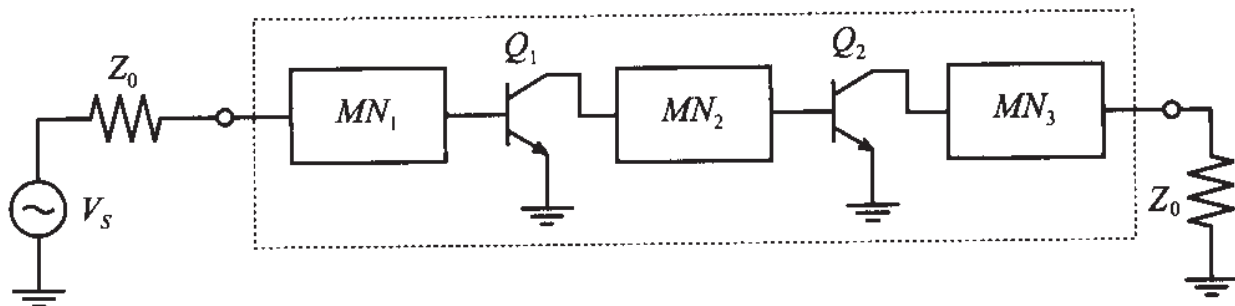


Figure 9-29 Dual-stage transistor amplifier.

Besides the typical input and output matching networks (MN_1 and MN_3), this configuration features an additional so-called **interstage matching network** (MN_2) for matching the output of stage 1 with the input of stage 2. In addition to providing appropriate matching, MN_2 can also be used to condition the gain flatness.

Under the assumption of optimally matched and lossless networks, let us summarize the most important dual-stage performance parameters. The total power gain G_{tot} of a dual-stage amplifier under linear operating conditions results in a multiplication of the individual gains G_1 and G_2 , or in dB

$$G_{\text{tot}}(\text{dB}) = G_1(\text{dB}) + G_2(\text{dB}) \quad (9.109)$$

An increase in gain performance is unfortunately accompanied by an increase in the noise figure, as discussed in Appendix H. Specifically, if F_1 and F_2 denote the noise figures associated with stages 1 and 2, we obtain a total noise figure

$$F_{\text{tot}} = F_1 + \frac{F_2 - 1}{G_1} \quad (9.110)$$

In addition, if the minimal detectable signal $P_{\text{in, mds}}$ at 3 dB above thermal noise at the input is given by $P_{\text{in, mds}} = kTB + 3 \text{ dB} + F_1$, the minimal detectable output power $P_{\text{out, mds}}$ becomes

$$P_{\text{out, mds}}(\text{dBm}) = kTB(\text{dBm}) + 3 \text{ dB} + F_{\text{tot}}(\text{dB}) + G_{\text{tot}}(\text{dB}) \quad (9.111)$$

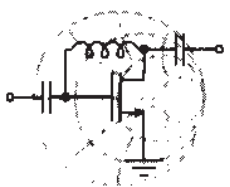
The dynamic properties are also affected. For instance, Rhode and Bucher (see Further Reading) have shown that the previously mentioned third-order intercept point changes to

$$IP_{\text{tot}}(\text{dBm}) = \frac{1}{1/IP_1(\text{dBm}) + 1/(G_2 IP_2)(\text{dBm})} \quad (9.112)$$

where IP_1 and IP_2 are the third order intercept points associated with stages 1 and 2. Finally, the total spurious-free dynamic range $d_{f\text{tot}}$ is approximately

$$d_{f\text{tot}}(\text{dBm}) = IP_{\text{tot}}(\text{dBm}) - P_{\text{out, mds}}(\text{dBm}) \quad (9.113)$$

Equation (9.113) also reveals that the addition of a second stage reduces the total dynamic range.



RF & MW →

Example 9-18: Transistor choices for multistage amplifier design

Design an amplifier with $P_{\text{out}, 1\text{ dB}} = 18 \text{ dBm}$ and a power gain not less than 20 dB. Using the transistor choices listed in Table 9-8, which shows pertinent characteristics at the operating frequency of $f = 2 \text{ GHz}$, determine the number of stages for the amplifier and discuss the choice of an appropriate transistor for each stage. In addition, estimate the noise figure F_{tot} and the third-order intercept point IP_{tot} of the amplifier.

Table 9-8 Transistor characteristics for Example 9-18.

| Transistor | $F[\text{dB}]$ | $G_{\text{max}}[\text{dB}]$ | $P_{\text{out}, 1\text{ dB}}[\text{dBm}]$ | $IP[\text{dBm}]$ |
|------------|----------------|-----------------------------|---|------------------|
| BFG505 | 1.9 | 10 | 4 | 10 |
| BFG520 | 1.9 | 9 | 17 | 26 |
| BFG540 | 2 | 7 | 21 | 34 |

Solution: Since the output power should be 18 dBm, the only transistor choice for the output stage of the amplifier is BFG540.

Because the output power of the amplifier $P_{\text{out},1\text{dB}} = 18 \text{ dBm}$ is much lower than $P_{\text{out},1\text{dB}}$ of the BFG540, it can operate at maximum gain of $G = 7 \text{ dB}$. This means that the remaining stages of the amplifier must be able to provide at least $20 \text{ dB} - 7 \text{ dB} = 13 \text{ dB}$ of gain. Thus, our amplifier should have at least three stages.

For the last stage to have 18 dBm output power, the second-stage transistor should be able to produce a power level of $P_{\text{out}_2,1\text{dB}} = 18 \text{ dBm} - 7 \text{ dBm} = 11 \text{ dBm}$, which eliminates BFG505 from the list of possible candidates. Since the BFG540 has a much higher power handling capability than necessary for the second stage, we choose BFG520.

Due to the fact that $P_{\text{out},1\text{dB}} = 11 \text{ dBm}$ is much lower than the 1-dB compression power of the BFG520, the second-stage transistor will also operate well below the compression point and the maximum gain will be equal to $G_{\text{max}} = 9 \text{ dB}$. Therefore, the transistor in the first stage has to have a minimum gain of $G = 13 \text{ dB} - 9 \text{ dB} = 4 \text{ dB}$ and be able to provide $P_{\text{out}_1} = 11 \text{ dBm} - 9 \text{ dB} = 2 \text{ dBm}$. Thus, the BFG505 is more than adequate for the task with $P_{\text{out}_1} = 2 \text{ dBm}$ and $G_1 = 4 \text{ dB}$. The input power to the amplifier is then $P_{\text{in}} = -2 \text{ dBm}$.

As shown in Appendix H, the noise figure of the entire amplifier is computed as

$$F_{\text{tot}} = F_1 + \frac{F_2 - 1}{G_1} + \frac{F_3 - 1}{G_1 G_2}$$

and is minimized if the gain of the first stage is high. The BFG505 cannot provide a gain higher than 6 dB because in this case (for a given P_{in}) it reaches the compression point. This difficulty is avoided if the BFG520 is used as the first stage. We can design the first stage for maximum gain and the second stage for necessary power to drive the output transistor. We can also adjust the gains of the individual stages so that none of the transistors reaches the compression point.

The block diagram of the resulting amplifier is shown in Figure 9-30, where the gain of each stage is chosen according to the preceding discussion. The noise figure of this amplifier is predicted as

$$F_{\text{tot}} = F_1 + \frac{F_2 - 1}{G_1} + \frac{F_3 - 1}{G_1 G_2} = 2.13 \text{ dB}$$

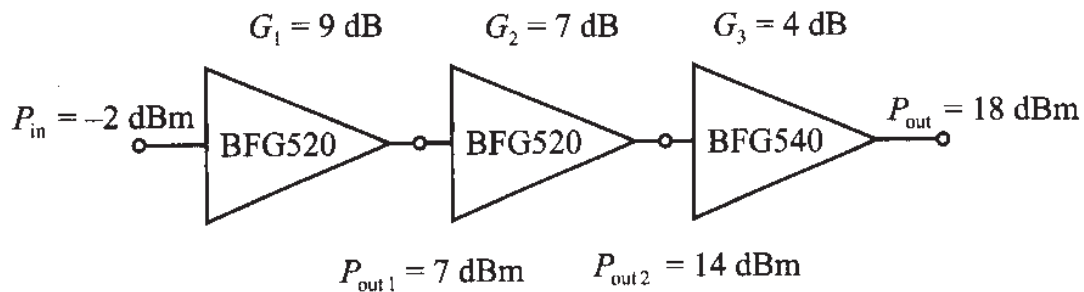


Figure 9-30 Block diagram of a three-stage amplifier.

The output power at the third-order intercept point is calculated using (9.112) and modified for a three-stage amplifier

$$IP_{\text{tot}} = \frac{1}{1/IP_3 + 1/(G_3 IP_2) + 1/(G_3 G_2 IP_1)} = 28 \text{ dBm}$$

where the preceding formula was obtained from (9.112) by first computing the IP of the first two stages and then resubstituting it into (9.112).

The above analysis is actually one of the first steps required in an amplifier design process. Here the crucial steps of picking suitable transistor types and deciding on the number of stages are made. They then become the starting point of a detailed performance analysis.

9.8 Summary

This chapter deals with a broad spectrum of amplifier design concepts. First, the various power relations are defined. Specifically, the transducer power gain

$$G_T = \frac{(1 - |\Gamma_L|^2)|S_{21}|^2(1 - |\Gamma_S|^2)}{|1 - \Gamma_S \Gamma_{\text{in}}|^2 |1 - S_{22} \Gamma_L|^2}$$

as well as the available and operating power gains are of key importance. We next establish the various input and output stability circle equations and examine the meaning of unconditional stability. Specifically, the factor

$$k = \frac{1 - |S_{11}|^2 - |S_{22}|^2 + |\Delta|^2}{2|S_{12}||S_{21}|} > 1$$

is employed to assess the unconditional stability of an active device. If the transistor turns out to be unstable, additional series or shunt resistances can be used to stabilize the device. Next the constant unilateral gain circles are established and displayed in the Smith Chart. The location and radius equations

$$d_{g_i} = \frac{g_i S_{ii}^*}{1 - |S_{ii}|^2(1 - g_i)} \text{ and } r_{g_i} = \frac{\sqrt{1 - g_i}(1 - |S_{ii}|^2)}{1 - |S_{ii}|^2(1 - g_i)}$$

provide insight as to where certain constant gain values are located under unilateral design conditions (inverse power gain is assumed negligible). The error committed by using the unilateral design approach over the bilateral method is quantified through the unilateral figure of merit. If the unilateral approach turns out to be too imprecise, a bilateral design has to be pursued, leading to the simultaneous conjugate matched reflection coefficients (Γ_{MS} , Γ_{ML}) at the input and output ports. The optimal matching

$$\Gamma_{MS}^* = S_{11} + \frac{S_{12}S_{21}\Gamma_{ML}}{1 - S_{22}\Gamma_{ML}} \text{ and } \Gamma_{ML}^* = S_{22} + \frac{S_{12}S_{21}\Gamma_{MS}}{1 - S_{11}\Gamma_{MS}}$$

results in amplifier designs with maximum gain. Starting from the operating power gain expression, circles of constant gain under optimal source matching are derived. Alternatively, starting with the available power gain expression, circles of constant gain under optimal load matching are derived.

We then investigate the influence of noise generated by an amplifier. Using the noise figure of a generic two-port network

$$F = F_{\min} + \frac{R_n}{G_S} |Y_S - Y_{\text{opt}}|^2$$

circle equations for the Smith Chart are computed. The noise figure circles can be used by the circuit designer to make trade-offs with the previously conducted constant gain analysis.

An investigation into reducing the VSWR as part of various input and output matching network strategies results in an addition set of circle equations that quantify the VSWR at the matching network ports:

$$\text{VSWR}_{IMN} = \frac{1 + |\Gamma_{IMN}|}{1 - |\Gamma_{IMN}|} \text{ and } \text{VSWR}_{OMN} = \frac{1 + |\Gamma_{OMN}|}{1 - |\Gamma_{OMN}|}$$

Combining the various circle representations permit the small-signal amplifier design based on constant operating gain, noise figure, and VSWR circles, jointly displayed in the Smith Chart.

For broadband design, we discuss the need to develop frequency compensated matching networks in an effort to widen the operational frequency range. The use of negative feedback loops is introduced as a way to flatten the power gain over the broadband frequency range.

In high-power amplifier applications issues related to the output power compression are of major concern since they limit the dynamic range of amplification. An important figure of merit is the 1-dB compression point:

$$P_{\text{out}, \text{1dB}}(\text{dBm}) = G_0(\text{dB}) - 1 \text{ dB} + P_{\text{in}, \text{1dB}}(\text{dBm})$$

Furthermore, an additional undesirable property is the occurrence of intermodular distortion due to the presence of nonlinearities. Finally, the influences of power compression, noise figure, and gain are investigated in the context of a multistage amplifier design.

Further Reading

I. Bahil and P. Bhartia, *Microwave Solid State Circuit Design*, John Wiley, New York, 1988.

G. Gonzalez, *Microwave Transistor Amplifiers, Analysis and Design*, Prentice Hall, Upper Saddle River, NJ, 1997.

K. C. Gupta, R. Garg, and R. Chada, *Computer-Aided Design of Microwave Circuits*, Artech, Dedham, MA, 1981.

Hewlett-Packard, RF Design and Measurement Seminar, Seminar Notes, Burlington, MA, 1999.

Hewlett-Packard, *S-Parameter Techniques for Faster and more Accurate Network Design*, Application Notes 95-1, 1968.

H. Krauss, C. Bostian, and F. Raab, *Solid Radio Engineering*, John Wiley, New York, 1980.

S. Y. Liao, *Microwave Circuit Analysis and Amplifier Design*, Prentice Hall, Englewood Cliffs, NJ, 1987.

S. J. Mason, "Power Gain in Feedback Amplifiers, *IRE Trans.*, Vol. 1, pp. 20–25, 1954.

D. Pozar, *Microwave Engineering*, John Wiley, New York, 1998.

B. Razavi, *RF Microelectronics*, Prentice Hall, Upper Saddle River, NJ, 1998.

U. L. Rohde and T. T. N. Bucher, *Communication Receivers, Principle and Design*, McGraw-Hill, New York, 1988.

J. M. Rollett, "Stability and Power-Gain Invariants of Linear Two-Ports," *IRE Trans.*, Vol. 9, pp. 29–32, 1962.

G. D. Vendelin, *Design of Amplifiers and Oscillators by the S-Parameter Method*, John Wiley, New York, 1982.

Problems

- 9.1 The available power of an RF source driving an amplifier connected to load $Z_L = 80 \Omega$ can be represented as

$$P_A = \frac{1}{2} \frac{|b_S|^2}{1 - |\Gamma_S|^2}$$

Based on the signal flow graph shown in Figure 9-2(b),

- (a) Find the power to the load P_L in terms of Γ_L , Γ_S , and b_S .
- (b) For $Z_S = 40 \Omega$, $Z_0 = 50 \Omega$, $V_S = 5V\angle 0^\circ$, find the available power P_A and the power at the load P_L .

- 9.2 Use the signal flow graph in Figure 9-2(b) and establish the validity of equation (9.8) in Section 9.2.2.

- 9.3 An amplifier is characterized by the following S-parameters: $S_{11} = 0.78\angle -65^\circ$, $S_{21} = 2.2\angle 78^\circ$, $S_{12} = 0.11\angle -21^\circ$, $S_{22} = 0.9\angle -29^\circ$. The input side of the amplifier is connected to a voltage source with $V_S = 4V\angle 0^\circ$, and impedance $Z_S = 65 \Omega$. The output is utilized to drive an antenna that has an impedance of $Z_L = 85 \Omega$. Assuming that the S-parameters of the amplifier are measured with reference to a $Z_0 = 75 \Omega$ characteristic impedance, find the following quantities:

- (a) transducer gain G_T , unilateral transducer gain G_{TU} , available gain G_A , operating power gain G
- (b) power delivered to the load P_L , available power P_A , and incident power to the amplifier P_{inc}

- 9.4 A FET is operated at $f = 5.5$ GHz and under bias conditions $V_{DS} = 3.2$ V and $I_D = 24$ mA. The S-parameters are $S_{11} = 0.73 \angle 176^\circ$, $S_{21} = 3.32 \angle 75^\circ$, $S_{12} = 0.05 \angle 34^\circ$, $S_{22} = 0.26 \angle -107^\circ$. In the absence of matching networks a load of $Z_L = 75 \Omega$ and a source of $Z_S = 30 \Omega$ are attached. Assume $Z_0 = 50 \Omega$.

- (a) Find G_{TU} , G_T , G_A , and plot the magnitude of G_{TU} for $10 \Omega \leq Z_L \leq 100 \Omega$.
- (b) Match the input side for the unilateral case and find G_{TU} .
- (c) Match both input and output for the unilateral case and compute $G_{TU} = G_{TU\max}$.

- 9.5 Unconditional stability in the complex Γ_{out} -plane requires that the $|\Gamma_s| = 1$ domain resides completely within the $|\Gamma_{\text{out}}| = 1$ circle, or $|C_s - r_s| < 1$, where

$$C_s = S_{22} + \frac{S_{12}S_{21}S_{11}^*}{1 - |S_{11}|^2} \quad \text{and} \quad r_s = \frac{|S_{12}S_{21}|}{1 - |S_{11}|^2}$$

- (a) Derive these two equations.
- (b) Find the circle equations for C_L and r_L and show that $|S_{12}S_{21}| < 1 - |S_{22}|^2$.

- 9.6 Prove that $|S_{11} - S_{22}^* \Delta|^2 = |S_{12}S_{21}|^2 + (1 - |S_{11}|^2)(|S_{22}|^2 - |\Delta|^2)$. This is a key identity in the stability factor derivation of Example 9.2.

- 9.7 A BJT has the following S-parameters (see the table below) as a function of four frequencies. Determine the stability regions and sketch them in the Smith Chart.

| Frequency | S_{11} | S_{12} | S_{21} | S_{22} |
|-----------|--------------------------|------------------------|-------------------------|-------------------------|
| 500 MHz | $0.70 \angle -57^\circ$ | $0.04 \angle 47^\circ$ | $10.5 \angle 136^\circ$ | $0.79 \angle -33^\circ$ |
| 750 MHz | $0.56 \angle -78^\circ$ | $0.05 \angle 33^\circ$ | $8.6 \angle 122^\circ$ | $0.66 \angle -42^\circ$ |
| 1000 MHz | $0.46 \angle -97^\circ$ | $0.06 \angle 22^\circ$ | $7.1 \angle 112^\circ$ | $0.57 \angle -48^\circ$ |
| 1250 MHz | $0.38 \angle -115^\circ$ | $0.06 \angle 14^\circ$ | $6.0 \angle 104^\circ$ | $0.50 \angle -52^\circ$ |

- 9.8 The S-parameters for a BJT at a particular bias point and operating frequency are as follows: $S_{11} = 0.60 \angle 157^\circ$, $S_{21} = 2.18 \angle 61^\circ$,

$S_{12} = 0.09 \angle 77^\circ$, $S_{22} = 0.47 \angle -29^\circ$. Check the transistor stability, stabilize it if necessary, and design an amplifier for maximum gain.

- 9.9 In this chapter we have derived the circle equations for constant operating power gain. It can be concluded that the maximum gain is obtained when the radius of the constant gain circle is equal to zero. Using this condition, prove that the maximum achievable power gain in the unconditionally stable case is

$$G_{T\max} = \frac{|S_{21}|}{|S_{12}|} (k - \sqrt{k^2 - 1})$$

where k is the stability factor ($k > 1$).

- 9.10 A BJT is operated at $f = 750$ MHz (and with the S -parameters given as follows: $S_{11} = 0.56 \angle -78^\circ$, $S_{21} = 0.05 \angle 33^\circ$, $S_{12} = 8.64 \angle 122^\circ$, and $S_{22} = 0.66 \angle -42^\circ$). Attempt to stabilize the transistor by finding a series resistor or shunt conductance for the input and output ports.
- 9.11 In Example 9-2 the stability factor k is derived based on the input stability circle equation. Start with the output stability circle equation and show that the same result (9.24) is obtained.
- 9.12 A BJT is operated at $f = 7.5$ GHz and is biased such that the S -parameter is given as $S_{11} = 0.85 \angle 105^\circ$. It is assumed that the transistor is unconditionally stable so that the unilateral approximation can be applied. Find the maximum source gain and plot the constant source gain circles for several appropriately chosen values of g_S .
- 9.13 A MESFET is used as a single-stage amplifier at 2.25 GHz. The S -parameters at that frequency and under given bias conditions are reported as $S_{11} = 0.83 \angle -132^\circ$, $S_{12} = 0.03 \angle 22^\circ$, $S_{21} = 4.9 \angle 71^\circ$, $S_{22} = 0.36 \angle -82^\circ$. For a required 18-dB gain, use the unilateral assumption by setting $S_{12} = 0$, and
- (a) Determine if the circuit is unconditionally stable.
 - (b) Find the maximum power gain under the optimal choice of the reflection coefficients.
 - (c) Adjust the load reflection coefficient such that the desired gain is realized using the concept of constant gain circles.
- 9.14 A BJT is used in an amplifier at 7.5 GHz. The S -parameters at that frequency and under given bias conditions are reported as $S_{11} = 0.63 \angle -140^\circ$,

$S_{12} = 0.08 \angle 35^\circ$, $S_{21} = 5.7 \angle 98^\circ$, $S_{22} = 0.47 \angle -57^\circ$. The design requires a 19 dB gain. Use the unilateral assumption and

- (a) Find the maximum power gain under the optimal choice of the reflection coefficients.
- (b) Adjust the load reflection coefficient such that the desired gain under stable operating conditions is realized.

- 9.15 A small-signal amplifier for a BJT operated at 4 GHz is appropriately biased and has the following S-parameters: $S_{11} = 0.57 \angle -150^\circ$, $S_{12} = 0.12 \angle 45^\circ$, $S_{21} = 2.0 \angle 56^\circ$, $S_{22} = 0.35 \angle -85^\circ$. If a unilateral design approach is pursued, estimate the error involved.
- 9.16 A BJT with $I_C = 10$ mA and $V_{CE} = 6$ V is operated at a frequency of $f = 2.4$ GHz. The corresponding S-parameters are $S_{11} = 0.54 \angle -70^\circ$, $S_{12} = 0.017 \angle 176^\circ$, $S_{21} = 1.53 \angle 91^\circ$, and $S_{22} = 0.93 \angle -15^\circ$. Determine whether the transistor is unconditionally stable and find the values for source and load reflection coefficients that provide maximum gain.
- 9.17 Using the same BJT discussed in the Problem 9.16, design an amplifier whose transducer power gain is 60% of $G_{T\max}$. In addition, ensure a perfect match on the input port of the amplifier.
- 9.18 A MESFET operated at 9 GHz under appropriate bias conditions has the following S-parameters: $S_{11} = 1.2 \angle -60^\circ$, $S_{12} = 0.02 \angle 0^\circ$, $S_{21} = 6.5 \angle 115^\circ$, and $S_{22} = 0.6 \angle -35^\circ$. Design an amplifier that stays within 80% of $G_{T\max}$. Moreover, ensure that $\text{VSWR}_{\text{out}} = 1$.
- 9.19 In Section 9.4.4 it is mentioned that the constant gain design for a matched input results in the circle equation

$$\left| \frac{S_{11} - \Gamma_S^*}{\Delta - S_{22}\Gamma_S^*} - d_{g_0} \right|^2 = r_{g_0}^2$$

Show that the center d_{g_0} and radius r_{g_0} are given by

$$r_{g_S} = \frac{r_{g_0} |S_{12}S_{21}|}{\left| |1 - S_{22}d_{g_0}|^2 - r_{g_0}^2 |S_{22}|^2 \right|}$$

and

$$d_{g_S} = \frac{(1 - S_{22}d_{g_0})(S_{11} - \Delta d_{g_0})^* - r_{g_0}^2 \Delta^* S_{22}}{\left| |1 - S_{22}d_{g_0}|^2 - r_{g_0}^2 |S_{22}|^2 \right|}$$

- 9.20 For the constant available gain circle $|\Gamma_S - d_{g_a}| = r_{g_a}$ [see (9.66)], show that

$$d_{g_a} = \frac{g_a(S_{11} - \Delta S_{22}^*)}{1 + g_a(|S_{11}|^2 - |\Delta|^2)} \text{ and } r_{g_a} = \frac{\sqrt{1 - 2kg_a|S_{12}S_{21}| + g_a^2|S_{12}S_{21}|^2}}{|1 + g_a(|S_{11}|^2 - |\Delta|^2)|}$$

- 9.21 A BFG197X transistor is biased at $V_{CE} = 8$ V and $I_C = 10$ mA and has the following S -parameters measured at $f = 1$ GHz: $S_{11} = 0.73\angle 176^\circ$, $S_{12} = 0.07\angle 35^\circ$, $S_{21} = 3.32\angle 75^\circ$, and $S_{22} = 0.26\angle 107^\circ$. Determine the unilateral figure of merit and compare the transducer gain of the amplifier designed under the unilateral and bilateral assumptions.

- 9.22 The BFG33 BJT is biased under $V_{CE} = 5$ V and $I_C = 5$ mA and has the following noise and S -parameters:

| | S_{11} | S_{12} | S_{21} | S_{22} | F_{\min} , dB | Γ_{opt} | R_n , Ω |
|----------|-------------------------|-----------------------|------------------------|------------------------|-----------------|-----------------------|------------------|
| 500 MHz | $0.72\angle -39^\circ$ | $0.05\angle 63^\circ$ | $6.22\angle 135^\circ$ | $0.78\angle -32^\circ$ | 2.3 | $0.64\angle 5^\circ$ | 58.5 |
| 1000 MHz | $0.45\angle -70^\circ$ | $0.08\angle 56^\circ$ | $5.13\angle 109^\circ$ | $0.61\angle -43^\circ$ | 2.5 | $0.56\angle 13^\circ$ | 67.5 |
| 2000 MHz | $0.18\angle -115^\circ$ | $0.12\angle 54^\circ$ | $3.24\angle 82^\circ$ | $0.49\angle -54^\circ$ | 3.0 | $0.52\angle 39^\circ$ | 49.7 |

Design a broadband low-noise amplifier with minimum gain of 10 dB and a noise figure not exceeding 3.5 dB.

- 9.23 Design a microwave amplifier using a GaAs FET whose S -parameters at $f = 10$ GHz are $S_{11} = 0.79\angle 100^\circ$, $S_{12} = 0.20\angle -21^\circ$, $S_{21} = 6.5\angle -73^\circ$, $S_{22} = 0.74\angle 152^\circ$. Analyze the trade-offs posed by stability, gain, and VSWRs.
- 9.24 A broadband amplifier with nominal characteristics of $\text{VSWR}_{\text{in}} = 4$, $\text{VSWR}_{\text{out}} = 2.8$, and $G_T = 10$ dB is used as part of a balanced amplifier design. Compute the worst input and output VSWR and the insertion gain of the balanced amplifier if the values listed can vary by as much as 10%.
- 9.25 In Section 9.7.3 we have listed equation (9.112) for the IP definition of a two-stage amplifier.
 (a) Derive a generalized formula for the IP computation of an N -stage amplifier.

- (b) Compute the total IP and the noise figure of the N -stage amplifier assuming that all stages are identical and have $IP_{\text{out}} = 35 \text{ dBm}$, $F = 2 \text{ dB}$, and $G = 8 \text{ dB}$.
- 9.26 Design a 15-dB broadband amplifier using a BJT with feedback loop. Calculate the value of the feedback resistor and find the minimum collector current of the transistor. Assume that the amplifier is operated at $T = 300^\circ \text{K}$.
- 9.27 A transistor has the following S -parameters: $S_{11} = 0.61 \angle 152^\circ$, $S_{12} = 0.1 \angle 79^\circ$, $S_{21} = 1.89 \angle 55^\circ$, and $S_{22} = 0.47 \angle -30^\circ$. Design an amplifier for minimum noise figure if $F_{\min} = 3 \text{ dB}$, $\Gamma_{\text{opt}} = 0.52 \angle -153^\circ$, and $R_n = 9 \Omega$.
- 9.28 Prove equation (9.113), which states the total spurious-free dynamic range.
- 9.29 An amplifier has a transducer gain of $G_T = 25 \text{ dB}$, and a 200 MHz bandwidth. The noise figure is given as $F = 2.5 \text{ dB}$ and the 1 dB gain compression point is measured as $P_{\text{out}, 1\text{dB}} = 20 \text{ dBm}$. Calculate the dynamic range and the spurious-free dynamic range of the amplifier if $IP_{\text{out}} = 40 \text{ dBm}$. Assume that the amplifier is operated at room temperature.
- 9.30 An amplifier has a gain of $G = 8 \text{ dB}$ at 1 GHz and lists a 1 dB compression point of $P_{\text{out}, 1\text{dB}} = 12 \text{ dBm}$ and the third order intercept point at $IP_{\text{tot}} = 25 \text{ dBm}$. Find the third order intercept points for the cascaded amplifier stages 2 and 3. What value of IP_{tot} is obtained in the limit of an infinite number of stages?
- 9.31 Derive a formula for the noise figure of a balanced amplifier. Make the assumption that the power gains and noise figures of the amplifiers in the individual branches are G_A , G_B , and F_A , F_B , respectively. Assume that the balanced amplifier uses 3 dB hybrid couplers at the input and output ports.

Oscillators and Mixers

With the advent of modern radio and radar systems came the need to provide stable harmonic oscillations at particular carrier frequencies to establish the required modulation and mixing conditions. While the carrier frequencies in the early days mostly reached into the low to mid MHz range, today's RF systems easily surpass the 1 GHz point. This has resulted in the need for specialized oscillator circuits capable of providing stable and pure sinusoidal responses. What makes the design of oscillators such a difficult task is that we exploit an inherently nonlinear circuit behavior that can only be described incompletely with linear system tools. Specifically, the small-signal linear circuit models utilized to represent the active device provide limited capabilities to handle the complicated feedback mechanism. Moreover, since an oscillator has to provide power to subsequent circuits, frequency-dependent output loading often plays an important role. It is for these reasons that the design process of oscillators remains more of an art than an exact engineering design task. This holds particularly true for the high-frequency regime, where parasitic component influences can significantly impact the overall system performance. Affected in part by the additional resonance effects of the passive circuit element, it is possible that the oscillator not only operates at the intended frequency but also at lower or higher harmonics. Certain system realizations may even cease to oscillate completely.

In the first part of this chapter we concentrate on the negative resistance and feedback harmonic oscillators as well as a number of Schottky diode mixers. Once the fundamental idea is mastered of how to generate oscillations, we investigate the basic Colpitts and Hartley resonators before moving to the modern RF circuit design approaches involving the *S*-parameters of the active device in conjunction with the various network configurations.

In the second part of this chapter, we turn our attention to the basic frequency translation tasks performed by mixers. Of the many different circuit implementations for a wide range of applications, the main emphasis in this chapter is placed on down-converters. A typical application of a mixer in a receiver system is to convert the RF input signal into a lower frequency intermediate signal that is generally more suitable for subsequent signal conditioning and processing. This conversion is accomplished by combining the RF input with a local oscillator signal as part of a multiplication operation that requires a nonlinear, at least quadratic transfer function. Primarily transistors and diodes are nowadays in use where present FET technology permits the construction of mixer circuits up to 50 GHz and with diode mixers already exceeding the 100 GHz mark.

10.1 Basic Oscillator Model

At the core of any oscillator circuit is a loop that causes a positive feedback at a selected frequency. Figure 10-1(a) illustrates the generic closed-loop system representation, while Figure 10-1(b) provides a two-port network description.

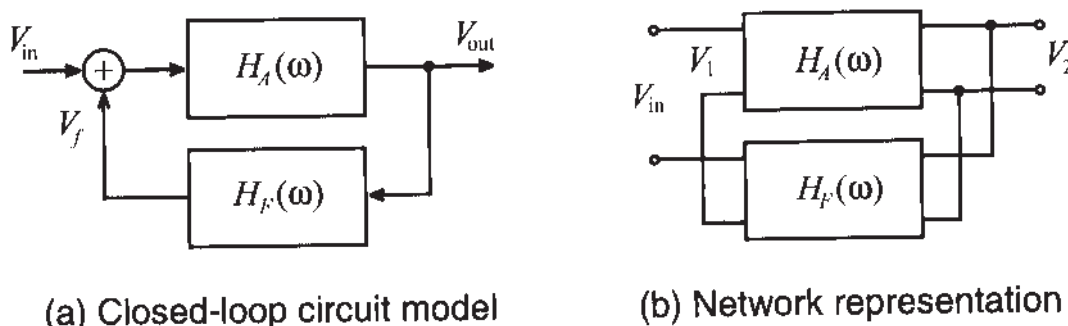


Figure 10-1 Basic oscillator configuration.

The mathematical condition for a circuit to oscillate can be established by combining the transfer functions of the amplification stage $H_A(\omega)$ with the feedback stage $H_F(\omega)$ to the closed-loop transfer function:

$$\frac{V_{\text{out}}}{V_{\text{in}}} = H_{CL}(\omega) = \frac{H_A(\omega)}{1 - H_F(\omega)H_A(\omega)} \quad (10.1)$$

Since there is no input to an oscillator, $V_{\text{in}} = 0$, to obtain a nonzero output voltage, V_{out} , the denominator in (10.1) has to be zero. This requirement leads to the **Barkhausen criterion**, which is also known as the loop gain equation:

$$H_F(\omega)H_A(\omega) = 1 \quad (10.2)$$

If the feedback transfer function $H_F(\omega)$ is written as a complex quantity [that is, $H_F(\omega) = H_{Fr}(\omega) + jH_{Fi}(\omega)$] and the amplifier transfer function possesses a real valued gain, $H_A(\omega) = H_{A0}$, we can re-express (10.2) as

$$H_{A0} = \frac{1}{H_{Fr}(\omega)} \quad (10.3a)$$

$$H_{Fi}(\omega) = 0 \quad (10.3b)$$

The conditions (10.2) and (10.3) apply only for a steady-state situation. Initially, we have to require that $H_{A0}H_{Fr}(\omega) > 1$. In other words, the loop gain has to be larger than unity to obtain an increasing output voltage. However, the voltage must reach a steady state (i.e., the amplitude eventually must stabilize). This nonlinear behavior of the oscillator is shown in Figure 10-2.

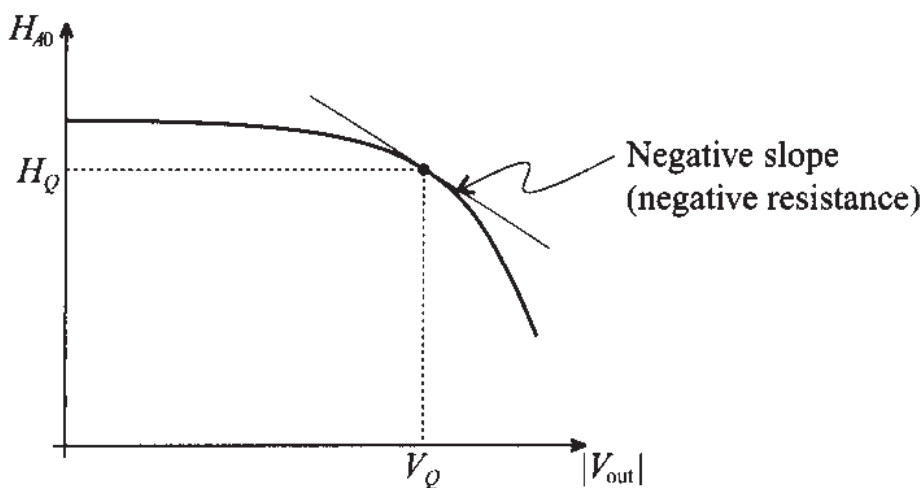


Figure 10-2 Output voltage versus gain characteristic.

A negative slope of the curve is needed to ensure a decrease in gain for increasing voltage. At point $|V_{\text{out}}| = V_Q$ for $H_{A0} = H_Q = H_{Fr}(\omega)$ the stable operating point is reached. A similar curve can be established for the frequency versus loop gain with a stable resonance frequency f_Q .

10.1.1 Negative Resistance Oscillator

To explain the idea behind an oscillator we need to understand the seemingly impossible concept of creating a negative resistance. The requirement of a negative resistance is best explained by investigating the series resonance circuit consisting of resistance R , inductance L , and capacitance C . As an input we use a current-controlled voltage source, as shown in Figure 10-3. The voltage source can represent the output of an active device, e.g. BJT or FET.

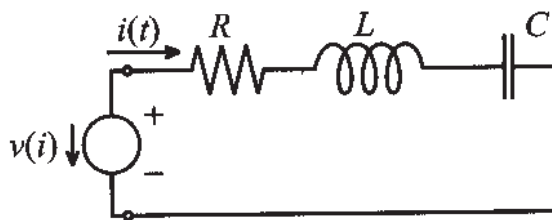


Figure 10-3 Series resonance circuit with voltage-controlled source term.

The governing equation in terms of the current is written as

$$L \frac{d^2 i(t)}{dt^2} + R \frac{di(t)}{dt} + \frac{1}{C} i(t) = -\frac{dv(i)}{dt} \quad (10.4)$$

If we set the right-hand side to zero (i.e., we reach steady state and the voltage amplitude is stable), we obtain the standard solution

$$i(t) = e^{\alpha t} (I_1 e^{j\omega_Q t} + I_2 e^{-j\omega_Q t}) \quad (10.5)$$

where $\alpha = -R/(2L)$ and $\omega_Q = \sqrt{1/(LC) - (R/(2L))^2}$. In general, because α is a negative quantity, the harmonic response of the resonance circuit will reduce to zero as time progresses. In the limit, as R reaches zero, an undamped sinusoidal response is obtained. The goal of an active element in the oscillator is therefore to generate a source response that compensates for the resistance in the circuit. This can only be achieved if a **negative resistance** is provided. Thus, if we succeed in selecting a nonlinear device whose voltage-current response is $v(i) = v_0 + R_1 i + R_2 i^2 + \dots$, then the terms may be adjusted in such a way as to compensate for R . Indeed, substituting the first two terms of this series expansion into (10.4), we see

$$L \frac{d^2 i(t)}{dt^2} + R \frac{di(t)}{dt} + \frac{1}{C} i(t) = -\frac{dv(t)}{dt} = -R_1 \frac{di(t)}{dt} \quad (10.6)$$

Combining the coefficients of the first derivative leads to

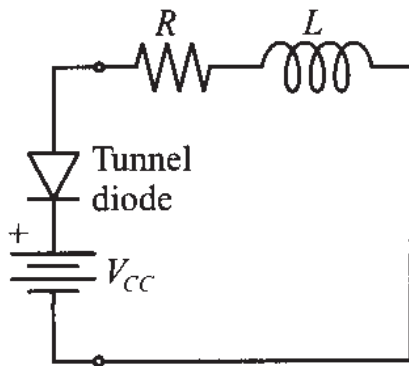
$$R + R_1 = 0 \quad (10.7)$$

as the requirement to set the attenuation coefficient to zero. It is now seen that (10.7) implies a device with a negative differential resistance:

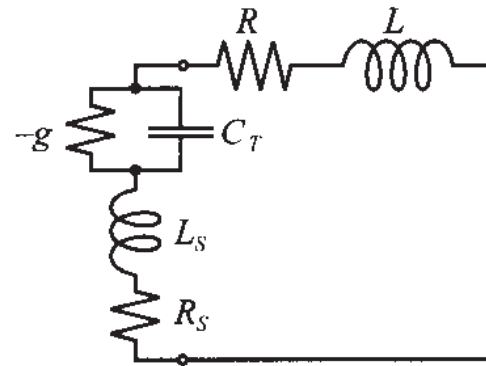
$$R_1 = -R \quad (10.8)$$

Moreover, to get the oscillations started, we require a positive attenuation coefficient, which implies R_1 to be less than $-R$. This situation is equivalent to the transfer function having poles in the right-hand side of the complex frequency domain.

A direct way to implement such a negative resistance condition is via a tunnel diode, whose electric circuit representation is discussed in Chapter 6 (see Figure 6-26). Figure 10-4 depicts both the circuit of a tunnel diode oscillator and the corresponding small-signal circuit model. Since the tunnel diode already possesses an inherent capacitance, an extra capacitor in the external circuit is not required.



(a) Tunnel diode oscillator circuit



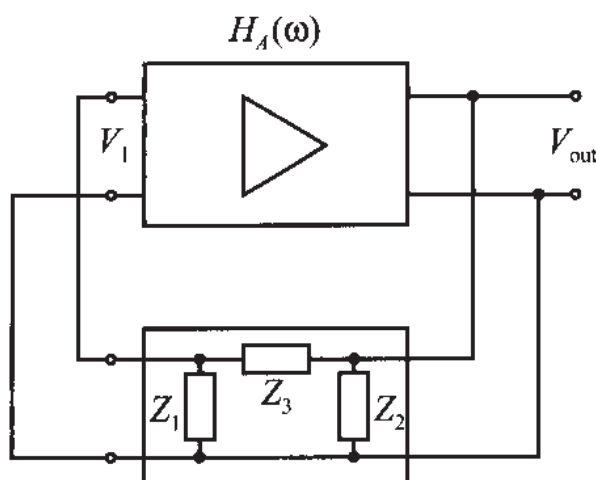
(b) Small-signal equivalent circuit

Figure 10-4 Tunnel diode oscillator circuit and its small-signal model.

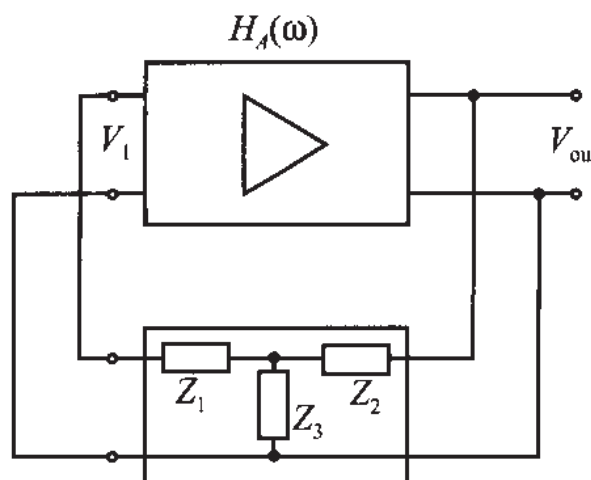
Circuits like the one shown in Figure 10-4 can be used for oscillators with resonance frequencies up to 100 GHz.

10.1.2 Feedback Oscillator Design

Because of their fundamental importance in the development of low-frequency as well as RF oscillators, let us next focus on the two-port feedback networks, shown generically in Figure 10-5.



(a) Pi-type feedback



(b) T-type feedback

Figure 10-5 Feedback circuits with Pi- and T-type feedback loops.

It is straightforward to find the transfer function of the feedback loop. For instance, for the Pi-network we obtain under high-impedance input and output assumptions

$$H_F(\omega) = \frac{V_1}{V_{\text{out}}} = \frac{Z_1}{Z_1 + Z_3} \quad (10.9)$$

More complicated is the computation of the transfer function $H_A(\omega)$ of the amplifier. This depends on the chosen active element and its electric equivalent circuit model. To demonstrate the concept, we use a simple, low-frequency FET model with voltage gain μ_V and output resistance R_B . The corresponding loop equation for the circuit depicted in Figure 10-6 is

$$\mu_V V_1 + I_B R_B + I_B Z_C = 0 \quad (10.10)$$

where $1/Z_C = Y_C = 1/Z_2 + 1/(Z_1 + Z_3)$.

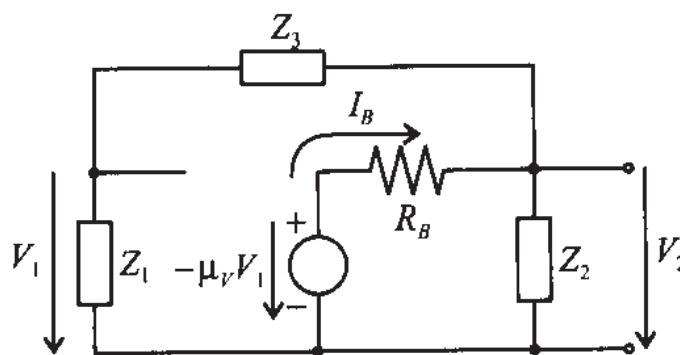


Figure 10-6 Feedback oscillator with FET electric circuit model.

Solving (10.10) for I_B and multiplying by Z_C gives us the output voltage V_{out} from which the voltage gain is found to be

$$H_A(\omega) = \frac{V_{\text{out}}}{V_1} = \frac{-\mu_V}{Y_C R_B + 1} \quad (10.11)$$

The closed-loop transfer function is thus

$$H_F(\omega) H_A(\omega) = \frac{-\mu_V Z_1 Z_2}{Z_2 Z_1 + Z_2 Z_3 + R_B (Z_1 + Z_2 + Z_3)} \equiv 1 \quad (10.12)$$

This equation allows us to design various oscillator types depending on the choice of the three impedances in the feed-back loop. To eliminate resistive losses, we choose purely reactive components $Z_i = jX_i$ ($i=1,2,3$). This ensures that the numerator is real. Further, to make the denominator real, it is necessary that $X_1 + X_2 + X_3 = 0$, which implies that one of the reactances has to be the negative sum of the others. It is understood that negative-valued reactances correspond to capacitors and positive-

valued reactances identify inductors. For instance, if we decide to use $X_3 = -(X_1 + X_2)$, then, upon substitution into (10.12), the result is

$$\frac{\mu_v X_1 X_2}{-X_2 X_1 + X_2(X_1 + X_2)} = \frac{\mu_v}{X_2} X_1 = 1 \quad (10.13)$$

It is apparent that X_1 and X_2 must have the same sign but different values according to (10.13). In Table 10-1 a few possible configurations of the feedback loop are summarized.

Table 10-1 Various feedback configurations for oscillator designs based on Figure 10-5(a)

| | | |
|----------------------------|---------------------|------------------|
| X_1, X_2 | | |
| X_3 | | |
| Hartley | Colpitts | Clapp |

Two often used realizations are the **Hartley oscillator**, where $X_1 = \omega L_1$, $X_2 = \omega L_2$, $X_3 = 1/(\omega C_3)$, and the **Colpitts oscillator**, where $X_1 = 1/(\omega C_1)$, $X_2 = 1/(\omega C_2)$, and $X_3 = \omega L_3$, as depicted in Figure 10-7, where a FET is employed as active device. Here resistors R_A , R_B , R_D , and R_S set the DC bias point. C_S is the RF bypass capacitor, and C_B denotes DC blocking capacitors.

The various choices of L and C element combinations are in practice limited by the range of realizable values for a given frequency. Often hybrid configurations are used; if, for instance, the inductance becomes very small, a capacitor connected in series can yield a larger effective inductive reactance (**Clapp oscillator**).

Besides the standard common-source (or common-emitter for a BJT) configuration, common-gate (common-base) and common-drain (common-collector) type oscillators can be constructed, as shown in Figure 10-8 where all DC biasing elements are omitted.

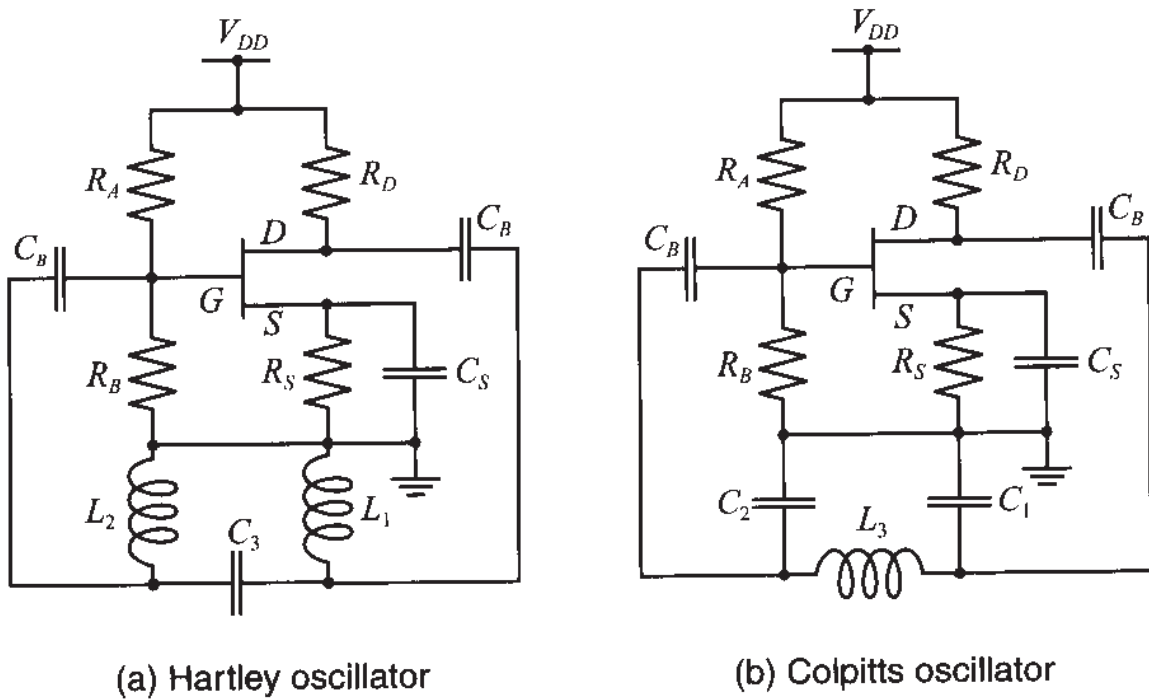


Figure 10-7 Hartley and Colpitts oscillators.

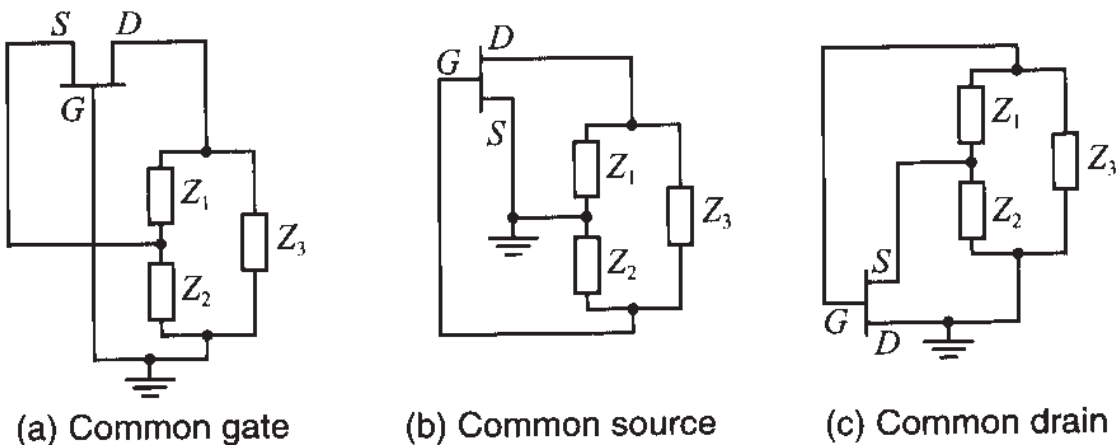


Figure 10-8 Common gate, source, and drain configurations.

10.1.3 Design Steps

What makes the oscillator design so complicated is that the nonlinear electric equivalent circuit describing the active device (BJT, FET) becomes increasingly complicated as the frequency increases. Moreover, the oscillator has to drive additional circuits and must therefore provide a certain amount of power. This output loading affects the oscillator in terms of frequency stability and waveform purity.

To provide the reader with a glimpse of the essential steps involved, we will at first examine the design of a low-frequency Colpitts oscillator. The *h*-parameter configuration with the appropriate feedback loop is depicted in Figure 10-9. The corresponding Kirchhoff voltage mesh equations involving input, output, and feedback loops are

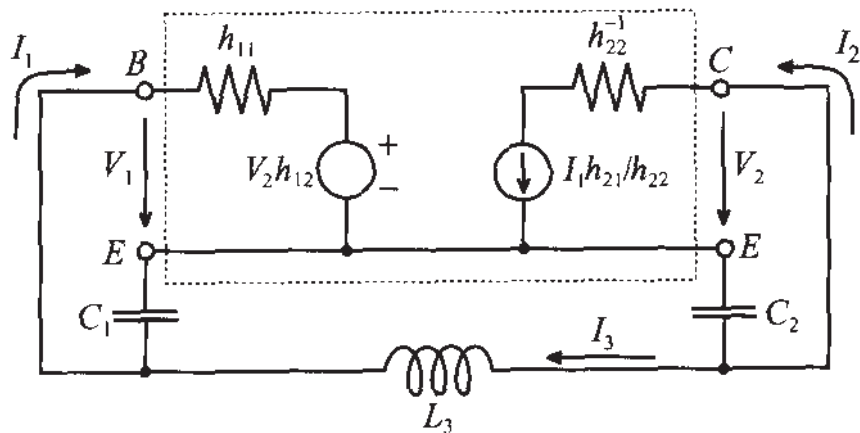


Figure 10-9 Colpitts oscillator design.

established by utilizing the output voltage $V_2 = V_{\text{out}} = I_2/h_{22} - I_1(h_{21}/h_{22})$. In matrix form for the unknown currents, we obtain

$$\begin{bmatrix} \left(h_{11} - jX_{C1} - \frac{h_{12}h_{21}}{h_{22}}\right) & \frac{h_{12}}{h_{22}} & jX_{C1} \\ -\frac{h_{21}}{h_{22}} & \left(\frac{1}{h_{22}} - jX_{C2}\right) & -jX_{C2} \\ jX_{C1} & -jX_{C2} & j(X_{L3} - X_{C1} - X_{C2}) \end{bmatrix} \begin{Bmatrix} I_1 \\ I_2 \\ I_3 \end{Bmatrix} = \begin{Bmatrix} 0 \\ 0 \\ 0 \end{Bmatrix} \quad (10.14)$$

Computing the determinant and setting its imaginary portion to zero results, after lengthy algebra, in the form

$$f = \frac{1}{2\pi} \frac{1}{\sqrt{C_1 C_2}} \sqrt{h_{22}/h_{11} + (C_1 + C_2)/L_3} \quad (10.15)$$

Furthermore, setting the real part of the determinant of (10.14) to zero, and assuming that $h_{12} \ll 1$, yields a quadratic equation in terms of the capacitor ratio C_1/C_2 :

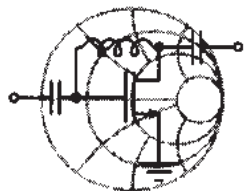
$$\frac{C_1^2}{C_2^2} (h_{11}h_{22} - h_{12}h_{21}) - \frac{C_1}{C_2} h_{21} + 1 = 0 \quad (10.16)$$

which, under the assumption that $h_{21}^2 \gg 4(h_{11}h_{22} - h_{12}h_{21})$, can be simplified to

$$C_1 \approx \frac{h_{21}}{(h_{11}h_{22} - h_{12}h_{21})} C_2 \quad (10.17)$$

The preceding treatment deals with the h -parameters as real quantities, an assumption that generally may not be applicable. In fact, even for moderately high frequencies, the h -parameters attain a significant phase angle. To incorporate the actual

frequency-dependent behavior, we need to resort to the equations given in Section 4.3.2. For these situations, explicit formulas as (10.15) and (10.17) are impossible to derive, and we must resort to a mathematical spreadsheet to find numerical results.



RF & MW

Example 10-1: Design of a Colpitts oscillator

For a 200 MHz oscillation frequency, a Colpitts BJT oscillator in common-emitter configuration has to be designed. For the bias point of $V_{CE} = 3$ V and $I_C = 3$ mA, the following circuit parameters are given at room temperature of 25°C: $C_{BC} = 0.1$ fF, $r_{BE} = 2$ kΩ, $r_{CE} = 10$ kΩ, $C_{BE} = 100$ fF. If the inductance should not exceed $L_3 = L = 50$ nH, find values for the capacitances in the feedback loop.

Solution: The first step involves the determination of the h -parameters. We compute the values for DC (i.e., $f \rightarrow 0$).

$$h_{11} = h_{ie} = \frac{r_{BE}}{1 + j\omega(C_{BE} + C_{BC})r_{BE}} = 2000 \Omega$$

$$h_{12} = h_{re} = \frac{j\omega C_{BC} r_{BE}}{1 + j\omega(C_{BE} + C_{BC})r_{BE}} = 0$$

$$h_{21} = h_{fe} = \frac{r_{BE}(g_m - j\omega C_{BC})}{1 + j\omega(C_{BE} + C_{BC})r_{BE}} = 233.32$$

$$h_{22} = h_{oe} = \frac{1}{r_{CE}} + \frac{j\omega C_{BC}(1 + g_m r_{BE} + j\omega C_{BE} r_{BE})}{1 + j\omega(C_{BE} + C_{BC})r_{BE}} = 0.1 \text{ mS}$$

At DC the h -parameters are real and we can find from (10.17) the ratio between the capacitances C_1 and C_2 :

$$C_1 = \frac{h_{21}}{(h_{11}h_{22} - h_{12}h_{21})} C_2 = 1166.6 C_2$$

Introducing a proportionality factor K such that $C_1 = KC_2$, equation (10.15) is rewritten as

$$f = \frac{1}{2\pi C_2 \sqrt{K}} \sqrt{\frac{h_{22}}{h_{11}} + (1+K) \frac{C_2}{L}} \quad (10.18)$$

Solving the resonance condition (10.15) for C_2 , we obtain

$$C_2 = \frac{\frac{1+K}{L} + \sqrt{\left(\frac{1+K}{L}\right)^2 + 16K\pi^2 f^2 \frac{h_{22}}{h_{11}}}}{8K\pi^2 f^2} = 12.68 \text{ pF}$$

where the inductance $L = 50 \text{nH}$ has been used.

From the known C_2 we next find $C_1 = 1166.6C_2$, or $C_1 = 14.79 \text{nF}$. In the preceding design, the transistor's h -parameters are given under DC conditions. In reality, however, the oscillator is operated at the resonance frequency of 200 MHz. Here the h -parameters have the following values:

$$h_{11} = h_{ie} = \frac{r_{BE}}{1 + j\omega(C_{BE} + C_{BC})r_{BE}} = (1881 - j473)\Omega$$

$$h_{12} = h_{re} = \frac{j\omega C_{BC} r_{BE}}{1 + j\omega(C_{BE} + C_{BC})r_{BE}} = 5.9 \times 10^{-5} + j2.4 \times 10^{-4}$$

$$h_{21} = h_{fe} = \frac{r_{BE}(g_m - j\omega C_{BC})}{1 + j\omega(C_{BE} + C_{BC})r_{BE}} = 219 - j55$$

$$\begin{aligned} h_{22} = h_{oe} &= \frac{1}{r_{CE}} + \frac{j\omega C_{BC}(1 + g_m r_{BE} + j\omega C_{BE} r_{BE})}{1 + j\omega(C_{BE} + C_{BC})r_{BE}} \\ &= (0.11 + j0.03) \text{ mS} \end{aligned}$$

As seen, the h -parameters at this frequency differ only slightly from the DC conditions. Therefore, the analysis should equally apply for this frequency setting and the oscillator will require only a minimal amount of tuning.

In practice, the situation often arises where the h -parameters at a given oscillation frequency differ significantly from their DC values, necessitating substantial tuning. The difference becomes more significant as the frequency increases.

10.1.4 Quartz Oscillators

Unlike electric resonance circuits, quartz resonators can offer a number of advantages. A much higher quality factor (up to $10^5 \dots 10^6$), improved frequency stability, and immunity to temperature fluctuations are among the chief benefits. Unfortunately, because quartz crystals are mechanical systems, they cannot be constructed to exceed approximately 250 MHz.

A quartz crystal exploits the piezoelectric effect whereby an applied electric field causes a mechanical deformation of the crystal. Depending on the geometric configuration and crystal cut, the crystal performs either longitudinal or shear vibrations at distinct resonance frequencies.

A typical electric circuit representation for a quartz crystal is shown in Figure 10-10. The circuit approximates the electric behavior at one of the resonance points for which the quartz is designed for.

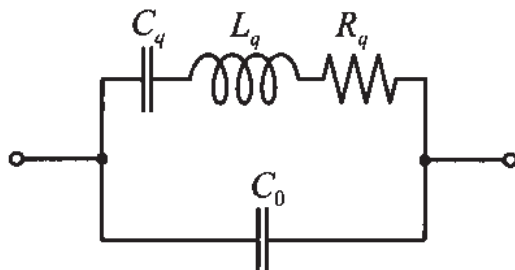


Figure 10-10 Quartz-resonator equivalent electric circuit representation.

The capacitor C_q along with R_q and L_q describes the mechanical resonance behavior while C_0 denotes the capacitance due to the external contacting of the crystal through electrodes. Normally, the ratio between C_q and C_0 can reach values as high as 1000. Moreover, the inductance L_q is typically in the range from 0.1 mH to 100 H.

The admittance of this model can be stated as

$$Y = j\omega C_0 + \frac{1}{R_q + j[\omega L_q - 1/(\omega C_q)]} = G + jB \quad (10.19)$$

The angular resonance frequency ω_0 is found by setting the imaginary component B to zero, or

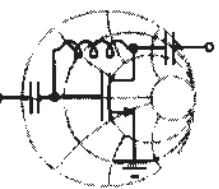
$$\omega_0 C_0 - \frac{\omega_0 L_q - 1/(\omega_0 C_q)}{R_q^2 + [\omega_0 L_q - 1/(\omega_0 C_q)]^2} = 0 \quad (10.20)$$

Solution of this equation (see Problem 10.4) using a Taylor series expansion (and retaining the first two terms) leads to approximate expressions for the series and parallel resonance frequencies:

$$\omega_0 = \omega_S \approx \omega_{S0} \left[1 + \frac{R_q^2}{2} \left(\frac{C_0}{L_q} \right) \right] \quad (10.21a)$$

$$\omega_0 = \omega_P \approx \omega_{P0} \left[1 - \frac{R_q^2}{2} \left(\frac{C_0}{L_q} \right) \right] \quad (10.21b)$$

where $\omega_{S0} = 1/\sqrt{L_q C_q}$ and $\omega_{P0} = \sqrt{(C_q + C_0)/(L_q C_q C_0)}$. A representative model is discussed next.



RF & MW →

Example 10-2: Prediction of resonance frequencies of quartz crystal

A crystal is characterized by the parameters $L_q = 0.1$ H, $R_q = 25 \Omega$, $C_q = 0.3$ pF, and $C_0 = 1$ pF. Determine the series and parallel resonance frequencies and compare them against the imaginary component of the admittance given by (10.19).

Solution: As a first approach to compute series and parallel resonance frequencies of the quartz crystal we use (10.21a) and (10.21b), respectively:

$$f_S = f_{S0} \left[1 + \frac{R_q^2}{2} \left(\frac{C_0}{L_q} \right) \right] = \frac{1}{2\pi\sqrt{L_q C_q}} \left[1 + \frac{R_q^2}{2} \left(\frac{C_0}{L_q} \right) \right] = 0.919 \text{ MHz}$$

$$f_P = f_{P0} \left[1 - \frac{R_q^2}{2} \left(\frac{C_0}{L_q} \right) \right] = \frac{1}{2\pi\sqrt{\frac{C_q + C_0}{L_q C_q C_0}}} \left[1 - \frac{R_q^2}{2} \left(\frac{C_0}{L_q} \right) \right] = 1.048 \text{ MHz}$$

The second approach is graphical. At resonance reactance and susceptance of the circuit equal zero; thus we can plot the imaginary portion of the admittance given by (10.19). Such a plot is shown in Figure 10-11, where the absolute value of the susceptance is plotted versus frequency.

Comparing the graphical results with the analytical approach (10.21), we see that they are virtually the same.

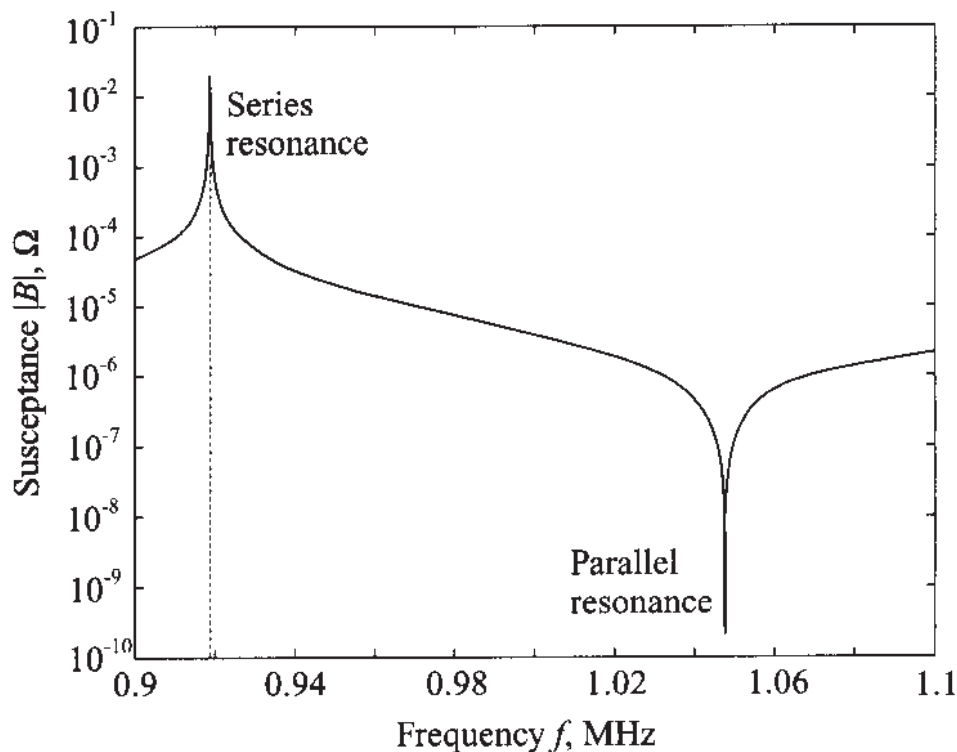


Figure 10-11 Susceptance response of a quartz element.

Care has to be exercised in selecting quartz crystals due to their multiple resonances. Depending on the crystal these responses can be very closely spaced and may result in an undesired oscillation frequency.

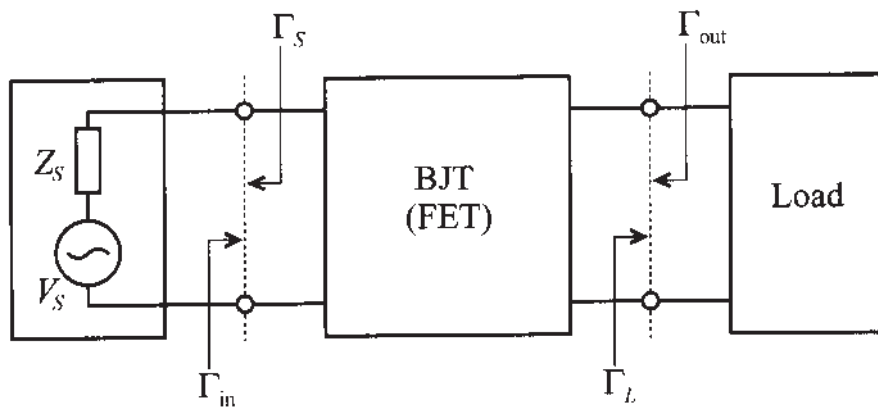
10.2 High-Frequency Oscillator Configuration

As the operating frequency approaches the GHz range, the wave nature of voltages and currents cannot be neglected. As outlined in previous chapters, reflection and transmission coefficients and the associated S -parameter representation are required to represent the circuit's functionality. This requires us to re-examine (10.1) from a transmission line point of view. The Barkhausen criterion has to be reformulated in the context of the reflection coefficients.

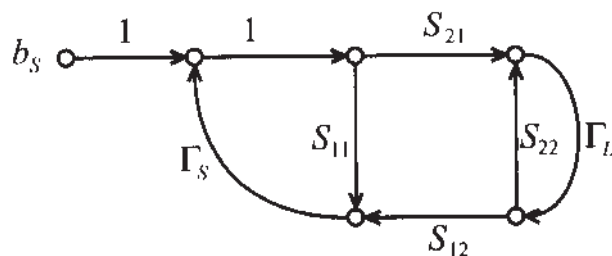
Toward re-expressing the loop gain in terms of transmission line principles, we recall our signal flow chart representation in Section 4.4.5 (see Figure 10-12).

The input reflection coefficient for matched source impedance ($Z_S = Z_0$) is

$$\Gamma_{\text{in}} = \frac{b_1}{a_1} = S_{11} + \frac{S_{12}S_{21}}{1 - S_{22}\Gamma_L} \Gamma_L = \frac{S_{11} - \Delta\Gamma_L}{1 - S_{22}\Gamma_L} \quad (10.22)$$



(a) Sourced and loaded transistor



(b) Equivalent signal flow graph

Figure 10-12 Sourced and loaded transistor and its flow chart model.

where $\Delta = S_{11}S_{22} - S_{12}S_{21}$. This is consistent with definitions given in Example 4-8. Conducting the computation with respect to the source term, $b_s = V_G\sqrt{Z_0}/(Z_G + Z_0)$, we can define the loop gain:

$$\frac{b_1}{b_s} = \frac{\Gamma_{in}}{1 - \Gamma_S \Gamma_{in}} \quad (10.23)$$

The equation implies that if

$$\Gamma_{in} \Gamma_S = 1 \quad (10.24)$$

at a particular frequency, the circuit is unstable and begins to oscillate.

The identical circuit situation applies if the output side is considered, implying the condition

$$\Gamma_{out} \Gamma_L = 1 \quad (10.25)$$

for oscillations to occur.

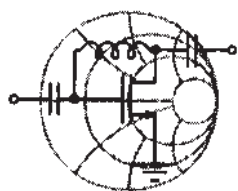
When the stability factor $k = (1 - |S_{11}|^2 - |S_{22}|^2 + |\Delta|^2)/(2|S_{12}||S_{21}|)$, see Chapter 9, is included, the preceding conditions for oscillation can be summarized as follows:

$$k < 1 \quad (10.26a)$$

$$\Gamma_{in}\Gamma_S = 1 \quad (10.26b)$$

$$\Gamma_{out}\Gamma_L = 1 \quad (10.26c)$$

Since the stability factor is dependent on the *S*-parameters of the active device we have to ensure that condition (10.26a) is satisfied first and foremost. If the *S*-parameters at the desired frequency do not ensure this requirement, we can switch to a common-base or common-collector configuration or add a positive feedback to increase instability, as the following example shows.



RF & MW

Example 10-3: Adding a positive feedback element to initiate oscillations

A BJT is operated at 2 GHz and has the following *S*-parameters specified in common-base configuration: $S_{11} = 0.94\angle 174^\circ$, $S_{12} = 0.013\angle -98^\circ$, $S_{21} = 1.9\angle -28^\circ$, and $S_{22} = 1.01\angle -17^\circ$. Determine how the Rollett stability factor is affected by adding an inductance to the base of the transistor ranging from 0 to 2 nH.

Solution: Using the definition for k gives us without inductance the value

$$k = (1 - |S_{11}|^2 - |S_{22}|^2 + |\Delta|^2)/(2|S_{12}||S_{21}|) = -0.25$$

Accounting for the inductance can be accomplished by redrawing the circuit in terms of two networks depicted in Figure 10-13.

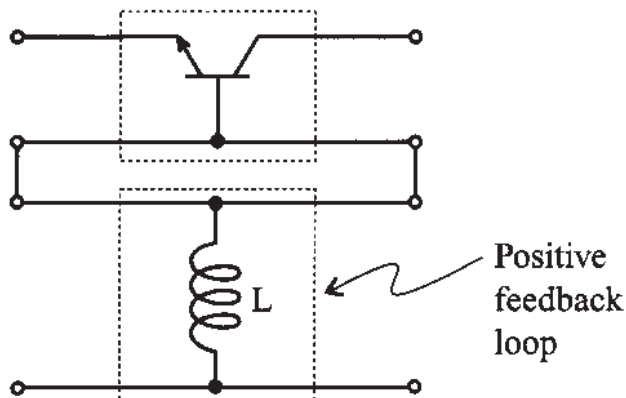


Figure 10-13 Network representation of the BJT with base inductance.

In this case the overall S -parameter representation can be found by first converting the transistor's S -parameters into impedance representation, followed by adding the Z -parameters of the inductor, and finally converting the result back into S -parameter form.

Using the conversion formulas described in Chapter 4, we find the Z -representation of the transistor in common-base configuration:

$$[\mathbf{Z}]_{\text{tr}} = \begin{bmatrix} -0.42 + j3.43 & -2.17 - j0.097 \\ -95.23 - j303.06 & -6.88 - j321.03 \end{bmatrix}$$

For the inductor the Z -matrix is given by

$$[\mathbf{Z}]_{\text{ind}} = j\omega L \begin{bmatrix} 1 & 1 \\ 1 & 1 \end{bmatrix} = \begin{bmatrix} j\omega L & j\omega L \\ j\omega L & j\omega L \end{bmatrix}$$

Adding $[\mathbf{Z}]_{\text{tr}}$ and $[\mathbf{Z}]_{\text{ind}}$ results in the Z -parameters of the entire circuit, which can then be converted into S -parameters.

To obtain the dependence of the Rollett stability factor as a function of feedback inductance, we have to repeat the preceding computations for each value of L . The result of such calculations is shown in Figure 10-14 (see also file ex10_3.m).

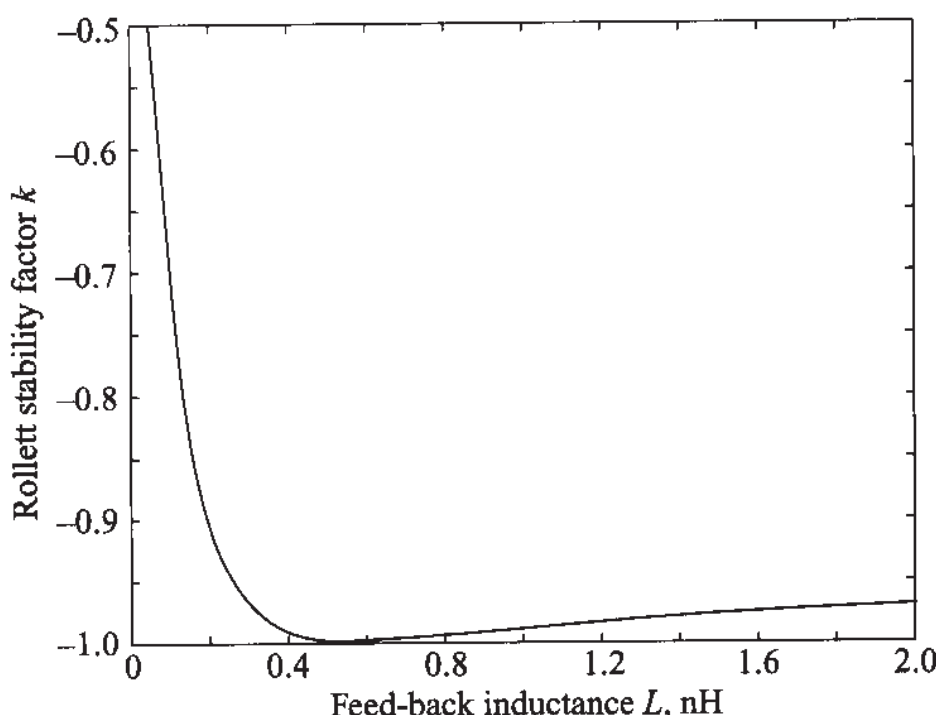


Figure 10-14 Rollett stability factor (k) as a function of feedback inductance in common-base configuration.

As seen from Figure 10-14, a maximum instability (minimum value of k) is obtained by adding a 0.6-nH inductor to the base.

At frequencies in the GHz range, even the lengths of the leads can be sufficient to create the desired inductance value in the base of the transistor.

It is interesting to note that if the oscillation condition is met either at the input or output port, the circuit is oscillating at both ports. This is directly seen by comparing the reflection coefficients at the input and output ports. We know that

$$\frac{1}{\Gamma_{\text{in}}} = \frac{1 - S_{22}\Gamma_L}{S_{11} - \Delta\Gamma_L} \equiv \Gamma_S \quad (10.27)$$

and solving for Γ_L yields

$$\Gamma_L = \frac{1 - S_{11}\Gamma_S}{S_{22} - \Delta\Gamma_S} \quad (10.28)$$

However, Γ_{out} can also be written as

$$\Gamma_{\text{out}} = \frac{S_{22} - \Delta\Gamma_S}{1 - S_{11}\Gamma_S} \quad (10.29)$$

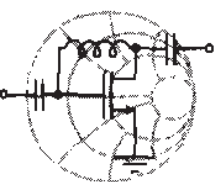
Therefore, we conclude that (10.28) is the inverse of (10.29), and thus

$$\Gamma_L = 1/\Gamma_{\text{out}} \quad (10.30)$$

as required by(10.26c).

10.2.1 Fixed-Frequency Oscillators

A very popular oscillator design approach involves the two-port design where the transistor configuration is first chosen such that it meets the requirement of $k < 1$ (an inductive feedback may have to be added). Next, we select Γ_L such that $|\Gamma_{\text{in}}| > 1$ or Γ_S such that $|\Gamma_{\text{out}}| > 1$. Either case implies the other condition. For instance, if $|\Gamma_{\text{out}}| > 1$ we conclude that $|\Gamma_{\text{in}}| > 1$ and vice versa. A proof is left as an exercise. The following example details these steps.



RF & MW

Example 10-4: Design of a fixed-frequency lumped element oscillator

A BFQ65 BJT manufactured by Philips Semiconductors is used in the common-base configuration with biasing conditions specified by $V_{CE} = 3$ V and $V_{BE} = 0.9$ V. For this case, the transistor has the following S -parameters measured at 1.5 GHz: $S_{11} = 1.47 \angle 125^\circ$, $S_{12} = 0.327 \angle 130^\circ$, $S_{21} = 2.2 \angle -63^\circ$, and $S_{22} = 1.23 \angle -45^\circ$. Design a series feedback oscillator that satisfies conditions (10.26) at $f = 1.5$ GHz.

Solution: As the first step in the design process we have to ensure that the transistor is at least potentially unstable. This can be tested by computing the Rollett stability factor:

$$k = (1 - |S_{11}|^2 - |S_{22}|^2 + |\Delta|^2) / (2|S_{12}||S_{21}|) = -0.975$$

Since k is less than unity, the transistor is indeed potentially unstable.

Next, we plot the input stability circle to choose a reflection coefficient for the input matching network. The center and radius of the input stability circle are computed base on the formulas provided in Chapter 9:

$$r_{in} = \left| \frac{S_{12}S_{21}}{|S_{11}|^2 - |\Delta|^2} \right| = 0.82$$

$$C_{in} = \frac{(S_{11} - \Delta S_{22}^*)^*}{|S_{11}|^2 - |\Delta|^2} = 0.27 \angle -57^\circ$$

Since $|C_{in}| < r_{in}$ and $|S_{22}| > 1$, the stable region is outside of the shaded circle, as illustrated in Figure 10-15.

According to Figure 10-15, we have a great deal of flexibility in choosing the reflection coefficient for the input matching network. Theoretically, any Γ_s residing inside of the stability circle would satisfy our requirements. In practice, however, we would like

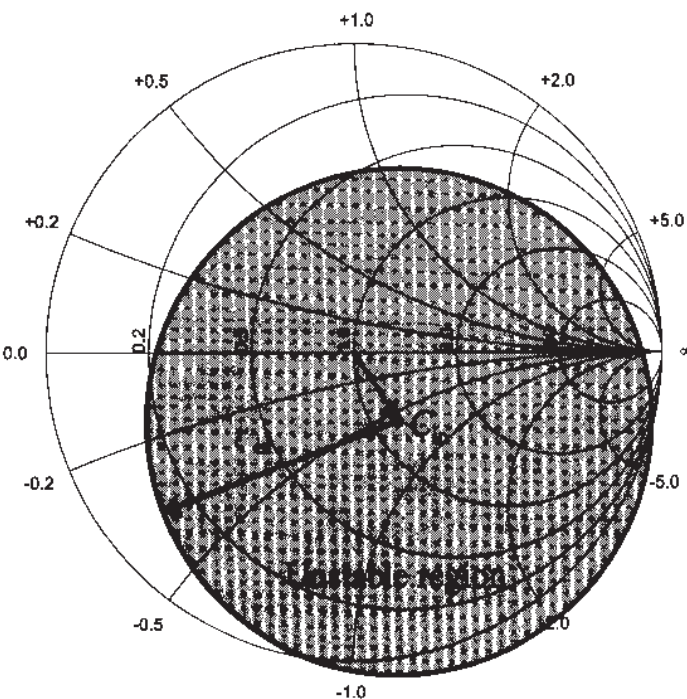


Figure 10-15 Input stability circle for the oscillator design.

to choose Γ_S such that it maximizes the output reflection coefficient:

$$\Gamma_{\text{out}} = S_{22} + \frac{S_{12}S_{21}}{1 - S_{11}\Gamma_S}\Gamma_S \quad (10.31)$$

From (10.31) it is obvious that Γ_{out} achieves its maximum value when $\Gamma_S = S_{11}^{-1}$. In this case we obtain an infinite output reflection coefficient, which from (10.26c) results in $\Gamma_L = 0$ (i.e., $Z_L = Z_0 = 50 \Omega$). The problem with such an approach is that in practical realizations it is almost impossible to achieve a perfect 50Ω matching. Moreover, as we approach $\Gamma_S = S_{11}^{-1}$, the oscillator becomes increasingly sensitive to changes in the load impedance. At $\Gamma_S = S_{11}^{-1}$, the slightest deviation from the 50Ω value results in ceasing all oscillations. Because of this phenomenon we choose Γ_S somewhat close, but not exactly equal, to S_{11}^{-1} .

After attempting several values for the source reflection coefficient, we finally select $\Gamma_S = 0.65 \angle -125^\circ$. From the knowledge of Γ_S the source impedance is computed as $Z_S = (13 - j25)\Omega$, which is realized by a series combination of a 13Ω resistor and a 4.3 pF capacitor, as shown in Figure 10-16.

Next the output reflection coefficient is computed using (10.31) with the result $\Gamma_{\text{out}} = 14.67 \angle -36.85^\circ$. To determine the

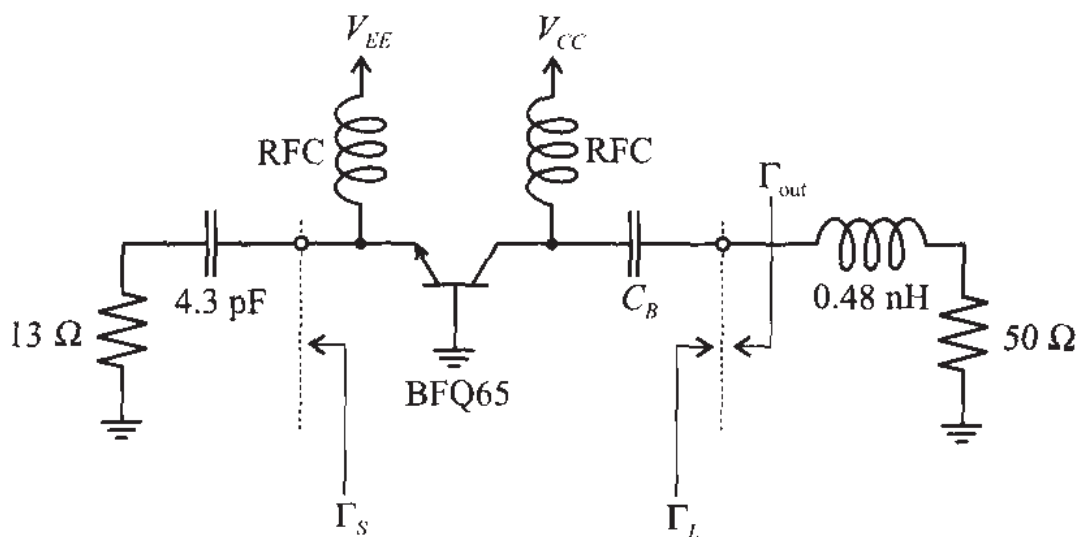


Figure 10-16 Series-feedback BJT oscillator circuit.

output matching network we utilize (10.26c) and obtain the value $\Gamma_L = \Gamma_{out}^{-1} = 0.068 \angle 36.85^\circ$. This corresponds to the impedance $Z_L = (55.6 + j4.57)\Omega = -Z_{out}$ and can be realized as a series combination of a 55.6Ω resistor with a 0.48 nH inductor.

The final point that has to be taken into account in our design is the fact that as the output power of the oscillator begins to build up, the transistor's small-signal S-parameters become invalid. Usually, the power dependence of the transistor's S-parameters results in a less negative $R_{out} = \text{Re}\{Z_{out}\}$ for increasing output power. Thus, it is necessary to choose $R_L = \text{Re}\{Z_L\}$ such that $R_L + R_{out} < 0$. In practice, a value of $R_L = -R_{out}/3$ is often used. However, we have to be careful with such a choice because it is only applicable if Γ_S is sufficiently far away from S_{11}^{-1} , as discussed previously. Another implication of $R_L \neq -R_{out}$ is a shift in the oscillation frequency.

In our design we have chosen $R_L = 50\Omega$, as shown in Figure 10-16. The output power for this oscillator at the fundamental frequency is $P_{out} = 16\text{ dBm}$, which corresponds to sinusoidal oscillations with 2 V amplitude. For our design the load resistance is very close to $-R_{out}$ so that the frequency shift is insignificant.

Although the component values assure that this oscillator project meets design specifications and the electric behavior is successfully modeled, the final circuit implementation will pose additional problems. This is apparent when considering, for instance, the 0.48 nH inductor, which is comparable with the inductance of

PCB through hole connections (vias) and parasitics of the individual components.

For high-frequency applications, a more realistic design requires the use of distributed elements. A typical oscillator example involving a FET with connection to a $50\ \Omega$ load is seen in Figure 10-17. Here, TL_i ($i = 1, \dots, 6$) represent microstrip lines.

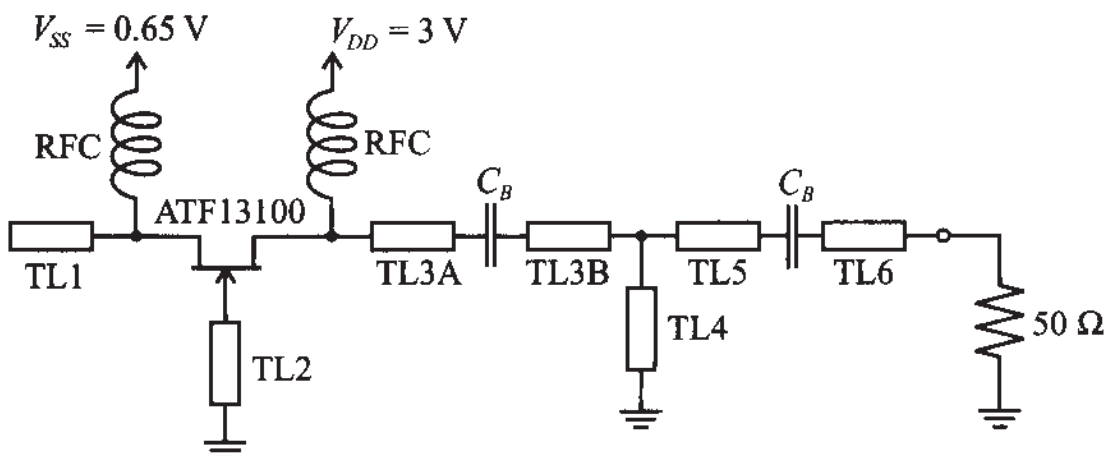
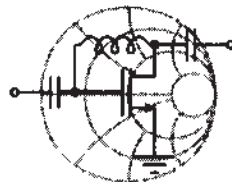


Figure 10-17 GaAs FET oscillator implementation with microstrip lines.

The design approach is presented in the following example, which provides details of how to increase the instability through a microstrip line attached to the common gate and how to select appropriate microstrip lines to match the load impedance.



RF & MW →

Example 10-5: Microstrip design of a GaAs FET oscillator

The S -parameters of the GaAs FET (Hewlett-Packard ATF13100) in common-gate configuration are measured at 10 GHz and have the following values: $S_{11} = 0.37\angle-176^\circ$, $S_{12} = 0.17\angle19.8^\circ$, $S_{21} = 1.37\angle-20.7^\circ$, and $S_{22} = 0.90\angle-25.6^\circ$. Design an oscillator with 10 GHz fundamental frequency. Furthermore, match the oscillator to a $50\ \Omega$ load impedance.

Solution: Similar to Example 10-4, we first check the stability of the transistor by computing the Rollett stability factor:

$$k = (1 - |S_{11}|^2 - |S_{22}|^2 + |\Delta|^2) / (2|S_{12}||S_{21}|) = 0.776$$

Even though $k < 1$ indicates that the transistor is potentially unstable, we can attempt to increase the instability by connecting a feedback inductor to the gate of the transistor. Following the same approach as discussed in Example 10-3, we plot the dependence of the stability factor as a function of inductance (see Figure 10-18).

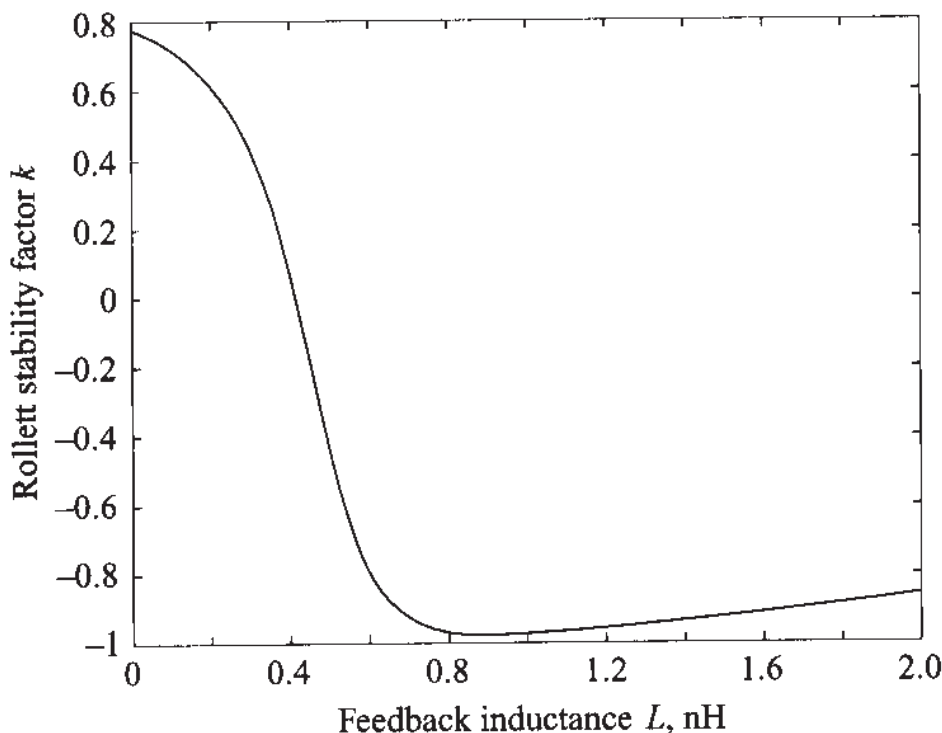


Figure 10-18 Stability factor for FET in common-gate mode as a function of gate inductance.

It is seen that maximum instability is achieved for $L = 0.9$ nH. Due to the high operating frequency of the oscillator, the use of lumped elements is undesirable and we have to replace the inductor by its distributed equivalent. One of the ways to realize an inductance is to replace it with a short-circuit transmission line stub. Referring back to Chapter 2, we can calculate the electrical length of the transmission line assuming 50Ω characteristic line impedance:

$$\Theta = \beta l = \tan^{-1}\left(\frac{\omega L}{Z_0}\right) = 48.5^\circ$$

The resulting *S*-parameters for the FET with a short-circuited stub connected to the gate contact are as follows:

$$[S] = \begin{bmatrix} 1.01\angle 169^\circ & 0.29\angle 148^\circ \\ 2.04\angle -33^\circ & 1.36\angle -34^\circ \end{bmatrix}$$

The next step in the design procedure is the development of an input matching network. As mentioned in Example 10-4, for a realizable oscillator we should choose a source reflection coefficient close to the inverse of the S_{11} parameter of the transistor. In our design we have selected $\Gamma_S = 1\angle -160^\circ$, which corresponds to a source impedance of $Z_S = -j8.8 \Omega$ and which can be realized as an open-circuit stub with a 50Ω characteristic impedance and 80° electrical length.

The output reflection coefficient is computed as

$$\Gamma_{\text{out}} = S_{22} + \frac{S_{12}S_{21}}{1 - S_{11}\Gamma_S} \Gamma_S = 4.18\angle 26.7^\circ$$

which is equivalent to $Z_{\text{out}} = (-74.8 + j17.1)\Omega$. To satisfy (10.26c), we would have to choose a load impedance of $Z_L = -Z_{\text{out}}$, but due to the power dependence of the transistor's *S*-parameters (see Example 10-4) we choose the real portion of the load impedance to be slightly smaller than $-R_{\text{out}}$:

$$Z_L = (70 - j17.1)\Omega$$

The transformation of the 50Ω load impedance to Z_L is done through a matching network consisting of a 50Ω transmission line with an electrical length of 67° and a short-circuit stub of 66° length.

The conversion of the electric parameters of the transmission lines into physical dimensions is done using the same approach as described in Example 2-5 in Chapter 2. The dimensions of the lines computed for a FR-4 substrate of 40 mil thickness are summarized in Table 10-2.

Based on the oscillator circuit diagram shown in Figure 10-17, the TL3 line is cut into two halves, TL3A and TL3B, to accommodate the blocking capacitor. The lines TL5 and TL6 can have any length since they are connected to a 50Ω load.

Table 10-2 Dimensions of the transmission lines in the FET oscillator

| Transmission line | Electrical length, deg. | Width, mil | Length, mil |
|-------------------|-------------------------|------------|-------------|
| TL1 | 80 | 74 | 141 |
| TL2 | 48.5 | 74 | 86 |
| TL3 | 67 | 74 | 118 |
| TL4 | 66 | 74 | 116 |

The microstrip line design allows for an extremely small circuit board implementation as seen by the individual line lengths.

10.2.2 Dielectric Resonator Oscillators

When dealing with microstrip line realizations, a **dielectric resonator** (DR) can be added to provide a very high-*Q* oscillator design (up to 10^5) with extraordinary temperature stability of better than $\pm 10 \text{ ppm}/^\circ\text{C}$. This resonator, simply called a **puck**, can either be placed on top or next to the microstrip line in a metallic enclosure. The electric field coupling between the strip line and the cylindrical resonator (see Figure 10-19), can be modeled near resonance as a parallel RLC circuit. The tuning screw permits a geometric adjustment which translates into a change of the resonance frequency.

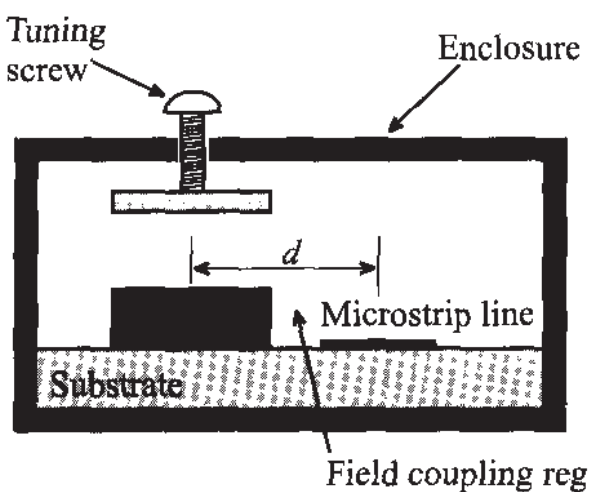


Figure 10-19 Dielectric resonator (DR) placed in proximity to a microstrip line.

We will not investigate the various waveguide modes (TE and TM modes) that are established inside the resonator, but rather concentrate on the use of DRs under TEM conditions.

In general, the circuit model of a DR (see Figure 10-20) is specified in terms of the **unloaded Q** , or Q_u ,

$$Q_u = \frac{R}{\omega_0 L} = \omega_0 R C \quad (10.32)$$

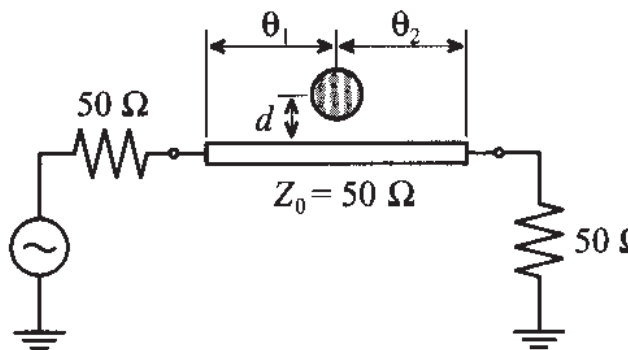
and the **coupling coefficient**, β ,

$$\beta = \frac{R}{R_{ext}} = \frac{R}{2Z_0} = \frac{\omega_0 Q_u L}{2Z_0} \quad (10.33)$$

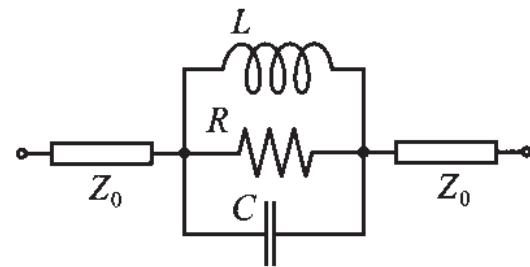
at the desired angular resonance frequency $\omega_0 = 1/(\sqrt{LC})$. The value of the external resistance R_{ext} is equal to twice the line impedance because of the symmetric termination into Z_0 . Similar to a transformer, the coupling coefficient quantifies the electromagnetic linkage between the resonator and the microstrip line, with typical values in the range of 2 to 20. Additionally, β is also employed to describe the relationship between the unloaded (Q_u), loaded (Q_L), and external (Q_E) quality factors:

$$Q_u = \beta Q_E = (1 + \beta) Q_L \quad (10.34)$$

For the oscillator design it is required to specify the DR behavior in terms of the S -parameters. The modified transmission line configuration is illustrated in Figure 10-20(b).



(a) Terminated microstrip line with DR



(b) Transmission line model

Figure 10-20 Placement of DR along a transmission line and equivalent circuit representation for S -parameter computation.

Recalling our discussion of parallel resonance circuits in Section 5.1.4, we can compute the impedance Z_{DR} as

$$Z_{DR} = \frac{R}{1 + j\omega RC - jR/(\omega L)} = \frac{R}{1 + jQ_u(\omega/\omega_0) - jQ_u(\omega_0/\omega)} \quad (10.35)$$

which simplifies to

$$Z_{DR} = \frac{R}{1 + jQ_u \left(\frac{\omega^2 - \omega_0^2}{\omega \omega_0} \right)} \approx \frac{R}{1 + j2Q_u \Delta f / f_0} \quad (10.36)$$

where $\Delta f = f - f_0$ is the deviation from the center frequency. The last equation is only valid around the resonance point, where $\omega + \omega_0 \approx 2\omega_0$. Normalized with respect to Z_0 near resonance, it is seen that

$$z_{DR} \approx \frac{R/Z_0}{1 + j2Q_u(\Delta f/f_0)} = 2\beta \quad (10.37)$$

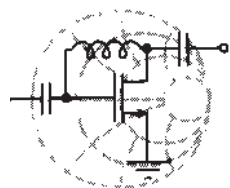
The transmission line segments on either side can now be included, leading to

$$[S]_{DR} = \begin{bmatrix} 0 & e^{-j\theta_1} \\ e^{-j\theta_1} & 0 \end{bmatrix} \begin{bmatrix} \frac{\beta}{\beta+1} & \frac{1}{\beta+1} \\ \frac{1}{\beta+1} & \frac{\beta}{\beta+1} \end{bmatrix} \begin{bmatrix} 0 & e^{-j\theta_2} \\ e^{-j\theta_2} & 0 \end{bmatrix} = \begin{bmatrix} \frac{\beta e^{-j2\theta_1}}{\beta+1} & \frac{e^{-j(\theta_1+\theta_2)}}{\beta+1} \\ \frac{e^{-j(\theta_1+\theta_2)}}{\beta+1} & \frac{\beta e^{-j2\theta_2}}{\beta+1} \end{bmatrix} \quad (10.38)$$

Depending on the direction, we can determine the reflection coefficient as either S_{11}^{DR} or S_{22}^{DR} . If the electric line length is equal on both sides of the DR, we obtain $\theta_1 = \theta_2 = \theta = (2\pi/\lambda)(l/2)$, and therefore

$$\Gamma_{in}(\omega_0) = \frac{\beta}{\beta+1} e^{-j2\theta} = \Gamma_{out}(\omega_0) \quad (10.39)$$

The selection and purchase of a DR can be carried out quickly and efficiently, often over the manufacturers' websites. The design engineer specifies a particular resonance frequency and board material (thickness, dielectric constants) and the manufacturer will provide a particular DR in terms of diameter, length, tuning screw extension, distance d from the microstrip line, and cavity material. In addition, the coupling parameter and the unloaded Q are given as well as the lumped parallel resonant circuit elements needed in the CAD simulation programs.



RF & MW

Example 10-6: Dielectric resonator oscillator design

Design an 8 GHz dielectric resonator oscillator (DRO) using a GaAs FET whose S -parameters at $f_0 = 8$ GHz are $S_{11} = 1.1 \angle 170^\circ$,

$S_{12} = 0.4\angle -98^\circ$, $S_{21} = 1.5\angle -163^\circ$, and $S_{22} = 0.9\angle -170^\circ$. A dielectric resonator that is used in the design has the following parameters at resonant frequency $f_{\text{res}} = f_0$: $\beta = 7$, $Q_u = 5000$. Find the length of the 50Ω microstrip line at the input port side of the FET, if the DR is located in the middle. Assume the DR is terminated with a 50Ω resistor. Examine the difference in the DRO response to the frequency fluctuations as compared to the conventional designs discussed previously.

Solution: The input stability circle of the FET at $f_0 = 8 \text{ GHz}$ is shown in Figure 10-21.

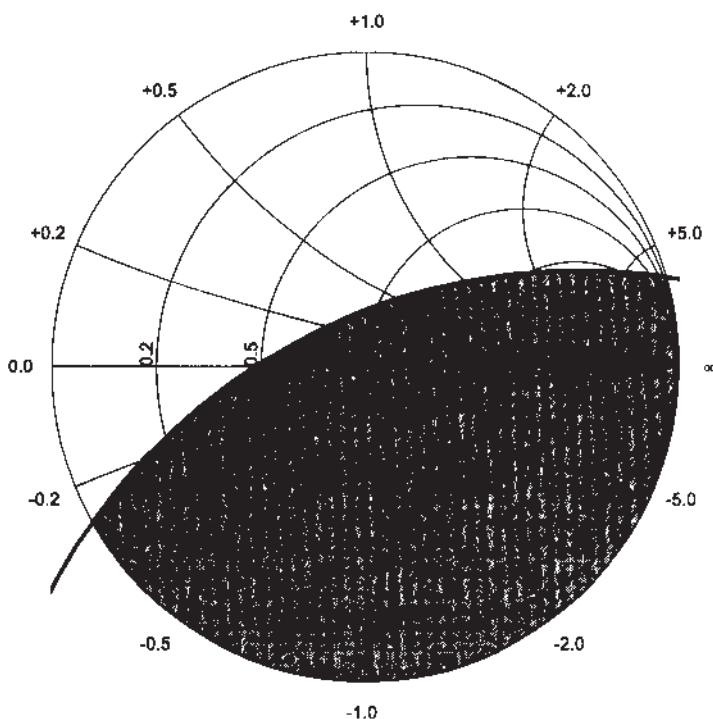


Figure 10-21 Input stability circle of the FET in the DRO design example.

To satisfy the oscillation conditions we have to chose a source reflection coefficient somewhere in the non-shaded area of Figure 10-21. Since the termination resistance for the dielectric resonator is equal to the characteristic line impedance, the output reflection coefficient of the DR is computed according to (10.39):

$$\Gamma_s = \frac{\beta}{\beta + 1} e^{-j2\Theta} = 0.875 e^{-j2\Theta}$$

As discussed in the previous examples, to maximize the output reflection of the transistor, we have to chose Γ_S close to the inverse of the S_{11} parameter. Since the absolute value of Γ_S is fixed, the best we can do is to select Θ such that the phase angle of Γ_S is equal to the phase angle of S_{11}^{-1} , or $-2\Theta = \angle S_{11}^{-1} = -\angle S_{11}$, leading to $\Theta = 85^\circ$. The resulting electric circuit for the input matching network of the oscillator is shown in Figure 10-22.

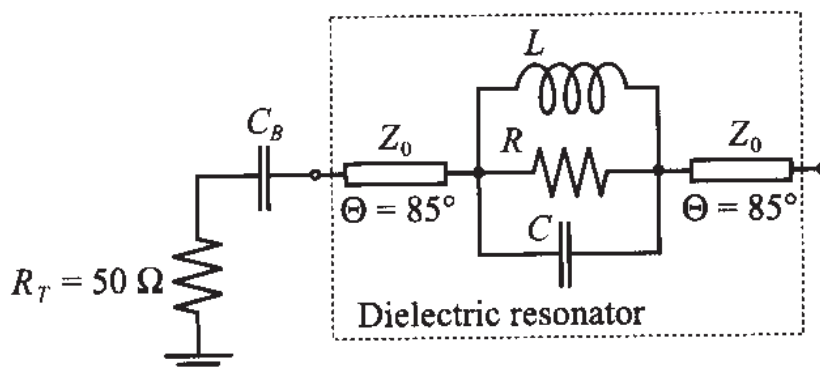


Figure 10-22 DR-based input matching network of the FET oscillator.

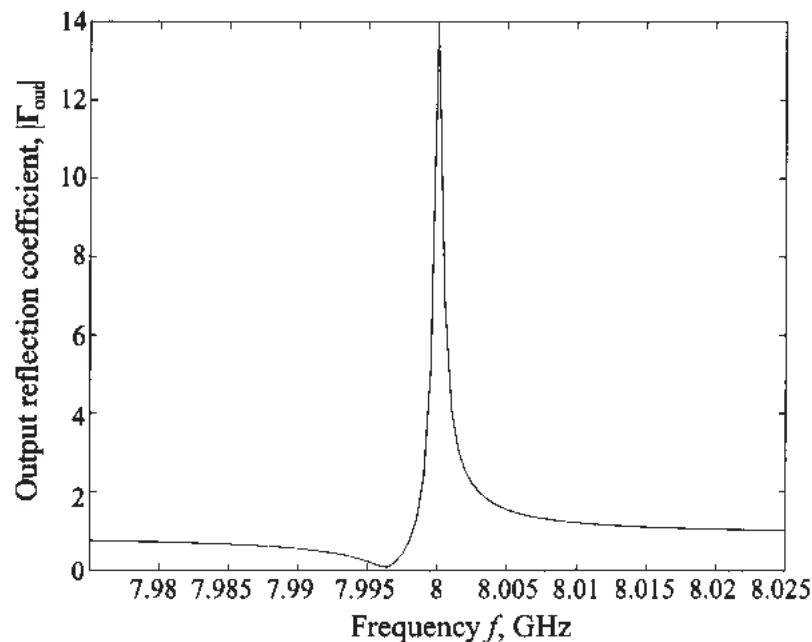
If the DR is not used in the input matching network of the transistor, then the simplest network that yields the same $\Gamma_S = 0.875 \angle -170^\circ$ at the oscillation frequency f_0 would be a series combination of a 3.35Ω resistor and a 4.57 pF capacitor. A comparison of $|\Gamma_{\text{out}}|$ for the DR versus no DR realization as a function of frequency is shown in Figure 10-23, where the FET S-parameters are assumed to be frequency independent and the DR is approximated by its equivalent circuit shown in Figure 10-20 with parameters computed using (10.32) and (10.33):

$$R = 2\beta Z_0 = 700 \Omega$$

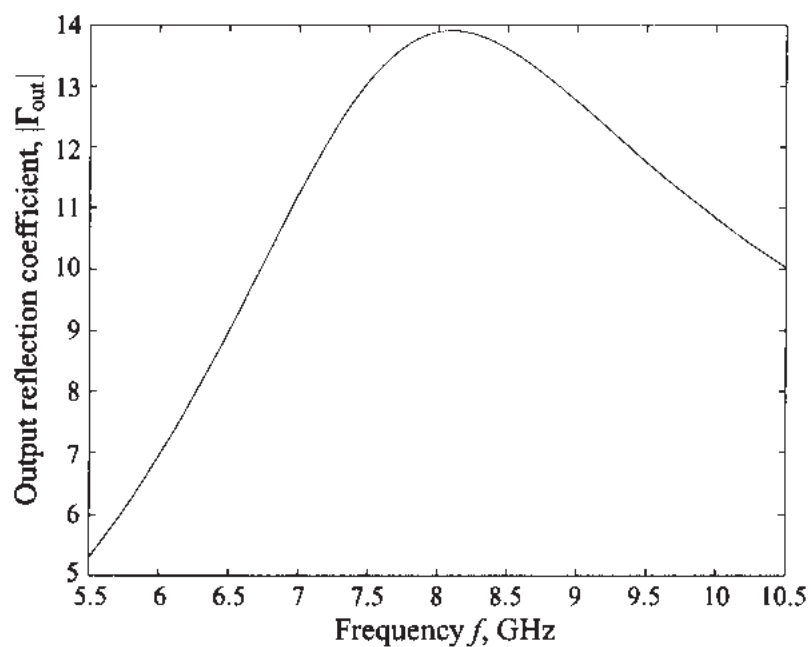
$$L = R/(\omega_0 Q_u) = 2.79 \text{ pH}$$

$$C = \omega_0^{-2} L^{-1} = 14.2 \text{ nF}$$

As clearly seen in Figure 10-23, the DRO design has a $|\Gamma_{\text{out}}| > 1$ in a much narrower frequency band than the conventional oscillator without the DR. This approach generally results in high selectivity and reduced drifts of the oscillation frequency. With the tuning screw small frequency adjustments can be done, typically in the range $\pm 0.01 f_0$ around the target frequency.



(a) Oscillator design with DR



(b) Conventional oscillator without DR

Figure 10-23 Frequency response of the output reflection coefficient for an oscillator design with and without DR.

The dielectric resonator is an inexpensive and easy way to improve the quality factor of an oscillator. Unfortunately, its geometric size depends on the resonance frequency and typically gets too large at low frequencies.

10.2.3 YIG-Tuned Oscillator

The dielectric resonator allows tuning over a very narrow band around the resonance frequency, typically between 0.01 and 1%. As an alternative, a magnetic element offers a wideband tunable oscillator design with a tuning range of more than a decade of bandwidth. Such a tunable element, often of spherical shape, derives its name from **yittrium iron garnet** (YIG), a ferrimagnetic material whose effective permeability can be externally controlled through a static magnetic bias field H_0 . This applied field directly influences the Q of the equivalent parallel resonant circuit consisting of conductance G_0 , inductance L_0 , and capacitance C_0 . Figure 10-24 depicts a typical YIG element oscillator circuit.

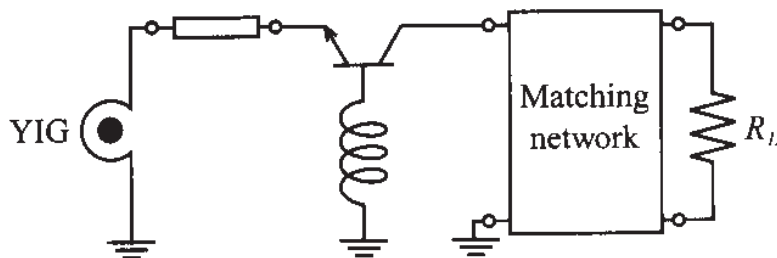


Figure 10-24 Oscillator design based on a YIG tuning element.

The unloaded quality factor is given as

$$Q_u = \frac{-4\pi(M_s/3) + H_0}{H_L} \quad (10.40)$$

where M_s is the saturation magnetization in the sphere and H_L is the resonance line width of 0.2 Oe. The saturation magnetization can be linked to the precessional motion of the magnetic moments at the angular frequency ω_m via

$$\omega_m = 2\pi\gamma(4\pi M_S) = 8\pi^2\gamma M_s \quad (10.41)$$

where γ is the gyromagnetic ratio recorded in 2.8 MHz/Oe. The resonance frequency follows from the bias field:

$$\omega_0 = 2\pi\gamma H_0 \quad (10.42)$$

From these equations the circuit elements of the parallel resonance circuit can be quantified. Specifically, the inductance is found to be

$$L_0 = \frac{\mu_0\omega_m}{\omega_0 d^2} \left(\frac{4}{3}\pi a^3 \right) \quad (10.42a)$$

with a being the radius of the YIG sphere. This also determines C_0 from the resonance condition $\omega_0^2 = 1/(L_0 C_0)$; that is,

$$C_0 = L_0 \omega_0^2 \quad (10.42b)$$

Finally, the conductance is

$$G_0 = \frac{d^2}{\mu_0 \omega_m Q_u \left(\frac{4}{3} \pi a^3 \right)} \quad (10.42c)$$

In (10.42a)–(10.42c) d is the diameter of the coupling loop.

10.2.4 Voltage-Controlled Oscillator

It is mentioned in Chapter 6 that certain diodes exhibit a large change in capacitance in response to an applied bias voltage. A typical example is the varactor diode, with its variable capacitance $C_V = C_{V0}(1 - V_Q/V_{\text{diff}})^{-1/2}$ that can be affected by the reverse bias V_Q . Figure 10-25 illustrates how the feedback loop for the Clapp oscillator can be modified, by replacing C_3 in Figure 10-25(a) with the varactor diode and an appropriate DC isolation. The modified circuit is shown in Figure 10-25(b). This circuit can readily be analyzed if a simplified BJT model ($R_L \ll h_{22}$) is employed.

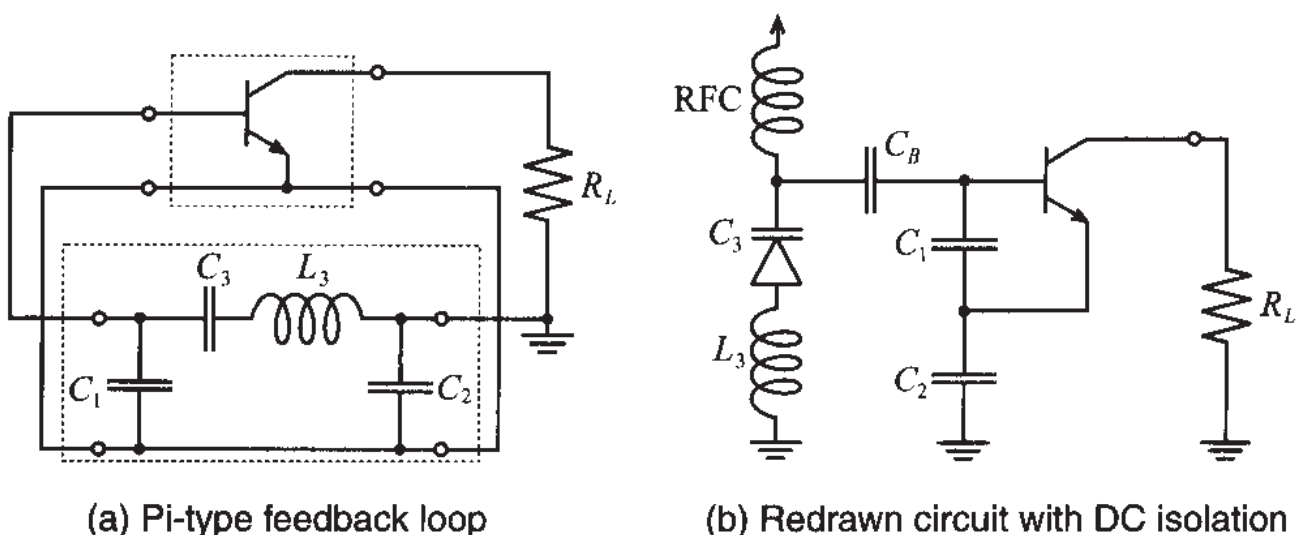


Figure 10-25 Varactor diode oscillator.

In Figure 10-26 the varactor diode and a transmission line element, whose length is adjusted to be inductive, form the termination circuit connected to the input of the oscillator. If the varactor diode and the transmission line segment is disconnected, the input impedance Z_{IN} can be computed from two loop equations:

$$v_{IN} - i_{IN}X_{C1} - i_{IN}X_{C2} + i_B X_{C1} - \beta i_B X_{C2} = 0 \quad (10.43a)$$

$$h_{11}i_B + i_B X_{C1} - i_{IN}X_{C1} = 0 \quad (10.43b)$$

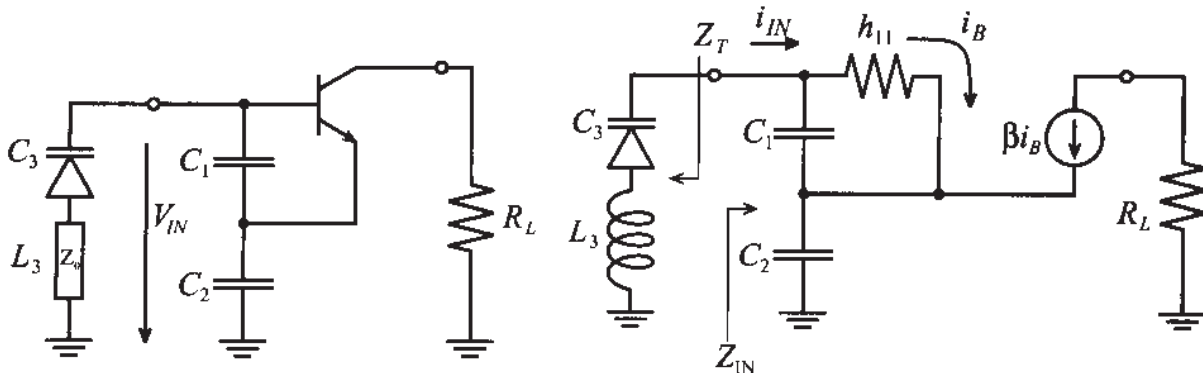


Figure 10-26 Circuit analysis of varactor diode oscillator.

Rearranging leads to

$$Z_{IN} = \frac{1}{h_{11} + X_{C1}} [h_{11}(X_{C1} + X_{C2}) + X_{C1}X_{C2}(1 + \beta)] \quad (10.44)$$

The equation can be simplified by noting that $(1 + \beta) \approx \beta$ and assuming that $h_{11} \gg X_{C1}$, which results in

$$Z_{IN} = \frac{1}{j\omega} \left[\frac{1}{C_1} + \frac{1}{C_2} \right] - \frac{\beta}{h_{11}} \left(\frac{1}{\omega^2 C_1 C_2} \right) \quad (10.45)$$

As expected from our previous discussion, the input resistance is negative. Therefore, with $g_m = \beta/h_{11}$,

$$R_{IN} = -\frac{g_m}{\omega^2 C_1 C_2} \quad (10.46a)$$

and

$$X_{IN} = \frac{1}{j\omega C_{IN}} \quad (10.46b)$$

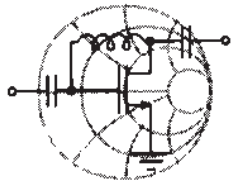
where $C_{IN} = C_1 C_2 / (C_1 + C_2)$. The resonance frequency follows from the previously established condition $X_1 + X_2 + X_3 = 0$ (see Section 10.1.2), or

$$j \left(\omega_0 L_3 - \frac{1}{\omega_0 C_3} \right) - \frac{1}{j\omega_0} \left[\frac{1}{C_1} + \frac{1}{C_2} \right] = 0 \quad (10.47)$$

with the result

$$f_0 = \frac{1}{2\pi} \sqrt{\frac{1}{L_3} \left(\frac{1}{C_3} + \frac{1}{C_2} + \frac{1}{C_1} \right)} \quad (10.48)$$

It can be concluded from (10.46a) that the combined resistance of the varactor diode must be equal to or less than $|R_{IN}|$ in order to create sustained oscillations.



RF & MW →

Example 10-7: Design of a varactor-controlled oscillator

A typical varactor diode has an equivalent series resistance of 45Ω and a capacitance ranging from 10 pF to 30 pF for reverse voltages between 30 V and 2 V . Design a voltage controlled Clapp-type oscillator with center frequency of 300 MHz and $\pm 10\%$ tuning capability. Assume that the transconductance of the transistor is constant and equal to $g_m = 115 \text{ mS}$.

Solution: To create sustained oscillations, we have to ensure that the series resistance of the varactor diode is smaller or equal to $|R_{IN}|$ over the entire frequency range as computed in (10.46a). From (10.46a) we can conclude that $|R_{IN}|$ achieves its minimum value at maximum frequency of operation. Substituting $\omega_{\max} = 2\pi f_{\max}$ (with $f_{\max} = 1.1f_0 = 330 \text{ MHz}$ being the maximum oscillation frequency) into (10.46a), it is found that the capacitances C_1 and C_2 are related as

$$C_1 = \frac{g_m}{\omega_{\max}^2 R_S C_2} = \frac{1}{k C_2} = \frac{1}{1.68 \times 10^{21} C_2} \quad (10.49)$$

where $R_S = 45 \Omega$ is the varactor's equivalent series resistance.

Since the maximum oscillation is obtained when the varactor capacitance has its minimum value, and the minimum frequency corresponds to the maximum C_3 , we can rewrite (10.48) as

$$f_{\min} = \frac{1}{2\pi} \sqrt{\frac{1}{L_3} \left(\frac{1}{C_{3\max}} + \frac{1}{C_2} + k C_2 \right)} \quad (10.50)$$

$$f_{\max} = \frac{1}{2\pi} \sqrt{\frac{1}{L_3} \left(\frac{1}{C_{3\max}} + \frac{1}{C_2} + k C_2 \right)} \quad (10.51)$$

where relation (10.49) is used to eliminate C_1 . Dividing (10.50) by (10.51) and taking the square of the result, the following quadratic equation is obtained for C_2 :

$$k(1 - \alpha^2)C_2^2 + \left(\frac{1}{C_{3\max}} - \frac{\alpha^2}{C_{3\min}} \right)C_2 + (1 - \alpha^2) = 0 \quad (10.52)$$

where $\alpha = f_{\min}/f_{\max}$. Solving (10.52) and substituting the result in (10.49) and (10.50) or (10.51), we find $C_1 = 12.4$ pF, $C_2 = 48$ pF, and $L_3 = 46.9$ nH as our desired values.

Unlike a mechanically adjustable dielectric resonator, the varactor diode permits dynamic tuning over a substantial frequency range.

10.2.5 Gunn Element Oscillator

The **Gunn element** can be employed to create oscillators from 1 to 100 GHz at low power outputs of roughly up to 1 W. It exploits a unique negative resistance phenomenon first discovered by Gunn in 1963. When certain semiconductor structures are subjected to an increasing electric field, they begin to shift, or transfer, electrons from the main valley to side valleys in the energy band structure. The accumulation of up to 90–95% of the electron concentration into these valleys results in a substantial decrease in effective carrier mobility and produces a technologically interesting *I-V* characteristic. Semiconductors with these band structures are primarily GaAs and InP. Figure 10-27 depicts a Gunn element and its current versus applied voltage response.

We notice that in the presence of an applied DC voltage to the Gunn element it behaves like a normal ohmic contact resistor for low field strength. However, if a certain threshold voltage V_0 is exceeded, **dipole domains** begin to be created below the cathode triggered by doping fluctuations. The formation of these domains lowers the current, as indicated in Figure 10-27 (b). The current then remains constant while the domains travel from cathode to anode. After collection, the process repeats itself. The frequency can be estimated from the drift velocity of the domain motion $v_d \approx 10^5$ m/s and the travel length L of the active zone of the Gunn element. For a length of 10 μm , we obtain

$$f = \frac{v_d}{L} = \frac{10^5 \text{ m/s}}{10 \times 10^{-6} \text{ m}} = 10 \text{ GHz} \quad (10.53)$$

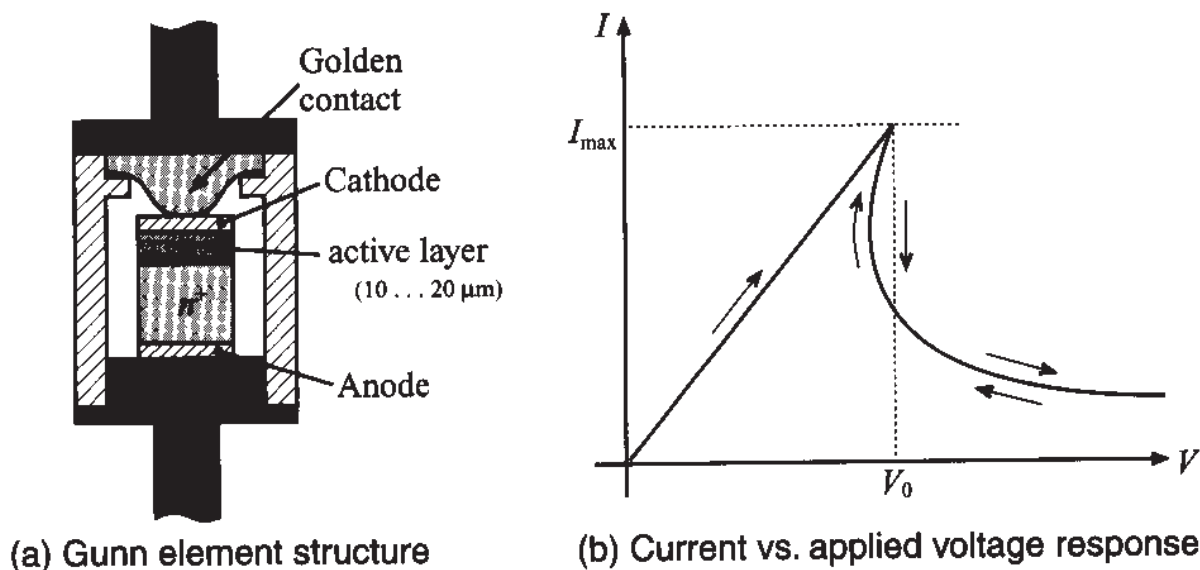


Figure 10-27 Gunn element and current versus voltage response.

If an external DC voltage is applied, the domain motion can be influenced and thus the resonance frequency is varied. The tuning range is approximately within 1% of the resonance frequency.

Figure 10-28 shows a microstrip line implementation of a Gunn element oscillator. Here the Gunn element is connected to a $\lambda/4$ microstrip line, which in turn is coupled to a dielectric resonator. The bias voltage for the Gunn element is fed through an RFC onto the microstrip line.

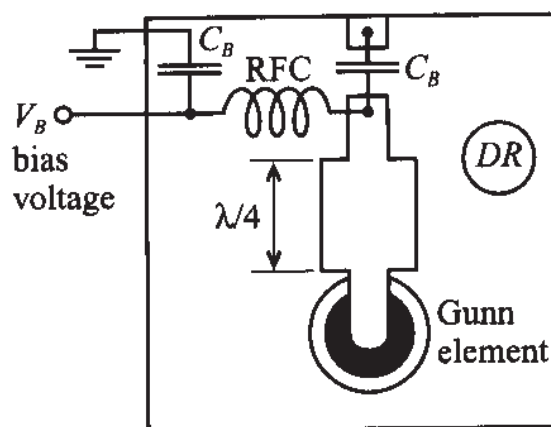


Figure 10-28 Gunn element oscillator circuit with dielectric resonator (DR).

10.3 Basic Characteristics of Mixers

Mixers are commonly used to multiply signals of different frequencies in an effort to achieve frequency translation. The motivation for this translation stems from the fact that filtering out a particular RF signal channel centered among many densely populated, narrowly spaced neighboring channels would require extremely high Q filters.

The task, however, becomes much more manageable if the RF signal carrier frequency can be reduced or downconverted within the communication system. Perhaps one of the best known systems is the downconversion in a **heterodyne receiver**, schematically depicted in Figure 10-29.

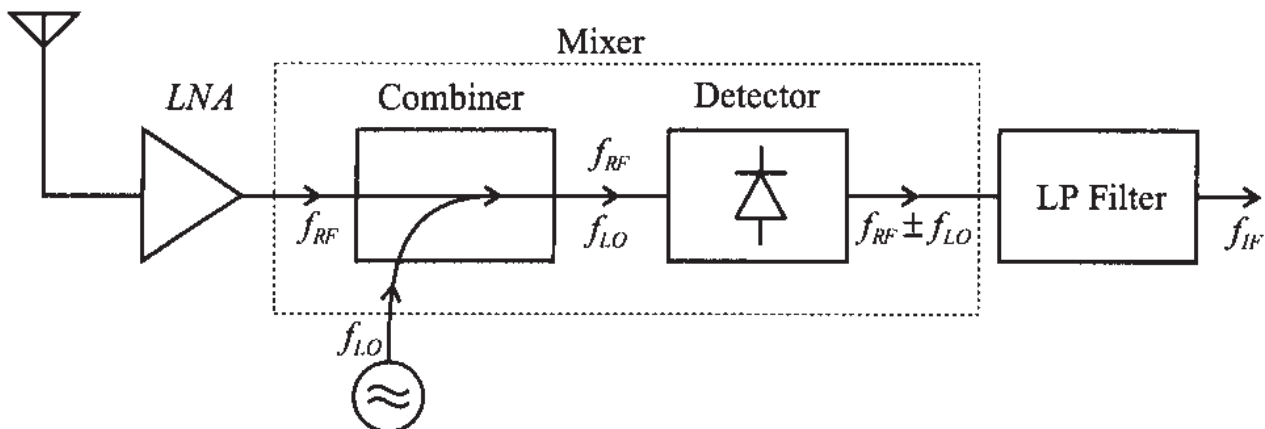


Figure 10-29 Heterodyne receiver system incorporating a mixer.

Here the received RF signal is, after preamplification in a low-noise amplifier (LNA), supplied to a mixer whose task is to multiply the input signal of center frequency f_{RF} with a **local oscillator** (LO) frequency f_{LO} . The signal obtained after the **mixer** contains the frequencies $f_{RF} \pm f_{LO}$, of which, after low-pass (LP) filtering, the lower frequency component $f_{RF} - f_{LO}$, known as the **intermediate frequency** (IF), is selected for further processing.

The two key ingredients constituting a mixer are the **combiner** and **detector**. The combiner can be implemented through the use of a 90° (or 180°) directional coupler. A discussion of couplers and hybrids is found in Appendix G. The detector traditionally employs a single diode as a nonlinear device. However, antiparallel dual diode and double-balanced quadrupole diode configurations are also utilized, as discussed later. In addition to diodes, BJT and MESFET mixers with low noise figure and high conversion gain, have been designed up to the X-band.

10.3.1 Basic Concepts

Before going into details of the circuit design, let us briefly review how a mixer is capable of taking two frequencies at its input and producing multiple frequency components at the output. Clearly a linear system cannot achieve such a task, and we need to select a nonlinear device such as a diode, FET, or BJT that can generate multiple harmonics. Figure 10-30 depicts the basic system arrangement of a mixer connected to an RF signal, $V_{RF}(t)$, and local oscillator signal, $V_{LO}(t)$, which is also known as the **pump signal**.

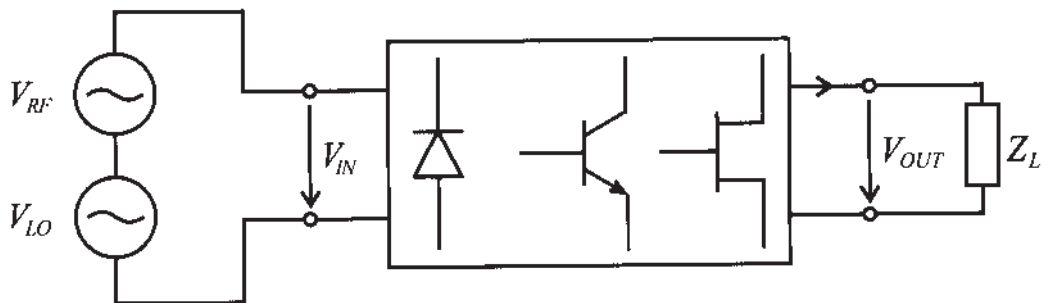


Figure 10-30 Basic mixer concept: two input frequencies are used to create new frequencies at the output of the system.

It is seen that the RF input voltage signal is combined with the LO signal and supplied to a semiconductor device with a nonlinear transfer characteristic at its output side driving a current into the load. Both diode and BJT have an exponential transfer characteristic, as expressed for instance by the Shockley diode equation discussed in Chapter 6:

$$I = I_0(e^{V/V_T} - 1) \quad (10.54a)$$

Alternatively, for a MESFET we have approximately a square behavior:

$$I(V) = I_{DSS}(1 - V/V_{T0})^2 \quad (10.54b)$$

where the subscripts denoting drain current and gate-source voltage are omitted for simplicity. The input voltage is represented as the sum of the RF signal $v_{RF} = V_{RF}\cos(\omega_{RF}t)$ and the LO signal $v_{LO} = V_{LO}\cos(\omega_{LO}t)$ and a bias V_Q ; that is,

$$V = V_Q + V_{RF}\cos(\omega_{RF}t) + V_{LO}\cos(\omega_{LO}t) \quad (10.55)$$

This voltage is applied to the nonlinear device whose current output characteristic can be found via a Taylor series expansion around the Q -point:

$$I(V) = I_Q + V\left(\frac{dI}{dV}\right)\Big|_{V_Q} + \frac{1}{2}V^2\left(\frac{d^2I}{dV^2}\right)\Big|_{V_Q} + \dots = I_Q + VA + V^2B + \dots \quad (10.56)$$

where the constants A and B refer to $(dI/dV)|_{V_Q}$ and $(1/2)(d^2I/dV^2)|_{V_Q}$, respectively. Neglecting the constant bias V_Q and I_Q , the substitution of (10.55) into (10.56) yields

$$\begin{aligned} I(V) &= A\{V_{RF}\cos(\omega_{RF}t) + V_{LO}\cos(\omega_{LO}t)\} \\ &\quad + B\{V_{RF}^2\cos^2(\omega_{RF}t) + V_{LO}^2\cos^2(\omega_{LO}t)\} \\ &\quad + 2BV_{RF}V_{LO}\cos(\omega_{RF}t)\cos(\omega_{LO}t) + \dots \end{aligned} \quad (10.57)$$

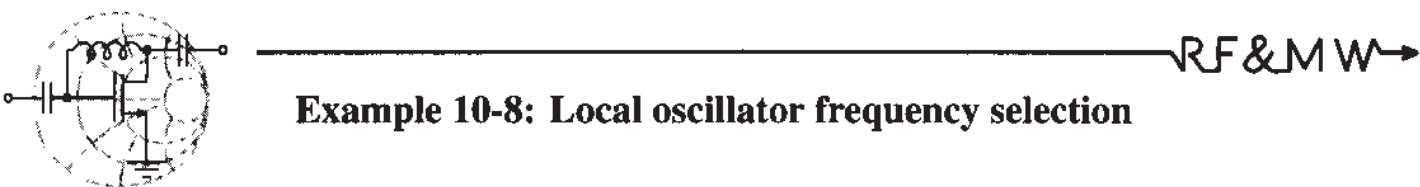
The factors containing the cosine square terms can be rewritten, via the trigonometric identity $\cos^2(\omega t) = (1/2)\{1 - \cos(2\omega t)\}$, into DC terms and terms involving $2\omega_{RF}t$ and $2\omega_{LO}t$. The key lies in the last term of (10.57), which becomes

$$I(V) = \dots + BV_{RF}V_{LO}\{\cos[(\omega_{RF} + \omega_{LO})t] + \cos[(\omega_{RF} - \omega_{LO})t]\} \quad (10.58)$$

This expression makes clear that the nonlinear action of a diode or transistor can generate new frequency components of the form $\omega_{RF} \pm \omega_{LO}$. It is also noted that the amplitudes are multiplied by $V_{RF}V_{LO}$, and B is a device-dependent factor.

Equation (10.58) is the Taylor series representation up to the third term, and thus up to **second-order intermodular product** (V^2B). Any higher-order products, such as **third-order intermodular product** (V^3C), are neglected. For diodes and BJTs these higher-order harmonic terms can significantly affect the performance of a mixer. However, the second-order intermodular product is the only surviving term if a FET with quadratic transfer characteristic is utilized. Thus, a FET is less prone to generate undesired higher-order intermodular products.

The following example discusses the down conversion process from a given RF signal frequency to a desired intermediate frequency.



Example 10-8: Local oscillator frequency selection

An RF channel with a center frequency of 1.89 GHz and bandwidth of 20 MHz is to be downconverted to an IF of 200 MHz. Select an appropriate f_{LO} . Find the quality factor Q of a bandpass filter to select this channel if no downconversion is involved, and determine the Q of the bandpass filter after downconversion.

Solution: As seen in (10.58), by mixing RF and LO frequencies through a nonlinear device we produce an IF frequency that is equal to either $f_{IF} = f_{RF} - f_{LO}$ or $f_{IF} = f_{LO} - f_{RF}$, depending on whether f_{RF} or f_{LO} is higher. Thus, to produce a $f_{IF} = 200$ MHz from $f_{RF} = 1.89$ GHz we can use either

$$f_{LO} = f_{RF} - f_{IF} = 1.69 \text{ GHz} \text{ or } f_{LO} = f_{RF} + f_{IF} = 2.09 \text{ GHz}$$

These two choices are equally valid and are both used in practice. When $f_{RF} > f_{LO}$ is chosen, the mixer is said to have **low-side**

injection, whereas when $f_{RF} < f_{LO}$ the design is called **high-side injection**. The first approach is generally preferred since lower LO frequencies are easier to generate and process.

Before down conversion, the signal has a bandwidth of $BW = 20$ MHz at a center frequency of $f_{RF} = 1.89$ GHz. Therefore, if we attempted to filter out the desired signal we would have to use a filter with $Q = f_{RF}/BW = 94.5$. However, after downconversion, the bandwidth of the signal does not change but the center frequency shifts to $f_{IF} = 200$ MHz, thus requiring a bandpass filter with a quality factor of only $Q = f_{IF}/BW = 10$.

This example shows that less selective filtering is required once the mixer has downconverted the RF signal.

10.3.2 Frequency Domain Considerations

It is important to place the previous section into a frequency domain perspective. To this end it is assumed that the angular RF signal is centered at ω_{RF} with two extra frequency components situated ω_w above and below ω_{RF} . The LO signal contains one single component at ω_{LO} . After performing mixing, according to (10.58), the resulting spectral representation contains both **upconverted** and **downconverted** frequency components. Figure 10-31 graphically explains this process.

Typically the upconversion process is associated with the modulation in a **transmitter**, whereas the downconversion is encountered in a **receiver**. Specifically, when dealing with modulation, the following terminology is common:

- Lower sideband, or LSB ($\omega_{RF} - \omega_{LO}$)
- Upper sideband, or USB ($\omega_{RF} + \omega_{LO}$)
- Double sideband, or DSB ($\omega_{RF} + \omega_{LO}, \omega_{RF} - \omega_{LO}$)

A critical question to answer is the choice of an LO frequency that shifts the RF frequency to a suitable IF level.

An interrelated issue is the problem of **image** frequencies mapping into the same downconverted frequency range. To understand this problem, assume an RF signal is downconverted with a given LO frequency. In addition to the desired signal, we have

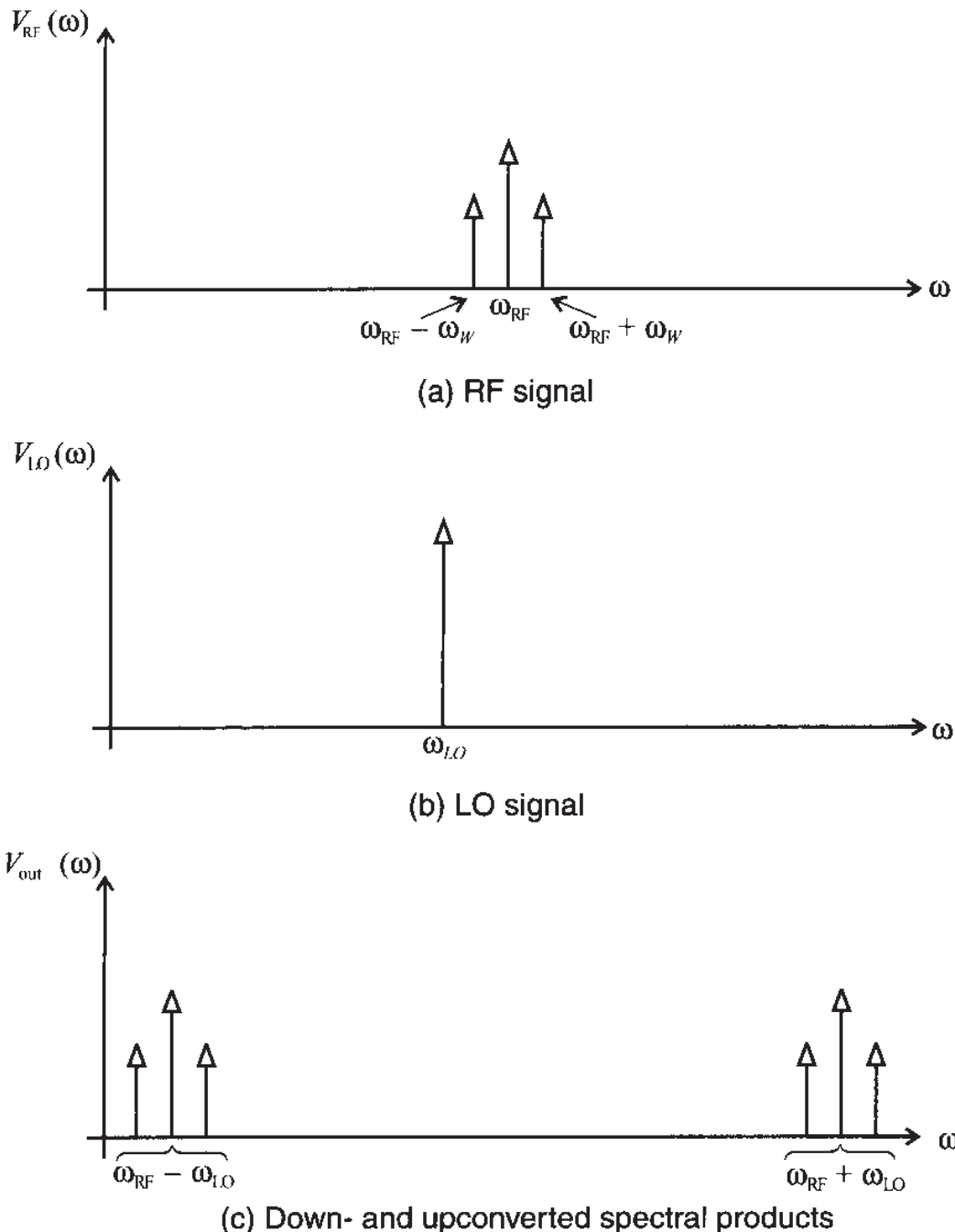


Figure 10-31 Spectral representation of mixing process.

placed symmetrically an interferer about IF (see Figure 10-32). The desired RF signal transforms as expected:

$$\omega_{RF} - \omega_{LO} = \omega_{IF} \quad (10.59a)$$

However, the image frequency ω_{IM} transforms as

$$\omega_{IM} - \omega_{LO} = (\omega_{LO} - \omega_{IF}) - \omega_{LO} = -\omega_{IF} \quad (10.59b)$$

Since $\cos(-\omega_{IF}t) = \cos(\omega_{IF}t)$, we see that both frequency spectra are shifted to the same frequency location, as Figure 10-32 illustrates.

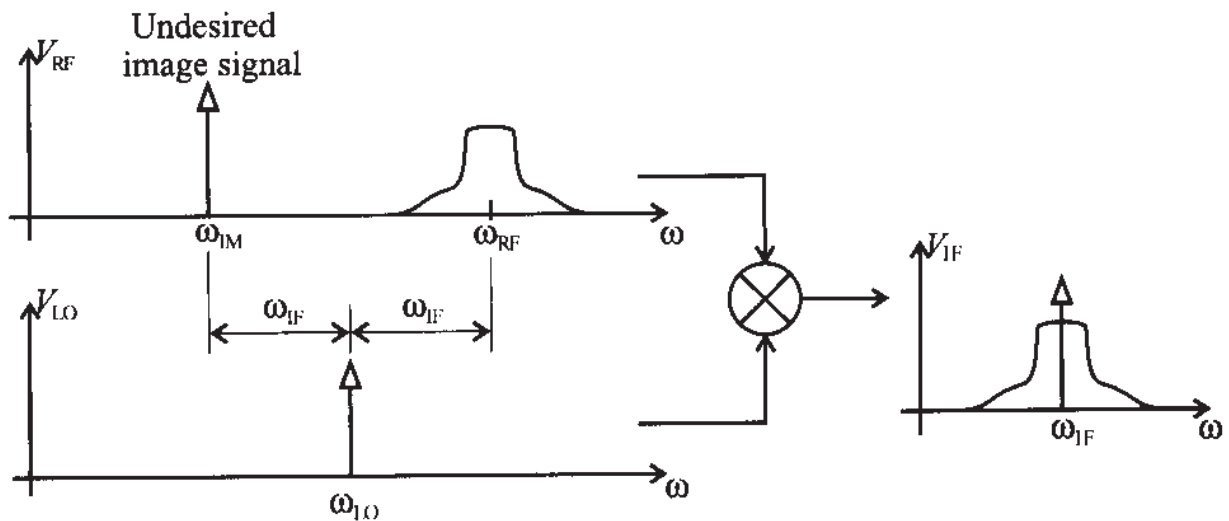


Figure 10-32 Problem of image frequency mapping.

To avoid the presence of undesired image signals that can be greater in magnitude than the RF signal, a so-called **image filter** is placed before the mixer circuit to suppress this influence, provided sufficient spectral separation is assured. More sophisticated measures involve an image rejection mixer.

10.3.3 Single-Ended Mixer Design

The simplest and least efficient mixer is the single-ended design involving a Schottky diode, as shown in Figure 10-33(a). The RF and LO sources are supplied to an appropriately biased diode followed by a resonator circuit tuned to the desired IF. In contrast, Figure 10-33(b) shows an improved design involving a FET, which, unlike the diode, is able to provide a gain to the incoming RF and LO signals.

In both cases the combined RF and LO signal is subjected to a nonlinear device with exponential (diode) or nearly quadratic (FET) transfer characteristic followed by a bandpass filter whose task is to isolate the IF signal. The two very different mixer realizations allow us to contrast a number of parameters important when developing suitable designs:

- Conversion loss or gain between the RF and IF signal powers
- Noise figure
- Isolation between LO and RF signal ports
- Nonlinearity

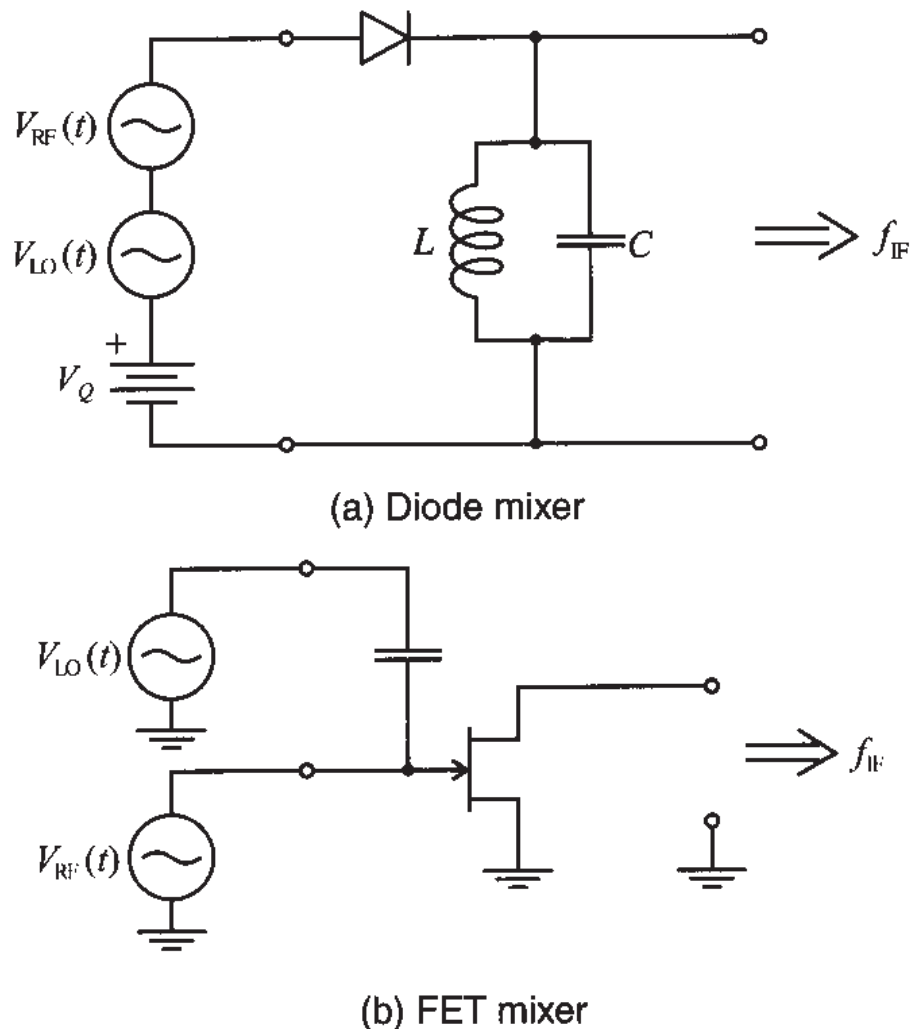


Figure 10-33 Two single-ended mixer types.

Since LO and RF signals are not electrically separated in Figure 10-33(a), there is the potential danger that the LO signal can interfere with the RF reception, possibly even reradiating portions of the LO energy through the receiving antenna. The FET realization in Figure 10-33(b) allows not only for LO and RF isolation but also provides signal gain and thus minimizes conversion loss. The **conversion loss (CL)** of a mixer is generally defined in dB as the ratio of supplied input power P_{RF} over the obtained IF power P_{IF} :

$$CL = 10 \log \left(\frac{P_{\text{RF}}}{P_{\text{IF}}} \right) \quad (10.60)$$

When dealing with BJTs and FETs, it is preferable to specify a **conversion gain (CG)** defined as the inverse of the power ratio.

Additionally, the noise figure of a mixer is generically defined as

$$F = \frac{P_{n_{\text{out}}}}{CG P_{n_{\text{in}}}} \quad (10.61)$$

with CG again being the conversion gain, and $P_{n_{out}}$, $P_{n_{in}}$ the noise power at the output due to the RF signal input (at RF) and the total noise power at the output (at IF). The FET generally has a lower noise figure than a BJT, and because of a nearly quadratic transfer characteristic (see Section 7.2) the influence of higher-order nonlinear terms is minimized. Instead of the FET design, a BJT finds application when high conversion gain and low voltage bias conditions are needed (for instance, for systems relying on battery operation).

Nonlinearities are customarily quantified in terms of **conversion compression** and **intermodular distortion (IMD)**. Conversion compression relates to the fact that the IF output power as a function of RF input power begins to deviate from the linear curve at a certain point. The point where the deviation reaches 1 dB is a typical mixer performance specification. As already encountered in the amplifier discussion, the intermodulation distortion is related to the influence of a second frequency component in the RF input signal, giving rise to distortion. To quantify this influence, a two-tone test is typically employed. If f_{RF} is the desired signal and f_2 is a second input frequency, then the mixing process produces a frequency component at $2f_2 - f_{RF} \pm f_{LO}$, where the $+$ - sign denotes up- or downconversion. The influence of this intermodulation product can be plotted in the same graph as the conversion compression (see Figure 10-34).

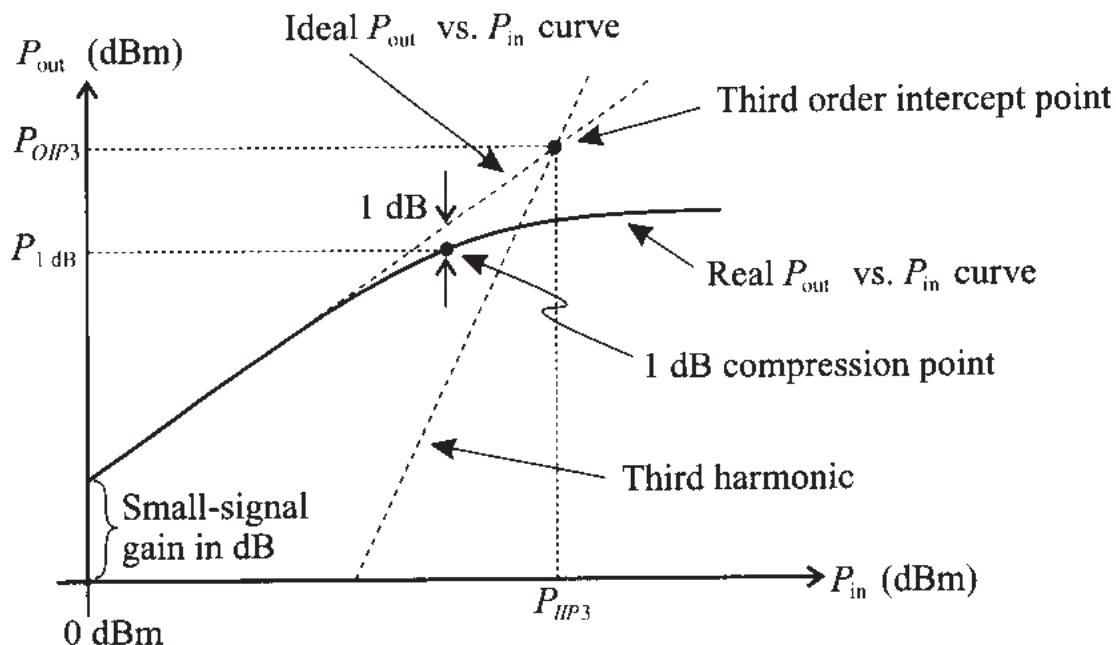


Figure 10-34 Conversion compression and intermodulation product of a mixer.

The intercept point between the desired linear output response and the undesirable third-order IMD response is a common figure of merit, indicating the ability of a mixer to suppress this influence.

Additional mixer definitions include distortion generated inside the mixer which is defined as **harmonic IMD**; **isolation** between RF and IF ports, which is directly linked to the influence of the combiner (hybrid coupler; see Appendix G); and **dynamic range**, which specifies the amplitude range over which no performance degradation occurs.

The circuit design of an RF mixer follows a similar approach as discussed when dealing with an RF amplifier. The RF and LO signals are supplied to the input of an appropriately biased transistor or diode. The matching techniques of the input and output side are presented in Chapter 8 and directly apply for mixers as well. However, one has to pay special attention to the fact that there is a large difference in frequencies between RF, LO on the input side, and IF on the output side. Since both sides have to be matched to the typical 50Ω line impedance, the transistor port impedances (or S-parameter representation) at these two different frequencies have to be specified. Furthermore, to minimize interference at the output side of the device, it is important to short circuit the input to IF, and conversely short circuit the output to RF (see Figure 10-35). Including these requirements as part of the matching networks is not always an easy task.

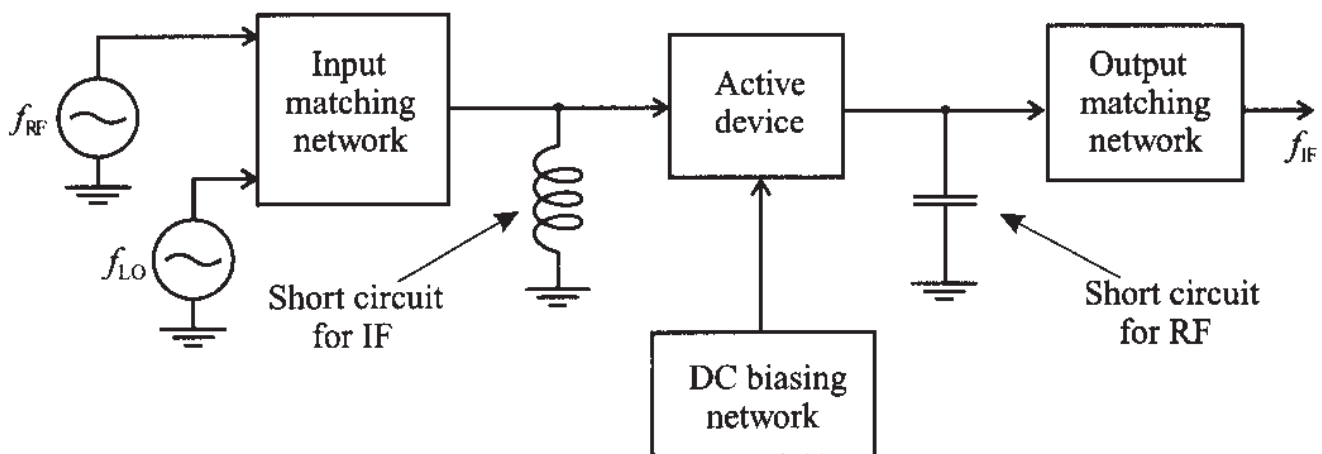
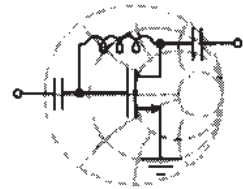


Figure 10-35 General single-ended mixer design approach.

These short-circuit conditions in general affect the transistor's behavior through internal feedback mechanism. Ideally, $\Gamma_{in}(\omega_{RF})$ should be known based on the short-circuit output condition and similarly $\Gamma_{out}(\omega_{IF})$ requires a short-circuit input condition. Typically, an additional load resistance is added to the output port to adjust the conversion gain. In the following example, the salient design steps are explained.



RF & MW →

Example 10-9: Design of a single-ended BJT mixer

For the DC-biasing topology shown in Figure 10-36, compute the values of the resistors R_1 and R_2 such that biasing conditions are satisfied. Using this network as a starting point, design a low-side injection mixer for $f_{RF} = 1900$ MHz and $f_{IF} = 200$ MHz. The BJT is measured at IF to have an output impedance of $Z_{out} = (677.7 - j2324)\Omega$ for short-circuit input, and an input impedance of $Z_{in} = (77.9 - j130.6)\Omega$ for short-circuit output at RF frequency. Attempt to minimize the component count in this design.

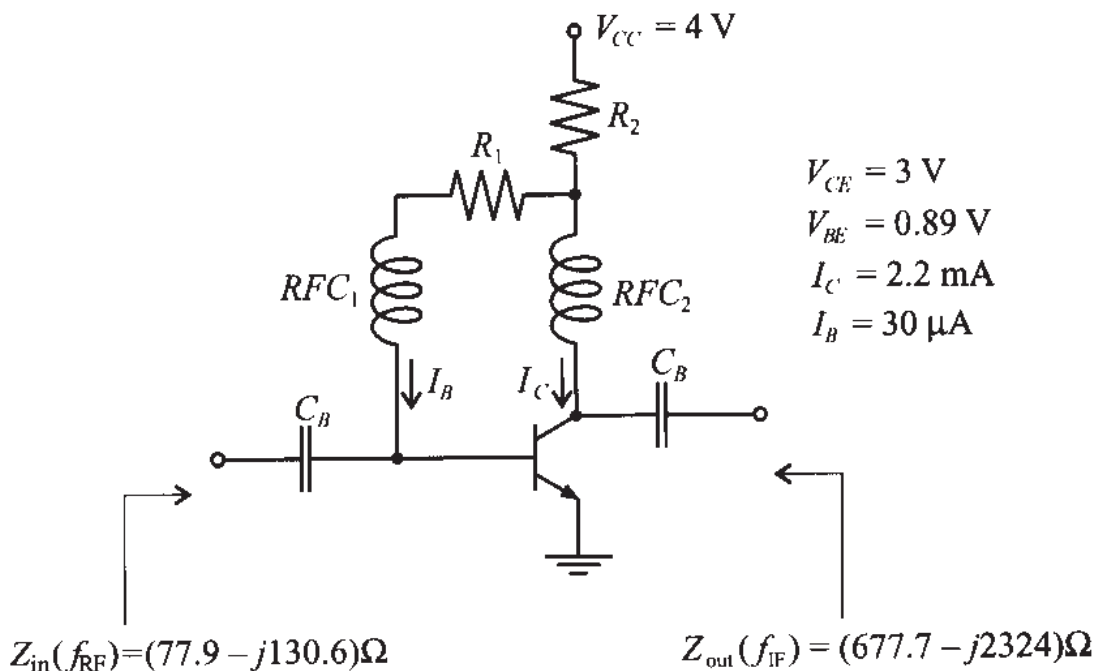


Figure 10-36 DC-biasing network for BJT mixer design.

Solution: Since the voltage drop across resistor R_2 is equal to the difference between V_{CC} and V_{CE} and the current is the sum of the base and collector currents, R_2 is computed as

$$R_2 = \frac{V_{CC} - V_{CE}}{I_C + I_B} = 448 \Omega$$

Similarly, the base resistor R_1 is computed as a ratio of $V_{CE} - V_{BE}$ over the base current:

$$R_1 = \frac{V_{CE} - V_{BE}}{I_B} = 70.3 \text{ k}\Omega$$

Before beginning the design of an input matching network, we have to decide on how to supply the LO signal. The simplest arrangement is to connect the LO source directly to the base of the transistor via a decoupling capacitor, as shown in Figure 10-37.

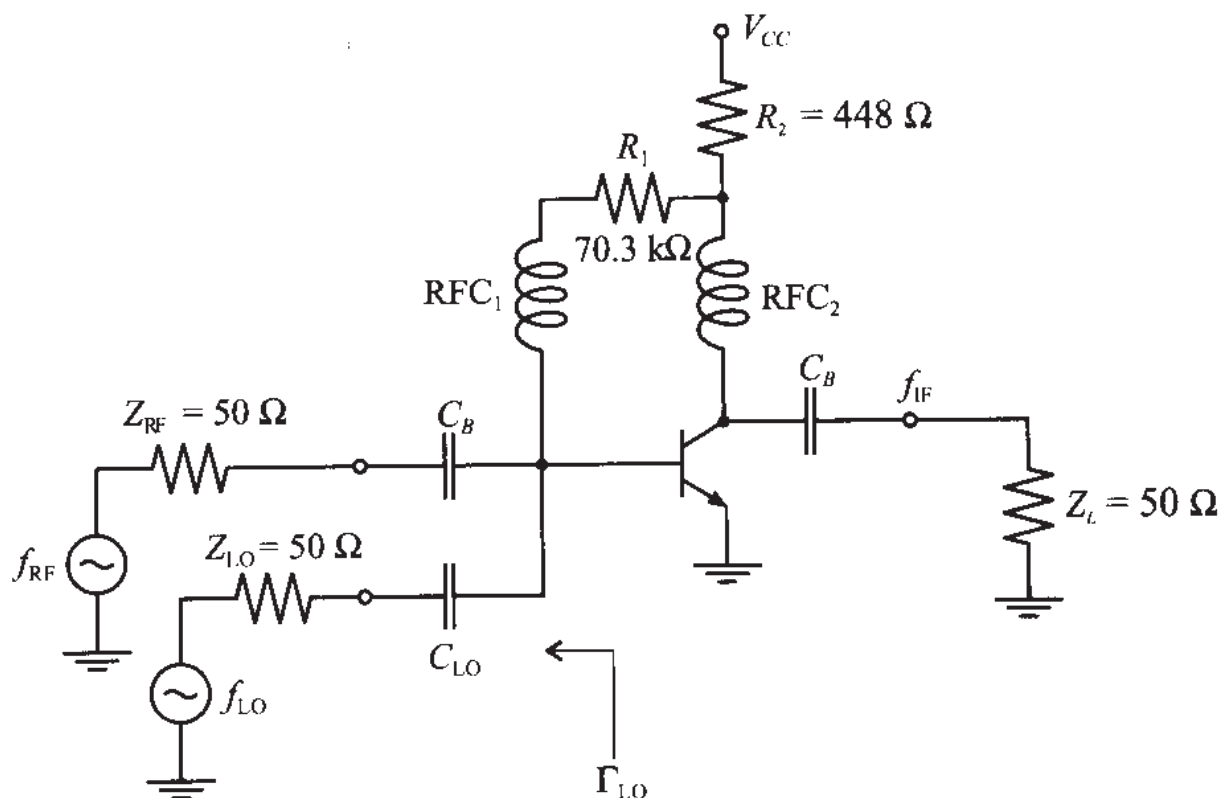


Figure 10-37 Connection of RF and LO sources to the BJT.

The value of this capacitor C_{LO} has to be chosen small enough so as to prevent RF signal coupling into the LO source. We arbitrary pick $C_{LO} = 0.2\text{ pF}$. In this case the series combination of C_{LO} and Z_{LO} creates a return loss RL_{RF} of only 0.24 dB, since

$$RL_{RF} = -20\log|\Gamma_{LO}|_{f_{RF}} = -20\log(0.9727) = 0.24\text{ dB}$$

Unfortunately, the LO frequency is very close to f_{RF} so that the same capacitance will attenuate not only the RF signal but the LO as well. We can compute the insertion loss IL_{RF} due to this capacitor at $f_{LO} = f_{RF} - f_{IF}$

$$IL_{RF} = -10\log\left(1 - |\Gamma_{LO}|^2\Big|_{f_{LO}}\right) = 13.6 \text{ dB}$$

Thus, if the LO source pumps at -20 dBm , only -33.6 dBm reaches the transistor. This seemingly high power loss is still tolerable since we can adjust the power provided by the local oscillator.

The presence of C_{LO} and Z_{LO} modifies the value of the input impedance. A new total input impedance Z'_{in} can be computed as a parallel combination of C_{LO} and Z_{LO} , and the input impedance of the transistor connected to the LO source is

$$Z'_{in} = \left(Z_{LO} + \frac{1}{j\omega_{RF}C_{LO}}\right) \parallel Z_{in} = (47.2 - j103.5)\Omega$$

The output impedance does not change since the input is shorted during the measurement of Z_{out} .

Knowing Z'_{in} , we can next design an input matching network using any of the methods described in Chapter 8. One of the possible topologies consists of a shunt inductor followed by a series capacitor, as shown in Figure 10-38, where we added the blocking capacitor C_{B1} to prevent DC short circuit to ground.

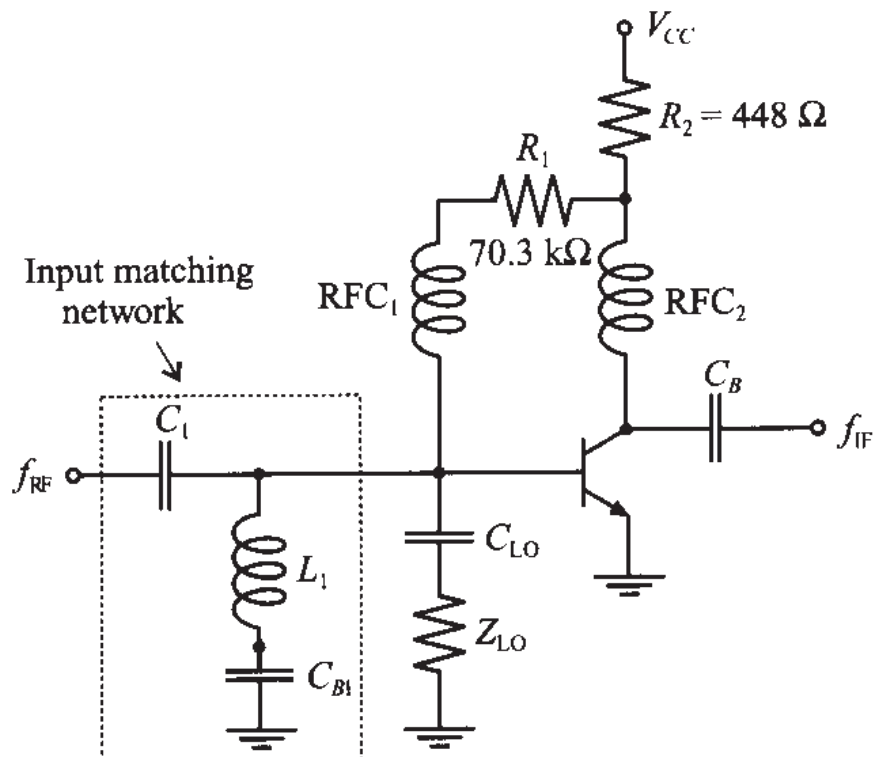


Figure 10-38 Input matching network for a single-ended BJT mixer.

There are several modifications that can be made to the circuit in Figure 10-38. First we notice that instead of biasing the base of the transistor through an RFC, we can connect R_1 directly to the contact between L_1 and C_{B1} . In this case we still bias the base of the transistor through L_1 and maintain isolation of the RF signal from the DC supply by grounding the RF through C_{B1} . One more task of this matching network is to provide a short-circuit condition for the IF signal. Even though the impedance of the inductor L_1 is rather small at f_{IF} , we still can lower it by choosing the value of C_{B1} such that L_1 and C_{B1} exhibit a series resonance at IF. For example, if we choose $C_{B1} = 120 \text{ pF}$, we still maintain a solid short circuit for the RF signal and we improve the path to ground for the f_{IF} signal. The modified input matching network is shown in Figure 10-39.

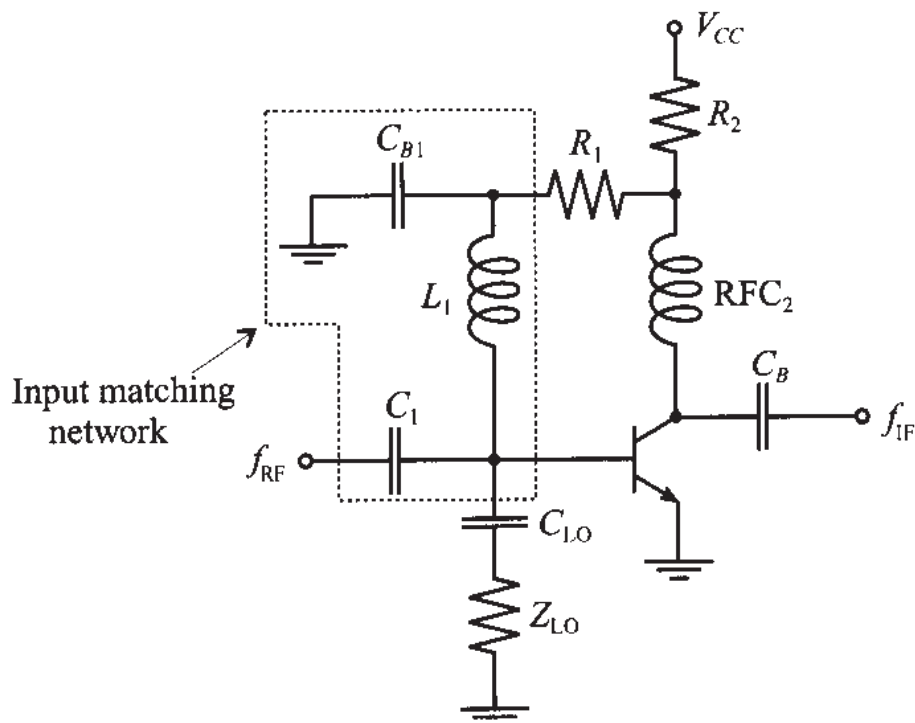


Figure 10-39 Modified input matching network.

The output matching network is developed using a similar approach. The original matching network again consisted of a shunt inductance L_2 followed by a series capacitance C_2 . The values are $L_2 = 416 \text{ nH}$ and $C_2 = 1.21 \text{ pF}$. This topology allows us to eliminate the RFC at the collector terminal of the transistor. However, the problem with this topology is that it does not provide a short circuit

to ground for the RF signal that may interfere with the output. To remedy this drawback we replace L_2 with an equivalent LC combination where the additional capacitance $C_3 = 120 \text{ pF}$ is chosen to provide solid ground condition for the f_{RF} signal and L_2 is adjusted to $L_2 = 5.2 \text{ nH}$. The complete circuit of the designed single-ended BJT mixer is shown in Figure 10-40.

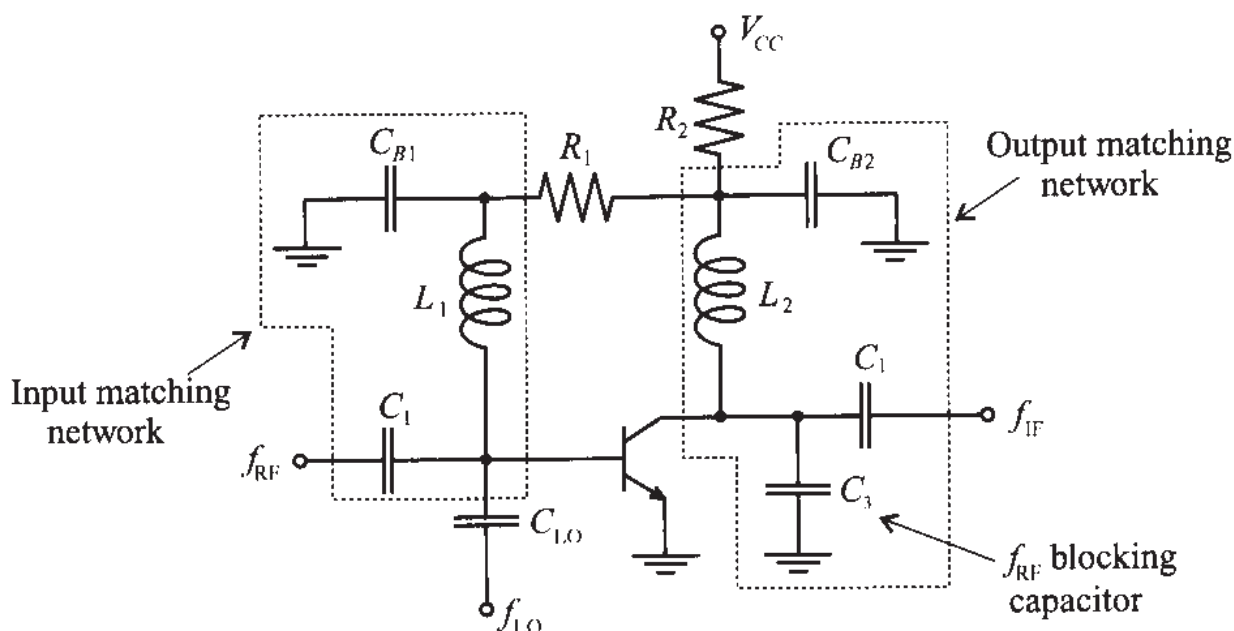


Figure 10-40 Complete electrical circuit of the low-side injection, single-ended BJT mixer with $f_{\text{RF}} = 1900 \text{ MHz}$ and $f_{\text{IF}} = 200 \text{ MHz}$.

This design shows the multiple purposes that a matching network can perform. At first glance they are often difficult to understand. Specifically, the dual network purposes of matching and isolation provide challenges for the circuit designer.

10.3.4 Single-Balanced Mixer

From the previous section it is seen that the single-ended mixers are rather easy to construct circuits. The main disadvantage of these designs is the difficulty associated with providing LO energy while maintaining separation between LO, RF, and IF signals for broadband applications. The balanced dual-diode or dual-transistor mixer in conjunction with a hybrid coupler offers the ability to conduct such broadband operations. Moreover, it provides further advantages related to noise suppression and spurious mode rejection. Spurs arise in oscillators and amplifiers due to parasitic resonances

and nonlinearities and are only partially suppressed by the front end. Thermal noise can critically raise the noise floor in the receiver. Figure 10-41 shows the basic mixer design featuring a quadrature coupler and a dual-diode detector followed by a capacitor acting as summation point.

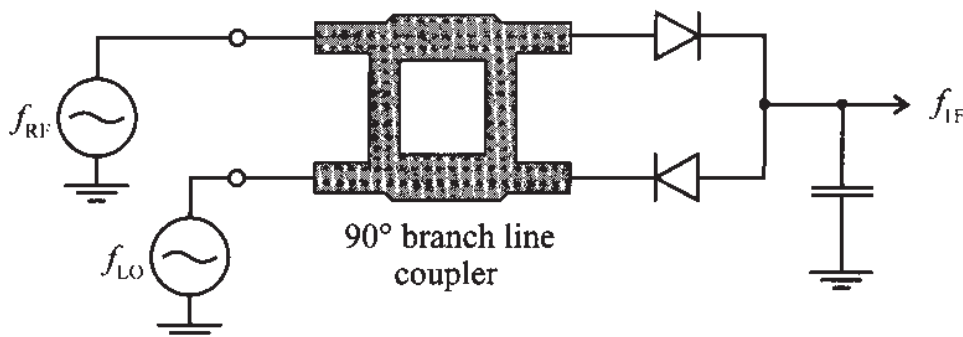


Figure 10-41 Balanced mixer involving a hybrid coupler.

Besides an excellent VSWR (see Appendix G), it can be shown that this design is capable of suppressing a considerable amount of noise because the opposite diode arrangement in conjunction with the 90° phase shift provides a good degree of noise cancellation. The proof is left as an exercise, see Problem 10.22.

A more sophisticated design, involving two MESFETs and 90° and 180° hybrid couplers is shown in Figure 10-42. The 180° phase shift is needed since the second MESFET cannot easily be reversed as done in the anti-parallel diode configuration seen in Figure 10-41. It is also important to point out that this circuit exhibits LO to RF as well as LO to IF signal isolation, but no RF to IF signal isolation. For this reason, a low-pass filter is typically incorporated into the output matching networks of each of the transistors in Figure 10-42.

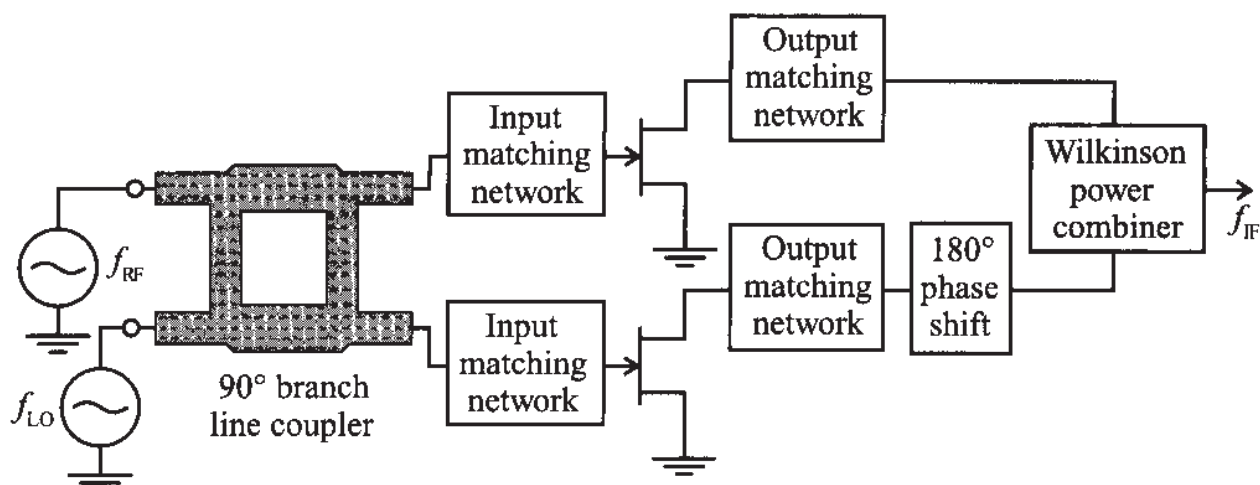


Figure 10-42 Single-balanced MESFET mixer with coupler and power combiner.

10.3.5 Double-Balanced Mixer

The double-balanced mixer can be constructed by using four diodes arranged in a rectifier configuration. The additional diodes provided better isolation and an improved suppression of spurious modes. Unlike the single-balanced approach, the double-balanced design eliminates all even harmonics of both the LO and RF signals. However, the disadvantages are a considerably higher LO drive power and increased conversion loss. Figure 10-43 depicts a typical circuit of the double-balanced design. All three signal paths are decoupled, and the input and output transformers enable a symmetric mixing with the LO signal.

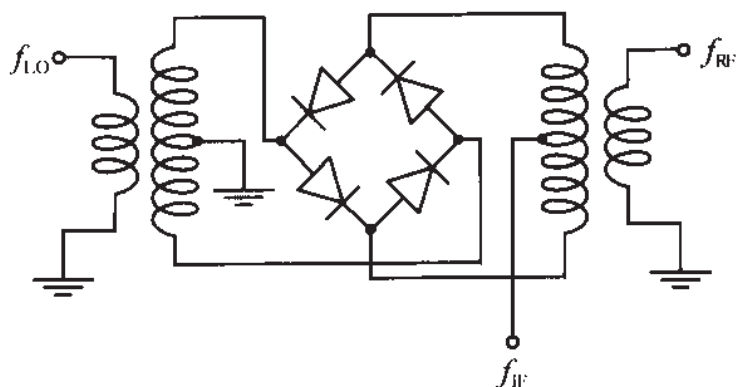


Figure 10-43 Double-balanced mixer design.

For design details of double-balanced mixers the reader is referred to the books by Vendelin and Mass listed at the end of this chapter.

10.4 Summary

Oscillators and mixers require a nonlinear transfer characteristic and are therefore more difficult to design than standard linear amplifiers. It is not uncommon to encounter circuits that perform as desired, but the design engineer does not understand exactly why they behave this way. Today's extensive reliance on CAD tools has often reduced our thinking to trial-and-error approaches. This certainly applies both to oscillators and mixer RF circuits.

One of the key design requirements of an oscillator is the negative resistance condition as a result of the feedback loop equation, which can be formulated as the Barkhausen criterion:

$$H_F(\omega)H_A(\omega) = 1$$

For instance, the feedback Pi-type network results in a host of different oscillator types, of which we discussed the Hartley, Colpitts, and Clapp designs. At frequencies up to approximately 250 MHz one of the passive feedback elements can be replaced by a

quartz crystal whose mechanical vibrations allow substantial improvements in frequency and temperature stability.

For higher frequencies the S-parameters again become the preferred design procedure. For a two-port oscillator, the stability condition and the input and output oscillation conditions assume primary importance:

$$k < 1, \Gamma_{in}\Gamma_S = 1, \Gamma_{out}\Gamma_L = 1$$

A typical approach would start with the test of the stability circle k . Next, from a particular output loading condition, the output reflection coefficient is determined from the knowledge of the input reflection coefficient. Conversely, the design can also be conducted from the input side. To enhance the Q -factor of the high-frequency performance a dielectric resonator can be added whose behavior is that of a parallel resonance circuit with normalized line impedance:

$$z_{DR} \approx \frac{R/Z_0}{1 + j2Q_u(\Delta f/f_0)} = 2\beta$$

Instead of the dielectric resonator a magnetically induced resonance condition can be established with the help of a YIG element. A Gunn diode finds applications in very high frequency oscillators. To add frequency tuning flexibility, a varactor diode is often employed to adjust the resonant circuit capacitively.

Besides oscillators, mixers are the second group of practical circuits directly exploiting the nonlinear transfer characteristic of active solid-state elements such as diodes and bi- and monopolar devices. The ability of a mixer to achieve frequency translation finds applications in heterodyne receiver and transmitter circuits. An RF signal ω_{RF} mixed with a local oscillator frequency ω_{LO} results in a main current product of

$$I(V) = \dots + BV_{RF}V_{LO}\{\cos[(\omega_{RF} + \omega_{LO})t] + \cos[(\omega_{RF} - \omega_{LO})t]\}$$

where the first term signifies upconversion and the second term downconversion. This second-term response can, for instance, be utilized as the required intermediate output signal in a receiver. To isolate the desired signal frequency, extensive filtering is required on the input (image filter) and output (low-pass) sides of the mixer. Single-ended, single-balanced, and double-balanced designs can be constructed by appropriate impedance matching of the source and load to the active device. One additional complication over the amplifier matching network design arises because of the need to isolate the RF and LO inputs from the IF output and, conversely, to isolate the IF output from both RF and LO input signals. While balanced mixers offer improved signal performance through partial cancellation of undesired harmonic responses, they require the additional complexity of couplers to accomplish the required phase shifts.

Further Reading

- Y. Anand and W. J. Moroney, "Microwave Mixer and Detector Diodes," *Proceedings of IEEE*, Vol. 59, pp. 1182–1190, 1971.
- R. J. Gilmore and F. J. Rosenbaum, "An Analytical Approach to Optimum Oscillator Design Using S-Parameters," *IEEE Trans. on Microwave Theory and Techniques*, Vol. 31, pp. 633–639, 1983.
- G. Gonzalez, *Microwave Transistor Amplifiers, Analysis and Design*, Prentice-Hall, Upper Saddle River, NJ, 1997.
- J. B. Gunn, "Effect of Domain and Circuit Properties on Oscillations on GaAs," *IBM Journal of Res. Development*, Vol. 10, pp. 310–320, 1966.
- J. M. Manley and H. E. Rowe, "Some General Properties of Nonlinear Elements," *Proceedings of IRE*, Vol. 44, pp. 904–913, 1956.
- S. A. Mass, *Microwave Mixers*, Artech House, Dedham, MA, 1986
- M. A. Smith, K. J. Anderson, and A. M. Pavio, "Decade-Band Mixer Covers 3.5 to 35 GHz," *Microwave Journal*, pp. 163–171, Feb. 1986.
- G. Vendelin, A. Pavio, and U. L. Rhode, *Microwave Circuit Design Using Linear and Nonlinear Techniques*, John Wiley, New York, 1990.
- G. Vendelin, *Design of Amplifiers and Oscillators by the S-Parameter Method*, John Wiley, New York, 1982.
- P. C. Wade, "Novel FET Power Oscillators," *Electronics Letters*, September 1978.

Problems

- 10.1 Derive the transfer function for the series resonance circuit depicted in Figure 10-3 with $v(i) = 0$ and zero initial conditions. In particular, show that $\omega_Q = (LC)^{-1/2}(1 - R^2C/(4L))^{1/2}$ and $\alpha = -R/(2L)$. For the values $R = 5 \Omega$, $L = 50 \text{ nH}$, and $C = 270 \text{ pF}$, plot the frequency response.
- 10.2 In Section 10.1.3 the Colpitts oscillator centered around the h -parameter description of the BJT in emitter configuration is derived. Follow similar steps and derive the Hartley oscillator. Specifically, find the oscillator frequency in terms of L_1 , L_2 , C_3 , and the h -parameters. Further, establish the ratio of L_2 to L_1 .

- 10.3 A Colpitts oscillator is to be designed for 250 MHz. At the bias point $V_{CE} = 2.7$ V and $I_C = 2$ mA, the following circuit parameters are given at room temperature of 25°C : $C_{BC} = 0.2$ fF, $r_{BE} = 3$ k Ω , $r_{CE} = 12$ k Ω , $C_{BE} = 80$ fF. If the inductance is fixed at 47 nH, find values for the capacitances in the feedback loop. Examine whether it is appropriate to use the h -parameters obtained under DC conditions.
- 10.4 In Section 10.1.4 the quartz element is discussed. Show that solving (10.20) results in the approximate series and parallel resonance conditions of equations (10.21a) and (10.21b). Hint: Use the Taylor Series expansion and retain the first two terms.
- 10.5 Quartz resonators are typically specified in terms of their series and parallel resonance frequency. For the electric equivalent circuit parameter of $R_q = 50$ Ω , $L_q = 50$ mH, $C_q = 0.4$ pF, and $C_0 = 0.8$ pF, find the series and parallel resonance frequencies based on (10.21a) and (10.21b). Plot the reactance of this quartz resonator over a suitable frequency range.
- 10.6 A particular crystal oscillator operates with the crystal in the parallel resonance mode. Then a lossless inductor is added in parallel with the crystal. If the combination of inductor and crystal is required to have the same reactance as the crystal originally did, will the oscillator frequency go up or down? Explain your answer.
- 10.7 In an oscillator design it is often required that we need the S -parameters of the transistor operating in common-base (CB) mode. Unfortunately, the manufacturer typically supplies the S -parameters for the transistor measured in common-emitter (CE) mode. We therefore have to convert them into CB S -parameters. The usual practice is that the S -parameters are first converted into Y -parameters, then the CE Y -parameters are converted into CB mode, and the result is finally converted into S -parameter representation. Derive CE to CB conversion formulas for the Y -parameter representation.
- 10.8 A GaAs MESFET chip has the following S -parameters in common-source configuration measured at 4 GHz: $S_{11} = 0.83 \angle -67^\circ$, $S_{21} = 2.16 \angle 119^\circ$, $S_{12} = 0.17 \angle 61^\circ$, $S_{22} = 0.66 \angle -23^\circ$. Using conversion formulas derived in the previous problem, compute the transistor S -parameters in common-base mode. Determine the stability circles for both configurations without and with a positive feedback of $L = 0.5$ nH at 4 GHz.

- 10.9 In Section 10.2.1 we discussed the case where Γ_L is chosen such that $|\Gamma_{in}|$ becomes greater than unity. Show that $|\Gamma_{in}| > 1$ implies $|\Gamma_{out}| > 1$ and vice versa.
- 10.10 In designing oscillators based on the S -parameter approach, it was stated that the following conditions must be satisfied: $k < 1$ and $\Gamma_S \Gamma_{in} = \Gamma_L \Gamma_{out} = 1$. By representing the input impedance as $Z_{in} = R_{in} + jX_{in}$ and output impedance $Z_{out} = R_{out} + jX_{out}$ as well as the source $Z_S = R_S + jX_S$ and load $Z_L = R_L + jX_L$ impedances, show that $R_{in} = -R_S$, $X_{in} = -X_S$, $R_{out} = -R_L$, and $X_{out} = -X_L$. This proves that the S -parameter design is equivalent to the negative resistance design.
- 10.11 An oscillator has to be designed for 3.5 GHz. The S -parameters of the BJT in common-base configuration are determined to be $S_{11} = 1.1 \angle 127^\circ$, $S_{12} = 0.86 \angle 128^\circ$, $S_{21} = 0.94 \angle -61^\circ$, and $S_{22} = 0.9 \angle -44^\circ$. By adding an inductance to the base, the instability can be enhanced. Determine the inductance for which the instability of the BJT is maximized.
- 10.12 In Section 10.2.2 the dielectric resonator is introduced and the S -parameters for the angular resonance frequency ω_0 are derived in (10.38). Show that near resonance (10.38) has to be modified to the form
- $$[S] = \begin{bmatrix} \frac{\beta}{1 + \beta + j2(Q_u \Delta f / f_0)} & \frac{1 + j2(Q_u \Delta f / f_0)}{1 + \beta + j2(Q_u \Delta f / f_0)} \\ \frac{1 + j2(Q_u \Delta f / f_0)}{1 + \beta + j2(Q_u \Delta f / f_0)} & \frac{\beta}{1 + \beta + j2(Q_u \Delta f / f_0)} \end{bmatrix}$$
- 10.13 Since $|\Gamma_{in}| > 1$ and $|\Gamma_{out}| > 1$, they cannot be displayed in a conventional Smith Chart. Extend the Smith Chart in such a way as to be able to display these quantities. What happens with the circles of constant resistance when the reflection coefficients are larger than unity?
- 10.14 Design a 7.5 GHz oscillator in common-emitter BJT configuration. The S -parameters at $V_{CE} = 5.0$ V and $I_C = 20$ mA are as follows: $S_{11} = 0.87 \angle -40^\circ$, $S_{12} = 0.25 \angle -32^\circ$, $S_{21} = 0.6 \angle 100^\circ$, and $S_{22} = 1.21 \angle 165^\circ$. Sketch the circuit, including the DC biasing network ($\beta = 80$).

- 10.15 A BJT is used in common-base configuration with biasing conditions specified at $V_{CE} = 3$ V and $V_{BE} = 0.9$ V. For this case, the transistor has the following S-parameters at 2.5 GHz: $S_{11} = 1.41 \angle 125^\circ$, $S_{12} = 0.389 \angle 130^\circ$, $S_{21} = 1.5 \angle -63^\circ$, and $S_{22} = 1.89 \angle -45^\circ$. Design a series feedback oscillator that satisfies the three conditions (10.26).
- 10.16 The S-parameters of a GaAs FET in common-source configuration are measured at 9 GHz and have the following values: $S_{11} = 0.30 \angle -167^\circ$, $S_{12} = 0.15 \angle 21.3^\circ$, $S_{21} = 1.12 \angle -23.5^\circ$, and $S_{22} = 0.90 \angle -25.6^\circ$. Design an oscillator with 9 GHz fundamental frequency and match the circuit to a $50\ \Omega$ load impedance. Use microstrip lines for a substrate FR-4 with 40 mil thickness ($\epsilon_r = 3.6$) and determine the widths and lengths of the elements.
- 10.17 A tunable oscillator involving a varactor diode has to be designed. For the varactor diode, the following data is known: equivalent series resistance of $35\ \Omega$ and a capacitance ranging from 15 pF to 35 pF for reverse voltages between 30 V and 2 V. Design a voltage controlled Clapp-type oscillator with center frequency of 300 MHz and $\pm 10\%$ tuning capability. Assume that transconductance of the transistor is constant and equal to $g_m = 115\text{ mS}$.
- 10.18 The output power of an oscillator can be approximated by

$$P_{\text{out}} = P_{\text{sat}} \left[1 - \exp\left(\frac{G_0 P_{\text{in}}}{P_{\text{sat}}}\right) \right]$$

where P_{sat} is the saturated output power, $G_0 = |S_{21}|^2$ is the small signal power gain, and P_{in} is the input power. For maximum output power we obtain

$$d(P_{\text{out}} - P_{\text{in}}) = 0 \text{ or } \frac{dP_{\text{out}}}{dP_{\text{in}}} = 1$$

Show that this leads to the maximum oscillator output power

$$P_{\text{out}}(\text{max}) = P_{\text{sat}} \left(1 - \frac{1}{G_0} - \frac{\ln G_0}{G_0} \right)$$

For a typical MESFET at 7 GHz, with $G_0 = 7\text{ dB}$ and $P_{\text{sat}} = 2\text{ W}$, find the maximum oscillator power.

- 10.19 The basic downconverting receiver system is shown in Figure 10-21. Draw a similar block diagram describing an upconversion transmitter system and explain its functionality.
- 10.20 When building BJT and diode-based mixers, the third-order intermodulation distortion (IMD) is an important design criterion. Ideally, over the entire range of RF input signal magnitudes the mixer should not generate any intermodulation. In reality, however, there may be a significant influence. Follow the same derivation as discussed in Section 10.3.1 and derive the first-, second-, and third-order harmonics for the combined mixer input signal $V = V_{RF}\cos(\omega_{RF}t) + V_{LO}\cos(\omega_{LO}t)$. If the RF signal is 1.9 GHz and the output IF is 2 MHz, determine all frequencies up to the third-order harmonics that are generated by this mixer.
- 10.21 Design a single-ended BJT mixer as shown in Figure 10-36. Compute values for the resistors R_1 and R_2 such that biasing conditions $V_{CE} = 2.5$ V, $V_{BE} = 0.8$ V, $I_C = 2.5$ mA, and $I_B = 40$ μ A are satisfied based on a supply voltage of $V_{CC} = 3.2$ V. RF and IF frequencies are $f_{RF} = 2.5$ GHz and $f_{IF} = 250$ MHz. The BJT is measured at IF to have an output impedance of $Z_{out} = (650 - j2400)\Omega$ for short-circuit input and an input impedance of $Z_{in} = (80 - j136)\Omega$ for short-circuit output at RF frequency.
- 10.22 For the balanced diode mixer in Figure 10-41 assume the following voltages:

$$v_{RF}(t) = V_{RF}\cos(\omega_{RF}t) \text{ and } v_{LO}(t) = [V_{LO} + v_n(t)]\cos(\omega_{LO}t)$$

where the constant amplitudes are such that $V_{RF} \ll V_{LO}$ and where the noise voltage v_n is much smaller than V_{LO} .

- (a) Find the currents through the upper diode $i_1(t)$ and lower diode $i_2(t)$ if the transfer characteristic is

$$i_n = C(-1)^{n+1}, (n = 1, 2)$$

where C is a constant, and v_1, v_2 is the respective diode voltage.

- (b) Explain how some of the noise cancellation occurs and show that the IF current, after suitable low-pass filtering (behind each diode), can be written as

$$\begin{aligned} i_{IF} &= -2CV_{RF}(V_{LO} + v_n)\sin[(\omega_{RF} - \omega_{LO})t] \\ &\equiv -2CV_{RF}V_{LO}\sin(\omega_{IF}t) \end{aligned}$$

Useful Physical Quantities and Units

Table A-1 Physical constants

| Quantity | Symbol | Units | Value |
|--------------------------|---------------|--------------|---------------------------|
| Permittivity in vacuum | ϵ_0 | F/m | 8.85418×10^{-12} |
| Permeability in vacuum | μ_0 | H/m | $4\pi 10^{-7}$ |
| Speed of light in vacuum | c | m/s | 2.99792×10^8 |
| Boltzmann's constant | k | J/K | 1.38066×10^{-23} |
| Electron charge | e | Coulomb | 1.60218×10^{-19} |
| Electron rest mass | m_0 | kg | 0.91095×10^{-30} |
| Electon volt | eV | J | 1.60218×10^{-19} |

Table A-2 Relevant quantities, units, and symbols

| Quantity | Symbol | Unit | Value |
|--------------|----------|--------------------------------|------------|
| femto | f | — | 10^{-15} |
| pico | p | — | 10^{-12} |
| nano | n | — | 10^{-9} |
| micro | m | — | 10^{-6} |
| milli | m | — | 10^{-3} |
| kilo | k | — | 10^3 |
| mega | M | — | 10^6 |
| giga | G | — | 10^9 |
| Mil | Mil | 0.001 inch = $25.4\mu\text{m}$ | |
| Conductivity | σ | S/m | |
| Resistivity | ρ | $\Omega \cdot \text{m}$ | |

International System of Units

| Quantity | Symbol | Unit | Dimensions |
|-----------------|----------|---------------------------|------------|
| Electric Charge | C | Coulomb | A · s |
| Current | A | Ampere | C/s |
| Voltage | V | Volts | J/C |
| Frequency | Hz | Hertz = cycles per second | 1/s |
| Electric field | E | V/m | |
| Magnetic field | H | A/m | |
| Magnetic flux | Wb | Weber | V · s |
| Energy | J | Joule | N · m |
| Power | W | Watt | J/s |
| Capacitance | F | Farad | C/V |
| Inductance | H | Henry | Wb/A |
| Resistance | Ω | Ohm | V/A |
| Conductance | S | Siemens | A/V |

Table A-3 Loss angle tangent for different dielectric materials

| Material | Loss Tangent | | | |
|--------------------|---------------------|---------------------|-----------------------|-------------------|
| | $f = 1 \text{ kHz}$ | $f = 1 \text{ MHz}$ | $f = 100 \text{ MHz}$ | $f = 3\text{GHz}$ |
| Aluminum oxide | 0.00057 | 0.00033 | 0.0003 | 0.001 |
| Barium titanate | 0.00044 | 0.0002 | | 0.0023 |
| Porcelain | 0.0140 | 0.0075 | 0.0078 | |
| Silicon dioxide | 0.00075 | 0.0001 | 0.0002 | 0.00006 |
| Araldite CN-501 | 0.0024 | 0.0190 | 0.0340 | 0.0270 |
| Epoxy resin RN-48 | 0.0038 | 0.0142 | 0.0264 | 0.0210 |
| Foamed polystyrene | <0.0002 | <0.0001 | <0.0002 | 0.0001 |
| Bakelite BM120 | 0.0220 | 0.0280 | 0.0380 | 0.0438 |
| Polyethylene | <0.0002 | <0.0002 | 0.0002 | 0.00031 |
| Polystyrene | <0.00005 | 0.00007 | <0.0001 | 0.00033 |
| Teflon | <0.0003 | <0.0002 | <0.0002 | 0.00015 |
| Sodium chloride | <0.0001 | <0.0002 | | <0.0005 |
| Water (distilled) | | 0.0400 | 0.0050 | 0.1570 |

Table A-4 American wire gauge chart

| Wire Size (AWG) | Diameter in Mils | Diameter in Millimeters | Area in Square Mils | Area in Square Millimeters |
|--------------------|---------------------|----------------------------|------------------------|----------------------------------|
| 1 | 289.3 | 7.34822 | 262934 | 169.6345 |
| 2 | 257.6 | 6.54304 | 208469 | 134.4959 |
| 3 | 229.4 | 5.82676 | 165324 | 106.6606 |
| 4 | 204.3 | 5.18922 | 131125 | 84.59682 |
| 5 | 181.9 | 4.62026 | 103948 | 67.06296 |
| 6 | 162.0 | 4.1148 | 82448.0 | 53.19212 |
| 7 | 144.3 | 3.66522 | 65415.8 | 42.20364 |
| 8 | 128.5 | 3.2639 | 51874.8 | 33.46752 |
| 9 | 114.4 | 2.90576 | 41115.2 | 26.52585 |
| 10 | 101.9 | 2.58826 | 32621.1 | 21.04581 |
| 11 | 90.7 | 2.30378 | 25844.2 | 16.67370 |
| 12 | 80.8 | 2.05232 | 20510.3 | 13.23244 |
| 13 | 72.0 | 1.8288 | 16286.0 | 10.50709 |
| 14 | 64.1 | 1.62814 | 12908.2 | 8.327859 |
| 15 | 57.1 | 1.45034 | 10242.9 | 6.608296 |
| 16 | 50.8 | 1.29032 | 8107.32 | 5.230518 |
| 17 | 45.3 | 1.15062 | 6446.83 | 4.159237 |

Table A-4 American wire gauge chart (Continued)

| Wire Size (AWG) | Diameter in Mils | Diameter in Millimeters | Area in Square Mils | Area in Square Millimeters |
|----------------------------|-----------------------------|------------------------------------|--------------------------------|---|
| 18 | 40.3 | 1.02362 | 5102.22 | 3.291754 |
| 19 | 35.9 | 0.91186 | 4048.92 | 2.612199 |
| 20 | 32.0 | 0.8128 | 3216.99 | 2.075474 |
| 21 | 28.5 | 0.7239 | 2551.76 | 1.646293 |
| 22 | 25.3 | 0.64262 | 2010.90 | 1.297354 |
| 23 | 22.6 | 0.57404 | 1604.60 | 1.035224 |
| 24 | 20.1 | 0.51054 | 1269.23 | 0.818860 |
| 25 | 17.9 | 0.45466 | 1006.60 | 0.649417 |
| 26 | 15.9 | 0.40386 | 794.226 | 0.512403 |
| 27 | 14.2 | 0.36068 | 633.470 | 0.408690 |
| 28 | 12.6 | 0.32004 | 498.759 | 0.321780 |
| 29 | 11.3 | 0.28702 | 401.150 | 0.258806 |
| 30 | 10.0 | 0.254 | 314.159 | 0.202683 |
| 31 | 8.9 | 0.22606 | 248.846 | 0.160545 |
| 32 | 8.0 | 0.2032 | 201.062 | 0.129717 |
| 33 | 7.1 | 0.18034 | 158.368 | 0.102172 |
| 34 | 6.3 | 0.16002 | 124.690 | 0.080445 |
| 35 | 5.6 | 0.14224 | 98.5203 | 0.063561 |
| 36 | 5.0 | 0.127 | 78.5398 | 0.050671 |
| 37 | 4.5 | 0.1143 | 63.6173 | 0.041043 |
| 38 | 4.0 | 0.1016 | 50.2654 | 0.032429 |
| 39 | 3.5 | 0.0889 | 38.4845 | 0.024829 |
| 40 | 3.1 | 0.07874 | 30.1907 | 0.019478 |
| 41 | 2.8 | 0.07112 | 24.6301 | 0.015890 |
| 42 | 2.5 | 0.0635 | 19.6350 | 0.012668 |
| 43 | 2.2 | 0.05588 | 15.2053 | 0.009810 |
| 44 | 2.0 | 0.0508 | 12.5664 | 0.008107 |
| 45 | 1.76 | 0.044704 | 9.73140 | 0.006278 |
| 46 | 1.57 | 0.039878 | 7.74371 | 0.004996 |
| 47 | 1.40 | 0.03556 | 6.15752 | 0.003973 |
| 48 | 1.24 | 0.031496 | 4.83051 | 0.003116 |
| 49 | 1.11 | 0.028194 | 3.87076 | 0.002497 |
| 50 | 0.99 | 0.025146 | 3.07907 | 0.001986 |

Skin Equation for a Cylindrical Conductor

The starting point of the skin effect analysis is Maxwell's equations expressed by the laws of Ampere and Faraday in differential form:

$$\nabla \times \mathbf{H} = \mathbf{J} = \sigma \mathbf{E} \quad (\text{B.1a})$$

$$\nabla \times \mathbf{E} = -\mu \left(\frac{\partial \mathbf{H}}{\partial t} \right) \quad (\text{B.1b})$$

where the displacement current density $\epsilon(\partial \mathbf{E} / \partial t)$ in (B.1a) is neglected inside a conductor. This is permissible since the electric field in conjunction with the dielectric constant is very small, even for rapidly changing fields, when compared with the conduction current. We evaluate these equations in a cylindrical coordinate system where E_z , E_r , and H_ϕ are the only non-zero components. Carrying out the curl in cylindrical coordinates, results in

$$\frac{1}{r} \frac{\partial}{\partial r} (r H_\phi) = \sigma E_z \quad (\text{B.2a})$$

$$-\frac{\partial H_\phi}{\partial z} = \sigma E_r = 0 \quad (\text{B.2b})$$

$$\frac{\partial E_z}{\partial r} - \frac{\partial E_r}{\partial z} = \mu \sigma \frac{\partial H_\phi}{\partial t} \quad (\text{B.2c})$$

The second equation is zero because H_ϕ does not depend on the z -coordinate. Consequently, E_r is also zero. Differentiating the last equation with respect to r , and then substituting the first into it, yields a second-order differential equation:

$$\frac{\partial^2 E_z}{\partial r^2} + \frac{1}{r} \left(\frac{\partial E_z}{\partial r} \right) - \mu \sigma \left(\frac{\partial E_z}{\partial t} \right) = 0 \quad (\text{B.3})$$

For time harmonic fields, the time derivative can be replaced by $j\omega$ and combined with $\mu\sigma$ to form the new parameter $p^2 = -j\omega\mu\sigma$. The final form

$$\frac{d^2 E_z}{dr^2} + \frac{1}{r} \left(\frac{dE_z}{dr} \right) + p^2 E_z = 0 \quad (\text{B.4})$$

is the standard Bessel equation with the solution $E_z = AJ_0(pr)$, where A is a constant and J_0 is the Bessel function of zeroth order. Substituting this solution into the time harmonic form of (B.2c) gives us

$$j\omega\mu H_\phi = ApJ_0'(pr) \quad (\text{B.5})$$

with the prime denoting differentiation with respect to the argument. The current is related to the line integral of H_ϕ along the outer perimeter, $r = a$, of the conductor: $H_\phi 2\pi a = I$. Thus, we can write

$$H_\phi = A \left(\frac{p}{j\omega\mu} \right) J_0'(pa) = \frac{I}{2\pi a} \quad (\text{B.6})$$

which allows us to determine the constant A . Substituting A into the solution of the Bessel equation leads to

$$E_z = \frac{j\omega\mu}{2\pi pa} I \left(\frac{J_0(pr)}{J_0'(pa)} \right) \quad (\text{B.7})$$

An interesting property of the Bessel function is the fact that $J_0'(pa) = -J_1(pa)$, which gives us, after a small algebraic manipulation, the final result

$$E_z = \frac{p}{2\pi\sigma a} I \left(\frac{J_0(pr)}{J_1(pa)} \right) \quad (\text{B.8})$$

This equation is used in Chapter 1. The validity of (B.8) for the case of zero frequency, or DC condition, can be proved easily. For low frequency we see that

$$J_0(pr) = 1 - \left(\frac{pr}{2} \right)^2 + \frac{(pr)^4}{(2 \cdot 4)^2} - \frac{(pr)^6}{(2 \cdot 4 \cdot 6)^2} + \dots \approx 1 \quad (\text{B.9a})$$

$$J_1(pa) = \frac{pa}{2} \left[1 - \frac{(pa)^2}{2 \cdot 4} + \dots \right] \approx \frac{pa}{2} \quad (\text{B.9b})$$

Substituting (B.9) into (B.8) yields Ohm's law for uniform current density J_z :

$$E_z = \frac{Ip}{2\pi a\sigma} \left(\frac{2}{pa} \right) = \frac{I}{\sigma\pi a^2} \equiv \frac{J_z}{\sigma} \quad (\text{B.10})$$

Complex Numbers

T

This appendix provides a brief summary of several useful concepts and definitions regarding complex numbers and their manipulations as repeatedly used throughout this textbook. Emphasis is placed on the basic definition of a complex number, its use in the magnitude computations, and its meaning in terms of the circle equation.

C.1 Basic Definition

A complex number z , such as the normalized impedance, can be represented in rectangular and polar forms as

$$z = x + jy = |z|e^{j\Theta} \quad (\text{C.1})$$

where the magnitude is given by

$$|z| = \sqrt{z \cdot z^*} = \sqrt{(x + jy) \cdot (x - jy)} = \sqrt{x^2 + y^2} \quad (\text{C.2})$$

and the phase is

$$\Theta = \tan^{-1}(y/x) \quad (\text{C.3})$$

The star notation denotes the complex conjugate (i.e., $z^* = x - jy$).

C.2 Magnitude Computations

Let us apply the preceding definition to a typical computation involving the magnitude of two complex numbers such as

$$|z + w^*|^2$$

where w is another complex number of the form $w = u + jv$. Substituting w yields

$$|z + w^*|^2 = (z + w^*) \cdot (z^* + w) = |z|^2 + |w|^2 + 2\operatorname{Re}\{z \cdot w\} \quad (\text{C.4})$$

where we used the fact that the terms $z \cdot w = ux - vy + j(uy + vx)$ and $z^* \cdot w^* = ux - vy - j(uy + vx)$ can be combined to $2\operatorname{Re}\{z \cdot w\}$. Here $\operatorname{Re}\{\dots\}$ represents the real part.

C.3 Circle Equation

Perhaps one of the most useful equations involving complex numbers in RF circuits is the circle equation

$$|z - w| = r \text{ or } |z - w|^2 = r^2 \quad (\text{C.5})$$

which forms the foundation of the Smith Chart. We can verify that this is indeed a circle equation by going through the magnitude computation

$$|z - w|^2 = (z - w) \cdot (z - w)^* = (x - u)^2 + (y - v)^2 = r^2 \quad (\text{C.6})$$

It is seen that u and v are the coordinates of the circle center in the complex z -plane and r is its radius, as depicted in Figure C-1.

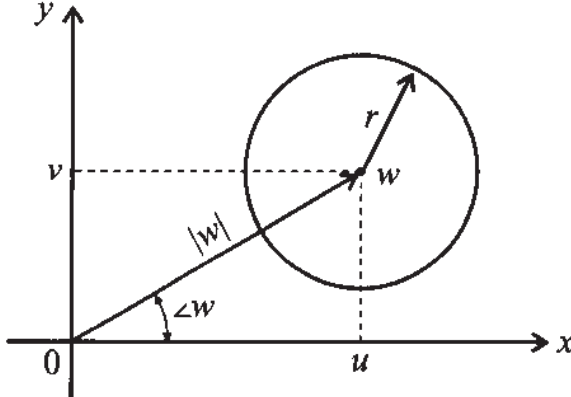


Figure C-1 Circle representation in the complex z -plane.

Matrix Conversions

Conversion between Z, Y, h, and ABCD representations

| | [Z] | [Y] | [h] | [ABCD] |
|--------|---|---|--|---|
| [Z] | $Z_{11} \ Z_{12}$ $Z_{21} \ Z_{22}$ | $\frac{Z_{22}}{\Delta Z} - \frac{Z_{12}}{\Delta Z}$ $-\frac{Z_{21}}{\Delta Z} \ \frac{Z_{11}}{\Delta Z}$ | $\frac{\Delta Z}{Z_{22}} \ \frac{Z_{12}}{Z_{22}}$ $-\frac{Z_{21}}{Z_{22}} \ \frac{1}{Z_{22}}$ | $\frac{Z_{11}}{Z_{21}} \ \frac{\Delta Z}{Z_{21}}$ $\frac{1}{Z_{21}} \ \frac{Z_{22}}{Z_{21}}$ |
| [Y] | $\frac{Y_{22}}{\Delta Y} - \frac{Y_{12}}{\Delta Y}$ $-\frac{Y_{21}}{\Delta Y} \ \frac{Y_{11}}{\Delta Y}$ | $Y_{11} \ Y_{12}$ $Y_{21} \ Y_{22}$ | $\frac{1}{Y_{11}} - \frac{Y_{12}}{Y_{11}}$ $\frac{Y_{21}}{Y_{11}} \ \frac{\Delta Y}{Y_{11}}$ | $-\frac{Y_{22}}{Y_{21}} - \frac{1}{Y_{21}}$ $-\frac{\Delta Y}{Y_{21}} - \frac{Y_{11}}{Y_{21}}$ |
| [h] | $\frac{\Delta h}{h_{22}} \ \frac{h_{12}}{h_{22}}$ $-\frac{h_{21}}{h_{22}} \ \frac{1}{h_{22}}$ | $\frac{1}{h_{11}} - \frac{h_{12}}{h_{11}}$ $\frac{h_{21}}{h_{11}} \ \frac{\Delta h}{h_{11}}$ | $h_{11} \ h_{12}$ $h_{21} \ h_{22}$ | $-\frac{\Delta h}{h_{21}} - \frac{h_{11}}{h_{21}}$ $-\frac{h_{22}}{h_{21}} - \frac{1}{h_{21}}$ |
| [ABCD] | $\frac{A}{C} \ \frac{\Delta ABCD}{C}$ $\frac{1}{C} \ \frac{D}{C}$ | $\frac{D}{B} - \frac{\Delta ABCD}{B}$ $-\frac{1}{B} \ \frac{A}{B}$ | $\frac{B}{D} \ \frac{\Delta ABCD}{D}$ $-\frac{1}{D} \ \frac{C}{D}$ | $A \ B$ $C \ D$ |

$$\Delta Z = Z_{11}Z_{22} - Z_{12}Z_{21}, \Delta Y = Y_{11}Y_{22} - Y_{12}Y_{21}, \Delta h = h_{11}h_{22} - h_{12}h_{21},$$

$$\Delta ABCD = AD - BC$$

Conversion from S-parameters to Z, Y, h, or ABCD representations

| | | | |
|--------|---|---|---------------------------------------|
| | $Z_{11} = Z_0 \frac{(1 + S_{11})(1 - S_{22}) + S_{12}S_{21}}{\Psi_1}$ | $Z_{12} = Z_0 \frac{2S_{12}}{\Psi_1}$ | $Z_{21} = Z_0 \frac{2S_{21}}{\Psi_1}$ |
| [Z] | $Z_{22} = Z_0 \frac{(1 - S_{11})(1 + S_{22}) + S_{12}S_{21}}{\Psi_1}$ where $\Psi_1 = (1 - S_{11})(1 - S_{22}) - S_{12}S_{21}$ | | |
| [Y] | $Y_{11} = \frac{(1 - S_{11})(1 + S_{22}) + S_{12}S_{21}}{Z_0\Psi_2}$ | $Y_{12} = \frac{-2S_{12}}{Z_0\Psi_2}$ | $Y_{21} = \frac{-2S_{21}}{Z_0\Psi_2}$ |
| | $Y_{22} = \frac{(1 + S_{11})(1 - S_{22}) + S_{12}S_{21}}{Z_0\Psi_2}$ where $\Psi_2 = (1 - S_{11})(1 - S_{22}) - S_{12}S_{21}$ | | |
| [h] | $h_{11} = Z_0 \frac{(1 + S_{11})(1 + S_{22}) - S_{12}S_{21}}{\Psi_3}$ | $h_{12} = \frac{2S_{12}}{\Psi_3}$ | $h_{21} = \frac{-2S_{21}}{\Psi_3}$ |
| | $h_{22} = \frac{(1 - S_{11})(1 - S_{22}) - S_{12}S_{21}}{Z_0\Psi_3}$ where $\Psi_3 = (1 - S_{11})(1 + S_{22}) + S_{12}S_{21}$ | | |
| [ABCD] | $A = \frac{(1 + S_{11})(1 - S_{22}) + S_{12}S_{21}}{2S_{21}}$ | $B = Z_0 \frac{(1 + S_{11})(1 + S_{22}) - S_{12}S_{21}}{2S_{21}}$ | |
| | $C = \frac{(1 - S_{11})(1 - S_{22}) - S_{12}S_{21}}{2S_{21}Z_0}$ | $D = \frac{(1 - S_{11})(1 + S_{22}) + S_{12}S_{21}}{2S_{21}}$ | |

Conversion from **Z**, **Y**, **h**, and **ABCD** representations to **S**-parameters.

| | | | |
|-----------------|--|---------------------------------------|---------------------------------------|
| | $S_{11} = \frac{(Z_{11} - Z_0)(Z_{22} + Z_0) - Z_{12}Z_{21}}{\Psi_4}$ | $S_{12} = \frac{2Z_{12}Z_0}{\Psi_4}$ | $S_{21} = \frac{2Z_{21}Z_0}{\Psi_4}$ |
| [Z] | $S_{22} = \frac{(Z_{11} + Z_0)(Z_{22} - Z_0) - Z_{12}Z_{21}}{\Psi_4}$ | | |
| | where $\Psi_4 = (Z_{11} + Z_0)(Z_{22} + Z_0) - Z_{12}Z_{21}$ | | |
| | $S_{11} = \frac{(1 - Z_0 Y_{11})(1 + Z_0 Y_{22}) + Y_{12}Y_{21}Z_0^2}{\Psi_5}$ | $S_{12} = \frac{-2Y_{12}Z_0}{\Psi_5}$ | $S_{21} = \frac{-2Y_{21}Z_0}{\Psi_5}$ |
| [Y] | $S_{22} = \frac{(1 + Z_0 Y_{11})(1 - Z_0 Y_{22}) + Y_{12}Y_{21}Z_0^2}{\Psi_5}$ | | |
| | where $\Psi_5 = (1 + Z_0 Y_{11})(1 + Z_0 Y_{22}) - Y_{12}Y_{21}Z_0^2$ | | |
| | $S_{11} = \frac{(h_{11}/Z_0 - 1)(h_{22}Z_0 + 1) - h_{12}h_{21}}{\Psi_6}$ | $S_{12} = \frac{2h_{12}}{\Psi_6}$ | $S_{21} = \frac{-2h_{21}}{\Psi_6}$ |
| [h] | $S_{22} = \frac{(h_{11}/Z_0 + 1)(h_{22}Z_0 - 1) + h_{12}h_{21}}{\Psi_6}$ | | |
| | where $\Psi_6 = (h_{11}/Z_0 + 1)(h_{22}Z_0 + 1) - h_{12}h_{21}$ | | |
| | $S_{11} = \frac{A + B/Z_0 - CZ_0 - D}{\Psi_7}$ | $S_{12} = \frac{2(AD - BC)}{\Psi_7}$ | $S_{21} = \frac{2}{\Psi_7}$ |
| [ABCD] | $S_{22} = \frac{-A + B/Z_0 - CZ_0 + D}{\Psi_7}$ | | |
| | where $\Psi_7 = A + B/Z_0 + CZ_0 + D$ | | |

Physical Parameters of Semiconductors

Table E-1 Properties of Ge, Si, and GaAs at 300°K

| Properties | Ge | Si | GaAs |
|--|----------------------|-----------------------|--------------------|
| Dielectric constant | 16.0 | 11.9 | 13.1 |
| Energy gap (eV) | 0.66 | 1.12 | 1.424 |
| Intrinsic carrier concentration (cm^{-3}) | 2.4×10^{13} | 1.45×10^{10} | 1.79×10^6 |
| Intrinsic resistivity ($\Omega \cdot \text{cm}$) | 47 | 2.3×10^5 | 10^8 |
| Minority carrier lifetime (s) | 10^{-3} | 2.5×10^{-3} | 10^{-8} |
| Electron mobility (drift) ($\text{cm}^2/\text{V}\cdot\text{s}$) | 3900 | 1350 | 8500 |
| Normalized effective mass of the electron (m_n^*/m_e) | 0.55 | 1.08 | 0.067 |
| Hole mobility (drift) ($\text{cm}^2/\text{V}\cdot\text{s}$) | 1900 | 480 | 400 |
| Normalized effective mass of the hole (m_p^*/m_e) | 0.37 | 0.56 | 0.48 |
| Electron affinity, χ (V) | 4.0 | 4.05 | 4.07 |
| Specific heat ($\text{J}/(\text{g} \cdot {}^\circ\text{K})$) | 0.31 | 0.7 | 0.35 |
| Thermal conductivity ($\text{W}/(\text{cm} \cdot {}^\circ\text{K})$) | 0.6 | 1.5 | 0.46 |
| Thermal diffusivity (cm^2/s) | 0.36 | 0.9 | 0.24 |

Long and Short Diode Models

The current flow through a diode under an applied forward bias voltage (see Chapter 6) can be evaluated based on the concentration of the injected **excess charge carriers** in each semiconductor region. Depending on the length of the semiconductor layers, we need to differentiate between a long and short diode model. In the following discussion the current flow is derived for both cases.

With reference to Figure F-1, let us examine the *pn*-junction under forward bias voltage V_A .

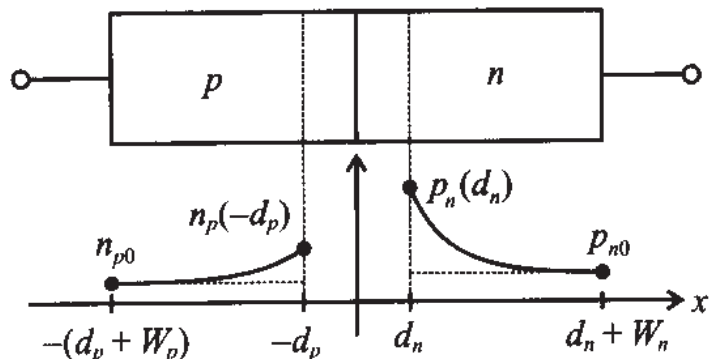


Figure F-1 *pn*-junction under forward bias.

Under this applied voltage the junction is no longer in thermal equilibrium, and minority concentrations are created that exceed the equilibrium condition n_{p0} in the *p*-layer and p_{n0} in the *n*-layer. Indeed, thermodynamic considerations predict the minority concentrations in each layer as

$$p_n(d_n) = p_{n0} e^{V_A/V_T} \text{ and } n_p(-d_p) = n_{p0} e^{V_A/V_T} \quad (\text{F.1})$$

The corresponding excess charge concentrations

$$\Delta p_n = p_n - p_{n0} \text{ and } \Delta n_p = n_p - n_{p0} \quad (\text{F.2})$$

begin to diffuse into the semiconductor layers, a process governed by the steady-state diffusion equation. For the n -layer, the equation reads

$$\frac{d^2(\Delta p_n)}{dx^2} = \frac{\Delta p_n}{D_p \tau_p} \quad (\text{F.3})$$

where D_p , τ_p are the diffusion constant of holes in the n -layer and excess charge carrier lifetime (on the order of $10^{-7} \dots 10^{-6}$ s), respectively. It is the so-called **diffusion length**

$$L_p = \sqrt{D_p \tau_p} \text{ and } L_n = \sqrt{D_n \tau_n} \quad (\text{F.4})$$

with respect to the length of each semiconductor layer that determines whether we have to deal with a long or short diode model. The general solution to (F.3) is $\Delta p_n = C_1 e^{x/L_p} + C_2 e^{-x/L_p}$, with two unknown constants to be determined through the boundary conditions on either end of the semiconductor layer. The following two cases are considered:

F.1 Long Diode ($W_n > L_p$, $\Delta p_n \rightarrow 0$ as $x \rightarrow \infty$)

Since the excess carriers completely decay to zero before reaching the end of the layer, only C_2 has to be specified and $C_1 = 0$. Applying (F.1) as a boundary condition, we can find C_2 and insert it into the general solution, with the result

$$\Delta p_n = p_{n0} (e^{V_A/V_T} - 1) [e^{-(x-d_n)/L_p}] \quad (\text{F.5})$$

In an identical way we can find for the p -layer ($W_p > L_n$, $\Delta n_p \rightarrow 0$ as $x \rightarrow -\infty$)

$$\Delta n_p = n_{p0} (e^{V_A/V_T} - 1) [e^{(x+d_p)/L_p}] \quad (\text{F.6})$$

F.2 Short Diode ($W_n < L_p$, $\Delta p_n \rightarrow 0$ as $x \rightarrow d_n + W_n$)

Here the situation is more complicated since the decay takes place over a finite distance. As a result, both coefficients have to be retained. The additional boundary condition on the right-hand layer now reads $p_n(d_n + W_n) = p_{n0}$. Going through the mathematics eventually leads to

$$\Delta p_n = p_{n0} (e^{V_A/V_T} - 1) \left(\frac{\sinh[(d_n + W_n - x)/L_p]}{\sinh[W_n/L_p]} \right) \quad (\text{F.7})$$

which can be further simplified by approximating the hyperbolic sine function, sinh, by its argument. This is permissible as long as the layer length is less than the diffusion

length ($W_n < L_p$). The final result is

$$\Delta p_n = p_{n0} (e^{V_A/V_T} - 1) \left(\frac{d_n + W_n - x}{L_p} \right) \quad (\text{F.8})$$

Similarly for the p -layer ($W_p < L_n$, $\Delta n_p \rightarrow 0$ as $x \rightarrow -(d_p + W_p)$)

$$\Delta n_p = n_{p0} (e^{V_A/V_T} - 1) \left(\frac{x - (d_p + W_p)}{L_p} \right) \quad (\text{F.9})$$

Similar to (6.14), equations (F.5), (F.6) or (F.8), (F.9) can be used to find the total current through the diode:

$$I = A [J_p(d_n) + J_n(d_p)] = A \left[(-q) D_p \left(\frac{d\Delta p_n}{dx} \right) \Big|_{d_n} + q D_n \left(\frac{d\Delta n_p}{dx} \right) \Big|_{-d_p} \right] \quad (\text{F.10})$$

Inserting (F.5), (F.6) or (F.8), (F.9) into (F.10) finally results in the Shockley equation:

$$I = I_0 (e^{V_A/V_T} - 1) \quad (\text{F.11})$$

where the reverse saturation current is for the long diode

$$I_0 = A \left[\frac{q D_p p_{n0}}{L_p} + \frac{q D_n n_{p0}}{L_n} \right] \quad (\text{F.12})$$

and for the short diode

$$I_0 = A \left[\frac{q D_p p_{n0}}{W_n} + \frac{q D_n n_{p0}}{W_p} \right] \quad (\text{F.13})$$

A typical numerical example for a short Si diode involves the following parameters:

$$A = 2 \times 10^{-5} \text{ cm}^2, D_n = 22 \text{ cm}^2/\text{s}, D_p = 9 \text{ cm}^2/\text{s}, N_A = 1.5 \times 10^{16} \text{ cm}^{-3}, \\ n_i = 1.5 \times 10^{10} \text{ cm}^{-3}, N_D = 3 \times 10^{16} \text{ cm}^{-3}, \tau_p = \tau_n = 10^{-7} \text{ s}, \\ W_n = W_p = 25 \mu\text{m}.$$

With these data we can compute the minority carrier electron and hole concentrations in thermal equilibrium:

$$p_{n0} = n_i^2 / N_D = 7.5 \times 10^3 \text{ cm}^{-3}, n_{p0} = n_i^2 / N_A = 15 \times 10^3 \text{ cm}^{-3}$$

Inserting into (F.13) results in a reverse saturation current of 0.5 fA.

Couplers

B

Branchline couplers and power dividers play important roles in RF circuits and measurement arrangements since they allow the separation and combination of RF signals under fixed phase references. Notably, in the mixer section of Chapter 10 and the measurement protocol of characterizing a device under test in Chapter 4, we see their usefulness. The purpose of this appendix is to discuss some of the couplers and dividers encountered most often in terms of their *S*-parameters and figures of merit.

G.1 Wilkinson Divider

The transmission line configuration and its microstrip line implementation of this power divider are shown in Figure G-1. The *S*-parameters for such a three-port network are given by the matrix

$$[\mathbf{S}] = \frac{-1}{\sqrt{2}} \begin{bmatrix} 0 & j & j \\ j & 0 & 0 \\ j & 0 & 0 \end{bmatrix} \quad (\text{G.1})$$

The figures of merit are the **return loss** at ports 1 and 2

$$RL_1 = -20\log|S_{11}| \text{ and } RL_2 = -20\log|S_{22}| \quad (\text{G.2})$$

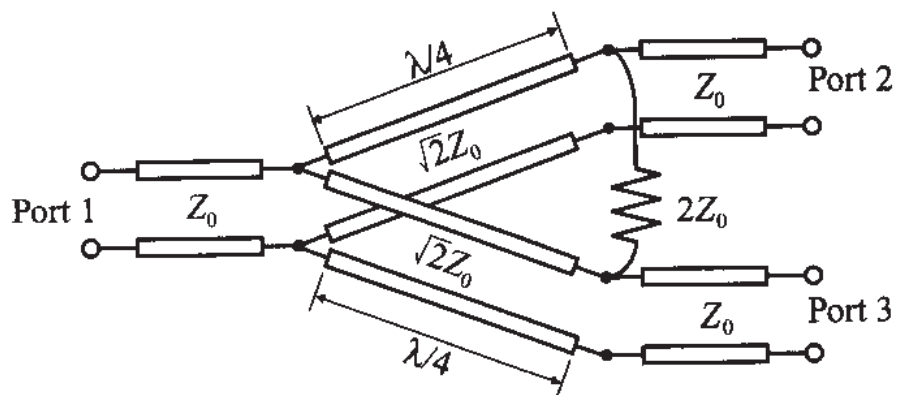
the **coupling** between ports 1 and 2

$$CP_{12} = -20\log|S_{21}| \quad (\text{G.3})$$

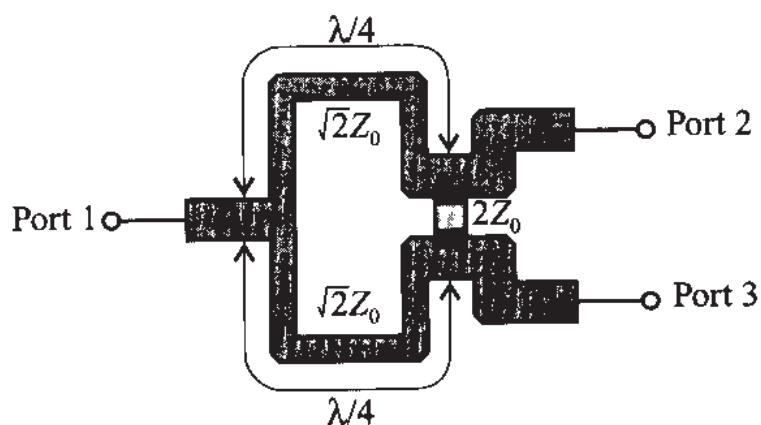
and **isolation** between ports 2 and 3

$$IL_{23} = -20\log|S_{23}| \quad (\text{G.4})$$

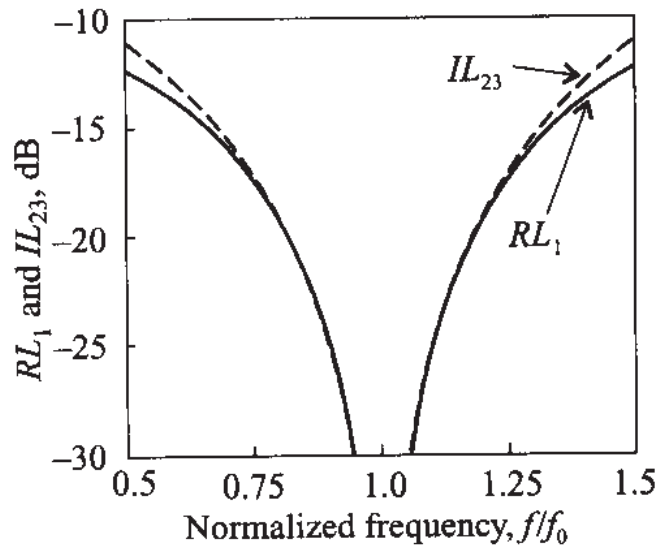
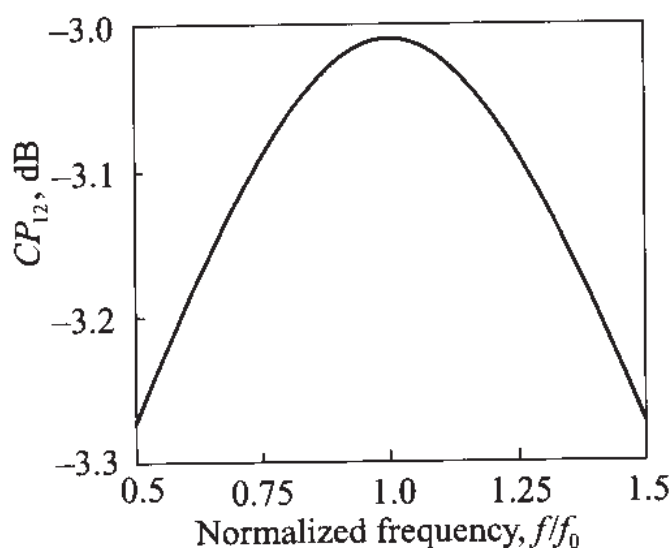
Figure G-2 provides a typical frequency response of RL_1 , CP_{12} , and IL_{23} for a center frequency of $f_0 = 1$ GHz.



(a) Transmission line model



(b) Microstrip line realization

Figure G-1 3 dB Wilkinson power divider.**Figure G-2** Frequency response of Wilkinson power divider.

Ideally, return loss and isolation should approach negative infinity at the center frequency and the coupling should be as close to the 3 dB value as possible. We also note that a coupler is not a broadband device. Typical frequency bandwidths do not exceed 20% of the center frequency.

The derivation of matrix (G.1) is most conveniently carried out by an even and odd mode analysis, as depicted in Figure G-3 for the computation of the S_{12} coefficient. We attach a source V_S to port 2 and terminated the other two ports with a Z_0 load. To make the circuit symmetric the source V_S at port 2 is divided into a series combination of two $V_S/2$ sources operating in phase. At port 3 two $V_S/2$ sources have a 180° phase shift and their sum is equal to zero. Also, the Z_0 load impedance connected to port 1 is replaced by the parallel combination of two $2Z_0$ impedances.

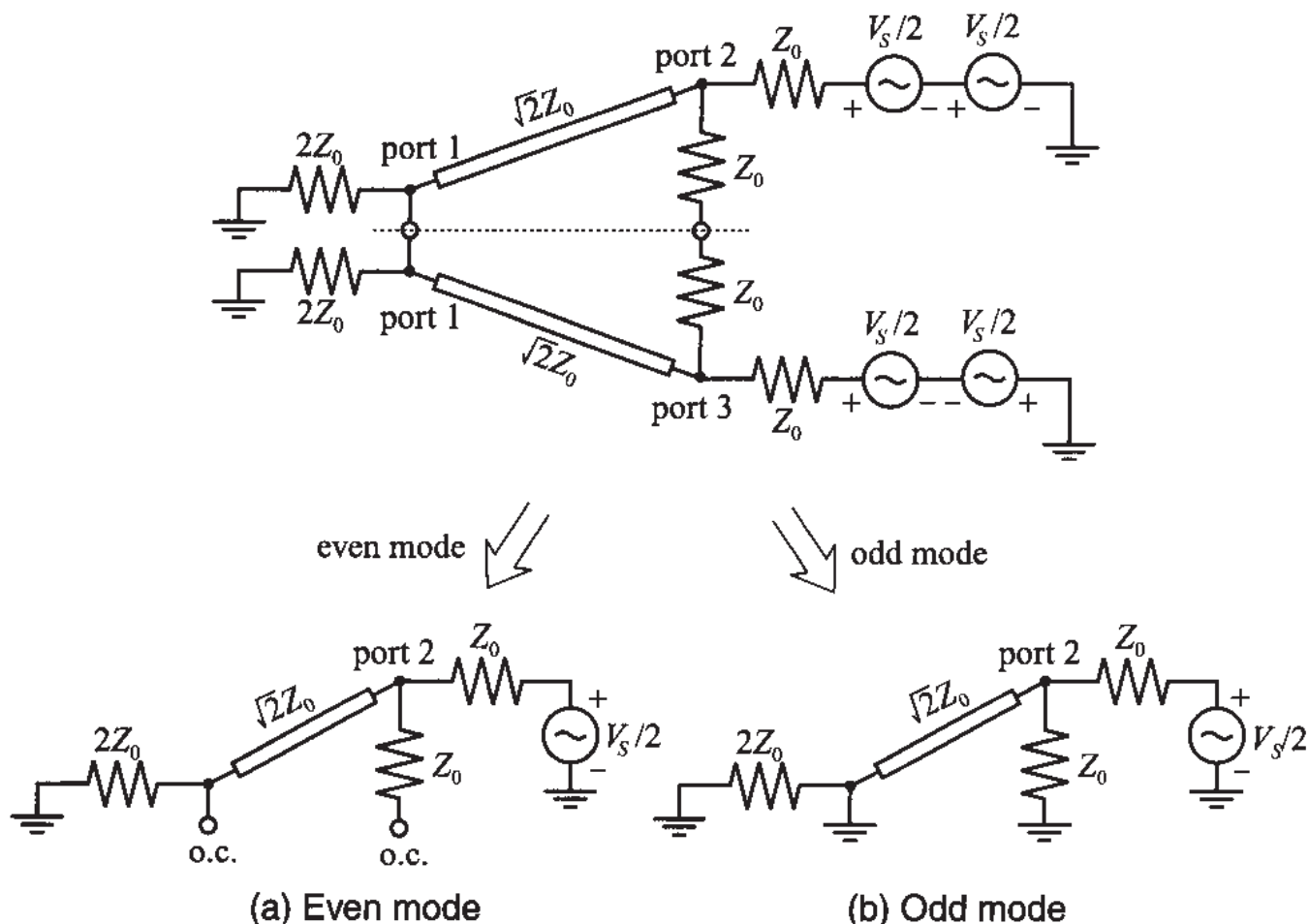


Figure G-3 Even and odd mode representation of Wilkinson divider
(o.c. = open circuit).

The reason for choosing the odd and even mode decomposition becomes immediately apparent. Let us consider at first the circuit in Figure G-3(a), which is driven by an even mode, meaning that the drive signals at ports 2 and 3 are in phase. In this case both ends of the $2Z_0$ cross impedance have the same potential. Thus, there is no current flow

and the impedance can be neglected. The input impedance seen at port 2 for this case is the impedance of a $\sqrt{2}Z_0$ quarter-wave transformer terminated with a $2Z_0$ load [i.e., $Z_2 = (\sqrt{2}Z_0)^2/(2Z_0) = Z_0$]. Consequently, in the even mode excitation, port 2 is perfectly matched and the voltage at port 2 is $V_2^e = 0.5(V_s/2) = V_s/4$. The corresponding voltage at port 1 can be found based on our discussion regarding the voltage distribution along a transmission line (see Chapter 2):

$$V_1^e = V^+(1 + \Gamma_0^e) \quad (G.5)$$

where $\Gamma_0^e = (2Z_0 - \sqrt{2}Z_0)/(2Z_0 + \sqrt{2}Z_0)$ is the even mode reflection coefficient at port 1. Therefore, the even mode voltage at port 1 is

$$V_1^e = V^+(1 + \Gamma_0^e) = jV_2^e \frac{\Gamma_0^e + 1}{\Gamma_0^e - 1} = \frac{-j\sqrt{2}}{4} V_s \quad (G.6)$$

and where the factor j is due to the $\lambda/4$ transmission line. For the odd mode excitation voltages at ports 2 and 3 have opposite polarities and there is a zero potential along the middle of the circuit. This means that the middle is shorted to ground. Since the input impedance seen from port 2 is again Z_0 and port 1 is grounded, we find that $V_1^o = 0$ and $V_2^o = V_s/4$.

The total voltage at ports 1 and 2 is found by adding the even and odd mode voltages. The corresponding S_{12} parameter is then computed as

$$S_{12} = \frac{V_1}{V_2} = \frac{V_1^e + V_1^o}{V_2^e + V_2^o} = -\frac{j}{\sqrt{2}} \quad (G.7)$$

An identical analysis for the port 3 to 1 configuration results in $S_{13} = -j/\sqrt{2}$. Furthermore, because the divider is a linear, passive network we conclude that $S_{21} = S_{12}$ and $S_{31} = S_{13}$. Also, both in the even and odd mode analysis port 2 is isolated from port 3 by either an open circuit or ground, we find that $S_{23} = S_{32} = 0$. Thus, all off-diagonal terms in (G.1) are verified.

In addition, $S_{22} = S_{33} = 0$ is due to the matching of the odd and even modes. This leaves us only to prove that $S_{11} = 0$. We notice that when port 1 is driven, the current through the $2Z_0$ resistor between ports 2 and 3 is again zero and has no influence on the circuit. Thus, the impedance Z_1 seen at port 1 is a parallel combination of two Z_0 terminations connected through $\sqrt{2}Z_0$ quarter-wave transformers

$$Z_1 = \frac{1}{2} \frac{(\sqrt{2}Z_0)^2}{Z_0} = Z_0 \quad (G.8)$$

This proves that port 1 is matched (i.e., $S_{11} = 0$).

G.2 Branch Line Coupler

There are two 3 dB branch line couplers of importance. According to their phase shifts, they are either referred to as 90° (quadrature) or 180° couplers. The S -parameter representation for the 90° coupler is

$$[S_{90}] = \frac{-1}{\sqrt{2}} \begin{bmatrix} 0 & j & 1 & 0 \\ j & 0 & 0 & 1 \\ 1 & 0 & 0 & j \\ 0 & 1 & j & 0 \end{bmatrix} \quad (\text{G.9})$$

and a circuit schematic is shown in Figure G-4.

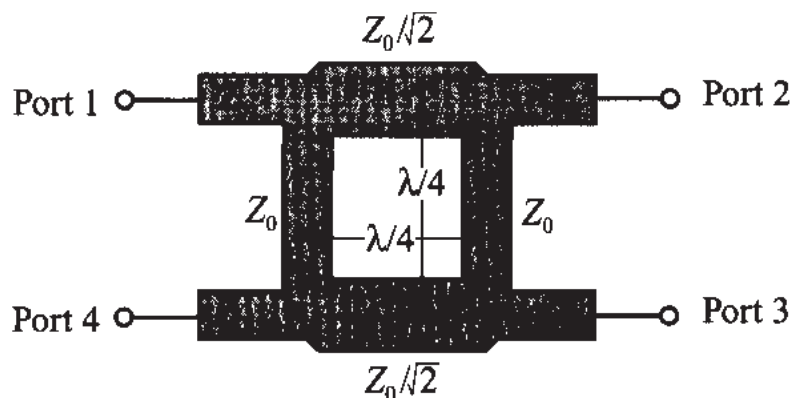


Figure G-4 Microstrip line realization of quadrature hybrid.

Besides return loss, isolation, and coupling definitions given in (G.2)–(G.4), the directivity of a branch coupler is a key parameter and defined as

$$D_{34} = -20\log|S_{34}| \quad (\text{G.10})$$

where D_{34} ideally approaches infinity at f_0 .

In our derivation of (G.9) we begin by using an even and odd mode analysis, as depicted in Figure G-5. We drive the hybrid at port 1 with an RF source V_S and terminate the remaining ports into the characteristic line impedance Z_0 . An equivalent circuit results if the source voltage at port 1 is written as the sum of an even (V_{1e}) and odd (V_{1o}) voltage such that $V_1 = V_S = V_{1e} + V_{1o}$ with $V_{1e} = V_S/2$ and $V_{1o} = V_S/2$. At port 4 we can enforce zero voltage condition by setting $V_4 = 0 = V_{4e} + V_{4o}$, where $V_{4e} = V_S/2$ and $V_{4o} = -V_S/2$.

The total transmitted voltage at port 2 due to the input voltage at port 1 can be established as

$$V_2 = (T_e + T_o) \frac{V_S}{2} = S_{21} V_S \quad (\text{G.11})$$

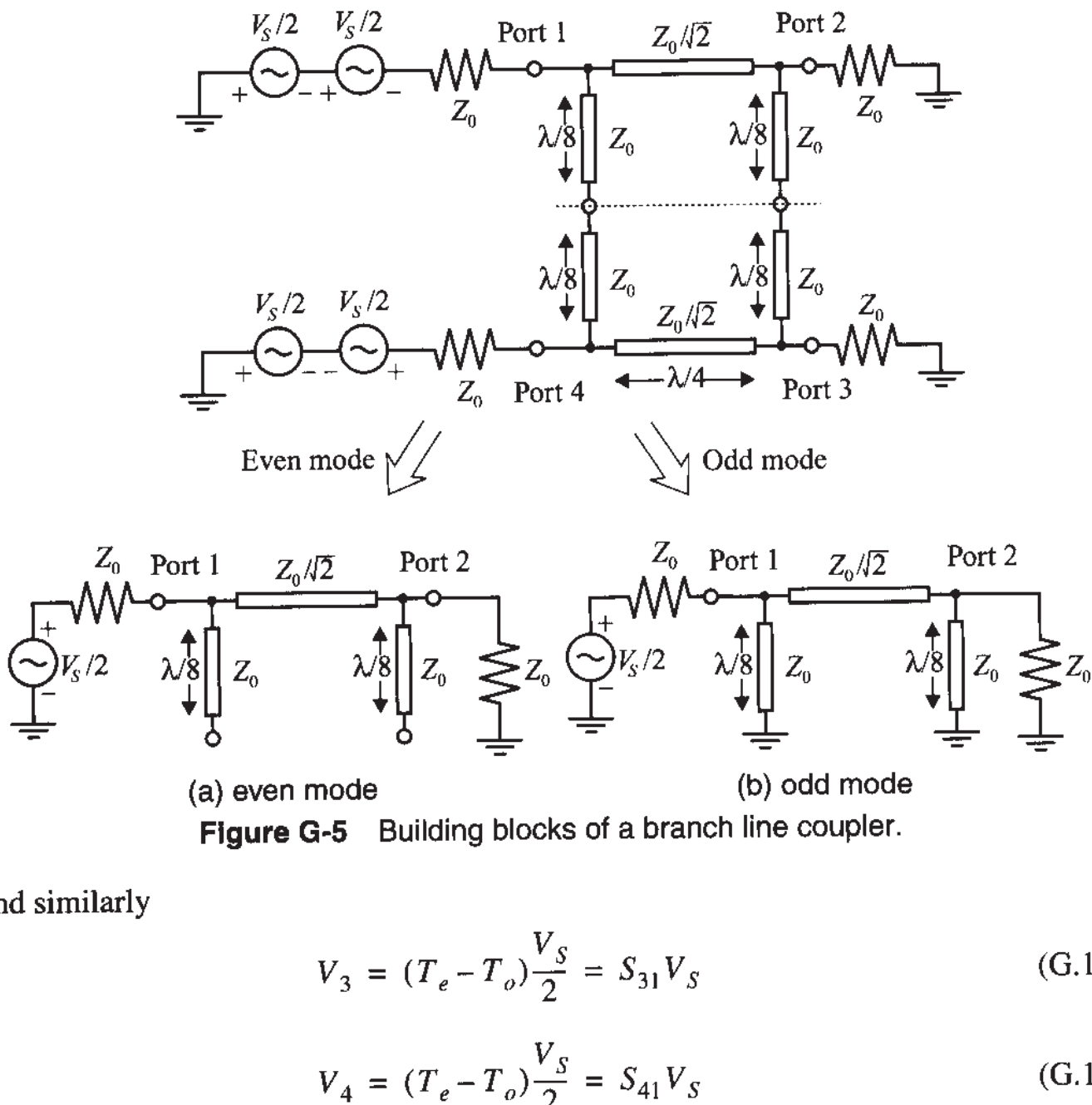


Figure G-5 Building blocks of a branch line coupler.

and similarly

$$V_3 = (T_e - T_o) \frac{V_s}{2} = S_{31} V_s \quad (\text{G.12})$$

$$V_4 = (T_e - T_o) \frac{V_s}{2} = S_{41} V_s \quad (\text{G.13})$$

The reflected signal at port 1 is

$$V_1 = (\Gamma_e + \Gamma_o) \frac{V_s}{2} = S_{11} V_s \quad (\text{G.14})$$

We must next turn our attention toward finding T_e , T_o , Γ_e , and Γ_o . The transmission line circuits in Figure G-5(a) and (b) can be represented as a three-element model involving either short or open-ended stub lines $\lambda/8$ in length.

The even mode and odd mode stub lines have an admittance of

$$Y_e = Y^{oc} = \frac{1}{Z_0} \tan\left(\frac{\pi}{4}\right) \quad \text{and} \quad Y_o = Y^{sc} = \frac{-1}{Z_0} \cot\left(\frac{\pi}{4}\right) \quad (\text{G.15})$$

The three-component circuit in *ABCD* network representation is then

$$\begin{aligned} \begin{Bmatrix} V_{U1} \\ I_{U1} \end{Bmatrix} &= \begin{bmatrix} 1 & 0 \\ jY_{e,o} & 1 \end{bmatrix} \begin{bmatrix} \cos(\beta l) & jY_A^{-1} \sin(\beta l) \\ jY_A \sin(\beta l) & \cos(\beta l) \end{bmatrix} \begin{bmatrix} 1 & 0 \\ jY_{e,o} & 1 \end{bmatrix} \begin{Bmatrix} V_{U2} \\ -I_{U2} \end{Bmatrix} \\ &= \begin{bmatrix} A & B \\ C & D \end{bmatrix} \begin{Bmatrix} V_{U2} \\ -I_{U2} \end{Bmatrix} \end{aligned} \quad (\text{G.16})$$

where $Y_A = 1/Z_A$ is the admittance of the $\lambda/4$ line element. Multiplying the three matrices and converting the result into *S*-parameter form yields, after some rather tedious computations, the following nonzero coefficients: $S_{21} = S_{12} = -j(Z_A/Z_0)$, $S_{43} = S_{34} = -j(Z_A/Z_0)$, and $S_{31} = S_{13} = -[1 - (Z_A/Z_0)^2]^{1/2} = S_{42} = S_{24}$. Setting $Z_A = Z_0/\sqrt{2}$ gives the desired matrix listed in (G.9). Again, it is noted that all four ports are matched into Z_0 .

The 180° coupler can be constructed by adjusting the lengths of the four transmission line segments and arranging the impedances in a ring configuration, as shown in Figure G-6.

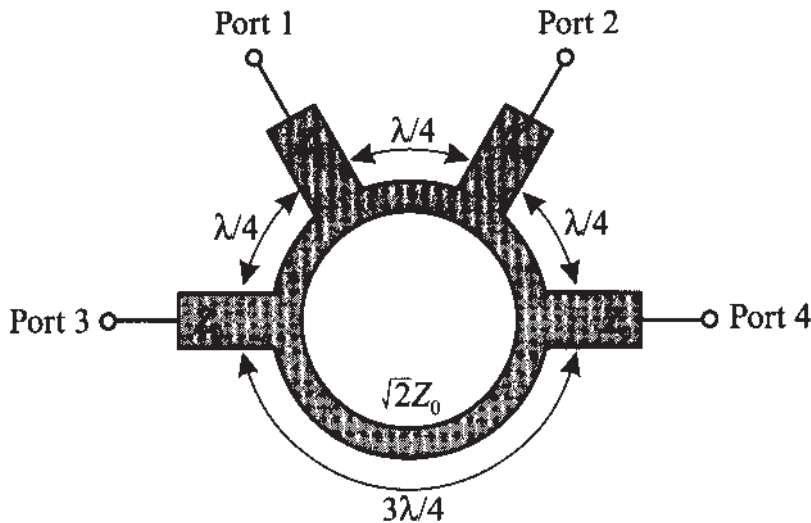


Figure G-6 A 180° ring coupler.

The *S*-parameter matrix for this configuration, also known as “rat race,” is given by

$$[\mathbf{S}_{180}] = \frac{-j}{\sqrt{2}} \begin{bmatrix} 0 & 1 & 1 & 0 \\ 1 & 0 & 0 & -1 \\ 1 & 0 & 0 & 1 \\ 0 & -1 & 1 & 0 \end{bmatrix} \quad (\text{G.17})$$

G.3 Lange Coupler

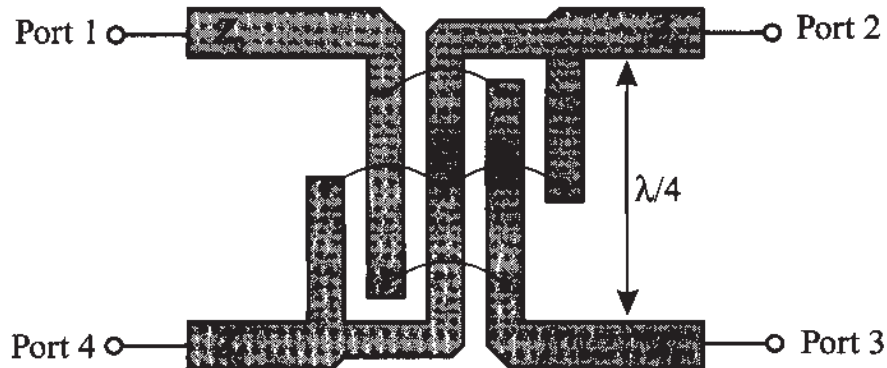


Figure G-7 A 3 dB Lange coupler.

A popular implementation of the quadrature hybrid in microstrip line form is the so-called Lange coupler shown in Figure G-7 for a four-strip configuration. Additional variations involve six- and eight-strip realizations. The interdigital form of the microstrips permits a very compact geometric size and provides for tight coupling.

Typical coupling values range between -5 and -1 dB. By choosing the length of the microstrip elements appropriately, a very broadband realization of up to 40% bandwidth can be achieved.

Further Reading

P. Karmel, G. Colef, and R. Camisa, *Introduction to Electromagnetic and Microwave Engineering*, John Wiley, New York, 1998.

J. Lange, "Interdigitated stripline quadrature hybrid," *IEEE Trans. on MTT*, Vol. 17, pp. 1150–1151, 1969.

Noise Analysis

The intent of this appendix is to provide an overview of the most important noise definitions and concepts as related to the noise figure analysis conducted in Chapter 9.

H.1 Basic Definitions

In a broad sense noise can be characterized as any undesired signal that interferes with the main signal to be processed. Examples of noisy signals are AC power coupling, crosstalk between circuits and electromagnetic (EM) radiation to name but a few sources. Mathematically we use **random variables** of Gaussian distribution and zero mean to describe the noise behavior. Although the mean is zero, the **root mean square** (RMS) value of a noisy voltage signal $v_n(t)$ is not. This can be expressed as

$$V_{n\text{RMS}} = \sqrt{V_n^2} = \left\{ \lim_{T_M \rightarrow \infty} \int_{T_1}^{T_1 + T_M} [v_n(t)]^2 dt \right\}^{1/2} \neq 0 \quad (\text{H.1})$$

where T_1 is an arbitrary point in the time and T_M is the measurement interval.

In 1928 Johnson first observed the fact that a resistor in the absence of any external current flow generates noise due to the random motion of charge carriers in the conductor. The **noise power** in a conductor is quantified as

$$P_n = kT\Delta f = kTB \quad (\text{H.2})$$

where k is Boltzmann's constant, T is the absolute temperature in °K, and $\Delta f = B$ is the **noise bandwidth** of the measurement system. The noise bandwidth is defined as the integration of the instrument's gain $G(f)$ over all frequencies normalized with respect to the maximum gain G_{\max} :

$$B = \frac{1}{G_{\max}} \int_0^{\infty} G(f) df \quad (\text{H.3})$$

We next turn our attention to the noise voltage. Let us consider the simple circuit shown in Figure H-1.

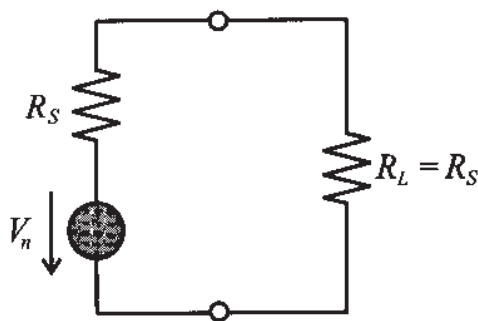


Figure H-1 Noise voltage of a circuit.

According to this circuit, the noise power is treated as if a noise voltage source drives a noiseless resistor R_S . Under matching condition $R_S = R_L$, the noise power of the resistor is given as

$$P_n = \frac{V_{n\text{RMS}}^2}{4R_S} = kTB \quad (\text{H.4})$$

from which the RMS noise voltage is found

$$V_{n\text{RMS}} = \sqrt{4kTB R_S} \quad (\text{H.5})$$

To keep the notation simple (and since no ambiguity will arise) the subscript RMS is dropped (i.e., $V_{n\text{RMS}} \equiv V_n$). In general, we represent a noisy resistor R as a noise voltage source in series with the noise free resistor R (Thévenin equivalent circuit) or as a noise current source $I_n = \sqrt{4kTB/R}$ in shunt with a noise free resistor, as shown in Figure H-2.

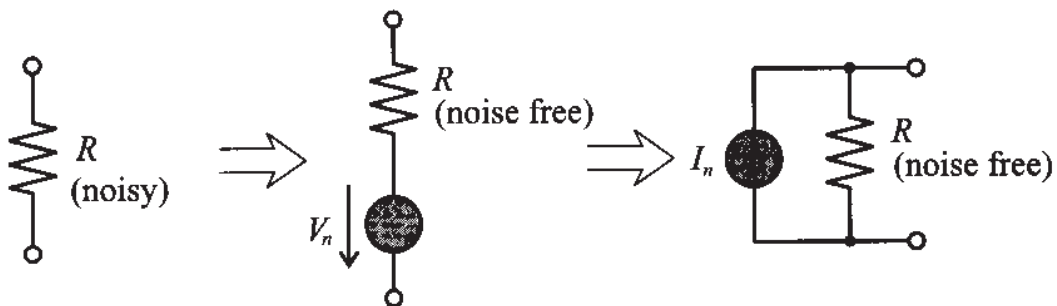


Figure H-2 Equivalent voltage and current models for noisy resistor.

If the bandwidth is eliminated from (H.5) we can define a so-called **spectral noise voltage** and a **spectral noise current**:

$$\overline{V_n} = V_n / \sqrt{B} \quad \text{and} \quad \overline{I_n} = I_n / \sqrt{B} \quad (\text{H.6})$$

whose units are given in $\text{V}/\sqrt{\text{Hz}}$ and $\text{A}/\sqrt{\text{Hz}}$.

Frequently, the **spectral density** $S(f)$ is used to quantify the noise content in a unit bandwidth of 1 Hz. For the thermal noise source associated with resistor R , it is given by

$$S(f) = \frac{V_n^2}{B} = 4kTR \quad (\text{H.7})$$

If $S(f)$ is a constant (i.e., independent of frequency), we speak of **white noise**. Care is required when noisy elements are added in a circuit. For instance, if two noisy resistors R_1 and R_2 are added, the associated noise sources V_{n1} and V_{n2} cannot be linearly summed. Instead, the resultant noise source V_n is

$$V_n = \sqrt{V_{n1}^2 + V_{n2}^2} \quad (\text{H.8})$$

provided both noise sources are **uncorrelated**. This is equivalent to saying that only power proportional voltage square quantities can be added because of their random distribution of amplitudes and phases as well as different nonharmonic frequencies.

If the noise sources are **correlated**, a correlation coefficient $C_{n1, n2}$ enters (H.8) such that

$$V_n^2 = V_{n1}^2 + V_{n2}^2 + 2C_{n1, n2}V_{n1}V_{n2} \quad (\text{H.9})$$

where $-1 \leq C_{n1, n2} \leq 1$. It is interesting to observe that if V_{n1} and V_{n2} are 100% correlated ($C_{n1, n2} = 1$), then $V_n^2 = V_{n1}^2 + V_{n2}^2 + 2V_{n1}V_{n2} = (V_{n1} + V_{n2})^2$ and the voltages can again be added, in agreement with Kirchhoff's linear circuit theory.

The thermal noise of a resistor is also referred to as an **internal noise** source, since no external current has to be impressed to observe the noise voltage. However, many noise mechanisms only occur due to externally impressed current flow through the device. They are collectively known as **excess noise**. Chief among them are the $1/f$ noise (also known as flicker noise, semiconductor noise, pink noise) and shot noise. The $1/f$ noise is most prominent at low frequencies and exhibits, as the name implies, an inverse frequency-dependent spectral distribution. It was first encountered in vacuum tubes as a result of "flickering" noticed on the plates. The **shot noise** is most important in semiconductor devices and can be attributed to the discontinuous current flow across junction potential barriers. As an example, in a semiconductor diode the reverse bias noise current I_{Sn} is given as

$$I_{Sn} = \sqrt{4qI_S B} \quad (\text{H.10})$$

where I_S is the reverse saturation current and q is the electron charge.

H.2 Noisy Two-Port Networks

The previous analysis can be expanded to two-port networks. Figure H-3 shows a noisy network and the equivalent noise-free network augmented by two current noise sources I_{n1} and I_{n2} .

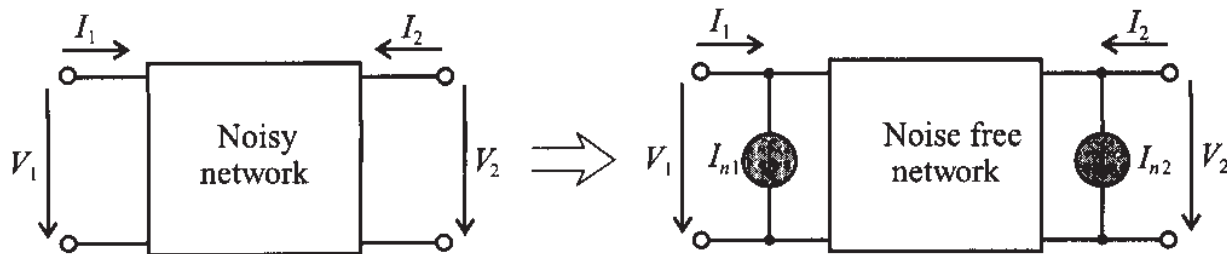


Figure H-3 Noisy two-port network and its equivalent representation.

In Y -parameter matrix representation we can write

$$\begin{Bmatrix} I_1 \\ I_2 \end{Bmatrix} = \begin{bmatrix} Y_{11} & Y_{12} \\ Y_{21} & Y_{22} \end{bmatrix} \begin{Bmatrix} V_1 \\ V_2 \end{Bmatrix} + \begin{Bmatrix} I_{n1} \\ I_{n2} \end{Bmatrix} \quad (\text{H.11})$$

A more useful representation is obtained when rearranging (H.11) as follows:

$$V_1 = -\frac{Y_{22}}{Y_{21}}V_2 + \frac{1}{Y_{21}}I_2 - \frac{1}{Y_{21}}I_{n2} \quad (\text{H.12a})$$

and

$$I_1 = \frac{Y_{11}Y_{22} - Y_{12}Y_{21}}{Y_{21}}V_2 + \frac{Y_{11}}{Y_{21}}I_2 + I_{n1} - \frac{Y_{11}}{Y_{21}}I_{n2} \quad (\text{H.12b})$$

Defining the transformed voltage and current noise sources

$$V_n = -\frac{1}{Y_{21}}I_{n2} \text{ and } I_n = I_{n1} - \frac{Y_{11}}{Y_{21}}I_{n2} \quad (\text{H.13})$$

we arrive at the network model shown in Figure H-4.

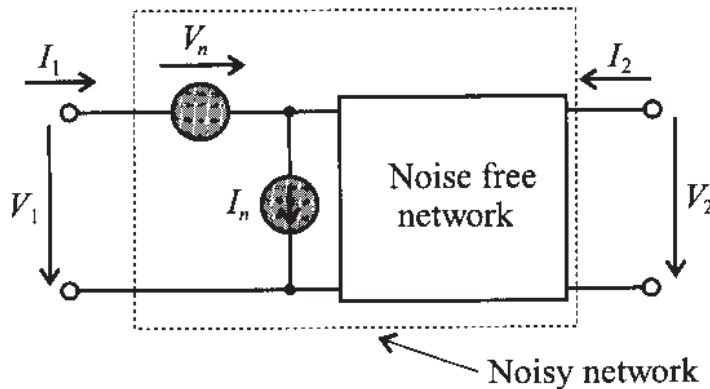
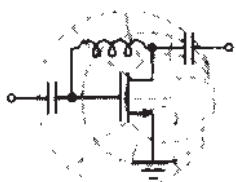


Figure H-4 Transformed network model with noise sources at the input.

To apply the various noise definitions and concepts to a practical example, let us consider a simplified BJT amplifier.



RF & MW

Example H-1: Noise analysis of a low-frequency BJT amplifier

In Figure H-5 a simplified BJT amplifier is treated as a two-port network consisting of the following parameters: $V_S = 25 \text{ mV}$, $R_S = 50 \Omega$, $R_{in} = 200 \Omega$, voltage gain $g_V = 50$, and measurement bandwidth $B = 1 \text{ MHz}$. The spectral noise voltage and current of the amplifier are given by the manufacturer as $\overline{V_n} = 9 \text{ nV}/\sqrt{\text{Hz}}$ and $\overline{I_n} = 9 \text{ fA}/\sqrt{\text{Hz}}$. Find the signal-to-noise ratio $\text{SNR} = 20\log(V_2/V_{n2})$ at the output.

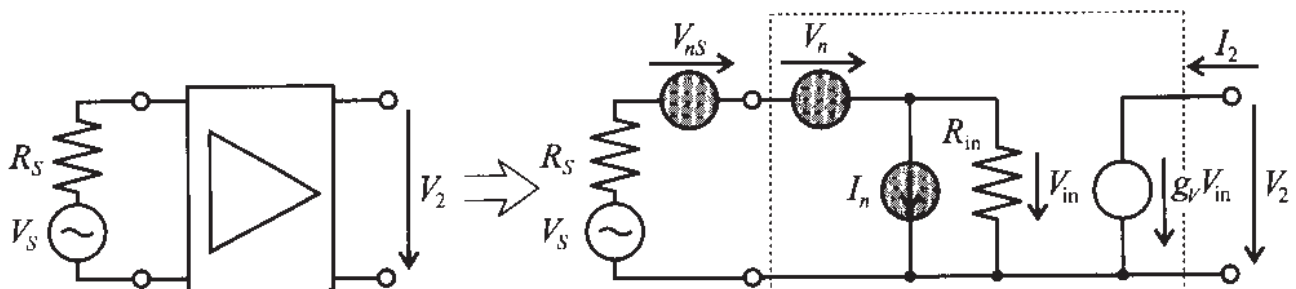


Figure H-5 Amplifier model and network representation with noise sources.

The output voltage V_2 is directly found from $V_2 = g_V R_{in} / (R_{in} + R_S) V_S = 1 \text{ V}$. The spectral noise sources of the network are next expressed in RMS noise voltage and current:

$$V_n = \overline{V_n} \sqrt{B} = 9 \mu\text{V} \quad \text{and} \quad I_n = \overline{I_n} \sqrt{B} = 9 \text{ pA}$$

The voltage source creates through the voltage divider rule the following noise voltage across R_{in} :

$$\frac{R_{in}}{R_{in} + R_S} V_n = 7.2 \text{ nV}$$

The noise current source is responsible for the noise voltage of

$$\frac{R_{in} R_S}{R_{in} + R_S} I_n = 0.36 \text{ nV}$$

Finally, the source resistor contributes the voltage

$$\frac{R_{in}}{R_{in} + R_S} V_{ns} = 728 \text{ nV}$$

where $V_{ns} = \sqrt{4kTBR_S} = 910 \text{ nV}$, assuming $T = 300^\circ\text{K}$.

Therefore, the total noise voltage at the output is

$$V_{n2} = g_V \sqrt{\left(\frac{R_{in}}{R_{in} + R_S} V_n\right)^2 + \left(\frac{R_{in} R_S}{R_{in} + R_S} I_n\right)^2 + \left(\frac{R_{in}}{R_{in} + R_S} V_{ns}\right)^2} = 36.4 \mu\text{V}$$

Finally, the signal to noise ratio is

$$\text{SNR} = 20 \log \left(\frac{V_2}{V_{n2}} \right) = 122.8 \text{ dB}$$

We notice that the noise voltage is dominated by the source.

The example makes clear how the noise voltages are individually computed, added, and amplified to provide the output noise voltage. This is in stark contrast to linear circuit theory.

H.3 Noise Figure for Two-Port Network

The **noise figure** is defined as the ratio between the SNR at the input to the SNR at the output port of a network. Specifically, Figure H-6 depicts the relevant power flow conventions, including the noise representation of the source Z_S .

The noise figure F can be cast into several equivalent representations. The first form involves the ratios of the signal to noise power at the input and output ports:

$$F = \frac{P_1/P_{n1}}{P_2/P_{n2}} = \frac{P_{n2}/P_2}{P_{n1}/P_1} \quad (\text{H.14})$$

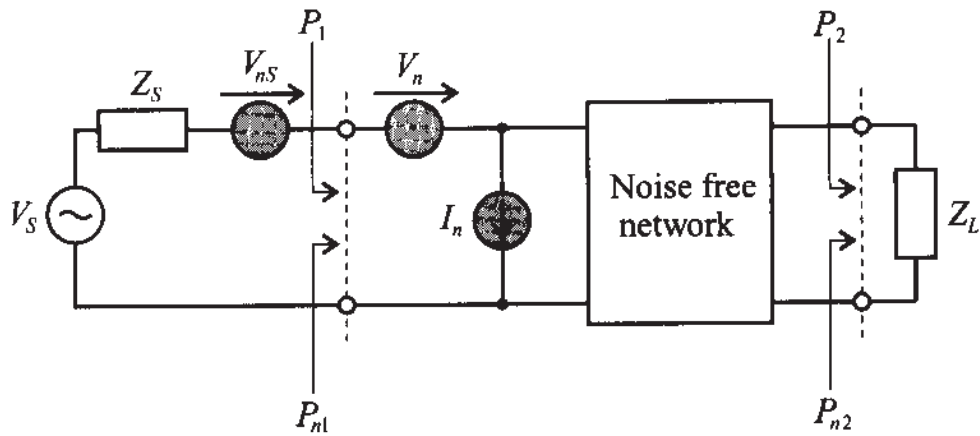


Figure H-6 Generic noise model for noise figure computation.

Employing the available power gain G_A from Section 9.2.3 to express $P_2 = G_A P_1$ and $P_{n2} = G_A P_{n1} + P_{ni}$, (H.14) is re-expressed as

$$F = 1 + \frac{P_{ni}}{G_A P_{n1}} \quad (\text{H.15})$$

where P_{ni} is the internally generated noise power within the amplifier.

Based on Figure H-6, we see that the signal power P_1 is

$$P_1 = \frac{1}{2} \frac{\text{Re}\{Z_{\text{in}}\}}{|Z_S + Z_{\text{in}}|^2} V_s^2 \quad (\text{H.16})$$

which is less than the power under source matching ($Z_S = Z_{\text{in}}^*$):

$$P_1|_{Z_S = Z_{\text{in}}^*} = \frac{1}{2} \left(\frac{|V_s|^2}{4 \text{Re}\{Z_{\text{in}}\}} \right) \quad (\text{H.17})$$

The thermal noise at the input side is with $Z_S = R_S + jX_S$:

$$P_{n1} = 4kTR_S B \frac{\text{Re}\{Z_{\text{in}}\}}{|Z_S + Z_{\text{in}}|^2} = V_{ns}^2 \frac{\text{Re}\{Z_{\text{in}}\}}{|Z_S + Z_{\text{in}}|^2} \quad (\text{H.18})$$

The power ratio is therefore

$$\frac{P_1}{P_{n1}} = \frac{V_s^2}{V_{ns}^2} \quad (\text{H.19})$$

The signal power P_2 is simply $P_2 = G_A P_1$, where P_1 is given by (H.16). For the noise power P_{n2} we set $P_{n2} = G_A P_{n1} + P_{ni}$, where the internally generated noise power P_{ni} takes into account the noise sources associated with the two-port network V_n and I_n . Thus, V_{ns}^2 in (H.18) has to be replaced by all three noise sources:

$V_{ns}^2 + V_n^2 + (I_n R_{in})^2$, where $R_{in} = \text{Re}\{Z_{in}\}$ is the input resistance of the network. Since the gain applies equally to signal and noise, it cancels and we arrive at

$$P_2/P_{n2} = \frac{V_s^2}{V_{ns}^2 + V_n^2 + (I_n R_{in})^2} \quad (\text{H.20})$$

The noise figure therefore takes the form

$$F = \frac{V_{ns}^2 + V_n^2 + (I_n R_{in})^2}{V_{ns}^2} = 1 + \frac{V_n^2 + (I_n R_{in})^2}{4kTBR_{in}} \quad (\text{H.21})$$

The preceding treatment does not take into account the fact that the same noise mechanisms are usually responsible for both V_n and I_n . Thus, these sources are, to a certain degree, correlated. This can be incorporated into the noise model by splitting I_n into an uncorrelated, I_{nu} , and a correlated current, I_{nc} , contribution, respectively. The correlated current contribution is related to the noise voltage V_n via a complex correlation factor $Y_C = G_C + jB_C$, such that $I_{nc} = Y_C V_n$. Since it is more convenient to deal with noise currents than voltages for our network, we convert the source into an equivalent Norton representation, as seen in Figure H-7.

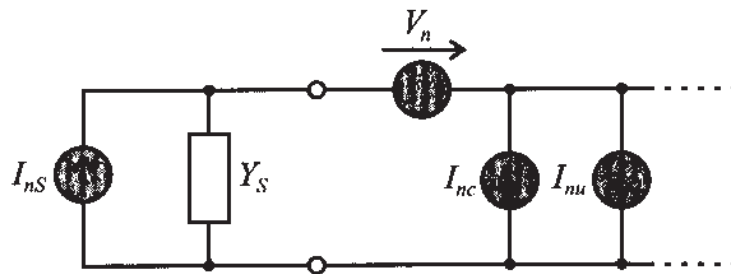


Figure H-7 Noise sources modeled at network input.

The total RMS noise current I_{ntot} under short circuit input conditions can be expressed as

$$I_{ntot}^2 = I_{ns}^2 + V_n^2(Y_S + Y_C)^2 + I_{nu}^2 \quad (\text{H.22})$$

where $I_{nc} = Y_C V_n$ and $I_n = V_n Y_S$ are combined because of their correlation. We can now rewrite (H.21) as

$$F = \frac{I_{ns}^2 + V_n^2(Y_S + Y_C)^2 + I_{nu}^2}{I_{ns}^2} \quad (\text{H.23})$$

Under the assumption that all noise sources are represented by an equivalent thermal noise source, we identify in (H.23)

$$I_{ns}^2 = 4kTBG_S : \text{noise due to the source } Y_S = G_S + jB_S \quad (\text{H.24})$$

$$I_{nu}^2 = 4kTBG_u : \text{noise due to the equivalent noise conductance } G_u \quad (\text{H.25})$$

$$V_n^2 = 4kTBR_n : \text{noise due to the equivalent noise resistance } R_n \quad (\text{H.26})$$

Inserting (H.24)–(H.26) into (H.23) gives

$$F = 1 + \frac{G_u + R_n|Y_S + Y_C|^2}{G_S} = 1 + \frac{G_u}{G_S} + \frac{R_n}{G_S}[(G_S + G_C)^2 + (B_S + B_C)^2] \quad (\text{H.27})$$

The circuit designer can minimize (H.27) through an appropriate choice of source admittance Y_S . This process is accomplished by first observing that the imaginary part can be chosen such that $B_S = -B_C$. This eliminates the $(B_S + B_C)^2$ term in (H.27). Next, the remaining expression is minimized with respect to G_S ; that is,

$$\frac{dF(B_S = -B_C)}{dG_S} = \frac{1}{G_{S\text{opt}}^2} \{R_n[2G_{S\text{opt}}(G_{S\text{opt}} + G_C) - (G_{S\text{opt}} + G_C)^2]\} = 0 \quad (\text{H.28})$$

which yields the explicit optimum value

$$G_{S\text{opt}} = \frac{1}{\sqrt{R_n}} \sqrt{R_n G_C^2 + G_u} \quad (\text{H.29})$$

The **minimum noise figure** is thus obtained by the optimal source admittance

$$Y_{S\text{opt}} = \left(\frac{1}{\sqrt{R_n}} \sqrt{R_n G_C^2 + G_u} \right) - jB_C \quad (\text{H.30})$$

Substituting (H.29) into (H.27) results in the expression

$$F_{\min} = 1 + \frac{G_u}{G_{S\text{opt}}} + \frac{R_n}{G_{S\text{opt}}} (G_{S\text{opt}} + G_C)^2 \quad (\text{H.31})$$

Eliminating G_u in (H.31) by using $G_u = R_n G_{S\text{opt}}^2 - R_n G_C^2$ from (H.29) gives

$$F_{\min} = 1 + 2R_n(G_{S\text{opt}} + G_C) \quad (\text{H.32})$$

This number is typically provided by the device manufacturer. It is dependent on frequency and bias conditions. Equation (H.32) can be incorporated into (H.27) with the result

$$F = F_{\min} - 2R_n G_{S\text{opt}} - 2R_n G_C + \frac{G_u}{G_S} + \frac{R_n}{G_S} [(G_S + G_C)^2 + (B_S - B_{S\text{opt}})^2] \quad (\text{H.33})$$

Replacing G_u by $G_u = R_n G_{S\text{opt}}^2 - R_n G_C^2$ and rearranging terms provides the final result

$$F = F_{\min} + \frac{R_n}{G_S} [(G_S - G_{S\text{opt}})^2 + (B_S - B_{S\text{opt}})^2] = F_{\min} + \frac{R_n}{G_S} |Y_S - Y_{S\text{opt}}|^2 \quad (\text{H.34})$$

This is the starting point of our noise circle analysis in Section 9.5. Based on the characteristic line impedance $Z_0 = 1/Y_0$, (H.34) is often expressed in terms of normalized noise resistance $r_n = R_n/Z_0$, conductance $g_S = G_S/Y_0$, and admittances $y_S = Y_S/Y_0$, $y_{S\text{opt}} = Y_{S\text{opt}}/Y_0$ in the form

$$F = F_{\min} + \frac{r_n}{g_S} |y_S - y_{S\text{opt}}|^2 \quad (\text{H.35})$$

H.4 Noise Figure for Cascaded Multiport Network

The previous noise figure discussion for a single two-port network, with P_{n1} being the input noise and $P_{n2} = G_A P_{n1} + P_{ni}$ being the output noise, can be extended to multiple cascaded networks, as shown in Figure H-8.

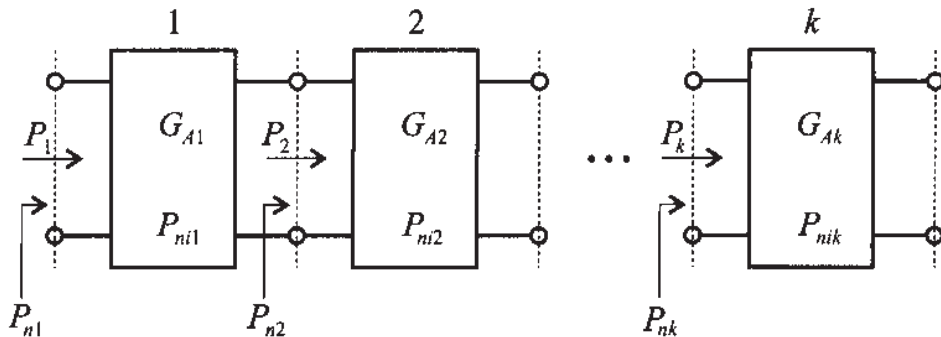


Figure H-8 Cascaded network representation.

In accordance with Figure H-8, we adopt a suitable notation such that G_{Ak} and P_{nik} denote power gain and internal noise generated by amplifier block $k = 1, 2, \dots$. Thus, for the noise power at the second amplifier section it is seen that

$$P_{n3} = G_{A2}(G_{A1}P_{n1} + P_{n1}) + P_{n2} \quad (\text{H.36})$$

or for the total noise figure F_{tot} we see

$$F_{\text{tot}} = \frac{P_{n3}}{P_{n1}G_{A1}G_{A2}} = 1 + \frac{P_{n1}}{P_{n1}G_{A1}} + \frac{P_{n2}}{P_{n1}G_{A1}G_{A2}} \quad (\text{H.37})$$

It is customary to retain the same noise figure expression for the individual blocks as derived for the single network; that is,

$$F_1 = 1 + \frac{P_{ni1}}{P_{n1}G_{A1}}, F_2 = 1 + \frac{P_{ni2}}{P_{n1}G_{A2}}, \dots, F_k = 1 + \frac{P_{nik}}{P_{nk}G_{Ak}} \quad (H.38)$$

For two networks this concept leads to the expression

$$F_{\text{tot}} = F_1 + \frac{F_2 - 1}{G_{A1}} \quad (H.39)$$

or for multiple cascaded networks

$$F_{\text{tot}} = F_1 + \frac{F_2 - 1}{G_{A1}} + \frac{F_3 - 1}{G_{A1}G_{A2}} + \dots + \frac{F_k - 1}{G_{A1}G_{A2}\dots G_{A(k-1)}} + \dots \quad (H.40)$$

The preceding considerations have important practical implications. For instance, if two amplifier stages with different gains and noise figures (F_1, G_{A1} and F_2, G_{A2}) are to be cascaded, which sequence of these stages results in the lowest noise figure? To answer this question, let us hypothetically assume amplifier block 1 (F_1, G_{A1}) is followed by amplifier block 2 (F_2, G_{A2}). The total noise figure for this configuration is

$$F_{\text{tot}}(1, 2) = F_1 + \frac{F_2 - 1}{G_{A1}} \quad (H.41)$$

On the other hand, if block 2 is followed by block 1, we obtain

$$F_{\text{tot}}(2, 1) = F_2 + \frac{F_1 - 1}{G_{A2}} \quad (H.42)$$

Under the assumption that $F_{\text{tot}}(1, 2)$ has a lower noise figure than $F_{\text{tot}}(2, 1)$, the following inequality must hold:

$$F_1 + \frac{F_2 - 1}{G_{A1}} < F_2 + \frac{F_1 - 1}{G_{A2}} \quad (H.43)$$

Rewriting (H.43)

$$(F_1 - 1)\left(1 - \frac{1}{G_{A2}}\right) < (F_2 - 1)\left(1 - \frac{1}{G_{A1}}\right) \quad (H.44)$$

allows us to define

$$NM_1 < NM_2 \quad (H.45)$$

where $NM_1 = (F_1 - 1)/(1 - G_{A1}^{-1})$ and $NM_2 = (F_2 - 1)/(1 - G_{A2}^{-1})$ are the **noise measures** of amplifiers 1 and 2, respectively. In other words, it is a combination of noise figure and gain that determines the noise measure as a basis of an overall noise performance comparison.

Introduction to MATLAB

A considerable number of MATLAB simulations have been created to enable the reader to reproduce the results presented in the examples. Moreover, it is hoped that these so-called **M-files** will stimulate and encourage the reader to develop code on his or her own relative to the RF topics covered in the ten chapters. This appendix is neither a tutorial of MATLAB nor a detailed discussion of the software written in support of this textbook. Rather, it is hoped that sufficient background is provided to understand how MATLAB routines are created, and how code can be written to reproduce some of the results and graphs presented in the text. Being a general-purpose mathematical spreadsheet tool, MATLAB does not replace specifically developed RF and MW CAD programs, such as MMICAD and ADS, with their powerful circuit analysis, optimization, and even layout utilities. Such dedicated simulation packages cannot be expected to be available to the general reader. For this reason, the authors have attempted to use MATLAB as a package that is widely available to students and at very reasonable cost. For more information regarding the use of MATLAB the reader should refer to the following Web site: <http://www.mathworks.com>.

This appendix first provides some general background as to how we created the M-files, followed by a brief example of how they are used in the context of a stability analysis, as done in Chapter 9. All M-files can be downloaded from our Web site: http://www.wpi.edu/ece/EM_RF_LAB/book.

I.1 Background

MATLAB is an easy-to-use mathematical spreadsheet with the capabilities to write special routines for mathematically evaluating the equations discussed in the main text and to display the results graphically. The authors have MATLAB implemented on a PC with a 450 MHz Pentium II processor, 128 MB RAM and 8 GB disk space. This does not constitute a mimimal configuration; it merely reflects the environment used during the writing of this textbook.

Upon executing MATLAB, a window is opened with a command line indicator >>. The appropriate directory can be checked with the command `pwd`, which yields

```
>>pwd
ans =
d:\RF\simulations
```

indicating that the directory is located on d-drive under subdirectories RF\simulations. Changing to a different directory can be initiated through the command `cd`, and a listing of the files within a directory is done with the commands `ls` or `dir`.

By way of an example from Chapter 2, let us consider the following command lines, which can be executed sequentially, each line terminated by pressing **ENTER**.

```
I=5
a=0.005
N=100
M=10
r=(0:N)/(M*a)
for k=1:N+1
    if(r(k)<=a)
        H(k)=I*r(k)/(2*pi*a*a)
    else
        H(k)=I/(2*pi*r(k))
    end
end
plot(r*1000,H,'k')
```

In the first line of the program we specify a current through the wire. The second line defines the wire radius. Variables `N` and `M` specify the number of points and the maximum distance from the center of the wire at which the magnetic field will be computed. In our case `M=10`, which means that we will look at distances ranging from 0 to 10 wire radii, and the number of points is set to `N=100`. The fifth line of the code defines a one-dimensional array of points that determine the actual position from the center of the wire. The command `(0:N)` creates an array of $N + 1$ elements with values of 0, 1, 2, 3, etc. After dividing this array by `N`, the values range between 0 to 1. Next, the array is scaled so that the distance changes from 0 to `M*a`. An alternative way to define this array would be `r=(0:M*a/N:M*a)`, where the parameter between the two colons defines the step size.

The next line of the code starts a `for` loop cycle for `k` ranging from 1 to `N+1`. For each `k` we take the corresponding radius from the array `r` and check whether it is less or greater than the wire radius. As discussed in Chapter 2, the field inside the wire is linear

$$H = \frac{Ir}{2\pi a^2}$$

with respect to the radial distance, whereas outside the wire we observe

$$H = \frac{I}{2\pi r}$$

The last line of the code instructs the program to plot a graph of the magnetic field H versus radius r . The graph is shown in black, which is specified in the last parameter of the `plot` instruction. Some of the possible choices for color include ‘k’—black, ‘r’—red, ‘y’—yellow, ‘b’—blue, and ‘g’—green. Other useful options for creating graphs include the following:

`semilogx`—logarithmic scale along x -axis, linear scale on y -axis
`semilogy`—logarithmic scale along y -axis, linear scale on x -axis
`loglog`—logarithmic scale on both axes
`polar`—polar plot

The entire list of commands can be entered in an interactive mode by using the command line. Alternatively, the commands can be placed in a file for batch-mode execution. For example, we can save this program in a file with name `field.m`; then to execute this program we simply type `>>field` on the MATLAB command line. Note that `.m` is a file extension reserved for use by MATLAB.

I.2 Brief Example of Stability Evaluation

Another useful capability of MATLAB is the creation of functions. For example, the following listing is a function that takes an array of S -parameter data (`s_param`) and computes two output parameters: the stability factor k and $|\Delta|$, denoted as `k` and `delta`.

```
function [K,delta] = K_factor(s_param)
% Usage: [K,delta] = K_factor(s_param)
%
% Purpose: returns K factor for a given s-parameter matrix
% if K>1 and delta<1 then circuit is unconditionally stable
% otherwise circuit might be unstable

s11=s_param(1,1);
s12=s_param(1,2);
s21=s_param(2,1);
s22=s_param(2,2);

delta=abs(det(s_param));
K=(1-abs(s11).^2-abs(s22).^2+delta.^2)./(2*abs(s12.*s21));
```

The first line in the listing defines a function `K_factor` that takes one input parameter `s_param` and returns two values as a result: `K` and `delta`, which are computed inside the function. Unlike program scripts, files containing functions must have the same name as the function name. Therefore, this function is stored in the file `K_factor.m`.

If the user does not know or forgot how to use the function, he or she can type `help K_factor` in the command line of MATLAB, and the comments that follow the first line in the function will be displayed.

The program file for creating the *S*-parameter matrix of a particular transistor and the stability check as well as the display of the stability circles is shown in the next file, entitled `test.m`

```
* s-parameters for hypothetical transistor
close all;

s11=0.7*exp(j*(-70)/180*pi);
s12=0.2*exp(j*(-10)/180*pi);
s21=5.5*exp(j*(+85)/180*pi);
s22=0.7*exp(j*(-45)/180*pi);

s_param=[s11,s12;s21,s22];

% check stability
[K,delta] = K_factor(s_param)

% create a Smith Chart
smith_chart;

% plot input and output stability circles
input_stability(s_param, 'r');
output_stability(s_param, 'b');

% create PostScript copy of the figure
print -deps 'fig9_8.eps'
```

This file is not a function; it is a collection of commands (program script) and therefore can have any name. In our case we use the name `test.m`.

We notice that the *S*-parameters are given in magnitude and phase and stored in an array called `s_param`. Next, a stability check is performed by passing on the `s_param` array into the M-file `K_factor.m`, whose task is to find the stability factor and $|\Delta|$ based on equations (9.24) and (9.29). After this we call three user-defined functions:

- `smith_chart`—creates a figure containing the Z-Smith Chart.

- `input_stability`—draws the input stability circles computed from the supplied S-parameters. Circles are drawn in the currently active figure (Smith Chart) and use a specified color (red in our case).
- `output_stability`—draws the output stability circles in the currently active figure.

The last line of the script creates a file called `fig9_8.eps`, which contains the figure stored in PostScript format. This is the format employed to produce most of the simulation results throughout the book.

I.3 Simulation Software on Compact Disk

I.3.1 Overview

The intent of the software contained on this CD is to provide support for the material covered in the textbook. All programs have been developed and tested using MATLAB Version 5.2. Although the authors believe that all routines should be compatible with earlier versions of MATLAB, this may not be the case. The software is maintained and regularly updated through our Web-site at www.wpi.edu/ece/EM_RF_lab/book.

I.3.2 Software Installation

The installation of the RF software involves the following steps:

1. Copy the entire directory `rf_matlab` onto the desired harddrive location.
2. Invoke MATLAB.
3. At the command prompt in the main MATLAB window type: `cd c:\rf_matlab`, (here it is assumed that all files are copied to disc-drive C)
4. At the MATLAB command line type `set_path`. This will add all necessary paths to the search tree of the MATLAB. If you do not wish to save this information for future use you can stop the installation process now. In this case you will be able to run all programs but all path information will be deleted after closing MATLAB. If you decide to store the path information for future use, continue with the next step.
5. In the MATLAB command window go to the `file\set path` option. This will launch the path browser.
6. In the path browser go to the `file\save path` option shown the main window.
7. At this step all path information is stored and you can begin to run the M-file routines from the command line.

I.3.3 File Organization

All files are organized in the directory structure shown below and the content of each folder is described in the table.

|  RF_matlab | Folder name | Description |
|--|--------------------|---|
|  ch01 | RF_matlab | Root directory |
|  ch02 | ch01-ch10 | Selected examples and figures for chapters 1 through 10. |
|  ch03 | | |
|  ch04 | | |
|  ch05 | | |
|  ch06 | | |
|  ch07 | | |
|  ch08 | | |
|  ch09 | | |
|  ch10 | | |
|  tools | | |
|  amplifiers | amplifiers | Programs for computation of stability factor and simultaneous complex-conjugate matching for the bilateral design |
|  circles | circles | Various circle equations |
|  gain | gain | Constant gain circles |
|  noise | noise | Constant noise circles |
|  quality | quality | Constant Q_n circles |
|  stability | stability | Stability circles |
|  conversion | conversion | Conversion routines between different two-port network representations |
|  global | global | Some useful routines for the computation of the input and output reflection coefficients, VSWR, etc. |
|  networks | networks | Routines for the definition of matching network circuit topologies |
|  smith | smith | Programs related to the construction and plotting of various arcs in the Smith Chart |

Additional information for each of the programs can be obtained by executing the command **help <program_name>**, where **<program_name>** is the name of the particular m-file. For example, to obtain help about the program **smith_chart.m**, you execute the command **help smith_chart** in MATLAB's main window.

Further Reading

Student Edition of MATLAB, The MathWorks, Inc., 1995.

Index

- A**
- ABCD*-matrix, 148, 194, 244–45
ABCD network representation, 156–61
of an impedance element, 157–58
of a T-network, 158–59
of a transmission line section, 159–61
- Active biasing networks, 449
design of, for BJT in common-emitter configuration, 452–53
- Active RF component modeling, 351–404
diode models, 352–57
linear diode model, 354–57
nonlinear diode model, 352–54
measurements, 385–97
of AC parameters of bipolar transistors, 387–92
of DC parameters of bipolar transistors, 385–87
of field effect transistor parameters, 392–93
scattering parameter device characterization, 393–97
transistor models, 357–85
large-signal BJT models, 357–66
large-signal FET models, 378–81
small-signal BJT models, 366–78
small-signal FET models, 382–85
- Active RF components, 271–350
bipolar-junction transistor (BJT), 312–28
brief history of, 312
construction of, 312–14
frequency response, 321–23
functionality of, 314–21
limiting values, 327–28
temperature behavior, 323–27
types of, 312
- high electron mobility transistors, 338–43
computation of HEMT-related electric characteristics, 341–42
construction of, 339
frequency response, 343
functionality of, 339–42
pseudomorphic HEMTs (pHEMTs), 339
- RF diodes, 293–311
BARRITT diodes, 311
Gunn diodes, 311
IMPATT diodes, 304–7
PIN diodes, 296–301
Schottky diode, 293–96
TRAPATT diodes, 311
tunnel diodes, 307–10
varactor diodes, 302–4
- RF field effect transistors, 328–38
construction of, 329–30
frequency response, 337
functionality, 331–37
limiting values, 337–38
- semiconductors, 272–93
See also Active RF component modeling; Bipolar-junction transistor (BJT); Field effect transistors
- Admittance matrix, 145
- Admittance Smith Chart, *See* Y-Smith Chart
- Admittance transformation, 121–26
parametric admittance equation, 121–25
Y-Smith Chart, 124–25
Z-Smith Chart, 121–24
ZY-Smith Chart, 125–26
- Admittance/Y-matrix, 145–48
- ADS, 351
- A/m, 598
- American Wire Gauge (AWG):
chart, 599–600
system, 13
- Ampere, 598
Ampere's law, 47, 48–51, 59, 61–62
- in differential (point) form, 48–49
- Amplifiers:**
- balanced amplifier design, 515–17
 - broadband, 511–22
 - characteristics of, 464
 - class A, 444
 - class AB, 445
 - class B, 445
 - class C, 446
 - classes of operation, 444–49
 - dynamic range, 523–24
 - efficiency computation, 446–49
 - gain compression, 523
 - high-power, 522–26
 - intermodulation distortion (IMD), 524–25
 - multistage, 526–29
 - power amplifier (PA), 4–6
 - power relations, 465–70
 - RF source, 465–66
- RF transistor amplifier designs, 463–538
- AT41410 BJT (Hewlett-Packard), 512–13
- ATF13100 (Hewlett-Packard), 560
- Attenuation behavior vs. normalized frequency, 223
- Available power, 466
- Available power gain, 468, 501–2
- Avalanche breakdown, 327
- Avalanche effect, 304
- B**
- Balanced amplifier design, 515–17
- Bandgap energy, 353
- Bandpass filters, 201, 210–17
with coupled line transmission line segments, 261–62
frequency transformation, 235–37
- Bandstop filters, 201, 210–17, 249
frequency transformation, 237–38
response, 212–13
- Bandwidth, 204
noise, 620
- Bandwidth factor, 249
- Barkhausen criterion, 540–41, 552
- BARRITT diodes, 311
- Base-width modulation, 367
- BFG403W BJT, 520–22
- BFG540 BJT, 527–28
- BFQ65 BJT, 557
- Biasing networks, 444–55
amplifier classes of operation and, 444–49
bipolar transistor biasing networks, 449–54
field effect transistor biasing networks, 455
- Bilateral matching, 508–9
- Binomial low-pass filters, 203
- Bipolar-junction transistor (BJT), 149–52, 312–28
bias conditions, setting for, 372–78
brief history of, 312
construction of, 312–14
forward active mode, 317–19
frequency response, 321–23
functionality of, 314–21
- GaAs field effect transistors (GaAs FETs), 312–14
- high electron mobility transistors (HEMTs), 312
- input/output impedances, determining for, 372–78
- internal resistances/current gain, 151–52
- limiting values, 327–28
- low-frequency hybrid network, description of, 149–51
- parameter nomenclature, 316
- parameters, 373
- reverse active mode, 314–15, 319–20
- saturation mode, 315, 320–21
- S-parameters, computing for, 372–78
- stabilization of, 481–83
- temperature behavior, 323–27
- types of, 312
- Bipolar transistor biasing networks, 449–54
- BJT, *See* Bipolar-junction transistor (BJT)
- Black box methodology, 143
- Blocking capacitors, 298–99
- Boltzmann's constant, 597
- Branches, 178
- Branch line coupler, 616–18
- Breakdowns, 327–28
- Broadband amplifiers, 511–22
balanced amplifier design, 515–17
design of, using frequency compensated matching networks, 512–15
negative feedback circuits, 517–22
- parameters of, 515
- Butterworth filters, 203, 220, 221–24
coefficients for, 223
compared to linear phasse Butterworth and Chebyshev filters, 229–31
- C**
- Calibration procedure, 190
- Capacitance, 598
- Capacitors:
chip, 25–26
high-frequency, 17–21
RF impedance response of, 18–20
- Carbon-composite resistors, 14
- Cascading networks, 155–56
- Cauer low-pass filters, 203
- Cellular phones, 3
- Center frequency, 202
- Chain/*ABCD*-matrix, 148
- Chain scattering matrix, 175–77
- Channel length modulation parameter, 335
- Characteristic line impedance, 63
- Charge:
electric, 598
electron, 597
excess charge carriers, 609
- Chebyshev bandpass filter design, 239–41
- Chebyshev filters, 203, 220, 224–31
coefficients for, 228–29
compared to Butterworth and linear phasse Butterworth filters, 229–31
- Chebyshev polynomials, 203, 224–25
- Chip capacitors, 25–26
- Chip resistors, 24–25
- Circle equation, 604
- Clapp oscillator, 545
- Class A amplifier, 444
- Class AB amplifier, 445
- Class B amplifier, 445
- Class C amplifier, 446
- Coaxial cable, 41–42
- Colpitts oscillator, 545–46
design, 547–49
- Commensurate line length, 243
- Complex numbers, 603–4
basic definition, 603
circle equation, 604
magnitude computations, 603–4
- Complex propagation constant, 62, 71–72
- Compressed Smith Charts, 109
- Computer-aided design (CAD), 119–21, 351
- Conductance, 598
- Conduction angle, 444
- Conduction parameter, 380
- Conductivity, 598
thermal, 608
- Conformal mapping, 65
- Constant current flow in a conductor, magnetic field generated by, 50–52

- Constant gain, 483–502
 bilateral design, 492–95
 operating and available power gain circles, 495–502
 unilateral design, 483–92
 applicability test, 491–92
 unilateral figure of merit, 490–92
- Constant gain circles, derivation of, 485–86
- Constant VSWR circles, 506–11
 design for given gain/noise figure, 509–11
- Conversion compression, mixers, 582
- Conversion gain (CG), mixers, 581
- Conversion loss (CL), mixers, 581
- Correlated noise sources, 622
- Coulomb, 597, 598
- Coupled filter, 253–62
 bandpass filter section, 257–58
 cascading bandpass filter elements, 259–60
 design example, 260–62
 odd/even mode excitation, 254–56
- Couplers, 612–19
 branch line coupler, 616–18
 dual-directional, 394–95
 Lange coupler, 619
 Wilkinson power divider, 612–15
- Coupling, 612
- Coupling coefficient, 564
- Coupling factor, 395
- Current, 598
- Cut-off frequency, 201, 202, 321
- Cylindrical conductor, skin equation for, 601–2
- D**
- Device under test (DUT), 168, 189, 195, 393, 395–96
- Dielectric constant, 608
- Dielectric resonator oscillators, 563–68
 design of, 565–68
- Diffusion length, 610
- Digital-to-analog converter (DAC), 4
- Dimensions, 6–8
- Diode models, 352–57
 linear diode model, 354–57
 nonlinear diode model, 352–54
- Diodes:
 Gunn, 311
 IMPATT, 304–7
 leakage, 354–55
 PIN, 296–301
 RF, 293–311
 Schottky, 293–96
 TRAPATT, 311
 tunnel, 307–10
 varactor, 302–4
- Dipole domains, 573
- Direct current (DC), transition from high-frequency modes of operation to, 1–6
- Directivity factor, 395
- Dispersion-free transmission, 72
- Dissipation factor d , 213
- Double-balanced mixer, 590
- Double-stub matching networks, 440–44
 design of, 442–44
- Downconverted frequency components, 578
- Drain saturation voltage, 332
- Dual-directional coupler, 394–95
- Dual-port network, flowchart analysis of, 181–84
- Dynamic Ebers-Moll chip-model, 359–61
- Dynamic range:
 amplifiers, 523–24
 mixers, 583
 spurious free, 525–26
- E**
- Early effect, 363
- Ebers-Moll BJT model, 351, 357–66, 387, 398
 dynamic Ebers-Moll chip-model, 359–61
 large-signal, transport vs. injection form of, 361–64
- popularity/acceptance of, 363
- Edison, Thomas, 2
- Effective dielectric constant, 65
- Effective width, 69
- Electrical length, 110
- Electric charge, 598
- Electric field, 598
- Electron affinity, 608
- Electron charge, 597
- Electron mobility, 608
- Electron rest mass, 597
- Electron volt, 597
- Elliptic low-pass filters, 203
- Emission coefficient, 352
- Emitter efficiency, 313
- Energy, 598
- Energy gap, 608
- Equivalent circuit representation, 45–47
- Equivalent noise resistance, 502
- Equivalent series resistance (ESR), 20
- Excess charge carriers, 609
- Excess minority carrier lifetime, 297
- Excess noise, 622
- External Q , 206
- F**
- Farad, 598
- Faraday's induction law, 2
- Faraday's law, 47, 51–53, 59
- Feedback loop, 180
- Feedback oscillator design, 543–46
- Femto, 598
- Field effect transistor biasing networks, 455
- Field effect transistors (FETs), 328–38
 construction of, 329–30
 frequency response, 337
 functionality, 331–37
 hetero FET, 329
 junction FET (JFET), 329
 limiting values, 337–38
 metal insulator semiconductor FET (MISFET), 329
 metal oxide semiconductor FET (MOS-FET), 329
 Metal Semiconductor FET (MESFET), 329
- Filter implementation, 241–53
 Kuroda's identities, 243–45
 unit elements (UEs), 243
- Filter Q , 206
- Filters:
 bandpass, 201, 210–17, 261–62
 binomial low-pass, 203
 Butterworth, 203, 220, 221–24, 229–31
 Cauer low-pass, 203
 Chebyshev, 203, 220, 224–31
 coupled, 253–62
 elliptic low-pass, 203
 high-pass, 201, 209–10, 233–35
 image, 580
 linear phase low-pass, 224
 low-pass, 201, 203, 206–9, 233
 RF filter design, 201–69
- Fixed-frequency oscillators, 556–63
 design of, 557–60
 GaAs FET oscillator, microstrip design of, 560–63
- Flat coils, 27–28
- Flow charts, 178–84
 branches, 178
 nodes, 178
- Forbidden regions, 415–17
- Forward active mode, 317–19
- Forward Early voltage, 365
- Forward power gain, 172
- Forward voltage gain, 172
- Frequency, 598
 center, 202
 cut-off, 201
- Frequency compensated matching networks, 512–15
- Frequency domain considerations, 578–80
- Frequency response, 417–22
 bipolar-junction transistor (BJT), 321–23
- field effect transistors (FETs), 337
- high electron mobility transistors (HEMTs), 343
- input reflection coefficient, 419
- matching networks, 417–22, 426
- RF field effect transistors, 337
- Wilkinson power divider, 613
- Frequency spectrum, 8–9
- Frequency transformation, 232–38
 bandpass filters, 235–37
 bandstop filters, 237–38
- G**
- GaAs field effect transistors (GaAs FETs), 312–14
- GaAs MESFET, 379
 determination of cut-off frequency of, 384–85
- Gain-bandwidth product, 372
- Gain compression, 523
- Generic RF system, block diagram of, 3
- Giga, 598
- Global positioning systems (GPS), 1, 2
- Gradual-channel approximation, 332
- Gummel-Poon BJT model, 351, 357, 363–65, 387, 398
- Gunn diodes, 311
- Gunn element oscillator, 573–74
- H**
- Harmonic distortions, 524
- Harmonic IMD, mixers, 583
- Hartley oscillator, 545–46
- Henry, 598
- Hertz, 598
- Hertz, Heinrich, 2
- Heterodyne receiver, 575
- Hetero FET, 329
- Heterojunction bipolar transistors (HBTs), 312–13
- High electron mobility transistors (HEMTs), 312, 338–43
 computation of HEMT-related electric characteristics, 341–42
 construction of, 339
 frequency response, 343
 functionality of, 339–42
 pseudomorphic HEMTs (pHEMTs), 339
- High-frequency capacitors, 17–21
 series loss tangent, 18
- High-frequency inductors, 21–24
- RF coils (RFCs), 21
- High-frequency resistors, 14–17
 surface mounted devices (SMDs), 14
- High-pass filters, 201, 209–10
 frequency transformation, 233–35
- High-power amplifiers, 522–26
- High-side injection, 578
- H-matrix, 148–49, 194
- Hole mobility, 608
- Hybrid circuits, 27–28
- Hybrid/h-matrix, 148–49, 194
- I**
- IEEE frequency spectrum, 8–9
- J*-layer, 296
- Image filter, 580
- Image frequencies mapping, 578–80
- Image impedance, 257
- Impact ionization, 304
- IMPATT diodes, 304–7
- Impedance:
 characteristic line, 63
 general definition, 63–64
 input impedance matching, 90–91
 intrinsic, 6, 7–8
 normalized impedance equation, 104
 wave, 64
- Impedance matching, using discrete components, 406–31
- Impedance matrix, 144–45
- Impedance transformation, 110–21, 232, 239–41
 computer simulations, 119–21

- for general load, 110–12
special transformation conditions, 115–19
open-circuit transformations, 116–17
short-circuit transformations, 117–19
standing wave ratio (SWR), 113–14
- I**mpedance/Z-matrix, 144–45, 148
Induced voltage, in a stationary wire loop, 52–53
Inductance, 598
Inductors:
high-frequency, 21–24
surface-mounted, 26–28
- I**njection version, 358
Input impedance matching, 90–91
Input matching network (IMN), 4, 506
Input reflection coefficient, frequency response of, 419
Input resistance, 367
Input stability circle equation, 471–72
Input VSWR, 506
Insertion loss (IL), 92–93, 204, 217–20
Institute of Electrical and Electronic Engineers (IEEE), 8–9
Intercept point (IP), 525
Interconnecting networks, 153–61
 ABCD network representations, 156–61
 cascading networks, 155–56
 parallel connection of networks, 154–55
 series connection of networks, 153–54
- Intermediate frequency (IF), 575
Intermodular distortion (IMD), 524
Internodulation distortion (IMD):
 amplifiers, 524–25
 mixers, 582
Internal noise source, 622
International System of Units, 598
Interstage matching network, 4, 526
Intrinsic carrier concentration, 608
Intrinsic impedance, 6, 7–8
Intrinsic resistivity, 608
Inverse Early voltage, 365
Isolation, 298, 583, 612
- J**
Joule, 598
Junction FET (JFET), 329
Junction grading coefficient, 352
- K**
Kilo, 598
Kirchoff's voltage and circuit laws (KVL/KCL), 39–41, 45, 58–62
Kuroda's identities, 242, 243–45
- L**
Lambda-quarter transformer, 81
Lange coupler, 619
Large-scale diode model, 352
Large-signal BJT models, 357–66
Large-signal Ebers-Moll circuit model, 358
Large-signal FET models, 378–81
 FET-related benefits, 378–79
 linear region, 380
 noninsulated-gate FET, 379
 reverse linear region, 381
 reverse saturation region, 380
 saturation region, 379–80
Large-signal S-parameters, 522–23
Lead resistance, 15
Leakage diodes, 354–55
Libra, 120
Linear active mode, 314
Linear diode model, 354–57
Linear phase behavior, 222
Linear phase low-pass filters, coefficients for, 224
Loaded Q, 205–6
Local oscillator (LO) frequency, 575
 selection of, 577–78
Long and short diode models, 609–11
Loop gain equation, 540
Loss factor, 218
- Loss tangent, 599
Low- to high-frequency circuit operations, evolution of, 1–36
- Low-pass filters, 201, 206–9
 actual attenuation profiles for, 203
 frequency transformation, 233
- Low-side injection, 577–78
- L-section matching networks, 406–15
 analytical approach to design of, 407–8
 graphical approach to design of, 410–12
- M**
Magnetic field, 598
Magnetic flux, 598
Magnitude computations, 603–4
Mapping:
 conformal, 65
 image frequencies, 578–80
- Matched load reflection coefficient, 493
Matched source reflection coefficient, 492
- Matching networks:
 design approaches, 406
 double-stub matching networks, 440–44
 forbidden regions, 415–17
 frequency compensated matching networks, 512–15
 frequency response, 417–22, 426
 impedance matching using discrete components, 406–31
 interstage matching network, 4, 526
 with lumped and distributed components,
 design of, 432–35
 microstrip line matching networks, 431–44
 narrow-band matching network, design of, 424–26
 quality factor, 422–26
 series C, shunt L matching network, 414
 series L, shunt L matching network, 414
 shunt C, series L matching network, 414
 shunt L, series L matching network, 414
 single-stub matching networks, 435–40
 T and Pi matching networks, 426–31
 transfer function of, 219
 two-component matching networks, 406–15
- MathCad, 134, 167
Mathematica, 134, 167
MATLAB, 120–21, 132, 134, 167, 631–35
 background, 631–33
 stability evaluation, brief example of, 633–35
- Matrix conversions, 605–7
Maximally flat filters, *See* Butterworth filters
Maximum gain, amplifier design for, 494–95
Maximum power hyperbola, 327
Maximum power transfer, 466
Maxwell, James, 2
Mega, 598
Mesa processing technology, 296
Metal-film resistors, 14
Metal film resistors, RF impedance response of, 16–17
Metal insulator semiconductor FET (MIS-FET), 329
Metal oxide semiconductor FET (MOSFET), 329
MEtal Semiconductor FET (MESFET), 329
 drain saturation current in, 333–35
 GaAs MESFET, determination of cut-off frequency of, 384–85
 idealized MESFET device structure, 382
 I-V characteristic of, 335–37
 small-signal MESFET model, 382
 SPICE modeling parameters for, 381
m.files, 134, 631
Micro, 598
Microstrip filter design, examples of, 245–52
Microstrip line matching networks, 431–44
 from discrete components to microstrip lines, 431–35
- Microstrip transmission lines, 42–44, 64–69
 design of, 67–68
- Microwave (MW), 2
- Mil, 598
Miller effect, 369–72
Milli, 598
Minimum detectable signal, 524
Minimum noise figure, 502, 628
 design of small-signal amplifier for, 504–6
- Minority carrier lifetime, 608
Mixers, 574–91
 basic characteristics of, 574–90
 basic concepts, 575–78
 conversion compression, 582
 conversion gain (CG), 581
 conversion loss (CL), 581
 double-balanced mixer, 590
 dynamic range, 583
 frequency domain considerations, 578–80
 harmonic IMD, 583
 intermodular distortion (IMD), 582
 local oscillator (LO) frequency, 575
 selection of, 577–78
 noise figure, 581–82
 single-balanced mixer, 588–89
 single-ended mixer design, 580–88
 BJT mixer, 584–88
 See also Oscillators
- Mixing process, spectral representation of, 579
- Modulation-doped field effect transistors (MODFETs). *See* High electron mobility transistors
- Monolithic and Microwave Integrated Circuit Analysis and Design (MMICAD), 120, 131, 134, 252, 351, 410
- Monopolar devices, 328
- Multistage amplifiers, 526–29
 transistor choices for desing of, 527–29
- N**
Nano, 598
Narrow-band matching network, design of, 424–26
N-channel, 328
Negative feedback, defined, 517
Negative feedback circuits, 517–22
Negative feedback loop broadband amplifier, design of, 520–22
Negative resistance oscillator, 541–43
Nodal quality factor, 422–24
Nodes, 178
Noise analysis, 620–30
 basic definitions, 620–22
 correlated noise sources, 622
 excess noise, 622
 internal noise source, 622
 noise bandwidth, 620
 noise figure:
 for cascaded multiport netwrok, 629–30
 for two-port network, 625–29
 noise power, 620–21
 noisy two-port networks, 623–25
 1/f noise, 622
 random variables, 620
 root mean square (RMS), 620
 shot noise, 622
 spectral density, 622
 spectral noise current, 621
 spectral noise voltage, 621
 uncorrelated noise sources, 622
 white noise, 622
- Noise figure, 502
 for cascaded multiport network, 629–30
 equivalent noise resistance, 502
 minimum, 502, 628
 See also small-signal amplifier for, 504–6
 mixers, 581–82
 optimum reflection coefficient, 503
 optimum source admittance, 503
 for two-port network, 625–29
- Noise figure circles, 502–6
- Noise measures, 630

- Noisy two-port networks, 623–25
 Noninsulated-gate FET, 379–81
 Nonlinear diode model, 352–54
 Normalized effective mass of the electron, 608
 Normalized impedance equation, 104
- O**
 Ohm, 598
 1 dB compression point, 523
 1/f noise, 622
 Open-circuit transformations, 116–17
 Open-circuit transmission, 79–80
 input impedance of, as a function of frequency, 80
 Operating point, 295
 Operating power gain, 468, 496–501
 circle derivation, 497–98
 constant operating power gain circles, amplifier design using, 498–500
 Optimum reflection coefficient, 503
 Optimum source admittance, 503
 Oscillations, adding positive feedback element to initiate, 554–56
 Oscillators, 479, 539–74
 basic model, 540–52
 Clapp oscillator, 545
 Colpitts oscillator, 545
 design, 547–49
 design steps, 546–49
 dielectric resonator oscillators, 563–68
 design of, 565–68
 feedback oscillator design, 543–46
 fixed-frequency oscillators, 556–63
 Gunn element oscillator, 573–74
 Hartley oscillator, 545
 high-frequency oscillator configuration, 552–74
 negative resistance oscillator, 541–43
 output voltage vs. gain characteristic, 541
 quartz oscillators, 550–52
 varactor diode oscillator, 570–73
 design of, 572–73
 voltage-controlled oscillator, 570–73
 YIG (yttrium iron garnet) oscillator, 569–70
 See also Mixers
- Output characteristic, 332
 Output conductance, 367
 Output matching network (OMN), 506
 Output stability circle equation, 471
 Output VSWR, 506
- P**
 Parallel connection of networks, 154–55
 Parallel-plate transmission line:
 circuit parameters for, 53–57
 derivation of equations, 59–62
 line parameters of, 56–57
 Parametric admittance equation, 121–25
 Parametric reflection coefficient equation, 106–8
 Passive networks, 449
 design of, for BJT in common-emitter configuration, 450–51
 P-channel, 328
 Permeability in vacuum, 597
 Permittivity in vacuum, 597
 Phase velocity, 7–8
 Physical constants, 597
 Pico, 598
 Pinch-off voltage, 333
 PIN diodes, 296–301
 computation of transducer loss of, 300–301
 Pi-network, matrix representation of, 146–48
 Pi-type matching network, 426–31
 design of, 429–31
 Planar printed circuit boards (PCBs), 42–43
 Power, 598
 Power amplifier (PA), 4–6
 circuit, knowledge required to build, 5–6
 Power derating curve, 324
 Power gain, 468
 available, 468, 501–2
 forward, 172
 operating, 468, 496–501
 reverse, 173
 transducer, 466–67
 unilateral, 467
 Printed circuit boards (PCBs), 10, 42–43
 Pseudomorphic HEMTs (pHEMTs), 339
 Puck, 563
- Q**
 Quality factor Q , 24, 205
 Quarter-wave transmission line, 80–84
 Quartz crystal:
 and piezoelectric effect, 550
 prediction of resonance frequencies of, 551–52
 Quartz oscillators, 550–52
 Quiescent point, 295
- R**
 Radio frequency coils (RFCs), 5, 298
 Radio frequency design, importance of, 2–6
 Radio frequency (RF), 2
 Random variables, 620
 Receiver, 578
 Reflection coefficient:
 input, 419
 matched load, 493
 matched source, 492
 normalized impedance equation, 104
 optimum, 503
 parametric reflection coefficient equation, 106–8
 in phasor form, 102–3
 representations, 102–3
 simultaneous conjugate matched, 493–94
 voltage, 69–71
 Rejection, 204
 Resistance, 598
 Resistivity, 598
 Resistors, 14
 chip, 24–25
 high-frequency, 14–17
 metal film, 16–17
 Return loss (RL), 91–93, 612
 Reverse active mode, 314–15, 319–20
 Reverse bias, 298
 Reverse collector and emitter saturation currents, 359
 Reverse power gain, 173
 Reverse saturation current temperature coefficient, 353
 Reverse voltage gain, 173
 RF amplifier, power relations of, 468–70
 RF behavior of passive components, 10–24
 high-frequency capacitors, 17–21
 high-frequency inductors, 21–24
 high-frequency resistors, 14–17
 RF coils (RFCs), 21
 RF impedance response of, 22–24
 RF diodes, 293–311
 BARRITT diodes, 311
 Gunn diodes, 311
 IMPATT diodes, 304–7
 PIN diodes, 296–301
 Schottky diode, 293–96
 TRAPATT diodes, 311
 tunnel diodes, 307–10
 varactor diodes, 302–4
 RF filter design, 201–69
 bandpass filters, 201, 210–17
 bandstop filters, 201, 210–17, 249
 response, 212–13
 basic resonator/filter configurations, 202–20
 coupled filter, 253–62
 bandpass filter section, 257–58
 cascading bandpass filter elements, 259–60
 design example, 260–62
 odd/even mode excitation, 254–56
 denormalization of standard low-pass design, 231–41
 frequency transformation, 232–38
 impedance transformation, 232, 239–41
 filter implementation, 241–53
 Kuroda's identities, 242, 243–45
 unit elements, 243
 filter types/parameters, 202–6
 high-pass filters, 201, 209–10
 insertion loss, 217–20
 low-pass filters, 201, 206–9
 actual attenuation profiles for, 203
 microstrip filter design, examples of, 245–52
 special filter realizations, 220–41
 Butterworth filters, 220, 221–24
 Chebyshev filters, 220, 224–31
 RF filters, calculation of quality factors for, 219–20
 RF impedance response:
 of capacitors, 18–20
 of metal film resistors, 16–17
 of RFCs, 22–24
 RF transistor amplifier designs, 463–538
 amplifiers:
 characteristics of, 464
 power relations, 465–70
 broadband amplifiers, 511–22
 constant gain, 483–502
 bilateral design, 492–95
 operating and available power gain circles, 495–502
 unilateral design, 483–92
 constant VSWR circles, 506–11
 high-power amplifiers, 522–26
 multistage amplifiers, 526–29
 noise figure circles, 502–6
 power gain (operating power gain), 468
 stability, 470–83
 circles, 470–73
 stabilization methods, 479–83
 unconditional, 473–79
 transducer power gain, 466–67
 Richardson constant, 294
 Richards transformation, 242–43, 263
 Ripple, 204
 Rollett stability factor, 474–76, 553–55, 557
 Root mean square (RMS), 620
- S**
 Safe operating area (SOAR), 327
 Saturation mode, 315, 320–21
 Saturation voltage, 314
 Scattering parameter device characterization, 393–97
 Scattering parameters (*S*-parameters), 168–95
 chain scattering matrix, 175–77
 conversion between Z-parameters and, 177–78
 definition of, 168–71
 generalization of, 184–88
 meaning of, 171–75
 practical measurements of, 188–93
 signal flow chart modeling, 178–84
 Schottky diode, 293–96
 Second-order intermodular products, 577
 Self-biased networks, 449
 Self-loop, 180–82
 Semiconductors, physical parameters of, 608
 Series connection of networks, 153–54
 Series C, shunt L matching network, 414
 Series loss tangent, 18
 Series L, shunt L matching network, 414
 Shape factor, 204
 Short-circuit transformations, 117–19
 Short-circuit transmission line, 76–78
 input impedance of, as a function of frequency, 77–78
 Shot noise, 622
 Shunt C, series L matching network, 414
 Shunt L, series L matching network, 414
 Siemens, 598
 Siemens, Werner, 2
 Signal flow chart:
 building blocks, 181

- input impedance computation of a transmission line based on use of, 187–88
modeling, 178–84
- Simultaneous conjugate match, 492
- Simultaneous conjugate matched reflection coefficients, derivation of, 493–94
- Single-balanced mixer, 588–89
- Single-ended mixer design, 580–88
BJT mixer, 584–88
- Single-/multi-port networks, 143–99
admittance/Y-matrix, 145–48
basic definitions, 144–52
chain/ABCD-matrix, 148
hybrid/h-matrix, 148–49
impedance/Z-matrix, 144–45, 148
interconnecting networks, 153–61
ABCD network representations, 156–61
cascading networks, 155–56
parallel connection of networks, 154–55
series connection of networks, 153–54
network properties/applications, 161–68
analysis of microwave amplifier, 164–68
interrelations between parameter sets, 161–64
- scattering parameters (S-parameters), 168–95*
- See also Scattering parameters (S-parameters)*
- Single-stub matching networks, 435–40
with fixed characteristic impedances, 436–38
design of, 436–38
using transmission lines with characteristic impedances, design of, 438–39
- Skin depth, 11–13, 54–57
- Skin equation for cylindrical conductor, 601–2
- Small-signal BJT models, 366–78
- Small-signal current gain, 367
- Small-signal diode model, 355
derivation of, 355–57
- Small-signal equivalent circuit model, 294
- Small-signal FET models, 382–85
- Smith, P. H., 101
- Smith Chart, 101–42, 436, 437, 442, 443, 463, 464, 487–88, 490, 505, 513–14
admittance transformation, 121–26
parametric admittance equation, 121–25
I-Smith Chart, 124–25
Z-Smith Chart, 121–24
ZY-Smith Chart, 125–26
compressed, 109
design of matching network using, 413
impedance transformation, 110–21, 418, 425
computer simulations, 119–21
for general load, 110–12
special transformation conditions, 115–19
standing wave ratio (SWR), 113–14
- key ingredient, 102
- one-to-one mapping, 109
- parallel connections, 126–27
of *R* and *C* elements, 127
of *R* and *L* elements, 127
- reflection coefficient, 102–8
in phasor form, 102–3
- series connections, 127–33
of *R* and *C* elements, 129–30
of *R* and *L* elements, 127–29
- T*-type network, 130–33
- Z-Smith Chart, 121*
- Sourced and loaded transmission line, 84–93
input impedance matching, 90–91
phasor representation of source, 85–87
power considerations for, 87–90
return loss and insertion loss, 91–93
- Source-field relations, 47–48
- Source gain circles, computation of, for unilateral design, 486–88
- Specific heat, 608
- Spectral density, 622
- Spectral noise current, 621
- Spectral noise voltage, 621
- Speed of light in vacuum, 597
- SPICE, 351, 354, 365
- Spurious free dynamic range, 525–26
- Stability, 470–83
circles, 470–73
for a BJT at different operating frequencies, 477–78
input, 471–72
output, 471
- Rollett stability factor, 474–76, 553–55, 557
- stability factor derivation, 476
- stabilization of a BJT, 481–83
- stabilization methods, 479–83
- stable vs. unstable region of a transistor, 479
- unconditional, 473–79*
- Standing wave ratio (SWR), 74–75, 113–14
voltage (VSWR), 75
- Standing waves, 72–75
- Steinmetz, Charles, 2
- Stopband width, 250
- Surface-mounted devices (SMDs), 14
- Surface-mounted inductors, 26–28
- "Switch off," 298
- T**
- Terminated lossless transmission line, 69–75*
input impedance of, 75–76, 105
open-circuit transmission, 79–80
propagation constant and phase velocity, 71–72
quarter-wave transmission line, 80–84
short circuit transmission line, 76–78
special termination conditions, 75–84
standing waves, 72–75
voltage reflection coefficient, 69–71
- Tesla, Nikolas, 2
- Thermal analysis, involving BJT mounted on heat sink, 326–27
- Thermal conductivity, 608
- Thermal diffusivity, 608
- Thin-film chip resistors, 14
- Third-order intermodular products, 577
- Threshold voltage, 333
- Through-Reflect-Line (TRL), 191–93, 195
- T* matching network, 426–31
design of, 427–29
- T*-network, 130–33, 134
determination of elements, 173–74
- Transceiver, 3
- Transconductance, 367
- Transducer power gain, 466–67
- Transfer function, 208
- Transistor models, 357–85
large-signal BJT models, 357–66
large-signal FET models, 378–81
small-signal BJT models, 366–78
small-signal FET models, 382–85
- Transition frequency, 321
- Transition time, 353
- Transmission coefficient, determination of, 86
- Transmission line analysis, 37–100
- Transmission lines:
coaxial cable, 41–42
configurations, 57
general equation, 58–64
general impedance definition, 63–64
Kirchhoff voltage and current law representations, 58–62
lossless transmission line model, 64
traveling voltage and current waves, 62–63
microstrip lines, 42–44
power considerations for, 87–90
sourced and loaded transmission line, 84–93
- terminated lossless transmission line, 69–75
two-wire lines, 41
- Transmission line theory, 37–41
- Transmitter, 578
- Transverse electric (TE) field wave propagation, 7, 44
- Transverse electromagnetic mode (TEM), 6–7
- Transverse magnetic (TM) field wave propagation, 7, 44
- TRAPATT diodes, 311
- Traveling voltage and current waves, 62–63
- T-type matching network, design of, 427–29
- Tunnel diodes, 307–10
- Tunneling, 308
- Two-component matching networks, 406–15
analytical approach to design of, 407–8
general, design of, 412–15
graphical approach to design of, 410–12
- Two-wire transmission lines, 41
- U**
- Unconditional stability, 473–79
- Uncorrelated noise sources, 622
- Unilateral figure of merit, 490–92
- Unilateral power gain, 467
- Unit elements (UEs), 243
- Units, 6–8
- Unloaded *Q*, 564
- Upconverted frequency components, 578
- V**
- Varactor diode oscillator:
circuit analysis of, 570–71
design of, 572–73
- Varactor diodes, 302–4
- V/m, 598
- Volta, A., 2
- Voltage, 598
drain saturation voltage, 332
forward Early voltage, 365
forward voltage gain, 172
induced, in a stationary wire loop, 52–53
inverse Early voltage, 365
Kirchoff's voltage law, 39–40, 45, 58–62
pinch-off voltage, 333
reflection coefficient, 69–71
reverse voltage gain, 173
saturation voltage, 314
spectral noise voltage, 621
voltage standing wave ratio (VSWR), 75
- Voltage-controlled oscillator, 570–73
- Voltage reflection coefficient, 69–71
- Voltage standing wave ratio (VSWR), 75
- Voltaic cells, 2
- Volts, 598
- W**
- Watt, 598
- Wave impedance, 64
- Wavelength, 6, 7–8
- Weber, 598
- White noise, 622
- Wilkinson power divider, 612–15
frequency response of, 613
- Wire diameter, conversion between AWG size and, 13–14
- Wireless local area networks (WLANS), 3
- Wire size standardization, 13–14
- Wire-wound resistors, 14–15
- WTG (wavelength toward generator) scale, 434
- Y**
- YIG (yttrium iron garnet) oscillator, 569–70
- Y*-matrix, 145, 194
- Y-Smith Chart, 124–25, 134*
- Z**
- Z*-matrix, 144–45, 194
- Z-Smith Chart, 121–24, 134*
- ZY-Smith Chart, 125–26, 134, 409–10*
use of, 126

YOU SHOULD CAREFULLY READ THE FOLLOWING TERMS AND CONDITIONS BEFORE OPENING THIS CD-ROM PACKAGE. OPENING THIS CD-ROM PACKAGE INDICATES YOUR ACCEPTANCE OF THESE TERMS AND CONDITIONS. IF YOU DO NOT AGREE WITH THEM, YOU SHOULD PROMPTLY RETURN THE PACKAGE UNOPENED.

Prentice-Hall, Inc. provides this program and licenses its use. You assume responsibility for the selection of the program to achieve your intended results, and for the installation, use, and results obtained from the program. This license extends only to use of the program in the United States or countries in which the program is marketed by duly authorized distributors.

LICENSE

You may:

- a. use the program;
- b. copy the program into any machine-readable form without limit;
- c. modify the program and/or merge it into another program in support of your use of the program.

LIMITED WARRANTY

THE PROGRAM IS PROVIDED "AS IS" WITHOUT WARRANTY OF ANY KIND, EITHER EXPRESSED OR IMPLIED, INCLUDING, BUT NOT LIMITED TO, THE IMPLIED WARRANTIES OF MERCHANTABILITY AND FITNESS FOR A PARTICULAR PURPOSE. THE ENTIRE RISK AS TO THE QUALITY AND PERFORMANCE OF THE PROGRAM IS WITH YOU. SHOULD THE PROGRAM PROVE DEFECTIVE, YOU (AND NOT PRENTICE-HALL, INC. OR ANY AUTHORIZED DISTRIBUTOR) ASSUME THE ENTIRE COST OF ALL NECESSARY SERVICING, REPAIR, OR CORRECTION.

SOME STATES DO NOT ALLOW THE EXCLUSION OF IMPLIED WARRANTIES, SO THE ABOVE EXCLUSION MAY NOT APPLY TO YOU. THIS WARRANTY GIVES YOU SPECIFIC LEGAL RIGHTS AND YOU MAY ALSO HAVE OTHER RIGHTS THAT VARY FROM STATE TO STATE.

Prentice-Hall, Inc. does not warrant that the functions contained in the program will meet your requirements or that the operation of the program will be uninterrupted or error free.

However, Prentice-Hall, Inc., warrants the CD-ROM(s) on which the program is furnished to be free from defects in materials and workmanship under normal use for a period of ninety (90) days from the date of delivery to you as evidenced by a copy of your receipt.

LIMITATIONS OF REMEDIES

Prentice-Hall's entire liability and your exclusive remedy shall be:

1. the replacement of any CD-ROM not meeting Prentice-Hall's "Limited Warranty" and that is returned to Prentice-Hall, or
2. if Prentice-Hall is unable to deliver a replacement CD-ROM or cassette that is free of defects in materials or workmanship, you may terminate this Agreement by returning the program.

IN NO EVENT WILL PRENTICE-HALL BE LIABLE TO YOU FOR ANY DAMAGES, INCLUDING ANY LOST PROFITS, LOST SAVINGS, OR OTHER INCIDENTAL OR CONSEQUENTIAL DAMAGES ARISING OUT OF THE USE OR INABILITY TO USE SUCH PROGRAM OR EVEN IF PRENTICE-HALL, OR AN AUTHORIZED DISTRIBUTOR HAS BEEN ADVISED OF THE POSSIBILITY OF SUCH DAMAGES, OR FOR ANY CLAIM BY ANY OTHER PARTY.

SOME STATES DO NOT ALLOW THE LIMITATION OR EXCLUSION OF LIABILITY FOR INCIDENTAL OR CONSEQUENTIAL DAMAGES, SO THE ABOVE LIMITATION OR EXCLUSION MAY NOT APPLY TO YOU.

GENERAL

You may not sublicense, assign, or transfer the license or the program except as expressly provided in this Agreement. Any attempt otherwise to sublicense, assign, or transfer any of the rights, duties, or obligations hereunder is void.

This Agreement will be governed by the laws of the State of New York.

Should you have any questions concerning this Agreement, you may contact Prentice-Hall, Inc., by writing to:

Prentice Hall
College Division
Upper Saddle River, NJ 07458

YOU ACKNOWLEDGE THAT YOU HAVE READ THIS AGREEMENT, UNDERSTAND IT, AND AGREE TO BE BOUND BY ITS TERMS AND CONDITIONS. YOU FURTHER AGREE THAT IT IS THE COMPLETE AND EXCLUSIVE STATEMENT OF THE AGREEMENT BETWEEN US THAT SUPERSEDES ANY PROPOSAL OR PRIOR AGREEMENT, ORAL OR WRITTEN, AND ANY OTHER COMMUNICATIONS BETWEEN US RELATING TO THE SUBJECT MATTER OF THIS AGREEMENT.

ISBN: 0-13-095323-7